ANL/FPP-80-1

STARFIRE

A COMMERCIAL TOKAMAK
FUSION POWER PLANT STUDY

VOLUME I

Distribution Category:
Magnetic Fusion Energy
(UC-20)

ANL/FPP-80-1
Volume I

ARGONNE NATIONAL LABORATORY
9700 South Cass Avenue
Argonne, Illinois 60439

STARFIRE - A COMMERCIAL TOKAMAK FUSION POWER PLANT STUDY

Argonne National Laboratory

McDonnell Douglas Astronautics Co. - East

General Atomic Company

The Ralph M. Parsons Company

September 1980

The facilities of Argonne National Laboratory are owned by the United States Government. Under the terms of a contract (W-31-109-Eng-38) among the U. S. Department of Energy, Argonne Universities Association and The University of Chicago, the University employs the staff and operates the Laboratory in accordance with policies and programs formulated, approved and reviewed by the Association.

MEMBERS OF ARGONNE UNIVERSITIES ASSOCIATION

The University of Arizona
Carnegie-Mellon University
Case Western Reserve University
The University of Chicago
University of Cincinnati
Illinois Institute of Technology
University of Illinois
Indiana University
The University of Iowa
Iowa State University
The University of Kansas
Kansas State University
Loyola University of Chicago
Marquette University
The University of Michigan
Michigan State University
University of Minnesota
University of Missouri
Northwestern University
University of Notre Dame
The Ohio State University
Ohio University
The Pennsylvania State University
Purdue University
Saint Louis University
Southern Illinois University
The University of Texas at Austin
Washington University
Wayne State University
The University of Wisconsin-Madison

Printed in the United States of America
Available from
National Technical Information Service
U. S. Department of Commerce
5285 Port Royal Road
Springfield, VA 22161

NTIS price codes
Printed copy: A99
Microfiche copy: A01

STARFIRE DESIGN TEAM

Argonne National Laboratory

C. C. Baker and M. A. Abdou

R. M. Arons
A. E. Bolon*
C. D. Boley
J. N. Brooks
R. G. Clemmer
C. B. Dennis
D. A. Ehst
K. E. Evans Jr.
P. A. Finn
R. E. Fuja
Y. Gohar
V. Z. Jankus
J. Jung
S. H. Kim
S. Piet†
R. F. Mattas
B. Misra
J. Rest
H. L. Schreyer
D. L. Smith
H. C. Stevens
L. R. Turner
S.-T. Wang

McDonnell Douglas Astronautics Company

D. A. DeFreece and C. A. Trachsel

N. G. Bond
D. A. Bowers
L. A. Carosella
J. W. Davis
M. J. Delaney
C. Dillow
D. E. Driemeyer
M. R. Gordinier
J. R. Haines
P. W. Heaton
G. D. Morgan
D. F. Ruester
P. B. Stones
L. M. Waganer
R. E. Watson
H. S. Zahn

General Atomic Company

D. W. Graumann

J. S. Alcorn
W. Y. K. Chen
R. L. Creeden
P. D. Drobnis
R. E. Field
T. Hino
E. R. Johnson
G. R. Lutz
R. Prater
H. Varga

*On leave from the University of Missouri - Rolla.

†Graduate student from M.I.T.

The Ralph M. Parsons Company

J. Kokoszenski and K. Barry

G. Arvay
R. Cavazo
M. Cherry
J. de La Mora
J. Geere
L. Gise
D. Hegberg
S. Huang
R. Jarvis
B. Kenessey
H. Klumpe
P. MacCalden
M. Mercado
R. Nixdorf
L. Pardee
W. E. Polk
A. Soderblom

Administrative Secretarial Staff - ANL

C. S. Bury
C. M. Hytry
C. A. Poore
M. L. Wilson

ABSTRACT

STARFIRE is a 1200 MWe central station fusion electric power plant that utilizes a deuterium-tritium fueled tokamak reactor as a heat source. Emphasis has been placed on developing design features which will provide for simpler assembly and maintenance, and improved safety and environmental characteristics. The major features of STARFIRE include a steady-state operating mode based on continuous rf lower-hybrid current drive and auxiliary heating, solid tritium breeder material, pressurized water cooling, limiter/vacuum system for impurity control and exhaust, high tritium burnup and low vulnerable tritium inventories, superconducting EF coils outside the superconducting TF coils, fully remote maintenance, and a low-activation shield. A comprehensive conceptual design has been developed including reactor features, support facilities and a complete balance of plant. A construction schedule and cost estimate are presented, as well as study conclusions and recommendations.

Acknowledgments

The STARFIRE team would like to greatfully acknowledge the support and interest of F. E. Coffman, J. E. Baublitz and C. R. Head of DOE's Office of Fusion Energy. Appreciation is also extended to S. Harkness and V. Maroni for their leadership and guidance during the early phases of this study.

We would also like to express our sincere appreciation to the many people who participated in the review of the STARFIRE study during its progress. Many people in the fusion community contributed their time and effort at the review held at ANL in the fall of 1979. In addition, special thanks are extended to the Utility Advisory Committee composed of Bill Wolkenhauer - Chairman (Washington State), Clint Ashworth (Pacific Gas and Electric), Fred Brunson (Union Electric Company), Ed Fiss (Duke Power Company), Robert Goodrich (Northwest Utilities), and Betty Jensen (Public Service Electric and Gas); and the Safety Advisory Committee composed of J. G. Crocker - Chairman (EG&G), J. L. Anderson (LASL), D. Cohn (MIT), H. Howe, Jr. (PPPL), M. Kazimi (MIT), L. Muhlestein (HEDL), J. Powell (BNL), and T. Shannon (ORNL).

In the area of plasma physics support, we would like to acknowledge the contributions of R. W. Conn (UCLA), G. Emmert (U. of Wisconsin), N. J. Fisch (PPPL), S. E. Attenberger (ORNL), and R. Harvey (GA).

The authors also wish to acknowledge with appreciation the helpful assistance and information supplied by the personnel at TSTA/LASL (J. L. Anderson, D. O. Coffin, R. H. Sherman, J. Bartlitt, F. Damiano, R. Jalbert) and also W. R. Wilkes, L. J. Wittenberg, M. Rodgers, T. R. Galloway, J. M. Mintz, and H. Garber in the area of tritium systems.

We would like to acknowledge the special efforts of the following McDonnell Douglas personnel: Don L. Kummer, Director of Fusion, for his participation, insight and support provided to STARFIRE; Bill Briggs, Manager Program Development, for development of the STARFIRE film; Dave Suitor for solid breeder development, Doug Riser for graphics and Ree Seeger for preparation of the manuscript. A special thanks is given to the Palomar Observatory and the California Institute of Technology for their kind permission to use the cover photograph of the Trifid Nebula in Sagittarius, taken through their 200 inch telescope.

A special appreciation is extended to Cyrilla Hytry, Carolyn Poore and Mela Wilson (all of ANL) for the final typing, editing and assembly of this report, and to Connie Bury for administrative support for the STARFIRE study.

EXECUTIVE SUMMARY

The STARFIRE study was initiated in the Spring of 1979 with the primary goal of developing a commercially attractive tokamak power reactor concept for central station electric power generation. This study has been carried out during a period of substantial progress in the tokamak fusion physics program. Also, a number of tokamak reactor design studies have identified several new features which could improve the reactor embodiment of the tokamak concept. The task of the STARFIRE study was to incorporate the results of recent tokamak research and reactor studies into an integrated design concept which would further advance the development of attractive tokamak-based reactor concepts.

Particular attention has been given to developing design concepts which will result in more attractive engineering features. The central theme has been to reduce the complexity of the design in order to develop a reactor concept which is more compatible with assembly and maintenance considerations. Design concepts were then examined in reasonable detail in order to establish their engineering credibility.

Plasma engineering has played an important role in the STARFIRE study. The philosophy here was to not necessarily adopt conservative plasma physics concepts based on proven theory and well-demonstrated experiments, as one would do in designing a near-term experiment, but rather to explore innovative physics ideas which would result in a more attractive reactor concept and which will provide guidance for future physics research.

Attention to safety and environmental features has been a major consideration in this study. Design efforts have examined both normal and off-normal conditions. Design choices have been strongly influenced by a desire to minimize vulnerable tritium inventories, reduce the use of scarce materials, minimize stored energies that could result in accidental releases of energy, and minimize long-term radioactive waste storage requirements.

Advisory committees for STARFIRE were established in two key areas. The first was a Utility Advisory Committee whose purpose was to provide input and guidance from the utility perspective on desirable features of a commercial fusion power plant. Because of the importance of carefully considering the

safety and environmental aspects of STARFIRE, a safety review committee was established. This committee's primary purpose was to provide review and recommendations for the development of the reactor and plant conceptual design.

The key features of STARFIRE are summarized in Table 1. Major design parameters are listed in Table 2 and an isometric view of the reactor is shown in Fig. 1.

A major effort has been devoted in STARFIRE to enhancing reactor maintainability and improving plant availability. The approach was to select design features and develop a design configuration that reduced the frequency of failure and shortened the replacement time. Relevant examples are: (1) steady state operation with lower hybrid current drive; (2) limiter/vacuum system for impurity control and exhaust; (3) vacuum boundary located at the shield with all mechanical seals (no welds); (4) all service connections (e.g., for high pressure coolant) are located outside the vacuum boundary (shield); (5) optimized modular design; (6) all superconducting EF coils are outside the TF coils; (7) conservative TF coil design; (8) fully remote maintenance permitting some repairs during reactor operation; (9) "remove and replace" maintenance approach (failed parts are replaced with spare parts

Table 1. Key Features of STARFIRE

- Steady-state plasma operation
- Lower hybrid rf for plasma heating and current drive
- ECRH-assisted startup
- Limiter/vacuum system for plasma impurity control and exhaust
- All superconducting EF coils outside TF coils
- Vacuum boundary at the shield, mechanical seals
- Total remote maintenance with modular design
- Water-cooled, solid tritium breeder blanket with stainless steel structure
- All materials outside the blanket are recyclable within 30 yr
- Less than 0.5 kg of vulnerable tritium inventory
- Minimum radiation exposure to personnel
- Conventional water/steam power cycle with no intermediate coolant loop and no thermal energy storage

Table 2. STARFIRE Major Design Parameters

Net electrical power, MW	1200
Gross electrical power, MW	1440
Fusion power, MW	3510
Thermal power, MW	4000
Gross turbine cycle efficiency, %	36
Overall availability, %	75
Average neutron wall load, MW/m^2	3.6
Major radius, m	7.0
Plasma half-width, m	1.94
Plasma elongation (b/a)	1.6
Plasma current, MA	10.1
Average toroidal beta	0.067
Toroidal field on axis, T	5.8
Maximum toroidal field, T	11.1
No. of TF coils	12
Plasma burn mode	Continuous
Current drive method	rf (lower hybrid)
Plasma heating method	rf (lower hybrid)
Plasma startup	ECRH-assisted, limited OH coil
TF coils material	$Nb_3Sn/NbTi/Cu/SS$
Blanket structural material	PCA[a]
Tritium breeding medium	Solid breeder (α-$LiAlO_2$)
Wall/blanket coolant	Pressurized water (H_2O)
Plasma impurity control	Limiter and vacuum system supplemented by low-Z coating, enhanced radiation and field margin
Primary vacuum boundary	Inner edge of shield

[a] Primary Candidate Alloy (PCA), an advanced austenitic stainless steel.

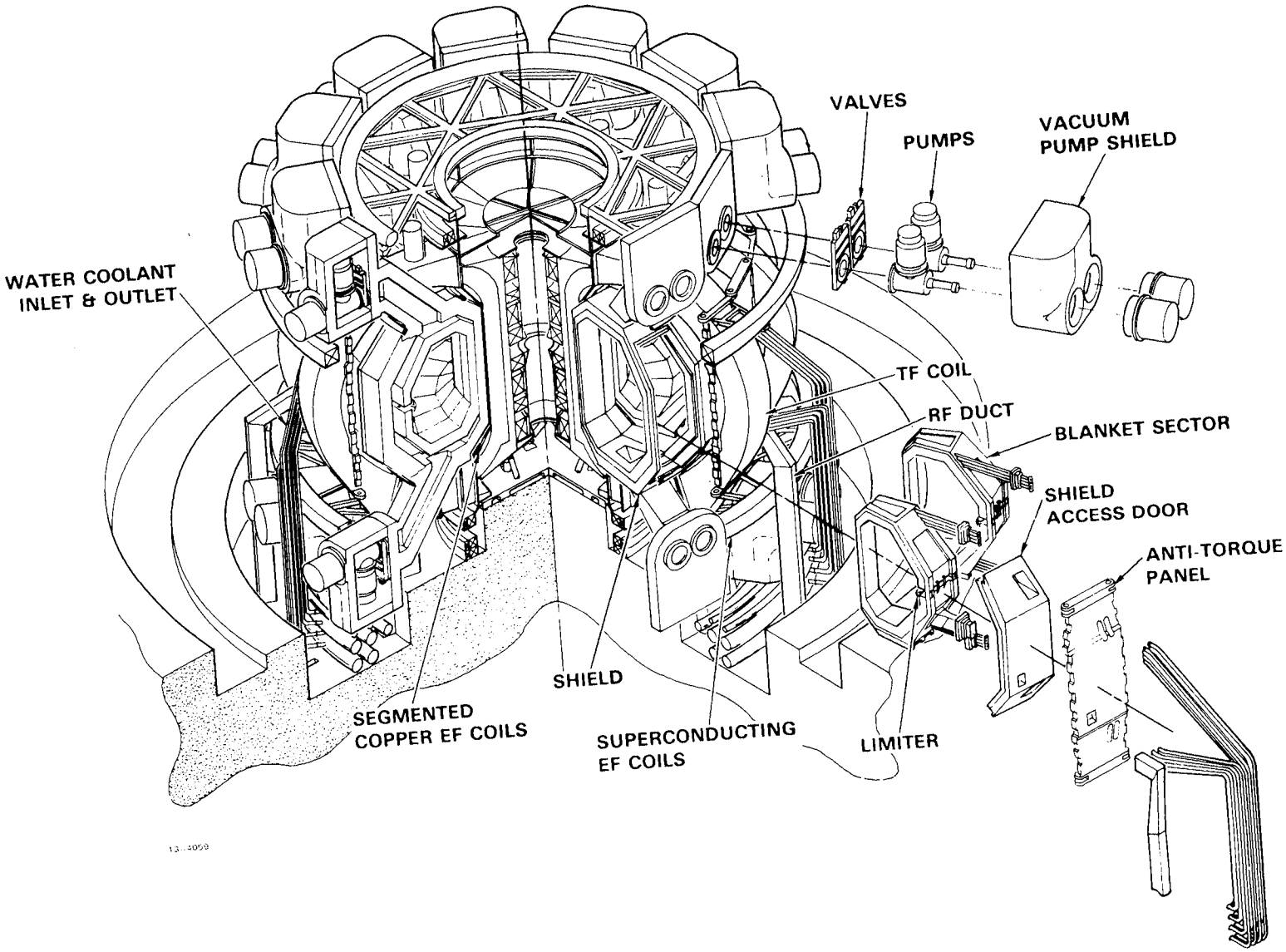

Fig. 1. STARFIRE reference design - isometric view.

and the reactor is operated while repairs are made in the hot cell) that minimizes downtime; (10) combining components for simplicity (e.g., TF coil room-temperature dewar provides support for the EF coils and shield); and (11) providing redundancy where it is justified (e.g., for the EF coils trapped below the reactor). These features as well as potential future improvements in component reliability provide optimism that the plant availability goal of 75% can be achieved.

Safety and environmental considerations have played a major role in the STARFIRE design effort. A solid tritium breeder was selected in preference to liquid lithium in order to minimize the stored chemical energy. The impurity control and exhaust system was selected and designed so that the tritium fractional burnup is maximized and the vulnerable tritium inventory in the fueling and vacuum pumping systems is minimized. Furthermore, the reactor design was developed to contain the tritium inside multiple barriers and to minimize the size of potential tritium releases. The shield was designed and all reactor materials selected so that recycling of all materials outside the blanket is possible in less than 30 yr. Radiation exposure of personnel has been minimized by the use of extensive remote maintenance operations and by providing adequate shielding. The use of resource-limited materials was minimized. Mechanisms for fast reactor shutdown and auxiliary cooling systems have been incorporated into the design. The beryllium coating on the first wall and limiter provide an inherent safety feature that terminates the plasma burn if the metal temperature reaches $\sim$ 900°C. Calculations show that the reactor will be automatically shut down in less than one second, if a hot spot forms on a small area of the first wall, without the need for any active control system. No major damage, other than some first wall coating ablation, will occur.

No runaway accident that could pose a major risk to the public was identified for STARFIRE. Furthermore, no plausible scenario could be formulated for the release of radioactive materials from the blanket (excluding corrosion products in the primary coolant loop) to the outside of the reactor building.

The use of water coolant, steam cycle and conventional materials in STARFIRE makes the heat transport and energy conversion system a state-of-the-art technology. Trade-off studies comparing helium and pressurized water

coolants show clear advantages for pressurized water cooling for STARFIRE conditions. The balance of plant has been designed to maximize the utilization of current power plant features.

The reactor configuration utilizes 12 toroidal field (TF) coils and 12 superconducting poloidal coils (EF and OH) located external to the TF coils. Additionally, four small normal conducting control coils (CF) are located inside the TF coils and outside the bulk shield to provide the necessary response time for plasma control while permitting good access for reactor maintenance. The magnet systems and shield are expected to last the full 40 year design life under normal operating conditions; however, provisions are incorporated for their replacement.

Blanket sectors, including the limiters and rf ducts, will require replacement every six years. The blanket was divided into large sectors to permit replacement with a minimum number of in-reactor maintenance actions. Twenty-four toroidal sectors of two different sizes are used to permit installation in the space between adjacent TF coils. The overall blanket installation was simplified by mounting the limiter, rf duct and ECRH duct to the sector for removal as a unit. Coolant connections to the blanket sector were located outside of the vacuum boundary to minimize the effects of irradiation on the joint and to permit use of mechanical seals. The penetrations through the vacuum boundary are sealed with elastomer seals located at the external shield surface.

Twelve rf ducts provide for heating and current drive of the plasma. These ducts are mounted in the blanket sector located between TF coils. An rf window and phase monitor are located in the duct near the shield while phase shifters, circulators and crossed field amplifiers are located in the reactor building basement where personnel access during operation is possible. Twenty-four ECRH ducts are provided for initial plasma breakdown and wall cleaning. Two ECRH ducts are located on each blanket sector between TF coils.

STARFIRE employs a DT burning, D-shape plasma to produce 3510 MW of fusion power. The plasma is operated at a moderate β of 6.7% and is moderately elongated, with a height-to-width ratio of 1.6. The plasma current is driven in steady state with 90 MW of lower hybrid rf power. The first wall

and all other components in the vacuum chamber are coated with Be. The impurity control system maintains a steady-state concentration of 14% helium and 4% Be in the plasma. The fairly low DT removal efficiency (15%) of the impurity control system permits a high fractional burnup of tritium (42%). Most of the plasma fueling is done automatically by DT neutrals recycling from the first wall and limiter. Additional fueling is done by gas puffing through the limiter.

In order to minimize the heat transport load on the limiter, as well as to establish a thermal equilibrium, the plasma is operated in an "enhanced radiation" mode, whereby a small amount of high-Z material, nominally iodine, is added along with the fuel stream. This serves to radiate most of the heating energy to the first wall and stabilizes the thermal operating point.

The plasma MHD equilibrium is of the low current, hollow profile type. The plasma position is controlled with two sets of coils, a main equilibrium field (EF) coil set and a control field (CF) coil set. The main EF coils are superconducting and are located outside of the TF coils. They are used to provide the basic positional equilibria. The CF coils consist of small copper coils inside the TF coils and are used to control position and to stabilize against plasma disruptions. To further aid in the latter task, the first wall is designed with a L/R time constant of 300 ms to stabilize against rapid vertical instabilities.

Most of the STARFIRE burn cycle is substantially different from pulsed reactor burn cycles. Plasma breakdown is done with 5 MW of electron cyclotron resonance heating (ECRH) and does not require a high voltage OH coil. The startup period takes 24 minutes and conforms to the desire that the fusion power should be ramped at a 5% per minute rate, to minimize thermal problems in the energy recovery and conversion systems. The OH coil as well as the OH and EF power supplies have modest requirements compared to pulsed reactor requirements.

Several shutdown scenarios have been developed for STARFIRE. The normal shutdown is basically the reverse of the startup period, whereby the fusion power is reduced at a 5% per minute rate by reducing the tritium fraction in the plasma. There are three types of rapid shutdowns. The fastest is an "abrupt" shutdown whereby a plasma disruption is induced by injecting excess

high-Z material. There is a more orderly "rapid" shutdown which also uses a disruption, but where most of the plasma energy is radiated uniformly to the first wall prior to the disruption. Finally, a "self-induced" shutdown occurs naturally as a result of hot spot formation on the first wall or limiter.

The results of the STARFIRE study show important incentives for developing the steady state option for tokamaks. Steady-state operation offers many engineering, technological and economical benefits in commercial reactors. Among these are: reactor reliability is increased, concerns about material fatigue are alleviated, electrical and thermal energy storage systems are not required; higher neutron wall load, and hence smaller size reactors, are acceptable; and the frequency of plasma disruption occurrence is greatly reduced. It has been estimated that the benefits of steady state can result in a saving in the cost of energy of as much as 30%.

The impurity control and exhaust system is one of the key components in a fusion reactor. It has a substantial impact on the engineering simplicity, reliability, maintainability, economics and safety of the power plant. Divertors and divertorless options were surveyed. It was concluded that the limiter/vacuum (also called "pumped" or "active" limiter) concept is a very attractive option for power reactors. It is relatively simple and inexpensive and deserves serious experimental verification. The results of STARFIRE indicate that a high efficiency exhaust system is not necessarily desirable. It is very beneficial to keep the removal efficiency low so that the tritium fractional burnup is high. This reduces the gas load in the exhaust system and simplifies the vacuum system design in addition to lowering the vulnerable tritium inventory in the fueling and vacuum systems.

A low-Z coating on all surfaces exposed to the plasma will probably be required in future tokamak reactors unless very low plasma edge temperatures can be established and maintained. Beryllium appears to be one of the best choices for the low-Z coating. Sputtering of the coating is predicted to be large but redeposition seems to extend the coating life to an acceptable level. However, there is a need for experimental investigations and theoretical work on the physics of the scrape-off region and the performance of low-Z coatings. There is also a need to develop in-situ low-Z coating techniques for fusion reactor applications.

Safety considerations provide major incentives for the development of solid breeders. Serious efforts have been devoted in STARFIRE to evaluation of solid tritium breeders and to the development of a design that optimizes their performance. The results are encouraging and show that the solid breeder option should continue to be pursued. However, the results of the detailed analyses in STARFIRE indicate potentially serious problem areas that must be further investigated before the viability of solid breeder blanket concepts can be cccurately assessed. The most critical problem concerns the tritium release characteristics of solid breeders.

Results of the economics analysis for the STARFIRE tokamak power plant indicate that fusion reactors can be developed to be economically competitive. The cost of energy estimated for STARFIRE is comparable to that of future light-water fission reactors and lower than for coal power plants. There are, of course, uncertainties in predicting the cost of energy for future fusion reactors. However, there appears to be no fundamental reason that fusion will not be economically competitive.

It is important to place in proper context the role of the STARFIRE study. STARFIRE represents the most comprehensive study performed to date on a commercial fusion reactor concept. It incorporates several design features in an attempt to develop an attractive tokamak reactor concept. Considerable effort has been devoted to developing credible engineering and physics solutions to key problem areas. In short, STARFIRE represents the best understanding that we have today of a commercial fusion reactor. Yet one must remember that fusion research is in the phase of transition from primarily plasma physics studies to a serious attack on developing the capability in fusion physics and technology which will be required to establish the engineering feasibility of fusion power. Several promising fusion concepts in addition to the tokamak are under development. The tokamak concept can be expected to undergo further development, most likely along lines described in this study. Thus, STARFIRE represents a "snapshot" of our current understanding and expectations for tokamak development. Further developments will occur which will hopefully lead to further improvement in the prospects for practical, economic, safe fusion power within the early part of the 21st century.

Table of Contents

****Volume I*****

Table of Contents (Continued)

Table of Contents (Continued)

Table of Contents (Continued)

1.0 INTRODUCTION

The primary objective of the STARFIRE study is to develop a conceptual design of a commercial tokamak electric power plant. Major guidelines for the study are as follows:

- Application - Commercial Central Station Electric Power Plant
- Confinement Concept - Tokamak
- Fusion Fuel Cycle - Deuterium/Tritium/Lithium

It is important to place in proper context the role of the STARFIRE Study. STARFIRE represents the most comprehensive study performed to date on a commercial fusion reactor concept. It incorporates several design features in an attempt to develop an attractive tokamak reactor concept. Considerable effort has been devoted to developing credible engineering and physics solutions to key problem areas. In short, STARFIRE represents the best understanding that we have today of a commercial fusion reactor. Yet one must remember that fusion research is in the phase of transition from primarily plasma physics studies to a serious attack on developing the capability in fusion physics and technology which will be required to establish the engineering feasibility of fusion power. Several promising fusion concepts in addition to the tokamak are under development. The tokamak concept can be expected to undergo further development, most likely along lines described in this study. Thus, STARFIRE represents a "snapshot" of our current understanding and expectations for tokamak development. Further developments will occur which will hopefully lead to further improvement in the prospects for practical, economic, safe fusion power within the early part of the 21st century.

The STARFIRE Study has been carried out during a period of substantial progress in the tokamak fusion physics program.[1] Also, a number of tokamak reactor design studies[2] have identified several new features which could improve the reactor embodiment of the tokamak concept. The task of the STARFIRE Study was to incorporate the results of recent tokamak research and reactor studies into an integrated design concept which would further advance the development of attractive tokamak-based reactor concepts.

Particular attention has been given to developing design concepts which will result in more attractive engineering features. The central theme here has been to reduce the complexity of the design in order to develop a reactor concept which is more compatible with assembly and maintenance considerations. Design concepts were then examined in reasonable detail in order to establish their engineering credibility.

Plasma engineering has played an important role in the STARFIRE Study. The philosophy here was to not necessarily adopt conservative plasma physics concepts based on proven theory and well-demonstrated experiments, as one would do in designing a near-term experiment, but rather to explore innovative physics ideas which would result in a more attractive reactor concept and which will provide guidance for future physics research.

Attention to safety and environmental features has been a major consideration in this study. Design efforts have examined both normal and off-normal conditions. Design choices have been strongly influenced by a desire to minimize vulnerable tritium inventories, reduce the use of scarce materials, minimize stored energies that could result in accidental releases of energy, and minimize long-term radioactive waste storage requirements. These considerations have played a major role in both reactor and plant design decisions.

The STARFIRE Study has endeavered to provide for input and review of the effort as it has been carried out. In addition to reviews carried out by DOE's Office of Fusion Energy, a comprehensive review was carried out in October, 1979, at ANL with approximately 60 representatives from all segments of the fusion community. The results at this review have been documented in an interium report.[3] Informal workshops were also held on tritium breeders, blanket design and current driven steady-state operating modes. In addition, STARFIRE progress was reported at several national and international meetings during the study period.[4-9] The objective here was to provide for a variety of mechanisms for feedback from the fusion community while the study was in progress so that recommended changes could be considered for incorporation into the reference design.

Advisory committees for STARFIRE were established in two key areas. The first was a Utility Advisory Committee whose purpose was to provide input from the utility perspective on commercial fusion power plants and to provide a mechanism for utility review of the design as it develops. Membership of the Utility Advisory Committee is shown in Table 1-1. The Utility Advisory Committee met with the STARFIRE Team in July, 1979, and March, 1980. The results of input from the Utility Advisory Committee are summarized in Appendix A.

Because of the importance of carefully considering the safety and environmental aspects of STARFIRE, a safety review committee was established. Membership of the committee is also shown in Table 1-1. This committee's primary purpose was to provide review and recommendations for the development of the reactor and plant conceptual design. The Safety Advisory Committee met with the STARFIRE team in October, 1979, and June, 1980.

Table 1-1. STARFIRE Advisory Committees

Utility

Bill Wolkenhauer-Chairman, Washington State
Clint Ashworth, Pacific Gas and Electric
Fred Brunson, Union Electric Company
Ed Fiss, Duke Power Company
Robert Goodrich, Northwest Utilities
Betty Jensen, Public Service Electric and Gas

Safety

J. G. Crocker-Chairman, EG&G Idaho, Inc.
J. L. Anderson, Los Alamos Scientific Laboratory
D. Cohn, Massachusetts Institute of Technology
H. Howe, Jr., Princeton Plasma Physics Laboratory
M. Kazimi, Massachusetts Institute of Technology
L. Muhlestein, Hanford Engineering Development Laboratory
J. Powell, Brookhaven National Laboratory
T. Shannon, Oak Ridge National Laboratory

A major feature of the design approach for STARFIRE was the formation of a multidisciplinary design team made up of personnel from a national laboratory and industry. The program was directed by Argonne National Laboratory and included an industrial team led by McDonnell Douglas Astronautics Company, which included General Atomic Company and The Ralph M. Parsons Company. In addition, the University of Wisconsin provided support in the area of plasma impurity control during the initial phase of the study.

This report is divided into three parts: Part A - Introductory and Overview Sections (Chapters 1 to 5), Part B - Design and Analysis (Chapters 6 to 23), and Part C - Appendices. Chapter 2 presents a comprehensive overview of all aspects of the STARFIRE study including a description of the reactor and plant, summaries of design analyses and summaries of design assumptions, conclusions and cost studies. Chapter 3 presents a detailed discussion of study conclusions while Chapter 4 presents a parameter list and Chapter 5 discusses the rationale for major design decisions.

Chapters 6 to 12 describe key plasma and engineering subsystems of the tokamak reactor. Chapters 13 to 18 describe major reactor supporting subsystems. Maintenance and operations are described in Chapter 19 while the balance of plant is described in Chapter 20. Safety and environmental analysis and economic analysis are reported in Chapters 21 and 22, respectively. The plant construction schedule is described in Chapter 23.

References

1. H. P. Furth, "U. S. Tokamak Reserach", PPPL-1598, Princeton Plasma Physics Laboratory (Oct. 1979).

2. C. C. Baker, G. A. Carlson, R. A. Krakowski, "Trends and Developments in Magnetic Confinement Fusion Reactor Concepts", to be published in Nuclear Technology, Sept. 1980.

3. "STARFIRE - A Commercial Tokamak Reactor - An Interim Report", ANL/FPP/TM-125, Argonne National Laboratory, Dec. 1979.

4. C. C. Baker, et al., "STARFIRE - A Commercial Tokamak Reactor", Proc. 8th Symposium on Engineering Problems of Fusion Research, San Francisco, California., Nov. 1979. (Also, 10 related STARFIRE Papers).

5. C. C. Baker, et al., "Energy Conversion Considerations of the STARFIRE Commercial Fusion Power Plant", 15th Intersociety Energy Conversion Engineering Conference, Seattle, Washington, August 18-22, 1980.

6. M. A. Abdou, et al., "STARFIRE - A Conceptual Design of a Commercial Tokamak Power Plant", 8th International Conference on Plasma Physics and Controlled Nuclear Fusion Research, Brussels 1-10 July, 1980.

7. C. C. Baker, "A Steady-State Tokamak Reactor with Non-Divertor Impurity Control - STARFIRE", Proc. of Eleventh Symposium on Fusion Technology, Oxford, England, September 15-19, 1980.

8. C. C. Baker et al., "An Overview of the STARFIRE Reference Commercial Tokamak Fusion Power Reactor Design", Proc. of the Fourth ANS Topical Meeting on The Technology of Controlled Nuclear Fusion, King of Prussia, Pennsylvania, Oct. 14-17, 1980. (Also, 14 related STARFIRE Papers).

9. C. C. Baker, et al., "STARFIRE, A Commercial Tokamak Power Plant Design", to be published in Nuclear Engineering and Design, submitted March, 1980.

Table of Contents

List of Figures

List of Tables

2.1 INTRODUCTION

A comprehensive conceptual design of the STARFIRE reactor and balance-of-plant has been developed. The detailed analyses and description of the reference design for the power plant systems are given in Chaps. 6 through 23 and Appendices A through I. The purpose of this chapter is to present an overview of the STARFIRE study and a brief description of the reference design.

The primary criteria for commercial attractiveness emphasized in the STARFIRE study are economics, safety, and environmental impact. The approach to meeting these criteria involved building upon experience from previous studies, developing additional innovative design concepts, and selecting features that simplify the engineering design and enhance reactor maintainability. Table 2-1 shows the key features of STARFIRE. The reactor is operated steady state with the plasma current maintained by lower-hybrid waves. This mode of

Table 2-1. Key Features of STARFIRE

- Steady-state plasma operation
- Lower hybrid rf for plasma heating and current drive
- ECRH-assisted startup
- Limiter/vacuum system for plasma purity control and exhaust
- All superconducting EF coils outside TF coils
- Vacuum boundary at the shield, mechanical seals
- Total remote maintenance with modular design
- Water-cooled, solid tritium breeder blanket with stainless steel structure
- All materials outside the blanket are recyclable within 30 yr
- Less than 0.5 kg of vulnerable tritium inventory
- Minimum radiation exposure to personnel
- Conventional water/steam power cycle with no intermediate coolant loop and no thermal energy storage

operation results in a reduction in the plant capital cost and an increase in the plant availability. The capital cost savings are due to the elimination of electrical and thermal energy storage, derating of power supplies and the reduction in the reactor size, which is made possible by the increase in the permissible wall loading. The improvement in reactor availability is brought about by the increase in component reliability, elimination of material fatigue as a life-limiting effect in the first wall, and the reduction in the probability of plasma disruption occurrence. The reactor design is

simplified by utilizing the lower-hybrid rf system, with its attractive engineering features, for the dual purpose of plasma heating and current drive. The problems associated with plasma initiation and startup have been eased by the use of electron cyclotron resonance heating to reduce the OH voltage.

The limiter/vacuum system concept has been selected for the plasma impurity control and exhaust system. Compared to divertors, the limiter/vacuum system greatly simplifies the reactor design and improves its reliability and accessibility. Detailed analysis showed that the system can be designed to credible engineering standards.

The characteristics of the plasma operating point and the plasma support systems in STARFIRE are different from those in previous conceptual designs. The major differences are due to the choice of the steady state operation and the limiter/vacuum system. These choices were motivated by the desire to simplify the engineering design. It was assumed in the early stages of the design that these options could be developed in the STARFIRE time frame. Fortunately, results from recent plasma physics experiments on noninductive current drive (see Chap. 7) and on limiters (see Chap. 8) are very encouraging and they suggest that these options can be developed in the next few years.

A major effort has been devoted in STARFIRE to enhancing reactor maintainability and improving plant availability. The approach was to select design features and develop a design configuration that reduced the frequency of failure and shortened the replacement time. Relevant examples are: (1) steady-state operation with current drive; (2) limiter/vacuum system for impurity control and exhaust; (3) vacuum boundary located at the shield with all mechanical seals (no welds); (4) all service connections (e.g., for high pressure coolant) are located outside the vacuum boundary (shield); (5) optimized modular design; (6) all superconducting EF coils are outside the TF coils; (7) conservative TF coil design; (8) fully remote maintenance permitting some repairs during reactor operation; (9) "remove and replace" maintenance approach (failed parts are replaced with spare parts and the reactor is operated while repairs are made in the hot cell) that minimizes downtime; (10) combining components for simplicity (e.g., TF coil room-temperature

dewar provides support for the EF coils and shield); and (11) providing redundancy of strategic components (e.g., for the EF coils trapped below the reactor). These features as well as potential future improvements in component reliability provide optimism, that the plant availability goal of 75% can be achieved.

The safety and environmental considerations have played a major role in the STARFIRE design effort. A solid tritium breeder was selected in preference to liquid lithium in order to minimize the stored chemical energy. The impurity control and exhaust system was selected and designed so that the tritium fractional burnup is maximized and the vulnerable tritium inventory in the fueling and vacuum pumping systems is minimized. Furthermore, the reactor design was developed to contain the tritium with multiple barriers and minimize the size of potential tritium releases. The shield was designed and all reactor materials selected to permit recycling of all materials outside the blanket in less than 30 yr. Radiation exposure of personnel has been minimized by the use of extensive remote maintenance operations and by providing adequate shielding. The use of resource-limited materials was avoided. Mechanisms for fast reactor shutdown and auxiliary cooling systems have been incorporated into the design. The beryllium coating on the first wall and limiter provide an inherent safety feature that terminates the plasma burn if the metal temperature reaches $\sim$ 900°C. Calculations show that the reactor will be automatically shut down in less than one second, if a hot spot forms on 10% of the first wall, without the need for any active control system. No major damage, other than some first wall coating ablation, will occur.

The use of water coolant, steam cycle and conventional materials in STARFIRE makes the heat transport and energy conversion system a state-of-the-art technology. The balance of plant has been designed to maximize the utilization of current power plant features. However, the reactor hall, hot cell and tritium facility are unique to fusion reactors. The tritium facility utilizes current day design practices of the Tritium Systems Test Assembly (TSTA). The reactor building houses the reactor and modules for auxiliary systems that may become contaminated.

The STARFIRE power plant design, shown in Fig. 2-1, represents a single 1200 MWe generating unit. The plant is part of a utility grid that normally uses the STARFIRE plant as a base load unit; however, the plant can load follow at 5% of full load per minute.

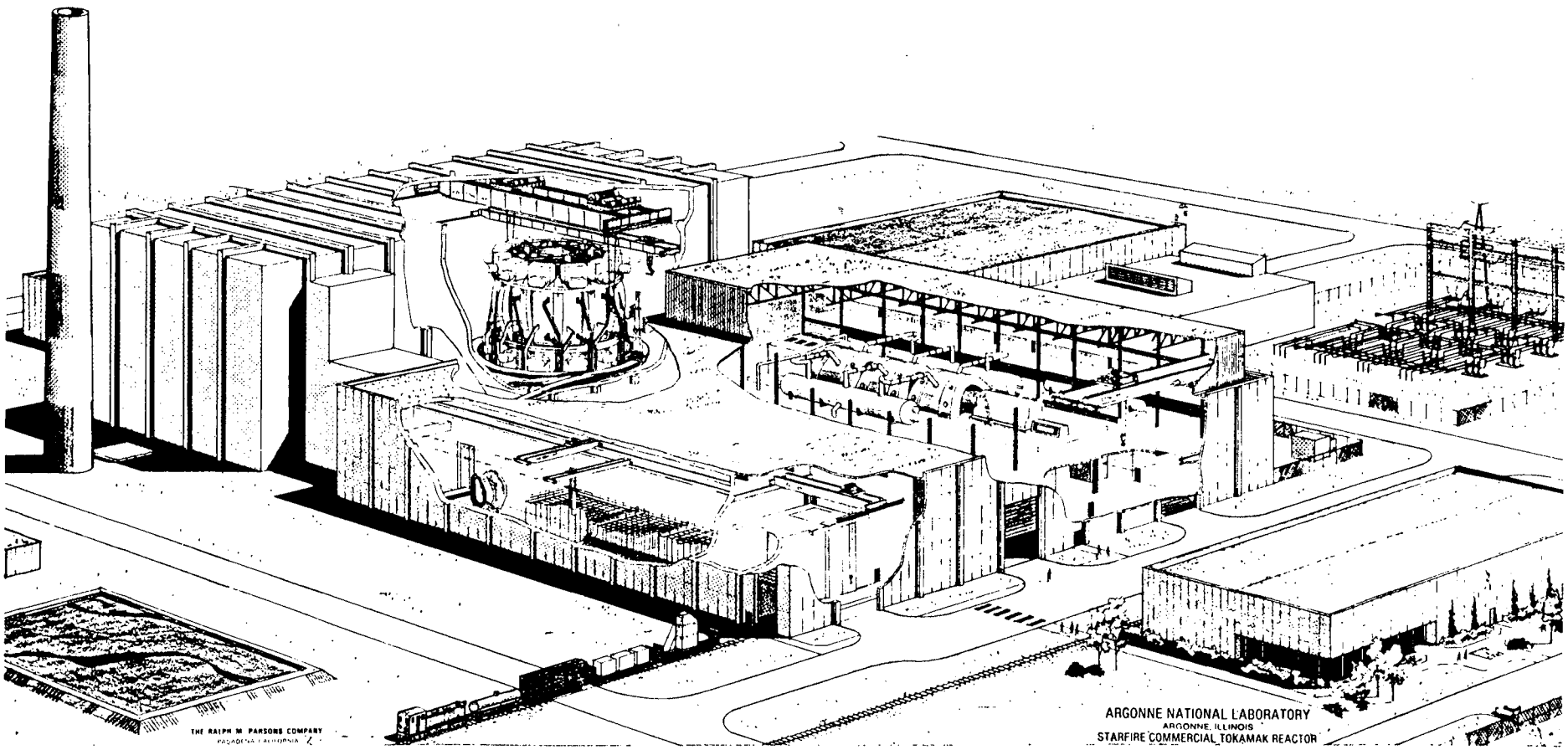

Figure 2-1. STARFIRE plant site.

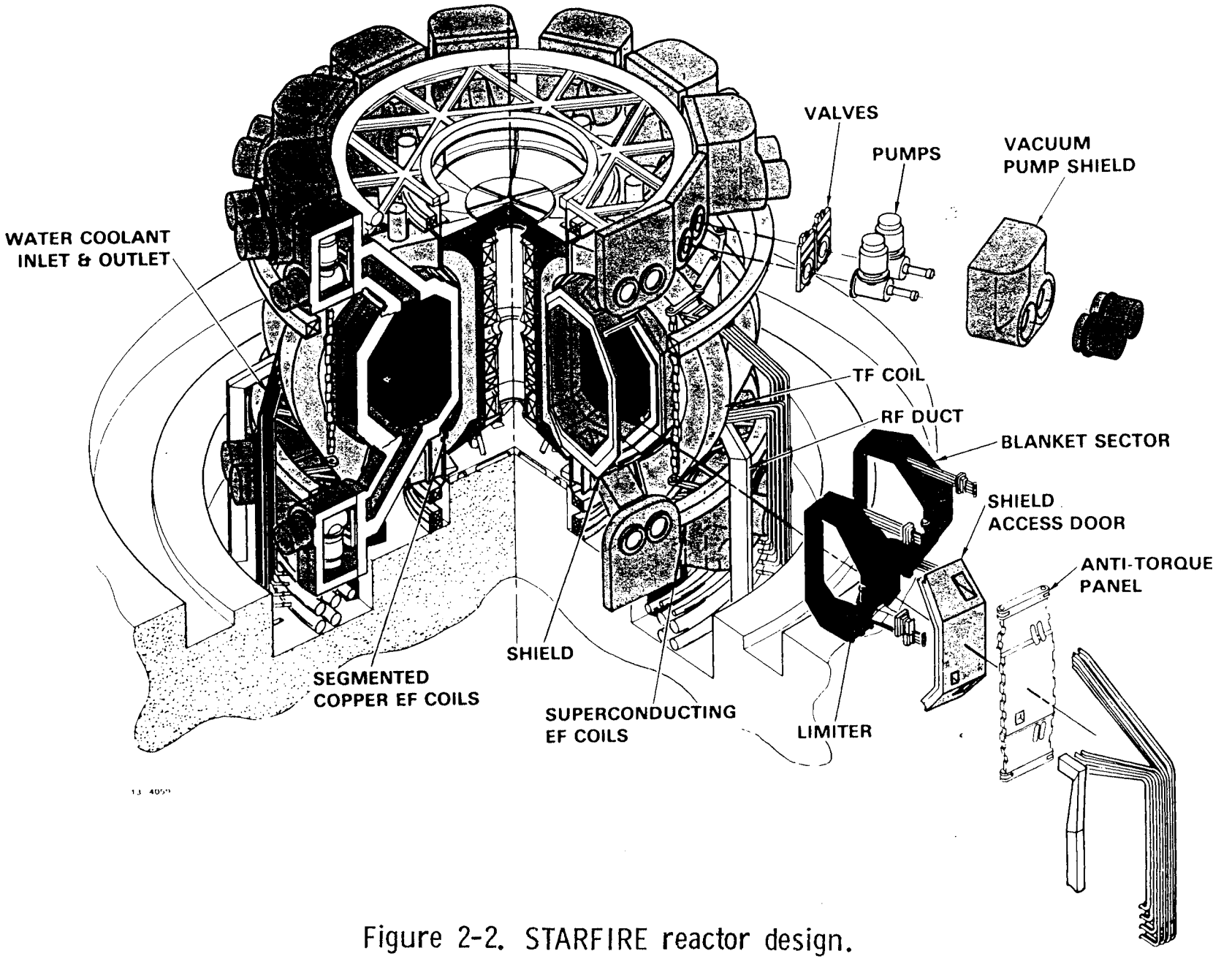

Figure 2-2. STARFIRE reactor design.

2.2 KEY ASSUMPTIONS

The STARFIRE reactor design was developed using the assumption that it was the tenth commercial plant constructed from a standardized design. This assumption provides a highly predictable machine that will have resulted from an extensive R&D program and utility operating experience from earlier plants. The first year of operation is assumed to be approximately 2020. Although this date does not directly enter in the design considerations, it is useful in considering the availability of certain advanced technologies.

Remote maintenance of all equipment within the reactor building has been the design basis; however, provision for personnel entry into the reactor building, on a contingency basis, has also been included in the design. A goal of an overall plant availability of 75% is justified on the basis of a maintainable design, a first wall life of greater than 6 years, and the assumption that STARFIRE is the tenth-of-a-kind power plant.

The major plasma physics assumptions and guidelines are discussed in detail in Chapters 6, 7, and 8. Key assumptions include ion heat transport which is three times faster than the neoclassical value, electron heat transport which is given by the empirical Alcator scaling, and particle transport which is taken as twice as fast as the empirical energy confinement time. Plasma cross-field transport at the edge is assumed to be Bohm diffusion with ion sound speed flow parallel to the field lines. The particle density and energy are assumed to fall exponentially in the scrape-off region. Neu- recycling at the plasma edge with some gas puffing is assumed to be an effective fueling mechanism. The plasma equilibrium with a somewhat hollow current profile is assumed to be stabilized by a conducting first wall for β's of at least 6.7%. Lower hybrid wave driven currents are calculated from standard quasilinear and Fokker-Planck theory. Linear theory is assumed when computing the transmission characteristics of the waveguide antenna and when performing the ray tracing calculation in the plasma.

The economic analysis assumes private utility ownership and a single generating unit at the site. Certain economic advantages would result from locating multiple units at one site. The construction plan assumes siting near navigable water for transportation of large assemblies to the site. Otherwise, siting would be nearly universal except that minor modifications would be

required for seismic zone 3. The plant lifetime for economic analyses was taken to be 30 years; the engineering design lifetime was taken to be 40 years.

2.3 REACTOR OVERVIEW

2.3.1 Reactor Configuration

The major reactor parameters for STARFIRE are listed in Table 2-2. These parameters were derived based on results from system analyses to minimize the cost of energy subject to constraints of physics, engineering, and technology. A discussion of these trade-off studies is given in Chap. 5.

The reactor design has a major radius of 7.0 m and operates at a first wall average neutron loading of 3.6 MW/m^2. The reactor delivers 1200 MWe to the grid in addition to providing 240 MWe for recirculating power requirements. The reactor operates with a continuous plasma burn and develops 4000 MW of useful thermal power. Approximately 3800 MW is provided to the main heat transport system and 200 MW is collected from the active limiter for use in feed water heating. An isometric view of the reactor is shown in Fig. 2-2. The reactor cross-section is shown in Fig. 2-3 and a top view is shown in Fig. 2-4.

The reactor configuration utilizes 12 toroidal field (TF) coils and 12 superconducting poloidal coils (EF and OH) located external to the TF coils. Additionally, four small normal conducting control coils (CF) are located inside the TF coils and outside the bulk shield to provide the necessary response time for plasma control while permitting good access for reactor maintenance. The magnet systems and shield are expected to last the full 40 year design life under normal operating conditions; however, provisions are incorporated for their replacement. Blanket sectors, including the limiters and rf ducts, will require replacement every six years. Vacuum pumps and the isolation vacuum valves will require replacement every two years.

The reactor configuration was developed to permit each component of the reactor to be replaced in a time consistent with its anticipated life (i.e., rapid replacement for components with short life) using remote maintenance techniques. Emphasis has been placed on overall reactor simplicity. This has led to combining components, where possible, to minimize the number of replaceable parts and to efficiently use the materials and space of various

Table 2-2. STARFIRE Major Design Parameters

Net electrical power, MW	1200
Gross electrical power, MW	1440
Fusion power, MW	3510
Thermal power, MW	4000
Gross turbine cycle efficiency, %	35.7
Overall availability, %	75
Average neutron wall load, MW/m^2	3.6
Major radius, m	7.0
Plasma half-width, m	1.94
Plasma elongation (b/a)	1.6
Plasma current, MA	10.1
Average toroidal beta	0.067
Toroidal field on axis, T	5.8
Maximum toroidal field, T	11.1
No. of TF coils	12
Plasma burn mode	Continuous
Current drive method	rf (lower hybrid)
Plasma heating method	rf (lower hybrid)
Plasma startup	ECRH-assist
TF coils material	Nb_3Sn/NbTi/Cu/SS
Blanket structural material	PCA[a]
Tritium breeding medium	Solid breeder (α-$LiAlO_2$)
Wall/blanket coolant	Pressurized water (H_2O)
Plasma impurity control	Limiter and vacuum system supplemented by low-Z coating, enhanced radiation and field margin
Primary vacuum boundary	Inner edge of shield

[a] Primary Candidate Alloy (PCA), an advanced austenitic stainless steel.

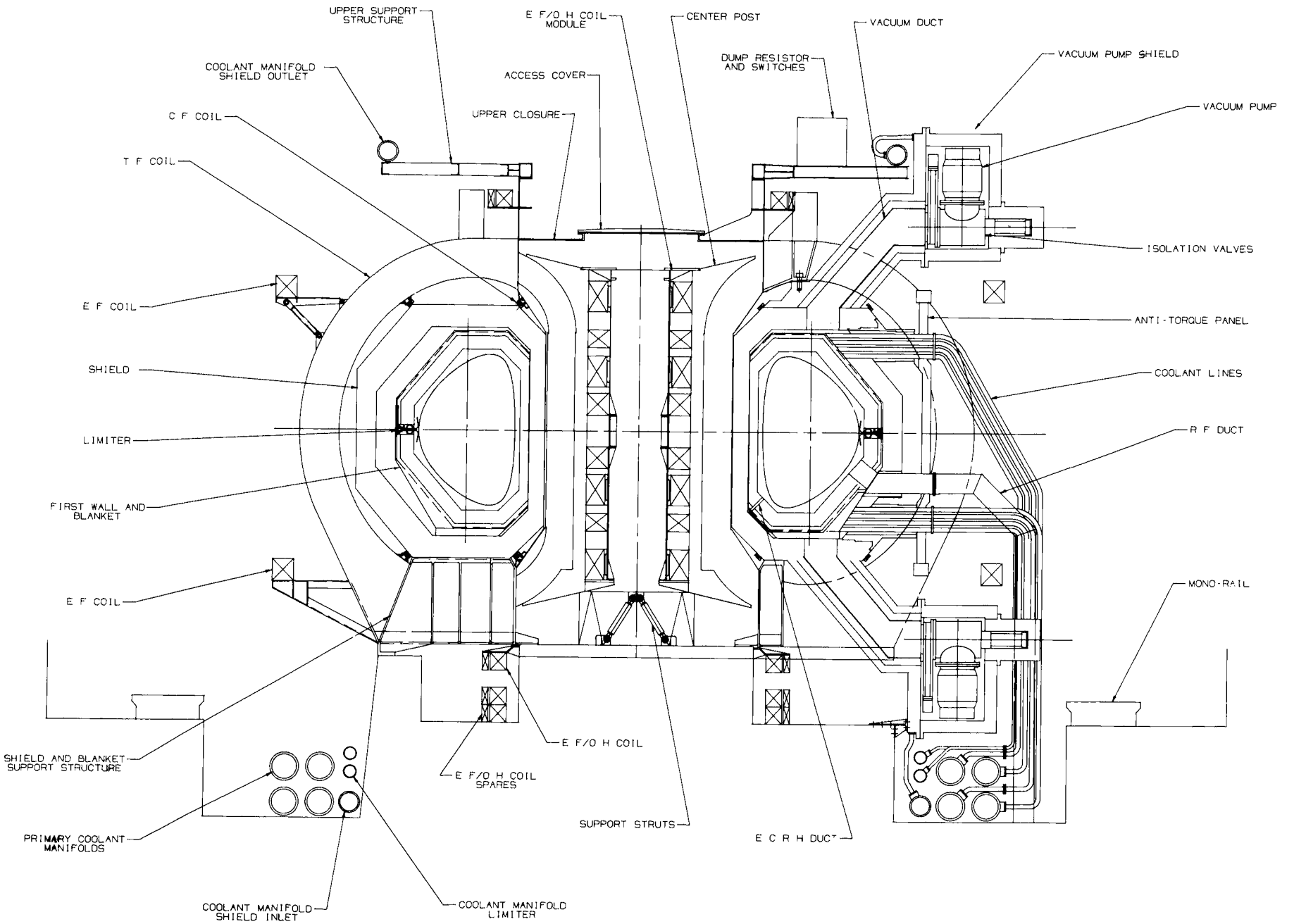

Figure 2-3. STARFIRE commercial tokamak - cross-section.

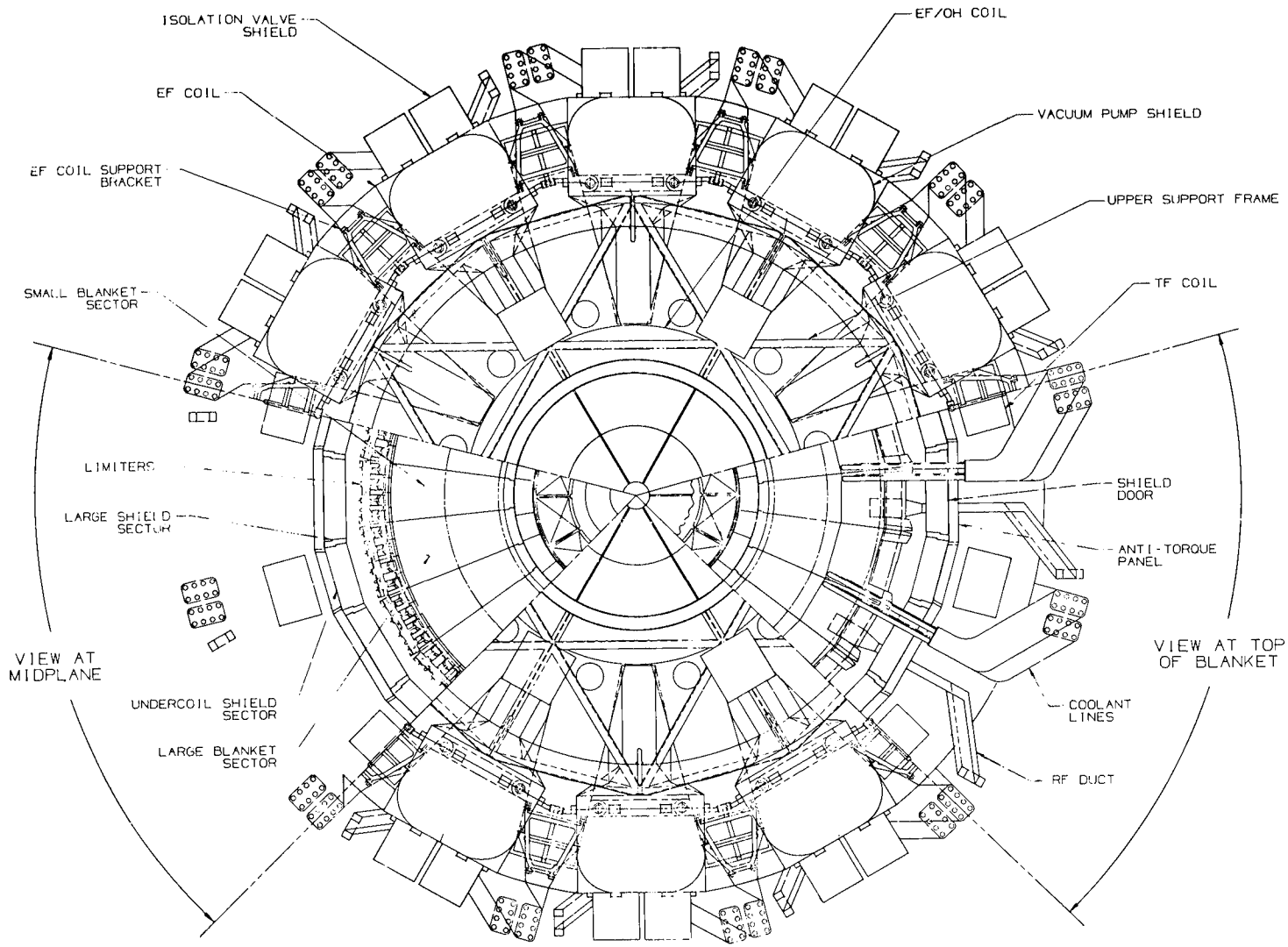

Figure 2-4. STARFIRE commercial tokamak - top view.

components. Modularization has also been emphasized so that all reactor components can be removed and replaced in a simple and practical manner. The remove and replace philosophy permits the reactor to resume operation while time-consuming repairs are made in the hot cell where more time and equipment is available.

The TF coil, and hence the reactor, configuration was developed primarily by the desire to keep the superconducting EF coils external to the superconducting TF coils so that their replacement is possible without fabrication of a new coil on the reactor. External placement of the EF coils increases the incentive to reduce the TF coil size to minimize the stored energy of the EF system. The TF coil outer radius is constrained to 13 meters by the clearance required for shield installation.

The TF coils are joined into a common vacuum tank at the center of the reactor. The common vacuum tank was chosen to minimize the heat leak to and the shield thickness at the magnet inner leg. The common TF coil vacuum tank also provides the vacuum boundary for the center post and EF/OH coils in the center region. Since the common vacuum tank does not contain a dielectric break, care was taken to minimize its thickness and hence the image currents in the vacuum tank so that the CF coils could properly control the plasma.

The EF/OH coils inside the center post are grouped in two modules to simplify their removal from the top of the reactor without significantly increasing the overhead crane or building height. The outer EF coils and upper EF/OH coil can be removed vertically. Spares have been provided for the lower EF/OH coils that are trapped under the reactor because the inherent complications of replacing a failed coil, even if only once in every few plant lifetimes, make it cost effective.

The shield is assembled as twenty-four sectors to permit its installation between TF coils. The 12 sectors that fit under the TF coils also incorporate dielectric breaks in every other sector. The other sectors incorporate an access door and two vacuum ducts. The sectors are joined together by a welded vacuum seal and are not expected to require frequent replacement (i.e., they are life-of-plant components).

The vacuum boundary location was selected at the shield interior with access door seals located at the outer surface in order to: 1) provide a

convenient way of pumping for the limiter slot system, 2) minimize the complexities of providing a vacuum boundary at the blanket/first wall and 3) permit the inboard vacuum seals which have limited access to remain intact during maintenance. The vacuum seals that must be opened for maintenance were located at the outer shield surface to provide access for maintenance and to reduce the damage to seal materials by radiation exposure. The shielding is effective enough to permit use of elastomer seals which can be sealed repeatably and easily. The vacuum pumps were located at the top and bottom of the reactor to minimize the neutron heating on the cryopanels and to permit the pumps to remain in-place during blanket replacement.

The blanket was divided into large sectors to permit replacement with a minimum number of in-reactor maintenance actions. Twenty-four toroidal sectors of two different sector sizes are used to permit installation in the space between adjacent TF coils. The overall blanket installation was simplified by mounting the limiter, rf duct and ECRH duct to the sector for removal as a unit. Coolant connections to the blanket sector were located outside of the vacuum boundary to minimize the effects of irradiation on the joint and to permit use of less than high integrity "leak-tight" mechanical seals. The penetration through the vacuum boundary is sealed with elastomer seals located at the external shield surface.

The limiter consists of 96 elements that form a near continuous toroidal ring at the outer midplane of the blanket. Four limiters are mounted on each blanket sector in front of a slot through the blanket that provides a path for particles to a plenum. Particles are then pumped by 24 vacuum pumps at the top and bottom of the reactor. An additional 24 vacuum pumps are provided to permit pump rejuvenation every two hours.

Twelve rf ducts provide for heating and current drive of the plasma. These ducts are mounted in the blanket sector located between TF coils. An rf window and phase monitor are located in the duct near the shield while phase shifters, circulators and crossed field amplifiers are located in the reactor building basement where personnel access during operation is possible. Twenty-four ECRH ducts are provided for initial plasma breakdown and wall cleaning. Two vacuum ducts are located on each blanket sector between TF coils.

Fuel is provided to the reactor by extracting bred tritium from a solid breeding blanket and injecting it into the plasma via gas puffing. Two gas ports are provided. Gas enters the plasma through the limiter which incorporates a drilled passage to the innermost protrusion of the plasma at the outer blanket midplane.

2.3.2 Plasma Engineering

STARFIRE employs a DT burning, D-shape plasma to produce 3510 MW of fusion power. The plasma is operated at a moderate β of 6.7% and is moderately elongated, with a height to width ratio of 1.6. The major plasma parameters and plasma engineering features of STARFIRE are listed in Tables 2-3 and 2-4, respectively. The plasma current is driven in steady state with 90 MW of lower hybrid rf power. The first wall and all other components in the vacuum chamber are coated with Be. The impurity control system maintains a steady-state concentration of 14% helium and 4% Be in the plasma. The fairly low DT removal efficiency (15%) of the impurity control system permits a high fractional burnup of tritium. For the same reason, most of the plasma fueling is done automatically by DT neutrals recycling from the first wall and limiter. Additional fueling is done by gas puffing.

In order to minimize the heat transport load on the limiter, as well as to establish a thermal equilibrium, the plasma is operated in an "enhanced radiation" mode, whereby a small amount of high-Z material, nominally iodine, is added along with the fuel stream. This serves to radiate most of the heating energy and stabilizes the thermal operating point.

The plasma MHD equilibrium is of the low current, hollow profile type. The plasma position is controlled with two sets of coils, a main equilibrium field (EF) coil set and a control field (CF) coil set. The main EF coils are superconducting and are located outside of the TF coils. They are used to provide the basic positional equilibria. The CF coils consist of small copper coils inside the TF coils and are used to control position and to stabilize against plasma disruptions. To further aid in the latter task, the first wall is designed with a time constant of 300 ms to stabilize against rapid vertical instabilities.

Table 2-3. STARFIRE Plasma Parameters

Parameter	Unit	Value
Major radius, R	m	7.0
Aspect ratio, A	—	3.6
Elongation, κ	—	1.6
Triangularity, d	—	0.5
Safety factor at limiter,	—	5.1
Average beta, β		0.067
Maximum toroidal field at coil, B_M	T	11.1
Toroidal field at plasma center, B_o	T	5.8
Plasma current, I_p	MA	10.1
Plasma volume, V_p	m^3	781
Average electron temperature, T_e	keV	17.3
Centerline electron temperature, T_{eo}	keV	22.5
Average ion temperature, T_i	keV	24.1
Centerline ion temperature, T_{io}	keV	31.3
Average fuel density, N_{DT}	m^{-3}	0.806×10^{20}
Center fuel density, N_{DT_o}	m^{-3}	1.69×10^{20}
Electron energy confinement time, τ_E	s	3.6
Ion energy confinement time, τ_I	s	10
Particle confinement time, τ_p	s	1.8
Fractional helium concentration, N_α/N_{DT}	—	0.14
Fractional beryllium concentration, N_{Be}/N_{DT}	—	0.04
Fractional iodine concentration N_I/N_{DT}	—	0.001
Fusion power, P_F	MW	3510 MW
Lower hybrid rf power to plasma, P_{rf}	MW	90
Average neutron wall load, P_{WN}	MW/m^2	3.6

Table 2-4. Plasma Engineering Features of STARFIRE

Operating Point	
Equilibrium type:	Elongated, D-shape, moderate β, hollow current profile
Equilibrium generation method:	Outside superconducting equilibrium field coil system
Position stabilization method:	Inside control field coils and conducting first wall with 300 ms time constant.
Burn Cycle	
Startup time:	$\sim$ 24 minutes
Method:	Tritium lean startup; vary rf power, DT density, T fraction; 5% per minute fusion power ramp.
Normal shutdown time:	$\sim$ 24 minutes
Emergency shutdown:	Induced disruption method, time $<$ 3 s
Plasma initiation method:	5 MW electron cyclotron resonance heating
Burn method:	Steady state, lower hybrid current drive
Thermal stabilization:	Enhanced radiation mode operation by iodine injection
Fueling	
Fueling method:	Recycling DT plus gas puffing

Because of the need to minimize the lower hybrid rf current drive power, the plasma density is lower and the plasma ion temperature is higher than most previous tokamak reactor designs. The plasma is operated with $T_i > T_e$, which makes better use of the available β. The tradeoffs, between the operating point and rf power, and the selection of density and temperature parameters are discussed in detail in Chap. 7.

Most of the STARFIRE burn cycle is substantially different from pulsed reactor burn cycles. Plasma breakdown is done with 5 MW of electron cyclotron resonance heating (ECRH) and does not require a high voltage OH coil. The startup period takes 24 minutes and conforms to the requirement that the fusion power should be ramped at a 5% per minute rate, to minimize thermal problems in the energy recovery and conversion systems. The OH coil as well as the OH and EF power supplies have modest requirements compared to pulsed reactor requirements. The steady state burn phase of the burn cycle has a thermal equilibrium maintained by the addition of iodine. The equilibrium and stability of the enhanced radiation mode of operation has been studied with a global code and with the 1-D WHIST code. These studies indicate that this mode of operation is feasible.

Several types of shutdown scenarios have been developed for STARFIRE. The normal shutdown is basically the reverse of the startup period, whereby the fusion power is reduced at a 5% per minute rate by reducing the tritium fraction in the plasma. There are three types of emergency shutdowns. The fastest is an "abrupt" shutdown whereby a plasma disruption is induced by injecting excess high-Z material. There is a more orderly "rapid" shutdown which also uses a disruption, but where most of the plasma energy is radiated away prior to the disruption. Finally, a naturally occurring "ablative induced shutdown" has been identified which occurs as result of a hot spot formation on the first wall or limiter.

Various fueling options for STARFIRE were studied. The high fractional burnup rate of 42% in STARFIRE permits a fairly low fueling rate from an external source. Gas puffing is the most desirable engineering option and has been adopted as the STARFIRE fueling method.

We have considered D-shaped plasma equilibria in toroidal geometry with pressure profiles characterized by a width parameter α. Using a diamagnetism function $F^2(\psi) = F_0^2 (1 - \delta\hat{\psi}^\gamma)$ and a pressure function $p(\psi) = \psi^\alpha$, it is possible to generate a broad range of low and high β equilibria with various axis and limiter values of the safety factor, q_a and q_b, respectively. The highest stable β is, in general, a function of A, κ, d, α, q_a and q_b, where A is the aspect ratio, κ is the elongation, and d determines the triangularity. This functional dependence is under active investigation in the physics community,

and the operating point for STARFIRE is based on a survey of equilibria and subsequent stability analysis.

2.3.3 Plasma Heating and Current Drive

The design of a tokamak reactor which can run in a steady state mode is basically different from the design of a pulsed tokamak, because the circulating power required to sustain the toroidal current against collisional dissipation may be a substantial fraction of the power plant's electric output. Consequently, the STARFIRE design focused on efforts to minimize the circulating electric power for steady state operation, and the resulting lower-hybrid rf system was optimized with this goal. In addition, the same system appears adequate to provide auxiliary heating during the startup phase to bring the plasma to ignition temperatures.

One obvious means of reducing rf power to the reactor is the selection of operating regimes with the lowest plasma currents. Accordingly, a large variety of MHD equilibria (solutions to the Grad-Shafranov pressure balance equation) were surveyed in order to identify the most desirable candidate. The aspect ratio, A, was selected after studying the power requirements for generating equilibria with $\beta_t = 0.25/A$. For a fixed reactor power, wall loading and toroidal field strength, the plasma current and electron density increase as A is reduced. This leads to increasing rf power at lower A. However, a larger A requires a larger major radius. This study concluded that A = 3.6 is best, with R = 7.0 m.

The selection of the plasma beta was another crucial decision. Generally, the higher the plasma current, the higher is the stable β_t which can be achieved. The increasing rf power required at higher β_t motivated the selection of a comparatively modest design value - $\beta_t = 6.7\%$. It was shown that hollow current density profiles can have favorable stability while requiring less total current than more conventional centrally peaked profiles.

An elongated ($\kappa = 1.6$), highly D-shaped plasma cross-section was chosen which requires I = 10.1 MA with $B_o = 5.8$T on axis. The plasma cross-section and lower hybrid system are shown in Fig. 2-5. The design of the equilibrium field (EF) coil system required to position and shape the poloidal flux surfaces is eased by the ability to locate large coils in the central hole. The

POWER BALANCE	MW
R F POWER TO PLASMA	90.4
(CURRENT DRIVE)	(66.5)
LOSSES	62.3
TOTAL R F ELECTRICAL POWER	152.7

POWER LOSSES		MW
A	GRILL	0.5
B	WAVEGUIDE	1.9
C	WINDOW (3)	0.2
D	WAVEGUIDE	18.2
E	CIRCULATOR	10.6
F	PHASE SHIFTER	1.5
G	C F A	21.8
ELECT. BLDG	POWER SUPPLIES	7.6
	TOTAL LOSSES	62.3

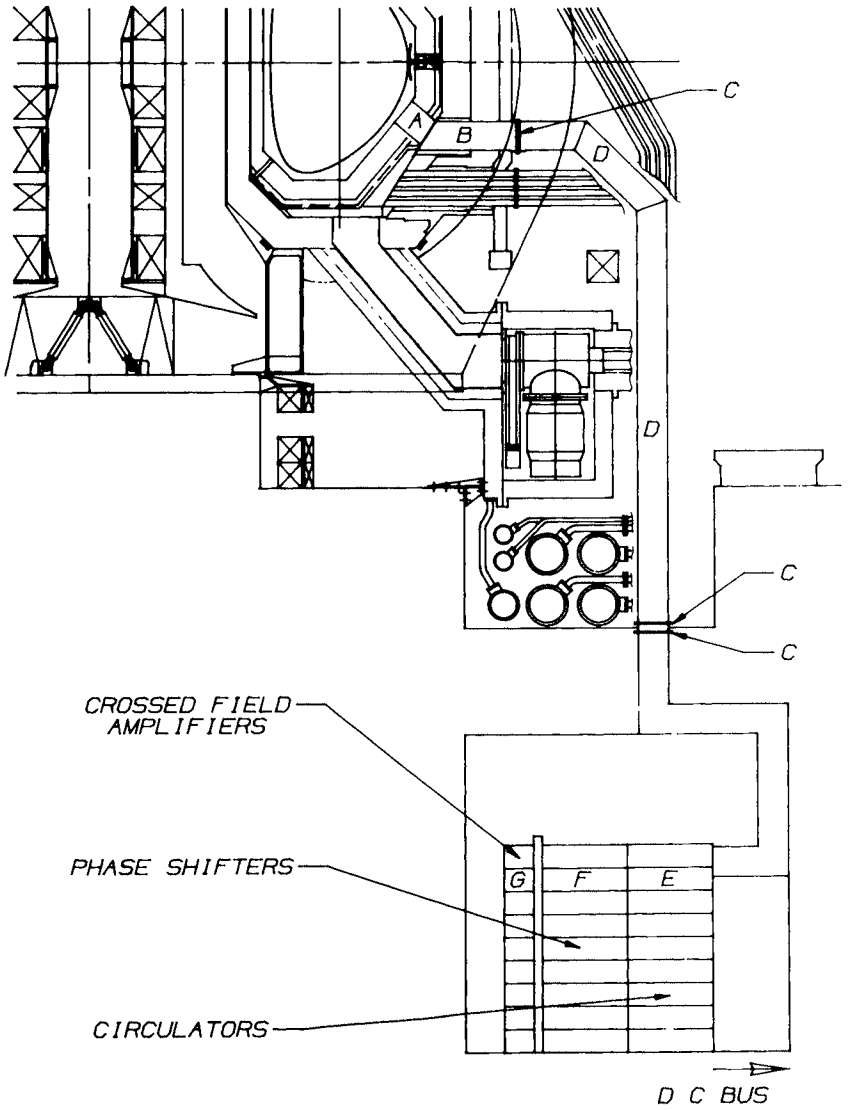

Figure 2-5. STARFIRE rf system showing plasma cross section.

safety factor profile does not allow double tearing modes, although other resistive modes have not been ruled out. Analysis with the BLOON and ERATO codes shows the equilibrium is stable to local interchange and ballooning modes but requires a close fitting conducting first wall/blanket to stabilize low-n kinks.

Lower hybrid current drive theory shows that the rf driving power is proportional to the local electron density where the current is generated, which makes the hollow current profiles especially attractive. In addition, for a fixed β, the average electron density ($\bar{n}_e$) may be reduced by operating the plasma at a higher temperature. Above 20 keV, the decreasing fusion reactivity of DT tends to offset these reductions in the rf power at low n_e. (Maximum Q occurs in the range 20-30 keV.) Despite low Q operation, the net electric output peaks for $T_e \simeq T_i \approx 11$ keV. However, the capital outlay for rf power supplies at 11 keV far exceeds that needed for auxiliary heating to ignition. The minimum cost of electricity appears when T_e = 17 keV, T_i = 24 keV, and $n_e = 1.2 \times 10^{20}$ m^{-3}, which results in a fusion power of 3510 MW.

Using the WKB form of the electromagnetic dispersion relation, the Landau damping of externally launched lower hybrid waves is computed in cylindrical geometry, and current generation is calculated from standard quasilinear/Fokker-Planck formulas. By minimizing the parallel wave index of refraction, $n_\parallel$, and adjusting the spectrum width, $n_{\parallel 1} - n_{\parallel 2}$, the equilibrium current density may be generated with a minimum amount of power. Wave accessibility (to avoid reflection) limits the lower bound on $n_{\parallel 2}$ to 1.40 in STARFIRE; setting $n_{\parallel 1} - n_{\parallel 2} = 0.46$ yields a hollow profile with a total parallel ("force-free") current of $I_\parallel$ = 9.1 MA. In equilibrium, due to the field line rotational transform, diamagnetic currents add another toroidal current density increment, with the result that 66.5 MW of driving power creates 10.1 MA of toroidal current. In these calculations, we have set the wave frequency at ν = 1.677 GHz, which exceeds the lower hybrid frequency at the point of deepest wave penetration and thus avoids parametric instabilities.

The Brambilla grill, a horizontal array of phased waveguides, is the ideal wave launcher in this rf frequency range. The waveguides have a vertical opening of 17.0 cm and transmit only the TE_{10} mode. The horizontal opening is 2.95 cm, and the guides are separated by 0.70 cm metal partitions. Phasing adjacent guides by $2\pi/3$ results in an asymmetric spectrum of

toroidally traveling waves with average $n_{\parallel} = 1.63$. We find a large number (N = 18) of guides is necessary to concentrate the spectral power into the range $n_{\parallel 1} - n_{\parallel 2} = 0.46$. The grill performance has been studied for a variety of electron edge density profiles, since this determines how well the grill couples to plasma waves. Two figures of merit appear. One is the average grill reflection coefficient, $\overline{R}$; the other is the fraction of transmitted power, ε, which is contained in the region $n_{\parallel} = 1.40 - 1.86$, and which is thus useful for driving toroidal current. Wave interference results in some power transmission at $n_{\parallel} = -3.2$, but, if reasonable control of the electron edge density is possible, ε will be in the range of 0.6 to 0.8. The overall $\overline{R}$ has been dramatically reduced in the STARFIRE design by replacing those waveguides with high individual reflection coefficients with passive reflectors. The final design has nine active and nine passive guides which results in $\overline{R} = 0.44$ and $\varepsilon = 0.74$. The total transmitted power to the plasma is thus 66.5 MW/ε = 90 MW.

In view of the large $\overline{R}$ of the grill, it is necessary to circulate the reflected power in a given waveguide directly into its neighboring guide. Thus a klystron drives the first of the nine active elements in an array, and circulators direct returning power through the other eight. Crossed field amplifiers (CFA's) are used to boost the reflected power to the required output level. Due to high reflection coefficients, the required amplifier gains are low, in the range 3-7 db. Present-day CFA's have achieved impressive efficiency in CW operation at low gains in this frequency range (η_{CFA} = 78% at 400 kW). We are confident that η_{CFA} = 85% is achievable with a modest R and D effort, and we have assumed this value in designing the STARFIRE system. Each CFA operates at 420 kW of rf output and requires a 20 to 30 kV power supply at 10 to 15 A, depending on the gain. Unlike klystrons, the CFA does not require a highly regulated power supply. The CFA may be operated with a cold cathode, eliminating costly heater power supplies and producing long-life operation (20,000 hours or 3 calendar years of STARFIRE operation).

Each waveguide facing the plasma is plated with Cu and Be to present a low sputtering, high conductivity surface. The wave intensity is low - 1.4 kW/cm^2 assuming 90 MW broadcast by a total launcher area of 6.4 m^2 - to

avoid nonlinear spectral modification; the electric fields are consequently well below the multipactor limit. A BeO window and dc break are located between the outboard legs of the toroidal field coils, and the electron cyclotron resonance region beyond is pressurized. Directional couplers monitor the phase on the vacuum side of each window to assure proper grill operation. Neutron damage to the window is negligible over the reactor lifetime, the fluence being less than 8×10^{11} neutrons/cm^2. The pressurized waveguide is routed through the building floor to a basement area (see Fig. 2-5) where the circulators, phase shifters and CFA's are located. Power supplies are in an auxiliary building. Inside the reactor hall, the rf equipment is passive, requiring little maintenance, while the CFA's and phase shifters are accessible during reactor operation if repair should prove necessary. By stacking four grills poloidally in each of the twelve reactor toroidal sectors, a system with 432 transmission lines and CFA's is achieved, with an input electric power of 153 MW (compared with 1200 MW net electric supplied to the grid). The redundancy in this system assures continued reactor operation in the event of single component failures. The total system cost, assuming prior amortization of an R & D program for CFA's and assuming mass production of the tubes, is \$33.5 M for the hardware, exclusive of power supplies. Power supply costs are \$14 M. This study concluded that a CFA system can provide lower hybrid power for current drive applications with much less circulating power than klystrons (which would require over 200 MW electric input) and at a fraction of the cost of a klystron system. The rf system is summarized in Table 2-5.

With minor modifications from the basic design given above, three of the twelve rf ducts can serve to heat and drive current during the startup phase of the tokamak discharge. These ducts contain grills with 36 waveguide elements with narrower openings. By appropriate phase control, these grills can heat the plasma at temperatures as low as $T_e = 0.5$ keV and can drive currents once T_e reaches $\sim$ 1.5 keV. A small OH coil and ECR heating serve to bring the discharge up to the temperatures at which the lower hybrid system functions. Beyond this point, we have demonstrated that there is a smooth evolution of the discharge towards the steady state.

Table 2-5. Lower Hybrid System Parameters

Parameter	Symbol	Value
wave frequency	ν	1.677 GHz
spectrum required	$n_{\|\|1} - n_{\|\|2}$	1.40 - 1.86
toroidal wave length	$\lambda_{\|\|}$	10.94 cm
parallel phase speed	ω/k	1.83×10^8 m/s
parallel current	$I_{\|\|}$	9.11 MA
toroidal current	I_p	10.1 MA
wave intensity at antenna	I	1.6 kW/cm^2
nine active/nine passive guides	N	9 + 9 = 18
phase difference	$\Delta\phi$	$2\pi/3$
narrow guide opening	b	2.95 cm
septum	d	0.70 cm
vertical guide opening	a	17.0 cm
edge density gradient	dn_e/dx	5.0×10^{10} cm^{-4}
vacuum distance	x_o	1.0 cm
spectral fraction driving current	ε	0.736
antenna reflection coefficient	$\overline{R}'$	0.443
power required to drive current	P_{LH}	66 MW
net heating power to plasma	P_h	90 MW
net electric power to rf system	P_e	152.7
CFA efficiency	η_{CFA}	85%

The rf system requires 432 CFA tubes operating at 420 kW with gains from 4.0 to 6.6 db.

2.3.4 Plasma Impurity Control and Exhaust

A plasma impurity control and exhaust system was developed for STARFIRE to satisfy the following goals: (1) engineering simplicity compatible with ease of assembly/disassembly and maintenance; (2) a high tritium burnup to minimize the tritium inventory in the fuel cycle; (3) a reasonable and reliable vacuum system that minimizes the number and size of vacuum ducts; and (4) manageable heat loads in the medium where the alpha and impurity particles are collected.

These goals are found to be best satisfied by a limiter/vacuum system together with a beryllium coating on the first wall, limiter, and all other surfaces exposed to the plasma. In order to minimize the heat load to the limiter, most of the alpha-heating power to the plasma is radiated to the first wall, by injecting a small amount of high-Z material, e.g. iodine, along with the DT fuel stream. The iodine atoms enhance the line-and-recombination radiation over most of the plasma volume. The helium removal efficiency of the limiter/vacuum system is intentionally kept low for three reasons: (1) to reduce the heat load on the limiter; (2) to simplify the vacuum system and reduce radiation streaming; and (3) to minimize the tritium inventory tied up in the vacuum and tritium processing systems. The major features of the STARFIRE impurity control and exhaust system are summarized in Table 2-6.

Figure 2-6 shows a cross section through the limiter, the limiter slot, the limiter duct, and the plenum region. The limiter consists of 96 segments that form one toroidal ring centered at the midplane and positioned at the outer side of the plasma chamber. This location was selected because: (1) it is the least likely place for a thermal energy dump from a plasma disruption; and (2) it assures symmetry in particle and heat load on the upper and lower branches of the limiter. Each of the limiter segments is 1 m high and 0.6 m wide. The physical dimensions of the system are shown in Fig. 2-6. The limiter slot, which is the region between the limiter and first wall, leads to a 0.4-m high limiter duct that penetrates the 0.7-m thick blanket. The limiter duct opens into a plenum region that is located between the blanket and shield and extends all the way around the torus. This plenum region is large enough so that it spreads the radiation leakage from the

Table 2-6. Major Features of STARFIRE Impurity Control/Exhaust

- o A limiter/vacuum system
  - One toroidal belt-type limiter centered around midplane
  - Simplified, credible engineering
- o Low-Z coating (beryllium) on all surfaces exposed to plasma
- o Enhance plasma radiation
  - To reduce heat load at collection plate
  - By injecting small amount of iodine
- o A low helium removal efficiency (25%)
  - Much simpler vacuum system
  - Less radiation streaming
  - High tritium burnup, low tritium inventory
  - Penalty: Modest increase in toroidal field (0.85 T on axis)
- o Simple vacuum system
  - Limiter duct penetrates blanket leading to a plenum region between blanket and bulk shield
  - Significantly reduced radiation streaming; less shielding and lower nuclear heat load in cryopanels

limiter duct into a larger surface area of the bulk shield. The conductance of the plenum region is large enough to permit locating the vacuum ducts in the bulk shield sufficiently removed from the midplane so that radiation streaming from the limiter duct in the blanket to the vacuum pumps is acceptable. There are 12 vacuum ducts at the top and another 12 at the bottom of the reactor. Each of these vacuum ducts has an equivalent diameter of 1 m and penetrates the bulk shield leading to the vacuum pumps. Fig. 2-7 shows an isometric view of the limiter system.

The basic principles of how the limiter works are rather simple. Ions that hit the front face of the limiter will be neutralized and reflected back into the plasma. Ions that enter into the limiter slot hit the back surface and are neutralized. Some of the scattered neutrals will directly reach the limiter duct and follow a multiple-scattering path into the plenum region and into the vacuum ducts where they are pumped out by the vacuum pumps. Other

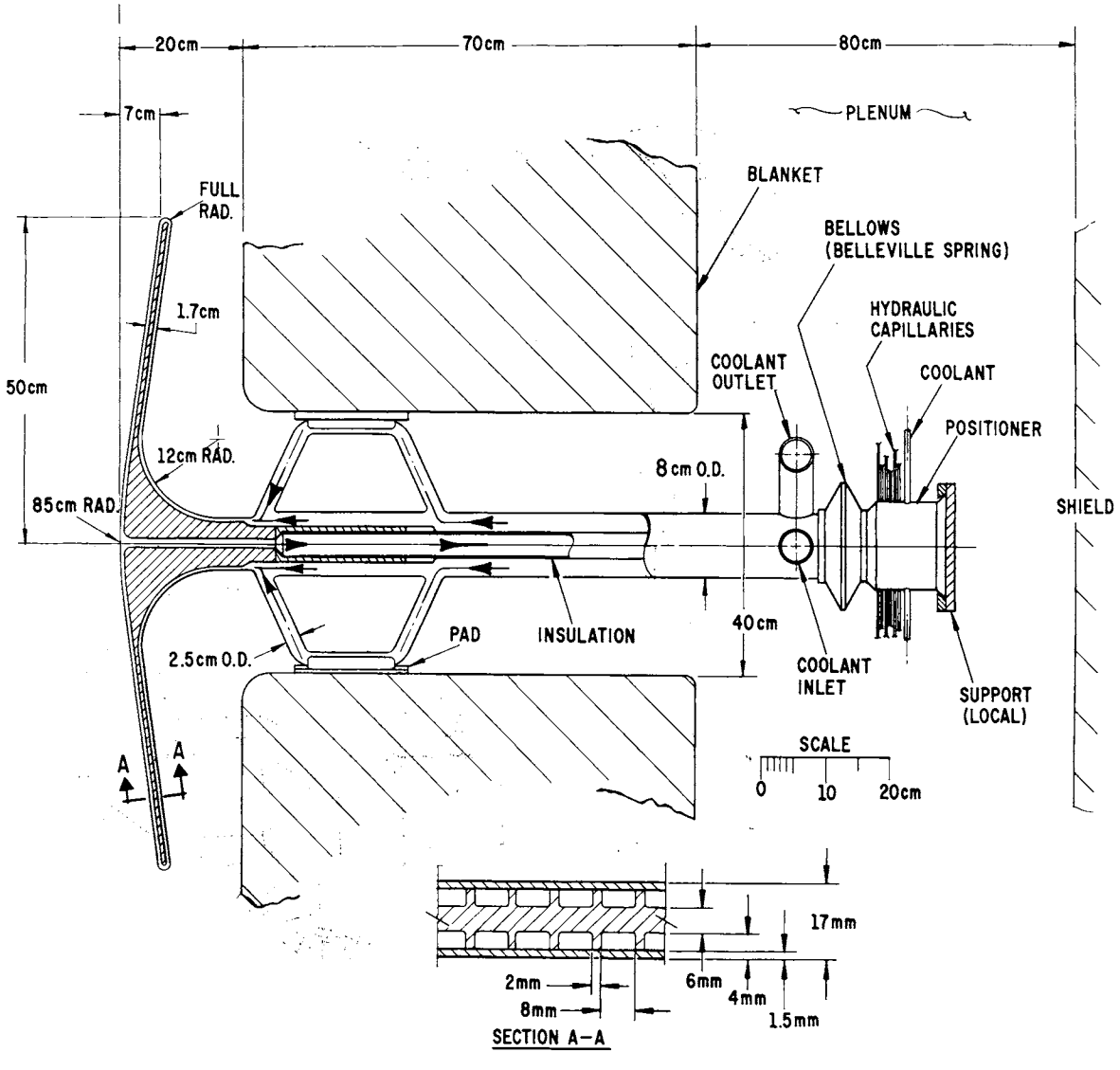

Figure 2-6. Cross section of the STARFIRE limiter design.

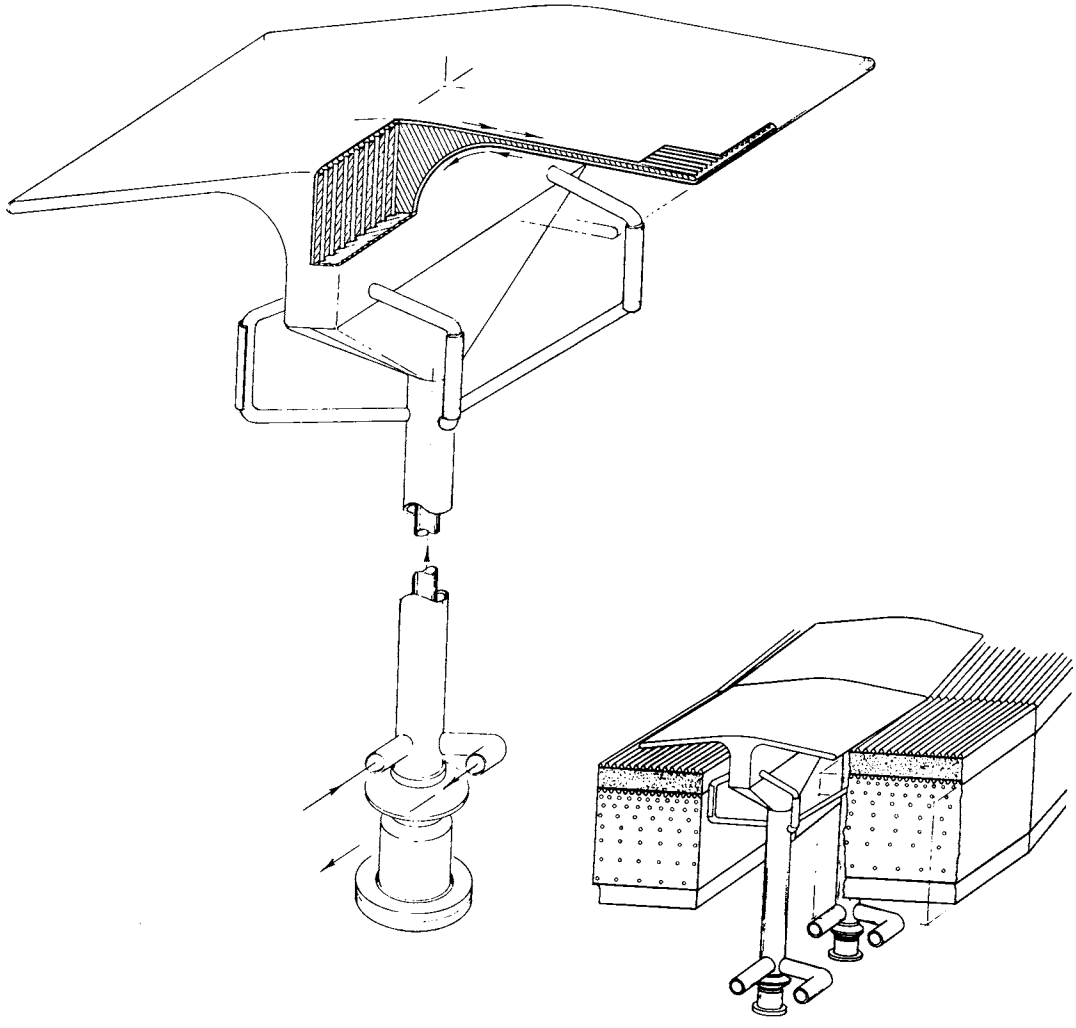

Figure 2-7. Isometric view of the STARFIRE limiter design.

particles neutralized at the back surface of the limiter will scatter back in the direction of the plasma. These neutrals have a high probability of being ionized and returned back to the limiter surface. Calculations show that this trapping or "inversion" effect is so large for helium that $\sim$ 90% of the helium entering the limiter slot will be pumped. This inversion effect greatly simplifies the limiter/vacuum system design in at least two ways:

1. Location of the Leading Edge -- Since the inversion probability is very high, the fraction of particles that enter the limiter slot need to be only slightly greater than the helium removal efficiency. This permits locating the two leading edges at the top and bottom of the limiter sufficiently away from the plasma edge and outward into the scrape-off region so that the peak heat flux at the leading edge is reasonably low.
2. Neutral Pressure -- This inversion effect causes the neutral gas pressure at the limiter duct to be considerably higher than the neutral pressure around the plasma. Such high pressure greatly simplifies the vacuum system design.

Hydrogen can charge-exchange as well as be ionized. These charge-exchange events significantly reduce the inversion probability for hydrogen because the resulting neutral will tend to make its way out of the slot region into the plasma. Therefore, the beneficial effect of higher helium pumping probability and enhanced hydrogen recycling into the plasma is obtainable in the limiter/vacuum system.

The plasma parameters related to the impurity control and exhaust system are shown in Table 2-7. The design parameters for the limiter and vacuum system are shown in Tables 2-8 and 2-9, respectively.

The charged particle flux in the scrape-off region falls off exponentially as e^{-x/δ_p} with δ_p = 10 cm and x being the distance into the scrape-off region. About 28% of the helium particles diffusing out of the plasma will enter into the limiter slot, i.e., between x = 8.7 cm and x = 20 cm. The transmission (pumping) probability for these particles is 0.9 giving an overall helium reflection coefficient R_α = 0.75 and helium removal efficiency $(1 - R_\alpha)$ of 0.25. The reflection coefficient for deuterium/tritium is 0.9.

The transport heat flux on the limiter (due to charged particles) varies as $e^{-x/\delta_E} \sin\theta$ in units of MW/m^2 with x in cm, δ_E = 5 cm, and θ being the angle between the field lines in the poloidal plane (nearly vertical in Fig. 2-6) and the surface of the limiter. The limiter surface from the tip (at plasma edge) to the top (or bottom) leading edge is slanted to spread the heat load. The leading edge (region where θ = 0 occurs) forms approximately one-half a cylinder shell with a diameter of 1.7 cm and extends from x $\sim$ 7 cm to x $\sim$ 8.7 cm. The location of the leading edge was determined from tradeoffs between the helium removal efficiency (and the associated toroidal-field margin) and the peak heat flux. The peak transport heat flux is $\sim$ 3.4 MW/m^2 and occurs at x = 7.8 cm. The average transport heat flux on the region of the leading edge is $\sim$ 2.2 MW/m^2. The front surface of the limiter (from the tip to the leading edge) receives an additional surface heat load of 0.9 MW/m^2 due to plasma radiation and charge-exchange. The magnitude of the volumetric nuclear heating depends on the specific limiter material and is in the range of 30 to 80 MW/m^3 for the materials to be discussed shortly.

Table 2-7. Plasma-Related Parameters for the Limiter/Vacuum System

Fusion alpha power ($P_{\alpha,}$), MW	703
Lower-hybrid power to plasma (P_{LH}), MW	90
Transport power to the limiter, MW	90
Helium production rate, s^{-1}	1.24×10^{21}
Alpha particle concentration (n_α/n_{DT})	0.14
Beryllium (low-Z coating) concentration (n_{Be}/n_{DT})	0.04
Iodine (radiation enhancement) concentration (n_I/n_{DT})	1.0×10^{-3}
Helium reflection coefficient, R_α	0.75
Toroidal-field margin at plasma center, T	0.85
Scrape-off region thickness, m	0.2
Particle confinement time (τ_p), s	1.8
Particle e-folding distance in scrape-off zone (δ_p), cm	10
Energy e-folding distance in scrape-off zone (δ_E), cm	5
Plasma-edge temperature (T_{edge}), keV	1.2

Water is selected as the limiter coolant because of its good heat transfer characteristics. This choice is consistent with the use of water cooling in the first wall and blanket. The limiter segments are connected so that the coolant passes through two segments (2 passes). The water inlet temperature to the first pass is 115°C, and with a temperature rise of 15°C per segment, the outlet temperature is 145°C for the second pass. The coolant pressure is 4.2 MPa (600 psia). The water temperature is kept low to minimize pressure stresses. Since the 200 MW of heat removed from the limiter represents only 5% of the reactor thermal power, this heat is used effectively for feedwater heating in the steam cycle without significant loss in thermal efficiency.

Table 2-8. Limiter Design Parameters

Coolant	Water			
Reference structural materials	Ta-5W, AMAX-MZC, FS-85, or V-20Ti			
Low-Z coating material	Beryllium			
Total heat removed from limiter, MW (90 MW transport, 56 MW radiation plus neutrals, and 54 MW nuclear)	200			
Average surface heat load, MW/m^2	2.3			
Peak surface heat load,[a] MW/m^2	4			
Coolant inlet temperature, °C	115			
Coolant outlet temperature (2-pass), °C	145			
Coolant pressure, MPa (psia)	4.2 (600)			
Coolant channel size, mm × mm	8 × 4			
Wall thickness, mm	1.5			
Maximum temperature, °C	Ta-5W	AMAX-MZC	FS-85	V-20Ti
Water side	193	182	192	191
Coating side	290	196	404	449

[a]Includes transport load (3.4 MW/m^2) plus load from radiation and charge-exchange neutrals.

Table 2-9. Vacuum System Parameters

Component	Dimensions (cm)	Conductance (m^3/s)
Limiter slots (2)	5650 × 10 × 50	4300
Limiter ducts (2)	3170 × 16 × 70	4100
Plenum	6000 × 67 × 600	13700
Vacuum ducts (24)	100 × 640 120 × 560	730
Vacuum pumps (24)	——	2900

Rated helium speed per pump, m^3/s	120
Rated DT speed per pump, m^3/s	200
Total helium pumping speed, m^3/s	490
Transmission probability[a] (helium)	0.9
Reflection coefficient (helium), R_α	0.75
Maximum helium pressure, Pa	0.016
Total DT pumping speed, m^3/s	480
Transmission probability[a] (DT)	0.40
Reflection coefficient (DT), R_{DT}	0.9
Maximum DT pressure, Pa	0.024
Tritium fractional burnup	0.42
Total gas load, $Pa\text{-}m^3/s$	18.7
DT gas load, $Pa\text{-}m^3/s$	10.85
Helium gas load, $Pa\text{-}m^3/s$	7.85
Temperature, °K	573
Number of vacuum pumps, on-line/total	24/48
Regeneration time, h	2
Maximum tritium inventory per pump, g	2.6

[a]Transmission probability per particle entering the limiter slot.

A large number of materials were evaluated as to their suitability for the limiter structure. The evaluation included the capability of withstanding high heat fluxes, resistance to radiation damage, fabricability, and compatibility with the surrounding environment. This resulted in identifying four reference alloys as the primary candidate materials. These included a copper alloy AMAX-MZC, and the refractory metal alloys of vanadium (V-20Ti), niobium (FS-85), and tantalum (Ta-5W). Three-dimensional thermal-hydraulic and stress analyses were carried out for these four materials. A summary of the results is shown in Table 2-10.

The limiter wall temperature at the coolant side is essentially the same, <200°C, for all materials with small differences due to axial conduction. At this low temperature, the corrosion rate of these materials in water should be acceptable. The maximum temperature in the structure (coating side) varies from 196°C in copper to 449°C in vanadium reflecting the large difference in the thermophysical properties. The ratio of the effective stress to the yield stress is also shown in Table 2-10. These results indicate that under normal operating conditions, all of the materials meet

Table 2-10. Thermal/Stress Analysis of Candidate Limiter Materials[a,b]

	Temperature (°C)		Maximum Effective Stress (MPa)	Yield Stress (MPa)	Effective Yield
	Outer	Inner			
Tantalum, Ta-5W	290	193	249	342	0.7
Niobium, FS-85	404	192	370	370	1.0
Vanadium, V-20Ti	449	191	537	452	1.2
Copper, AMX-MZC	196	182	178	431	0.4

[a] Coolant: Pressure = 600 psi, T_{in} = 115°C, T_{out} = 145°C
Channels = 4 x 8 mm, 1.5 mm thick at outer side.

[b] Peak heat load = 4 MW/m^2.

the allowable stress criteria of Code Case 1592. However, only AMAX-MZC and Ta-5W can meet the more restrictive criteria of 0.75 of the yield strength. Since the thermal stress component dominates the total stress in the limiter, the materials with the highest thermal conductivity and lowest thermal expansion will experience the lowest stress. It should be noted, however, that the results in Table 2-10 are based on conservative assumptions. Furthermore, several modifications in the reference limiter design that can significantly reduce the thermal stress have been identified and are discussed in Sec. 8.4. Therefore, all the four alloys in Table 2-10 are considered viable candidates and the selection of one of them must be made based on additional data from future experimental results in areas such as resistance to radiation damage. For the purposes of this report, the alloy Ta-5W is identified as the reference structural material whenever the need arises to provide only one set of parameters.

The limiter and the first wall are coated with beryllium to eliminate sputtering of the underlying high-Z structural materials. Beryllium is selected as the low-Z coating because its properties make it superior to other candidates. Estimates of the erosion of the beryllium coating were made. The coating on the first wall will erode at a rate of 0.14 mm/yr; therefore, a 1.2-mm coating is adequate for a 7-yr life. The limiter coating will sputter by all ion species with a spatially varying rate. Redeposition of beryllium from the plasma and first wall will also occur. The net effect is that the coating will erode on the wall while it grows on the limiter. The STARFIRE design is developed such that there is no net erosion or growth on the leading edge. This is accomplished by maintaining a beryllium density in the plasma of $\sim 4\%$ of the hydrogen ion density. There will be a net growth of beryllium on the rest of the limiter averaging ~ 0.6 mm/yr. A simple grinding process in place can be performed if necessary to restore the beryllium coating to its original thickness.

The response of the limiter to off-normal conditions was considered as an integral part of the design. The important off-normal events are: (1) plasma disruptions; and (2) loss-of-coolant flow. The concerns with plasma disruptions are the thermal energy dump and the induced electromagnetic forces. The limiter is intentionally located at the outer side of the plasma and centered around the midplane, where a thermal energy dump from a plasma disruption is unlikely. However, when a plasma thermal energy dump on the

limiter occurs, only the coating will be affected. The rate of ablation of beryllium is small enough that several disruptions per year with thermal energy dumps on the limiter can be tolerated.

The electromagnetic forces will always be induced in the limiter in the case of a plasma disruption regardless of where the plasma energy dump occurs. Three electromagnetic effects are produced, with the magnitude strongly dependent on the plasma disruption (current decay) time. The first is a uniform pressure, acting on the outside panels of the limiter. For a plasma disruption time of >10 ms, the maximum induced stress due to this uniform pressure is 0.6 MPa (90 psi) which is a small fraction of the yield stress for the copper, tantalum, niobium, and vanadium alloys. The second effect is a force tending to bend the limiter arm about a toroidal axis. Accommodating this force required an iterative process in the limiter design. In particular, providing a thick root for the limiter (see Fig. 2-6) was found necessary to reduce the moment's arm and the magnitude of the force. With the present reference design, the maximum bending stress is 154 MPa (22000 psi), which is < 40% of the yield stress for the reference structural materials when the plasma disruption time is >10 ms. The third electromagnetic effect is a torque that tends to twist the limiter about a radial axis. For a plasma disruption time of 10 ms, the maximum torque is 46 kN-m resulting in an effective stress which is <60% of the yield stress for all of the four primary structural materials. The magnitude of these forces and torques is reduced substantially at longer, and perhaps more realistic, plasma disruption (current decay) times. The reference limiter design can withstand the electromagnetic effects without any permanent deformation for an unlimited number of plasma disruptions.

2.3.5 Magnets

The magnet systems provide the plasma with confinement and a stable equilibrium configuration as well as some current initiation. The magnets must be superconducting, except for a few control coils carrying relatively low current; otherwise they would consume unacceptable amounts of electrical power. The magnets are large components which experience large forces, which must be resisted with structural material in a manner which minimizes heat conduction to

the magnets operating at liquid helium temperature. Most importantly, they must be extremely reliable, as a magnet replacement is a laborious and time-consuming process.

The superconducting toroidal field (TF) coils and poloidal field (PF) coils have been designed with a cabled conductor consisting of a copper stabilizer and NbTi superconductor, except for the inner turns of the TF coils, where field requirements in excess of 9 T have led to the choice of Nb_3Sn superconductor. In both the TF and PF coils, each cable conductor is contained in its own structure, which bears against the structure of neighboring conductors to transmit radial and axial forces. All coils are bath-cooled by pool boiling liquid helium at 4.2°K. The structure around the conductor contains transverse and longitudinal channels, to carry liquid helium to where cooling is needed and to carry helium vapor away.

The superconducting toroidal field coil system for STARFIRE is a logical, straight-forward extension of present superconducting magnet technology. Table 2-11 is a summary of selected TF coil features and parameters.

The TF coils bear radially inward against the G-10 fiberglass-epoxy centerpost support cylinder, within whose bore is located the inner ohmic heating (OH) and equilibrium field (EF) coils. All of these elements share a common vacuum volume. The centerpost region is surrounded by a common vacuum tank section with individual vacuum tanks surrounding each TF coil outer leg.

The 24 kA conductor for the TF coils is a three level, unsoldered, uninsulated "Rutherford cable", consisting of sixteen 1500 ampere cables, each of which is a six-around-one bundle of similarly configured subcables. Inherent in a cabled conductor design, particularly when employing Nb_3Sn, is its limited ability to support hoop and transverse bearing loads (the latter occurring in the centerpost region of a TF coil). Therefore, in the selected design, the conductor is sandwiched between two pretensioned stainless steel strips for hoop load support, and flanked by two bearing load support strips. Stainless steel is employed for these support elements due to its high elastic modulus and strength.

Nb_3Sn is employed only in the high field (9-11 tesla) region. A bronze diffusion geometry is envisioned, with a tantalum barrier to shield the

surrounding stabilizer material of the composite strand. The Nb is reacted with the Sn of the bronze matrix after the cabling process is complete, but before coil winding.

The NbTi alloy is specified for the three 0-9 tesla field grades. Grading is based upon three centerpost region parameters: amount and type of superconductor required (determined by magnetic field); amount of copper stabilizer required (determined by magnetoresistance, radiation degradation, cryostability and protection criterion limit); and required bearing load support (determined by cumulative radial bearing load).

The STARFIRE reactor has three sets of poloidal field (PF) coils. These are the ohmic heating (OH) coils, the equilibrium field (EF) coils, and correction field (CF) coils. Even though STARFIRE operates in a steady-state mode, it incorporates a small OH coil to provide an inductive voltage over several seconds to initiate a plasma current. The EF coils provide the field which maintains the plasma at equilibrium with the desired position, shape, and current profile. The correction field coils, which link the TF coils, respond to displacements of the plasma to correct those displacements and thus stabilize the plasma. They can respond to plasma motion more quickly without excessive power demands than can the EF coils that are located outside the TF coils. Parameters for the OH and EF coils are given in Table 2-12. The CF coils, because they link the TF coils and must be demountable, are constructed of water-cooled copper.

The EF and OH coils must be superconducting; normal conducting coils would consume an unacceptable amount of power. Being superconducting, these coils must be outside the TF coil system to facilitate maintenance and possible coil replacement. External location of the EF coils exposes the outer TF coil region to large fields, which interact with the TF coil current to generate large out-of-plane (overturning) loads. The magnitude of the overturning moment on each coil is about 1.5×10^9 N m. The centerpost region of the TF coil reacts a small portion of this load. The major portion of the load is reacted in the outer curved coil region, where the distributed out-of-plane load is transmitted from the helium vessel to the surrounding vacuum tank by closely packed pairs of cold-to-warm tiebars. The individual coil vacuum tanks are in-turn supported by substantial intercoil shear panels.

Table 2-11. STARFIRE Toroidal Field Coil Parameters

Number of Coils	12
Total Ampere Turns	2×10^8 A-turns
Total Stored Energy	50 GJ
Total Inductance	174 H
Peak Field	11.1 T
Current	24 kA
Total Weight	6×10^6 kg
Coil Straight Section Height	8 m
Mean Radius of Outer Coil Leg	13 m
Conductor:	
Superconductor	Nb_3Sn/NbTi
Stabilizer	Copper
Configuration	Cable
Coil Cooling	He Bath, 4.2°K
Structural Material	Austenitic, High Mn Stainless Steel

Table 2-12. Ohmic-Heating and Equilibrium-Field Coil Parameters

	OH Coils	EF Coils
Superconductor/stabilizer	NbTi/Cu	NbTi/Cu
Conductor configuration	Cable	Cable
Stability	Cryostable	Cryostable
Cooling	Bath Cooled	Bath Cooled
Operating temperature	4.2°K	4.2°K
Operating current	100 kA	100 kA
Average current density	1400 A/cm	1400 A/cm
Total amp-turns	51 MA-turns	86 MA-turns
Total amp-meters	600 MA-m	2900 MA-m
Peak field	8.0 T	4.5 T
Maximum dB/dt (normal operation)	0.6 T/s	0.2 T/s
Stored energy (self)	1.1 GJ	10.0 GJ
Self inductance*	55 mH	500 mH

* Based on equivalent parallel current of 200 kA.

2.3.6 First Wall/Blanket

The primary functions of the first-wall/blanket of a commercial tokamak reactor are to provide the first physical barrier for the plasma, to convert the fusion energy into sensible heat and provide for the heat removal, to breed tritium and provide for tritium recovery, and to provide some shielding for the magnet system. The first wall must withstand high particle and energy fluxes from the plasma, high thermal and mechanical stresses and elevated temperature operation. Also, the wall must not be a source of excessive plasma contamination. The first wall may or may not be integral with the blanket. The blanket must withstand high neutron fluences, elevated temperature operation, thermal and mechanical stresses, and be compatible with the chemical environment, the plasma and the vacuum.

In the present study, the technological and design aspects of various first-wall/blanket concepts have been considered in the selection of potentially viable designs for STARFIRE. The objectives of the present study involve identification of key technological constraints of candidate tritium-breeding-blanket design concepts, establishment of a basis for assessment and comparison of the critical problem areas and design features of each concept, and development of optimized first-wall/blanket designs for STARFIRE. The major emphasis has been placed on the development of a blanket design that is safe and environmentally acceptable. The primary guidelines established to meet these criteria are low tritium inventory in the blanket, minimal long-lived activation products and minimal stored energy.

Since breeding of tritium is considered essential, and since lithium is the only viable tritium-breeding medium, lithium in some form is required in the blanket. On the basis of engineering and design considerations, liquid lithium provides many advantages for the tritium breeder; however, because of perceived safety problems associated with a liquid lithium system, an *a priori* decision was made to focus the present study on the use of solid lithium compounds for breeding. Although previous studies have assessed the viability of alternate blanket options, a technical evaluation of the design and safety problems associated with liquid lithium, liquid lithium alloys, and molten salt breeding materials was not performed in the present study. The primary objective was to assess the design and performance characteristics of a blanket concept based on solid tritium breeding materials.

The development of the reference STARFIRE first-wall/blanket design involved numerous tradeoffs in the materials selection process for the breeding material, coolant, structure, low-Z coating, neutron multiplier and reflector. The coolant and structural material selections were greatly influenced by the choice of the solid breeder concept which was used as a basis for the STARFIRE design. The most important criteria considered in the selection of potentially viable solid breeding materials include breeding performance, chemical stability, compatibility and tritium release characteristics. Of the two types of solid breeding materials considered as primary candidates, viz., intermetallic compounds and oxide ceramics, only selected ceramics appear to have satisfactory tritium release characteristics. The α-$LiAlO_2$ is selected for the reference design on the basis of the best combination of these critical materials requirements. It is one of the most stable compounds considered and compatibility should not be a major problem; however, adequate tritium breeding is attainable only with the aid of a neutron multiplier. The high tritium solubility and greater reactivity with the structural materials were primary factors in the elimination of Li_2O as the reference breeding material.

Pressurized water, both H_2O and D_2O, and helium were considered for the coolant. Major concerns regarding the use of helium relate to difficult neutron shielding problems, large manifold requirements, leakage into plasma chamber, lower tritium breeding because of the large structure requirements and the high temperatures required for the energy conversion system. An acceptable structural material for use with high temperature helium in a radiation environment has not been identified. Also, design constraints associated with the use of helium as a first-wall coolant appear to be prohibitive. Major advantages of the water coolant are its characteristically low operating temperature and its excellent heat transfer characteristics. However, the use of water with the intermetallic compound breeder materials is probably not acceptable because of the high reactivity, and hence, safety concern. Although D_2O has several neutronic advantages compared to H_2O, the cost is considered prohibitive.

The choices of breeding material and coolant limit the number of viable candidate structural materials. Key factors in the selection of the advanced austenitic stainless steel relate to the steady state reactor operation and

the low operating temperatures characteristic of a water-cooled system. Because of the high thermal stress factor associated with austenitic stainless steel, acceptable first wall lifetimes could not be attained with a cyclic burn. Also, radiation damage effects are less severe at the proposed operating temperatures than at temperatures above 500°C.

The low-Z coating concept for the first-wall is incorporated as part of the plasma impurity control system. The low-Z coating concept provides flexibility in that the structural material can be selected primarily on the basis of structural requirements and the coating can be selected primarily on the basis of surface-related properties. Favorable properties such as high thermal conductivity, high heat capacity and compatibility with hydrogen were important considerations in the selection of beryllium as the first-wall coating/cladding material. A primary consideration in the selection of the candidate coating/cladding is that it can be used on all components exposed to the plasma. This is important because considerable redistribution of the material throughout the chamber is expected as a result of sputtering and ablation.

An effective neutron multiplier is required to obtain adequate tritium breeding with the $LiAlO_2$. Two candidate materials are proposed. Beryllium provides good neutronics performance and can be easily incorporated into the blanket design since it has low density, high thermal conductivity and high heat capacity. Because of the concern regarding limited resources of beryllium, an alternate neutron multiplier Zr_5Pb_3, is also proposed. This compound retains some of the beneficial neutron characteristics of lead but remains solid at the operating temperatures.

Low activation, low cost and inherent safety characteristics were key factors in the selection of graphite over water and stainless steel as the reflector.

A schematic diagram of the reference STARFIRE blanket concept is given in Fig. 2-8 and the key reference parameters are summarized in Table 2-13. The water-cooled blanket module, with a thickness of 68 cm, consists of 1-cm thick first wall, a 5-cm thick neutron multiplier, a 1-cm thick second wall, a 46-cm thick breeding zone, and a 15-cm thick reflector zone that contains the blanket support structure and the manifolding. The modules are 2-3 m wide by $\sim$ 3 m high depending on the location within the reactor. The module

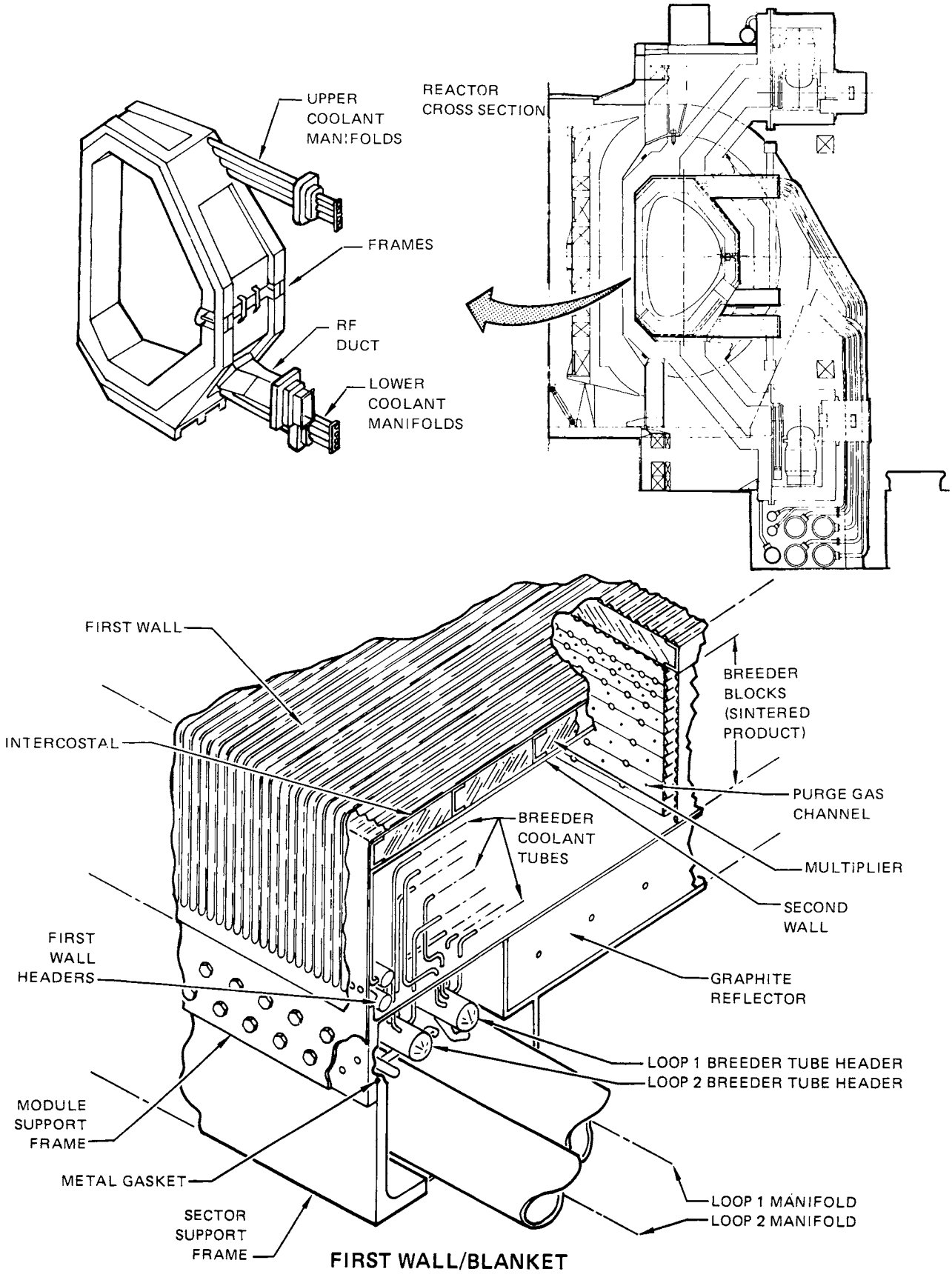

Figure 2-8. STARFIRE blanket concept.

Table 2-13. Summary of First-Wall/Blanket Design Parameters

First-Wall		
	Form	Be-coated panel
	Structural material	Austenitic stainless steel[a]
	Outer wall structural thickness, mm	1.5
	Maximum structural temperature, °C	<423
	Coating/cladding	Beryllium
	Coating/cladding thickness, mm	1.0
	Coolant	Pressurized water, H_2O
	Coolant outlet temperature, °C	320
	Coolant inlet temperature, °C	280
	Coolant nominal pressure, MPa	15.2
	Coolant velocity, m/s	6.1
Neutron Multiplier		
	Material Options	Be / Zr_5Pb_3
	Maximum temperature, °C	490 / 840
	Thickness, m	0.05 / 0.05
	Theoretical density, g/cm^3	1.8 / 8.9
	Effective density, %	70 / 100
	Total mass, kg	51,800 / 356,000
Breeding Region		
	Structural material	Austenitic stainless steel[a]
	Maximum structural temperature, °C	425
	Breeder material	α-$LiAlO_2$ (natural Li with Be) (60% ^6Li with Zr_5Pb_3)
	Theoretical density, g/cm^3	3.4
	Effective density, %	60
	Grain size, 10^{-6} m	0.1
	Maximum/minimum temperature, °C	850/500
	Region thickness, m	0.46
	Coolant	Pressurized water, H_2O
	Coolant outlet temperature, °C	320
	Coolant inlet temperature, °C	280
	Coolant nominal pressure, MPa	15.2
	Tritium processing fluid	He (0.05 MPa)
Reflector		
	Material	Graphite
	Thickness, m	0.15
	Maximum temperature, °C	<800
	Structure	Austenitic stainless steel (low Mo)
	Structure temperature, °C	300-400

[a] Prime Candidate Alloy, an advanced titanium-modified Type 316 austenitic stainless steel.

walls and all support structures in the high-radiation zone are fabricated from an advanced low-swelling austenitic stainless steel. The internal structure is integrally cooled to remove the nuclear heating and maintain the structure below 400°C.

The first wall, which is a water-cooled austenitic stainless steel panel coil, is an integral part of the blanket module. The corrugated plasma side of the first-wall panel is constructed of 1.5-mm thick advanced austenitic stainless steel. The 3.5-mm thick back plate is formed from the same material. The pressurized water coolant is maintained between 280 and 320°C throughout the first wall and blanket. For the average neutron wall loading of 3.6 MW/m^2, the average surface heat flux on the first wall is 0.92 MW/m^2 with a peak-to-average value of $\sim$ 1.2. The maximum structural temperature in the stainless steel wall is $\sim$ 450°C for the reference conditions. For steady state operation at these relatively low temperatures, an estimated wall design life of six years is considered reasonable for the advanced austenitic stainless steel. The proposed panel-type construction provides integral cooling of the blanket wall and avoids the necessity for a large number of pressure boundary tube welds in the high radiation zone. Also, the panel-type structure is perceived to have less vibration problems than an unsupported tube bank.

A $\sim$ 1-mm thick beryllium coating or cladding on the first wall serves to protect the plasma from the high-Z wall material. This thickness will provide sufficient material to withstand the predicted surface erosion for the reference blanket lifetime of six years. The beryllium coating/cladding on the inboard wall will also accommodate the projected number ($\sim$ 10 per wall lifetime) of plasma disruptions for the assumed conditions.

A 50-mm thick neutron multiplier is placed directly behind the first wall to permit adequate breeding with the $LiAlO_2$ breeding material. Two neutron multiplier options, beryllium and Zr_5Pb_3, are carried in the reference design. Beryllium is generally considered to be the most favorable neutron multiplier, however, resource limitations are a concern. The present analysis indicates that beryllium requirements for several hundred reactors are only a few percent of the estimated U.S. beryllium reserves. An important part of the present study was to provide an alternative to beryllium. The Zr_5Pb_3

with an estimated melting temperature of 1400°C provides some of the benefits of a lead multiplier while maintaining the design simplicity of the solid materials. Approximately 30% of the neutron heating is deposited in the multiplier zone. The back side of the first-wall panel and a water-cooled panel (second wall) between the multiplier and breeder region provides cooling that maintains the maximum multiplier temperature at 480°C for beryllium and 850°C for Zr_5Pb_3. Structural webs between the first and second walls provide support for the first wall. The overall reactor analyses of the energy conversion system, the shield, the remote maintenance and repair, and safety are based on the blanket design option with the Zr_5Pb_3 neutron multiplier.

The 46-cm tritium-breeding zone consists of a packed bed of α-$LiAlO_2$ with 1.25-cm diameter stainless steel coolant tubes spaced appropriately throughout the zone to maintain a maximum breeder temperature of 850°C (Fig. 2-9). The spacing of the horizontal tubes increased from $\sim$ 2 cm at the front of the breeder zone to $\sim$ 10 cm at the back. There are approximately 60,000 coolant tubes in the blanket. The nominal coolant pressure is 15.2 MPa (2200 psi) with a coolant inlet temperature of 280°C and an outlet temperature of 320°C. The relatively low temperature of the austenitic stainless steel tubes (< 400°C) and the oxide film on the water side of the tubes provide an adequate tritium barrier for inleakage into the coolant. Natural lithium is used for the beryllium neutron multiplier option; however, 60% enriched ^6Li is required to achieve adequate tritium breeding with the Zr_5Pb_3 neutron multiplier option. The $LiAlO_2$ is in the form of low density (60%) sintered product with a tailored bimodal pore distribution, i.e., a small grain size (< 1 μm) and a fine porosity within particles that are fairly coarse ($\sim$ 1 mm) with a much coarser porosity between particles. The sintered $LiAlO_2$ is perforated with $\sim$ 2-mm diameter holes through which low-pressure (0.5 atm) helium passes to recover the tritium from the breeder. The low density ceramic with a tailored microstructure is proposed to facilitate percolation of tritium (as T_2O) to the helium purge channels. A breeder lifetime of six years before lithium burnup becomes excessive is considered feasible.

The reflector consists primarily of $\sim$ 15 cm of graphite. The support structure to which the blanket modules are attached also serves as the containment for the graphite reflector. In order to conserve space and

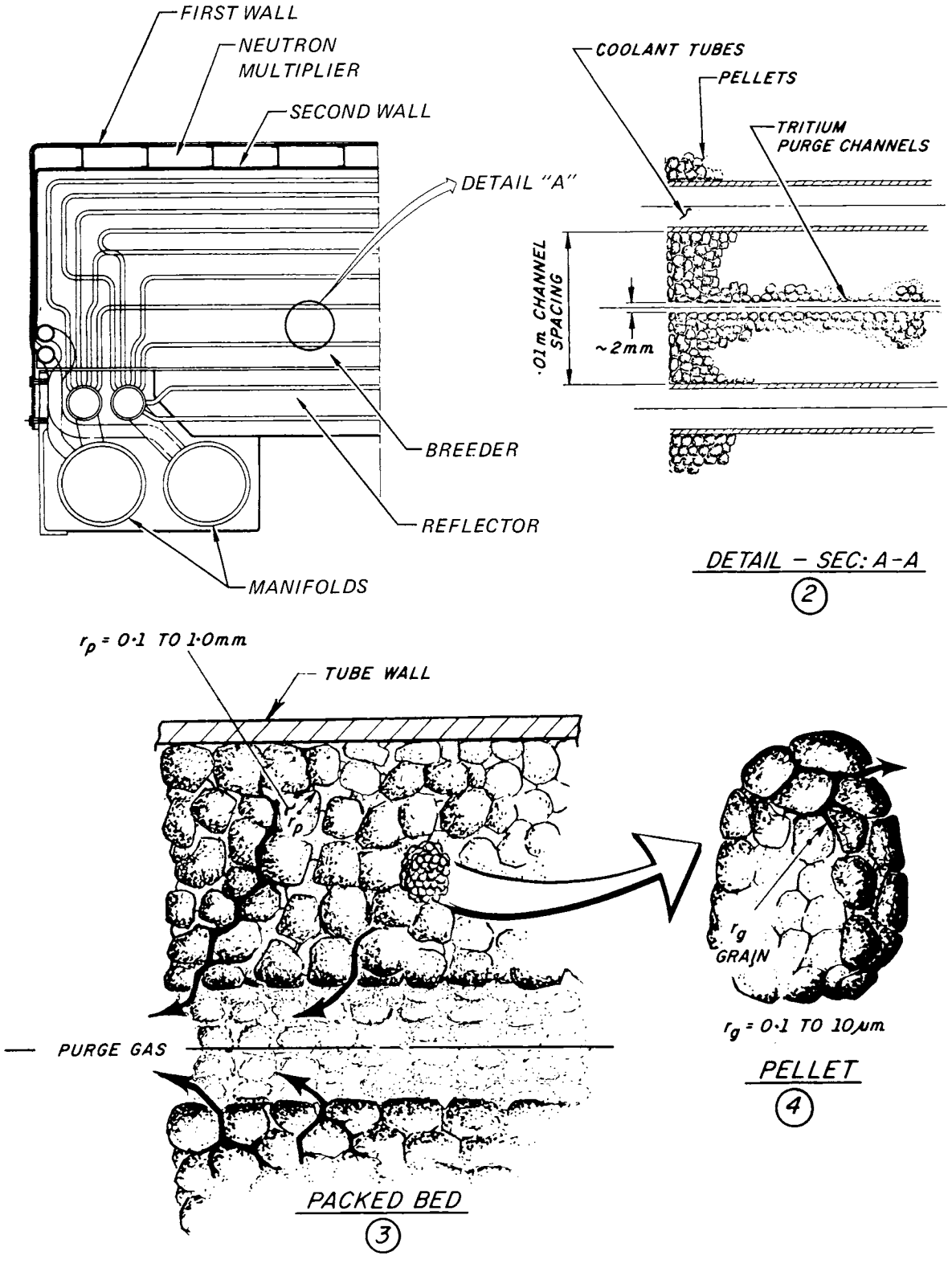

Figure 2-9. Schematic diagram of STARFIRE blanket concept showing solid breeder microstructure and bimodal pore distribution and tritium removal scheme.

improve the vacuum characteristics of the blanket, the manifolds and headers for the blanket are imbedded in the reflector region. The large number of coolant tubes are joined to the headers in a vented chamber that is isolated from both the breeder region and the vacuum chamber. This concept provides both safety and reliability benefits since the most probable coolant leakage problem is at the coolant tube-to-header welds. A coolant-tube weld failure in this chamber would not likely lead to coolant ingress into the breeder region. Also, a small leak at a weld would not destroy the vacuum, and therefore, might not require immediate reactor shutdown. Isolating the geometrically complex manifolds and headers from the plenum region with a relatively smooth rear-blanket surface should substantially improve the vacuum characteristics of the blanket. A modified austenitic steel with low molybdenum content is used in this low-flux region to reduce the long-term activation.

A two-loop coolant system is provided in the blanket to reduce the consequences in the event of a loss-of-flow or loss-of-coolant accident. One loop provides coolant for the first-wall and alternate tube banks in the breeder region beginning with the first row of tubes. The second loop provides coolant for the second wall and the remaining coolant tubes in the blanket. Under the reference plasma shutdown conditions, cooling provided by either loop is sufficient to prevent excessive temperatures in all regions of the blanket. The two-loop concept will also reduce the pressure release and activation release in the event of a coolant-tube failure.

For plasma stability, an electrical conducting path equivalent to 2 cm of stainless steel is required near the first wall. The conductivity of the first wall and the neutron multiplier meets this requirement in the modules. Bimetallic contacts between the modules are provided adjacent to the multiplier region to complete the current path. Upon cooling, these contacts recess into the module wall to allow for sector removal.

The inner blanket is similar in most respects to the outer blanket just described. The major differences, which relate to the breeder zone thickness, the reflector, and the coolant flow direction, are designed to minimize the inner blanket/shield thickness. The breeding zone thickness is reduced from 46 to 35 cm and the graphite reflector is eliminated with a modest penalty

on tritium breeding capability. Vertical coolant flow in the inner blanket eliminates the need for manifolds in the back of the blanket module, thereby improving the effective shielding capability of the inner blanket/shield.

2.3.7 Radiation Shielding System

The shield design in STARFIRE has evolved from a comprehensive approach that involved the following considerations: (1) recognition of the importance of the shield system and its impact on reactor component reliability, simplicity, maintainability, and economics; (2) a full accounting of shielding considerations in the selection process of key reactor subsystems from the early stages of the reactor design; examples of this are the choices of the limiter instead of divertor for plasma impurity control and exhaust and the selection of lower-hybrid rf system for plasma auxiliary heating in preference to neutral beams; and (3) comprehensive trade-off analyses for determining the material composition and dimensions of the shield components.

The design criteria for the shield included: (a) protection of all reactor components from excessive nuclear heating and radiation damage; (b) the biological dose rate outside the shield at 24 h after shutdown should be sufficiently low, $\sim$ 1-2 mrem/h, to facilitate personnel access into the reactor building; and (c) material composition and dimensions of the shields were selected so that all reactor components, including the shields, outside the blanket are recyclable within 50 years or less.

The shield system in STARFIRE consists of the blanket, primary bulk shield, penetration shield, component shield, and biological shield. Table 2-14 shows the material compositions and dimensions of the bulk shield (inboard and outboard regions) and penetration shields. State-of-the-art analyses, including multidimensional Monte-Carlo calculations, were performed for the reference design.

The space problems in the inboard region have been resolved by trade-off studies as discussed in Chap. 5. The inboard blanket/shield thickness, Δ_{BS}^{i}, is 1.2 m. This includes space for 9-cm vacuum gaps between the blanket and shield, shield and TF coils and thermal insulation inside the TF vacuum tank; 3-cm vacuum tank (alloy Fe14Mn2Ni2Cr, referred to as Fe-1422) and 7-cm helium vessel (stainless steel). The inner blanket is 37-cm thick and must breed

Table 2-14. Material Composition and Dimensions of Bulk and Penetration Shields

Component	Major Radius (m)	Thickness (m)	Composition
(A) Inboard Shield[a]			
Shield Jacket	4.47	0.02	Fe-1422
Shield 1	4.45	0.15	10% Fe-1422 + 10% H_2O + 80% W
Shield 2	4.30	0.075	10% Fe-1422 + 10% H_2O + 80% B_4C
Shield 3	4.225	0.15	10% Fe-1422 + 10% H_2O + 80% W
Shield 4	4.075	0.075	10% Fe-1422 + 10% H_2O + 80% B_4C
Shield 5	4.00	0.075	10% Fe-1422 + 10% H_2O + 80% W
Shield 6	3.925	0.075	10% Fe-1422 + 10% H_2O + 80% B_4C
Shield Jacket	3.85	0.02	Fe-1422
(B) Outboard Shield[b]			
Shield Jacket	10.54	0.02	Fe-1422
HFS Shield	10.56	0.50	5% Ti6Al4V + 65% TiH_2 + 15% B_4C + 15% H_2O
MFS Shield	11.06	0.40	70% Fe-1422 + 15% B_4C + 15% H_2O
LFS Shield	11.46	0.18	Fe-1422
(C) Vacuum System Shield			
Shield Jacket	---	0.02	Fe-1422
(C-1) Upper Duct-Shield			
Shield 1	---	0.30	5% Ti6Al4V + 65% TiH_2 + 15% B_4C + 15% H_2O
Shield 2	---	0.28	70% Fe-1422 + 15% B_4C + 15% H_2O

Table 2-14. (Continued)

Component	Major Radius (m)	Thickness (m)	Composition
(C-2) Lower Duct-Shield			
Shield 1	---	0.30	5% Ti6Al4V + 65% TiH_2 + 15% B_4C + 15% H_2O
Shield 2	---	0.18	70% Fe-1422 + 15% B_4C + 15% H_2O
(C-3) Pump Pod Shield	---	0.48	70% Fe-1422 + 15% B_4C + 15% H_2O
(D) RF-System Shield			
In the Plenum	---	0.10	Fe-1422
Outside the Bulk Shield	---	0.15 max.	Fe-1422

(a) The major radius is for the outer surface at the reactor midplane.

(b) The major radius is for the inner surface at the reactor midplane.

tritium as the breeding margin with the solid breeder is small. The inboard shield is 54 cm thick and consists of alternating layers of tungsten and boron carbide with water for cooling and Fe-1422 for structure as shown in Table 2-14.

Table 2-15 shows the maximum radiation effects in the inboard section of the TF coils. The maximum radiation-induced resistivity in the copper stabilizer after 40 yr operation, is 2.2×10^{-10} Ω•m, assuming a magnet anneal every 10 yr with 83% recovery. The maximum radiation dose in the shield dielectric break is 7.4×10^{7} Gy after 40 yr operation.

The outboard bulk shield is 1.1 m-thick. It includes 2-cm shield jacket at the plenum region with the rest divided into three regions. The first region, in the high flux zone, is 0.5-m-thick and has a material composition of 5% Ti alloy + 65% TiH_2 + 15% B_4C + 15% H_2O. The second region, middle zone, is 0.40-m-thick with the material composition as 70% Fe-1422 + 15% B_4C + 15% H_2O. The third region, outer zone, is 0.18-m-thick of Fe-1422. At reactor shutdown, the biological dose rate in the reactor building is ∿ 130 mrem/h and is dominated by the contribution from the decay of ^{56}Mn and ^{54}Mn. Due to the short half-life of ^{56}Mn, the biological dose rate in the reactor building decays very rapidly and reaches ∿ 1.5 mrem/h at 24 h after shutdown. These dose rates are calculated with all shielding in place. Although the STARFIRE plans call for fully remote maintenance, the dose rate of 1.5 mrem/h shows that personnel access into the reactor building with all shielding in place is permissible within one day after shutdown. This provides a degree of confidence in improving the plant availability factor, if desired, by allowing some maintenance tasks to be carried out in contact or semi-remote mode.

One of the important shield considerations is radiation streaming through void regions that penetrate the blanket and bulk shield regions. In general, the direct radiation flow in neutral beam ports, divertors, etc., has been one of the primary sources of design complexity and shielding difficulties in previous tokamak designs. In the STARFIRE design, a serious effort has been devoted to minimizing possible design difficulties associated with these penetrations. The STARFIRE design features the selection of a lower-hybrid rf system in preference to a neutral beam heating system and a limiter impurity control concept rather than divertors. A great advantage of the rf and limiter/vacuum systems is the elimination of any direct radiation streaming

Table 2-15. Maximum Radiation Effects in the TF Coil (in the inboard region)

Maximum nuclear heating in the superconductor (MW/m^3)	1.54×10^{-5}
Maximum nuclear heating in the helium tank (MW/m^3)	3.18×10^{-5}
Maximum nuclear heating in the vacuum tank (MW/m^3)	4.76×10^{-5}
Maximum dose in the electrical insulator[(a)] (Gy)	$1.22 \times 10^{+7}$
Maximum dose in the thermal insulator[(a)] (Gy)	$2.39 \times 10^{+7}$
Maximum dose in the dielectric break[(a)] (Gy)	$7.41 \times 10^{+7}$
Maximum fast neutron fluence ($E > 0.1$ MeV) in the superconductor[(a)] (n/m^2)	$1.87 \times 10^{+21}$
Maximum radiation induced resistivity in the Cu stabilizer[(a)] (Ω-m)	2.17×10^{-10}

(a) After 40 years of operation.

path from the plasma to the reactor exterior. These design features have helped reduce the shielding problems to a manageable level and brought about overall simplicity in the shield design.

Radiation streaming through the limiter duct increases the nuclear heating rate by about a factor of 10 in a relatively small region of the bulk shield (centered around the midplane). This presents no difficulty in the shield design. The maximum nuclear heating in the cryopanels of the vacuum pumps is ~ 0.3 kW/m^3, which poses no difficult heat removal problems.

The STARFIRE design employs an rf-wave launching method for the plasma heating as well as for the plasma current drive. From a radiation shielding standpoint, the rf system is very attractive in that bends can be tolerated in the rf ducts and also that the waveguide structural materials (PCA stainless steel in the reference design) along with the water coolant flowing

through the structure prevent, to a substantial degree, the direct radiation flow from coming out through the waveguides.

In order to hinder radiation streaming into the plenum region, the duct portion inside the plenum is completely surrounded by a 0.1-m thick Fe-1422 shield. In addition, the duct portion in the reactor room is fully shielded by the same material of 0.15 m, which is aimed primarily at reducing the impact of the rf penetration on the potential increase in the post-shutdown biological dose inside the reactor building.

2.3.8 Radioactivity

The most important concern with regard to induced-activation is the production of radioisotopes with very long half-lives (> 50 — 100 yr) in relatively large volumes of materials; this results in (1) requirements for permanent radwaste storage, and (2) depletion of some resource-limited materials. An important strategy for fusion reactor development, therefore, is to avoid generating any large inventories of high-level, long-term activation products so that a majority of the reactor construction materials could be recycled on a reasonably short time-scale, e.g., a human generation of $\sim$ 30 yr after component replacement or reactor decommissioning. This strategy has been adopted in STARFIRE and has considerably affected the material selection.

2.3.8.1 Component Activation and Material Recycling

The importance of the major radioisotopes has been examined in terms of radioactivity and radioactivity-related parameters such as biological hazard potential (BHP) in air and BHP in water. With regard to material recycling, an effort has been devoted to establishing a criterion for potential material recycling categorization. In addition to the conventional waste level classification by specific radioactivity concentration (Ci per unit volume), a criterion based on the contact biological dose has been suggested and used for the recycling analysis.

It is found that the magnitude of high-level, long-term radwaste from STARFIRE is dominated by the PCA first wall/blanket structural material. It is shown, however, that the average annual discharge rate of PCA from STARFIRE

is only about 9.5 m^3 ($\sim$ 75 metric tons in weight) which is considerably less than a typical annual discharge of high-level waste from an LMFBR of the same power. Note that because the power density is lower in fusion than in fission systems, the reactor material volume that is potentially activated is larger. However, the degree of biological hazard potential associated with STARFIRE is significantly lower. For example, the BHP-air of STARFIRE varies as air volumes of 57 km^3, 0.03 km^3 and 0.004 km^3 per kWth reactor power at post-shutdown times of 1 yr, 100 yr and 1000 yr, respectively. These values are compared to the corresponding BHP-air's of $\sim$ 550 km^3, $\sim$ 100 km^3 and 80 km^3 in a typical LMFBR system.

Figure 2-10 shows the time-dependent radioactivity concentration contributed by each constituent element of the PCA first wall structure. In addition to the PCA activation, the radioactive products generated in the blanket come from the Zr_5Pb_3 neutron multiplier and the $LiAlO_2$ tritium breeder. The long-term activation of the $LiAlO_2$ breeder is governed solely by ^{26}Al (half-life of 7.2 x 10^5 yr) and its concentration is $\sim$ 2 Ci/m^3 at times greater than a few months after shutdown. Recycling of $LiAlO_2$ or Li is desirable and appears to be technically feasible but needs to be addressed in future studies in detail.

The activation level of most reactor components external to the blanket, including the major penetration subsystems, decays to a category of low-level waste in 30 yr at most. Thus, the potential for recycling of materials from most reactor components is excellent. Table 2-16 classifies major reactor components according to high (R) and low (N) potential for recycling the material.

2.3.8.2 Decay Afterheat

The total decay-heat in the Zr_5Pb_3 multiplier design is $\sim$ 88 MW at shutdown which is $\sim$ 2.2% of the total reaction thermal power. This decay-heat is reduced to $\sim$ 40 MW within 24 hr, followed by a rapid decrease beyond that time period, reflecting the decay of the most dominant radioactive isotope of ^{89}Zr (78 hr). Approximately half of the decay-power comes solely from the Zr_5Pb_3 activation decay. The decay heat from the alternate neutron multiplier of beryllium is about an order of magnitude lower than that from Zr_5Pb_3.

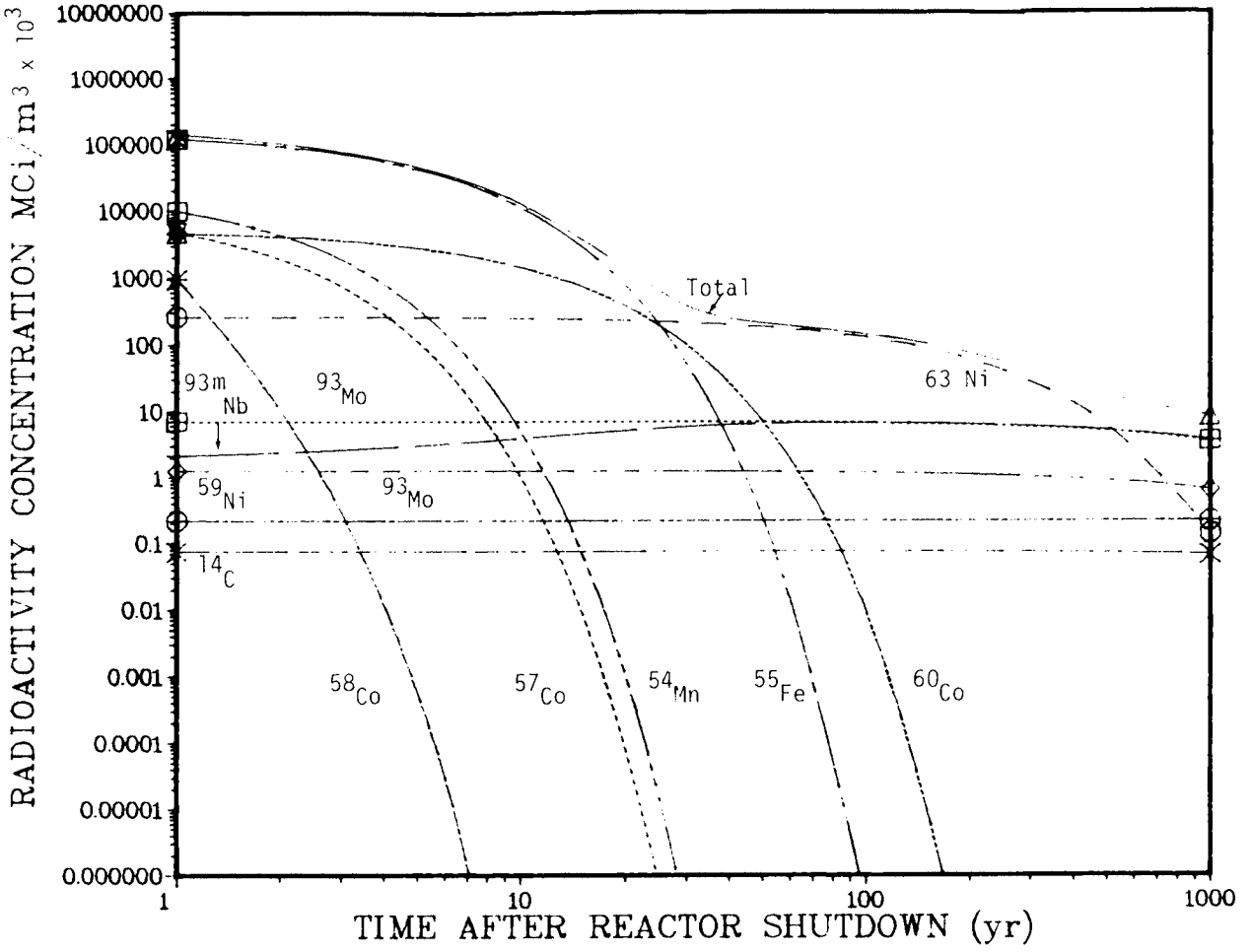

Figure 2-10. Isotopic radioactivity contribution for STARFIRE - PCA First Wall.

Table 2-16. A Classification of STARFIRE Component Radioactivities

Component	Mass (Mg)	Class[a]
First Wall/Blanket		
PCA	450	N
Zr_5Pb_3	329	R
$LiAlO_2$	605	N-R[b]
C	163	R
Bulk Shield	8770	R
Vacuum Shield	6688	R
TF-Magnets	6240	R
OH/EF-Magnets	1931	R
CF-Magnets	140	R
Support Structure	1852	R
Reactor Building	175400	R

(a) R: The contact biological dose rate at the surface of 1 m-diameter sphere is below 2.5 mrem/hr within 30-50 yr after component replacement or reactor decommissioning; the potential for recycling is high.

N: The biological dose is greater than 2.5 mrem/hr; the potential for recycling is low.

(b) The dose is high but since it comes from Al, which can be chemically separated, recycling potential for lithium is high.

2.3.8.3 Reactor Room Activation

Three different gases – air, nitrogen (N_2) and carbon-dioxide (CO_2) - were considered for the reactor building. The magnitude of induced-activation was compared for the three gases. It was found that the residual radioactivity in both air and N_2 atmospheres is only about a factor of 4 lower than the current maximum permissible concentration (MPC) for ^{14}C. The isotope ^{14}C is produced in both air and nitrogen via the (n,p) reaction. In addition, the activation of argon in the air makes a large contribution during reactor operation and for a short time after shutdown. The CO_2 activity is due largely to the $^{16}O(n,p)^{16}N$ reaction. The ^{16}N isotope has a 7.1 s decay half-life. Therefore, its activity decays very quickly (in about 10 minutes). Beyond this time period, the CO_2 activation is determined by the radioactivity of ^{14}C which comes in this case from the $^{13}C(n,\gamma)$ reaction.

2.3.9 Heat Transport and Energy Conversion

The thermal energy deposited in the blanket, first wall and limiter is delivered via the heat transport system to the steam power conversion system where it is converted to electricity. Two separate heat removal systems are utilized, a dual loop circuit for the blanket/first wall and a single loop for the limiter.

The dual loop system was chosen for the blanket/first wall in order to virtually eliminate the possibility of a complete loss of coolant in the blanket, and to reduce the building over-pressure occurring as a consequence of certain loss of coolant events. The primary coolant system consists of piping and valves, pumps, pressurizers, steam generators, water makeup and conditioning equipment, and instrumentation and controls. Inlet and outlet ring manifolds are located beneath the reactor. Each circuit incorporates two vertical straight-tube-and-shell steam generators, two vertical single-stage shaft seal pumps and a single pressurizer, all located within the reactor building. The main piping and manifolds are about 1 m diameter, and piping and valving are incorporated such that individual blanket segments, steam generators or pumps can be isolated from the rest of the system. Because of the steady-state operating mode, a thermal energy storage system is not required, and tritium concentrations in the primary coolant are maintained low enough such that an intermediate loop is not needed.

Primary coolant at 15.2 MPa (2200 psi) leaves the blanket at 320°C and is returned at 280°C. The pressure drop through the system is about 1.0 MPa (150 psi) and the electric power required to pump the primary coolant is about 30 MW.

The thermal energy deposited in the limiter, about five percent of the total power, is transported via the single loop limiter feedwater circuit and utilized for feedwater heating in the power conversion system. This system incorporates piping and valves, pumps, a pressurizer, feedwater heaters, a water conditioning system and the appropriate controls and instrumentation. Water coolant at an operating pressure of 700 psi leaves the limiter at 145°C and is cooled to 115°C in the feedwater heat exchangers. Coolant is transported via ring manifolds beneath the reactor and piping beneath the building floor. The pumping power is less than 3 MW. As in the primary loop,

system components are located within the reactor building and are mounted in standard modules. This modularity approach is consistent with the total remote, remove-and-replace maintenance philosophy for those systems which are potentially contaminated with tritium or activated particulates.

When the reactor is shut down, initial cooling of the blanket and first wall is provided by one of the primary loops. However, as the heat load decreases and the coolant temperature drops, the residual heat removal system takes over this task. This lower pressure system is plumbed into both of the primary loops at the inlet and outlet ring manifolds so that cooling may be provided through either of the primary loop blanket circuits. The system is sized for a maximum heatload of 60 MW, the blanket and first wall afterheat generation rate approximately 12 h after shutdown and the earliest time at which blanket maintenance would begin.

2.3.10 Tritium Systems

The fuel cycle for STARFIRE is shown in Fig. 2-11. The system is designed to reprocess tritium for fueling, process the tritium produced in the blanket, control the amount and location of tritium in the plant and process tritiated wastes. Fully redundant and modular units, multiple processing paths and location in a separate tritium facility provide maximum reliability, availability and maintainability. The existence of multiple, isolated pathways reduces both the impact of a single unit's failure and the magnitude of an associated-tritium release.

The high fractional burnup (0.42) for STARFIRE results in a minimized tritium inventory in all fuel processing systems. This reduces the magnitude of a possible tritium release in the reactor building to approximately 10 g (as T_2O). In the tritium facility as much as 50 g of T_2 could be released if multiple failures occur in an isotope separation unit.

The inventory in the STARFIRE plant is designated "vulnerable" or "nonvulnerable" (Table 2-17) depending upon the degree of control which can be enforced on a system and also the physical state of the tritium in that system. The tritium within the blanket (10 kg) is considered "nonvulnerable" since it is tenaciously retained by the solid breeding material and thus is relatively immobile. The tritium in the pump and fuelers (in the reactor building) is considered "mobile." The total "vulnerable" inventory for STARFIRE is less than 400 g.

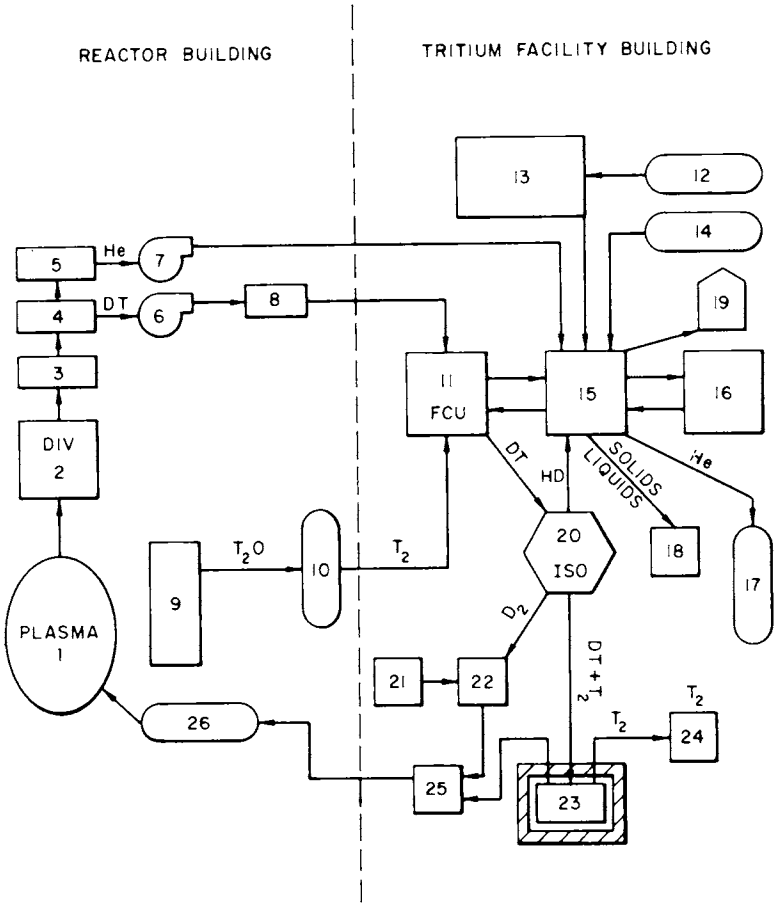

1. Plasma Chamber
2. Limiter Plates
3. Debris Separator
4. D-T Cryocondensation Pump
5. Helium Pump
6,7. Regeneration Pumps
8. Metal Bellows Pumps
9. Breeder Blanket
10. Electrolysis Unit
11. Fuel Cleanup Unit
12. Tertiary Enclosures
13. Atmospheric Tritium Recovery System
14. Secondary Enclosures, Purge Streams
15. Tritiated Waste Treatment
16. Tritiated Water Recovery Unit
17. Helium (tritium-free)
18. Tritiated Waste -- Liquids and Solids
19. Detritiated Gases: N_2, O_2, CO_2, Ar
20. Isotopic Separation Unit
21. D_2 Supply
22. D_2 Storage
23. DT and T_2 Storage
24. T_2 Shipment/Receiving
25. Fuel Blender
26. Gas Fueling

Figure 2-11. Fuel cycle scenario for STARFIRE.

Table 2-17. Reference STARFIRE Tritium Parameters

Plasma Parameters	
Plant Availability	0.75
Thermal Power (MW)	4000
Energy Per Fusion (pJ)	3.22
Ion Density (ions/m^3)	8.06×10^{19}
Plasma Volume (m^3)	783
Particle Confinement Time (s)	1.8
Reflection Coefficient	0.9
Fractional Burnup	0.42
Tritium Mass Flow Rates (g/d)	
Tritium Burnup	536
Tritium Fueled	1296
Tritium Exhausted	760
Tritium Bred	562
Deuterium Mass Flow Rates (g/d)	
Deuterium Burned	360
Deuterium Fueled	865
Impurity Mass Flow Rates (g/d)	
Helium Exhaust	712
Iodine Exhaust	$\sim$ 50
Protium Exhaust	$\sim$ 10
Carbon Exhaust	$\sim$ 10
Nitrogen Exhaust	$\sim$ 10
Oxygen Exhaust	$\sim$ 10

The design goal for tritium releases from the STARFIRE fusion plant is less than 5000 Curies per year in all forms (gas, liquid and solid waste) averaged over operating, standing, and maintenance phases and including in-plant releases. The sources and amounts of tritium release are shown in Table 2-17. The primary release pathway is leakage in the coolant system.

2.3.11 Electrical Storage and Power Supplies

The STARFIRE electrical system is somewhat simpler than that for a pulsed device due to the steady state operation. There is no requirement for an energy storage system, and the electrical energy required for startup of the power system is taken directly from the local power grid. Some capacitive energy storage is provided for use in conjunction with the correction field (CF) coil power supply. Major parameters of the electrical power system are shown in Table 2-18.

The TF coil power supply charges the TF coil and compensates for the power losses in the normal temperature current carrying devices which make up the interconnections between superconducting coils. Because the coils are de-energized infrequently, the charging voltage (100 V) and the charging time (12 h) are moderate. Dump switches which open in the event of a TF coil fault are provided so that coil energy can be dissipated in dump resistors.

The EF coil power supply is a 1417 volt system. A free-wheeling diode is connected across the power supply output terminals. In order to protect against loss of phase, failed thyristor, or over-current conditions, standard protection schemes and equipment are provided. A dump circuit is incorporated to limit the voltage across the coil to 85 kV during emergency shutdown. A form of liquid rheostat is utilized to increase the dump resistance from 0 ohm to 0.8 ohms during the 2.5 seconds over which the energy is removed from the coil.

The CF coil power system provides the energy dissipated in the normal coils, bus work, thyristors, etc. Energy is transferred between each of the four CF coils and a common energy storage device (capacitors) via a dc-ac-dc

Table 2-18. Electrical Power System Parameters

Toroidal Field Coil Power Supply	
Primary Voltage	13.8 kV
Input Power	3.2 MVA
TF System Charging Voltage	100 V
TF System Charging Time	12 h
Equilibrium Field Coil Power Supply	
Input Voltage	13.8 kV
Input Power	290 MVA
Power Supply Voltage	1417 V
Ohmic Heating Coil Power Supply	
Primary Voltage	13.8 kV
Input Power	3.2 MVA
Charging Voltage	12 V
Correction Field Coil Power Supply	
Primary Voltage	13.8 kV
Power Supply	3 MVA
Power Supply Voltage	5000 V
Energy Storage Capacity	10 Megajoules

converter system. Energy is delivered to the coils through a force commutated chopper switch and returned to storage from the coils by way of a force commutated inverter, transformer and rectifier.

The 12 volt ohmic heating coil power supply with series blocking diodes in the bus from the power supply is connected across the ohmic heating coil. A series combination of an adjustable resistor and a diode is in parallel with this superconducting coil. The series combination is connected so as to block current during the coil charging period. The use of blocking diodes in series with the 12 volt, 200 kiloampere power supply protects the power supply from the coil reverse voltage and eliminates the necessity of mechanical switches to perform this function.

2.3.12 Support Structure

The primary requirement in the design of the reactor support structure system was to safely react all loads acting on reactor components resulting from magnetic, thermal, pressure, gravity and seismic forces. Additional key considerations were the simplification of routine maintenance tasks (e.g., blanket sector changeout) and the design of structural components to serve multiple functions where practical.

The design of the support structure system was strongly influenced by the large out-of-plane magnetic forces acting on the TF coils, which result from the requirement that all superconducting EF coils be located outside the TF coils. This requirement, which precludes "interlocking" of superconducting coils, was considered fundamental to achieving a maintainable reactor design for which a failed superconducting TF or PF coil could be replaced within acceptable downtimes.

The method selected to react the forces was to surround the helium vessel of each TF coil with a room-temperature vacuum tank, and to rigidly connect the outer legs of the tanks of adjacent TF coils with thick vertical steel panels. The forces acting on each helium vessel are transmitted to the surrounding vacuum tank through struts fabricated from a high strength fiberglass having low thermal conductivity. The tank beams the loads to the pinned joints which attach the panel corners to the dewar. The loads for each coil are equal in magnitude and opposite in direction on either side of the midplane; thus the loads in each panel are balanced out by attaching its vertical sides to the vacuum tank surface to effect a shear tie along the sides.

Other major components of the system are the centerpost, thermal isolation struts, blanket/shield support pedestals, upper and lower vacuum pump support assemblies, and EF coil vacuum tanks and supports. The centerpost, constructed of fiberglass laminate, reacts the centering forces from all twelve TF coils, and reacts a small part of the TF coil out-of-place forces as two torques acting in opposite directions on the centerpost top and bottom. The centerpost loads are reacted to the building floor through a set of fiberglass thermal isolation struts.

The blanket/shield support pedestal is a beam-and-web structure which attaches to the bottom of each TF coil vacuum tank to react loads from the blanket and shield sectors to the building floor. The overhead support frame support assembly provides support for dump resistors and supports vacuum pump assembly and duct shielding. The two large-diameter EF coils are supported from the TF coil vacuum tanks by tripod-shaped beam assemblies.

All metallic components of the system are constructed of Nonmagne 30, a nonmagnetic austenitic manganese steel with low nickel and chrome content, selected to reduce activation of the structure and to minimize the use of resource-limited elements.

2.3.13 Cryogenic Systems

The cryogenic system for STARFIRE is a single central system which supplies the required quantities of liquid helium and liquid nitrogen to the user locations near the reactor and in the fueling facility. By far the largest cryogenic requirement is for the superconducting toroidal field coils, with lesser requirements for the superconducting EF/OH coils, the fueling and tritium processing system, and the vacuum system cryopumps. The cryogenic system is a relatively straightforward system requiring no new technology, but should benefit from future improvements in reliability, economy and operating efficiency.

Cryogenic refrigeration is supplied at two temperature levels. Vaporization of liquid nitrogen at 80°K is used for thermal shielding of the liquid helium cooled components and precooling of warm helium gas in the helium refrigerator-liquifier. This liquid nitrogen is supplied to the user systems from a central pressurized storage dewar. The nitrogen gas is returned to the closed cycle nitrogen liquefaction plant where it is condensed and returned to the supply dewar. The nominal liquefaction capability of the nitrogen plant is 1,500 ℓ/h.

Refrigeration at 4.2°K is supplied by pumping liquid helium from the central LHe storage dewar through LN_2 shielded vacuum jacketed transfer lines to the location of the component requiring cryogenic refrigeration. The liquid helium is vaporized and returned to the central helium refrigerator-liquifier as either cold or warm gas depending on the user requirements. The

return helium gas is liquified and returned to the central supply dewar. The nominal liquefaction capability of the liquid helium system is 26.5 kℓ/h. A large medium pressure helium gas storage facility supplies make up gas to the system and is used to store the helium when the cryogenic system is warmed up.

The major parameters of the cryogenic system are listed in Table 2-19.

Table 2-19. Cryogenic System Parameters

Liquid Helium Supply Rate	
TF Coils	15,000 ℓ/h
EF/OH Coils	6,600 ℓ/h
Other	4,900 ℓ/h
Helium Refrigeration of 4.2-4.5°K	20 kW
Liquid Helium Storage	100,000 std. m^3
Gaseous Helium Storage	70,000 std. m^3
Liquid Nitrogen Supply Rate	
Helium Liquifier - Refrigerator	900 ℓ/h
TF Coils	100 ℓ/h
EF/OH Coils	50 ℓ/h
Other	450 ℓ/h
Liquid Nitrogen Storage (@ 0.3 MPa)	40,000 ℓ
Total System Electrical Power	7 MW

2.3.14 Instrumentation and Control

The conceptual design of STARFIRE has not included the detail required to completely specify and design the I&C system. The system description anticipates future developments in I&C technology.

It is estimated that up to 50,000 signals will require processing and that a 1 millisecond update rate will be required. Other key features of the system are:

- o Distributed network architecture
- o Integrated safety system
- o Multiple redundant elements for improved reliability
- o Modular instrumentation -- integral with subsystems
- o Wireless data links -- 2.5 MHz and 50 MHz

Architecture

A distributed network should be a good match for the available computer and instrumentation technology, taking advantage of what appears to be a natural evolution toward distributed intelligence in control systems. In addition, it provides improved response for direct digital control loop computation times compatible with plasma and electromechanical requirements. It further provides considerable reduction of network communications traffic to the control room through exchange of only summary and setpoint control information with local controllers.

Central control room displays are provided in the form of color graphic diagrams on flat panels of convenient size, which are capable of providing either summary information or any desired depth of detail to suit operational requirements at any particular time. Commands will be given by voice, leaving the operators free to concentrate upon plant operations, except where hand/eye or simulated touch are appropriate, as in controlling remote handling equipment.

A central data base is maintained at the supervisory level, which centralizes information requests and updates. This central data base is also used by other supervisory level computer systems. These service the control room displays; provide historical records of normal and alarm conditions;

provide sequencing information for startup, shutdown, and response to unusual conditions; and provide archive access to outside users, such as power dispatch controllers, utility management, and regulatory agencies.

Access is also provided to a plant simulation computer, for use in evaluating unusual situations and predicting plant responses to various commands. Since this system is capable of 100 times concurrent real-time simulations, it is assumed to be a large supercomputer located remotely and shared by many plants of the STARFIRE design.

Integrated Safety System

Safety functions have been integrated into the design of the STARFIRE I&C System. It is anticipated that this will be possible because of hardware advances which will provide electrical isolation between various sensors and measuring subsystems, distribution of intelligence to multi-fold dedicated subsystem controllers, and economical multiply redundant elements at all levels of the I&C System. This will provide operators with all information relevant to any potentially hazardous situations.

Redundancy

Redundancy will be employed extensively to permit reliable operation with a minimum of system downtime, particularly in the area of the reactor itself.

Modularity

It is intended that instrumentation be integrally designed with subsystems and components. All plasma instrumentation is intended to be similarly carried with and installed as part of the blanket modules and be modular with the annual blanket replacement cycle, so that a complete new redundant set of all required instrumentation will be installed each year. This means that such instrumentation will have six-fold redundancy and need only be designed for a six year service life in the reactor environment.

Wireless Data Links

Use of wireless transmission is designed to achieve electrical noise and fault isolation, reduction of labor and containment wall penetrations, and elimination of radiation effects on cables and connectors. In addition, maintainability and replacement are simplified. These links may use light, microwaves, or both.

Remote Maintenance

Requirements for remote maintenance will dictate many features of the reactor subsystems designs, but systems using industrial robot technology will be available for performance of the required functions remotely. It is expected that by the time of STARFIRE, such systems will be capable of performing such tasks as visual recognition of objects, grasping, feeling, hearing, and connecting basic operations and movements to perform complex operations with a minimum of human supervision.

Development Areas

It is anticipated that much of the technology required for STARFIRE I&C will be developed on natural evolutionary lines, independent of the Fusion Energy program. Three areas requiring specific development have been identified, however. These include the development of radiation-resistant sensors, electronics, and optical components; provision for a plasma access as a deliberate part of reactor design; and development of fully engineered plasma instrumentation modules and systems.

2.3.15 Material Inventory

The material requirements for a single STARFIRE reactor have been tabulated and are presented in Appendix C. The material requirements for the remainder of the plant would typically be common with current generating systems.

Table 2-20. Materials Inventory for Each STARFIRE Reactor Categorized by Material

Material	Initial Requirements Volume (m^3)	Initial Requirements Mass (tonnes)	Life of Unit Requirements[a] Volume (m^3)	Life of Unit Requirements[a] Mass (tonnes)
PCA				
FW	3.6	28.6	30.6	214.5
SW	2.6	20.5	22.1	153.8
Breeder	22.2	174.7	188.7	1310.3
Reflector	5.7	44.7	48.4	335.3
Jacket	19.0	149.3	161.5	1119.8
Headers & Manifolds	4.1	32.2	34.9	241.5
		450.0		3375.2
H_2O (Primary)				
FW	2.0	2.0		
SW	1.3	1.3		
Breeder	11.3	11.3		
Reflector	5.7	5.7		
Headers & Manifolds	29.5	29.5		
H_2O (Shield)	9.3	9.3		
Inner Shield				
Outer Shield	144.8	144.8		
Vacuum Duct Shield	175.0	175.0		
Zr_5Pb_3[b]				
Multiplier	36.8	328.0	73.6	656.0
$LiAlO_2$ (60% enriched)[b]				
Breeder	178.1	606.5	356.2	1213.0
C[b]				
Reflector	102.0	164.0	204.0	328.0
W[d]				
Inner Shield	44.0	840.0		
Outer Shield	0.0	0.0		
Vacuum Duct Shield	0.0	0.0		
		840.0		
B_4C				
Inner Shield	26.3	66.0		
Outer Shield	144.8	362.0		
Vacuum Duct Shield	174.8	437.0		
		865.0		
TiB4				
Inner Shield	0.0	0.0		
Outer Shield	25.9	117.0		
Vacuum Duct Shield	6.6	30.0		
		147.0		
TiH_2				
Inner Shield	0.0	0.0		
Outer Shield	336.0	1310.0		
Vacuum Duct Shield	86.1	336.0		
		1646.0		
Fe1422 (Low Mo steel)				
Inner Shield	12.1	95.9		
Outer Shield	487.0	3858.0		
Vacuum Duct Shield	736.0	5830.0		
RF Duct Shield	6.9	55.0		
TF Magnet Vacuum Tank	123.0	974.0		
Common Dewar	8.8	69.9		
Anti-Torque Panel	132.4	1050.9		
Blanket/Shield Pedestal	52.8	418.0		
Equipment/Coil Supports	4.1	32.2		
OH Magnet Vacuum Tank	6.9	54.9		
EF Magnet Vacuum Tank	31.4	249.1		
		12,687.9		

Table 2-20. Materials Inventory for Each STARFIRE Reactor Categorized by Material (Continued)

Material	Initial Requirements Volume (m^3)	Initial Requirements Mass (tonnes)	Life of Unit Requirements[a] Volume (m^3)	Life of Unit Requirements[a] Mass (tonnes)
Cu				
TF Coil Stabilizer	179.3	1598.0		
OH Coil Stabilizer	8.6	77.1		
CF Coil Conductor	15.7	140.0		
EF Coil Stabilizer	41.9	372.9		
		2188.0		
G-10 Insulator				
TF Coils	32.1	61.0		
OH/EF Coils	45.8	87.0		
Centerpost Supports	0.7	1.4		
Centerpost	147.0	279.3		
		428.7		
Nb_3Sn				
TF Magnet	6.4	51.0		
NbTi				
TF Magnet	8.9	57.0		
OH, EF Magnets	5.1	33.0		
		90.0		
Ta5W[b,c]				
Limiter	1.9	32.0	3.8	64.0
Be				
FW Coating	0.5	1.0	4.3	8.5
Limiter Coating	0.1	0.2	0.9	1.7
		1.2		10.2
304 Stainless Steel				
TF Magnet Helium Tank	143.0	1124.0		
TF Coil	293.1	2304.0		
OH Magnet Helium Tank	12.8	101.0		
OH Magnet Helium Tank	10.2	80.2		
EF Magnet Helium Tank	62.1	488.0		
EF Coil	49.4	388.0		
		4,485.2		

Notes:

[a] For reactor only Life-of-unit requirements are same as initial requirements except where otherwise indicated.

[b] Life of unit requirements for these materials are twice the initial requirements, to account for anticipated recycling within a short period of time following removal from the reactor.

[c] Tantalum (as Ta-5W) is only one of several candidates for the reference design limiter (see Sec. C-3).

[d] Tungsten can be replaced by another shielding material (see Sec. C-3).

2.4 BALANCE OF PLANT

The balance of plant facilities for STARFIRE are a combination of features common to any large power plant, and elements peculiar to the fusion technology. For example, the steam generators, turbine-generator and main condenser components of the power conversion system are generic to power plants. The tritium reprocessing facilities, the electrical and rf power supply building, and the hot cell, in which fully remote repair and maintenance functions are performed, are unique to a fusion power plant.

In the overall plan of this fusion power plant, closely related facilities are combined into the same buildings that are then located to achieve a functional and economical layout. The principal buildings and their spatial relationships are summarized below:

1. The reactor building contains the tokamak fusion reactor and supporting systems.
2. To the south of the reactor building is the turbine and support building that contains the energy conversion equipment, a reactor service area in which blanket sections and other new reactor subsystems are prepared, a plant auxiliary area that houses the closed loop cooling water system, and the hot cell.
3. The electrical and rf power supply building is placed to the east of the reactor building and the tritium reprocessing and cryogenics building is located to the north of the reactor building.
4. The administration, facility control and site service complex is located to the south of the turbine and support building.

The balance of the plant facilities are shown on the site plan of Fig. 2-1 and in layouts of Chap. 20.

2.4.1 Site Plan

Principal site elements include buildings, roads, walks, fencing, and surface and subsurface mechanical and electrical equipment and utilities, most notably the large natural draft hyperbolic cooling towers. The site elements are located and arranged to minimize piping, electrical, and utility runs and at the same time provide adequate separation between buildings and other elements.

2.4.2 Facility Buildings

The reactor building is a steel-lined, hardened ribbed box structure constructed of reinforced concrete designed for DBE seismic loading and 0.16 MPa (24-psig) internal pressure. Modifications of the primary coolant loop have resulted in decreasing the maximum anticipated overpressure to 100 kPa (15 psi). The 1.5 m thick building outside walls and roof prevent penetration by tornado missiles, withstand a tornado-induced differential pressure, and provide adequate shielding.

The reactor building houses the reactor and related systems that can potentially become contaminated. These systems are modularized to permit removal. A partial height, shielding wall and sliding doors separate the module area from the reactor to minimize activation of materials in the system module area. The pressure boundary of the building is lined with steel to provide a leak-tight boundary and minimize tritium release in the event of a loss of primary coolant within the building.

The reactor building is 120 m long and 50 m wide (inside clear dimensions), and consists of three levels in addition to the crane maintenance balcony. A 600-tonne-capacity bridge crane spans the width of the building and runs its entire length. The reactor and system modules are located on the ground level.

The first level below ground is a pipe chase. All pipelines, conduits, and other connections between the reactor and the modules are routed through the pipe chase to provide clearance for the remote maintenance equipment on the ground floor. The pipe chase, reactor hall, and system module areas are subject to overpressure under accident conditions. Access to the pipe chase is by two removable hatches, one at each end of the building on the ground floor.

The second level below ground is the routinely occupied subgrade floor, which is not subject to overpressure, significant radiation, or a tritium atmosphere. The rf system components and HVAC mechanical and electrical equipment are located on this level.

The remote maintenance system is employed in the reactor building and also extends to the hot cell. The equipment runs on a solid monorail track, arranged to allow movement of system components into position to perform remote maintenance and repair functions on the process module equipment, the ATR systems, the HVAC equipment, as well as the reactor itself.

In addition to the floor mounted equipment, the overhead bridge cranes and electromechanical bridge manipulators assist in the maintenance functions by providing access to the top and upper equipment areas of the reactor and various modules not accessible to other systems. The 60-tonne bridge crane at the process module end of the building is capable of lifting and removing process equipment for repair and replacement.

Preparation of blanket segments and other new reactor subsystems, equipment, and parts is carried out in the reactor service area, a ground level high bay area between the hot cell and turbine building, and adjacent receiving end of this building, where there is also access for large vehicles and other equipment. Storage spaces for new blanket segments and other reactor and process module components are provided.

The hot cell is a carbon steel lined, concrete-hardened structure designed for DBE seismic loading. The building outside walls and roof are thick enough to prevent penetration by tornado missiles, to withstand a tornado-induced differential pressure, and to provide adequate shielding.

The hot cell contains three process areas. The liquid waste processing equipment separates activated particulate matter from tritiated water that is then returned to the tritium reprocessing building. The remote maintenance and repair shop contains equipment for shield door seal and latch mechanism replacement and for repair of failed process module components. The blanket module and solid waste processing cell contains the equipment required to bake out tritium from spent blanket segments and to reduce the segments into pieces conveniently sized for storage in canisters. Both wet and dry solid waste storage facilities are provided in the blanket module and solid waste processing cell. Wet storage for 600 m^3 of spent blanket segments and dry storage for 400 m^3 of discarded shield doors, pumps, valves, and piping is available.

The portion of the tritium reprocessing building that contains potentially contaminated areas is hardened in accordance with applicable seismic and tornadic design criteria, and is lined with carbon steel to minimize the escape to atmosphere of potential tritium release from process equipment. Tritium-free areas of the building are occupied on an every day basis and are separated from potentially contaminated areas by an air lock. Piping to and from the reactor building and hot cell is double walled, with quick-acting isolation valves located close to the building walls. The piping is routed to the reactor building pipe chase in an underground tunnel.

2.4.3 Mechanical Systems

The power conversion system consists of components of conventional design for use in large central generating stations. The thermodynamic cycle and its components resemble the thermal cycle of a pressurized water reactor plant. The 4000-MW of thermal energy generated by the reactor is transferred to the power conversion system by the heat transport system.

The facility heat rejection system consists of three hyperbolic natural draft cooling towers; eight wet pit, vertical-type centrifugal pumps; a chlorination package; an evaporation pond; and a raw water reservoir for makeup. The cooling towers are reinforced concrete, approximately 150 m in diameter at the basin, 100 m in diameter at the top, and 165 m in height. The pump house provided for the pumps and chlorination package contains a well with individual compartments for each pump and filter.

The closed loop cooling water system provides demineralized and deionized cooling water to reactor auxiliary components and reactor building cooling systems during normal plant operation. It consists of three half-capacity pumps, three one-third-capacity heat exchangers, a surge tank, and the necessary piping, controls and instrumentation. The system is connected to the standby cooling water system to provide cooling water to the atmospheric tritium cleanup systems and the solid waste pools during normal operation. The connections include isolation valves that close automatically when the standby cooling water system goes into operation, or when the closed loop cooling water system is shut down for any reason.

The standby cooling water system provides demineralized and deionized cooling water to the residual heat removal system, atmospheric tritium

removal systems, solid waste pools, and control building chillers during abnormal operating conditions. Operation of the system occurs, for example, during an incident when the reactor has been shut down, offsite power is unavailable, and the plant is using the onsite standby power source. The system operates whenever the reactor is shut down and maintains the blanket temperature within specified limits by removing the residual or decay heat. The system cools the blanket indirectly by providing the cooling medium to the residual heat removal system that in turn cools the blanket. The standby cooling water system also provides cooling water to the three atmospheric tritium removal (ATR) systems located in the reactor building, the tritium reprocessing building, and the hot cell. Components of the system include a dry cooling tower, two full-capacity pumps, a surge tank and the necessary instrumentation and controls.

2.4.4 Building Services

The reactor hall is provided with six recirculation systems by which the atmosphere gas (CO_2) is filtered and conditioned. The recirculation systems are divided into two groups of three units each, supplied from two different power sources. A total of four units operate normally, and two units are on standby, thereby allowing flexibility of operation. In the event of a loss-of-coolant accident, the fan coil units are capable of maintaining the temperature of the reactor building atmosphere at or below 54.4°C.

The reactor hall is at a negative pressure with respect to the environment, and two 100% capacity pressure control fans are provided. When the concentration of tritium within the reactor hall is detected to be above the normal concentration, the pressure control fans are de-energized, and automatic isolation of the building takes effect. This operation calls for automatic shift of the atmospheric air cleanup system from the normal 10% to full capacity operation. The atmospheric cleanup system provides for removal of tritium and/or particulates within the reactor hall.

The hot cell employs 100% recirculation of filtered and tempered air to the different zones. Two 100% capacity pressure control fans are provided to maintain differing pressure requirements among confinement zones. The

assignment of pressure zones ensures confinement of the potentially contaminated atmosphere and prevents its migration to other parts of the facility. Pressure assignments are such that the flow of air is from areas of lesser to areas of higher potential for radioactive contamination. The design incorporates isolation of the hot cell when it is determined that the concentration of tritium in the hot cell atmosphere is beyond the normally acceptable concentration. Upon isolation, the atmospheric tritium removal system located inside the hot cell runs at full capacity.

The tritium reprocessing area, which has the highest potential for radioactive contamination within the tritium reprocessing building, is provided with a dedicated recirculating HVAC system. Minimum outdoor purge air for ventilation is filtered and conditioned for supply to the area. As in the hot cell and the reactor hall, it is expected that the atmospheric tritium removal system will operate at 10% capacity during normal operating modes. Full capacity operation will be in effect upon the detection of an unacceptably high concentration of tritium in the area.

2.4.5 Electrical Systems

The plant is designed with adequate auxiliary electrical equipment, standby power and protection to ensure operation of the essential station auxiliary equipment during normal operation and all emergency conditions.

Offside power is used for startup and shutdown, i.e., the plant is not designed with "black starting" capability. Power is generated continuously so that an intermediate energy storage system is not required. Major electrical equipment associated with power generation, auxiliary electrical power supply and distribution, onsite standby power generation, and extra-high voltage (EHV) switchyard systems have been identified. These systems and equipment are within state of the art technology or technology currently being developed.

A double bus system is used as a minimum to supply power to equipment required for continuous operation and/or orderly shutdown. The distribution of power to two or more identical items of equipment is such that a failure of a

power supply bus does not result in a complete loss of a particular mechanical or electrical function. All vital control and protection systems and equipment are powered from uninterruptible power supply (UPS) systems.

A function of the main generator and its connections is to generate 1440-MWe power (gross), to deliver power to the plant unit auxiliary transformers, and to deliver the net electrical power through the main step-up transformer and switchyard to the EHV transmission system network. The generator is provided with a breaker to allow isolation of the generator during startup, shutdown, and maintenance, while the main step-up transformers and the unit auxiliary transformers supply offsite power for the auxiliary system.

It is anticipated that a minimum of two full-capacity EHV transmission lines will be connected to the switchyard of the plant. The primary function of the switchyard is to provide an onsite EHV switching facility that can provide a power outlet for the unit and that can receive and provide the offsite power required for startup and shutdown when the main generator is off the line. The arrangement of the switchyard is based on a double-bus, breaker-and-a-half scheme that provides the flexibility and reliability required for a plant of this size.

The auxiliary electrical power supply and ac distribution system provides continuous power to the plant auxiliary equipment for startup, normal operation, and shutdown. Each auxiliary electrical power supply bus has two sources of power supply, one from the unit auxiliary transformers, and the other from the reserve station service transformer is implemented when the unit auxiliary power supply fails. Electrical loads that are vital for an orderly shutdown of the plant are grouped separately. Feeders to coil and rf power supplies are duplicated or divided so that a single switchgear bus or feeder failure does not result in loss of a function.

Power at 480 V is provided by double-ended load center type substations located throughout the plant approximately in the center of their respective loads. Each transformer of a double-ended unit is fed from a different 13.8-kV bus for better flexibility and service continuity.

Reliable and continuous dc battery power is required for a variety of uses, such as "trip" and "close" of electrically operated circuit breakers, solenoid-operated valves, control systems, vital lighting, the station annunciators, and devices used during turbine coast-down. Through dc/ac inverters, the batteries are also used to provide power to the turbine-generator and reactor protection system, and to instrumentation required for an orderly shutdown.

The function of the onsite standby ac power system is to generate an onsite ac source of auxiliary power if the preferred offsite source is lost. This system consists of two redundant, onsite gas-turbine generators. Each generator is connected to a pair of redundant 4160 V switchgear bus systems. The connected loads on these buses consist of equipment and systems required for an orderly shutdown of the plant.

Facilities electrical services provide adequate lighting including emergency lighting; provide the necessary grounding for systems and equipment, including a separate grounding system for "low" signal level instrumentation and controls; provide necessary systems for communication, including telephone, public address (PA and PAX), and sound-powered telephone systems for testing and maintenance where required; provide adequate lightning protection; and provide necessary cathodic protection.

Electrical equipment is arranged and located to minimize length of runs for interconnections and to facilitate maintenance and testing. Major electrical equipment is located in separate electrical rooms with adequate space provided for cable and raceway connections. Raceways are grouped for ease of installation and common mechanical protection. They are dedicated to the particular type of cable, and those containing different types of cable are separated. Raceways and cables serving the onsite standby ac power systems and associated with redundant equipment required for an orderly shutdown are physically separated and isolated from their redundant counterparts, and are designed to withstand DBE seismic forces.

2.5 PLANT CONSTRUCTION

The schedule for plant construction shows that six years will be required between the time the first concrete is poured until initial power delivery. The pacing time in the construction schedule is the reactor building and reactor. Approximately three years is required to prepare the reactor building for initial installation of the reactor components. Two years is required for reactor erection and one year is allowed for reactor and plant tests. Reactor building construction proceeds until the roof over the reactor area is complete and the 600 tonne overhead crane is complete. One end of the reactor building is left open and temporary crane rails extended to permit direct entry of major reactor components. Modularization, with factory assembly and checkout, of reactor components is used where possible. Off-site winding of magnets and fabrication of blanket and shield sectors is planned with water shipment to the site. The overall construction schedule is discussed in Chap. 23. Further reductions in overall construction time may be achievable with advances in modularization of plant components and improvements in current transportation capabilities.

2.6 OPERATION AND MAINTENANCE

A goal of the STARFIRE design has been to maximize utility compatibility not only in current practice but also with anticipated trends for future utility operations. The Utility Advisory Group has provided insight to current utility practice.

Startup power is drawn from the grid and after plasma initiation the reactor power is brought up slowly to minimize the thermal stress effects on the blanket and steam generators. Once operating, the plant has the ability to load-follow at a rate of 5% of rated power increase or decrease per minute, although the plant is designed as a base load unit. The plant will normally operate continuously with one scheduled shutdown per year for maintenance. It is anticipated, however, that 1 to 3 other major shutdowns per year will occur as a result of component failures. Once the reactor is

shut down it can be restarted to full power in approximately 1/2 h; however, approximately 12 h will be required for a restart if the TF coils are discharged for maintenance or if the vacuum chamber has been breached briefly. After major vacuum chamber breaches 36 hours is required for restart.

Three major startup conditions are anticipated:

1. Startup after maintenance that requires opening of the vacuum chamber to the building environment. Opening the vacuum chamber requires the blanket sectors be cooled down to near ambient temperature and the TF coils to be discharged (e.g., for blanket replacement). Thirty-six hours are required to clean the vacuum walls for startup.

2. Startup after maintenance at the reactor where it is unnecessary to breach the vacuum. TF coil discharge is necessary to permit maintenance equipment manuevering about the reactor. TF coil recharging will require 12 h. In addition, if the primary coolant loop has been shut down, approximately 13 h is required for warm up.

3. Startup after shutdown not requiring reactor maintenance (turbine trip etc.). The TF coil charge is maintained and the primary loop is kept hot.

The plant is expected to operate at full power under normal conditions; however, the fueling ratio can be adjusted to reduce the power. In event of redundant component failures the reactor power can be reduced to the appropriate level and operation continued until the failure can be corrected. Redundant systems, where continued operation at reduced power is possible, include the vacuum system where power reduction is necessary after four pump failures and the steam generators where shutdown for excessive leakage would require operation at 50% power during repairs.

Shutdown sequence of the reactor is normally the reverse of startup and requires approximately 1 h to reach a hot shutdown and approximately 20 h to reach a cold shutdown.

The STARFIRE reactor and maintenance facility designs have been developed based on the assumption that a mature fusion economy exists and that all facets of the design have been demonstrated in previous power plants. The premise that a fully understood technical basis exists for STARFIRE leads to the assumption that components can be replaced periodically to prevent

unscheduled failures from dominating the maintenance needs. The plant availability goal is 75% and the system reliability requirements have been established accordingly based on the projected time for replacement of system components.

The complexities of a fusion system will reduce the achievable availability as compared with PWR'S if the same technology is assumed. However, advances in automated maintenance technology and simultaneous development of the maintenance system and reactor designs are believed to offer benefits that make the 75% availability goal reasonable. The maintenance system must receive as much attention from the outset of the design as any other major system in order to achieve this goal. The reactor maintenance schedule was developed to fit within the typical utility Balance-of-Plant maintenance scenario. It includes an annual shutdown for four weeks (28 days) to perform maintenance and inspection, and a four-month (120 days) shutdown every ten years for overhaul of the turbine-generator. During this period the TF coil system is also annealed. This results in an average annual scheduled outage of 37 days.

In addition, current utility experience indicates that approximately 20 days downtime per year is caused by failures in the balance-of-plant (BOP). As a result of these constraints the following downtime allocations were made as listed in Table 2-21.

Table 2-21. Downtime Allocations

Balance-of-Plant		Reactor	
Scheduled	Unscheduled	Scheduled	Unscheduled
37 days	20 days	37 days	34 days

The 37 days of reactor scheduled maintenance is derived from the assumption that the reactor will be maintained simultaneously with the BOP on a noninterference basis. The total of 57 days outage required for BOP maintenance leaves 34 days for reactor unscheduled maintenance if the 75% availability (91 days outage/year) is to be achieved.

A total remote maintenance facility has been designed for all equipment located within the reactor building and hot cell. The major benefit is that this approach minimizes radiation exposure to maintenance workers. All known or foreseen maintenance operations are planned as remote; however, operational flexibility has been provided by design of the reactor shielding to permit personnel access within 24 h after reactor shutdown.

The reactor design was developed to permit removal of all components, however, the vacuum pumps and isolation valves and the blanket require scheduled, routine maintenance. Shield door seals, limiters and rf grilles are replaced with blanket sectors. Ease of replacement of these items has therefore been emphasized. Reactor scheduled maintenance does not dominate annual plant downtime, therefore, several scheduled operations can be added without affecting reactor availability. Failure of life-of-plant items such as the magnets or shield can be permitted to result in longer outages since their failure will be infrequent.

The blanket sectors are expected to require replacement every six years. An annual replacement sequence is planned whereby four sectors are replaced each year to level out the maintenance tasks and permit the reactor scheduled maintenance to fit within the normal utility practice of a four week per year outage for the balance-of-plant maintenance. Blanket sectors are removed as a unit with limiters, rf grilles and ECRH ducts in place. When the sectors are changed shield door seals are replaced. Total time for replacing two sectors is $\sim$ 10 days.

Vacuum pumps and valves require replacement every two years, hence 1/2 are replaced at each scheduled outage. Total time for replacement of 1/2 the vacuum pumps and valves is 20 days annually.

The maintenance facilities consist of the reactor building, the hot cell, the reactor service area and the remote maintenance control room. Remote maintenance developments in major nuclear facilities have been utilized in developing the STARFIRE maintenance approach and design.

The reactor building contains the reactor, selected support system modules, and required maintenance equipment. The reactor is located at one end of the building. The support system modules are organized within the

central area. The other end of the building contains the crane bay maintenance area, the personnel airlock to the crane bay maintenance area, the equipment airlock between the hot cell and the main floor of the reactor building, laydown space for the support system modules, and parking space for the reactor building maintenance machines. The reactor and the support system are maintained with (1) equipment that is mounted on a monorail system; (2) overhead cranes; and (3) bridge-mounted electro-mechanical manipulators. All viewing is by means of remote CCTV. Building area lighting and special lighting in maintenance areas are required.

A shield wall isolates the reactor from the support system modules and permits maintenance of the modules while the reactor is operating. This wall serves as a neutron shield for the modules and as a missile shield for the reactor. Doors provide ingress and egress for the monorail system.

The support system modules located in the reactor building are limited to only those subsystems which are potentially contaminated with significant radioactive contamination. These are:

- o Tritium processing and cleanup
- o Reactor building HVAC
- o Coolant water
- o Steam generators
- o Primary loop components
- o Limiter feedwater loop components
- o Vacuum pumps

The modules are designed for total remote maintenance using monorail-mounted maintenance machines and the overhead cranes and electro-mechanical manipulators. The modules are positioned within the reactor building to provide adequate access for the remote maintenance machines. Maintenance of the support system modules is accomplished by removing and replacing a whole module or by removing and replacing a failed subcomponent within a module. The failed module or subcomponent is transported to the hot cell, on the monorail, for further repair or disposal.

A single monorail system provides maintenance access to the reactor and to the support system modules and allows equipment and material movement in the reactor building and the hot cell. The large monorail track provides

stability for the maintenance machines as well as the required load carrying capacity. While a maintenance machine is in position to perform a given task, additional stability is obtained by locking the machine to the monorail. Power and control for the maintenance machines is supplied by busbars on the monorail. Machines have been defined for maintenance of the reactor. The machines are preprogrammed for all planned activity. Intermediate checkpoints will be programmed into operational sequences to stop equipment for verifying position and for performing inspections.

The hot cell is located outside of the reactor building to localize contamination products and permit independent operation. An equipment air lock connects the reactor building to the hot cell. Communication between the hot cell and the reactor building is via a monorail system. The equipment airlock and hot cell are sized to handle all reactor building components.

The hot cell consists of a central corridor containing the monorail. At one end of the corridor is the air lock entrance to the reactor building. At the opposite end of the corridor is a decontamination chamber. The decontamination chamber is connected to the turbine and support building by another airlock. All processing, handling and storage within the hot cell is on either side of the monorail corridor. Shield doors isolate the monorail corridor from the cells. Turntable switches connect the monorail with these cells.

Specific tasks performed in the hot cell are:

- o Blanket disposal
- o Solid waste packaging
- o Holdup treatment of nontritiated liquid and gaseous wastes
- o Remote maintenance of activated components
- o Decontamination of non-activated components for out-of-cell handling
- o Emergency tritium cleanup
- o Wet and dry storage of activated components

Maintenance and repair of activated components takes place in the hot cell remote maintenance and repair shop. All maintenance and repair work is done using servo-manipulators, overhead bridge cranes and bridge mounted electro-mechanical manipulators. Typical maintenance operations include reactor shield door seal renewal, reactor shield door latch repair, rf duct

repair, limiter replacement, blanket repair, fuel system repair, vacuum pump isolation valve repair, support system module and subcomponent repair, and maintenance equipment repair. Once repaired, testing and check-out of the refurbished components takes place. Some repair work on nonactivated components may be carried out in the hot cell. A case-by-case evaluation will be necessary to determine if decontamination is more expedient than remote maintenance.

Decontamination of nonactivated components takes place in the decontamination chamber. From the decontamination chamber the components can enter the reactor service area through an air lock. The reactor service area provides hands-on repair and testing of decontaminated, nonactivated components.

2.7 POWER FLOW

The reactor delivers 4000 MW_{th} to the power conversion system which generates 1440 MWe. A circulating load of 240 MWe results in 1200 MWe of power deliverable to the grid. A power flow diagram is shown in Fig. 2-12.

2.8 ECONOMICS

The total direct and indirect costs are summarized in Table 2-22 for both 1980 constant year dollars and 1986 then-current dollars. Also shown is the total busbar energy cost for the fusion generated energy along with the major contributors to the costs. These costs are higher than are currently being projected for new fission plants. However, it must be noted that the cost of energy shown here is for the initial year of operation. The levelized cost of energy (for 30-yr economic life) is actually comparable to those estimated for future LWRs and is lower than that for coal. The reason for this is that, for a given power plant, the cost of energy increases from year to year because of escalation in fuel, maintenance and operation costs. The cost of fuel is negligible in STARFIRE while it represents $\sim$ 25% and 40% of the cost of energy in LWR and coal, respectively.

The cost estimate of STARFIRE is specific to this system, reflecting the unique ground rules applying to this study. It should be noted that this study is a preconceptual design with some subsystems not fully developed or defined. For these subsystems, the cost estimates were determined with implicit design allowances to account for the lack of complete definition. Fortunately, many of the balance of plant and heat transport systems are similar to

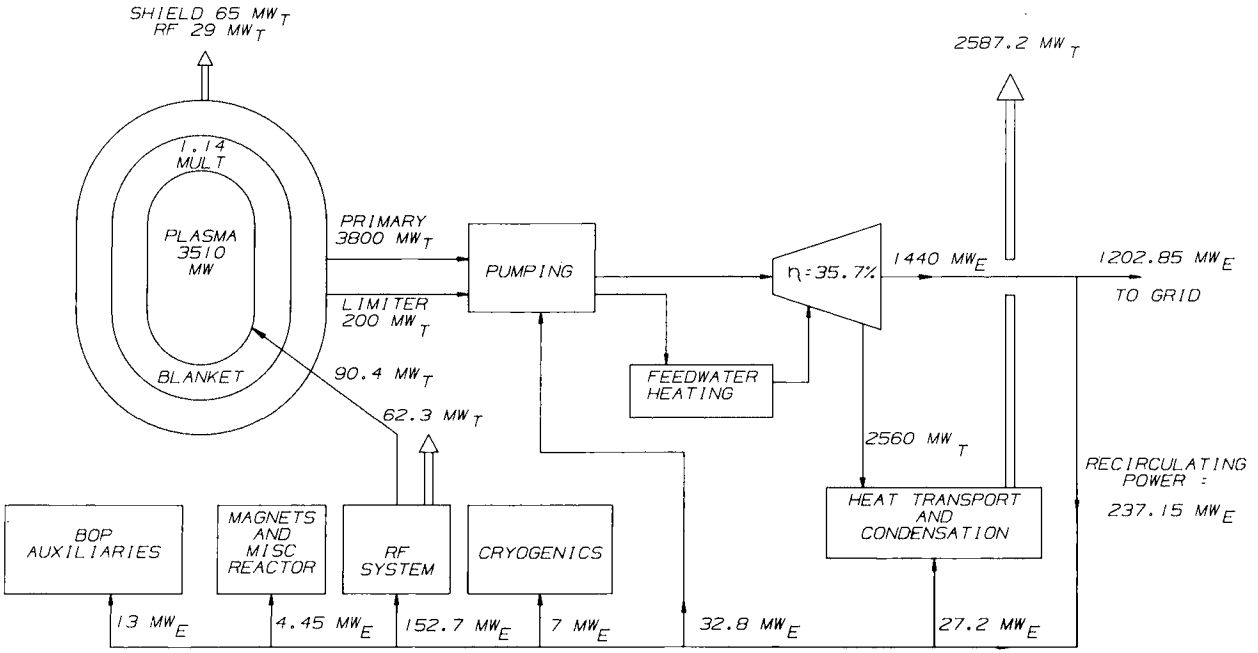

Figure 2-12. Power flow diagram.

Table 2-22. STARFIRE Summary Costs

ACCOUNT NUMBER	ACCOUNT TITLE	COSTS (1980 $ x 10^{-6})		
20	LAND AND LAND RIGHTS	3.30		
21	STRUCTURES AND SITE FACILITIES	346.58		
21.02	Reactor Building		157.44	
21.03	Turbine Building		35.92	
21.07	Hot Cell Building		53.69	
21.99	Contingency Allowance		44.95	
22	REACTOR PLANT EQUIPMENT	968.62		
22.01	Reactor Equipment		589.26	
22.01.01	Blanket and First Wall			82.36
22.01.02	Shield			186.07
22.01.03	Magnets			171.57
22.01.04	RF Heating and Current Drive			33.49
22.01.05	Primary Structure and Support			52.74
22.01.07	Power Supply, Switching and Energy Storage			52.90
22.02	Main Heat Transfer and Transport Systems		69.84	
22.05	Fuel Handling and Storage Systems		38.60	
22.06	Other Reactor Plant Equipment		43.75	
22.06.01	Maintenance Equipment			38.30
22.06.02	Special Heating Systems			0.00
22.06.03	Coolant Receiving, Storage and Make-Up Systems			0.24
22.06.04	Gas Systems			0.08
22.06.05	Inert Atmosphere System			0.00
22.07	Instrumentation and Control		23.41	
22.07.01	Reactor I&C Equipment			7.61
22.07.02	Monitoring Systems			1.76
22.07.03	Instrumentation and Transducers			14.04
22.98	Spare Parts Allowance		66.38	
22.99	Contingency Allowance		117.68	
23	TURBINE PLANT EQUIPMENT	249.68		
23.01	Turbine-Generators		77.33	
23.03	Heat Rejection Systems		44.34	
24	ELECTRIC PLANT EQUIPMENT	117.28		
25	MISCELLANEOUS PLANT EQUIPMENT	40.77		
	TOTAL DIRECT COST	1726.48		
91	CONSTRUCTION FACILITIES, EQUIPMENT AND SERVICES (10%)	172.65		
92	ENGINEERING AND CONSTRUCTION MANAGEMENT SERVICES (8%)	138.12		
93	OTHER COSTS (5%)	86.32		
	SUBTOTAL	2123.57		

Table 2-22. STARFIRE Summary Costs (continued)

		1980 CONSTANT	1986 THEN-CURRENT
94	INTEREST DURING CONSTRUCTION	246.70	671.69
95	ESCALATION DURING CONSTRUCTION	0.00	462.63
	TOTAL CAPITAL	2400.27	3197.89
	$/kWe	2000	2665

TOTAL BUSBAR ENERGY COST

	ANNUAL COST ($ x 10^{-6})	
	1980 CONSTANT	1986 THEN-CURRENT
ANNUALIZED COST OF CAPITAL	240.43	479.68
OPERATIONS AND MAINTENANCE	19.41	26.01
SCHEDULED COMPONENT REPLACEMENT	17.36	23.26
FUEL	0.33	0.44
TOTAL ANNUAL COST	277.13	529.39
COST OF ELECTRICITY (Mill/kWh)	35.1	67.1

those of PWR systems, thus enhancing the cost credibility. The direct capital costs associated with the reactor plant equipment, the balance of plant equipment, land and all the related structures and site facilities, were estimated based upon supplier quotes, historical data and analogous systems. The indirect costs related to construction are assessed based upon DOE recommendations with modifications specific to this design. Time related costs account for both interest and escalation during construction. The annual costs include the annuallized capital cost, the operations and maintenance costs, the fuel costs and any scheduled component replacement costs. Given these costs along with the plant capacity (net power output) and the plant availability, the busbar energy cost is determined. These costs are presented in both constant year 1980 dollars and then - current year dollars, which represents a nominal first year facility cost.

2.9 SAFETY

The incorporation of safety considerations into the design process, even at the conceptual stage as in STARFIRE, is done to ensure that the environmental and safety advantages inherent in fusion are fully realized. The emphasis on

safety must include the concern for the safety of the general public, the plant personnel, and the plant itself -- in that order.

Fusion power will have several significant safety advantages compared to current methods of generating electricity. The nuclear safety aspects are decidedly improved when compared to fission reactors: the problems of accidental criticality and of prompt criticality are not applicable; the prospects and consequences of a loss-of-coolant accident are less; and the biological hazards of radioisotopes in the plant are much lower. Generally, the concerns regarding safeguarding against diversion of weapons-grade material, such as Pu or U-235, are eliminated. Fusion, like fission, does not involve combustion in air; thus the routine chemical releases are much lower than for fossil power plants. The dangers due to fuel mining and other associated activities, including transportation, will be greatly reduced. Radioactive waste storage requirements will be less complicated due to the absence of fission products and actinides. Low-level radioactive waste production should be less than for fission plants. Radiation doses to the general public due to routine or accidential releases of radioactivity will also be reduced.

Most recent safety evaluations of light water reactors (LWRs) and fast breeder reactors (FBRs) have concluded that, for an adequate analysis to be conducted of public risk associated with the different concepts, the total fuel cycle must be examined. In this regard, utilizing D-T for fuel should be preferable to LWRs or FBRs. The deuterium and lithium involved are not radioactive. Only the initial, start-up requirements of tritium, which is approximately 10 kg, need to be shipped to the plant. The rest of the tritium fuel cycle is contained within the plant. The breeding ratio of STARFIRE is sufficiently low that shipment of excess tritium from the site is not necessary.

It is important to note that no runaway-type accidents which would affect the public or the plant personnel have been identified by this study. No method of generating electricity is capable of completely eliminating environmental impact and risk to society; however, fusion will reduce the adverse effects and potential impacts to very low levels.

The primary emphasis in this study of deterministic methods rather than on probabilistic methods was due mainly to the timing involved. It was not possible to do a quantified probabilistic risk assessment, due to lack of sufficient design details, statistical operating data, and physical models pertaining to hazard rates. Future efforts undoubtedly will be directed at performing a detailed probabilistic risk assessment.

In the context of a Preliminary Hazards Analysis (PHA), the following sources of hazards were identified for the STARFIRE design:

- o Tritium inventory
- o Induced activity in the first wall, blanket, magnet, shield and structural materials
- o Pressurized water primary coolant
- o Corrosion products in the primary coolant
- o Stored energy in the superconducting magnet system
- o Cryogenics
- o Kinetic and self-inductive energy associated with plasma current
- o RF heating

The following potential accidents were identified for STARFIRE. Safeguards were incorporated into the design to the extent possible, which prevent their occurrnce or limit the damage.

- o Tritium release, both in a continuous and a pulsed mode.
- o Loss of coolant flow to the first wall and/or blanket
- o Failure of the resistive dump for the superconductive magnet system
- o A superconducting magnet becoming locally normal
- o Gross rupture of the magnets' helium cryogenic system
- o Failure of first wall due to plasma disruption
- o Production of missiles as the result of an accident
- o Hydrogen detonations or explosions

Table of Contents

3.1 INTRODUCTION

The results of the STARFIRE study have increased our confidence in the potential of tokamaks as power reactors. The study has identified new and important directions for the development of fusion reactors, in general, and tokamaks, in particular, to further enhance their potential for commercial applications. Study conclusions regarding specific technical areas are discussed in the appropriate chapters of this report. This chapter summarizes some of the key and broad conclusions of the study.

3.2 STEADY STATE

The results of the STARFIRE study show important incentives for developing the steady state option for tokamaks. Steady-state operation offers many engineering, technological and economical benefits in commercial reactors. Among these are: reactor reliability is increased, serious concerns about material fatigue are eliminated, electrical and thermal energy storage systems are not required; higher neutron wall load, and hence smaller size reactors, are acceptable; and the frequency of plasma disruption occurrence is greatly reduced. It has been estimated (see Chap. 5) that the benefits of steady state can result in a saving in the cost of energy as much as 30%.

Recent experimental results on noninductive current drivers are encouraging (see Chap. 7). However, the current driver to be developed for commercial power reactors should be reliable with simple engineering features and low electrical power requirements. A lower hybrid (LH) system was selected for the current driver in STARFIRE because of its attractive engineering features. Crossed-field amplifiers provide an inexpensive, highly efficient and long-lived power source in the LH frequency range. In addition, the transmission system is attractive due to flexibility in routing the transmission line and high reliability in the reactor environment.

Wave accessibility is a severe constraint for the LH system and forced the STARFIRE designers to use a hollow current profile for the plasma MHD equilibrium. Stability analysis shows that this profile may require close fitting conducting walls to operate even at the moderate β of 6.7% selected for the reference design. Efforts were made in the design of the first wall/blanket to satisfy the conducting wall requirements, but the engineering solutions add to the complexity of the reactor.

Extensive efforts were made in STARFIRE to minimize the electrical power requirements for the LH current driver. Nevertheless, the reference design calls for 150 MW of electrical power to drive the relatively low plasma current of 10.1 MA. This represents $\sim$ 10% of the plant gross electrical output, which is relatively large. Therefore, strong incentives exist for additional efforts to further improve the performance of the LH current driver. Other potential current drivers must also be seriously explored.

3.3 IMPURITY CONTROL AND EXHAUST (Limiter/Vacuum System)

The impurity control and exhaust system is one of the key components in a fusion reactor. It has a substantial impact on the engineering simplicity, reliability, maintainability, economics and safety of the power plant. Divertors and divertorless options were surveyed. It was concluded that the limiter/vacuum (also called "pumped" or "active" limiter) concept is a very attractive option for power reactors. It is relatively simple and inexpensive and deserves serious experimental verification.

The main advantages of the limiter/vacuum system, as identified in STARFIRE, are: (1) it is a mechanical system (it does not require magnets); (2) it has minimal impact on access and breeding blanket space; (3) it can be designed to dramatically reduce radiation streaming; (4) the surface area available for particle collection is relatively large; and (5) it permits designing for higher tritium fractional burnup and lower tritium inventory in the vacuum pumps and fueling system.

The STARFIRE study finds it an important design approach to radiate most of the alpha-power from the plasma to the large surface area of the first wall. This reduces the heat load on the particle collection medium (limiter or divertor target plate) to a manageable level and it deposits more energy in the primary coolant of the first wall. One means of enhancing plasma radiation is by injecting small amounts of high-Z material along with the DT fuel stream. The large ignition margin in commercial reactor-size plasmas makes operation in such an enhanced radiation mode feasible.

A low-Z coating on all surfaces exposed to the plasma will probably be required in future tokamak reactors unless very low plasma edge temperatures

can be established and maintained. Beryllium appears to be one of the best choices for the low-Z coating. Sputtering of the coating is predicted to be large but redeposition seems to extend the coating life to an acceptable level. However, there is a need for experimental results and theoretical work on the physics of the scrape-off region and the performance of low-Z coatings. There is also a need to develop in-situ low-Z coatings techniques for fusion reactor applications.

Four materials have been identified as the most promising for the limiter structure. These are alloys of copper (AMAX-MZC), tantalum (Ta-5W), niobium (FS-85) and vanadium (V-20Ti). These alloys can withstand the high heat fluxes on the limiter. Available data indicates that these alloys have many properties that are suitable for the reactor environment. Unfortunately, the data base is not complete and more information is required in the areas of corrosion and radiation effects for all of these alloys.

The results of STARFIRE indicate that a high efficiency exhaust system is not necessarily desirable. It is very beneficial to keep the removal efficiency low so that the tritium fractional burnup is high. This reduces the gas load in the exhaust system and simplifies the vacuum system design in addition to lowering the vulnerable tritium inventory in the fueling and vacuum systems.

3.4 ENERGY CONVERSION

A detailed first wall/blanket design has been developed to meet many of the conflicting requirements on this system. The study focused on solid tritium breeders in order to minimize the stored chemical energy. The reference design is based on $LiAlO_2$ solid breeder, improved austenitic stainless steel structure and water coolant.

Safety considerations provide major incentives for the development of solid breeders. Serious efforts have been devoted in STARFIRE to evaluation of solid tritium breeders and to the development of a design that optimizes their performance. The results are encouraging and show that the solid breeder option should continue to be pursued. However, the results of the detailed analyses in STARFIRE indicate potentially serious problem areas that must be

further investigated before the viability of solid breeder blanket concepts can be accurately assessed. The most critical of these problems concerns the tritium release characteristics of solid breeders. Analytical models show that in the absence of radiation effects, the tritium inventory in the solid breeder blanket can be kept to only a few kilograms, which is acceptable. The nonmobility of solid breeders makes the tritium tied in the blanket nonvulnerable. However, the results show that radiation effects, such as radiation-induced trapping of tritium within the grains and pore closure, may increase the tritium inventory in the solid breeders to unacceptably high level. There is a serious lack of an adequate data base on solid breeders, particularly in the area of radiation effects. Specific information that need to be developed are discussed in Chap. 10.

All the ternary oxides such as $LiAlO_2$, Li_2TiO_3 and Li_2SiO_3 are found to require a neutron multiplier to yield a tritium breeding ratio greater than one. From a neutronics viewpoint, the best neutron multipliers are beryllium, lead and bismuth. Beryllium resources are limited and both lead and bismuth have low melting points. The STARFIRE study identified Zr_5Pb_3 as a promising neutron multiplier. The detailed Monte Carlo calculations show a net tritium breeding ratio of $\sim$ 1.04. While this is slightly higher than the breeding ratio needed ($\sim$ 1.02), it does not provide a conservative margin against uncertainties in nuclear data, calculational methods and design requirements. The adequacy of the margin needs to be assessed by conducting neutronics integral experiments. In addition, efforts to identify, evaluate, and develop information for neutron multipliers should be considered as an important part of solid tritium breeder development. The use of Pb, Bi and the PbBi alloy in STARFIRE was ruled out because of their low melting points and the desire to develop a solid blanket. However, future work should reconsider the use of such neutron multipliers if an additional margin in the tritium breeding ratio is found necessary. It should be noted that other tritium breeding materials, such as natural lithium, Li_7Pb_2 and Li_2O, do not require a neutron multiplier.

Trade-off studies comparing helium and water coolants were performed. The results show clear advantages for the use of pressurized water for the STARFIRE conditions. The study also identified the key technology development requirements that are necessary for effective utilization of the helium cooling option (see Sec. 5.4).

3.5 ECONOMICS AND MAINTAINABILITY

Results of the economics analysis for the STARFIRE tokamak power plant indicate that fusion reactors can be developed to be economically competitive. The cost of energy estimated for STARFIRE is comparable to that of future light-water fission reactors and lower than for coal power plants. There are, of course, uncertainties in predicting now the cost of energy for future fusion reactors. However, there appears to be no fundamental reason that fusion will not be economically competitive. In fact, fusion has some inherent features that lead to economic advantages. The most important of these concerns fuel. The fusion fuel in not only abundant, but its cost is negligible. In contrast, the cost of fuel presently represents $\sim$ 25% and 40% of the cost of energy in fission light-water reactors (LWR) and coal, respectively. Therefore, the cost of energy for a given LWR or coal power plant continues to rise from year to year due to escalation in fuel prices, while the cost of energy for a fusion power plant remains essentially unchanged. In addition, the attractive safety and environmental features, besides being desirable in their own right, can result in cost savings due, for example, to elimination of or reduction in the requirements for extensive and redundant protective systems.

The cost of energy is directly proportional to the capital cost and inversely proportional to the plant availability factor. The capital cost estimates for STARFIRE are the most comprehensive estimates made to date for a fusion reactor. Confidence in these estimates is enhanced by the details in the definition of the reference design and by the use of an extensive data base for costing materials and labor. Furthermore, roughly one-half of the direct capital cost is attributable to the balance-of-plant, for which most of the cost estimates are based on direct quotes from manufacturers (see Chap. 22).

The greatest uncertainties in the economics of future tokamak power plants concern the plant availability factor. This is crucially dependent on component reliability (low frequency of component failure) and maintainability (short downtime to replace failed components). The data base for the reliability of components in the fusion reactor environment is lacking, and such information must be obtained as a part of the technology development program. Definitive information on reactor maintainability will come only from experience with operation and maintenance of future fusion devices.

The STARFIRE design attempted to maximize component and reactor reliability and maintainability. Component reliability is enhanced by the choice of steady state mode of operation; by locating, whenever feasible, key components (e.g., poloidal coils, vacuum pumps) away from the harsh radiation environment; and by developing a design in which the engineering burden is optimally shared among reactor components (e.g., radiating the α-power from the plasma to the first wall in order to reduce the heat load on the particle-collection medium to a manageable level). Special attention was given to maximizing the reliability of components that are difficult to replace. For example, conservative design margins were incorporated into the design of the TF coils since their replacement requires long downtimes.

Simplifying the reactor design has been a key approach in STARFIRE to enhancing component reliability and maintainability. The choices of the lower-hybrid current driver and the limiter/vacuum system concept have contributed significantly to simplifying STARFIRE. Other features found important in enhancing reactor maintainability include: modularity; locating the vacuum boundary at the shield with all mechanical seals; placing all service connections outside the vacuum boundary; and locating all superconducting EF coils outside the TF coils. A low number, 12, of TF coils was used to increase accessibility. There remains a great incentive for further reducing the number of TF coils. Therefore, more accurate information on the allowable field ripple in reactor-size plasmas is needed. The STARFIRE maintenance plan calls for a "remove and replace" approach; i.e., the failed components are replaced with stand-by units and the reactor is operated while the failed parts are repaired in the hot cell. This approach seems necessary in order to achieve reasonable availability goals.

3.6 SAFETY

The safety and environmental considerations have been emphasized in STARFIRE. The choice of a solid breeder in preference to liquid lithium was motivated by the desire to minimize the stored chemical energy. Significant effort was devoted to minimizing the vulnerable tritium inventory. This was achieved by selecting the limiter/vacuum system and designing it for a low particle removal efficiency in order to maximize the fractional tritium

burnup. The reactor was designed to contain the tritium with multiple barriers and to minimize the size of tritium release. The choice of CO_2 for the reactor building eliminates the need for routine releases of radioactive gases.

No runaway accident that could pose a major risk to the public can be identified for STARFIRE. Furthermore, no plausible scenario could be formulated for the release of radioactive materials from the blanket (excluding corrosion products in the primary coolant loop) to the outside of the reactor building. The reasons such a release appears extremely unlikely include: the stored energy in the blanket is not sufficient to melt and vaporize the blanket structure; the massive shield (which also serves as the vacuum boundary) surrounding the blanket has a very large thermal capacity and serves as a containment barrier for the blanket; and the reactor building provides additional containment. In addition, mechanisms for rapid reactor shutdown have been incorporated into the design and auxiliary cooling systems are provided to serve as a backup in cases of off-normal conditions involving the primary coolant. A dual primary coolant loop system was designed to avoid complete loss of coolant. The beryllium coating on the first wall and limiter provides an inherent safety feature that terminates the plasma burn if the metal temperature exceeds $\sim$ 900°C. Calculations show that the reactor will be automatically shut down in less than one second if a hot spot forms on a small area (< 10%) of the first wall without the need for an active control system. No major damage, other than ablation of some of the coating on the first wall, is predicted.

There are many safety concerns that remain in the reactor design, but the concerns here are limited mainly to the loss of capital investment of failed components. STARFIRE has emphasized the safety considerations in the selection of the design features, but the analysis of off-normal conditions was limited to only a few key problems. Much work remains to be done in the analysis of off-normal conditions.

The reactor has been designed so that all materials outside the blanket can be recycled within 30 yr after component removal or reactor decommissioning. Radiation exposure of personnel has been minimized by extensive use of remote maintenance operations and by providing adequate shielding.

TABLE OF DESIGN PARAMETERS

This chapter presents a table of design parameters for the STARFIRE reactor and balance of plant. The format and content of this table follows that suggested in Ref. 1 to facilitate comparison of designs resulting from studies of various reactor types. More detailed information about specific reactor subsystems and the balance of plant may be found in Chap. 2, STARFIRE Overview, or in the Chapters and Appendices of this report which discuss the topic of interest.

References

1. DOE Letter RS&A: CRH: #478, March 7, 1979.

		Unit	Value
1.	Characteristic Machine Dimensions		
1.1	Reactor Envelope		
1.1.1	Height	m	28.6
1.1.2	Width	m	33.0 dia.
1.1.3	Length	m	N.A.[a]
1.2	First Wall		
1.2.1	Major Radius	m	7.0
1.2.2	Minor Radius	m	2.14
1.2.3	Volume	m^3	950
1.2.4	Inner Surface Area	m^2	780
2.	Plasma Parameters		
2.1	Plasma Dimensions		
2.1.1	Major Radius, R	m	7.0
2.1.2	Minor Radius, a	m	1.94
2.1.3	Plasma Elongation		1.6
2.2	Centerline Fuel Density (n_{DTO})	m^{-3}	1.7×10^{20}
2.3	Average Density ($\bar{n}_{DT}$)	m^{-3}	0.806×10^{20}
2.4	τ_E, Electron Energy Confinement Time	s	3.6
2.5	τ_e, Ion Energy Confinement Time	s	10
2.6	τ_i, Particle Confinement Time	s	1.8
2.7	$n\tau_E$ (Averaged Through Plasma)	s/m^3	2.9×10^{20}
2.8	β_o, Peak Toroidal Beta		0.194
2.9	$<\beta>$, Average Toroidal Beta		0.067
2.10	β_{PO}, Centerline Poloidal Beta		N.A.
2.11	$<\beta p>$, Average Poloidal Beta		2.91
2.12	I_p, Plasma Current	MA	10.1
2.13	T_{io}, Centerline Ion Temperature	keV	31.3
2.14	$\bar{T}_i$, Average Ion Temperature	keV	24.1
2.15	T_{eo}, Centerline Electron Temperature	keV	22.5
2.16	$\bar{T}_e$, Average Electron Temperature	keV	17.3
2.17	Z_{eff}, Effective Plasma Ion Charge		3.4
2.18	q, Plasma Safety Factor		5.1
2.19	Volt-Seconds	Volt-s	N.A.
2.20	Reactor Cycle		Steady State
2.20.1	Burn Pulse Length	s	N.A.
2.20.2	Total Pulse Length	s	N.A.
2.21	Fuel Cycle (i.e., D-T, D-D, etc.)		D-T
2.22	Plasma Heating Method		Lower Hybrid
2.23	Plasma Heating Power	MW	90.4
2.24	Plasma Heating Energy or Freq.	Hz	1.677×10^9
2.25	Plasma Energy Gain, Q_p (Plasma Fusion Power/Plasma Heating Power)		39

		Unit	Value
3.	**Power Output**		
3.1	Plasma Fusion Power (Peak)	MWth	3510
3.2	Plasma Fusion Power (Total Cycle Time Average)	MWth	3510
3.2.1	Thermal Power	MWth	4000
3.3	Power to First Wall/Blanket (Peak Neutron)	MWth	2810
3.4	Power to First Wall/Blanket (Total Cycle Time Average) (Fusion Neutron Power)	MWth	2810
3.4.1	Nuclear Heating in First-Wall/Blanket	MW	3205
3.5	Blanket Power Amplification Factor		1.14
3.6	Power to Direct Convertor (Peak)	MWth	N.A.
3.7	Power to Direct Convertor (Total Cycle Time Average)	MWth	N.A.
3.8	Power to Divertor (Peak)	MWth	N.A.
3.9	Power to Divertor (Total Cycle Time Average)	MWth	N.A.
3.10	Plasma Chamber Power Density (Total Cycle Time Average)	MW/m^3	3.7
3.10.1	Plasma Power Density	MW/m^3	4.5
3.11	Nuclear Island Power Density[b] (Total Cycle Time Average)	MW/m^3	0.13
3.11.1	Engineering Power Density[g]	MW/m^3	0.30
3.12	Plant Gross Electrical Output	MWe	1440
3.13	Plant Net Electrical Output	MWe	1200
3.14	Thermal Cycle Efficiency	%	35.7
3.15	Direct Convertor Efficiency	%	N.A.
3.16	Net Plant Efficiency	%	30
4.	**Reactor Coolant System**		
4.1	Blanket Coolant Type		H_2O
4.2	Blanket Outlet Temperature (Hot Leg)-Peak/Average	°C	320/320
4.3	Blanket Inlet Temperature (Cold Leg)-Peak/Average	°C	280/280
4.4	Blanket Outlet Pressure-Peak/Average	MPa	15.0/15.0
4.5	Blanket Inlet Pressure-Peak/Average	MPa	15.2/15.2
4.6	Blanket Coolant Flow Rate	kg/s	10823
4.7	Blanket Coolant Pipe Material		PCA
4.8	First Wall Coolant Type		H_2O
4.9	First Wall Outlet Temperature-Peak/Average	°C	320/320
4.10	First Wall Inlet Temperature-Peak/Average	°C	280/280
4.11	First Wall Outlet Pressure-Peak/Average	MPa	15.0/15.0
4.12	First Wall Inlet Pressure-Peak/Average	MPa	15.2/15.2
4.13	First Wall Coolant Flow Rate	kg/s	5811
4.14	Total Number of First Wall/Blanket Coolant Loops		2

		Unit	Value
4.	Reactor Coolant System (cont'd)		
4.15	Type of Blanket Coolant Circulator		Vertical, 1-Stage
4.16	Power Input to Each Circulator	MWe	5.5
4.17	Peak First-Wall/Blanket Temperature in Case of Loss of Coolant Flow[f]		
4.17.1	First Wall Be Coating	°C	710
4.17.2	Multiplier	°C	720
4.17.3	Breeder	°C	670
4.17.4	First Wall Structure	°C	710
4.18	Energy Storage	J	N.A.
5.	Intermediate Coolant System		N.A.
6.	Steam Generation System		
6.1	Steam Outlet Temperature	°C(°F)	299 (800)
6.2	Steam Outlet Pressure	MPa(psia)	6.3 (910)
6.3	Steam Flow Rate	kg/s(lb/hr)	2060 (16.4×10^6)
6.4	Feedwater Temperature	°C(°F)	235 (455)
6.5	Number of Steam Generators per Loop		2
6.6	Number of Sectors per Steam Generator		6
6.7	Steam Generator Materials, Shell/Tube		Low Carbon Stl/Inconel 600
7.	Shield Coolant System		
7.1	Total Energy Deposited in the Shield	MWth	65
7.2	Shield Coolant Type		H_2O
7.3	Shield Outlet Temperature-Peak/Average	°C	60/60
7.4	Shield Inlet Temperature-Peak/Average	°C	43/43
7.5	Coolant Outlet Pressure-Peak/Average	MPa	0.48/0.48
7.6	Coolant Inlet Pressure-Peak/Average	MPa	0.34/0.34
7.7	Coolant Flow Rate	kg/s	1300
8.	Reactor Auxiliary Systems		
8.1	Vacuum Pumping System		
8.1.1	Plasma Chamber Pressure (Base)	Pa	1×10^{-6}
8.1.2	Plasma Chamber Volume	m^3	950
8.1.2.1	Plasma Volume	m^3	781
8.1.3	Number of Pumps		48 (24 on line, 24 regenerating)

		Unit	Value
8.	Reactor Auxiliary Systems (cont'd)		
8.1.4	Capacity of Each Pump	$Pa\text{-}m^3$	2.7×10^5
8.1.5	Helium Pumping Speed of Each Pump	m^3/s	120
8.2	Magnet Cooling System		
8.2.1	Cooling Load	W	23,300
8.3	Plasma Heating System		
8.3.1	Heat Removal From rf System	MW	90
8.4	Plasma Fueling System		
8.4.1	Type		Gas Puffing
8.4.2	Fuel Composition (i.e., %D, %T, etc.)		50%D, 50%T
8.4.3	Fueling Rate	kg/s	1.5×10^{-5} (T) 1.0×10^{-5} (D)
8.4.4	Pellet Size (if used)	m	N.A.
8.4.5	Pellet Injection Frequency (if used)	s	N.A.
8.5	Tritium Processing and Recovery System		
8.5.1	Total Tritium Inventory	kg	11.6
8.6	Impurity Control System		
8.6.1	Type		Limiter/Vacuum
9.	Reactor Components		
9.1	First Wall/Blanket		
9.1.1	Structural Material		PCA[c]
9.1.2	Breeding Material/Neutron Multiplier		α-$LiAlO_2$/ Zr_5Pb_3
9.1.3	Breeding Ratio		1.044
9.1.4	Number of Sectors		24
9.1.5	Weight of Sector	Tonnes	65 (Large) 60 (Small)
9.1.6	Weight of Largest Single Component	Tonnes	65
9.1.7	Dimensions of Largest Component	m x m x m	3.9 x 12.4 x 13.8 high
9.1.8	First Wall Loading (Peak/Average)		
9.1.8.1	14.1 MeV neutrons	MW/m^2	4.0/3.6
9.1.8.2	Alpha Particle Flux	MW/m^2	(very small)
9.1.8.3	Electro-Magnetic Radiation Plus Charge Exchange Neutrals[d] (Peak/Average)	MW/m^2	1.17/0.90
9.1.8.4	Plasma Thermal Conduction (Particle Transport)	MW/m^2	<0.01
9.1.8.5	Wall Life	$MW\text{-}yr/m^2$	16
9.2	Shielding		
9.2.1	Material		
9.2.1.1	Inboard		W, Steel, B_4C, H_2O

		Unit	Value
9.	Reactor Components (cont'd)		
9.2.1.2	Outboard		Ti-6-4, TiH_2, B_4C, Steel, H_2O
9.2.1.3	Ducts		Steel, B_4C, H_2O, Ti-6-4, TiH_2
9.2.2	Number of Sectors		12 large, 12 small
9.2.3	Weight of Each Sector	Tonnes	179 Large Sec. 226 Small Sec.
9.2.4	Weight of Largest Single Component	Tonnes	411 (Large Sec. Plus 2 Ducts)
9.2.5	Dimensions of Largest Component	m x m x m	3.5x7.8x12.75
9.3	Magnets		
9.3.1	Toroidal Field Magnets		
9.3.1.1	Superconducting	yes/no	yes
9.3.1.2	Conductor/Stablizer Material		Nb_3Sn/Cu, NbTi/Cu
9.3.1.3	Structural Material		316 LN stainless
9.3.1.4	Operating Temperature	K	4.2
9.3.1.5	Coolant		Liquid He, Bath Cooling
9.3.1.6	Maximum Stress in Coil	N/m^2	$550x10^6$
9.3.1.7	Maximum Force Transmitted to Building	N/m^2	N.A.
9.3.1.8	Maximum Field	T	11.1
9.3.1.9	Field on Plasma Axis	T	5.8
9.3.1.10	Number of Magnets		12
9.3.1.11	Field Ripple-Plasma Edge/Plasma Axis	%	$\pm 1.14/\pm 0.06$
9.3.1.12	Stored Energy	J	$50x10^9$
9.3.2	Equilibrium Field Magnets		
9.3.2.1	Superconducting	yes/no	yes
9.3.2.2	Conductor/Stabilizer Material		NbTi/Cu
9.3.2.3	Structural Material		316 LN stainless
9.3.2.4	Operating Temperature	K	4.2
9.3.2.5	Coolant		Liquid He, Bath Cooling

		Unit	Value
9.	Reactor Components (cont'd)		
9.3.2.6	Maximum Stress in Coil	N/m^2	550×10^6
9.3.2.7	Maximum Force Transmitted to Building	N/m^2	N.A.
9.3.2.8	Maximum Field	T	4.5
9.3.2.9	Field on Axis	T	0.35
9.3.2.10	Number of Magnets		6
9.3.2.11	Field Ripple-Edge/Center	%	0/0
9.3.2.12	Stored Energy	J	10×10^9
9.3.3	Ohmic Heating Magnets		
9.3.3.1	Superconducting	yes/no	yes
9.3.3.2	Conductor Material		NbTi/Cu
9.3.3.3	Structural Material		316 LN stainless
9.3.3.4	Operating Temperature	K	4.2
9.3.3.5	Coolant		Liquid He, Bath Cooling
9.3.3.6	Maximum Stress in Coil	N/m^2	550×10^6
9.3.3.7	Maximum Force Transmitted to Building	N/m^2	N.A.
9.3.3.8	Maximum Field	T	8.0
9.3.3.9	Field on Axis	T	<0.005
9.3.3.10	Number of Magnets		8
9.3.3.11	Field Ripple-Edge/Center	%	0/0
9.3.3.12	Stored Energy	J	1.1×10^9
9.3.4	Correction Field Magnets		
9.3.4.1	Superconducting	yes/no	no
9.3.4.2	Conductor Material		Cu
9.3.4.3	Structural Material		Cu
9.3.4.4	Operating Temperature	K	353
9.3.4.5	Coolant		H_2O
9.3.4.6	Maximum Stress in Coil	N/m^2	14×10^6
9.3.4.7	Maximum Force Transmitted to Building	N/m^2	N.A.
9.3.4.8	Maximum Field	T	7.7
9.3.4.9	Field on Axis	T	0.26
9.3.4.10	Number of Magnets		4
9.3.4.11	Field Ripple-Edge/Center	%	0/0
9.3.4.12	Stored Energy	J	30×10^6
9.4	Energy Transfer and Storage		
9.4.1	Plasma Preparation		
9.4.1.1	Type		Electron Cyclotron Resonance Heating

	Unit	Value
9. Reactor Components (cont'd)		
9.4.1.2 Energy Per Unit	MJ	15
9.4.1.3 Total Energy	MJ	15
9.4.1.4 Peak Power Transfer Rate	MW	5
9.4.1.5 Transfer Time	s	3
9.4.1.6 Depth of Discharge	%	N.A.
9.4.1.7 Recharge Time	s	N.A.
9.4.1.8 Pulse Frequency	s	CW
9.4.1.9 Switching Requirements		
9.4.1.9.1 Current, Power Supply Output	A	11-15
9.4.1.9.2 Volts, Power Supply Output	V	25×10^3
9.4.1.9.3 Number of Power Supplies		432
9.4.2 Primary Power Supply		N.A.
9.4.3 Current Drive Power Supply		
9.4.3.1 Type		Solid State Rectifier DC
9.4.3.2 Input Power	MWe	152.9
9.4.3.3 On Time	s	Continuous
9.4.4 Poloidal Coil Supplies		
9.4.4.1 Main Equilibrium Coil Supply		
9.4.4.1.1 Type		Solid State Rectifier, Inverter
9.4.4.1.2 Peak Power Rating	MVA	290
9.4.4.1.3 On Time	s	1440
9.4.4.2 Correction Coil Supply		
9.4.4.2.1 Type		Solid State Rectifier/ Inverter
9.4.4.2.2 Peak Power Rating	MW	33
9.4.4.2.3 Average Power Rating	MW	2
9.4.4.2.4 On Time	s	Continuous
9.4.4.3 Ohmic Heating Coil Supply		
9.4.4.3.1 Type		Variable Dump Resistor
9.4.4.3.2 Peak Power Rating	MW	150
9.4.4.3.3 On Time	s	14
9.4.4.3.4 Emergency Shutdown Equilibrium Coil Supply		
9.4.4.4.1 Type		Variable Dump Resistor
9.4.4.4.2 Peak Power Rating	GW	10
9.4.4.4.3 On Time	s	3

			Unit	Value
10.	Electrical Power Requirements			
	10.1	Cold Start Power from Grid	MWe vs. s	300 vs. 60
	10.2	Auxiliary Power Requirements (Normal Operation)	MWe	240
	10.2.1	Electrical Energy Storage (EF Coils)	MWe	None
	10.2.2	Magnet Power Supply (other than energy storage)[e]	MWe	3.3
	10.2.3	First-Wall/Blanket Circulators	MWe	30
	10.2.4	Limiter Coolant Circulators	MWe	2.8
	10.2.5	Shield Coolant Circulators	MWe	1.0
	10.2.6	Refrigeration System	MWe	7.0
	10.2.7	Vacuum System (Roughing)	MWe	0.15
	10.2.8	Plasma Heating System	MWe	152.9
	10.2.9	Miscellaneous Reactor Plant Auxiliaries	MWe	(Incl. in 10.2.13)
	10.2.10	Feed Pump System	MWe	N.A.(Turbine Driven)
	10.2.11	Condensing System	MWe	6
	10.2.12	Heat Rejection System	MWe	21.2
	10.2.13	Misc. BOP Auxiliaries (Transformer Cable)	MWe	13.0
11.	Buildings			
	11.1	Reactor Building		
	11.1.1	Characteristic Dimensions	m x m x m	120x50x44 High
	11.1.2	Enclosed Volume	m^3	2.55×10^5
	11.1.3	Minimum Wall Thickness for Shielding	m	1.5
	11.1.4	Internal Pressure, Normal/Accident (gage)	MPa	-0.0001/+0.165
	11.1.5	Containment Atmosphere		CO_2
	11.2	Electrical Energy Storage Building		N.A.
	11.3	Reactor Service Building		
	11.3.1	Characteristic Dimensions	m x m x m	($4160\ m^2$)x23 High
	11.3.2	Special Functions (i.e., hot cells, blanket processing equipment, etc.)		o Hot Cells o Waste Processing and Storage o New Component Receiving

		Unit	Value
12. Reactor Maintenance			
12.1	Blanket/First Wall Replacement	% Surface Area/Yr.	16.7
		Tonnes/yr.	139.6
12.2	Radioactive Material Storage Requirement, Years/Volume	$Yr./m^3$	(See Chap. 12)

[a] NA = Not Applicable.

[b] The "Nuclear Island" is defined as everything covered by Account No. 22 in PNL-2648, "Fusion Reactor Design Studies--Standard Accounts for Cost Estimates."

[c] PCA = Prime Candidate Alloy; a titanium-modified 316 austenitic stainless steel.

[d] Includes electro-magnetic radiation components from synchrotron, Bremsstrahlung, and impurity inputs.

[e] Transformer losses, conductor and rectifier.

[f] Values for 600 s after shutdown.

[g] Defined as MWth rating divided by volume enclosed by and including field coils.

TABLE OF CONTENTS

LIST OF FIGURES

LIST OF TABLES

5.1 INTRODUCTION

Numerous tokamak reactor design and system studies[1-17] were carried out in the United States and worldwide over the past decade. These studies have elucidated many of the important features of tokamaks, have helped focus the fusion research and development program by identifying key physics and technology problems, and have served as an invaluable vehicle for developing innovative design concepts to enhance the potential of the tokamak as a power reactor. These studies have also demonstrated the presence of a wide range of design parameters and a diversity of design concepts. The primary objective of the STARFIRE study was to select the most attractive set of design parameters and concepts that make tokamaks economically competitive and environmentally acceptable. This objective has been fulfilled by building upon the experience gained from previous studies, by developing new innovative design concepts, and by performing trade-off studies as the basis for key design selections. The tools for these trade-off studies included the ANL Systems Code[10] and the MDAC code.[11]

The most important decisions that had to be made in the course of the STARFIRE study relate to the choices of (a) the plasma burn mode, pulsed, or steady state; (b) the impurity control and exhaust scheme, divertor, or divertorless approach; (c) breeding material and coolant; (d) key reactor parameters affecting the reactor size and performance (power rating, major radius, aspect ratio, neutron wall load, etc.); and (e) important reactor features affecting maintainability. The rationale for the decisions made in these areas is presented, in respective order, in this chapter. The reasons for many of the other specific design choices in STARFIRE are discussed throughout the report.

5.2 PLASMA BURN MODE (STEADY STATE)

Except for the Culham MKII study,[8] previous conceptual designs for tokamaks were based on pulsed plasma operation. Although these studies developed attractive solutions to many of the problems of pulsed operation, there remains a significant economic penalty associated with the inherent features of such a mode of operation. The necessity of pulsed operation in conventional tokamak designs is dictated by the limitations on the maximum volt-seconds that can be provided by the Ohmic heating (OH) coils. Fortunately, recent theoretical and experimental evidence[18-25] indicates the possibility that the toroidal plasma current may be maintained with noninductive external momentum sources to the

electrons. Since many of these sources, e.g. rf, can be operated continuously, this suggests that steady state may be an achievable mode of operation for tokamaks. As discussed below, steady state offers a potential for substantial reduction in the cost of energy as well as in the cost and lead time for technology development. Therefore, steady state has been selected as the mode of plasma operation in STARFIRE.

Steady-state operation offers many technological and engineering advantages. Among these are:

(1) Component and system reliability is increased. Engineering experience indicates that the rate of unexpected failures is higher for components that are subjected to cyclic loads.

(2) Material fatigue is eliminated as a serious concern; particularly for the first wall and blanket structure, which is seriously affected by thermal cycling.

(3) Higher surface heat loads on the first wall are acceptable since higher thermal stresses can be tolerated. The higher surface heat load limits can be beneficially utilized by significantly reducing the reactor size and/or enhancing the plasma radiation to the first wall in order to reduce the particle heat transport load to the limiter (or the divertor target plate).

(4) The frequency of plasma disruptions is greatly reduced. Accommodating the thermal energy dump and the electromagnetic forces associated with plasma disruptions currently represents a key engineering design problem, particularly for the first wall. Most plasma disruptions occur during startup and shutdown.

(5) The electrical energy storage is significantly reduced or eliminated and power supplies can be derated. Since plasma shutdown and startup occurs only every several months (depending on maintenance schedule), slow shutdown and startup is permissible. The reduction in the power supplies and energy storage represents a large saving in the capital cost.

(6) For a given thermal power, the electrical power output is increased by increasing the plasma duty cycle to unity.

(7) Thermal energy storage is not required. In pulsed reactors, thermal energy storage is necessary to level the plant electrical output and to prevent thermal cycling of the turbine generator. Furthermore, the need for an intermediate coolant loop is reduced.

(8) An ohmic heating solenoid is not needed or at least its requirements are greatly reduced, and external placement of the EF coils is simplified.

The above discussion illustrates qualitatively the benefits of steady-state operation. However, making quantitative estimates of these benefits is very difficult because it requires a detailed comparison of pulsed and steady-state reactor designs that are developed on consistent bases. No such designs are available. Furthermore, the difficulty of comparison is compounded by the lack of quantitative data on the reliability of fusion reactor components as a function of operating conditions. However, an attempt to estimate a range of potential economic benefits based on current experience is desirable. Such an attempt is discussed below.

Improvements in component reliability and elimination of material fatigue as a life-limiting effect in the first wall are anticipated to be among the most important benefits of steady state. However, they are the most difficult to quantify. As an example, consider the case of the first wall.

The lifetime of the first wall and blanket structure is determined by fatigue and bulk radiation damage (e.g. swelling, loss of ductility, etc.). The fatigue life depends strongly on the number and characteristics of the loading/unloading cycles (e.g. surface heat load and burn/dwell time) but it is also dependent on the thermophysical and mechanical properties of the material as well as the specific first-wall/blanket design. Several studies[26-28] have addressed the fatigue and bulk radiation damage effects on the first wall. The present uncertainties are too large to permit an accurate comparison of the achievable lifetime in steady state relative to pulsed operation. Nevertheless, some general observations can be noted. One case is that of stainless steel. The thermophysical properties of stainless steel are poor. Therefore, the thermal stresses in typical reactor design conditions tend to be high and the number of cycles to failure is relatively low, corresponding approximately to 1-2 yr lifetime for a surface heat load of $\sim$0.5 MW/m^2. Thus, even if thermal cycling is eliminated, the lifetime of the first wall is limited to $\sim$1-2 yr

depending on the wall load. Conversely, the newly improved austenitic stainless steel, PCA, can operate up to ∿15-20 MW-yr/m^2 which is the limit from bulk radiation damage effects. Since the thermophysical properties of PCA remain the same as ordinary stainless steel, there is considerable lifetime advantage for PCA in eliminating thermal cycling.

In order to assess the improvement in the lifetime of the first wall due to elimination of thermal cycling, it is necessary to consider a specific reactor design, In the case of STARFIRE, the average neutron wall load and surface heat load on the first wall are 3.6 and 0.9 MW/m^2, respectively. The lifetime of the PCA first wall is estimated to be ∿6 yr. If STARFIRE were pulsed under these loading conditions, the lifetime would be very short (<1 yr) and there would be an unacceptably large decrease in plant availability. However, it would be imprudent to design a pulsed reactor with such loading conditions. An optimum pulsed reactor would have lower wall loads, with lower power or larger reactor size, and/or a different structural material. A lower power or larger reactor size entail an economic penalty. The development of radiation-resistant structural materials that have good thermal stress factors is always desirable but involves significant cost and long lead time.

In view of the difficulties in deriving quantitative estimates for improvement in component reliability, it is assumed here that the frequency of failure as defined in STARFIRE would increase by ∿20-40% if the reactor were to be pulsed. Such a number reflects only a judgment based on current engineering experience. This increase in frequency of failure reduces the plant availability from 0.75 to ∿0.65-0.7 and increases the cost of energy by ∿7-13%.

The benefits of reducing the probability of plasma disruptions are also difficult to quantify. There is no reliable data on the frequency and characteristics of plasma disruptions in pulsed reactors. Engineering analysis in this study (see Chaps. 8 and 10) and other studies[29] show that accommodating plasma disruptions may require extensive design measures depending on the frequency of occurrence and the disruption conditions (e.g. current and thermal energy decay times). If plasma disruptions were to require a replacement of a component (e.g. the inboard wall) only once every three years, the plant availability factor would be reduced by more than 3%.

The savings in the cost of electrical energy storage and power supplies can also be estimated. If STARFIRE were pulsed with a burn cycle of 30-s

startup/30-min burn/30-s shutdown, the cost of power supplies and energy storage would be ∿265 million dollars. This is to be compared to 54 million dollars for the reference STARFIRE (steady state). The reduction in the cost of power supplies and energy storage of 211 million dollars results in a saving in the cost of energy of 12% (see Chap. 22).

The increase in the plant electrical output by making the plasma duty cycle unity can be estimated once a burn cycle is defined for a comparative pulsed system. The dwell time for torus evacuation varies from one design to another. A minimum of ∿40 s is estimated for the size of STARFIRE. With start-up, burn, and shutdown times of 30 s, 30 m, and 30 s, respectively, the plasma duty cycle is ∿0.98. Thus, the saving in the cost of energy due to making the plasma duty cycle unity is ∿2%. The reduction in the cost of energy due to elimination of the thermal energy storage has been estimated to be ∿1.5%.

According to our present understanding, there is no fundamental difference between the impurity control requirements for steady-state and pulsed reactors with a burn time of several minutes or longer. Since the plasma dwell time is 40 s or longer, the burn time should be >5 min to achieve a reasonable plasma duty cycle in a pulsed commercial tokamak. Furthermore, the plasma ash must be continuously removed in beta-limited pulsed systems to keep the fusion power at a reasonably constant level during the plasma burn.

Based on the above estimates, the combined benefits of steady-state operation result in ∿25-30% saving in the cost of energy.

The penalty for steady-state operation comes primarily from the potential problems associated with a noninductive current driver; in particular: (1) the electrical power requirements; (2) the capital cost; and (3) reliabilty and engineering complexity of the current driver. Methods to reduce these penalties in the STARFIRE design have been attempted. The most important of these are: (a) selecting a single system for the dual purpose of plasma heating and current driver; and (b) minimizing the power requirements for driving the current. It appears that the power requirements for driving the current can be kept about the same or below those for plasma heating. Therefore, the capital cost increment and the complexity associated with the current driver can be eliminated by utilizing the plasma heating system to also serve as the current driver. A strong incentive remains, however, to minimize the power requirements for the current driver as it directly affects the plant net electrical power output.

As discussed below, a lower-hybrid (LH) rf system was selected for plasma heating and current drive. Methods to minimize the power requiements for this system have been developed and are discussed in detail in Chap. 7. The LH system requires ∿153 MW of electrical power to deliver 90 MW into the plasma. Since the 90 MW delivered to the plasma is converted to electrical power at an efficiency of 36%, the net recirculating power penalty for the OH current drive is ∿120 MW. With the plant net electrical power output of 1200 MW, the penalty associated with the current drive corresponds to ∿10% increase in the cost of energy. Therefore, the net benefit of steady-state operation in STARFIRE is ∿15-20% saving in the cost of energy. This is a substantial saving and there are very few changes in a tokamak design that could result in such a large reduction in the cost of energy. Although the development of the steady-state option will require extensive experimental and theoretical plasma physics effort, it is anticipated that this will be more than compensated for by the reduction in the cost and lead time of technology development for many reactor components. Much larger savings are potentially realizable if the performance of the LH current driver can be further improved or substantially better alternatives for the current driver are developed.

Once the decision was made to design a steady-state tokamak, the STARFIRE designers were faced with the task of deciding which current driver should be selected for detailed study. Lower-hybrid waves were chosen principally because they have engineering features compatible with power reactors and they were previously the most extensively studied option for reactor application. Our preliminary work compared them with lower frequency (Alfven and magnetosonic waves and concluded the lower-hybrid waves were in fact a good choice based on a number of considerations: the tubes, transmission line, and launcher are standard rf hardware and can be easily adapted to a reactor environment; at low intensities the antenna theory agrees well with experiments; and experimentally, the plasma heating is efficient and roughly in agreement with theory. In addition, lower-hybrid current drive is readily calculated from simple models — WKB (ray tracing) is appropriate, trapped electrons play no role, and the shear Alfven and ion-hybrid resonances do not appear. Thus, our choice of lower-hybrid waves gives a high degree of confidence in our design. We have not, however, ruled out other drivers from being ultimately more suitable.

5.3 IMPURITY CONTROL AND EXHAUST

Many of the previous reactor design studies employed divertors. The results of these studies show that present concepts for poloidal and bundle divertors are rather complex. Specifically, they require magnets, enhance radiation streaming, tend to complicate maintenance, and increase the physical size of the reactor. Therefore, it seems prudent to seriously explore divertorless concepts.

An evaluation of divertorless schemes shows that the "pumped limiter" (also called limiter/vacuum system) is an attractive concept with many inherently simple features that are very desirable in a commercial power reactor. Among the advantages of the limiter/vacuum system, as compared to divertors, are:

(1) It is a mechanical system that does not require magnets.

(2) It has minimal requirements on space; the limiter fits naturally into the scrape-off region.

(3) Because of its location inside the first wall, the surface area available for the limiter is relatively large, thus permitting operation at reasonable heat fluxes.

(4) The system is flexible enough to permit designing for low hydrogen removal efficiency; this leads to higher tritium fractional burnup, low tritium inventory, reduced gas loads, and more attractive requirements for the effective pumping speed.

(5) The limiter/vacuum system can be designed to dramatically reduce radiation streaming.

(6) The limiter can be replaced simultaneously with the first wall with no special maintenance requirements.

(7) The system is simple and inexpensive. This feature is not only attractive from reactor maintainability and economics, but it also means that the physics and engineering testing necessary to qualify the concept can be done in relatively short times at a modest cost.

Therefore, the limiter/vacuum concept has been adopted for the impurity control and exhaust system in STARFIRE.

5.4 CHOICE OF BREEDER AND COOLANT

The choices of coolant and tritium breeding material have a substantial impact on the design, operation, maintenance, safety, and economics of a fusion power plant. Therefore, a great deal of attention was devoted in the STARFIRE study to the choices of coolant and breeder material. The solid tritium breeder, $LiAlO_2$, and pressurized water coolant were selected for the reference design. The rationale for this selection is presented in this section.

The promising coolant types are liquid metals, molten salts, helium, and water. Liquid lithium offers unique advantages. It can simultaneously perform the functions of tritum production, heat deposition, and heat transport resulting in a simple low-pressure system. It is also compatible with most structural materials. The major problem with liquid lithium is the large stored chemical energy. The associated safety problems are of concern. Previous design studies[30] and experience from the LMFBR program indicate that special design features, e.g. multiple barriers between liquid lithium and air and water, can reduce the probability of lithium fires to very low levels. However, these preventive design measures are costly. Furthermore, liquid lithium has other disadvantages that include difficult problems in maintenance and cleanup of spills, a need for an intermediate coolant, and MHD effects. Therefore, it seems prudent at this stage of fusion research and development to seriously explore other options that offer intrinsic safety features. It was in this spirit that a decision was made in the STARFIRE study to focus on solid breeders. No detailed comparison between liquid lithium systems and the reference solid breeder/water system was attempted. Such a study should be performed in the future.

Extensive trade-off studies were made to select the specific solid breeder and the coolant. The reasons for the specific choices of the reference design are discussed in the following two subsections. Detailed examination of specific technical areas is presented in Chap. 10.

5.4.1 Choice of Tritium-Breeding Material

The major solid breeder candidates are Li_7Pb_2, Li_2O, and the ternary oxides such as $LiAlO_2$, Li_2TiO_3, and Li_2SiO_3. Important criteria considered in the selection of potentially viable solid breeding materials include chemical stability, compatibility, neutronics properties, and tritium release characteristics.

The α-$LiALO_2$ is selected on the basis of the best combination of these materials requirements. It is one of the most stable compounds considered and compatibility should not be a major problem. Adequate breeding is attainable with the aid of a neutron multiplier and the tritium release characteristics are nearly as good as any of the candidate compounds. The primary advantages of α-$LiAlO_2$ compared to γ-$LiAlO_2$ relate to the higher density, which will result in a thinner breeding zone, and the fact that α is the stable phase at temperatures below $\sim$900°C. The major disadvantages of Li_2TiO_3 are its poor breeding performance and the lack of a data base. A slight potential advantage of this compound is its lower long-term activation compared to the aluminate. The silicate is similar to the above compounds, but because of its lower melting temperature, its chemical stability and compatibility characteristics are not as good.

The allowable operating temperature ranges for the candidate compounds have been predicted from available thermodynamic data. The low-temperature limits, which are defined by tritium diffusion kinetics in the solid, are based on very small ($\sim$1 μm) grain size. The upper temperature limits are based on sintering characteristics of the solids which would close interconnected porosity and increase the diffusion path. Allowances for radiation-induced trapping of tritium at the lower temperatures and radiation-induced sintering at the higher temperatures are included.

The ceramics are preferred over the intermetallic compounds for the reference solid breeding material because of the larger allowable operating temperature ranges. On the basis of this criterion, Li_2O and $LiAlO_2$ appear to have an advantage. However, the calculated solubility of tritium in Li_2O at these temperatures and at reasonable T_2O partial pressures in the tritium-processing stream ($>10^{-1}$ Pa) is much greater. Also, compatibility of Li_2O with the structural material is a major concern.

Li_7Pb_2 was excluded on the basis of its reactivity with the water coolant and compatibility problems with the structural material at the high temperatures required for helium cooling.

5.4.2 Choice of Coolant

The most suitable coolant candidates with solid tritium breeders are water and helium. The water coolant can be D_2O or H_2O either as steam or liquid.

Heavy water has several advantages compared to H_2O. The requirements on the processing of tritium from the water coolant is less difficult for D_2O since both deuterium and tritium are used for the plasma fuel. Another important advantage of D_2O relates to its neutronics properties. D_2O has a lower neutron slowing down power and a smaller neutron capture cross section than H_2O. Therefore, D_2O has less negative impact on the tritium breeding ratio and it gives more uniform lithium burnup and energy deposition as shown in Chap. 10. However, the very high cost of D_2O makes it economically undesirable. Steam was given some consideration but was found to offer no overall advantages over pressurized water or helium.

The choice between helium and pressurized water (H_2O) was a difficult decision involving several issues. This difficulty can be appreciated by examining Table 5-1 which shows a large number of technical areas of the reactor design affected by the choice of one of these two cooolants. Therefore, a comparative study of helium and pressurized light water was performed. The early comparison was performed using the ANL systems code[10] and showed clear benefits for the choice of pressurized water for the typical conditions of STARFIRE. After the STARFIRE design was completed, the comparative study was repeated on "a point basis". Starting with the reference pressurized water system, the areas most affected by the choice of coolant were examined and the performance characteristics and costs for a helium system were estimated and compared to the reference water design. The results of this point comparison confirmed the prudence of the earlier decision to use water. Key points from this point design comparison are discussed below.

5.4.2.1 Gross Thermal Efficiency

In reference to Table 5-1, the first area of comparison is the thermal conversion efficiency. Helium cooling is an advanced technology with potentially higher conversion efficiency than pressurized water. The reason for this is that a helium gas can be operated at high temperatures (e.g. 700-900°C) with reasonably low pressures (e.g. 700-1000 psi) while water requires high pressures at low temperatures (critical temperature $\sim$370°C). However, a key problem that must be clearly realized is that there is no structural material identified at present that (a) can operate at high temperatures; (b) is resistant to radiation damage; and (c) is compatible with impurities in helium. Structural mate-

Table 5-1. Key Areas of Comparison Between Helium and Water Coolants in STARFIRE

1. Gross thermal efficiency
2. Pumping power requirements
3. Inner blanket, shield thickness (void space with helium)
4. Primary coolant loop plus steam generator cost
5. Outer blanket/shield thickness
   - — Outer leg of the TF coil
   - — Design of EF coils
6. Shielding
   - — Streaming through helium ducts
   - — Crud in water loops
7. Achievable tritium breeding ratio in solid breeders
8. Ease of in-situ tritium recovery from solid breeders with narrow temperature range
9. Chemical reactivity
10. Coolant leakage
11. Overpressure on reactor building
12. Requirements for an intermediate coolant loop
13. Cost of coolant and coolant purification (e.g. crud and tritium)

rial temperatures <500°C are not capable of utilizing the full potential of helium. Modified austenitic stainless steel, PCA, is used in STARFIRE with water and is judged to be the only acceptable material with helium if no aggressive materials development program is pursued. This is a key assumption in this comparison.

The problems of cooling the first wall with helium are particularly severe. The heat deposited in the STARFIRE first wall is ∿20% of the reactor thermal power and the surface heat load on the wall is high, ∿0.9 MW/m^2. Attempts to design a helium-cooled first wall resulted in large pumping power requirements. Therefore, it is assumed in this study that for the helium case, the first wall is cooled with water while the helium is used only for cooling the blanket. The helium coolant exit temperature is 475°C and the water from the first wall is used for feedwater heating in the steam turbine cycle. The maximum coolant temperature for the reference pressurized water case is 320°C.

The obtainable thermodynamic efficiency depends on the steam temperature which in turn depends on the pinch-point temperature difference in the steam generator. To keep the cost of the steam generator reasonable, a pinch point of ∿10°C is normally maintained with water and ∿30-100°C with helium. The higher pinch point necessary with helium is due to its poorer heat transport properties. The gross thermal conversion efficiency with water is calculated as 35.7%, based on a steam temperature of 299°C (570°F) and a pressure of 6.3 MPa (910 psi) and assuming minor improvement in steam turbine technology as discussed in Chaps. 13 and 20. A steam temperature of 427°C (800°F) and pressure of 13.1 MPa (1900 psi) are assumed with helium. The resulting pinch-point in this case is only 13°C which increases the size of the steam generator. The gross thermal conversion efficiency for the helium case is taken to be 40%. Since 20% of the thermal power is removed by water from the first wall and 200 MW of heat is removed by low temperature water from the limiter, the assumed conversion efficiency for helium alone is >40%. Optimisitc conditions are assumed here for helium. A comparison of helium performance assumed in this study with that in present gas-cooled reactors[31] is shown in Table 5-2.

5.4.2.2 Pumping Power

Another major difference between the two coolants is the pumping power requirements. These are low with water, ∿0.3-0.8% of the thermal power. The pumping power for helium is generally large and is roughly inversely proportional to the square of the helium pressure and coolant temperature rise. The operating pressure in current gas-cooled reactors (see Table 5-2) is ∿700 psia. However, studies for recent gas-cooled fast reactor (GCFR) designs show significant economic incentives for technology development to accommodate high helium coolant pressures.[32] A pressure of 1500 psia is assumed for helium in this comparative study. Considerations of tritium release from solid breeders necessitates a small coolant temperature rise, ΔT, in the blanket. The reference water design in STARFIRE uses $\Delta T = 40°C$. Such a small ΔT would result in very large pumping power for helium. Therefore, a ΔT of 175°C is assumed for the helium case. (This will result in a higher blanket tritium inventory.) Under these conditions, the pumping power requirements for helium are ∿6% of the thermal power transported by helium. Since 20% of the thermal power is removed by water in the first wall, the pumping power for the helium case is ∿4.7% of the reactor thermal power. The fact that this pumping power is added to the

circulating fluid as thermal energy and converted to electric power must also be accounted for.

5.4.2.3 Inner Blanket/Shield Thickness

In STARFIRE, the use of a solid breeder is an important feature. All useful solid breeders that satisfy the tritium recovery and material compatibility constraints require a neutron multiplier and have much lower tritium breeding potential than liquid lithium. The relatively large percentage of the structural material required with the helium coolant makes development of blanket designs with a reasonably conservative margin in the tritium breeding ratio very difficult. It was concluded from the neutronics analysis that a blanket breeding region must be placed on the inner side of the torus. This conclusion strongly impacts the helium/water comparison in view of the negative effect of void space in the inner blanket on tokamak reactor performance and economics. For a given plasma geometry, beta, and maximum toroidal field, the fusion power varies with the inner blanket/shield thickness, Δ_{BS}^{i}, as

$$P_f \sim \left(\frac{R - a - \Delta_v - \Delta_{BS}^{i}}{R}\right)^4 ,$$

where R is the major radius, a is the plasma half-width, and Δ_v is the scrape-off thickness. For STARFIRE, R = 7 m, a = 1.94 m, and Δ_v = 0.2 m. The required blanket/shield thickness with water coolant is Δ_{BS}^{i} = 1.2 m.

Helium requires $\Delta_{BS}^{i} = 1.2 + \delta$, where δ is the equivalent thickness of the void space for the helium coolant in the inner blanket. Solid breeder blanket module designs were developed in sufficient detail to permit reasonable estimates of δ. A typical value for δ was found to be $\sim$0.38 m with 0.18 m void in the blanket region and 0.2 m equivalent void space for manifolds and headers. The void space can be reduced by increasing the helium pressure. Furthermore, clever routing of the coolant manifolds and locating the headers further away from the midplane in the inboard blanket will substantially reduce δ, but will also significantly increase the coolant pumping power requirements. In keeping with the spirit of this comparison of considering an optimistic case for helium, the value of δ is taken as only 0.18 m; thus Δ_{BS}^{i} for the helium case is 1.38 m. This reduces the thermal power for the helium case by $\sim$18%.

Table 5-2. Comparison of Typical Helium Coolant Conditions in Present Gas-Cooled Reactors with Conditions Assumed in This Study

	Fort St. Vrain HTGR DEMO	Peach Bottom HTGR Prototype	Conditions Assumed in the Present Study[a]
Reactor coolant exit temperature (helium inlet to steam generator), °C	776	734	475
Steam temperature, °C	538	538	427
Gross thermal efficiency, %	40.7	39.9	40[b]
Steam generator pinch point, °C	146	98	13
Coolant pressure, psi	700	350	1500
Steam pressure, psi	2400	1450	1900
Temperature rise of helium in reactor, °C	372	400	175

[a]For the purpose of comparing helium coolant performance to the reference pressurized water coolant in STARFIRE.

[b]Assuming roughly a 2-point improvement in thermal efficiency due to advances in steam turbine technology.

5.4.2.4 Cost of Heat Transport System

Tables 5-3 and 5-4 show the heat transport parameters for water (reference STARFIRE case, see Chap. 13) and helium, respectively. The water system utilizes two loops while the helium system incorporates four parallel loops beyond the dual ring manifold system. Each water loop utilizes two steam generators and two pumps while only one steam generator and one helium circulator are used in each helium loop.

Table 5-3. Water Heat Transport System Parameters

Coolant	Water
Heat load	3800 MW
Water temperature	
Reactor outlet	320°C
Reactor inlet	280°C
Operating pressure	2200 psi
No. of independent loops	2
Maximum pipe size (i.d.)	0.99 m
Maximum velocity	20 m/s
Gross system pumping power	30 MW
No. of pumps	4
No. of steam generators	4
Steam temperature	299°C (570°F)
Steam pressure	6.3 MPa (910 psi)

Component costs for the two systems were estimated as shown in Table 5-5. The costs for the water system were taken from the reference STARFIRE case (see Chap. 22). The costs for the helium case were estimated by using unit costs or by scaling from the more detailed cost estimates of HTGR and GCFR. The hot leg of the helium piping incorporates a thermal barrier as in the HTGR designs. As shown in Table 5-5, most components in the gas-cooled system are more expensive, reflecting the larger volumetric flow rate of coolant to be handled. On a per unit thermal power basis, the helium heat transport system cost is almost twice that of a water-cooled system.

Table 5-4. Helium Heat Transport System Parameters

Coolant	Helium
Heat load (total)	3105 MW
Blanket (helium)	2484 MW
First wall (water)	621 MW
Helium temperature	
Blanket outlet	475°C
Blanket inlet	300°C
Operating pressure	1500 psi
No. of loops	4
Maximum pipe size (i.d.)	1.13 m
Maximum velocity	103 m/s
Gross system pumping power	150 MW
No. of helium circulators	4
No. of steam generators	4
Steam temperature	427°C (800°F)
Steam pressure	13.1 MPa (1900 psi)

5.4.2.5 Other Areas of Comparison

The above discussion addressed only the first four areas of comparison given in Table 5-1. It is in these four areas that major differences in the performance and economics between water and helium are found. The other areas are important but it is not clear at present that any one of them will make so large a difference as to change or overwhelmingly strengthen the impact of the first four areas. A brief discussion of these other areas follows.

One difference between helium and water is the outer blanket/shield thickness, Δ^{o}_{BS}. As discussed earlier for the inboard region, Δ^{o}_{BS} will have to be increased with helium. This results in an increase in the major radius of the outer leg of the TF coil, thereby increasing the cost of the TF and the externally located equilibrium field (EF) coils.

Another difference between the two coolants is shielding requirements. The large-size helium manifolds will result in significant radiation streaming. Adequate shield has to be provided around the helium manifolds. In addition to the

Table 5-5. Comparison of Cost Estimates for the Heat Transport System of Helium and Water-Cooled Systems

Component	Cost Estimate (millions $)	
	Water Cooled	Helium[a] Cooled
Piping and manifolds	26.1	35.5
Valves	6.1	5.9
Pumps/circulators	2.4	14.0
Pressurizers	6.3	(b)
Coolant makeup and cleanup	4.2	5.5
Steam generators	18.0	40.0
Additional components for water-cooled first wall	(b)	10.2
TOTAL	63.1	111.1

[a]Helium system incorporates water-cooled first wall dissipating 20% of the power.

[b]Not applicable.

cost of the shield, the large-size manifolds and the shields that surround them complicate the space problem between the outer legs of the TF coils. On the other hand, some of the corrosion products with water will be transported throughout the heat transport system. Since these corrosion products are radioactive, shielding of the heat transport pipes for the water coolant is necessary if personnel access into the reactor building after shutdown is required.

Helium-cooled blankets require a larger amount of structural material than that for water. As indicated earlier, the most promising solid breeders (ternary oxides, e.g. $LiAlO_2$) have low tritium breeding potential. The increase in parasitic absorption in the structural material makes it difficult in most cases to attain a tritium breeding ratio greater than one with helium cooling. This problem can be resolved if it is shown that the tritium release characteristics of Li_2O are substantially better than currently predicted or if the compatibilty problems associated with Li_7Pb_2 can be solved.

In order to keep the tritium inventory in the blanket low, solid breeders have to operate in a narrow temperature range. As discussed earlier, a low coolant temperature rise in the blanket makes the pumping power with helium unacceptably large. It appears therefore, that a high tritium inventory in the blanket may be unavoidable with helium cooling.

A disadvantage of water is its reactivity with lithium and some of the lithium compounds. A major advantage of helium is that it is chemically inert. The chemical reactivity of water with the ternary oxides of lithium is generally weak.

Helium leakage is of concern. It is estimated that the entire inventory of the helium coolant is lost roughly once every year due to leakage. This problem is compounded by the use of a high helium pressure to minimize the coolant pumping power.

The maximum overpressure for which the reactor building is designed depends to some extent on the coolant pressure. Helium shows an advantage here as its operating pressure is lower than that for water. However, in designs such as STARFIRE, the thickness of the reactor building wall is determined more by the biological shielding requirements rather than overpressure considerations.

The STARFIRE study has shown that an intermediate coolant loop between the primary water coolant and the steam cycle is not necessary to keep the tritium leakage to the environment low. This is expected to be also the case for helium cooling. If, for other presently unknown reasons, either of the two coolants is shown to require an intermediate coolant loop, this can result in a significant impact on the present comparison.

Water represents a sink for tritium. While this has the favorable effect of preventing tritium permeation to other regions of the reactor, it is a cause for concern in cases of accidents involving release of water. This problem can be circumvented by keeping the tritium concentration in the water coolant sufficiently low. As discussed in Chap. 14, this requires continuous or periodic processing of water to remove tritium. However, the cost for this capability is estimated to be small relative to the economic impact of the first four major areas of Table 5-1.

5.4.2.6 Comparison of Power Plant Economics

Table 5-6 shows the key points regarding the comparison of performance and economics for pressurized water and helium coolants. A dominant effect is the increase in the inner blanket/shield thickness when the helium coolant is used. For the same maximum magnetic field (11.1 T), plasma average beta (0.067) and the same reactor plasma size (major radius = 7 m, minor radius = 1.94 m), the fusion power in the helium case is ∿18% lower than in the reference water case. This effect, together with the larger helium pumping requirements, because the net electric power to be lower with helium despite its larger thermal conversion efficiency. The cost of the heat transport system is considerably higher for helium. The reference power plant costs for STARFIRE were modified for the helium case to reflect reductions in the costs of the turbine plant equipment, the electric plant equipment, and other accounts. These reductions are due to the lower electric power generation with helium.

The cost per unit power is shown to be significantly higher, ∿13%, with helium cooling. Therefore, the choice of pressurized light water over helium for STARFIRE is clearly justified.

Helium has many attractive features but it is not economically competitive if constaints based on the present state-of-the-art are imposed. However, it is strongly emphasized here that helium cooling cannot be ruled out now as an option for fusion reactors. Rather, it is hoped that the present results can help identify the technology development requirements that are necessary for effective utilization of the helium cooling option. One of the most important of these requirements appears to be the development of high temperature (>600°C) structural materials that are compatible with impurities in helium. For example, there seems to be a great incentive for attempting to resolve the compatibility problems between the vanadium alloys (low long-term radioactivity and good resistance to radiation damage) and the achievable minimum level of impurities in helium. Another important area is resolving the problem of void space in the inner blanket. A key to this is the use of a breeding material whose tritium breeding capability is large enough so that placing a breeding module in the inboard blanket is not necessary. The only breeding materials that offer this potential are natural lithium, some of the lithium-lead compounds, and Li_2O.

Table 5-6. Summary of Key Points in the Water and Helium Coolants Comparison for STARFIRE

	Water	Helium
Pressure, psi	2200	1500
Inner blanket/shield thickness, m	1.20	1.38
Maximum magnetic field, T	11.1	11.1
Magnetic field on axis, T	5.80	5.52
Thermal power, MW	4000[a]	3305[a,b]
Coolant temperature, °C		
Reactor exit	320	475
Reactor inlet	280	300
Gross thermal efficiency, %	35.7	40
Coolant pumping power, MW	33	153
Other auxiliary power, MW	207	207
Net electric power,[c] MW	1200	1011
Cost of primary coolant loop	63	111
Direct plant capital cost, M$	1700	1620
$/kWe (relative units)	1.0	1.13

[a] Includes 200 MW in the limiter, which is removed by a separate water coolant.

[b] 621 MW of this power is deposited in the first wall and is removed by a water coolant.

[c] Account is made for the fact that the pumping power is added to the coolant as thermal energy; efficiency of helium circulator = 0.8.

5.5 KEY REACTOR PARAMETERS

The major design parameters that characterize a tokamak reactor are the reactor power, the neutron wall load, aspect ratio, plasma elongation, major radius, plasma beta, magnetic field, scrape-off region thickness, and blanket/shield thickness. A brief review of the considerations that were factored into selection of these major parameters is presented below. It should be noted that many of the tradeoffs presented below were carried out early in the STARFIRE study. Other tradeoffs that focused on specific subsystems were performed during the various phases of the design. Therefore, some of the parameter values used in parts of the tradeoffs presented below are slightly different from those in the final reference design.

5.5.1 Reactor Power

It has been shown[14] that tokamak reactors exhibit an economy of scale; i.e. larger power reactors have lower cost of energy. However, three considerations important to the utilities limit the desirable power rating of a plant. The first is the difficulty of raising the capital for larger power plants. The second relates to the cost of reserve electric power capacity that the utility must provide to compensate for scheduled and unscheduled outages. The cost of reserve capacity increases with the size of the individual power plant. The third is the maximum capacity of a single turbine generator, postulated to be in the range of 1400 MWe, by the year 2000. Based on recommendations by the Utility Advisory Committee for STARFIRE, the most desirable power rating at present is in the range of 3000-4000 MW for thermal power and ∿1250 MW for electrical power. Therefore, the fusion power for STARFIRE was selected as 3510 MW. Accounting for 90 MW of rf power injected into the plasma, this corresponds to a thermal power of ∿4000 MW, based on 19.5 MeV per fusion reaction. With the gross thermal conversion efficiency of 36%, the gross electrical output is 1440 MW. The circulating power for the rf system and other auxiliary systems is 240 MW. Thus, the net electrical power output is 1200 MW.

5.5.2 Neutron Wall Load and Structure Life

A key parameter that has a substantial impact on the physical size of the reactor is the neutron wall load. The neutron wall load, P_{nw}, is related to the fusion power, P_f, as

$$P_f = P_{nw} A_w \left(\frac{17.6}{14.1}\right) = P_p V ,$$

where A_w is the surface area of the first wall, P_p is the average fusion power density in the plasma, and V is the plasma volume. For the same P_f, higher P_{nw} results in a smaller surface area, higher power density, smaller reactor volume, and potentially lower cost. This underlines the motivation for developing designs with higher wall loads. Figure 5-1 shows the relationship between the major radius and the neutron wall load for P_f = 3200 MW and a plasma elongation of 1.6.

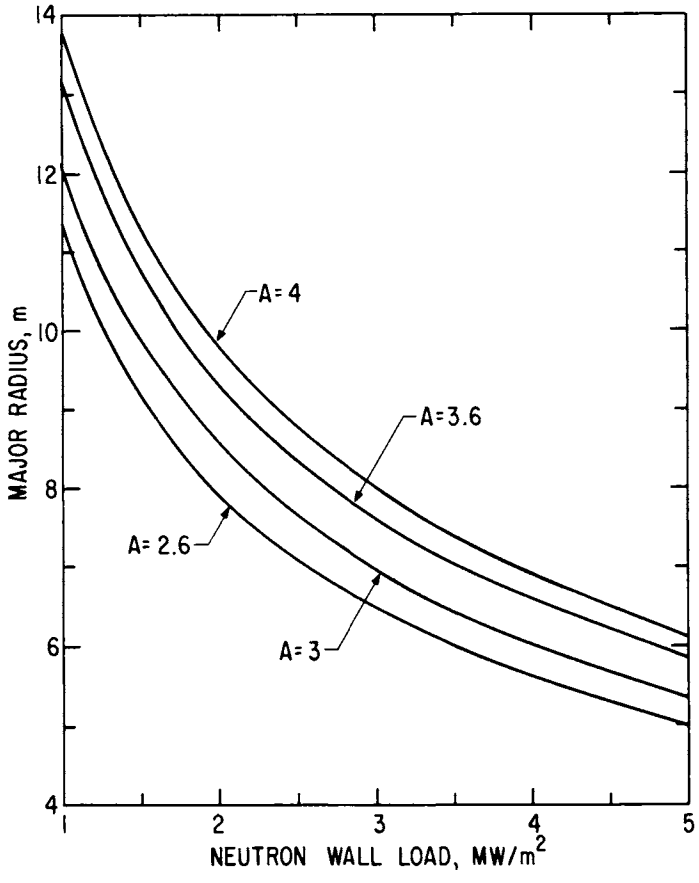

Figure 5.1 Major radius as a function of neutron wall load at four values of the aspect ratio, A. Results based on: fusion power = 3200 MW, and plasma elongation = 1.6.

There are limitations, however, on the ability to produce and use high wall loads. The upper limits on the use of high wall loads are dictated primarily by the first-wall cooling capability and the structure lifetime. Constraints such as the maximum operating temperature and thermal stresses place

an upper bound on the allowable wall load. For typical structural materials such as stainless steel in pulsed reactor systems, the neutron wall load will be limited to $\sim$2.0 MW/m^2 for helium coolants. Higher wall loads are possible with water and lithium coolants. In general, the maximum allowable wall load is higher for steady-state reactors.

For a given fluence lifetime, the neutron wall load should be limited so that the frequency of structure replacement is not excessive. In order to limit the fractional increase in the cost of energy due to the plant downtime for replacement of the structural material to δ, the structure lifetime must be sufficiently long to satisfy the following inequality:[33]

$$t_w > \frac{t_d}{365\ \delta},$$

where t_w is the structure lifetime in years and t_d is the total cumulative downtime in days for replacement of the structural material. For example, in order to limit the increase in the cost of energy to 10% (i.e. $\delta = 0.1$) when the downtime is 125 days, the structure lifetime must be greater than 3.4 yr.

For a given structural material and a fluence lifetime, the loss of energy production resulting from choosing high P_{nw} and short t_w must be weighed against the economic gain realized by designing a small size reactor. Figure 5-2 shows the cost of energy as a function of the neutron wall load at two values of the integral neutron wall load, I_w, of 5 and 20 MW-yr/m^2 and at two different values for the total cumulative downtime, t_d, for replacement of the structural material. For I_w = 5 MW-yr/m^2 and downtime of 125 days, the neutron wall load should be kept in the range of 2-2.5 MW/m^2. For $I_w \sim$ 20 MW-yr/m^2 the cost of energy decreases significantly as the neutron wall load is increased from 1 to 2 MW/m^2. A smaller but significant, saving in the cost of energy (COE) is realizable by increasing P_{nw} from 2 to 3 MW/m^2. A slight change in COE is noticeable in the range $P_{nw} \sim$ 3-4 MW/m^2. The reasons for the modest increase in COE as P_{nw} is increased beyond $\sim$4 MW/m^2 will become evident from discussions later in this section.

It is clear from Fig. 5-2 that the achievable lifetime of the structural material has a significant impact on the cost of energy. By eliminating short plasma pulses and designing STARFIRE for steady-state operation, it is anticipated that a fluence lifetime of 16 MW-yr/m^2 or greater is obtainable with selected candidate structural materials. There are several important advantages

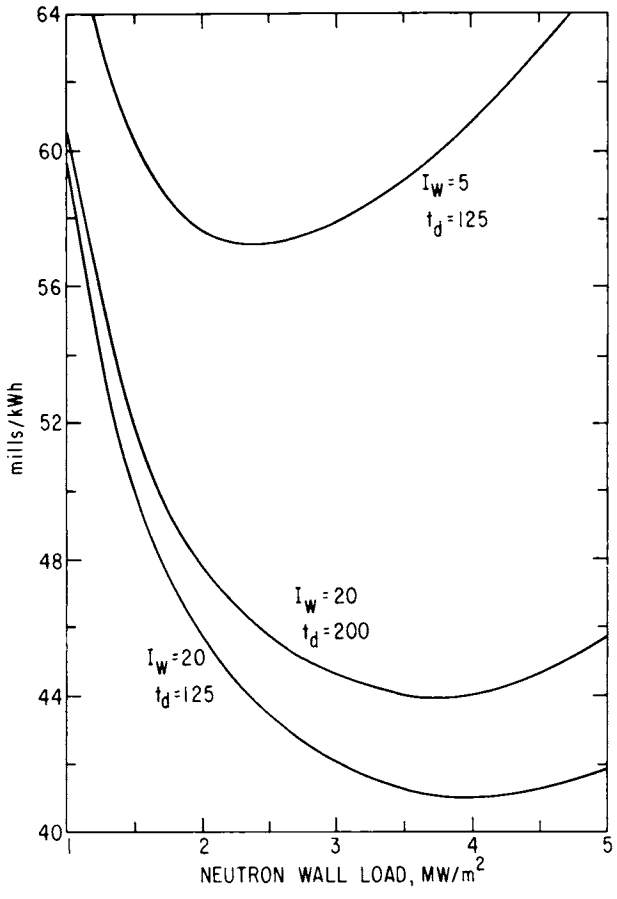

Figure 5-2. Cost of energy as a function of neutron wall load. I_w is the integral neutron wall load in MW-yr/m^2 and t_d is the total downtime in days for replacement of the structural material. Results are based on fusion power of 3200 MW, aspect ratio of 3.6, plasma elongation of 1.6 and β_t = 0.067.

for such long life: (a) the cost of energy is substantially reduced because of less frequent replacement and higher availability factor; (b) when the frequency of replacement is substantially reduced, the cost of energy becomes less sensitive to moderate variations in the downtime. This is quite important as it permits flexibility in the reactor design not available otherwise for designs driven primarily by the need for achieving very short downtimes; (c) a less frequent replacement of the structural material results in a lower inventory of radioactive materials for which storage has to be provided. (It should be noted that even for the candidate structural materials with no long-term activation, adequate radioactive storage is necessary for two to five decades); and (d) the demand on material resources is less with longer life.

For a given fusion power, plasma elongation and aspect ratio, a higher wall load implies a higher plasma power density, P_p. This varies as $P_p \sim \beta^2 B^4$. Since the plasma β is limited by stability considerations, a high P_{nw} is obtainable only by providing a higher magnetic field as shown in Fig. 5-3. This figure shows the maximum toroidal magnetic field, B_m, required as a function of aspect ratio and neutron wall load. The two different scales for B_m on the left and right of Fig. 5-3 correspond to two different plasma impurity control schemes as discussed in Sec. 5.5.4. For $P_{nw} > 2$ MW/m^2, there is $\sim$1 T increase in the required B_m for every 1 MW/m^2 increase in P_{nw}. The economically attractive range for P_{nw} of 3-4 MW/m^2 requires a maximum toroidal field in the range of 10-12 T which is considered acceptable for the STARFIRE design as discussed shortly.

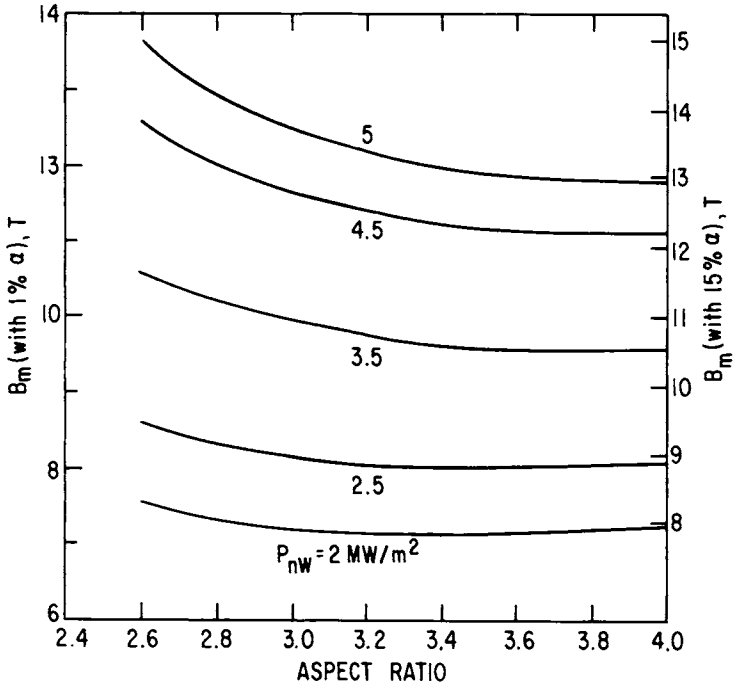

Figure 5-3. B_m as a function of A at several values of P_{nw}. The LHS scale is for n_α/n_{DT} = 0.01 and the RHS scale is for n_α/n_{DT} = 0.15. (P_f = 3200 MW, β_t = 0.24/A, Δ_{BS}^i = 1.2 m, Δ_v = 0.1 m, $\bar{T}$ = 8 keV, κ = 1.6.)

In light of the above considerations, a neutron wall load of 3.6 MW/m^2 has been selected for STARFIRE. This moderately high wall load appears to be a reasonable choice that makes it possible to design a relatively small size reactor without excessive requirements on first-wall cooling capability,

maximum toroidal magnetic field, and frequency of structural material replacement.

5.5.3 Plasma Beta

Previous systems studies[14] have indicated significant economic benefits for operating at high average plasma toroidal beta, β_t. However, the maximum realizable β_t is limited by plasma stability considerations.

The reference value, $\beta_t = 0.067$, appears attainable on the basis of the stability analysis of Chap. 6. An important constraint in the STARFIRE design was the desire to keep the plasma current, I, small in order to minimize the lower-hybrid power needed to maintain the plasma current. Generally speaking, operation with higher current stabilizes the plasma to higher β_t. Results from Table 6-3 are summarized in Table 5-7. These results suggest that β_t = 0.067, 0.10, and 0.12 may be achieved for I = 10.1 MA, 11.2 MA, and 12.9 MA, respectively. The electric power, P_{LH}, required for the lower-hybrid system is estimated to be 150 MW, 166 MW, and 192 MW for the three cases. Since the gross electric power is held fixed, the increase in P_{LH} represents the penalty of higher β_t values. The benefit is a reduction in the toroidal magnetic field strength, B_m. Increasing β_t from 0.067 to 0.10 reduces the plant net electric output by 1.3%, which has a direct capital cost equivalent of $\sim$22 M\$ in addition to $\sim$4 M\$ increase in the cost of the lower-hybrid system. The corresponding reduction in the magnetic field from 11.1 to 9.1 T reduces the cost of the magnets and support structure by $\sim$70 M\$. Therefore, the cost per unit power for the case of $\beta_t = 0.10$ is $\sim$2.5% lower than that for $\beta_t = 0.067$ (Table 5-7). Thus, the higher β_t cases offer some economic benefits. In addition, they may eliminate the need for the development of the Nb_3Sn superconductor. However, it is not clear yet, without experimental evidence, whether the higher β_t values are achievable and what additional degree of engineering complexity, e.g. in wall stabilization, may be required. Therefore, the lower β_t value of 0.067 is used in the reference design. In the following tradeoffs, the relationship β_t = 0.24/A, where A is the aspect ratio, is assumed. This relationship is based on recent theoretical analysis (see Chap. 6).

5.5.4 Toroidal Magnetic Field

Figure 5-3 showed the maximum toroidal field (B_m) required as a function of aspect ratio and neutron wall load for P_f = 3200 MW, κ = 1.6, β_t = 0.24/A,

Table 5-7. Higher Beta Designs for STARFIRE.

(P_f = 3510 MW, R = 7.0 m, A = 3.6, $\kappa \stackrel{f}{=}$ 1.6, d = 0.5, α = 1.4, $\bar{n}_e = 1.18 \times 10^{20}$ m^{-3}.)

β_t	0.067	0.100	0.120
q_a	1.21	1.10	∿1.1
I, MA	10.1	11.2	12.9
B_m, T	11.1	9.1	8.3
P_{LH}, MW	150	166	192
Net electric power, MW	1200	1184	1158
Cost per unit power (relative units)	1.00	0.975	0.984

Δ_v = 0.1 m, and Δ^i_{BS} = 1.2 m. The scale on the left side of Fig. 5-3 shows the required B_m if an efficient plasma impurity control mechanism is provided such that n_α/n_{DT} is ∿0.01. The scale on the right shows the B_m required if a less efficient impurity control mechanism is utilized such that n_α/n_{DT} is ∿0.15. Figure 5-4 provides more details about the variation of B_m with the impurity level for the case of P_{nw} = 3.6 MW/m^2, aspect ratio of 3.6 and $T_i \sim T_e$ = 14 keV. The rf power required to drive the plasma current decreases with T_e. The dependence of B_m on T_e is shown in Fig. 5-5.

There exists at present considerable experience with NbTi superconductors. However, it has been shown that a magnetic field of ∿10 T is the maximum practical limit for NbTi cooled to 4.2 K at atmospheric pressure. On the other hand, Nb_3Sn is capable of generating higher fields. Although present experience with Nb_3Sn is limited, the progress in the current technology development program indicates that the Nb_3Sn technology will be available in the STARFIRE time frame. Therefore, the 10-T limit of NbTi was not imposed as a constraint in the STARFIRE study; the required value of the toroidal field was determined from engineering and economic tradeoffs for the overall reactor system.

5.5.5 Plasma Elongation

The elongation (κ = b/a) of a D-shaped plasma has a significant impact on the plasma performance, the reactor design characteristics, and economics. In

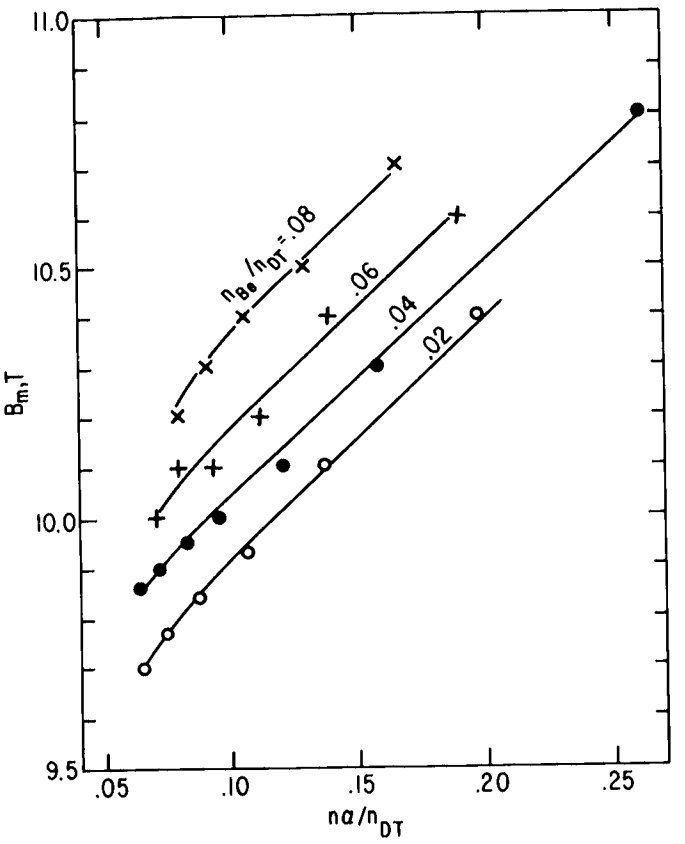

Figure 5-4. Variation of the maximum magnetic field with the α-particle concentration, n_α/n_{DT}, and other impurity concentration, n_{Be}/n_{DT}. (P_f = 3200 MW, P_{nw} = 3.6 MW/m^2, κ = 1.6, A = 3.6, β_t = 0.067, $\bar{T}_i \sim T_e$ = 14 keV, Δ^i_{BS} + 1.2 m, Δ_v = 0.1 m, R = 7 m.)

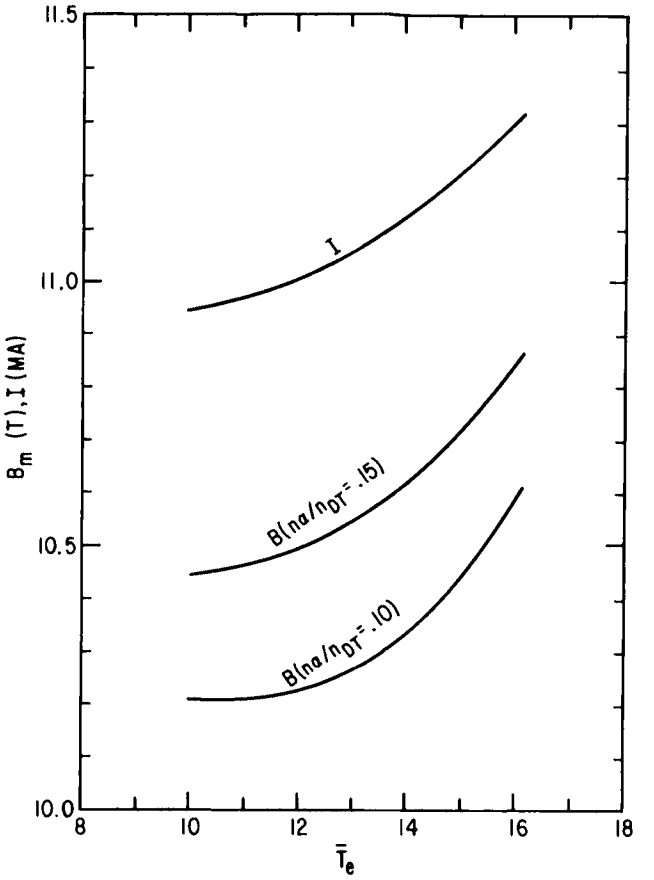

Figure 5-5. Variation of the maximum magnetic field and plasma current with the average electron temperature, T_e. (P_f = 3200 MW, κ = 1.6, A = 3.6, R = 7 m, β_t = 0.067, Δ^i_{BS} = 1.2 m, Δ_v = 0.1 m.)

particular, at higher κ the achievable β_t is higher but the required EF coil system becomes more complex and costly. Based on previous work,[10,34] a value of $\kappa = 1.6$ was selected for STARFIRE. This is believed to be nearly the upper limit on elongation if the important design goal of locating most of the EF coils external to the TF coils is to be achievable.

5.5.6 Power Requirements for Current Drive

Since STARFIRE will operate in a steady-state mode, a particularly important aspect of the design is the mechanism for plasma current drive. As discussed in Sec. 5-2, lower-hybrid rf is the selected option for current drive. An important impact of the current drive system on the reactor performance and economics is the electrical power requirements for this system. The dependence of the magnitude of this power for the rf system on key plasma and reactor design parameters is discussed in Chap. 7.

5.5.7 Major Radius and Aspect Ratio

With the fusion power and neutron wall load selected, the surface area of the plasma is defined. For a given κ, the aspect ratio (A) or the major radius (R) should be selected in order to fully define the plasma geometry. As shown previoulsy in Fig. 5-1, at $P_{nw} = 3.6$ MW/m^2, the major radius increases from 6 m to $\sim$7.3 m if A is increased from 2.6 to 4.0.

The size of the reactor building, length of piping, etc., are strongly affected by the size of the reactor, in particular, by the value of R + a, where a is the plasma minor radius. Notice that the variation of R + a as the aspect ratio is changed is less than the variation in R alone. Despite the reduction in the capital cost of several items that are sensitive to size at smaller values of R, economic optimization does not necessarily favor the selection of minimum R. This is true for both pulsed and steady-state reactors although for different reasons.

For pulsed reactors, the optimum size is significantly affected by the central core radius, r_v. For a given magnetic field for the OH coil, decreasing r_v reduces the available volt-seconds and shortens the burn time resulting in a lower reactor electrical output.

For steady-state reactors with no OH coils the problem of the central core radius disappears. In this case, the plasma current has to be driven by external

means. If the electrical power requirement for the current driver were negligibly small, then the smallest aspect ratio should be chosen so that the major radius is minimum, provided of course that there is adequate space on the inner side of the torus to accommodate the TF coils and support cylinder. This is illustrated by the case P_{rf} = 10 MW in Fig. 5-6 which displays the cost of energy as a function of the aspect ratio.

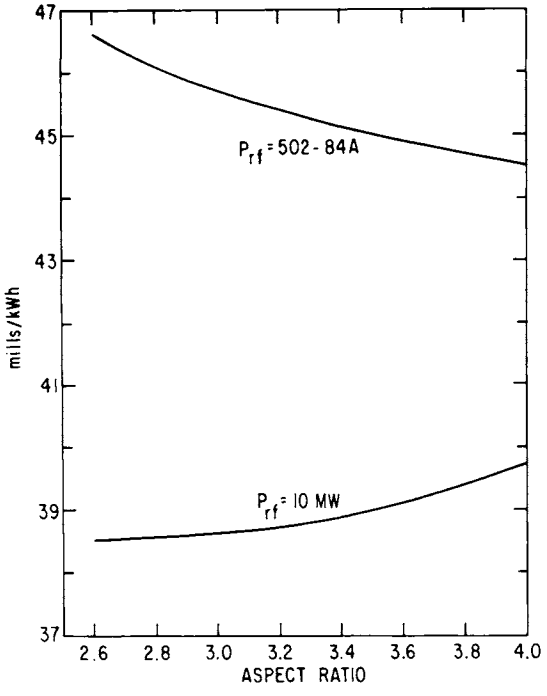

Figure 5.6. Cost of energy as a function of aspect ratio for a steady-state reactor in two cases for the electrical power, P_{rf}, required for the current-drive system: P_{rf} = 10 and P_{rf} = 502 - 84A where A is the aspect ratio.

As discussed earlier in Sec. 5.2, the electrical power requirement, P_{rf}, for the lower-hybrid current drive system appears to be relatively large, and it increases with lower aspect ratio. Figure 5-6 shows the dependence of the cost of energy on aspect ratio for the case where P_{rf} = 502 - 84A, with P_{rf} in MWe. In this case, the cost of energy decreases as A increases up to A $\sim$ 4. As discussed in Chapt. 7, further work significantly reduced the LH power requirements. This reduces the optimum aspect ratio somewhat below A = 4. Therefore, A = 3.6 was adopted for STARFIRE. This results in a major radius R = 7 m. The maximum magnetic field required is nearly minimum at A = 3.6 as evident from results in Fig. 5-3.

5.5.8 Inner Blanket/Shield Thickness

The thickness, Δ^i_{BS}, of the blanket and shield on the inner side of the torus, or more precisely the distance in midplane from the plasma side of the first wall to the location of the maximum toroidal magnetic field, has a substantial impact on the reactor size, the required strength of the magnetic field, and reactor economics. A comprehensive investigation of the optimum value for Δ^i_{BS} has been carried out previously.[35] The details of this previous work will not be repeated here, but the results are briefly stated.

For a given P_f, P_{nw}, β_t, and major radius, the advantages of a smaller Δ^i_{BS} are (1) lower maximum magnetic field; and (2) larger central core (OH) radius, r_v. In pulsed tokamaks, the impact of the value of Δ^i_{BS} on r_v is large and becomes critical for low P_f, high P_{nw} designs. In a steady-state tokamak with no OH solenoid, the primary incentive for reducing Δ^i_{BS} is to reduce the maximum magnetic field required.

On the other hand, there are several penalties for making Δ^i_{BS} too small. The increase in the radiation field when Δ^i_{BS} is decreased results in (a) increases in the resistivity of the stabilizer material and a need for increasing the amount of the stabilizer to satisfy the cryogenic stability requirements; (b) a decrease in the critical current density of the superconductor necessitating the use of more superconductor; and (c) an increase in the heat generation rate in the TF coil. The increase in the power requirements for the TF coil cryogenic system can be so large that the reactor net electrical power output is seriously reduced.

In STARFIRE, a value of Δ^i_{BS} = 1.2 m was selected based on careful considerations of the above tradeoffs. This value includes a 9-cm vacuum gap between the blanket and shield, shield and TF coils, and thermal insulation inside the vacuum tank. The shield consists of a combination of tungsten, boron carbide, and a structural material. If the 37-cm thick breeding blanket in the inboard region were to be replaced with more effective shielding material, Δ^i_{BS} could have been reduced further. This inboard blanket is necessary to achieve a tritium breeding ratio >1 with the solid breeder.

5.5.9 Outer Leg of the TF Coils

For a given major radius (R), plasma inner radius (a) and inner blanket/shield thickness (Δ^i_{BS}), the position of the inner leg of the TF coil is defined.

In order to fully define the D-shape of the TF coil, the size of the vertical or horizontal bore must be selected. We will discuss this choice in terms of R_2, the major radius of the midpoint of the outer leg of the TF coil. R_2 is the sum of the major radius, first-wall minor radius, outer blanket/shield thickness (Δ^o_{BS}), vacuum plenum thickness (Δ_p), clearance (Δ_c) in the midplane from the outer edge of the shield to the TF coil and half of the TF coil thickness. The choice of R_2 has a significant impact on many of the reactor characteristics and cost as discussed below.

With the reactor parameters previously defined in this section (R, a, Δ_v, B_m, Δ^i_{BS}) the only remaining parameters that affect R_2 are Δ^o_{BS} and Δ_c. The necessary value of Δ^o_{BS} varies with blanket and shield material and coolant choices. As a goal, the materials in the shield should be chosen to have inherently low long-lived radioactivity even if they are less efficient in radiation attenuation. For the reference material choices, the required Δ^o_{BS} is $\sim$1.8 m. The plenum region thickness varies slightly with position with an average $\Delta_p \sim 0.6$ m. The clearance from the outer edge of the shield to the TF coils is required for several engineering reasons; the most dominant of which is to provide clearance for installation of the shield. The required R_2 is $\sim$13 m.

The economics analysis shows a substantial penalty for increasing R_2. The cost of energy increases by $\sim$3% for each additional meter increase in the value of R_2 beyond 13 m. The cause of this penalty is that the value of R_2 directly influences the size and weight of the TF coils and their support structure, the size of the reactor building, the length of the piping for the heat transport system, and the size of the externally located EF coils. For example, by increasing R_2 from 13 to 15 m, the ampere-turns and stored energy in the EF coils nearly double.

It should be noted that in order to keep the field ripple at the plasma to an acceptable level, the value of R_2 is larger for a smaller number of TF coils. A relatively small number, 12, of TF coils has been chosen for STARFIRE to enhance reactor maintainability. The resulting field ripple at the plasma edge is $\pm$1.14%. While such a field ripple is higher than the values considered acceptable for near-term physics devices, it is judged to be acceptable in STARFIRE because of the much larger plasma volume and better particle confinement. Should future results prove otherwise, a field-ripple correction system

(e.g. iron blocks)[36] should be provided in preference to increasing R_2, which is costly. There is also a possibility that a much higher field ripple is tolerable. If such a result is found in the future, the most effective way of capitalizing on it would be to decrease the number of TF coils in order to further enhance reactor accessibility and maintainability.

5.6 DESIGN CONFIGURATION

Several design configuration decisions were motivated primarily by a desire to provide easier assembly and maintenance procedure for STARFIRE. Examples include locating the vacuum boundary at the shield rather than the first wall, locating all superconducting poloidal coils outside of the TF coils, selecting the minimum number of the coils subject to constraints on ripple, and the radial dimension of the outer leg of the TF coil (see previous section). Additional key requirement in developing the STARFIRE reactor configuration is that it permits removal of each component in a time consistent with its anticipated life. Short-lived components are designed for rapid replacement at the expense of, if necessary, the ease of replacing longer life components. As an example, blanket sectors are afforded more rapid replacement than sheild sectors by providing shield access doors through the vacuum boundary to permit blanket replacement. This permits the shield to be designed so that it normally remains in place and permits long life welded seals and a close fitting stepped joint to be used in the centerpost region.

The reactor configuration is developed primarily around the desire to keep the superconducting EF coils external of the superconducting TF coil so that coil replacement is possible without in-place manufacturing of a new coil. The external EF coil location places a large incentive on minimizing TF coil size to reduce the stored energy requirement and resultant capital costs of the EF coils.

The TF coils utilize a common dewar at the centerpost to minimize the inner blanket shield thickness and to minimize the cryogentic heat leak to the coils. The common dewar vacuum tank encloses the centerpost, core EF/OH coils, and TF coils to simplify the overall design. The small EF/OH coils at the center of the reactor were located inside the centerpost to permit their removal without distrubing the TF coils. The centerpost coils are grouped in two modules to simplify yet permit their removal without increasing the overall

building height. Infrequent maintenance will require warming of all coils simultaneously.

Spare coils are provided for the EF/OH coils trapped under the reactor because the complications of installing a new coil, even if only once in every few plant lifetimes, make it cost effective.

The reactor support structure is integrated into the other reactor components to maximize access and utilize materials effectively. For example, the TF coil room temperature vacuum tank provides support for the EF coils without significantly effecting the structural thickness requirements. The dominant out-of-plane forces on the TF coil system are reacted through a room temperature shear panel that also acts as shielding. Room temperature structure was used to permit large access openings for blanket removal while providing adequate coil restraint.

References

1. R. G. Mills, et al., "A Fusion Power Plant," MATT-1050, Princeton Plasma Physics Laboratory (1974).

2. G. L. Kulcinski, et al., "A Wisconsin Toroidal Fusion Reactor Design, UWMAK-I," UWFDM-68, Univeristy of Wisconsin (1974).

3. R. W. Conn, et al., "A Conceptual Tokamak Reactor Design, UWMAK-II," University of Wisconsin (1975).

4. C. Baker, et al., "Characteristics of a First-Generation Commercial Fusion Power Plant," GA-A13661, General Atomic Co. (1975).

5. W. M. Stacey, Jr., C. C. Baker and M. Roberts, "Tokamak Experimental Power Reactor Studies," Proc. 6th Intern. Conf. Plasma Physics and Controlled Nuclear Fusion Research, October 6-13, 1976, Berchtesgaden, Federal Republic of Germany; also ERDA-76/139, U. S. Energy Research and Development Administration (1976).

6. R. W. Conn, et al., "UWMAK-III, A Noncircular Tokamak Power Reactor Design," UWFDM-150, University of Wisconsin (1976).

7. D. W. Kearney, et al., "Conceptual Design Study of a Noncircular Tokamak Demonstration Fusion Power Reactor," GA-A13992, General Atomic Company (1976).

8. R. Hancox and J. T. D. Mitchell, Proc. 6th Intern. Conf. on Plasma Physics and Controlled Nuclear Fusion, Berchtesgaden, FRG, Vol. 3 (IAEA, 1976), p. 193.

9. D. Steiner, et al., "ORNL Fusion Power Demonstration Study: Interim Report," ORNL/TM-5813, Oak Ridge National Laboratory (1977).

10. M. Abdou, et al., "ANL Parametric System Studies," ANL/FPP/TM-100 (1977).

11. D. DeFreece, et al., "Fusion First Wall/Blanket Systems Analysis," EPRI Report RP-472-1 (1977).

12. F. Casali and G. Casini, "FINTOR, A Minimum Size Toakamk DT Reactor," The FINTOR Group, J. R. C. EURATOM, Ispra (1977).

13. D. R. Cohn, et al., "High Field Compact Tokamak Reactor," RR-78-2, MIT plasma Center (1978).

14. M. Abdou, et al., "Impact of Major Design Parameters on the Economics of Tokamak Power Plants," IAEA-TC-145/44 (1978).

15. J. T. D. Mitchell, "Blanket Replacement in Toroidal Fusion Reactors," Proc. 3rd Top. Mtg. on Technology of Controlled Nuclear Fusion, CONF-78058, Vol. 2 (1978), p. 954.

16. B. Badger, et al., "NUMAK, A Tokamak Reactor Design Study," UWFDM-330, University of Wisconsin (1979).

17. M. Abdou, et al., "Impact of Technology and Maintainability on Economic Aspects of Tokamak Power Plants," Proc. 7th IAEA Conf. on Plasma Physics and Controlled Nuclear Fusion Research, IAEA-CN-37/I-4 (IAEA, Vienna, 1979), Vol. III, p. 357.

18. N. J. Fisch, Phys. Rev. Lett. 41, 873 (1978).

19. C. F. F. Karney and N. J. Fisch, Phys. Fluids 22, 1817 (1979).

20. D. J. H. Wort, Plasma Phys. 13, 258 (1971); P. C. Thonemann, W. T. Cowhig and P. A. Davenport, Nature 169, 34 (1952); N. A. Borzunov, et al., Dokl. Akad. Nauk SSR 152, 581 (1963) [Sov. Phys. - Dokl. 8, 914 (1964)]; R. A. Demirkhanov, et al., Zh. Tekh. Fiz. 35, 212 (1965) [Sov. Phys. - Tech. Phys. 10, 174 (1965)]; S. Yoshikawa and H. Yamato, Phys. Fluids 9, 1814 (1966); K. Hirano, K. Matsuura and A. Mohri, Phys. Lett. A 36, 215 (1971); S. M. Osovets and I. A. Popov, Proc. 5th European Conf. on Controlled Fusion and Plasma Physics, Vol. 1 (1972), p. 8; M. Fukuda, et al., J. Phys. Soc. Japan 41, 1376 (1976); M. Fukuda and K. Matsura, J. Phys. Soc. Japan 44, 1344 (1978).

21. D. A. Ehst, Nucl. Fusion 19, 1369 (1979).

22. S. Y. Yuen, et al., Nucl. Fusion 20, 159 (1980).

23. C. Chu, et al., General Atomic Co., GA-A15027 (1978); R. Klima, et al., Sov. J. Plasma Phys. 5, 277 (1979); N. J. Fisch, et al., Princeton Plasma Physics Laboratory, PPPL-1624 (1979); K. Kato, Phys. Rev. Lett. 44, 779 (1980); D. K. Bhadra, Nucl. Fusion 20, 619 (1980); N. J. Fisch, et al., Princeton Plasma Physics Laboratory, PPPL-1657 (1980).

24. K. L. Wong, Phys. Rev. Lett. 43, 438 (1979); R. McWilliams, et al., Phys. Rev. Lett. 44, 245 (1980); R. J. LaHaye, et al., Nucl. Fusion 20, 218 (1980); K. L. Wong, et al., Princeton Plasma Physics Laboratory, PPPL-1662 (1980).

25. T. Yamato, et al., Phys. Rev. Lett. 45, 716 (1980).

26. D. L. Smith, et al., "Fusion Reactor Blanket/Shield Design Study," ANL/FPP-79-1, Argonne National Laboratory (1979).

27. J. S. Karbowski, et al., "Tokamak Blanket Design Study Final Report," ORNL/TM-7049, Oak Ridge National Laboratory (1980).

28. R. Mattas and D. L. Smith, "Modeling of Life-Limiting Properties of Fusion Reactor Structural Materials," ANL/FPP/TM-84, Argonne National Laboratory (1977).

29. "ETF Interim Design Description Document," ETF Design Center (1980).

30. D. L. Smith and R. E. Gold, "Liquid Metals in Tokamak Reactor Blankets," Proc. 2nd Intern. Conf. on Liauid Metal Technology in Energy Production, Richland, Washington (1980), to be issued.

31. M. M. El-Wakil, Nuclear Energy Conversion (American Nuclear Society, LaGrange Park, Illinois, 1978).

32. G. Melese d'Hospital, "Review of Gas Cooled Reactors Thermal Hydraulics," GA-A15866, General Atomic Company (1980).

33. M. Abdou and Z. El-Derini, "A Comparative Study of the Performance and Economics of Advanced and Conventional Structural Materials in Fusion Systems," Proc. 1st Top. Conf. on Fusion Reactor Materials, Miami Beach, Florida; J. Nucl. Mater. 85 & 86, 57 (1979).

34. K. Evans, et al., "Equilibrium Field Coil Considerations for Tokamak Reactors," Proc. 3rd ANS Top. Mtg. on the Technology of Controlled Nuclear Fusion, CONF-780508, Vol. 2 (1978), p. 1084.

35. M. Abdou, "Radiation Considerations for Superconducting Fusion Magnets," J. Nucl. Mater. 72, 147 (1978).

36. L. R. Turner, et al., "Iron Shielding to Decrease Toroidal-Field Ripple in a Tokamak Reactor," Proc. 3rd ANS Top. Mtg. on the Technology of Controlled Nuclear Fusion, CONF-780508, Vol. 2 (1978), p. 883.

Table of Contents

List of Figures

List of Figures (cont'd)

List of Tables

6.1 SUMMARY AND INTRODUCTION

STARFIRE uses a DT burning, D-shape plasma to produce 3510 MW of fusion power. The plasma is operated at a moderate β of 6.7% and is moderately elongated, with a height to width ratio of 1.6. The major plasma parameters and plasma engineering features of STARFIRE are listed in Tables 6-1 and 6-2, respectively. The plasma current is driven in steady state with 90 MW of lower hybrid rf power. The first wall and all other components in the vacuum chamber are coated with Be. The impurity control system maintains a steady-state concentration of 14% helium and 4% Be in the plasma. The fairly low DT removal efficiency (10%) of the impurity control system permits a high fractional burnup of tritium. For the same reason, most of the plasma fueling is done automatically by DT neutrals recycling from the first wall and limiter. Additional fueling is done by gas puffing.

In order to minimize the heat transport load on the limiter, as well as to establish a thermal equilibrium, the plasma is operated in an "enhanced radiation" mode, whereby a small amount of high-Z material, nominally iodine, is added along with the fuel stream. This serves to radiate most of the α-heating energy and stabilizes the thermal operating point.

The plasma MHD equilibrium is of the low current, hollow profile type. The plasma position is controlled with two sets of coils, a main equilibrium field (EF) coil set and a control field (CF) coil set. The main EF coils are superconducting and are located outside of the TF coils. They are used to provide the basic positional equilibria. The CF coils consist of small copper coils inside the TF coils and are used to control position and to stabilize against plasma disruptions. To further aid in the latter task, the first wall is designed with a time constant of 300 ms to stabilize against rapid vertical instabilities.

Because of the need to minimize the lower hybrid rf current drive power, the plasma density is lower and the plasma ion temperature is higher than most previous tokamak reactor designs. The plasma is operated with $T_i > T_e$, which makes better use of the available β. The tradeoffs between the operating point and rf power, and the selection of density and temperature parameters are discussed in detail in Chap. 7.

Table 6-1. STARFIRE Plasma Parameters

Parameter	Unit	Value
Major radius, R	m	7.0
Aspect ratio, A	—	3.6
Elongation, κ	—	1.6
Deity, D	—	0.5
Safety factor at limiter, q_b	—	5.1
Toroidal beta, β	—	0.067
Maximum toroidal field at coil, B_M	T	11.1
Toroidal field at plasma center, B_o	T	5.8
Plasma current, I_p	MA	10.1
Plasma volume, V_p	m^3	781
Average electron temperature, T_e	keV	17.3
Centerline electron temperature, T_{eo}	keV	22.5
Average ion temperature, T_i	keV	24.1
Centerline ion temperature, T_{io}	keV	31.3
Average fuel density, N_{DT}	m^{-3}	0.806×10^{20}
Centerline fuel density, N_{DT_o}	m^{-3}	1.69×10^{20}
Electron energy confinement time, τ_E	s	3.6
Ion energy confinement time, τ_I	s	10
Particle confinement time, τ_p	s	1.8
Fractional helium concentration, N_α/N_{DT}	—	0.14
Fractional beryllium concentration, N_{Be}/N_{DT}	—	0.04
Fractional iodine concentration N_I/N_{DT}	—	0.001
Fusion power, P_F	MW	3510 MW
Lower hybrid rf power to plasma, P_{rf}	MW	90
Average neutron wall load, P_{NW}	MW/m^2	3.6

Table 6-2. Plasma Engineering Features of STARFIRE

Operating Point	
Equilibrium type:	Elongated, D-shape, moderate β, hollow current profile
Equilibrium generation method:	Outside superconducting equilibrium field coil system
Position stabilization method:	Inside control field coils and conducting first wall with 300 ms time constant.
Burn Cycle	
Startup time:	$\sim$ 24 minutes
Method:	Tritium lean startup, vary rf power, DT density, T fraction, 5% per minute fusion power ramp.
Normal shutdown time:	$\sim$ 24 minutes
Emergency shutdown:	Induced disruption method, time < 3 s
Plasma initiation method:	5 MW electron cyclotron resonance heating
Burn method:	Steady state, lower hybrid current drive
Thermal stabilization:	Enhanced radiation mode operation by iodine injection
Fueling	
Fueling method:	Recycling DT plus gas puffing

Most of the STARFIRE burn cycle is substantially different from pulsed reactor burn cycles. Plasma breakdown is done with 5 MW of electron cyclotron resonance heating (ECRH) and does not require a high voltage OH coil. The startup period takes 24 minutes and conforms to the requirement that the fusion power should be ramped at a 5% per minute rate, to minimize thermal problems in the energy recovery and conversion systems. The OH coil as well as the OH and EF power supplies have modest requirements compared to pulsed reactor

requirements. The steady state burn phase of the burn cycle has a thermal equilibrium maintained by the addition of iodine. The equilibrium and stability of the enhanced radiation mode of operation have been studied with a global code and with the 1-D WHIST code. These studies indicate that this mode of operation is feasible.

Several types of shutdown scenarios have been developed for STARFIRE. The normal shutdown is basically the reverse of the startup period, whereby the fusion power is reduced at a 5% per minute rate by reducing the tritium fraction in the plasma. There are three types of emergency shutdowns. The fastest is an "abrupt" shutdown whereby a plasma disruption is induced by injecting excess high-Z material. There is a more orderly "rapid" shutdown which also uses a disruption, but where most of the plasma energy is radiated away prior to the disruption. Finally, a naturally occurring "ablative induced shutdown" has been identified which occurs as a result of a hot spot formation on the first wall or limiter.

Various fueling options for STARFIRE were studied. The high fractional burnup rate of 42% in STARFIRE permits a fairly low fueling rate from an external source. Gas puffing is the most desirable engineering option and has been adopted as the STARFIRE fueling method.

6.2 MHD EQUILIBRIUM AND STEADY STATE OPERATING POINT

6.2.1 Equilibrium and Stability Survey

This section describes the considerations leading to the choice of the reference equilibrium operating point. We have considered D-shaped plasma equilibria in toroidal geometry (as defined in Ref. 1 and 2) with pressure profiles characterized by a width parameter α. Using a diamagnetism function[2] $F^2(\psi) = F_0^2 (1 - \delta\hat{\psi}^\gamma)$ and a pressure function $P(\psi) = \psi^\alpha$ it is possible to generate a broad range of low and high β equilibria with various axis and limiter values of the safety factor, q_a and q_b, respectively. The highest stable β is, in general, a function of A, κ, d, α, q_a and q_b, where A is the aspect ratio, κ is the elongation, and d determines the triangularity. This functional dependence is under active investigation in the physics community, and the operating point for STARFIRE is based on a survey of equilibria and subsequent stability analysis.

Stability to the n = 1 external kink and to ballooning modes increases linearly with κ up to $\kappa \sim 1.6$ and levels off for higher values.[1,3] Likewise, stability increases with d for $\kappa \simeq 1.6$, up to $d \approx 0.5$.[1,3] This desirability of D-shapes has been confirmed for a variety of diffuse[4] and surface current equilibria.[5] The difficulty of designing the EF coil system, however, increases at large values of κ and d and it was found that $\kappa = 1.6$ and $d = 0.5$ are an appropriate choice for STARFIRE. Broad pressure profiles (low α) appear to yield the highest β stable to ideal modes,[1] and for STARFIRE we have chosen $\alpha = 1.4$. Steady-state auxiliary heating associated with the current-drive mechanism will yield some control over the pressure profile width, but α must remain somewhat uncertain until more detailed one-dimensional plasma transport calculations have been developed. The aspect ratio was retained as an explicit variable in the system trade-off studies performed in Chap. 5. On the basis of those studies, where the maximum stable β was taken as $\beta = 0.25\ A^{-1}$,[1,6] the value A = 3.6 was selected.

For the four fixed parameters $\kappa = 1.6$, $d = 0.5$, $A = 3.6$, and $\alpha = 1.4$, an equilibrium survey was performed over a matrix of q_b and β values. [In our discussions, β is the volume averaged quantity,[2] which is distinct from the r.m.s. value occasionally used in the literature.[1]] In the survey $q_a \equiv 1.0$; from the equilibria it is possible to use a simple scaling law to obtain lower β solutions by increasing q_a.[7] When analyzing this variety of equilibria (Fig. 6-1), several key criteria can be used to quickly eliminate unattractive solutions:

1. Assuming $q_a \gtrsim 1.0$ for stability, we can only scale these $q_a = 1$ solutions to lower β values; this makes solutions in Fig. 6-1 with $\beta \lesssim 0.07$ uninteresting.

2. Assuming negative current density is not compatible with the wave drive mechanism, those solutions above the dashed line in Fig. 6-1 may be discarded.

3. In order to avoid the double tearing mode,[8] the safety factor profile is required to be monotonic from the magnetic axis to the limiter, which tends to eliminate some very high β solutions (those above the dotted line in Fig. 6-1).

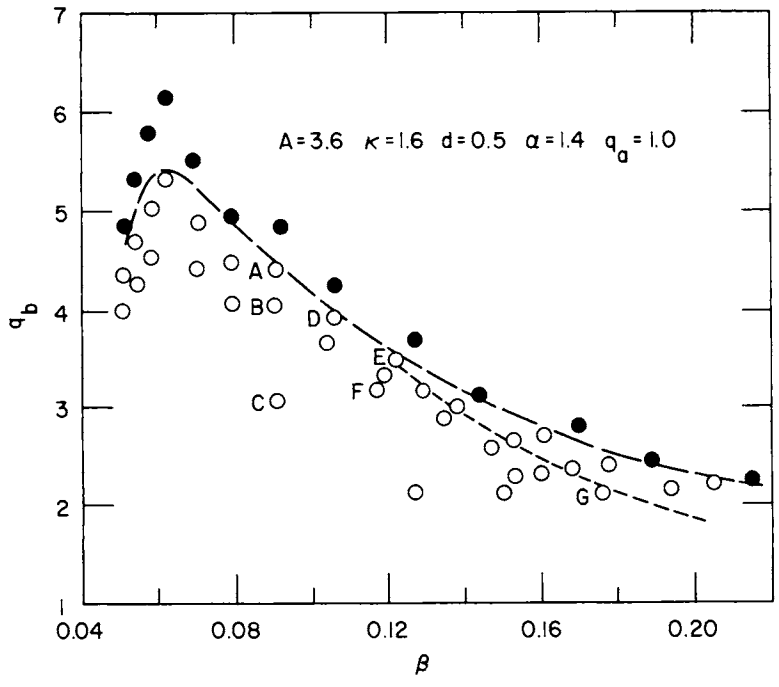

Figure 6-1. MHD equilibrium solutions for STARFIRE survey; each point represents a different γ-δ combination [$(F^2(\psi) = F_0^2\ (1-\delta\hat{\psi}^\gamma)$].

As discussed in Chap. 7, driving the toroidal current with lower hybrid waves is made easier with low current equilibria with hollow current profiles. Sykes[9] showed that hollow profiles are compatible with high β stability, and we use the sequence A, B, C on Fig. 6-1 to illustrate the consequences for STARFIRE. Table 6-3 shows the decrease in I as q_b is raised for the sequence C → B → A, all of which have $\beta = 0.09$. Figure 6-2 shows that the decrease in I is accomplished by removing current density from the interior of the plasma; and an analysis with the BLOON code[10,11] showed that all three cases are equally stable to ballooning and interchange modes when the equilibria are scaled to $\beta = 0.067$. Thus, for a given β, the stable equilibria with lowest current appear to have hollow profiles. Favorable stability of paramagnetic surface currents has also been suggested by other analyses.[6,12-14]

Table 6-3. Equilibria with A = 3.6, κ = 1.6, d = 0.5, α = 1.4

Equilibrium	β (q_a = 1.0)	I (q_a = 1.0)	γ	β_p	q_b (q_a = 1.0)	δ (1.0)
A	0.0909	11.8	1.70	2.91	4.40	0.217
B	0.0904	12.2	1.70	2.75	4.04	0.201
C	0.0910	14.5	1.75	2.17	3.06	0.160

Equilibrium	q_a (β = 0.067)	q_b (β = 0.067)	γ	β_p	δ (0.067)	I (β = 0.067)
A	1.207	4.399	1.70	2.91	0.160	10.1
D	1.333	3.909	1.75	2.88	0.159	10.2
E	1.466	3.511	1.80	2.85	0.158	10.3

Equilibrium	q_a	β (q_a)	B_o (β)	I (B_o)	δ (β)	γ	β_p	BLOON Stable
A	1.21	0.0671	5.80	10.1	0.160	1.70	2.91	yes
A	1.07	0.0822	5.24	10.1	0.196	1.70	2.91	no
A	1.01	0.0893	5.03	10.1	0.213	1.70	2.91	no
F	1.10	0.100	4.75	11.2	0.208	1.80	2.57	yes
F	1.03	0.110	4.53	11.1	0.229	1.80	2.57	no
G	1.29	0.100	4.75	12.9	0.164	1.99	2.05	yes
G	1.09	0.130	4.17	12.9	0.213	1.99	2.05	marginal
G	0.954	0.160	3.76	12.9	0.263	1.99	2.05	no

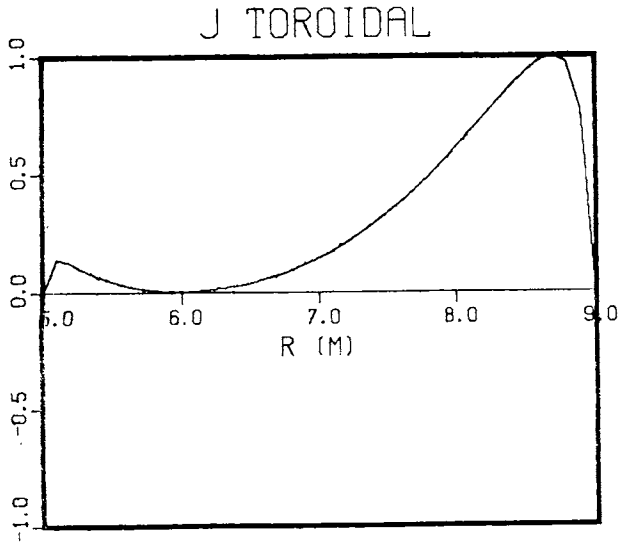

(A)

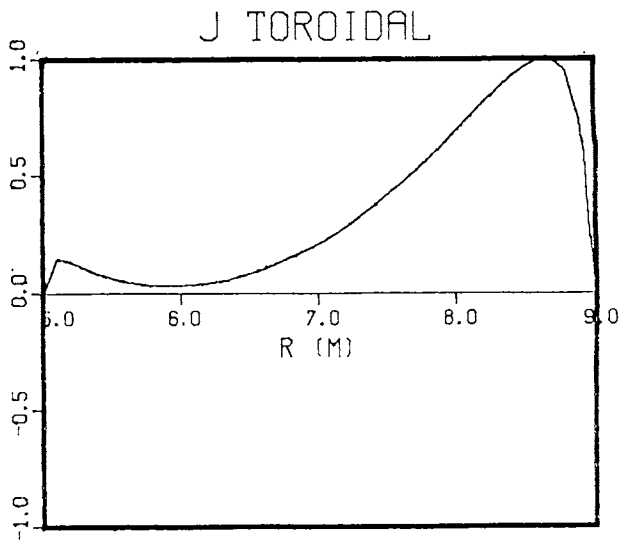

(B)

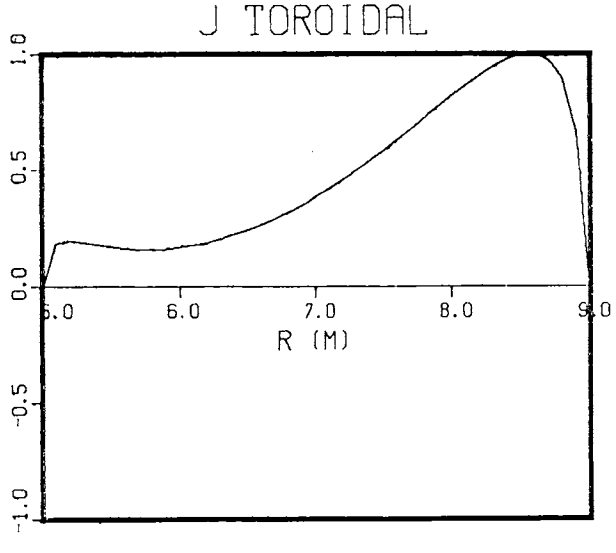

(C)

Figure 6-2. Current density profiles for equilibria A, B, and C in Fig. 6-1.

The remaining hollow current equilibria, residing near the dashed line in Fig. 6-1, may be compared by scaling all solutions to the same β value with the following relationships,[7]

$$\tilde{\beta}/\beta = \lambda^{-2}$$

$$\tilde{q}_b/q_b = \lambda$$

$$\tilde{\delta}/\delta = \lambda^{-2}$$

$$\tilde{q}_a/q_a = \lambda\,[1-\tilde{\delta}]^{-\frac{1}{2}}\,[1-\delta]^{-\frac{1}{2}}$$

$$\tilde{I}/I = \lambda^{-1} \quad .$$

The results for three examples, A, D, and E are tabulated in Table 6-3. BLOON results for these three cases yield approximately equal stability, but $q(\psi)$ is not monotonic for E (see Fig. 6-3). In fact, A has the lowest current, which suggests I may be minimized for a given β by making q_a as small as possible ($q_a \approx 1.0$). This insensitivity of stability to total current for $q_a \approx 1$ has been found by other investigators;[6,9,10,15-19] Ref. 15 graphically displays the q_a^{-2} variation of maximum β at high q_a, due to ballooning limitations, and the precipitous drop in stability for $q_a < 1$, due to the kink and internal modes. The results in Ref. 15 are for a fixed ratio q_b/q_a and confirm our conclusions that stability is least dependent on total current for q_a slightly above unity.

A remaining option to be explored is operation at higher β values and higher total current. Three cases, A, F, and G, in Table 6-3 and Fig. 6-4, were chosen and analyzed with BLOON for various β values with q_a near unity. In addition to the β-q_a scaling, we allowed the magnetic field on axis, B_0, to vary as $B_0 \sim \beta^{-\frac{1}{2}}$ to keep the fusion power constant. In addition, I was scaled as $I \sim B_0$. The results indicate that an increase of I from 10.1 MA to 11.2 MA or 12.0 MA would permit increases in β from 0.067 to 0.10 or $\sim$ 0.12, respectively. Assuming constant reactor power, these imply reductions in the maximum field from 11.1 T to 9.1 T or $\sim$ 8.3 T, respectively. Such reductions in B might justify the increases in rf power required to drive the higher currents. Finally, we note from Table 6-3 that reducing q_a to 1.07 for equilibrium A does not result in stable, higher β plasma; and we conclude that for I = 10.1 MA, the largest stable β lies between 0.067 and 0.082.

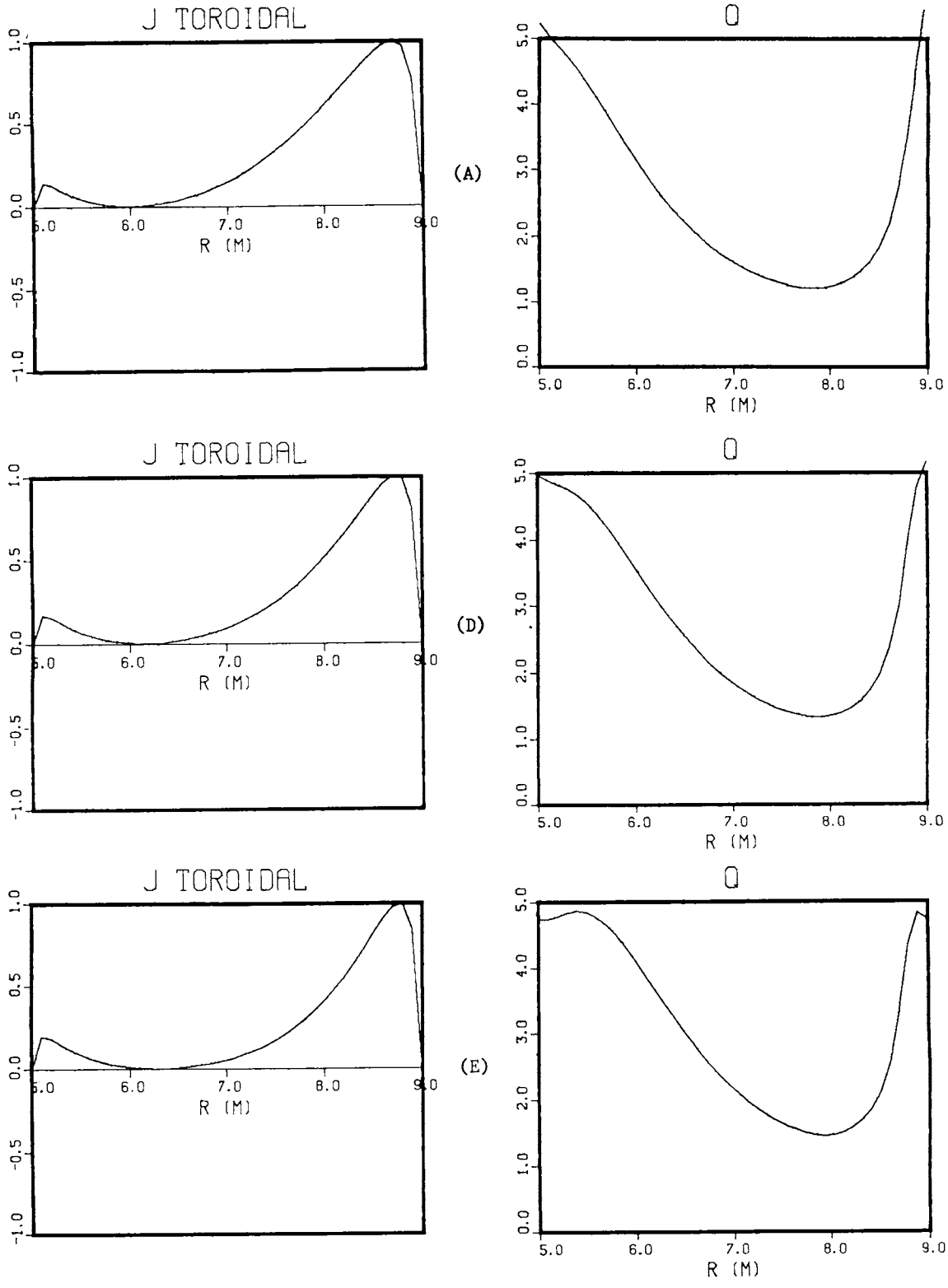

Figure 6-3. Current density and safety factor profiles for equilibria A, D, and E in Fig. 6-1.

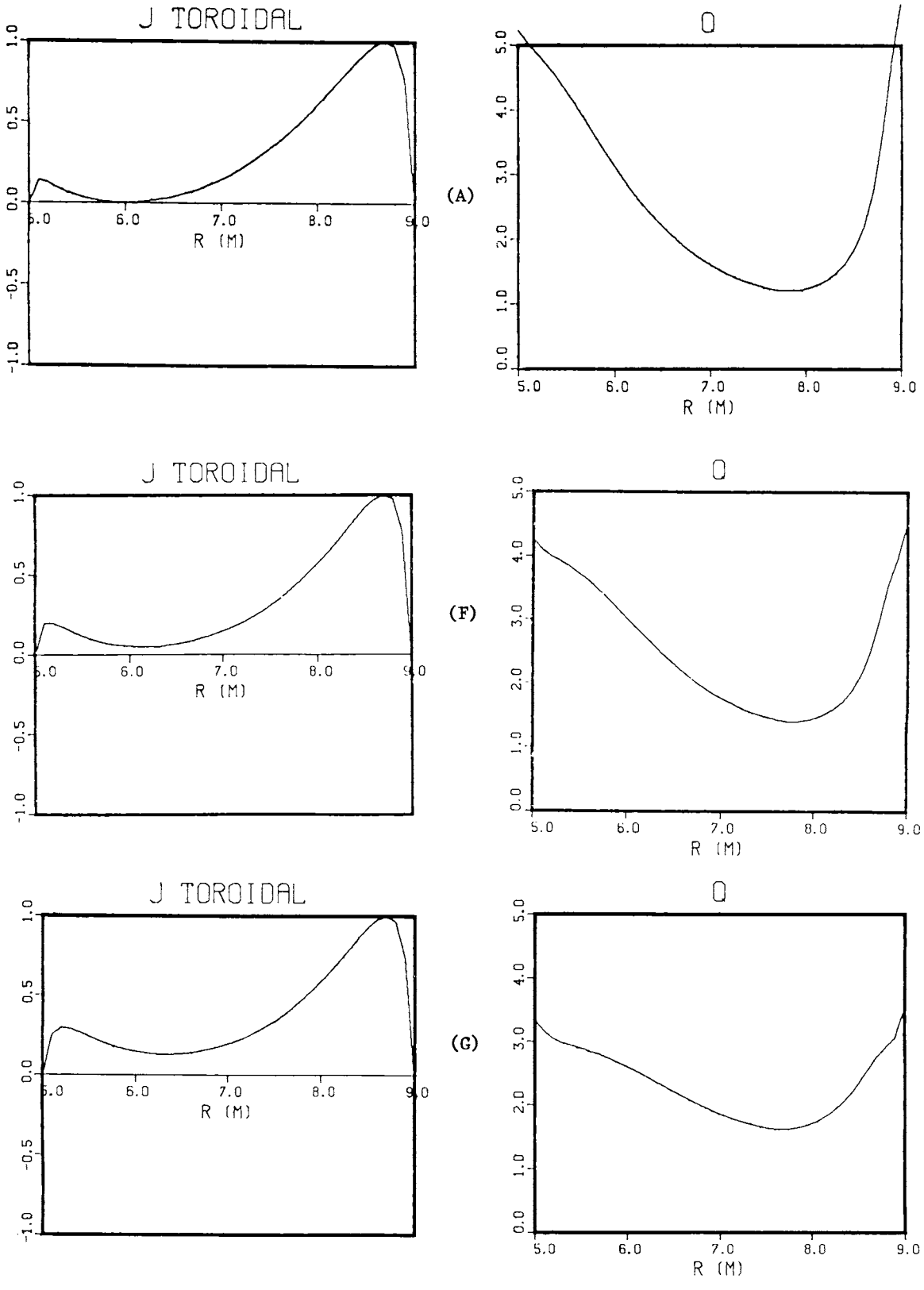

Figure 6-4. Current density and safety factor profiles for equilibria A, F, and G in Fig. 6-1.

The large number of instabilities and the great variety of MHD equilibria makes surveys of equilibria a difficult task; many solutions found stable with BLOON may be unstable to other modes; on the other hand even higher β equilibria may exist which are completely stable to all modes. The two parameters, A and α, have not been varied in our stability survey, and the stability trends published in Ref. 1 may be incorrect for our considerations. In particular, our emphasis on low I equilibria forced the consideration of high β_p equilibria, and An and Bateman[20] have recently found that, for large κ, stability trends with A and α are reversed at high β_p relative to the low β_p scaling. Closer attention should also be given to the current density and safety factor profiles, which, as shown in Ref. 21, have strong influences on stability.

The reference equilibrium for STARFIRE (A in Fig. 6-4), with A = 3.6, κ = 1.6, d = 0.5, α = 1.4, β = 0.067, q_a = 1.21 and q_b = 5.12 has a beta in accord with the upper limits calculated for the JET device. Bernard and his coworkers found β = 0.10 was possible with wall stabilization[22] at the JET values of κ = 1.68 and A = 2.37. If $\beta \propto A^{-1}$, this would yield β = 0.066 for the STARFIRE value, A = 3.6. The studies in Ref. 22 were limited to monotonic current profiles, but other work has shown that hollow current profiles are stable at $\beta > 0.10$ in JET, provided a conducting wall surrounds the plasma.[23]

We turn now to a detailed study of the STARFIRE reference equilibrium, considering a larger class of modes than the interchange and ballooning modes of this section.

6.2.2 Plasma Stability of the STARFIRE Reference Equilibrium

Two main categories of MHD instability have been considered. In the first, the instability is driven by the interaction of the plasma pressure gradient with the magnetic field curvature; these are the interchange and ballooning modes. These instabilities move and stretch magnetic field lines, especially in regions of unfavorable curvature, so that some minimum magnetic field line tension is needed to effect stabilization. These modes therefore result in an upper limit on beta. The ballooning mode typically is most unstable at a large toroidal mode number. The other category of instability is the kink mode, which is driven by plasma electrical currents parallel to the magnetic field. The kink modes have small toroidal mode number, and they are

generally the strongest instability, having exponential growth rates $\gamma \sim V_A/R$, where V_A is the poloidal Alfvén velocity and R is the major radius. The kink mode may be stabilized by a conducting wall in close proximity to the plasma surface. A special case of the kink mode is the n = 0 axisymmetric mode, which is considered separately.

The equilibrium of the STARFIRE reactor is established by a system of superconducting equilibrium field (EF) coils located outside the toroidal field coils. This location for the EF-coils facilitates reactor maintenance and disassembly, but it makes control of the plasma position and shape difficult because of the large distance between the coils and the plasma surface. In STARFIRE, this difficulty is compensated for by having a lower hybrid current drive system, which reduces the need for an ohmic heating induction coil. This allows the center bore of the toroidal field coil center post, normally the exclusive location of the OH-coil, to be used for the placing of some EF-coils. These inner EF-coils, together with the main outside EF coils, provide for a good plasma shape. In addition, the rf current drive provides a plasma current density profile which is maximum near the plasma boundary, where the outside EF-coils can be most effective at determining the plasma shape.

Figure 6-5 shows the flux surfaces of the STARFIRE equilibrium. In the following, these surfaces are labeled from $N_\psi = 1$ on the axis to $N_\psi = 30$ on the boundary. The hollow current density profile is shown in Fig. 6-6, along with the pressure, safety factor, and poloidal flux profiles.

The BLOON code is used to analyze the local interchange mode and the ballooning mode. For the interchange mode, two criteria are applied: stability near the magnetic axis (on-axis stability) is determined by use of the Yavlinski criterion,[24] and the Mercier criterion[25] is applied off the magnetic axis. The Euler equation derived from the energy principle in the limit of large toroidal mode number is used in the ballooning mode analysis of each of the 30 flux surfaces found for the equilibrium shown in Fig. 6-5. Generally, the ballooning mode places a lower limit on beta than do the interchange modes.

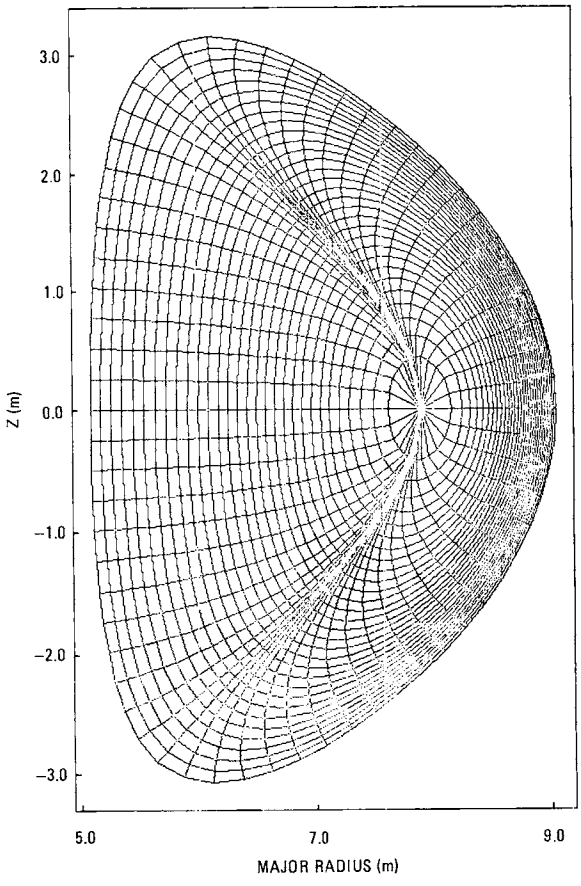

Figure 6-5. Flux surfaces of STARFIRE equilibrium.

For the STARFIRE equilibrium, the off-axis interchange critical beta is 11.5%, and the on-axis interchange critical beta is 8.7%. These limits lie well above the STARFIRE design beta of 6.7%.

Figure 6-7 shows the square of the ballooning mode frequency calculated as a function of flux surface, for several different toroidal magnetic field magnitudes. When the square of the frequency is negative, it indicates a growing mode. The effect of the magnetic field is to reduce the mode growth rate, and when the growth rate is less than 10^{-4} of the inverse poloidal Alfvén time, the mode is considered to be stabilized.

Figure 6-7 shows that two spatial regions tend to be unstable. The first is a broad region between the 10th and 20th flux surfaces, and the other is narrowly peaked around the 27th flux surface at the outside of the plasma. This latter mode is questionable, for several reasons. First,

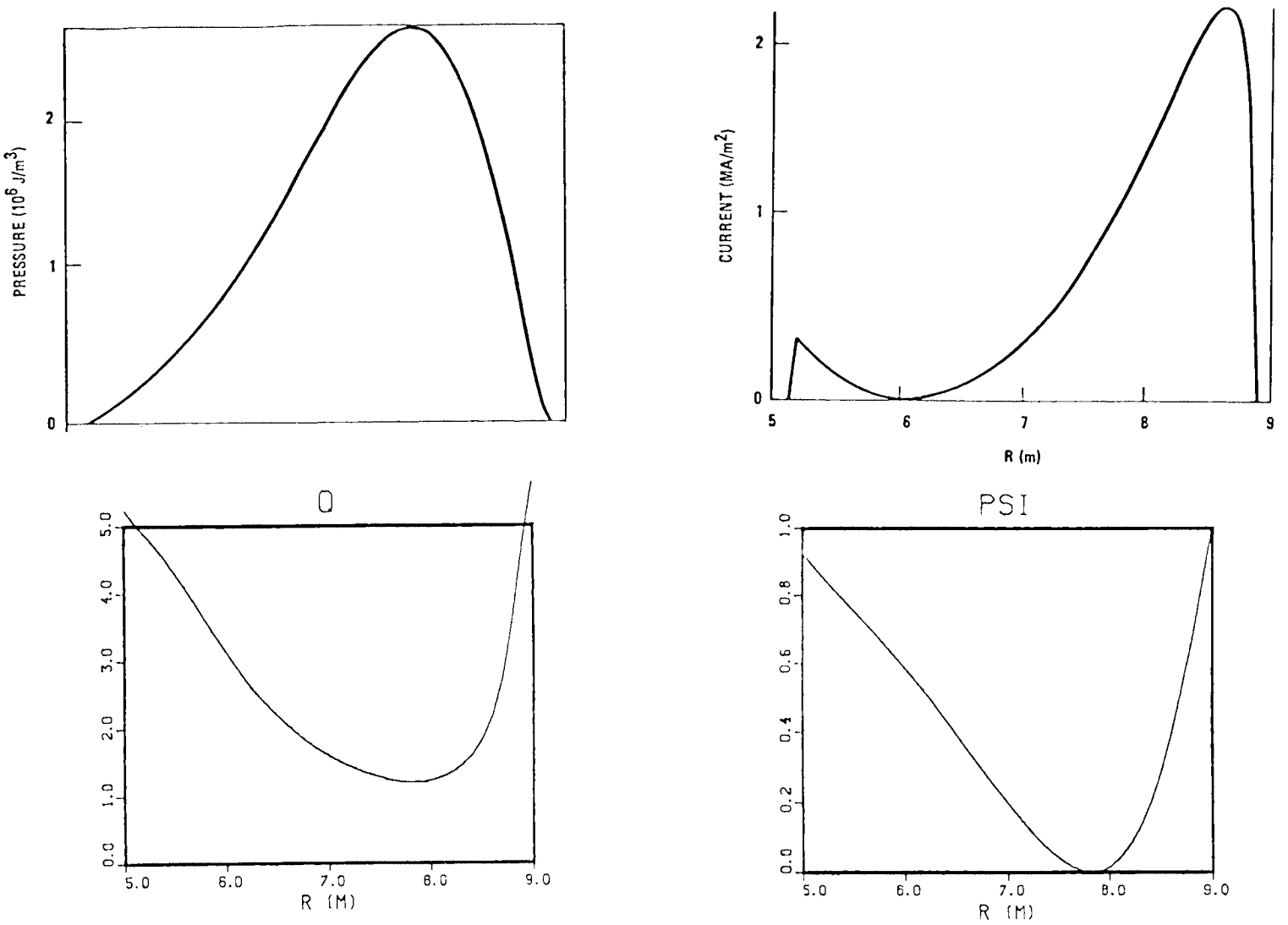

Figure 6-6. Pressure, current density, safety factor and flux surface profiles for the reference STARFIRE equilibrium.

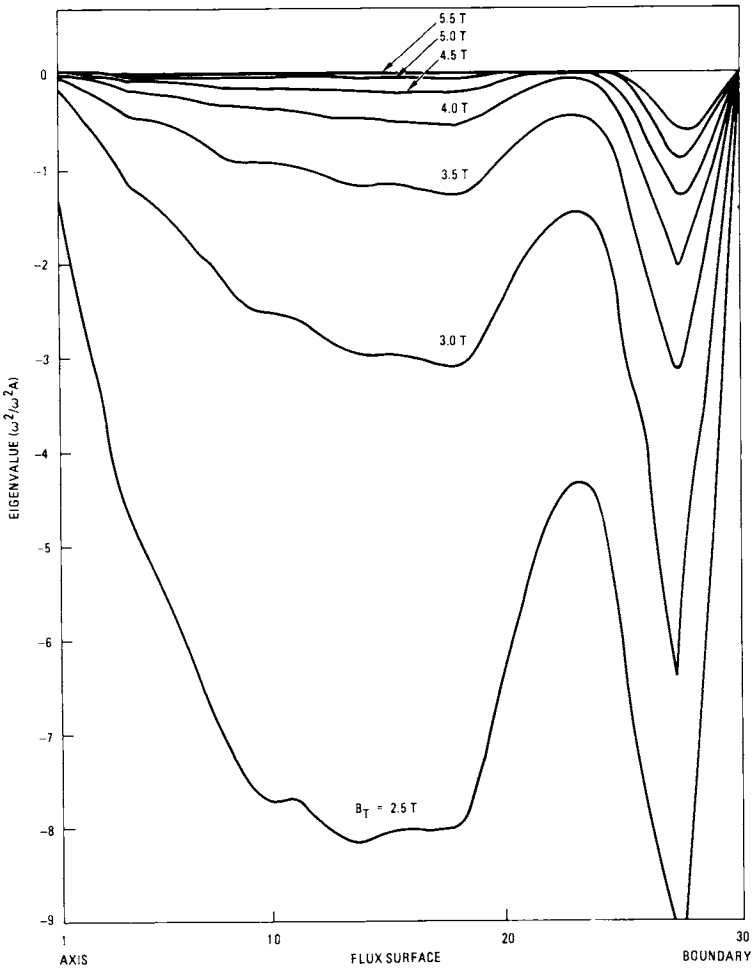

Figure 6-7. Ballooning mode frequency squared (normalized to the poloidal Alfvén frequency squared) as a function of flux surface, for several toroidal field magnitudes.

the code assumes that the radial gradient in the current density is small over the scale of the distance between flux surfaces; clearly from Figs. 6-5 and 6-6, this is not the case and the code results are suspect. Second, radial corrections to the eigenvalue due to finite toroidal mode number tend to make this mode stable for reasonable mode numbers. For these reasons, the critical beta is taken to be the minimum beta necessary for stabilization of the broad unstable mode appearing around N_ψ = 18. This stabilization takes place for toroidal fields above 5.0 T, corresponding to beta below 8.2%. This is also well above the 6.7% STARFIRE design level.

The kink mode analysis is performed using the code ERATO.[22,26] The Lagrangian

$$L = \delta W_p + \delta W_v - \omega^2 \int \rho |\vec{\xi}|^2 \, d^3r$$

including plasma displacements $\vec{\xi}$ must be obtained to evaluate the MHD stability, where ω is the instability frequency, ρ is the plasma density, δW_p is the plasma potential energy, and δW_v is the vacuum potential energy. In the ERATO code, the displacement is expanded in toroidal eigenmodes $\xi = \xi_0 e^{-in\phi}$, where n is the eigenmode number and ϕ is the toroidal angle. A matrix eigenvalue equation is obtained by applying a variational principle to the Lagrangian, and the equation is solved for a given equilibrium by an inverse vector iteration process using an initial guess for the eigenvalue (mode growth rate, γ).

The accuracy of the eigenvalue depends on the number of grid points used by the computer in calculating flux surface quantities and derivatives. The larger the number of grid points, the more accurate the result but the more computer time required. The approach adopted here is to evaluate the eigenvalue for several values of N_ψ, the number of flux surfaces derived from the equilibrium calculations, and note the trend of the eigenvalue as N_ψ is increased and greater accuracy is achieved. Approximately, good convergence of the eigenvalue requires $N_\psi > 4nq_b$. For this reason, mode numbers higher than 3 or 4 cannot be analyzed due to the excessive number of grid points which must be used.

For the STARFIRE equilibrium, the growth rates of the n = 0,1,2, and 3 modes were examined. In this study, internal kink modes are considered under the assumption of a fixed plasma boundary shape. Stabilization of these modes may be achieved by use of a conducting wall surrounding the plasma. While some modes may be stable without the conducting wall in a circular equilibrium,[26] all low mode number kinks are unstable when the plasma cross-section is elongated.

Figure 6-8 shows the calculated growth rate for the n = 0,1,2,3 modes as a function of the inverse square of N_ψ (i.e., the inverse of the number of grid points). The safety factor on axis, q_a, is 1.27, which is above the minimum value required for interchange stability according to the Mercier

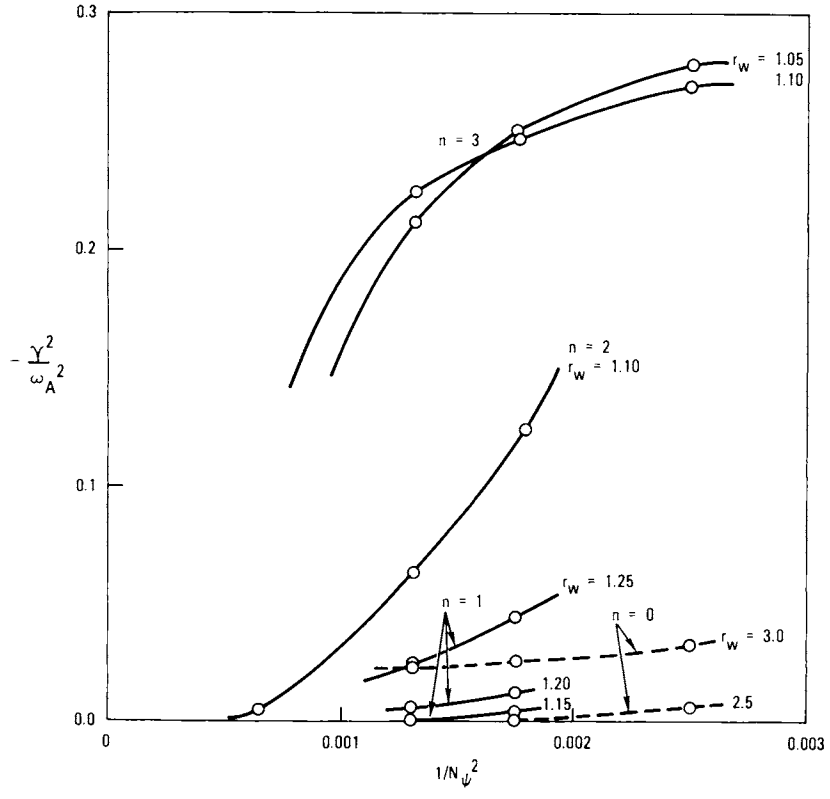

Figure 6-8. Calculated growth rate for the n = 0, 1, 2, 3 modes as a function of the inverse square of N_ψ.

criterion described in the previous section. The growth rate for each mode is plotted for several r_w, which is defined as the ratio of the distances from the plasma center to the conducting wall and to the plasma boundary. For the n = 0 mode, the square of the growth rate, γ^2, is about 0.1 ω_A^2 when r_w is infinite, where ω_A is the Alfvén frequency V_A/R, and V_A is the poloidal Alfvén speed and R is the major radius.

The stabilizing effect of the conducting wall can be clearly seen, since for the n = 0 mode, γ^2/ω_A^2 drops to 0.02 for r_w = 3.0 and to 0 for r_w = 2.5. As the mode number n increases, the instability becomes of smaller scale, so that the induced electrical currents in the wall must be closer to the plasma in order to effect stabilization. For the n = 1 mode, r_w must be less than about 1.15 for stabilization. For larger n, eigenvalue convergence becomes poorer, but the trend is toward stabilization for $r_w \sim 1.1$.

The pattern of local plasma displacements due to the unstabilized kink mode is shown in Fig. 6-9 for mode numbers 1 and 3. The pattern of plasma

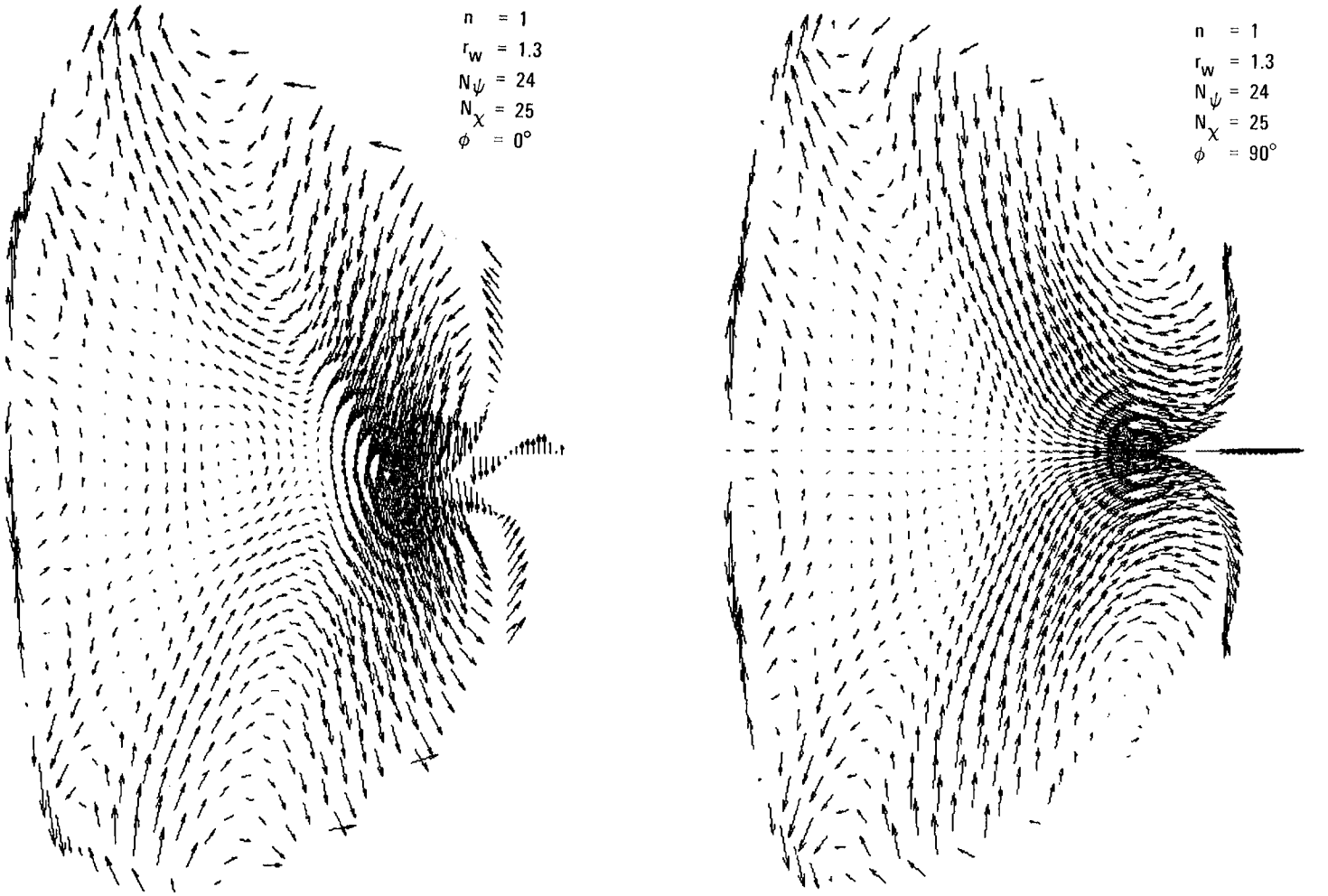

Figure 6-9. Plasma displacements for the kink mode with N_ψ = 24 (sheet 1 of 2).

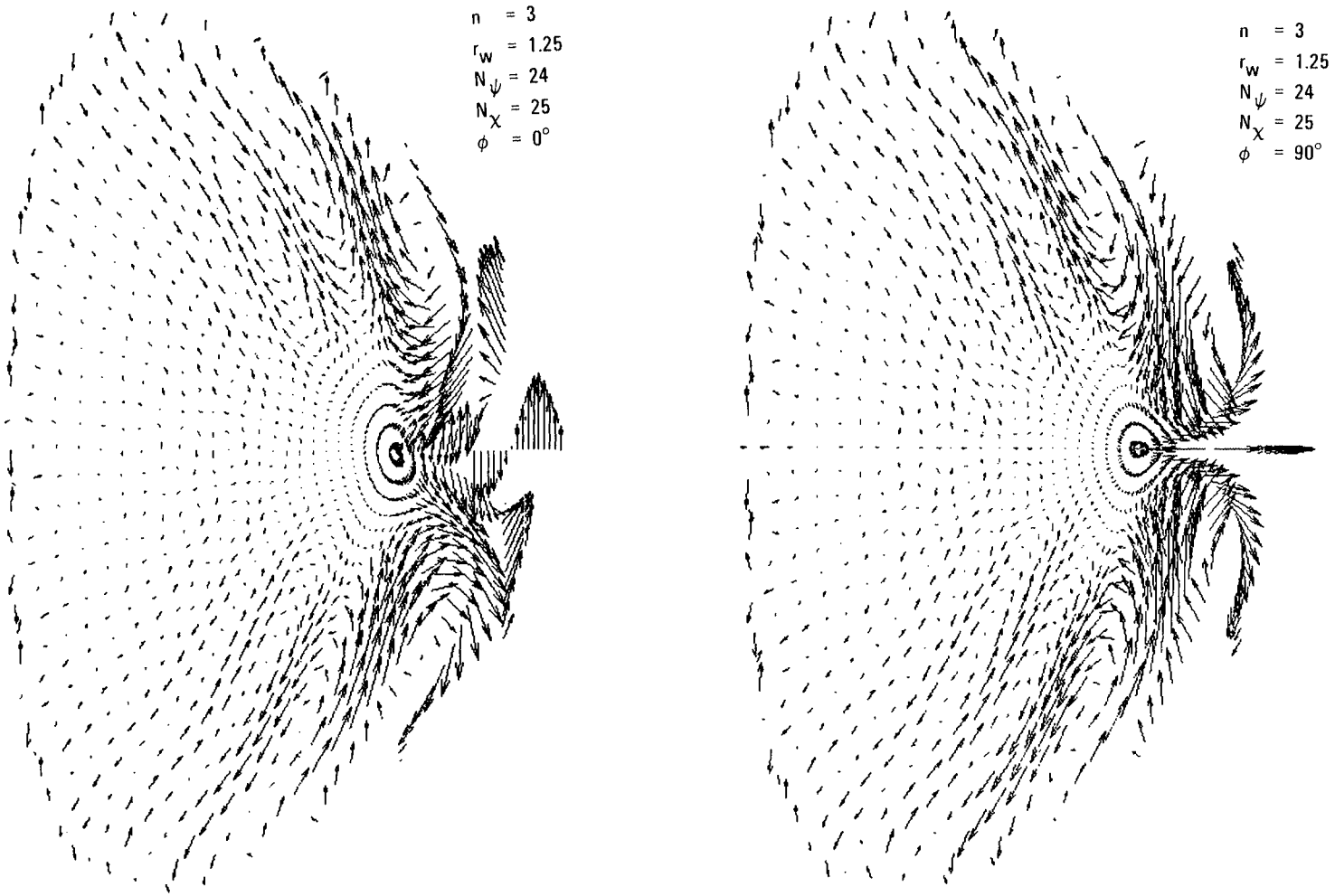

Figure 6-9. Plasma displacements for the kink mode with N_ψ = 24 (sheet 2 of 2).

motions is that of small-scale vortices in the direction across the flux surfaces. These displacements can cause rapid radial plasma transport. When the wall is moved close enough to the plasma to cause stabilization of the kink mode, the displacement vectors become very small, and what displacements remain tend to lie along the flux surface, as shown in Fig. 6-10. These residual plasma motions cause little cross-field transport.

In conclusion, the calculated critical beta for the interchange and ballooning modes lies above 8%, well in excess of the 6.7% design value for STARFIRE; the low-order kink modes -- n = 0, 1,2,3 -- have been shown to be stabilized by a close-fitting conducting shell.

The most troublesome MHD instabilities may be the kink modes with toroidal mode numbers in the range of 4 to 10. These modes, and all higher modes, lie outside the range amenable to numerical analysis due to their small size relative to the numerical grid spacing. In addition, the $n \to \infty$ result of the BLOON calculation may not accurately gauge the stability of large but finite n modes; Ref. 27 displays a hollow current equilibrium for which the

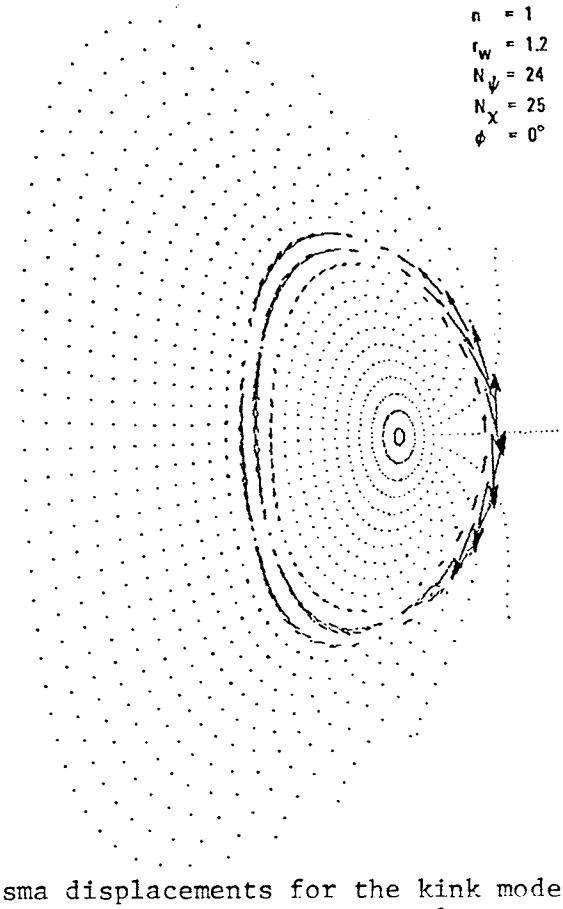

Figure 6-10. Plasma displacements for the kink mode with $N_\psi = 24$ for n = 1, $r_w = 1.2$, and $\phi = 0°$.

$n \sim 150$ mode cannot be analyzed with BLOON. Kinks with large mode number may cause only moderately enhanced energy transport due to their fine scale, since the radial extent of the vortex is approximately proportional to $n^{-\frac{1}{2}}$, while the minor azimuthal angle of the vortex extent is proportional to n^{-1}. The intermediate modes may have sufficient extent to cause rapid transport, while not being amenable to wall stabilization owing to their small scale and distance from the wall. This difficulty with the kink modes is a characteristic of hollow current profiles in the STARFIRE case. If kink mode losses are too severe, the hollowness of the current density profile may need to be relaxed.

The conducting shell which surrounds the plasma and stabilizes the low mode number kinks must have toroidal continuity to be effective. In the STARFIRE design, these requirements are satisfied by conducting electrical jumpers between the toroidal segments of the blanket. This system is described in Chap. 10.

6.2.3 Plasma Control

6.2.3.1 Introduction

The elongated equilibrium of the STARFIRE reactor is generated by superconducting EF-coils exterior to the TF-coils. In this exterior coil system the equilibrium is sensitive to changes in such plasma properties as the current density profile or plasma beta, because of the shallow magnetic well of the EF-coil system. Also, the plasma is unstable to axisymmetric vertical motions. Unless stabilized, the plasma motions due to these effects can grow rapidly until the plasma contacts the vacuum chamber wall, and the resulting plasma-wall interaction is likely to trigger a major disruption of the plasma current.

For an EF-coil system which closely surrounds the plasma, the plasma may be intrinsically stable to vertical and radial motions due to the flux-conserving nature of the EF-coils.[28] However, coil maintenance and replaceability require that linked superconducting coils be avoided, while power requirements exclude demountable interior copper coils. The conflicting requirement of stability and maintainability may best be reconciled in a hybrid system comprising superconducting EF-coils outside the TF-coil and normal conducting control field (CF) coils inside the TF-coil. The exterior

coil system carries the total average current necessary to generate the desired plasma equilibrium, but because of the large system inductance, the current in the exterior coils can be varied only on a fairly long time scale of several seconds. The fastest time scale for plasma stabilization is limited by the L/R time of the first wall, so the inner copper coils should at least be capable of reacting on that time scale.

The dynamics of the plasma column position are analyzed in the next section. The currents required in the stabilizing coils to react to given plasma displacements or parameter changes are estimated using the General Atomic MHD equilibrium code.[29] The resistive and reactive power requirements for the control coils are also estimated. While this analysis is based on a low β, circular plasma approximation, the results should be adequate as first order estimates of the control system requirements for STARFIRE.

6.2.3.2 Plasma Horizontal Motion

The equation of horizontal (radial) motion of a toroidal plasma column of circular cross section is[30]

$$M\ddot{R} = \frac{1}{2}\mu_0 I_p^2 \left(\ln\frac{8R}{a} + \beta_p + \frac{\ell_i - 3}{2}\right) - 2\pi R I_p B_V \qquad (1)$$

where M is the total plasma mass $2\pi^2 R a^2 M_i n_i$, R is the plasma major radius, I_p is the plasma toroidal current, a is the plasma minor radius, M_i is the ion mass, and n_i is the plasma density. The quantity β_p is given by $\beta_p = 2\mu_0\bar{p}/B_p^2$, where $\bar{p}$ is the average plasma pressure, B_p is the poloidal magnetic field, and ℓ_i is the plasma internal inductance. The vertical field B_V includes contributions due to the poloidal field coils, B_{v0}, which is assumed constant in time during a plasma excursion due to the weak coupling to the plasma current, as well as the contribution, B_u, due to induced currents in a conducting shell surrounding the plasma, and the contribution, B_v due to control coils.

For a shift in plasma radial position of X, Eq. (1) can be expanded about the equilibrium major radius R_0, $R = R_0 + X$, and the minor radius $a = a_0(1 + X/2R_0)$. The resulting expression describes conservation of toroidal magnetic flux and the expression for B_V becomes $B_V = (B_{v0} + B_v) \times (1 - nX/R_0) + B_u$, where n is the index of curvature of the externally applied vertical field which is determined by the locations and currents of the exterior equilibrium field coils.

From Eq. (1), the radial expansion force is a function of the plasma current I_p, the internal inductance ℓ_i and the poloidal beta β_p. Motion of the plasma column may be triggered by changes in these parameters on a time scale in which the vertical field B_{v0} is unable to respond. Changes in ℓ_i or β_p may be brought on by MHD activity which rapidly changes the profiles of current density or pressure. Overall changes in I_p may occur due to minor disruptions. In order to prevent rapid subsequent loss of plasma equilibrium, a change in the magnetic fields B_v and B_u must occur.

As perturbations to Eq. (1), the following parameter disturbances are considered:

$$I_p = I_{p0}\,(1 - \mu X/R_0)(1 + \delta I_p/I_{p0})$$

$$\ell_i = \ell_{i0}\,(1 + \delta\ell_i/\ell_{i0})$$

$$\beta_p = \beta_{p0}\,(1 + \delta\beta_p/\beta_{p0})\ ,$$

where the quantities subscripted with a zero are the equilibrium quantities, and μ is a constant chosen to conserve the poloidal magnetic flux.

For the case of small displacements, $X/R_0 \ll 1$, Eq. (1) may be linearized to yield

$$\Gamma\,\frac{X}{R_0} = \frac{B_v + B_u}{B_{v0}} - \delta S\ , \qquad (2)$$

where

$$\Gamma = \frac{1}{2\Lambda_0} + n - \mu - 1$$

$$\Lambda_0 = \ln\frac{8R_0}{a_0} + \beta_{p0} + \frac{\ell_{i0} - 3}{2}$$

$$B_{v0} = \frac{\mu_0 I_0 \Lambda_0}{4\pi R_0}$$

$$\delta S = \frac{\delta I_p}{I_{p0}} + \frac{\delta\beta_p + \frac{1}{2}\,\delta\ell_i}{\Lambda_0}$$

The left-hand term of Eq. (1) is neglected, since it describes motion on the time scale of the poloidal Alfvén time, and only the persisting motion is

sought in Eq. (2). If there is no conducting wall, the displacement grows at the poloidal Alfvén speed when $\Gamma > 0$ or oscillates at the Alfvén frequency when $\Gamma < 0$. When a conducting shell is present, the growth rate becomes the resistive time constant of the wall. Thus, it is important to have a conducting wall and to design the reactor to have $\Gamma < 0$ for stability. In the STARFIRE design, these conditions are maintained by making the vacuum chamber wall and the neutron multiplier behind the first wall into toroidally continuous conductors of low electrical resistance, and by providing vacuum vertical field of the proper curvature.

6.2.3.3 Vertical Motion

The horizontal motion of a plasma column is stable if $\Gamma < 0$ is satisfied. However, the vertical motion is unstable when the curvature index of the vertical field is negative, as it must be for an elongated plasma. The growth rate for this instability is also of the order of the poloidal Alfvén time, if no conducting shell exists to slow the motion.

The equation of motion of the plasma column for a vertical displacement Z may be given by

$$M\ddot{z} = 2\pi R_0 I_p B_r, \tag{3}$$

where B_r is the radial component of the magnetic field due to the equilibrium coils,

$$B_{vr} \cong -nzB_{v0}/R_0 ,$$

plus the radial field due to image currents flowing in an inductive first wall of minor radius r_u,

$$B_u \cong -\tau_u \dot{z} \mu_0 I_0 / 2\pi r_u^2 ,$$

where $\tau_u = 1/2\ \sigma\mu_0 d_u r_u$ is the L/R time constant of the wall and d_u is the thickness of the wall, assumed small in comparison to the plasma minor radius. For the persisting mode, Eq. (3) reduces to

$$\dot{z} + z\frac{\gamma}{\tau_u} = \xi\frac{b_0}{\tau_u} , \tag{4}$$

where

$$\gamma = -\frac{1}{2}\left(\frac{r_u}{R_0}\right)^2 n\Lambda_0, \quad \xi = \frac{r_u^2}{2R_0 b_0}\Lambda_0 \frac{B_d}{B_{v0}} \quad ,$$

B_d is the radial component of a magnetic field disturbance, and b_0 is the dimension of the plasma in the z-direction.

The solution to Eq. (4) is

$$\frac{z}{b_0} = \frac{\xi}{\gamma}\left(1 - e^{-\gamma t/\tau_u}\right) \tag{5}$$

for a step-function disturbance. The growth rate of the motion is

$$\tau = \frac{-2}{n\Lambda_0}\left(\frac{R_0}{r_u}\right)^2 \tau_u \quad , \tag{6}$$

which, for STARFIRE parameters ($n \cong -0.5$, $\Lambda_0 \cong 5$) is about four times the first wall time constant of 300 ms. Because the vertical displacement is unstable even if the initial disturbance is small, feedback control of every disturbance must be made on a time scale of about τ_u or shorter, in order to limit the displacement to a small fraction of the plasma minor radius.

6.2.3.4 Equilibrium Calculations

The temporal behavior of the gross plasma motions has been analyzed in the previous sections to determine the stability of the plasma and the time response required of the feedback system. In this section, the efficiency of a particular design for the correcting coil locations is analyzed, and the magnitude of the required feedback currents is determined.

The method used is to first obtain a base plasma equilibrium using only the poloidal field coils which are located outside the toroidal field coil envelope, assuming the desired plasma current, β_p, and current density profile, using the MHD equilibrium code (see Fig. 6-5). This determines the poloidal coil currents, which are assumed to be constant over the time scale of plasma motions. Then, a sudden change in the plasma parameters is postulated in order to model minor disruptions (plasma current δI_p) or MHD activity (current density profile or $\delta\beta_p$). These changes, in general, lead to poorly centered and badly shaped flux configurations, which can lead to loss of plasma confinement and a major plasma disruption. Currents are then placed

at the locations of the four correction coils. These locations are constrained by engineering and design requirements.

The equilibrium for an increase of plasma currents by $\delta I_p / I_p = 0.05$ is shown in Fig. 6-11(a). The ratio of the radial displacement X to the minor radius a_0 is $X/a_0 = 0.13$, or about that obtained from Eq. (2). Figure 6-11(b) shows the equilibrium pulled back by the control coils, which requires a total of about 3 MA turns. The magnetic well due to the EF-coils is quite shallow in the radial direction due to the large separation of the coils from the plasma. The elongation of the controlled equilibrium decreases due to the change in the vertical field curvature; thus, the equilibrium change due to plasma current decrease may, even if controlled, result in an equilibrium configuration with reduced critical beta. However, if the equilibrium is uncontrolled, a major disruption is a likely consequence due to the strong interaction between the plasma and the first wall.

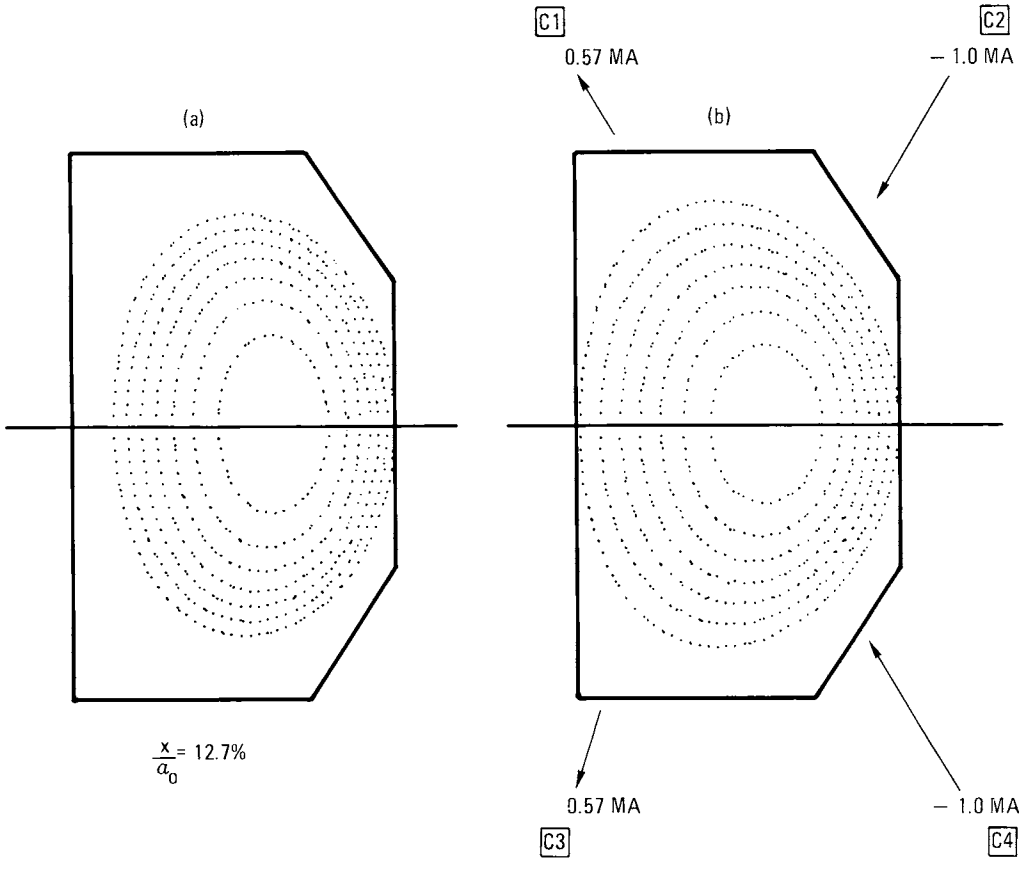

Figure 6-11. (a) shifted equilibrium due to increase in plasma current of 5% and (b) corrected equilibrium.

For the STARFIRE hollow current equilibrium, free energy exists for a collapse to a flat or peaked current profile. Under some conditions, then, the hollow current system may not be stable, and rapid filling of the profile may occur. This abruptly changes the internal inductance ℓ_i, resulting in a shift in major radius. Figure 6-12(a) shows the equilibrium shift that can be expected from a change in current profile from that of Fig. 6-12(c) to that of Fig. 6-12(d) ($\delta\ell_i = 0.2$). The resultant major radius shift is $X/a_0 \simeq 0.06$, and the total control coil current is about 2.2 MA.

When the expansion force decreases or the vertical field increases, the equilibrium shifts in the inward direction. Figure 6-13(a) shows the equilibrium when $\delta I_p/I_p = 0.1$. Since the plasma moves against a stronger vacuum vertical field generated by the EF-coils on the midplane at small major radius, the displacement is much smaller than the corresponding outward shift. The total current requirements for the control coils is less than 0.5 MA.

Vertical displacements are difficult to model in this manner because the iterative equilibrium calculation does not converge. In order to obtain convergence, first the gross up-down symmetry must be generated by adjusting the currents of the control coils; and second, the rapid movement of the equilibrium must be suppressed by fixing the flux at positions near the plasma. This second restriction can be relaxed as the plasma equilibrium converges.

The converged equilibria shown in Fig. 6-14 are obtained by this scheme. Off-midplane equilibria with vertical displacements as large as $z/b_0 \simeq 0.14$ can be maintained with a control coil current total of 1.1 MA; of course, the plasma elongation and cross-sectional area must be considerably reduced.

The total current required to feedback stabilize the shifted equilibrium is shown in Fig. 6-15 as a function of relative displacement. Total current requirements for vertical shifts is less than that for expected horizontal motions.

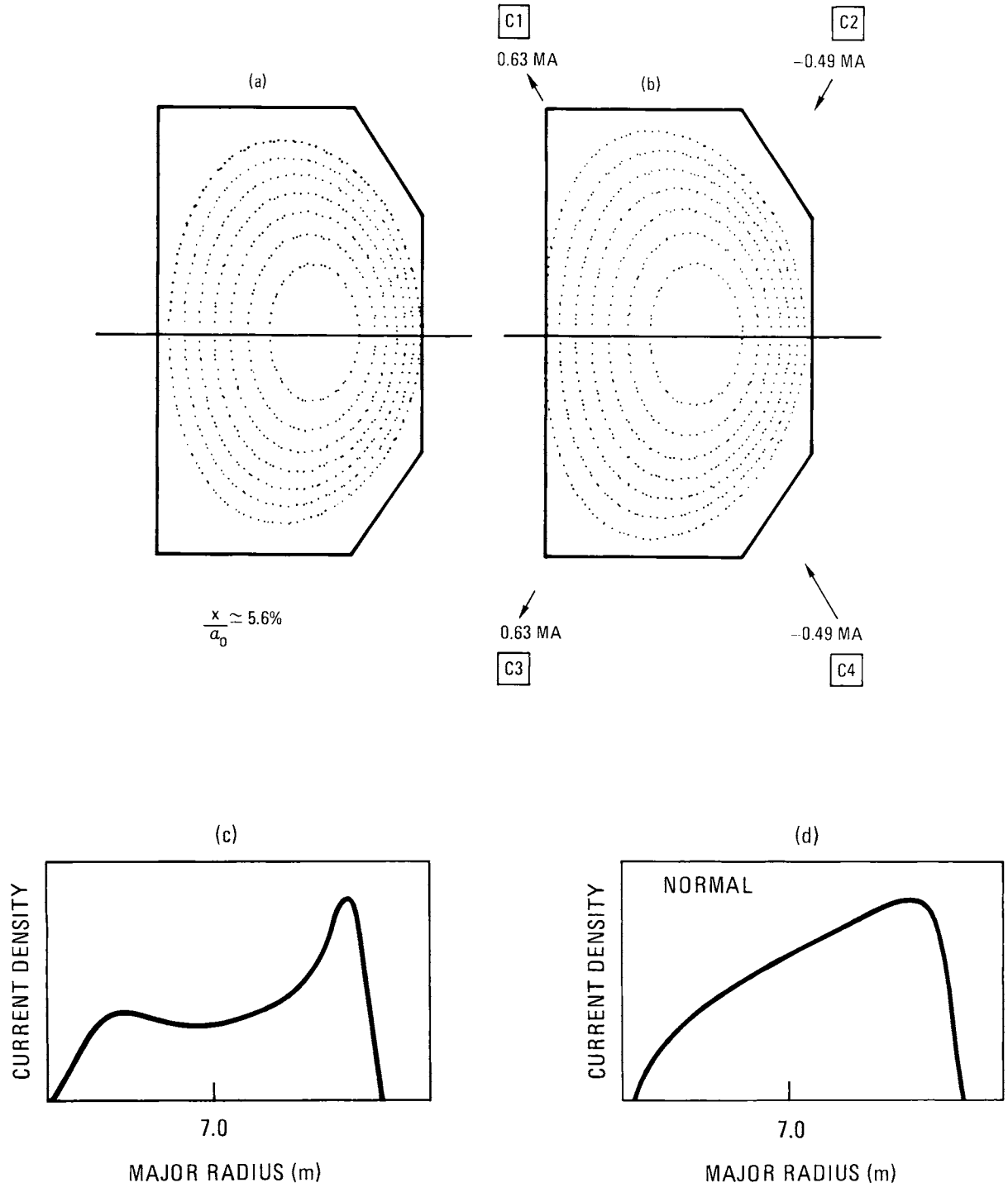

Figure 6-12. (a) Shifted equilibrium due to change in current density profile, (b) corrected equilibrium, (c) normal hollow current density profile, and (d) current density profile for cases (a) and (b).

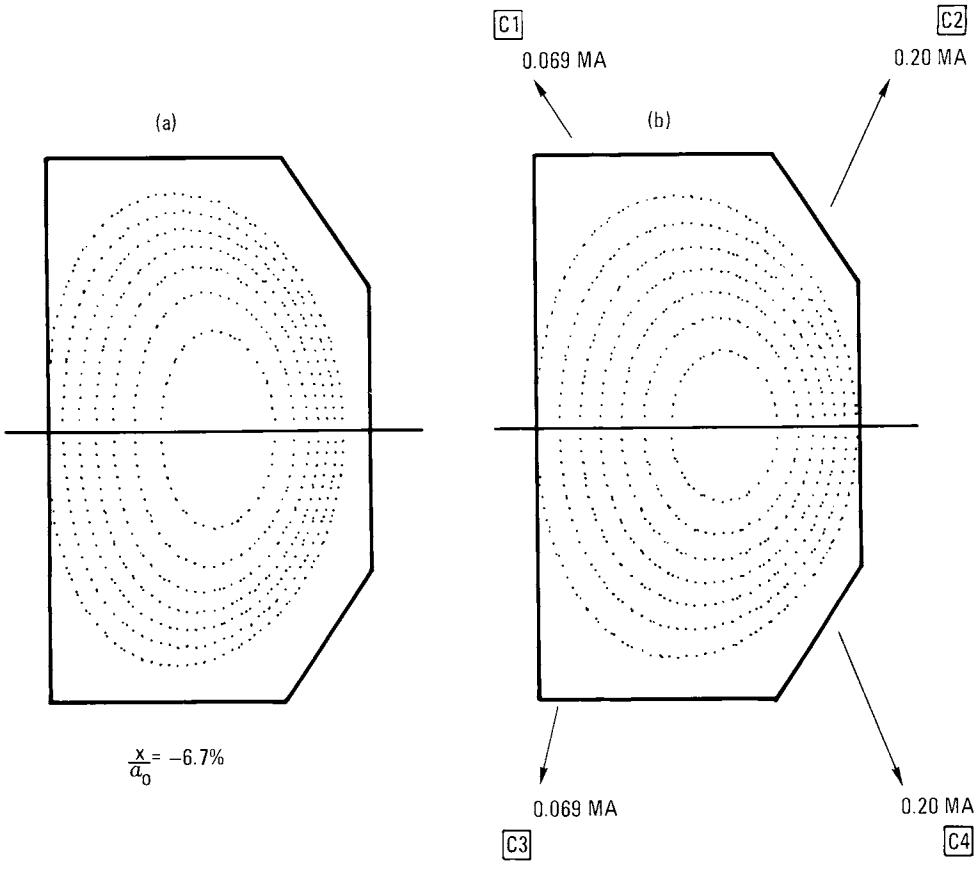

Figure 6-13. (a) Shifted equilibrium due to a decrease in plasma current of 10%, and (b) restored equilibrium.

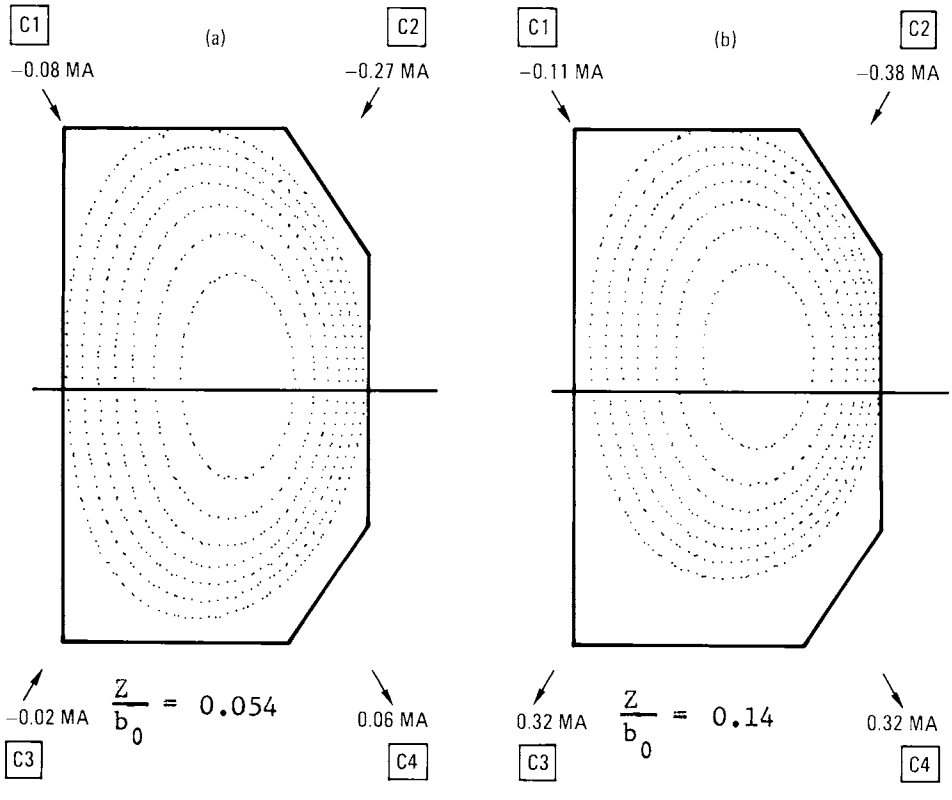

Figure 6-14. Examples of off-midplane equilibria.

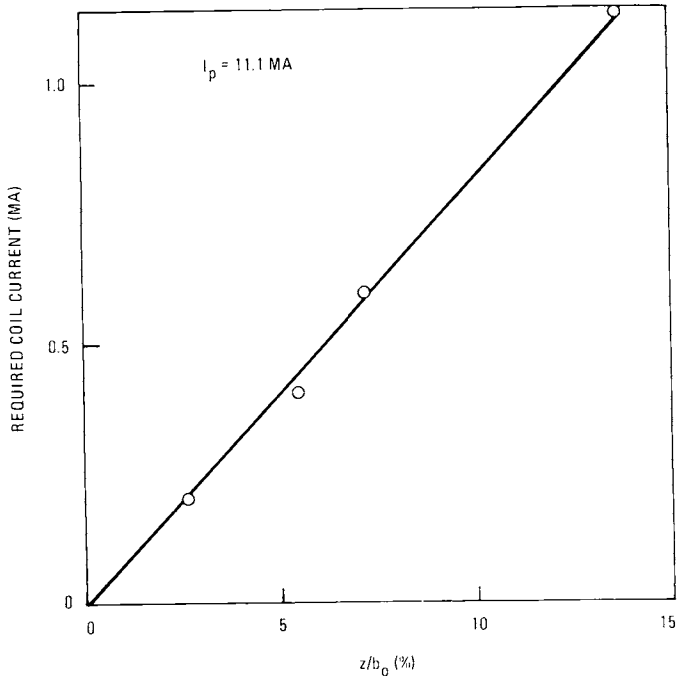

Figure 6-15. Required coil current versus vertical displacement.

6.2.3.5 Power Requirements

Since the currents required for the control field coils have been calculated and the geometry of the coils is known, the power supply for plasma control can be specified. The time constant for increasing the control field coil current to the required value is the resistive L/R time of the first wall, τ_u. Then the power required is

$$P = \frac{\sum_c \frac{1}{2} L_c I_c^2}{\tau_u} + \sum_c R_c I_c^2$$

where L_c, R_c, and I_c are the inductance, resistance, and current, respectively, of the c'th control coil, and mutual inductances are neglected. The coils are made such that the resistive term is negligible compared to the inductive term. Then the peak (inductive) power is inversely proportional to the first wall time constant. The average dissipative power can be reduced to acceptable levels (2 MW) by designing the coils with sufficiently low resistances. For the design values, the peak inductive power is 33 MW and the total stored energy is 10 MJ.

6.3 BURN CYCLE

6.3.1 Startup

Because STARFIRE is a steady state device, its burn cycle differs substantially from pulsed reactor designs. In particular, the startup and shutdown phases appear to be much easier than for pulsed operation, in terms of the plasma driving system requirements. This is basically due to the lack of any time limitations for the startup or shutdown; these can be as long as necessary to minimize power supply and heating requirements. Also, because of the lower hybrid current drive, there is no particular concern about volt-second losses during startup. In contrast to pulsed operation, which typically requires a large and expensive power supply system (e.g., see Ref. 31), STARFIRE requires far more modest supplies. No electrical storage is needed because the power requirements are low enough to be taken directly from the grid.

The startup and shutdown phases of the STARFIRE burn cycle have been analyzed using a profile-averaged time dependent code coupled to a magnetohydrodynamic code (see Ref. 32). A model for computing the plasma current as a function of ohmic heating (OH), equilibrium field (EF) coil voltages, and lower hybrid rf power is included. The plasma burn cycle code solves particle balance equations for each constituent plasma species [deuterium-tritium (DT), helium, and wall sputtered and high-Z impurities] and solves energy balance equations for the ions and electrons. Plasma heating by alpha-particle and rf drive is treated. Radiative (bremsstrahlung, line, recombination) and transport losses are treated, the former with a coronal equilibrium model, and the latter with an empirical electron and neoclassical ion confinement model. The plasma MHD equilibrium code solves the Grad-Shafranov and pressure balance equations for the two-dimensional flux function. The coupled dynamics of the plasma, poloidal coils, rf system, and the power supply system are modeled by the four mesh equivalent circuit shown in Fig. 6-16. Both the OH and EF coil systems are represented as a single equivalent inductance, and the plasma is represented as a series combination of inductance

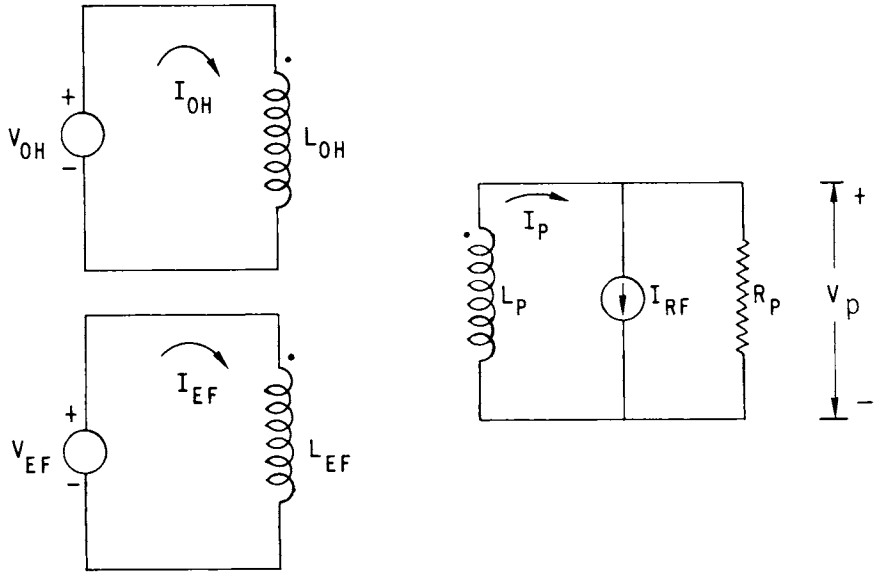

Figure 6-16. Plasma current drive model.

and resistance, both of which vary with time. The rf current drive is represented as a controlled current source in the plasma loop. The coupled system of Fig. 6-16 is described by the following set of equations:

$$L_{OH} \frac{dI_{OH}}{dt} - M_{OH,p} \frac{dI_p}{dt} = V_{OH} \tag{7}$$

$$V_p = - \frac{d}{dt} (L_p I_p) + M_{OH,p} \frac{dI_{OH}}{dt} + M_{EF,p} \frac{dI_{EF}}{dt} \tag{8}$$

$$I_p = \frac{V_p}{R_p} + I_{RF} \tag{9}$$

$$I_{EF} = f(I_p, \beta) \tag{10}$$

The required current, I_{EF}, needed to maintain MHD equilibrium is a function of I_p and β and is determined by these quantities as the plasma evolves

through a sequence of equilibria during the burn cycle. The plasma resistance, R_p, is computed at every time step using the neoclassical Spitzer resistivity. The rf current, I_{RF}, is computed as a function of rf power P_{RF}, according to the following algorithm (whose derivation is discussed in Sec. 7.4):

$$I_{RF} = 0 \quad , \; T_e < 1.4$$

$$I_{RF} = \frac{P_{RF}}{8.2 \times 10^{-19} \frac{N_e}{T_e} (1 + 0.16 \sqrt{T_e})} \quad , \; 1.4 < T_e < 6.2 \qquad (11)$$

$$I_{RF} = \frac{P_{RF}}{1.35 \times 10^{-19} \; N_e \; (2.4 - \alpha_T) \; \frac{16}{(1 + \alpha_T) \; T_e} (1.4/\alpha_T - 1)} \quad , \; 6.2 < T_e$$

where N_e and T_e are the average values of electron density and temperature respectively. All units are MKS except temperature which is in keV. The temperature profile factor α_T (see Sec. 7.1) is given by

$$\alpha_T = 1.5 - 0.07 \; T_e \qquad (12)$$

A number of possible burn cycle scenarios were developed for STARFIRE in the course of the study; the selected reference burn cycle is typical. The startup phase of the reference STARFIRE burn cycle is shown in Figs. 6-17 through 6-21. The plasma burn cycle starts when the previously evacuated torus is filled with fresh DT gas. The initial tritium fraction of this gas is 4%, i.e., the gas is 96% D. Five MW of electron cyclotron resonance heating (ECRH) power is then applied to the plasma through a series of waveguides built into the first wall. The ECRH breaks down the fill gas to an ionized plasma at several hundred eV temperature in 10 ms (see Sec. 6.3.4 for a complete description of the plasma initiation process). Next, the previously reverse-biased OH coil is discharged through a dump resistor circuit. This circuit (see Chap. 15) is designed to keep the OH voltage approximately constant during the discharge, to minimize the EF voltage requirements. The OH coil is completely discharged in about 14 seconds; it is then disconnected from the dump resistor circuit and has no further role in the burn cycle. The OH

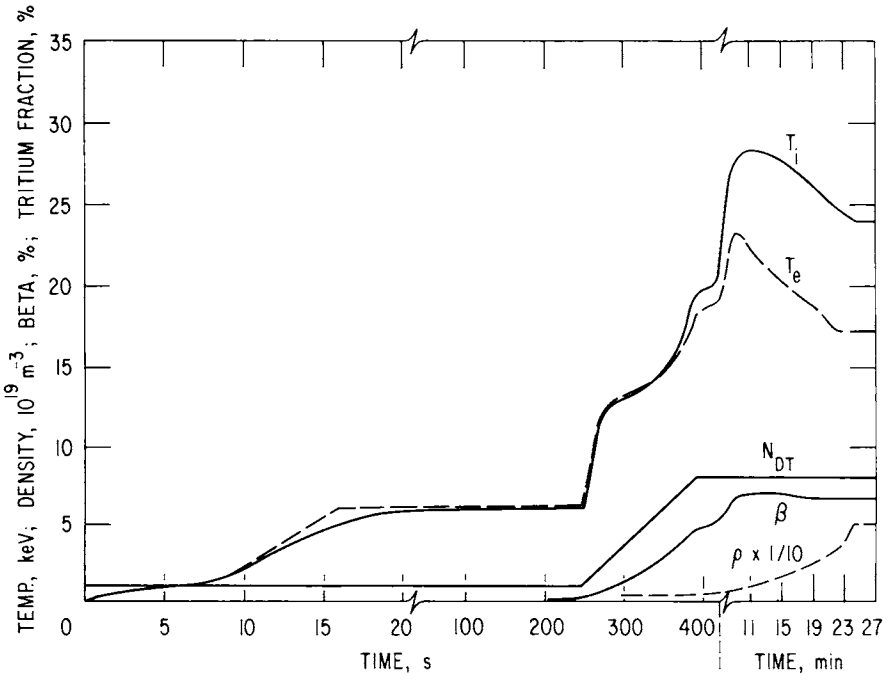

Figure 6-17. Plasma temperature, DT density, beta, and tritium fraction during the startup period.

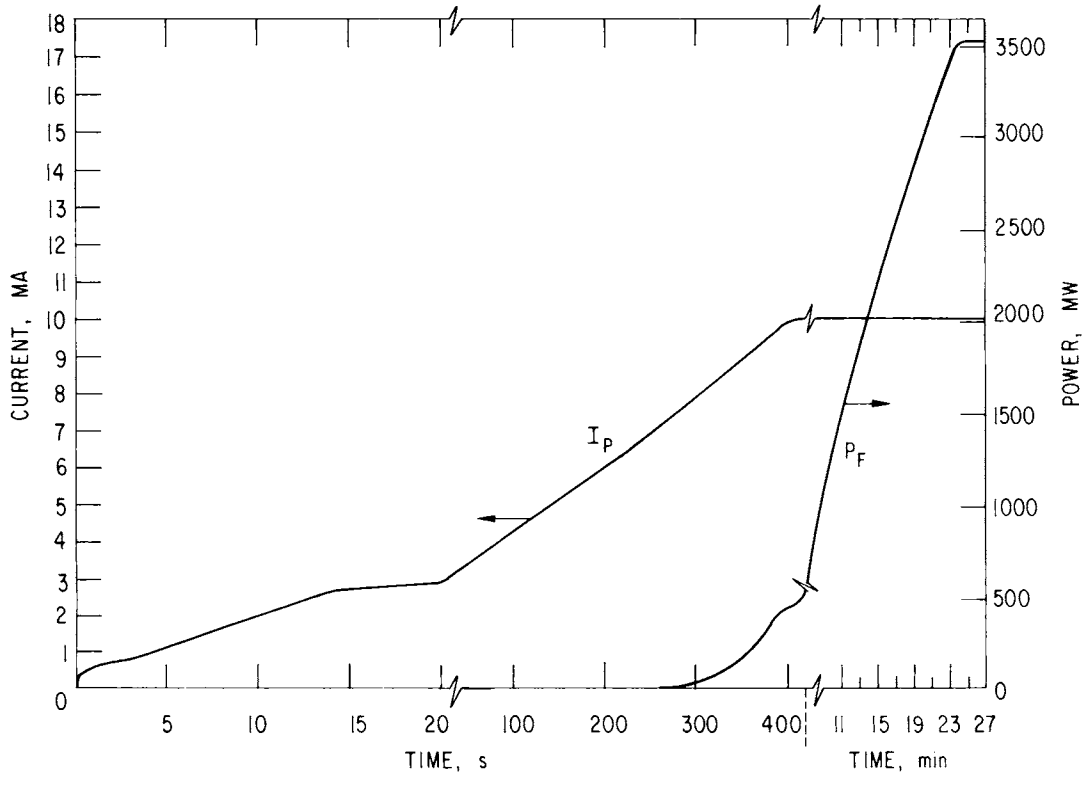

Figure 6-18. Plasma current and fusion power during startup.

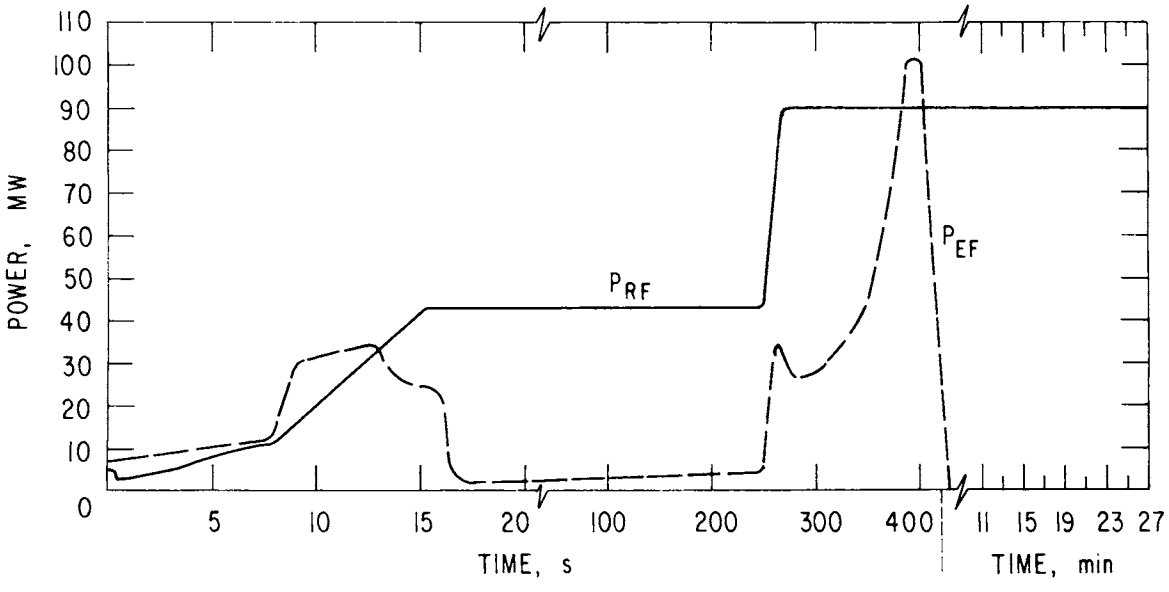

Figure 6-19. RF and EF power during startup.

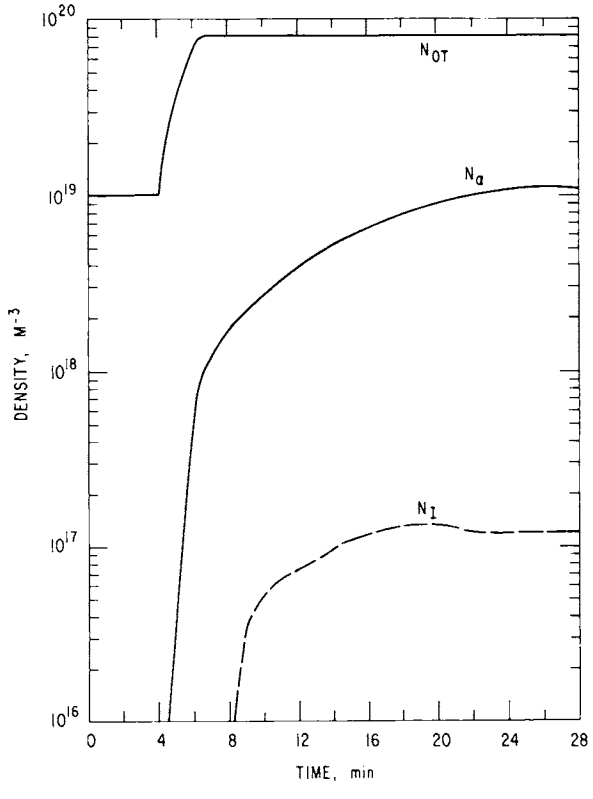

Figure 6-20. Ion densities during startup.

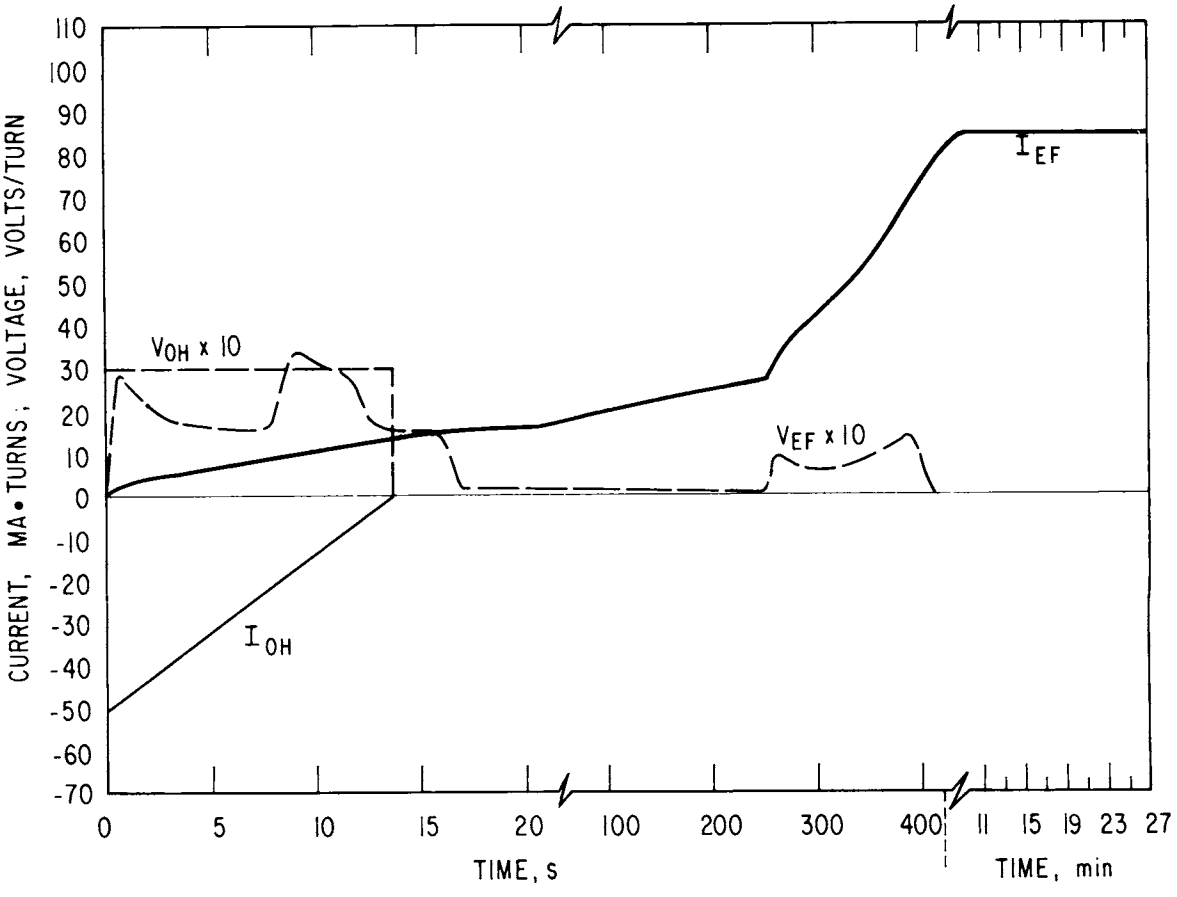

Figure 6-21. OH and EF waveforms during the startup period.

coil supplies about 25 V-s to the plasma. The coil consists of a few turns located in the center of the torus and is used only to achieve an initial plasma current of $\sim$ 2 MA. If it proved possible to induce current immediately, i.e., at low temperatures, with the rf system, then even this small coil could be eliminated.

During this "ohmic heating" period, a variable amount of rf power is applied to the plasma, first with the ECRH system, for about the first three seconds, and thereafter with the lower hybrid system (this is shown as a single rf power in Fig. 6-19). For about the first half of the OH period, the rf power is varied so as to gradually heat the plasma to a temperature of $\sim$ 1.4 keV where the lower hybrid waves can begin inducing current. The rf power is then linearly increased up to about half of the full power and kept constant for $\sim$ 250 seconds. During this 250 s period, which can be described as the main current inducement period, the plasma temperature is held constant at $\sim$ 6 keV, and the rf drive induces its share of the plasma current. This share consists of the total volt seconds needed by the

plasma minus the contribution of the OH coil and minus the expected contribution of the EF coil. During this period, the plasma density is held constant to a low value of about 10% of the maximum value. This combination of low density and moderate temperature minimizes the current inducement time and hence the supplied rf energy, according to the algorithm of Eq. (11). It should be noted, however, that this is not a serious restriction since there would be little problem in operating with a higher density and extending this phase, if necessary.

The next phase of the startup is the main plasma heating phase. At the start of this phase the rf power is brought up to the full 90 MW level. This is done in 15 seconds (and not faster) to provide for a reasonable power load change from the grid. The plasma DT density is also brought up to full value, in $\sim$ 200 s, but a 4% tritium fraction is still maintained. The reason for using this level of tritium is to have some fusion power, to aid in heating the plasma, but to not have enough to thermally stress the first wall, blanket, steam generators and turbines. The combination of rf power, and the α-heating power from fusion serve to heat the plasma to near full temperatures. Therefore, at the end of this phase, the plasma is at full density, current and approximately at full temperature.

The last and longest phase of the startup period is the fusion power ramp phase. During this phase the tritium fraction is increased from 4% to 50% in $\sim$ 17 minutes, in such a way as to linearly increase the fusion power to the full 3510 MW level. The fusion power scales with the tritium fraction, P, as $P_F \sim P(1-P)$ and so for a desired linear increase in fusion power the tritium fraction is changed as per this relation. Control of the tritium fraction is done by increasing the tritium content of the fueling stream. The slight deviation of the fusion power from a linear ramp shown in Fig. 6-18, is due to the variations in ion temperature. The duration of this phase is set at 17 minutes to meet the requirement of a 5% per minute increase in fusion power. If needed, this rate could easily be made faster or slower by changing the rate of increase of the tritium fraction.

In order to provide for a thermal equilibrium during the fusion ramp phase, and the subsequent burn period, iodine atoms are slowly added to the plasma, as shown in Fig. 6-20. The iodine serves to increase the X-ray

power loss of the plasma, and hence, to radiate most of the α-heating power. The iodine is added according to a simple control algorithm intended to maintain a constant value of $\beta = 0.067$. About 0.1% of iodine must eventually be added. The general subject of plasma thermal stabilization with iodine, or other high-Z material, is discussed more fully in Sec. 6.3.3. As shown in Fig. 6-17, β is held fairly constant by the control algorithm; the fine variations in β are due to the changes in the ion and electron temperature, and the buildup of helium, as the plasma evolves through a series of slightly different thermal equilibria.

During the startup period, the EF current is monotonically increased in order to keep the plasma in MHD equilibrium. The EF current and EF voltage required during the startup are shown in Fig. 6-21. The maximum reactive power of the EF power supply is set during the startup and is given by

$$P_{EF}^{REACTIVE} = V_{EF}^{MAX} \times I_{EF}^{MAX} = 290 \text{ MVA}.$$

This is only about 20% of the estimated value that would be needed if STARFIRE were operated in a pulsed mode. The maximum draw of power from the grid is determined by the sum of rf and EF instantaneous powers as shown in Fig. 6-19. For a value of 150 MW of rf input power (for 90 MW output) and assuming a 95% conversion efficiency for the EF supply, the maximum power from the grid is about 250 MW, a reasonable value. If necessary, the EF power peak at $\sim$ 400 s could be reduced by resorting to a non-linear ramp of the fuel density.

6.3.2 Shutdown

6.3.2.1 Normal Shutdown

Two basic types of shutdown are envisioned for STARFIRE, a "normal" shutdown used once or twice a year to routinely shut the plant down, and an "emergency" shutdown used in accident or other non-routine situations.

Like the startup period, the normal shutdown phase of STARFIRE is not restricted by time limitations. The reference shutdown scenario is divided into two parts, fusion ramp down and current ramp down. The fusion ramp down phase is essentially the reverse of the last phase of the startup, i.e., the fusion ramp up phase. For shutdown, the fusion power is reduced, at a 5% per minute rate, by reducing the plasma tritium fraction from 50% to 4%. At the

same time the iodine concentration is reduced to zero to keep the plasma in thermal equilibrium. At the end of this first phase of the shutdown the plasma is in the state shown at the start of Figs. 6-22 and 6-23 which illustrates the second and final phase of the shutdown. During this phase, the DT density (not shown) is held constant at its full value, but with a 4% tritium fraction. The lower hybrid rf power is ramped down linearly from 90 MW to 10 MW. This causes the plasma to cool and the remaining fusion power to fall off. The plasma current also falls, for two reasons; it decays resistively because of the reduction in rf drive, and secondly, because of the transformer action of the EF coil as the EF current is reduced. Towards the end of the shutdown, the rf power is held to a small level to keep the plasma from extinguishing too abruptly. Finally, the rf power is terminated and the plasma is extinguished.

During the shutdown period energy is extracted from the EF coil and fed back to the grid as shown. The maximum value of this power is (-) 70 MW as shown. The EF power supply requirements for the shutdown are less than for the startup; the same supply is therefore used for both periods.

6.3.2.2 Emergency Shutdown

As discussed above, the normal shutdown period for STARFIRE takes about 25 minutes and would be done once or twice a year, for the normal maintenance period. A faster shutdown capability is needed for emergency conditions, such as loss of coolant, turbine trips, etc. Several types of emergency shutdown scenarios have been developed for STARFIRE; these are summarized in Table 6-4.

One way of shutting down the plasma is to induce a plasma disruption. During a disruption the plasma extinguishes completely in a fraction of a second, so the fusion power is essentially stopped immediately. A disruption can be initiated by injecting excess high-Z material (iodine, etc.) into the plasma. This can be done with the normal high-Z gas injection system. The addition of as little as 1 mg of excess iodine would more than double the iodine content of the plasma and should cause an immediate disruption. The time needed for this type of shutdown should, therefore, be limited by the time needed to detect an emergency condition and initiate a shutdown command.

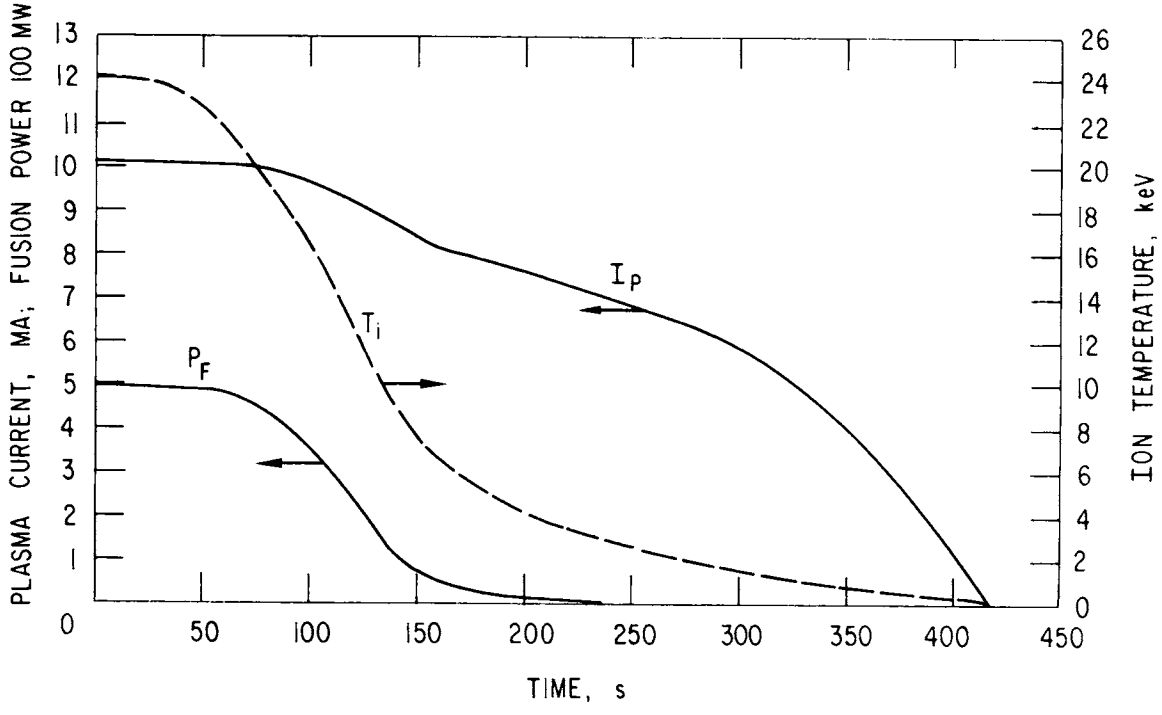

Figure 6-22. Fusion power, ion temperature and plasma current during the last phase of the normal shutdown period.

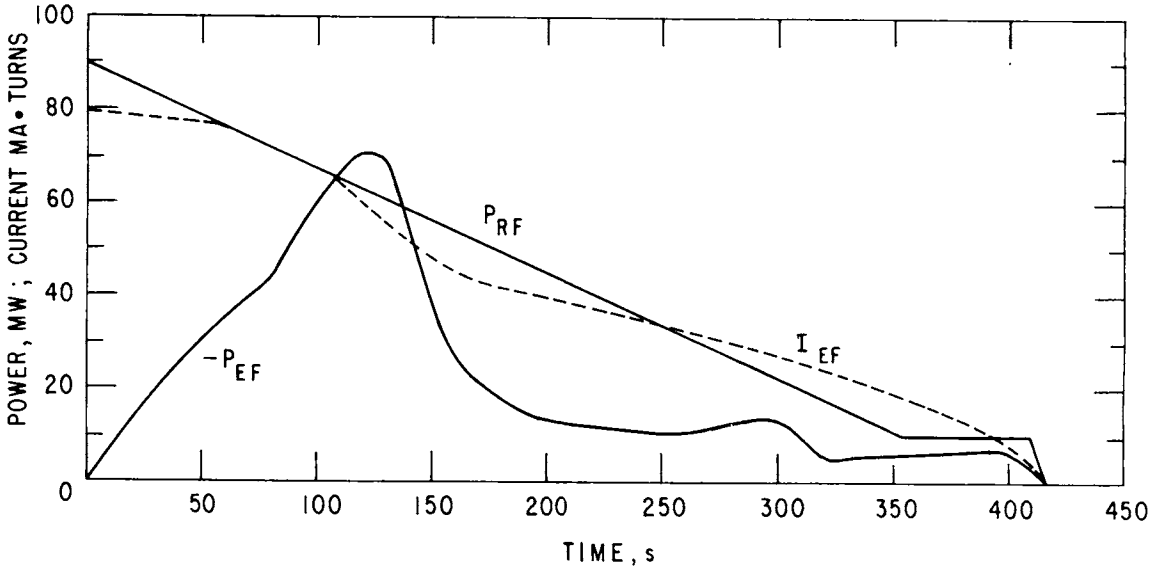

Figure 6-23. RF and EF powers and EF current during the last phase of the normal shutdown period.

Table 6-4. STARFIRE Shutdown Scenarios

Type of Shutdown	Purpose	Time for Complete Shutdown	Method
Normal Shutdown	Reduce fusion power slowly for normal shutdown	1450 s	Reduce tritium fraction
Abrupt Shutdown	Emergency shutdown - stop power immediately	$\lesssim$ 100 ms	Induce a plasma disruption by injection of excess high-Z material
Rapid Shutdown	Emergency shutdown - reduce power quickly	2.5 s	Terminate refueling and rf power
Ablative Induced Shutdown	Occurs automatically if small hot spot develops	$\sim$ 0.5 s	Ablating beryllium causes plasma to cool and disrupt

STARFIRE is designed to take a large number of plasma disruptions each year with no damage except for the ablation of a small amount of beryllium coating on the first wall. However, frequent occurrence or induction of plasma disruptions is undesirable. Therefore, exercising the option of emergency shutdown by inducing a plasma disruption is limited only to those critical failures in the system that require instantaneous shutdown.

An alternate emergency shutdown, labeled as a "rapid" shutdown in Table 6-4 was also developed. This type of shutdown also involves a disruption except that most of the plasma energy is dissipated prior to the disruption. This type of shutdown might be used for a less critical situation where it was still desired to shut the plasma quickly.

The rapid shutdown scenario is shown in Figs. 6-24 through 6-26. The shutdown is controlled through the lower hybrid system and the refueling system. Shutdown is initiated by turning off the rf power in about 0.6 s, as shown. At the same time, both the DT refueling and iodine injection are stopped. The DT density then falls off because of both burnup by fusion and pumping by the limiter vacuum system. The fusion power falls off accordingly as $P_F \sim N_{DT}^2$. The plasma ion and electron temperatures do not fall at first,

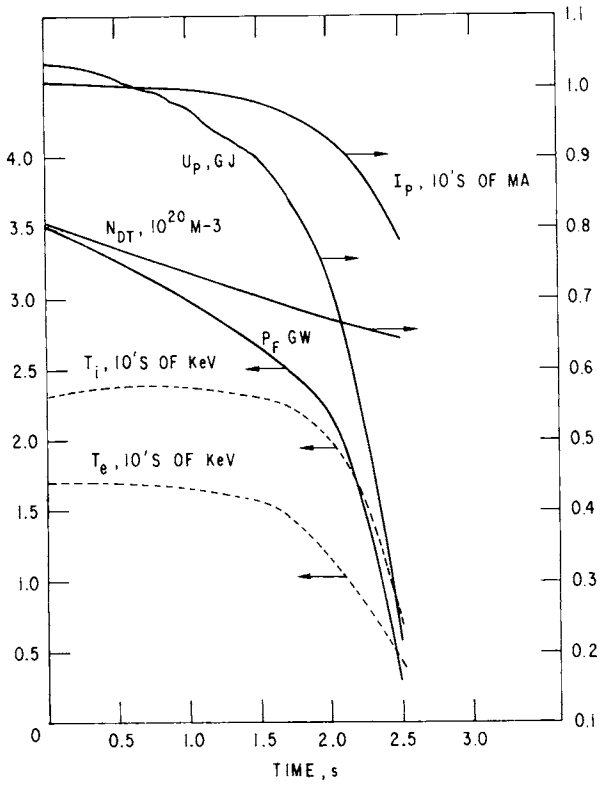

Figure 6-24. Plasma parameters during a rapid shutdown.

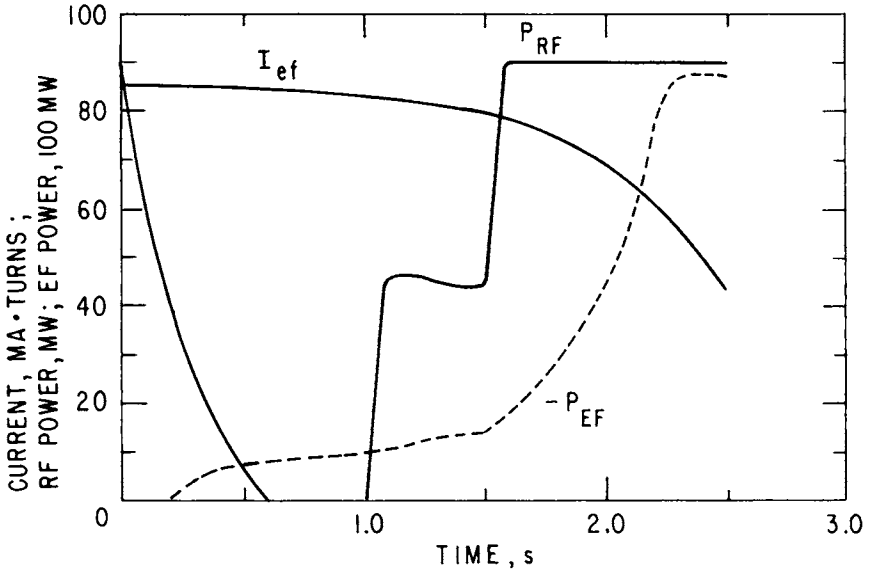

Figure 6-25. Plasma parameters during a rapid shutdown (continued).

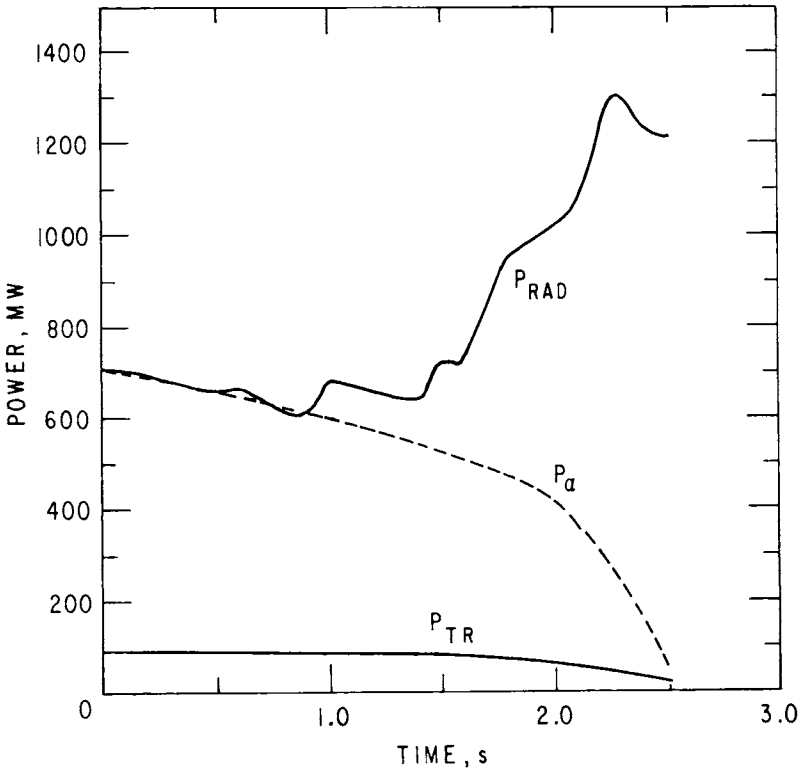

Figure 6-26. Plasma power balance terms during a rapid shutdown.

because there is still an approximate power balance between alpha and rf heating, and radiation and transport losses. At about 1.5 seconds into the shutdown, however, radiation starts to increase substantially and T_i and T_e fall rapidly. Because of the characteristics of the line and recombination radiation from iodine (or other high-Z material), radiation losses increase rapidly with falling temperatures, in spite of the decrease in the electron density and the iodine density (not shown). Eventually the point is reached, at 2.5 seconds, when the EF current cannot be reduced fast enough to keep the plasma in MHD equilibria. At that point the plasma is driven into the inner wall and disrupts. The purpose of reducing the power output of the rf system (in stages) is to extend the time until disruption to 2.5 seconds; if this were not done the disruption would occur sooner. The key difference between this type of shutdown and the "abrupt" shutdown is that the plasma thermal energy, U_p, is reduced to 20% of its full value by the time the disruption occurs. Also, the plasma magnetic energy, which scales as $\sim I_p^2$, is reduced to $\sim$ 60% of full value. However, it is not clear at this time

whether this soft disruption type shutdown really is needed, i.e., whether the abrupt type of shutdown might just as well be used.

The requirements on the EF system, for the rapid shutdown, are shown in Fig. 6-25. Since the EF coil stores 10 GJ at full current, a large amount of power is involved in reducing the EF current in 2.5 seconds. As discussed in Chap. 15, a variable dump resistor/interrupting switch system is used to reduce I_{EF} in a controlled manner during a rapid shutdown. This is a fairly cheap system, because it uses a mechanical switch instead of a longer lifetime, more expensive solid state switch. This can be done because of the very infrequent use of this system. The dump resistor system is designed for a nominal rating of 10 GW. When the power reaches approximately this level the resistance is not increased any further. I_{EF} is then larger than required for MHD equilibrium and the plasma disrupts (at 2.5 s).

The third type of shutdown has been called an "ablative induced shutdown." As its name implies, this shutdown is not induced by external control but occurs naturally as a result of the ablation of Be coating from the first wall or limiter. This type of shutdown was studied by inputting different rates of Be ablation into the plasma dynamic code. The ablation rates studied correspond to various degrees of hot spot formation on the first wall. It was found that if as little as 10^{22} Be atoms per second ablate into the plasma, this will cause a disruption in a maximum of 0.7 seconds, even if nothing else is done to terminate the plasma. This shutdown is shown in Fig. 6-27 for this value of ablation rate. An ablation rate of 10^{22} s^{-1} corresponds to as little as 1% of the wall area increasing in temperature by about 500°C (see Chap. 10). The mechanism for this shutdown is that the incoming Be cools the plasma, not by radiation, but simply by diluting the plasma with excess ions and electrons. The rapid decrease in electron temperature then causes the radiation power to increase which, in turn, further decreases T_e and so forth. At about 0.7 seconds, the plasma extinguishes abruptly. In this simulation the EF current was allowed to decrease as fast as necessary to accommodate the falling plasma pressure. Since this could not be done in actuality, the plasma would actually terminate sooner. Therefore, the value of 0.7 seconds represents an upper limit to the shutdown time. The plasma also terminates sooner for higher Be ablation rates. These results tend

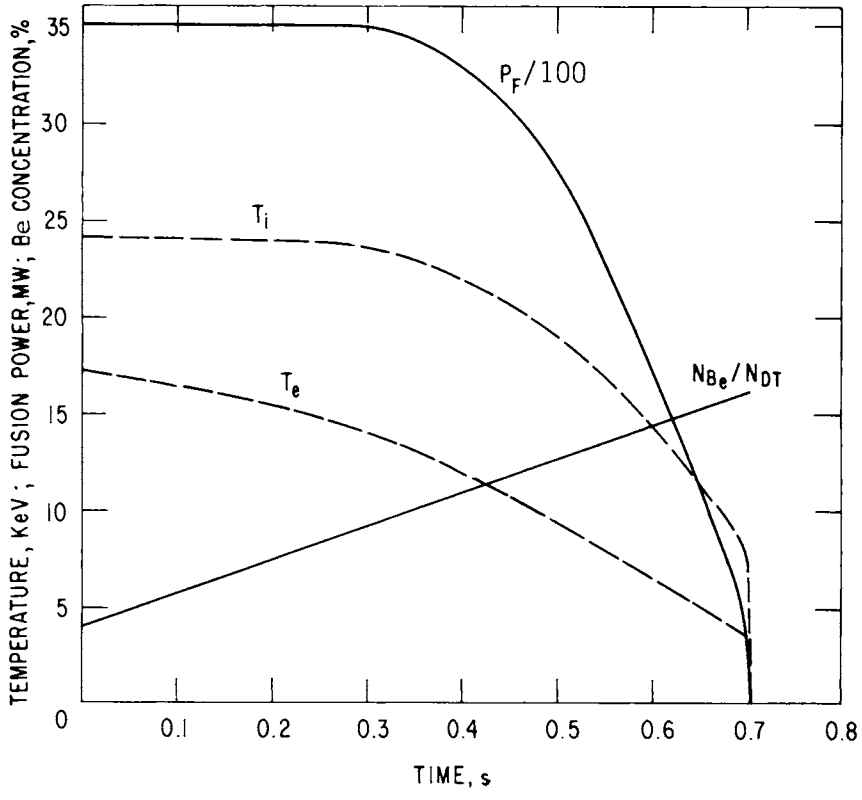

Figure 6-27. Plasma parameters during beryllium ablation shutdown.

to confirm the general safety feature of fusion; any accident serious enough to affect the first wall will almost immediately shut the plasma down before there is any major damage to the first wall. This would include water leaks or virtually any introduction of foreign material into the plasma.

6.3.3 Burn Phase

6.3.3.1 General Features

The normal burn phase of STARFIRE lasts on the order of six months, the exact time depending on the need to shut the plant down for maintenance. The plasma current is driven in steady state by the lower hybrid rf system. Impurities in the plasma, specifically the helium from fusion and beryllium from sputtering of the boundary, are held to values of 14% and $\sim$ 4%, respectively, by the impurity control system (see Chap. 8).

During the burn phase the current in the main set of EF coils is kept constant, to provide for the basic MHD equilibrium. Vertical and horizontal motions of the plasma are stabilized by feedback control of the current in the inner, CF coils. These coils also serve to stabilize against plasma disruptions. The CF coils are driven by a 33 MW solid state power supply operating out of a small capacitor bank. The plasma is also stabilized by means of eddy currents set up in the conducting path composed of the first wall plus jumper cables.

During the burn phase, the STARFIRE plasma is operated in an "enhanced radiation mode" whereby iodine atoms are fed into the plasma to enhance X-ray radiation. This has two purposes: to control the plasma thermal equilibrium, and to radiate most of the α-heating and rf energy from the plasma to the first wall, thereby minimizing the transport power to the limiter.

The basic thermal equilibrium of the plasma can be developed with a simple global power balance as follows; the plasma can be divided into a core region, where almost all of the fusion reactions are taking place, and an edge region between the core and the boundary. The power balance for the core can be written as:

$$P_\alpha + P_{rf} = P_{TR}^{core} + P_{rad}^{core} \qquad (13)$$

where P_α is the α-heating power to the plasma, P_{rf} is the lower hybrid rf power, P_{TR}^{core} is the heat transport loss power from the core to the edge region, and P_{rad}^{core} is the core radiation loss. For STARFIRE, P_α = 703 MW and P_{rf} = 90 MW. The total heating power is therefore about 800 MW. At equilibrium this must be balanced by transport and radiation losses as per Eq. (13). The transport power is given by:

$$P_{TR}^{core} = \frac{U_e}{\tau_e} + \frac{U_i}{\tau_i}$$

where U_e and U_i are the kinetic energies of the electrons and ions, respectively, and τ_e and τ_i are the energy containment times. The kinetic energies for STARFIRE are:

$$U_e = 432 \text{ MJ}$$

$$U_i = 488 \text{ MJ} \quad .$$

The containment times can be estimated using the common prescription of empirical scaling for the electrons and one-third neoclassical for the ions. This gives for τ_e:

$$\tau_e = 5 \times 10^{-21} N_e \bar{a}^2 = 3.6 \text{ s}$$

where $N_e = 1.18 \times 10^{20}$ m^{-3} and $\bar{a}^2 = \kappa a^2$ where $\kappa = 1.6$ and $a = 1.9$ m. For ions, using the banana regime coefficient as defined in Ref. 32, one obtains $\tau_i = 10$ s. The core transport power is then:

$$P_{TR}^{core} = 170 \text{ MW}$$

Therefore, for a power balance, the core radiation power, from Eq. (13) would have to be: $P_{rad}^{core} = 623$ MW. Normally the core radiation would be almost entirely from bremsstrahlung and would typically be less than 100 MW. Therefore, a STARFIRE-like plasma would not be in thermal equilibrium. By adding a high-Z material to the plasma, the radiation can be enhanced and the plasma brought into thermal equilibrium. A suitably chosen high-Z atom will be only partially stripped, even in the plasma center. It will, therefore, enhance the line and recombination radiation through electron capture and release as well as enhancing bremsstrahlung through electron acceleration in the presence of highly charged ions. It should be noted that a power balance could possibly be achieved by enhancing the transport power by such means as ripple coils. However, this might have the undesired effect, for STARFIRE, of increasing the heat load to the limiter, unless excess transport power could be radiated away at the plasma edge.

For the edge region, the power balance can be written as:

$$P_{TR}^{core} = P_{TR}^{lim} + (P_{rad}^{edge} + P_{cx} + P_{misc}) \qquad (14)$$

where the left-hand term is the heat transport from the core to the edge region, P_{TR}^{lim} is the heat transport power to the limiter, and the three terms in brackets are respectively the radiation power from the edge, the charge exchange loss power, and a miscellaneous term associated with the ionization of recycling neutrals. Based on estimates of the charge exchange flux, and average edge temperature, as discussed in Sec. 8.2.6.1, the charge exchange power would be about 50 MW. However, this value, as well as the other loss

terms are somewhat uncertain. In general the transport power to the limiter will be some fraction γ, of the transport power to the edge, viz:

$$P_{TR}^{lim} = \gamma P_{TR}^{core} \tag{15}$$

For the STARFIRE reference case we have used an estimated value of $\gamma = 0.5$, i.e., half the power to the edge region will be transported to the limiter. This gives about 90 MW of transport power to the limiter.

The high-Z material used for enhanced radiation should ideally have the following characteristics: (1) it should enhance the radiation throughout the discharge and particularly in the center, (2) the amount needed should not significantly increase the plasma pressure (and hence increase β), and (3) its chemistry should be compatible with the reactor boundaries, the vacuum system and the tritium processing system. Based on these criteria, we have evaluated several candidate elements. It appears that elements with atomic number $Z < 18$, i.e., argon and below do not radiate enough energy for reasonable impurity ion concentrations. Feasible elements are in the general range of Kr to Xe, i.e., $Z = 36$-54. The noble gases are, of course, ideal from the chemical interaction standpoint. On the basis of radioactive isotope considerations, iodine is a somewhat better choice than xenon, and has been selected as the reference, "high-Z" material for STARFIRE. However, xenon, krypton and possibly other elements are feasible backup choices. Based on the burn cycle calculations discussed earlier, an amount of iodine equal to about 0.1% of the DT density is needed in STARFIRE. This value of iodine concentration is, of course, somewhat uncertain because of uncertainties in the various models used; however, any concentration in this order of magnitude is small enough to be acceptable.

The aforementioned burn cycle calculations used fixed plasma profiles with averaging done over the profiles. Further 1-D studies of the enhanced radiation mode of operation were performed, and are described in the next section.

6.3.3.2 1-D Code Studies of STARFIRE Burn Phase

In order to further analyze the feasibility of the enhanced radiation mode of operation, a simulation of the main phase of the STARFIRE burn cycle was undertaken with the one-dimensional, time-dependent plasma transport code WHIST. This code has been developed over the past several years by teams at Oak Ridge National Laboratory and elsewhere.[33] Because of its ability to provide a detailed treatment of radially dependent processes such as radiation, transport, and refueling, WHIST constitutes a very useful tool for the analysis of tokamak discharges. For various choices of plasma transport laws, it advances the particle and energy diffusion equations in time using a conservative spatial differencing scheme and an implicit time treatment which ensures numerical stability.[34] Because of a number of differences between WHIST and the codes used to generate the STARFIRE reference design (e.g., the treatment of non-circularity and impurity control), we do not seek an exact match of plasma parameters, but rather a general confirmation of the enhanced radiation mode concept.

The problems considered here concern only the main part of the burn, so that the full current, densities, and temperatures are assumed to be present initially. The D, T, and α species, the electron and ion temperatures, and the current are allowed to diffuse according to a combination of Alcator, magnetic ripple, and neoclassical transport laws. The transport coefficients are given, more specifically by:

(a) Empirical expressions for the electron heat conductivity (χ_e) and diagonal particle diffusion coefficients (D),

$$\chi_e = (5 \times 10^{19}\ m^{-1}s^{-1})/n_e\ ,$$

$$D = \frac{1}{5}\chi_e\ ;$$

(b) The ripple-trapping contribution to the ion heat conductivity[35,36] (the banana-drift contribution is negligible in the STARFIRE discharge), and

(c) Neoclassical expressions appropriate to the banana-plateau regime,[37] with each neoclassical transport coefficient modified by an overall factor of three.

Virtually all of the plasma heating is provided by α energy deposition, taken to be instantaneous, and the rf source; ohmic heating contributes less than a percent. The rf heating is modeled by a source term in the electron energy equation given in Ref. 2:

$$P_{rf} = \frac{3e^4 \ln \Lambda}{5(2\pi)^{3/2}\varepsilon_0^2 m_e^{1/2}} \frac{n_e^2}{\sqrt{T_e}} \exp\left(-\frac{m_e c^2}{2n_1^2 T_e}\right) \ln\left(\frac{n_1}{n_2}\right), \qquad (16)$$

with the parallel indices of refraction $n_1 = 1.86$ and $n_2 = 1.40$. This source term is added at spatial mesh points beginning with the limiter and extending inward until 90 MW have been deposited in the plasma.

While gas puffing has proved to be an effective refueling mechanism in present day experiments, no simple and successful 1-D transport model is now available. WHIST provides a gas-puffing option, but if it is used to refuel STARFIRE, the fuel accumulates at the edge and execution times increase exorbitantly. For the purposes of this study, therefore, the decision was made to postulate refueling profiles (source terms in the D and T density equations) which, in combination with particle diffusion processes, give rise to the design density profiles. The value of the source at each spatial point was adjusted at fixed time intervals (typically 15 or 20 ms) via feedback from the actual density at that point.

A trace iodine species was added for purposes of producing enhanced radiation. In principle, the iodine belongs in the list of diffusing species, but since its source profile is no better understood than that of the fuel, a simplified approach was adopted; this was that the iodine profile was taken to be identical to the deuterium profile and its height was adjusted so that the average electron temperature remained at its design value. Since various averages can be defined, it should be remarked that, for the purposes of this analysis, this average was two-thirds of the average kinetic energy per electron, or

$$\tilde{T}_e = \int_o^a r n_e(r) T_e(r) dr \left[\int_o^a r n_e(r) dr\right]^{-1},$$

which is $\tilde{T}_e = 19.5$ keV for the STARFIRE design. (In interpreting these integrals, one should note that WHIST accounts for the plasma elongation

by introducing effective concentric circular cross sections, but it does not account for the shift and compression of flux surfaces.)

The initial state of the plasma was taken to have the reference design fuel and temperature profiles, an iodine concentration of 0.17% relative to $n_D + n_T$, a parabolic current profile, and a guess for the α profile (bell-shaped, with an average density of 0.95×10^{19} m^{-3}). After the first few hundred milliseconds, both the fuel profiles and the average electron temperature remained steady. The iodine concentration necessary to enforce the desired T_e was 1.65×10^{17} m^{-3}, or 0.20% of the fuel density. The average ion temperature, defined as in the equation above with n_i in place of n_e, decreased during the first second by 10% from its initial value of 27.4 keV, and then rose over a period of several seconds to a constant final value of 26.6 keV. The temperature profiles also changed rapidly during the first second, developing points of inflection and becoming hotter in the center and cooler at the edge. After approximately 10 s, they stabilized to the shapes indicated in Fig. 6-28. Note that both the final $T_e(r)$ and the final $T_i(r)$ are practically flat from the magnetic axis out to about 0.4 m (T_e is hollow by about 0.1%); each then exhibits a nearly constant downward gradient out to the scrapeoff region. The slight increase in the local electron temperature at r = 1.35 m corresponds to the innermost penetration of the rf heating, where the rf power density is a maximum. The fusion power developed with both the initial temperature profiles and the final profiles is very similar, and is within 10% of the STARFIRE reference value.

Figure 6-29 indicates the calculated, steady-state refueling profiles for both D and T. The differences, which arise from the small fraction of DD reactions and the mass dependence of the neoclassical transport coefficients, are practically negligible. It is of interest that the profiles are peaked much more strongly at the edge than at the center.

The steady-state power balance figures for this discharge are shown in Table 6-5. Overall, radiation accounts for 85% of the power loss, and atomic radiation from iodine exceeds bremsstrahlung and cyclotron radiation by a factor of 3, in justification of the enhanced radiation concept. The power balance split is plotted as a function of position in Fig. 6-30. Note that transport losses are peaked in the region where the rf power is deposited; the rf power is transported to adjacent regions which therefore show transport gains.

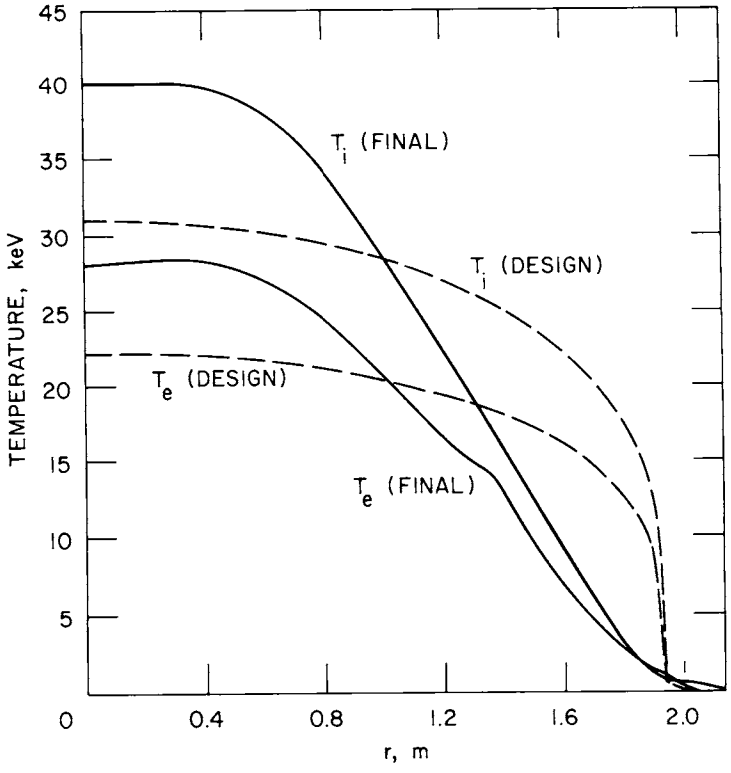

Figure 6-28. 1-D code results for steady-state $T_e(r)$ and $T_i(r)$. Also shown are design profiles. In this figure and in Figs. 6-29 and 6-30, r is the distance from the magnetic axis (taken to be centered) in the horizontal plane.

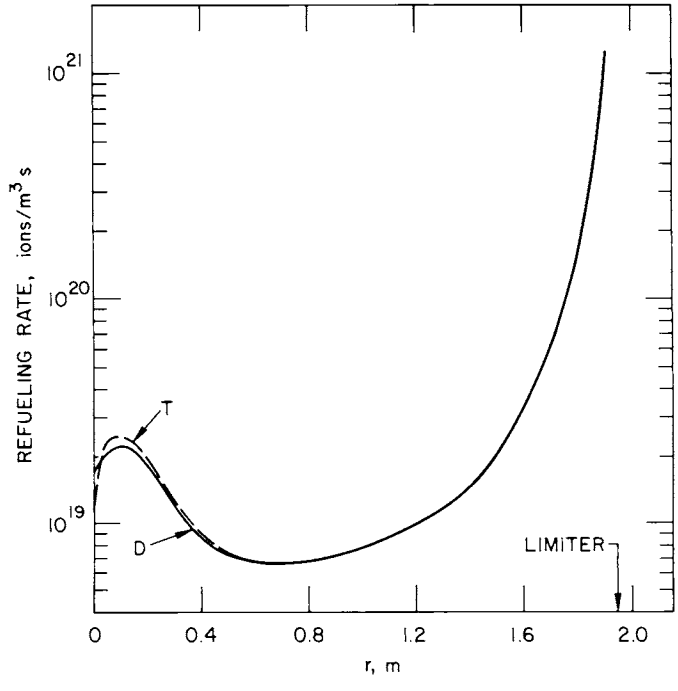

Figure 6-29. 1-D code results: steady-state refueling profiles.

Table 6.5 Steady State Power Balance from WHIST Code Results. Units are MW.

	Electrons	Ions
α heating	434	212
rf heating	90	—
Ohmic heating	1	—
Temperature equilibration	183	-183
Radiation (bremsstrahlung and cyclotron)	-152	—
Radiation (atomic)	-473	—
Transport	-83	-29

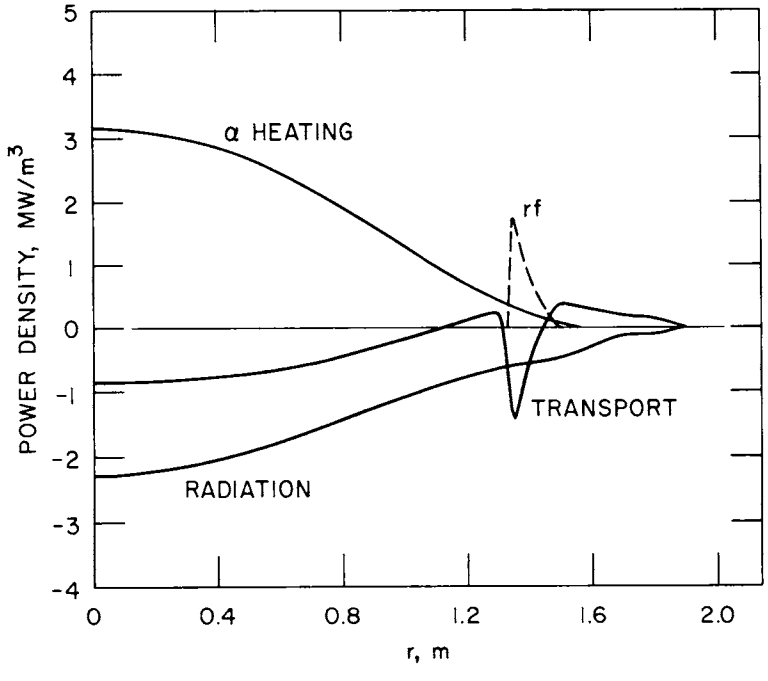

Figure 6-30. 1-D code results: steady-state power balance profiles.

The existence and properties of the steady state depend strongly on the toroidal field ripple. The case just discussed pertained to a nominal peak-to-average ripple of 1.5% at the edge and 0.3% at the center, with 12 TF coils. These ripple values are considered nominal in the sense that the theory yielding the ripple-trapping ion conductivity[35,36] assumes concentric, circular zero-order flux surfaces, which differ appreciably from the STARFIRE flux surfaces. Thus one would probably not be justified in taking literally the ripple values; the WHIST results, however, should give the correct trends.

To test the sensitivity to ripple, runs were made with several values of the edge ripple, keeping 12 TF coils and a fixed edge-to-center ratio of 5. With 4% edge ripple, the average ion temperature dropped by at least 50%, giving conditions inappropriate to a reactor like STARFIRE. When the ripple was decreased to 2.3%, however, a steady burn resulted with a fusion power equal to about 90% of that in the case discussed above but also with 50% more transport power. A further decrease of the ripple to 1.1% led to conditions suggesting a thermal runaway. The possibility of exploiting the high sensitivity to ripple as a burn control mechanism has been discussed by Petrie and Rawls.[38].

To test the sensitivity to the iodine density profile, a number of runs were made using different profiles, generally more peaked toward the center than in the case discussed. It was found that more peaked iodine profiles also result in acceptable enhanced radiation equilibria with the ion and electron temperature becoming lower in the center and higher at the edge than those shown in Fig. 6-28. In general, it appears that a fairly wide range of temperature profiles can be obtained, by varying the iodine refueling profile.

Finally, on the important question of plasma stability, it should be noted that while the enhanced radiation mode is not inherently stable, the present results have shown that feedback control of the iodine concentration appears to serve as an effective control measure. For example, the plasma temperature profiles, shown in Fig. 6-28, converged to stable values, by feedback controlling the iodine concentration on a relatively long time scale. More analysis of this subject is needed, however, to quantify the effects of different iodine refueling methods and transport laws on stability. Other high-Z materials may also aid the stability; e.g., krypton

may be inherently more stable than iodine, because of its radiation vs. temperature characteristics, and this needs further examination. Passive thermal stabilization by such means as ripple transport and radial motion may also serve as a significant help for STARFIRE like devices.[39]

6.3.3.3 Refueling System

The parameters pertaining to the refueling system requirements for STARFIRE, during the steady-state burn phase, are shown in Table 6-6. Because of the high recycling rate of 90% for DT ions diffusing from the plasma (see Chap. 8), the required external refueling rate is fairly small, being only about 16% of the total refueling rate. Because of this, and because it is clearly the simplest engineering option, gas puffing has been adopted as the reference refueling system for STARFIRE.

Other fueling schemes were examined as backups to gas puffing. For pellet injection, the low plasma density ($n_{DT} \sim 8 \times 10^{19}$ m^{-3}) in the reactor limits pellet diameters to less than 20 mm to avoid large density fluctuations. Such small pellets are found to penetrate only a small percentage of the distance to the magnetic axis, even assuming the unlikely injection speed of 9000 m/s. Snowplow plasma guns, on the other hand, are compact, inexpensive, and promise excellent fuel penetration. If fuel densities of 1×10^{24} m^{-3} are achieved, plasma penetration should occur for fuel energies $\sim$ 200-600 eV, corresponding to 1.1 MJ gun operation (assuming 50% efficiency). A system having 70-cm long coaxial electrodes of 5 and 10 cm radii could be fired at 105 kV. The gun could be installed in the vacuum plenum between the blanket and shield. An insulating gasket between the electrodes can be well protected from neutrons, and impurity injection can be minimized by beryllium plating the cathode. Snowplow plasma guns, therefore, constitute a backup option for gas puffing.

6.3.4 Plasma Initiation

An electron cyclotron resonance heating (ECRH) system has been chosen as the plasma breakdown system for STARFIRE. An important advantage of the ECRH approach is that it circumvents the creation of a multipole field null and the need for inducing a large voltage spike around the plasma, both of which are required for a conventional avalanche type breakdown and preheat.

Table 6-6. Plasma Refueling Parameters

	Parameter	Value
1)	DT ion content in plasma	6.29×10^{22}
2)	Gross DT diffusion rate (before recycling)	3.49×10^{22} s^{-1}
3)	DT burnup rate	2.50×10^{21} s^{-1}
4)	Total required DT fueling rate (#2 + #3)	3.75×10^{22} s^{-1}
5)	DT recycling rate (from wall and limiter)	3.14×10^{22} s^{-1}
6)	Required external fueling rate (#4 - #5)	6.0×10^{21} s^{-1}

For example, in the Argonne EPR design[40] a complex field null near the first wall was created by a combination of the OH and EF coils and an initiation coil set. The current in the initiation coils was then resistively ramped to zero providing a 500 V spike for $\sim$ 10 ms. This provided breakdown of the gas in the channel defined by the field null, and the rising OH voltage then took over the job of plasma heating while the radius of the discharge was slowly increased until the whole vacuum chamber was filled. Startup utilizing ECRH eliminates the need for an initiation coil set. The ECRH input is also sufficient to preheat the plasma to a few 100 eV, at which point the lower hybrid system can take over. These features led to the selection of ECRH for plasma breakdown and preheating.

Successful plasma heating with microwave power at the electron cyclotron frequency has been demonstrated in the Elmo Bumpy Torus (EBT),[41,42] in mirror experiments, and more recently in tokamaks in both the U.S.S.R[43,44] and the U.S.[45] This has prompted a vigorous program focusing on the development of high frequency microwave sources. Prospects for utilizing electron cyclotron resonance heating (ECRH) on larger machines such as

STARFIRE are encouraging, especially in light of recent advances in cyclotron resonance maser (gyrotron) technology.[46,47] Varian has already demonstrated pulsed gyrotrons capable of generating ∿ 250 kW of power at an efficiency of 35%, and work is now proceeding on an extension of the technology to a steady-state mode of operation.

A second attractive feature of ECRH breakdown is the simple power distribution system. Ordinary waveguides can be used to deliver the microwave power to the plasma where high (> 90%) absorption efficiencies are expected. The only complication is that for effective absorption the wave must be injected from the high field (inboard) side of the vacuum chamber. Fortunately the small dimensions of the waveguide structure (inside diameter ∿ 6 cm) and any launching mechanisms that may be required (typically horn antennas) enable the ECRH system to have a minimal impact on the engineering of the reactor, in spite of the inboard injection requirement.

The initiation scenario envisioned for STARFIRE is as follows: After an initial pumpdown to low pressures (∿ 10^{-6} torr) to reduce impurities, the vacuum chamber is back filled with deuterium to a pressure of ∿ 10^{-4} torr. The ECRH system is then turned on. A rapid breakdown ensues, culminating in a plasma with a hot (few hundred eV) electron component at the upper hybrid resonance and a cold (tens of eV) background plasma filling the remainder of the vacuum chamber. This initial phase takes ∿ 10 ms. Thereafter, the gradual buildup of plasma current causes the cold background plasma to begin equilibrating with the hot resonance layer. This equilibration occurs in ∿ 5 s and results in a more or less uniform plasma temperature of a few hundred eV. At this point the ECRH system is turned off, the lower hybrid system is turned on, and the main stratup period starts.

The ECRH breakdown system appears to be naturally compatible with the remainder of the startup scenario. ECRH breakdown reduces the volt second requirements on the OH coil set, and it completely eliminates the complexities of initiation coils and the multiple field considerations associated with avalanche breakdown. These savings must, of course, be weighed against the addition of the ECRH power supplies and power distribution system to determine the actual cost benefits of the ECRH approach. However, it seems clear that the reduction in the complexity of the coil set afforded by the lower hybrid current drive will favor the ECRH system under most conceivable cost

situations. In addition, the active ECRH development program and the promising early results should lead to a well developed ECRH technology in the STARFIRE time frame.

The reference case ECRH breakdown calculation for the STARFIRE reactor was computed using the model described in Appendix I. The reference breakdown results are shown in Fig. 6-31. In this case, the vacuum chamber is initially filled with deuterium gas at a pressure of $\sim 10^{-4}$ torr, with an amount of oxygen equal to 0.1% of the deuterium density also present due to desorption of physically bonded oxygen from the first wall and fuel contamination. Once the ECRH power is turned on, local gas breakdown occurs in the neighborhood of the ECRH waveguides resulting in a cold, low density ($\sim 10^{16}$ m^{-3}) plasma that quickly fills the vacuum chamber. Resonance absorption at the electron cyclotron resonance (ECR) layer then causes a rapid increase in the local electron temperature. This increase is quickly quenched by the density buildup, and soon thereafter absorption at the upper hybrid resonance (UHR) begins to dominate absorption at the ECR resonance.

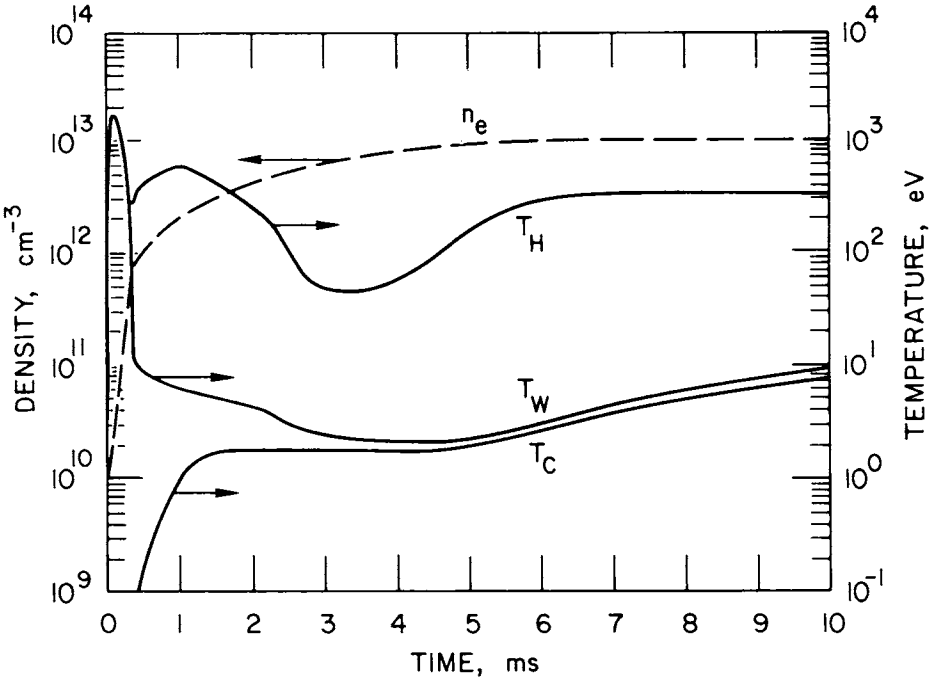

Figure 6-31. Reference case ECRH breakdown calculation.

Because the UHR resonance layer is much narrower than the ECR layer, the temperature of UHR layer (T_H) rapidly becomes much larger than that of the ECR layer (T_W), even though the two layers never physically separate. T_H rises until the UHR absorption reaches its maximum (at $n_e \sim 2 \times 10^{18}$ m^{-3}) and then falls rapidly to a minimum of $\sim$ 40 eV while the bulk of neutral gas in the vacuum chamber is ionized. As the ionization losses begin to decrease (due to the reduction in the background neutral density), T_H slowly begins to rise and eventually reaches an equilibrium at $\sim$ 300 eV. During this time, T_W has fallen to a value that is just slightly larger than the bulk electron temperature T_C.

The ECRH breakdown is thus completed in $\sim$ 10 ms. It results in a low temperature ($\sim$ 10 eV), moderately dense ($\sim 10^{19}$ m^{-3}) plasma filling the bulk of the vacuum chamber with a thin ($\sim$ 2 cm) wide layer near the center of the chamber that is resonance heated to a temperature of $\sim$ 300 eV. The initial current induced by the OH coils thus flows primarily in the UHR layer but will spread out as the field transform produces a more uniform plasma temperature. This occurs in about 5 s after which the entire plasma has been heated to $\sim$ 400 eV. The plasma is then able to absorb microwave energy at the lower hybrid frequency; therefore, the lower hybrid system is used to increase the plasma temperature from 400 eV to ignition.

It was found that the oxygen impurity fraction has little effect on the initial plasma breakdown. In fact, an increase in this fraction from 0.1% to 5% does not change the breakdown time and only lowers T_H from 320 to 280 eV. Any problem of starting up with higher impurity fractions would therefore occur after breakdown. For example, a 10^{19} m^{-3} dense plasma containing 5% oxygen is found to require $\sim$ 0.1 MW/m^3 of input power density in order to burn through the impurity radiation barrier at 40 eV. Since the bulk breakdown plasma must still be heated past this radiation barrier, nearly 80 MW of input power would be required to initiate the STARFIRE system for a 5% oxygen concentration. From these considerations, oxygen impurities should make up to more than 0.1% of the initial plasma density. (If higher Z impurities are involved this percentage will be lower.) The impurity radiation barrier is then $\sim$ 3 MW which is substantially less than the 5 MW that is provided by the ECRH system.

It should be noted here that the ECRH breakdown process may lend itself to startup with a higher impurity fraction than is indicated by the above consideration. This is due to the hot resonance layer which becomes the current channel once the OH flux begins to change. The hot region of the plasma spreads outward from this resonance layer as the plasma current builds up; consequently the entire vacuum chamber is not burning through the impurity radiation barrier at the same time. This spatial effect will cause the impurity radiation losses to be lower than the previous estimate which assumed that the temperature increase was uniform across the plasma. Startup with a higher impurity fraction could thus be accommodated for a given input power. Unfortunately, the magnitude of this spatial effect is difficult to quantify; therefore its influence has not been included in the present design, other than to recognize that it represents an inherent design margin.

6.3.4.1 System Implementation

Based upon the requirements identified by the breakdown model, an ECRH system design has been developed. The system is composed of 24, 160 GHz gryotrons, each delivering $\sim$ 210 kW to the plasma for about five seconds. This power is distributed using 24, 6 cm ID, overmoded waveguides. The guides are composed of PCA stainless steel whose interior has been coated with copper to reduce power losses. Near the first wall, an additional coating of beryllium is added to minimize impurity sputtering. Two guides are routed in parallel with each of the 12 lower hybrid rf ducts through the shield. They then separate and travel along the outside of the blanket sector to the lower inboard side (see Fig. 6-32) where they penetrate the blanket and open into the vacuum chamber. For startup purposes, random phase and polarization are adequate; consequently special wave launching mechanisms such as horn antennas are not required.

The gyrotrons (shown schematically in Fig. 6-33) are composed of a plasma gun that emits electrons into a cyclotron resonance cavity. There the thermal energy of the electron beam is converted to microwave power which is passed through a vacuum window into the waveguide. The residual beam power ($\sim$ 65% of the total) is deposited on a water cooled beam dump upon exiting from the resonance chamber. Superconducting magnets are utilized to create the resonance fields due to the high frequencies required. As was

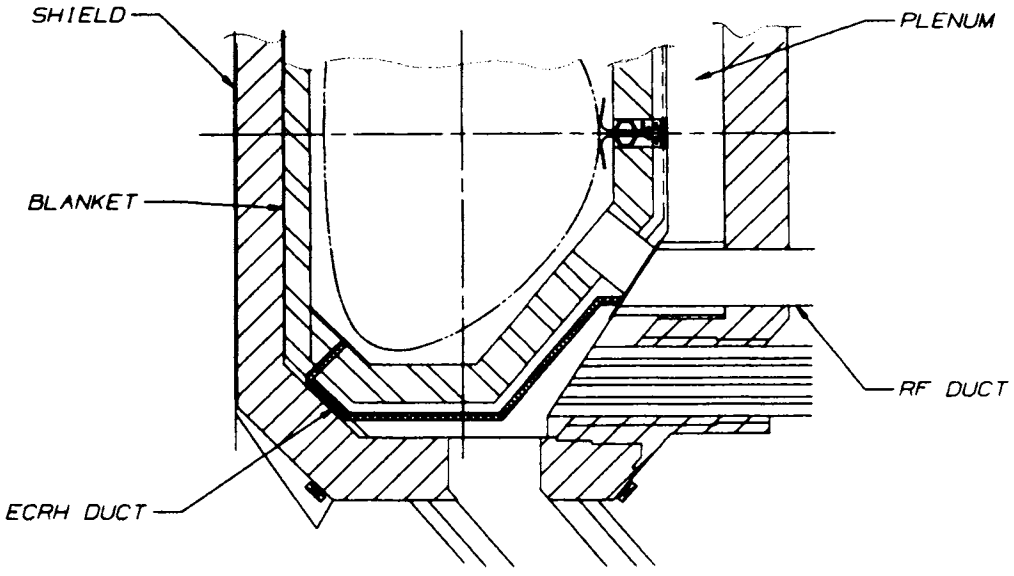

Figure 6-32. Plasma cross section showing location of the ECRH ducts.

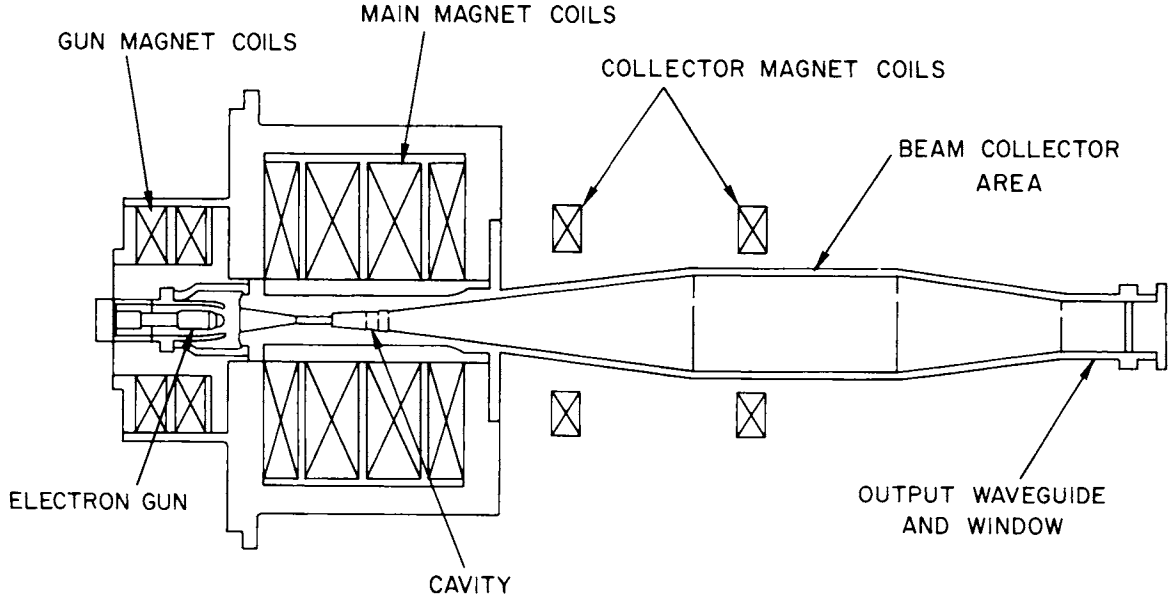

Figure 6-33. Layout drawing of a CW gyrotron with tapered output guide.

indicated earlier, Varian has already produced pulsed ($\sim$ 10 ms) gyrotrons capable of delivering $\sim$ 250 kW of peak power at an efficiency of $\sim$ 35%; therefore, this value has been used in the present case to establish the input power requirement of 600 kW per gyrotron. The waste heat disposal system must thus be sized to handle 9.36 MW for five seconds. Each gyrotron is 1.5 m long and 0.6 m in diameter. Therefore, they can be conveniently located in the basement of the reactor building along with the lower hybrid cross field amplifiers.

The power supply system for the gyrotrons must deliver 14.4 MW of high voltage power (24 x 600 kW). In the present design, this is provided by two 7.2 MW power supplies, each driving 12 gyrotrons. Aydin has shown[48] that this multiple gyrotron approach offers a number of advantages provided that switch tubes are used as series modulator/regulators to allow individual control of the gyrotron operating voltages. A layout of the power supply substation is shown in Fig. 6-34. It measures 17 m wide by 27 m long and requires no building.

In summary, plasma breakdown and preheating utilizing microwaves at the ECR frequency has been shown to be an effective means of initializing the STARFIRE burn cycle. It capitalizes on the coil simplifications provided by the lower hybrid current drive system, and, because the remaining OH coils need only drive enough current to stabilize and not to heat the plasma, the ECRH input allows the size of the OH power supplies to be reduced. The system consists of 24 gyrotrons that deliver 5 MW of power to the plasma for five seconds. This provides complete breakdown of the fill gas in $\sim$ 10 ms, with a more gradual heating to a few hundred eV once a plasma current has been established by the changing OH coil flux. At this point, microwave absorption at the lower hybrid resonance is possible, and the lower hybrid system is then used to bring the plasma up to ignition temperatures.

Economic trade-offs between the more conventional avalanche breakdown system and the present design have not been attempted. It seems likely, however, that the reduced complexity of the coil set necessary for the ECRH approach more than offsets the costs of the ECRH power supply and distribution systems. A future study should involve an evaluation of the economic benefits of the ECRH breakdown scenario.

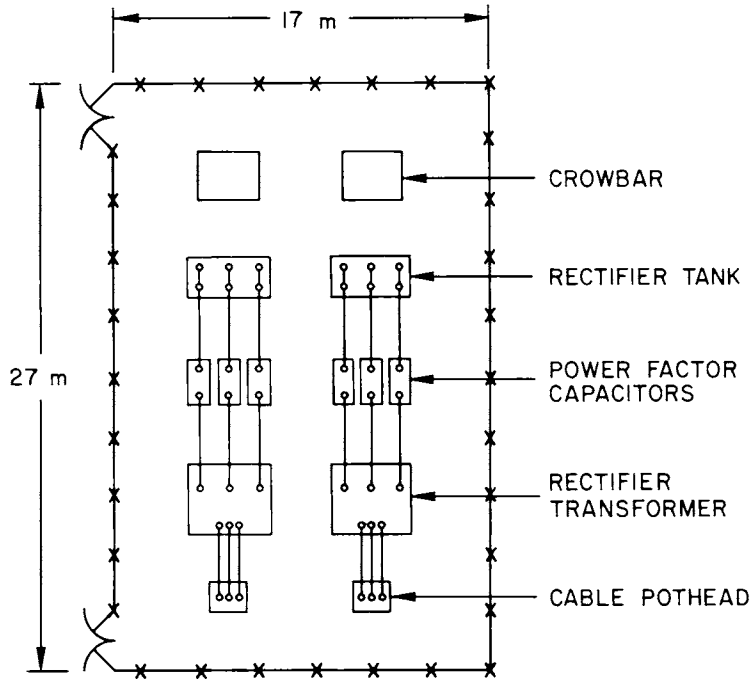

Figure 6-34. Gyrotron power supply layout.

Additional future work in this area could focus on some of the simplifying assumptions, regarding the propagation and absorption of microwave energy, that have been made in the present study. This would involve the coupling of a ray-tracing calculation with the present time evolution, and the introduction of spatial resolution into the code. Such a model would be quite useful, but it would be very time consuming to develop. Another area for future work might, therefore, be to consider the initial breakdown of gas near the waveguides. Questions about arcing in the guides and runaway electron populations could then be addressed.

References

1. A. M. M. Todd, et al., Nucl. Fusion 19, 743 (1979).

2. D. A. Ehst, Nucl. Fusion 19, 1369 (1979).

3. Y-K. Peng, et al., Phys. Fluids 21 (1978) 467.

4. R. L. Miller, et al., Phys. Rev. Letters 43, 765 (1979).

5. E. Rebhan, et al., Nucl. Fusion 18, 1639 (1978).

6. D. A. D'Ippolito, et al., Proc. Finite Beta Theory Workshop 75, (Varenna, 1977).

7. K. Evans, Jr., "High β_t Equilibria in Tokamaks," Argonne National Laboratory, ANL/FPP/TM-98 (1977).

8. R. B. White, et al., Proc. 6th International Conf. on Plasma Physics and Controlled Nuclear Fusion Research, Berchtesgaden (IAEA, 1976). Vol. 1, 569.

9. A. Sykes, et al., Phys. Rev. Letters 39, 757 (1977).

10. D. Dobrott, et al., Phys. Rev. Letters 39, 943 (1977).

11. R. W. Moore, "BLOON Users' Manual," General Atomic Company, GA-A15353 (1979).

12. D. A. D'Ippolito, et al., Proc. 6th International Conf. on Plasma Physics and Controlled Nuclear Fusion Research, Berchtesgaden (IAEA, 1976), Vol. 1, 523.

13. D. A. D'Ippolito, et al., Phys. Fluids 21, 1600 (1978).

14. H. C. Lui, Phys. Fluids 23, 153 (1980).

15. G. Bateman, Proc. Finite Beta Theory Workshop 49, (Varenna, 1977).

16. G. Bateman and Y-K. Peng, Phys. Rev. Letters 38, 829 (1977).

17. D. Dobrott, et al., Proc. 7th International Conf. on Plasma Physics and Controlled Nuclear Fusion Research, Innsbruck (IAEA, 1978), paper CN-37-P-4, Vol. i, 717.

18. L. A. Charlton, et al., Phys. Rev. Letters 43, 1395 (1979).

19. R. A. Dory, et al., Proc. 7th International Conf. on Plasma Physics and Controlled Nuclear Fusion Research, Innsbruck (IAEA, 1978) Vol. i, 579.

20. C. H. An, et al., "High Ballooning Modes in Highly Elongated Tokamaks," Oak Ridge National Laboratory, ORNL/TM-7074 (1980).

21. H. R. Strauss, et al., Nucl. Fusion 20, 638 (1980).

22. L. C. Bernard, et al., "Stabilization of Ideal MHD Modes," General Atomic Company, GA-A15236 (1979).

23. R. Gruber, et al., Proc. 7th International Conference on Plasma Physics and Controlled Nuclear Fusion Research, Innsbruck, (IAEA, 1978), Vol. i, 593.

24. Y. N. Yavlinski, Nuc. Fusion 13, 951 (1973).

25. C. Mercier, Nucl. Fusion 1, 47 (1960).

26. D. Berger, et al., Proc. Plasma Physics and Controlled Nuclear Fusion Research (IAEA, Vienna, 1976) Vol. 2, 411.

27. L. A. Charlton, et al., "Applicability of High-n Ballooning Theory", Oak Ridge National Laboratory, ORNL/TM-7198 (1980).

28. M. S. Chu and R. W. Miller, Phys. Fluids, 21, 817 (1978).

29. F. W. McClain and B. B. Brown, General Atomic Company, GA-A14490 (1977).

30. V. S. Mukhovatov and V. D. Shafranov, Nucl. Fusion, 11, 605 (1971).

31. J. N. Brooks and R. Kustom, Nucl. Tech., 46, 61 (1979).

32. W. M. Stacey, et al., Argonne National Laboratory, ANL/CTR/76-3 (1976).

33. WHIST lacks an up-to-date documentation. Some examples of its use appear in R. W. Conn and J. Kesner, J. Nucl. Mater., 63, 1 (1976); W. A. Houlberg and R. W. Conn, Nucl. Fusion, 19, 81 (1979); A. T. Mense and G. A. Emmert, Nucl. Fusion, 19, 361 (1979); W. A. Houlberg, S. E. Attenberger, and A. T. Mense, Nucl. Fusion, 20, 811 (1980); W. A. Houlberg, H. C. Howe, and S. E. Attenberger, Oak Ridge National Laboratory, TM-7124 (1980); a review of tokamak transport codes is given by J. T. Hogan, in Methods in Computational Physics, Vol. 16 (edited by J. Killeen), (1976).

34. W. A. Houlberg and R. W. Conn, Nucl. Sci. Eng., 64, 141 (1977).

35. T. E. Stringer, Nucl. Fusion, 12, 689 (1972); J. W. Conner and R. J. Hastie, Nucl. Fusion, 13, 221 (1973).

36. N. A. Uckan, K. T. Tsang, and J. D. Callen, Oak Ridge National Laboratory, TM-5438 (1976).

37. F. L. Hinton and T. B. Moore, Nucl. Fusion, 14, 639 (1974).

38. T. W. Petrie and J. M. Rawls, Nucl. Fusion, 20, 419 (1980).

39. L. Bromberg and D. R. Cohn, Massachusetts Institute of Technology, DFC/RR-79-19-R (1980).

40. J. Norem, Argonne National Laboratory, ANL/FPP-TM/76 (1977).

41. R. A. Dandl, et al., Nucl. Fusion, 11, 411 (1971).

42. R. A. Dandl, Bul. APS Sec. 2 19, (9), 906 (1974).

43. V. E. Golant, et al., Proc. Third International Symp. on Toroidal Plasma Confinement, E5 (1973).

44. V. V. Alikaev, et al., Proc. Fifth Conf. Plasma Physics and Controlled Nuclear Fusion Research, TR-33 (1975).

45. R. M. Gilgenbach, et al., Phys. Rev. Letters, 44, 647 (1980).

46. H. R. Jory, et al., "Final Report, Millimeter Wave Study Program," Varian Associates, ORNL/SUB-75-49438-2 (1975).

47. S. Hegji, et al., "Development Program for a 200 KW, CW, 28 GHz Gyroklystron," Varian Associates, ORNL/SUB-76-01617-5 (1977).

48. "Elmo Bumpy Torus Proof-of-Principle Project Definition Study," Appendix E, McDonnell Douglas Astronautics Corporation Staff Report, MDC-E2160 (1979).

TABLE OF CONTENTS

LIST OF FIGURES

LIST OF FIGURES (Contd.)

LIST OF TABLES

7.1 LOWER-HYBRID CURRENT DRIVE THEORY

The confidence that a tokamak may be operated with a steady-state toroidal current is based on a large body of theoretical and experimental work[1-9] on wave-driven currents. While the theory is well developed, the experimental evidence to date is somewhat circumstantial,[8] the best results appearing on JFT-2[9] in which half the plasma current (15 kA) was generated for 20 ms with 125 kW of power. A definitive demonstration of toroidal, collisionless, lower-hybrid-driven currents awaits further results from tokamak research on devices such as JFT-2, Versator, and PLT. (The idea of a steady-state mode of operation is further bolstered by a variety of proposed particle injection schemes which have also been published.[10])

Quasilinear theory[1,2,4] predicts the local current density generated by toroidally travelling lower-hybrid waves is:

$$j_{\parallel}(r) = e\, n_e(r) \int_{-\infty}^{\infty} dv\, v\, f(v) , \tag{1}$$

where

$$f(v) = N \exp\left(- \int \frac{w\, dw}{1 + w^3 D}\right), \tag{2}$$

and the local wave power dissipation is

$$p_{LH}(r) = 1.7 \times 10^{-31}\, K\, n_e^2 T_e^{-1/2}\, \ell n\, \Lambda\, f(w_1)\, \ell n \left[\frac{1 + w_2^3 D}{1 + w_1^3 D}\right]^{1/3} . \tag{3}$$

We have defined the following quantities:

m_e = electron mass

e = electron charge

$n_e(r)$ = local electron density

$T_e(r)$ = local electron temperature

ω = wave angular frequency

$k_{\parallel} = 2\pi\lambda_{\parallel}^{-1}$ = wave number parallel to $\underline{B}$

$n_{\parallel} = ck_{\parallel}/\omega$ = parallel index of refraction

$E_{\parallel}$ = wave electric field parallel to $\underline{B}$

$D = D(E_{\parallel})$ = ratio of quasilinear to collisional diffusion coefficients

$w = v/\sqrt{T_e/m_e}$

$w_1 = \omega/\left(k_{\parallel 1}\sqrt{T_e/m_e}\right)$

$\ell n\ \Lambda$ = Coulomb logarithm.

All units are MKS except for temperature which is in units of keV.

The earliest theory[1] assumed a flat wave spectrum of uniform energy density within the range of phase speeds $\omega/k_{\parallel 1}$ to $\omega/k_{\parallel 2}$ and considered the electron distribution, f, a function only of parallel velocity. Subsequent calculations with a fully two-dimensional velocity distribution[2] show Eqs. (1)-(3) are still applicable provided K = 0.392. In the range of interest $w_1^3 D >> 1$, and Eqs. (1)-(3) may be combined into a useful expression:

$$p_{LH}(r) = j_{\parallel}(r) \times 2.2 \times 10^{-21}\, n_e(r)\, \frac{\ell n\left(n_{\parallel 1}/n_{\parallel 2}\right)}{n_{\parallel 2}^{-2} - n_{\parallel 1}^{-2}}\ , \qquad (4)$$

where we set $\ell n\ \Lambda = 18$. In the design of STARFIRE we compute the total required lower-hybrid power from Eq. (4) as:

$$P_{LH} = \int_{r_c}^{a} p_{LH}(r) 4\pi^2 R\, r\, dr\ , \qquad (5)$$

where R is the major radius, r_c is the furthest depth of wave penetration, and a is the plasma minor radius; the lower-hybrid calculation assumes a cylindrical plasma. In order to minimize P_{LH}, a number of strategies are suggested by Eq. (4):

(1) $j_{\parallel}(r)$ is generally reduced by selection of the lowest current plasma equilibria;

(2) $p_{LH}(r)$ is reduced by generating current density where $n_e(r)$ is low, near the plasma edge;

(3) for a fixed β_t (and, hence, approximately fixed fusion power) P_{LH} is reduced by operation at high temperatures and low average electron density, $\bar{n}_e$;

(4) for a fixed $\bar{n}_e$, and surface current equilibria, the edge density of n_e (and thus P_{LH}) is reduced by the choice of narrow density profiles;

(5) $\bar{n}_e$ and P_{LH} are lowered by the minimization of high-Z impurities in the plasma; and

(6) $p_{LH}(r)$ is reduced by operation with the lowest $n_{\parallel_2}$ and narrowest spectra (smallest $n_{\parallel_1} - n_{\parallel_2}$).

Criteria (1) and (2) were used in Chap. 6 in the selection of the 10.1 MA, surface current equilibrium. The fourth criterion was satisfied by selecting a narrow $n_e(r)$ and broad $T_e(r)$:

$$\begin{cases} n_e(r) = \bar{n}_e\left(1 + \alpha_n\right)\left[1 - (r/a)^2\right]^{\alpha_n} + n_{edge} & (6) \\ T_e(r) = \bar{T}_e\left(1 + \alpha_T\right)\left[1 - (r/a)^2\right]^{\alpha_T} + T_{edge}\,, & (7) \end{cases}$$

where $\alpha_n = 1.1$ and $\alpha_T = 0.3$. Corresponding to these model profiles for the wave current drive calculation, the two-dimensional flux surface profiles used in the power balance calculation were

$$\begin{cases} n_e(\hat{\psi}) = n_{e_0}\hat{\psi}^{\alpha_n} \\ T_e(\psi) = T_{e_0}\hat{\psi}^{\alpha_T}\,, \end{cases}$$

where $\hat{\psi} = \left[\psi_{limiter} - \psi\right]\left[\psi_{limiter} - \psi_{magnetic\ axis}\right]^{-1}$ and $\psi(\rho,z)$ is the equilibrium poloidal flux solution found in Chap. 6 with a pressure profile $p(\psi) = p_0\hat{\psi}^{\alpha_n+\alpha_T} = p_0\hat{\psi}^{\alpha}$, α being 1.4. A broad T_e profile is consistent with central alpha particle heating and surface heating from the waves, as demonstrated by the transport calculations of Chap. 6. A narrow n_e profile assumes fuel deposition near the magnetic axis.

In order to assess the effects of impurities and to determine the optimum plasma temperature, the lower-hybrid power was explicitly determined for a number of cases. This calculation of wave damping and current generation is subject to several constraints on the acceptable solutions. First,

$$\int_{r_c}^{a} j_t(r) 2\pi r \, dr = I = 10.1 \text{ MA} , \tag{8}$$

where j_t is the toroidal current density. Since the average location of the inboard and outboard j_t maxima in Fig. 6-6 represents a 14% penetration towards the magnetic axis, we set $1 - (r_c/a) = 0.14$ for the cylindrical calculation. Next,

$$\omega = 1.8 \, \omega_{LH}(r = r_c) , \tag{9}$$

since we require ω to exceed

$$\omega_{LH} = \sqrt{\frac{\omega_{pi}^2}{1 + \omega_{pe}^2 \Omega_e^{-2}}} , \tag{10}$$

where ω_{pj} is the plasma frequency of the j-th species and Ω_e is the electron cyclotron frequency, in order to avoid parametric instabilities.[11] P_{LH} is minimized by setting $n_{\parallel_2}$ as small as possible without violating the accessibility criterion[12] (which would result in reflecting the wave power); that is, $n_{\parallel_2}$ is the solution to

$$\frac{n_e(r_c)}{n_0} = y^2 \left[2y^2 n_{\parallel_2}^2 - \left(n_{\parallel_2}^2 - 1 \right) - \left\{ \left[2y^2 n_{\parallel_2}^2 - \left(n_{\parallel_2}^2 - 1 \right) \right]^2 - \left(n_{\parallel_2}^2 - 1 \right)^2 \right\}^{1/2} \right] , \tag{11}$$

where $y = (\omega/\Omega_e)\sqrt{M/m_e}$, $n_0 = 9.72 \times 10^{18}\ B_c^2$, B_c is the toroidal field at r_c, and M is an effective ion mass.[12] The consequence of the accessibility criterion, Eq. (11), is that penetration to higher n_e plasma requires larger $n_{\parallel_2}$ values, which results in larger P_{LH} according to Eq. (4).

Figure 7-1 displays the consequences of temperature variation on a reactor with R = 7.0 m, B = 11.1 T, $\beta_t = 0.067$, A = 3.6, $\kappa = 1.6$, d = 0.5, $\alpha = 1.4$, $\alpha_n = 1.1$, and $\Delta = 1.4$ m. The field on axis, B_0, is related to B at the toroidal magnets by the inboard blanket/shield/scrape-off distance, Δ, as $B_0 = B[1 - A^{-1} - \Delta R^{-1}] = 5.8$ T. The equilibrium used in Fig. 7-1, that labeled F in Fig. 6-1, has I = 11.1 MA. A fixed beryllium fraction, $\bar{n}_{Be}/\bar{n}_{DT} = 0.04$, and a high alpha particle reflection coefficient, $\mathcal{R}_\alpha = 0.7$, are assumed. In these calculations $\bar{T}_i \sim \bar{T}_e$, and higher $\bar{T}_e$ results in larger alpha particle fractions $\left(\bar{n}_\alpha/\bar{n}_{DT} \sim \bar{n}_{DT}\tau\langle\sigma v\rangle\right)$; $\bar{n}_\alpha/\bar{n}_{DT}$ is 0.04 at $\bar{T}_e$ = 8 keV and is 0.17 at 31 keV. Nevertheless, $\bar{n}_e$ is roughly inversely proportional to $\bar{T}_e$, being 3.2×10^{20} m^{-3} at 8 keV and 0.69×10^{20} m^{-3} at 31 keV. Accordingly, due to the accessibility constraint, $n_{\parallel_2}$ is large at low $\bar{T}_e$ (1.51 at 10 keV) and low at high $\bar{T}_e$ (1.18 at 31 keV). This combination of high $n_\parallel$ and large $\bar{n}_e$ at low temperatures results in the large values of P_{LH} in the low temperature range of the figure. On the other hand, the fusion power, P_f, peaks around $\bar{T}_e \sim \bar{T}_i = 10$ keV and drops inversely with temperature. Maximum power multiplication, measured by $Q \equiv P_f/P_{LH}$, occurs for $\bar{T}_e \gtrsim 20$ keV.[4,5] Operation at maximum Q does not necessarily result in the lowest cost of power, however. Using the algorithm, $P_n = 0.34\left(P_f \times 1.2\right) - P_{LH}/0.9$, the approximate net electric production is also shown in Fig. 7-1, assuming 1.2 for blanket energy multiplication, 0.34 for thermal to electric efficiency, and 0.9 for electric to rf power efficiency. Since $Q >> 1$, we see P_n peaks close to the maximum of P_f, i.e. near 10-12 keV. Using the ANL systems code,[13] the capital cost of electricity, C, was computed. The penalty for operating near $\bar{T}_e \sim 10$ keV is the great additional capital cost of rf power supplies beyond what is needed for rf heating to ignition. The conclusion drawn from this figure is that C is minimum around $\bar{T}_e \sim 14$ keV, between the maxima of P_f and Q.

The STARFIRE design imposed an additional constraint, namely, the neutron wall load, W, should not exceed 3.5-3.7 MW-m^2 (see Chap. 5). As seen in Fig. 7-1, this restriction is violated below $\bar{T}_e \sim 18$ keV, so an additional reactor survey was performed, and the results are shown in Figs. 7-2 and 7-3.

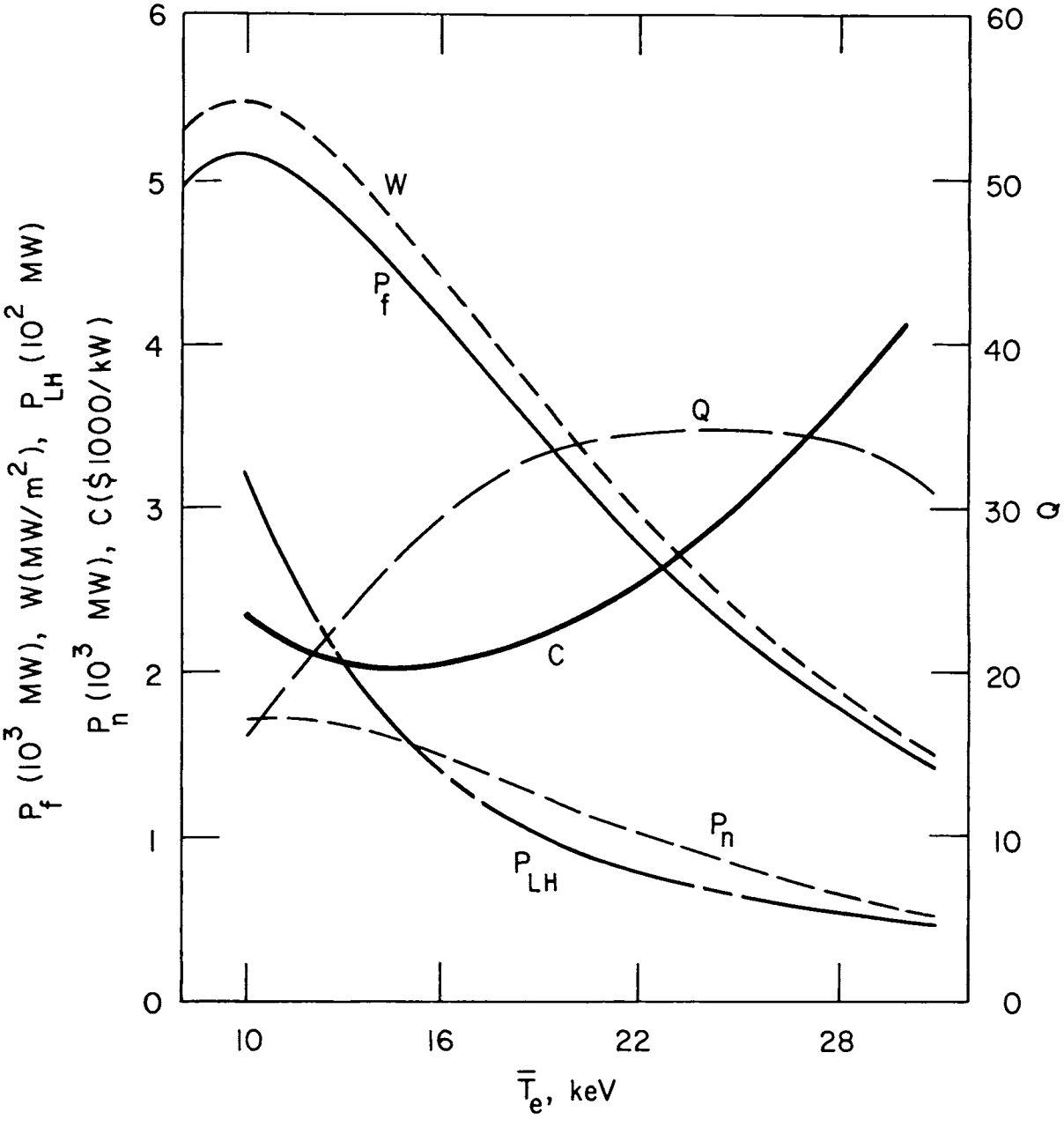

Figure 7-1. Fusion power (P_f), lower-hybrid current drive power (P_{LH}), net electric power (P_n), Q ($\equiv P_f/P_{LH}$), neutron wall load (W), and capital cost of electricity (C) at various operating temperatures; R = 7.0 m, B_0 = 5.8 T, β_t = 0.067, A = 3.6, κ = 1.6, d = 0.5, α = 1.4, α_n = 1.1, Δ = 1.4 m, and equal ion and electron containment times ($\bar{T}_i \sim \bar{T}_e$).

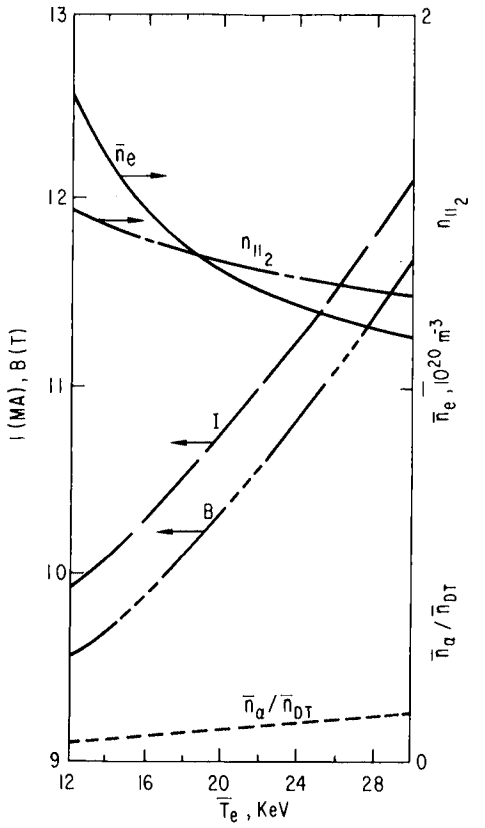

Figure 7-2. Magnet strength (B), toroidal current (I), alpha fraction ($\bar{n}_\alpha/n_{DT}$) and electron density ($\bar{n}_e$) at constant power and wall load but different $\bar{T}_e$; P_f = 3200 MW, W = 3.5 MW/m^2, R = 7.06 m, $\bar{\beta}_t$ = 0.067, A = 3.6, κ = 1.6, d = 0.5, α = 1.4, α_n = 1.1, Δ = 1.3 m, $\mathcal{R}_\alpha$ = 0.7, and $\bar{T}_i \sim \bar{T}_e$. The lower limit of accessibility, $n_{\parallel 2}$, increases with $\bar{n}_e$; 20% current penetration is assumed, with $\omega = 2\omega_{LH}(r_c)$.

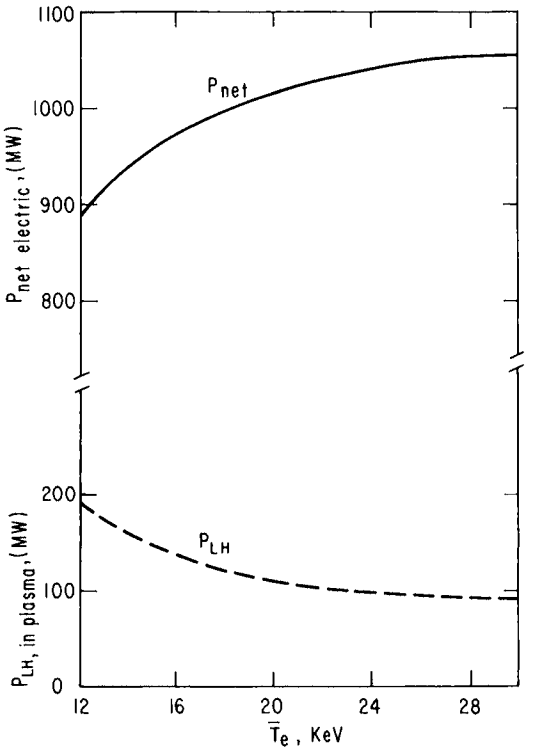

Figure 7-3. Lower-hybrid current drive power (P_{LH}) for the reactor of Fig. 7-2; net electric power (P_n) assumes 1200 MW of gross electric power minus $P_{LH}/0.6$. Results for P_{LH} appear independent of wall load, magnet strength, and major radius in the range W = 3.5-4.0 MW/m^2, B = 10.3-11.5 T, R = 6.6-7.1 m.

Equilibrium F was again used as $\bar{T}_e$ was varied, but this time P_f and W were kept constant at 3200 MW and 3.5 MW m^{-2}, respectively. Since the geometry (R = 7.1 m) and β_t (= 0.067) were held constant and since $\langle\sigma v(T_i)\rangle\bar{T}_i^{-2}$ is a decreasing function of $\bar{T}_i \sim \bar{T}_e$, the B value must increase at $T_e \gtrsim 10$ keV in order to keep P_f constant. (That is, $P_f \sim R^3\kappa A^{-2}\beta_t^2 B^4\langle\sigma v\rangle\bar{T}_i^{-2}$.) Since $I \propto B$, the total current increases at higher $\bar{T}_e$. However, this increase in I is offset by the decrease in $\bar{n}_e$ and $n_{\parallel_2}$ at high $\bar{T}_e$ (Fig. 7-2), with the result that P_{LH} drops significantly in going from 10 keV to 20 keV. Assuming the P_f = 3200 MW results in a gross electric output of 1200 MW, and assuming 60% electric to rf conversion, the net electric output is calculated and displayed in Fig. 7.3. Comparing the figures we find modest increases in P_n and decreases in rf power supply requirements above $\bar{T}_e$ = 20 keV, but this high temperature operation requires increasingly strong toroidal fields ($B \gtrsim 11$ T). Based on these considerations the STARFIRE reference design, with W = 3.72 MW-m^{-2}, P_f = 3510 MW, and B = 11.1 T, was selected with $\bar{T}_e$ = 17.3 keV, $\bar{T}_i$ = 24.1 keV, and $\bar{n}_e = 1.18 \times 10^{20}$ m^{-3} (see Chap. 4). The hot ion mode of operation is a consequence of empirical energy confinement for electrons and neoclassical containment of ions (see Sec. 6.3).

Having described the rationale for selecting $\bar{n}_e$, $\bar{T}_e$, α_n, and α_T for Eqs. (6) and (7), we proceed to a detailed description of the lower-hybrid waves for the STARFIRE reference plasma. For $n_{edge} = 5 \times 10^{17}$ m^{-3} and $1 - r_c/a = 0.14$, the electron density at the greatest depth of penetration is $n_e(r_c/a) = 5.69 \times 10^{19}$ m^{-3}. The effective ion mass for the DT, alpha, and beryllium content (Table 6-1) is M = 2.325 amu, and the lower-hybrid frequency at $r = r_c$ is $\omega_{LH}(r_c) = 5.883 \times 10^9$ s^{-1}, so, from Eq. (10), $\omega = 1.054 \times 10^{10}$ s^{-1} and $\nu = \omega/2\pi = 1.677$ GHz. We set B_c = 5.1 T when computing n_0, assuming waves launched from the outboard side of the plasma (see Fig. 7-16); then we solve Eq. (11) for $n_e(r_c)/n_0 = 0.225$ and y = 0.7676. The result is $n_{\parallel_2} = 1.40$; any waves with slower phase speeds will penetrate beyond $r = r_c$. In fact, according to linear theory,[12] waves with $n_\parallel > [1 - y^2]^{-\frac{1}{2}} = 1.565$ could penetrate beyond $r = r_c$ as far as the lower-hybrid resonance $(k_r \to \infty)$ which occurs at $n_e = n_0 y^2[1 - y^2]^{-1} = 3.63 \times 10^{20}$ m^{-3}. We note that this resonance does not occur within the STARFIRE plasma, and we need not concern ourselves with nonlinear effects and mode conversion associated with the resonance.

For spatial regions where the density is above cutoff $(\omega_{pe} > \omega)$ the slow wave branch of the dispersion relation is a propagating wave, called the lower-

hybrid wave, and in this region a WKB, or ray tracing, calculation is performed. We will find that the full electromagnetic dispersion relation is appropriate to STARFIRE since the waves do not approach close to the lower-hybrid resonance. Following Stix,[14] we write the WKB form of the dispersion relation:

$$0 = An^4 - Bn^2 + C \,, \tag{12}$$

where

$$\begin{cases} A = \varepsilon_1 \sin^2\theta + \varepsilon_3 \cos^2\theta \\ B = (\varepsilon_1^2 - \varepsilon_2^2)\sin^2\theta + \varepsilon_3\varepsilon_1(1 + \cos^2\theta) \\ C = \varepsilon_1^2(\varepsilon_1^2 - \varepsilon_2^2) \,, \end{cases}$$

and $n = c|\underline{k}|/\omega$, $n_\parallel \equiv n\cos\theta$, $n_\perp \equiv n\sin\theta$, $\underline{k}$ is the wave vector, and $\underline{k}\cdot\underline{B} \equiv |\underline{k}||\underline{B}|\cos\theta$. The explicit expressions for ε_1, ε_2, and ε_3, generalized to multicomponent plasmas,[12] are

$$\varepsilon_1 = 1 + \frac{\omega_{pe}^2}{\Omega_e^2 - \omega^2} - \frac{\omega_{pi}^2}{\omega^2}$$

$$\varepsilon_2 = \frac{\omega_{pe}^2\Omega_e}{\omega(\Omega_e^2 - \omega^2)}$$

$$\varepsilon_3 = 1 - \frac{\omega_{pe}^2}{\omega^2} - \frac{\omega_{pi}^2}{\omega^2} \,,$$

where we have adopted the appproximation $\Omega_i^2 << \omega^2 << \Omega_e^2$ and defined ω_{pi} in terms of M. Equation (12) may be rewritten as

$$0 = \varepsilon_1 n_\perp^4 + \left[(\varepsilon_1 + \varepsilon_\varepsilon)(n_\parallel^2 - \varepsilon_1) + \varepsilon_2^2\right]n_\perp^2 + \varepsilon_3\left[(n_1^2 - \varepsilon_1)^2 - \varepsilon_2^2\right] \,,$$

which has the solution

$$n_\perp^2 = \left\{ -\left[(\varepsilon_3 + \varepsilon_1)(n_\parallel^2 - \varepsilon_1) + \varepsilon_2^2 \right] \pm \sqrt{\left[(\varepsilon_3 + \varepsilon_1)(n_\parallel^2 - \varepsilon_1) + \varepsilon_2^2 \right]^2 - 4\varepsilon_1\varepsilon_3 \left[(n_\parallel^2 - \varepsilon_1)^2 - \varepsilon_2^2 \right]} \right\} \Big/ 2\varepsilon_1 \, . \tag{13}$$

The lower-hybrid wave is the larger value of $n_\perp^2$, corresponding to the upper sign. The method of solution we choose is to follow the wave propagation numerically, evaluating Eq. (13) at each spatial point. All waves have $\omega = 1.054 \times 10^{10}\ s^{-1}$, and this relation determines $n_\perp(r)$ for a mode of given $n_\parallel$ value. We will be interested in fairly narrow spectra, $n_{\parallel_1} - n_{\parallel_2} \ll n_{\parallel_2}$, and we will find the wave dispersion is similar for all modes within the spectrum. The polarization of the waves is found from the wave equation[14]

$$0 = \begin{pmatrix} \varepsilon_1 - n_\parallel^2 & -i\varepsilon_2 & n_\perp n_\parallel \\ i\varepsilon_2 & \varepsilon_1 - n^2 & 0 \\ n_\perp n_\parallel & 0 & \varepsilon_3 - n_\perp^2 \end{pmatrix} \begin{pmatrix} E_r \\ E_y \\ E_\parallel \end{pmatrix} .$$

We assume $E_y = 0$, $k_\perp = k_r$, and find

$$\frac{E_r}{E_\parallel} = \frac{n_\perp / n_\parallel}{1 - (\varepsilon_1 / n_\parallel^2)} \, . \tag{14}$$

To illustrate the wave properties, consider the mode with $n_\parallel = 1.4$. At the point of deepest penetration ($r = r_c$), we find from Eqs. (13) and (14) that $n_\perp = 32.36$ and $E_r/E_\parallel = 40.57$. Thus $n_\perp \gg n_\parallel$ and $E_r \gg E_\parallel$, but since $n_\perp/n_\parallel \neq E_r/E_\parallel$, the wave is not electrostatic.

The wave energy density can also be found. The "electric" energy density including both electric field energy and particle kinetic energy, is obtained from the dielectric function,[14]

$$\underline{\underline{K}} = \begin{pmatrix} \varepsilon_1 & -i\varepsilon_2 & 0 \\ i\varepsilon_2 & \varepsilon_1 & 0 \\ 0 & 0 & \varepsilon_3 \end{pmatrix}.$$

The electric energy density is

$$\mathscr{E}_{\underline{\underline{K}}:\underline{E}} \equiv \frac{\varepsilon_0}{2}\,\underline{E} : \frac{\partial}{\partial\omega}(\omega\underline{\underline{K}}) : \underline{E} = \frac{\varepsilon_0}{2}\left[E_r^2\frac{\partial}{\partial\omega}\left(\omega\varepsilon_1\right) + E_\parallel^2\frac{\partial}{\partial\omega}\left(\omega\varepsilon_3\right)\right].$$

In the limit $\omega^2 << \Omega_e^2$, we have

$$\mathscr{E}_{\underline{\underline{K}}:\underline{E}} = \frac{\varepsilon_0}{2}E_\parallel^2\left[\left(\frac{E_r^2}{E_\parallel^2}+1\right) + \frac{E_r^2}{E_\parallel^2}\left(\frac{\omega_{pe}^2}{\Omega_e^2}+\frac{\omega_{pi}^2}{\omega^2}\right) + \frac{\omega_{pe}^2}{\omega^2}\right]. \tag{15}$$

The portion of $\mathscr{E}_{\underline{\underline{K}}:\underline{E}}$ associated only with electric field energy is

$$\mathscr{E}_{\underline{E}} \equiv \frac{\varepsilon_0}{2}E^2 = \frac{\varepsilon_0}{2}E_\parallel^2\left(\frac{E_r^2}{E_\parallel^2}+1\right).$$

Typically, approximately half of $\mathscr{E}_{\underline{\underline{K}}:\underline{E}}$ is particle kinetic energy and half is electric field energy. The wave magnetic energy density, $\mathscr{E}_{\underline{B}}$, is found from Faraday's law, $-(\partial\underline{B}/\partial t) = \nabla\times\underline{E}$, or $i\omega\underline{B} = \left(-ik_rE_\parallel + ik_\parallel E_r\right)\hat{y}$. Thus

$$\mathscr{E}_{\underline{B}} = \frac{B^2}{2\mu_0} = \frac{\varepsilon_0}{2}n_\parallel^2E_\parallel^2\left(\frac{E_r}{E_\parallel}-\frac{k_r}{k_\parallel}\right). \tag{16}$$

Obviously, the wave is strictly electrostatic only when $E_r/E_\parallel = k_r/k_\parallel$.

Table 7-1 illustrates the contributions to the total wave energy density $\left(\mathscr{E} = \mathscr{E}_{\underline{B}} + \mathscr{E}_{\underline{\underline{K}}:\underline{E}}\right)$ at three spatial points. All values are normalized to $(\varepsilon_0/2)E_\parallel^2$. The magnetic energy, $\mathscr{E}_{\underline{B}}$, is 25% of $\mathscr{E}$ at the first spatial point and decreases to 16% at $1 - r/a = 0.11$ (12% at $1 - r/a = 0.14$). This value of

$\mathcal{E}_B/\mathcal{E}$ is large enough to warrant the inclusion of electromagnetic terms in the STARFIRE calculation; however, it was found *a posteriori* that the electrostatic approximation did in fact yield fairly accurate results. Note that the kinetic energy density, $\mathcal{E}'_{\underline{\underline{K}}:\underline{E}} - \mathcal{E}'_{\underline{E}}$, exceeds $\mathcal{E}'_{\underline{E}}$ at higher densities but becomes smaller at the plasma edge. Naturally, in a vacuum $\mathcal{E}_{\underline{\underline{K}}:\underline{E}} \equiv \mathcal{E}_{\underline{E}}$. Also note the normalized $\mathcal{E}'$ in the table increases at higher densities. When wave energy dissipation is small, this implies $E_\parallel$ will decrease at higher densities. This decrease of $E_\parallel$ in the absence of dissipation is due to the increasing contribution to $\mathcal{E}$ from particle kinetic energy and also to the increasing polarization of $\underline{E}$ perpendicular to the toroidal $\underline{B}$ field lines.

Table 7-1. Relative Contributions of Kinetic, Electric Field, and Magnetic Field Energy Density to the Total Wave Energy Density

1 - r/a	$\mathcal{E}'_{\underline{\underline{K}}:\underline{E}} - \mathcal{E}'_{\underline{E}}$	$\mathcal{E}'_{\underline{E}}$	$\mathcal{E}'_{\underline{B}}$	$\mathcal{E}'$	$\mathcal{E}'_{\underline{B}}/\mathcal{E}'$
0	14.5	28.1	13.9	56.5	0.25
0.05	795	1006	465	2266	0.21
0.11	1922	1682	700	4304	0.16

Note: Primes indicate normalization to $(\varepsilon_0/2)E_\parallel^2$; e.g. $\mathcal{E}' = \mathcal{E}/\left(\varepsilon_0 E_\parallel^2/2\right)$.

The radial component of the wave group velocity[14] is

$$v_{gr} = \partial\omega/\partial k_r \,, \tag{17}$$

where $\omega\left(k_r\right)$ is found from Eq. (13) with $n_\perp = ck_r/\omega$. At $r = r_c$ we find, for example, $\left|v_{gr}\right| = 7 \times 10^5$ m/s. In general, $\partial\omega/\partial k_r$ has the opposite sign of ω/k_r; the lower-hybrid wave is a "backward" wave. The wave intensity, $\bar{\mathcal{I}}$, is

$$\bar{\mathcal{I}} = v_{gr}\mathcal{E}$$

$$= v_{gr}\left[\mathcal{E}_{\underline{\underline{K}}:\underline{E}}\left(E_\parallel\right) + \mathcal{E}_{\underline{B}}\left(E_\parallel\right)\right] \,, \tag{18}$$

and, assuming uniform radiation over the tokamak surface area (i.e. neglecting the spatial localization of wave energy within the resonance cones[15-18]), the equation for wave damping is

$$p_{coll}(r) + p_{LH}(r) = \frac{1}{r}\frac{d}{dr} r \left| v_{gr}(r) \right| \mathscr{E}\left(E_{\parallel}\right) . \tag{19}$$

The nonresonant collisional dissipation is given in Ref. 6, and p_{LH} is given in Eq. (3). The collisional power dissipation is three orders of magnitude less than the resonant, quasilinear power dissipated in STARFIRE. The assumption of uniform wave intensity is not completely justified. However, the waveguide sources are distributed toroidally around the tokamak, and it is expected that turbulence and nonlinear effects may smear the poloidal extent of the resonance cones to some degree.[19-21]

Equation (19) is nonlinear since $D = D\left(E_{\parallel}\right)$.[1,4] For the STARFIRE parameters, we find the following solution subject to the constraints previously discussed in this section. With $n_{\parallel_2} = 1.40$ and $n_{\parallel_1} = 1.86$, an incident wave power of $P_{LH} = 66.5$ MW ($\bar{\mathscr{G}} = 0.092$ MW-m^{-2} averaged over the surface) results in a total current parallel to the field lines $I_{\parallel} = 9.107$ MA with a parallel current density, $j_{\parallel}(r)$, extending 14% of the distance into the plasma. The wave heating profile, $P_{LH}(r)$, and $j_{\parallel}(r)$ are shown in Figs. 7-4 and 7-5.

It is possible to compute an exact ideal MHD equilibrium since our calculation was done for a cylindrical approximation to the plasma. Pressure balance, $\underline{j} \times \underline{B} = \nabla p$, and Ampere's law, $\nabla \times \underline{B} = \mu_0 \underline{j}$, may be combined to yield the following coupled equations:

$$\frac{1}{r}\frac{d}{dr} rB_{\theta} = -\frac{\mu_0}{B_{\theta}}\frac{dp}{dr} - \frac{B_z}{B_{\theta}}\frac{dB_z}{dr} , \tag{20}$$

$$\frac{dB_z}{dr} + \frac{\mu_0}{B^2} B_z \frac{dp}{dr} = -\frac{\mu_0 B_{\theta}}{B} j_{\parallel}(r) . \tag{21}$$

Here $B^2 = B_{\theta}^2 + B_z^2$, B_{θ},B_z being the large aspect ratio versions of the poloidal and toroidal fields. These equations are solved for $B_{\theta}(r)$ and $B_z(r)$ with $p(r)$ specified as $2n_e(r)T_e(r)$ and with $j_{\parallel}(r)$ given by the output of the wave-damping calculation. The boundary conditions are $B_{\theta}(0) = 0$ and $B_z(r = a) = B_0 = 5.8$ T.

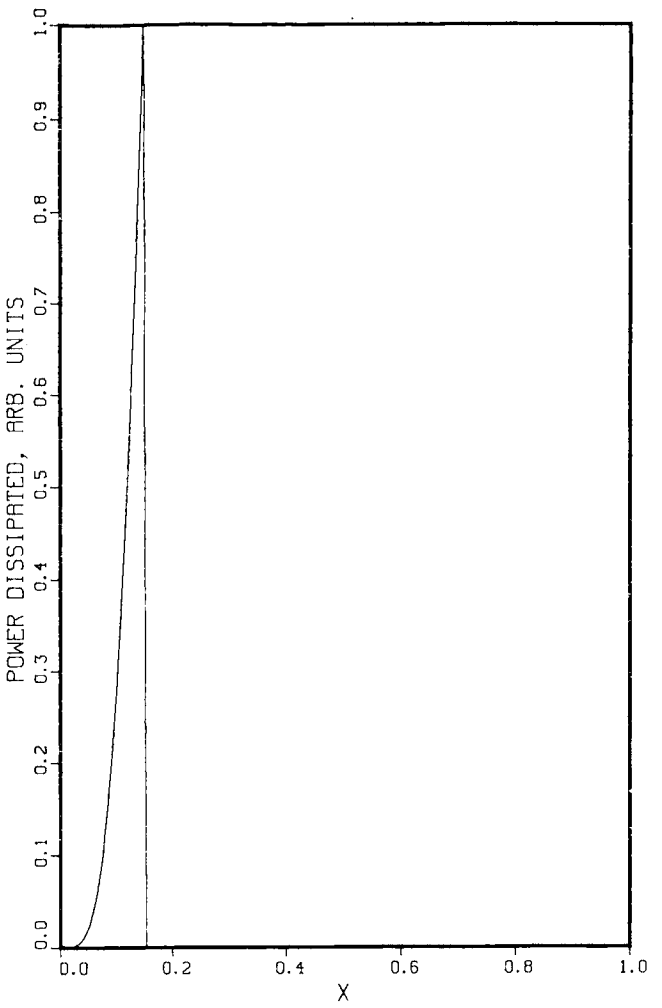

Figure 7-4. Lower-hybrid power dissipation profile from waves with $1.40 \leq n_{\parallel} \leq 1.86$ (rectangular spectrum) for steady-state operation of STARFIRE. Abscissa measures penetration from the outside, $x = 1 - r/a$.

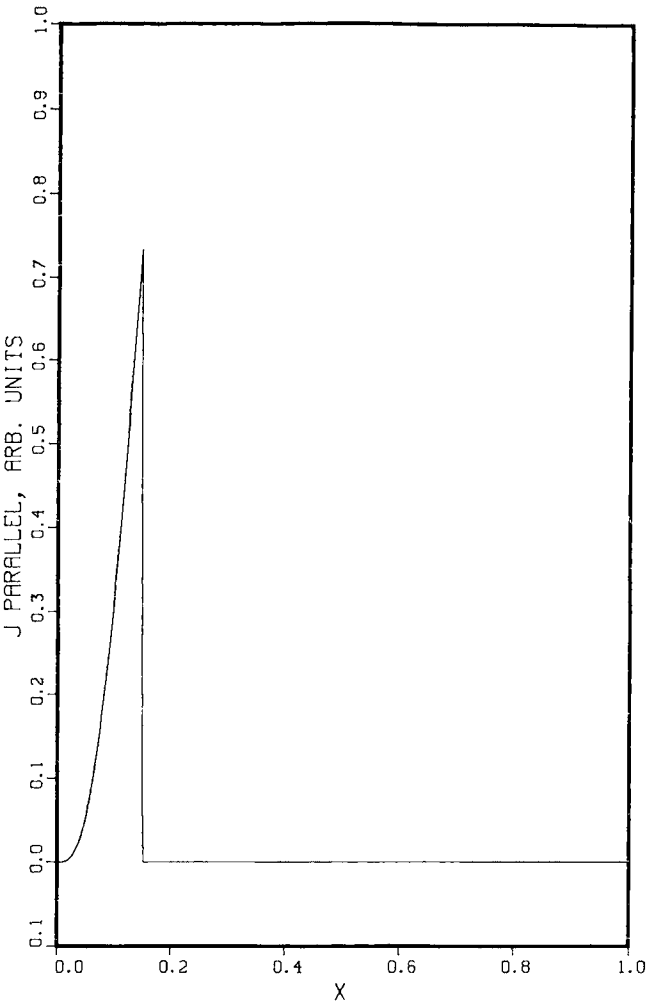

Figure 7-5. Parallel current density profile corresponding to Fig. 7.4.

The significance of computing the exact equilibrium is that, due to the rotational transform $aB_\theta(r)/RB_z(r)$, diamagnetic currents contribute to the z ("toroidal") component of the current density. Thus, $j_t > j_\parallel$, and for STARFIRE, while $I_\parallel = 9.1$ MA, we find I = 10.1 MA, as required by Eq. (8). This solution of the current drive-equilibrium equations is displayed in Figs. 7-6 to 7-9. Note in the region where the current density is largest that the plasma is paramagnetic, due to the predominance of force-free currents. This cylindrical equilibrium is qualitatively similar to the screw pinch configuration of Sakanaka and Goedbloed[22] which possesses good stability according to a sigma-stability analysis. Similar surface current equilibria have been computed in toroidal geometry,[23] and experimental data from SPICA[24] imply the existence and stability of surface current profiles in transient, ohmically driven discharges.

From a quantitative point of view, the acutely peaked current profile in Fig. 7-9 may be unstable to tearing modes.[25] Considerable theoretical and experimental evidence[26-31] shows that sharply peaked surface currents in ohmically driven discharges erode and diffuse inward. The same mechanism which may account for this ohmic current penetration may lead to a benign redistribution of $j_\parallel$.[32] On the other hand, STARFIRE is not driven by ohmic currents, and, by the proper selection of the lower-hybrid wave spectrum, it may be possible to tailor the current profile so as to avoid tearing modes.[33] (We note that plasma disruptions can also be attributed to a variety of tearing modes.[30,34-37] In Refs. 37 and 38 it is discussed how local heat transport near the plasma edge can affect temperature profiles, and, hence, conductivity and current profiles near mode rational surfaces in ohmic discharges, and the consequences for tearing mode behavior are pointed out. It appears possible with wave-driven currents to have more direct control over the current profile, and so the STARFIRE study has adopted the position that plasma disruptions may be practically eliminated. Disruptions are postulated to be possible only due to failures in the position and profile monitoring systems or in the CF coils and waveguide phase controllers.) In addition, the low aspect ratio and high plasma temperature in STARFIRE also tend to reduce resistive tearing mode growth rates.[39,40] For STARFIRE the ratio of the resistive magnetic diffusion time to the poloidal Alfven time is large, $S = 1.4 \times 10^9$, and the stability parameter, $\Lambda = \beta_p^{5/6} A^{-2} S^{1/3}$, is likewise large ($\Lambda \sim 90$). Reference 40 shows that for $\Lambda \gtrsim 60$ the resistive tearing mode boundaries have retreated so far that ideal stability is almost a sufficient requirement for overall stability.

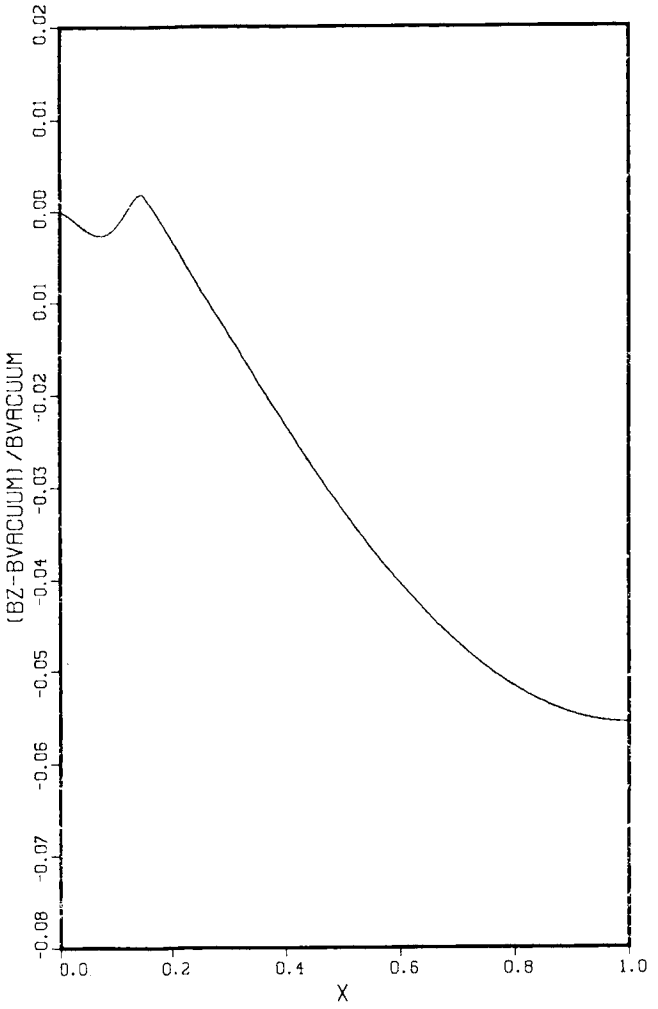

Figure 7-6. Diamagnetism corresponding to Fig. 7-4; ordinate is $(B_Z - B_V)/B_V$, where B_V is the vacuum field.

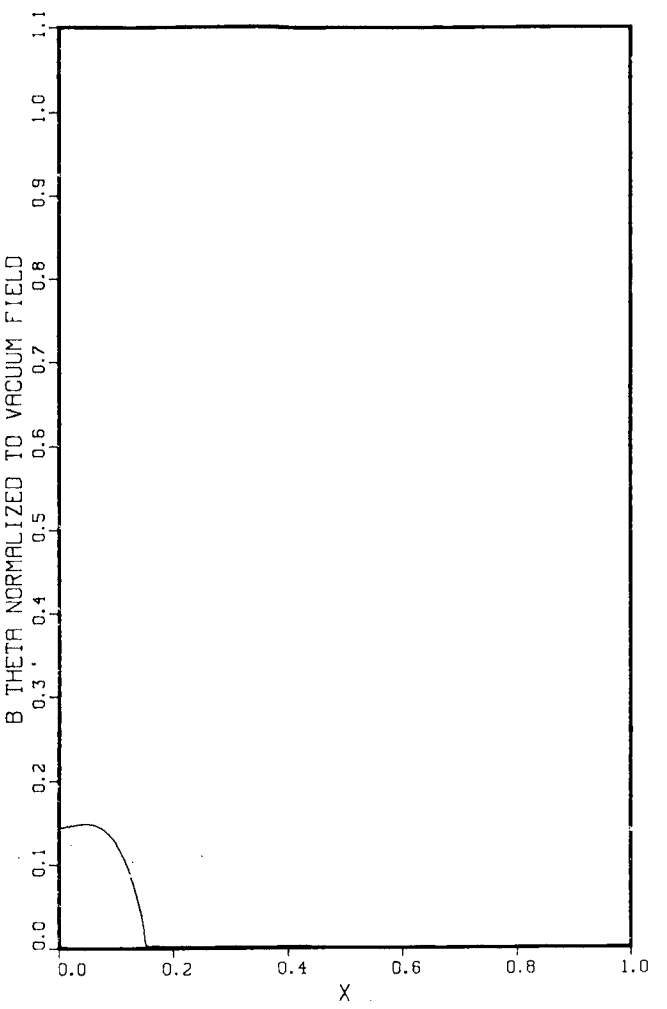

Figure 7-7. Theta component of equilibrium magnetic field corresponding to Fig. 7-4, normalized to the vacuum field.

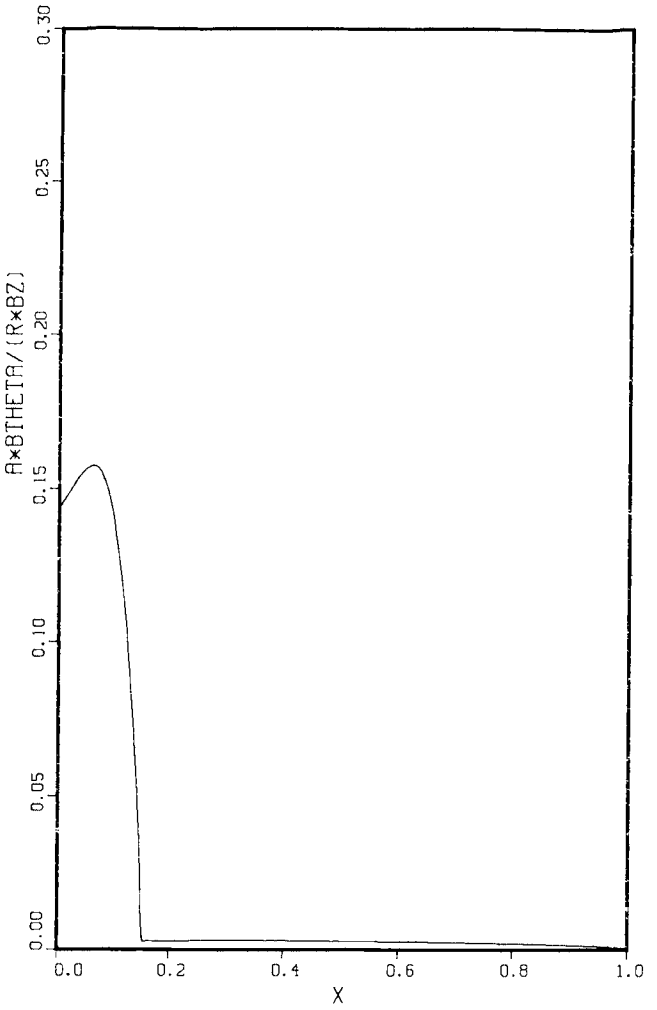

Figure 7-8. Rotational transform, aB_θ/RB_z, corresponding to Fig. 7-4.

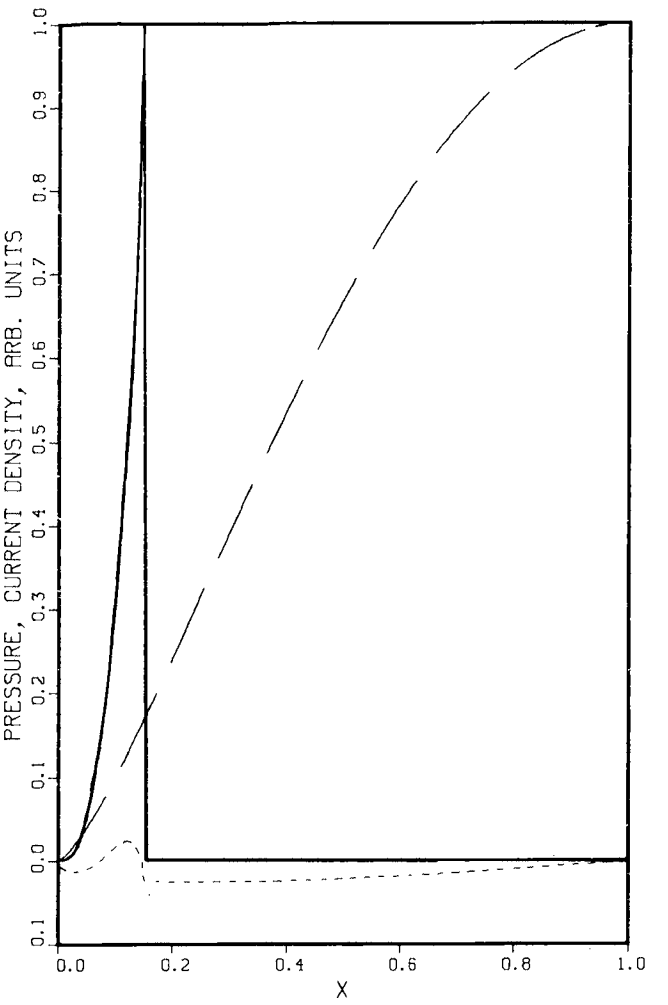

Figure 7-9. Cylindrical pressure profile (dashed), z component of current density (solid), and θ component of current density (dotted) in equilibrium for steady-state STARFIRE. This solution corresponds to the profiles in Figs. 7-4 to 7-8.

The actual demonstration that the desired two-dimensional STARFIRE MHD equilibrium can be formed with lower-hybrid-driven currents is not possible with our present-day understanding of wave-driven currents. Two-dimensional equilibria need to be calculated, and tearing mode theory needs to be reformulated for the proper version of Ohm's law pertinent to noninductive currents. We note also that tearing modes can arise from nonideal effects such as viscosity and have even been predicted in purely collisionless plasmas.[41] It is also conceivable that a true steady state is impossible, with the current profile oscillating between hollow and flat distributions. Such a phenomenon appears to account for the sawtooth oscillations and internal disruptions in present experiments;[34,42] in this case the ohmic current density becomes increasingly peaked on axis as ohmic heating raises the central conductivity, and the j peak is flattened by an m = 1, n = 1 mode, only to repeat the cycle once again. An analogous situation in STARFIRE can be envisioned whereby currents are driven on the surface, and double tearing modes grow and nonlinearly flatten j, to be followed by renewed wave-driven current at the low-density plasma surface.

From this section we determined that a spectrum peaked between $n_{\parallel} = 1.40$ and $n_{\parallel} = 1.86$ is necessary to drive the desired currents with 66.5 MW of power. The following section describes the theoretical model and the equations governing antenna behavior.[43-45]

7.2 WAVEGUIDE ANTENNA THEORY

The waveguide structure is illustrated schematically in Fig. 7-10. As this figure indicates, the waveguides open into the wall defined by the y-z plane, with the x axis pointing toward the plasma. The toroidal field (assumed to be straight) is parallel to the z axis. Along this direction there is a series of N ports, with the edges of the p-th port located at $z = z_p$ and $z_p + b_p$ (thus the width is b_p). The ports are separated by a series of perfectly conducting slabs, the width of the slab separating ports p and p + 1 being $d_p = z_{p+1} - (z_p + b_p)$. The ports are taken to extend indefinitely in the y direction.

Within the waveguides ($x \leq 0$), the fields are taken to be[43] (in MKS units)

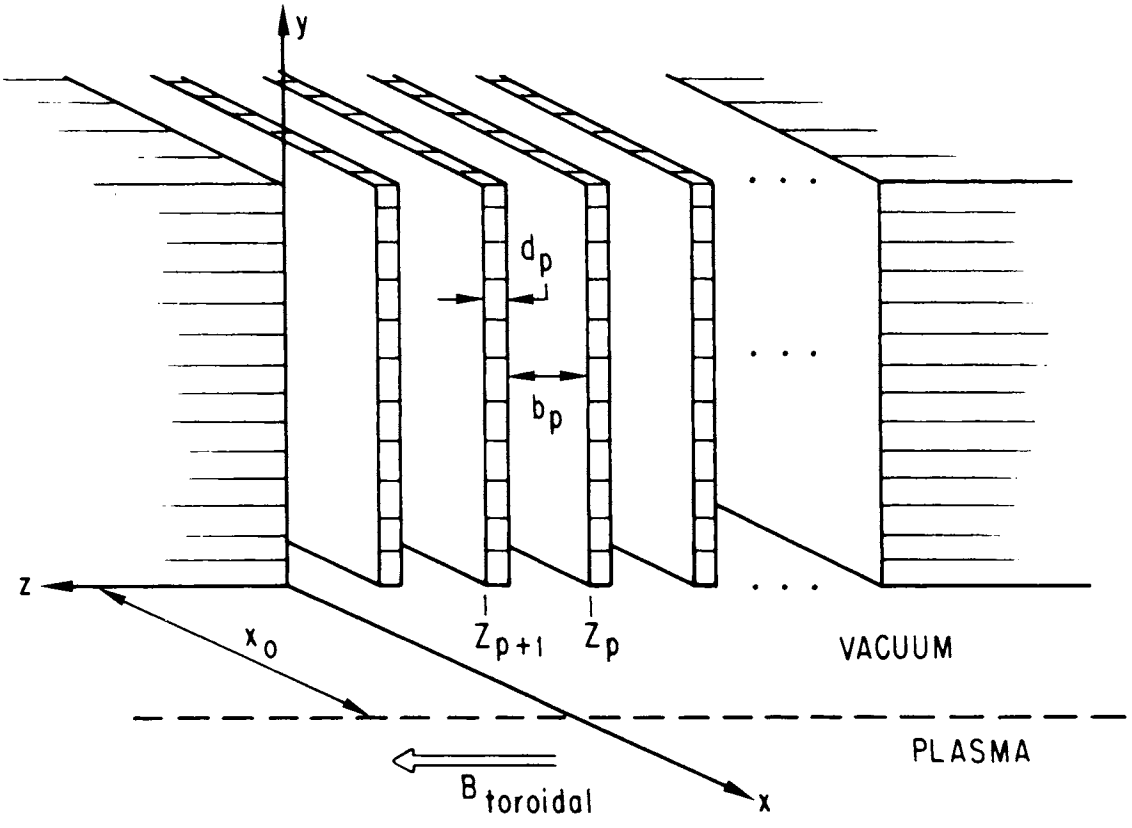

Figure 7-10. Grill geometry for antenna theory.

$$E_z(x,z) = E_0 \sum_{p=1}^{N} \theta_p(z) \sum_{n=0}^{M} \left(\delta_{n0} \alpha_p e^{ik_{np}x} + \beta_{np} e^{-ik_{np}x} \right) \times \cos \frac{n\pi (z - z_p)}{b_p}, \tag{22a}$$

$$B_y(x,z) = -\frac{E_0}{c} \sum_{p=1}^{N} \theta_p(z) \sum_{n=0}^{M} \frac{k_0}{k_{np}} \left(\delta_{n0} \alpha_p e^{ik_{np}x} - \beta_{np} e^{-ik_{np}x} \right) \times \cos \frac{n\pi (z - z_p)}{b_p}, \tag{22b}$$

$$E_x(x,z) = -\frac{ic}{k_0}\frac{\partial B_y(x,z)}{\partial z}, \tag{22c}$$

where $\theta_p(z)$ is unity for z within the p-th waveguide $\left(z_p \leq z \leq z_p + b_p\right)$ and zero elsewhere. The n-sums extend over propagating and evanescent modes. The angular frequency $\omega_0 = 2\pi\nu$ and the waveguide widths are assumed here to satisfy $\pi/b_p > \omega_0/c$, so that there is only a single propagating mode n = 0 in each waveguide. The wave vectors are then given by

$$k_{0p} = \frac{\omega_0}{c} = k_0 , \tag{23a}$$

$$k_{np} = i\left[\left(n\pi/b_p\right)^2 - k_0^2\right]^{\frac{1}{2}}, \qquad n \geq 1 . \tag{23b}$$

The number of evanescent modes is, in principle, infinite but is truncated to M for computational practicality. The dimensionless complex excitation coefficients α_p are input parameters; the complex coefficients β_{np} for the reflected wave and for the evanescent modes are to be determined. The constant E_0 is an overall multiplicative factor. Note that the magnetic field is purely transverse to the waveguide axis x, while the electric field has both transverse and longitudinal components.

Solving for the time-averaged Poynting vector in the x-direction, one sees that the total power delivered by the waveguide array to the plasma is

$$P = \frac{E_0^2}{2\mu_0 c}\sum_p b_p\left[\left|\alpha_p\right|^2 - \left|\beta_{op}\right|^2\right], \tag{24}$$

per unit length in the y direction.

Outside the waveguides, there is a vacuum region of width x_0 (possibly zero) followed by the plasma region. In the vacuum $\left(0 \leq x \leq x_0\right)$ the fields are written as

$$E_z(x,z) = E_0\int_{-\infty}^{\infty} dk_z\, e^{ik_z z}\,\sigma\left(k_z\right)\left[e^{ik_x x} - Y\left(k_z\right)e^{-ik_x x}\right], \tag{25a}$$

$$B_y(x,z) = -\frac{E_0}{c}\int_{-\infty}^{\infty} dk_z \frac{k_0}{k_x} e^{ik_z z}\,\sigma(k_z)\left[e^{ik_x x} + Y(k_z)e^{-ik_x x}\right], \tag{25b}$$

$$E_x(x,z) = -\frac{ic}{k_0}\frac{\partial B_y(x,z)}{\partial z}, \tag{25c}$$

where

$$k_x = \begin{cases} \left(k_0^2 - k_z^2\right)^{\frac{1}{2}}, & |k_z| < k_0 \\ i\left(k_z^2 - k_0^2\right)^{\frac{1}{2}}, & |k_z| > k_0 \end{cases} \tag{26}$$

The Fourier coefficients $\sigma(k_z)$ and $Y(k_z)$ are as yet unknown. If there is no plasma, Y vanishes.

Within the plasma ($x \geq x_0$), the fields are represented as

$$\begin{pmatrix} E_z(x,z) \\ E_x(x,z) \\ B_y(x,z) \end{pmatrix} = E_0 \int_{-\infty}^{\infty} dk_z\, e^{ik_z z} \begin{pmatrix} \mathscr{E}_z(x,k_z) \\ \mathscr{E}_x(x,k_z) \\ \mathscr{B}_y(x,k_z) \end{pmatrix}, \tag{27}$$

and the Fourier amplitudes on the right-hand side satisfy equations which depend on the particular plasma model chosen. In the model for lower-hybrid waves used here,[43,44] these equations are

$$\frac{\partial^2 \mathscr{E}_z}{\partial x^2} + \left(k_0^2 - k_z^2\right)\left(1 - \frac{x - x_p}{L}\right)\mathscr{E}_z = 0, \tag{28a}$$

$$ik_z \frac{\partial \mathscr{E}_z}{\partial x} - \left(k_0^2 - k_z^2\right)\mathscr{E}_x = 0. \tag{28b}$$

The magnetic field follows from Faraday's law:

$$i\omega_0 \mathscr{B}_y = ik_z \mathscr{E}_x - \frac{\partial \mathscr{E}_z}{\partial x}. \tag{29}$$

In Eq. (28a) a constant electron density gradient has been assumed, and $L = \varepsilon_0 m_e \omega_0^2 / \left(e^2 \, dn_e/dx\right)$ is the cutoff length into the plasma, at which the electron plasma frequency equals the driving frequency.

Equation (28a) has two types of solutions, depending on the sign of $k_0^2 - k_z^2$. Defining

$$a\left(k_z\right) = L^{2/3}\left|k_0^2 - k_z^2\right|^{1/3} , \tag{30a}$$

$$\bar{x} = \frac{x - x_0}{L} , \tag{30b}$$

one has, for $\left|k_z\right| < k_0$,

$$\mathcal{E}_z\left(x,k_z\right) = c_0\left(k_z\right)\mathrm{Ai}\left[a(\bar{x} - 1)\right] . \tag{31a}$$

and for $\left|k_z\right| > k_0$,

$$\mathcal{E}_z\left(x,k_z\right) = c_1\left(k_z\right)\left\{\mathrm{Ai}\left[a(1 - \bar{x})\right] + i\mathrm{Bi}\left[a(1 - \bar{x})\right]\right\} , \tag{31b}$$

where Ai and Bi are Airy functions. The functions $c_0\left(k_z\right)$ and $c_1\left(k_z\right)$ are as yet undetermined.

Now the fields are to be matched at the interfaces between the various regions. At the waveguide-vacuum interface, E_z is continuous for all z, and B_y is continuous for values of z corresponding to the waveguide openings. These requirements lead to the following system of linear equations relating the β's to the α's:

$$\sum_{n'p'}\left[\delta_{nn'}\delta_{pp'} + \frac{k_{np}b_{p'}}{\pi\left(1 + \delta_{n0}\right)} J_{np,n'p'}\right]\beta_{n'p'}$$

$$= \sum_{p'}\left[\delta_{n0}\delta_{pp'} - \frac{k_{np}b_{p'}}{\pi\left(1 + \delta_{n0}\right)} J_{np,0p'}\right]\alpha_{p'} , \tag{32}$$

where $J_{np,n'p'} = J_{n'p',np}$ is the dimensionless integral

$$J_{np,n'p'} = \frac{1}{b_p b_{p'}} \int_{-\infty}^{\infty} dk_z \frac{1 + Y(k_z)}{1 - Y(k_z)} e^{ik_z(z_p - z_{p'})} \frac{k_z^2}{k_x}$$

$$\times \frac{1 - (-1)^n e^{ik_z b_p}}{k_z^2 - (n\pi/b_p)^2} \frac{1 - (-1)^{n'} e^{-ik_z b_{p'}}}{k_z^2 - (n'\pi/b_{p'})^2} . \tag{33}$$

This integral contains the function $Y(k_z)$, which is determined when the fields are matched at the vacuum-plasma interface. The matching calculations result in

$$Y(k_z) = \eta(k_z) \frac{1 - Z(k_z)}{1 + Z(k_z)} , \tag{34}$$

where, for $|k_z| < k_0$,

$$\eta(k_z) = \exp\left[2ix_0(k_0^2 - k_z^2)^{\frac{1}{2}}\right] . \tag{35a}$$

$$Z(k_z) = ia^{\frac{1}{2}} \frac{Ai(-a)}{Ai'(-a)} , \tag{35b}$$

and for $|k_z| > k_0$,

$$\eta(k_z) = \exp\left[-2x_0(k_z^2 - k_0^2)^{\frac{1}{2}}\right] , \tag{36a}$$

$$Z(k_z) = a^{\frac{1}{2}} \frac{Ai(a) + iBi(a)}{Ai'(a) + iBi'(a)} . \tag{36b}$$

With the information in Eqs. (33)-(36), Eq. (32) is a closed linear system for the reflection parameters β_{np}. In terms of these parameters, the electric field amplitudes are:

$$\begin{pmatrix} c_0(k_z) \\ \\ c_1(k_z) \end{pmatrix} = \frac{T(k_z)}{2\pi} \eta^{-\frac{1}{2}} \frac{\eta - Y}{1 - Y} \begin{pmatrix} [Ai(-a)]^{-1} \\ \\ [Ai(a) + iBi(a)]^{-1} \end{pmatrix} \tag{37}$$

where

$$T(k_z) = -ik_z \sum_{np} (\delta_{n0}\alpha_p + \beta_{np}) \frac{1 - (-1)^n e^{-ik_z b_p}}{k_z^2 - (n\pi/b_p)^2} . \tag{38}$$

Of course the electric field is continuous at $k_z = k_0$. The k_z spectrum of the square of the electric field, $I(x,k_z)$, which is defined by

$$\int_{-\infty}^{\infty} dz \left|E_z(x,z)\right|^2 = \int_{-\infty}^{\infty} \frac{dk_z}{2\pi} I(x,k_z), \tag{39}$$

is then (for x in the plasma)

$$I(x,k_z) = \left| T\, \eta^{-\frac{1}{2}} \frac{\eta - Y}{1 - Y} g(\bar{x}) \right|^2 , \tag{40}$$

where

$$g(\bar{x}) = \begin{cases} \dfrac{Ai[a(\bar{x} - 1)]}{Ai(-a)} & |k_z| < k_0 \\ \dfrac{Ai[a(1 - \bar{x})] + iBi[a(1 - \bar{x})]}{Ai(a) + iBi(a)} & |k_z| > k_0 . \end{cases} \tag{41}$$

This concludes the development of the important equations of the waveguide theory. Essentially, one ends up with a system of N × (M + 1) simultaneous linear equations [cf. Eq. (32)], where N is the number of ports and M is the number of evanescent modes accounted for. The coefficients in these equations involve integrals over known functions, which can be evaluated by standard numerical techniques. The accuracy of the final spectra increases rapidly with the number of evanescent modes, and for accuracy to three or four figures it was found sufficient to take M = 2.

We now consider the behavior of the results as the number of ports, the vacuum distance, and the density gradient are varied, with the other parameters held fixed. We set ν = 1.677 GHz and, assuming equal outgoing power in each guide, α_p = 1.0. It is desirable to keep the septa as thin as possible, but waveguide fabrication difficulties limit this to d_p = 0.7 cm, for all guides.

The minimum number of guides needed to define a traveling wave is three per wavelength, so we require an increasing phase difference of $2\pi/3$ between all neighboring guides.

First we consider the characteristics of the central peak in the spectrum of the electric field, as a function of the number N of waveguides. For sufficiently large N, this peak is expected to occur at a value of k_z such that $2\pi/k_z$ equals the grill width associated with a phase difference of 2π, or $3(b_p + d_p)$; thus for $n_{\|}^c = 1.63$ (the average value required for current drive), we expect $b_p = 2.95$ cm. This is borne out by Fig. 7-11, which shows the central peak for N = 6, 12, 18, and 24 at fixed values of x_0 and dn_e/dx and with x at the cut-off distance into the plasma. Another important feature is the fact that the product of the width and the number of ports is approximately constant. This is a diffraction effect, since the trend remains when the plasma parameters are varied, or when the plasma is removed (the value of the product, however, varies from case to case). Note also the peak at $k_z = k_0$, corresponding to waves propagating with the free-space wavelength, which disappears as N is increased. For any given range of k_z, plots like Fig. 7-11 allow for an estimate of the minimum number of ports necessary to concentrate the spectrum in that range.

Figure 7-12 displays the side bands radiated by a typical grill.[46] These smaller peaks in the spectrum occur at intervals separated by $\Delta n_{\|} = \Delta k_z k_0^{-1} = 2\pi \left| n_{\|}^c \right| / \Delta\phi$, where $n_{\|}^c$ is the location of the (central) largest peak and where $\Delta\phi$ is the phase difference between adjacent guides. Since $n_{\|}^c = 1.63$ and $\Delta\phi = 2\pi/3$, we see $\Delta n_{\|} = 4.89$. Thus, in Fig. 7-12, relative maxima occur at $n_{\|} = 1.63 - 4.89$, $n_{\|} = n_{\|}^c = 1.63$, and $n_{\|} = 1.63 + 4.89$. Only lower-hybrid waves with $1.40 < n_{\|} < 1.86$ generate useful current density in STARFIRE; so in evaluating antenna spectra one figure of merit we consider is the fractional intensity, ε, lying within the range of interest,

$$\varepsilon \equiv \int_{1.40\ k_0}^{1.86\ k_0} dk_z\ I\left(x_c, k_z\right) \left[\int_{-\infty}^{\infty} dk_z\ I\left(x_c, k_z\right) \right]^{-1} ,$$

where x_c denotes the cut-off distance into the plasma. Another figure of merit is the average reflection coefficient, $\bar{R}$, defined by

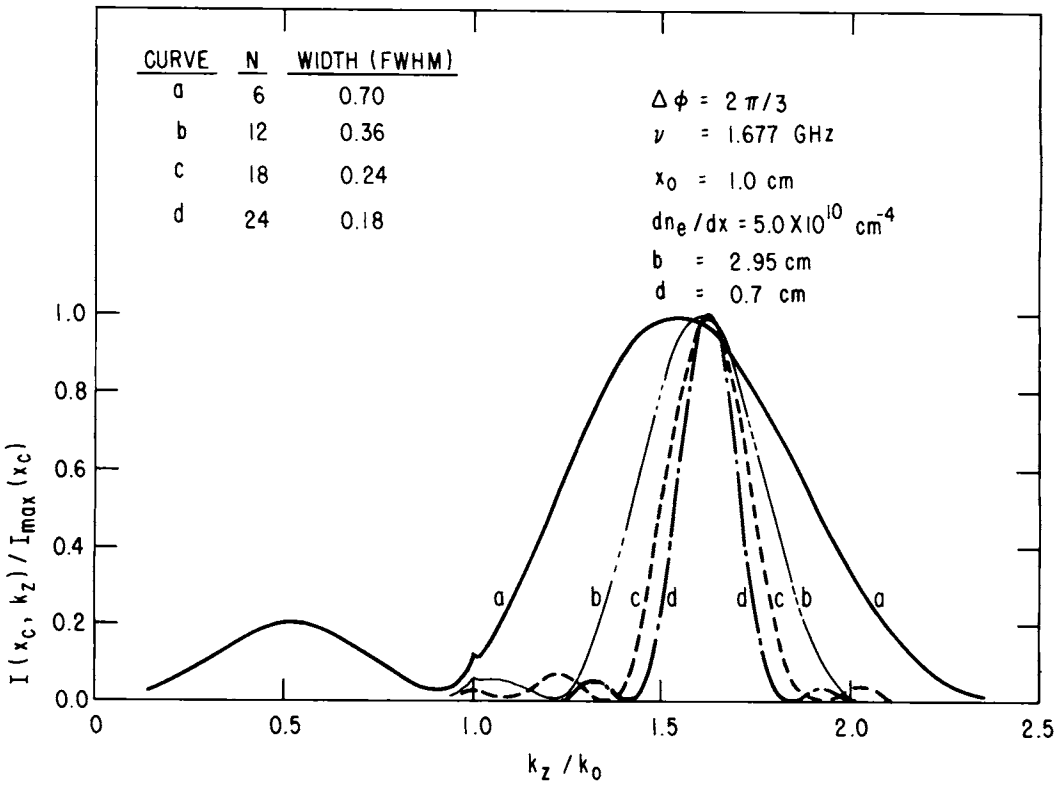

Figure 7-11. Grill spectra for differing numbers of grill elements, N; all active elements.

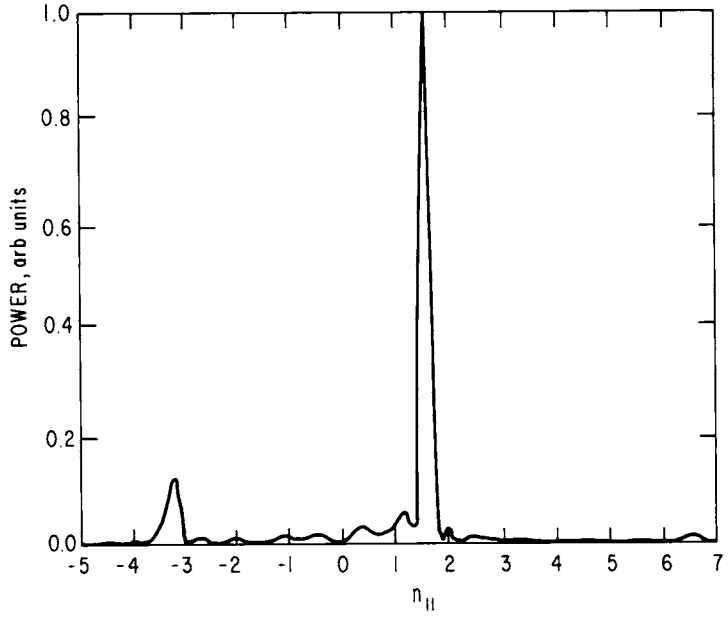

Figure 7-12. Grill spectrum showing secondary peaks; 18 elements, $\Delta\phi = 2\pi/3$, $\nu = 1.677$ GHZ, b = 2.95 cm, d = 0.7 cm, $x_0 = 1.0$ cm, $dn_e/dx = 5 \times 10^{10}$ cm^{-4}. Active guides are numbers 1, 2, 3, 8, 9, 10, 14, 16 (steady-state STARFIRE design).

$$\bar{R} = \sum_p b_p \left|\beta_{0p}\right|^2 \Big/ \sum_p b_p \left|\alpha_p\right|^2 = \frac{1}{N}\sum_{p=1}^{N} \left|\beta_{0p}\right|^2 .$$

We now fix the number of ports at 18 and vary the vacuum thickness x_0, with the density gradient held constant at 5.0×10^{10} cm^{-4}. Generally it is desired to minimize $\bar{R}$ (maximize $1 - \bar{R}$) and maximize ϵ. As Fig. 7-13 indicates, a tradeoff is involved in identifying the optimal thickness. The reflection coefficient always increases with x_0,[43,44] but ϵ also increases with x_0, at least until the reflection coefficient becomes prohibitively large. The reason for the trend in ϵ is that modes with $\left|k_z\right| > k_0$ tend to be damped out as they cross the vacuum, and the damping increases with $\left|k_z\right|$; thus modes with large $\left|k_z\right|$, hence far from the desired interval, become proportionally less represented as x_0 increases.

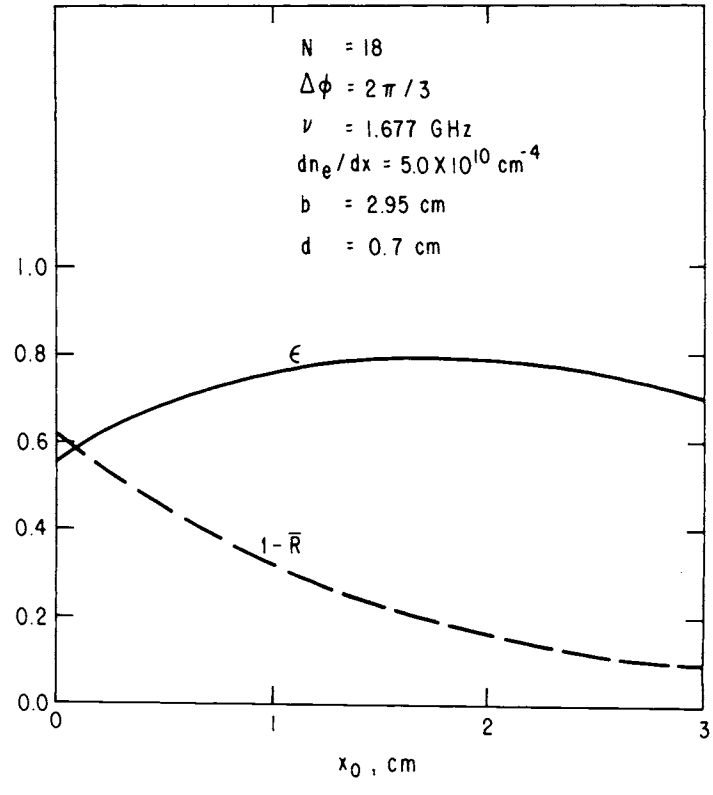

Figure 7-13. Transmission coefficient $(1 - \bar{R})$ and ϵ versus x_0 for fixed density gradient; N = 18 (all active).

Finally, we consider the behavior of $\bar{R}$ and ε as the electron density gradient is varied, keeping N = 18 and working with a representative vacuum distance of 1.0 cm. These results are shown in Fig. 7-14, which illustrates that a trade-off again is involved. Brambilla[43] has given detailed arguments concerning the existence of an optimal density gradient for the reflection coefficient. It is fortunate that ε varies rather slowly from its maximum value in the region where $1 - \bar{R}$ peaks, so that a simultaneous optimization is possible.

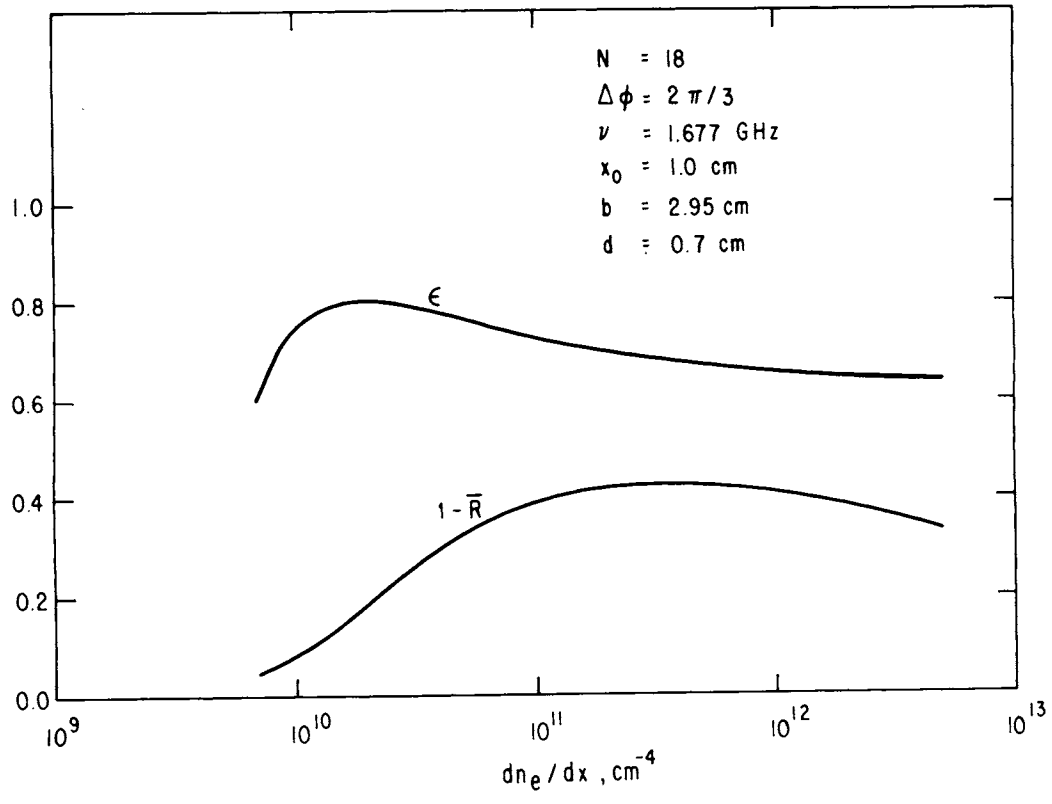

Figure 7-14. Transmission coefficient $(1 - \bar{R})$ and ε versus dn_e/dx for fixed x_0; N = 18 (all active).

7.3 RF SYSTEM DESIGN

Before identifying desirable plasma-edge conditions (x_0 and dn_e/dx of the antenna theory) and computing antenna coupling to the plasma it is necessary to specify the power flow paths in the rf system. This section describes the transmission system, rf sources, and associated hardware and itemizes the power losses in order to permit an optimized design.

Rectangular waveguides appear best suited to carry the rf power. From Sec. 7.2, a narrow opening, b = 2.95 cm, in the horizontal (toroidal) direction is required. To transmit power at ν = 1.677 GHz a vertical opening, a, of 17.0 cm is convenient; only the TE_{10} mode will propagate. The waveguide structure is plated with a thin (several mils) layer of copper which reduces power loss in the guides, since surface currents flow to a skin depth of 2×10^{-4} cm at this frequency. A thin layer of beryllium will form an additional coating on the waveguide surfaces in contact with the plasma. Beryllium is chemically and electrically similar to copper and, since it has a low sputtering and electron emission coefficient, it will be an ideal coating. In the relatively hot waveguide structure facing the plasma typical temperatures of 250°C are expected, and power attenuation in the guides would be about 1.4×10^{-2} db/m. Most of the waveguides, away from the first wall, will operate at 60°C with only 1.2×10^{-2} db/m.

Radiation effects over the reactor lifetime will ultimately increase the resistivity of the copper and beryllium plating; structural damage from high energy particles occurs near one micron of the surface, which is comparable to the skin depth. However, the affected waveguides, those near the first wall, initially account for an estimated 0.5 MW of rf losses and a hundred-fold increase in resistivity could be permitted before the losses reach 5.0 MW and begin to impact the reactor's power balance. Moreover, waveguide baking during maintenance periods may be expected to anneal the metals, removing neutron damage and partly recovering the initial low resistivity.

As shown in Fig. 7-11 the spectrum is better defined as the number of guides in the array is increased. For example, going from sixteen guides to twenty typically increases ε from 77% to 79%. For the same conditions, however, the reflection coefficient may increase from 77% to 78% in going to the larger number of guides. These changes are small and tend to counteract each other in determining overall system efficiency. This insensitivity to N at

large values of N leads us to believe that an eighteen-element array will perform optimally and result in a fairly compact, almost square antenna design. The resulting configuration, shown in Fig. 7-15, has four arrays stacked in the poloidal direction; all guides poloidally adjacent are in phase, in order to approximate the uniform y-dependence of the antenna theory. The total waveguide area facing the plasma, assuming ducts like that in the figure are located in each of the twelve toroidal sectors, is 6.2 m^2. In order to accommodate up to 90 MW of rf heating to ignition the waveguide-averaged intensity is only 1.5 kW/cm^2. This is well below the breakdown capacity of waveguides; the multipactor limit[47] for our guides is ∿25 kV/cm, and we do not expect fields above ∿6 kV/cm. Intensities as high as 10 kW/cm^2 have been achieved without breakdown.[48] However, the linear antenna theory appears incorrect at intensities above ∿1 kW/cm^2. Some experiments[49,50] indicate significant electron densities build up inside the guides at high power levels, leading to a permittivity greater than ε_0 and a loss of control of wave phase. Other experiments[51] with dielectric loaded guides also find high power spectra in disagreement with Brambilla's theory. In this case ponderomotive wave pressure appears to modify the plasma's edge density. Hopefully, careful surface preparation[52] will reduce the electron density problem, and the higher edge electron temperature in a reactor may reduce the ponderomotive effects compared to present-day experiments. STARFIRE also employs directional couplers on the vacuum side of the waveguide windows in order to constantly monitor individual guide phases; a control system adjusts phases to create the desired spectrum. There is good reason to believe that in the next few decades our understanding of plasma response at high intensity will mature to the point that higher intensity and smaller antenna surface area may be used.

The waveguide window is combined with the phase monitors and a dc break to electrically isolate the antenna, which is in contact with the plasma. The window is located between the TF coils, and beyond that point the guide is pressurized at one to two atmospheres with SF_6 (see Fig. 7-16). Thus the ECR region, where $\Omega_e(B) = \omega$, falls in the pressurized guide, 3 m outboard of the window, and ECR breakdown is not a concern. The windows are fabricated from a single 3-mm thick slab of BeO which is grooved on the surface to inhibit surface multipactor.[47] The low loss tangent ($\tan \theta_\ell = 0.001$) of BeO results in a small heating rate. The dielectric constant is $\varepsilon_r = 6.6$, and the wave attenuation[53] is $\alpha = 0.397$ db/m. The transmission efficiency of the window is thus

WG #	R
1	.44
2	.29
3	.47
4	1.00
5	1.00
6	1.00
7	1.00
8	.51
9	.52
10	.53
11	1.00
12	1.00
13	1.00
14	.38
15	1.00
16	.45
17	1.00
18	.39

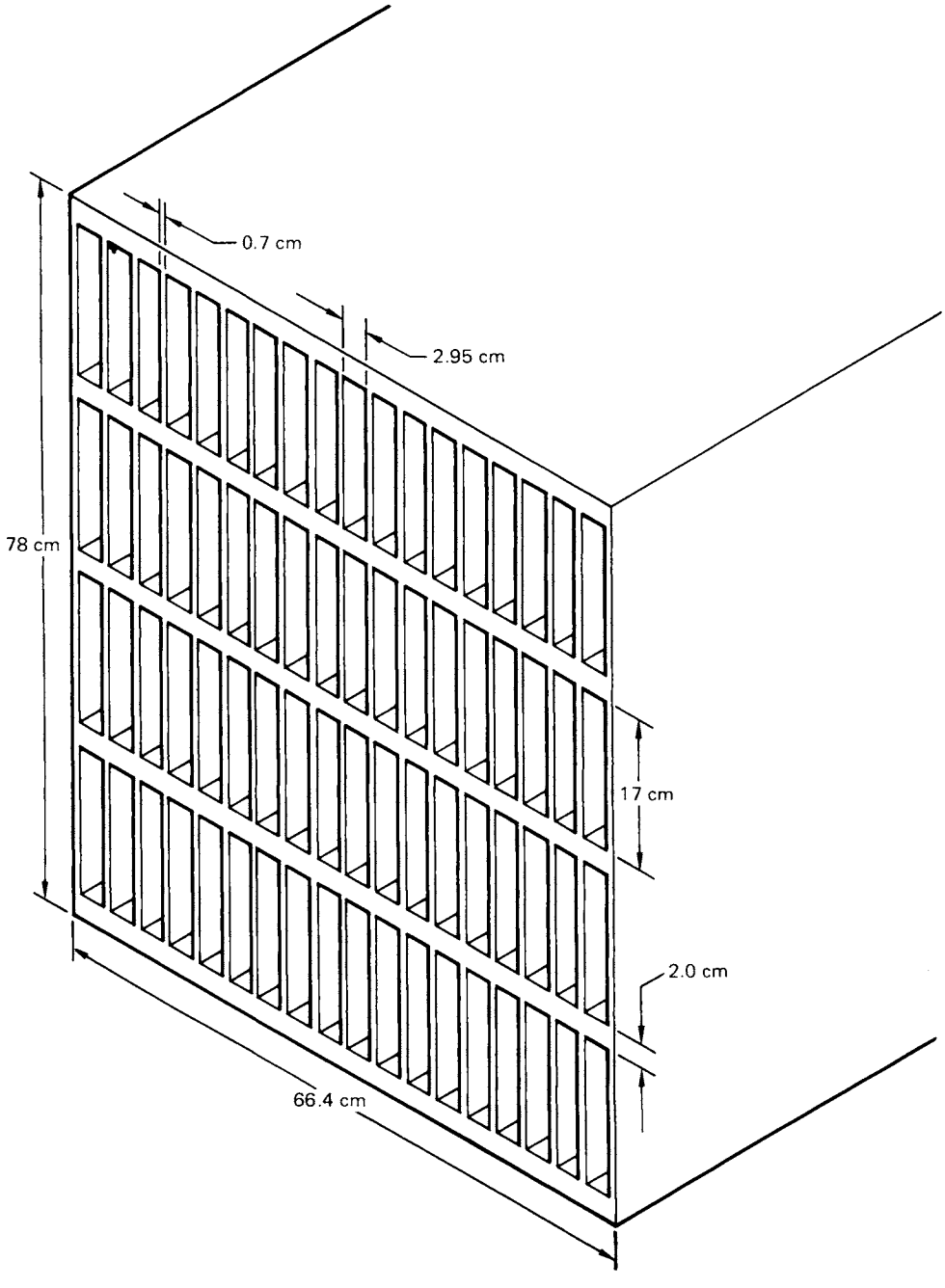

Figure 7-15. Waveguide duct facing the plasma; matrix is composed of four 18-element grills with vertically adjacent waveguides in phase. Electric field vector in guides is in the horizontal direction (TE_{10} mode).

POWER BALANCE	MW
R F POWER TO PLASMA	90.4
(CURRENT DRIVE)	(66.5)
LOSSES	62.3
TOTAL R F ELECTRICAL POWER	152.7

POWER LOSSES		MW
A	GRILL	0.5
B	WAVEGUIDE	1.9
C	WINDOW (3)	0.2
D	WAVEGUIDE	18.2
E	CIRCULATOR	10.6
F	PHASE SHIFTER	1.5
G	C F A	21.8
ELECT. BLDG	POWER SUPPLIES	7.6
	TOTAL LOSSES	62.3

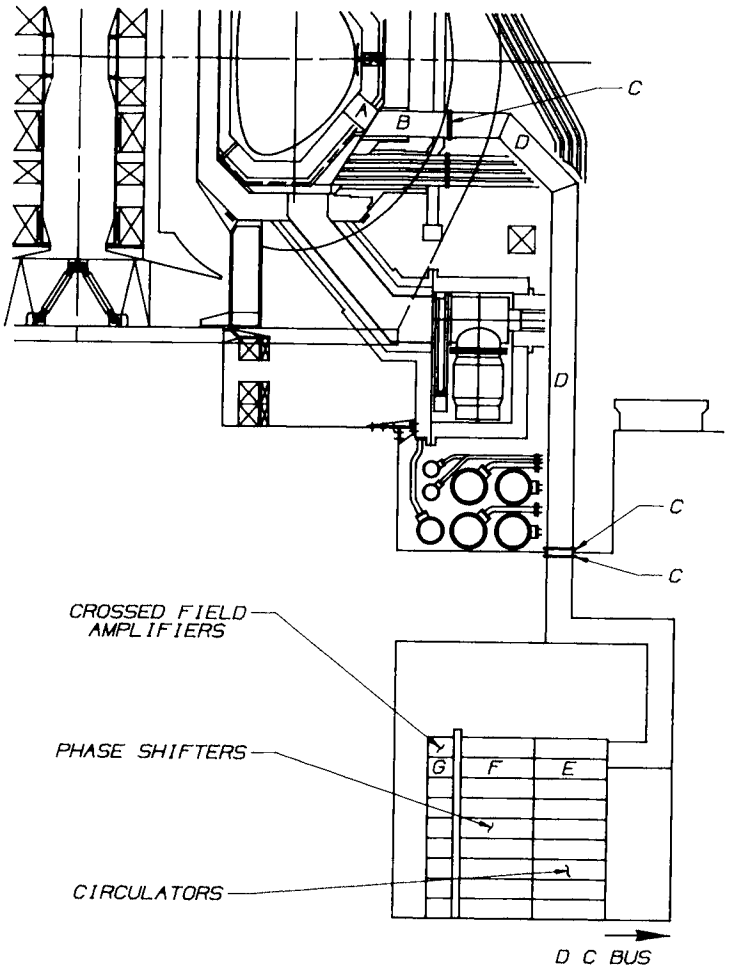

Figure 7-16. RF generation and transmission system; power supplies are in an auxiliary building. A similar system is located between each of the twelve toroidal field coils.

$$\eta_w = 10^{-(0.0397\times3\times10^{-3})} = 0.99973 .$$

The electric field strength in the window is found to be twenty-five times less than the dielectric strength of BeO.[47] A window of this design, which is much thinner than a quarter wavelength, will have minimal influence on wave transmission.[47] In addition, it appears to be sufficiently rigid to withstand the static gas pressure on one side and the thermal stresses of operation. Losses from rf transmission amount to no more than 160 W in an individual window; this small amount of heat is easily dissipated by edge cooling the window. BeO has a high thermal conductivity (χ = 2.4 W/cm-°C at 50°C); therefore in a worst-case situation the temperature variation across the window is less than 6°C, and the thermal stress would not exceed 5 ksi, which is small compared to the compressional strength of over 100 ksi for BeO. Reference 54 cites examples of similar waveguide windows which have performed up to these standards in neutron-free environments.

According to the neutronics calculations of Chap. 11, the windows receive during the reactor's lifetime a total dose less than 8×10^{11} neutrons/cm^2. This leads to negligible swelling and negligible changes in thermal conductivity in BeO,[47] thus suggesting the possibility that the windows may never need to be replaced.

Beyond the windows the waveguides pass below the reactor floor to a complex of circulators, phase shifters, and high-power amplifier tubes. The electronic configuration is the high efficiency system which was proposed in Ref. 54 and which is diagrammed in Fig. 7-17. Due to the high reflected power found in Sec. 7.2 it is most appropriate to simply circulate the reflected power into low gain crossed-field-amplifier (CFA) tubes, such as magnetrons or amplitrons,[55,56] and return the power to the reactor in an adjacent waveguide. In our design a klystron oscillator drives the CFA of the first waveguide in an 18-element array and subsequently power is circulated in a "daisy-chain" manner to each of the other active elements in the array. We assume a 96% transmission efficiency for the circulators[54] and a 0.1 db loss in the phase shifters, which assumes small improvements can be made over present-day performance.

Since the CFA is a low-gain device its efficiency is defined differently from other amplifiers. Denoting the rf output power, rf input power, and electrical input power respectively as P_2, P_3, and P_4, the efficiency is

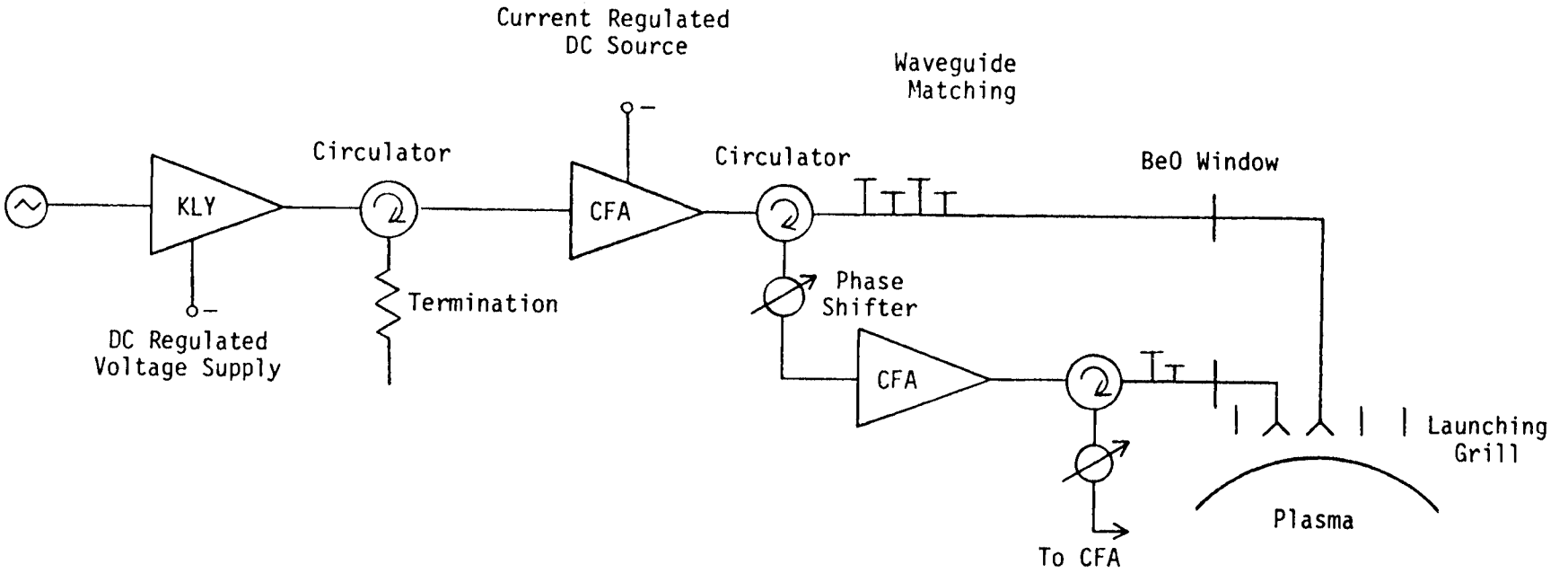

Figure 7-17. Electronic configuration of rf system which circulates reflected power to adjacent CFA's; this figure is reproduced from Ref. 54 [S. Y. Yuen, et al., MIT Plasma Fusion Center Report RR-79-22 (1979)].

$$\eta_{CFA} = (P_2 - P_3)/P_4 \ . \tag{56}$$

The super power amplitron developed by Raytheon[56] has achieved $\eta_{CFA} = 0.78$ at $P_2 = 400$ kW and 3 GHz CW with gains in the range 8-10 db. In addition, the tube is attractive because it does not require a highly regulated power supply, in marked contrast with klystrons. Tubes with several kilogauss magnets are expected to require 20-30 kV power supplies and to draw 10-15 A, depending on the gain required. We assume power supplies will be available to convert ac to dc at a high efficiency, $\eta_{PS} = 0.95$. Discussions with Raytheon indicate there is a high likelihood that a CFA could be developed with $\eta_{CFA} = 0.85$ at 428 kW, 1.677 GHz, and gains of 4-7 db, so we have adopted this η_{CFA} value in our design.

We are now in a position to evaluate the overall lower hybrid system efficiency as a function of ε and $\bar{R}$. Referring to Fig. 7-17 and Table 7-2, the transmission efficiency of power flowing from a CFA to the waveguide opening at the first wall is $\eta_{out} \equiv \eta_C\eta_{TL}\eta_W\eta_G = 0.8774$; the transmission efficiency for the reflected power traveling from the waveguide mouth through the circulator and a phase shifter and into an adjacent CFA is $\eta_{in} \equiv \eta_G\eta_W\eta_{TL}\eta_C\eta_P = 0.8574$. Recalling that $P_{LH} = 66.5$ MW is needed to sustain the toroidal current, an antenna output $P_h = P_{LH}\varepsilon^{-1}$, is needed to supply this, due to the inefficiency associated with the spectral sidebands. Assuming for the moment that all eighteen guides in a horizontal array are actively supplying power, then the output of a single guide (assuming twelve ducts each with four banks of arrays) must be $P_1 \equiv P_h[12 \times 4 \times 18]^{-1}[1 - \bar{R}]^{-1}$, where $[1 - \bar{R}]$ is the overall transmission coefficient of the antenna. Thus, including transmission losses, the CFA output is $P_2 \equiv P_1\eta_{out}^{-1} = P_{LH}\varepsilon^{-1}\eta_{out}^{-1}[1 - \bar{R}]^{-1}/864$. The power reflected into the j-th waveguide, given by the reflection coefficient $R_j \equiv |\beta_{0j}|^2/|\alpha_j|^2$ in the antenna calculation, is R_jP_1. Therefore, the input power to the adjacent CFA, including transmission losses, is

$$P_{3j} \equiv R_jP_1\eta_{in} = P_{LH}\varepsilon^{-1}\eta_{in}R_j[1 - \bar{R}]^{-1}/864 \ .$$

The dc power to the j-th CFA is

$$P_{4j} \equiv (P_2 - P_{3j})\eta_{CFA}^{-1} \ ,$$

and the electric power to the j-th transformer/rectifier is

Table 7-2. RF System Performance

Component	Efficiency	RF Power Loss (12 Ducts) (MW)
Waveguide through blanket (0.70 m)	$\eta_G = 0.9979$	0.5
Waveguide, blanket to basement (32.6 m)	$\eta_{TL} = 0.9166$	20.1
Windows, three per waveguide	$\eta_W = 0.9992$	0.2
Circulator	$\eta_C = 0.9600$	10.6
Phase shifter	$\eta_P = 0.9772$	1.5
CFA	$\eta_{CFA} = 0.8500$	21.8
Power supply	$\eta_{PS} = 0.9500$	7.6

$$P_{ej} \equiv P_{4j}\eta_{PS}^{-1} .$$

Combining these expressions, the net electric power to the rf system is

$$P_e^{18} \equiv 12 \times 4 \times \sum_{j=1}^{18} P_{ej}$$

$$= P_{LH}\varepsilon^{-1}\eta_{PS}^{-1}\eta_{CFA}^{-1}\eta_{out}^{-1}[1 - \bar{R}]^{-1}\left[1 - \eta_{in}\eta_{out}\bar{R}\right] , \qquad (42)$$

provided all waveguides have $R_j < \eta_{in}^{-1}\eta_{out}^{-1}$.

Table 7-3 presents the results of surveys of antenna and system performance for a variety of plasma-edge conditions, assuming eighteen active elements (864 CFA tubes). For any edge density gradient it is seen that there is a vacuum distance which minimizes the required electric power. Evidence from Alcator A shows that the vacuum distance can be controlled with the placement of local "virtual" limiters[57] near the first wall. These limiters serve mainly to define the low electron density edge region, and, being close to the wall, they are shielded from the high energy particle flux seen by the main limiter. Our survey also indicated wide variation in the minimum P_e^{18} value (167 MW at $dn_e/dx = 5 \times 10^{10}$ cm^{-4} to 203 MW at $dn_e/dx = 5 \times 10^{12}$ cm^{-4}). Hopefully, with a series of local limiters of different widths and separations, it will be possible to tailor the edge density in order to obtain optimum

coupling to the plasma. We have made this assumption for the STARFIRE design and, accordingly, we take the edge conditions to be $dn_e/dx = 5 \times 10^{10}$ cm^{-4} and $x_0 = 1.0$ cm.

For some of the high $\bar{R}$ cases in Table 7-3 individual R_j values exceed $\eta_{in}^{-1}\eta_{out}^{-1}$. In these cases an individual reflection coefficient is so high (greater than unity) that the input rf power to a CFA would exceed the output power. Even for the best cases in the table (lowest P_e^{18} values) the average reflection is quite high ($\bar{R} \gtrsim 0.6$). Rather than circulate so much power through the expensive tubes and rf hardware, one obvious improvement is to modify the basic 18-element grill by simply stoppering those guides with individual $R_j \sim 1.0$. This idea of combining active and passive guides having been tested,[58] and the experimental results are in excellent agreement with the theory. Individual passive guides must be plugged or tuned so the outgoing power has the requisite phase corresponding to an all-active grill system.

Table 7-3. Net Electric Power Requirements Versus Plasma Edge Density (18-Active Element Grill)

dn_e/dx (cm^{-4})	x_0 (cm)	ε	$\bar{R}$	P_e^{18} (MW)
2×10^{10}	0.0	0.7351	0.6356	170.1
	0.2	0.7603	0.6793	172.9
	0.5	0.7857	0.7360	181.9
	1.0	0.8024	0.8085	208.8
5×10^{10}	0.0	0.5604	0.3833	188.7
	0.3	0.6470	0.4834	171.7
	0.5	0.6912	0.5457	167.4
	0.7	0.7260	0.6021	166.7
	1.0	0.7634	0.6759	171.4
	1.5	0.7884	0.7724	194.5
	2.0	0.7888	0.8368	232.2
5×10^{11}	0.5	0.5234	0.3875	202.3
	1.5	0.7498	0.7038	181.2
	2.0	0.7794	0.7887	204.2
	2.5	0.7761	0.8503	———
5×10^{12}	1.0	0.6359	0.6649	203.1
	1.5	0.7245	0.7665	209.0
	2.0	0.7617	0.8326	———
	3.0	0.7442	0.9064	———

The passive guides, while they are not connected to high power amplifiers, nevertheless help to define the spectrum and keep ε at a large value. The power flow formulas are modified only slightly from the all-active grill equations above:

$$P_1 = P_{LH}\varepsilon^{-1}[1 - \bar{R}']N^{-1}M^{-1} \tag{43}$$

$$P_2 = P_1\eta_{out}^{-1} \tag{44}$$

$$P_{3j} = R_j P_1 \eta_{in} \tag{45}$$

$$P_{4j} = \left(P_2 - P_{3j}\right)\eta_{CFA}^{-1} \tag{46}$$

$$P_e^N = P_{LH}\varepsilon^{-1}\eta_{PS}^{-1}\eta_{CFA}^{-1}\eta_{out}^{-1}\left(1 - \bar{R}'\right)^{-1}\left(1 - \eta_{in}\eta_{out}\bar{R}'\right) . \tag{47}$$

M is 4 × 12, N is the number of active guides in an 18-element array, and primes denote an average over the active elements only.

By reducing N, which eliminates CFA's from the system, the total system cost may be reduced and the value of $\bar{R}'$ decreased. However, if N is too small the spectrum departs too much from the N = 18 case and ε decreases. In addition, smaller N requires larger CFA outputs which eventually can appreciably exceed the $P_2 \sim 400$ kW which was demonstrated for the super power amplitron.[56] We surveyed various possibilities and compromised on N = 9, i.e. half active and half passive elements. The reference STARFIRE configuration is summarized in Table 7-4 which shows individual reflection coefficients as well as the array average. Note the average reflection coefficient $\bar{R}'$ = 44% which is considerably lower than the corresponding R' = 68% in Table 7-3. Thus, even though ε is slightly smaller, the active/passive arrangement requires only 153 MW electric compared to the 171 MW of Table 7-3. The heat input to the plasma, P_h = 90.4 MW, was shown in Chap. 6 to be adequate for ignition. The maximum power carried by any waveguide is $P_1 + R_{10}P_1$ = 575 kW, which is well within the guides' capacity. CFA output at 428 kW with gains of 4.0 to 6.6 db are required, with supplies rated at 300 to 400 kW dc output. Each horizontal array is driven by a 100-kW klystron which powers the number two CFA in the chain. Note that the adoption of N = 9 reduces the number of CFA's and power supplies from 864 to 432, reducing the capital cost of rf hardware by a factor of two. Additional

Table 7-4. Antenna and System Performance for Reference Active/Passive Grill (N = 9)

Waveguide No.	R_j	P_{3j} (kW)	CFA Gain (db)	P_{4j} (kW)	$R_j P_1$ (kW)
1	0.44	140	4.8	338.	164.
2	0.29	93	6.6	394.	109.
3	0.47	151	4.5	326.	176
4	1.00		passive		
5	1.00		passive		
6	1.00		passive		
7	1.00		passive		
8	0.51	164	4.2	310.	192.
9	0.52	167	4.1	306.	196.
10	0.53	172	4.0	301.	201.
11	1.00		passive		
12	1.00		passive		
13	1.00		passive		
14	0.38	123	5.4	358.	144.
15	1.00		passive		
16	0.45	146	4.7	331.	171.
17	1.00		passive		
18	0.39	126	5.3	355.	147.

$\varepsilon = 0.7359$; $\bar{R}' = 0.4433$; $P_e^9 = 152.7$ MW

$P_h = 90.4$ MW; $P_1 = 376$ kW; $P_2 = 428$ kW

$x_0 = 1.0$ cm; $dn_e/dx = 5 \times 10^{10}$ cm^{-4}

cost reductions appear feasible if larger circulating power is permitted (P_e^N > 150 MW), provided higher power CFA's could be developed.

From the power flow calculations the power losses in different parts of the system were calculated, and these are itemized in Table 7-2. Note that the CFA's dissipate about one-third of the 62 MW of power lost in the conversion of the 152.7 MW of ac power to the 90.4 MW of plasma heating; the waveguide dissipates another third. The placement of the circulators, phase shifters, and CFA's directly under the tokamak (Fig. 7-16) is crucial in keeping the net electric driving power at a reasonable level. It is estimated that an additional 15 m of travel for each transmission line would incur an extra 10 MW of dissipated power. The present configuration does permit access to the active electronics and conveniently locates the power supplies in an auxiliary building. The coax dc bus to the power supplies is sized to yield negligible power loss. It appears possible that further reductions in P_e could be achieved by shortening the waveguide runs. The dogleg configuration in the basement area of Fig. 7-16 could be eliminated with further optimization. In addition, the circulators are passive (low mairtenance) ferrite devices which might be located within the 3-m thick floor. This would have an added advantage of reducing neutron leakage into the basement.

The rf system design, optimized for steady-state current drive, is summarized in Table 7-5. The choice of CFA tubes appears excellent for the present application; preliminary analysis of a klystron-powered system indicated circulating power much in excess of 200 MW as well as considerably higher capital costs.

The lower-hybrid current drive option has attractive engineering and operating features which recommend its use over such options as particle beam drivers and other wave candidates. These stem from the redundancy within the system, flexibility in transmission line location, and high reliability of the components. For example, the rf system has sufficient over capacity so that if a failure occurs in a single array of slots (1/48th of the system) the reactor can continue to operate unless the vacuum system is breached. This design feature permits maintenance without shutting down the reactor.

In addition, the system components are located in three different areas of the plant as shown in Fig. 7-16. Active rf components are located outside the reactor building to provide maximum access to the reactor and minimize the

Table 7-5. RF System Summary

Quantity	Value	Explanation
	I. Tokamak Parameters (Input to WKB Analysis of Wave Damping)	
R	7.0 m	Major radius
A	3.6	Aspect ratio
S	1.33	Shape factor
$\tilde{a}$	2.59 m	SR/A
B_0	5.8 T	Field on axis
B_c	5.1 T	Field near antenna
$\bar{T}_e$	17.3 keV	Average electron temperature
α_T	0.3	Temperature profile
T_{edge}	0.025 keV	Edge electron temperature
$\bar{n}_e$	1.18×10^{20} m^{-3}	Average electron density
α_n	1.1	Density profile
n_{edge}	5×10^{17} m^{-3}	Edge electron density
$\bar{n}_D, \bar{n}_T$	0.403×10^{20} m^{-3}	Fuel ion density
$\bar{n}_\alpha/\bar{n}_D$	0.284	Alpha fraction
$\bar{n}_{Be}/\bar{n}_D$	0.08	Beryllium fraction
M	2.325 amu	Effective ion mass
$r_c/\tilde{a}$	0.86	Furthest wave penetration
$n_e(r_c)$	0.569×10^{20} m^{-3}	Density at furthest penetration
$T_e(r_c)$	15.1 keV	Temperature at furthest penetration
	II. Lower Hybrid System Parameters	
ν	1.677 GHz	Wave frequency
ω	1.054×10^{10} s^{-1}	Wave angular frequency
$\omega_{LH}(r_c)$	5.883×10^{9} s^{-1}	Lower-hybrid frequency at r_c
$\bar{n}_\parallel$	1.40-1.86	Spectrum required
$\bar{\lambda}_\parallel$	10.94 cm	Toroidal wave length
$\omega/\bar{\kappa}_\parallel$	1.83×10^{8} m/s	Parallel phase speed
$w(r_c)$	3.56	$\omega/\bar{\kappa}_\parallel v_e$ at r_c
$I_\parallel$	9.11 MA	Parallel current
I	10.1 MA	Toroidal current
$\mathcal{I}$	1.5 kW/cm^2	Wave intensity at antenna
N	9 + 9 = 18	Nine active/nine passive guides
$\Delta\phi$	$2\pi/3$	Phase difference
b	2.95 cm	Narrow guide opening
d	0.70 cm	Septum
a	17.0 cm	Vertical guide opening
dn_e/dx	5.0×10^{10} cm^{-4}	Edge density gradient
x_0	1.0 cm	Vacuum distance
ϵ	0.736	Spectral fraction driving current
$\bar{R}'$	0.443	Antenna reflection coefficient
P_{LH}	66.5	Required to drive current
P_h	90.4	Net heating to plasma
P_e^9	152.7	Net electric to rf system

number of remote maintenance operations required. The rf duct, which is routed through the reactor floor space to a basement area, has two dielectric windows provided at the building liner to assure integrity of the liner. The basement area was chosen for location of the circulators, phase shifters, and amplifiers to minimize the duct length and resultant rf losses. The basement area is specifically designed for the rf components and is shown in the balance-of-plant (BOP) layout in Chap. 20. A circular crane is provided to assist in component handling. The bends and lengthy ducting together with the thick floor of the building provide adequate shielding so that maintenance personnel can replace components during reactor operation.

The electrical power supplies are located in the electrical building as shown in the BOP layout of Chap. 20. This arrangement permits replacement of individual power supplies while the reactor continues to operate. The electrical building location was chosen for the power supplies because of space limitations in the reactor building basement.

The rf grill design is shown in the engineering layout of Fig. 7-18. The grill assembly is mounted to the blanket and is replaced every six years as part of the blanket sector, as discussed in Chap. 19. The grill assembly protrudes through the shield door as a part of an assembly that contains other penetrations. This interface is discussed in Chap. 11. An elbow attaches to the grill assembly outside the shield. The elbow incorporates the phase monitor and beryllium oxide dielectric window. The window is located at the interface of the grill assembly and elbow to permit its removal for replacement if necessary, yet it provides a vacuum tight boundary so that plasma cavity pumpdown can be started without having all external structure and cooling lines in place. Each time the elbow is removed for blanket replacement, a refurbished duct is installed. Refurbishment is expected to include seal and phase monitor replacement and a general inspection.

Cooling water is directed to the first wall from the reactor building floor by a tube in the rf duct. At the first wall the water is manifolded and forced to flow past the first wall at 3 m/s. The coolant then flows through the duct cross section where it bath cools the separate rf guides as it exits near the initial inlet at the reactor building floor.

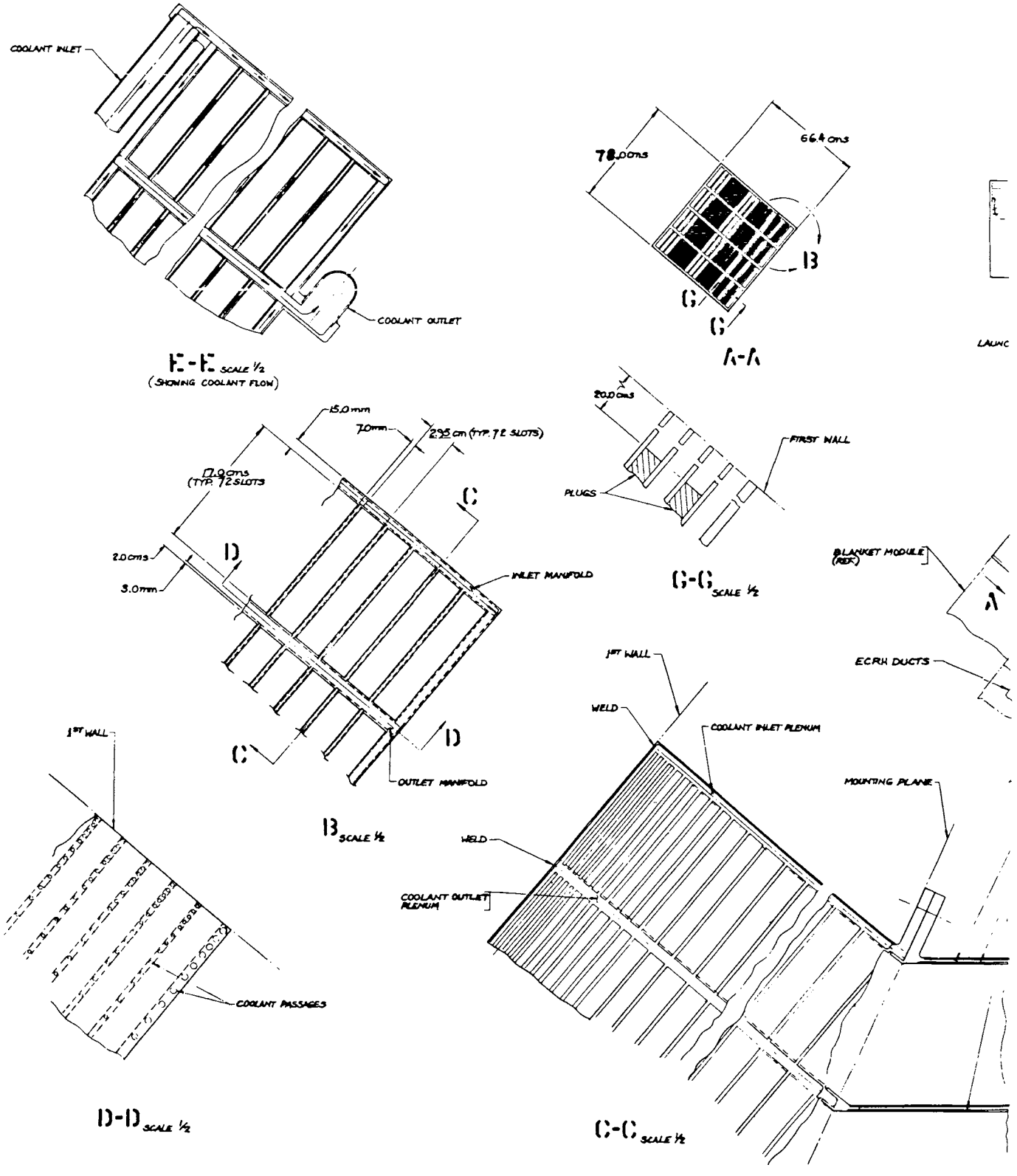

Figure 7-18. Engineering layout of rf duct; in Sec. A-A the passive guides are shown shaded.

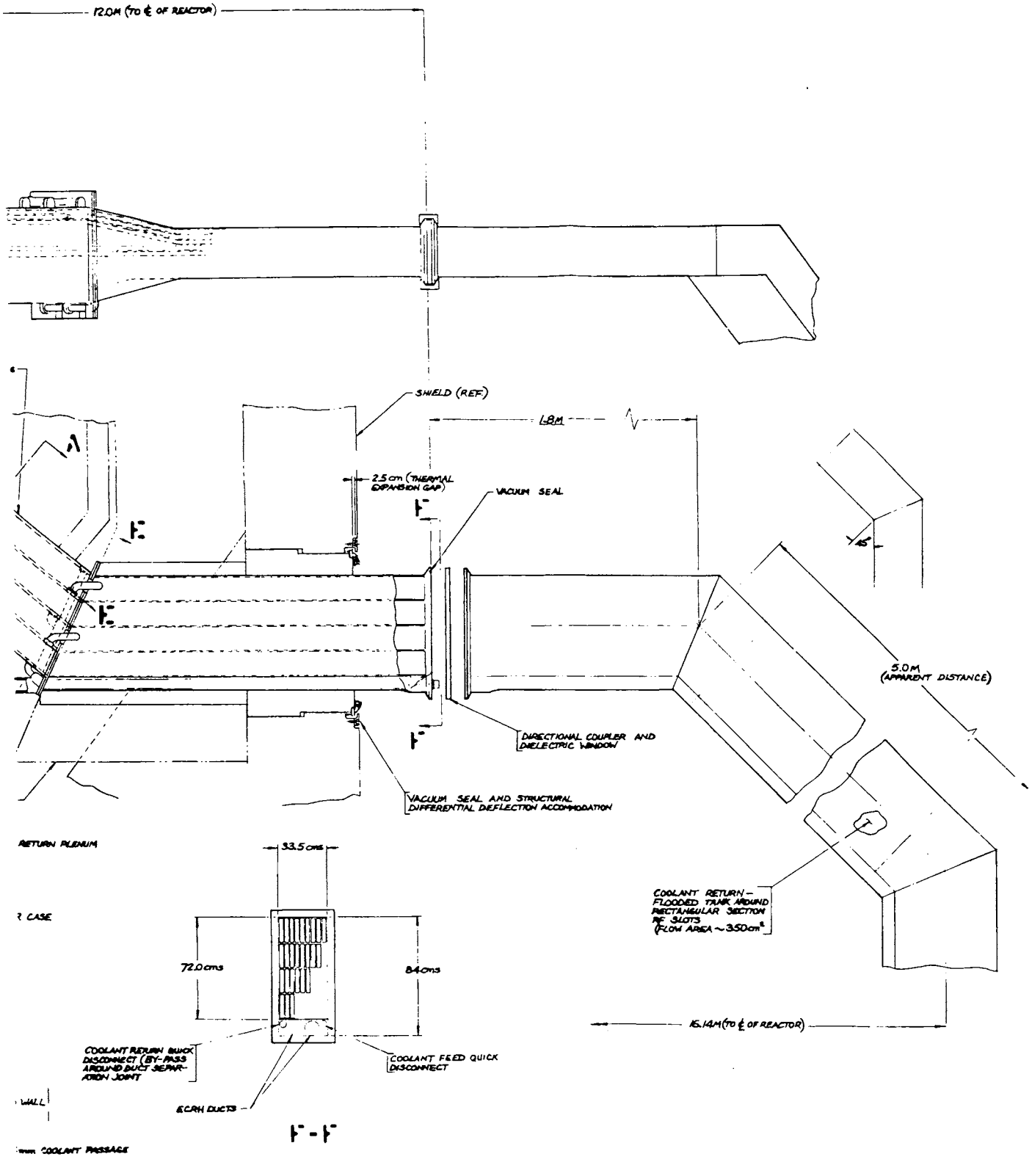
12.0M (TO ℄ OF REACTOR)
SHIELD (REF.)
1.8M
2.5 cm (THERMAL EXPANSION GAP)
VACUUM SEAL
45°
5.0M (APPARENT DISTANCE)
DIRECTIONAL COUPLER AND DIELECTRIC WINDOW
VACUUM SEAL AND STRUCTURAL DIFFERENTIAL DEFLECTION ACCOMMODATION
COOLANT RETURN — FLOODED TRIAX AROUND RECTANGULAR SECTION RF SLOTS (FLOW AREA ~ 350cm²)
15.14M (TO ℄ OF REACTOR)
RETURN PLENUM
? CASE
33.5 cms
72.0 cms
84 cms
COOLANT RETURN BLOCK DISCONNECT (BY-PASS AROUND DUCT SEPARATION JOINT
COOLANT FEED QUICK DISCONNECT
ECRH DUCTS
WALL
COOLANT PASSAGE

Within the reactor hall, the total heat load to each of the twelve ducts is approximately 3.8 MW of which 0.5 MW results from the first wall flux, 2.2 MW results from nuclear heating, and 1.1 MW results from rf losses. Total system heating in the ducts within the reactor hall is 45 MW. The inlet coolant temperature is 35°C and the outlet temperature is 46°C. Pressure loss of the system is expected to be ∿20 psi.

Each grill assembly is fabricated from PCA steel. PCA steel was chosen based on its selection as a material for the first wall and blanket. The uncertainties of material properties under irradiation conditions results in the desire to minimize the number of different materials used near the plasma. Changes in choice of a blanket structure would likely result in a change in the rf duct structure. PCA steel is acceptable for the grill because it is being used at lower stresses (50-psi coolant) and lower temperatures (315°C maximum) than the first wall and should therefore have a longer life.

The grill is designed to minimize the amount of welding required near the first wall, again because of the uncertainties. Minimum welding at the first wall is accomplished by constructing the grill of four machined plates, each of which contains a 1 × 18 matrix of broached slots with cross-drilled holes (see section DD of Fig. 7-18) for cooling passages. The machined slots are 2.95 cm × 17 cm and the drilled cooling passages are 3 mm diameter. The only welding required near the first wall is to join the individual slotted plates together. The weld zone is in the low pressure manifold region at the back of the machined and welded assembly; rectangular extruded tubes are welded to each machined slot. The bank of extruded tubes is enclosed by a steel tank which forms the outlet coolant passage and provides bath cooling.

7.4 LOWER-HYBRID HEATING AND CURRENT DRIVE FOR STARTUP

The same rf system described in the previous section for steady-state current drive may also be used, with slight modification, to initiate the tokamak discharge. Previous studies, using Landau damping of lower-hybrid waves coupled to one-dimensional transport calculations,[59] have shown that reactor-size tokamaks may be ignited with reasonable amounts of rf power. The results reported in this section focus on different requirements, viz., the dynamic phase of current drive and the ability to maintain MHD equilibrium during this phase.

Lower-hybrid theory[1,2] points out that significant current density is generated when the ratio of phase speed to electron speed, w, is about 3-4. Thus (see Table 7-5) we found w = 3.56 at the peak current density of the steady-state configuration, which was achieved with $n_{\parallel} = 1.40\text{-}1.86$. Lower $\bar{T}_e$ values during startup accordingly require higher $n_{\parallel}$ to generate current. Therefore, three of the twelve rf ducts in the STARFIRE design house a special grill geometry designed to broadcast higher $n_{\parallel}$ spectra when $\bar{T}_e$ is low; by adjusting the waveguide phases these grills can essentially duplicate the spectrum of Fig. 7-12 for the steady-state portion of the burn. For the dynamic zero-dimensional calculation described in Sec. 6.3.1 an algorithm was developed to model the rf heating and current drive. This algorithm will be shown *a posteriori* to fit the actual performance of the special grills.

For simplicity the pressure profile is assumed constant during the startup with $\alpha = 1.4$. The combination of low-power ohmic heating and ECRH initially creates a peaked temperature profile; we take $\alpha_T = 1.1$. We assume the special grills are initially phased at π with power concentrated near $|n_{\parallel}| \sim 5$. Since the spectrum is symmetric no net momentum is launched, but heating occurs where the local temperature is $T_e \sim 1$ keV. We desire to heat the central portion of the plasma, with $T_{e_0} = 1$ keV corresponding to $\bar{T}_e \sim 0.5$ keV. Once $\bar{T}_e$ is raised to ~1.4 keV, central heating (at $T_{e_0} \sim 2.9$ keV) requires a guide phasing that results in an asymmetric spectrum $(n_{\parallel} \sim 3)$; at this point the LH waves begin to drive current. During this low β_t phase the MHD equilibrium demands centrally peaked current profiles. This is accomplished by reducing $n_{\parallel}^c$ to ~1.6 while $\bar{T}_e$ increases to 6.2 keV. Wave accessibility to the magnetic axis during this period requires $\bar{n}_e < 0.3 \times 10^{20}$ m^{-3}. An analytic expression in Ref. 4 relates total rf current to power dissipated:

$$P_{rf} = 1.3 \times 10^{-20} I_{rf} R n_{e_0} \left[1 - \left(r_c^2/a^2\right)\right]^{\alpha_n/\alpha_T} \frac{\ell n\left(n_{\parallel 1}/n_{\parallel 2}\right) G}{\left(n_{\parallel 2}^{-2} - n_{\parallel 1}^{-2}\right)} \quad . \qquad (48)$$

With $\alpha_n = 0.3$, $\alpha_T = 1.1$, $r_c = 0$, $n_{\parallel 1} - n_{\parallel 2} \sim 0.9$, $n_{\parallel 1} = 5.3\, T_{e0}^{-\frac{1}{2}}$, and $G \sim 1$ we obtain the formula given in Sec. 6.3.1 for the interval $1.4 < \bar{T}_e < 6.2$, when T_e is in units of keV. Once $n_{\parallel}^c \sim 1.6$ the phases are fixed so all twelve ducts become available to further heat and drive current. Waves with $n_{\parallel} \sim 1.6$ heat the location where $T_e \sim 14$ keV, so as $\bar{T}_e$ increases from 6.2 keV to 17.3 keV, the waves heat and drive current closer to the plasma edge. The tendency to heat the surface flattens the temperature profile, which is modeled by taking $\alpha_T = 1.5 - 0.07\, \bar{T}_e$. The increase in α_n and tendency to drive current in the low n_e edge region allows increases of $\bar{n}_e$ to the steady-state value of 1.2×10^{20} m^{-3}. MHD equilibrium is simultaneously satisfied during this phase since the increase in β_t automatically leads to hollow current profiles. Again, using Eq. (48) with $n_{\parallel 2} = 1.40$, $n_{\parallel 1} = 1.86$, but taking $\left[1 - \left(r_c^2/a^2\right)\right] \sim 13\left[\left(1 + \alpha_T\right)\bar{T}_e\right]^{-1}$, the P_{rf} versus I_{rf} relationship is formulated for 6.2 keV $< \bar{T}_e$, as given in Sec. 6.3.1.

To illustrate the consistency of this picture we have tabulated the relevant parameters at several time steps from the startup phase shown in Figs. 6-17 to 6-19, as well as MHD parameters and I_{rf} calculated from the algorithms given above; this is given in Table 7-6. Four stages in the evolution of the MHD equilibrium are shown in Fig. 7-19. The first example, labeled $\beta_p = 0.950$, is typical of the discharge profiles through the first 250 s, when $\bar{T}_e \lesssim 6.2$ keV and β_t is very low. During this time the current density peaks at the magnetic axis, so $r_c = 0$. After 300 s the $\bar{T}_e$ and β_t values increase. The profile at 368 s is approximately given by the example labeled $\beta_p = 1.96$; notice the current density peaks outboard of the magnetic axis and is beginning to flatten. By 386 s $\bar{T}_e$ has reached 17.7 keV and $\beta_t = 0.044$. The corresponding equilibrium, labeled $\beta_p = 2.24$, is already hollow. The final state, for which $\bar{T}_e = 17.3$ keV and $\beta_t = 0.067$, is, of course, the last equilibrium, labeled $\beta_p = 2.91$. All the equilibria in the startup sequence were computed with $F^2(\psi) = F_0^2(1 - \delta\hat{\psi}^{1.7})$; increasing β_p values correspond to larger δ values (see Sec. 6.2.1 for further discussion). The four equilibria in Fig. 7-19 have boundary-to-axis safety factor ratios of $q_b/q_a = 2.7$, 3.0, 3.2, and 4.2 and do not constitute a flux conserving sequence. However, due to the very long time taken for startup,

Table 7-6. Current Drive and Heating During Startup (Zero-D, Dynamic Code)

Time(s)	β_p	β_t	$\bar{T}_e$ (keV)	$\bar{n}_e$ (10^{20} m^{-3})	P_{rf} (MW)	I_{rf} (MA)	I (MA)	α_T
4	1.14	1.7×10^{-4}	0.74	0.11	1.4	0.0	0.99	1.1
9	0.80	4.9×10^{-4}	1.75	0.11	15.0	2.45	1.77	1.1
15	0.99	0.0015	5.45	0.11	40.2	18.5	2.77	1.1
17	1.09	0.0017	6.29	0.11	40.2	24.1	2.86	1.1
300	1.10	0.014	13.1	0.39	90.0	14.7	7.99	0.6
368	1.97	0.033	15.6	0.77	90.0	10.0	9.18	0.4
386	2.25	0.044	17.7	0.88	90.0	14.4	9.69	0.3

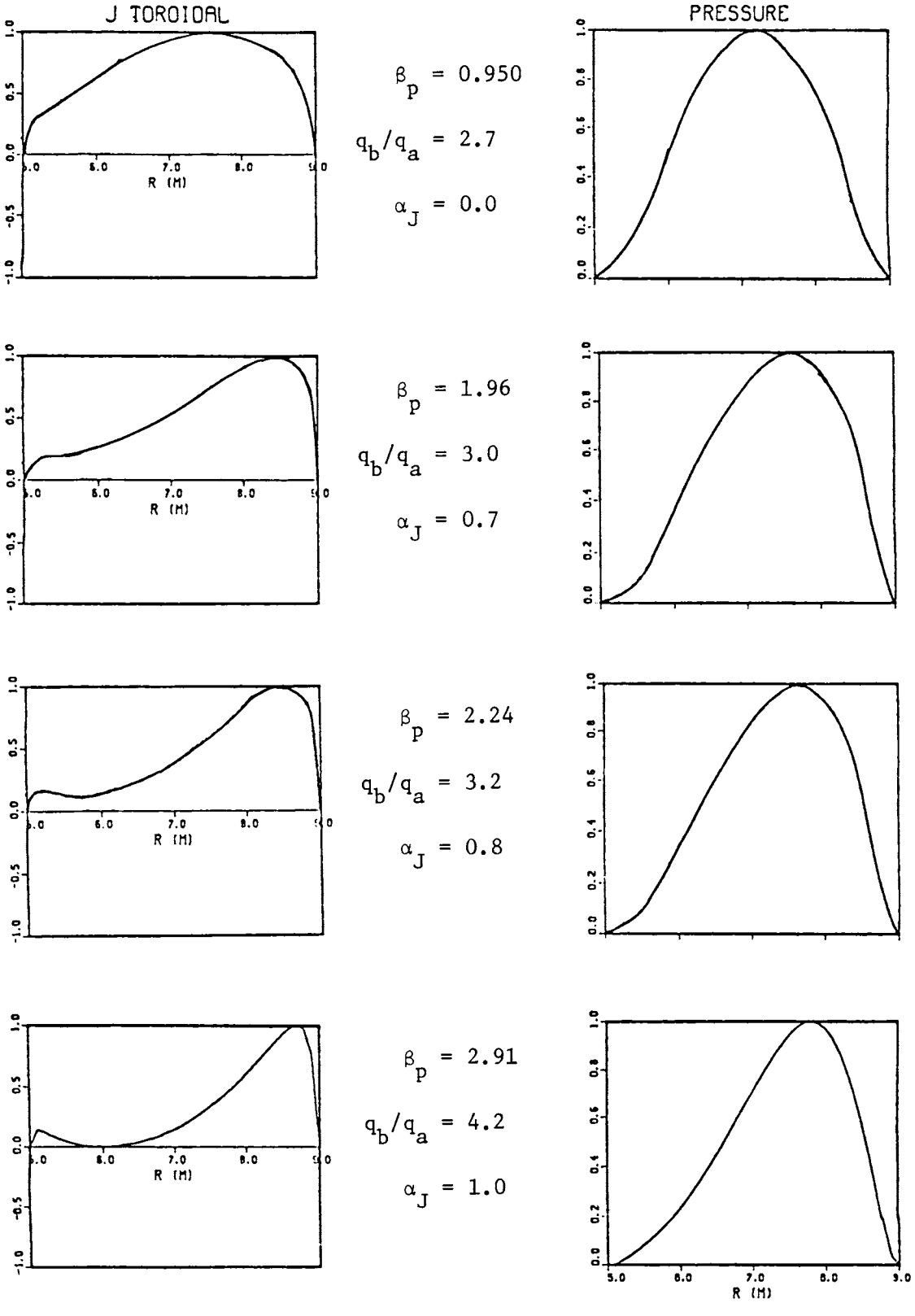

Figure 7-19. Toroidal equilibria during startup showing current density profile evolving from low β_t peaked profiles to a high β_t hollow profile; α_J is proportional to δ and indicates the degree of diamagnetism.

flux conservation should not be a constraint on the STARFIRE current profile.

Prior to 4 s, heating results from ECRH, and at 4 s the lower-hybrid system adds an additional 1.4 MW of heating, as shown by the P_{rf} column in Table 7.6. However, there is not yet any rf current drive, the total I being driven by the EF coils and small OH coil. By 9 s, $\bar{T}_e$ has risen high enough that substantial rf current can be driven. From this point on, I_{rf}, carried by the plateau in the electron distribution function, exceeds the net plasma current, I. This is a result of the reverse emf from -d(LI)/dt which drives ohmic reverse current in such a way as to retard the increase in I. One consequence of this is the long delay from 17 s to 400 s in Fig. 6-18, which is essentially the decay time for the reverse current. In order to obtain $I_{rf} \gtrsim 20$ MA with only 40 MW of rf power it is essential to keep $\bar{n}_e$ low during this period. Once $\bar{T}_e > 6.2$ (after 250 s), all twelve rf ducts are employed, and P_{rf} is raised to 90 MW. Subsequently, as $\bar{n}_e$ is raised to its final value, I_{rf} falls and eventually becomes $I_{rf} = I = 10.1$ MA.

The three special rf ducts for the startup phase have the same vertical dimensions and outside horizontal dimension as the unit shown in Fig. 7-15, but they differ by having 36 openings (instead of 18) with narrower b = 1.375 cm and thinner septa, d = 0.5 cm. These grills are operated at $\nu = 1.677$ GHz, but the phase difference between guides is adjusted during startup to vary the spectrum. Table 7-7 summarizes the spectra resulting from activating only 18 of the 36 elements with different relative phases. The spectrum is continuously tunable in the range from $n_{\parallel}^c = 4.7$ to $n_{\parallel}^c = 1.58$, as assumed for the startup simulation. The $\Delta\phi = \pi$ phasing has a symmetric spectrum (and cannot drive current), but ε rapidly rises to 0.8-0.9 for the other phasings. By activating more or fewer waveguides the width $\Delta n_{\parallel}$ of the spectral peak may be adjusted, $\Delta n_{\parallel}$ becoming ~ 0.4 when N = 36. The reflection coefficient varies considerably for differing $\Delta\phi$ and fixed plasma edge conditions. It might be necessary, therefore, to actively control x_0 and dn_e/dx during the startup phase in order to obtain the best coupling to the plasma.

The final illustration, Fig. 7-20, displays the results of the cylindrical equilibrium calculation at five times during the startup. The plasma conditions at each time step were taken from Table 7-6. By varying the $n_{\parallel}^c$ values it is evident that central heating and current drive does occur at early times and is followed later by surface current generation. The P_{rf} and I_{rf} values

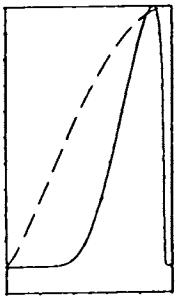

t = 4 s

$n_{\parallel}^{c}$ = 4.7

$\Delta n_{\parallel}$ = 0.8

P_{rf} = 3.0 MW

I_{rf} = 0

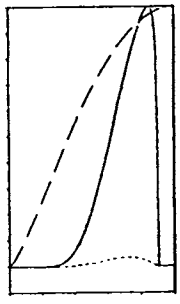

t = 9 s

$n_{\parallel}^{c}$ = 3.1

$\Delta n_{\parallel}$ = 1.2

P_{rf} = 17 MW

I_{rf} = 2.3 MA

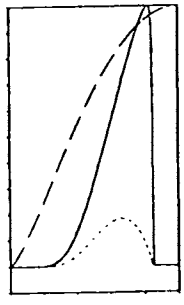

t = 15 s

$n_{\parallel}^{c}$ = 2.1

$\Delta n_{\parallel}$ = 0.8

P_{rf} = 55 MW

I_{rf} = 15.5 MA

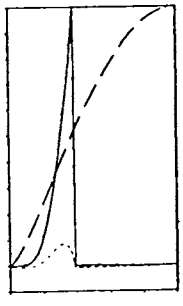

t = 300 s

$n_{\parallel}^{c}$ = 1.63

$\Delta n_{\parallel}$ = 0.46

P_{rf} = 90 MW

I_{rf} = 14.8 MA

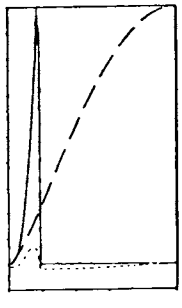

t = 386 s

$n_{\parallel}^{c}$ = 1.63

$\Delta n_{\parallel}$ = 0.46

P_{rf} = 90 MW

I_{rf} = 14.8 MA

Figure 7-20. Cylindrical equilibria during startup. Curves are identified as in Fig. 7-9 except at t = 4 s when the solid curve is rf heating (no rf current density).

Table 7-7. Special Grill Performance for Startup

N = 18, ν = 1.677 GHz, b = 1.375 cm,
d = 0.5 cm, x_0 = 1.0 cm,
$dn_e/dx = 5 \times 10^{10}$ cm^{-4}

$\Delta\phi$	$n_{\parallel}^{c}$	$\Delta n_{\parallel}$
$2\pi/2$	4.7	0.8
$2\pi/2.5$	3.8	0.8
$2\pi/3$	3.1	0.8
$2\pi/4$	2.36	0.76
$2\pi/5$	1.88	0.76
$2\pi/6$	1.58	0.78

in the figure agree qualitatively with the dynamic code values (Table 7-6), derived from the algorithms of Sec. 6.3.1. Quantitative agreement would be expected if the wave damping routine were directly coupled to the dynamic code.

A detailed engineering design of the special grill systems has not been performed, but, on the basis of the analysis in Sec. 7.3, these systems will be similar to the other nine rf assemblies. Therefore, special requirements for these grills will not greatly impact the overall performance and cost of the lower hybrid system. The capital cost (see Sec. 22.5.3.4) for the lower hybrid system is only a few percent of the total power plant cost, so, in view of the attractiveness of starting up with lower hybrid driven currents, the increased complexity of adding the special grills is more than compensated by the enhanced tokamak performance.

References

1. N. J. Fisch, Phys. Rev. Lett. 41, 873 (1978).

2. C. F. F. Karney and N. J. Fisch, Phys. Fluids 22, 1817 (1979).

3. D. J. H. Wort, Plasma Phys. 13, 258 (1971); P. C. Thonemann, W. T. Cowhig and P. A. Davenport, Nature 169, 34 (1952); N. A. Borzunov, et al., Dokl. Akad. Nauk SSR 152, 581 (1963) [Sov. Phys. - Dokl. 8, 914 (1964)]; R. A. Demirkhanov, et al., Zh. Tekh. Fiz. 35, 212 (1965) [Sov. Phys. - Tech. Phys. 10, 174 (1965)]; S. Yoshikawa and H. Yamato, Phys. Fluids 9, 1814 (1966); K. Hirano, K. Matsuura and A. Mohri, Phys. Lett. A 36, 215 (1971); S. M. Osovets and I. A. Popov, Proc. 5th European Conf. on Controlled Fusion and Plasma Physics, Vol. 1 (1972), p. 8; M. Fukuda, et al., J. Phys. Soc. Japan 41, 1376 (1976); M. Fukuda and K. Matsura, J. Phys. Soc. Japan 44, 1344 (1978).

4. D. A. Ehst, Nucl. Fusion 19, 1369 (1979).

5. S. Y. Yuen, et al., Nucl. Fusion 20, 159 (1980).

6. R. Prater, et al., General Atomic Co., GA-A15229 (1978).

7. C. Chu, et al., General Atomic Co., GA-A15027 (1978); R. Klima, et al., Sov. J. Plasma Phys. 5, 277 (1979); N. J. Fisch, et al., Princeton Plasma Physics Laboratory, PPPL-1624 (1979); K. Kato, Phys. Rev. Lett. 44, 779 (1980); D. K. Bhadra, Nucl. Fusion 20, 619 (1980); N. J. Fisch, et al., Princeton Plasma Physics Laboratory, PPPL-1657 (1980).

8. K. L. Wong, Phys. Rev. Lett. 43, 438 (1979); R. McWilliams, et al., Phys. Rev. Lett. 44, 245 (1980); R. J. LaHaye, et al., Nucl. Fusion 20, 218 (1980); K. L. Wong, et al., Princeton Plasma Physics Laboratory, PPPL-1662 (1980).

9. T. Yamamoto, et al., Phys. Rev. Lett. 45, 716 (1980).

10. B. R. Kusse, Electric Power Research Institute, EPRI-108 (1976); A. Mohri, et al., Proc. 7th Intrrn. Conf. on Plasma Physics and Controlled Nuclear Fusion Research, Innsbruck (IAEA, 1978), Vol. 3, 311; T. Ohkawa, Nucl. Fusion 10, 185 (1970); W. M. Manheimer, et al., Naval Research Laboratory, NRL-MR4142 (1979).

11. M. Porkolab, et al., Phys. Rev. Lett. 38, 230 (1977); M. Porkolab, Phys. Fluids 20, 2058 (1977).

12. M. P. Hacker, et al., General Atomic Co., GA-A14933 (1978).

13. M. Abdou, ed., Argonne National Laboratory, ANL/FPP/TM-100 (1978).

14. T. H. Stix, The Theory of Plasma Waves (McGraw-Hill, New York, 1962).

15. R. J. Briggs, et al., Phys. Rev. Lett. 29, 852 (1972).

16. P. M. Bellan, et al., Phys. Fluids 17, 1592 (1974).

17. P. M. Bellan, et al., Phys. Fluids 19, 995 (1976).

18. P. L. Colestock, Nucl. Fusion 18, 740 (1978).

19. R. E. Slusher, et al., Phys. Rev. Lett. 40, 400 (1978).

20. E. Ott, Phys. Fluids 22, 1732 (1979).

21. J. R. Wilson, Phys. Rev. Lett. 43, 1392 (1979).

22. P. H. Sakanaka, et al., Phys. Fluids 17, 919 (1974).

23. L. W. Mann, et al., Nucl. Fusion 19, 1029 (1979).

24. C. Bobeldijk, et al., Proc. 6th Intern. Conf. on Plasma Physics and Controlled Nuclear Fusion Research (IAEA, Vienna, 1977), Vol. 1, p. 493.

25. H. P. Furth, et al., Phys. Fluids 16, 1054 (1973).

26. I. H. Hutchinson, et al., Nucl. Fusion 16, 447 (1976).

27. B. Carreras, et al., Nucl. Fusion 19, 583 (1979).

28. Yu. N. Dnestrovskŭ, et al., Sov. J. Plasma Phys. 5, 289 (1979).

29. B. Carreras, et al., Oak Ridge National Laboratory, ORNL/TM-7161 (1980).

30. T. H. Stix, Phys. Rev. Lett. 36, 521 (1976).

31. B. Carreras, et al., Oak Ridge National Laboratory, ORNL/TM-6570 (1978).

32. J. Hogan, Oak Ridge National Laboratory, Personal Communication (1979).

33. A. H. Glasser, et al., Phys. Rev. Lett. 38, 234 (1977).

34. B. B. Kadomtsev, Sov. J. Plasma Phys. 1, 389 (1975).

35. B. Carreras, et al., Oak Ridge National Laboratory, ORNL/TM-6175 (1978).

36. B. V. Waddell, et al., Oak Ridge National Laboratory, ORNL/TM-6213 (1978).

37. A. Sykes, et al., Phys. Rev. Lett. 44, 1215 (1980).

38. B. Carreras, et al., Oak Ridge National Laboratory, ORNL/TM-6403 (1978).

39. A. H. Glasser, et al., Phys. Fluids 19, 567 (1976).

40. R. J. Hastie, et al., Nucl. Fusion 17, 515 (1977).

41. P. K. Kaw, et al., Phys. Rev. Lett. 43, 1398 (1979); B. Coppi, et al., Phys. Rev. Lett. 42, 1058 (1979).

42. J. D. Callen, et al., Proc. 7th Intern. Conf. on Plasma Physics and Controlled Nuclear Fusion Research (IAEA, Vienna, 1978), Vol. 1, p. 415.

43. M. Brambilla, Nucl. Fusion 16, 47 (1976).

44. V. Krapchev and A. Bers, Nucl. Fusion 18, 519 (1978).

45. C. D. Boley, Argonne National Laboratory, ANL/FPP/TM-135 (1980).

46. D. A. Ehst and C. D. Boley, Proc. of the Annual Controlled Fusion Theory Conference, Tucson, Arizona, April 23-25, 1980.

47. B. W. Reed, et al., Princeton Plasma Physics Laboratory, PPPL-1410 (1977).

48. L. Dupas, et al., Proc. 8th Intern. Conf. on Plasma Physics and Controlled Nuclear Fusion Research (IAEA, Vienna, 1980), Paper IAEA-CN-38/T.1.1.(b), to be issued.

49. J. J. Schuss, et al., Phys. Rev. Lett. 43, 274 (1979); T. Fujii, et al., Proc. 7th Intern. Conf. on Plasma Physics and Controlled Nuclear Fusion (IAEA, Vienna, 1978), Vol. 1, 85.

50. M. Porkolab, Masschusetts Institute of Technology, Personal Communication (1980).

51. R. W. Motley, et al., Phys. Rev. Lett. 24, 1799 (1979); R. W. Motley, et al., Princeton Plasma Physics Laboratory, PPPL-1642 (1980).

52. N. Suzuki, et al., Proc. 8th Intern. Conf. on Plasma Physics and Controlled Nuclear Fusion (IAEA, Vienna, 1980), Paper IAEA-CN-38/T.2.3, to be issued.

53. R. E. Collin, Field Theory of Guided Waves (McGraw-Hill, New York, 1960), p. 182.

54. S. Y. Yuen, et al., MIT Plasma Fusion Center, Report RR-79-22 (1979).

55. C. H. Dix and W. H. Aldous, Microwave Valves (Ieffe Books, London, 1966), p. 215ff.

56. "Final Report, Ultra High Power Amplitron," Rome Air Development Center, Report RADC-TDR-64-Vol. I.

57. L. S. Scaturro, et al., Nucl. Fusion 18, 1717 (1978); A. M. Razdow, USDOE Report, CONF-791057 (1979).

58. R. W. Motley, et al., Nucl. Fusion 20, 222 (1980); R. W. Motley, Princeton Plasma Physics Laboratory, PPPL-1651 (1980).

59. R. W. Harvey, et al., Nucl. Fusion 19, 1529 (1979).

TABLE OF CONTENTS

LIST OF FIGURES

LIST OF FIGURES (Contd.)

LIST OF TABLES

LIST OF TABLES (Contd.)

8.1 INTRODUCTION

Previous reactor design studies have shown that plasma impurity control and exhaust is one of the most difficult systems in tokamaks. Therefore, the STARFIRE study has devoted a significant effort to the development of a credible and attractive design for this system. This chapter develops the design concept and presents detailed analyses to support the design choices and to predict the performance characteristics of the reference impurity control and exhaust system in STARFIRE.

An assessment of the impurity control and exhaust system based mostly on previous work in this area identified five basic problems: (1) high heat load on the particle collection medium; (2) high tritium inventory in the fueling system and vacuum pumps; (3) very large vacuum-pumping speed requirements; (4) significant neutron and gamma-ray streaming through the vacuum ducts leading to high heat loads on the pumping cryopanels and difficult shielding requirements; and (5) engineering complexity inherent to some specific concepts for plasma ash removal. The STARFIRE approach to solving these problems is discussed below.

The origin and solution to the first problem of high heat load on the particle collection medium are highly dependent on the characteristics of plasma operation. In steady-state, the alpha power plus any auxiliary heating power must be removed from the plasma region. In STARFIRE, the alpha power is 700 MW and the rf power is 90 MW, giving a total of 790 MW. In conventional designs, only less than half of this energy is radiated leaving more than 400 MW to be transported to the particle collection medium. Previous designs for divertors showed that the surface area of the particle collection medium is limited to $\sim$20 m^2. For these designs, the average heat load would be >20 MW/m^2 and, given the fact that the particle heat load drops exponentially across the scrape-off region, the peak heat load would be >50 MW/m^2. Such an extremely high heat load is beyond the capability of any suitable structural material. The STARFIRE approach to solving this problem consists of two parts:

(a) Enhancing plasma radiation to reduce the transport power to the particle collection medium. This is accomplished by injecting small amounts of high-Z material (iodine) along with the DT fuel. Most of the alpha energy is thus radiated to the first wall which has a large surface area.

(b) Increasing the surface area of the collection medium. One convenient method of accomplishing this is to minimize the angle between the direction of incidence of the charged particles and the surface of the collection medium. There are limitations on the size and position of the collection medium, which vary from one impurity control concept to another.

The second, third, and fourth problems of high tritium inventory, large pumping speeds, and troublesome radiation streaming are strongly interrelated as to the origin of the problems and the approach to solving them. Previous studies strived to achieve a high helium removal efficiency approaching unity. This removal efficiency is defined as the probability that a particle diffusing out of the plasma will be pumped rather than reflected into the plasma. By requiring a helium removal efficiency of $\sim$1, the fraction of deuterium (D) and tritium (T) recycled into the plasma (reflection coefficient) becomes low and the gas load to the vacuum pumps increases. A low tritium reflection coefficient results in a low tritium fraction burnup and an increase in the tritium inventory requirements in the fueling system. The increase in the DT gas load in the vacuum pumping system leads to an increase in (a) the tritium inventory in the vacuum pumps; (b) the required pumping speed; and (c) the required capacity of the vacuum pumps. The intensity of radiation streaming is critically dependent on the size and shape of the vacuum ducts. Again, requiring high helium removal efficiency requires a high conductance vacuum pumping system, which can only be realized by large-size vacuum ducts with no significant bends.

A key part of the STARFIRE solution to these problems is to design for only a modest helium removal efficiency. As will be discussed in Sec. 8.3, it can be shown that steady-state plasma operation is achievable with a helium removal efficiency as low as 10-20%. The penalty of such a low removal efficiency is a high alpha particle equilibrium concentration in the plasma. In STARFIRE, this is compensated for by a modest increase in the strength of the toroidal field to keep the fusion power the same. It should be noted that the significant charge-exchange with hydrogen tends, in general, to make the tritium removal efficiency lower than that for helium.

The solutions outlined for the four problems above can be applied to any design concept for impurity control and exhaust. However, the degree of success varies considerably from one concept to another. This degree of success is an important figure of merit in selecting a design concept.

The fifth problem of engineering complexity is specific to the particular design concept selected for the impurity control and exhaust system. The magnitude of the problem is greatly dependent on the configurational and component requirements of the specific concept and how they integrate with the rest of the reactor system. Divertor and divertorless concepts were surveyed. Present design concepts for poloidal and bundle divertors are found to be inherently complex. Specifically, they require magnets, enhance radiation streaming, complicate maintenance, and significantly increase the physical size of the reactor. Therefore, it seems prudent to seriously explore divertorless concepts.

An evaluation of divertorless schemes shows that the "pumped limiter" (also called limiter/vacuum system) is an attractive concept with many inherently simple features that are very desirable in a commercial power reactor. Among the advantages of the limiter/vacuum system, as compared to divertors, are:

(1) It is a mechanical system that does not require magnets.

(2) It has minimal requirements on space; the limiter fits naturally into the scrape-off region.

(3) Because of its location inside the first wall, the surface area available for the limiter is relatively large, thus permitting operation at reasonable heat fluxes.

(4) The system is flexible enough to permit designing for low hydrogen removal efficiency; this leads to higher tritium fractional burnup, low tritium inventory, reduced gas loads, and more attractive requirements for the effective pumping speed.

(5) The limiter/vacuum system can be designed to dramatically reduce radiation streaming.

(6) The limiter can be replaced simultaneously with the first wall with no special maintenance requirements.

(7) The system is simple and inexpensive. This feature is not only attractive for reactor maintainability and economics, but it also means that the physics and engineering testing necessary to qualify the concept can be done in present facilities, in a relatively short time and at a modest cost.

Several variants of the limiter were discussed earlier in the literature (see for example, Refs. 1-6). The present work represents the first comprehensive attempt to develop a detailed design supported by physics and engineering analyses.

Section 8.2 introduces the limiter/vacuum system concept and summarizes the reference design. The plasma engineering considerations of impurity control and exhaust are discussed in Sec. 8.3. The engineering aspects of the limiter are analyzed in Sec. 8.4. These include structural and coating materials, thermal hydraulics, stresses, neutronics, and electromagnetic considerations. The analyses include both steady state and off-normal conditions. Section 8.4 is concluded with a description of the mechanical design for the limiter and its support. Tradeoffs and design analysis for the vacuum system are presented in Sec. 8.5.

8.2 REFERENCE DESIGN SUMMARY

A serious effort has been made in the STARFIRE study to develop a plasma impurity control and exhaust system that satisfies the following goals: (1) have manageable heat loads in the medium where the alpha and impurity particles are collected; (2) have a reasonable and reliable vacuum system that minimizes the number and size of vacuum ducts; (3) have a high tritium burnup to minimize the tritium inventory in the fuel cycle; and (4) have engineering simplicity compatible with ease of assembly/disassembly and maintenance.

These goals are found to be best satisfied by a toroidal limiter/vacuum system together with a beryllium coating on the first wall, limiter, and all other surfaces exposed to the plasma. In order to minimize the heat load to the limiter, most of the alpha-heating power to the plasma is radiated to the first wall, by injecting a small amount of high-Z material, e.g. iodine, along with the DT fuel stream. The iodine atoms enhance the line-and-recombination X-ray radiation over most of the plasma volume. The helium removal efficiency of the limiter/vacuum system is intentionally kept low for three reasons: (1) to reduce the heat load on the limiter; (2) to simplify the vacuum system and reduce radiation streaming; and (3) to minimize the tritium inventory tied up in the vacuum and tritium processing systems. The major features of the STARFIRE impurity control and exhaust system are summarized in Table 8-1.

Table 8-1. Major Features of STARFIRE Impurity Control/Exhaust

- A limiter/vacuum system
  - — One toroidal belt-type limiter centered around midplane
  - — Simple, inexpensive, credible engineering
- Low-Z coating (beryllium) on all surfaces exposed to plasma
- Enhanced plasma radiation
  - — To reduce heat load at collection plate
  - — Achieved by injecting small amount of iodine
- A low helium removal efficiency (25%)
  - — Much simpler vacuum system
  - — Less radiation streaming
  - — High tritium burnup, low tritium inventory
  - — Penalty: Modest increase in toroidal field (0.85 T on axis)
- Simple vacuum system
  - — Limiter duct penetrates blanket leading to a plenum region between blanket and bulk shield
  - — Significantly reduced radiation streaming; less shielding and lower nuclear heat load in cryopanels

Figure 8-1 shows a cross section through the limiter, the limiter slot, the limiter duct, and the plenum region. The limiter consists of 96 segments that form one toroidal ring centered at the midplane and positioned at the outer side of the plasma chamber. This location was selected because: (1) it is the least likely place for a thermal energy dump from a plasma disruption; and (2) it helps the symmetry in particle and heat loads on the upper and lower branches of the limiter. Each of the limiter segments is 1 m high and $\sim$0.6 m wide. The physical dimensions of the system are shown in Fig. 8-1. The limiter slot, which is the region between the limiter and first wall, leads to a 0.4-m high limiter duct that penetrates the 0.7-m thick blanket. The limiter duct opens into a plenum region that is located between the blanket and shield and extends all the way around the torus. This plenum region is large enough so that it spreads the radiation leakage from the limiter duct into a larger surface area of the bulk shield. The conductance of the plenum region is large

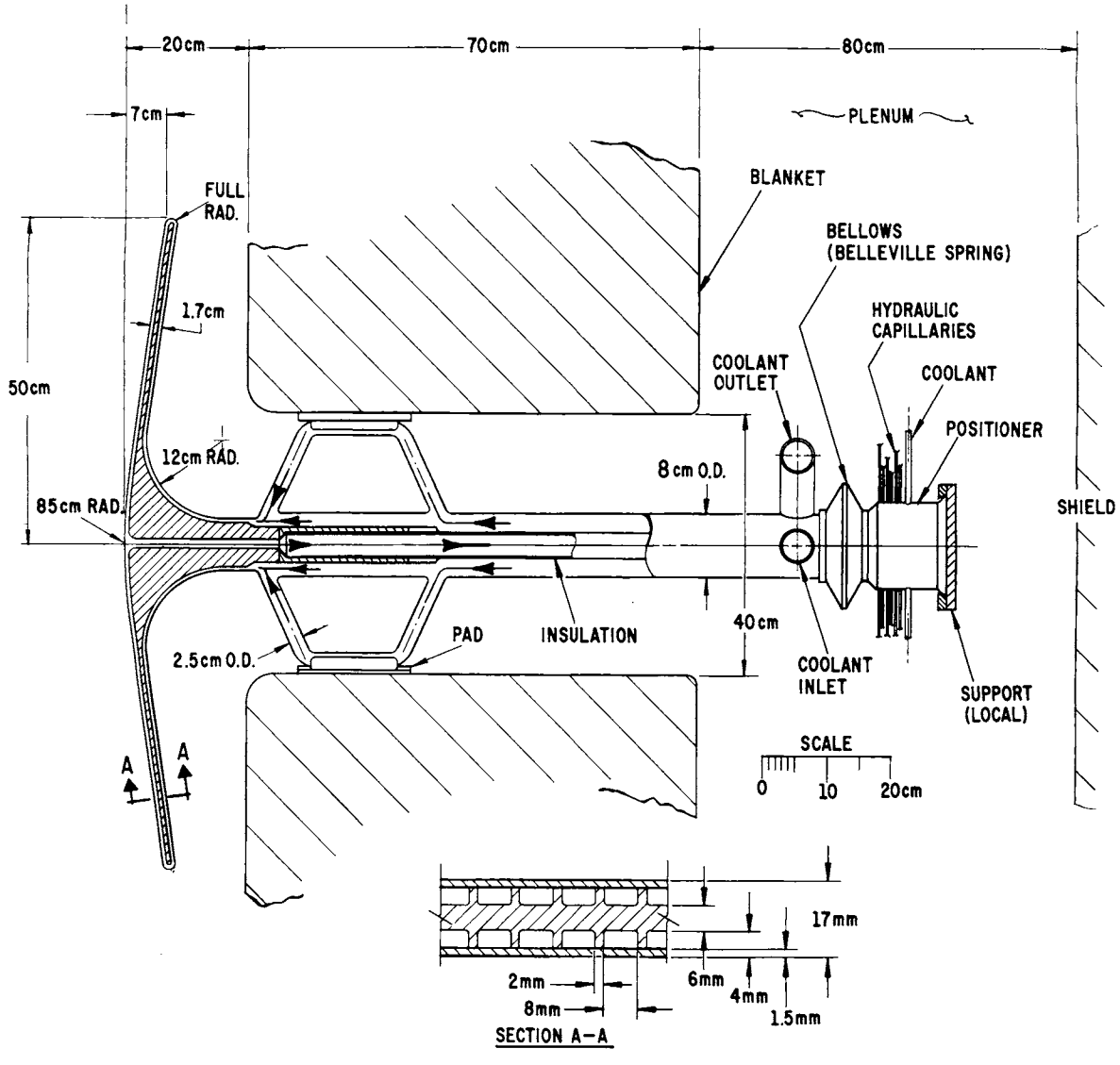

Figure 8-1. Cross section of the STARFIRE limiter design.

enough to permit locating the vacuum ducts in the bulk shield sufficiently removed from the midplane so that radiation streaming from the limiter duct in the blanket to the vacuum pumps is acceptable. There are 12 vacuum ducts at the top and another 12 at the bottom of the reactor. Each of these vacuum ducts has an equivalent diameter of 1 m and penetrates the bulk shield leading to the vacuum pumps.

The basic principles of how the limiter works are rather simple. Ions that hit the front face of the limiter will be neutralized and reflected back into the plasma. Ions that fall into the limiter slot hit the back surface and are neutralized. Some of the scattered neutrals will directly reach the limiter duct and follow a multiple-scattering path into the plenum region and out the vacuum ducts where they are removed by the vacuum pumps. Other particles neutralized at the back surface of the limiter will scatter back in the direction of the plasma. These neutrals have a high probability of being ionized and returned back to the limiter surface. Calculations show that this trapping or "inversion" effect is so large for helium that ∿90% of the helium entering the limiter slot will get pumped. This inversion effect greatly simplifies the limiter/vacuum system design in at least two ways:

(1) Location of the Leading Edge: Since the helium inversion probability is very high, the fraction of particles that enters the limiter slot needs to be only slightly greater than the helium removal efficiency. This permits locating the two leading edges at the top and bottom of the limiter sufficiently away from the plasma edge and inward into the scrape-off region so that the peak heat flux at the leading edge is reasonably low.

(2) Neutral Pressure: This inversion effect causes the neutral gas pressure at the limiter duct to be considerably higher than the neutral pressure around the plasma. Such hign pressure greatly simplifies the vacuum system design.

Hydrogen can charge-exchange as well as be ionized. These charge-exchange events significantly reduce the inversion probability for hydrogen because the resulting neutral will tend to make its way out of the slot region into the plasma. Therefore, the beneficial effect of higher helium pumping probability and enhanced hydrogen recycling into the plasma is obtainable with the limiter/vacuum system.

The plasma parameters related to the impurity control and exhaust system are shown in Table 8-2. The design parameters for the limiter are shown in Table 8-3.

Table 8-2. Plasma-Related Parameters

Fusion alpha power (P_α), MW	703
Lower-hybrid power to plasma (P_{LH}), MW	90
Transport power to the limiter, MW	90
Helium production rate, (particles per second)	1.24×10^{21}
Alpha particle concentration (n_α/n_{DT})	0.14
Beryllium (low-Z coating) concentration (n_{Be}/n_{DT})	0.04
Iodine (radiation enhancement) concentration (n_I/n_{DT})	1.0×10^{-3}
Helium reflection coefficient, R_α	0.75
Toroidal-field margin at plasma center, T	0.85
Scrape-off region thickness, m	0.2
Particle confinement time (τ_p), s	1.8
Particle e-folding distance in scrape-off zone (δ_p), cm	10
Energy e-folding distance in scrape-off zone (δ_E), cm	5
Plasma-edge temperature (T_{edge}), keV	1.2

The charged particle flux in the scrape-off region falls off exponentially as e^{-x/δ_p} with δ_p = 10 cm and x as the distance into the scrape-off region. About 28% of the helium particles diffusing out of the plasma will fall into the limiter slot, i.e. between x = 8.7 cm and x = 20 cm. The transmission (pumping) probability for these particles is 0.9 giving an overall helium reflection coefficient R_α = 0.75 and helium removal efficiency (1 - R_α) of 0.25. The reflection coefficient for deuterium/tritium is 0.9.

The transport heat flux on the limiter (due to charged particles) varies as 16 e^{-x/δ_E} sin θ in units of MW/m^2 with x in cm, δ_E = 5 cm, and θ being the angle between the field lines in the poloidal plane (nearly vertical in Fig. 8-1) and the surface of the limiter. The limiter surface from the tip (at the plasma edge) to the top (or bottom) leading edge is slanted to spread the heat

Table 8-3. Limiter Design Parameters

Coolant	Water			
Reference structural materials	Ta-5W, AMAX-MZC, FS-85, or V-20Ti			
Low-Z coating material	Beryllium			
Total heat removed from limiter, MW (90 MW transport, 56 MW radiation plus neutrals, and 54 MW nuclear)	200			
Average surface heat load, MW/m^2	2.3			
Peak surface heat load,[a] MW/m^2	4			
Coolant inlet temperature, °C	115			
Coolant outlet temperature (2-pass), °C	145			
Coolant pressure, MPa (psia)	4.2 (600)			
Coolant channel size, mm × mm	8 × 4			
Wall thickness, mm	1.5			
Maximum temperature, °C	Ta-5W	AMAX-MZC	FS-85	V-20Ti
Water side	193	182	192	191
Coating side	290	196	404	449

[a]Includes transport load (3.4 MW/m^2) plus load from radiation and charge-exchange neutrals.

load. The leading edge (region where $\theta = 0$ occurs) forms approximately one-half a cylindrical shell with a diameter of 1.7 cm and extends from $x \sim 7$ cm to $x \sim 8.7$ cm. The location of the leading edge was determined from tradeoffs between the helium removal efficiency (and the associated toroidal-field margin) and the peak heat flux. The peak transport heat flux is ~ 3.4 MW/m^2 and occurs at $x \sim 7.8$ cm. The average transport heat flux on the region of the leading edge is ~ 2.2 MW/m^2. The front surface of the limiter (from the tip to the leading edge) receives an additional surface heat load of 0.9 MW/m^2 due to plasma radiation and charge-exchange neutrals. The magnitude of the volumetric nuclear heating depends on the specific limiter material and is in the range of 30 to 80 MW/m^3 for the materials to be discussed shortly.

Water is selected as the limiter coolant because of its good heat transfer characteristics. This choice is consistent with the use of water cooling in the first wall and blanket. The limiter segments are connected so that the coolant passes through two segments (2 passes). The water inlet temperature to the first pass is 115°C and, with a temperature rise of 15°C per segment, the outlet temperature is 145°C for the second pass. The coolant pressure is 4.2 MPa (600 psia). The water temperature is kept low to minimize pressure stresses. Since the 200 MW of heat removed from the limiter represents only 5% of the reactor thermal power, this heat is used effectively for feedwater heating in the steam cycle without significant loss in thermal efficiency.

A large number of materials were evaluated as to their suitability for the limiter structure. The evaluation included the capability of withstanding high heat fluxes, resistance to radiation damage, fabricability, and compatibility with the surrounding environment. This resulted in identifying four reference alloys as the primary candidate materials. These included a copper alloy AMAX-MZC, and the refractory metal alloys of vanadium (V-20Ti), niobium (FS-85), and tantalum (Ta-5W). Three-dimensional thermal-hydraulic, and stress analyses were carried out for these four materials. A summary of the results is shown in Table 8-4.

Table 8-4. Thermal/Stress Analysis of Candidate Limiter Materials[a,b]

	Temperature (°C)		Maximum Effective Stress (MPa)	Yield Stress (MPa)	Effective / Yield
	Outer	Inner			
Tantalum, Ta-5W	290	193	249	342	0.7
Niobium, FS-85	404	192	370	370	1.0
Vanadium, V-20Ti	449	191	537	452	1.2
Copper, AMX-MZC	196	182	178	431	0.4

[a] Coolant: Pressure = 600 psi, T_{in} = 115°C, T_{out} = 145°C
Channels = 4 × 8 mm, 1.5 mm thick at outer side.

[b] Peak heat load = 4 MW/m^2.

The limiter wall temperature at the coolant side is essentially the same, <200°C, for all materials with small differences due to axial conduction. At this low temperature, the corrosion rate of these materials in water should be acceptable. The maximum temperature in the structure (coating side) varies from 196°C in copper to 449°C in vanadium reflecting the large difference in the thermophysical properties. The ratio of the effective stress to the yield stress is also shown in Table 8-4. These results indicate that under normal operating conditions, all of the materials meet the allowable stress criteria of the ASME Code Case 1592. However, only AMAX-MZC and Ta-5W can meet the more restrictive criteria of 0.75 of the yield strength. Since the thermal stress component dominates the total stress in the limiter, the materials with the highest thermal conductivity and lowest thermal expansion will experience the lowest stress. It should be noted, however, that the results in Table 8-4 are based on conservative assumptions. Furthermore, several modifications in the reference limiter design that can significantly reduce the thermal stress have been identified and are discussed in Sec. 8.4. Therefore, all the four alloys in Table 8-4 are considered viable candidates and the selection of one of them must be made based on additional data from future experimental results in areas such as resistance to radiation damage.

The impact of a specific material choice for the limiter on the performance of other reactor components is very small. For the purposes of this report, all the four alloys identified in Table 8-4 are considered as reference materials. The small differences that may result in the reactor design due to the choice of any of these four materials will be noted where appropriate.

The limiter and the first wall are coated with beryllium to eliminate sputtering of the underlying high-Z structural materials. Beryllium is selected as the low-Z coating because its properties make it superior to other candidates. Estimates of the erosion of the beryllium coating were made. The coating on the first wall will erode at a rate of 0.14 mm/yr; therefore, a 1.2-mm coating is adequate for a 7-yr life. The limiter coating will sputter by all ion species with a spatially varying rate. Redeposition of beryllium from the plasma and first wall will also occur. The net effect is that the coating will erode on the wall while it grows on the limiter. The STARFIRE design is developed such that there is no net erosion or growth on the leading edge. This is accomplished by maintaining a beryllium density in the plasma of $\sim$4% of the hydrogen ion density. There will be a net growth of beryllium

on the rest of the limiter averaging ∿0.6 mm/yr. A simple grinding process in place can be performed if necessary to restore the beryllium coating to its original thickness.

The response of the limiter to off-normal conditions was considered as an integral part of the design. The important off-normal events are: (1) plasma disruptions; and (2) loss-of-coolant flow. The concerns with plasma disruptions are the thermal energy dump and the induced electromagnetic forces. The limiter is intentionally located at the outer side of the plasma and centered around the midplane, where a plasma energy dump is least likely. However, in the unlikely event that a plasma thermal energy dump on the limiter occurs, only the coating will be affected. The rate of ablation of beryllium is small enough that several disruptions per year with the thermal energy dump on the limiter can be tolerated.

The electromagnetic forces will always be induced in the limiter in the case of a plasma disruption regardless of where the plasma energy dump occurs. Three electromagnetic effects are produced, with the magnitude strongly dependent on the plasma disruption (current decay) time. The first is a uniform pressure, acting on the outside panels of the limiter. For a plasma disruption time of >10 ms, the maximum induced stress due to this uniform pressure is 0.6 MPa (90 psi), which is a small fraction of the yield stress for the copper, tantalum, niobium, and vanadium alloys. The second effect is a force tending to bend the limiter arm about a toroidal axis. Accommodating this force required an iterative process in the limiter design. In particular, providing a thick root for the limiter (see Fig. 8-1) was found necessary to reduce the moment arm and the magnitude of the force. With the present reference design, the maximum bending stress is ∿154 MPa (22,000 psi), which is <40% of the yield stress for the reference structural materials when the plasma disruption time is >10 ms. The third electromagnetic effect is a torque that tends to twist the limiter about a radial axis. For a plasma disruption time of 10 ms, the maximum torque is 46 KN-m resulting in an effective stress which is <60% of the yield stress for all of the four primary structural materials. The magnitude of these forces and torques is reduced substantially at longer, and perhaps more realistic, plasma disruption (current decay) times. The reference limiter design can withstand the electromagnetic effects without any permanent deformation for an unlimited number of plasma disruptions.

The major components of the vacuum system are shown in the STARFIRE reactor cross section of Fig. 8-2. The design parameters for the vacuum system are given in Table 8-5. The vacuum system consists of the limiter slots, limiter ducts, plenum region, vacuum ducts, and vacuum pumps. There are 48 compound cryopumps operating on 24 vacuum ducts. Two pumps are provided on each duct so that regeneration can be accomplished during plasma operation. Each pump has a rated helium pumping speed of 120 m^3-s^{-1}. The vacuum system is designed to produce a base pressure of $\sim 1.3 \times 10^{-6}$ Pa (10^{-8} torr). Tritium inventories in the pumps are minimized by the achievement of a very high tritium fractional burnup (42%) and by minimizing the pump regeneration time (2 h). The maximum tritium inventory in a single pump is only 2.6 g.

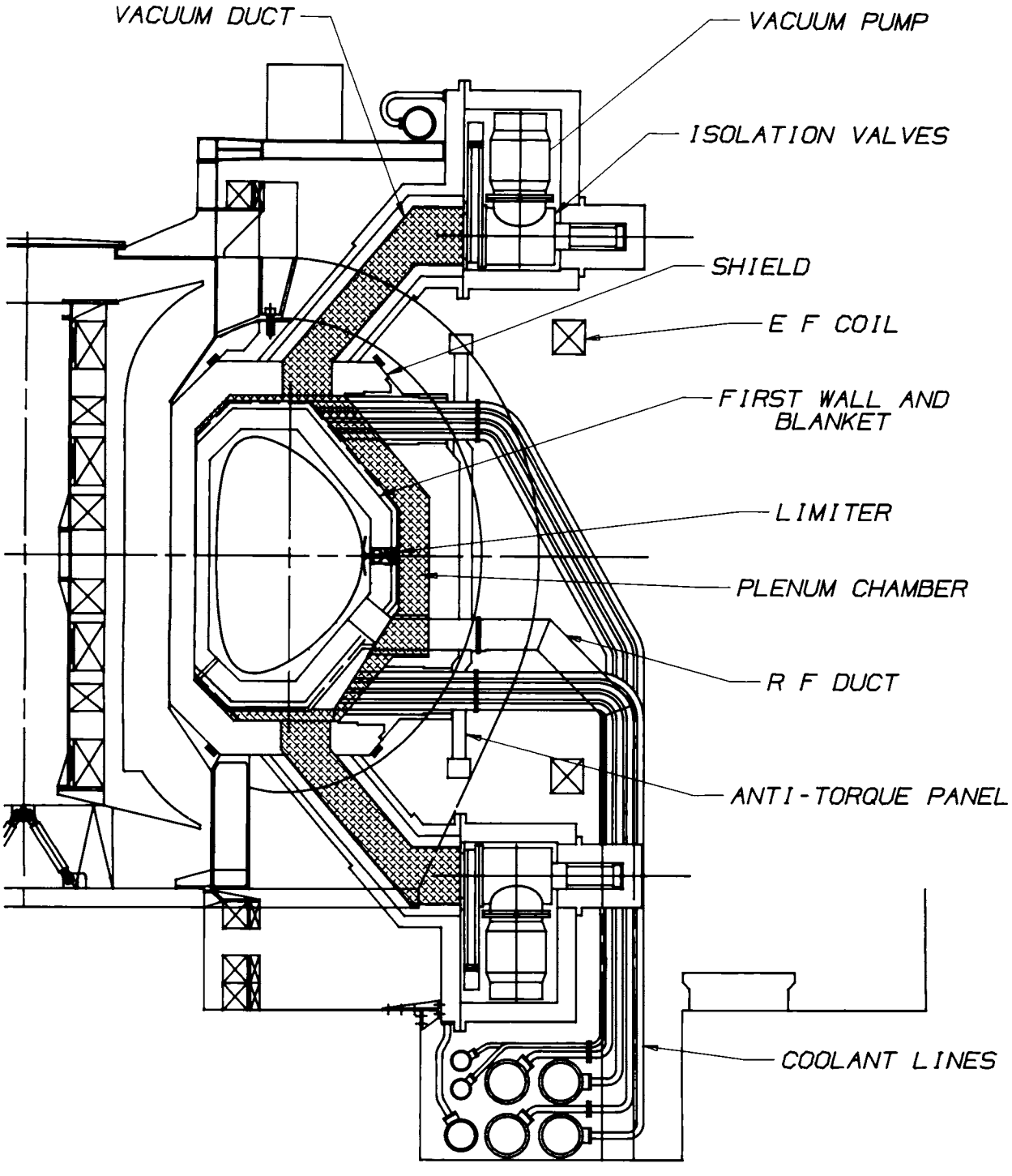

Figure 8-2. A cross section of the STARFIRE reactor showing the components of the vacuum system.

Table 8-5. Vacuum System Parameters

Component	Dimensions (cm)	Conductance (m^3/s)
Limiter slots (2)	5650 × 10 × 50	4300
Limiter ducts (2)	3170 × 16 × 70	4100
Plenum	6000 × 67 × 600	13700
Vacuum ducts (24)	100 × 640 120 × 560	730
Vacuum pumps (24)	——	2900

Rated helium speed per pump, m^3/s	120
Rated DT speed per pump, m^3/s	200
Total helium pumping speed, m^3/s	490
Transmission probability[a] (helium)	0.9
Reflection coefficient (helium), R_α	0.75
Maximum helium pressure, Pa	0.016
Total DT pumping speed, m^3/s	480
Transmission probability[a] (DT)	0.40
Reflection coefficient (DT), R_{DT}	0.9
Maximum DT pressure, Pa	0.024
Tritium fractional burnup	0.42
Total gas load, Pa-m^3/s	18.7
DT gas load, Pa-m^3/s	10.85
Helium gas load, Pa-m^3/s	7.85
Temperature, °K	573
Number of vacuum pumps, on-line/total	24/48
Regeneration time, h	2
Maximum tritium inventory per pump, g	2.6

[a]Transmission probability per particle entering the limiter slot.

8.3 PLASMA ENGINEERING FOR THE LIMITER/VACUUM SYSTEM

8.3.1 Introduction

As discussed in the previous section the impurity control system for STARFIRE is based upon a limiter/vacuum system which collects and pumps some of the particles diffusing out of the plasma. Both the limiter and the first wall are coated with a layer of beryllium to eliminate sputtering of the underlying high-Z structural materials. In addition to these measures, the toroidal field coils are designed with sufficient field capability to accommodate a moderately high concentration of helium in the plasma.

In order to minimize the heat load to the limiter, most of the alpha-heating power to the plasma is radiated to the first wall, by injecting a small amount of iodine, along with the DT fuel stream. The iodine atoms enhance the line-and-recombination X-ray radiation over most of the plasma volume. The helium removal efficiency of the limiter/vacuum system is intentionally kept low for two reasons: (1) to reduce the heat load on the limiter; and (2) to minimize the tritium inventory tied up in the vacuum and tritium processing systems.

In order to have an equilibrium in the plasma, helium must be removed at the same rate that alpha particles are being produced. However, as discussed in Ref. 4, it is only necessary to remove a fraction of the helium ion outflux to achieve steady-state conditions. In particular, the steady-state concentration of helium in the plasma scales with the helium reflection coefficient, R_α, of the impurity control system as $N_\alpha \sim 1/(1 - R_\alpha)$. Although N_α is minimized by removing all of the helium outflux, values of R_α as high as 0.9 (i.e. 10% pumping) were shown in Ref. 4 to still yield reasonable values of helium concentration. Because at least some tritium is removed along with the helium, there is an incentive to operate at a high value of R_α in order to minimize the tritium throughput in the vacuum and tritium processing systems.

The specific dimensions of the STARFIRE limiter depend on estimates for the transport heat load and on the various scrape-off parameters. While these are somewhat uncertain at this time, a parametric analysis has shown that the overall limiter concept is not very sensitive to many of these parameters. For example, if the heat load were doubled, due for example to a lower than expected value of the energy containment time, it would still be possible to design an effective limiter, though at somewhat reduced performance.

The function of the beryllium coating in STARFIRE is to eliminate sputtering of the structural materials of the limiter and first wall, both of which could lead to unacceptable amounts of high-Z material in the plasma. A critical issue for low-Z coatings is their erosion by sputtering. Although an estimate of erosion for the wall coating depends on uncertain estimates of the neutral charge-exchange flux, it appears that a 1-mm thick beryllium wall coating would last about 7 yr, approximately the same as the lifetime of the wall structural material. Recoating the wall could be done during a maintenance period as described in Chaps. 10 and 19. The erosion problem of the limiter is reduced considerably by the fact that beryllium ions arriving at the limiter will tend to stick and recoat the surface at the same time that sputtering tends to erode it. Because beryllium sputtered from the wall generally will be transferred to the limiter, and because additional beryllium can also be added to the plasma, it appears that instead of erosion, the coating can be made to grow on the limiter. While definitive work in this area must await a vigorous experimental program, it appears that the coating growth can be held to a maximum of 1.7 mm/yr at the front tip of the limiter. This would permit a multi-year operation before a simple grinding process would be needed.

8.3.2 Physics of the Scrape-off Region

In this section, estimates for the particle and energy fluxes to the limiter are developed. A coordinate system for this discussion is shown in Fig. 8-3. The tip of the limiter, on the front face, defines the start of the scrape-off zone. For present day tokamaks, the charged particle flux in the scrapeoff has been shown, by probe measurements, to fall off exponentially as e^{-x/δ_p} where x is the distance into the scrape-off zone (see Fig. 8-3) and δ_p is the e-folding distance for particle flow.[7-9] Such a fall-off can be explained by the simple argument of flow along the field lines and diffusion perpendicular to the field lines.[10] The value of δ_p for present devices is $\sim$2 cm, the exact value depending on the size of the device and on the type of limiter used.[7-9] The value of δ_p for STARFIRE can be estimated by considering a particle that, on its orbit around the torus, has just missed hitting the limiter tip. In order to return to the vicinity of the limiter, the particle must make one revolution poloidally and hence q revolutions toroidally, where q is the safety factor at the plasma edge. In so doing, the particle diffuses outwards in minor radius and hits the limiter at an average (rms) distance of

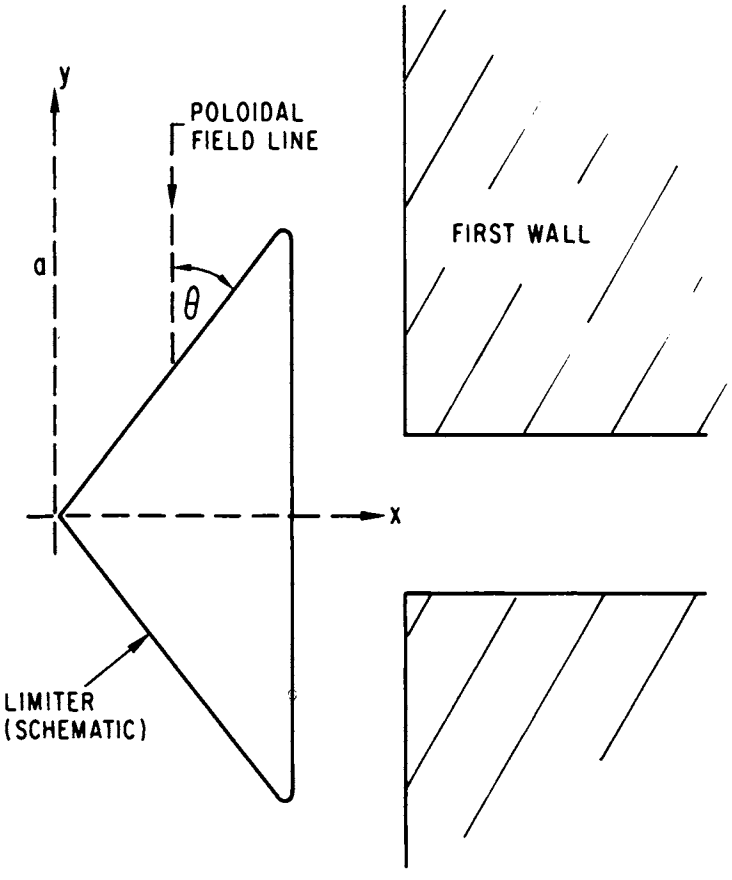

Figure 8-3. Limiter coordinate system.

δ_p from the tip. This distance is given by $\delta_p = \sqrt{D_\perp \tau}$, where $D_\perp$ is the radial diffusion coefficient characteristic of the edge region, and τ is the time for the particle to return to the limiter. This time is given by $\tau = L/V_\parallel$, where L is the path length travelled and $V_\parallel$ is the speed along the field line. For the typical conditions of Bohm diffusion, flow velocity at the sound speed,[10] an ion mass of 2.5 AMU, and for $T_e \approx T_i$ at the edge:

$$D_\perp(m^2/s) = 0.063 \frac{T_e(eV)}{B(T)}$$

$$V_\parallel = \sqrt{KT_e/M_i} .$$

The particle e-folding distance is then:

$$\delta_p(m) = 3.18 \times 10^{-3}\sqrt{L/B}\, T_e^{1/4} . \quad (1)$$

where L is in meters, B is in tesla, and T is in eV.

Experimentally, there is some ambiguity concerning the values of the diffusion coefficient and the sound speed in the scrape-off region. However, if the diffusion coefficient were a fraction C_1 of Bohm and the speed were a fraction C_2 of the sound speed, then δ_p in Eq. (1) would only change by the factor $\sqrt{C_1/C_2}$. Accordingly, there is a broad combination of C_1's and C_2's that would give rise to the same value of δ_p.

For the STARFIRE limiter system, $L = 2\pi Rq$ where R = 7 m is the major radius and q = 5.1, giving L = 224 m. The computed electron-edge temperature for STARFIRE (see Sec. 8.3.3.1) is 1200 eV. Although there are uncertainties in this value, there is only a very weak, fourth-root dependence of δ_p on T_e. Using T_e = 1200 eV and the value of B_0 = 5.8 T in the plasma center as an average value in Eq. (1) gives a value for δ_p of ~10 cm, which has been taken as the STARFIRE reference value. The value of δ_p does not appear to be critical to the limiter concept as discussed in Sec. 8.2.6. However, if it were necessary, or desirable, it might also be possible to control this value. For example, turbulence introduced by applying low-frequency rf waves to the plasma edge might serve to spread out the particle flux.

The power or energy heat flux to the limiter depends on the temperature fall-off rate as well as the particle fall-off rate. A number of calculations[10,11] have predicted that plasma temperature will fall off at about the same rate as particle flux and this is generally supported by probe measurements.[7-9] This has accordingly been assumed for STARFIRE. The energy flux to the limiter is proportional to the product of particle flux and particle temperature and will therefore fall off at a rate given by e^{-x/δ_E} where $\delta_E = \delta_p/2$ = 5 cm is defined as the energy e-folding distance. More generally, the heat flux to both the top and bottom of the limiter can be expressed as:

$$q(x) = q_0 e^{-x/\delta_E} \sin\theta , \quad (2)$$

where the first two terms on the right-hand side of Eq. (2) represent the heat flux perpendicular to the plane y = ±a and the sin θ term represents the effect of spreading the heat out geometrically (see Fig. 8-3). The angle θ is the

angle that the poloidal field lines make with the limiter (at the location of the limiter these poloidal field lines are almost exactly vertical). The constant q_0 is given by:

$$P_{TR}^{lim} = N_S 2\pi R_L q_0 \int_0^{\infty} e^{-x/\delta_E} \, dx \, , \tag{3}$$

where P_{TR}^{lim} is the transport heat load to the limiter, $N_S = 2$ is the number of limiter surfaces (top and bottom), and $2\pi R_L$ is the circumference of the limiter where $R_L = 9$ m is the limiter major radius. Equation (3) gives for q_0:

$$q_0 = \frac{P_{TR}^{lim}}{N_S 2\pi R_L \delta_E} \, . \tag{4}$$

For a value of $P_{TR}^{lim} = 90$ MW (see Chap. 6), the heat flux is:

$$q(x) = 16 \, e^{-x/\delta_E} \sin\theta \, , \quad (MW/m^2) \, . \tag{5}$$

At the leading edges of the limiter, $\sin\theta = 1$ (by definition) while on the front face of the limiter $\sin\theta \approx 1/7$. The heat flux varies from about 2.3 MW/m^2 at the limiter tip to 0.6 MW/m^2 just before the leading edges. The maximum heat flux of 4 MW/m^2 occurs at the leading edges where $x/\delta_E = 1.4$ and $\sin\theta = 1$. One design option for the limiter is to shape the front face so as to have a more constant heat load on it,[6] and/or to shape the tip so as to eliminate any heat load on the tip ($\theta = 0$). This requires deviating from the simple straight line geometry of the front face which has advantages in fabrication and maintenance.

8.3.3 Plasma Edge Physics and Particle Recycling

The plasma edge region can be defined as the region between the "core" plasma, where most of the fusion reactions are taking place, and the scrape-off region. The edge region is important to impurity control in two major respects: the edge temperature affects the sputtering coefficients of charged particles hitting the limiter and neutrals hitting the wall; and secondly, recycling of particles in the edge region affects the total flux of particles out of the plasma. With respect to the latter point, a high flux will, in general, make

it easier to remove helium, but can increase the sputtering rate. Too low a flux can make it difficult to remove helium at a fast enough rate. Unfortunately, the plasma edge region is not adequately understood. Detailed codes, e.g. Refs. 12 and 13, as well as experiments, are currently being developed which could add insight into the physics of the edge region. For STARFIRE we have defined a reference edge temperature on the basis of a simple model for power balance. In the absence of more definitive information, we have defined a reference particle flux based on scaling from present experimental results. These reference calculations are discussed in the remainder of this section.

The total charged particle flow to the limiter can be defined in terms of an average particle confinement time τ_p for the plasma as a whole as:

$$I_j = \frac{N_j}{\tau_p} , \tag{6}$$

where I_j is the flow of the j-th species, in particles (ions or electrons) per second, and N_j is the total number of particles in the plasma. For a density N_j and plasma volume V_p, $N_j = N_j V_p$. The value of τ_p reflects the core confinement time, which could be much greater than the average, and the edge confinement time, which could be much smaller than the average. The value of τ_p, for present devices, seems to lie in the general range of

$$\frac{1}{2} \lesssim \frac{\tau_p}{\tau_E} \lesssim 3 ,$$

where τ_E is characterized as the energy replacement time.[14-15] One general physical picture for the particle flux is that particles take a relatively long time to diffuse out of the core, but once in the edge region they undergo rapid recycling; the overall value of τ_p is then some average of the core and edge processes. For STARFIRE we have adopted a reference particle containment time of $\tau_p = \tau_E/2 = 1.8$ s, where τ_E is the electron energy containment time using empirical scaling (see Chap. 6).

On this subject, a conclusion based on work done for the INTOR design study[15] is that edge recycling could play a larger role for future devices than for present devices, leading to a smaller τ_p and a higher particle flux. This would basically be due to the larger size of future machines which could prevent recycling neutrals from reaching the core. Associated with this could

be a fairly high edge density and fairly low edge temperature. While definitive conclusions must await further experiments and calculations, there are several reasons why this scenario could be different for STARFIRE.

First, STARFIRE makes use of a broad plasma temperature profile and a narrow density profile (see Chap. 6). A higher edge temperature would also result from the direct deposition of 90 MW of rf power fairly close to the plasma edge. Finally, the average plasma density in STARFIRE is about half that of most previous designs, owing to the need to minimize the rf current drive power. All of these effects tend to imply a low edge density and less recycling. While the reference particle containment time is at the lower end of present measurements, it is probably somewhat higher than if the rapid-recycling phenomena occurred. The effect of different values of τ_p on the limiter performance is discussed in Sec. 8.3.6.

8.3.4 Edge Temperature

If the particle and power flows to the limiter are specified, the edge temperature can be computed by simple conservation of energy. Specifically, the heat tranport power to the limiter can be expressed as:

$$P_{TR}^{lim} = \gamma\left(kT_e\right)I \ , \tag{7}$$

where I is the total number of charged particles diffusing from the plasma per second, γ is (by this definition) the heat transmission coefficient of the plasma sheath at the limiter, and T_e is the electron edge temperature. Equation (7) assumes convective flow of heat in the scrapeoff region, i.e. each particle carries its respective kinetic energy from the edge region to the start of the sheath region. The value of γ, as well as the sheath potential ϕ, for the case of a geometry where flow is parallel to the field lines (i.e. normal incidence) have been computed by several authors, e.g. Refs. 16-18. Fig. 8-4, for example, shows the variation of these parameters as a function of the electron re-emission coefficient of the boundary, for the parallel flow case. The parameter α is the ratio of average ion-to-electron energy in the scrape-off region. A value of $\alpha = 1$ is probably typical for STARFIRE. For the STARFIRE limiter geometry, the angle of incidence is only about 22 deg, and this introduces several key uncertainties, among them: (1) the value of electron re-emission of the beryllium surface coating for off-normal incidence is unknown;

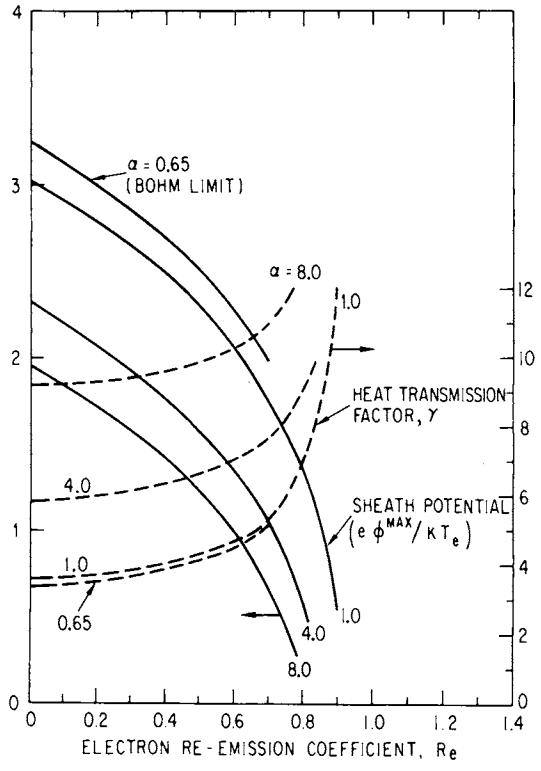

Figure 8-4. Normalized sheath potential and heat transmission factor as a function of electron re-emission coefficient.

and (2) the sheath potential may be influenced by possible finite gyroradius effects. For a normal incidence flux, the electron re-emission coefficient of beryllium (assumed equal to the secondary electron coefficient) is fairly low, reaching a maximum of only 0.5 at 100 eV and falling to zero by 2.5 keV.[19] From Fig. 8-4 this would imply a fairly high sheath potential and low value of γ. However, for off-normal incidence there is some expectation that R_e would increase. Furthermore, for a purely electron repelling sheath (i.e. ignoring any gyroradius effects), ϕ would tend to diminish with the angle of incidence. For these reasons, we have adopted a reference value of $\phi/kT_e = 1$ for STARFIRE which is considerably lower than for the normal-incidence geometry case. This is conservative in the sense that a low sheath potential results in more sputtering of the limiter (see Sec. 8.3.6). The corresponding reference heat transmission factor (from Fig. 8-4) is $\gamma = 5$. This value (by the present definition) is in the range found experimentally for similar boundary geometries in present devices, e.g. Ref. 20. The current I in Eq. (7) is given by:

$$I = \frac{(N_{DT} + N_{\alpha} + N_z + N_e)V_p}{\tau_p} , \tag{8}$$

which for the STARFIRE densities yields $I = 9.25 \times 10^{22}$ particles per second. For the value of $P_{TR}^{lim} = 90$ MW and $\gamma = 5$, the edge temperature is given by:

$$T_e = \frac{90 \times 10^6 \text{ J/s}}{5 \times 9.25 \times 10^{22} \text{ s}^{-1} \times 1.6 \times 10^{-19} \text{ J/eV}} = 1200 \text{ eV} . \tag{9}$$

8.3.5 Limiter/Vacuum System Performance

There are three important performance parameters of the limiter/vacuum system: the helium concentration permitted in the plasma; the tritium fractional burnup; and the sputtered beryllium concentration in the plasma. The third parameter also depends on first-wall sputtering. Based on the exponential fall-off of particle flux in the scrape-off region, discussed earlier, and on the coordinate system of Fig. 8-3, the fraction of particles entering the limiter slots is given by:

$$f_{slot} = e^{-x_1/\delta_p} - e^{-x_2/\delta_p} , \tag{10}$$

where x_1 and x_2 are respectively the coordinates of the start of the slot region and the first wall. For $\delta_p = 10$ cm, $x_1 = 8.7$ cm, $x_2 = 20$ cm, this fraction is $f_{slot} = 0.28$. This is the same for all particle species. The efficiency of pumping particles that enter the slot region will depend on the species, and can be denoted by a value η_j for the j-th species. The total fraction of charged particle outflux from the plasma that is removed is then given by a removal efficiency:

$$\varepsilon_j = f_{slot}\eta_j . \tag{11}$$

Alternatively the overall particle reflection coefficient can be written as

$$R_j = 1 - \varepsilon_j . \tag{12}$$

As mentioned previously, the pumping efficiency will depend on the various vacuum system conductances, the speed of the vacuum pumps, and on the neutral/ plasma interactions in the slot region. For helium, these interactions consist of electron impact ionization and the subsequent acceleration of the ionized helium back to the limiter because of a presheath electric field. Hydrogen can similarly be trapped by this process but tends to be preferentially released because of charge-exchange events. This occurs because a charge-exchange event exchanges the charge of an incoming ion with a neutral in the slot region, but the resulting neutral can still make its way out of the slot region. Because of these processes, the neutral pressure in the slot region can be much greater than the equivalent neutral pressure of the entering plasma, i.e. the pressure resulting from the thermalization of incoming particles with the wall surface temperature. Preliminary calculations by Jacobsen[21] show a three-order of magnitude difference, for example. Recent experiments in Alcator[22] have also shown the existence of a pressure differential in a limiter system. Monte Carlo calculations by Seki, et al.[23] have also indicated a significant increase in pumping efficiency for helium and the relative release of hydrogen due to the interactions in the slot region. Based on the data from the latter referenced calculations, we have estimated the inversion probability of the limiter, defined as the probability that a neutral atom coming from the back surface of the limiter and entering the slot region will be ionized and returned to the back surface, for helium as 0.99 and for DT as 0.4. As shown in Sec. 8.5, this results in overall limiter pumping efficiencies of $\varepsilon_\alpha = 0.25$ and $\varepsilon_{DT} = 0.10$. The corresponding reflection coefficients are therefore $R_\alpha = 0.75$ and $R_{DT} = 0.90$.

At equilibrium, the removal of helium by the limiter/vacuum system must equal the alpha-particle production rate by fusion:

$$J_\alpha = \frac{N_\alpha V_p}{\tau_p}\left(1 - R_\alpha\right), \tag{13}$$

where J_α is the production rate, in particles per second, and the right-hand side of Eq. (13) is the removal rate. Solving Eq. (13) for N_α and dividing by N_{DT} gives the fractional concentration of helium in the plasma:

$$\frac{N_\alpha}{N_{DT}} = \frac{J_\alpha \tau_p}{N_{DT} V_p \left(1 - R_\alpha\right)}. \tag{14}$$

For the STARFIRE values of $J_\alpha = 1.25 \times 10^{21}\ s^{-1}$, $N_{DT} = 0.806 \times 10^{20}\ m^{-3}$, $V_p = 783\ m^3$, $\tau_p = 1.8$ s, and $R_\alpha = 0.75$, the fractional concentration from Eq. (14) is 14%.

The fractional burnup of tritium is defined as the ratio of tritium fused per second to the tritium pumped plus fused per second or:

$$f_{Bu} = \frac{J_\alpha}{\left(N_{DT}V_p/2\tau_p\right)\left(1 - R_{DT}\right) + J_\alpha}\ , \tag{15}$$

where the tritium fused is obviously the same as the alpha-particle production rate. The fractional burnup can be related to the helium concentration by combining (14) and (15) to give:

$$\left(f_{Bu}\right)^{-1} = \left[2\left(\frac{N_\alpha}{N_{DT}}\right)\frac{\left(1 - R_\alpha\right)}{\left(1 - R_{DT}\right)}\right]^{-1} + 1\ . \tag{16}$$

This shows the tradeoff between minimizing the helium concentration in the plasma on one hand, and maximizing the tritium burnup on the other, as well as the advantage obtained by having as high an R_{DT} as possible. For the values of $N_\alpha/N_{DT} = 0.14$, $R_\alpha = 0.75$, and $R_{DT} = 0.9$ the fractional burnup is then: $f_{Bu} = 0.42$. This represents a significant increase over most previous reactor designs and results in a significant decrease of tritium inventory. Even if there were no selective pumping of helium, i.e. if $R_{DT} = R_\alpha$, the fractional burnup of tritium would be 22% which is still fairly high. These high values of tritium burnup result from the choice of a moderate-to-low pumping efficiency limiter system.

The above analysis of limiter performance has used the same particle confinement time for all ion species. It should be noted that helium may well have a shorter confinement time than hydrogen due to a possible faster recycling in the edge region of reactor size devices. This could occur because of the absence of charge-exchange events for helium which could lead to a shallower penetration of the edge region for helium than for hydrogen. If the confinement times were different, then the helium concentration, in Eq. (14), would be multiplied by the ratio of τ_α/τ_{DT} (see Ref. 4). This could result in a substantial reduction of helium concentration in the plasma, for a given limiter/vacuum system.

8.3.6 Low-Z Coating Considerations

8.3.6.1 Need for Low-Z Coating

A number of studies have discussed the need for a low-Z coating on the exposed surfaces of a fusion reactor, e.g. Refs. 24-27. The function of the coating is to prevent sputtering of the underlying structural material, in the case of STARFIRE, the stainless steel of the first wall and the tantalum of the limiter. Even though STARFIRE operates in an enhanced radiation mode, with the intentional addition of a high-Z material, nominally iodine, the sputtering of bare iron and tantalum could result in too much radiation. A possibly more serious concern is the occurrence of a runaway self-sputtering cascade whereby iron and tantalum ions, accelerated through even a modest sheath potential, would have sputtering coefficients in excess of unity, at the limiter. The resulting self-sputtering avalanche would then proceed with the confinement time of the plasma ions and would quickly lead to excessive levels of high-Z impurities. This avalanche behavior seems to have been responsible for hollow discharges associated with high-edge temperatures in PLT when tungsten limiters were used.[28] According to one analysis,[16] the plasma-edge temperature in a fusion reactor with a normal-incidence-type limiter would have to be at or below $\sim$300 eV to prevent a self-sputtering cascade for high-Z materials. For the shallow incidence limiter of STARFIRE the exact limiting value of edge temperature is uncertain but the estimated value of 1200 eV is far in excess of the threshold. For low-Z materials, self-sputtering rates are less than one at all incident energies.

The requirements for surface properties of the limiter/first-wall system are low hydrogen and self-sputtering yields, minimum plasma degradation by sputtered material (undesirable radiation loss), low thermal desorption, good thermal conductivity and thermal shock characteristics to cope with disruptions, and compatibility with other structural materials. Bulk properties required are: high mechanical strength, good radiation resistance, good electrical and thermal conductivity and thermal shock characteristics to cope with disruptions, requirements argue for a coating/substrate system, where the surface coating would be chosen primarily on the basis of compatibility with the plasma, and the substrate would be chosen primarily for mechanical and radiation considerations. The dominant constraint concerning the compatibility of the wall surface with the plasma seems to be hydrogen and self-sputtering yields. This is due to the fact that other erosion mechanisms can be minimized and perhaps eliminated

in present machines by careful attention to design and operating parameters. Based on its thermal, mechanical, and sputtering properties (see Sec. 8.4) beryllium has been chosen as the reference coating material for STARFIRE.

A number of other factors have influenced the choices of low-Z materials. Since wall materials become plasma impurities, high-Z wall atoms, when fully ionized, produce electrons that must be confined at the expense of DT fuel, if the overall plasma beta is fixed. Low-Z atoms produce less plasma degradation. Low-Z materials, since their self-sputtering yields are less than one, seem natural candidates for in-situ recoating which can be done by doping the plasma impurity level above the equilibrium impurity fraction.[29] Surface segregation phenomena, either Gibbsian or radiation-induced solute segregation, may also be useful in controlling the constituents of the top monolayer, which in turn controls the sputtered species.[30] These segregation phenomena can control sputtering both by altering the surface concentrations and by altering the ion/neutral ratio of the atoms.

8.3.6.2 Sputtering of the First Wall

During the operation of STARFIRE, the first wall will receive a steady flux of DT neutrals arising from charge-exchange (cx) reactions at or near the plasma edge. The wall will also receive a small percentage of the charged particle flux, i.e. the flux not going to the limiter; but this is small compared to the charge-exchange flux and has been neglected in this analysis. In general, the charge-exchange flux will tend to be nonuniform and will have a complex energy distribution, due to the many charge-exchange events that a single atom can typically undergo before impinging on the wall. However, an estimate of the charge-exchange flux, adequate to define the erosion problem of the first wall, can be computed using the global model of Ref. 24. This model predicts a total charge-exchange flow to the wall given by:

$$I^0_{DT} = I_{DT} \frac{A_{cx}\gamma}{1 - R^w_{DT}A_{cx}\gamma}, \tag{17}$$

where I_{DT} is the DT ion flow to the limiter (of which an approximately equal amount in the form of recycling and gas-puffed neutrals return to the plasma), A_{cx} is the probability of a neutral entering the edge region being charge-exchanged, γ is the probability that the neutral is returned to the first wall,

and R_{DT}^{W} is the reflection coefficient for DT atoms off the first wall. For STARFIRE, $R_{DT}^{W} = 1$ because the first wall should quickly be saturated with DT. The charge-exchange probability is given by:

$$A_{cx} = \frac{\langle\sigma v\rangle_{cx}}{\langle\sigma v\rangle_{cx} + \langle\sigma v\rangle_{I}} , \tag{18}$$

where $\langle\sigma v\rangle_{cx}$ and $\langle\sigma v\rangle_{I}$ are the rate coefficients for charge-exchange and ionization respectively. In STARFIRE, if the last 10% of the plasma is taken as the predominant region for charge-exchange, then based on the reference temperature profile, the average temperature for use in computing A_{cx} is about 5 keV. For this value, using the rate coefficient data of Ref. 25 and using the Monte Carlo code estimate of $\gamma = 0.75$ from Ref. 24 gives an overall value of $\gamma A_{cx} = 0.65$ and a charge-exchange flow of $I_{DT}^{0} = 1.85\ I_{DT}$. The charge-exchange flow to the wall is therefore about twice the charged DT flow to the limiter. The latter is given by:

$$I_{DT} = \frac{N_{DT} V_p}{\tau_p} = 3.5 \times 10^{22}\ s^{-1} , \tag{19}$$

and so the charge-exchange flow is $I_{DT}^{0} = 6.5 \times 10^{22}\ s^{-1}$.

The sputtering rate of the wall coating is given by:

$$S_z^W = I_{DT}^{0} Y_{DT}^{0} , \tag{20}$$

where S_z^W is the sputtering rate in atoms/s and Y_{DT}^{0} is the sputtering coefficient for DT on beryllium, in sputtered atoms per incident atom. For an average temperature of charge-exchange neutrals of 5 keV, the average sputtering coefficient, based on the formula of Smith,[31-32] is $Y_{DT}^{0} = 0.0061$. The sputtering rate is therefore $S_z^W = 3.95 \times 10^{20}$ atoms/s.

Based on the sputtering rate, the lifetime of the wall coating can be computed as:

$$\tau_w = \frac{A_w \rho d}{S_z^W} , \tag{21}$$

where τ_w is the lifetime, A_w is the wall area, d is the coating thickness, and ρ is the atom density of the coating. For the above value of S_z^w, $A_w = 755\ m^2$ and for $\rho = 1.22 \times 10^{29}$ atoms/m^3 (i.e. the theoretical density), $\tau_w = 2.3 \times 10^{11}$ d where τ_w is in seconds and d is in meters. The lifetime from this formula is tabulated for different coating thicknesses as follows:

d (mm)	τ_w
0.1	∿9 mo
0.5	3.5 yr
1.0	7 yr
2.0	14 yr

8.3.6.3 Sputtering of the Limiter

Sputtering of the limiter low-Z coating is a more complicated process than the sputtering of the first wall for several reasons: (1) the limiter will be sputtered by all of the ion species; (2) beryllium ions impinging on the limiter will tend to stick to the surface as well as to sputter; and (3) the sputtering rates will differ on different parts of the limiter because the plasma temperature and particle flux are not constant in the scrape-off region. In general, for an area element dA on the limiter surface, at location x from the tip (see Fig. 8-3) having thickness dx and length $2\pi R_L$, the thickness of the coating eroded in a time Δt is given by:

$$d = \left\{ \Gamma_{DT}(x) S_{DT}(x) + \Gamma_{\alpha}(x) S_{\alpha}(x) + \Gamma_z(x) \left[S_z(x) - \left(1 - R_z\right) \right] \right\} \frac{\Delta t}{\rho} , \qquad (22)$$

where d is the thickness eroded, the Γ's are the flux of particles of the respective species to the area element, the S's are the sputtering coefficients at a distance x into the scrape-off zone, R_z is the reflection coefficient for beryllium on beryllium, and ρ is the atomic density of beryllium in the coating. The particle fluxes are computed in analogy to the energy flux in Eqs. (2)-(5), viz:

$$\Gamma_j(x) = \frac{I_j}{N_S 2\pi R_L \delta_p} e^{-x/\delta_p} \sin\theta \qquad (23)$$

for each species j, where I_j is given by Eq. (6). Combining Eqs. (6), (23), and (22) then gives:

$$d = \frac{\left\{N_{DT}S_{DT}(x) + N_\alpha S_\alpha(x) + N_z\left[S_z(x) - \left(1 - R_z\right)\right]\right\} V_p \Delta t\, e^{-x/\delta_p} \sin\theta}{4\pi R_L \tau_p \delta_p \rho} . \qquad (24)$$

The sputtering coefficients in Eq. (24) will depend on the energy of a particle impinging on the limiter. This in turn depends on the temperature of the particle and on the energy acquired in the sheath region. For an electron temperature profile in the scrape-off region given by:

$$T_e(x) = 1.2\, e^{-x/\delta_p} \quad \text{(keV)} , \qquad (25)$$

and for a sheath potential of $e\phi = kT_e$, the energy of an impinging ion is given by:

$$U_j(x) = kT_e(x)\left[3/2 + Z_j\right] , \qquad (26)$$

where Z_j is the charge state of the ion, and where it is assumed that the ion temperature in the scrapeoff is equal to the electron temperature. The charge states are given by $Z_{DT} = 1$, $Z_\alpha = 2$, and $Z_z = 4$.

Because of the limiter geometry and the uncertainties associated with the sheath potential, it is uncertain at what angle the ions strike the limiter. However, a computation of the sputtering coefficients using the energy [Eq. (26)] in the formula of Ref. 32 is probably a reasonable estimate, inasmuch as the sheath potential will tend to yield a normal incidence impingement. Table 8-6 shows the sputtering coefficients computed in this manner for several locations on the limiter. As shown in this table, the sputtering coefficients are lowest at the limiter tip and increase towards the leading edge. This is due to the reduction in ion energy with distance into the scrape-off zone which brings the sputtering coefficients closer to their peak values, which occur at an energy at about 200 eV for DT, 400 eV for helium, and 800 eV for beryllium.

Table 8-6. Sputtering Coefficients at the Limiter

x (cm)	S_{DT}	S_α	S_z
0	0.0076	0.033	0.182
3.5	0.010	0.044	0.236
7[a]	0.014	0.056	0.296

[a]Leading edge.

For this reason, if the sheath potential were higher than the reference value the sputtering would be reduced. In this context, it should be noted that high-Z ion sputtering, particularly the iodine used for thermal control in STARFIRE, may be significant, even though its concentration is very small. However, because the uncertainties associated with the sheath physics are much more critical for the analysis of high-Z sputtering, we have ignored this contribution in this analysis.

The leading edge is clearly the most critical area of the limiter since it receives the highest particle flux and because the sputtering coefficients are at their highest. However, from Eq. (24) it is seen that for the proper concentration of beryllium in the plasma, there will be zero erosion at the leading edge. Physically this can occur if as much beryllium recoats the limiter as is eroded. The concentration of beryllium needed to achieve this condition is found by setting Eq. (24) to zero which gives:

$$\frac{N_{z_0}}{N_{DT}} = \frac{S_{DT}(X_L) + (N_\alpha/N_{DT})S_\alpha(X_L)}{1 - S_z(X_L) - R_z}, \tag{27}$$

where X_L = 7 cm is the location of the leading edge and N_{Z_0} is the required value of beryllium in the plasma. Using the data from Table 8-6, R_z = 0.05 (see Ref. 25), and N_α/N_{DT} = 0.14, Eq. (27) gives the required fractional concentration of beryllium N_{z0}/N_{DT} = 0.033. Therefore, from this analysis, if the beryllium concentration in the plasma is held to 3.3% there will be no erosion of the leading edge. If the concentration is less there will be erosion and if the concentration is more there will be a net growth of the coating.

This suggests a means for ameliorating the leading-edge erosion. The amount of beryllium naturally in the plasma will be due to sputtering from the first wall and the limiter itself and can be estimated as follows. The buildup of beryllium in the plasma, due to sputtering, is given by:

$$\frac{dN_z}{dt} = \frac{S_z^W}{V_p} + \frac{N_{DT}}{\tau_p}\bar{S}_{DT} + \frac{N_\alpha}{\tau_p}\bar{S}_\alpha + \frac{N_z}{\tau_p}\left[\bar{S}_z - \left(1 - R_z\right)\right], \tag{28}$$

where the first term on the right-hand side of Eq. (28) is the contribution from wall sputtering [see Eq. (20)] and $\bar{S}_{DT}$, etc. is the average sputtering coefficient at the limiter. At equilibrium, Eq. (28) is set to zero which gives for the beryllium concentration:

$$\frac{N_z}{N_{DT}} = \frac{0.011 + \bar{S}_{DT} + \left(N_\alpha/N_{DT}\right)\bar{S}_\alpha}{1 - \bar{S}_z - R_z}. \tag{29}$$

Using the weighted average of values of sputtering coefficients from Table 8-6 in Eq. (29) then gives an estimate of the concentration as $N_z/N_{DT} = 0.030$. Therefore, the naturally sputtered beryllium concentration is somewhat less than the required value for no leading-edge erosion. However, the extra beryllium needed can easily be added to the plasma along with the fuel stream. In effect, then, there would be a net transfer to beryllium from the wall and from an outside source to the plasma, and then to the limiter. Since it is unlikely that the exact amount of beryllium could be maintained for exactly no net erosion, it is probably easier to allow for a slight excess. This case has been analyzed as discussed in Sec. 8.3.2 and it was found that an equilibrium can still be reached on the leading edge whereby the sum of thermal vaporization and sputtering is equal to the recoating rate.

The strategy for STARFIRE is then to maintain a beryllium concentration of 3.3% in the plasma, to provide for a nominal condition of no erosion on the leading edge (a more conservative reference value of 4% has been assumed for the purposes of computing power balance, β, etc.). This value is in excess of what would be needed to keep the rest of the limiter front face from being eroded; there will therefore be a net growth of coating on the rest of the limiter. The rate of growth is given by Eq. (24). Using the value of ρ =

1.22×10^{29} atoms/m^3, V_p = 783 m^3, R_L = 9 m, δ_p = 0.1 m, sin θ = 1.7, gives a growth rate at the locations in Table 8-6 of:

X (cm)	Coating Growth Rate (mm/yr)
0	∿1.7
3.5	∿0.6
7	0

As discussed in Sec. 8.4, these growth rates are low enough to permit several years worth of operation before the excess coating needs to be removed.

8.3.7 Parametric Study of the Limiter/Vacuum System

In this section we analyze the effect of different values of key parameters on the performance of a limiter/vacuum system. The key parameters studied are (1) the transport power to the limiter P_{TR}^{lim}; (2) the particle containment time τ_p; (3) the particle and energy fall-off rates in the scrape-off region δ_p and δ_E; and (4) the maximum tolerable heat flux on the limiter q^{max}. The first three parameters depend on the plasma physics while the last parameter depends on engineering considerations.

The performance of the limiter/vacuum system can be defined in terms of the concentration of helium maintained in the plasma and the required value of the toroidal magnetic field, and these have been used to quantify the effect of variations in parameters (1)-(4) above. The limiter is assumed to be of the same shape as the reference design except that the leading edge can be displaced by a different distance from the tip. This distance is denoted by X_L. Using the model equations for the particle and heat fluxes to the limiter as developed earlier, the heat flux on the leading edge is given by:

$$q_L = \frac{P_{TR}^{lim}}{4\pi R_L \delta_E} e^{-X_L/\delta_E} . \qquad (30)$$

Setting this value equal to q^{max}, i.e.:

$$q_L = q^{max} , \qquad (31)$$

and using Eqs. (30) and (31), the required displacement of the leading edge is given by:

$$X_L = -\delta_E \log\left[\delta_E q^{max} \frac{4\pi R_L}{P_{TR}^{lim}}\right] . \tag{32}$$

The percentage of particles entering the limiter slot region is given by Eq. (10) as:

$$f_{slot} = e^{-(X_L+a)/\delta_p} - e^{-(X_L+a+b)/\delta_p} , \tag{33}$$

where a = 1.7 cm is the width of the leading edge and b = 11.3 cm is the slot width. The helium reflection coefficient of the limiter system is given by:

$$R_\alpha = 1 - \eta_\alpha f_{slot} \tag{34}$$

where η_α = 0.9 is the efficiency of pumping those helium ions that enter the slot region. Using Eq. (14) and using the appropriate numerical values for STARFIRE, the helium concentration in terms of τ_p and f_{slot} is given by:

$$\frac{N_\alpha}{N_{DT}} = 0.0220 \frac{\tau_p}{f_{slot}} . \tag{35}$$

Combining Eqs. (32), (33), and (35) and using the relation $\delta_p = 2\delta_E$ then gives:

$$\frac{N_\alpha}{N_{DT}} = 0.0029\, \tau_p \sqrt{\frac{P_{TR}^{lim}}{\delta_p q^{max}}} \Bigg/ \left[e^{-a/\delta_p}\left(1 - e^{-b/\delta_p}\right)\right] . \tag{36}$$

Finally for a fixed temperature and β-limited plasma the toroidal magnetic field, B, required to maintain a given fusion power, scales as

$$\left(\frac{B}{B_0}\right)^2 = 1 + 0.13 + 1.5 \frac{N_\alpha}{N_{DT}} , \tag{37}$$

where B_0 is the field required for a completely clean plasma. The factor of 0.13 corresponds to a 4% beryllium concentration and a 0.1% iodine concentration. The difference between B and B_0 represents the "field margin" necessary to offset the added impurity pressure.

Figure 8-5 shows the effect of variations in δ_p on the fractional helium concentration from Eq. (36) and on the magnetic field from Eq. (37), using a value of B_0 = 9.8 T (corresponding to a β of 6.7%) and for the reference values of P_{TR}^{lim} and τ_p. As shown, the performance of the limiter system is fairly insensitive to δ_p within about a factor of two from the reference value of δ_p = 10 cm. This dependence would be even less sensitive for ratios of δ_p/δ_E greater than two, but it would be somewhat more sensitive for smaller ratios.

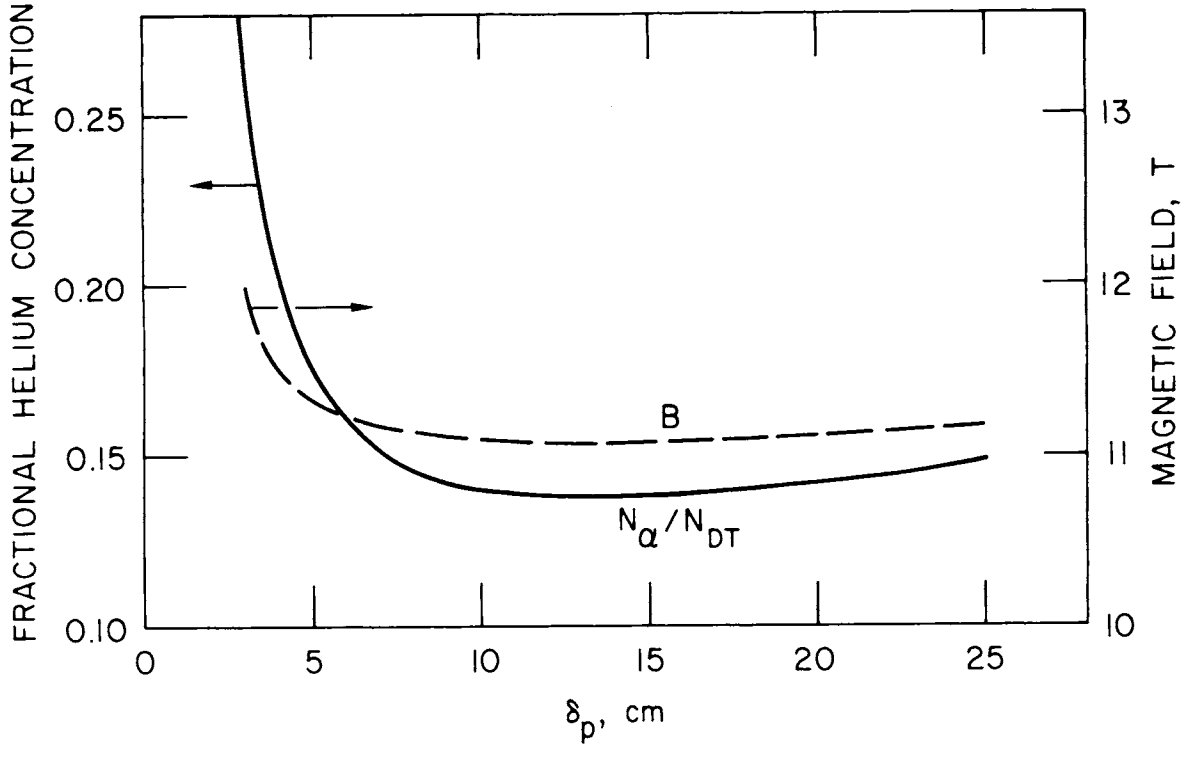

Figure 8-5. Sensitivity of the fractional helium concentration and the required toroidal field to changes in the particle e-folding distance.

Figure 8-6 shows the effect of different values of τ_p and P_{TR}^{lim} on the magnetic field. Here too there is a fairly broad region of parameter space where the limiter/vacuum system operates successfully, without requiring unreasonable

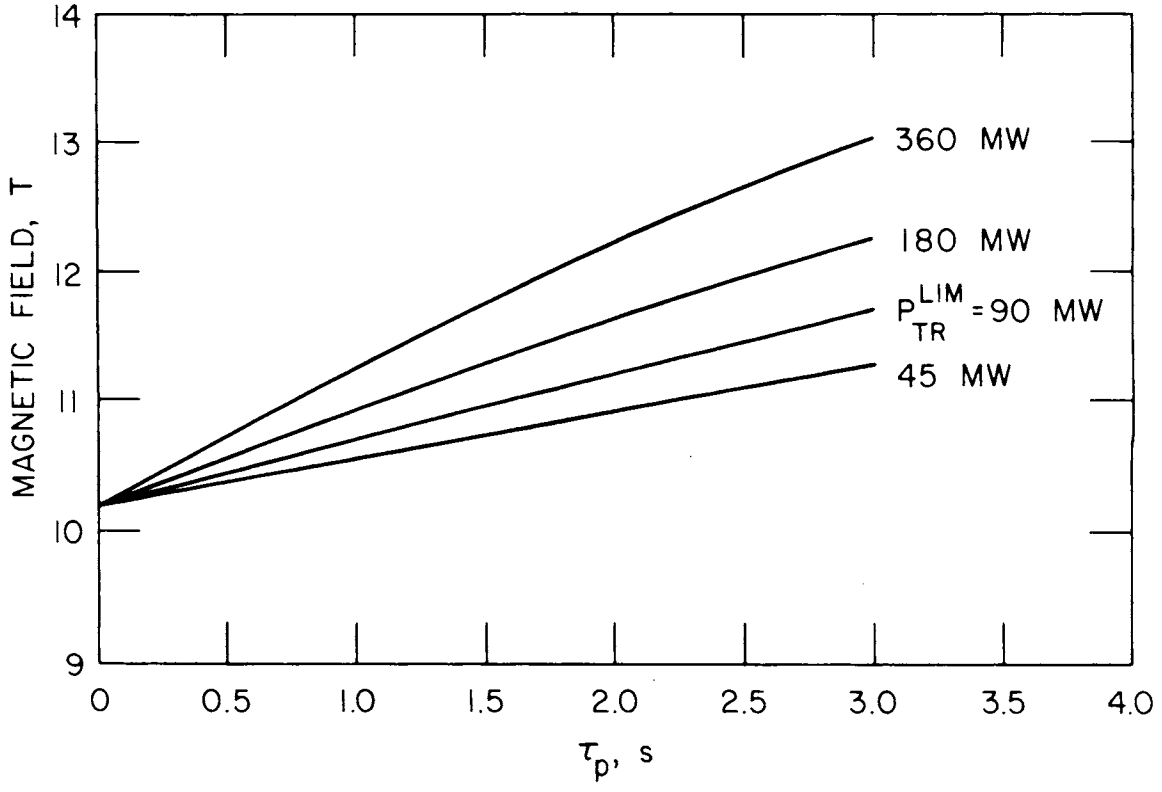

Figure 8-6. Sensitivity of the required toroidal field to changes in the particle containment time and the limiter transport power.

values of B. This is particularly true since high values of P_{TR}^{lim}, which could arise if the energy containment time were smaller than expected, would probably be associated with small values of τ_p. The sensitivity of the limiter system to q^{max} was not plotted but can be seen from Eq. (36) to behave inversely to P_{TR}^{lim}. Improvements in the power flux handling capability are seen to be helpful, but not essential, except for the case of very high transport loads and long particle confinement times.

8.4 LIMITER ENGINEERING

8.4.1 Introduction

This section is devoted to the engineering aspects of the limiter design. Section 8.4.2 evaluates the properties of a large number of structural materials for the limiter applications. Based on this broad survey, four reference alloys are identified as the most promising candidates. These include a copper alloy (AMAX-MZC) and the refractory metal alloys of vanadium (V-20Ti), niobium (FS-85), and tantalum (Ta-5W). Section 8.4.3 compares the candidate materials for the coating/cladding materials. The rationale for selecting beryllium as the reference low-Z material is discussed.

Detailed thermal-hydraulics and stress analyses for the four reference structural materials are presented in Sec. 8.4.4 and 8.4.5, respectively. The analyses cover both steady-state and off-normal conditions. The thermal-hydraulics section emphasizes the loss-of-coolant events. The stress analysis section covers in more detail the response of the limiter to the electromagnetic forces and torques induced due to plasma disruptions. The magnitudes of these forces and torques are derived in Sec. 8.4.6.

The neutronics analysis of the limiter/vacuum system is presented in Sec. 8.4.7. The mechanical design of the limiter and its support is described in Sec. 8.4.8.

8.4.2 Limiter Materials

The requirements for the limiter materials are similar to those of the first-wall materials except that the limiter material must, in addition, be capable of withstanding a surface heat flux of $\sim$4 MW/m^2. The limiter structure must still be resistant to radiation damage, capable of elevated temperature operation, and environmentally compatible with its surroundings. In addition, it is desirable that the material exhibit low activation, and its properties should not be affected by the formation of transmutation products. The high surface heat flux can potentially influence the lifetime of the limiter by increasing the average temperature and by introducing large thermal and stress gradients in the material. The average material temperature will affect the type and degree of radiation damage, the compatibility with the coolant, and the mechanical and physical properties. Large thermal gradients can result in

large thermal stresses and swelling gradients. These gradients can produce additional creep and crack growth in the limiter during normal operation.

Several factors influence the limiter's ability to withstand a high surface heat flux, including the physical properties of the material, the limiter design, and the power cycle of the reactor. This subsection will discuss the properties of potential limiter materials and their impact upon the limiter operation. The effects of temperature, radiation, and chemical environment will be considered in comparing the various materials. Reference alloys, which most closely meet the requirements for the limiter, will then be selected and analyzed in detail for the conditions expected in STARFIRE.

The desirable properties of a limiter structural material are listed in Table 8-7. A low coefficient of thermal expansion, a high thermal conductivity, and a low elastic modulus are the properties required to minimize the temperature and stress gradients. A high heat capacity will help minimize the temperature gradient during thermal shock conditions. High strength materials are also desirable since the allowable thermal stresses are based upon the tensile strength of the materials. Radiation should not significantly alter these properties during the limiter lifetime. The other desirable properties are the same as those required for the first wall/blanket structural material, but because of the potentially high temperature and stress gradients, the effects of swelling, crack growth, and creep could be more severe than in the first wall. In particular, the rates of crack growth will be dependent upon the reactor operating cycle. A cyclic mode of operation that imposes a large cyclic stress on the limiter could result in a considerably reduced lifetime due to accelerated crack growth compared with a continuous mode of operation. This problem is discussed in detail in Sec. 10.6 for the first-wall materials.

8.4.2.1 Potential Limiter Materials

The number of potential limiter materials is large, and several classes of materials have been surveyed to determine the best candidates for the limiter. The materials classes, including stainless steels, nickel alloys, refractory metal alloys, and copper alloys, along with their principal advantages and disadvantages, are shown in Table 8-8. It is clear that no single group of alloys offers all of the desired properties. Many of the alloys can be

Table 8-7. Desirable Characteristics of Limiter Materials

Property	Desirable Value	Purpose
Thermal conductivity	High	Minimize thermal stress
Thermal expansion	Low	
Young's modulus	Low	
Specific heat	High	Minimize effect of thermal shock
Yield strength	High	Maximize allowable stress
Ultimate tensile strength	High	
Uniform elongation	High	Maximize ability to withstand off-normal events
Total elongation	High	
Swelling	Low	Minimize dimensional and physical property changes
Creep	Low	Minimize dimensional changes
Fatigue	Low	Prevent catastrophic failure
Crack growth	Low	
Corrosion	Low	Prevent wall thinning and coolant channel plugging
Stress corrosion cracking	Low	Prevent catastrophic failure
Transmutations	Low	Prevent alloy compositional change
Sputtering	Low	Reduce wall thinning and plasma impurities

Table 8-8. Materials Considered for Limiter

Material	Advantages	Disadvantages
Stainless steel	Large data base. Resistant to radiation damage. Experience with fabriction.	Poor thermophysical properties.
Nickel alloys	High strength. High temperature capability. Experience with fabrication.	Poor resistance to radiation.
Refractory metal alloys	High temperature capability. Desirable thermophysical properties. Resistant to radiation damage.	High ductile-brittle transition temperature. Susceptible to hydrogen embrittlement. Coolant corrosion. Potentially difficult fabrication.
Copper alloys	High thermal conductivity. Experience with fabrication.	Limited irradiation data base. Low temperature operation. Potentially high swelling.

eliminated from consideration because they do not have adequate properties in one or more crucial areas. The purpose of this section is to reduce the number of potential limiter materials to only a few reference alloys which can then be examined in more detail.

Some of the alloys can be eliminated from consideration based upon the primary requirement that the limiter material must be capable of withstanding a high heat flux. A simple model of a tube which contains a coolant of pressure P, and which receives a uniform heat flux Q, was analyzed in order to compare the heat flux capabilities of various alloys. The maximum allowable heat flux for the tube was determined by setting the stresses due to the coolant pressure and thermal gradient equal to an allowable stress of 0.75 of the yield strength. This allowable stress level was chosen because it is desirable to maintain the stress of irradiated metals below the yield strength due to the greatly reduced ductility that is likely to result from irradiation. The tensile stress, σ, from the coolant pressure, P, is given by

$$\sigma = \frac{\left(R_0/R_I\right)^2 + 1}{\left(R_0/R_I\right)^2 - 1} P \ , \tag{38}$$

where R_0 and R_I are the outer and inner tube radii respectively. The maximum thermal hoop stress, σ_{th}, occurs at the tube inner radius and is given by[33]

$$\sigma_{th} = \frac{E\alpha}{2(1-\nu)} \left[\frac{\left(R_0^2 T_0 - R_I^2 T_I\right) - R_0^2\left(T_I - T_0\right)}{R_0^2 - R_I^2} - \frac{T_I - T_0}{\ell n\left(R_I/R_0\right)} - T_I \right] , \tag{39}$$

where E is Young's modulus, α is the thermal expansion coefficient, ν is Poisson's ratio, and T_0 and T_I are the temperatures at the outer and inner tube surfaces, respectively. The thermophysical and mechanical properties used in the calculations are given in Appendix E. The parameters chosen for the comparison are a wall thickness of 1.5 mm, a tube diameter of 2 cm, and a coolant pressure of 400 psi. The results of the calculations are shown in Fig. 8-7. The temperature plotted in Fig. 8-7 are the temperatures at the tube inner surface where the tensile hoop stresses are greatest. Overall, the copper alloy and the refractory metal alloys, with the exception of the titanium

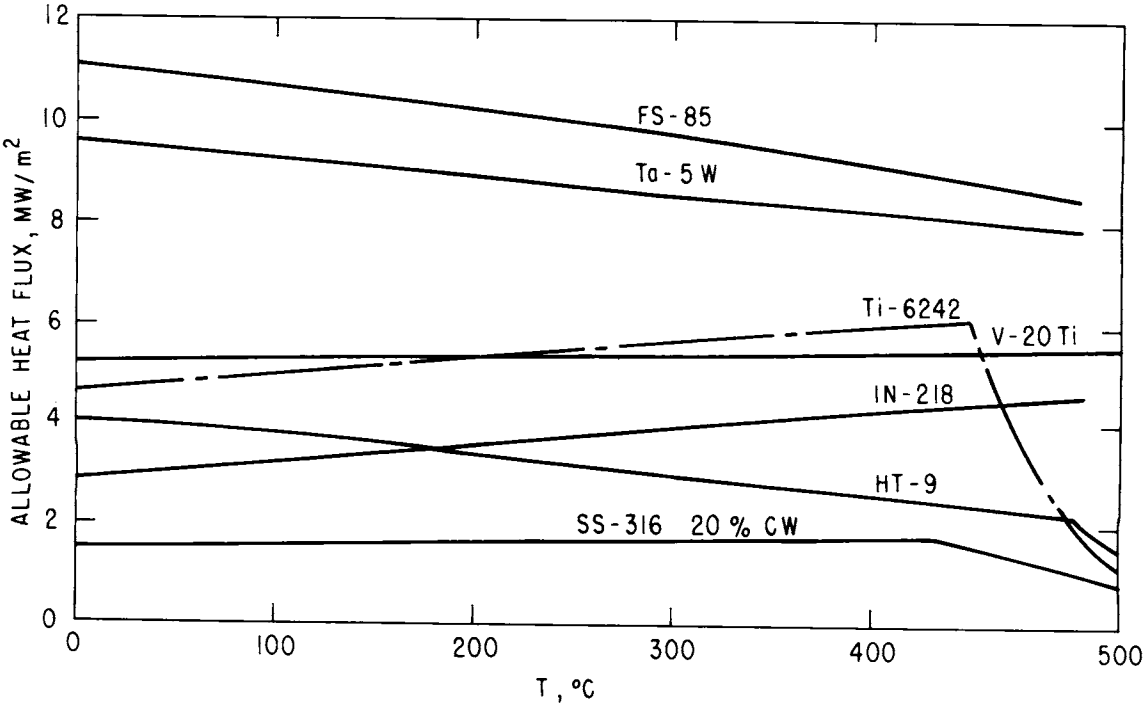

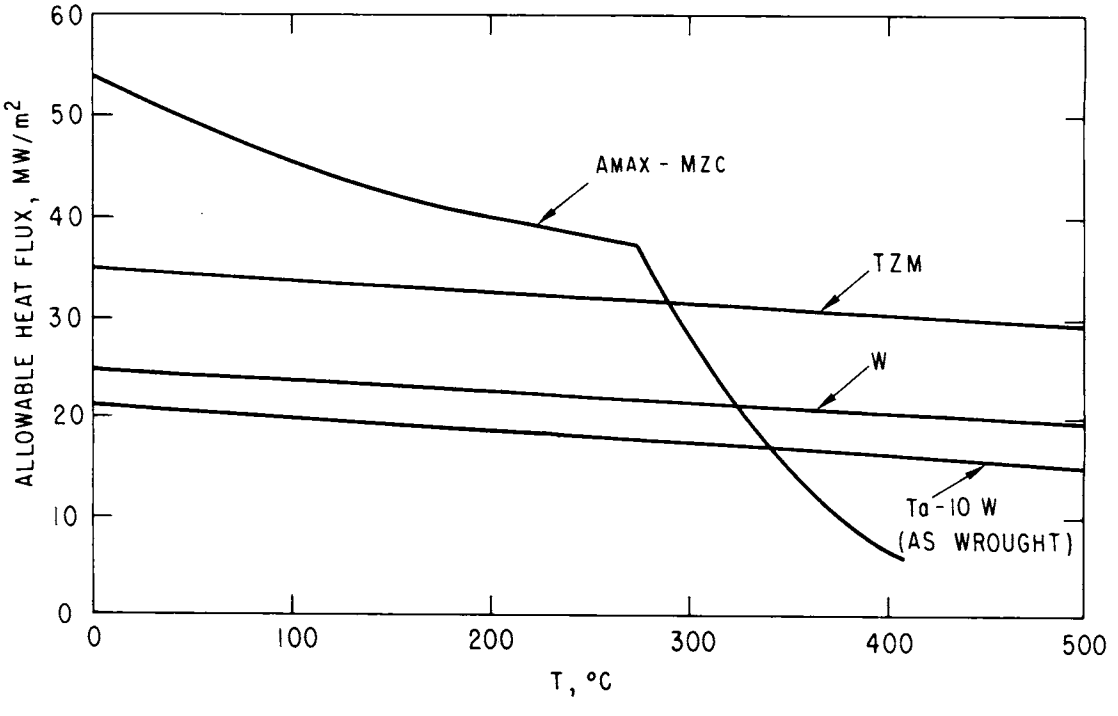

Figure 8-7. Heat flux limits for potential limiter materials.

alloy, exhibit the highest potential to withstand a high heat flux. The stainless steels, Type 316 and HT-9, can be eliminated from further consideration because of their relatively poor thermophysical properties. The nickel alloy, Inconel 718, appears to be only marginal in its ability to withstand a high heat flux, and has also been eliminated from further consideration.

Other materials can be eliminated from consideration based upon deficiencies in other properties. Although the molybdenum alloy, TZM, and tungsten are capable of withstanding a high heat flux, they are both susceptible to radiation damage. The ductile-brittle transition temperature (DBTT) of these materials has been observed to increase to ~400°C after irradiation,[34,35] which is at or above the standard operating temperatures of the limiter. In addition, the alloys of both molybdenum and tungsten are generally difficult to fabricate. Therefore, they have also been eliminated from consideration. The titanium alloy and the vanadium alloy exhibit a similar level of resistance to thermal stress. However, vanadium alloys have a superior resistance to radiation, and titanium alloys appear to be particularly susceptible to hydrogen embrittlement.[36] Thus only the vanadium alloy will be considered.

8.4.2.2 Reference Alloys

Four reference alloys with the potential for successfully handling the limiter heat flux have been selected for further consideration. As shown in Table 8-8, they include a copper alloy (AMAX-MZC) and refractory metal alloys of vanadium (V-20Ti), niobium (FS-85), and tantalum (Ta-5W). The copper alloy was chosen because it combines high strength and a high thermal conductivity that is close to that of pure copper.[37] The vanadium alloy was chosen because of its known resistance to radiation damage, while the niobium and tantalum alloys were chosen because of their high heat flux limits and potential resistance to radiation damage. The primary concerns of the copper alloy are first the very limited data on the effects of radiation; second, its low operating safety margin due to its low melting point compared with the other materials (see Table 8-9); and third, its ability to be fabricated into a usable form while maintaining its cold-worked strength properties. Welding or brazing will alter the strength of the material. The primary concerns of the refractory metal alloys are first, the possible corrosive and embrittling effects of the reactor environment; and second, the loss of ductility due to irradiation hardening and the increase in the DBTT during operation. This

Table 8-9. Reference Limiter Alloys

Material	Composition (wt-%)	Melting Point (°K)	Density (g/cm^3)
AMAX-MZC	Magnesium - 0.06 Zirconium - 0.15 Chromium - 0.40 Copper - Bal.	1356	8.9
FS-85	Tungsten - 10 Tantalum - 27 Zirconium - 0.8 Niobium - Bal.	2741	8.6
V-20Ti	Titanium - 20 Vanadium - Bal.	2163	6.1
Ta-5W	Tungsten - 5 Tantalum - Bal.	3269	16.6

section will consider the physical properties of the reference alloys and the effect of the reactor environment upon their operational lifetime. The limiter is expected to operate at low-to-moderate temperatures, and therefore the properties have been evaluated for temperatures $\leq$600°C.

The properties of concern for the alloys in the unirradiated condition include the thermophysical, tensile, and thermal creep properties. The thermophysical properties of the four alloys are shown in Fig. 8-8. It is evident that the principal advantage of AMAX-MZC is its extremely high thermal conductivity which is a factor of 5-10 higher than the conductivity of the other alloys. Although the thermal expansion coefficient is also the highest in AMAX-MZC, its thermal conductivity more than compensates for this disadvantage. The tensile properties of the four alloys are shown in Fig. 8-9. Note that the properties of the Ta-5W alloy are shown for both the fully annealed and 40% cold-worked conditions. The Ta-5W alloy is a solution strengthened alloy, like Type 316 stainless steel, and as such, cold work has a significant effect upon its strength. For both the tensile strength and ductility, the cold-worked and annealed Ta-5W alloy bracket the range of properties. Thermal creep of the reference alloys is not expected to be a problem, with the possible exception of AMAX-MZC. The transition metal alloys, being high-melting

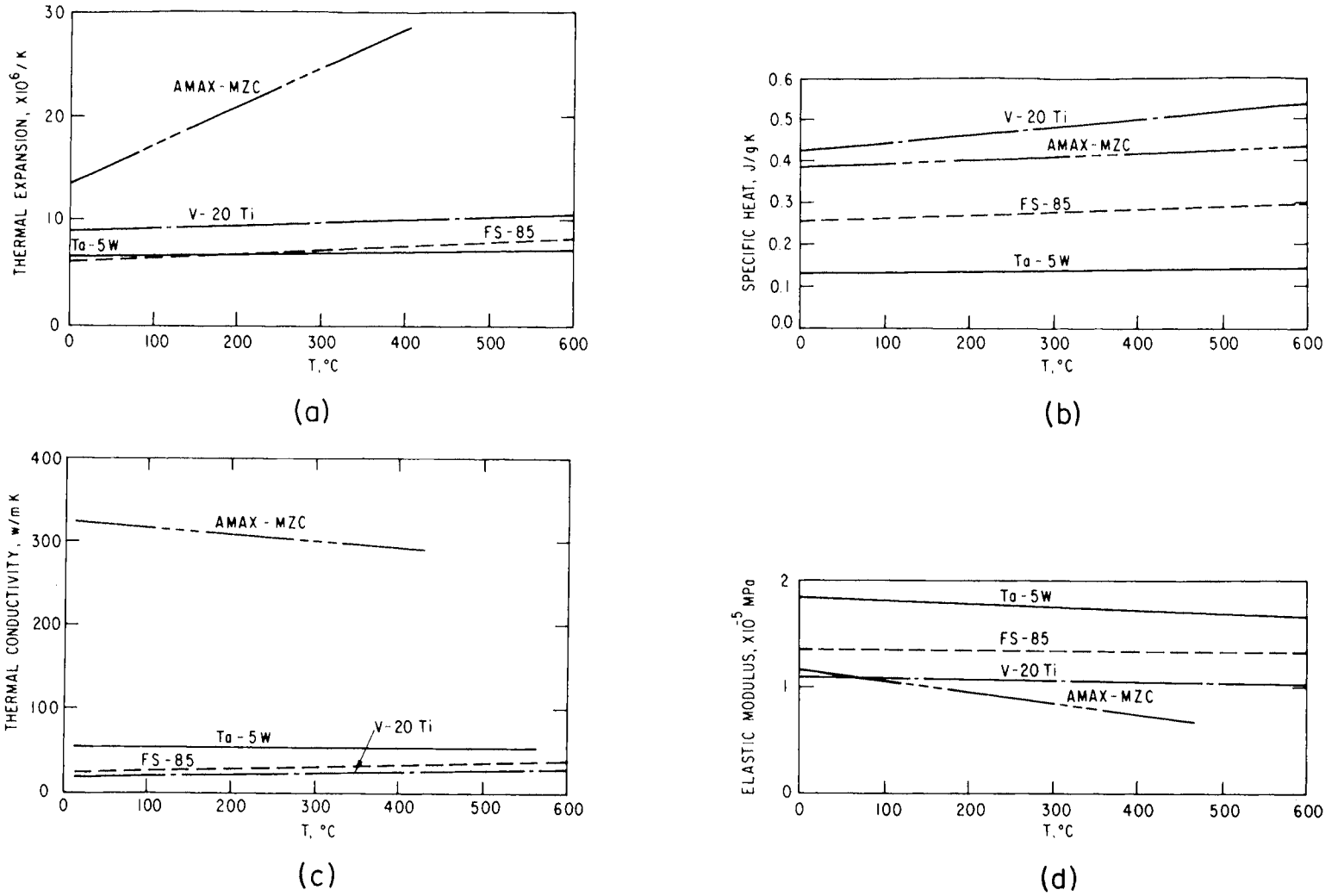

Figure 8-8. Thermophysical properties of candidate limiter materials: (a) thermal conductivity; (b) specifc heat; (c) thermal expansion; and (d) elastic modulus.

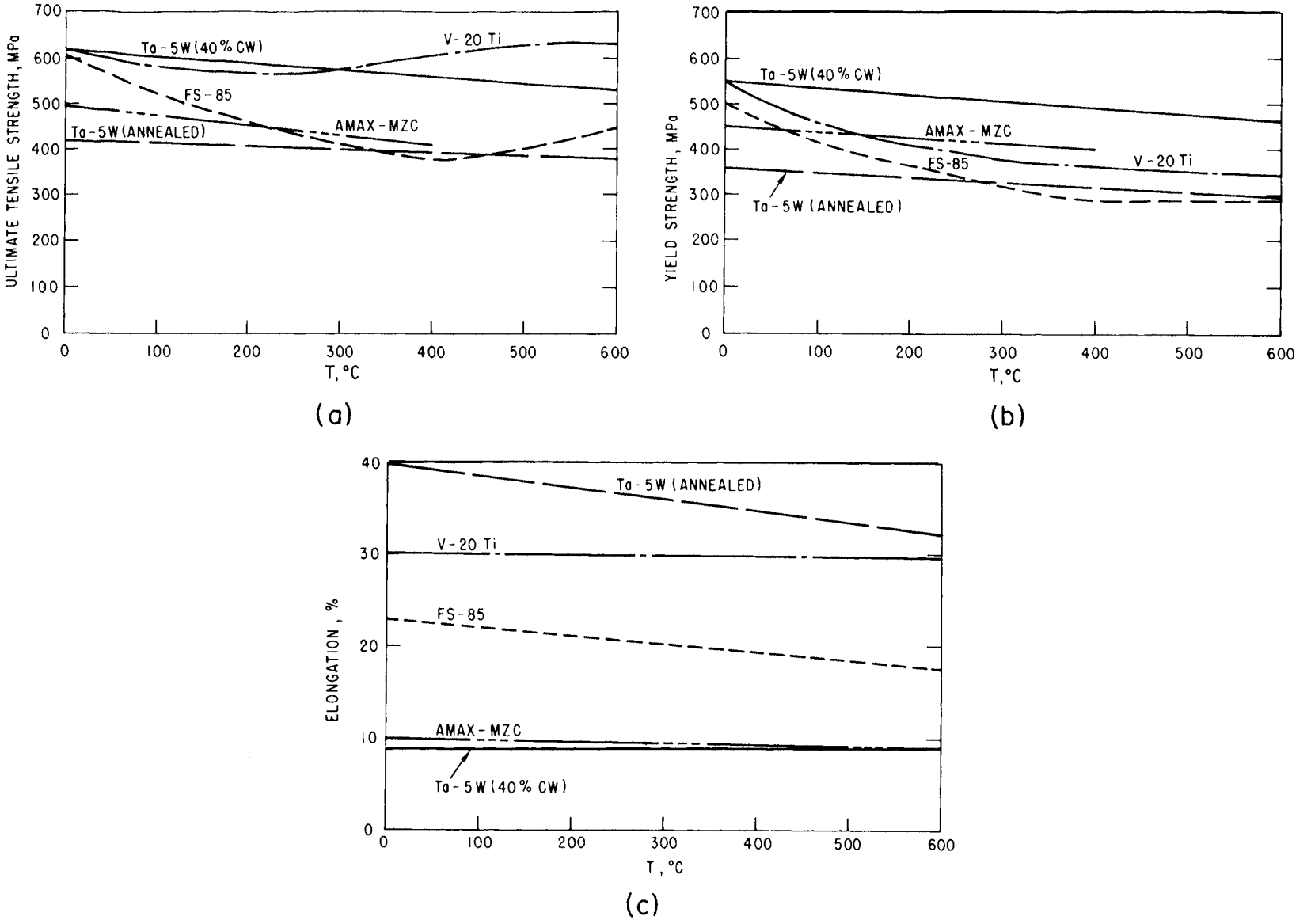

Figure 8-9. Tensile properties of candidate limiter materials: (a) ultimate tensile strength; (b) 0.2% yield strength; and (c) total elongation.

point metals, all exhibit low thermal creep in the temperature range contemplated for STARFIRE.[38] The limited data on thermal creep in AMAX-MZC show that significant thermal creep occurs at temperatures >300°C[37] indicating that the useful temperature range would be limited for this material.

Compatibility of the limiter materials with the reactor environment is also a major concern. In STARFIRE, the limiter must be compatible with the water coolant as well as the deuterium and tritium from the plasma. The corrosion rate of the materials in water will depend upon the temperature, coolant flow rate, alloy composition, and water chemistry. In general, there is insufficient information on the reference alloys to predict their corrosion rates in STARFIRE, but there is some information on similar alloys from which order of magnitude estimates can be made. Copper and copper alloys have been examined for potential use in light-water reactors and have been found to have high corrosion rates (>100 mg/dm^2-mo) at 260°C in water containing 10 to 30 cm^3 of dissolved oxygen (STP) per kilogram.[39] However, the presence of hydrogen in water can reduce corrosion rates by a factor of up to 200. The corrosion rate of 70-30 copper-nickel in degassed water at 260°C has been measured at only 5 mg/cm^2-mo.[39] The corrosion rates of pure niobium or vanadium in water are also high,[39,40] but alloying is expected to reduce the rates. For example, the corrosion rate of pure niobium exposed to 360°C water is estimated to be 110 mg/cm^2-mo compared with 30 mg/dm^2-mo for a Nb-40Zr alloy.[40] Tantalum and niobium alloys have excellent corrosion resistance to acid environments, but are much less resistant to corrosion in alkaline environments.[41] A Ta-10W alloy tested in 260°C water containing 30 cm^3 of dissolved oxygen per liter had a corrosion rate of 8 mg/dm^2-mo.[42] For comparison, a corrosion rate of 10 mg/dm^2-mo is representative of the corrosion rates for a stainless steel water-cooled reactor.[39] In summary, the corrosion rates of the reference alloys are probably acceptable for the low temperature (145°C coolant outlet) operating conditions of STARFIRE, but further experimental work is needed to determine the best coolant chemistry conditions to minimize corrosion.

Protium, deuterium, and tritium introduced into the limiter materials is a concern because of the potential of hydrogen embrittlement. Copper and copper alloys can become embrittled by hydrogen if there is also a significant amount of oxygen dissolved in the metal.[43] Reduction of the oxygen content to low levels should eliminate this concern, however. The other three alloys are susceptible to hydrogen embrittlement due to the formation of a brittle

hydride phase at low temperatures. The hydrogen (plus deuterium and tritium) can be introduced into the material by either absorption and diffusion from the plasma side or by galvanic action on the coolant side. The equilibrium concentration of hydrogen in the three refractory metal alloys can be estimated from thermodynamic data for the pure elements, as shown in Fig. 8-10.[44-47]

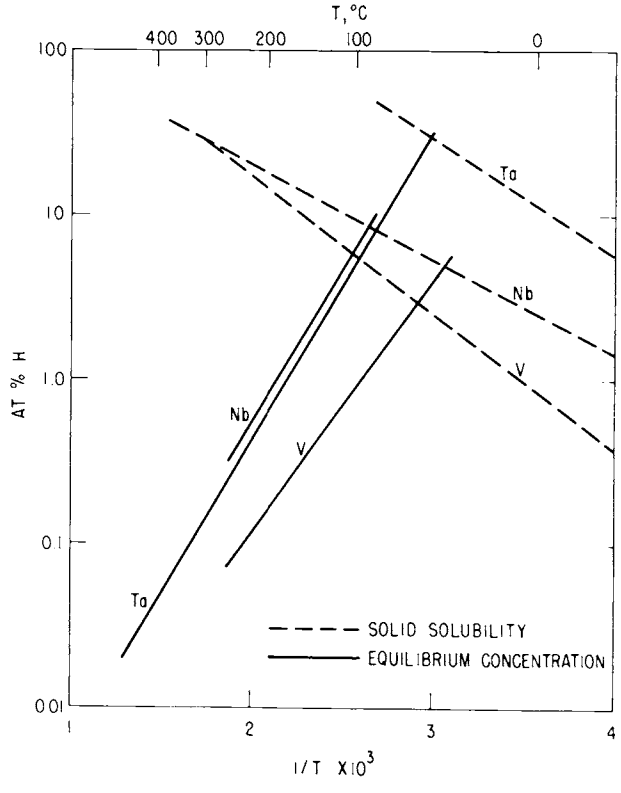

Figure 8-10. Equilibrium hydrogen concentration at 0.13 Pa hydrogen pressure and hydrogen solid solubility in refractory metals.

The maximum estimated partial pressure of deuterium and tritium at the limiter is $\sim 10^{-3}$ torr (0.13 Pa). At this pressure, the equilibrium concentration of hydrogen in the metal is at least a factor of 100 below that required for hydride formation during normal operation at 200-300°C. As the temperature is lowered, the solubility of the hydrogen decreases while the concentration of hydrogen increases for a constant hydrogen partial pressure. If the partial pressure is maintained at 0.13 Pa (10^{-3} torr) as the temperature is lowered, hydride formation is predicted above room temperature for all three metals. The kinetics of the reaction at these temperatures is low, however, and barriers to hydrogen diffusion such as the beryllium coating or an oxide layer

are expected to prevent the hydrogen from reaching the levels necessary for embrittlement. In addition, the partial pressure of tritium and deuterium will be much less than 10^{-3} torr during reactor shutdown. The joining of a refractory metal to a dissimilar metal could produce a galvanic action that would result in the introduction of hydrogen into the metal from the coolant. In fact, hydrogen embrittlement in tantalum has been observed due to this process.[48] Therefore, care should be taken in the selection of other metals in the limiter cooling system to insure against this form of embrittlement. With proper control, however, all of the reference alloys should be capable of an acceptable level of corrosion resistance.

Neutron irradiation is known to induce swelling, accelerate creep, alter the strength, decrease the ductility, and produce compositional changes in structural metals. All of these changes can potentially affect the heat carrying capacity and the lifetime of the limiter materials. The amount of information available on irradiation effects on the reference alloys is sparse, and thus a rigorous evaluation of the operating lifetime is not possible. Rather, the available data will be used to indicate general trends and, where possible, to determine areas of major concerns.

Swelling in metals is caused by the segregation of radiation produced vacancies into voids during irradiation at temperatures from 0.3 to 0.5 of the absolute melting temperature, T_m. Several factors, including temperature, neutron flux rate, total neutron fluence, helium generation rate, cold work, grain size, and precipitate structure can influence the amount of swelling. With the exception of V-20Ti, swelling in the reference alloys has not been investigated. Copper exhibits a peak swelling at $\sim$325°C (0.44 T_m) and the rate of swelling is high ($\sim$1%/dpa).[49] Alloying the copper can reduce the observed swelling,[50] but it is not known what, if any, reduction in swelling will be observed in AMAX-MZC. Therefore, to reduce the amount of swelling, the temperature of AMAX-MZC should be kept significantly below 325°C. Pure niobium, vanadium, and tantalum exhibit swelling peaks at $\sim$600°C (0.32 T_m), 550°C (0.38 T_m), and 650°C (0.28 T_m), respectively.[51-53] These temperatures are far higher than the expected limiter operating temperatures of 200-300°C, and thus void swelling in the refractory metals should be low. The swelling rates of the refractory metals exhibit a less than linear dependence with neutron fluence, and the swelling rates are considerably below

that of pure copper. Alloying can significantly reduce the swelling in the refractory metals. In the case of V-20Ti, no swelling has been observed up to a fast neutron fluence of 6×10^{22} n/cm^2 ($\sim$30 dpa).[52] Additions of molybdenum, vanadium, titanium, zirconium, and hafnium have been shown to reduce the void swelling in niobium.[54] Limited data on the tantalum alloy, T-111, indicate densification rather than swelling after irradiation at 414°C and 643°C to a fluence of 1.9×10^{22} n/cm^2 (>0.1 MeV).[34] No explanation for the densification was given.

Neutron irradiation is known to reduce the ductility of metals at low temperatures. Since the limiter is designed to operate in the elastic range, residual ductility is only necessary to prevent catastrophic failure during an off-normal event. The amount of ductility required will depend upon the severity of the event, and cannot be realistically estimated at this time. However, the greater the amount of residual ductility, the more likely the limiter is to successfully withstand off-normal conditions. Unfortunately, there is no available information on copper and copper alloys near the range of interest, and only limited data are available on the refractory alloys. Vanadium alloys and pure niobium appear to retain the greatest amount of ductility, while Nb-1Zr, tantalum, and T-111 appear to become highly embrittled by neutron fluences of $1\text{-}3 \times 10^{22}$ n/cm^2 (ε > 1 MeV).[34] Although the values for the total elongation of irradiated Nb-1Zr, tantalum, and T-111 were 8-15%, the values for the uniform elongation were as low as 0.2% at room temperature. In comparison, the uniform elongation of vanadium alloys and pure niobium at room temperature were 2.5% and 10.1% respectively. The reduced ductility at low temperatures in tantalum and niobium alloys represents a potential problem area for these materials, and further experimental work is needed to more carefully evaluate the influence of radiation on the ductility of the reference alloys.

Radiation is expected to accelerate creep in all of the reference alloys at the limiter operating temperatures, similar to the effect of radiation on creep in stainless steels. Again, there is insufficient data to evaluate the magnitude of this effect. However, if the radiation creep rates are similar to the creep rates in stainless steel, the thermal stresses would be expected to relax to low values in 2000-5000 h. (See Sec. 10.6 for details on creep relaxation in stainless steels.) After this time, the highest stresses would then occur when the temperature gradient is removed and not during normal

operation. The stresses produced when the temperature gradient is removed would be equal in magnitude but opposite in sign to the original thermal stresses. Since the primary stresses in the limiter are expected to be low, the dimensional changes due to radiation creep are expected to be low for all the reference alloys.

The fusion neutron spectrum introduces radiation effects that do not occur in fission reactors. First, helium production rates in the limiter materials will be significantly higher. Helium can alter the swelling rates and induce embrittlement. Helium embrittlement is a high temperature phenomena ($T > 0.5\ T_m$) and should not effect the limiter operation. Since the refractory metal alloys would operate significantly below the void swelling range, helium should have little influence on swelling. The copper alloy, AMAX-MZC, may operate in the swelling regime, and therefore, the high helium production rate may be important. Second, compositional changes could be large. As shown in Sec. 8.4.7, the only reference alloy whose composition would be significantly changed is Ta-5W. Six years of operation will increase the tungsten content to $\sim$20 wt-%. The principal effect of the increased tungsten is a higher tensile strength and reduced ductility.[38] These changes are not expected to have a serious impact on the limiter operation, since radiation displacement damage alone will reduce the ductility of Ta-5W to low levels.

8.4.2.3 Summary

A summary of the various properties of the reference alloys is shown in Table 8-10. No single alloy stands out as being the best for limiter applications. The AMAX-MZC alloy certainly is capable of withstanding high heat fluxes, but is limited in the temperature of operation because thermal creep becomes significant at temperatures $\geq$300°C. Swelling in this alloy could also be a problem since the swelling peak in pure copper is at $\sim$325°C. For STARFIRE, the AMAX-MZC alloy would probably be limited to low temperature operation ($T < 200$°C). The operating safety factor of this material is the lowest of the four reference alloys, because of its low melting point. The V-20Ti alloy appears to have the best radiation resistance, but it also has the lowest thermal stress resistance of the reference alloys. Radiation damage in both FS-85 and Ta-5W could result in unacceptably low ductility. Since FS-85 and Ta-5W are high melting point materials, however, they can be operated at high temperatures and are more likely to remain undamaged by an off-normal event.

The corrosion resistance of the refractory alloys to the water coolant will limit the temperature of operation. Unfortunately, there is insufficient data to make a final choice for the limiter material at this time. In particular, more information is required in the areas of corrosion and radiation effects for all of the alloys.

Table 8-10. Reference Limiter Alloys Properties

Property	AMAX-MZC	Vi-20Ti	FS-85	Ta-5W
Thermal stress resistance	O	●	O	O
Tensile strength	●	O	O	O
Thermal creep	●	O	O	O
Corrosion	O?	O?	O?	O?
Stress corrosion cracking	?	?	?	?
Swelling	●?	O	O	O
Loss of ductility	?	O?	●?	●?
Change in tensile strength	?	O	O	O
Radiation creep	O?	O?	O?	O?
Transmutation effects	O	O	O	O

O Acceptable.

● Potential problem.

? Insufficient data for evaluation.

O? Appears acceptable but more data needed.

●? Appears to be a problem but more data needed.

8.4.3 Coating/Cladding Materials

8.4.3.1 Criteria for Material Selection

Selection of the appropriate material for the plasma-exposed surfaces of the plasma chamber components is an important consideration in the design of the plasma chamber and the impurity control system. The plasma chamber materials in general, and the limiter materials in particular, must withstand the high thermal and particle fluxes, maintain their structural integrity under high neutron radiation and thermal stresses, and not be a source of excessive plasma contamination. The critical criteria for the selection of candidate

first-wall/limiter materials relate to the plasma-wall interactions. Several materials should withstand the plasma environment for acceptable lifetimes; however, the impacts of different materials on plasma performance and effects arising from plasma-wall interactions severely limit the choices of materials. The coating/cladding concept is proposed because of its flexibility which allows the coating/cladding material to be selected primarily on the basis of its surface properties and the substrate material to be selected primarily on the basis of its structural and compatibility properties. The coating concept was originally proposed for the ANL Experimental Power Reactor first wall.[24,25]

As discussed in Sec. 8.3, high-Z impurities eroded from the surfaces of the plasma chamber components severely impact the plasma performance. Also, high-Z impurities eroded from the wall can become energetic ions or neutrals which subsequently impact the first-wall components and produce high self-sputtering yields. Sputtering yields greater than unity can lead to a propagating effect and an excessive buildup of impurities in the plasma or excessive erosion of the wall. A second important surface-related consideration in the selection of the limiter coating/cladding material arises from effects of redeposition of wall-eroded material. Material eroded from one region of the plasma chamber, e.g., the first wall, can deposit on the limiter. If the first-wall and limiter materials are different, the composition of the limiter would be changed by the deposition of the wall material on the limiter. A similar type of problem could exist if the wall materials are a compound consisting of different elements. Non-uniform erosion or deposition of the different elements will change the surface composition of the wall and hence its properties, e.g., sputtering coefficients. Although limited information exists, a third consideration relates to the electronic characteristics of the first surface material, viz., electronic conductor versus electronic insulator. Since both energetic electrons and ions will strike the limiter surface, the electronic properties and charge state of the surface could have important implications. For example, non-uniform charge buildup such as could occur with an insulator may enhance arcing. Also, cracking of an insulator coating could affect the charge state of the limiter surface and the effective reflection coefficient for electrons. Although further analyses are needed, highly conducting surfaces are presently perceived to be preferred over insulator materials.

Table 8-11 summarizes the important considerations in the selection of the primary candidate coating/cladding materials.

Table 8-11. Considerations for Selection of Coating/Cladding Material for Limiter

Atomic number (Z)
Physical sputtering yields
Chemical reactivity with hydrogen
Blistering erosion
Compatibility with candidate substrate materials
Melting temperature
Vapor pressure
Elemental composition
Thermal conductivity
Radiation damage resistance
Thermal expansion coefficient
Electronic conductivity
Fabricability

8.4.3.2 Candidate Coating/Cladding Materials

The materials considered for the limiter coating/cladding have generally been classified into the four categories listed in Table 8-12. The primary criteria for the identification of these candidate materials is chemical stability, viz., melting temperature and vapor pressure, at acceptable operating temperatures and moderate or low effective atomic numbers. The compounds listed are generally representative of the class of materials available.

Table 8-12. Materials Considered for the Limiter Coating/Cladding

Low-Z elements	Be, B, C
Low-Z compounds	BeO, B_4C, BN
Moderate-Z compounds	SiC, SiO_2, SiN, Al_2O_3, MgO
Transition metal compounds	TiC, TiB_2, VB_2

It is possible that more complex compounds, e.g., ternary compounds, with favorable characteristics may exist. Erosion mechanisms considered for the coating/cladding materials include physical sputtering by plasma particles, neutron sputtering, chemical sputtering, and blistering. Because of the physical sputtering, desorption mechanisms are not considered to be a significant source of plasma contamination for STARFIRE conditions.

The major mechanism of wall erosion during operation is predicted to be physical sputtering caused by energetic plasma particles (D, T, He, and impurities) striking the limiter. A significant data base for physical sputtering of candidate wall materials has been developed in recent years. It is generally concluded that physical sputtering yields of monoenergetic ions normally incident on candidate wall materials are known or can be predicted within a factor of 2 (a factor of 1.5 in many cases). This accuracy is considered to be within the range of other uncertainties in plasma-wall interaction analyses and adequate for the present study. Physical sputtering yields used in the present study are based on a model developed by Smith,[31,32] which gives the energy-dependent physical sputtering yields for various plasma particles incident on candidate first-wall materials. The expression for the physical sputtering yields, which is based on both theoretical and experimental considerations, is given in terms of the atomic and mass numbers of the incident and target atoms, the surface binding energy of the target material, and the energy of the incident particle. The general shapes of the sputtering yield curves are based on theoretical models, whereas the magnitudes of the yields are derived primarily from experimental data. Characteristics of the original sputter-yield curves[31] include: (a) a direct energy dependence at low incident particle energy; (b) a 1/E dependence at high incident particle energies; and (c) a peak at intermediate energies where the yield is relatively insensitive to energy. The recent modification[32] incorporates a threshold energy term into the expression to give an asymptotic approach to zero sputtering at the threshold rather than the abrupt cutoff originally presented. The sputtering yield in atoms per ion is given by:

$$S(E) = \frac{20}{U_0} Z_1^2 Z_2^2 \frac{M_1}{M_2} \frac{\left(E - E_{th}\right)}{\left[\left(E - E_{th}\right) + 50\ Z_1 Z_2\right]^2}, \qquad (40)$$

where

$$E_{th} = \frac{(M_1 + M_2)^2}{4\, M_1 M_2} U_0 , \qquad \text{for } M_1 \leq M_2 ,$$

$$E_{th} = \frac{M_2}{M_1} U_0 , \qquad \text{for } M_1 > M_2 , \tag{41}$$

where Z_1, Z_2 and M_1, M_2 are the atomic numbers and mass numbers of the incident particles and target atoms, respectively; U_0 is the binding energy in eV; and E is the incident particle energy in eV. Parameters required for the calculation of the physical sputtering yields for several candidate wall materials are given in Table 8-13. As shown in Appendix E, the calculated values are in fairly good agreement with reported experimental data including the recent compilation of Roth, et al.[53] Although several models have been proposed, the present model gives an adequate representation over the energy range of interest and it can be easily combined with the Maxwellian distribution function to give the Maxwellian-averaged sputtering yields. Representative sputtering yield curves for monoenergetic D^+, He^{++}, and self-ions on selected wall materials are given in Figs. 8-11 through 8-13.

As indicated in Sec. 8.3, the effective Z of the transition metal compounds does not appear to be acceptable on the basis of impact on plasma performance. Subsequent self-sputtering erosion by the energetic transition metal ions is also identified as a major problem. Since other important properties of the transition-metal compounds are not substantially superior to those of the moderate-Z and low-Z compounds, this class of materials is not proposed for the primary candidate limiter material. The moderate-Z compounds have also been eliminated from further consideration since they appear to be marginal because of their impact on plasma performance, and to a first order, they do not offer other significant advantages over the low-Z compounds.

The candidate low-Z compounds are refractory-type materials that offer potential for high-temperature operation. The calculations indicate that these materials would permit acceptable plasma performance and they also appear to meet most of the other criteria listed in Table 8-11. The major questions regarding the viability of these materials relate to their electronic properties

Table 8-13. Parameters for Calculation of Physical-Sputter Yields for Metallic Wall Materials

Wall Material	Z	M	U_0, eV
Be	4	9.0	3.4
B	5	10.8	5.7
C	6	12.0	7.4
Al	13	27.0	3.4
Si	14	28.1	4.7
Ti	22	47.9	4.9
V	23	50.9	5.3
Fe	26	55.9	4.3
Nb	41	92.9	7.6
Mo	42	95.9	6.8
W	74	183.9	11.1
BeO	6.0	12.5	6.1
B_4C	5.2	11.0	4.2
BN	6.0	12.4	6.1
MgO	10.0	20.2	5.1
Al_2O_3	10.0	20.4	6.2
SiC	10.0	20.0	4.2
SiO_2	10.0	20.0	6.4
TiC	14	30	4.2
TiB_2	11.3	23.2	4.2
VB_2	11.7	24.2	4.2

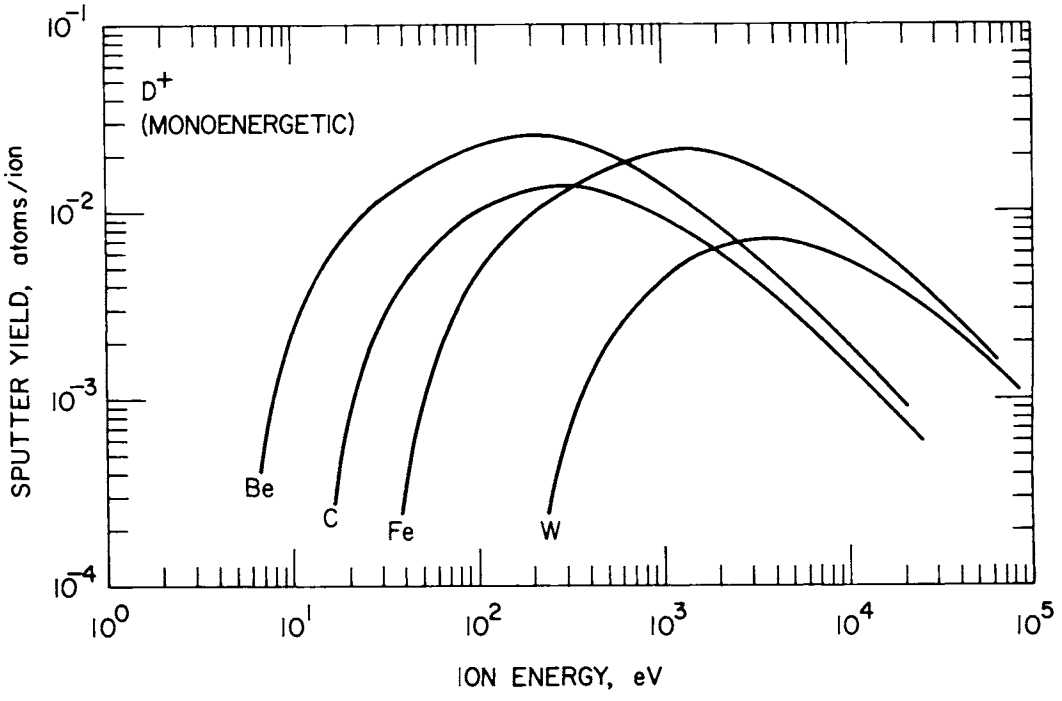

Figure 8-11. Calculated energy-dependent physical sputter yields of candidate first-wall materials bombarded with monoenergetic deuterium ions.

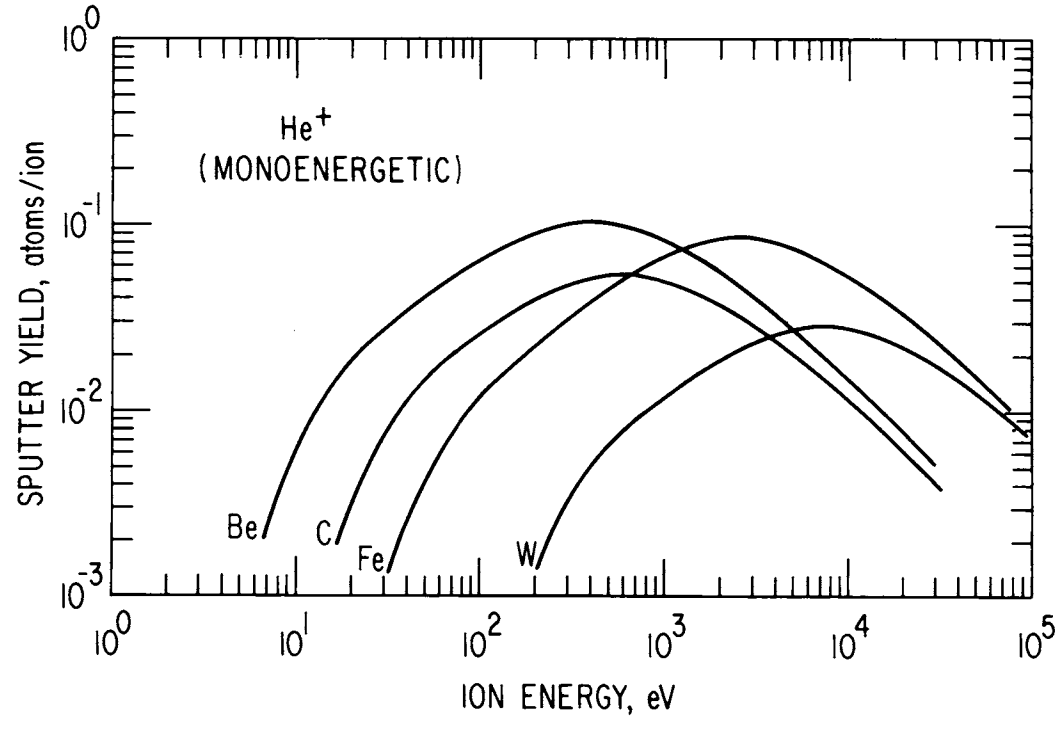

Figure 8-12. Calculated energy-dependent physical sputter yields of candidate first-wall materials bombarded with monoenergetic helium ions.

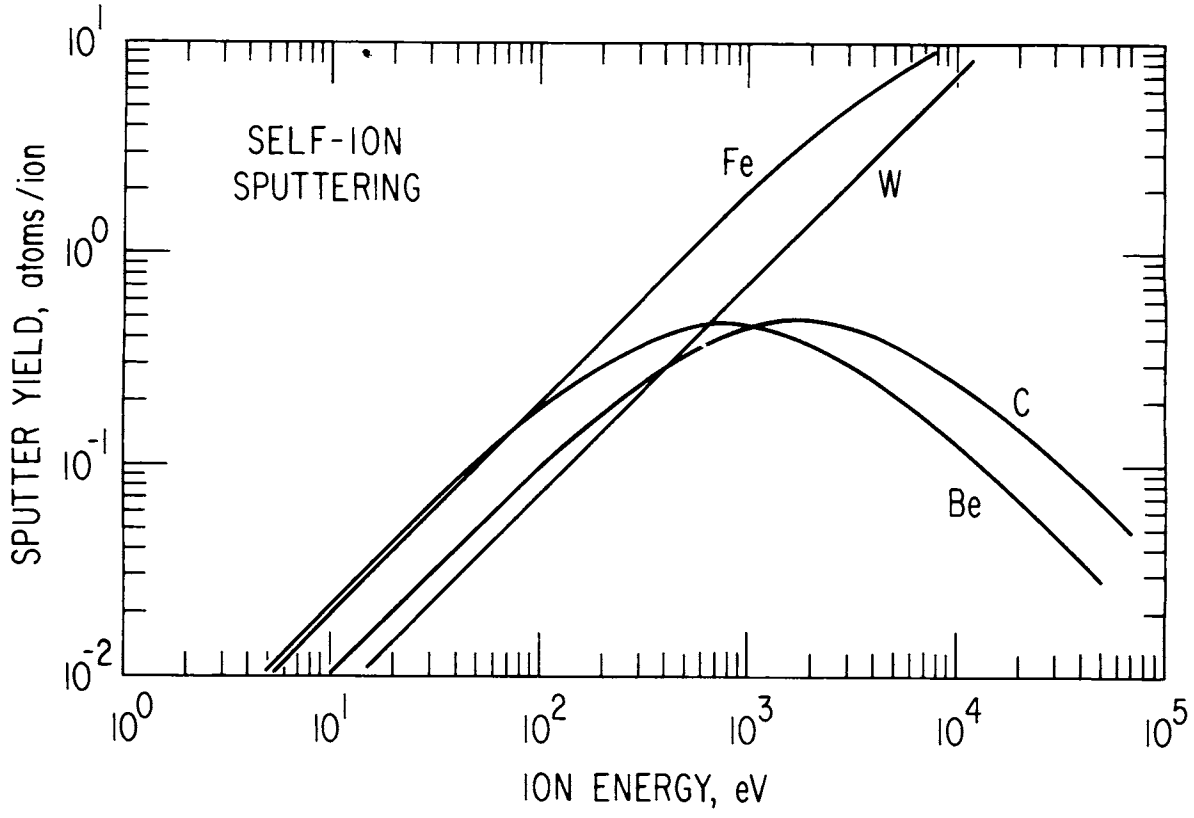

Figure 8-13. Calculated energy-dependent self-sputtering yield for several candidate wall materials.

and problems arising from the use of a two-component material. Since the STARFIRE limiter operates at relatively low temperature, the high-temperature properties are not a great advantage. Because of the uncertainties arising from the compound (two element) nature of these materials and the importance of electronic structure, the low-Z elements are presently selected for the primary candidate limiter coating/cladding materials.

The erosion rates of graphite are predicted to be excessive because of the chemical sputtering that occurs as a result of chemical interactions with the hydrogen isotopes. The anticipated temperature ranges for the limiter coating are within the methane (CH_4) formation region predicted by Balooch and Olander [56] and the enhanced sputtering-yield range observed by several other investigators.[57-60] Although some efforts to suppress the chemical sputtering of graphite have recently been indicated,[61-62] detailed results are not presently available. However, it is difficult to understand how the reported surface passivation can be retained under anticipated STARFIRE conditions where high-radiation damage levels and substantial total wall erosion are predicted.

The thermodynamics of the hydrogen-carbon system have been extensively studied and probably provide the best basis at present for assessment of the chemical effects. Present evidence is not sufficient to conclude that carbon or graphite would be an acceptable coating for the limiter of STARFIRE.

Beryllium and boron are selected as the primary candidate coating/cladding materials for the limiter and beryllium is selected for the reference design. Table 8-14 presents important properties of these two primary candidate materials.

8.4.3.3 Evaluation of Reference Coating/Cladding

Beryllium has many properties that not only make it suitable for the limiter coating/cladding but make it superior to other candidates. The important property requirements and the relative merits of beryllium are summarized as Table 8-15.

A potential method for applying beryllium to the limiter is plasma spraying. This technique has been successfully employed to apply coatings and to produce tubing and free-standing beryllium parts.[64] Present plasma-spray devices can apply beryllium at a rate of $\sim$1 kg/h. At this rate, a 1-mm thick coating can be applied to a 1-m^2 surface area in $\sim$1.8 h. The structure of plasma-sprayed beryllium is layered, resulting in an inhomogeneity in the physical properties. The grain size, impurity content, and amount of porosity can vary depending on the conditions used for spraying. Sintering of the plasma-sprayed coating will occur at elevated temperatures, and the temperature where sintering begins depends upon the original porosity. A layer with 12% porosity will begin to sinter at $\sim$1000°C. Coatings produced from high-purity powders are difficult to densify even at 1250°C. Beryllium does not penetrate deeply into the substrate material because of its low atomic weight. Therefore, the surface of the substrate material should be roughened by grit blasting, special machining or etching to increase the bond strength of the beryllium coating. Further development work is required to determine the proper technique for application of beryllium coatings on the limiter.

Boron is also a prime candidate coating material. Primary advantages compared to beryllium include slightly lower physical sputtering yields and higher melting temperature. The major disadvantages relative to beryllium are a much lower thermal conductivity and a higher hydrogen solubility and permeability.

Table 8-14. Properties of Beryllium and Boron

Property	Beryllium	Boron
Atomic number	4	5
Atomic weight	9.01	10.81
Density, g/cm^3	1.85	2.34
Crystal structure	HCP	MC
Melting temperature, °C	1284	2300
Boiling temperature, °C	2970	2550 (s)
Vapor pressure, Pa (°C)	10^{-4} (850) 10^{-2} (993) 10^{0} (1192) 10^{1} (1335) (ℓ)	10^{-4} (1557) 10^{-2} (1877) ——— ———
Heat of fusion, J/g	1083	2077
Heat of vaporization, J/g	24,790	46,740
Heat capacity, J/g-°C		
500°C	2.25	2.09
1000°C	2.92	2.61
1500°C	3.59 (ℓ)	3.13
Coefficient of thermal expansion, $°C^{-1}(10^{-6})$		
25-100°C	11.6	5.0
25-500°C	15.9	5.5
25-1000°C	18.4	6.1
Thermal conductivity, w/m-°K		
50°C	150	27
300°C	125	18
600°C	96	14
Electrical Resistivity, μΩ-cm		
400°C	15	15

Table 8-15. Summary of Favorable Characteristics of Beryllium for Limiter Coating/Cladding

Atomic number	Beryllium is the lowest atomic number of any material that is solid at the proposed operating temperature.
Physical sputtering	Maxwellian averaged deuterium and tritium sputtering yields for an incident energy of 1200 eV (0.015, 0.023 atom/ion) are less than those for aluminum and steel but about 50% greater than that for carbon. However, the estimated self-sputtering yield is only 0.4 atom/ion compared to values of 0.39 for carbon, 1.9 for aluminum, and 20 for steel. Very few elements have self-sputtering yields lower than beryllium.
Blistering	Microstructural tailoring has been shown to be effective in substantially reducing the tendency to blistering of beryllium.[a]
Hydrogen reactions	Hydrides are not stable under the predicted operating conditions and chemical sputtering of beryllium has not been observed. The solubility of hydrogen is very low and the reported permeability of hydrogen is significantly lower than that for either tungsten or molybdenum. Therefore, tritium inventory in the beryllium and tritium migration into the coolant should be minimal.
Melting temperature	Although beryllium is not refractory, its melting temperature is adequate for the water-cooled limiter.
Thermal conductivity	Beryllium has a very high conductivity compared to most metals (about one-third that of copper and ∿10 times higher than carbon). The high thermal conductivity tends to minimize surface temperatures and thermal stresses. The coating/cladding can be thicker to accommodate sputtering erosion.
Vapor pressure	The vapor pressure is low at the proposed operating temperatures. Since the vapor pressure increases relatively rapidly above 800°C, vaporization will aid in quenching the plasma in the event of a loss of coolant.
Radiation damage	Radiation swelling reportedly occurs in beryllium under certain conditions. Microstructural tailoring to incorporate some porosity should tend to alleviate this problem. Since the coating is not a structural component, moderate swelling should be acceptable.
Toxicity	Toxicity is not considered a major problem under the controlled atmospheres and handling procedures required for activated materials and for tritium.

[a] See Ref. 63.

8.4.4 Thermal-Hydraulic Analysis

Figure 8-1 schematically presents the conceptual design of the limiter with a length of ∿1 m exposed to the plasma. The coolant channel details are also shown in Fig. 8-1. The limiter surface exposed to the particle and radiation heat flux is covered with 1-mm thick beryllium coating. To simplify thermal-hydraulic calculations, heat flow across the central metal structure between the inlet and the outlet side of the coolant channels was assumed to be negligible. The leading edge is the most important region of the limiter from the standpoint of thermal hydraulics and thermal stresses as it receives the highest heat flux. Figure 8-14 shows the geometric model used in establishing the temperature distribution and the resultant stresses in the nose (leading edge) section. For geometrical modeling, each coolant channel between the inlet and the outlet headers was divided into 15 regions of which 5 regions represent the leading edge.

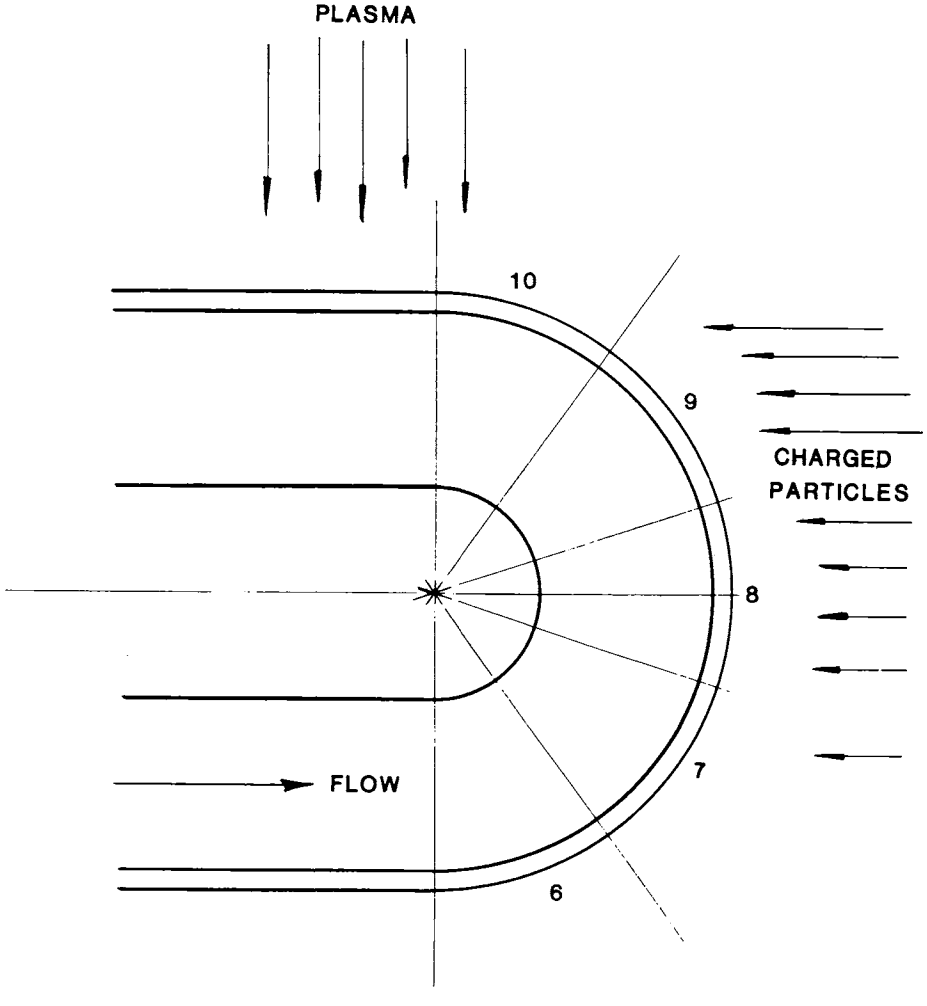

Figure 8-14. Geometric model of nose section.

The heat flux due to plasma radiation and charge-exchange neutrons was taken to be 0.9 MW/m^2 on the limiter surface facing the plasma, 0.6 MW/m^2 in the leading edge regions 8, 9, and 10, and zero at the back surface of the limiter. The charged particle flux on the limiter as discussed in Sec. 8.3 is given by

$$q(x) = 16\, e^{-x/10} \sin\theta \,, \tag{42}$$

where

$q(x)$ = surface heat flux at distance x, MW/m^2

x = distance from the outermost position of the limiter in relation to plasma edge, cm

θ = angle between the direction of particle incidence (in the poloidal plane) and the limiter surface.

The surface heat flux at the nose section based on Eq. (42) is found to be as follows:

Region[a]	Heat Flux (Transport) (MW/m^2)
6	1.28
7	2.52
8	3.34
9	2.11
10	0.94

[a]See Fig. 8-14.

In addition to the radiation and particle fluxes, there is volumetric heat generation in the beryllium coating, structural material, and coolant. The nuclear heating rates in these materials are based on neutronic calculations corresponding to average neutron heat load of 3.6 MW/m^2 on the first wall.

The total energy deposited on the limiter and its supports is of the order of 200 MW. Hence, it is desirable to recover as much of this heat as possible to improve the overall thermodynamic efficiency of the power

conversion system. Three refractory materials (tantalum, niobium, and vanadium alloys) and one copper alloy (AMAX-MZC) were selected as the primary candidate structural materials (see Sec. 8.4.2) for this study with pressurized water as the coolant for each case. To minimize pressure stresses, it was decided to limit both the inlet temperature and temperature rise of water to relatively low values. However, it was necessary to keep the temperature high enough to permit utilizing the thermal energy of the limiter for feedwater heating. A two-pass flow arrangement with 15°C temperature rise across each pass was selected for this study. The inlet temperature of the water for the first pass was assumed to be 115°C which leads to 145°C as the outlet temperature for the second pass. As the radiation heat flux on the limiter represents a significant part of the total heat load on the limiter, the choice of flow direction has some significance in selecting the minimum coolant inlet pressure. It may be noted that the temperature rise between Region 1 and Region 8 amounts to one-third of the total temperature rise across the limiter. Hence, the coolant is designed to flow from Region 1 to Region 15 (see Fig. 8-14). The coolant flow rate based on 200-MW heat load is 1550 kg/s.

Heat transfer calculations show that the convective heat transfer coefficient, h, should be relatively high (e.g., h $\sim$ 5.7 W/cm^2-°C, i.e. 10^4 Btu/h-ft^2-°R) to minimize the large temperature drop at the coolant-structure interface, and thus prevent departure from nucleate boiling (DNB) and boiling burnout due to the high surface heat fluxes at the leading edge. The cross section of the coolant channel (see Fig. 8-15) was selected based on the assumption that the coolant velocity must be of the order of 8 m/s (25 ft/s) to assure large heat transfer coefficients (h $\gtrsim$ 5.7 W/cm^2-°C). This subject is discussed in more detail in Sec. 8.4.4.3.

Based on the above set of operating conditions, both steady-state and transient analyses were carried out using a 405-node (27 nodes in each region) geometric model. The nodal representation is shown in Fig. 8-15 (for Region 8 for the sake of simplicity). A three-dimensional thermal hydraulic computer program was used to establish the temperature distribution. Temperature-dependent properties were used in all calculations whenever such data was available. The thermal-hydraulic analyses are summarized below.

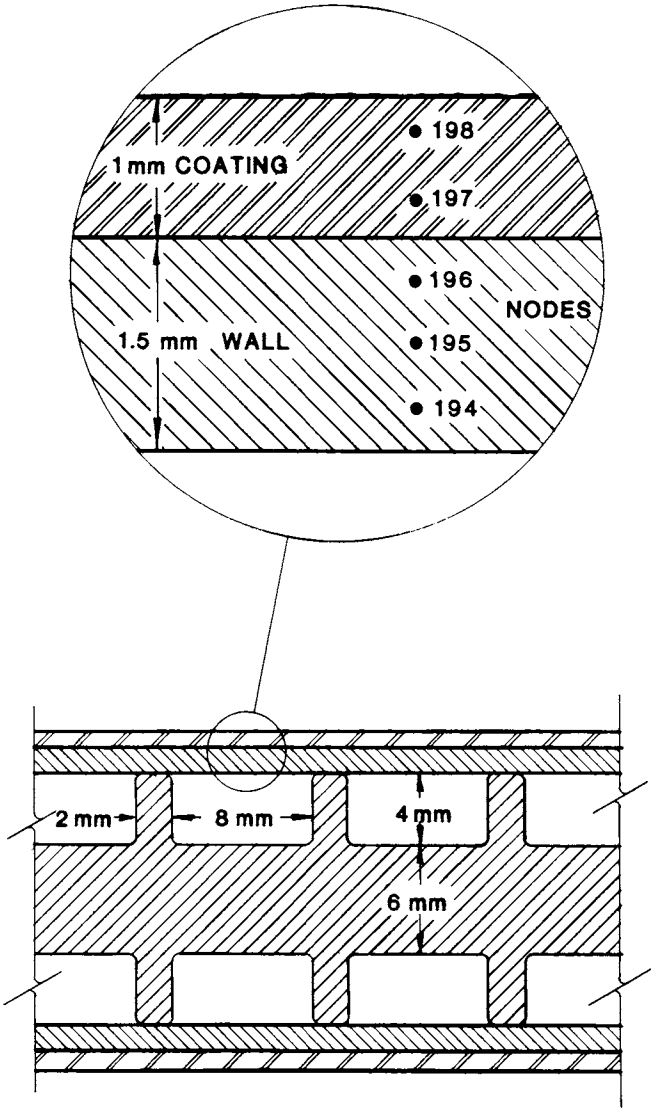

Figure 8-15. Coolant channel cross section and node representation.

8.4.4.1 Steady-State Temperature Distribution

The temperature distribution in the nose section of the limiter for the four structural materials is summarized in Table 8-16. The inlet temperature of the coolant is taken as 130°C, representing the flow conditions for the second pass of the two-pass limiter design. The temperature of the structure in contact with the beryllium coating (T_{WO}) and the temperature of the structure in contact with the coolant (T_{WI}), along with the maximum temperature (T_{max}) that occurs at the web section of the structure, are summarized in Table 8-16. As expected, Region 8 represents the high-temperature region. The highest temperatures for four structural materials (tantalum, vanadium,

Table 8-16. Summary of Steady-State Temperature Distribution

	Temperature (°C)				
Region:	6	7	8	9	10
Tantalum Alloy					
T_{max} [a]	197.4	241.1	290.3	283.8	238.6
T_{WO} [b]	195.1	237.3	285.0	278.7	234.9
T_{WI} [c]	158.6	174.8	193.1	190.8	174.5
Vanadium Alloy					
T_{max}	270.9	352.0	448.9	433.2	355.5
T_{WO}	265.5	343.6	433.1	421.8	346.8
T_{WI}	159.3	174.1	191.3	189.4	175.5
Niobium Alloy					
T_{max}	249.4	321.6	404.0	393.3	322.6
T_{WO}	244.7	214.0	393.2	383.1	314.9
T_{WI}	158.7	173.9	191.5	189.3	173.0
Copper Alloy					
T_{max}	158.4	174.0	191.7	189.6	174.3
T_{WO}	160.2	177.1	196.3	194.0	177.5
T_{WI}	154.9	167.6	182.2	180.6	168.6

[a] T_{max} = maximum temperature of structure at the web section.

[b] T_{WO} = maximum wall temperature at center of the coolant channel wall.

[c] T_{Wi} = maximum wall temperature in contact with the coolant.

niobium, and copper) are found to be 290, 449, 404, and 196°C, respectively. It may be noted that T_{max} for copper alloy occurs at the midsection of the coolant channel and not at the web region. This is caused by axial conduction due to high thermal conductivity of copper alloy. The inner wall temperature (T_{WI}) ought to be the same for all materials. The small differences in the values of T_{WI} are due to axial conduction.

Table 8-17 summarizes the estimated temperature of (1) the beryllium coating (T_{Be}); (2) structural material in contact with the coating, (T_{WO}); and (3) structural material in contact with the coolant (T_{WI}) for all of the 15 regions of the limiter with tantalum alloy as the structural material. As can be seen from Table 8-17, the coating temperatures are only a few degrees higher than the structural material, except at the leading edge. At the leading edge, the temperature drop across the 1-mm coating is 32°C.

8.4.4.2. Transient Thermal Analysis Under Off-Normal Design Conditions

Flow disruptions are not uncommon events in any power reactor system. Since such events have both safety and economic implications, a series of transient analyses was carried out to determine the response of the limiter in the case of a coolant flow failure. It was assumed that the coolant flow decays in 2 s from its full value to zero as a result of some flow disruption initiating event. The response time of the instrumentation and control system is of the order of 2 s. Two plasma shutdown scenarios were envisioned. The first case assumes the plasma shutdown time to be 3 s; and the second case assumes the plasma shutdown time to be 10 s. The flow disruption and plasma fusion power decay events were assumed to be linear with time. At the end of plasma shutdown, the only thermal energy that needs to be considered is the decay heat in the structural material and in the beryllium coating. A third case analyzed assumes the plasma is not shut down following a flow disruption. Flow decay and fusion power decay scenarios are shown graphically in Fig. 8-16.

The transient analyses were limited to tantalum alloy. The outer surface of the limiter was assumed to radiate thermal energy to the surrounding first wall that is maintained at 400°C. The inner surface of the coolant channels was assumed to be thermally insulated.

The temperature of the beryllium coating at the midsection of the coolant channel (Node No. 198, see Fig. 8-15) and the temperature of the structural

Table 8-17. Summary of Steady-State Temperature Distribution for Tantalum Alloy

Region	Temperature (°C)		
	T_{Be} [a]	T_{WO} [b]	T_{WI} [c]
1	159.6	155.6	141.2
2	177.4	170.4	147.7
3	139.2	139.0	135.7
4	139.7	139.5	136.2
5	140.6	140.2	136.9
6	206.1	195.1	158.6
7	174.8	193.1	190.8
8	317.4	285.0	193.1
9	310.0	278.7	190.8
10	253.5	234.9	254.1
11	277.7	254.1	182.9
12	280.6	257.0	185.8
13	272.1	250.4	185.0
14	235.0	220.1	174.6
15	151.8	151.7	148.7

[a] T_{Be} = surface temperature of beryllium coating.

[b] T_{WO} = outer surface temperature of structure

[c] T_{WI} = wall temperature in contact with coolant.

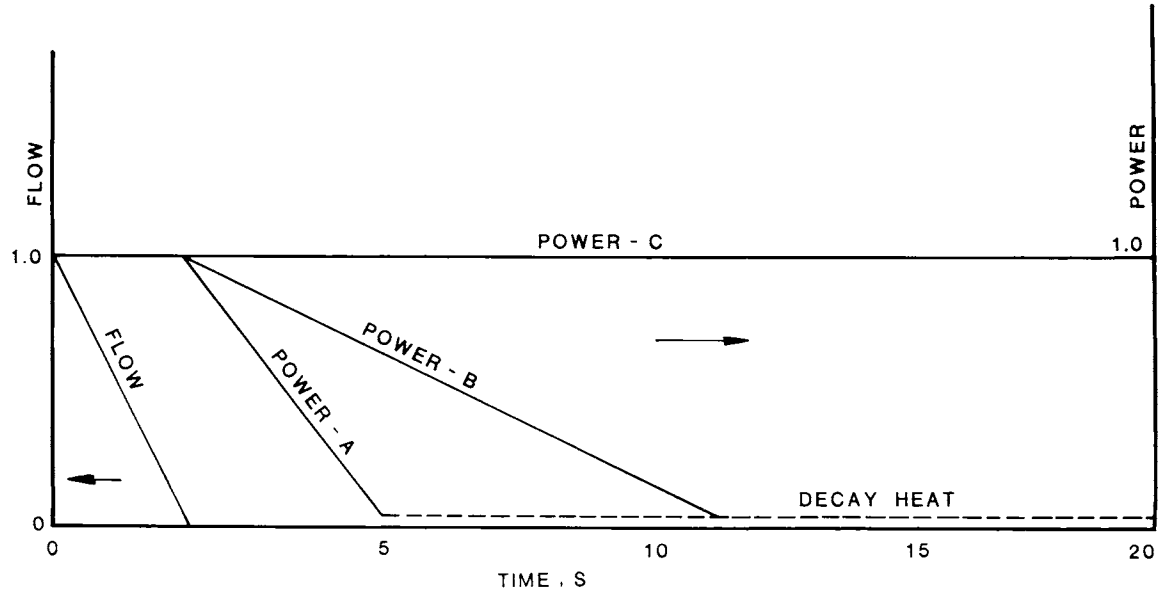

Figure 8-16. Schematic representation of coolant flow, plasma energy, and decay heat during plasma shutdown.

material in contact with the beryllium coating (Node No. 196) are selected for plotting (temperature versus time). Figure 8-17 shows the transient temperature response for the case of 3-s plasma shutdown. The structural material temperature rises from its steady-state value of 293°C to 435°C following flow disruption. The peak temperature occurs 4 s after flow disruption starts. For the case of 10-s plasma shutdown, the peak temperature approaches 681°C (see Fig. 8-18). In each case, the temperatures start to go down after reaching the peak values. As expected, the temperatures begin to rise slowly again due to decay heat in the coating and in the structural materials (see Fig. 8-19). Since the time duration over which the peak temperature occurs is so small (less than 2 s), the structural material is expected to sustain no significant damage. The beryllium coating temperatures for the above two cases are also shown in Figs. 8-17 through 8-19. As the thermal conductivity of beryllium is quite high, the surface temperature of the coating is only a few degrees higher, except at the leading edge, than the corresponding structural material temperature. The temperature drop across the 1-mm coating is approximately 10°C/(MW/m^2). Hence, the maximum coating temperature can be obtained by adding 32°C to T_{max} values as given in Table 8-16 (for Region 8 only).

A severe but extremely unlikely case was also analyzed. In this case, the coolant flow is lost but no action is taken to shut the plasma down. The

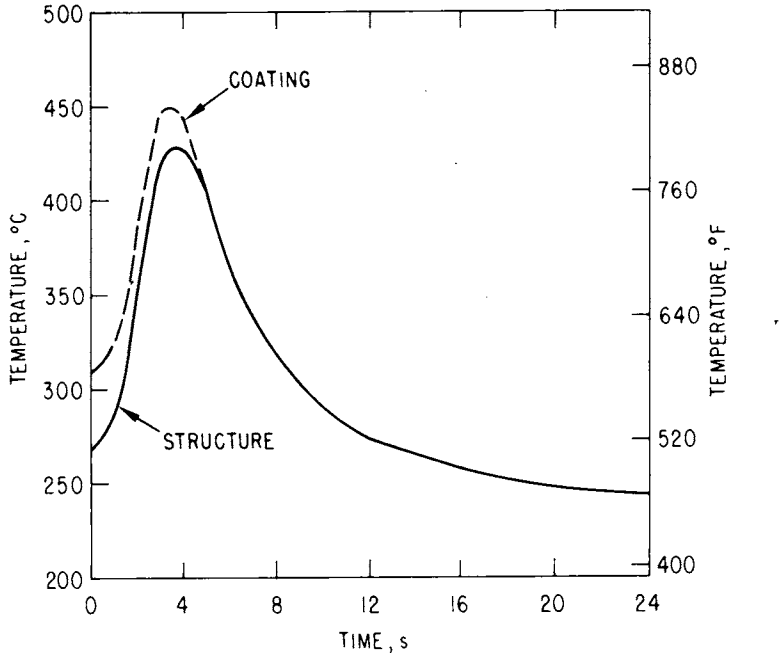

Figure 8-17. Temperature response of beryllium coating and structure: 3-s plasma shutdown.

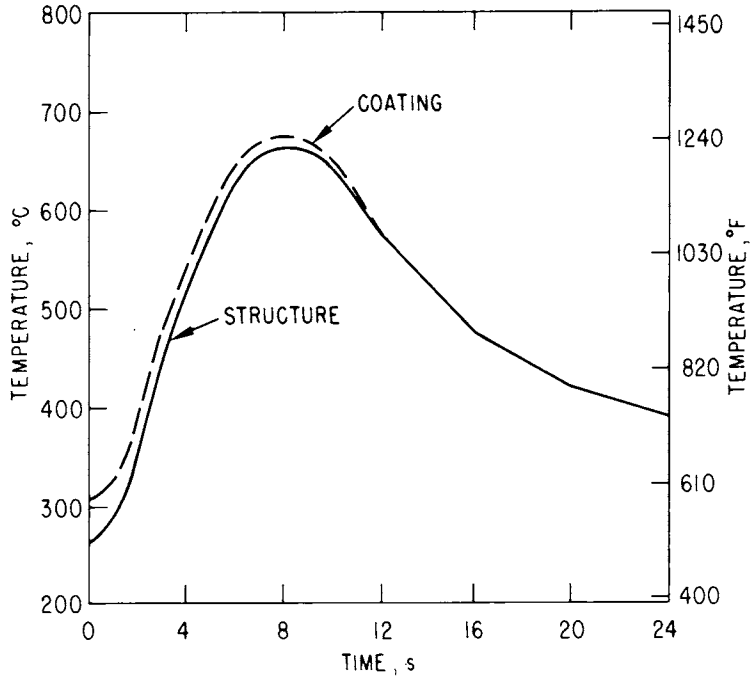

Figure 8-18. Temperature response of beryllium coating and structure: 10-s plasma shutdown (time: 0-24 s).

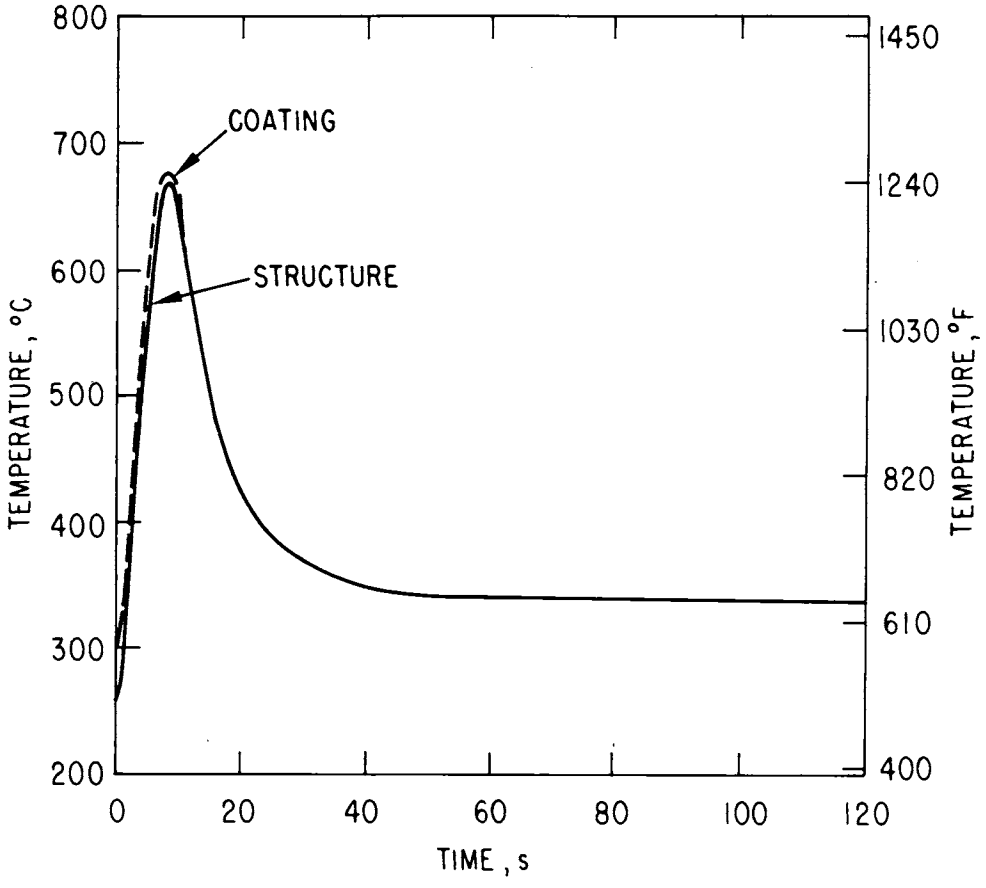

Figure 8-19. Temperature response of beryllium coating and structure: 10-s plasma shutdown (time: 0-120 s).

temperature versus time for both beryllium coating and the structural material is shown in Fig. 8-20. Both the coating and the structural material temperatures are expected to rise until the plasma energy is just equal to the energy transfer to the surroundings by thermal radiation. Since the melting point of beryllium is 1285°C, coating temperatures beyond this point do not correctly represent the state of the beryllium coating. At temperatures above 1000°C, the vapor pressure of beryllium becomes significant in the high vacuum environment of the toroidal chamber. Plasma physics calculations (see Chap. 6) show that plasma quenching due to buildup of beryllium will occur before beryllium coating approaches the melting point, and it will automatically result in a plasma shutdown. Hence, the case analyzed here represents a hypothetical situation that merely shows how high the structural material temperature would rise to attain thermal equilibrium. It may be noted that based on black-body radiation, the equilibrium surface temperature of the leading edge would be ∿2500°C, assuming no axial or circumferential heat conduction from the leading edge.

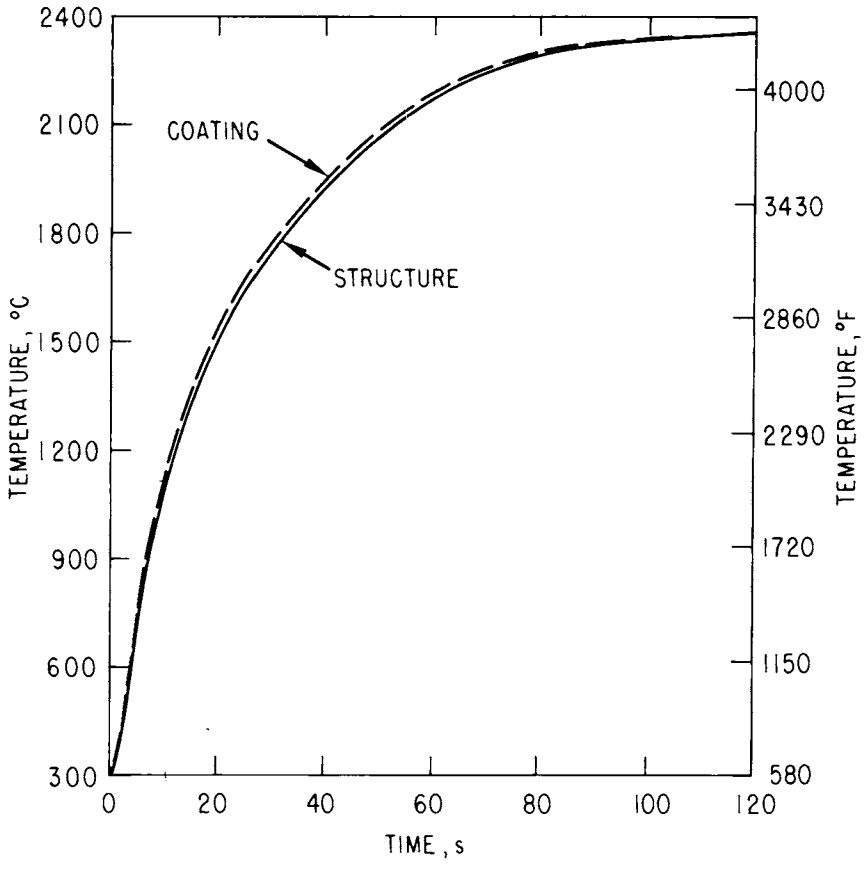

Figure 8-20. Temperature response of beryllium coating and structure: continuous plasma.

8.4.4.3 Selection of Coolant Pressure

One of the most important criteria used to select the coolant pressure is the heat transfer characteristics of the coolant at the leading edge. At peak heat fluxes of the order of several MW/m^2, subcooled nucleate boiling is likely to occur when the wall temperature exceeds the saturation temperature of the coolant corresponding to the system pressure. The subcooling, ΔT_{sub} (defined as $\Delta T_{sub} = T_{saturation} - T_{bulk}$) should be sufficiently high so that the peak heat flux at the leading edge will not exceed the critical heat flux. Of the large number of empirical correlations that have been published in the literature, only three were selected for this analysis. These are: (1) Jens and Lottes equation;[65] (2) Gunther correlation;[66] and (3) Westinghouse correlation.[67] To be conservative, estimates of ΔT_{sub} from the above correlation were based on operation under off-design conditions such as displacement of the leading edge or failure of the plasma radiation enhancement system which may give rise to a 100% increase in the peak heat flux. The calculated values of

ΔT_{sub} from the above correlations varied between 14°C to 34°C. As the uncertainty in the empirical correlations is quite large, a conservative approach was taken by setting the subcooling requirements at 55°C (132°F).

The total length of the coolant flow passage between the inlet and the outlet regions of the limiter is approximately 2 m per pass. The frictional pressure drop per pass was estimated to be 310 kPa (45 psi). The pressure loss at the inlet and at the outlet headers, and across the sharp bend of the nose section is found to be 83 kPa (12 psi). Based on a two-pass coolant flow system, the pressure drop between the inlet header of the first pass and the nose section of the second pass is 552 kPa (80 psi). As noted earlier, the coolant temperature rise per pass is 15°C under normal operating conditions. Under off-design conditions, the coolant temperature rise per pass may be as large as 30°C per pass. This leads to an estimated bulk temperature of the coolant at the nose section of the second pass equal to 155°C (311°F), and thus sets a limit on the saturation temperature of coolant (i.e. T_{sat} = 155 + 55 = 210°C). Hence, the minimum coolant pressure at the nose section of the second pass must be at least 1.93 MPa (280 psia). Based on pressure loss of 552 kPa (80 psia), the coolant inlet pressure at the first pass becomes 2.48 mPa (360 psia). To provide an added margin of safety due to uncertainty in the pressure loss calculations, the coolant inlet pressure may be assumed to be 2.76 MPa (400 psia). Using ΔT_{sub} = 55°C and coolant pressure = 1.93 MPa as the design basis, the critical heat fluxes as calculated from the Jens and Lottes equation,[65] Westinghouse correlation,[67] and Gunther correlation[66] were found to be 9, 17, and 12 MW/m^2, respectively. Therefore, the critical heat fluxes calculated by all of the above three empirical correlations are two to four times the normal operating heat flux. Thus, a very conservative safety margin has been provided in this system.

A check of ΔT_{sat} (defined as $\Delta T_{sat} = T_{wall} - T_{sat}$) for subcooled nucleate boiling was made using the Jens and Lottes correlation. The ΔT_{sat} corresponding to 3.4 MW/m^2 was found to be 25°C. If the peak heat flux increases to 6.8 MW/m^2, then ΔT_{sat} increases to only 30°C. (Note: $\Delta T_{sat} \propto \sqrt[4]{\text{peak heat flux.}}$) Hence, the maximum wall temperature in contact with the coolant is expected to be 241°C (466°F).

The convective heat transfer coefficient corresponding to the operating conditions presented above is calculated to be 7.38 W/cm^2-°C (13,000 Btu/hr-ft-°R).

Hence, the use of heat transfer coefficients of 5.68 W/cm^2-°C (10,000 Btu/hr-ft-°R) in these analytical studies is conservative.

Based on the analytical results presented above, it may be concluded that operation of the limiter with a coolant inlet temperature of 115°C and coolant inlet pressure of 2.8 MPa (400 psia) is expected to provide adequate margin of safety, even during operation under off-design conditions such as displacement of the leading edge giving rise to 100% increase in heat flux.

An additional degree of conservatism is introduced by selecting a design pressure of 4.2 MPa (600 psia). This pressure is also used in the stress analysis.

8.4.5 Stress Analysis

The limiter is a critical component of the reactor and, consequently, a high degree of reliability is required. One aspect of assuring reliability is to show that the maximum stresses under normal operating conditions are below the allowable design stress for that temperature. In this section we compute, by means of prudent engineering assumptions and elementary calculations, the maximum stress and compare this stress with the allowable design stress. This provides a measure of the adequacy of the design and provides some guidance for more sophisticated numerical analysis.

Under steady-state conditions the maximum heat load occurs at the leading edge of the limiter. The approach adopted is to superimpose stresses due to three loading conditions. The first case is a solution from shell theory for internal pressure and uniform wall temperature. The second involves a correction to obtain an average plane strain solution while the third is the stress distribution for a linear thermal distribution through the wall. Then the stress in the wall at the point where the conditions are worst is used to provide a comparison with the allowable stress.

The allowable design stresses and failure criteria are basically the same for the limiter as for the first-wall/blanket components. Several design codes already exist which consider the allowable component stresses for various stress classifications, including primary stresses, secondary stresses due to sustained loads and temperature gradients, and peak stresses. The design code used for stress analysis of reactor components is ASME Code Case 1592 for Class 1 components in elevated temperature service, and it will be used here as a starting

point for the stress analysis in the limiter.[68] Code Case 1592 is intended to cover a wide variety of design configurations and service conditions, and the design criteria are therefore usually quite conservative. Since different stress classifications have different degrees of significance, the code assigns a different allowable stress for each classification. The allowable stresses are given in terms of the stress intensity, S_{mt}, which is calculated from the tensile and creep properties of the structural materials. At lower temperatures, the value of S_{mt} is either two-thirds of tensile yield or one-third of ultimate stress, and at high temperatures, S_{mt} is the stress necessary to produce a given amount of thermal creep during the expected component lifetime. In the case of the reference limiter materials, S_{mt} is one-third of the ultimate stress for the normal operating temperatures. Code Case 1592 limits the primary mean stress, i.e., coolant stress, to a value of S_{mt}, and it limits the combined primary mean stress plus the primary local membrane stress to a value of 1.5 S_{mt}. See Sec. 10.6.2 for additional information on stress analysis.

Because of the high heat fluxes received by the limiter, special consideration must be given to the allowable thermal stresses. Code Case 1592 limits the combined primary and secondary stress range, including thermal stress, to a value of 3 S_{mt}. For the reference limiter materials, 3 S_{mt} is the ultimate tensile strength. This value is used because it is assumed that the stresses will shake down to the elastic strain range shortly after startup. However, Code Case 1592 does not specifically include radiation effects or the effect of thermal stress on crack growth rates in the determination of allowable stress. The additional effects of radiation creep and embrittlement could result in a nonconservative design stress and premature failure. In fact, under some circumstances the allowable stress range of 3 S_{mt} for unirradiated components is considered nonconservative.[69] Therefore, it is felt that the allowable stress level for STARFIRE should be modified. The loss of ductility during irradiation suggests that the allowable stress for the combined primary and secondary stresses should be below the yield strength to avoid any plastic deformation. In order to provide a safety factor, a value of 0.75 of the 0.2% yield strength has been selected as the maximum allowable primary plus secondary stress in the limiter.

The electromagnetic forces built up in the limiter during a disruption must be accommodated without permanent deformation if the limiter is to be

reuseable. Since these forces are dynamic in nature and last for such a short time, creep is not a factor. Instead, an elastic analysis with the appropriate temperature-dependent properties is sufficient for this investigation. Since the force calculations are difficult to compute with a high degree of accuracy, due to many uncertainties in plasma disruption characteristics, simple structural models are adequate.

A major research effort is needed to ultimately provide the capability for predicting the behavior of the limiter. The limitations of time and resources in the present study suggested that a more modest engineering approach should be attempted. Radiation effects are not included. Instead, conservative assumptions are made to develop models that reasonably characterize the physical structure and for which analytical elastic solutions are available. By showing that the maximum effective stress is reasonably low, this approach provides some assurance that the design is realistic and that a final detailed stress analysis would show that the limiter meets design criteria. Section 8.4.5.1 presents the analysis for the steady-state conditions and Sec. 8.4.5.2 is devoted to an analysis of the effects of electromagnetic loads from plasma disruption. Section 8.4.5.3 summarizes the conclusions of the stress analysis.

8.4.5.1 Steady-State Stresses at Leading Edge

The leading edge of the limiter is subjected to a maximum heat flux of 4 MW/m^2. The purpose of this analysis is to indicate whether or not the worst state of stress in the limiter walls is acceptable for each of the four reference candidate materials.

The basic configuration of the leading edge of the limiter is shown in Fig. 8-21. Since the outer wall forms a 180-deg segment, a reasonable model for determining the effect of temperature and pressure on wall stress is to use the cylindrical model which is also shown in Fig. 8-21. The ends of the cylinder, which correspond to the edges of a typical cooling channel, constrain the cylindrical wall from expanding radially when the wall is subjected to a uniform temperature, T_s, and pressure, P. Since the thickness-to-radius ratio is small, shell theory is appropriate for this aspect of the analysis.

In addition to the stress induced by a uniform temperature, additional stresses result from the temperature gradient through the wall. Thermal stress theory provides results that are applicable for this case.

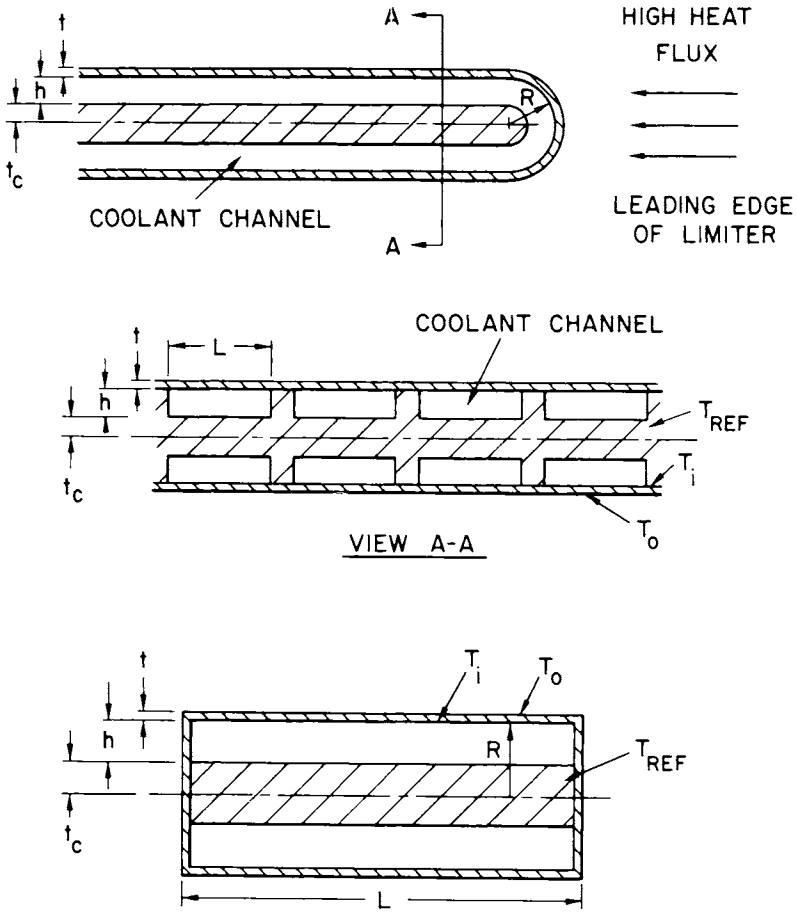

Figure 8-21. Schematic drawing of the leading edge model.

Let T_0 and T_i denote the temperatures at the outer and inner surfaces of the wall, respectively. If the temperature of the structural core is given by T_{ref}, then the average wall temperature, T_{ave}, and the temperature difference, ΔT, between the wall and the core are given by

$$T_{ave} = (T_0 + T_i)/2 , \qquad \Delta T = T_{ave} - T_{ref} . \tag{43}$$

The thermal stress analysis predicts stresses only if there is a gradient. If the temperature distribution through the wall is assumed to be linear, then the temperature difference between the outer and inner points of the wall

$$T_g = T_0 - T_i \tag{44}$$

appears in the stress formulas.

With the notation shown in Fig. 8-21, the shell equations for stress resultants and normal displacement, w, are given as follows: (70)

$$M_x = -2\mu^2 D\left(\frac{PR^2}{Et} + R\alpha T_s\right) [G(\delta) \sin \mu x \sinh \mu x + F(\delta) \cosh \mu x \cos \mu x] , \quad (45)$$

$$M_s = \nu M_x , \quad (46)$$

$$N_x = 0 \text{ (assumed)} , \quad (47)$$

$$N_s = \frac{Et}{R} w - E\alpha t T_s , \quad (48)$$

$$w = \left(\frac{PR^2}{Et} + R\alpha T_s\right) [1 - G(\delta) \cosh \mu x \cos \mu x + F(\delta) \sinh \mu x \sin \mu x] . \quad (49)$$

The bending moments in the longitudinal (x) and circumferential (s) directions are given by M_x and M_s, respectively, and the corresponding membrane forces are N_x and N_s. The bending stiffness is:

$$D = \frac{Et^3}{12(1 - \nu^2)} , \quad (50)$$

where t is the thickness, E denotes Young's modulus, and ν is Poisson's ratio. The coefficient of thermal expansion is α. R denotes the radius of the shell and P the internal pressure. The parameters μ and δ are defined by:

$$\mu^2 = \left[\frac{3(1 - \nu^2)}{R^2 t^2}\right]^{\frac{1}{2}} , \quad (51)$$

$$\delta = \frac{\mu L}{2} , \quad (52)$$

and the functions of δ given in Eqs. (45) and (49) are

$$F(\delta) = (\cos \delta \sinh \delta - \sin \delta \cosh \delta / H(\delta) , \quad (53)$$

$$G(\delta) = (\sin \delta \cosh \delta + \cos \delta \sinh \delta)/H(\delta) , \quad (54)$$

where

$$H(\delta) = \sinh \delta \cosh \delta + \sin \delta \cos \delta \ . \tag{55}$$

By definition, the membrane stresses are:

$$\sigma_x^m = 0 \ , \qquad \sigma_s^m = \frac{N_s}{t} \ , \tag{56}$$

and the maximum bending stresses are:

$$\sigma_x^b = \pm \frac{6}{t^2} M_x \ , \qquad \sigma_s^b = \nu \sigma_x^b \ , \tag{57}$$

for the outer and inner surfaces, respectively.

For this analysis, w is assumed to be zero at the ends. However, the end plates of the shell (or channel walls) is also subjected to a temperature distribution which is approximately linear with a radial coordinate, r.

The change in radius of the end cap due to this temperature field is:

$$\Delta R = \int_0^R \alpha r \frac{\Delta T}{R} \, dr = \alpha R \frac{\Delta T}{2} \ , \tag{58}$$

which is one-half the free radial expansion of the cylindrical shell. Thus, an appropriate value to use for the shell analysis is

$$T_s = \frac{\Delta T}{2} \ . \tag{59}$$

The axial membrane strain predicted by this shell theory is

$$e_x^m = \frac{-\nu \sigma_s^m}{E} \ , \tag{60}$$

and the average strain for the complete shell is

$$\bar{e}_x^m = \frac{2}{L} \int_0^{L/2} e_x^m \, dx \ . \tag{61}$$

The use of Eqs. (47), (48), and (55) together with integration formulas yields

$$\bar{e}_x^m = \nu\alpha T_s - \frac{\nu}{R}\left(\frac{PR^2}{Et} + R\alpha T_s\right)\left[1 - \frac{H}{2}\left(F^2 + G^2\right)\right]. \tag{62}$$

In addition, with no constraints the shell wall would expand with a thermal strain

$$\bar{e}_x^t = \frac{\alpha\Delta T}{2}, \tag{63}$$

which accounts for the remaining strain due to the difference in temperature between the wall and the core. In actual fact, the edges of the channel prevent this expansion so in addition to the stresses from shell theory, a uniform axial stress

$$\sigma_x^t = -E\left(\bar{e}_x^m + \bar{e}_x^t\right) \tag{64}$$

must be superimposed.

Because the radial stress, σ_r, is zero on the outer surface and -P on the inner surface, it is assumed to be negligible everywhere. However, there are additional contributions to the axial and circumferential components of the stress tensor due to the thermal gradient through the wall. The circumferential component is (see Ref. 71, p. 290)

$$\sigma_s^g = \frac{\alpha E}{r^2}\left[\frac{r^2 + a^2}{b^2 - a^2}\int_a^b Tr\, dr + \int_a^r Tr\, dr - Tr^2\right], \tag{65}$$

in which r is the radial coordinate, r = a and r = b denote the radii of the inner and outer wall surfaces, respectively, and T is the temperature distribution through the wall.

For convenience introduce a mid-surface coordinate, z, such that

$$r = r_0 + z, \qquad r_0 = \frac{a + b}{2}. \tag{66}$$

The linear temperature distribution is given by

$$T = \frac{(T_0 + T_i)}{2} + \frac{(T_0 - T_i)}{2} \frac{2z}{t} . \tag{67}$$

However, it can be shown from Eq. (65) that the stress contribution due to a uniform temperature is zero so there is no loss of generality if Eq. (67) is replaced with

$$T = (T_0 - T_i) \frac{z}{t} = T_g \frac{z}{t} .$$

Then it is easily shown that

$$\frac{r^2 + a^2}{b^2 - a^2} \int_a^b Tr \, dr = T_g \frac{t}{6} (r_0 + z) ,$$

$$\int_a^r Tr \, dr = \int_{-h/2}^z Tg \frac{z}{t} (r_0 + z) \, dz ,$$

$$= \frac{T_g}{t} \left[r_0 \left(z^2 - \frac{t^2}{r} \right) + \frac{2}{3} \left(z^3 + \frac{t^3}{8} \right) \right] ,$$

$$Tr^2 = T_g \frac{2z}{t} (r_0^2 + z^2) .$$

With the assumption that $z << r_0$, one has

$$\frac{1}{r^2} \simeq \frac{1}{r_0^2} \left(1 - \frac{2z}{r_0} \right) ,$$

and

$$\sigma_s^g \simeq - \frac{\alpha E T_g}{12 r_0} \left(t + 24 r_0 \frac{z}{t} \right) . \tag{69}$$

At the midplane:

At the midplane:

$$\sigma_s^g\Big|_{z=0} \simeq \frac{-\alpha E T_g t}{12 r_0} . \tag{70}$$

and at the outer and inner surfaces:

$$\sigma_s^g\Big|_{z=\pm(t/2)} = \mp \alpha E T_g . \tag{71}$$

Again, since the strain in the axial direction must be zero, the axial stress component due to the temperature gradient is

$$\sigma_x^g = \nu \alpha_s^g - \alpha E T , \tag{72}$$

with T given by Eq. (68). Thus, the components σ_s^g and σ_x^g vary linearly through the wall with negative values on the outer surface and positive values on the inner surface.

The final values of the non-zero components of the stress tensor for any point are obtained from the sum

$$\begin{aligned} \sigma_x &= \sigma_x^b + \sigma_x^t + \sigma_x^g , \\ \sigma_s &= \sigma_s^m + \sigma_s^b + \sigma_s^g . \end{aligned} \tag{73}$$

Simple superposition is appropriate since the theory of linear elasticity has been utilized throughout the analysis.

For a multiaxial state of stress, which is represented by the present case, there is a problem in determining whether or not the worst stress state is acceptable since the allowable stress is frequently a scalar associated with a uniaxial state of stress. To handle the actual multi-dimensional state of stress, an "effective" stress is defined based on a von Mises yield surface. For plane stress, the effective stress is defined by

$$\sigma = \left(\sigma_x^2 + \sigma_s^2 - \sigma_x \sigma_s + 3\tau^2\right)^{\frac{1}{2}} , \tag{74}$$

in which τ is the shear stress (zero for this problem). For uniaxial stress

($\sigma_x \neq 0$, say), the effective stress reduces to $\sigma = |\sigma_x|$, whereas for pure shear $\sigma = \sqrt{3}|\tau|$. A state of hydrostatic stress does not affect σ. If the scatter of most material property data is taken into account, then the use of σ as a simple measure for determining the reserve capacity of a structural member is justified and widely accepted.

To determine the stress components, values for several parameters are required. The geometrical parameters are given as follows:

$$R = 0.85 \text{ cm}, \qquad L = 0.80 \text{ cm}, \qquad t = 0.15 \text{ cm}. \tag{75}$$

The heat transfer analysis presented in Sec. 8.4.4 provided the steady-state temperature distribution for each of the candidate materials. These results provided the outer and inner surface temperatures, the average wall temperature, the difference in temperature between the inner and outer surfaces, the reference temperature in the core region, and the difference between the average wall temperature and reference temperature that are summarized in Table 8-18. As discussed in the previous section on thermal hydraulics, the maximum coolant pressure required is 2.8 MPa (400 psia). For conservatism, a value of 4.2 MPa (600 psia) is used in the stress calculations.

The material properties are functions of temperature. Table 8-19 shows nominal values for Young's modulus, E, Poisson's ratio, ν, and the coefficient of thermal expansion, α, based on the average wall temperature for each material. Also given are the corresponding values of yield stress (based on 0.2% permanent deformation) and the ultimate stress to which maximum values of the effective stress can be easily compared.

A computer program was written based on the equations in this section. In general, σ is a function of x and r (or z) and a search over the domain is necessary to determine the maximum value of σ. As expected, the four worst points were located on the outer and inner surfaces at the center and ends of the cylinder wall. Of these points, the maximum values of σ were always located on the outer surface at an end. Components of the stress tensor separated into parts due to pressure and temperature for this point are given in Table 8-20 for each material. The reason that this point is the critical one is immediately apparent since the contributions from each load provide stress values with the same sign. For the other points, this was not the case. Also given in the table are the effective stress determined from the total values of the stress components and the ratio of the effective stress to the yield stress.

Table 8-18. Temperatures (°C) in Limiter Wall

Material	T_0	T_i	T_{ave}	T_g	T_{ref}	ΔT
Tantalum, Ta-5W	279	193	236	86	145	91
Niobium, FS-85	393	192	293	201	143	150
Vanadium, V-20Ti	433	191	312	242	144	168
Copper, AMAX-MZC	196	182	189	14	140	49

Table 8-19. Material Properties for Average Wall Temperature

	E				Yield Stress		Ultimate Stress	
Material	MPa $\times 10^5$	psi $\times 10^6$	ν	α 10^{-6}/°C	MPa	psi $\times 10^3$	MPa	psi $\times 10^3$
Tantalum, Ta-5W	1.81	26.2	0.3	6.6	342	50	391	57
Niobium, FS-85	1.33	19.2	0.3	7.3	370	54	490	71
Vanadium, V-20Ti	1.17	16.9	0.3	10.6	452	66	602	87
Copper, AMAX-MZC	0.96	13.9	0.3	20.8	431	63	460	67

Table 8-20. Stresses (MPa) at Critical Point in Limiter

Material	$\sigma_s^{P(1)}$	$\sigma_x^{P(1)}$	$\sigma_s^{G(2)}$	$\sigma_x^{G(2)}$	$\sigma_s^{T(3)}$	$\sigma_x^{T(3)}$	$\sigma_s^{(4)}$	$\sigma_x^{(4)}$	σ	Ratio of σ to Yield Stress
Tantalum, Ta-5W	-12	-38	-103	-82	-185	-242	-197	-280	249	0.73
Niobium, FS-85	-12	-38	-195	-156	-305	-370	-317	-408	371	1.00
Vanadium, V-20Ti	-12	-38	-300	-240	-458	-576	-470	-585	537	1.19
Copper, AMAX-MZC	-12	-38	-28	-22	-102	-167	-114	-205	178	0.41

(1) Contribution due to pressure.

(2) Contribution due to temperature gradient.

(3) Total contribution due to temperature.

(4) Final values of stress components.

The results shown in Table 8-20 indicate that under normal operating conditions, all of the materials meet the allowable stress criteria of Code Case 1592. However, only AMAX-MZC and Ta-5W can meet the more restrictive criteria of 0.75 of the yield strength. Since the thermal stress component dominates the total stress in the limiter, the materials with the highest thermal conductivity and the lowest thermal expansion will experience the lowest total stress. Note that the Ta-5W alloy is in the annealed condition, and its tensile strength will increase during operation due to irradiation hardening. The strength increase will result in a greater operating safety margin. Since the AMAX-MZC alloy is already in the cold-worked and aged condition, its tensile properties are not likely to increase during reactor operation. In addition, the welding or brazing required for limiter fabrication would reduce the strength of AMAX-MZC in the heat-affected zone. Based upon these considerations, AMAX-MZC and Ta-5W are preferred. However, other factors including toughness, ductility, creep, strength as fabricated, and loss of ductility must also be considered.

It should be emphasized that the present limiter does not represent the optimum design. There are potentially several modifications which could reduce the thermal stress. One such modification would be to eliminate the internal ribs at the leading edge of the limiter that receives the highest heat flux. This would eliminate one large component of the thermal stress while not sigficantly increasing the primary stresses. Another modification would be to make the internal structure of the limiter from a material with a higher coefficient of thermal expansion than the outer skin. The dimensional change in the outer skin could thus be offset by the dimensional changes in the internal structure which is at lower temperatures. A third modification would be to predeform the outer skin such that it is bowed outward between the internal ribs. Part of the dimensional change produced by the surface heat load would then be accommodated by additional bowing rather than just the lateral expansion considered here, and would result in a lowered value of thermal stress. Further modeling and experimental effort is required to determine the degree to which these modifications would improve the limiter design.

8.4.5.2 Stress Due to Plasma Disruptions

Electromagnetic forces on various sections of the limiter due to plasma disruptions represent an important aspect of the limiter design. In this sec-

tion, stress calculations are performed to evaluate their effect. The magnitudes of the forces and torques used below are derived in Sec. 8.4.6.

During a plasma disruption, three basic force fields act on the limiter as shown in Fig. 8-22. These fields are functions of time and depend on the plasma disruption time. Instead of considering all possibilities, a worst case approach is adopted in which the maximum values of each force are used as base figures. If the structure is assumed to remain elastic and each force is considered to be a step function in time, the maximum possible dynamic load factor is two. In other words, a static analysis based on twice the predicted maximum values for each force provides a very conservative approach. However, if the predicted stresses are below allowable values, then the limiter will certainly be able to withstand the actual loads during disruption.

The first load we consider is a uniform pressure N^e acting on the outside panels of the limiter except at the leading edge and root support areas. This pressure acts in the same direction as the coolant pressure. The maximum values of N^e are 55 psi for a zero disruption time, and 0.55 psi for a disruption time of 10 ms. This indicates the extremely unlikely occurrence of the peak value of 55 psi. In any case, suppose we consider a figure of 110 psi superimposed on the coolant pressure of 600 psi. For the region of interest, the coolant channel wall can be considered as a plate infinitely long with fixed edges on the two parallel sides. If b denotes the width of the panel and q the pressure, then the two components of the bending moment at the edge of the plate (the worst case as given on p. 87 of Ref. 72) are

$$M_1 = 0.0833\ qb^2 , \qquad M_2 = \nu M_1 .$$

The corresponding bending stresses are

$$\sigma_1 = \frac{6M_1}{t^2} , \qquad \sigma_2 = \frac{6M_2}{t^2} ,$$

where t is the wall thickness. For q = 710 psi, b = 0.8 cm, and t = 0.15 cm, the result is

$$\sigma_1 = 10{,}100 \text{ psi } (70 \text{ MPa}) , \qquad \sigma_2 = 3{,}030 \text{ psi } (21 \text{ MPa}) .$$

The corresponding effective stress from Eq. (67) is

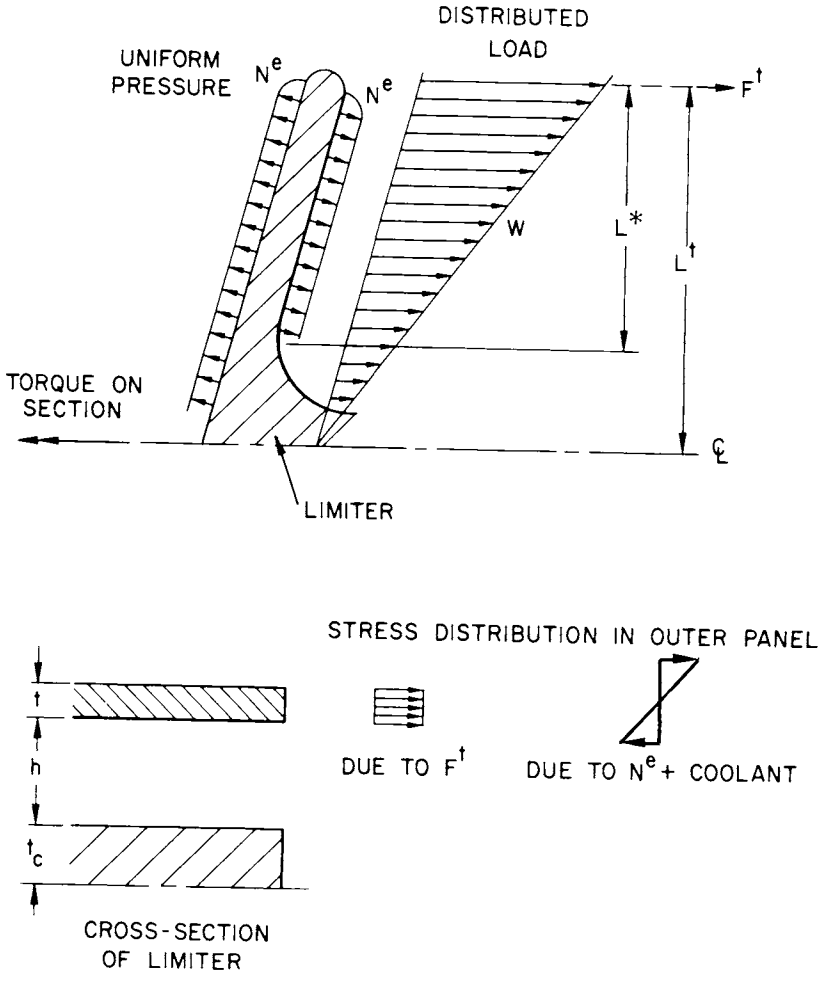

Figure 8-22. Nomenclature for electromagnetic stress calculations.

$$\sigma = 9000 \text{ psi } (62 \text{ MPa})$$

which is less than 20% of the yield stress for each of the four reference materials.

For the second load, W, which is distributed and acts towards the first wall, the moment at the root of the limiter is equal to that provided by a tip force F^t. That is, the maximum applied bending moment is

$$M_{max} = F^t L^t .$$

The maximum computed value of F^t for an instantaneous plasma disruption is 583 lb (2600 N), so double this value will be used for the static analysis.

Suppose the bending stress σ^b is taken to be uniform over the outer flange of thickness t. Then the moment carrying capacity is

$$M = 2\sigma^b t\left[t_c + h + (t/2)\right]b$$

in which b is the width of the limiter segment. However, this expression holds for the thinnest section of the limiter, and not at the centerline where the maximum moment occurs. The maximum bending stress will occur at the transition point, a distance L^* from the tip. The applied moment at this point is $F^t L^*$ which should be used in the stress calculation.

For $L^* = 40$ cm, b = 50 cm, t = 0 15 cm, h = 0.4 cm, $t_c = 0.3$ cm, and $F^t =$ 1166 lb, the result of combining these two equations to obtain σ^b is

$$\sigma^b_{max} = 26{,}000 \text{ psi } (177 \text{ MPa})$$

which is < 50% of the yield stress for each of the candidate materials. Actually this stress should be combined with the previous stress to obtain the maximum stress on the outer surface. However, the combination of these two electromagnetic forces will not produce significant plastic deformation. In addition, these forces are considerably reduced at longer plasma disruption times as shown in Sec. 8.4.6.

The third load consists of a torque applied to the limiter support with a maximum value of 68,100 N-m for instanteous plasma disruptions. This torque is created by large transverse shear forces which should not cause the limiter itself to deform because of the high resistance to shear of this particular section geometry. The most vulnerable part of the system is the region immediately behind the limiter. As shown in Fig. 8-23, we assume this section is adequately modeled as a solid rectangular beam with a height b and width w, each reduced by twice the channel opening, 2L. The effective length of this section is $L_e = 25$ cm after which the torque is transmitted to the blanket.

According to Ref. 73, the maximum shear stress occurs on the perimeter at the middle of the longer side and equals

$$\tau = \frac{T}{ab^2w},$$

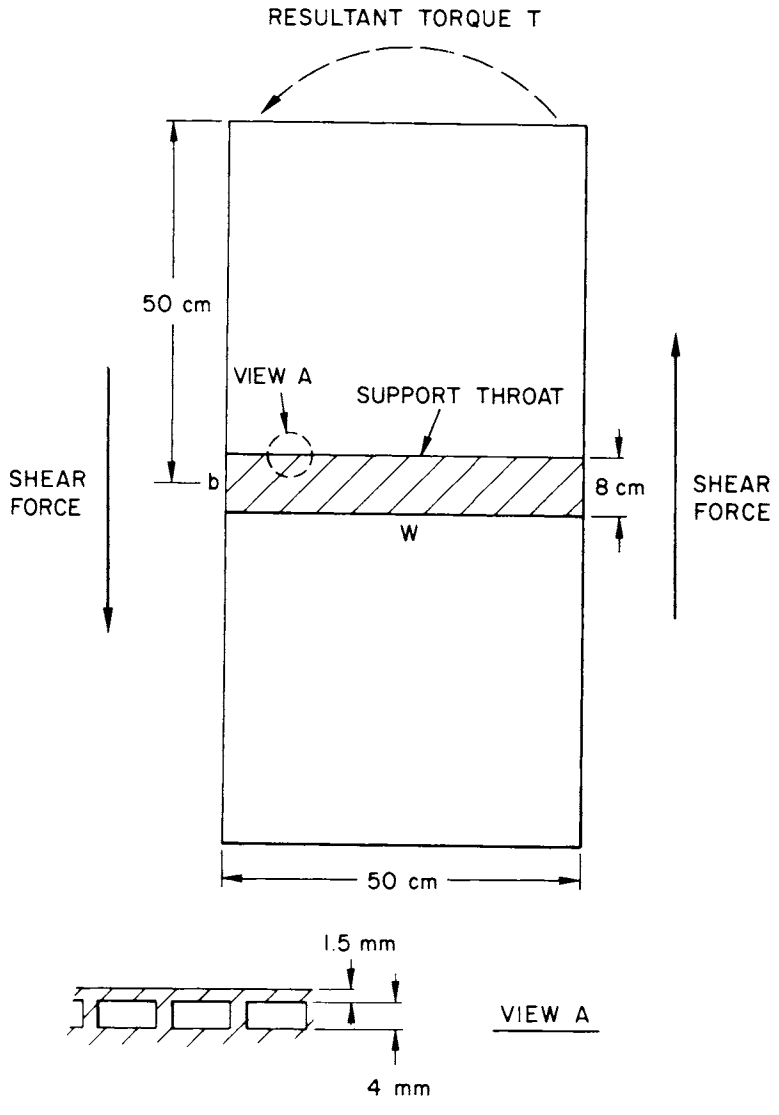

Figure 8-23. Schematic Drawing showing limiter support.

where T is the applied torque and

$$\alpha = 0.3$$

is a parameter appropriate for the aspect ratio w/b. If a maximum dynamic load factor of 2 is used then T = 136,200 N-m. With b = 8 - 0.8 = 7.2 cm and w = 50 - 0.8 = 49.2 cm, it follows that

$$\tau = \frac{136{,}200 \text{ N-m}}{0.3(0.072 \text{ m})^2(0.492 \text{ m})} = 177 \text{ MPa}$$

and from Eq. (74), the effective stress is

$$\sigma = 306 \text{ MPa} .$$

From Table 8-19 we see that this stress for the case of an instanteneous plasma disruption is below the yield stress for any of the candidate materials. The torque T = 68,100 N-m at a plasma disruption time $\tau = 0$ is reduced by a factor of 2 when $\tau = 25$ ms.

8.4.5.3 Conclusion

The existing limiter design is feasible with perhaps minor modifications required according to which material is used. Under steady-state conditions, the simplified analysis shows that for all materials except the vanadium alloy, the yield stress will not be exceeded. However, the greatest load is caused by thermal stresses which will relax over a period of time. Unfortunately, if the reactor is shut down, reverse thermal stresses will occur and if there are a large number of cycles, fatigue and cracking may become a factor. Only detailed analyses and experiments can provide the quantitative information that is required for a complete understanding of the stress history of a limiter. Several modifications for reducing the thermal stress have been identified in Sec. 8.4.5.1. Any of these modifications provides for a significant improvement in the safety margin.

In general, electromagnetic disruptive stresses can be large but the effective stress is below the yield stress for the most severe case of zero plasma disruption time. For the longer plasma disruption (current decay times) these stresses are substantially reduced.

A comprehensive stress analysis would incorporate the spatial variation of temperature through the entire body, a more accurate account of boundary conditions, creep, and the effects of radiation including radiation-enhanced creep, swelling, hardening, and possible changes in ductility. A life cycle which incorporates planned and disruptive shutdowns should be analyzed to ensure that the limiter meets lifetime expectations. The possibility of extensive crack growth would be considered part of this analysis.

The capability for incorporating most of these effects exists in many current large scale finite difference and finite element computer codes. Two

primary features are generally lacking however. The first is a reasonably accurate constitutive model for each of the candidate materials under the range of loading conditions experienced by the limiter. Numerous one-dimensional data are frequently available but the description of material under a multiaxial state of stress and an associated failure criterion are usually based on very limited data. The interaction of creep, plasticity, radiation, and failure is especially complex and results from numerical analyses must be interpreted with the understanding that material models may be limited in scope. The second feature that restricts the scope of the analysis is the lack of an efficient procedure for incorporating the possibility of crack progression in two- and three-dimensional structural models. The use of special finite elements or other assumptions limits the physical effects which can be studied in many cases.

Even if a complete analytical capability existed, it should be emphasized that a preliminary analysis of the type given here is necessary and would have to be performed. These calculations indicate that the design is reasonable, that the limiter would be expected to perform its function, and that a good model is available for the detailed, but necessarily expensive, stress analysis that must ultimately be performed.

8.4.6 Electromagnetic Effects on the Limiter due to a Plasma Disruption

A plasma disruption will induce eddy currents in the limiter, which will interact with the poloidal and toroidal magnetic fields to produce pressure, force, and torques on the limiter. In this section the magnitudes of the pressure, force, and torques are calculated. Section 8.4.5 analyzed the stresses resulting from these loads.

As the plasma current drops to zero, the magnetic flux produced by that current decreases. Eddy currents are established in the limiter, shown in Fig. 8-24, which tend to compensate for the flux decrease by producing additional flux to replace it. The decrease in flux parallel to one of the limiter arms produces a toroidal current flowing one way on one face of the arm and the other way on the opposite face; these currents cause a pressure tending to explode the limiter arm. The decrease in flux perpendicular to the limiter arms and horizontal section cause circulating currents in those planes.

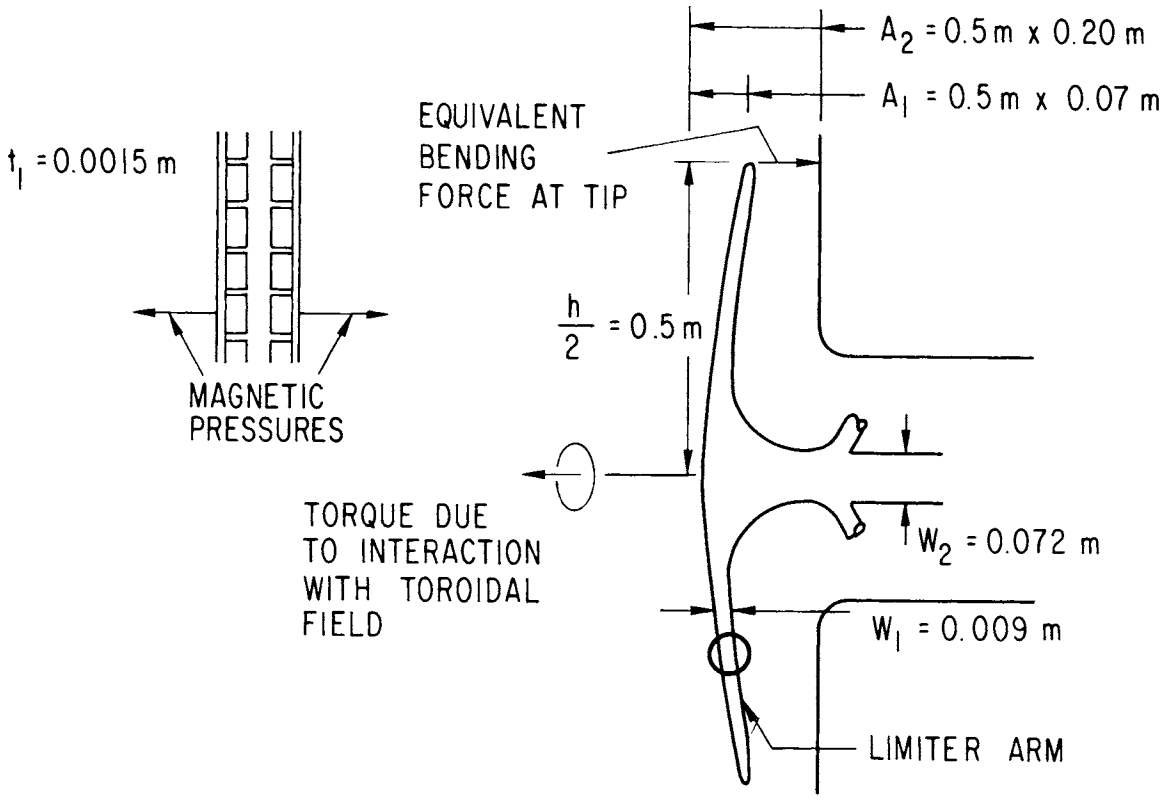

Figure 8-24. Limiter schematic.

These currents, pressures, forces, and torques are analyzed below. An analysis of an earlier, hollow limiter design, which was replaced by the solid limiter largely because of problems from the eddy current forces and torques, appears in Appendix H.

8.4.6.1 Limiter Analysis

The Model -- We treat separately eddy currents due to flux changes parallel to and perpendicular to an arm of the limiter; the arm is the part that extends upward or downward, roughly parallel to the first wall. To calculate the eddy current response to changes in flux parallel to an arm, we model the conducting path by the two plane currents in opposite directions, with crossovers between the planes at each end as shown in Fig. 8-25(a). The flux Φ, field B, and self-inductance L are given by

$$\Phi = Bw\ell$$

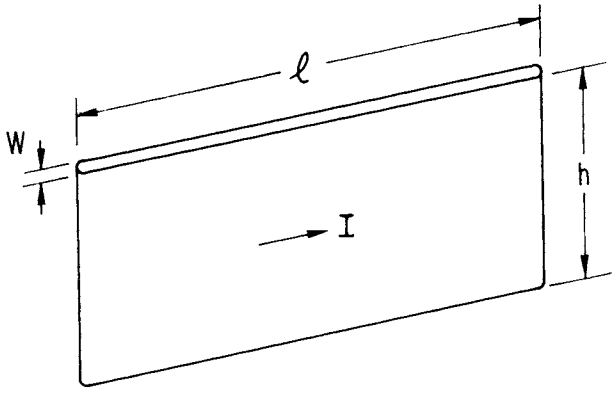

a. MODEL FOR FLUX PARALLEL TO ARMS

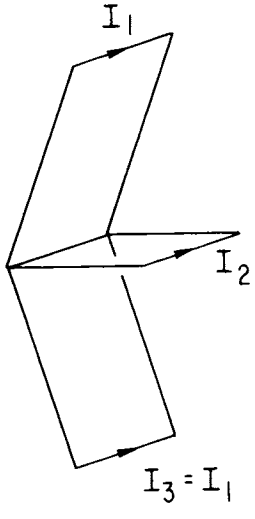

b. MODEL FOR FLUX PERPENDICULAR TO ARMS

Figure 25. Models for solid limiter.

$$B = \mu_0 I/h$$

$$L = \Phi/I = \mu_0 w\ell/h$$

where w is the separation of the planes, 0.0155 m; ℓ is the length of the limiter, 0.5 m; and h is the height of the limiter, 1.0 m. With these values L = 0.0097 μH. Also, the resistance $R = \rho 2\ell/ht_1$, where t_1 is the current carrying thickness of a plate, 0.0015 m, and ρ is the electrical resistivity. With these values, R = 93 μΩ and the L/R time τ = 0.10 ms.

To calculate the eddy current response to changes in flux perpendicular to the two arms and the horizontal section, we model the three faces by three current loops as shown in Fig. 8-25(b). The resistance of the side common to the three loops is neglected, because of its much greater thickness. The resistance of the other nine sides is taken to be $R = \rho \ell^2/2Aw$, with ρ the resistivity, ℓ the length of the side, w the thickness, and A the area of the triangle defined by the side and the centroid of the loop.[74] The resistances are summed for the three sides to give the resistance of each loop. For loops 1 and 3, $w_1 = 0.009$ m and $R_1 = R_3 = 93$ μΩ. For loop 2, $w_2 = 0.072$ m and $R_2 = 12.8$ μΩ.

Because the current is not really concentrated in a filamentary loop, the mutual inductance between two faces is not given correctly by Neumann's formula. Instead we calculate the mutual inductance M_{ij} between loops i and j by $M_{ij} = B_{ij}A_i/I_j$, where B_{ij} is the component of field due to loop j at the centroid of loop i and perpendicular to loop i, A_i is the area bounded by loop i, and I_j is the current in loop j. Self-inductance L_i is given by a similar expression. Calculations yield:

$$L_1 = L_3 = 1.110\ \mu H$$

$$L_2 = 0.668\ \mu H$$

$$M_{12} = M_{21} = M_{23} = M_{32} = 0.202\ \mu H$$

$$M_{13} = M_{31} = 0.009\ \mu H\ .$$

The L/R time τ of the system can be found from the equation:

$$\begin{vmatrix} L_1 - \tau R_1 & M_{12} & M_{13} \\ M_{21} & L_2 - \tau R_2 & M_{23} \\ M_{31} & M_{32} & L_3 - \tau R_3 \end{vmatrix} = 0 \qquad (76)$$

or, imposing the condition $I_3 = I_1$,

$$\begin{vmatrix} L_1 + M_{13} - \tau R_1 & M_{12} \\ 2M_{12} & L_2 - \tau R_2 \end{vmatrix} = 0\ . \qquad (77)$$

The above values for inductances and resistance yield two values for the L/R times, τ_ℓ and τ_s, with corresponding relationships between the currents I_1 and I_2 for each:

$$\tau_\ell = 53.7 \text{ ms} ; \quad I_{1\ell} = 0.0520\ I_{2\ell}$$

$$\tau_s = 10.4 \text{ ms} , \quad I_{1s} = -1.324\ I_{2s} . \tag{78}$$

Response to Instantaneous and Exponential Plasma Disruptions - For an instantaneous plasma disruption, the initial current I_0 is that required to maintain the flux Φ_p previously produced by the plasma. Afterwards it decays with the L/R time τ. For a single mode,

$$I_0 = \Phi_p/L$$

and

$$I = I_0 \exp(-t/\tau) .$$

Interaction with a time-independent toroidal field, B_{TF}, perpendicular to the current direction yields a force per unit length F/ℓ

$$F/\ell = B_{TF} I_0 \exp(-t/\tau) .$$

If the initial field was B_{po}, the induced field, B_{in}, is given by

$$B_{in} = B_{po} \exp(-t/\tau) ,$$

and the induced force per unit length by

$$F/\ell = \frac{1}{2} I\ B_{in}$$

$$= \frac{1}{2} I_0 B_{po} \exp(-2t/\tau) .$$

In comparison to the poloidal field from the plasma, the field from the EF coils can be neglected.

For an L/R time τ and an exponential plasma discharge with time constant τ_0, the current is given by

$$I = \frac{I_0}{(1 - \tau_0/\tau)} \left[e^{-t/\tau} - e^{-t/\tau_0} \right] . \tag{79}$$

The maximum current I_{max} occurs at time t_{max}, given by

$$t_{max} = \frac{-\tau_0 \, \ell n(\tau_0/\tau)}{(1 - \tau_0/\tau)} \tag{80}$$

and is given by

$$I_{max} = \frac{I_0}{(1 - \tau_0/\tau)} \left[\left(\frac{\tau_0}{\tau}\right)^{(\tau_0/\tau)(1-\tau_0/\tau)^{-1}} - \left(\frac{\tau_0}{\tau}\right)^{(1-\tau_0/\tau)^{-1}} \right] . \tag{81}$$

Forces and torques resulting from interaction between the current and the time-independent toroidal field show the same time variation.

The eddy current I interacts with the field of a plasma B_p and its own field B_s to give a magnetic force per unit length:

$$F/\ell = IB . \tag{82}$$

All the current interacts with the plasma field but only half with the self-field, since the self-field varies from zero to its peak value across the current-carrying layer:

$$F/\ell = \left(B_p + \frac{1}{2} B_s \right) I .$$

Now

$$B_p = B_{p0} \exp(-t/\tau_0) ,$$

but B_s is proportional to the current,

$$B_s = B_{p0}(1 - \tau_0/\tau)^{-1} \left[\exp(-t/\tau) - \exp(-t/\tau_0) \right] .$$

Hence:

$$F/\ell = \frac{I_0 B_{po}}{2\mu_0(1 - \tau_0/\tau)^2}\left\{e^{-t/\tau} - (1 - 2\tau_0/\tau)e^{-2t/\tau_0} - 2\tau_0/\tau\ e^{-t[(1/\tau)+(1/\tau_0)]}\right\}. \quad (83)$$

If I is given by a combination of modes with different L/R times, Eq. (80) and Eq. (81) cannot be used to give the peak currents and the time at which it occurs. Instead, the current must be found by Eq. (79) for each mode and summed at different times to find the peak current.

8.4.6.2 Results

Three electromagnetic effects have to be evaluated: the magnetic pressure tending to explode the limiter, the forces tending to bend the limiter arm about a toroidal axis, and the torque tending to twist the limiter about a radial axis.

For an instantaneous disruption, the pressure is of magnitude, $p = B^2/2\mu_0$. For the conservative value, B = 1 T, $p = 0.40 \times 10^6$ N/m^2 = 55 psi. For disruption times τ_0 long compared with the L/R time τ = 0.10 ms, the pressure is reduced by a factor τ/τ_0. Thus for a disruption time of 10 ms, the pressure is only 0.55 psi.

For an instantaneous plasma quench, the induced currents I_1 and I_2 will initially maintain the flux ϕ_1 through the 0.5 m × 0.07 m projected area of the arm and ϕ_2 through the 0.5 m × 0.20 m horizontal area of the support. For a plasma field of 1 T and in the vertical direction, the fluxes are:

$$\phi_1 = 1\ T \times 0.5\ m \times 0.07\ m = 0.035\ Wb$$

$$\phi_2 = 1\ T \times 0.5\ m \times 0.2\ m = 0.1\ Wb.$$

The currents I_1 and I_2 are then given by

$$\phi_1 = (L_1 + M_{13})I_1 + M_{12}I_2$$

$$\phi_2 = 2M_{12}I_1 + L_2I_2$$

with the solution I_1 = 3.733 kA and I_2 = 146.102 kA. To find the time dependence of I_1 and I_2, these values are combined with the relations of Eq. (78), which yields

$$I_1 = 7.52 \exp(-t/53.7) - 2.76 \exp(-t/10.4)$$
$$I_2 = 144.64 \exp(-t/53.7) + 2.09 \exp(-t/10.4) \quad (84)$$

with I_1 and I_2 in kA and t in ms.

The current I_1 reaches its maximum value of 5.20 kA at time t = 8 ms. The equivalent tip force tending to bend the arm is conservatively estimated to be

$$F = 0.5 \text{ m} \times 1 \text{ T} \times 5.20 \text{ kA} = 2.60 \text{ kN} = 583 \text{ lb.}$$

For non-zero plasma disruption times, each of the exponential time dependence in Eq. (84) must be replaced as in Eq. (79). Results appear in Table 8-21.

Table 8-21. Currents and Equivalent Tip Forces for the Solid Limiter with Various Disruption Times τ_0

τ_0 (ms)	t_{max} (ms)	I_1 (kA)	F_{Tip} (kN)	F_{Tip} (lb)
0	7	5.20	2.60	583
10	25	4.45	2.23	500
25	40	3.49	1.74	392
100	75	1.81	0.91	203

The torque tending to twist the limiter arises from interactions between the toroidal field (4.54 T) and radial currents:

$$N = wiB_T\ell$$
$$= (2 \times 0.07 \text{ m} I_1 + 0.20 \text{ m} I_2) \, 4.54 \text{ T} \times 0.5 \text{ m}$$
$$= 0.3178 \, I_1 + 0.454 \, I_2 ,$$

which upon substitution of Eq. (84) becomes

$$N = 68.1 \text{ kN-m } \exp(-t/53.7) + 0.07 \text{ KN-m } \exp(-t/10.4) \quad (85)$$

for an instantaneous plasma disruption. For a non-zero disruption time, the torque will have a time dependence as in Eq. (79). Because the second term in Eq. (85) is negligible compared to the first, it can be ignored; t_{max} and N_{max} can be found from Eqs. (80) and (81), using τ = 53.7 ms. Torques appear in Table 8-22.

Table 8-22. Torque on Solid Limiters for Various Disruption Times τ_0

τ_0 (ms)	t_{max} (ms)	N (kN-m)	N (lb-ft)
0	0	68.1	50,100
10	21	46.3	34,100
25	36	35.0	25,800
100	72	17.8	13,100

8.4.7 Neutronics Analysis

A detailed analysis of the neutronics performance and shielding requirements for the limiter/vacuum system is presented in Chap. 11. Calculations based on a three-dimensional geometrical model were made using the Monte Carlo method. In this subsection, a brief summary of the key points is given.

An important concern with the vacuum system design is radiation streaming into the vacuum pumps and the exterior of the reactor. The cryopanels in the compound cryopumps operate at low temperatures, $\sim$4.2°K. High nuclear heating rates due to radiation streaming into the pumps can result in: (a) a large increase in the temperature of the cryocondensation panels, thereby reducing their pumping speed; and (b) an increase in both the power requirements for cryogenic cooling and the flow rates of the helium coolant. Significant neutron streaming through the vacuum ducts and vacuum pumps will result in activation of components in the exterior of the reactor. This problem can be generally solved by placing adequate shields around the ducts and pumps.

The potential problem with radiation streaming through the vacuum system was a key factor in selecting the limiter/vacuum concept for STARFIRE in preference to other impurity control and exhaust schemes such as divertors. The limiter/vacuum concept is flexible enough to permit development of a good design in which the radiation streaming problems can be reduced to a manageable level. As can be seen from Fig. 8-1, a neutron must undergo a large number of collisions before reaching the vacuum pumps. As a result, the nuclear heating rate in the aluminum cryocondensation panels is only $\sim$0.3 mW/cm^3. The temperature rise across the 1-mm thick cryopanel, and hence the effect on pumping speed, is negligibly small. Another feature of the design is the reduction of the neutron flux at the outer surfaces of the pump to an average value of $\sim 5 \times 10^{13}$ m^{-2}s^{-1}. A shield that is 0.5-m thick around the vacuum ducts and pumps is more than adequate to protect adjacent reactor components and to reduce induced activation so that the reactor building is accessible within 24 h after shutdown. Comparison of these results with those for divertors[77-80] leads to an important conclusion. The limiter/vacuum concept is the first impurity control and exhaust scheme for which a shield design has been developed that adequately protects all reactor components and permits personnel access into the reactor building at a modest shield cost.

The neutronic performance of the limiter has been analyzed for two of the primary reference materials, Ta-5W and V-20Ti. The tantalum alloy has some unique neutronics characteristics but the vanadium-titanium alloy is more representative of the other candidate materials of copper and niobium alloys.

For the Ta-5W, the average nuclear heating rates (based on an average neutron wall load of 3.6 MW/m^2) are $\sim$80, 60, and 35 MW/m^3 in the regions of the limiter arms (long branches in the scrape-off region), limiter root (thick part around the midplane) and the limiter support (horizontal part in the limiter duct that penetrates the blanket, see Fig. 8-1), respectively. The reason for this strong spatial variation in the limiter heating rates is that the neutron and gamma-ray "backshine" into the limiter is affected considerably by the void region (limiter duct) behind the limiter. Notice that the upper parts of the limiter arms are in the shadow of the first wall/blanket (see Fig. 8-1) while the limiter root and limiter support are more directly affected by the mostly void limiter duct region. The average nuclear heating rates in a V-20Ti limiter are about a factor of three lower than that with Ta-5W. The

reason is that tantalum has large radiative capture and gamma-ray absorption cross sections.

The total neutron and gamma-ray energy deposition in the limiter (arms, root, and support) is ∿54 MW for V-20Ti compared to ∿163 MW for Ta-5W. This heat together with the energy deposited in the limiter by plasma radiation and particles is removed by low-temperature (145°C) water and is used for feedwater heating in the steam cycle. Operating the limiter at low temperature helps avoid the large stresses associated with high pressure cooling. Thus, it is desirable to minimize the energy deposition in the limiter in order not to significantly affect the thermodynamic efficiency for the reactor plant. It seems that the relatively high nuclear heating in Ta-5W is a disadvantage. However, this disadvantage is compensated for by the fact that a good fraction of the high nuclear heat in Ta-5W is an excess energy that is self-generated by the exothermic radiative capture reaction.

The rate and effects of nuclear transmutations in the limiter materials were analyzed. The most important result concerns the unusually high rate of transmutations in tantalum. As mentioned above, tantalum has a large radiative capture cross section. Furthermore, the presence of the lead-zirconium compound, with its relatively large (n,2n) and inelastic cross sections, immediately behind the first wall causes the flux of low energy neutrons to be significant in the limiter region. If the limiter shown in Fig. 8-1 were to completely surround the plasma poloidally as well as toroidally the rate of the (n,γ) reactions in the tantalum limiter would have been ∿0.5 for every fusion neutron. Fortunately, the limiter area is only ∿7% of the first wall surface and the effect of this strong parasitic absorption on the tritium breeding ratio is reduced to only ∿6%. However, the local fractional change of tantalum to other elements remians high. Table 8-23 shows the percentage burnup of tantalum in the Ta-5W limiter. The principal transmutation chain for tantalum is rather simple. ^{181}Ta is converted to ^{182}Ta via an (n,γ) reaction. ^{182}Ta either decays to ^{182}W or undergoes an (n,γ) reaction to produce ^{183}Ta, which in turn either decays to ^{183}W or is converted to ^{184}Ta. The final effect of the $^{181}Ta(n,\gamma)$ reaction is the production of several tungsten isotopes. For bare no-coating) limiter and first wall, ∿21% of the tantalum is converted into tungsten after irradiation, yielding an integral neutron wall load of 16 MW-yr/m^2 (which is the end of life according to the scheduled maintenance plan). This large increase in the tungsten content of the tantalum alloy will significantly

reduce its ductility but will increase its mechanical strength as discussed in Sec. 8.4.2. It is therefore not clear at present whether such a high transmutation rate will rule out the tantalum alloys as candidates for the limiter material. Methods to reduce this rate of transmutation were investigated. The most effective method is to use a strong neutron absorber for the coating material on the limiter and first wall in order to reduce the low energy neutron component within the tantalum limiter. Boron can serve this function well because of the large $^{10}B(n,\alpha)$ cross section and because it is a strong candidate as a low-Z coating as discussed in Sec. 8.4.3. Table 8-23 shows that a 2-mm thick coating can reduce the tantalum burnup to 17%. Unfortunately, ^{10}B is depleted in a short time and maintaining the $^{10}B(n,\alpha)$ reaction rate at the desired level will require recoating every few months. A 2-mm thick Li_2O coating would also reduce the tantalum burnup to ~12%. However, the low thermal conductivity of Li_2O will almost surely preclude its use as a coating material. Adding boron to the limiter water coolant also helps reduce the rate of the tantalum transmutation, but this can only be used as a secondary measure since the exterior surfaces of the limiter are where shielding against low energy neutrons is most effective.

Table 8-23. Tantalum Burnup for Ta-5W Limiter

Case	Ta(n,γ) Reaction/DT Neutron	Burnup[a] (%)
Bare limiter	0.042	21
2-mm thick beryllium coating	0.045	22
2-mm thick boron coating	0.029	14
2-mm thick Li_2O coating	0.026	12
2-mm thick Li_2O coating and water is borated	0.025	11

[a]After irradiation to an integral neutron wall load of 16 MW-yr/m^2.

8.4.8 Limiter Mechanical Design

The selected limiter system design consists of 96 individual limiters that form a continuous toroidal ring in front of a 40-cm slot through the outer blanket. The ring is made up of 96 straight segments which approximate a circle to within a total roundness variation of 1/2 cm. Each limiter incorporates an actuator which permits radial positioning to assure a proper match with the plasma contour.

The limiter system continuously absorbs 200 MW of plasma power without injecting excessive impurities into the plasma or eroding significantly. A beryllium coating covers all exposed limiter surfaces to minimize the effects of impurities.

The reference limiter design is fabricated from Ta-5W (or any of the other three reference alloys discussed earlier) and is water cooled. It is shown in Fig. 8-26 in isometric form. A cross section through the limiter and vacuum slot of the blanket is shown in Fig. 8-1. It consists of a limiter head, a transition zone, and circular support stem. Four tubular legs mounted to the transition section and limiter support stem position the unit against slide pads on the blanket sidewalls. A hydraulic positioning device, using an expansion bellows section, is located at the rear of the unit next to the rear anchor support fitting. The limiter positioning and support load is taken by a horizontal bracket fastened to the rear of the blanket sector support structures. The positioner hydraulic lines, coolant lines, and instrumentation lead lines are located outside the blanket envelope to minimize blockage of the vacuum slot. The limiter coolant tubing inside the shield boundary is also made from Ta-5W. A transition from Ta-5W to steel is made at the mechanical joint to the coolant bundle that is located outside the shield.

The coolant flows up the stem where it spreads out to the outer surface of the limiter. The coolant then flows at 8 m/s along the skin through milled coolant channels to the front face where the coolant merges and returns through holes that lead back to the support system.

The limiters are connected so that coolant passes through two limiters before exiting to provide a sufficient temperature rise for feedwater heating. A 115°C base inlet temperature plus a 15°C bulk coolant temperature rise in each pass results in an outlet temperature of 145°C. The maximum coolant

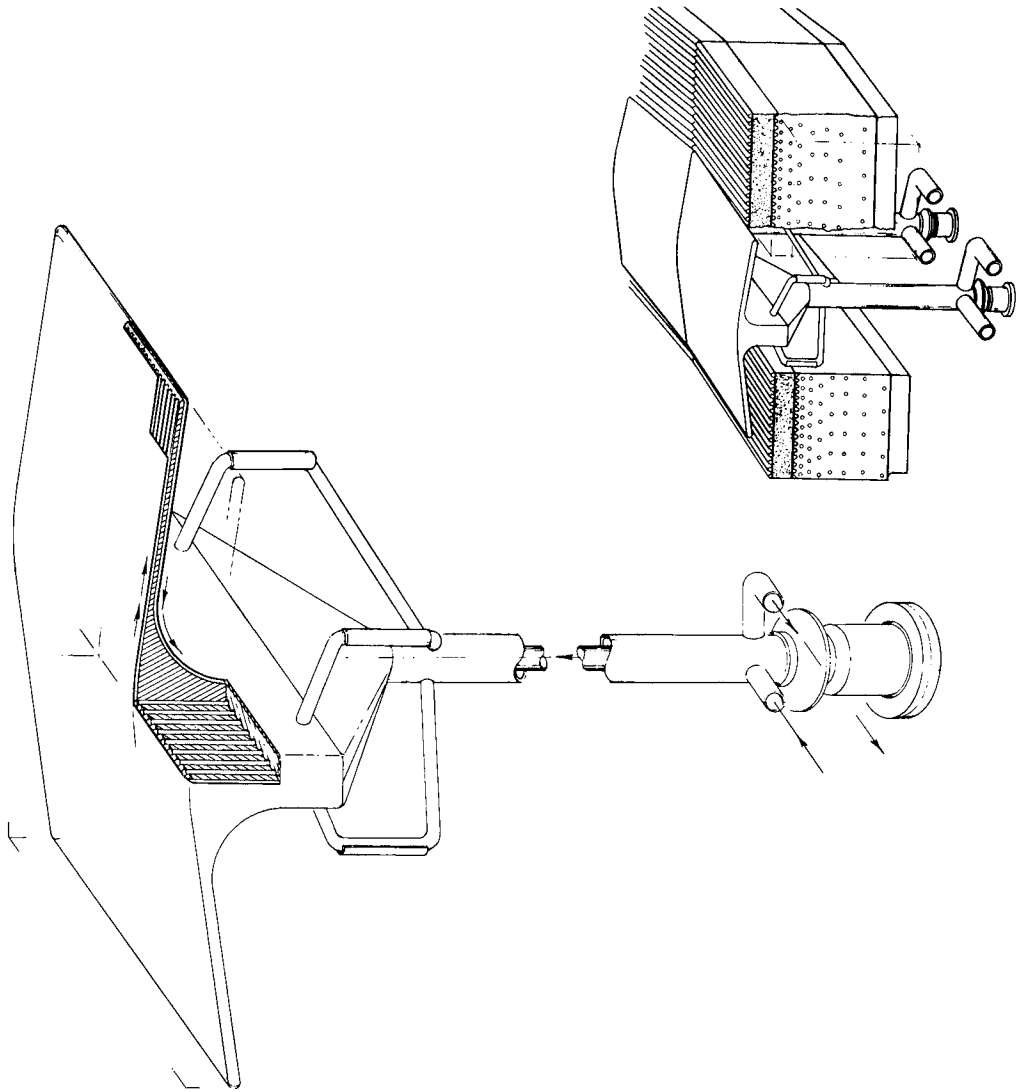

Figure 8-26. An isometric view of the STARFIRE limiter design.

pressure is 4.2 MPa (600 psi). The presssure drop per pass is 310 KPa (45 psi). A series of 4 mm × 8 mm channels with a 2-mm partition wall and a 1.5-mm frontal cover plate form the coolant passages.

Investigation of other cooling methods may permit a further decrease in the system pressure. Use of subnucleate boiling and a finned structure may improve the heat transfer characteristics. Another factor to be included is the centrifugal effects that would force steam bubbles away from the heated surface as the coolant passes the curved leading edge where the heat flux is highest.

The transition neck from the coolant inlet to the panel is designed for minimum pressure drop as are the concentric inlet/outlet trunk supply lines. The support leg tubes use bypass inlet coolant produced by a small pressure differential inherent in the transition piece to cool the tubular support and pad. Similarly, the support base and positioner assembly are also cooled with a very small inlet bypass flow.

The Limiter Head Fitting - The portion of the limiter interfacing with the plasma is shown in cross section in Fig. 8-1. The thin flat ended blades are 50 cm in length by 1.7-cm thick. It is attached, through a gentle arc, to the neck which tapers to a 9-cm thick rectangular section. Parallel channels are milled into the outside surfaces as shown in Fig. 8-1, Sec. AA, to form 4-mm deep by 8-mm wide coolant passages yet leave a 2-mm wide partition for support of the outer skin. A 1.5-mm plate covers the base milled structure forming leak-tight structure.

Transition and Trunk - The neck of the limiter head piece is rectangular in cross section and requires a transition to the circular trunk section. The transition consists of two flattened funnel-shaped pieces, one inside the other, stiffened and welded to withstand the 4.2 MPA (600 psi) operating pressure. The hot outlet coolant flows out through the inner transition piece while the incoming coolant flows in the annulus between the concentric pieces. The transition piece acts as both flow distributor, inlet-to-outlet coolant insulator, and structural support extension.

The trunk section, composed of two concentric tantalum alloy pipes, is joined to the transition piece and to the positioner/mounting case at the far end. The outer pipe is designed for the 4.2 MPa (600 psi) pressure while the

inner pipe contains a thermal insulator and is designed for only the pressure differential. The tubular trunk section of 11-cm outer diameter by ∿80 cm long serves to carry the coolant and form the base support for the limiter. Two coolant nozzles, the inlet and outlet, are located near the positioner.

Positioner/Support Base - A hydraulic mechanism has been selected to provide the 1 to 2-cm adjustment required for the accurate positioning of the limiter relative to the plasma. A piston is used to provide the motion within the 11-cm trunk tube diameter while hydraulic tap monitors indicate position. The fluid is coolant water conditioned to 600 psi and discharged as necessary to the coolant system. Position control is attained by pressure balancing the piston across any given set of the many pressure ports which both positions and provides indication through the use of multiple sets of small (capillary) tubes.

Differential motion between the base support and the limiter is taken up through one or possibly two convolution bellows-type section. The bellows is designed to adequately flex at both full operating pressure (600 psi) and through maximum tension loading during a plasma disruption. A further definition of the control system necessary to determine the position of the limiter or its support base relative to the plasma location is required.

Fabrication - The process for fabrication of the limiter can be selected from one of several choices. The panel and neck section (nose piece) is to be fabricated from one-piece shaped block. Cutting of the coolant channels on the outer surfaces will be done by either chemical or straight milling process. The remaining channels, transition preparations, and manifolding are made using conventional practices. A 1.5-mm sheet of tantalum alloy is then joined to the outer surface of the finished base by pressure bonding, electron-beam or resistance welding, with roll bonding being preferred. Transition pieces of tantalum are then joined to the nose section providing the coolant manifolding and structural support to the final tubular trunk section.

If the alternate material, AMAX-MZC copper, is used for the limiter, a method of joining the 40% cold-worked material without loss of strength properties must be identified.

8.5 VACUUM SYSTEM

8.5.1 Design Criteria and Objectives

The primary requirement for the STARFIRE vacuum system is to remove the helium ash. Other design objectives are to achieve good reliability and maintainability while minimizing tritium inventory and neutron streaming. These design objectives tend to conflict with one another. For example, while it is desirable to maximize helium pumping in order to maximize plasma purity it would then be necessary to have large vacuum ducts which would result in excessive neutron and gamma streaming. Also, highly efficient removal of helium ash will remove large amounts of unburnt fuel; tritium inventories in the vacuum pumps and fuel recycle systems would then be large. The tradeoffs between tritium inventories and plasma purity are discussed in Sec. 14.2. In order to best satisfy the conflicting design objectives, a number of trade studies were performed. The resulting vacuum system serves to minimize neutron streaming while providing adequate helium pumping.

The vacuum system configuration is illustrated in Fig. 8-2 and the components are defined as follows: The two limiter slots are the regions between the back of the limiter and the first wall, above and below the reactor midplane. The limiter duct is the orifice which extends from the limiter slots through the blanket to the plenum region. Since the limiter requires cooling lines and structural support, the limiter duct is divided in two. The plenum region is the open space behind the blanket; it serves to provide a high-conductance pathway to the vacuum ducts, while providing a tortuous path for streaming neutrons. The limiter ducts, the limiter slots, and the plenum region are symmetric about the reactor midplane and they extend around the torus circumference. The vacuum ducts are the circular ducts which connect the vacuum-pumps to the plenum region.

8.5.2 Vacuum System Optimization

The slot regions behind the limiter receive about 28% of the particle flux (F = 0.28). This flux consists of deuterium and tritium ions, helium ions, beryllium ions, and electrons. The helium ions are neutralized on the back surfaces of the limiter. Some of the helium atoms are scattered directly into the limiter duct where they are eventually pumped; those traveling back up the slot are nearly all ionized by the incoming stream of hot electrons.

Once ionized, they are accelerated back into the limiter slot. This phenomenon can be described by a trapping or "inversion probability", κ, which for helium has been estimated at 0.99. The trapping of hydrogen is less frequent since the deuterium/tritium neutrals can charge-exchange with other DT with a probability roughly equal to that of electron ionization. The neutrals created from charge-exchange can escape. Therefore, the inversion probability for DT is less than for helium ($\kappa_{DT} = 0.8$). This insures that a large fraction of the DT returns to the plasm yielding a higher fractional burnup.[81]

A transmission probability, ε, is defined as the probability that a particle entering the limiter slots will be trapped by the compound cryopumps. The dependence of ε on κ and on the geometric configuration of the limiter/vacuum system is derived as follows:

The pressure of neutrals in the plasma is assumed to be zero as is the pressure at the compound cryopump. A mass flow balance in the limiter slots then requires that

$$\frac{dP_i}{dt} = \phi_i - C_R P_i - C_S P_i(1 - \kappa_i) , \tag{86}$$

where P_i is the pressure of species i in the slot region, ϕ_i is the input gas load of species i, κ_i is the inversion probability of species i, C_R is the effective conductance of the vacuum system, C_S is the conductance of the limiter slots, and t is time. At steady-state operation, Eq. (86) reduces to

$$\phi_i = C_R P_i\left[1 + \gamma(1 - \kappa_i)\right], \tag{87}$$

where $\gamma = C_S/C_R$ is the conductance ratio of the limiter slots to the vacuum system.

The transmission probability, ε, of species i is given by:

$$\varepsilon_i = \frac{C_R P_i}{\phi_i} . \tag{88}$$

Substitution of Eq. (88) into Eq. (87) yields:

$$\varepsilon_i = \frac{1}{1 + \gamma(1 - \kappa_i)}, \tag{89}$$

which shows the dependence of ε on on κ, the inversion probability, and on γ, the geometric configuration of the vacuum system design. This relationship is shown in graphical form in Fig. 8-27.

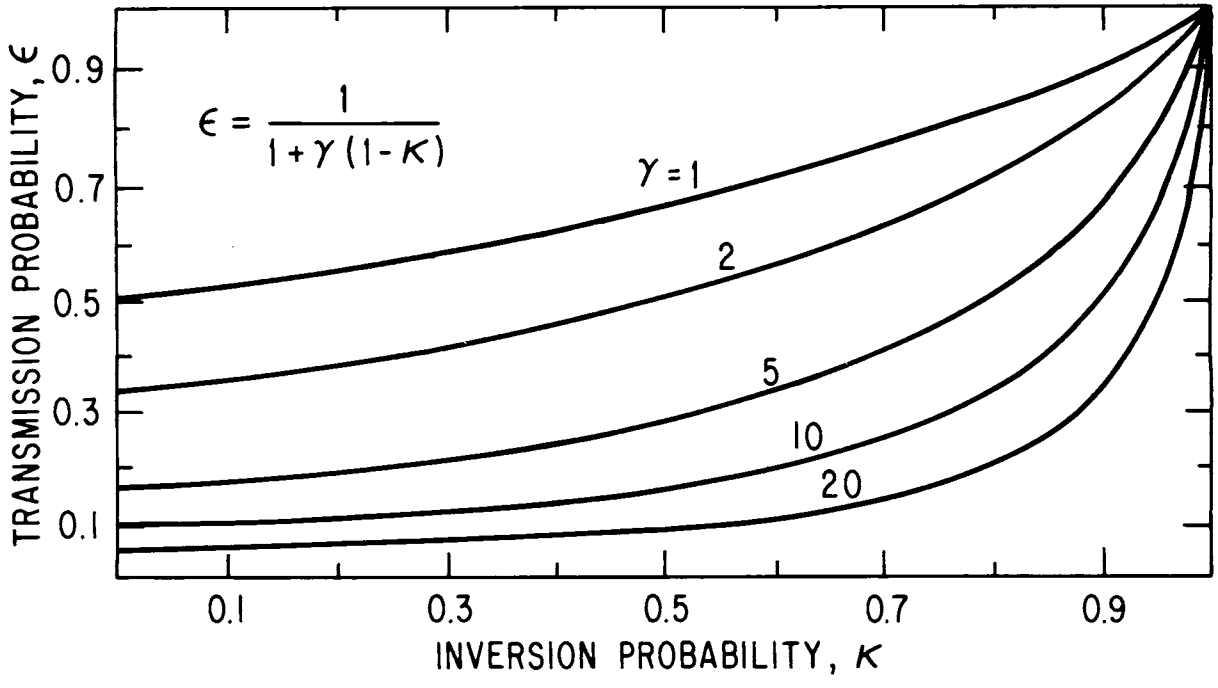

Figure 8-27. Dependence of transmission probability, ε, on inversion probability, κ, and on γ.

The reflection coefficient, R, for species i is given by $R_i = 1 - F\varepsilon_i$, where F is the particle fraction entering the limiter slots. For the STARFIRE design, effective impurity control requires that $R_{He} \leq 0.75$ to satisfy impurity requirements. Since $\kappa_{He} = 0.99$, and $F = 0.28$, ε_{He} must be at least 0.9.

For the STARFIRE design, the vacuum system has to provide a high conductance path from the limiter slots to the compound cryopumps, while also minimizing neutron streaming, i.e., eliminating any direct line-of-sight paths to unshielded areas. An optimized design was arrived at by performing parametric trade studies on the various possible components of the vacuum system. The analyses were done by comparing the reciprocal conductances[82,83] of various

component configurations and optimizing each in terms of the total vacuum system design. The tube conductance (C_t) of each component was calculated for helium gas at an appropriate temperature. Some of the components were treated as long rectangular ducts. At room temperature, the appropriate conductance equation is:

$$C_t = \frac{0.122\ a^2b^2}{(a + b)\ell}, \quad \text{if } a > 10b \tag{90}$$

where a, b, and ℓ are in cm and C_t is in m^3/s. For the conductance of the vacuum ducts (C_{VD}), aperture effects are significant. Therefore, in the same units

$$C_t = \frac{0.0332\ b^3}{\ell} \tag{91}$$

and

$$C_a = 0.0250\ b^2, \tag{92}$$

where

$$C_{VD} = \frac{C_a C_t}{C_a + C_t}. \tag{93}$$

A representative sampling of some of the trade studies is shown in Table 8-24. The items with footnote "a" are the STARFIRE reference design. The dimensions of the plenum are 12 m high and 1.0 m wide ($\sim$0.33 m of which is used for coolant manifolding). Its impedance is very low, being 0.7×10^{-3} s/m^3 for the reference case (Table 8-24). Thus it provides a high conductance path for vacuum pumping while reducing line-of-sight neutron streaming. A change in temperature has little impact on the impedance; however, a major reduction in its width produces an order of magnitude increase in its impedance. The limiter ducts are each 0.16 m in height and extend circumferentially around the torus through the 0.70-m blanket. Changes in the surface temperature and duct height have minor impact on the impedance which is an order of magnitude greater than the plenum's. The 48 cryopumps (24 on-line at a given time each with a helium speed of 120 m^3/s) were oversized in terms of helium speed to reduce their impedance (of the same magnitude as the limiter ducts) and to provide system reliability in the event of one or more pump failures.

Table 8-24. Parameterized Vacuum Conductance Analysis for Helium

Component	Dimensions (cm) a	Dimensions (cm) b	Length (cm) ℓ	Temp. (K)	Component Conductance (m^3/s)	Reciprocal Conductance (10^{-3} s/m^3)
Limiter slots (2)	5650	10	50	673	4320	0.23[a]
	5650	10	50	773	4630	0.22
	5650	10	40	773	5780	0.17
	5650	5	50	773	1160	0.86
Limiter ducts (2)	3170	16	70	573	4090	0.24[a]
	3170	16	70	673	4420	0.23
	3170	14	70	673	3390	0.30
	4600	16	70	673	6430	0.16
	6000	16	70	573	7750	0.13
Plenum (2)	6000	67	600	473	13660	0.07[a]
	6000	67	600	573	15140	0.07
	6000	76	600	573	19380	0.05
	6000	40	600	573	5380	0.19
	6000	80	600	473	20360	0.05[b]
Vacuum ducts (24)	——	100	640	293	730	1.37[a]
	——	120	560			
	——	100	800	293	850	1.17
	——	100	1000	293	700	1.42
	——	100	1200	293	600	1.67
	——	120	1000	293	1190	0.84
	——	120	1200	293	1010	0.99
	——	150	1000	293	2240	0.45
Vacuum pumps[c] (24)	——	——	——	——	2400	0.42
	——	——	——	——	2880	0.35[a]
	——	——	——	——	3360	0.30

[a] Reference STARFIRE vacuum design.

[b] RF ducts not included.

[c] Helium pump speeds.

The major impedance in the vacuum design are the 24 vacuum ducts. Good pumping performance requires that they have a large diameter and be as short as possible; neutron streaming considerations require that they have a small diameter and be bent. Their size was optimized to satisfy both requirements.

Each duct is composed of a front section 6.4 m long × 1.0 m equivalent diameter and a back section 5.6 m long × 1.2 m diameter. As seen in Table 8-24, the impedance is less than one would obtain from a shorter duct which was 1-m diamter its entire length. However, the impedance of the vacuum ducts is twice that of the rest of the vacuum system. Thus, the addition of the limiter ducts and the plenum to the vacuum design has only increased the total impedence by 20%. However, these components provide a tortuous path for radiation streaming, thereby dramatically reducing its effects (Sec. 11.3.1).

Table 8-25 lists the vacuum system conductances for the reference STARFIRE design. The total conductance of the 24 vacuum ducts is 730 m^3/s. The conductance of the plenum region is two orders of magnitude greater than that of the vacuum ducts. The conductance of the limiter ducts and the total speed of the compound cryopump are each an order of magnitude greater than the conductance of the vacuum ducts. The effective conductance of the vacuum system for helium is 490 m^3/s. Using the appropriate DT conductance ratio and κ_{DT} yields a transmission probability of 0.4 for DT from Fig. 8-27. The associated reflection coefficient is 0.9 which yields a fractional burnup of 0.42; this is a very efficient use of tritium fuel. A reflection coefficient of 0.9 for tritium produces a minimum total gas load (Q) of 18.7 Pa-m^3/s (7.9 Pa-m^3 for helium) as seen in Fig. 8-28. Use of the equation, P = Q/S yields pressures of 16 mPa (1.2×10^{-4} torr) for helium and 24 mPa for DT in the limiter slot. Recent experiments on Alcator[22] indicate that even higher pressures are likely to be attainable.

The vacuum/limiter concept thus satisfies the design objectives for it preferentially removes helium from the system, thus achieving reasonable impurity control while maintaining a high fractional burnup of tritium. The configuration chosen has a reasonable conductance while minimizing radiation streaming.

In order to verify the results of the analytical conductance formulas and to calculate the vacuum system performance more precisely, a two-dimensional Monte Carlo code was developed and used to perform vacuum trade analyses. The results are discussed below.

A geometrical representation of the configuration shown in Fig. 8-29 (not drawn to scale) was generated. The dimensions of all surfaces were assigned variables and varied. Ions entering the region behind the limiter follow magnetic field lines until they strike the limiter and are neutralized. The

Table 8-25. STARFIRE Limiter/Vacuum System

Limiter slot conductance, m^3/s	4300
Limiter duct conductance, m^3/s	4100
Plenum conductance, m^3/s	13700
Vacuum duct conductance, m^3/s	730
Total helium pump speed, m^3/s	2900
Effective conductance, m^3/s, helium	490
Conductance ratio (γ), helium	8.8
Conductance ratio (γ), DT	8.1
Effective conductance, m^3/s, DT	480
Particle fraction to limiter (F)	0.28
Inversion probability (κ), helium	0.99
Transmission probability (ε), helium	0.9
Reflection coefficient (R), helium	0.75
Inversion probability (κ), DT	0.8
Transmission probability (ε), DT	0.4
Reflection coefficient (R), DT	0.9
Fractional burnup, tritium	0.42
Limiter helium gas load (Q), Pa m^3/s	7.9
Limiter DT gas load (Q), Pa m^3/s	10.8

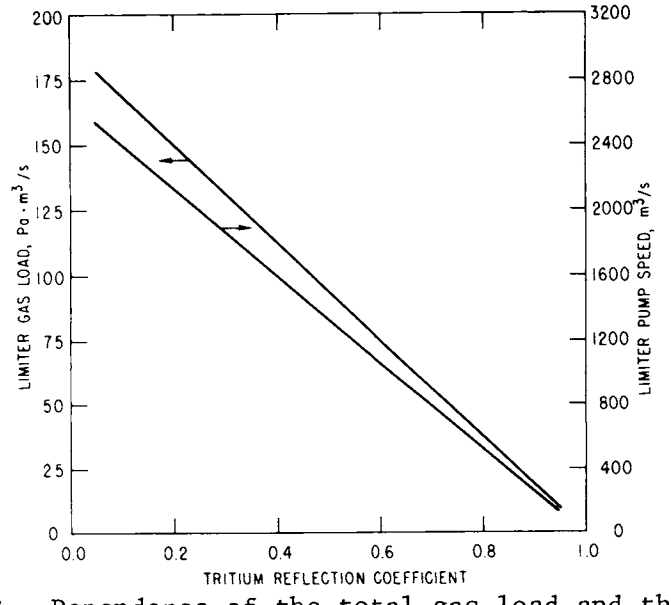

Figure 8-28. Dependence of the total gas load and the pump speed on the tritium reflection coefficient.

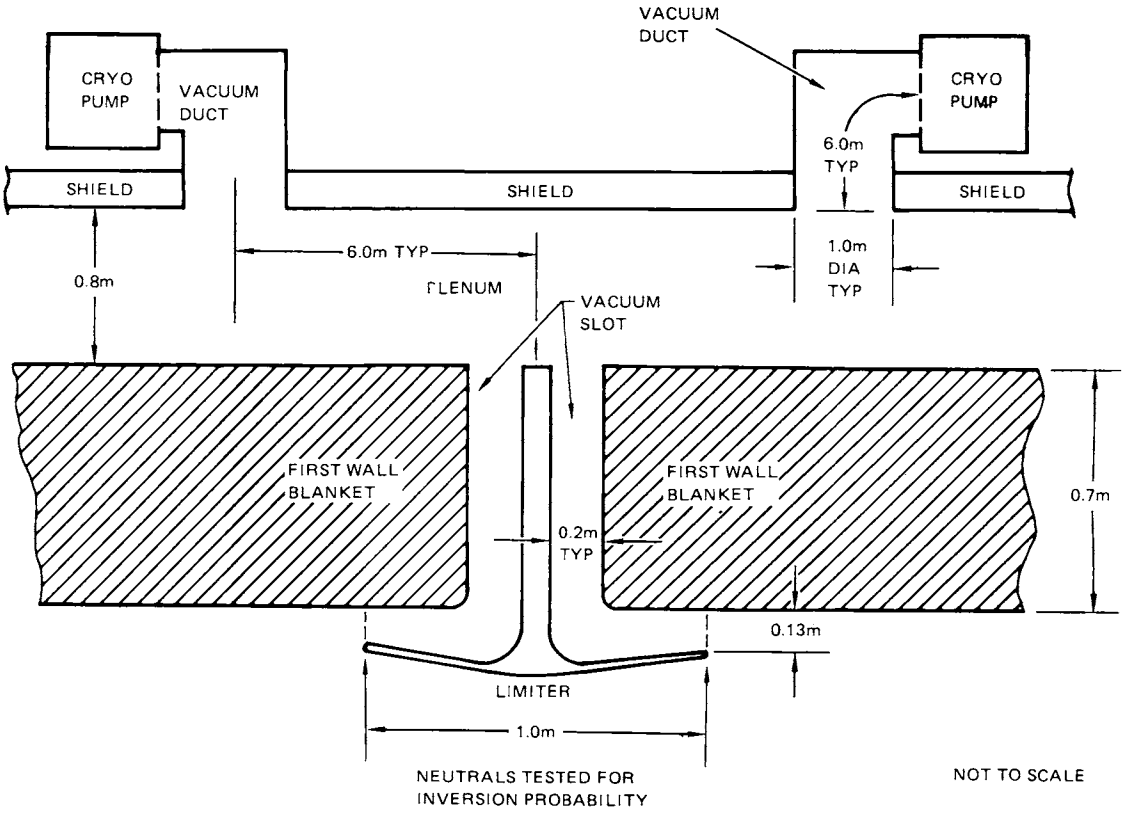

Figure 8-29. Geometric representation of the STARFIRE limiter/vacuum system configuration for Monte Carlo calculations.

neutrals travel through the vacuum duct system in free molecular flow unless they travel back toward the plasma through the limiter slot. In this region the neutrals have a probability of being reionized and then returning to the limiter as discussed above.

To simulate these events, neutrals are initiated from random points on either side of the limiter. Their direction is assumed to be random, with the overall distribution of directions assuming a cosine shape. The neutrals are traced through the system with a new, random direction assigned each time a boundary is reached. The neutrals often return to the limiter and travel toward the plasma. Such neutrals (see Fig. 8-29) have a probability (inversion probability) of being ionized and returned to the limiter. If an ion is returned to the limiter, it is reinitiated from the limiter in a random direction.

Neutrals which are incident on the vacuum pumping duct are treated as follows. In three dimensions a pump duct is not always in the location depicted; the neutral may actually be incident on the shield surface between

pumps. To account for this, the probability of striking a duct is assigned. This probability was taken to be twelve (the number of ducts in the upper or lower half of the torus) times the duct diameter divided by the circumference of the machine at the duct inlets. If the neutral has hit a wall, it is randomly reinitiated. If it has entered the duct it is subject to a pumping probability. This probability (P) is simply,

$$\frac{1}{P} = \frac{1}{P_D} + \frac{1}{P_p} - 1 , \tag{94}$$

where P_D is the throughput probability of the duct and P_p is the capture probability of the pump. P_p is assumed in all cases to be equal to 0.2. Neutrals which are not pumped are reinitiated from the duct inlet into the plenum region. At any given time only one neutral is traced through the system until it is either pumped or re-enters the plasma. One thousand samples were found to be sufficient for each geometrical configuration for each inversion probability. This was verified by running up to 5000 samples and noting where the pumping probability and standard deviations began to converge. The standard deviation for all data was approximately 0.04.

The results of four trade studies are presented in Figs. 8-30 through 8-33. Pumping probability is plotted as a function of inversion probability for various slot widths, plenum widths, duct diameters, and number of pumps. The basic system configuration for all cases is shown in Fig. 8-29. The appropriate dimension was varied for each study. As discussed previously, the pumping probability must be $\sim$0.9 for STARFIRE to operate as designed. In this region, the width of the plenum and slots have little effect on the system performance in the ranges studied. It is seen that the system performance is very sensitive to the duct size and number of vacuum pumps. Presently, 12 pumps are located around the top and 12 around the bottom of the torus, between each pair of TF coils. Though it is possible to add more pumps, the present number (24) should be adequate. The system actually incorporates 48 pumps to permit pump regeneration during operation. To improve the system performance, it would be preferable to increase the pump diameter. The upper limit on pump diameter results from nuclear heating in the pumps and the desire to keep induced activation caused by neutron streaming to a minimum. Analyses indicated (Sec. 11.2.1) that pump diameters may be increased by as much as 20% before neutron heating[84] becomes significant.

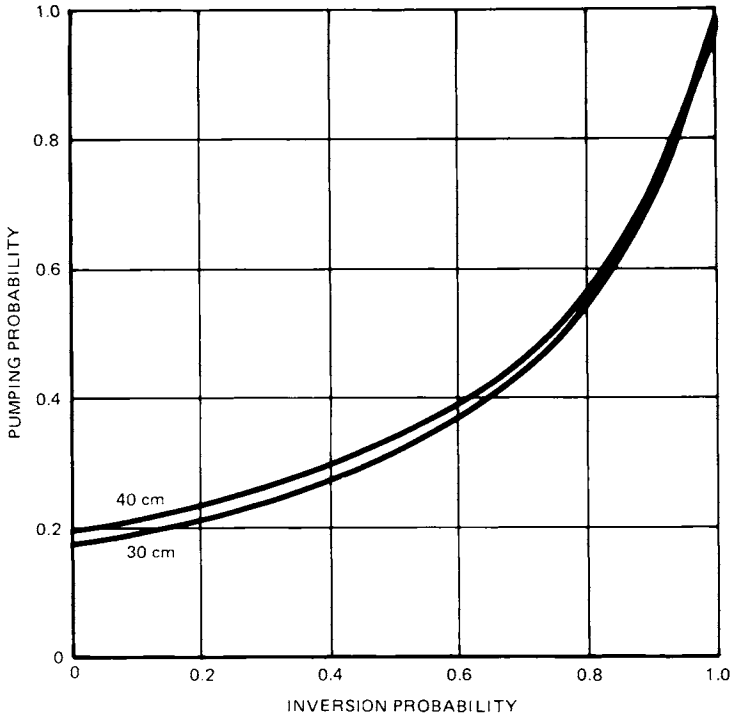

Figure 8-30. STARFIRE performance for different slot widths.

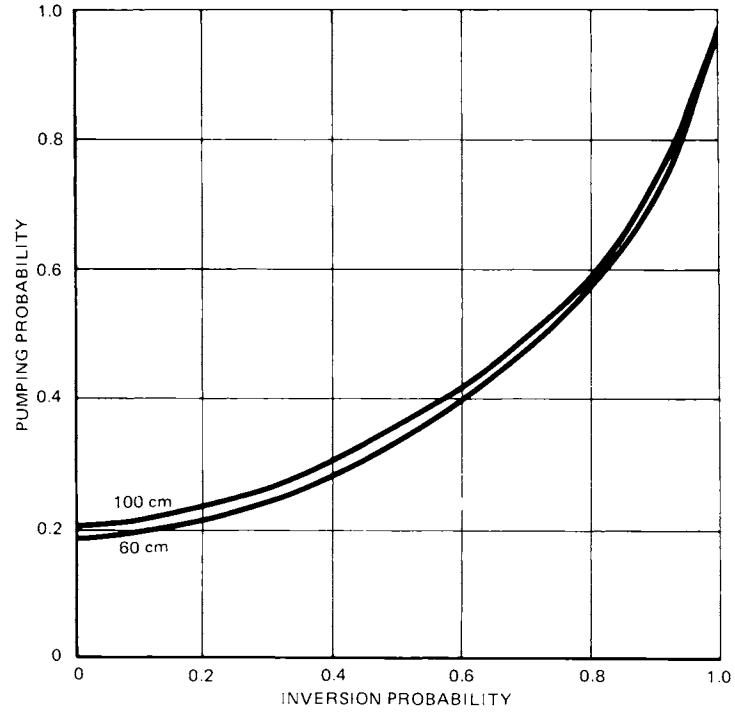

Figure 8-31. STARFIRE performance for different plenum widths.

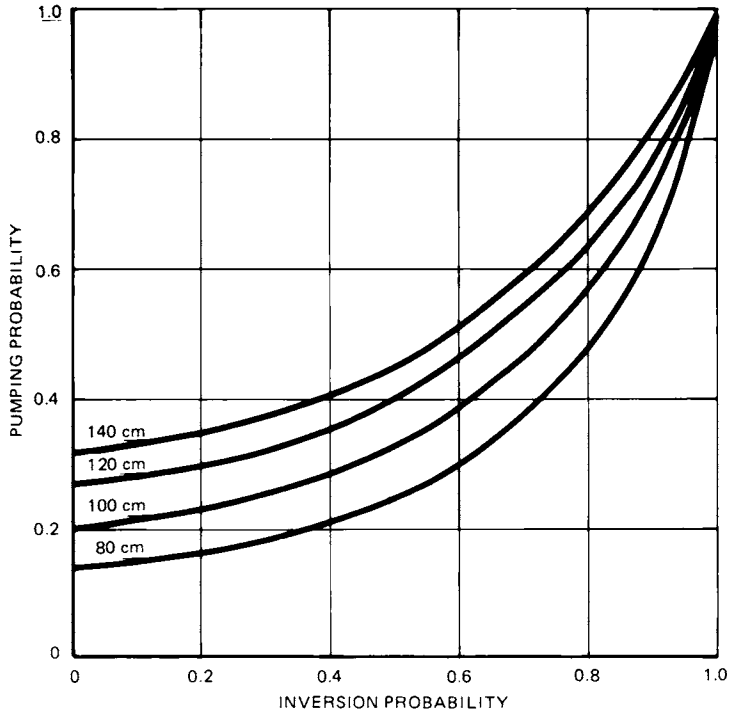

Figure 8-32. STARFIRE performance for different duct diameters.

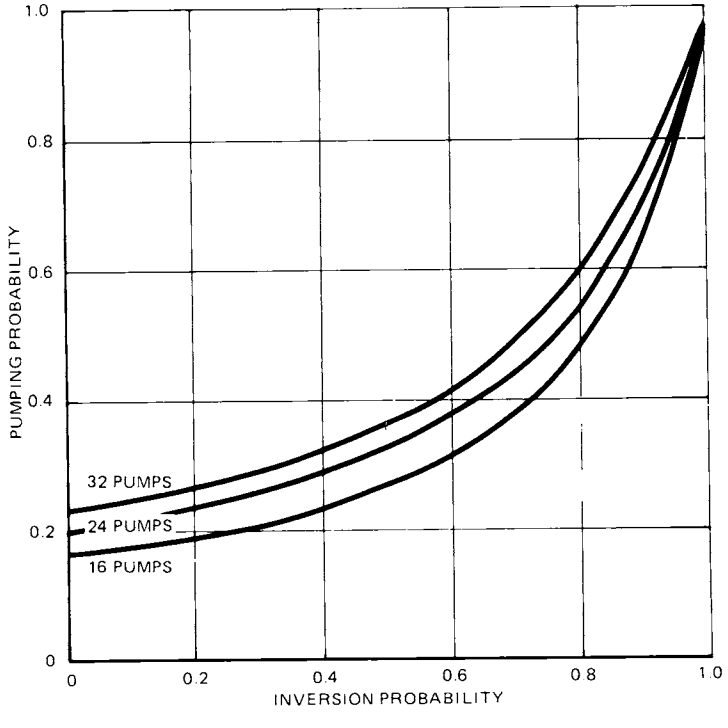

Figure 8-33. STARFIRE performance for different numbers of vacuum pumps.

The predicted performance of the reference limiter vacuum system configuration (Fig. 8-29) is shown in Fig. 8-34. With an inversion probability of 0.99, a pumping probability of 0.9 is calculated. This result confirms the results of the conductance model. However, it is noted that in the region of pumping probabilities above 0.7 the system performance is quite sensitive to small changes in inversion probability. For this reason, it will be necessary to accurately determine the inversion probability.

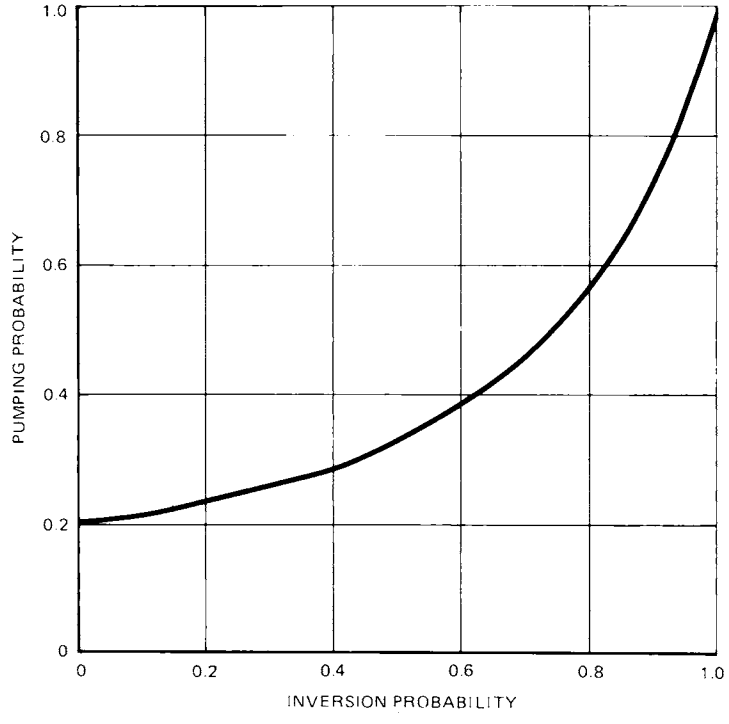

Figure 8-34. Predicted pumping performance of the design shown in Fig. 8-29.

8.5.3 Vacuum System Component Selection and Design

The STARFIRE vacuum system must perform the following functions:

(1) produce a clean, high vacuum of approximately 1.3×10^{-6} Pa for initial plasma startup;

(2) continuously pump helium ash during the burn and interface with the limiter system; and

(3) regenerate the cryopumps and interface with the tritium recovery system.

Primary considerations in the selection of valves and pumps for the vacuum system are to: (1) contain tritium; (2) minimize tritium inventory; (3) minimize radioactive waste; (4) perform the roughing, regeneration, and high vacuum pumping functions. A description of the reference design and the rationale used in the selection of the various components is provided in this section.

8.5.3.1 Roughing and Regeneration Pumps

Vacuum pumps capable of operation from atmospheric pressure to ∿0.01 Pa are required for rough pumping the torus and for regenerating the high vacuum cryopumps. These pumping systems must also be capable of transferring gases into the fuel processing system at pressures around 1 atm.

Rough pumping the STARFIRE system to ∿0.01 Pa can be accomplished in less than 2 h with four 1-m^3/s roots blowers and mechanical pump systems. Figure 8-35 shows the predicted pump-down curve. Unfortunately, the elastomeric seals and organic lubricants found in these pumps may not be compatible with tritium and become sources of radioactive waste when replaced during maintenance.

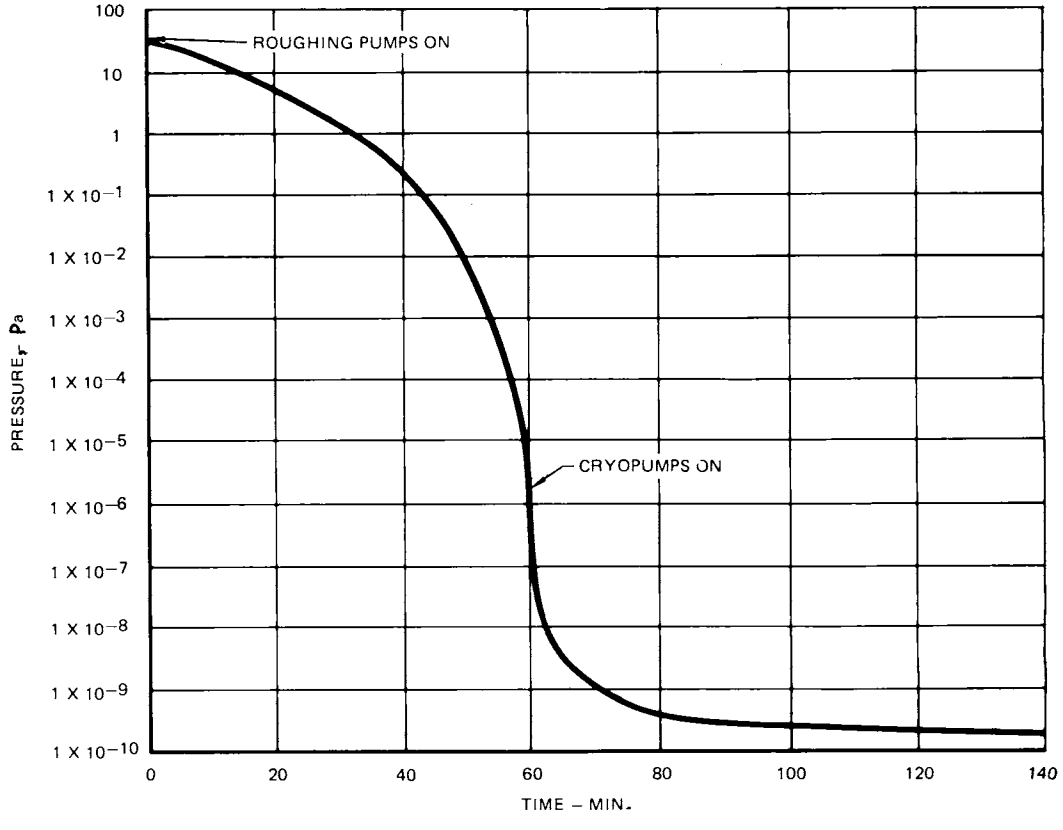

Figure 8-35. Pumpdown of the STARFIRE vacuum vessel.

Improved pump design could potentially alleviate these problems. Tritium containment can be enhanced by providing double containment for all components in which the tritium pressure exceeds 1.3 Pa (10^{-2} torr).

A completely oilless Normetex "scroll" pump will be evaluated on TSTA. This pump is not lubricated and has no shaft seals. Functionally, it will serve the same purpose as a roots blower, and will also require a mechanical backing pump. Since it is organic free, it would be preferable to present day roots blowers.

The roughing pumps will also be used in regeneration of the high vacuum cryogenic pumps and will interface with the fuel processing system. All metal roughing pumps, such as metal bellows pumps, may be useful for transferring high-pressure streams of radioactive gas. The regeneration process is discussed in detail in Sec. 8.5.3.2.

8.5.3.2 High Vacuum Pumping System

The STARFIRE high vacuum pumping system consists of 48 cryopumps, 1.2 m in diameter each, on 24 vacuum ducts. Two pumps are provided on each duct so that regeneration can be accomplished during plasma operation (Fig. 8-36). Compound cryopumps operating at 4.2 K were selected for use on STARFIRE. This decision was based on the following considerations: (1) high pumping speeds; (2) cleanliness; (3) reliability/maintainability; (4) tritium compatibility; and (5) no moving parts.

Liquid helium cryopumps[85,86] exhibit high pumping speeds for helium and the hydrogen isotopes and may be fabricated in irregular shapes and dimensions. No organics, working fluids, or elastomers are required in such pumps, ensuring a high degree of cleanliness. Such pumps have neither moving parts nor working fluids, minimizing their maintenance requirements. This also makes liquid helium cryopumps quite compatible with a tritium environment, because the amount of solid, radioactive waste is minimized. Cryopumps trap gases by cryocondensation and cryosorption, rather than by compression and transfer via higher pressure pumps. This characteristic provides for better containment of the radioactive gases. Cryotrapping is an alternative to cryosorption pumping of helium, but it was not selected because the injection of a condensable gas adds a great deal of complexity to the system design. The fuel processing system would also be affected by the selection of cryotrapping.

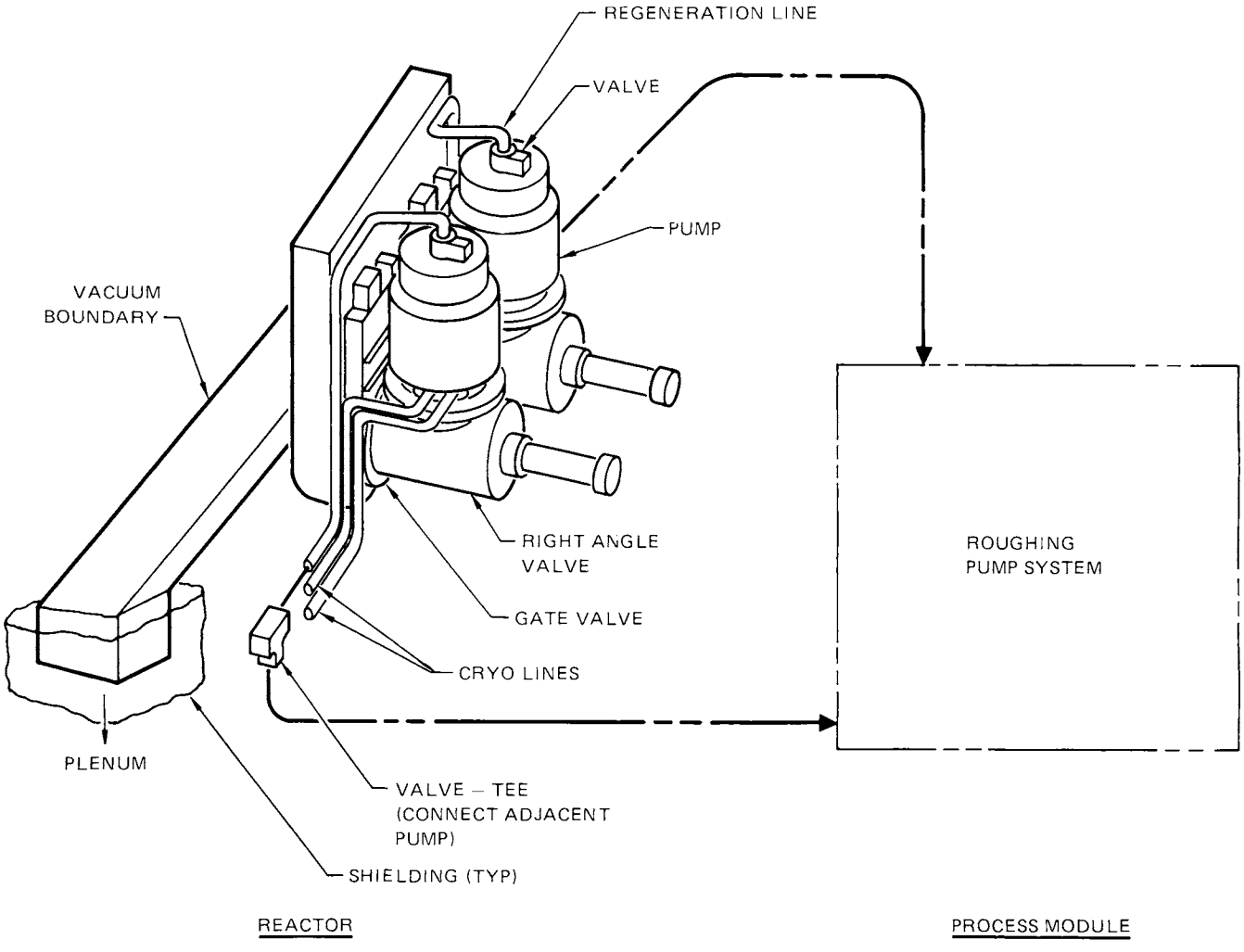

Figure 8-36. Vacuum duct and pump configuration.

Turbomolecular pumps have many desirable characteristics but were not chosen for the following reasons. It is not clear that turbomolecular pumps can be built as large as needed for STARFIRE. Large turbomolecular pumps must be mounted vertically, which may present design problems. Finally, the high rotating speeds and critical dimensions involved in their operation make their reliability appear questionable.

The STARFIRE cryopump configuration is shown in Fig. 8-37. It is a compound cryopump with cryocondensation and cryosorption elements operating at 4.2 K. The cryocondensation element will pump D_2 and T_2 and most impurity gases. This element also provides an optically tight shield for the cryosorption surface so that only noncondensable gases such as helium are pumped by the

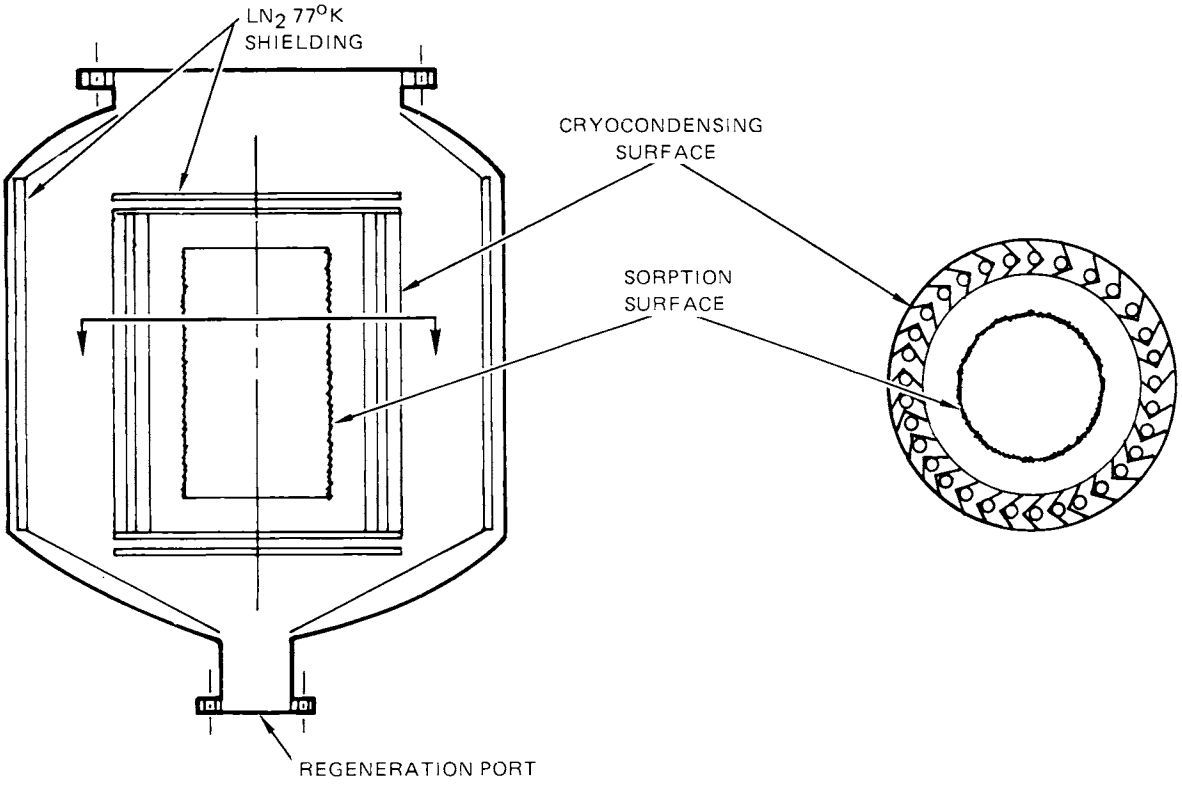

Figure 8-37. Section view of liquid helium cryopump.

adsorbent, ensuring optimum pumping performance. The cryosorption surface is designed so that high helium pumping speeds can be maintained for the 2-h operating interval between regeneration periods. At a helium generation rate of 1×10^{-4} std m^3/s, 0.72 std m^3 of helium will be pumped during 2 h of operation. Each of the 24 pumps must then have a capacity of 0.3 std m^3. Previous studies indicate that ~400 g of Mole Sieve 5A distributed over a 0.3-m^2 cryogenic (4.2 K) surface will suffice. The cryosorption surface shown in Fig. 8-37 has 3700 g of Mole Sieve 5A distributed over 2.7 m^2. Molecular sieve, a zeolite, was chosen over charcoal as the adsorbent. Charcoal would react with tritium producing tritiated hydrocarbons, thus complicating the fuel processing system.

The metal structure of the cryogenic surfaces must be designed so that maximum thermal performance can be achieved with minimal material thickness. Material thicknesses must be minimized to reduce the effects of neutron heating and to allow rapid thermal cycling during regeneration of the pumping surfaces. The vacuum system dimensions and the key performance parameters for the reference design are shown in Table 8-5.

As is noted above, the limiter/vacuum system preferentially removes helium ash and therefore a high-tritium fractional burnup is attained. The result is that the gas loads are rather low. (The total gas load is only 18.7 Pa m^3/s, and therefore the vacuum pump capacity requirements are relaxed.) It is desirable to minimize pump regeneration cycles for another reason, namely, to minimize tritium inventories in the vacuum pumps. As is shown in Table 8-5, with the 42% fractional burnup and a 2-h regeneration cycle, the maximum amount of tritium in a vacuum pump is only 2.6 g. This translates to less than 0.02 std m^3 of DT gas per pump. A vacuum pump failure resulting in the total release of the maximum DT inventory of one pump would result in a DT pressure in the plenum of less than 2 Pa. Therefore, a separate surge tank for each vacuum pump is not required. It is noted that minimization of the regeneration time has significant implications upon valve lifetime as discussed below. The composition of the plasma exhaust is shown in Table 8-26. The compound cryopump has different chevrons and pumping surfaces which could, in principle, achieve a high degree of chemical separation. The first elements encountered by particles entering the pump are the liquid nitrogen chevrons. These should remove a high percentage of the condensable impurities. The cryocondensation surfaces pump the hydrogenic species plus some of the more volatile species. The cryosorption surface is designed to pump helium gas. However, while achieving chemical separation at the pump and separate regeneration of each stage would simplify fuel purification, it would require placing movable valves or conductance limiters between each stage. Experience at TSTA has shown that careful temperature control is required to maintain chemical separation during the regeneration process. This can be very time consuming and affect the 2-h regeneration cycle. For these reasons it is assumed that the species are not regenerated separately.

Another question that is of some concern is that of the effects of particulate debris. In the reference design, the first wall is coated with beryllium. Wall erosion processes result in sputtered beryllium atoms. These beryllium atoms have a very high sticking probability and are most likely deposited on the limiter. The structural materials for the first wall and limiter are stainless steel and tantalum, respectively. It may be possible that particulates of these species (which have gamma-emitting activated products) could pass through the plenum and vacuum ducts to the pumps. It is not possible to place a filter in front of the inlet to the compound cryopumps because this would cause unacceptable conductance losses. However, a filter or trap could be placed between the outlet of the cryopumps and the regeneration pumps.

Table 8-26. Plasma Exhaust Composition

Chemical Element	g/d	at-%	Principal Molecular Species
D	503	29	DT, D_2
T	760	29	DT, T_2
He	712	41	He
H	10	1	HD, HT
I	∿50	0.1	(HDT)I
O	∿10	0.1	$(HDT)_2O$, O_2
N	∿10	0.1	$N(HDT)_3$, N_2, NO_x
C	∿10	0.1	$C_2(HDT)_2$, $C(HDT)_4$, CO_x
(P, S, Be, Al)	?	?	MH_x, MD_x, M
(Be, SS, Ta)	?	?	Particulates

The regeneration pumps are required to pump the cryopump gas at ∿0.01 Pa and pressurize it to ∿1 kPa. These pumps should be oil free. Various kinds of pumps which could be used for this purpose are discussed in Sec. 8.5.3.1. The outlet from the regeneration pumps is pressurized to ∿10^5 Pa (1 atm) by metal bellows pumps staged in series and the gas is transferred to the tritium facility for processing.

8.5.3.3 Valves

The valve configuration for each cryopump will consist of a gate valve in series with a right-angle valve as shown in Fig. 8-38. Both valves will be of all metal construction and ∿1.2-m diameter. The function of the right-angle valve will be to isolate the cryopump from the operating system during the regeneration period (every 2 h). The gate valve will be cycled only when it is necessary to repair or maintain the right-angle valve. Such a scheme will minimize valve maintenance requirements. Polymide or metal seals will be employed on the valves. It is necessary to maximize valve cycle life in order to minimize the periods between cryopump regeneration and thus the tritium inventory. Effects of pump regeneration times on tritium inventory are discussed in Chap. 14.

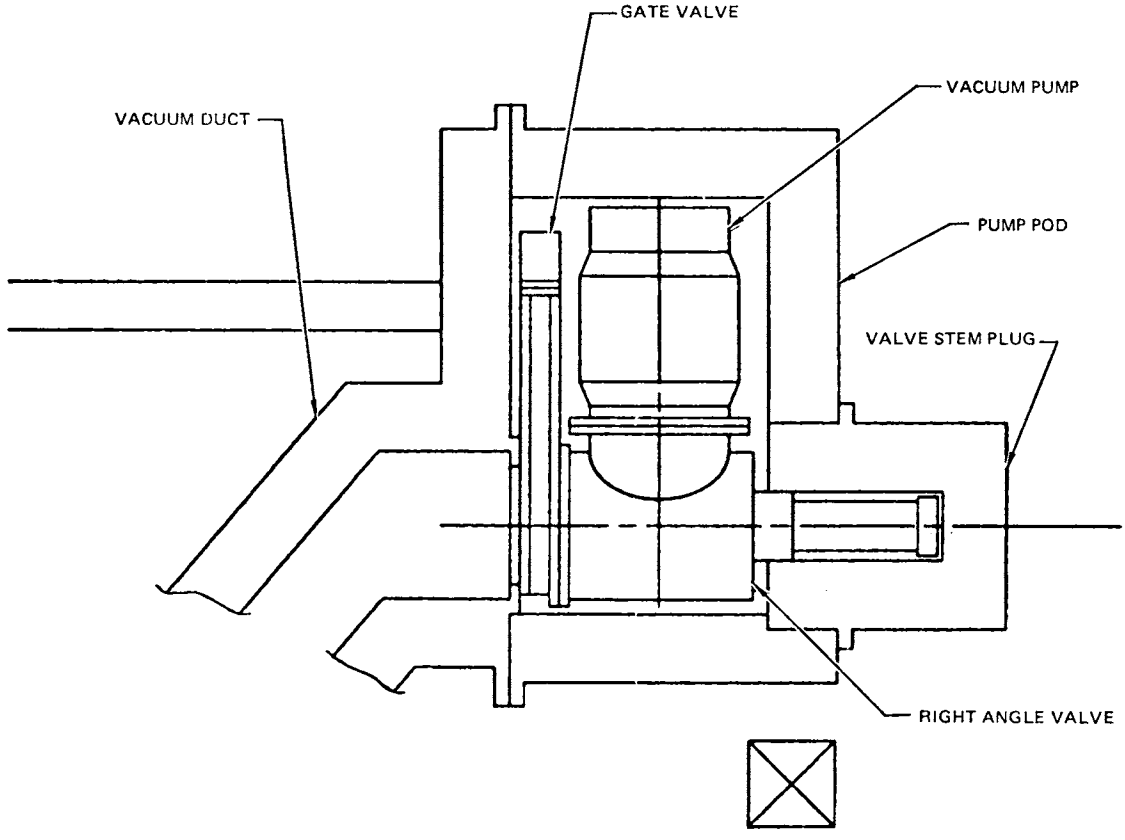

Figure 8-38. STARFIRE cryopump confiugration.

A right-angle valve was selected as the primary regeneration valve because such valves are capable of achieving a higher number of cycles between failures than gate valves. A gate valve was selected as the secondary valve to keep the connecting duct length short (and vacuum conductance high) and because it will be cycled very infrequently. Its anticipated cycle life of a few hundred cycles will probably make it maintenance free for the life of the plant. Presently, large all-metal, right-angle valves have a seal life of about 500 cycles. The seal is considered to have failed when the leak rate through the valve is 1×10^{-10} Pa m^3/s. Since the total continuous gas load during operation will be about 30 Pa m^3/s, it is obvious that a valve leak rate of even 0.1 Pa m^3/s would not affect plasma operation and could be tolerated. Furthermore, the pressure in the cryopump will be below 130 Pa for all but a few seconds, significantly reducing the pressure difference across the valve and thus the leak rate. Based on these considerations a valve life of 8000 cycles was selected. This will permit a regeneration cycle of once every 2 h and a valve seal life of 2 yr.

References

1. V. A. Vershkov and S. V. Mirnov, Nucl. Fusion 14, 383 (1974).

2. W. Bieger, et al., Proc. Intern. Symp. on Plasma Wall Interaction (Pergamon Press, Oxford, 1977), p. 609.

3. J. F. Schivell, Princeton Plasma Physics Laboratory, PPPL-1342 (1977).

4. J. N. Brooks, Proc. 3rd ANS Top. Mtg. on the Technology of Controlled Nuclear Fusion, CONF-780508-2 (1978), p. 873.

5. J. A. Schmidt, TFTR Physics Group, Report No. 11 (1979).

6. R. W. Conn, et al., Proc. IEEE Symp. on Engineering Problems of Fusion Research, IEEE Pub. No. 79CH1441-5-NPS (1979), p. 568.

7. G. M. McCracken, et al., Princeton Plasma Physics Laboratory, PPPL-1569 (1979).

8. S. K. Erents and G. M. McCracken, Proc. 4th Intern. Conf. on Plasma Surface Interactions in Controlled Fusion Devices, Garmisch, FRG (1980), J. Nucl. Mater., to be issued.

9. A. M. Razdow, Proc. USDOE Workshop on Hydrogen Recycling, CONF-791057 (1979).

10. R. E. Waltz and K. H. Burrell, Nucl. Fusion 17, 5 (1977).

11. K. Audenaerde, G. A. Emmert and M. Gordinier, University of Wisconsin, UWFDM-273.

12. M. R. Gordinier and R. W. Conn, University of California-Los Angeles, UCLA Rep. PPG-478 (1980).

13. J. M. Ogden, et al., Princeton Plasma Physics Laboratory, PPPL-1608 (1980).

14. K. Bol, et al. (PLT Group), Proc. 7th Conf. on Plasma Physics and Controlled Nuclear Fusion Research, Innsbruck, IAEA Pub. 495 (1978), p. 11.

15. INTOR Group, "Preliminary Copy of Final Report (1979).

16. J. N. Brooks, Proc. 4th Intern. Conf. on Plasma Surface Interactions in Controlled Fusion Devices, Garmisch, FRG (1980), J. Nucl. Mater., to be issued.

17. P. F. Harbour and M. F. A. Harrison, J. Nucl. Mater. 76 & 77, 513 (1978).

18. G. Fuchs and A. Nicolai, ibid., 573.

19. N. R. Wheten, Methods of Experimental Chemistry (Academic Press, 1963).

20. DIVA Group, Nucl. Fusion 18, 9 (1978).

21. R. Jacobsen, Princeton Plasma Physics Laboratory, Personal Communication (1979).

22. ALCATOR Group, Proc. 8th Intern. Conf. on Plasma Physics and Controlled Nuclear Fusion Research, Brussels, Belgium, July 1-10, 1980, to be issued.

23. Y. Seki, et al., Japan Atomic Energy Research Institute Memo NO. 8506 (1979).

24. W. M. Stacey, Jr., et al., Argonne National Laboratory, ANL/CTR-76-3 (1976).

25. W. M. Stacey, Jr., et al., ANL/FPP-TM-91 (1977).

26. General Atomic Co., GA-A14000 (1976) and GA-A13534 (1975).

27. "Oak Ridge Tokamak Experimental Power Reactor Study," ORNL/TM-5572 through ORNL/TM-5577 (1976); and M. Roberts and E. S. Bettis, ORNL/TM-5042 (1975).

28. S. Suckewer, Proc. Workshop on New Diagnostics Related to Impurity Release, Germantown, Md., CONF-79-05-85 (1979).

29. J. Norem, Proc. 4th Intern. Conf. on Plasma Surface Interactions in Controlled Fusion Devices, Garmisch, FRG (1980), J. Nucl. Mater., to be issued.

30. N. Q. Lam, G. K. Leaf and H. Wiedersich, J. Nucl. Mater., 88, 289 (1980).

31. D. L. Smith, J. Nucl. Mater. 75, 20 (1978).

32. D. L. Smith, Proc. Workshop on Sputtering Caused by Plasma Surface Interactions, CONF-79-07-75 (1979).

33. P. O. Benham and R. Hoyle, Thermal Stress (Pittman and Sons, Ltd., London, 1964).

34. F. W. Wiffen, Nucl. Metallurgy 18, 176 (1973).

35. J. M. Steichen, J. Nucl. Mater. 60, 13 (1976).

36. J. W. Davis and D. L. Smith, J. Nucl. Mater. 85 & 86, 71 (1979).

37. P. W. Taubenblat, W. R. Opie and Y. T. Hsu, Metals Engineering Quarterly 12, 41 (1972).

38. T. C. Tietz and J. W. Wilson, Behavior and Properties of Refractory Metals (Stanford University Press, Stanford, 1965).

39. D. J. DePaul, ed., Corrosion and Wear Handbook for Water-Cooled Reactors, TID-7006 (1957).

40. W. C. Berry, Energie Nucl. 4, 204 (1962).

41. W. K. Boyd, "The Use of Titanium, Zirconium, Tantalum, and Columbium in Chemical Environments," in Process Industries Corrosion (National Association of Corrosion Engineers, Houston, Texas, 1975), p. 207.

42. C. R. Breden, et al., Argonne National Laboratory, ANL-4519 (1951).

43. Metals Handbook, 9th Ed., Vol. 2 (American Society for Metals, Metals Park, Ohio, 1979).

44. T. Schober and A. Carl, Scripta Met., 397 (1977).

45. J. A. Pryde and J. S. T. Tsong, Trans. Faraday Soc., 65, 2766 (1969).

46. K. Natesan and D. L. Smith, Nucl. Technol. 22, 138 (1974).

47. C. Veleckis and R. K. Edwards, J. Phys. Chem. 73, 683 (1969).

48. M. Schussler, Corrosion Data Survey on Tantalum (Fansteel, Inc., 1972).

49. M. Gomolinski and G. Bubee, J. Nucl. Mater. 43, 59 (1972).

50. D. E. Mazey and F. Menzinger, J. Nucl. Mater. 48, 15 (1973).

51. L. J. Pivnke and J. W. Davis, McDonnell Douglas Astronautics Co., COO-4247-2 (1979).

52. R. E. Gold, et al., Westinghouse Electric Corp., COO-4540-1, Vol. 2 (1978).

53. J. F. Bates and A. L. Pitner, Nucl. Technol. 16, 406 (1972).

54. B. A. Loomis, Argonne National Laboratory, Personal Communication (1980).

55. J. Roth, et al., "Data on Low Energy Light Ion Sputtering, Max-Planck-Institut fur Plasmaphysik, IPP 9/26 (1979).

56. M. Balooch and D. R. Olander, J. Chem. Phys., 63, 4772 (1975).

57. F. B. Behrisch, et al., J. Nucl. Mater. 60, 321 (1976).

58. J. Roth, et al., J. Nucl. Mater. 63, 222 (1976).

59. N. P. Busharov, et al., J. Nucl. Mater. 230 (1976).

60. B. Feinberg and R. S. Post, J. Vac. Sci. Technol. 13, 443 (1976).

61. G. L. Kulcinski, University of Wisconsin, Personal Communication on INTOR Study (1980).

62. P. Trester, Proc. Workshop on Plasma-Materials Development, Albuquerque, New Mexico, June 24-25, 1980, to be issued.

63. S. K. Das and M. Kaminsky, Proc. 6th Symp. Engineering Problems of Fusion Research, IEEE Pub. No. 75CH1097-5-NPS (1975), p. 1151.

64. J. W. Dunmur, "Plasma-Sprayed Beryllium," in Beryllium Science and Technology, Vol. 2., D. R. Floyd and J. N. Lowe, eds. (Plenum Press, New York, 1979), p. 135.

65. M. M. El-Waki, Nuclear Heat Transport (International Text Book Co., 1971).

66. W. H. McAdams, Heat Transmission (McGraw-Hill Book Co., Inc. 1954).

67. L. S. Tong and J. Weisman, Thermal Analysis of Pressurized Water Reactors (American Nuclear Society, 1970).

68. ASME Boiler and Pressure Vessel Code, 1977 Code Cases - Nuclear Components, Case N-47 (ASME, 1977), pp. 1592-1610.

69. D. Burgren, Design Methods for Power Plant Structures (C. P. Press, Jamaica, New York, 1975).

70. H. Kraus, Foundations of the Theory of Thin Elastic Shells (J. Wiley & Sons, Inc., New York, 1967), p. 137.

71. B. A. Boley and J. H. Weiner, Theory of Thermal Stresses (J. Wiley & Sons, Inc., New York, 1960).

72. S. Timoshenko and S. Woinowski-Krieger, Theory of Plates and Shells (McGraw-Hill Book Co., Inc. New York, 1959), p. 87.

73. S. Timoshenko and G. H. MacCullough, Elements of Strength of Materials (D. Van Nostrand Co., Inc., 1956), p. 265.

74. L. Turner, IEEE Trans. Mag., MAG-13, 119 (1978).

75. "UWMAK-III, A Noncircular Tokamak Power Reactor Design," University of Wisconsin, UWFDM-150 (1976).

76. T. Yang, et al., "Reactor Application of an Improved Bundle Divertor," Westinghouse Electric Corp., WFPS-TME-104 (1978).

77. T. F. Yang, et al., "A Compact Poloidal Divertor Reference Design for TNS," Westinghouse Electric Corp., WFPS-TME-055 (1977).

78. M. Abdou, "Problems of Fusion Reactor Shielding," Georgia Institute of Technology, GTFR-10 (1979).

79. M. Abdou, et al., "An Assessment of Radiation Shielding and Personnel Access," in Report on U.S. Contributions to the International Tokamak Reactor Workshop on INTOR (1979).

80. Y. Gohar, C. W. Maynard and E. Cheng, Proc. 2nd Top. Mtg. on The Technology of Controlled Nuclear Fusion, CONF-760935-P3 (1976).

81. R. W. Conn, I. N. Sviatoslavsky and D. K. Sze, Proc. 8th Symp. on Engineering Problems of Fusion Research, IEEE Pub. 79CH1441-5-NPS (1979), p. 568.

82. A. Guthrie and R. K. Wakerling, eds., Vacuum Equipment and Techniques (McGraw-Hill Book Co., Inc., New York, 1949).

83. D. J. Santeler, D. H. Holkeboer, D. W. Jones and F. Pagano, "Vacuum Technology and Space Simulation," NASA-SP-105 (1966).

84. T. S. Chou and H. J. Holama, J. Vac. Sci. Technol. 16, 81 (1979).

85. D. O. Coffin and C. R. Walthers, Proc. 8th Symp. on Engineering Problems of Fusion Research, IEEE Pub. 79CH1441-5-NPS (1979), p. 513.

86. P. W. Fisher and J. S. Watson, J. Vac. Sci. Technol. 16, 75 (1979).

Table of Contents

List of Figures

List of Figures (Cont'd)

List of Tables

9.1 INTRODUCTION

The magnet systems of the reactor provide confinement, equilibrium, shaping, current initiation, and stabilization to the plasma. Physically, the magnets are among the largest components of the reactor. They experience large forces, which must be resisted with structural material in a manner which minimizes heat conduction to the magnets operating at liquid helium temperature. Most importantly, they must be extremely reliable, as a magnet replacement is a laborious and time-consuming process.

The magnets must be superconducting, except for a few control coils carrying relatively low current; otherwise they would consume unacceptable amounts of power. There are four primary areas in which these superconducting magnets represent an extrapolation beyond existing technology: 1. the large size of the magnets, with accompanying large forces and stored energy; 2. a reliable Nb_3Sn conductor, produced in large quantities; 3. a pulsed cryostable magnet with acceptably low ac losses; and 4. operation of a superconducting magnet for years in a radiation environment. It is envisioned, however, that these extrapolations can be carried out in a straightforward way from present superconducting magnet technology, and that no technological breakthroughs are required.

The superconducting magnets, both toroidal field (TF) coils and poloidal field (PF) coils, have been designed with a cabled conductor consisting of copper stabilizer and NbTi superconductor, except for the inner turns of the TF coils, where field requirements in excess of 9 T have led to the choice of Nb_3Sn superconductor.

In both the TF and PF coils, each cable conductor is contained in its own structure, which bears against the structure of neighboring conductors to transmit radial and axial forces. All coils are bath-cooled by pool boiling liquid helium at 4.2 K. The structure around the conductor contains transverse and longitudinal channels, to carry liquid helium to where cooling is needed and to carry helium vapor away.

The safety of the public, the operating personnel, and the reactor itself, as well as reliable operation, have weighed heavily in the design choices that have been made.

Within this chapter, the TF coils are described in Sec. 9.2, the equilibrium field coils and ohmic heating coils in Sec. 9.3, and the copper, normal-conducting, correction field coils in Sec. 9.4. Safety considerations not treated explicitly in those three sections are described in Sec. 9.5.

9.2 TOROIDAL FIELD COIL SYSTEM

9.2.1 Introduction

The superconducting toroidal field (TF) coil system for STARFIRE, despite its impressive size, and stored energy, is a logical, straightforward extension of present superconducting magnet technology. Thus, the primary challenge of the STARFIRE TF coils comes not from developmental technology, but rather from the application of sound engineering judgment to insure a harmonious synthesis of operational reliability, reactor compatibility, and minimum overall cost. The TF coil system could, of course, benefit significantly from future technological developments, such as low activation, higher strength structural materials, improved superconductors, better insulators, or innovative design features.

Comparison of the STARFIRE TF coils with those presently envisioned for the Engineering Test Facility (ETF)[1] shows that much of the development needed for the STARFIRE coils will have been carried out for the successful construction of ETF.

	ETF	STARFIRE
Peak field (tesla)	11.4	11.1
Stored energy (GJ)	38	50
Mean radius of coil outer leg (m)	11.3	13

A summary of basic STARFIRE TF coil system parameters is presented in Table 9-1.

9.2.1.1 Design Constraints

The constraints to which the toroidal field coils have been designed are presented here under two generic headings: Geometrical Constraints and Functional Constraints.

Geometrical Constraints--The geometrical constraints are set by machine size requirements, and spatial demands for other reactor components within

Table 9-1. STARFIRE Toroidal Field Coils Basic Parameters

Number of Coils	12
Total Ampere Turns	2×10^8
Total Stored Energy	50 GJ
Total Inductance	174 H
Peak Field	11.1 T
Current	24 kA
Total Weight (12 Magnets)	6×10^6 kg
Coil Straight Section Height	8 m
Mean Radius of Outer Coil Leg	13 m
Conductor:	
Superconductor	Nb_3Sn/NbTi
Stabilizer	Copper
Configuration	Cable
Coil Cooling	ℓHe Bath, 4.2 K
Structural Material	Austenitic, Stainless Steel

and around the toroidal field coil envelope. The vacuum tank outer radius of 3.8 m in the centerpost region is set by the plasma chamber dimensions and requisite inboard blanket and shield thickness (the shield requirement being set largely by the maximum allowable lifetime neutron fluence to the coil conductor and insulator components). A further radial allowance for vacuum tank wall, vacuum space, liquid nitrogen shield, and the helium vessel leads to a peak field radius of 3.66 m. This sets the peak field of 11.1 tesla and ampere turn requirement of 203×10^6. The 13 m outer leg mean equatorial radius is set by internal space demands versus the desire to minimize the overall reactor size.

The corresponding number of coils, 12, has been selected based upon maximum allowable field ripple (± 1.14% at the plasma edge) and intercoil access considerations (blanket sectors).

In summary, the basic geometrical constraints are:

- Number of TF coils 12
- Centerpost outer radius of TF coil vacuum tank 3.8 m
- Mean radius of TF coil outer leg at equator 13.0 m

Functional Constraints

- Peak Toroidal Field: The peak field requirement of 11.1 tesla is set by the need for 5.8 tesla at the 7.0 m plasma axis and the maximum permissible radius of the coil in the centerpost region, as described above.
- Maximum Allowable Field Ripple at Plasma: The calculated value for a 12 coil array of the indicated imposed dimensions is ± 1.14% which is compatible with physics requirements. The corresponding ripple at the plasma axis is ± 0.06%.
- Coils Must Accommodate Plasma Neutron Heat Flux and Normal Operational ac Heat Loads Without Jeopardizing Stability: The lifetime fluence shielding requirements for the TF coil centerpost region materials (copper, insulation) result in a very modest heat flux. Since STARFIRE operates in a steady state mode, the operating ac loads are negligible.
- Coils Must Absorb Plasma Disruption Without Going Normal: This is a significant concern for STARFIRE due to the external location of the EF coil system. It is discussed in Sec. 9.2.9.
- Coils Must be Cryogenically Stabilized Against a "Maximum Credible" Normal Operating Disturbance: The only such disturbance is local transient mechanical motion of a conductor in response to the magnetic field loads. This condition is discussed in Sec. 9.2.4.
- Coils Must Meet All Above Requirements Following Exposure to the Design Lifetime Neutron Plasma Fluence: This requirement is discussed in Sec. 9.2.4.
- Coils Must Meet the Above Requirements Without Replacement of Major Components Throughout the Design Reactor Lifetime.
- TF Coil System Must Survive All Perceived Credible Accident Conditions Without Endangering Personnel or Causing Unacceptable

Damage to Other Reactor Components: This requirement includes such mishaps as a severed coil circuit, resulting in arcing and unequal coil currents. This situation is discussed in Sec. 9.5.2.

The following quantified parameters are associated with the above functional constraints:

Centerpost plasma neutron heatload: 0.5 kW

Total lifetime insulator dose (maximum): 5×10^9 rad

Operating poloidal field experienced:

$B_{||}$ and $B_{\perp} \sim 0.5$ tesla average

Plasma disruption field experienced:

B = 0.7 tesla in 0.5 s

Conductor stability criterion:

100 mJ/cm^3 over 1 meter

Peak design dump voltage: 2.5 kV

9.2.1.2 Design Considerations

Basically, all of the TF coil design considerations fall into five closely interrelated generic categories: performance, reliability, reactor compatibility, cost, and safety. All of these factors underlie the identification of key issues and other basic design considerations discussed below, and the resultant selected design features.

Key Issues -- The key specific issues confronted in design of the STARFIRE toroidal field coils are the following:

- Accommodation of the eddy current heat loads induced in the coil/helium vessel structure by a plasma disruption
- Support of the coils against the out-of-plane (overturning) loads generated by interaction of their current with the fringing field of the externally located equilibrium field (EF) coils
- Verification of a coil's ability to sustain a low liquid level induced quench without damage, based upon a selected protection scheme

- Ease and location of manufacture
- Minimization of shutdown and end of life radioactivity

Other Basic Design Considerations -- In addition to the above key issues, several other important aspects of the TF coil design were addressed in depth:

- Selection of appropriate superconductor material
- Coil cooling method
- Selection of an appropriate conductor/support configuration
- Coil materials integrity versus total neutron fluence
- Coil influence on overall reactor cost
- Maintainability

9.2.2 TF Coil Design

Figure 9-1 is an elevation section of STARFIRE, showing one toroidal field coil, and associated reactor elements. The TF coils bear radially inward against the centerpost support cylinder, within whose bore are located the OH coils and the inner EF coils. All of these elements share a common vacuum volume. The centerpost region is surrounded by a common vacuum tank section, while each TF coil outer region is housed within its own vacuum tank section.

Table 9-2 is a summary of selected TF coil features, while Table 9-3 lists the basic calculated parameters of this system. Figure 9-2 depicts the basic dimensions of one constant tension TF coil.

9.2.3 Conductor

The 24 kA conductor is a three level, unsoldered, uninsulated "Rutherford cable", whose general structure is depicted in Fig. 9-3. The conductor consists of sixteen 1500 ampere cables, each of which is a six-around-one bundle of similarly configured subcables.

A three-level uninsulated, unsoldered cable design was selected, in lieu of a monolithic or soldered cable design, for the following reasons:

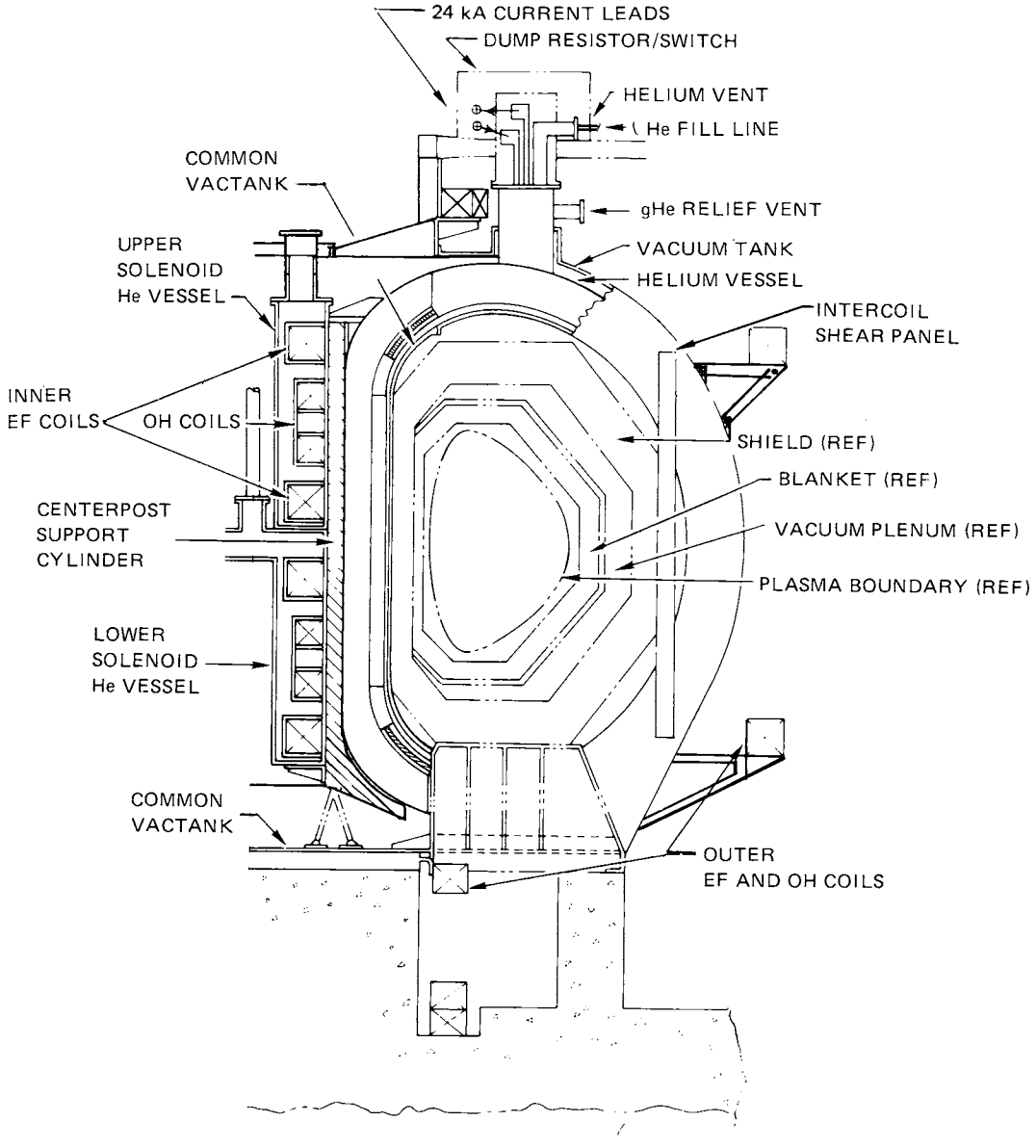

Figure 9-1. Toroidal field coil elevation showing related reactor elements.

Table 9-2. Summary of Selected Features of TF Magnets

- CONDUCTOR
  - Superconductor Material:
    - High Field (9-11 T) Region: Nb_3Sn
    - All Other Coil Regions: NbTi
  - Stabilizer:
    - Material: Copper, RRR = 150:1 (minimum)
    - Maximum Current Density: 6 kA/cm^3 (coil protection limit)
  - Operating Current: 24 kA
  - Geometry: Rutherford cable, unsoldered, uninsulated
  - Number of Field Grades: Four (0-5 T, 5-7 T, 7-9 T, 9-11 T)
- COOLING
  - Type: Liquid helium bath
  - Operating Conditions:
    - Saturated: 4.2 K, 1 atm nominal
    - Peak Bath Temperature: 4.5 K
- COIL
  - Type: Pancake (spiral) wound
    - Bifurcated (two symmetric sections)
  - Conductor Support: Interturn stainless steel strip, plus flanking strip for bearing load support
  - Ground, Interturn and Interlayer Insulation Material:
    - Epoxy fiberglass laminate (G-10CR)
- HELIUM VESSEL
  - Material: Austenitic stainless steel (316 LN)
  - Configuration:
    - Coil cavity bifurcated
    - Trapezoidal cross section in centerpost region
    - Rectangular cross section in outer, curved region
  - Support:
    - Centering Loads: by cold centerpost
    - Support Cylinder: G-10CR Fiberglass
    - Out-of-plane Loads: G-10CR structures to vacuum tank, plus intercoil shear elements in centerpost region

Table 9-2 (Continued)

- VACUUM TANK
  - Material: Austenitic stainless steel (14 Mn-2Ni-2Cr)
  - Configuration: Common vacuum tank around coil/He vessels in centerpost regions
  - Out-of-plane Load Support: Intercoil shear panels, removable
- COIL CIRCUIT
  - Connection: All coils in series
  - Design Charging Time: 12 hours
  - Protection Circuit: Switch/dump resistor, parallel circuit between each coil
  - Dump Resistor Resistance: 0.1 Ω each

1. To minimize ac losses from the poloidal field system and plasma disruption.

2. As a conventional, modular fabrication method for producing high current conductor at reasonable cost, and with good area reduction of the composite superconducting elements.

3. For optimal cryogenic stability, by virtue of its high effective surface to area cooling characteristics.

4. For ease of coil winding by virtue of its flexibility.

5. To minimize hoop load strain (significant for Nb_3Sn).

Inherent in a cabled conductor design, particularly when employing Nb_3Sn, is its limited ability to support hoop and transverse bearing loads (the latter occurring in the centerpost region of a TF coil). Therefore, in the selected design, the conductor is sandwiched between two pretensioned stainless steel strips for hoop load support, and flanked by two bearing load support strips. Stainless steel is employed for these support elements due to its high elastic modulus and strength.

In the high field region of the STARFIRE TF coils (9 - 11 tesla), Nb_3Sn has been selected, based upon anticipated fabrication and metallurgical advances during the next two or three decades. Ten tesla is about the upper

Table 9-3. STARFIRE Toroidal-field Coils - Calculated Parameters

Total Ampere Turns	203×10^6
Total Stored Energy	50 GJ
Total Inductance	174 H
Total Weight	6×10^6 kg
Total Coil Height (less chimney and supports)	15.3 m
Centerpost Straight Section Height	8.04 m
Coil/Helium Vessel Radial Thickness is Centerpost Region	1.125 m
Field Ripple at Plasma Extremity	± 1.14%
Field Ripple at Plasma Axis	± 0.06%
Mean Perimeter of One Coil	40 m
Average Conductor Current Density	4000 A/cm^2
Average Coil/Helium Vessel Current Density in Centerpost Region	1000 A/cm^2
Plasma Disruption Heat Load to Entire Coil/ Helium Vessel Structure, Delayed EF coil decay:	
- Centerpost Region (from plasma decay)	10 MJ
- Outer Coil Region (EF coil decay)	1 MJ
Overturning Moments per TF-coil, Due to EF coils	
- Outer Coil Region	806×10^6 Nm
- Centerpost Region	678×10^6 Nm

practical limit for employment of NbTi alloys cooled with 4.2 K liquid helium at one atmosphere.

Nevertheless, Nb_3Sn is an inherently brittle compound, requiring special design and manufacturing techniques to accommodate its limited tolerance for tensile strain. Therefore an alloy of NbTi with Ta, operating at a bath temperature in the 3 K range, should be regarded as a viable alternative. In any case NbTi alloy is specified for the 0 - 9 tesla field grades.

Four conductor grades are employed, as shown in Figs. 9-4 through 9-7. Grading is based upon three centerpost region parameters: amount and type of superconductor required (as a function of magnetic field); amount of copper stabilizer required (a function of magnetoresistance, radiation degradation,

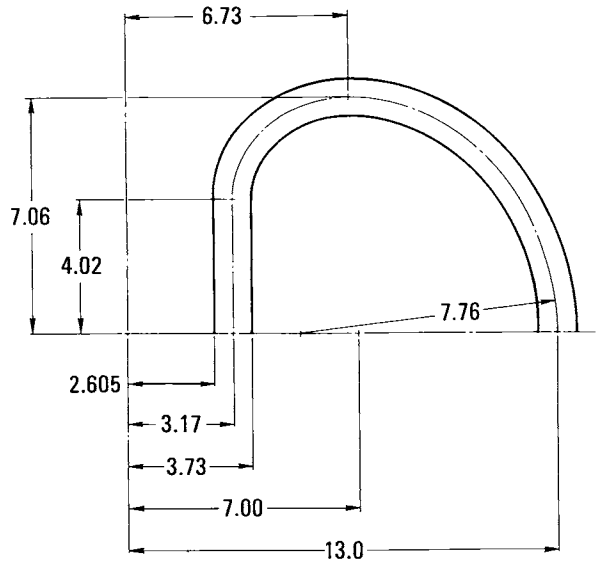

Figure 9-2. Dimensions of coil/helium vessel, constant tension shape.

cryostability and protection criterion limit); and required bearing load support (a function of cumulative radial bearing load).

Nb_3Sn is employed only in the high field (9 - 11 tesla) region. A bronze diffusion geometry is envisioned, with a tantalum barrier to shield the surrounding stabilizer material of the composite strand. The Nb is reacted with the Sn of the bronze matrix after the cabling process is complete, but before coil winding.

Note that in the high field region, six composite strands surround one copper strand to form a subcable. With each lower field grade of conductor, the number of composite strands in a subcable is reduced, the 0-5 tesla grade having a single NbTi/Cu composite strand surrounded by six copper strands.

9.2.3.1 Conductor Support Modules

The conductor is housed within a multi-component stainless steel strip support frame. Collectively, these support elements carry almost all of the hoop, radial bearing (centerpost) and circumferential bearing (outer region) loads generated within the coil. The allowable combined stress is

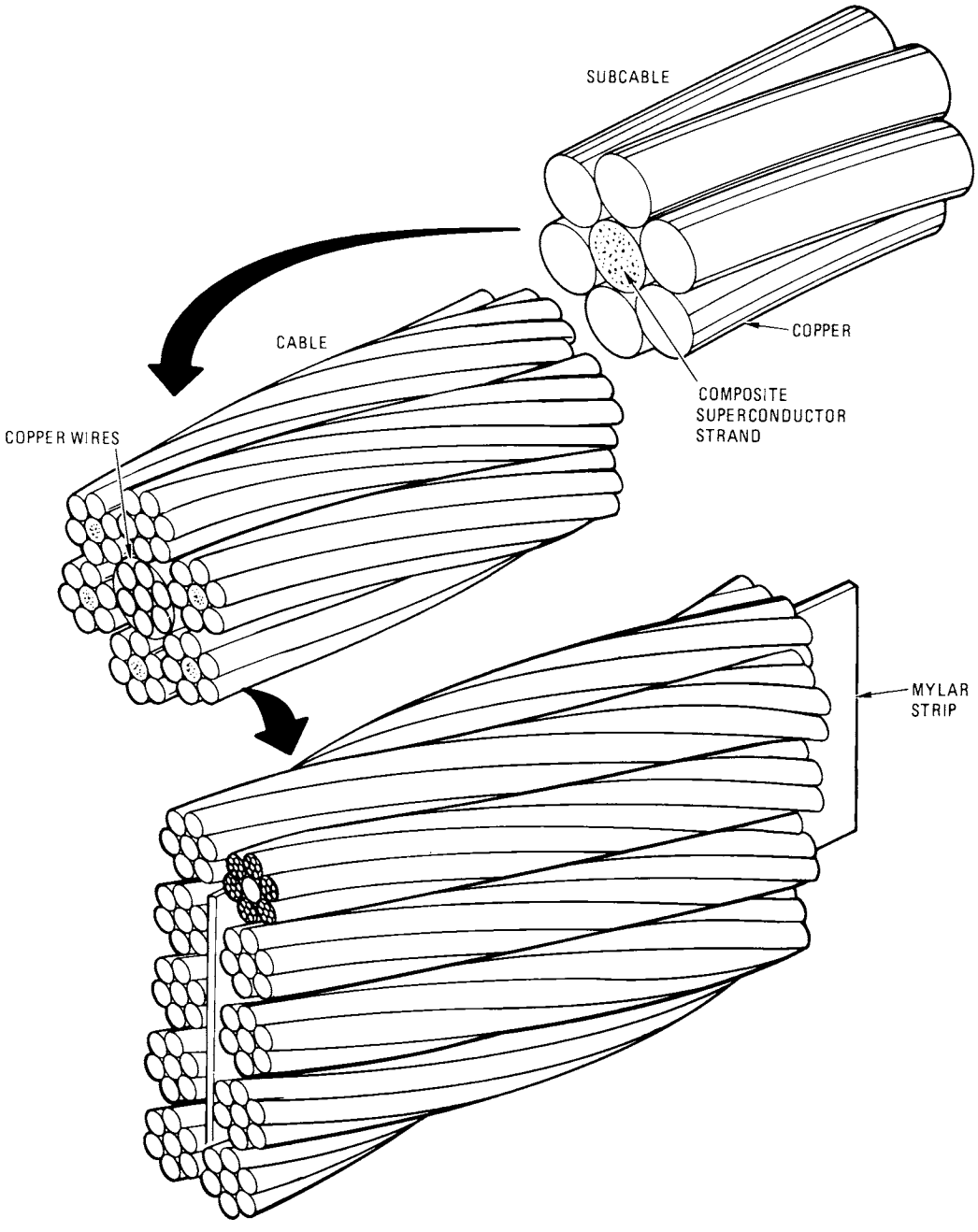

Figure 9-3. Three level cabled conductor.

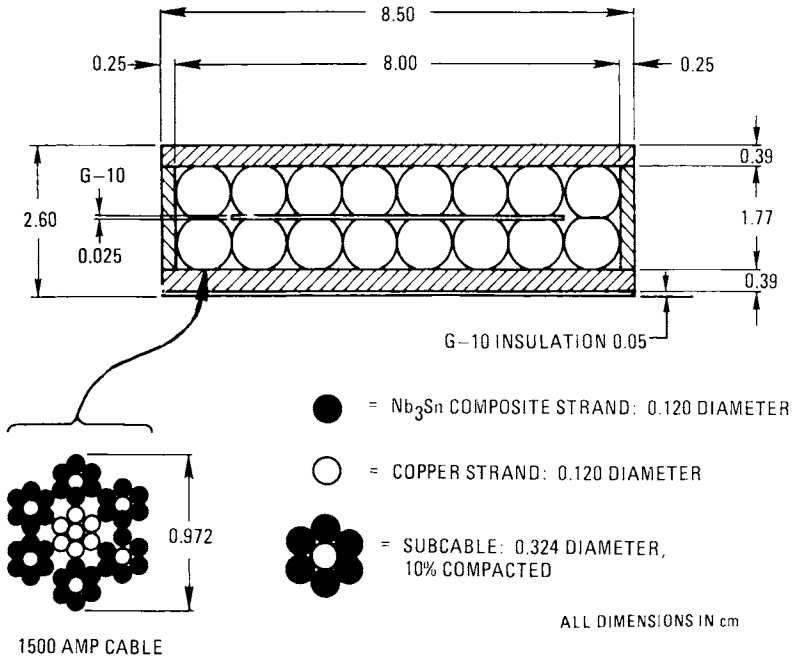

Figure 9-4. 24 kA conductor/support module, high field region (9-11 tesla).

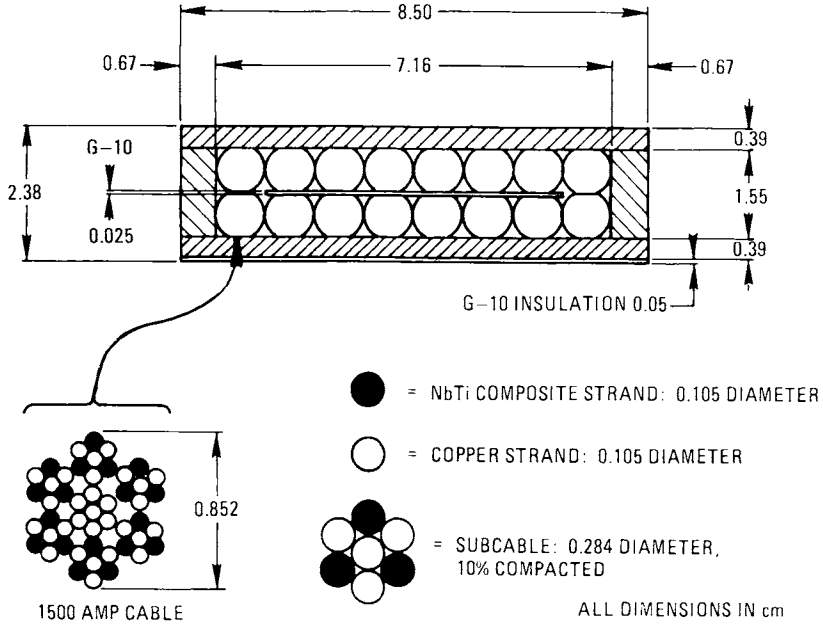

Figure 9-5. 24 kA conductor/support module, 7-9 tesla field region.

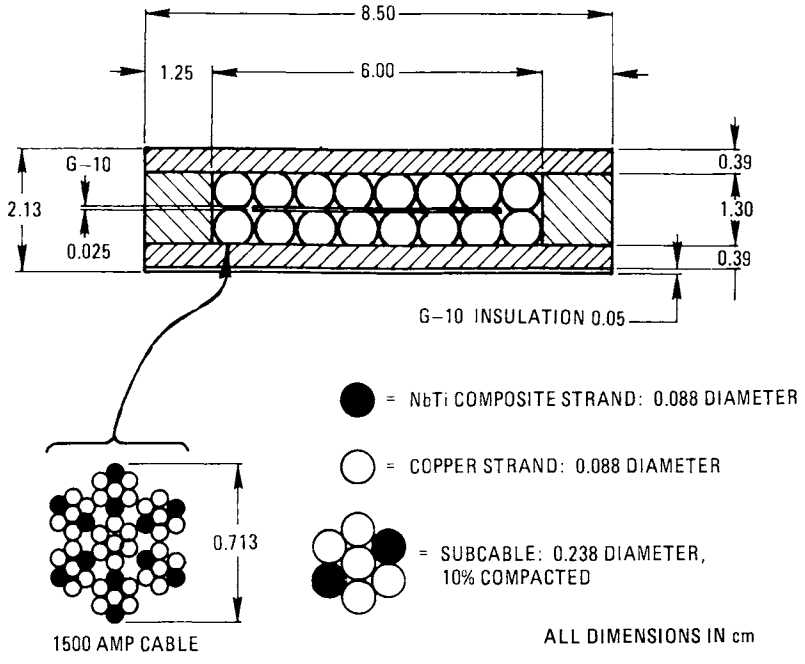

Figure 9-6. 24 kA conductor/support module, 5-7 tesla field region.

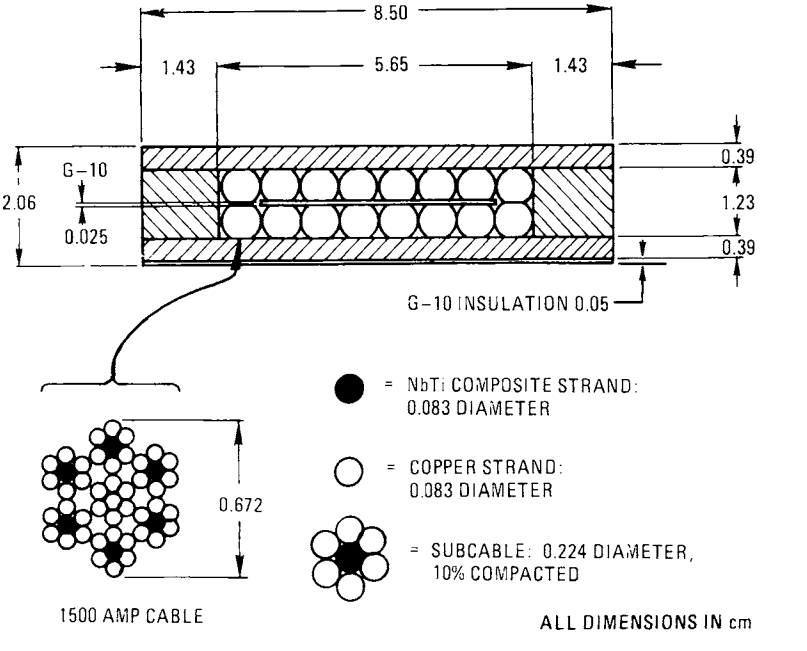

Figure 9-7. 24 kA conductor/support module, low field region (0-5 tesla).

550 MN/m^2 (80,000 psi) for 316 LN, or equivalent. The conductor and its support strips are collectively referred to as a "conductor support module" since these components are wound simultaneously. Yet in a pancake wound coil, the coil support module must be of constant width. Hence the stainless steel sidewall strips which flank the conductor in this design must become progressively thicker with diminishing centerpost radius, in order to bear the cumulative radial loads. Fortunately, in this and similar designs, the required conductor area, and hence width for a given number of cables, is diminishing proportionately.

This is emphasized in Fig. 9-8 which shows the high and low field conductor support modules together. Also indicated are the helium ventilation cutouts in the sidewall support strips.

9.2.4 Cooling and Cryostability

Bath cooling has been selected in lieu of forced flow, based upon considerations of design simplicity and operational reliability.

Forced flow cooling introduces complexities of conductor design, pumping, and parallel path manifolding which more than offset any potential benefits of improved heat transfer. In principle, forced flow cooling through simple well defined channels is well understood and is characterized by relatively high heat transfer rates (example: "hollow" monolithic conductor). However, the flow path geometries of cables or braided conductor presently under consideration for large TF coils are torturous. Proper understanding of such geometries will require considerable analytical and experimental effort. Certainly a far greater body of practical operational experience exists for bath cooling of large superconducting coils.

The possibilities of coolant path blockage or pump failure are reliability concerns for a forced flow system. Bath cooling on the other hand is inherently reliable so long as the coils remain fully immersed in liquid.

9.2.4.1 Cryogenic System

Each coil is independently immersed in liquid helium within its own stainless steel helium vessel. However, all twelve helium vessels (plus the centerpost support cylinder and solenoidal coils within its bore) share a

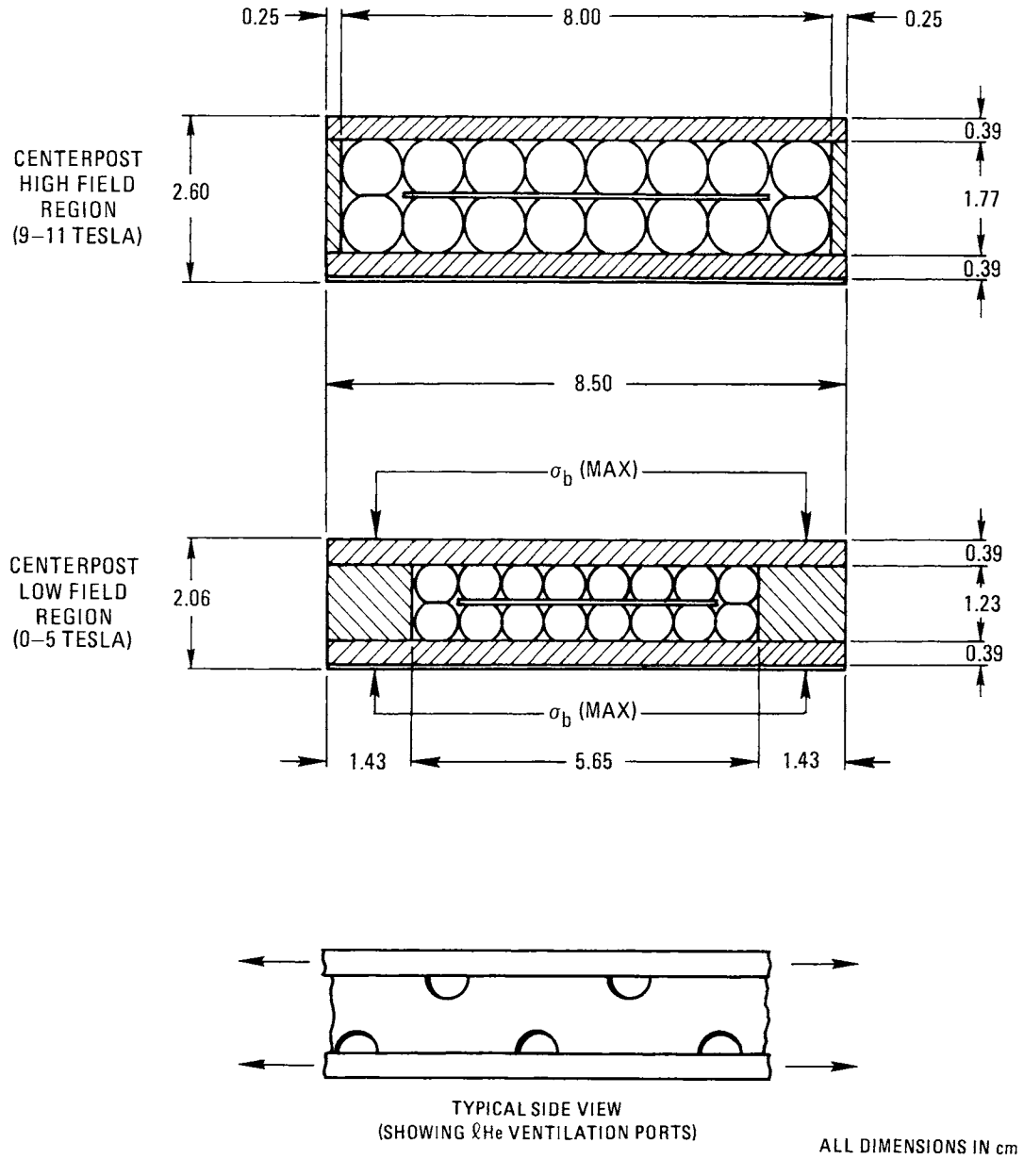

Figure 9-8. Conductor/support modules.

common vacuum volume. A locally stiffened sheet aluminum thermal radiation shield is interposed between the helium vessels and vacuum tank in both the centerpost and outer regions. This shield is cooled with liquid nitrogen convectively circulating through attached tubing. Both the helium vessels and thermal radiation shield are wrapped with multilayer aluminized mylar insulation. Collectively the helium vessels, vacuum tank, thermal radiation shield, multilayer insulation and associated plumbing comprise the TF coil cryostat.

Figure 9-9 is a detailed section of the coil and helium vessel, at the inner radius of the centerpost region. Shown here are detailed relationships of the cabled conductor support modules; interturn, interlayer and ground insulation, and the helium vessel. Despite its solid looking appearance in the centerpost cross section, 26 percent of the coil/helium vessel volume is helium. Much of this is interstitial cabled conductor space; also only about 25% of the interlayer and coil-to-ground volume is occupied by insulation material, as evidenced in Fig. 9-9.

Transverse helium migration through each conductor support module is allowed by the twist pitch of the cabled conductor and by the cutouts (or "mouseholes") in the stainless steel side strip. Vertical helium flow is allowed by the diagonal performation and radial groove pattern in the interlayer insulation, and by the diagonal, interrupted pattern of the coil-to-helium vessel (ground) insulation.

Each coil has a pair of room temperature conductor leads, in order that it can be connected to adjacent coils through a dump resistor/switch circuit. These leads are cooled by helium boil-off gas. Additional boil-off gas is removed through the helium ventline, through which the &He fill line counterflows. In addition, a gaseous helium relief vent is provided, set to open at 3.0 atm absolute pressure.

Table 9-4 shows the coil/helium vessel component fractions in the centerpost cross section.

Table 9-5 gives the component weights per coil.

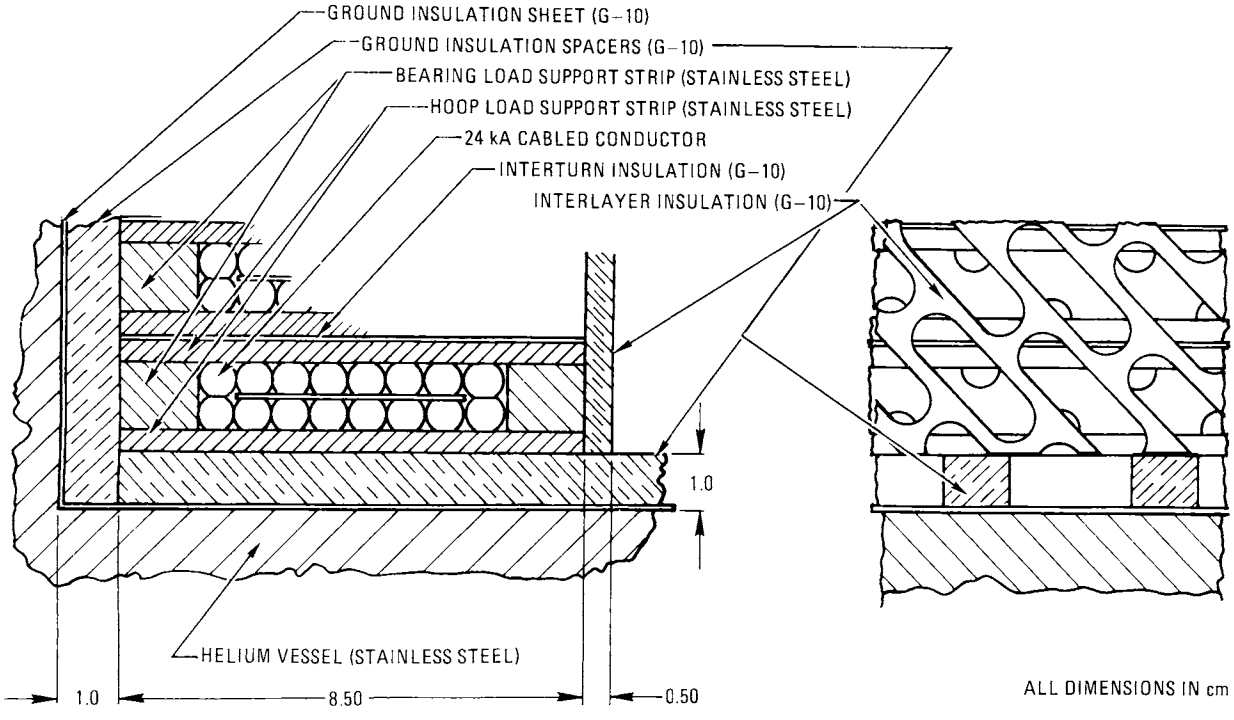

Figure 9-9. Coil detail: inner radius conductor region.

Table 9-4. Coil/Helium Vessel Component Fractions (in Centerpost Region)

	Area (cm^2) Per Coil	Fraction Percent
Conductor, Net	4,231	22.7
Support Strip	5,980	32.0
Insulation	700	3.8
Helium Vessel	2,916	15.6
Helium	4,831	25.9
	18,658	100.0

Table 9-5. Coil/Helium Vessel Component Weights Per Coil (kg)

Conductor	151,300
Support Strip	192,000
Insulation	5,100
Helium Vessel	93,700
Helium	2,400
	444,500

9.2.4.2 Cryogenic Stability of Conductor

The design criterion selected for the stability analysis is that the conductor must recover from a transient disturbance of 100 mJ/cm^3 (15 K) over a 1 meter length. The recovery of a 1500 amp cable in the high field region (9 - 11 tesla) was calculated upon the quasistatic relation:

$$A_{cu} \times C.P._{eff} < Q \left(\frac{W}{cm^2} \right) \text{limit}$$

where

the copper resistivity is given by

$$\rho_{cu} = \left(\frac{171}{150} + 0.455\ B + 3.8 \right) \times 10^{-8} = 1.10 \times 10^{-7}\ \Omega\text{-cm}$$

for a neutron fluence degradation factor of 3.8, based upon four 10-year anneal cycles and a total fluence of 5×10^9 rad (see Fig. 9-10). The effective cooled perimeter ($C.P._{eff}$) equals one-half of a circular envelope of a 1500 amp cable. The Q (limit) of 0.35 W/cm^2 is based upon the saturated liquid helium heat transfer curve shown in Fig. 9-11. These parameters yield a required copper current density of 3315 A/Cm^2 in the high field region. In the low field region (0 - 5 tesla), the cryogenic stability limit is about 6000 A/cm^2 (in the copper), which coincides with our selected coil protection limit.

9.2.4.3 TF Coil Heating Due to Plasma Disruption

For a viable commercial fusion reactor, a plasma disruption will necessarily be a relatively rare event, occurring perhaps once or twice a year. Nevertheless the inevitable eddy current heating resulting from such an event must not drive the TF coils out of the superconducting mode - that is, to quench.

This condition has been carefully analyzed, as described in Sec. 9.2.9. The results demonstrate that the selected cabled conductor absorbs relatively little of this energy. Some 10 MJ of eddy current heat is generated within the stainless steel helium vessels; fortunately even this amount can be absorbed by the liquid helium without raising the bath to the conductor critical temperature (the point at which resistive current sharing begins).

Had this bath heating proven excessive, it would have been necessary to employ other design expedients. Consideration was given for example to a relatively thick (2 - 3 cm), electrically continuous liquid nitrogen shield, particularly in the centerpost region.

9.2.5 Coil Cross Section and Support

Figure 9-12 shows cross-sections of one coil/helium vessel in both the centerpost and outer region. Figure 9-13 is an elevation section of one TF coil/cryostat, centerpost support cylinder and associated elements in the upper region. Figure 9-14 is an isometric view illustrating the transition of the helium vessel from the centerpost to outer region.

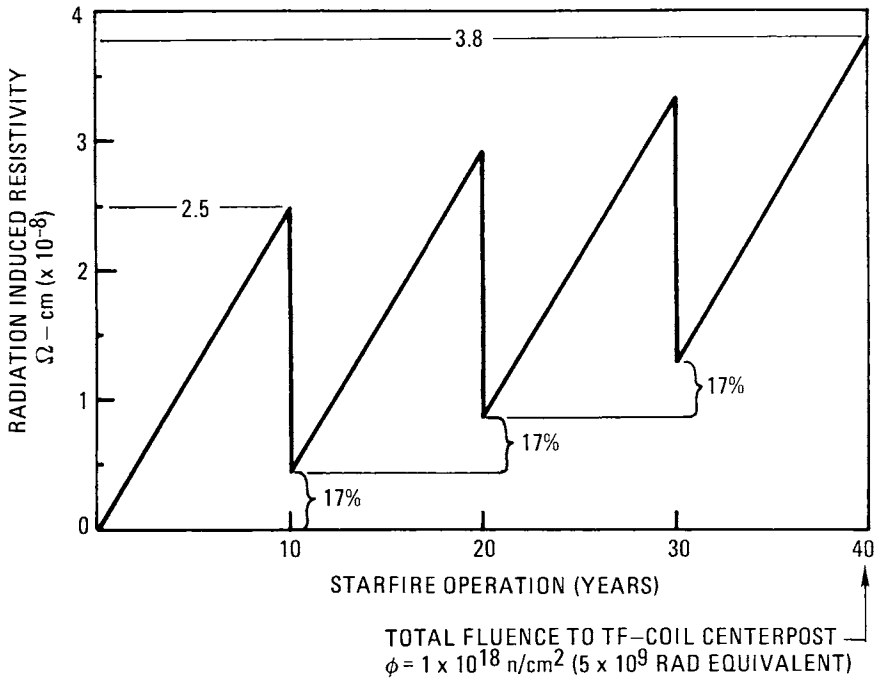

Figure 9-10. Radiation induced resistivity of copper at 4.2 K, as a function of fast neutron fluence, and anticipated 10 year room temperature anneal cycle.

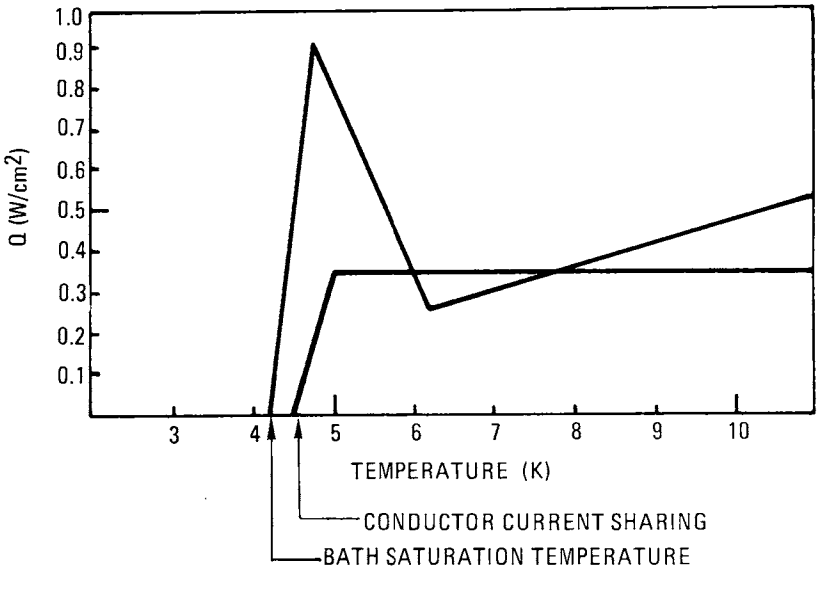

Figure 9-11. Cooling versus heat generation in conductor normal zone.

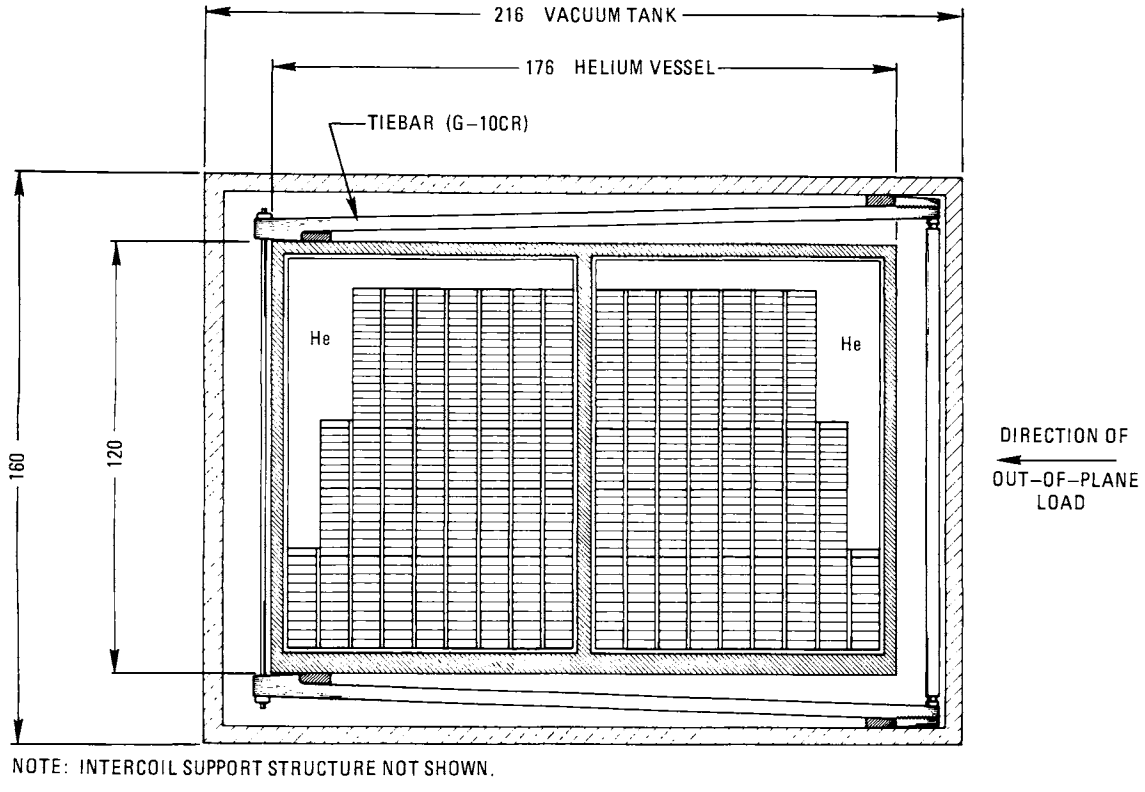

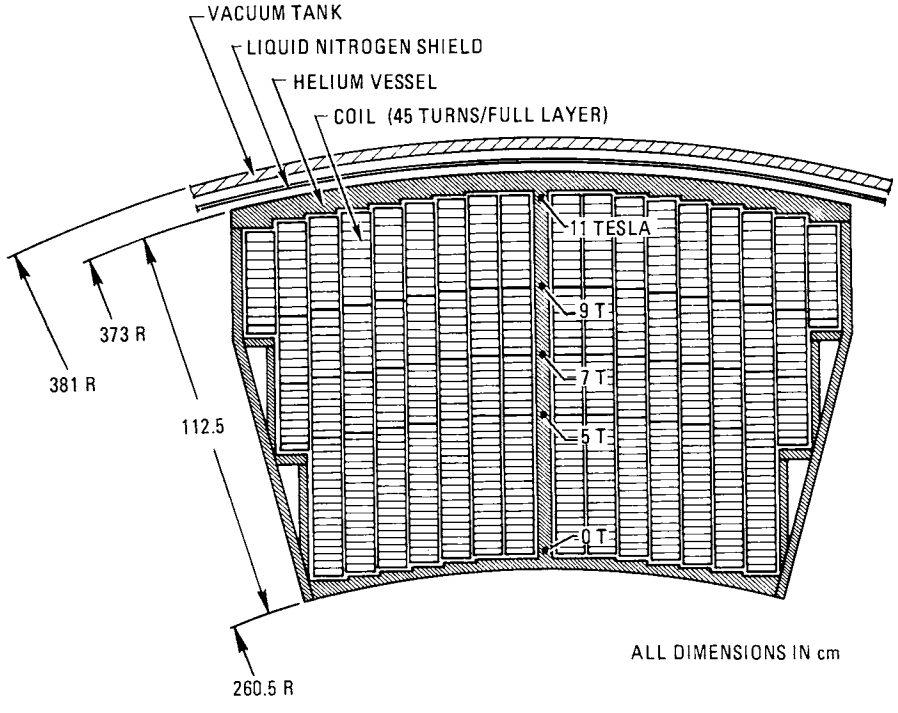

Figure 9-12. Section through one coil in centerpost and outer region.

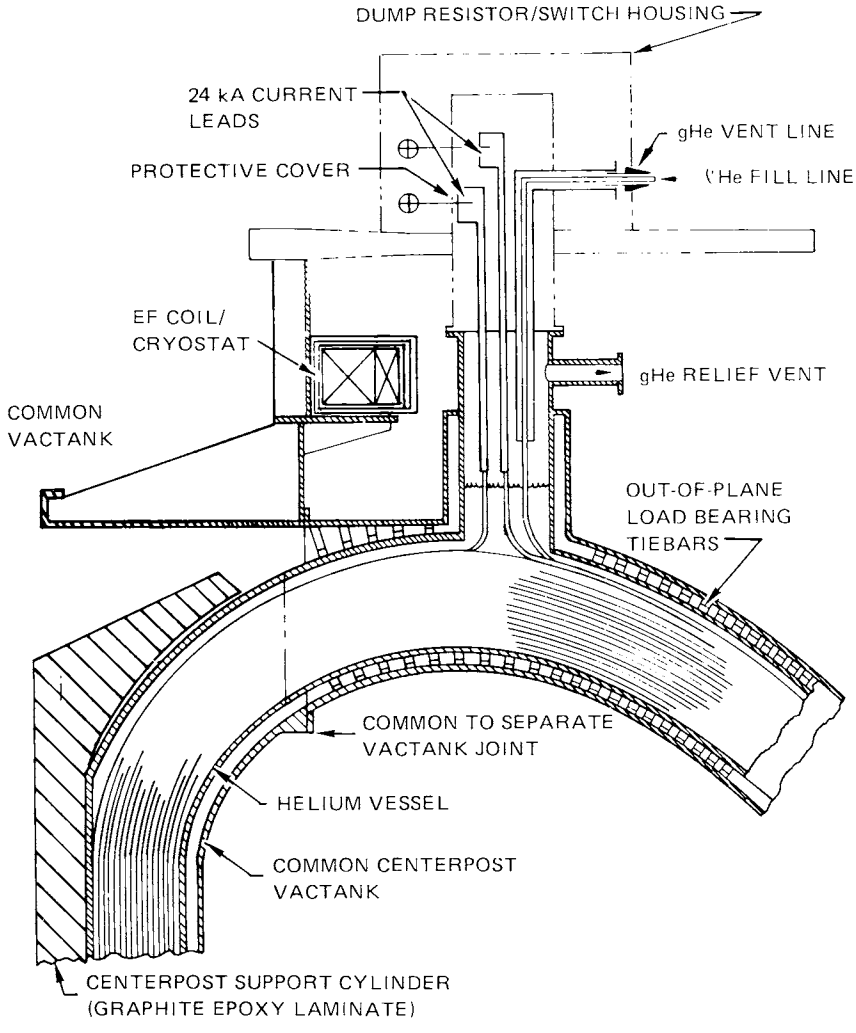

Figure 9-13. TF coil/cryostat and related elements section view of upper region.

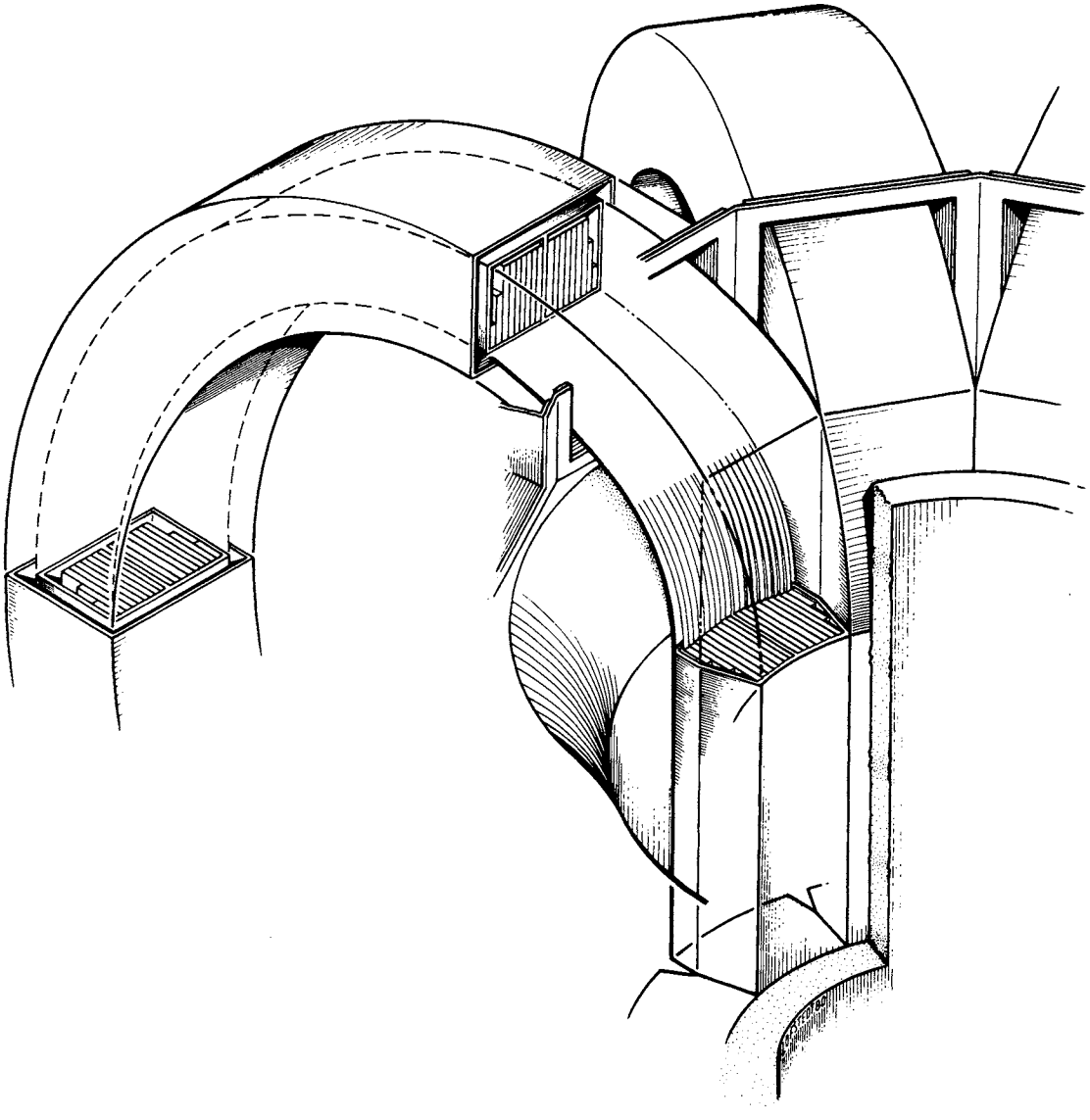

Figure 9-14. Cryostat details.

The coils are spiral wound, the 14 full height pancakes having 45 turns each. The pancakes are wound directly onto the inner wall (which is the outer radius element as shown in the centerpost section) and the central radial spine of the helium vessel. One-half of a coil is wound, and then the side and outer wall elements are installed. The coil/helium vessel is then inverted, and the process is repeated for the other half.

9.2.5.1 Centering Load Support

In the straight, centerpost region the i dl x B (Lorentz) forces on each conductor are directed radially inward towards the machine axis. This accumulated load of about 70 MN/m^2 (10,000 psi) average at the coil inner radius must be borne by the centerpost support cylinder (Fig. 9-13). Thus, in this region the inner radius helium vessel wall must bear against the "outer" turn of each coil layer (through interposed ground insulation, of course). Also, the flanking partial height coil layers must bear against brackets attached to the helium vessel sidewalls (Fig. 9-12).

9.2.5.2 Hoop Load Support

In its outer, curved portion, the coil is self-supporting against hoop loads by virtue of the conductor support strip. Therefore, the coil layers do not bear against the outer helium vessel wall except in the straight centerpost region, as seen in the upper view of Fig. 9-12 and in Fig. 9-13. This radial gap between coil and helium vessel outer wall is used as required for interlayer crossovers.

9.2.6 TF Coil Support Against EF Coil Generated Out-of-Plane Loads

The STARFIRE equilibrium field (EF) coils are located outside of the TF coil envelope to improve machine maintainability by allowing intact removal of the outer EF coils if required for repair, replacement or access to other major reactor components. Current designs for ETF and INTOR also incorporate external EF coils.

Along with its overall topology advantage, external location of the EF coils exposes the outer TF coil region to large fields, which interact with the TF coil current to generate large out-of-plane (overturning) loads. This

field results both from the EF coil currents, and from the fact that, for machine accessibility reasons, the EF coils must necessarily be few in number.

As discussed in Sec. 9.2.6.1 below, the magnitude of the overturning moment on each coil is about 1.5×10^9 N•m. In the selected design, the centerpost region of the TF coil bears a small portion of this load, reacted by shear plates to adjacent helium vessels; thus the twelve helium vessel centerpost regions act together to resist the resultant torsion load. In the outer, curved coil region, the distributed out-of-plane load is transmitted from the helium vessel to the surrounding vacuum tank by closely packed pairs of cold-to-warm tiebars. The individual coil vacuum tanks are in turn supported by substantial intercoil shear panels. These features are shown and described below in Sec. 9.2.6.2.

9.2.6.1 Analysis

External location of the widely spaced high current EF coils exposes the outer TF coil regions to large fringing fields, which interact with the TF coil current to generate large out-of-plane (overturning) loads. The upper and lower hemispheres containing the TF coils tend to rotate about the machine vertical axis in opposite directions, each TF coil contributing a force. These loads are described in Sec. 16.4.

The loads, shown in Fig. 9-15, originate in the conductor in the liquid helium vessel. This vessel contains these loads as a pressure against one side. In the centerpost regions, the loads are reacted directly to the centerpost and balanced torsionally from top to bottom; no connection to the warm structure being required. The distribution of the loads is such, however, that the loads in the outer limb of the TF coil are too great to be either transferred to, or resisted by the centerpost torsional system. Accordingly, a bracing system is required between the outer limbs of the TF coils. This bracing must be penetrated radially for rf heating ducts and blanket cooling lines, and it must be removable to allow blanket/shield removal. A shear panel concept has been selected, the panels being placed between the coils, forming a cylinder around the machine vertical axis. Each panel carries 70% of the overturning force, about 65 MN/coil (14×10^6 lb) from the top and the bottom of the machine, to resist the overturning moment through its shear connection to the warm shells. The support structure is discussed further in Chapter 16.

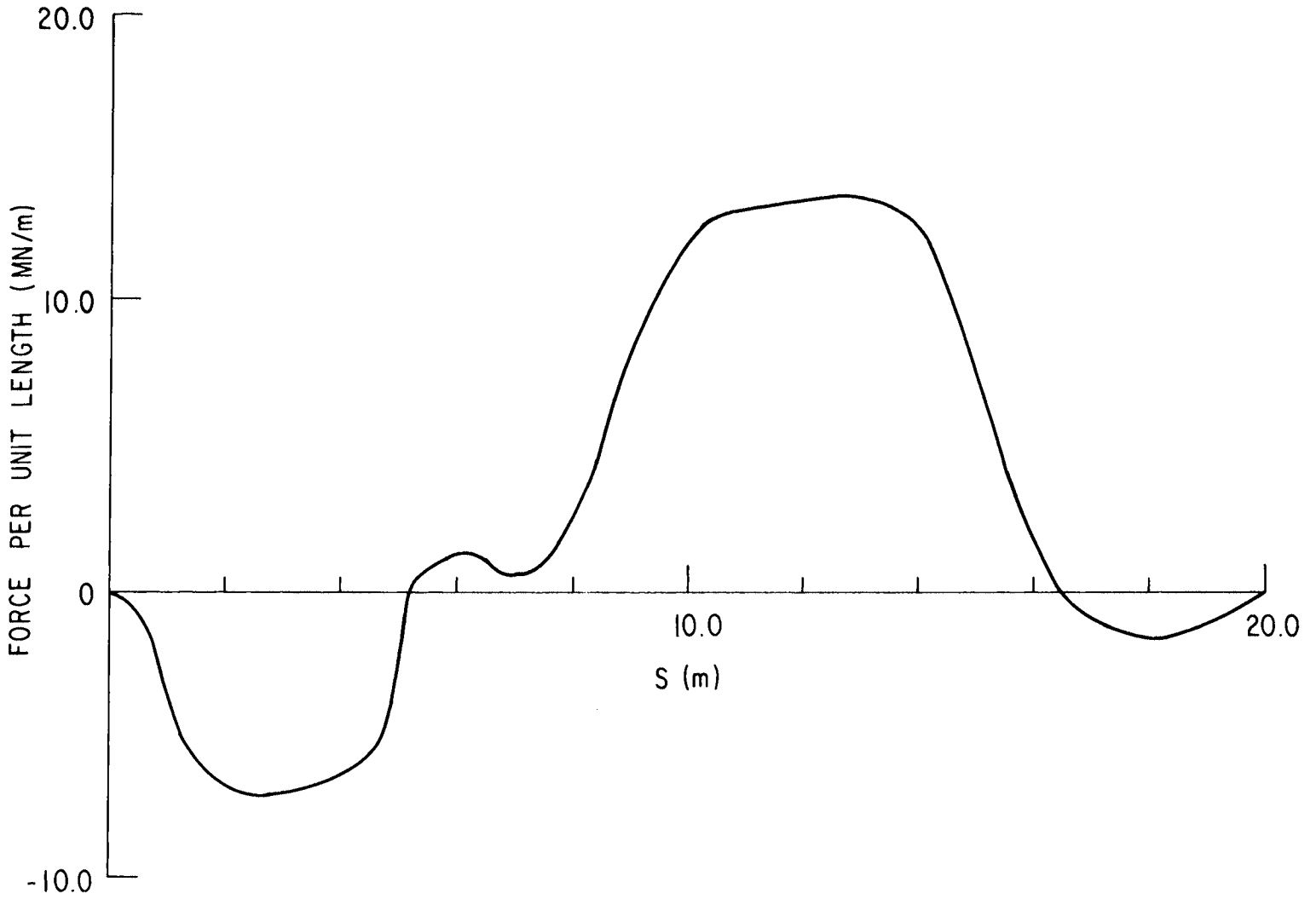

Figure 9-15. Out of plane load on TF Coil as a function of S, the circumferential distance around the coil, measured from the midplane position on the TF coil inboard leg.

The loads associated with the brace system originate in the conductors in the cold helium vessel. These loads must be carried to the warm shell by an attachment system which conducts minimum heat across the vacuum. The tiebar system developed for this is shown in Fig. 9-12 and 9-16.

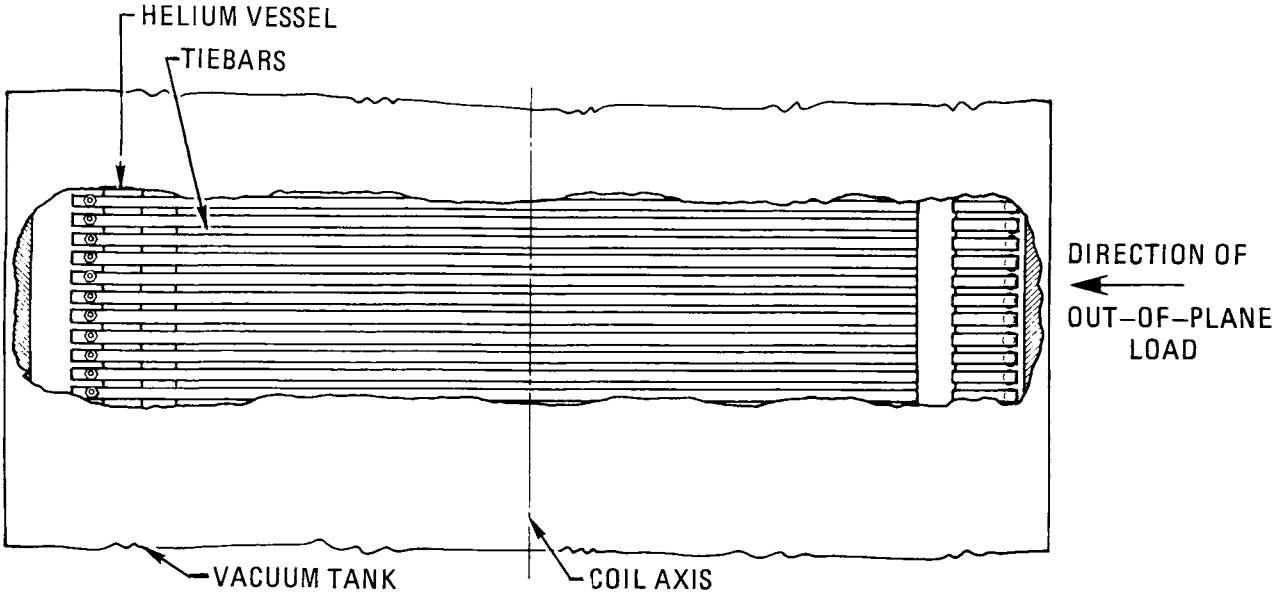

Figure 9-16. Cutaway view of one coil showing support bars in high load region.

The basis of the design is support of the running load with minimal heat transfer. To achieve a uniformly high stress level, it was decided to use a tensile application of as high quality as possible. In order to obtain long paths, these ties stretch the entire width of the coil. A further feature of the design is the large relative movement induced by the thermal contraction of the helium vessel. In order to handle this, the ties must generate minimum stress during relative lateral displacement of their ends.

The adopted design has pivoting ends of hook form; simple pin ends were not used since the pin heads would take space and prevent the ties from being installed "shoulder to shoulder" where necessary. This would make the struts wider, inducing very large moments between the points of origin of the loads (the box webs) and the strut centerlines. The beams to take this moment on the helium vessel would constitute a considerable structure which would increase the width of the coil by some inches. The moment associated with the hook is carried by separate struts and ties which do not cross from cold to

warm walls. The resulting design minimizes both material content and conducting cross section.

An important feature of this design is that it will take up to 140,000 N/cm (80,000 lb/in) along the coil, the maximum calculated value. The configuration does not change at all as the loading decreases, this being accommodated by pitching the tiebars at increasing intervals. For instance, at a load of 20,000 lb/in, these assemblies can be installed at 10 cm pitch. Where the load reverses, it is easy to invert the design; and indeed at the crossover point the "normal" and "inverted" systems can be intermingled. The quantity of ties needed, 17,000, should lead to economies of production.

The achieved heat leak for the entire system is only of the order of 500 watts. A benefit of the design expected to be realized is that in a major coil bending situation the ties will allow deflections of the inner helium vessel larger than those of the outer vessel. This will have the effect of raising the inner helium vessel bending stresses, effectively raising the bending load which the coil can carry.

9.2.6.2 Out-of-Plane Load Support

In the outer coil region the out-of-plane load path is as follows (again referring to Fig. 9-12, upper view):

- The out-of-plane (circumferential) running load is generated within the coil by the i dl x $B_{polodial}$ forces along each conductor. The coil remains under compression (that is, the layers do not pull away from each other, or from the helium vessel central web) due to the self-generated field.
- The helium vessel central radial web bears the coil out-of-plane load and transmits it to the inner and outer helium vessel walls.
- The epoxy-fiberglass (G-10) tiebars support the coil/helium vessel structure, transferring the running load to the vacuum tank (see also Fig. 9-16).
- The vacuum tanks of the outer TF-coil region are mutually selfsupported by the intercoil shear panels (see Fig. 9-1 above).
- The combined moment of inertia of the interconnected helium vessel and vacuum tank in the outer coil region is sufficient to support the out-of-plane running load between the intercoil shear panels and the centerpost support.

- A significant fraction of the out-of-plane loading must be borne in torsion by the centerpost components. In the basic scheme, the TF coil helium vessels are supported by the upper and lower flared portions of the centerpost support cylinder. An alternative design concept is to install shear wedges between helium vessels, just beyond their straight sections.

9.2.7 Quench Protection and Power Supplies

The STARFIRE TF coil system, including an inherently reliable coil protective (energy dump) system, must be designed to withstand a quench, or rapid transition from the superconducting to resistive state, without damage. Such an occurrence would probably never transpire during the course of a machine's lifetime, but it must be regarded as a possibility. The primary threats to a coil under such a circumstance are excessive voltage and temperature.

As a first principle, all of the TF coils should be connected in series to a single power supply, in order to insure that all carry the same current. Secondly, the total dump resistance should be distributed uniformly among the coils in order to minimize the peak voltage. These intercoil dump resistors must be short circuited by a mechanical breaker during normal operation. A dynamic computer analysis was used to predict actual parameters within a quenching coil with reasonable accuracy, accounting for such time dependent factors as normal region size, coolant pressure, and decaying current. The results are presented in the analysis subsection below.

9.2.7.1 Power Supply and Protection Circuitry

The circuit diagram for the TF coil power supply leads and energy dump system is shown in Fig. 9-17. The coils are charged in 12 hours during plant startup but function in a steady state mode during normal operation.

Since the stored energy of the fully charged TF coil system is 50 GJ, coil damage would result in the event of a single coil quench if this energy were dissipated internally. To avoid this, the system is discharged rapidly by forcing the current to flow through resistors placed between the coils in the circuit and activated by mechanical switches. The 12 water-cooled resistors and mechanical switches are located above the reactor, between the coil "chimneys".

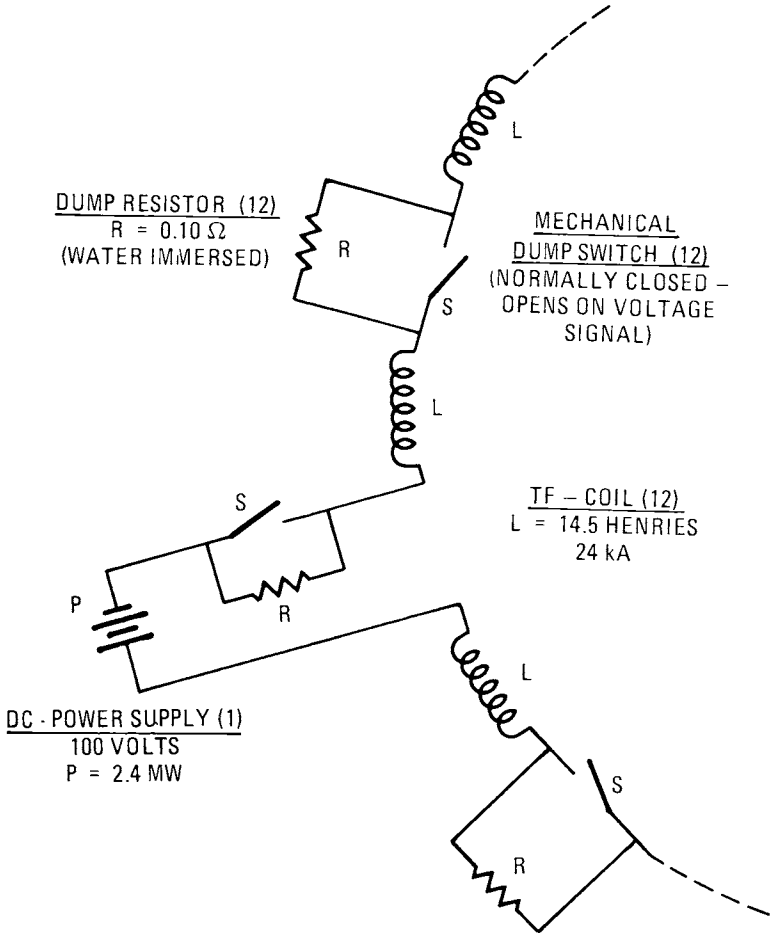

Figure 9-17. TF coil operating/protection circuit.

During startup and normal operation, the power supply charges the coils with the dump resistors (R) bypassed by the closed switches (S). If a coil is detected to be quenching (by a voltage signal), the switches are opened, forcing the current to flow through the dump resistors. The power supply must be isolated during the dumping process because an appreciable voltage would be imposed on the power supply due to any unbalance in the coil inductance or external resistance. Since the power supply is a low-voltage and high-current device, it could be damaged by such an applied voltage.

All power and dump leads are room temperature copper conductors rated for 24,000 amps. The 24 power leads to the TF coils are cooled by boil-off helium gas from the coil cryostats in order to minimize heat conduction to the superconductors.

Connected in series, the 12 coil toroidal arrangement has an inductance of 174 henries. A single current-regulated power supply rated at 100 volts and 24,000 amps charges the magnet system in 12 hours. The resistance of the power leads is small and can be neglected in the charging time calculation.

9.2.7.2 Quench Protection

A magnet quench analysis for the case of a low liquid level and a normal region starting in the gas space has been performed using a code called "QUENCH" which has been developed at GA (not to be confused with other widely used codes of the same name). This computer program accurately accounts for all the important processes in the cryostat during a magnet quench. It calculates liquid level, cryostat pressure, coil temperature, normal region dissipation, energy deposited into the helium bath, current decay, etc. The results show that the magnet will not suffer damage, provided either that the dump resistors are utilized or alternatively that all the liquid in the 12 cryostats is expelled at about the same time. If, however, all the energy in the TF coil system were to be dumped into one coil it would be severely damaged by both voltage breakdown and overheating.

The computer program is basically a two-dimensional, time-dependent thermal transient code with liquid helium cooling in the region just below the liquid level. The behavior of thermal transport in the third dimension is assumed from the 2-D results since the thermal properties in the turn-to-turn direction are about the same as in the layer-to-layer direction.

The assumed magnet geometry consists of an arc at the top and bottom and two straight sections. The thermal conductivity is assumed to be temperature independent. Magnetoresistivity and radiation induced resistivity are included in the total resistivity but do not change during the calculation. The heat capacities of the support structure, copper and superconducting material are lumped together. Local temperature dependent resistivities and specific heats enable the calculation of ohmic heating in the winding structure as the stored energy of the field is dissipated in the equivalent LR circuit. The compressibility of liquid helium is also accounted for. The pressure relief valve is set at 3 atm absolute.

Figure 9-18 shows the coil parameters as a function of time for a conductor current density of about 6000 A/cm^2 and an average field of 5 T. It shows the peak resistive voltage over the normal region is only 280 volts, while the peak temperature is at 85 K at that time. The peak temperature rises up to 90 K in 170 seconds and would probably not exceed 100 K when the

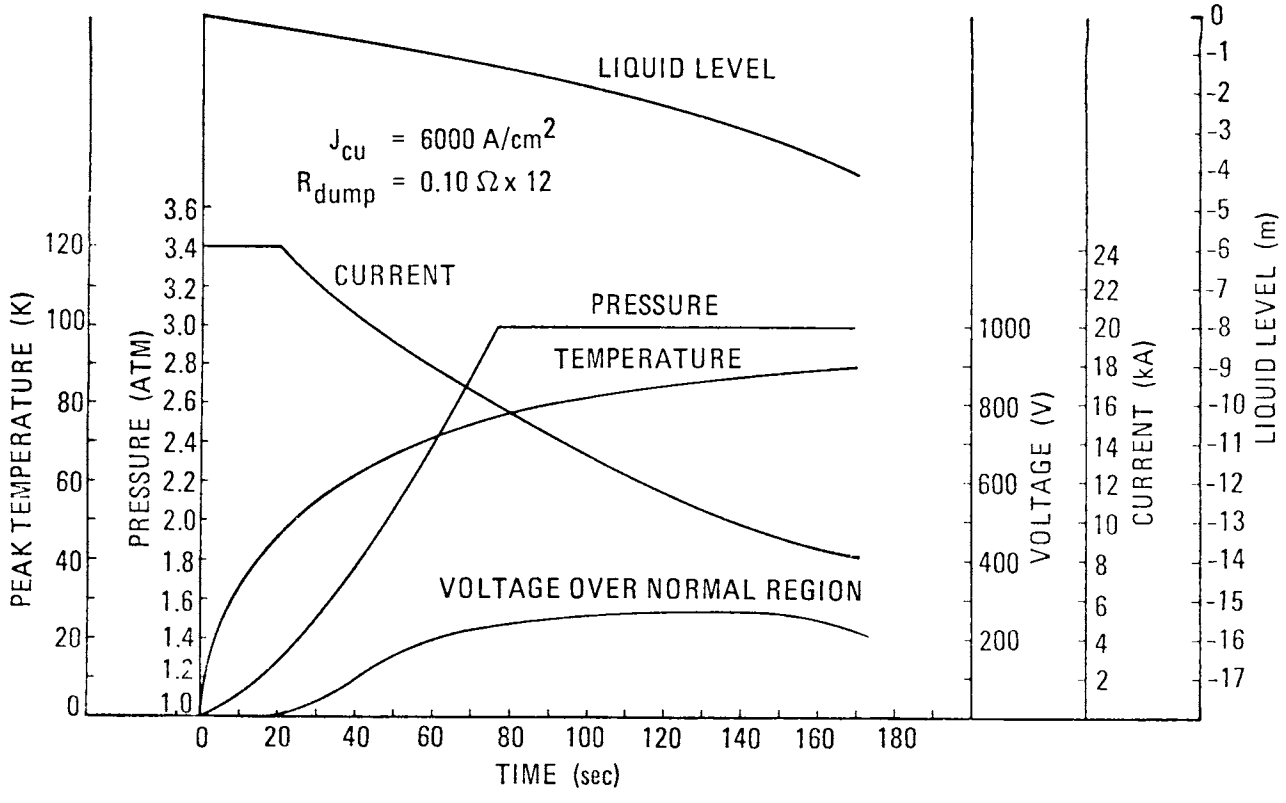

Figure 9-18. Coil quench data.

current has decayed to zero. The voltage over the dump resistor is proportional to the current, which decreases with time. The maximum voltage relative to the ground is about the same as the voltage over the dump resistor since the resistive voltage over the normal region is small compared to it.

The conclusion, therefore, is that the magnet can be protected with a modest dump voltage. The resistive voltage drop within the magnet is small and the peak temperatures will not damage the magnet.

9.2.8 Other Considerations

9.2.8.1 Ease and Location of Manufacture

Each STARFIRE TF coil/helium vessel assembly is about 15 m high (excluding "chimney" and leads) x 10.5 m wide, and weighs 4.5×10^5 kg (10^6 lb).

There are a number of perceived advantages to completing each coil and helium vessel assembly at a central facility, versus performing this work at the reactor site. The disadvantage lies in transporting such a massive item over long distances, especially where waterways are not available. (Lighter-than-air vessels have been suggested for overland transport, but may not be practical due to the size required, and their vulnerability to weather.)

The point of view adopted by STARFIRE is that it is certainly feasible to fabricate the TF coils either at a central facility or at the reactor site. Therefore the approach to use would be determined by the ecomonics for any given reactor site. Certainly it would appear that whenever water transport is available over the whole route, the assemblies should be completed at the central facility. And, by the year 2020, overland movement of comparable masses may be relatively commonplace and hence economically attractive.

Economic considerations would also determine whether all TF coils would be tested at full field at the central fabrication facility before shipment to site. Experience with earlier reactors in the STARFIRE series may provide the confidence that such tests are unnecessary. If, however, it is too expensive to achieve the quality assurance required to provide that confidence, it may be more economical to provide a test installation at the fabrication facility, in which each coil could be tested before shipment. The test installation could consist, for example, of an inventory of eleven TF coils.

9.2.8.2 Minimization of Shutdown and End-of-Life Radioactivity

The choice of materials involves two main items, the coil conductor and the cryostat (helium vessel and vacuum tank).

From a radioactivity standpoint, pure aluminum would be preferable to copper for conductor stabilizer material. However, in either case the superconductor elements (niobium, titanium and tin) produce the dominant activation

problem. Since the superconductor and stabilizer material are intimately bound together, it appears that they cannot be separated and separately disposed of following machine shutdown.

Structural grade aluminum and austenitic stainless steel are the two candidate materials considered for the large cryostat elements. Stainless steel was selected because of its high strength and high modulus of elasticity as compared with aluminum are particularly important for cryostat support of the out-of-plane loads.

9.2.8.3 Maximum Operation Reliability

High reliability is achieved through a combination of sound, straightforward design, good manufacturing practice, and comprehensive component and system testing. An important design consideration here is selection of a maximum allowable total fast neutron fluence to the conductor and insulation materials.

9.2.8.4 Maintainability

The removal and replacement of a TF coil following an in-service failure would be a costly, time consuming operation. The principal difficulties would be removal of machine components surrounding the coil. Nevertheless, the coils should be desitned for possible removal from the toroidal array.

9.2.8.5 Coil Materials Integrity Under Neutron Fluence

The two principal considerations in this regard are mechanical degradation of the coil insulation, and electrical degradation of the conductor stabilizer (copper).

Irradiation tests at Brookhaven National Laboratory and elsewhere indicate that epoxy-fiberglass laminate (NEMA G-10) maintains about 80% of its mechanical strength up to 5×10^9 rad (corresponding to about 5×10^{18} n/cm^2).

At this same fluence, the resistivity of pure copper increases by about 5×10^{-8} Ω-cm. However, for STARFIRE it is anticipated that the TF coils will be brought up to room temperature approximately once every ten years for scheduled reactor maintenance. Each such "anneal" will remove 80% of the copper's radiation degradation, so that at the end of its 40-year operating life, the radiation induced resistivity figure will not exceed 3.8×10^{-8} Ω-cm. This is the basis upon which the conductor is designed, as indicated in Sec. 9.2.4.2 above.

9.2.9 Analysis of TF Coil Heating due to Plasma Disruption

9.2.9.1 General Considerations

When a plasma disruption occurs, the centerpost region of the TF coils will experience the fast poloidal field variation due to the abrupt disappearance of the plasma current. The first wall, blanket and shield will slow down the field variation somewhat. A reasonable time duration is about 0.5 s at the TF coil centerpost region. The field variation in the TF coil outer leg region will depend on the manner in which the poloidal coils are controlled after the disruption. Since the poloidal coils are relatively far away from the plasma, it should be possible to control the poloidal coils independently after the plasma disruption. A reasonable time for de-energizing the poloidal coils may be one minute.

The selected cabled conductor effectively reduces the amount of heating to reasonably low values. The coil helium vessels, on the other hand, are relatively thick and relatively large in dimension. Each stainless steel helium vessel forms a D-shaped tubular conducting structure 40 m in circumference, about 1.5 m x 1.0 m in cross sectional dimensions, and 5 cm in wall thickness. Since the helium vessels form part of the coil structural support against out of plane loads, the wall thickness must be above a certain minimum (> 5 cm). Under a pulsing poloidal field, such large scale metallic objects will develop significant amounts of eddy current heating. Since the helium vessels are kept in contact with the bath, the heat generated will eventually flow into the bath be removed through the refrigeration system. Moreover, the heat input will raise the bath temperature and pressure; therefore, excessive heating may decrease the stability margin of the conductor and lead to coil quench.

9.2.9.2 Heating in Superconductor

A three-leveled cable conductor will be utilized in the TF coils as described above. The pulsed field loss calculations were carried out for the 6 T field region, which represents the average conditions for the four field grades. The relevant conductor parameters are listed in Table 9-6.

The distribution of poloidal field generated by the plasma current and the poloidal coils was computed using the 2-D magnetic field code EFFI. The mean square values of the perpendicular and parallel field components were then calculated. Table 9-7 is a summary of the field computations.

It is expected that the filament and superconducting strand coupling eddy current losses are the dominant loss components as compared to hysteresis loss. Since the coupling eddy current loss depends strongly on the transverse conductivity of the cables, the accurate estimation of the losses will require a reliable estimate of the effective transverse conductivity $\sigma_{T,eff}$.

The eddy current loss can be decomposed into the loss due to the coupling of the superconducting filaments in the strand, and the loss due to the coupling of the strands (sub-cables) in the first level cable (higher level cables).

Actual measurements of effective transverse conductivity carried out by R. Schermer at LASL on the 30 MJ coil conductor[2] indicated that for the first level cable with completely uninsulated strands, the effective transverse conductivity is a hundred times less than a solder-filled cable with the same strand construction. The solder-filled cable has a conductivity comparable to Cu. Similarly, the second level cable with uninsulated strands shows an additional factor of two reduction in $\sigma_{T,eff}$ as compared with the solder-filled second level cable. The measurements of $\sigma_{T,eff}$ on the final cable were not carried out due to its large size. However, a conservative estimate is that in going from the second level cable to the final cable, $\sigma_{T,eff}$ will drop by another factor of two.

For a sinusoidal time varying field, the loss per unit volume due to the perpendicular field component is estimated to be[3]

$$P_{e,\perp}/V = 10^{-16} \times \frac{\sigma}{4}\left(\frac{H\omega L}{2\pi}\right)^2\left[1 + (L/2\pi\delta)^4\right]^{-1} \ (W/cm^3) \quad , \qquad (1)$$

Table 9-6. Parameters Relevant to Loss Analysis for STARFIRE Toroidal-Field Coil Conductor

Ampere-turns per Coil	16.9 MA-turns
Coil Perimeter	40.0 m
Current per Turn	24 kA
Conductor (6 T typical):	
- Configuration	3-level, noninsulated cable, 7 x 7 x 14 strand
- Strand Diameter	0.0897 cm
- S/C Strands per Cable	252
- Copper Strands per Cable	434
- Cu:SC Ratio in S/C Strands	3.82:1
- S/C Strand Twist Pitch	2 cm
- First Level Cable Twist Pitch	8 cm
- Second Level Cable Twist Pitch	24 cm
- Final Cable Twist Pitch	120 cm
- ρ_{Cu}	6×10^{-8} Ω-cm
- ρ_{eff} of First Level Cable	6×10^{-6} Ω-cm
- ρ_{eff} of Second Level Cable	1.2×10^{-5} Ω-cm
- ρ_{eff} of Final Cable	2.4×10^{-5} Ω-cm

where σ = conductivity of matrix in Ω-cm

L = twist pitch of the filaments in cm

H = field amplitude in Oersteds

$\omega = 2\pi f$ with f being the frequency

δ = skin depth = $\left(2\pi\omega\sigma \times 10^{-9}\right)^{-1/2}$ (cm) ,

Table 9-7. Poloidal Field Distribution Along the STARFIRE Toroidal-Field Coil Perimeter

Field Point Location		Field Components (T)		Field Components (T)	
R(m)	Z(m)	Radial (B_r)	Vertical (B_z)	Parallel ($B_{\parallel}$)	Perpendicular ($B_{\perp}$)
3.05	0.53	-5.0×10^{-2}	7.3×10^{-1}	5.0×10^{-2}	7.3×10^{-1}
3.05	2.63	-4.6×10^{-1}	2.75×10^{-1}	4.6×10^{-1}	2.75×10^{-1}
3.10	4.56	-3.6×10^{-1}	-2.1×10^{-1}	3.1×10^{-1}	-2.8×10^{-1}
3.79	6.03	-8.3×10^{-2}	-2.0×10^{-1}	-7.0×10^{-2}	-2.1×10^{-1}
4.79	6.78	-2.4×10^{-1}	-1.7×10^{-1}	-4.5×10^{-2}	-2.9×10^{-1}
6.19	7.20	-3.4×10^{-1}	-4.8×10^{-1}	-4.4×10^{-1}	-3.8×10^{-1}
7.59	7.14	-1.9×10^{-1}	-7.0×10^{-1}	-7.3×10^{-1}	-5.7×10^{-2}
9.19	6.58	-8.9×10^{-2}	-8.4×10^{-1}	-7.9×10^{-1}	3.1×10^{-1}
10.79	5.40	4.4×10^{-2}	1.08×10^{0}	-7.4×10^{-1}	7.9×10^{-1}
12.51	2.68	3.6×10^{-1}	-7.5×10^{-1}	8.0×10^{-2}	8.7×10^{-1}
12.92	0.99	1.5×10^{-1}	-5.8×10^{-1}	6.3×10^{-2}	6.0×10^{-1}
Average Field		$\langle B_{\parallel}^2 \rangle = 3.04 \times 10^{-1}$ (T^2)			
		$\langle B_{\perp}^2 \rangle = 2.29 \times 10^{-1}$ (T^2)			

and the loss per unit volume due to the parallel field component is

$$P_{e,\parallel}/V = 10^{-16} \frac{\sigma}{2} \left(H\omega R_o\right)^2 \left[\frac{(\ell/L)^2}{1 + (\sqrt{2}\ \ell/\pi\delta)^4} + \frac{1}{16}\right] (W/cm^3) \ , \qquad (2)$$

where R_o = radius of the cable

ℓ = characteristic distance for field reversal.

Results of the analysis are summarized in Table 9-8. It can be seen that the total energy deposition in all 12 TF coils per disruption is about

Table 9-8. Pulsed Field Loss in STARFIRE Toroidal-Field Coil Conductor Due to Plasma Disruption

	Superconductor Strand	1st Level Cable	2nd Level Cable	Final Cable
Power Loss per Unit Volume (W/cm^3)	9.53×10^{-3}	1.52×10^{-3}	6.85×10^{-3}	8.58×10^{-2}
Volume per Coil (m^3)	6.29	10.5	12.22	12.22
Power per Coil (W)	6.00×10^4	1.60×10^4	8.38×10^5	1.05×10^6
Total Power for 12 Coils = 12.6×10^6 W				
Total Energy Deposition per Disruption [a] = 6.3×10^6 J				

[a]Assuming all poloidal coil currents decay in 0.5 s.

6.3 MJ if all the poloidal currents decay in 0.5 s. However, as explained earlier, it is reasonable to assume that only the plasma current decays in 0.5 seconds while the poloidal coils can be controlled to de-energize in one minute or more. Under such a condition, the heating will be 1.6 MJ in the centerpost region, and 3.9×10^4 J in the outer leg region.

9.2.9.3 Heating in the Helium Vessel and Shield

If a room temperature or liquid nitrogen temperature flux shield is used to slow down the field pulse experienced by a coil helium vessel, then these two metallic structures constitute two coupled inductors, and the energy deposition in each can best be computed by a circuit simulation procedure. Variations in the external field is simulated by the introduction of the third inductor which is driven by a voltage source. Figure 9-19 is a sketch of the electrical circuit involved.

The currents in the three inductors I_i, i = 1-3 are described by the set of coupled differential equations:

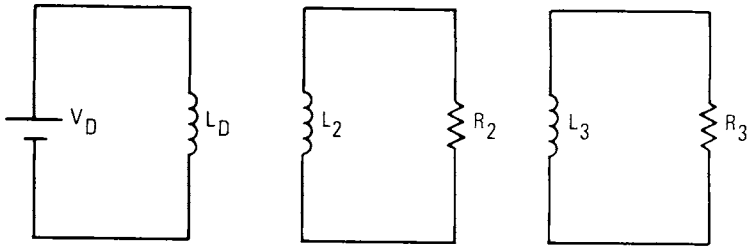

L_D = DRIVE COIL
L_2 = FLUX SHIELD
L_3 = HELIUM VESSEL

Figure 9-19. Circuit depicting the pulsed field heating in the flux shield and the helium vessel in the outer leg region.

$$\sum_{k=1}^{3} M_{jk} \dot{I}_k = V_j \qquad j = 1\text{-}3 \quad , \tag{3}$$

where V_j is the voltage drop in each inductor loop and M_{jk} are elements of the inductance matrix. The set of equations can be solved numerically given the initial conditions I_j $(t = 0)$, and the waveform of the driving voltage $V_D(t)$.

Outer Leg Region -- In this case, the drive coil is used to deliver the field change experienced by the TF coil. A 10 m section of the helium vessel and vacuum vessel was simulated in the analysis. The drive coil with larger dimensions was used. The parameters of the circuit elements involved are summarized in Table 9-9.

Two cases were studied for both a "fast" and a "slow" decay time. One of them involves using an aluminum shield, the other involves using a stainless steel shield. The results are also shown in Table 9-9. It can be seen that the Al shield is more efficient than the stainless steel one. However, if the poloidal coil currents are controlled after the disruption to have a slow decay time, then the heating in the center leg region will be much reduced (see Table 9-9), and a stainless steel shield will be sufficient.

Table 9-9. Parameters and Results in Calculating the Heating on Outer Leg Portion of Helium Vessels

	Shield (Vacuum Vessel)	Helium Vessel	Drive Coil [a]
Height (m)	10.0	10.0	10.0
Radius (m)	1.0	0.9	4.0
Thickness (cm)	3.0	5.0	10.0
Resistivity (μΩ)			
Stainless Steel Case	50.0	50.0	--
Aluminum Case	2.5	50.0	--
"Fast" Decay			
Current Decay Time (s)	--	--	0.5
Energy Deposition [b] (MJ)			
Stainless Steel Case	21.1	15.3	--
Aluminum Case	71.5	6.6	--
Unshielded Case	--	16.8	--
"Slow" Decay			
Current Decay Time (s)	--	--	60.0
Energy Deposition [b] (MJ)			
Stainless Steel Case	0.18	0.13	--
Aluminum Case	0.60	0.06	--

[a] Used to simulate poloidal field pulse.

[b] Scaled to give total heating in all 12 toroidal-field coil outer legs.

Centerpost Region -- The helium vessel of each coil forms a conducting loop by itself. However, since all 12 helium vessels are closely packed into a ring in the centerpost, and a common flux shield is used to slow down the field pulse (see Fig. 9-20), the inner and outer walls of all the helium vessels effectively form two connected loops with equal and opposite shielding currents flowing in them (Fig. 9-20). The effective resistance of each loop is increased due to the fact that shielding currents must flow through the side walls as well. The entire system consists of four inductors;

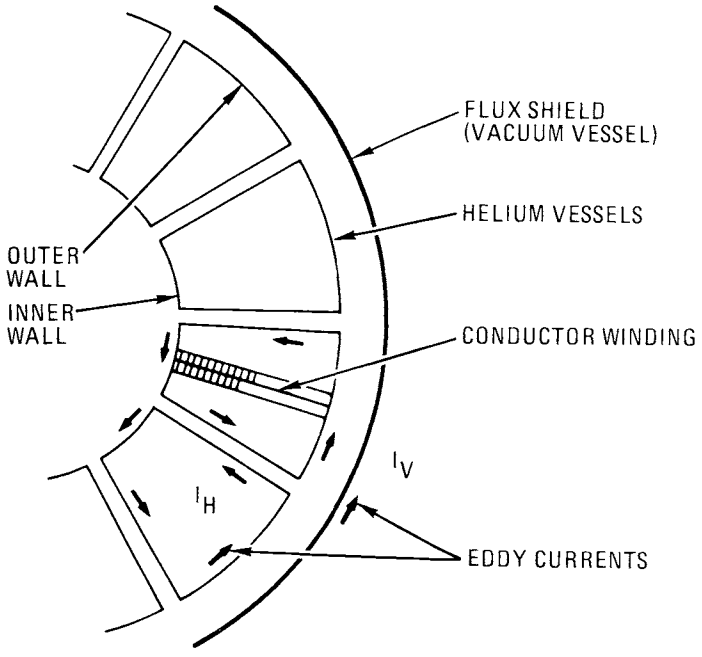

EQUIVALENT EDDY CURRENT PATTERN

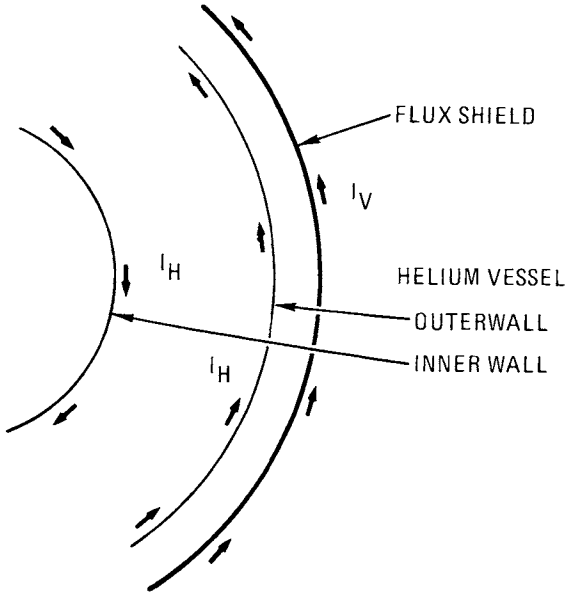

Figure 9-20. Eddy current flow pattern in the centerpost helium vessels and flux shield.

however, the condition that the inner and outer loops simulating the helium vessel inner and outer walls have equal and opposite currents can be used to eliminate one inductor from the system, and only three equations are required to fully describe the system (Fig. 9-21.)

The parameters for the analysis are summarized in Table 9-5 and 9-6. Again, two cases involving an Al shield and a stainless steel one are considered, and the results for both are shown in Table 9-10. It can be seen that the performance of the Al shields is much better than the stainless steel one. However, the presence of a low resistance loop placed between the OH coil and the plasma may strongly affect the operation of the OH coil. Furthermore, to be compatible with the material used for the outer leg vacuum vessel, it may be required to adopt the stainless steel shield.

Because it is not possible to further slow down the field perturbations created by the disruption of the plasma current, the 9.3 MJ of energy deposited in the helium vessels cannot be reduced very much further.

9.2.9.4 Conclusions

Due to the utilization of low loss cabled conductor, the heating in the conductor is not the dominant heat source. On the other hand, the coil helium vessels are relatively thick and massive metallic objects, and the eddy current heating in the helium vessels represents the majority of the heat load.

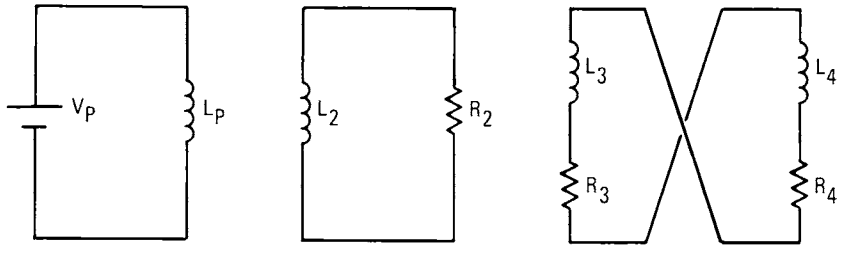

L_P = PLASMA
L_2 = FLUX SHIELD
L_3 = HELIUM VESSEL OUTER WALL
L_4 = HELIUM VESSEL INNER WALL

Figure 9-21. Circuit depicting the pulsed field heating in the flux shield and the inner and outer walls of the helium vessel in the centerpost region.

Table 9-10. Parameters and Results in Calculating the Heating in the Centerpost Helium Vessel

	Shield (Vacuum Vessel)	Helium Vessel	Plasma
Height (m)	10.0	10.0	6.21
Radius (m)	4.475	--	7.0
Inner Wall (m)	--	4.384	--
Outer Wall (m)	--	3.075	--
Thickness (cm)	3.0	5.0	388.00
Resistivity (μΩ-cm)			
Stainless Steel Case	50.0	50.0	--
Aluminum Case	2.5	50.0	--
Current Decay Time (s)	--	--	0.5
Energy Deposition[a] (MJ)			
Stainless Steel Case	64.1	9.30	--
Aluminum Case	153.1	1.12	--
Unshielded Case	--	10.4	--

[a]Total for 12 toroidal-field coils.

By controlling the poloidal coils after the disruption so that the poloidal coils are de-energized in more than one minute, the total heating can be limited to about 11 MJ, which will raise the helium bath temperature by 0.19 K, but should not cause significant problems.

The results of the pulsed field heating in the STARFIRE TF coils due to plasma disruption can be summarized as the following (with stainless steel vacuum vessels):

No delayed decay in poloidal coils:

Total heating for 12 coils per disruption

Conductor	6.3 MJ
He vessel	9.5 MJ
Vacuum vessel	85.2 MJ

With delayed decay (1 min) in poloidal coils:

Total heating for 12 coils per disruption

Conductor	1.6 MJ
He vessel	9.5 MJ
Vacuum vessel	64.4 MJ

9.3 EQUILIBRIUM FIELD COILS AND OHMIC HEATING COILS

9.3.1 Introduction

The STARFIRE reactor has three sets of poloidal field (PF) coils. These are the ohmic heating (OH) coils, the equilibrium field (EF) coils, and correction field (CF) coils. Even though STARFIRE operates in a steady-state mode, it incorporates OH coils to provide an inductive voltage over several seconds to initiate a plasma current. The EF coils provide the field which maintains the plasma at equilibrium with the desired position, shape, and current profile. The correction field coils, which link the TF coils, respond to displacements of the plasma to correct those displacements and thus stabilize the plasma. They can respond to plasma motion more quickly without excessive power demands than the EF coils, which are located outside the TF coils. Because they are of similar design and construction, the superconducting OH and EF coils are treated together in this section. Parameters for the OH and EF coils are given in Table 9-11. The CF coils, because they link the TF coils and must be demountable, are constructed of water-cooled copper; they are described in Sec. 9.4.

9.3.2 EF and OH Coil Locations

The EF coils must be superconducting; normal conducting coils would consume an unacceptable amount of power. Being superconducting, the EF coils must be outside the TF coil system. Superconducting EF coils which interlink the TF coils could be manufactured only by in-situ winding, a difficult and time consuming process that would appreciably lengthen the construction time for STARFIRE. Moreover, all the EF coils would have to be removed and later rewound if a TF coil had to be replaced.

EF coils outside the TF coil system present certain problems. First the stored energy is large: 9.7 GJ for the EF coil system. However as the coils are superconducting, no electrical power save refrigeration is required to maintain this energy. Even the charging power is not excessive; it peaks at 87 MW because the coils are charged over a comfortable seven minute period. The EF system cannot respond quickly to correct a plasma current displacement; supplementary copper CF coils, located inside the TF coil system, are required to perform such corrections.

Table 9-11. Ohmic-Heating and Equilibrium-Field Coil Parameters

	OH Coils	EF Coils
Superconductor/Stabilizer	NbTi/Cu	NbTi/Cu
Stability	Cryostable	Cryostable
Cooling	Bath Cooled	Bath Cooled
Operating Temperature	4.2 K	4.2 K
Operating Current	100 kA	100 kA
Average Current Density	1400 A/cm^2	1400 A/cm^2
Total Amp-turns	51 MA-turns	86 MA-turns
Total Amp-meters	600 MA-m	2900 MA-m
Peak Field	8.0 T	4.5 T
Maximum dB/dt (Normal Operation)	0.6 T/s	0.2 T/s
Stored Energy (Self)	1.1 GJ	10.0 GJ
Self Inductance*	55 mH	500 mH
Mutual Inductance with Plasma*	-0.15 mH	-0.49 mH
Mutual Inductance M_{EF-OH}*	-0.024 mH	

*Based on equivalent parallel current of 200 kA.

Other problems resulting from the external EF coil location are the overturning moments on the TF coils and ac losses in the TF coils during a scheduled or unscheduled change in EF coil current. These are described above in Sec. 9.2.

The same arguments apply also to the OH coil system, except that the problems are less severe for the OH coils than for the EF coils, since the OH system has only 1.1 GJ stored energy compared to the 9.7 GJ of the EF system.

The actual positions and currents of the OH coils are determined by three conditions: (1) that they produce a large flux linking the plasma but a low field in the plasma region, (2) that the currents in the coils are manageable, and (3) that the coils not interfere with other reactor components. Similarly, the positions and currents of the EF coils are determined by the conditions that they provide the location, shape, and current profile desired for the plasma, that the current be manageable, and that these coils also not interfere

Table 9-12. Equilibrium-Field and Ohmic-Heating Coil Locations and Currents

Coil #	R_1 (cm)	ΔR (cm)	H_1 (cm)	ΔH (cm)	I (MA-turns)
OH Coils					
1	104	78	180	126	-13.82
2	92	90	341	72	-9.08
3	600	25	914	72	-2.51
EF Coils					
4	92	90	65	90	-11.35
5	104	78	487	126	13.82
6	527	66	914	72	6.69
7	1397	86	535	90	-10.89

with other reactor components. In addition, the EF coil system and OH coil system should be uncoupled magnetically in order that the charging or discharging of one system not induce voltage in the other.

The coil locations and currents listed in Table 9-12 and illustrated in Fig. 9-22 satisfy these conditions. There are seven coils above the reactor mid-plane, with another seven located symmetrically below the midplane. Coils 1-3 are OH coils, and coils 4-7 are EF coils. OH coils 1 and 2 are inboard of the TF coils, and coil 3 is above. EF coils 4 and 5 are inboard, coil 6 is above, and coil 7 is outboard. OH coil 3 and EF coil 6 are located close together, so they can share a support system. Coils 1, 2, 4, and 5 have the same outer diameter, for ease of assembly.

9.3.3 Forces on EF and OH Coils

The six OH coils and eight EF coils all exert magnetic forces on each other. In addition, the plasma exerts magnetic forces on all the poloidal coils. Because the plasma, OH coil, and EF coil currents all vary differently with time, the time development of these forces is rather complex. The plasma current builds up gradually over 7 min; the EF coil current builds up over the same time, but not with an identical time profile.

Several options are possible for the time development of the OH coil current, since only the change in current determines the volt-seconds delivered to the plasma. For example, it could rise from zero to some final value I_o, or from $-I_o/2$ to $+ I_o/2$. The time development which has been chosen consists of gradually driving the current to $-I_o$ before plasma initiation, and then driving it to zero at a constant rate for 14 s. The detailed time histories of the currents are described in Chapter 7. For calculating the forces on the coils, the following simplified time histories were assumed:

$$
\begin{aligned}
I_{OH} &= I_o\ (t/14-1) && 0 \le t < 14 \\
&= 0 && t \ge 14 \\
I_p &= I_o\ \ 0.015\ t && 0 \le t < 20 \\
&= I_o\ (0.00175\ t + 0.265) && 20 \le t < 420 \\
&= I_o && t \ge 420 \\
I_{EF} &= I_o\ \ 0.00975\ t && 0 \le t < 20 \\
&= I_o\ (0.00073\ t + 0.1804) && 20 \le t < 220 \\
&= I_o\ (0.003295\ t - 0.3839) && 220 \le t < 420 \\
&= I_o && t \ge 420
\end{aligned}
\qquad (4)
$$

where time t is in seconds, and I_o = 200 kA for the OH and EF coils and 10.1 MA for the plasma.

The forces were calculated as follows: First the fields were calculated at the positions of the seven EF and OH coils above the reactor midplane; fields from the plasma, all OH coils, and all EF coils were calculated separately, assuming full current in each; then the axial force F_Z and radial force per unit circumferential length F_r/ℓ were calculated from

$$
\begin{aligned}
F_Z &= -2\ \pi r\ nIB \\
F_r/\ell &= nIB_Z,
\end{aligned}
\qquad (5)
$$

again assuming full current and again calculating forces from plasma, OH coils, and EF coils separately. Finally the forces calculated from the Eq. (5) were scaled for both current and field according to Eq. (4) and summed for different values of time. The resulting forces are shown in Figs. 9-23, 9-24, and 9-25.

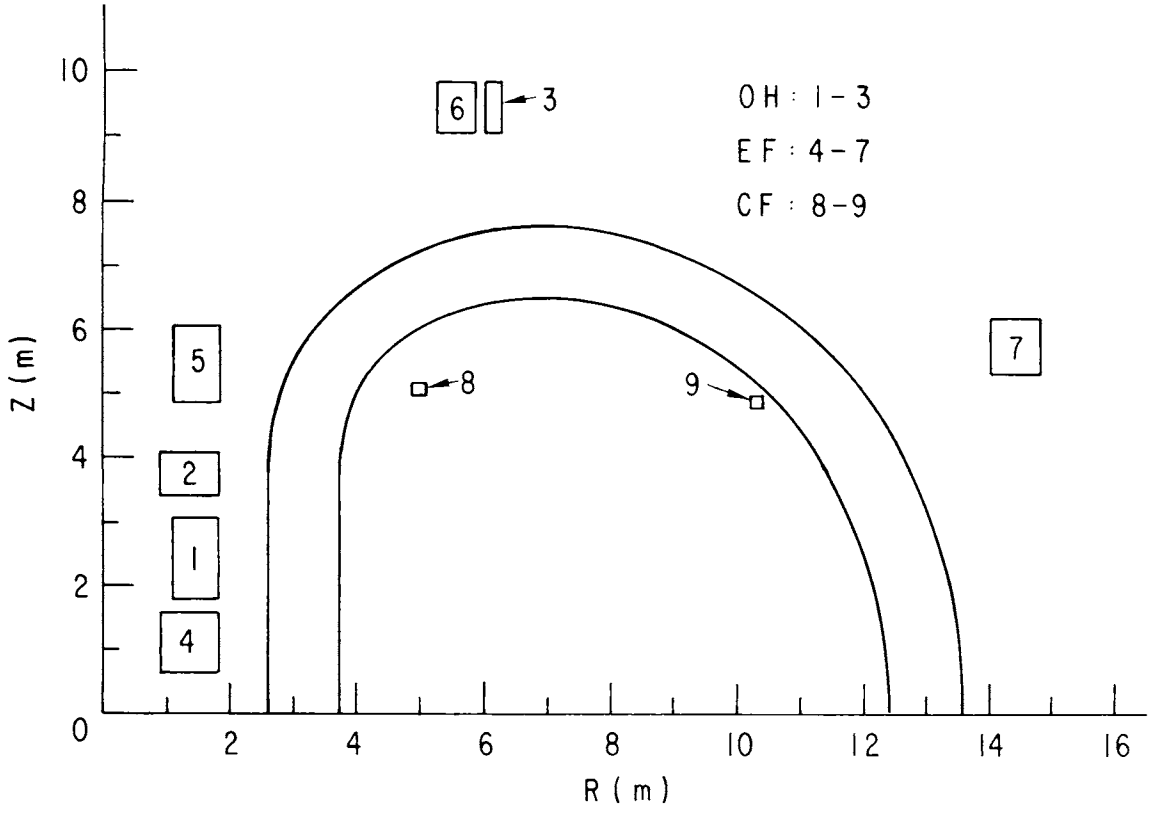

Figure 9-22. Poloidal Coil Locations.

Because the current in the OH coils is greatest when those in the EF coils and plasma are zero, and vice versa, the forces on the OH coils are predominantly the forces they exert on each other. Consequently, they all experience this maximum force at the start of plasma current initiation.

Similarly, almost all of the forces on the EF coils reach their maximum when the plasma and EF coil currents attain their full values. The only exception is the axial force on coil #6, at which the radial fields from the plasma and EF coils nearly cancel; the maximum force is reached earlier, at 290 s, when the differing time development of the EF and plasma currents make the net field larger.

Although the forces are large, they are not unmanageable. For example, when the OH coils are carrying full current, coil #1 experiences an axial force of 90.0 MN directed toward coil #2, and coil #2 experiences a force of 107.5 MN directed toward coil #1. The larger force divided by the smaller area (7.75 m^2) corresponds to a compressive stress of only 13.9 MN/m^2(2010 psi).

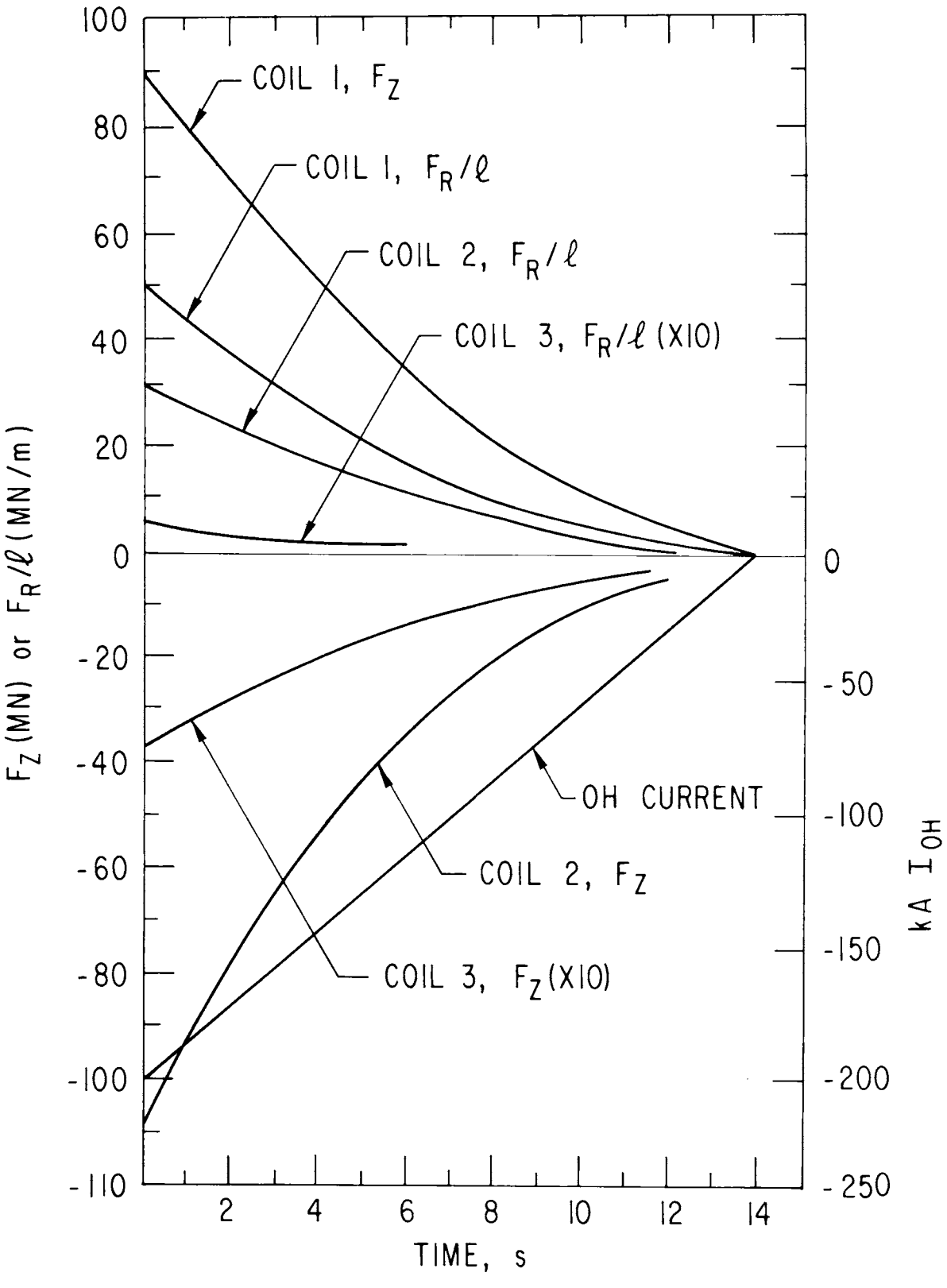

Figure 9-23. OH Coils: Forces and Current.

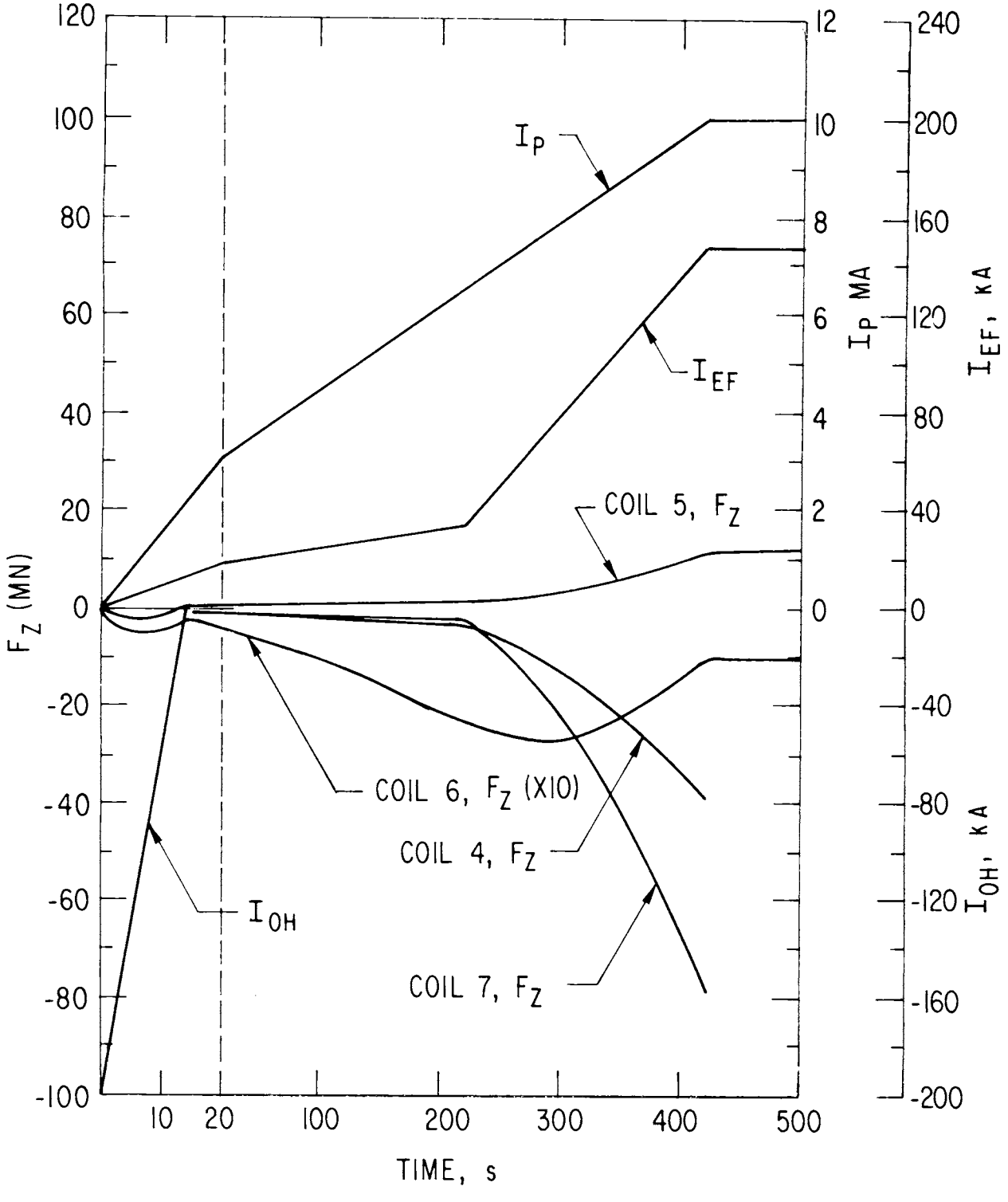

Figure 9-24. EF coils, axial forces and currents.

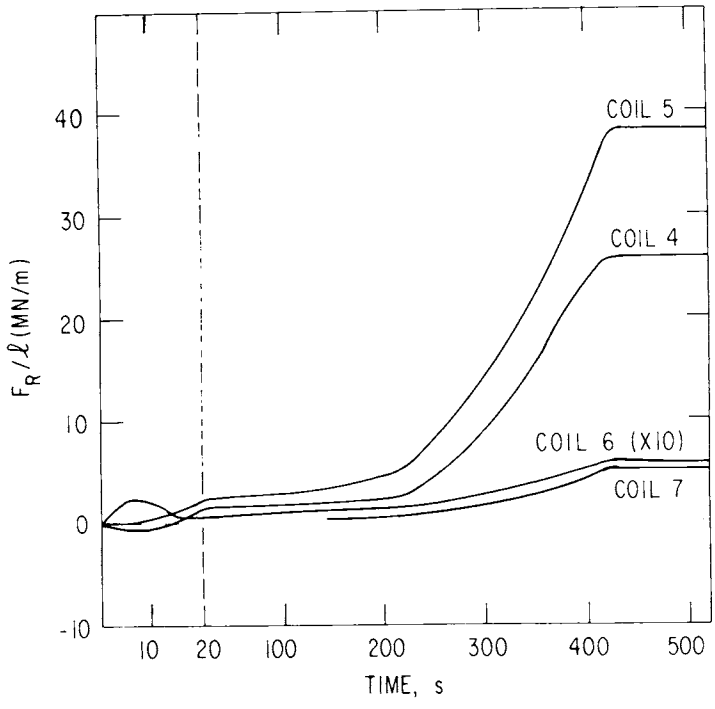

Figure 9-25. Radial force per unit length on EF coils.

A potentially more troublesome force is that on coil #7, the 28.8 m diameter EF coil. The axial force of 79.1 MN must be supported at the twelve TF coils it encircles. To first approximation, the coil and cryostat between two neighboring TF coils can be treated as a straight box beam 107 cm wide by 112 cm high and 5 cm thick (42" x 44" x 2" thick), clamped at both ends and acted upon by a distributed force of 0.874 MN/m (4985 lb/in). The calculated peak displacement is 0.89 mm (.0352"). A cryostat with thinner walls, 102 cm by 107 cm by 2.5 cm thick, (40" x 42" x 1") would have a displacement of 1.93 mm (.0758").

A calculation treating the coil and cryostat between two TF coils as a curved beam, supported and slope guided at each end,[4] yields a peak displacement of 0.92 mm (.0361) and a roll at the support of only 0.005°, justifying the simpler straight beam analysis. These displacements from the force are acceptable.

9.3.4 Conductor for EF and OH Coils

The conductor design chosen for the EF and OH coils is a flat cable consisting of 26 basic cables wrapped around a central pultruded fiberglass strip, 11.9 cm by 0.2 cm, as shown in Fig. 9-26. The strip serves to ensure

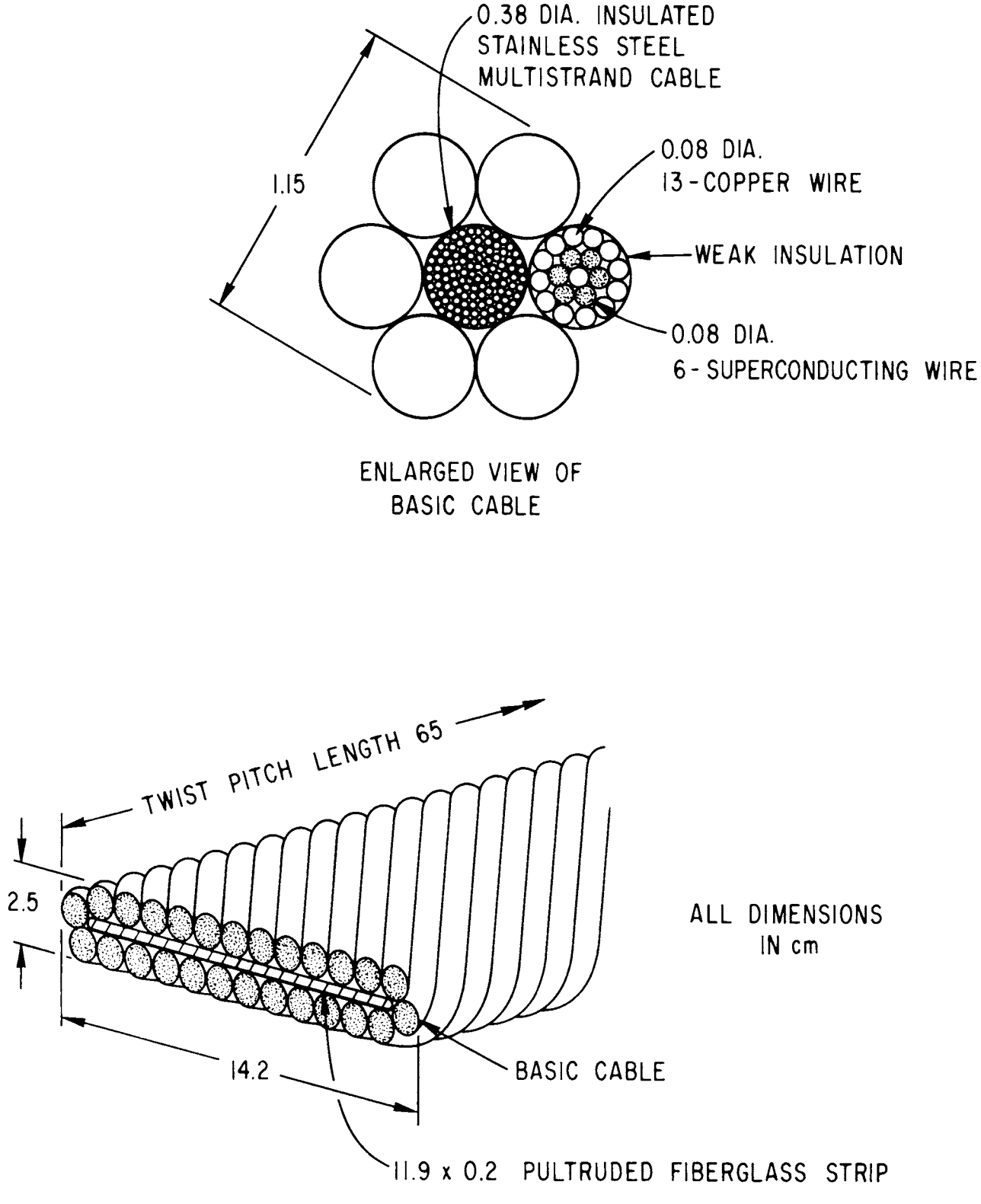

Figure 9-26. Cabled conductor for OH and EF coils.

mechanical and dimensional stability during the conductor cabling and coil winding. The conductor carries 100 kA; equivalent 200 kA operation is achieved by operating coils located symmetrically above and below the midplane in parallel.

Each basic cable consists of six copper and superconductor subcables cabled around a central 0.38 cm diameter stainless steel multistrand cable. The stainless steel is introduced to increase the tensile strength of the basic cable. The subcables are electrically insulated from each other to reduce eddy current losses in the cable during charging and discharging.

Each subcable consists of six 0.08 cm diameter superconducting wires cabled around a copper wire of the same size and with twelve more copper wires cabled around the superconducting wires (see Fig. 9-26).

In this cable, the superconducting wires are all fully transposed in order that the transport current be equally shared among the wires and that there be no large ac losses from circulating currents in the superconductor.

Good electrical contact, attained through soldering, between the superconductor wires and copper wires in each subcable provides cryostability for the cable, while the electrical insulation between subcables reduces eddy current losses. In this way, the conductor provides the compromise between cryostability and low ac losses which is required for a pulsed cryostable magnet. The heat flux on the surface of the cable when the superconducting wires are in the normal state will be 0.2 W/cm^2; the heat flux due to the ac losses is estimated to be 0.01 W/cm^2.

9.3.5. Coil Layout

The coils are pancake wound. Each cable is enclosed top, bottom, and on one side by a fiberglass laminate spacer (G-10), which transmits axial and radial stresses. The top and bottom of the spacer have only fifty percent coverage, to permit helium flow past the conductor. On the other side of the conductor is a pultruded fiberglass band, with a longitudinal central groove and fully cut-out "mouse holes". The central groove and mouse holes permit free flow of helium coolant horizontally and vertically (see Fig. 9-27).

Two stainless steel bands 0.476 cm thick are wound with the conductor to support against the hoop tension resulting from the magnetic forces.

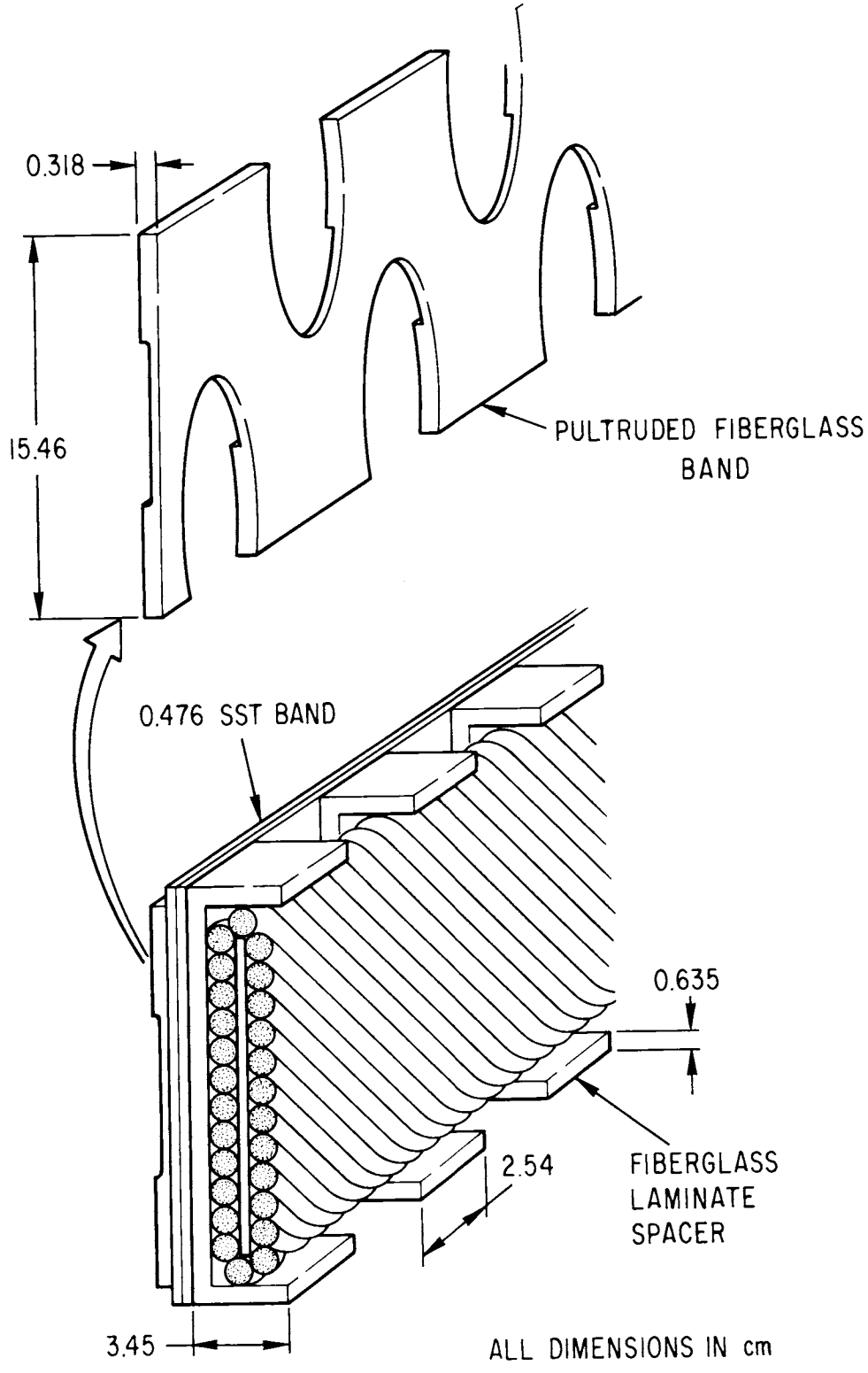

Figure 9-27. Support for OH and EF coil conductor.

Coil structure, with layer-to-layer helium channels, banding, and helium vessel are shown in Fig. 9-28. Plates of G-10, 25 cm thick, are placed between pancakes. Both sides of the G-10 plate will have cooling channels (0.64 cm x 0.47 cm) in the radial direction. The two plates at the top and bottom will be 5 cm thick to have additional cooling channels. After outer banding, the whole coil will be tied down together using stainless steel beams and placed in the cryostat. The weights of the materials which make up the OH and EF coils are given in Table 9-13.

Table 9-13. Equilibrium-Field and Ohmic-Heating Coil Material Weights

Material	Weight (metric ton)
Copper	450
NbTi	33
Stainless Steel	1057
G-10	87
Pultruded Fiberglass	90

9.3.6 Winding and Transportion to Site

The off-site winding and transporting of the OH and EF coils should provide no particular difficulty, with the possible exception of the 30 m diameter coils (Coil #7) which encircle the TF coil system. We make the assumption that by the time STARFIRE is built, transportation needs unrelated to fusion have led to a nationwide transportation system capable of carrying the 500 tonne, 15 m by 11 m TF coils. All the EF and OH coils other than coil #7 are smaller and can be carried by the same system. Even if they had to be wound on site, no great difficulty or delay is expected because they are circular and have at most 140 turns.

Coil #7, 30 m in diameter, could be wound either on a rotating coil form from a stationary conductor-feed station or on a stationary coil from a conductor feed station traveling on a circular track around the coil form.

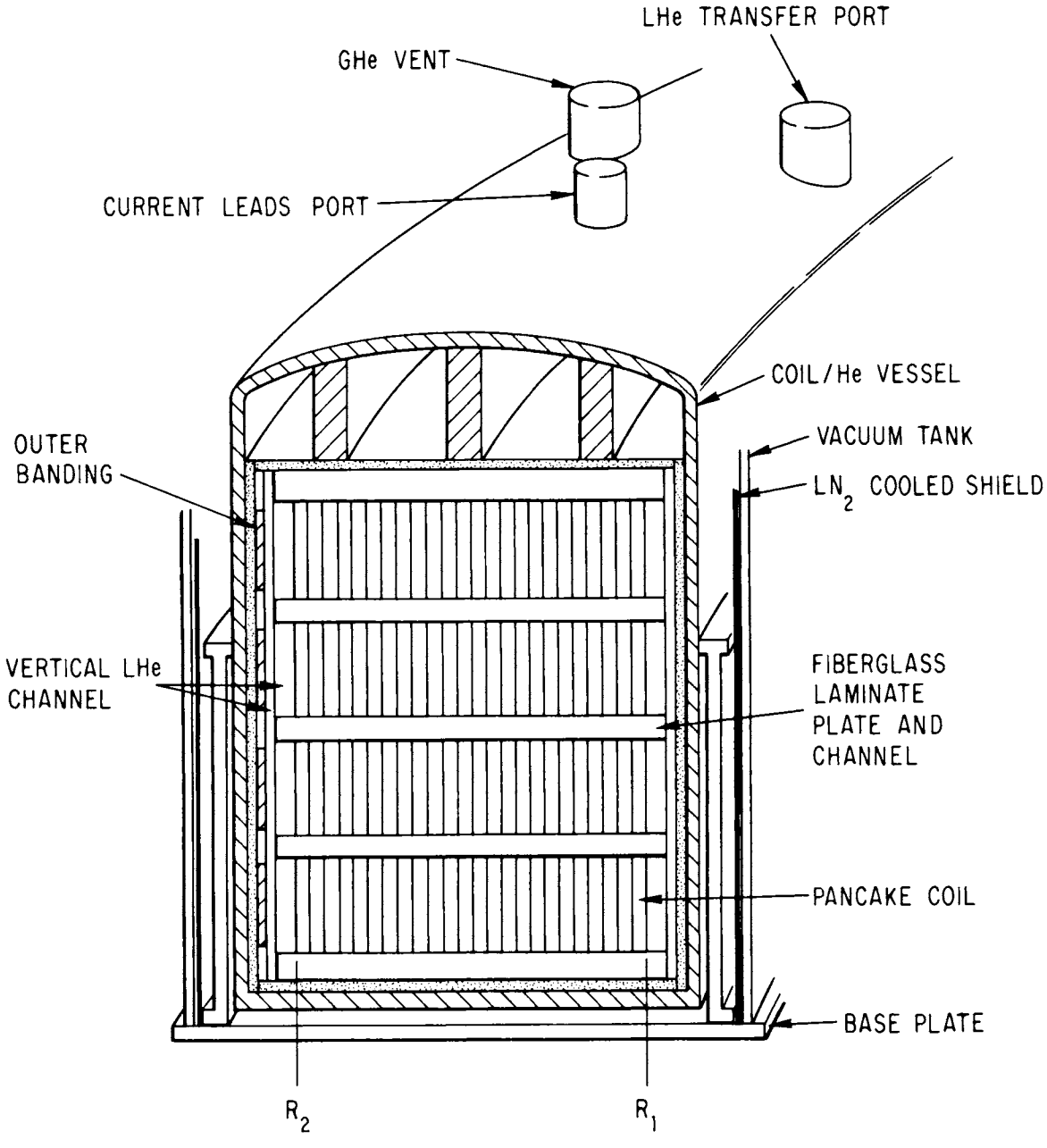

Figure 9-28. Structure of outer OH and EF coils.

9.4 CORRECTION FIELD COILS

9.4.1 Function

The correction field (CF) coils of STARFIRE are used to control the vertical position of the plasma. These coils are not energized until the plasma is off center; then the power supplies are turned on to restore the plasma to its correct position.

9.4.2 Parameters

The four CF coils typically operate at about 10% duty factor. They are placed outside the blanket and shield so that they experience a relatively low neutron dosage. The locations of the coils relative to the plasma and the ampere-turns of each coil are shown in Fig. 9-29. The design parameters for these coils are shown in Table 9-14.

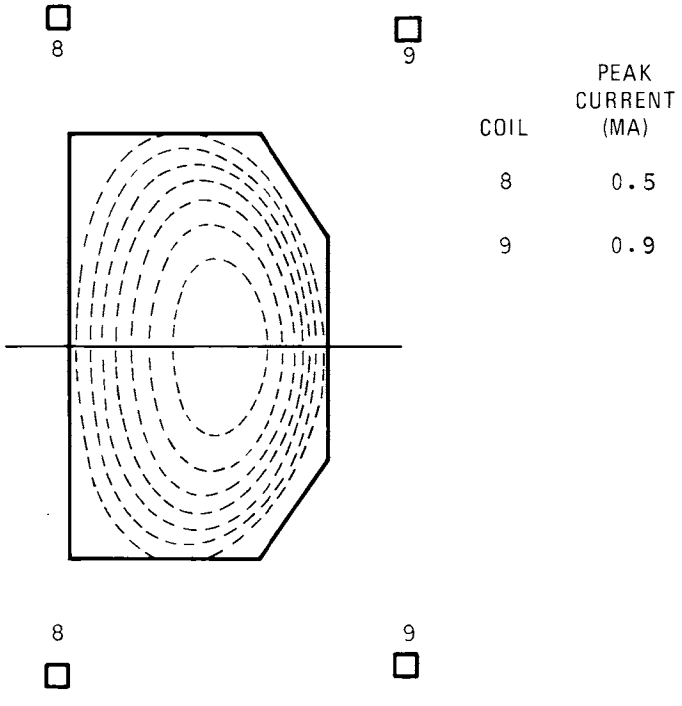

Figure 9-29. STARFIRE correction field coil location.

Table 9-14. STARFIRE Correction Field Coil Design Parameters

Coil Number	Coil 8	Coil 9
R (m)	4.807	10.159
Z (m)	5.044	4.864
Amp-Turns	-0.5×10^6	-0.9×10^6
V_{max} (v)	$\simeq 200$	$\simeq 10$
B_r (T)	-0.02	-0.02
B_z (T)	-0.02	-0.11
f_r (N/m)	1.0×10^4	9.9×10^4
f_z (N/m)	1.0×10^4	1.8×10^4
ΔR (m)	0.3	0.3
ΔZ (m)	0.2	0.3
σ_t (N/m^2)	1.0×10^6	1.4×10^7
F_z (N)	3.0×10^5	1.1×10^6

Peak I^2R power (total) = 2.3 MW.

Peak inductive power (total) = 210 MW.

9.4.3 Design Considerations

The CF coils are placed in regions of significant poloidal magnetic field, so there will be radial as well as vertical loads acting on them. It is necessary to design the coils for very high reliability due to the difficulties associated with their maintenance.

Nevertheless, the coils must be segmented, the joints being designed for easy assembly and disassembly. Since they must be actively cooled to remove the resistive and radiation heating, the coolant connection at the joints should be designed for the same degree of maintainability and accessibility.

The coil design chosen for the STARFIRE CF coils is very similar to the one adopted for the top and bottom field shaping coils of the GA PGFR design.[5] The current ratings are similar, and the radiation dosage and radial and vertical forces are less for the STARFIRE CF coils than for the PGFR F-coils. Thus, it is reasonable to utilize the same design concept.

The most critical part of the CF coil design lies in the demountable joints. Figure 9-30 is a joint concept applicable to the STARFIRE. As shown, each joint consists of two pressure plates and a number of clamping bolts which will apply the necessary pressure to all ten individual joints. Sufficient frictional force can be generated between the joints to overcome the hoop force. Alumina insulation slabs will be placed between turns and between the clamping bolts and also the pressure plates to achieve the necessary insulation. Each coil segment has its own coolant circuits whose connections must be made independently of the clamping assembly.

9.5 MAGNET SAFETY

9.5.1 Superconducting Magnet Quench

The safety concern which is unique to superconducting magnets is the magnet quench, a means by which the energy stored in the magnetic field is converted to other forms. A quench is initiated when a portion of the current carrying conductor, perhaps because of a temperature rise, loses its superconducting property and becomes normal-conducting. Current flowing through the normal region generates heat, which raises the temperature of more conductor and drives it too from the superconducting to the normal state. The temperature of the conductor rises at a rate which, if permitted to continue, would lead to damage and eventual melting of the conductor and other magnet components. At the same time, liquid helium coolant is vaporized; if the vapor is not vented fast enough, the cryostat will be overpressurized and may burst.

For safety, a large superconducting magnet is designed so that it cannot quench, but also so that even if it does quench, no harm will result. The primary step in preventing quenches is to make the magnet cryostable, i.e., to adjust the design of the heat transfer to the helium coolant and the Joule

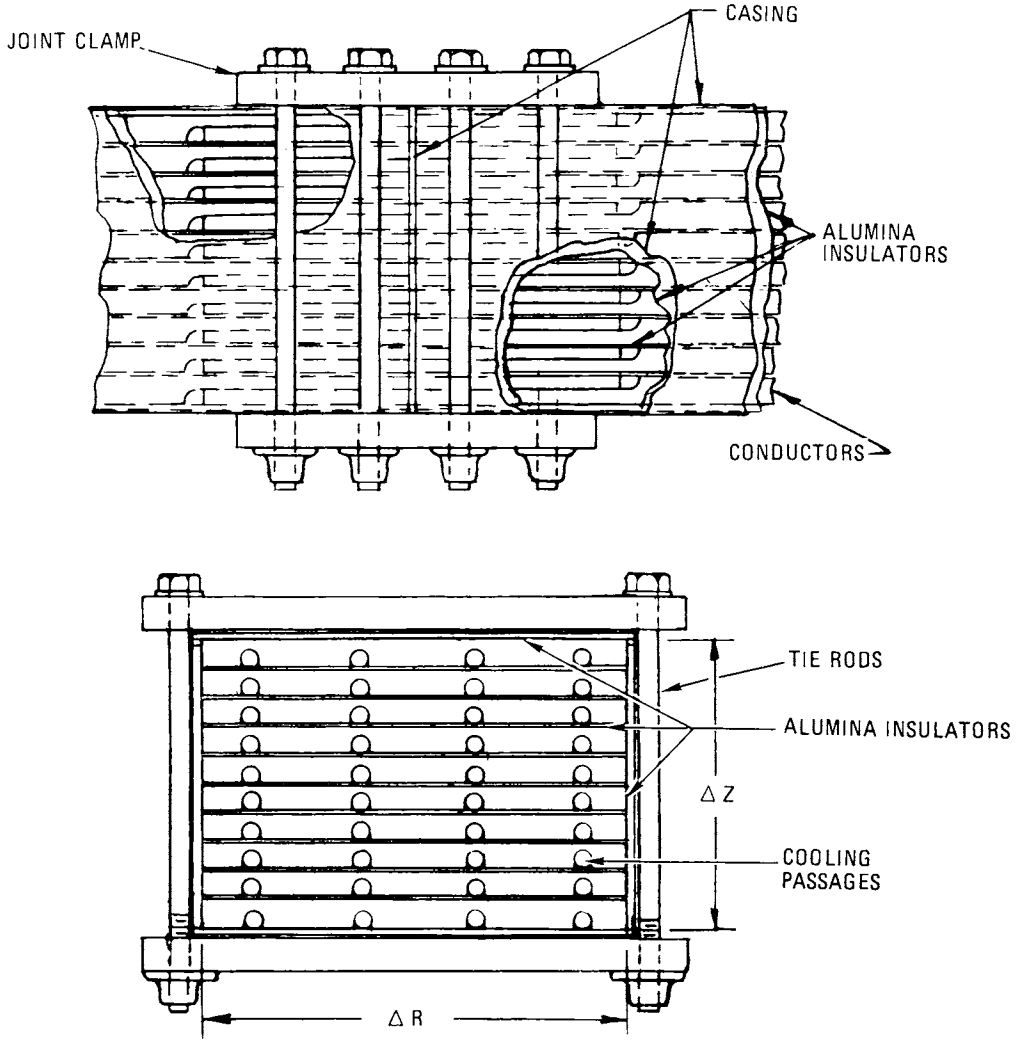

Figure 9-30. STARFIRE correction field coil joint concept design.

heating of the conductor when it is normal, so that if a normal region of conductor does develop, it will shrink and disappear rather than propagate. Thus, it is only under abnormal conditions that a cryostable magnet can quench.

It is informative to consider the accidental quenches of two early large cryostable magnets, the Argonne National Laboratory (ANL) bubble chamber magnet and the Fermi National Accelerator Laboratory (FNAL) bubble chamber magnet.[6] The quench of the ANL magnet occurred as follows: wishing to operate the magnet as quickly as possible and knowing the time required to fill the magnet with liquid helium and the time required to charge it to full field, the operating crew began charging it before it was completely filled. However, because of a problem with the liquid transfer, the magnet

was fully charged before it could be fully filled. A power supply problem then caused voltage pulses to the magnet and quenched the upper turns of the magnet.

The quench of the FNAL magnet was also caused by a low liquid level. Because of a defective liquid level indicator, the problem was not recognized until another, lower level indicator gave a warning. A decision was made to discharge the magnet through the dump resistors. Eddy currents produced by the discharge heated and quenched the upper coils. The helium pressure rose, and more coils quenched after the rupture disk broke and helium vapor and liquid were expelled.

Note that both of these quenches were avoidable, the first by a more conservative start up procedure and the second by the provision of redundant liquid level indicators. Note also that both quenches proceeded from a low liquid level; a low level is certainly one appropriate initiator from which to analyze a quench and its consequences. Finally note that there are newer cryostable magnets which never have quenched, e.g., the superconducting dipole built at ANL and used for MHD research in Moscow. The stability analysis of the STARFIRE TF coils, describing why they are expected not to quench, is given in Sec. 9.2.4.2. The quench protection analysis, describing what will happen if they do, is given in Sec. 9.2.7.2.

9.5.2 Out-of-Plane Forces on TF Coils due to Unequal Currents

Series connection of TF coils does not make unequal currents impossible, but it does make them highly unlikely. A break in the conducting path (due to a lead failure, joint failure, or conductor break between coils) can result in arcing. The most likely consequence of the arcing is the reestablishment of the original current path and the gradual decay, in around 25 minutes, of the TF coil current and field. However, it is possible that the arcing will lead to different current paths and unequal currents through the coils.

With series connected coils, such an occurrence is very rare, perhaps happening only once in many tokamak reactor lifetimes. By contrast, with separately connected TF coils, the probability of a serious current inequality is much larger, perhaps once per reactor lifetime. Because the destruction and replacement of a TF coil must have a very low probability, series connection should be retained on safety grounds.

Because large scale motion of the TF coils could lead to a serious accident situation, the out-of-plane forces developed in the worst current imbalance situation must be resisted by the TF coil support system. A scenario has been analyzed in which the current in one coil drops to zero and the other coils are free-wheeling and remain superconducting. The coils neighboring the zero-current coil carry 130% of normal operating current and experience an out of plane force of 400 MN (90×10^6 lb). In Sec. 9.2.6, it was shown that under normal operation the out of plane force on the TF coils from the external EF coils is 65 MN per coil half. Thus, the support structure needed for normal operation must withstand 130 MN per coil or one-third of the force described above. Moreover, the intercoil support panels are designed to one-third or less of ultimate stress. Consequently, if the TF coils experience the currents described above, they may suffer some damage, but they will not collapse together. We conclude then that even under the very worst conditions the damage would be confined to the reactor magnet and adjacent structure.

9.5.3 Fringe Magnet Field

The magnitude of the magnetic field outside the tokamak reactor has been assessed. The field originates from the TF, EF, and OH coils; locations of all three are shown in Fig. 9-1 and 9-22. The fringe field from the TF coils is very small, less than 10 gauss everywhere outside the reactor building. The fringe field is predominantly from the EF coils, with the OH coils adding about 6% and the plasma cancelling about 12% of the EF coils' contribution. For distances R greater than about 30 m, the field is given by

$$B = 12.39 \times 10^6/R^3 \qquad (6)$$

with B in gauss and R in meters. Contours of constant field appear in Fig. 9-31, superimposed on the site plan. Several points should be mentioned.

1. No building other than the reactor building itself (in which there are no personnel) lies within the 200 G contour, which traditionally is the point at which one worries about steel tools and other objects being pulled into the magnet.

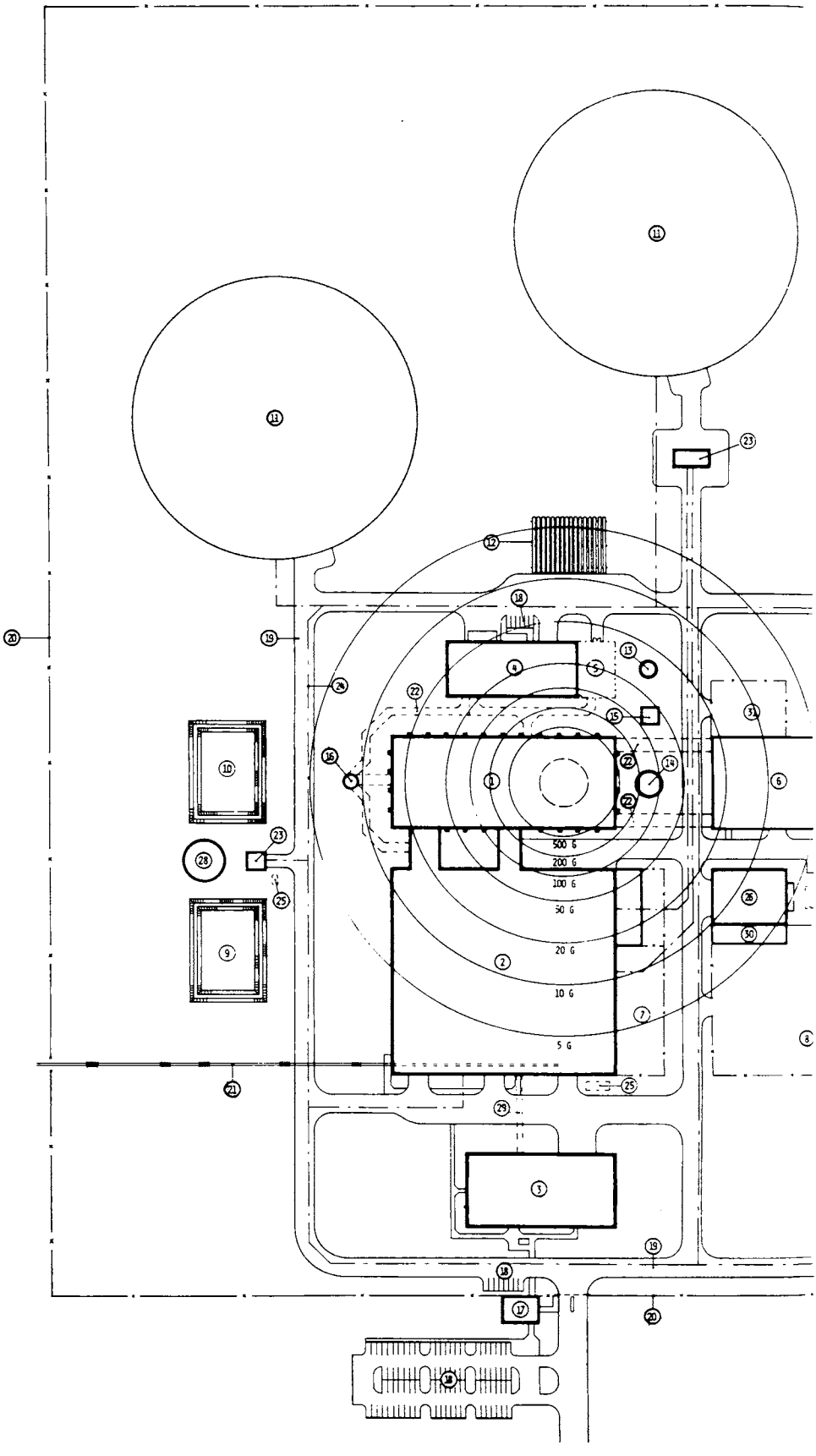

Figure 9-31. Maximum STARFIRE f

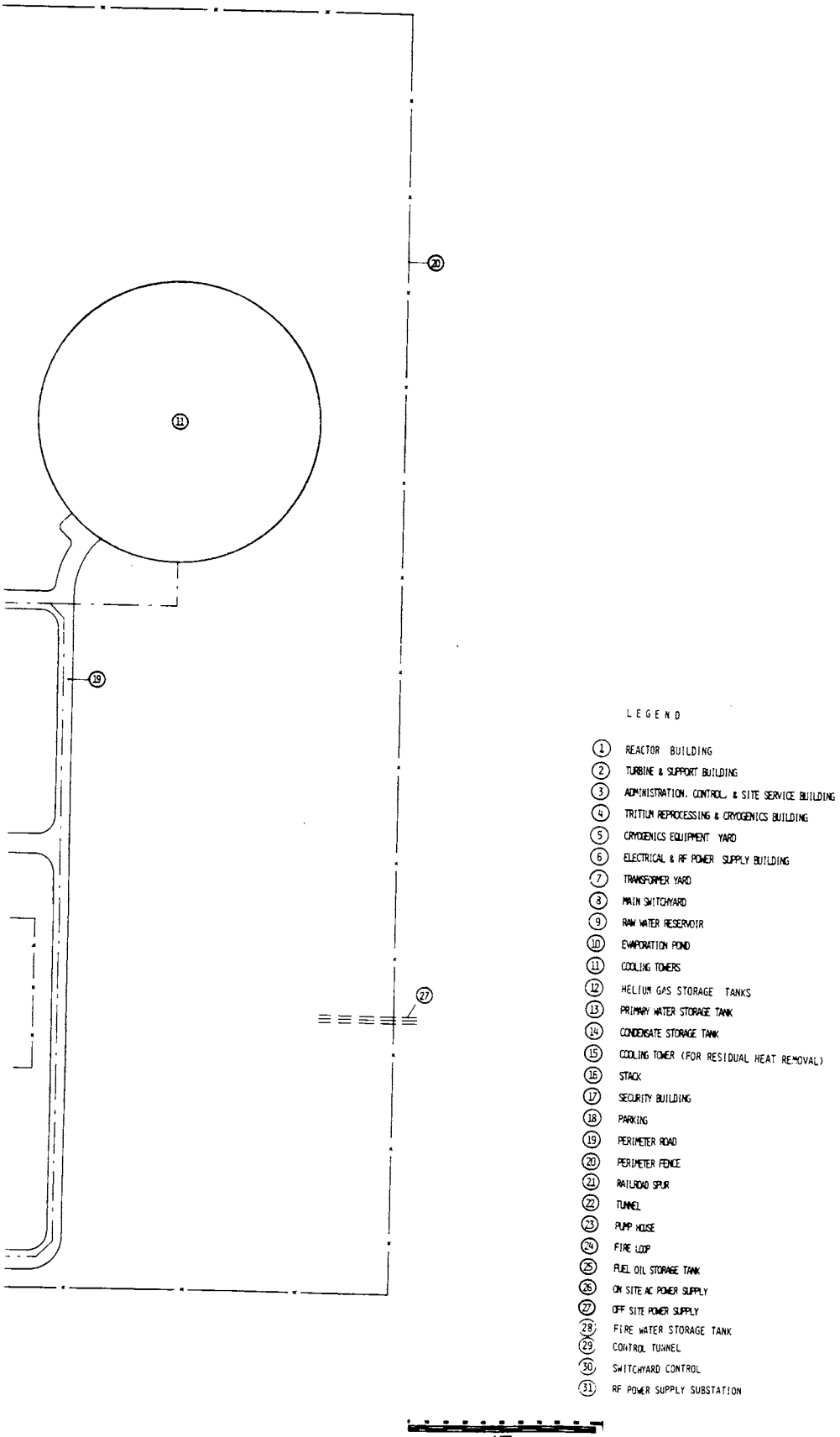

field, superimposed on site plan.

2. No one will normally work within the 100 G contour, which was specified as the interim safety standard for an eight-hour work day.

3. The cryogenics building lies almost entirely outside the 100 G contour. Studies at the Francis Bitter National Magnet Laboratory show that cryogenics and refrigeration systems for superconducting magnets are capable of performing in a 200 G environment.

4. The control room lies far outside the 5 G contour. Other sensitive controls in other buildings can be located in magnetically shielded rooms if necessary.

5. The field outside the perimeter fence is everywhere less than 5 G. In fact, the highest field at the perimeter fence is 3.1 G.

In conclusion, the fringe field from the magnets presents no safety problems.

References

1. "ETF Interim Design Description Document," ETF Design Center, Oak Ridge National Laboratory (1980).

2. J. D. Thompson, J. J. Wollan, B. Turch, R. I. Scherman, "Losses in a Build-up Conductor for Large Pulsed Coils," Proc. 8th Symposium on Engineering Problems of Fusion Research San Francisco (1979) pp. 1739-1742.

3. W. J. Carr, Jr. "Parallel Field Losses in Twisted Miltifilament Superconductors," Proc. 6th Symposium on Engineering Problems of Fusion Research, San Diego, (1975) pp. 152-155.

4. R. J. Roark and W. C. Young Formulas for Stress and Strain, Fifth Edition, McGraw Hill, New York, (1975) p. 273.

5. G.A. TNS Project, Status Report for FY-78, General Atomic Company, GA-A15100, Vol. VI (1978).

6. John R. Purcell, "Experience with Quench Protection of Multi-Megajoule Superconducting Coils," International Symposium on Superconductive Energy Storage, Osaka, Japan, (1979).

Table of Contents

Table of Contents (cont'd)

List of Figures

List of Figures (cont'd)

List of Figures (cont'd)

List of Figures (cont'd)

List of Figures (cont'd)

List of Figures (cont'd)

List of Tables

List of Tables (cont'd)

List of Tables (cont'd)

List of Tables (cont'd)

List of Tables (cont'd)

10.0 FIRST-WALL/BLANKET

The primary functions of the first-wall/blanket of a commercial tokamak reactor are to provide the first physical barrier for the plasma, to convert the fusion energy into sensible heat and provide for the heat removal, to breed tritium and provide for tritium recovery, and to provide some shielding for the magnet system. The first wall must withstand high particle and energy fluxes from the plasma, high thermal and mechanical stresses and elevated temperature operation. Also, the wall must not be a source of excessive plasma contamination. The first wall may or may not be integral with the blanket. The blanket must withstand high neutron fluences, elevated temperature operation, thermal and mechanical stresses, and be compatible with the chemical environment, the plasma and the vacuum.

In the present study, the technological and design aspects of various first-wall/blanket concepts have been considered in the selection of potentially viable designs for STARFIRE. The objectives of the present study involve identification of key technological constraints of candidate tritium-breeding-blanket design concepts, establishment of a basis for assessment and comparison of the critical problem areas and design features of each concept, and development of optimized first-wall/blanket designs for STARFIRE. The major emphasis has been placed on the development of a blanket design that is safe and environmentally acceptable. The primary guidelines established to meet these criteria are low tritium inventory in the blanket, minimal long-lived activation products and minimal stored energy.

Since breeding of tritium is considered essential, and since lithium is the only viable tritium-breeding medium, lithium in some form is required in the blanket. On the basis of engineering and design considerations, liquid lithium provides many advantages for the tritium breeder; however, because of perceived safety problems associated with a liquid lithium system, an *a priori* decision was made to focus the present study on the use of solid lithium compounds for breeding. Although previous studies have assessed the viability of alternate blanket options,[1] a technical evaluation of the design and safety problems associated with liquid lithium, liquid lithium alloy, and molten salt breeding materials was not performed in the present study. The primary objective was to assess the design and performance characteristics of a blanket concept based on solid tritium breeding materials.

Important materials properties and the major parameters that impact materials selection and design criteria are discussed in the following section. Subsequent sections in this chapter summarize the design issues and constraints imposed by the various blanket concepts. Also included in this chapter are analyses conducted to evaluate the tritium release characteristics from the breeder materials, the neutronics performance, the thermal hydraulics performance, structural limitations and predicted lifetime, electromagnetic effects, and safety. Based on results of the analyses performed, a reference blanket design for STARFIRE is proposed. Details of the reference design are presented in Sec. 10.9.

The development of the reference STARFIRE first-wall/blanket design involved numerous tradeoffs in the materials selection process for the breeding material, coolant, structure, low-Z coating, neutron multiplier and reflector. The coolant and structural material selections were greatly influenced by the choice of the solid breeder concept which was used as a basis for the STARFIRE design. The most important criteria considered in the selection of potentially viable solid breeding materials include breeding performance, chemical stability, compatibility and tritium release characteristics. Of the two types of solid breeding materials considered as primary candidates, viz., intermetallic compounds and oxide ceramics, only selected ceramics appear to have satisfactory tritium release characteristics. The α-$LiAlO_2$ is selected for the reference design on the basis of the best combination of these critical materials requirements. It is one of the most stable compounds considered and compatibility should not be a major problem; however, adequate tritium breeding is attainable only with the aid of a neutron multiplier. The high tritium solubility and greater reactivity with the structural materials were primary factors in the elimination of Li_2O as the reference breeding material.

Pressurized water, both H_2O and D_2O, and helium were considered for the coolant. Major concerns regarding the use of helium relate to difficult neutron shielding problems, large manifold requirements, leakage into plasma

chamber, lower tritium breeding because of the large structure requirements and the high temperatures required for the energy conversion system. An acceptable structural material for use with high temperature helium in a radiation environment has not been identified. Also, design constraints associated with the use of helium as a first-wall coolant appear to be prohibitive. Major advantages of the water coolant are its characteristically low operating temperature and its excellent heat transfer characteristics. However, the use of water with the intermetallic compound breeder materials is probably not acceptable because of the high reactivity, and hence, safety concern. Although D_2O has several neutronic advantages compared to H_2O, the cost is considered prohibitive.

The choices of breeding material and coolant limit the number of viable candidate structural materials. Key factors in the selection of the advanced austenitic stainless steel relate to the steady state reactor operation and the low operating temperatures characteristic of a water-cooled system. Because of the high thermal stress factor associated with austenitic stainless steel, acceptable first wall lifetimes could not be attained with a cyclic burn. Also, radiation damage effects are less severe at the proposed operating temperatures than at temperatures above 500°C.

The low-Z coating concept for the first-wall is incorporated as part of the plasma impurity control system. The low-Z coating concept provides flexibility in that the structural material can be selected primarily on the basis of structural requirements and the coating can be selected primarily on the basis of surface-related properties. Favorable properties such as high thermal conductivity, high heat capacity and compatibility with hydrogen were important considerations in the selection of beryllium as the first-wall coating/cladding material. A primary consideration in the selection of the candidate coating/cladding is that it can be used on all components exposed to the plasma. This is important because considerable redistribution of the material throughout the chamber is expected as a result of sputtering and ablation.

An effective neutron multiplier is required to obtain adequate tritium breeding with the $LiAlO_2$. Two candidate materials are proposed. Beryllium provides good neutronics performance and can be easily incorporated into the blanket design since it has low density, high thermal conductivity and high heat capacity. Because of the concern regarding limited resources of beryllium an alternate neutron multiplier, Zr_5Pb_3, is also proposed. This compound retains some of the beneficial neutron characteristics of lead but remains solid at the operating temperatures.

Low activation, low cost and inherent safety characteristics were key factors in the selection of graphite over water and stainless steel as the reflector.

A schematic diagram of the reference STARFIRE blanket concept is given in Fig. 10-1 and the key reference parameters are summarized in Table 10-1. The water-cooled blanket module, with a thickness of 68 cm, consists of 1-cm thick first wall, a 5-cm thick neutron multiplier, a 1-cm thick second wall, a 46-cm thick breeding zone, and a 15-cm thick reflector zone that contains the blanket support structure and the manifolding. The modules are 2-3 m wide by $\sim$ 3 m high depending on the location within the reactor. The module walls and all support structures in the high-radiation zone are fabricated from an advanced low-swelling austenitic stainless steel. All internal structure is integrally cooled to remove the nuclear heating and maintain the structure below 400°C.

The first wall, which is a water-cooled austenitic stainless steel panel coil, is an integral part of the blanket module. The corrugated plasma side of the first-wall panel is constructed of 1.5-mm thick advanced austenitic stainless steel. The 3.5-mm thick back plate is formed from the same material. The pressurized water coolant is maintained between 280 and 320°C throughout the first wall and blanket. For the average neutron wall loading of 3.6 MW/m^2, the average surface heat flux on the first wall is 0.92 MW/m^2

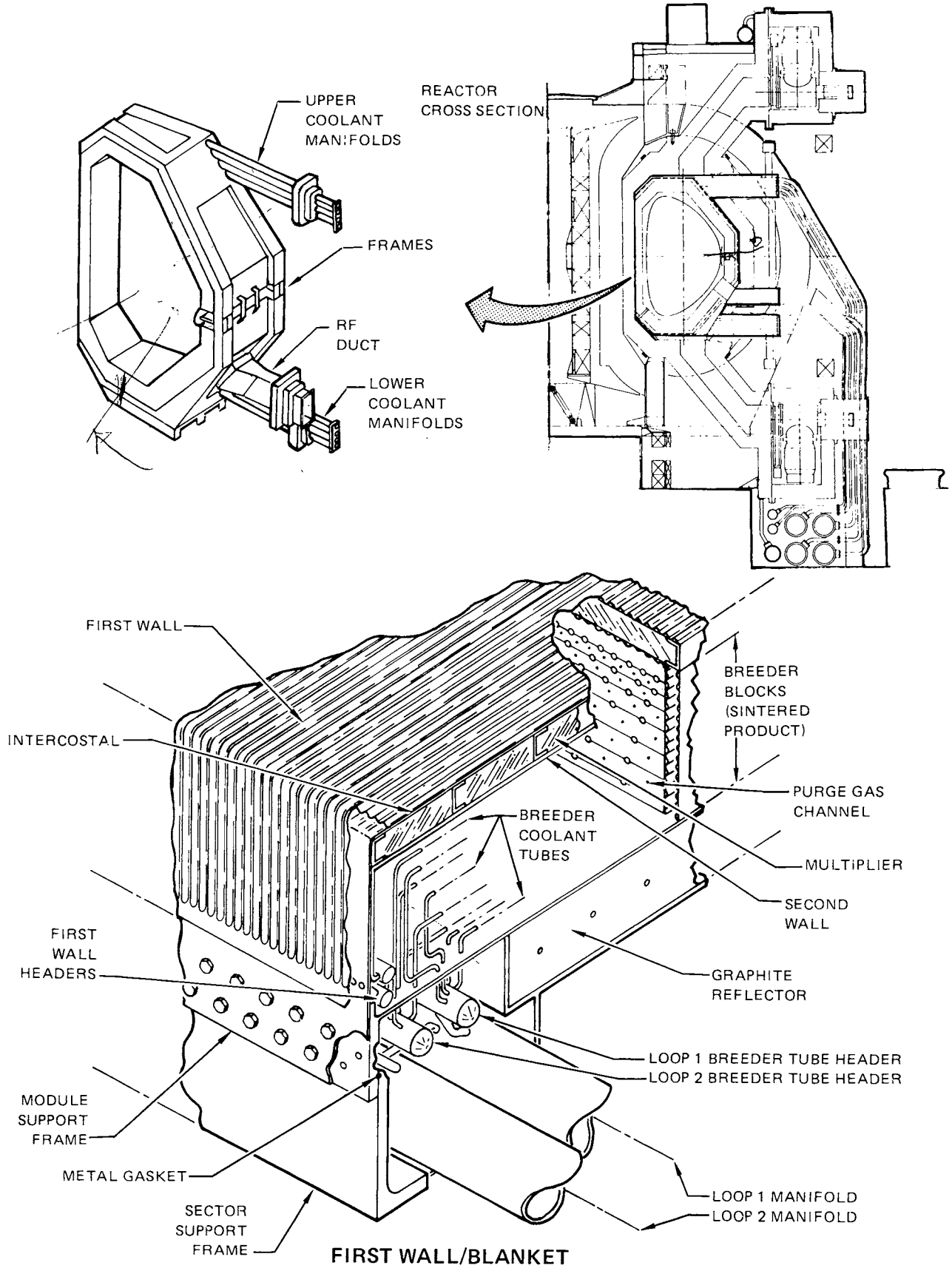

Figure 10-1. STARFIRE blanket concept

Table 10-1. Summary of First-Wall/Blanket Design Parameters

First-Wall	
Form	Be-coated panel
Structural material	Austenitic stainless steel[a]
Outer wall structural thickness, mm	1.5
Maximum structural temperature, °C	<423
Coating/cladding	Beryllium
Coating/cladding thickness, mm	1.0
Coolant	Pressurized water, H_2O
Coolant outlet temperature, °C	320
Coolant inlet temperature, °C	280
Coolant nominal pressure, MPa	15.2
Coolant velocity, m/s	6.1

Neutron Multiplier		
Material Options	Be	Zr_5Pb_3
Maximum temperature, °C	490	840
Thickness, m	0.05	0.05
Theoretical density, g/cm^3	1.8	8.9
Effective density, %	70	100
Total mass, kg	51,800	356,000

Breeding Region	
Structural material	Austenitic stainless steel[a]
Maximum structural temperature, °C	425
Breeder material	α-$LiAlO_2$ (natural Li with Be) (60% ^6Li with Zr_5Pb_3)
Theoretical density, g/cm^3	3.4
Effective density, %	60
Grain size, 10^{-6} m	0.1
Maximum/minimum temperature, °C	850/500
Region thickness, m	0.46
Coolant	Pressurized water, H_2O
Coolant outlet temperature, °C	320
Coolant inlet temperature, °C	280
Coolant nominal pressure, MPa	15.2
Tritium processing fluid	He (0.05 MPa)

Reflector	
Material	Graphite
Thickness, m	0.15
Maximum temperature, °C	<800
Structure	Austenitic stainless steel (low Mo)
Structure temperature, °C	300-400

[a] Prime Candidate Alloy, an advanced titanium-modified Type 316 austenitic stainless steel.

with a peak-to-average value of $\sim$ 1.2. The maximum structural temperature in the stainless steel wall is $\sim$ 423°C for the reference conditions. For steady state operation at these relatively low temperatures, an estimated wall design life of six years is considered reasonable for the advanced austenitic stainless steel. The proposed panel-type construction provides integral cooling of the blanket wall and avoids the necessity for a large number of pressure boundary tube welds in the high radiation zone. Also, the panel-type structure is perceived to have less vibration problems than an unsupported tube bank.

A $\sim$ 1-mm thick beryllium coating or cladding on the first wall serves to protect the plasma from the high-Z wall material. This thickness will provide sufficient material to withstand the predicted surface erosion for the reference blanket lifetime of six years. The beryllium coating/cladding on the inboard wall will also accommodate the projected number ($\sim$ 10 per wall lifetime) of plasma disruptions for the assumed conditions.

A 50-mm thick neutron multiplier is placed directly behind the first wall to permit adequate breeding with the $LiAlO_2$ breeding material. Two neutron multiplier options, beryllium and Zr_5Pb_3, are carried in the reference design. Beryllium is generally considered to be the most favorable neutron multiplier, however, resource limitations are a major concern. The present analysis indicates that beryllium requirements for several hundred reactors are only a few percent of the estimated U.S. beryllium reserves. An important part of the present study was to provide an alternative to beryllium. The Zr_5Pb_3 with an estimated melting temperature of 1400°C provides some of the benefits of a lead multiplier while maintaining the design simplicity of the solid materials. Approximately 30% of the neutron heating is deposited in the multiplier zone. The back side of the first-wall panel and a water-cooled panel (second wall) between the multiplier and breeder region provides cooling that maintains the maximum multiplier temperature at 490°C for beryllium and 840°C for Zr_5Pb_3. Structural webs between the first and second walls provide support for the first wall. The overall reactor analyses of the energy conversion system, the shield, the remote maintenance and repair, and safety are based on the blanket design option with the Zr_5Pb_3 neutron multiplier.

The 46-cm tritium-breeding zone consists of a packed bed of α-$LiAlO_2$ with 1.25-cm diameter stainless steel coolant tubes spaced appropriately throughout the zone to maintain a maximum breeder temperature of 850°C (Fig. 10-2). The spacing of the horizontal tubes increases from $\sim$ 2 cm at the front of the breeder zone to $\sim$ 10 cm at the back. There are approximately 60,000 coolant tubes in the blanket. The nominal coolant pressure is 15.2 MPa (2200 psi) with a coolant inlet temperature of 280°C and an outlet temperature of 320°C. The relatively low temperature of the austenitic stainless steel tubes (< 400°C) and the oxide film on the water side of the tubes provide an adequate tritium barrier for inleakage into the coolant. Natural lithium is used for the beryllium neutron multiplier option; however, 60% enriched ^6Li is required to achieve adequate tritium breeding with the Zr_5Pb_3 neutron multiplier option. The $LiAlO_2$ is in the form of a low density (60%) sintered product with a tailored bimodal pore distribution, i.e., a small grain size (< 1 μm) and a fine porosity within particles that are fairly coarse ($\sim$ 1 mm) with a much coarser porosity between particles. The sintered $LiAlO_2$ is perforated with $\sim$ 2-mm diameter holes through which low-pressure (0.5 atm) helium passes to recover the tritium from the breeder. The low density ceramic with a tailored microstructure is proposed to facilitate percolation of tritium (as T_2O) to the helium purge channels. A breeder lifetime of six years before lithium burnup becomes excessive is considered feasible.

The reflector consists primarily of $\sim$ 15 cm of graphite. The support structure to which the blanket modules are attached also serves as the containment for the graphite reflector. In order to conserve space and improve the vacuum characteristics of the blanket, the manifolds and headers for the blanket are imbedded in the reflector region. The large number of coolant tubes are joined to the headers in a vented chamber that is isolated from both the breeder region and the vacuum chamber. This concept provides both safety and reliability benefits since the most probable coolant leakage problem is at the coolant tube-to-header welds. A coolant-tube weld failure in this chamber would not likely lead to coolant ingress into the breeder region. Also, a small leak at a weld would not destroy the vacuum, and therefore, might not require immediate reactor shutdown. Isolating the geometrically complex manifolds and headers from the plenum region with a relatively smooth rear-blanket surface should substantially improve the vacuum characteristics of the blanket. A modified austenitic steel with

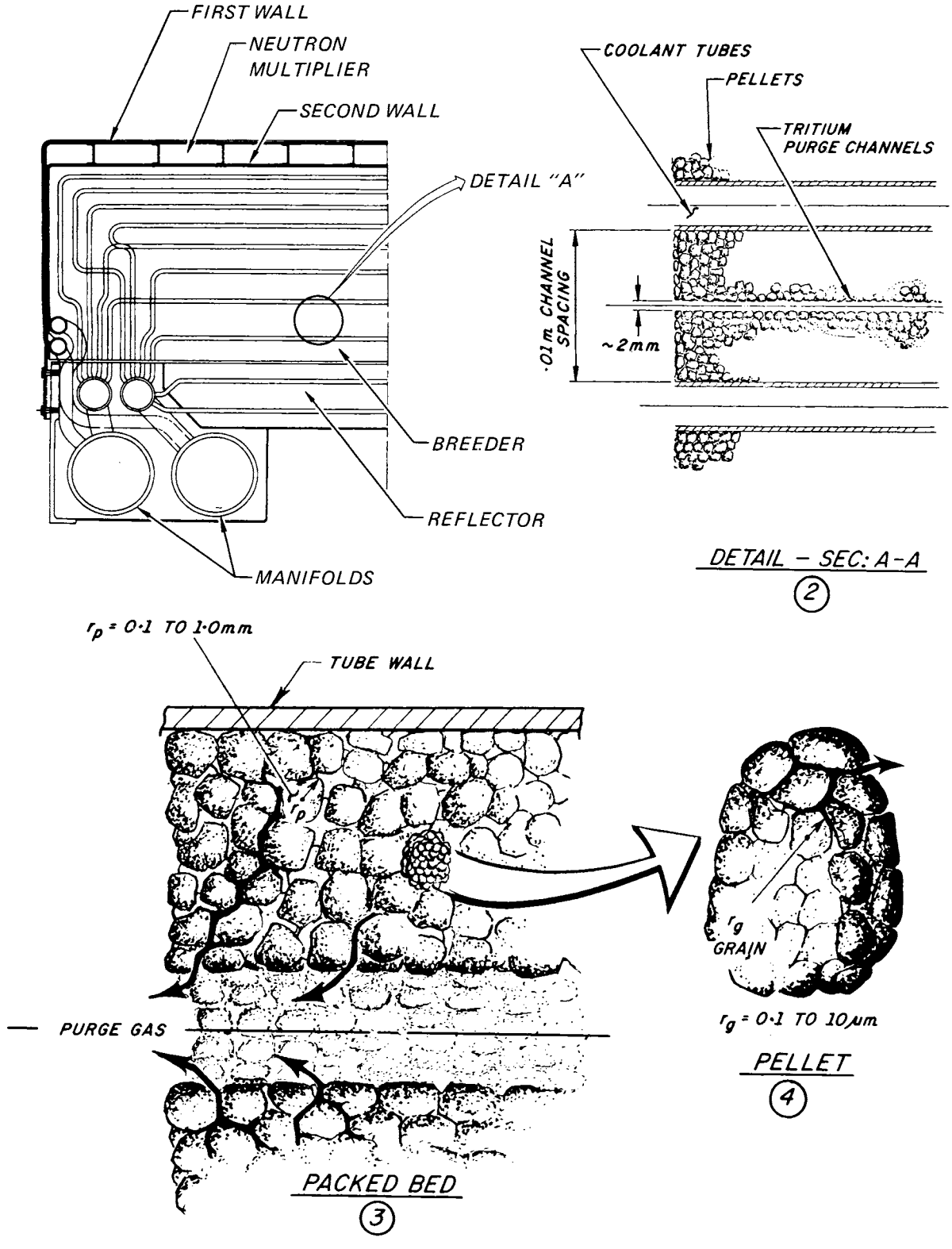

Figure 10-2. Schematic diagram of STARFIRE blanket concept showing solid breeder microstructure with bimodal pore distribution and tritium removal scheme.

low molybdenum content is used in this low-flux region to reduce the long-term activation.

A two-loop coolant system is provided in the blanket to reduce the consequences in the event of a loss-of-flow or loss-of-coolant accident. One loop provides coolant for the first-wall and alternate tube banks in the breeder region beginning with the first row of tubes. The second loop provides coolant for the second wall and the remaining coolant tubes in the blanket. Under the reference plasma shutdown conditions, cooling provided by either loop is sufficient to prevent excessive temperatures in all regions of the blanket. The two-loop concept will also reduce the pressure release and activation release in the event of a coolant-tube failure.

For plasma stability, an electrical conducting path equivalent to 2 cm of stainless steel is required near the first wall. The conductivity of the first wall and the neutron multiplier meets this requirement in the modules. Bimetallic contacts between the modules are provided adjacent to the multiplier region to complete the current path. Upon cooling, these contacts recess into the module wall to allow for sector removal.

The inner blanket is similar in most respects to the outer blanket just described. The major differences, which relate to the breeder zone thickness, the reflector, and the coolant flow direction, are designed to minimize the inner blanket/shield thickness. The breeding zone thickness is reduced from 46 to 28 cm and the graphite reflector is eliminated with a modest penalty on tritium breeding capability. Vertical coolant flow in the inner blanket eliminates the need for manifolds in the back of the blanket module, thereby improving the effective shielding capability of the inner blanket/shield.

10.1 MATERIALS SELECTION AND PROPERTIES

The development of the STARFIRE first-wall/blanket design involved numerous tradeoffs in the materials selection process for the breeding material, coolant, structure, neutron multiplier, and reflector. A major objective of the present study was to determine the key materials requirements for the various applications and to assess the potential of the candidate materials on the basis of the existing data base. Sensitivity studies were conducted to evaluate the impact of uncertainties in the materials data base

on operating constraints and to provide a basis for identifying critical materials development needs. This section summarizes (1) the important properties and criteria used in the selection of candidate materials, (2) the materials considered in the assessment and the proposed primary candidate materials for each application, and (3) the materials data base for the primary candidate materials. Additional materials property data are given in Appendix E.

The STARFIRE study has focused on the use of solid tritium-breeding materials, hence, the selection of other materials is strongly influenced by this decision. Table 10-2 summarizes the primary candidate materials considered for STARFIRE and indicates the materials selected for the reference design and the alternate material choices. The selection of the reference breeding materials was based to a great extent on the evaluation of the tritium release characteristics. Operating temperature constraints imposed by the breeding material and the structural material were important considerations in the selection of the reference coolant. Radiation effects and materials compatibility were major factors considered in the selection of the structural material. Because of the limited breeding capability of the $LiAlO_2$ and most of the other candidate breeding materials, a neutron multiplier is required in the reference design. Consistent with the choice of a solid breeding material, the reference neutron multipliers were selected from the few candidate materials that are solid at the operating temperatures. System compatibility and safety were key issues considered in the selection of the reflector.

10.1.1 Tritium Breeding Materials

An important function of a DT fusion reactor blanket is to breed tritium. Lithium in some form has been identified as the only element from which adequate tritium breeding appears feasible. Liquid lithium, molten lithium salts and solid lithium compounds have been proposed as the tritium-breeding material in various blanket concepts. Most of these proposed concepts and candidate breeding materials have been summarized in a recent blanket design study report.[1] In the STARFIRE study a major emphasis has been placed on safety and environmental acceptability, with primary goals that include low tritium inventory in the blanket, minimal long-lived activation products and minimal stored energy. Although a technical evaluation of the safety problems

Table 10-2. Candidate and Reference First-Wall/Blanket Materials

	Breeder	Coolant	Structure	Neutron Multiplier	Reflector
A.	α-$LiAlO_2$	Pressurized water	Austenitic SS (adv. alloy)	Be, Zr_5Pb_3	Graphite
B.	γ-$LiAlO_2$ Li_2ZrO_3	Pressurized water (D_2O)	Ferritic steel	Zr Pb	H_2O/SS
C.	Li_2SiO_3 Li_7Pb_2 Li_2O Li_2TiO_3	Helium Steam	Ti alloy V alloy Ni alloy	BeO Pb-Bi eut. Bi PbO	D_2O/SS ZrC SiC

A - Reference material for STARFIRE.

B - Alternate or backup materials

C - Other materials considered for STARFIRE.

associated with the liquid lithium system was not performed in the present study, the solid breeder materials are perceived to have some safety advantages. An *a priori* decision was made to focus the present study on concepts that utilize solid lithium compounds for the tritium-breeding material with a primary objective to assess the viability of blanket designs based on solid breeders. This section summarizes the important criteria for the selection of candidate solid breeder materials, the breeding materials considered for STARFIRE, and the properties of the primary candidate materials. Key areas where the data base is grossly inadequate are also identified.

10.1.1.1 Selection Criteria for Breeding Material

Several important criteria must be considered in the selection of candidate solid breeding materials for a fusion reactor blanket. The criteria evaluated in the present study include:

- tritium breeding capability
- chemical stability
- tritium recovery

- compatibility with system and environment
- physical properties
- radiation effects on properties
- fabrication considerations
- residual activation.

The most important initial criteria include the tritium breeding potential, chemical stability, and tritium recovery considerations. The other criteria relate primarily to design and operating constraints for the blanket.

Tritium Breeding -- The primary purpose of including lithium in a fusion reactor blanket is to breed tritium from $^{6}Li(n,\alpha)t$ and $^{7}Li(n,n'\alpha)t$ reactions. At least one triton must be bred for each fusion reaction, however, a production rate of $\sim$ 1.2 tritons per fusion neutron is typically required to compensate for plasma chamber surface coverage. Higher breeding ratios allow for increased design flexibility. The tritium breeding capability of lithium compounds is affected by the lithium atom density and number and species of other atoms in the compound. Most of the candidate compounds will require a neutron multiplier to provide adequate breeding capability. Li_2O and Li_7Pb_2 are among the few solid lithium compounds capable of adequate breeding without the aid of a neutron multiplier. Enrichment of ^{6}Li may also be essential to provide adequate breeding.

Chemical Stability -- Since much of the fusion energy is deposited in the breeding material, and since generation of sensible heat in the blanket is generally regarded as essential, the breeding material must operate at elevated temperature. To remain solid under proposed blanket operating conditions, the melting point and decomposition temperature must be relatively high and the vapor pressure of the compound, its constituents and related impurity compounds must be sufficiently low.

Tritium Recovery -- There is a clear consensus that in-situ tritium recovery from fusion blankets is by far the most desirable if not the only viable method of tritium recovery from solid breeders. Mobile solid blanket concepts have been proposed as a means of tritium recovery, however, the feasibility of this concept is questioned primarily on the basis of breeding capability and design complexity, particularly for the tokamak configuration.

The economics of a batch-type tritium recovery scenario is generally regarded as unacceptable. Important aspects of tritium release include:

- tritium diffusivity in the solid
- thermodynamic equilibria (T_2O)
- desorption kinetics
- grain boundary migration
- percolation through porosity in packed bed
- convective transfer in processing fluid.

Tritium recovery is important because it directly affects the blanket inventory which in turn impacts the system safety considerations, the required tritium breeding rate and the system economics.

Compatibility -- Compatibility of the lithium compounds with other materials in the system and with the environment is recognized as an important consideration with respect to both safety and operating limitations. Corrosion of the structural material, reactions with the coolant, and compatibility with the tritium recovery fluid or its impurities are of primary concern. Because the stoichiometry of the compounds will be changed by burnup of the lithium, the compatibility problems become more complex.

Physical Properties -- The physical properties of the candidate breeder materials are important to the viability of proposed blanket designs. Critical properties include melting and vaporization temperatures, thermal conductivity, density, thermal expansion, and heat capacity. In addition, electrical conductivity may be important to the response of the blanket during plasma disruptions. Some properties such as thermal conductivity are sensitive to microstructure, fabrication method and porosity.

Radiation Effects -- A fusion reactor blanket will be exposed to a severe radiation environment. For projected blanket lifetimes corresponding to 10-20 MW-y/m^2, the solid breeder material near the first wall could experience a neutron fluence of up to 5×10^{27} n/m^2 and a lithium atom burnup of 20-30 percent. Additional damage will also be produced by the highly energetic tritium and helium recoils produced by the n-Li reaction. It is important that properties of the breeding material not be severely degraded by the radiation damage. Of particular concern is the potential effect of radiation induced sintering on the tritium release characteristics. With lithium burnup of

several percent, the chemical composition of some of the solid breeder compounds could change enough to alter their physical characteristics.

Fabrication -- Methods for manufacturing solid lithium breeder compounds have not been extensively developed. Because of the importance of microstructure, grain size and interconnected porosity to the tritium release characteristics, processes to control these during manufacture are important. Several of the candidate materials react with air, H_2O, CO_2 and other common impurities. Techniques must be defined for proper handling of a blanket module between manufacture and use to ensure that the desired characteristics are maintained. Different materials will have different fabrication requirements which will impact the system economics. Although it appears that laboratory scale techniques are available for the candidate materials, extrapolation to an industrial scale will require further development.

Activation Concerns -- Neutron activation of the breeder material is an important consideration because of afterheat generation and waste disposal concerns. If the breeder material is to be recycled, activation could restrict manual fabrication and severely impact cost. In addition to activation of the primary constituents of the various materials, activation of impurities could be important.

10.1.1.2 Candidate Solid Breeding Materials

A wide spectrum of lithium compounds have been proposed as candidate breeding materials in the various fusion reactor system design studies conducted during the past several years.[1-6] These materials can generally be classified as binary ceramics, ternary ceramics, and binary intermetallic compounds. Table 10-3 summarizes those compounds considered to offer the most potential on the basis of tritium breeding capability and chemical stability under anticipated operating conditions.

Tritium recovery from solid breeding materials has been identified as a key consideration in the selection of the primary candidate breeding materials (see Sec. 10.3 for detailed analysis). Based only on the diffusion-controlled tritium release characteristics, the estimated operating temperature limits for the candidate solid breeding materials are given in Table 10-4. These results indicate that only the ceramics appear to have sufficient

Table 10-3. Potential Tritium Breeding Materials Based on Tritium Breeding and Chemical Stability Considerations

Breeder	M.P. °C	Li Atom Density g/cm^3	Stability	Tritium Breeding
Li_2O	1700	0.93	Significant vapor pressure above 1200°C (sublimes).	Neutron multiplier not required if breeding in inner blanket.
$LiAlO_2$	1610	0.27	Low vapor pressure ∿ 1400°C $\alpha \rightarrow \gamma$ phase transformation.	Neutron multiplier required. ^6Li enrichment for most multipliers.
Li_2SiO_3	1200	0.36	Reduced solidus (∿ 1030°C) if not stoichiometric. Crystalline/amorphous transformation.	Slightly better than $LiAlO_2$.
Li_4SiO_4	1250	0.54	Similar to Li_2SiO_3.	Slightly better than Li_2SiO_3.
Li_2TiO_3	1550	0.33	Limited data.	Questionable breeding even with very effective neutron multiplier.
Li_2ZrO_3	1616	∿ 0.33	Limited data.	Zr provides some neutron multiplication.
Li_2Si	760	0.36	Reduced solidus if not stoichiometric. Reacts vigorously with H_2O.	Neutron multiplier required.
LiAl	700	0.36	Reacts vigorously with H_2O.	Neutron multiplier required.
Li_7Pb_2	726	0.49	Reduced solidus if not stoichiometric. Reacts vigorously with H_2O.	Excellent breeding since Pb is an effective multiplier.
Li_3Bi	1145	0.47	Reduced solidus if not stoichiometric. Reacts vigorously with H_2O.	Excellent breeding since Bi is an effective multiplier.

Table 10-4. Temperature Limits of Solid Breeders Based on Diffusion-Controlled Tritium Release

Breeder	T_{min} (°C)[a]	T_{max} (°C)[b]
Li_2O	410	910
$LiAlO_2$	500	850
Li_2SiO_3	420	610[d]
Li_2TiO_3	420	820
Li_2ZrO_3	420	860
Li_4Si	480	350
LiAl	300	310
Li_7Pb_2	320	330
Li_3Bi	320[c]	580[d]

[a] Requires < 1 μm grain size; maximum tritium inventory of 1-2 kg from diffusive holdup. Modest allowance for radiation-induced trapping of T.

[b] Assumes significant radiation-induced sintering occurs above 0.6 T_m which increases diffusion path.

[c] Estimated values based on data for similar materials.

[d] Solidus temperature for nonstoichiometric compositions is much lower than melting temperature of stoichiometric compound.

temperature ranges for adequate tritium release. Major limitations and concerns for each of the candidate materials are summarized in Table 10-5. Although Li_7Pb_2 and Li_3Bi are particularly attractive from a neutronics viewpoint, the questionable tritium release characteristics and the compatibility concerns with water coolant prevent this material from being a primary candidate. The maximum operating temperatures are considered to be inadequate for a practical helium-cooled system.

The Li_2O is generally considered to be an attractive candidate because of its high lithium atom density and its potential for breeding without the aid of a neutron multiplier. The major questions regarding the viability of Li_2O as a breeding material relate to the thermodynamic equilibria with

Table 10-5. Assessment of Candidate Solid Breeder Materials

Material	Major Limitations
Li_7Pb_2, Li_3Bi	- Low melting temperature not appropriate for He coolant. - Reactive with H_2O - safety. - Unacceptable tritium release.
LiAl, Li_2Si	- Same as Li_7Pb_2. - Effective neutron multiplier required.
Li_2O	- Unacceptable tritium release (thermodynamic). - Compatibility with structure. - Chemical stability (LiOH).
$LiAlO_2$	- Effective neutron multiplier required. - Tritium release uncertain (T,ϕt).
Li_2SiO_3	- Effective neutron multiplier required. - Chemical and microstructural stability under irradiation. - Tritium release uncertain (T,ϕt).
Li_2ZrO_3	- Similar to $LiAlO_2$ except tritium release more questionable (thermodynamic).
Li_2TiO_3	- Similar to $LiAlO_2$ except tritium breeding more difficult (Ti).

T_2O and the impact on tritium inventory, to stability in the tritium processing fluid and to compatibility with candidate structural materials. Although the thermodynamic data base for the Li_2O-H_2O-LiOH system is not well established, calculations given in Sec. 10.3 indicate that acceptable tritium recovery may not be attainable because of the high tritium solubility for projected operating conditions. The calculated equilibria must be experimentally verified before Li_2O can be eliminated from consideration solely on this basis. Although limited data are available on the compatibility of Li_2O under conditions of interest, compatibility with the structural materials and stability in the tritium processing fluid are areas of much concern.

The Japanese have reported severe corrosion of several structural materials by Li_2O in short term (100 h) tests at temperatures above 800°C.[7] Preliminary compatibility tests conducted at Argonne National Laboratory have also indicated extensive corrosion of Type 316 stainless steel, a ferritic steel (HT-9) and Inconel 625 alloy after exposure to Li_2O at 600°C for $\sim$ 2000 h.[8] Although these results are preliminary and the purity of all materials have not been well characterized, indications are that corrosion may well be a serious problem. Additional effects produced by compositional variations in Li_2O that result from lithium burnup, e.g., LiOT formation, or by chemical interactions with the tritium-processing fluid, may be even more critical. Also, stress-corrosion phenomena could severely impact the integrity of the structural material.

Weight loss data for Li_2O exposed to helium with low moisture content[9] and predicted gas phase equilibria over Li_2O at high temperature[10] indicate that considerable mass transfer of lithium in the tritium processing stream may occur (see Appendix E). The weight-loss measurements on Li_2O indicate loss rates in excess of 1% per hour at temperatures of 1000°C. Primarily on the basis of these three concerns, Li_2O is not included as a primary candidate for the breeding material in STARFIRE.

The four ternary ceramics listed in Table 10-5 are all potential candidates and all will require use of a neutron multiplier. Except for tritium breeding, $LiAlO_2$ is considered the most favorable of these materials. The Li_2ZrO_3 has better breeding properties than the aluminate, but tritium inventory is predicted to be larger and other materials properties are less

well defined. The Li_2TiO_3 is similar to the aluminate, however, tritium breeding will be more difficult because of poorer neutronic performance of titanium. The Li_2SiO_3 should provide a better breeding performance than $LiAlO_2$ but compatibility and stability problems are of greater concern. The maximum operating temperature will be less because of the lower melting temperature. This limitation may be even more critical because of the nonstoichiometry that results from lithium burnup. Another major concern expressed about the use of the silicates is their well known tendency to form the amorphous (glass) structure. Microstructural changes under irradiation could significantly impact the tritium release characteristics.

Although considerable uncertainties exist in the materials data base for the candidate breeding materials, $LiAlO_2$ gives the greatest confidence for successful operation and is selected as the reference material.

10.1.1.3 Data Base for Primary Candidate Materials

The data base for the candidate breeding materials is given in Appendix E. Critical values for the primary candidates, viz., α- and γ-$LiAlO_2$ are summarized in this section. Most of the data have been obtained from materials' handbooks referenced in Appendix E; however, an excellent review of data for solid breeders has been published by Johnson, et al.[9] Table 10-6 summarizes the data base for $LiAlO_2$.

A low density (60%) sintered product of the α-$LiAlO_2$ is selected for the reference design to facilitate tritium recovery. The tailored microstructure (Fig. 10-2) with a bimodal pore distribution and a relatively high porosity should tend to optimize the tritium (T_2O) migration to the helium processing stream. As discussed in more detail in Sec. 10.3, very small grain size ($\sim$ 1 μm or less) is essential because of the very low tritium diffusivity. Since the kinetics of tritium migration will have such a major impact on the tritium inventory in the solid breeder blanket, this should be the dominant factor in establishing the desired structure. Preliminary analyses conducted as part of this effort (see Appendix E) provide a basis for selecting the microstructure; however, additional effort is required for further optimization. Determination of desirable microstructures, pore morphology, and porosity is of primary importance because critical

Table 10-6. Materials Data Base for $LiAlO_2$

Crystal Structure	α	Rhombohedral
	γ	Tetragonal
Density, g/cm^3	α	3.4
	γ	2.56
Molecular Weight		65.92
α-γ Transformation, °C		$\sim$ 900
Melting Temperature, °C		1610
Lithium Atom Density, g/cm^3		0.27
Coefficient of Thermal Expansion, $°C^{-1}$		12.4×10^{-6}
Heat Capacity, J/g·°K		1.6 (est.)
Thermal Conductivity, w/m·°K		(60% dense)
500°C		4.7 (est.)
800°C		3.5 (est.)
Stability		Low vapor pressure < 1200°C Appreciable vapor pressure > 1400°C
T Diffusion Coefficient, cm^2/s		
500°C		5×10^{-17} (est.)
800°C		5×10^{-11} (est.)
Chemical Compatibility		Slightly soluble in hot water Hygroscopic in air
Tritium Breeding		Requires effective neutron multiplier
Activation Products		^{26}Al
Radiation Damage		Swelling/densification (?) Tritium trapping Radiation-induced sintering

properties, such as thermal conductivity and effective density, strongly impact design and neutronic performance. Also, radiation effects, such as sintering, will be sensitive to the original microstructure.

The α-$LiAlO_2$ is preferred over γ-$LiAlO_2$ primarily because of its higher density (and hence, Li atom density) and because α-$LiAlO_2$ is the stable phase at the projected operating temperatures. Limited observations generally indicate that the γ-α transformation is very sluggish during thermal aging at temperatures below 900°C;[11] however, the kinetics will likely be enhanced under irradiation. Because of the substantial density change, this transformation is important. The relatively high porosity should accommodate considerable volume change, however, any transformation might significantly impact the grain structure and tritium release. One concern regarding the use of α-$LiAlO_2$ relates to the limited sintering temperature ($\sim$ 900°C) to avoid the γ transformation. Pressure-assisted sintering or other sintering aids, which may be necessary, will require further development. The proposed process for obtaining small grain size and desired porosity has been developed at Argonne for the fuel cell program.[12] Further development work[13] has shown that $LiAlO_2$ can be fabricated with a bimodal pore distribution, i.e., a small grain size and fine porosity within particles (agglomerates) that are fairly coarse ($\sim$ 1 mm) with a much coarser porosity between the particles. Additional information on fabrication of $LiAlO_2$ is given in Appendix E.

Although the data base for $LiAlO_2$ is greater than for most of the other candidate breeding materials, several properties are not well known. The thermal conductivity has been estimated from data for similar ceramics with allowances for porosity. The estimated temperature-dependent curve for 60% dense $LiAlO_2$ conforms to the conductivity shown in Fig. 10-3 for Li_2O with $\sim$ 90% theoretical density. Since the thermal conductivity is sensitive to the microstructure, reliable data must be obtained on material with the appropriate microstructure.

Since tritium diffusivity data are not available for $LiAlO_2$, the estimates given in Table 10-6 are based on hydrogen diffusivity in single crystal Al_2O_3.[14] Data on polycrystalline material are not relevant for the present analyses. The diffusivity of hydrogen in these types of ceramics are

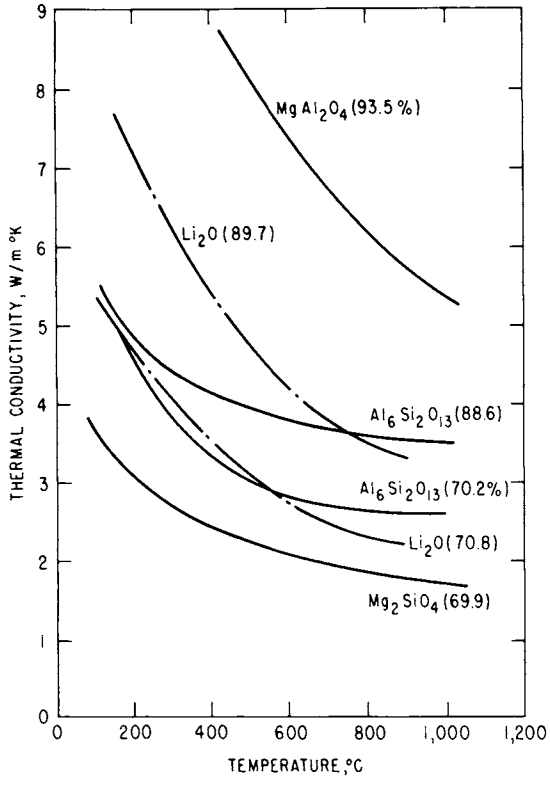

Figure 10-3. Thermal conductivities of oxides with effective densities given in parentheses.

generally quite similar when considered in terms of temperature variations. For example, single crystal Al_2O_3 and BeO have diffusivities of $\sim 5 \times 10^{-14}$ cm^2/s at temperatures that differ by only about 75°C. Data for Al_2O_3 should give a reasonable approximation for the present study.

Of the candidate ceramics considered, $LiAlO_2$ is probably the most stable chemically. It is slightly soluble in hot water and is moderately hygroscopic in air. Further studies on the stability under proposed conditions, i.e., moist He with excess tritium or hydrogen, should be conducted. Although the chemical energy release should be small in the event of a coolant leak into the breeder, the high surface-to-volume ratio of the porous breeder could lead to substantial pressure transients within the module if the high pressure water leaks rapidly into the high temperature breeding zone.

Since very little radiation damage data exist for $LiAlO_2$, the following assessment is mostly qualitative. The major considerations are possible swelling or densification, enhanced recrystallization or sintering caused by the radiation, and trapping of tritium by defects or cavities. An important aspect of

the radiation damage analysis relates to the effects of the high energy tritium and helium with recoil ranges of $\sim$ 30 and $\sim$ 4 μm, respectively. Swelling could occur as a result of vacancy coalescence, gas generation, or α-γ transformation. In contrast to metals, helium is typically more mobile than hydrogen in ceramic oxides. Therefore, if low tritium inventories can be maintained, buildup of helium should not be excessive. The relatively high porosity proposed should accommodate some swelling with little impact on the structural containment. Some microcracking of the brittle ceramic may occur and must be accommodated in the design.

Recrystallization or sintering are believed to be extremely important since they may have a substantial effect on the tritium release characteristics (see Sec. 10.3). Thermal sintering characteristics of ceramic oxides are generally quite consistent, with significant sintering at $\sim$ 0.8 T_m (absolute melting temperature). However, enhanced sintering has been observed and is generally expected in a radiation environment. Since the high energy (MeV) tritium and helium recoils have ranges much greater than the proposed grain size, considerable ion-induced damage and intergranular sputtering are expected. The small grain size and fine pore structure desired for tritium release is probably more susceptible to radiation-induced sintering than a more coarse structure. Estimates of the radiation-induced sintering characteristics are based on observed data for mixed oxide fission reactor fuels that undergo fission product damage. Significant restructuring typically occurs at $\sim$ 0.6 T_m. For the present study a maximum temperature of 0.6 T_m or $\sim$ 850°C is recommended for $LiAlO_2$. Experimental verification is required for the appropriate microstructures and for conditions of target lithium atom burnups since stoichiometric changes and chemical interactions (excess T) may produce enhanced synergistic effects.

Radiation-induced trapping of hydrogen at defects has been observed in many materials and is predicted to occur in the $LiAlO_2$ and other candidate breeding materials. Probably the most pertinent data base for assessing this effect is the surface effects studies conducted as part of the fusion materials development program. The high energy deuterium and helium implant studies (see Refs. 15 and 16) have indicated substantial trapping of the light ions in surface regions. Trapping efficiencies as high as 50 at % have been observed in the surface regions of several materials.[17] The mechanisms

and effects observed in these studies are similar in many ways to the conditions anticipated in the blanket region. Although further analyses and experiments are needed for a more accurate assessment, radiation-induced tritium trapping may increase the diffusive holdup (see Sec. 10.3) by at least a factor of 10 and possibly as much as a few atomic percent tritium in the ceramic.

The thermochemical data for the H_2O-ceramic oxide systems are summarized in Sec. 10.3. Since complete data for the relevant phase equilibria do not exist, calculations based on ideal solution behavior have been used to estimate equilibrium tritium concentrations in the breeder materials as a function of T_2O pressure.

The neutronic data are summarized in Sec. 10.4 with the neutronics analysis.

10.1.2 Coolant Selection

The choice of coolant has a major impact on the selection of other blanket materials, e.g., the structural material, and upon the operating parameters of the reactor system. In all previous reactor studies only four types of coolants have been evaluated extensively, viz., lithium, helium, water and molten salts. Reference 1, which presents a review of those four blanket coolants, has been used as a basis for the assessment of the candidate coolants and the selection of the reference coolant for STARFIRE. Additional information is included in the STARFIRE Interim report[18] and in Appendix E. Since the choice of coolant also impacts the energy conversion system, shielding maintenance and repair, tritium systems, and reactor building design, important implications relevant to these systems are discussed in their respective chapters. This section focuses on the blanket implications and summarizes the important criteria for the selection of candidate coolants, the coolants considered for STARFIRE, and the important properties of the primary candidate materials.

10.1.2.1 Selection Criteria for Coolant

Several important criteria must be considered in the selection of the coolant for a fusion reactor blanket. The criteria evaluated in the present study are summarized in Table 10-7. Each type of coolant has characteristic

Table 10-7. Considerations for Selection of Coolant

Physical Properties

- operating temperature limits (T_{max}, T_{min}, ΔT)
- operating pressure
- heat capacity
- thermal conductivity
- electrical conductivity

Thermal-Hydraulic Characteristics

- heat transfer coefficient
- heat flux limits
- velocity requirements
- pumping power requirements
- containment difficulty

Neutronic and Radiation Properties

- neutron moderating properties
- induced radioactivity
- shielding characteristics
- neutron absorption properties (breeding)
- radiolytic decomposition

Chemical Compatibility

- reactivity with environment
- compatibility with reactor materials

Tritium Considerations

- tritium solubility and activity
- processing difficulty

Magnetic Interactions

- magneto-hydrodynamic effects

Economics and Resources

- cost
- resources and availability

Maintenance and Repair

- cleanup of spills
- damage from breach of containment

compatibility problems with other blanket materials and a limited range of acceptable operating temperatures.

Since liquid lithium was not included as a candidate breeding material in the STARFIRE design, liquid metals were not considered for the coolant. It makes little sense to use lithium as the coolant without also using it as the breeding material. Although molten salts have some advantages compared to water as a reactor coolant, primarily low pressure operation, the disadvantages generally outweigh the advantages. Hence, molten salts were not seriously considered for the STARFIRE design. Pressurized water and helium remain as the primary candidates. The relative merits of H_2O and D_2O were evaluated in some detail. Although steam and boiling water possess some attractive features, the apparent advantages of these systems were not sufficient to include them as primary candidates in the present study. In general, the comparative analyses presented in this section for the choice of coolant are qualitative. More quantitative support is contained in the following sections on neutronics, thermal hydraulics, tritium recovery and mechanical design.

10.1.2.2 Helium Coolant

Helium has been used as a fission reactor coolant and has been proposed as a candidate fusion reactor coolant. The major incentive for the use of helium is the inherent safety associated with its being chemically inert. Also, helium does not interact significantly with the magnetic field (MHD effects) and it does not produce any significant radioactivity. Key problem areas related to the use of helium as a coolant include the relatively high temperature requirements for acceptable energy conversion efficiencies, the possible leakage of helium into the plasma chamber, relatively low first-wall heat flux limits, significant pumping power requirements, and the relatively large manifolds required. The properties of helium are well documented in handbooks and fission reactor studies, and therefore, are not reproduced here in detail. Table 10-8 summarizes the ranges of operating parameters typically considered for fusion reactor first-wall/blanket applications.

Table 10-8. Typical Helium Operating Parameters

Pressure:	5-10 MPa
Maximum Temperature:	500-1000°C
Coolant Velocity:	30-100 m/s
Film ΔT:	100-250°C
C_p (5 MPa):	5.2 J/g·°K

Table 10-9 summarizes the generic favorable and unfavorable characteristics of helium coolant. Since high helium temperatures are required to permit efficient energy conversion, high temperature structural materials are generally required. Coolant outlet temperatures of 600-800°C have been proposed in most helium-cooled power reactor designs.[1] Nickel-base alloys are generally proposed for the structural material in helium-cooled designs because of their high temperature properties. However, as discussed in Sec. 10.1.3, the predicted radiation damage resistance of these alloys does not appear to be adequate for acceptable blanket lifetime. At present, structural material limitations are believed to limit the maximum outlet temperature to ∿ 500°C. This restriction severely compromises many of the advantages of helium coolant.

Experience in helium-cooled fission reactors and other high pressure helium systems has demonstrated the difficulty in containment of high pressure helium in complex elevated-temperature systems. It is questionable whether high pressure helium can be adequately contained in the complex geometries required and under the severe conditions encountered within the vacuum chamber of a fusion reactor. Proposed tube-type[1] and cannister[19] first wall designs typically require in excess of 50,000 to 100,000 pressure-tight welds in the vacuum chamber. Leak rates as high as the helium-generation rate in the plasma (∿ 50 cm^3/s STP) would substantially impact the plasma performance and the impurity control system. There is generally a tradeoff between pumping power and first-wall heat flux. Previous analyses have indicated that surface heat fluxes in excess of 0.5 MW/m^2 are difficult to accommodate without excessive structural material temperatures or relatively high pumping power.[1]

Table 10-9. Assessment of Helium as Coolant for STARFIRE

Unfavorable	Favorable	Characteristic
X		Leakage and leak detection in first wall
X		Difficult shielding (large penetrations)
X		Large manifolds and ducts
	X	Chemical reactivity
X		Low first-wall load limit
X		Requires high coolant outlet (structure) temperature
	X	Relatively easy cleanup of leak
X		Relatively high pressure
	X	Magnetic interaction (MHD)
X		High pumping power
	X	Potential for tritium processing
X		Poor heat transfer coefficient
	X	Compatible with conventional structural materials
X		High coolant velocity to enhance heat transfer
	X	Existing technology base
X		Low thermal inertia (heat capacity)

Because of the large duct size typically required for helium and the fact that helium does not significantly attenuate neutrons, shielding is a major problem for helium-cooled systems. The large ducts that must pass between the magnets create serious neutron streaming problems. Also, economic penalties occur because of the lack of attenuation in the inner blanket that results from relatively large helium coolant channels and manifolds.

10.1.2.3 Pressurized H_2O

Pressurized water is an attractive coolant because of its good thermal-hydraulic properties. The major problems associated with water coolant

relate to its high operating pressure, low operating temperature, reactivity with some candidate breeding materials and difficult tritium extraction.

Water has a high heat capacity (4.46 J/g·°K) and a density of ∿ 0.95 g/cm^3 for the conditions of interest. The critical temperature is 374°C with a critical pressure of 20.4 MPa. The equilibrium pressure at 320°C is 10.4 MPa.

Typical operating pressures in pressurized water fission reactors are ∿ 14 MPa with maximum temperatures of ∿ 320°C. This provides an overpressure equivalent to ∿ 23°C. With a 320°C maximum coolant temperature, the efficiency of the energy conversion system is limited theoretically to ∿ 36%. However, problems associated with higher pressure usually outweigh the benefits of the modest efficiency improvements attainable at higher temperatures.

Water reacts vigorously with lithium at elevated temperatures and to a lesser degree with the intermetallic lithium compounds considered for the breeding materials. For this reason concepts incorporating pressurized water in blankets with intermetallic lithium compound breeding materials are probably not viable. The chemical reactivity of water with the candidate ceramic breeding materials is much less, and therefore, not considered prohibitive. The major concern involves pressure transients that could arise from injection of pressurized water into the high temperature porous ceramic in the event of a coolant tube leak.

Tritium recovery from water is very difficult and expensive. Therefore, tritium migration into the coolant from the vacuum chamber or the breeding zone should be minimized. Characteristic oxide films formed on coolant channel walls tend to provide excellent tritium barriers. Analyses of this problem are presented in Chap. 14.

Water also serves as an efficient neutron moderator. This is particularly detrimental for systems which require a neutron multiplier since a high energy neutron spectrum typically provides much better neutron multiplication. For this reason the amount of water in the first wall should be minimized. Quantitative analyses are presented in Sec. 10.4.

10.1.2.4 Pressurized D_2O

In most respects D_2O is similar to H_2O as a coolant. The primary differences relate to the neutronics performance and tritium recovery. As

discussed in more detail in Sec. 10.4, the degraded moderating properties of D_2O relative to H_2O result in significantly better tritium-breeding performance. Also, since deuterium is a fuel component, the degree of isotopic separation required in the recovery of tritium from the coolant is reduced for the case of D_2O.

The major disadvantage of D_2O relative to H_2O relates to cost. The estimated cost of D_2O is $\sim$ 200 \$/kg. For the total inventory required and the anticipated makeup, the economic penalties associated with the use of a D_2O coolant appear to be excessive.

10.1.2.5 Reference Coolant

Pressurized H_2O is selected as the reference coolant for STARFIRE. Further justification for this choice is given in the following sections. Important advantages associated with the choice of water coolant include: (1) the operating temperature is compatible with both the breeding material and the structure, (2) the neutronics performance appears to be acceptable, (3) first-wall heat fluxes can be accommodated, (4) manifold sizes are tolerable, and (5) the recirculating power is minimal. The major penalty associated with the pressurized water system is the limited energy conversion efficiency attainable. The primary safety concern relates to the pressure transients that arise in the event of a coolant leak into the breeding zone.

10.1.3 Structural Materials

The structural materials for the STARFIRE first-wall/blanket must maintain their mechanical integrity and dimensional stability for adequate lifetimes under the severe radiation, thermal, chemical and stress conditions imposed in a fusion reactor environment. The candidate materials must be resistant to radiation damage, capable of elevated temperature operation, compatible with other blanket materials, and capable of withstanding high surface heat fluxes. In addition, the structural material should have adequate resources and be readily fabricable. The selection of the reference structural material for STARFIRE is strongly influenced by the choice of breeding material and coolant, both of which impact the reactor operating characteristics. The goal lifetime for the first wall/blanket is 6 years,

which corresponds to an average integrated neutron wall loading of $\sim$ 16 MW/m^2 (see Sec. 10.5 for lifetime evaluation). This section summarizes the important criteria for the selection of candidate structural materials, the structural materials considered for STARFIRE, and the key properties of the primary candidate alloys. Reference 1 is used as a basis for the present analysis and additional materials properties data are presented in Appendix E.

10.1.3.1 Selection Criteria for the Structural Material

A large number of materials properties and operating parameters influence the selection of the structural material. Key properties include physical, mechanical, chemical and neutronic properties. Key parameters include operating temperatures, heat fluxes, lifetime neutron fluences, and stress requirements. Table 10-10 lists the critical properties of the structural materials that have been used in the assessment of candidate materials. A low coefficient of thermal expansion, a high thermal conductivity, and a low elastic modulus are important physical property characteristics that are required to minimize the temperature and stress gradients. A high heat capacity will help minimize the temperature gradient during thermal shock conditions. High strength materials are desirable since the allowable stresses are based upon the tensile and creep strength of the materials. A high ductility is desirable to accommodate strain transients during off-normal conditions. A high degree of radiation swelling and creep can produce dimensional changes that interfere with normal operation or can lead to component failure. Fatigue and crack growth, which can lead to failure, are largely dependent upon design and the reactor operational cycle. A cyclic mode of operation that imposes a large cyclic stress could result in a premature failure compared with a continuous mode of operation.

10.1.3.2 Candidate Structural Materials

A number of potential structural materials have been surveyed for STARFIRE. Six classes of materials which have been considered in some detail include austenitic stainless steels, ferritic stainless steels, nickel alloys, titanium alloys, vanadium alloys, and niobium alloys. Aluminum alloys were not considered because of their low operating temperatures, and molybdenum alloys were not considered primarily because of difficulties in fabrication.

Table 10-10. Desirable Characteristics of Structural Materials

Property	Primary Variables[a]	Desirable Value	Purpose
Thermal Conductivity	T	High	Minimize thermal gradients and thermal stress
Thermal Expansion	T	Low	
Young's Modulus	T	Low	
Specific Heat	T	High	Minimize effect of thermal shock
Yield Strength	T,ϕt	High	Maximize allowable stress
Ultimate Tensile Strength	T,ϕt	High	
Uniform Elongation	T,ϕt	High	Maximize ability to withstand off-normal events (e.g., plasma dump, magnetically induced torques)
Total Elongation	T,ϕt	High	
Swelling	T,ϕt	Low	Minimize dimensional changes and physical property changes
Creep	T,ϕt,σ,ϕ	Low	Minimize dimensional changes, avoid catastrophic failure
Fatigue	T,ϕt,$\Delta\sigma$,$\Delta\epsilon$,f	Low	Avoid catastrophic failure
Crack Growth	T,ϕt,Δk,f	Low	
Corrosion	T,ϕ,ϕt,Ch	Low	Avoid wall thinning and coolant channel plugging
Stress Corrosion Cracking	T,ϕ,ϕt,Ch,Δk,f	Low	Avoid catastrophic failure
Neutron Cross Sections	ϕt	Low	Minimize alloy compositional changes and reduce activation

[a] T $\equiv$ temperature, ϕ $\equiv$ neutron flux, ϕt $\equiv$ neutron fluence, σ $\equiv$ stress, $\Delta\sigma$ $\equiv$ change in stress during operational cycle, $\Delta\epsilon$ $\equiv$ change in strain during operational cycle, Δk $\equiv$ change in stress intensity during operational cycle, f $\equiv$ operational cycle frequency, Ch $\equiv$ chemical composition.

Table 10-11 summarizes the primary favorable and unfavorable characteristic properties of each class of structural alloys. Since the STARFIRE blanket design focuses on the use of solid tritium breeding materials, this constraint and the choice of water coolant are key considerations in the assessment of the candidate structural materials. Another important parameter is the steady state operating scenario proposed for STARFIRE.

Vanadium and niobium alloys offer several potential advantages as structural materials. They maintain their mechanical properties at high operating temperatures ($\geq$ 650°C) and typically exhibit low thermal stresses during operation. Vanadium alloys have been shown to be the most resistant to radiation damage of all alloys tested to date and they produce no long-lived activation products. Unfortunately, both alloy systems are susceptible to severe oxidation at elevated temperatures, and they are not compatible with either high temperature water or helium coolants. Therefore, they are not considered to be viable candidates for the STARFIRE reference design.

The major concerns relating to the use of titanium-base alloys are compatibility with the hydrogen (DT) environment, creep strength at elevated temperatures, and radiation damage effects. Titanium alloys have a high permeability for hydrogen and recent data indicate that oxide and nitride surface films are not effective hydrogen barriers.[20] Permeation rates of tritium from the plasma chamber into the water coolant appear to be excessive for conditions of interest. Titanium and zirconium alloys are known to be particularly susceptible to hydrogen embrittlement under certain conditions. The equilibrium tritium concentrations in titanium are in excess of 1000 wppm at pressures of $\sim 10^{-1}$ Pa and temperatures below 300°C.[21] The common titanium-base alloys generally exhibit a sharp decrease in creep strength at $\sim$ 450-500°C. Since the available data on radiation effects is very limited, it is difficult to assess the performance and limitations of titanium alloys in a radiation environment. Enhanced precipitation with the formation of planar defect structures has been observed in stressed titanium alloys under fission-reactor irradiation.[22] While titanium alloys are readily fabricable, welding must be done in an inert environment and post-weld stress relieving is recommended for certain applications. Titanium alloys can be used with helium and water coolants, however, the operating temperatures for the helium and water coolants will be limited by the kinetics of the

Table 10-11. Potential Structural Materials

Material Class	Alloys	Principal Advantages	Principal Disadvantages
Austenitic Stainless Steel	316, 20% CW	Large data base Fabrication experience	Poor thermophysical properties Large swelling
	PCA	Low swelling High irradiated ductility	Poor thermophysical properties
Ferritic Stainless Steels	HT-9 9Cr-1Mo	Large unirradiated data base Low swelling and creep	Ferromagnetic DBTT increased by irradiation
Titanium Alloys	Ti-64 Ti-6242 Ti-5621	Fabrication experience Potentially low activation	Lack of irradiation data base Hydrogen embrittlement
Nickel Alloys	Inconel 625 PE-16 Inconel 718	Low swelling and creep High temperature capability	High activation Susceptible to radiation embrittlement
Vanadium Alloys	V-15Cr-5Ti V-10Cr-3Ti	Radiation resistant High temperature operation Low activation	Little fabrication experience Not compatible with H_2O or He coolants
Niobium Alloys	Nb-1Zr FS-85 Cb-753	High temperature operation Desirable thermophysical properties	Little fabrication experience Not compatible with H_2O or He coolants

oxidation mechanisms. Titanium is also compatible with high-purity lithium. However, certain alloying elements in candidate alloys, e.g., Al and Sn, are highly soluble in lithium and may substantially affect the compatibility. Although no data are available on the compatibility of titanium alloys with Li_7Pb_2 and Li_2O, compatibility with the stoichiometric compounds is probably satisfactory at relatively low temperatures of interest for water coolants. However, decomposition of the lithium compounds may lead to compatibility problems. Further studies are required to assess the importance of these compatibility problems. Because of these limitations, titanium alloys are not included as primary candidates for the STARFIRE structural material.

High nickel alloys generally exhibit better high temperature strength than either the austenitic or ferritic stainless steels. They are also more resistant to radiation swelling and tend to exhibit low radiation creep rates. The major concern of nickel alloys relates to the effect of radiation on ductility. Helium will be generated in large amounts in nickel exposed to a fusion neutron spectrum, and the presence of helium will lead to embrittlement at temperatures $\gtrsim 600°C$.[23] In addition, nickel alloys are particularly prone to loss of ductility due to thermal aging and to low-temperature radiation-hardening embrittlement.[24] The net result of the radiation embrittlement is to reduce the permissible operating temperatures and allowable stresses that were possible with unirradiated material, and therefore, to eliminate their primary advantage over the stainless steels. Irradiation of nickel will also result in the formation of long lived activation products. Nickel alloys have, therefore, also been eliminated as reference structural materials primarily on the basis of their predicted radiation performance.

Austenitic stainless steels and ferritic steels are selected as the primary candidate structural materials for STARFIRE. For the steady-state operation proposed for STARFIRE and for the relatively low operating temperatures characteristic of a water-cooled system, an advanced austenitic stainless steel should provide acceptable performance. The titanium modified austenitic stainless steel, designated as the prime candidate alloy (PCA) in the Magnetic Fusion Energy Alloy Development Program, is selected as the reference alloy. A stabilized ferritic steel is proposed as the alternate structural material

for STARFIRE. The materials data base for these two primary candidate alloys are summarized in the following section and additional data are presented in Appendix E.

10.1.3.3 Data Base for Primary Candidate Structural Materials

Austenitic stainless steels are the best characterized of all of the candidate structural materials and are probably the easiest to fabricate. The 20% cold-worked Type 316 stainless steel is generally regarded as the reference alloy in this class. The primary disadvantages of this alloy are its relatively high swelling rates and elevated temperature embrittlement after fission reactor irradiation, and its relatively poor physical properties that can lead to excessive thermal stresses. In an effort to reduce swelling and embrittlement, a titanium modified austenitic stainless steel, designated PCA, has been developed. The reduced swelling of PCA makes it preferable to Type 316 stainless steel; however, the thermophysical and unirradiated mechanical properties are essentially the same. The thermal stress problem associated with austenitic steels is less critical for STARFIRE because it will operate in a continuous rather than a cyclic mode, thereby reducing the fatigue and crack growth effects. Except for the radiation effects, the data base for the PCA alloy is derived from Type 316 stainless steel. Ferritic steels, or more precisely martensitic steels, have been studied in recent years and were found to exhibit both low swelling and low irradiation creep. Their thermophysical properties are superior to those of austenitic stainless steel, which would result in a lower thermal stress under the same operating conditions. The principal concerns of the ferritic steels are their magnetic properties, difficult welding characteristics, and relatively high ductile-to-brittle transition temperature (DBTT). These alloys are ferromagnetic, and as such, could strongly interact with the large magnetic fields in STARFIRE. However, preliminary experiments indicate that these materials saturate in a high magnetic field and may not adversely affect plasma performance.[25] The data base used for evaluation of the ferritic steels is derived primarily from the Sandvic HT-9 alloy, although a modified 9Cr-1Mo alloy developed in the breeder program is a potential candidate.

Table 10-12 gives the nominal compositions of the PCA alloy and the HT-9 alloy. Representative values of selected thermal, physical, and elastic properties of these alloys obtained from handbooks are summarized in Table 10-13. Additional property data for these alloys are given in Appendix E.

Fabrication - Type 316 stainless steel, in common with virtually all of the 300 series austenitic stainless steels, possesses excellent formability and fabricability characteristics. Weldability is excellent by all of the fusion welding processes. For the 20% CW 316 SS it is probably prudent to try to design the first wall such that the weld zones, which will respond differently than the cold-worked matrix to neutron irradiation, are not exposed to the highest neutron fluences. The ferritic alloys have a microstructure consisting of tempered martensite. Typical heat treatments involve austenitizing at 1050°C for one hour followed by either air cooling or oil quenching; tempering is usually carried out at 600° to 750°C for one hour followed by air cooling. Fusion welding of the Cr-Mo-V steels is rated as difficult because of a tendency toward cracking in the weld heat-affected-zones. This is the result of the formation of hardened martensite in both the fusion and heat-affected zones due to the very rapid cooling which follows the welding process. To minimize this tendency it is generally necessary to preheat the weld zone areas to 200-400°C and to provide a final postweld heat treatment at about 650-700°C.

Mechanical Properties - The mechanical strengths of PCA (20% cold-worked 316) and HT-9 are compared in Fig. 10-4 in terms of the allowable stress intensity, S_{mt}.[26,27] At low temperatures, S_{mt} is 1/3 of the ultimate tensile strength, while at high temperatures, S_{mt} is 2/3 of the 100,000 h creep-rupture stress. (See Sec. 10.6 for additional information on S_{mt}.) Overall,

Table 10-12. Nominal Composition of PCA Alloy and HT-9 Alloy

PCA	65Fe-14Cr-16Ni-2Mo-0.3Ti-0.5Si-0.05C
HT-9	85Fe-12Cr-1Mo-0.5W-0.3V-0.20C

Table 10-13. Selected Properties of Type 316 Stainless Steel and Type HT-9 Ferritic Steel

Property	316	HT-9
Melting Temperature, °C	∿ 1430	1427/1482
Density, g/cm^3	7.97	7.75
Poisson's Ratio - 400°C	0.294	0.265
Young's Modulus (GPa)		
- 20°C	193	200
- 400°C	167	175
Heat Capacity (J/kg·°K)		
- 20°C	465	490
- 400°C	560	680
Mean Thermal Expansion ($°C^{-1} \times 10^{-6}$)		
- 20-100°C	15.6	10.6
- 20-400°C	17.7	11.3
Thermal Conductivity (W/m-°K)		
- 20°C	18	∿ 29
- 400°C	19.5	∿ 29
Thermal Stress Figure of Merit[a]		
- 400°C	0.220	0.105
Electrical Resistivity (10^{-6} Ω-cm)		
- 20°C	78	--
- 400°C	97	∿ 90
Corrosion in Water, μm/y	0.5	2

[a] $\tau = \frac{\alpha E}{k\ (1-\nu)}$

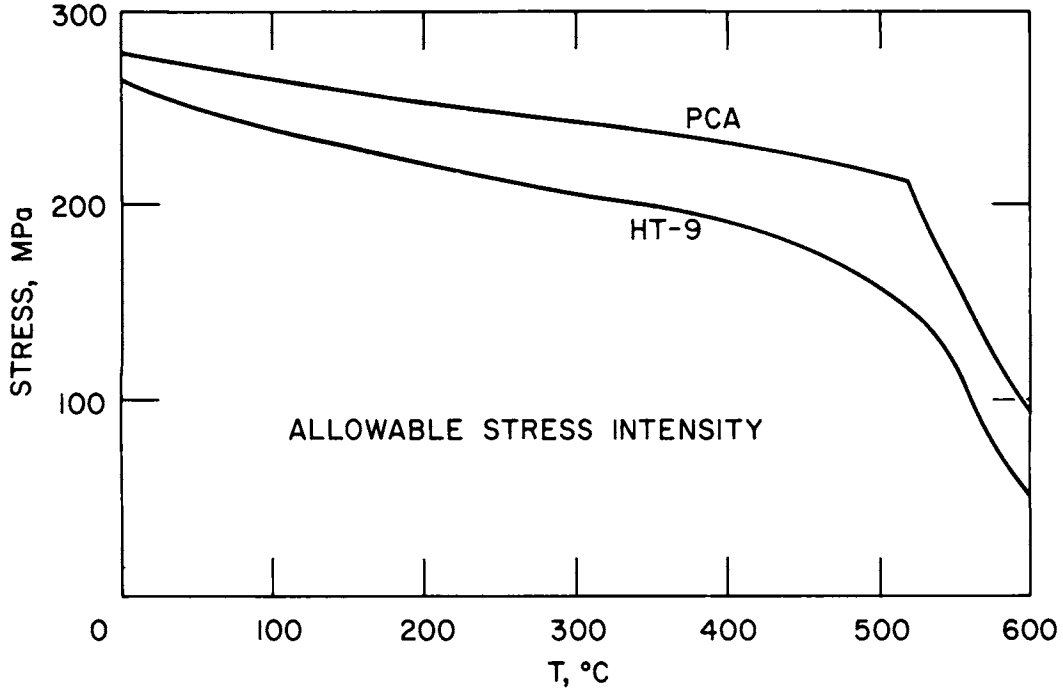

Figure 10-4. Allowable 300,000-hr design stress intensity (S_{mt}) for HT-9 and Type 316 stainless steel based on ASME Boiler and Pressure Vessel Code Case N47 for elevated temperature service.

PCA is marginally stronger than HT-9. Both materials show a slowly decreasing strength with temperatures up to ∿ 550°C, at which point the creep strength decreases rapidly. For the operating temperatures in STARFIRE (< 450°C), both materials have adequate strength properties. The limited data available on the fatigue and crack growth properties of ferritic steels indicate that they are similar to those of austenitic stainless steels. Under the same operating conditions, fatigue and crack growth problems are expected to be more severe in PCA than HT-9 because of the significant differences in thermophysical properties. However, since STARFIRE operates in a continuous mode, fatigue and crack growth should not pose major problems for either material. Additional mechanical property data are given in Appendix E.

Compatibility - Since pressurized water has been selected as the coolant for STARFIRE, compatibility of the structural material with water is an important requirement. The corrosion rates of steels in water depend upon the purity of the water, in particular the oxygen content. The oxygen

concentration in pressurized water systems is generally controlled by an overpressure of hydrogen. Nominal corrosion rates for austenitic and ferritic steels in high purity water are given in Table 10-13. These corrosion rates are sufficiently low that the structural integrity of the alloys is not significantly affected. The major concern relates to radioactive mass transport. Since this is primarily a safety concern, a detailed discussion of the relevant data is presented in Sec. 21.7.

The major compatibility problem concerning the mechanical integrity of the structure relates to the susceptibility of austenitic stainless steels to stress corrosion cracking. Again water chemistry is a key factor in avoiding this problem. The ferritic steels are less susceptible to stress corrosion cracking than the austenitic stainless steels.

Radiation Effects - The radiation effects on structural materials that are of primary interest for STARFIRE are swelling, creep, and loss of ductility. Since the strength properties, viz., ultimate and yield strength, of these two alloys are affected only modestly by neutron irradiation, unirradiated values are used for the present study. Swelling and creep can produce dimensional changes during operation, while the loss of ductility will limit the temperatures of operation and the ability of the structural material to withstand off-normal events. Swelling in Type 316 stainless steel is considerably higher than has been observed in ferritic steels.[26,28] Recently, new austenitic alloys, such as PCA, have been developed which show improved resistance to swelling.[29] Figure 10-5 compares the swelling in 20% cold worked Type 316 stainless steel, PCA, and HT-9 for fast reactor conditions. The swelling in PCA is assumed to be one-tenth of the swelling in Type 316 stainless steel. The additional helium generated by the 14 MeV neutrons is expected to influence the swelling. Experiments conducted in the Oak Ridge National Laboratory's High Flux Isotope Reactor (HFIR), where high concentrations of helium are generated in austenitic stainless steel, indicate that swelling is increased over EBR-II irradiations, and swelling above 0.5 T_m is much higher due to gas driven swelling.[30] However, at temperatures below 0.5 T_m, high helium production has a minimal effect in 20% cold-worked Type 316 stainless steel because the dislocations provide effective nucleation sites for helium bubbles. Therefore, the low swelling rates in PCA and HT-9 coupled with operating temperatures considerably below 0.5 T_m suggests that the total swelling should be low in STARFIRE.

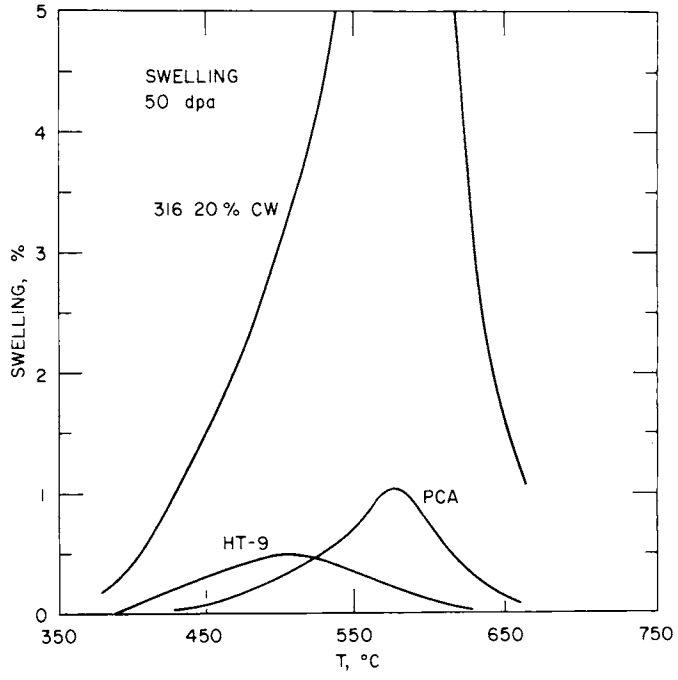

Figure 10-5. Temperature dependent swelling response of austenitic and ferritic steels as a function of temperature.

Irradiation creep will produce dimensional changes at temperatures where thermal creep is insignificant. The assumed in-reactor creep for PCA and HT-9 are shown in Fig. 10-6 for a constant stress level of 100 MPa and a reactor fluence of 50 dpa.[26,31] The radiation creep in PCA is similar to that of Type 316 stainless steel except that the creep rate has been reduced in the range of 500-600°C to account for the reduced swelling in PCA. At temperatures < 400°C, HT-9 exhibits significantly lower radiation creep than PCA. The influence of swelling and creep on component lifetime are discussed in Sec. 10.6.

Radiation can reduce the ductility of structural materials in several ways. Radiation hardening can reduce the ductility by forcing plastic strain to occur in highly localized regions (channel fracture). In bcc metals, radiation can cause an increase in the DBTT such that brittle fracture is possible above room temperature. Finally, helium produced during irradiation can form into bubbles along grain boundaries, which results in greatly reduced

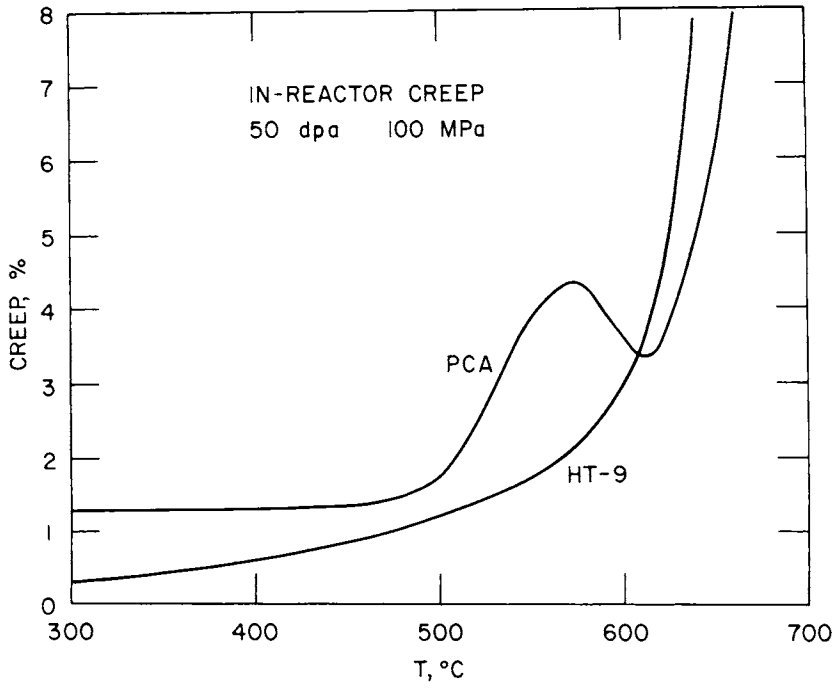

Figure 10-6. Temperature dependent in-reactor creep properties for PCA and HT-9.

ductility at temperatures $\geq 0.5\ T_m$. All of these embrittlement mechanisms can result in restricted operation of the structural material. The DBTT of HT-9 has been observed to increase to 100-150°C with irradiation, which means that this material may not be capable of withstanding impact type loads at lower temperatures. The loss of ductility in 20% cold worked Type 316 stainless steel due to irradiation can be severe, particularly at high helium concentrations, as shown in Fig. 10-7.[33] The low ductility will restrict operation to temperatures $\leq$ 500°C. Both HT-9 and PCA are expected to exhibit greater ductility after irradiation than Type 316 stainless steel, but their ductility will also be significantly reduced. The degree of ductility required for safe operation is open to question, but a uniform elongation of 0.5 to 1.0% is generally regarded as the minimum necessary.

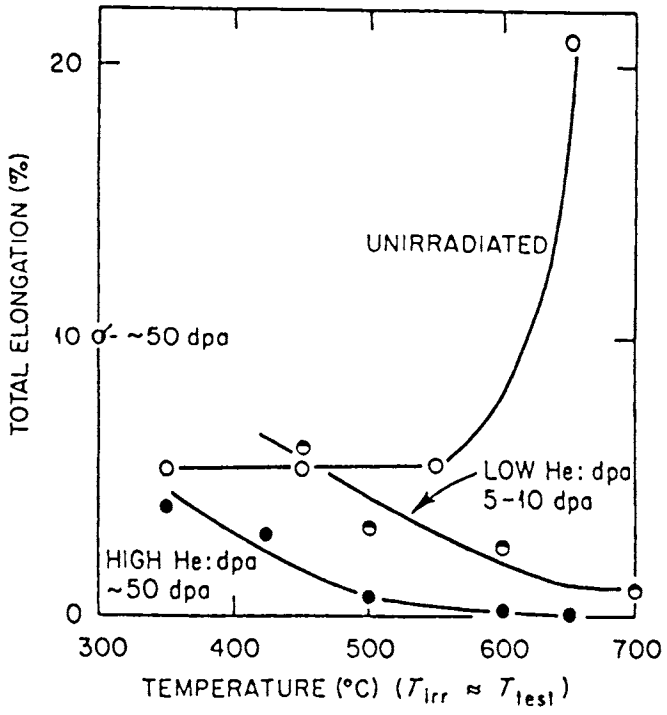

Figure 10-7. Uniform elongation of 20% cold-worked 316 stainless steel after irradiation.

10.1.4 Neutron Multipliers

Aside from its neutronic properties, the neutron multiplier should be capable of transmitting heat efficiently to the structural material and coolant, should not be significantly altered by irradiation, and should be compatible with the surrounding materials. Since the STARFIRE design emphasizes the use of solid breeding materials, it is also desirable for the neutron multiplier to remain in the solid state during operation. Therefore, a reasonably high melting point is also required. In general, the mechanical property requirements are minimal, since the multiplier will be completely supported by the structural material. Rather, the properties of the multiplier should be tailored such that the induced stresses in the structural material are minimized. A summary of the desirable characteristics for the neutron multipliers is shown in Table 10-14.

Table 10-14. Desirable Characteristics for Neutron Multipliers

Property	Desirable Value	Purpose
Thermal Conductivity	High	Reduce thermal gradients and internal stress
Thermal Expansion	Similar to or less than structural material	Minimize stress in structural material
Specific Heat	High	Reduce temperature excursions during accidents
Density	Low	Minimize load carried by structural material
Tensile Properties	High	Support own weight
Swelling	Low	Minimize dimensional changes and stress on structural material
Corrosion	Low	Minimize chemical interaction with structural material
Transmutations	Low	Reduce changes in neutronics and reduce gas production

Neutronically, the elements Be, Bi, Pb, Zr and their combinations would be acceptable for the neutron multiplier concept of STARFIRE. A list of the candidate multiplier materials along with their relevant thermophysical properties is shown in Table 10-15. A more complete set or property values along with their sources is given in Appendix E. Both Pb and Bi, as well as PbBi alloys have low melting points which are not consistent with the STARFIRE design concept of a solid blanket, and therefore, are not considered prime candidates. However, this does not imply that these materials are unacceptable for other design concepts. If these materials were to be employed in the liquid state, the primary consideration would be their compatibility with the structural material. Austenitic stainless steels exhibit poor corrosion resistance to liquid Pb and Bi at temperatures of $\sim 500°C$.[33] Ferritic stainless steels have a greater resistance to corrosion, and the refractory metals,

Table 10-15. Properties of Candidate Neutron Multipliers

Material	Density (g/cm^3)	Specific Heat[a] (J/kg K)	Thermal Conductivity[a] (W/m°K)	Thermal Expansion[a] x 10^{-6} (°C)	Melting Point (°C)
Be	1.8	1923	188	13	1284
BeO	3.0	1042	200	8	2520
Pb	11.3	127	35	29	327
PbO	9.5	209	2.8	50	888
Bi	9.8	56.4	6.0	13	271
Zr	6.5	275	21	6	1852
Zr_5Pb_3	8.9	220	21	20	∿ 1400
PbBi	10.5	125	10	27	125

[a] @ 25°C

Mo, Nb, Ta, and W, all have good corrosion resistance to ∿ 800°C. The poor corrosion resistance of austenitic stainless steels is due to the high solubility of nickel in liquid Pb and Bi.[34] Since chromium has a higher solubility in liquid Pb and Bi than iron, low alloy steels exhibit less corrosion than chromium stainless steels. Corrosion in ferritic alloys can be inhibited to varying degrees by small additions of zirconium or titanium to the liquid metals.[34] It is unlikely that austenitic stainless steels could be used in direct contact with these liquid metals, because of the corrosion problems.

Lead oxide is eliminated from further consideration because of its extremely poor thermal conductivity and high coefficient of thermal expansion. This combination of properties would result in high temperature gradients and thermal stresses. It is also possible that the large thermal expansion would create high stresses in the structural material. Beryllium oxide, and

zirconium, although having acceptable thermophysical properties, are only marginally acceptable neutronically (see Sec. 10.4 for neutronic considerations), and have also been eliminated as prime candidates.

The remaining materials, Be, and Zr_5Pb_3, have acceptable thermophysical and neutronic properties. Beryllium is particularly appealing because it combines the lowest density with the highest specific heat and thermal conductivity of the candidate materials. Little is known about the properties of Zr_5Pb_3, and it should be noted that the thermophysical properties shown in Table 10-15 are only estimated. It has been included because it offers greater neutron multiplication than pure zirconium and a significantly higher melting point than pure lead. Properties of these two primary candidates are discussed in more detail below.

10.1.4.1 Beryllium

The physical and mechanical properties of pure beryllium are well known because of its application in the aerospace and nuclear industries. Beryllium products can be produced in the hot pressed, rolled, extruded, or wrought conditions. The tensile properties of wrought beryllium at 538°C compare favorably with annealed Type 316 stainless steel, but the thermal creep rate of beryllium is significantly higher than the creep rate of Type 316 stainless steel.[35] The mechanical properties of beryllium depend upon the impurity concentration, grain size, and surface finish, and, in general, the most favorable properties are obtained with the purest material with the smallest grain size. Beryllium also exhibits a ductile-brittle transition temperature which depends upon the grain size and can reach as high as 200°C.[36] See Appendix E for further information on the properties of beryllium.

The impurities which have the greatest impact on the mechanical properties are BeO, Al, Si, and Mg. BeO is present in commercial beryllium in concentrations of 1-2%. Its presence can improve the mechanical properties by increasing the high temperature creep strength, tensile strength, and recrystallization temperature.[37] The amount of BeO lying on the grain boundaries is the primary factor influencing the recrystalization temperature. The presence of Al, Si, or Mg can result in a reduction of the high temperature creep strength.[37] It is believed that these elements can form low

melting point phases that become liquid above 760°C. Surface damage caused by machining operations can also reduce the tensile strength and ductility of beryllium.[38]

The corrosion behavior of beryllium has been examined in oxygen, nitrogen, and water environments.[39] The reaction of beryllium with both oxygen and nitrogen follows the parabolic rate law after the initial stages. Significant oxidation appears between 600 and 700°C and increases gradually until 825°C, after which the temperature of oxidation increases rapidly until actual burning commences at 1200°C. The reaction of beryllium with nitrogen follows the same pattern, but the reaction rates are lower. The corrosion of beryllium in high temperature water shows a wide variation in behavior. However, high purity beryllium in deionized water at 315°C exhibited corrosion rates of < 20 mg/cm^2/mo. Porous beryllium can exhibit much greater rates of corrosion due to the open porosity. Beryllium can also interact with steel to form a hard surface coating.[40] In particular, beryllium has a high affinity for nickel, and the compound NiBe predominates on the surface of high nickel steel. Other compounds which can form include $FeBe_2$ and BeC. The extent of the interaction with stainless steel should be small, however, at the operating temperatures of the structural material.

The helium generated during reactor operation could produce extensive swelling. The amount of helium predicted to be generated in STARFIRE is 8300 appm/yr. The bubbles that will form from this helium can result in both swelling and a degradation of the mechanical properties. The magnitude of the helium bubble swelling increases continuously with temperature. Large volume increases have been observed by either irradiating beryllium above 700°C or irradiating at low temperatures and then annealing above 700°C. There appears to be a ceiling to the volume increase of $\sim$ 30% that is probably due to the link up of the bubbles, thus creating an open path to the surface.[41] It is recommended, therefore, that a beryllium with 70% theoretical density and interconnected porosity be used to accommodate the predicted swelling. Since the helium gas that will be generated and released from the beryllium could pressurize the multiplier region of the blanket, a venting system may be required to alleviate the pressure.

Resource limitations are of major concern regarding the use of beryllium as a neutron multiplier. The estimated reserves and resources of beryllium in the United States are 2.5×10^7 and 7.4×10^7 kg, respectively[42,43] (see Appendix C). The corresponding world reserves and resources are estimated at 3.8×10^8 kg and 1.1×10^9 kg, respectively. The STARFIRE blanket requires 5×10^4 kg of beryllium for the design with a beryllium neutron multiplier. The beryllium burnup is estimated to be $\sim$ 0.5%/y or 250 kg/y for each reactor. For a 30 year lifetime the burnup for each reactor corresponds to $\sim$ 0.01% of the U.S. resources or 0.03% of the U.S. reserves. For 10^5 MWe generating capacity (83 reactors) the total beryllium burnup would be $\sim$ < 1% of the U.S. resources. In addition, allowances would have to be made for the in-reactor inventory. The beryllium would have to be recycled in order to meet the needs of more than a couple hundred reactors. Since beryllium produces very little activation except for tritium, recycle does not appear to be a difficult problem. Minimal refabrication would be required since the multiplier zone consists of simple 5-cm thick slabs of beryllium with a 70% theoretical density. The relatively high cost of beryllium ($\sim$ 215 $/kg) also provides an incentive for recycling. In general, the energy multiplication provided by beryllium will more than offset the inventory cost.

10.1.4.2 Zr_5Pb_3

The limited data on the zirconium-lead system indicates that the intermetallic compound Zr_5Pb_3 exists with a hexagonal crystal structure.[44] No physical property data are available for this material so that its characteristics can only be implied from information on other intermetallic compounds. Some information is available from the related systems of Zr-Sn and Zr-Bi. In both cases intermetallic compounds exist which are near the composition of Zr_5Pb_3. In the Zr-Sn system, the compound Zr_5Sn_3 has a melting point of 1985°C, and in the Zr-Bi system, Zr_3Bi_2 has a melting point of 1495°C.[44,45] A partial phase diagram for the Zr-Pb system indicates a melting temperature of $\sim$ 1400°C for Zr_5Pb_3.[45]

In general, intermetallic compounds are high hardness, low ductility materials.[46] Young's modulus in many alloy systems is observed to be a maximum at the composition of an intermetallic compound. At sufficiently

high temperatures ($\sim 0.65\ T_m$), these materials can show enhanced ductility. The increase in ductility and decrease in strength at elevated temperatures is often associated with disordering of the low temperature ordered crystal structure. The creep rates of these compounds have also been related to their ordered structure, and they often exhibit low thermal creep rates up to the temperature where disordering occurs.

The corrosion behavior of intermetallic compounds is not well characterized.[46] In many cases, intermetallic compounds and metal alloys have similar corrosion behavior. In other cases, intermetallic compounds can be susceptible to low temperature disintegration which is believed to be due to accelerated diffusion of oxygen or nitrogen along grain boundaries. Data are not sufficient to accurately predict the corrosive behavior of Zr_5Pb_3 with any of the candidate structural materials. Selective oxidation of the zirconium would likely occur upon exposure to water or air at elevated temperature with a change in the stoichiometry and the possibility of formation of a lower melting phase.

The radiation effect which is of primary concern for the neutron multiplier is the swelling behavior. Swelling can be the result of the formation of internal voids, as in austenitic stainless steel, or the result of He gas bubble formation. Since the helium generation rate in Zr_5Pb_3 is predicted to be very low, swelling from bubble formation should not be excessive; however, void swelling is a possibility. Recently, the void swelling in long range ordered alloys has been examined using dual heavy ion and helium implantation techniques.[47] A cobalt alloy containing 23 w/o V and 16 w/o Fe was tested at 570, 625, 680, and 750°C to damage levels of 70 dpa. At all temperatures, only small cavities, $\sim$ 10 mm in diameter, were observed, and the total swelling was low. This limited information indicates that swelling in Zr_5Pb_3 may not be a major problem.

10.1.4.3 Reference Neutron Multiplier

The available data indicate that beryllium would have considerable advantages over Zr_5Pb_3 as a neutron multiplier material. It is less dense and would operate at lower temperatures than Zr_5Pb_3. In an accident, such as a loss of coolant, its high specific heat and high thermal conductivity would provide a wider margin of safety. The major problem associated with

the use of beryllium is the resource limitation. Because of the handling requirements associated with tritium and radioactive materials, the toxicity of beryllium causes little added problems. Since little is known about Zr_5Pb_3, its potential as a neutron multiplier cannot be adequately assessed at this time. In particular, more information is required about its physical properties, its corrosion properties, and its response to radiation. Reference blanket designs based on both beryllium and Zr_5Pb_3 are proposed. The Zr_5Pb_3 provides a potential alternative to the beryllium resource problem.

10.1.5 Coating/Cladding Material

Selection of the material that serves as the first physical barrier to the plasma is a critical consideration in the design of the first-wall. As discussed in Sec. 8.0, low-Z materials appear essential since high-Z impurities eroded from the first wall and plasma chamber components, e.g., the limiter, can severely impact the plasma performance. Also, impurities eroded from the first wall can become energetic ions that subsequently strike the limiter. Since higher Z ions produce sputtering yields greater than unity at modest energies (of the order of 100 eV), excessive erosion of the limiter is predicted if the first wall is constructed of other than low-Z materials. It is also concluded that portions of the first wall must survive a modest number of large transient surface heat fluxes that result from plasma disruptions. Significant amounts of wall material ablated or vaporized during a disruption will most likely deposit at other regions of the plasma chamber. Because of the extensive material redistribution in the plasma chamber that arises both from sputtering during normal operation and ablation during a disruption, a single material for all plasma chamber components provides important advantages that may be essential. For example, deposition of armor material, such as graphite, on a metal first wall could substantially affect erosion rates or the integrity of the metal wall. Likewise, deposition of elements from a compound, e.g., TiC or TiB_2, could result in a nonstoichiometric surface layer with properties much different than the ideal compound. It is concluded in the present design study that all first wall components, including the limiter, should be constructed of the same material and that the surface material should be a single element with a low-Z (probably < 10).

The recommended approach for incorporating low-Z materials into the first wall of STARFIRE is the low-Z coating (cladding) concept originally advocated in the ANL Experimental Power Reactor Study.[48] A major advantage of this concept relates to the greater flexibility of materials choices in that the surface material or coating can be selected primarily on the basis of its surface properties while the substrate can be selected primarily on the basis of its structural and compatibility characteristics. This concept permits use of low-Z materials that would not otherwise be viable candidates.

10.1.5.1 Coating/Cladding Requirements

Properties of the coating/cladding material that are important considerations in the selection of candidate materials are summarized in Table 10-16. The importance of atomic number and wall erosion processes, e.g., physical and chemical sputtering and blistering, have been discussed earlier in this section and in Sec. 8.0. The physical properties are important for both normal and off-normal or accident conditions. The melting temperature should be high enough for the material to remain solid under anticipated conditions. Since many materials effects, e.g., cavity formation under irradiation, typically occur at certain fractions of the absolute melting temperature (T_m), there tends to be optimum operating temperature ranges for most materials. High thermal conductivity is generally very beneficial for both normal operation and plasma disruption conditions. High heat capacities and heats of vaporization tend to minimize the potential for ablation or evaporation during a plasma disruption. Vaporization of the wall at the normal operating temperature should not be a source of excessive plasma contamination, however, increased vaporization rates at higher temperatures could serve as an inherent safety feature for plasma control. The mechanical integrity and radiation responses are considered to be less critical for the coating/cladding concept than if the low-Z material were a structural component. Because of the relatively low resource requirements for the proposed first-wall concept, purification, material cost, and residual activation are less critical.

Table 10-16. Summary of Important Properties and Requirements for First-Wall Coating/Cladding Materials

Property	Justification	Evaluation of Beryllium
Atomic Number (Z)	Impact of impurity on plasma performance Higher-Z particles produce higher sputtering yields	Be has the lowest Z of any material that is solid at the proposed operating temperature
Physical Sputtering	Impact on plasma performance Source for self-sputtering Wall erosion	D,T sputtering of Be compares favorably with most materials at predicted energy (1200 eV) Self-sputtering yield is lower than nearly all materials (except B)
Hydrogen Reactions	Tritium inventory Tritium permeation to coolant Impact on chemical stability Chemical sputtering	Solubility of H in Be is lower than most metals Permeability of H in Be is lower than most metals Hydrides are not stable under anticipated conditions Chemical sputtering of Be has not been reported
Blistering	Same as physical sputtering	Experimental evidence indicates that very low blistering erosion rates occur with tailored microstructures
Melting Temperature	Operating temperature limits Melting caused by disruptions	Operating temperature of $\sim 0.5\ T_m$ is attractive for coating (swelling, creep, ductility)
Thermal Conductivity	Heat flux limits Thermal stresses	Thermal conductivity is very high relative to most metals ($\sim$ one-third that of copper)
Heat Capacity	Energy absorption during disruption	Heat capacity per g is higher than most metals (5-6 times Cu; $\sim$ 2 times Al; $\sim$ 4 times SS)
Heat of Vaporization	Ablation during disruption	Heat of vaporization per g is 3-6 times that of most structural materials (slightly greater than that of Al)

Table 10-16. (Continued)

Property	Justification	Evaluation of Beryllium
Vapor Pressure	Plasma contamination	Vapor pressure is very low (< 10^{-6} Pa) at operating temperature Rapid increase in vapor pressure may aid in quenching plasma in event of a loss of coolant
Thermal Expansion	Coating/substrate compatibility Thermal Stresses	Expansion coefficient is similar to that of steel substrate
Resources	Cost/availability	Coating/cladding concept requires very small resource (< 10,000 Kg per reactor life, partially recoverable)
Purity	Impact on plasma performance	Common impurities should present no major problem
Fabrication	Cost and capability	Demonstrated methods probably adequate
Radiation Damage	Integrity and lifetime	Low-Z materials typically give high gas production Radiation swelling of Be has been observed Gas release and swelling can probably be accommodated in coating at operating temperature with appropriate microstructural tailoring
Residual Activation	Handling and environmental impact	Very low activation except for tritium
Toxicity	Handling and environmental impact	Normal precautions for handling irradiated material and tritium should be adequate Adequate fabrication handling procedures have been demonstrated

10.1.5.2 Candidate Coating/Cladding Materials

The same materials that were considered for the limiter coating/cladding are also evaluated for the first-wall application. The four classes of materials are summarized in Table 10-17. The primary criteria for the identification of these candidate materials are chemical stability, viz., melting temperature and vapor pressure, at acceptable operating temperatures and moderate or low effective atomic numbers. The compounds listed are generally representative of the class of materials available. Other more complex compounds with similar characteristics may also be credible.

Table 10-17. Materials Considered for the First-Wall Coating/Cladding

low-Z (< 10) elements	Be, B, C
low-Z compounds	BeO, B_4C, BN
moderate-Z (< 18) compounds	SiC, SiO_2, SiN, Al_2O_3, MgO
transition metal compounds	TiC, TiB_2, VB_2

On the basis of the analyses conducted as part of the present study, beryllium has been selected as the low-Z coating/cladding for the first wall as well as for the limiter and other components in the plasma chamber. In general, beryllium possesses several desirable properties that make this material superior to other materials for the first wall application. Boron is presently regarded as the primary backup material. Important properties of these two materials are summarized in Table 10-18. The basis for physical sputtering values and the assessment of other plasma/wall interactions are presented in Sec. 8.4.3. Additional materials properties data for other candidate materials are summarized in Appendix E.

A general evaluation of beryllium for the first-wall coating/cladding application is given in Table 10-16. Boron possesses two primary advantages compared to beryllium, viz., a higher melting temperature and a slightly lower sputtering yield. The major disadvantages of boron are its much lower thermal conductivity and a higher hydrogen solubility and permeability. Although graphite possesses many favorable properties, its reactivity with

Table 10-18. Properties of Beryllium and Boron

Property	Beryllium	Boron
Atomic number	4	5
Atomic weight	9.01	10.81
Density, g/cm^3	1.85	2.34
Crystal structure	HCP	MC
Melting temperature, °C	1284	2300
Boiling temperature, °C	2970	2550(s)
Vapor pressure, Pa (°C)	10^{-4} (850)	10^{-4} (1557)
	10^{-2} (993)	10^{-2} (1877)
	10^{0} (1192)	--
	10^{1} [1335(ℓ)]	--
Heat of fusion, J/g	1083	2077
Heat of vaporization, J/g	24,790	46,740
Heat capacity, J/g °C		
500°C	2.25	2.09
1000°C	2.92	2.61
1500°C	3.59(ℓ)	3.13
Coefficient of thermal expansion, $C^{-1}(10^{-6})$		
25-100°C	11.6	5.0
25-500°C	15.9	5.5
25-1000°C	18.4	6.1
Thermal conductivity, w/m•°K		
50°C	150	27
300°C	125	18
600°C	96	14
Electrical resistivity, μΩ•cm		
400°C	15	15

hydrogen (chemical sputtering) is considered prohibitive for the range of operating temperatures and surface heat and particle fluxes predicted for the first-wall components.

None of the candidate compound materials have overall properties that are superior to those of beryllium. Concerns regarding variations in stoichiometry of the compounds resulting from erosion and redistribution, and the higher self-sputter yields generally make use of these materials questionable.

10.2 MECHANICAL DESIGN

The mechanical design of the first-wall/blanket system was developed concurrent with, and as an integral part of, the STARFIRE reactor design. Consistent with project guidelines, emphasis was placed on identifying those design options which could best be combined into a first-wall/blanket design that was safe and environmentally and economically attractive.

The most important factors in evaluating and comparing the design options were materials selection, neutronics (both tritium breeding and activation), reactor maintainability, system reliability, and fabrication. Development of the first-wall/blanket mechanical design was most strongly influenced by the various materials options examined during the study for the breeder, coolant, neutron multiplier, and structure. A previous blanket design study,[1] which summarized previously proposed blanket design concepts, was used as a basis for the present study. In the STARFIRE study the mechanical design effort focused only on the use of solid tritium-breeding materials. The majority of effort was more specifically focused on options using the water coolant, which was selected for the reference design.

The most important design requirements and considerations differ significantly among the basic zones or regions of the first-wall/blanket system. The first wall must withstand high surface heat fluxes with the resultant high temperature gradients and thermal and mechanical stresses. Also, the first wall must withstand a limited number of plasma disruptions and must not be a significant source of plasma contamination. The amount of water coolant and structure must be minimized to maximize blanket tritium breeding ratios. The solid neutron multiplier, required for most of the candidate solid breeders, must

be cooled and must be structurally supported during normal operation and plasma disruptions. The latter consideration is especially important for neutron multipliers that contain a large percentage of lead. The solid breeder must be cooled, yet kept within a specific temperature range to assure acceptably low tritium inventories at steady-state conditions. A means must be provided for removing the tritium from the blanket on a continuous or periodic basis without requiring removal of the breeder. Previous design studies indicated that blanket concepts involving frequent or continuous removal of breeder to extract tritium were not feasible for STARFIRE.[1] Some considerations of major importance to the overall first-wall/blanket system design were structural support, removal of neutronic afterheat following reactor shutdown, and system reliability with respect to the avoidance of reactor shutdown caused by off-nominal operating conditions (e.g., loss of coolant).

The various candidate design options were developed in an iterative manner using the results of neutronics, thermal-hydraulics, and structural analyses performed as needed to adequately define the options. In the development of the options and their subsequent evaluations and comparisons, the first-wall/blanket was considered as a complete system to properly determine the effects of various choices on the overall reactor design. For purposes of discussion, however, the following subsections discuss individually each of the basic regions or zones which comprise the first-wall/blanket design. For each zone, the more important design requirements and considerations are discussed together with the design options developed for that zone. The basic geometric envelopes evaluated are discussed in Sec. 10.2.1. Design options developed for the first wall, neutron multiplier, and breeder zones are discussed in Sec. 10.2.2 through 10.2.4, respectively, while Sec. 10.2.5 and 10.2.6 summarize the reflector and coolant manifold zones, respectively.

10.2.1 Blanket Geometric Envelope Concepts

Numerous variations of two basic blanket concepts shown in Fig. 10-8, the module concept and the tube bank concept, were examined to determine which combination of geometric concept and breeder/multiplier arrangement could best be utilized in the overall reactor design.

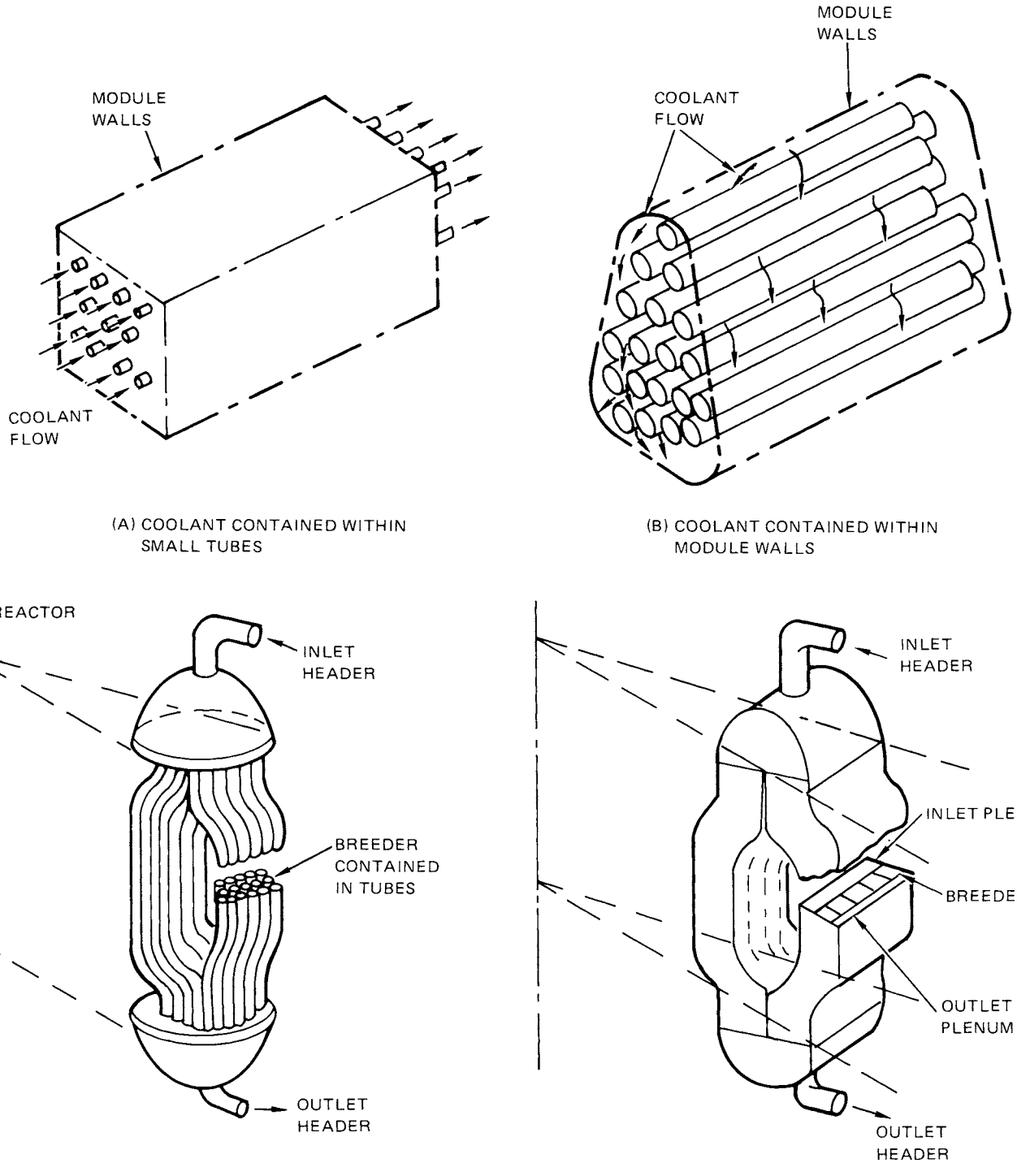

Figure 10-8. Blanket geometric and pressure containment concepts.

10.2.1.1 Module Concept

For this concept, individual modules are built up into blanket sectors, or orange-slice-shaped sections. The number of modules per sector is dependent on numerous design considerations. Each module contains the breeder (and multiplier if present) behind a first wall. Coolant for the interior of the module can be contained either within a relatively large number of small-diameter coolant tubes or by the module walls themselves.

In the pressurized tube concept, the tubes are embedded in the breeder (and the multiplier in some cases). Heat generated within the breeder is conducted through the breeder and the tube walls to the coolant.

In the pressurized module concept, the coolant flows over the breeder and multiplier, which are contained within metal structure for support, for protection from erosion by the coolant, and in some cases for reasons of compatibility with the coolant. This concept is considered more suitable for gas coolant than for water which in general would be used at considerably higher pressures. Analyses for various designs using the pressurized module concept showed that it consistently resulted in higher structural volume and larger void fractions than the pressurized tube concept, making it less desirable from the standpoints of tritium breeding ratio and blanket packaging efficiency.

10.2.1.2 Tube Bank Concept

The first wall and blanket for this concept are comprised of banks of tubes which contain the coolant. The tube axes are oriented vertically, with bends near the top and bottom at a shallow angle to the vertical to encompass the plasma chamber. The first wall tubes are relatively small in diameter (2-4 cm), with breeder zone tubes being much larger in diameter (20-80 cm). Tubes terminate in large hemispherical or cylindrical headers at the reactor top and bottom, located between adjacent TF coils to minimize reactor size. The solid breeder is contained inside the breeder zone tubes in the form of small spherical pellets. Analyses showed that for He coolant, directing the flow vertically through packed beds of spheres in the tubes led to very high pumping power requirements; as much as 50% (work basis) of total reactor thermal output. To obtain reasonable coolant pumping powers with gas coolant, either the

breeder had to be contained in an annulus inside the breeder tubes, or the space for coolant flow between spheres had to be increased by some artifice to be a significant fraction of sphere diameter.

One variation of this concept is the monolithic cell, in which long vertical cells of roughly rectangular cross section contain the breeder spheres. An inlet plenum at the front face directs coolant into the cell; the coolant flows through the breeder zone radially outward from the plasma center to a similar outlet plenum at the rear of the blanket. The first wall is in general a separate tube bank cooled by water or gas.

Both the tube bank concept and the monolithic cell variation were considered inferior to module concepts, both in terms of their impact on the reactor design and their relative disadvantages as breeding blankets. These concepts were considered only for solid breeders which required very short diffusion paths for adequate tritium release or which had to be removed from the reactor to extract tritium. In general, direct contact of breeding material and coolant was not considered acceptable and blanket concepts that required blanket removal for tritium processing were not economically viable.

10.2.2 First Wall

A critical consideration in the first wall design for a commercial tokamak reactor is protection of the metal first wall from erosion during normal operation and from ablation or vaporization during plasma disruptions. The design concern is twofold, in that excessive sputtering could severely impact plasma performance and erosion could result in a relatively short first wall design life due either to rapid erosion of a thin wall or excessively high thermal strains in a thick wall. The relative merits of bare first walls, armor or tiles, and coatings are summarized. The mechanical designs of forced-circulation-cooled first wall concepts are evaluated and the advantages of an integrated first-wall/blanket are assessed.

10.2.2.1 First Wall Concepts

Bare First Wall -- As discussed in Chap. 8, from the standpoint of plasma performance the use of high-Z materials (such as steel) as the first physical barrier to the plasma does not appear to be viable. Construction of

a forced circulation-cooled first wall from low-Z materials is not considered feasible. Therefore, the bare first-wall concept is not proposed for STARFIRE.

Armor or Liner -- Graphite has often been proposed and analyzed as a candidate low-Z material for armor, interposed between the first wall and the plasma and generally fabricated as tiles. Although graphite has a high vaporization temperature ($\sim$ 2000°C) it has a low conductivity, which limits its ability during normal operation to radiate the surface heat flux (and neutronic heat) from its back face to the first wall without approaching the vaporization temperature limit at the front face. This limitation results in a neutron wall load limit of $\sim$ 2 MW/m^2 for designs with armor covering all the first wall, and $\sim$ 3 MW/m^2 for designs with only the inner first wall covered. The former value is not acceptable for STARFIRE. The latter value is marginal, and in addition some other form of protection, such as a coating, would still be necessary for the remainder of the first wall surface area. As discussed in Chap. 8, excessive chemical sputtering makes graphite unacceptable for the first-wall application. Further analyses and development work are required to identify a suitable material for this application.

Coatings -- The addition of a coating or cladding of a low-Z material was determined to have a number of distinct advantages compared to armor for the first wall mechanical design. The coating concept provides additional flexibility in the materials options since the coating material can be selected primarily on the basis of its surface-related properties and the substrate can be selected primarily on the basis of its structural properties. Additional materials related considerations are presented in Chaps. 8 and 10. Also, the fabrication complications of an armor system and its attachment to the first wall are eliminated, which simplifies the first-wall/blanket system. In-situ coating refurbishment/repair techniques are also considerably simpler than in-situ replacement of armor tiles. Second, it permits neutron wall loading values much higher than those considered acceptable with the armor or radiatively-cooled liner. The candidate coatings have high vaporization and melting temperatures; coupled with good thermal conductivity (e.g., beryllium). As a result, maximum allowable temperatures for coatings of reasonable thicknesses are not exceeded for any wall loading values which could realistically be considered for STARFIRE. An added benefit of the coatings' good thermal conductivity is that it aids in conducting heat from

hotter to cooler regions of the first wall, which in effect increases the wall loading capability for any specific first wall design. The low-Z coating concept is selected for the reference STARFIRE first-wall design.

10.2.2.2 First Wall Mechanical Design

Various first-wall design concepts were studied in conjunction with the blanket concepts discussed in Sec. 10.2.1. The three basic mechanical design concepts studied were tubes, ribbed panels with channels having rectangular cross-section, and embossed panels consisting of one flat sheet welded to a second sheet having embossed (formed) half-channels. These concepts are illustrated in Fig. 10-9. Within the materials constraints presented in Sec. 10.1 and the thermal-hydraulic analyses in Sec. 10.5, helium is not considered a viable first-wall coolant for STARFIRE. Therefore, the first-wall design study focused primarily on a water-cooled wall constructed of advanced austenitic stainless steel.

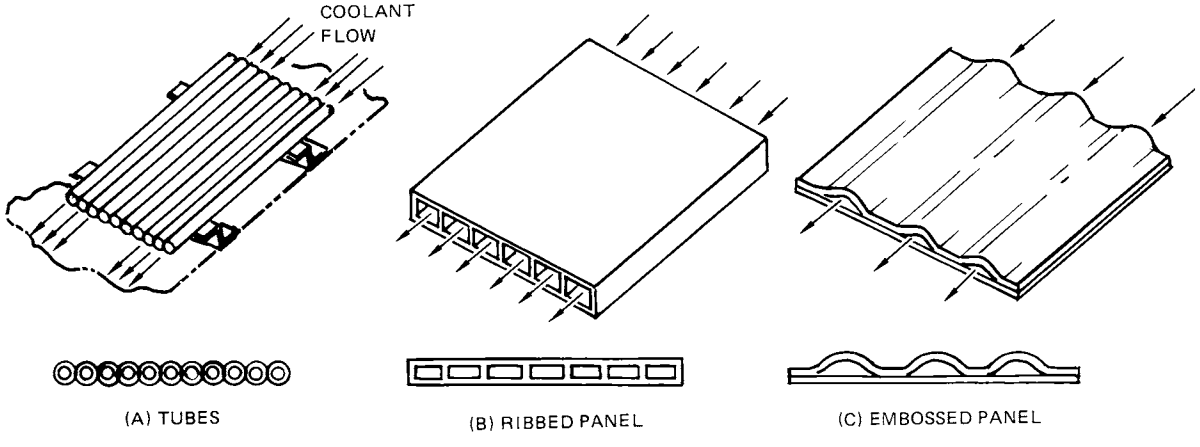

Figure 10-9. First wall design concepts.

Tubes -- The use of discrete tubes containing pressurized coolant has been proposed many times for tokamak first wall designs.[1] A design in which tubes are free standing, i.e., not mounted to each other or to supporting structure across the face of the first wall, results in a minimum of structural material, which enhances tritium breeding. However, the tube concept can result in a large equivalent volume of coolant in the first wall, which will significantly degrade the tritium breeding if the coolant is water and a neutron multiplier is used. Neutronics studies (Sec. 10.4) indicated that the presence of a small equivalent thickness of water coolant can reduce breeding even more than an equal thickness of stainless steel structure. Both ribbed panels and embossed panels can be designed to provide a relatively low equivalent thickness of water. The tube concept also presents considerable fabrication problems in welding the tube to intermediate supports and to manifolds.

For a single bank of contiguous tubes, it was considered necessary to support the tubes at discrete points along the first wall, so that motions due to thermal straining, flow-induced vibrations, and seismic events would not result in chafing of adjacent tubes. The use of two staggered banks of tubes with significant lateral and vertical space between adjacent tubes would alleviate these problems but would add more steel and coolant to the first wall, further degrading tritium breeding. Supporting the tubes results in added thermal strain problems for both the tubes and supports. The supports must be attached to the blanket front face and to the individual tubes. The required welding of the tubes at the support could result in problems of tube weakening or perforation and of local distortion. Adequate cooling of the tube supports is also a major problem.

Ribbed Panels -- In this concept, first wall coolant flows through channels of square or rectangular cross-section. The channels are formed by joining a front and rear wall with vertical ribs which separate adjacent channels. Major advantages of the ribbed panel concept compared to the tubes relate to simpler support, reduced concern over vibration and fretting problems and the possibility of using the first wall panel as an integral part of the blanket.

If a ribbed panel is designed with square channels, it has similar thermal-hydraulic and heat transfer characteristics to tubes of the same hydraulic diameter, and uses more steel than the tubes due to its less efficient structural shape for containing pressure. However, if the channels are designed with rectangular channels, the equivalent thickness of coolant present in the first wall can be reduced. This is important for designs with water coolant, since the moderating properties of water are quite detrimental to tritium breeding if a neutron multiplier is used.

The fabrication of ribbed-panel first walls from stainless steel would involve joining the ribs to the insides of the front and rear walls. Two state-of-the-art methods for accomplishing this joint are electron beam (EB) welding, and diffusion bonding; even better methods are likely to be developed in the future. Diffusion bonding would require heating the complete structure to temperatures at which the initial cold worked (CW) properties would be reduced to those of annealed material. It is believed that the greater radiation damage resistance of CW material would also be lost. The radiation damage characteristics of an EB weld zone are not known, but its microstructure changes from that of the CW condition are greater than those for the resistance weld used in embossed panels (see below). Since the loss of the CW conditions' radiation damage resistance was considered proportional to changes in microstructure, the EB weld was accordingly considered less desirable than resistance welding for first wall application.

The relatively large amount of welding required is considered a major disadvantage of this concept. This is particularly important for austenitic stainless steel since it is cold-worked to improve its radiation damage resistance. Welding may be less critical for other types of structural materials.

Embossed Panels -- The coolant channels for this first wall concept are formed by joining together two stainless steel sheets, one or both of which are embossed or corrugated to form a channel shape. The sheets are joined between adjacent channels by a continuous resistance weld or a roll-bonding process accomplished by passing two rollers along the outsides of the two-sheet assembly and flowing an electric current between the rollers through the sheets. The embossed shapes in each sheet can be semi-circular, semi-elliptical or trapezoidal.

The embossed panel concept has several significant advantages for a tokamak first wall design. First, it minimizes the equivalent volume of water coolant required in the first wall compared to the tube concept. Second, the resistance weld method used to bond sheets together between channels is believed to cause minimal impact on the radiation damage resistance of the structural material. Examination of the weld zone of resistance welded material shows that the microstructure is not markedly changed in the weld area. Since the microstructure is important for radiation damage resistance, the roll-bonding process is believed to be a good method for first wall fabrication. Any separation or cracking of welds between channels results only in a minute passage of coolant between adjacent channels. This is not significant since the flow is in the same direction across the first wall for all channels. The probability of a leak through a front or rear sheet to the plasma region or to the multiplier region is considered to be very low.

The major advantage of the embossed panel concept relative to the ribbed panel relates to the much simpler fabrication processes. The advantages relative to the tube concept are the simpler support requirements, reduced vibration and fretting problems, and the potential for using the first-wall panel as an integral part of the blanket.

10.2.2.3 Mechanical/Structural Integration of First-Wall/Blanket

An important decision in the evolution of the first wall/blanket mechanical design is whether or not to make the first wall easily separable from the blanket for replacement or repair operations. The first wall and the blanket have a number of fundamentally different design requirements and functions. Also, previous design studies have tended to predict first wall design lifetimes considerably lower than for the breeding blankets used with those designs. For the solid breeder concepts, blanket lifetimes are limited by burnup to values that may be similar to the first wall.

A first wall which can be separated from the blanket in a relatively easy fashion offers advantages to the economics of the reactor design if first wall design life is significantly less than blanket design life, and if the use of a separate first wall results in a significant reduction in maintenance time, leading to reduced reactor downtime and increased reactor availability. A first-wall/blanket design with an easily separable first wall

will, in general, be more complex than one in which the first wall and blanket are integrated both mechanically and structurally.

The most significant factors in the separate versus integral first wall decision related to: (1) the sector removal concept for first wall and blanket maintenance; (2) negligible reduction in maintenance times for replacing the first wall only versus replacing the first wall and blanket as a unit; and (3) additional reactor volume required for first wall designs made for easy separation from blankets. The sector removal concept was determined to be a better approach than individual module removal (or repair) in terms of first-wall/blanket maintainability. Thus, a first-wall/blanket sector must be pulled out of the reactor in order to gain access to the first wall. The total time required to remove a failed first-wall assembly from the blanket and to replace it with a new first-wall assembly was considered to be equal to or greater than the time required to simply position a new first-wall and blanket sector for insertion into the reactor. The rest of the maintenance operations and time lines, which comprise nearly all the total down time, are the same for both concepts.

It is important to note that for the separate first-wall concept to be viable, not only the first wall but also the next few centimeters of structural material must be replaced at the same time, since the radiation damage in this region of the blanket will be similar. For designs with the multiplier in front of the-breeder, this would require replacement of at least the multiplier zone and its coolant panels or tubes in addition to replacement of the first wall. This further complicates the overall first-wall/blanket design. In addition, design concepts with easily removable first wall components were shown to require more volume than integrated concepts in order to permit simple first wall removal operations. This affects reactor economics since for a given neutron wall loading and total thermal megawatt rating, increased reactor size results in increased capital costs and thus increased cost of electricity. A larger amount of structural material and coolant required for the separated first-wall concept will be detrimental to the breeding capability if a neutron multiplier is used.

10.2.3 Neutron Multiplier Zone

Only solid multipliers were given serious consideration in the present study. Four arrangements of a solid tritium breeder and neutron multiplier were examined. The choice of arrangement for a given materials combination is dependent upon materials compatibility considerations, the tritium breeding performance, thermal-hydraulics performance, and mechanical design considerations. The four arrangements examined, shown in Fig. 10-10, are discussed in this section in order of their relative complexity from the standpoint of mechanical design.

10.2.3.1 Breeder Only

A blanket concept with no neutron multiplier is the most desirable from the standpoint of design simplicity. However, this concept is feasible only if the selected breeder can achieve required breeding performance without a multiplier for a specific reactor and blanket design combination. Few solid breeding materials exist that will provide adequate breeding without a neutron multiplier. Incorporation of a neutron multiplier into the blanket greatly increases the materials compatibility problems, e.g., structure-multiplier and coolant-multiplier compatibility, and substantially increases the design complexity and fabrication difficulties. These aspects are particularly important since there are only a limited number of candidate neutron multiplier materials available (see Sec. 10.1 and 10.4).

10.2.3.2 Homogeneous Breeder and Multiplier

Potentially a breeding material and a neutron multiplier can be homogeneously mixed together. For this concept to be feasible, the breeder and neutron multiplier must be compatible over the design life of the blanket, both for normal operation and for off-nominal or accident situations. The multiplier must also be compatible with the tritium generated by the breeder. Design complexity is similar to that for the concept with no multiplier. Thermal-hydraulic characteristics of the two concepts may differ because of different materials properties, e.g., thermal conductivities. It is possible to divide the breeding region into zones depthwise, with varying breeder/multiplier volumetric ratios and enrichment levels of ^{6}Li to optimize the breeding performance.

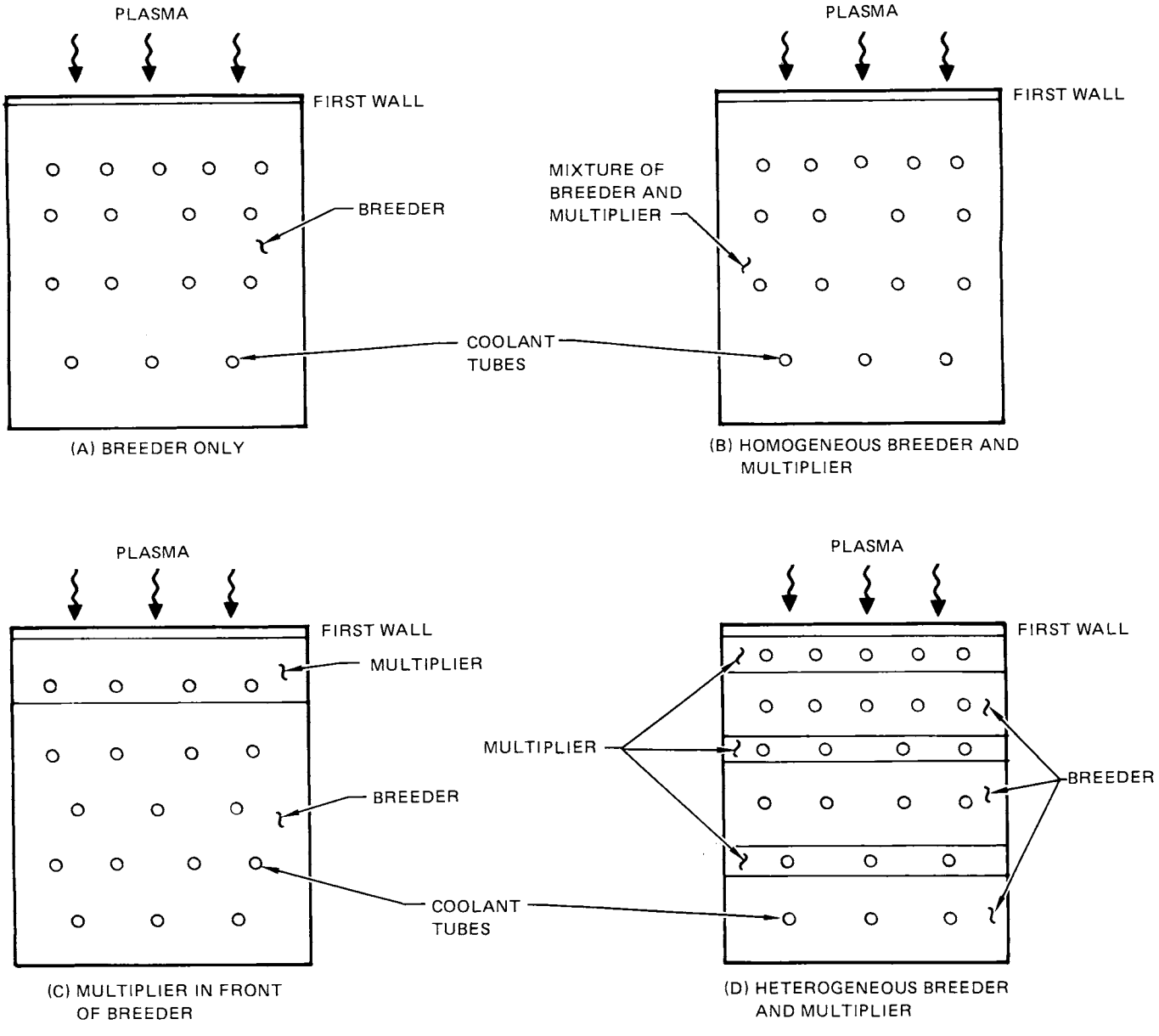

Figure 10-10. Possible arrangements of solid breeder and solid neutron multiplier.

10.2.3.3 Multiplier in Front of Breeder

In this concept, the multiplier is separated from the breeder primarily for reasons of chemical compatibility. This increases design complexity because the multiplier must be cooled separately from the breeder. Thermal-hydraulic characteristics of this part of the coolant system must be integrated with those for the breeder and first wall. Since the multiplier is a single region, it must be structurally supported as a separate entity from the breeder. The first wall, in general, can be used to remove part of the multiplier's neutronic heat. Tritium breeding ratio can be changed only by varying the thickness of the multiplier and breeder zones and by varying the ^{6}Li enrichment level in the breeder. The two most important mechanical design considerations for this concept relate to the multiplier cooling and structural support.

Multiplier Cooling -- For the multiplier thicknesses considered (typically 4 to 8 cm), cooling of the multiplier can be accomplished either by passing coolant tubes through the interior of the multiplier and/or by cooling both the front and back faces of the multiplier. The choice of cooling method is dependent on materials constraints and on the results of thermal-hydraulic and tritium breeding analyses. If the first wall can be used to cool the front face, then it is desirable from the standpoints of mechanical design simplification and tritium breeding to eliminate coolant tubes from the multiplier interior. Cooling of the back face can be best accomplished with a ribbed or embossed coolant panel, either of which permits heat transfer between two flat sheets in contact.

Multiplier Structural Support -- Locating the solid multiplier in front of the breeder presents an added complication to the design, not only because of cooling requirements, but because of the magnetic forces induced during plasma disruptions. These forces act uniformly over the multiplier (as well as any nearby structure) and tend to pull it toward the plasma chamber. In addition, the first-wall/blanket structure must support the multiplier mass and react all seismic and gravity loads. This is particularly important for those multiplier compounds containing large percentages of lead because of its high density.

The candidate solid multipliers considered generally have little if any inherent structural strength at the proposed operating temperatures. Accordingly, it was decided that the multiplier should be contained by a structural assembly which could withstand any forces transmitted to it as loads in bearing from the multiplier. Considering also the cooling and isolation requirements for the multiplier, the structural approach judged most logical was to use (if possible) cooling panels for the front and rear faces to act as load-carrying structure. The addition of intercostals perpendicular to the flow channel direction to join the two panels, breaks them into smaller load-carrying panels. The further addition of intercostals, parallel to the coolant channel and connected to both panels, couples the panels together into a structural beam as shown in Fig. 10-11. Depending on the structural concept selected for the rest of the blanket, the multiplier loads can then be transmitted directly into intermediate frames in the-breeder zone attached to the intercostals. If the second set of intercostals is not added, then the module

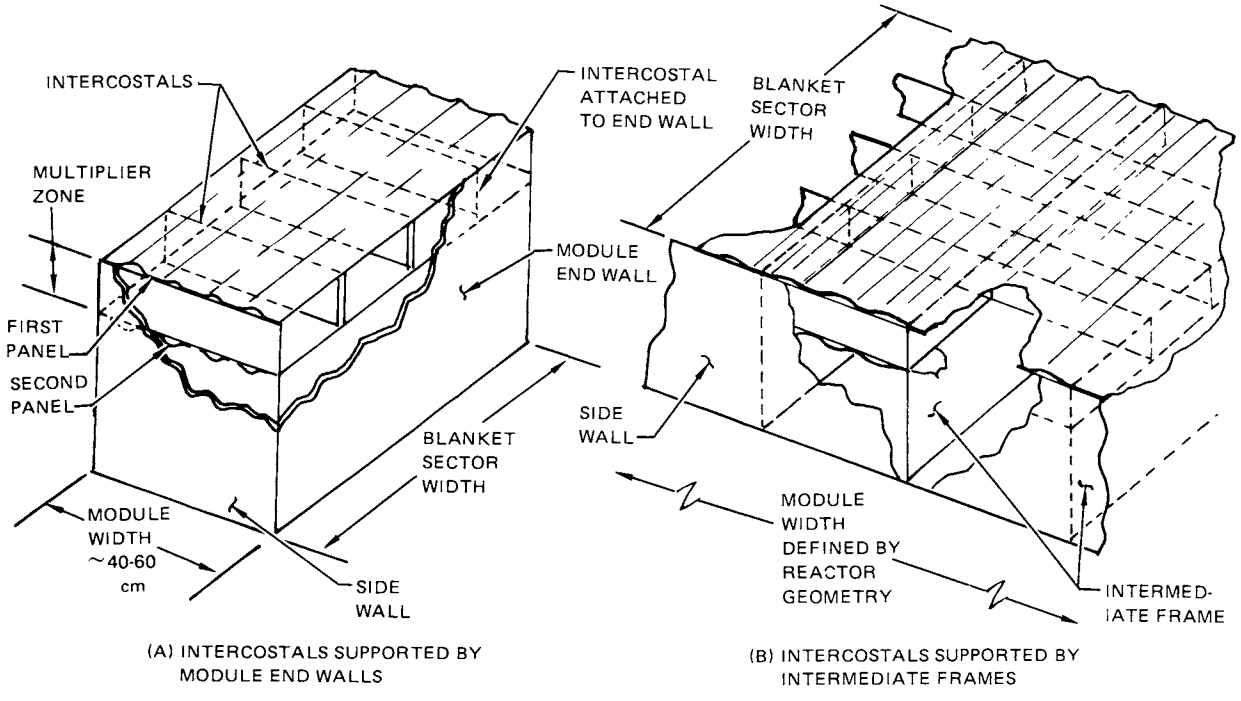

Figure 10-11. Neutron multiplier support concepts (multiplier in front of breeder).

walls to which the original intercostals transmit their loads must be brought relatively close together (∿ 40 to 60 cm) to keep intercostal thicknesses reasonable. The choice of multiplier structural support concept is thus strongly dependent on both the multiplier cooling requirements and on the mechanical design of the remainder of the blanket.

10.2.3.4 Heterogeneous Breeder and Neutron Multiplier

In this concept the multiplier is also separated from the breeder for reasons of compatibility. From the standpoint of mechanical design this is the most complex and least desirable concept because a breeder/multiplier partition must be provided, which increases the structure fraction requirement. Thermal-hydraulics and tritium removal systems also become more complex. The heterogeneous concept would be preferred over that with the multiplier in front of the breeder, only if advantageous from the standpoint of neutronics, e.g., better breeding performance or lower fractional burnup of ^{6}Li. The breeder and multiplier can be fabricated in the shapes of slabs, blocks or cylinders, each of which are penetrated by coolant tubes.

Although a number of design concepts are possible for multiplier cooling, the most efficient method for the breeder and multiplier material combinations studied was to pass water coolant tubes through each multiplier zone. Each breeder zone would be similarly cooled. The relative volumes of breeder and multiplier required for adequate breeding, coupled with their relatively poor thermal conductivities (beryllium being an exception to the rule) and resistance to heat transfer at the interface between zones, did not permit a simpler design in which only the breeder or only the multiplier was cooled. In addition, either the breeder or multiplier regions must be contained within pressure tight chambers to assure no physical contact between regions. This complicates blanket fabrication and the provisions for the flow of helium purge gas through the breeder.

10.2.4 Tritium Breeder

The STARFIRE study focused only on the use of solid breeding materials and the blanket design effort concentrated on the ceramic oxides that offered the most potential for tritium recovery. These materials characteristically

have relatively low densities, low thermal conductivities, and high melting temperatures. The low thermal conductivities will create large thermal gradients within the breeding materials. As discussed in Sec. 10.1 and 10.3, tailored microstructures with relatively high porosities are required to facilitate tritium-recovery. In general, these compounds are not highly reactive with water or the candidate structural materials. Of the ceramics considered, Li_2O is the most reactive. It is concluded that these materials cannot be used in direct contact with the candidate neutron multipliers. The major safety concerns relate to pressure transients that could result from a leak of the high pressure water into the high-temperature, highly-porous breeding material.

Three important considerations in mechanical design concepts for breeder zones are: (1) coolant tube configuration; (2) breeder fabrication method; and (3) breeder zone internal structure. These design aspects are discussed in the following paragraphs.

10.2.4.1 Coolant Tube Configurations

Three basically different coolant tube configurations were studied: radial-flow tubes, straight horizontal-flow tubes with tube-sheet manifolds, and U-bend tubes with horizontal flow. These configurations are shown schematically in Fig. 10-12. Each concept has differing requirements for the placement of inlet and outlet plenums. The radial tube orientation also results in designs fundamentally different from those with straight or U-bend tubes.

Radial-Flow Tubes -- In this concept, the coolant tubes have their axes oriented perpendicular to the plane of the first wall. The tubes extend through the breeder zone from a forward plenum between the multiplier and breeder to a rear plenum between the breeder and reflector zones. This concept was not considered in depth, primarily because of severe design problems related to thermal-hydraulic characteristics of the coolants and to thermal characteristics of the breeders. The key problem is tailoring of the flow velocity with depth in any given radial tube, to match the depthwise exponential reduction in volumetric heating in the breeder while keeping the breeder within the minimum and maximum temperature range required for adequate tritium removal (Sec. 10.3). An array of rather closely spaced small diameter tubes is required

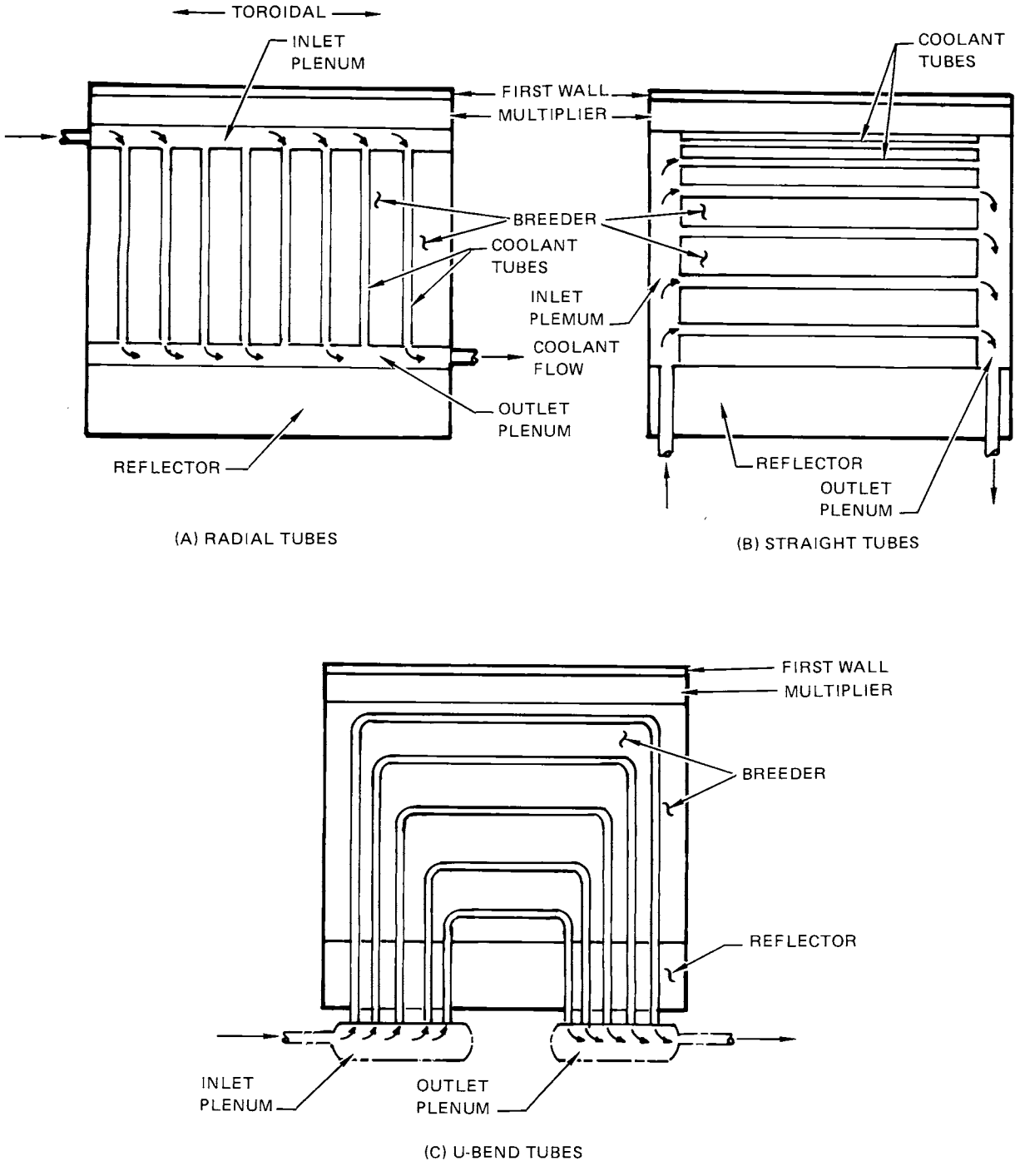

Figure 10-12. Breeder coolant tube configuration concepts.

at the front of the blanket. Tube quantity and spacing is thereby established for the full blanket depth. Because of the lower heating rates at the rear of the blanket, appropriate cooling characteristics in this region are not easily attainable with this concept. From the standpoint of thermal-hydraulics, meeting all the design requirements for the solid breeders is extremely difficult with radial flow. Also, the volumetric fraction of water coolant in the blanket is quite high and net tritium breeding may not be adequate. For helium coolant, neutron streaming through the tubes is an added problem.

Straight Tubes -- For this concept the coolant tube axes are oriented horizontal and parallel to the first wall plane. The tubes pass through the breeder across the width of the blanket from one side of the sector to the other. The tube ends connect to inlet and outlet plenums at the sector sides.

The coolant tubes are arrayed from the front to the back of the blanket in layers or "banks". The spacing of the banks plus the flow rate and flow velocity in the tubes for each bank are all varied as required to assure equal pressure drops and coolant temperature increases for each tube. The plenums are connected to large manifold tubes at the rear of the blanket. The plenums would be designed to withstand the coolant static pressure, and would also be utilized as blanket module support structure. Overall thermal stress problems are not considered difficult due to the low temperature difference (40°C water coolant ΔT) across the blanket width. However, assuring isolation of the breeder from the coolant in the event of a tube end weld leak could be more difficult than for the U-bend tube concept. Although the plenum regions have large volumetric fractions of steel and coolant, this is probably not a prohibitive problem for tritium breeding since the plenums represent only small local areas $\sim$ 10 cm thick or less at the blanket sides. The structure and coolant volume fractions through most of the breeding zone would be similar to those for the U-bend tube concept. Fabrication of the blanket structure and coolant system are straightforward, and the concept is adaptable to any of the candidate breeder fabrication options (Sec. 10.2.4.2). A major concern for this concept is the large number of pressure welds in the high radiation regions.

U-Bend Tubes -- The coolant tubes for this concept are in the shape of a flat-bottomed U. The tube portion representing the bottom of the U, which is the longest part of the tube, extends horizontally from one side of the

blanket sector to the other. The tube ends terminate at the rear of the blanket behind the breeder zone near either side of the sector. The plane of the tube bends is perpendicular to the first wall. Tube spacing, internal diameter, and flow velocity can be varied to match breeder neutronic heating rates depthwise, and to maintain equal pressure drops and coolant temperature increases in the tubes.

The tube ends are connected to inlet and outlet manifolds located behind the breeder in the reflector region. The breeder zone is isolated from the plenum region by joining the tube walls to the flat plate separating the breeder and plenum regions, through which the tubes pass. The joints can be made by welding or brazing between the tube and plate, or by brazing the ends of flexible C-section circular rings to the tube and plate, respectively. Major advantages of the U-tube concept include elimination of pressure welds in the high radiation regions, minimization of expansion stresses at tube ends, flexibility of tube spacing and isolation of pressure welds from breeder region.

10.2.4.2 Breeder Fabrication Methods

Important factors that influence the solid breeder fabrication methods include the tailored microstructure required to facilitate tritium release, the need for the helium purge channels in the breeding material, and the complexity of blanket assembly procedures. As discussed in Sec. 10.1 and 10.3, a low-density material with a fine grain size ($\leq$ 1 μm) and a bimodal pore distribution is believed to be the most desirable microstructure. Three potential methods for fabrication of the solid breeding material in the blanket modules are sintered blocks, vibratory compaction, and slip casting.

Since direct contact of the breeding material and the coolant was not considered acceptable, the proposed tritium processing method involves passing a high-purity, low-pressure helium gas through the breeding material. The helium would flow through a large number of small ($\sim$ 2 mm) diameter holes spaced approximately equidistant from and parallel to the adjacent coolant tubes. The holes are thus located where the breeder temperature is highest. Since the flowrate of the helium processing stream is low, only 1-2 MWth of power is removed from the blanket by the helium processing stream. A major consideration in the selection of the viable breeder fabrication methods

relates to the formation of these channels for the helium. Since all of the tritium must pass across the channel surfaces, the tritium should not be restricted by nonporous or low porosity tubes. Also, neutronics consideration (parasitic absorption) and compatibility limitations at the high temperatures severely restrict the choices of materials that could be used to form the channels. It is concluded that the most appropriate method is to form the channels by the breeding material itself. As a result, the methods of breeder fabrication that can be used are limited. Important aspects of possible breeder fabrication processes are briefly described.

Sintered Product -- This term is defined to be the form of solid breeder produced by baking the breeder within a mold at high temperature to form a monolithic block with the desired breeder density. The breeder cannot be baked with the coolant tubes embedded within it, because the time/temperature combination required would degrade the radiation damage resistance of the tubes. Therefore, the breeder must be made in block or slab form, with preformed depressions and helium purge gas channels, then fitted around the coolant tubes as they are assembled in banks to completely fill the breeder cavity. The desired breeder material density and microstructure can readily be obtained by this method (see Sec. 10.1.1). However, its use constrains the blanket assembly method options and increases fabrication difficulties because of the requirement to fit-up the many different pieces.

Vibratory Compaction -- This method involves partial or complete filling of the breeder cavity with fine particles of breeder, followed by compaction of the material using vibrating or pulsating devices which act on the free surface of the breeder to gradually achieve the required density. For blanket concepts with tubes oriented parallel to the first wall, sequential filling/compacting operations are difficult and may require such operations to be performed after each tube bank is sequentially installed, which again constrains blanket assembly method options. It is considered difficult to achieve uniform breeder density throughout the breeder zone and to prevent voids or pockets in small regions not readily filled by the incoming flow of breeder powder. Formation of the helium channels is also more difficult with this process.

Slip Casting -- This method permits formation of the breeder as a solid block around the complete array of coolant tubes. The powder is poured into the breeder cavity as a wet slurry, which makes prevention of void formation easier. The assembly and slurry are baked to drive out the liquid agent, resulting in a solid block of breeder with embedded coolant tubes. Helium purge channels are formed subsequently by "rodding out" the breeder, or by inserting rods of low-melting-point material (e.g., wax) which gradually melt away during the bakeout leaving the purge channel voids in their place. This is the simplest of the proposed breeder fabrication methods. It has the least impact on blanket fabrication complexity and does not constrain the choice of blanket fabrication option, However, it is questionable whether all the liquid agent can be driven off at bakeout temperatures low enough to preclude degradation of coolant tube cold-worked structural properties, and whether breeder shrinkage during bakeout can be accommodated. The microstructure of the ceramic can be less well controlled by this method compared to the sintered produce.

10.2.4.3 Structure

Breeder zone structure is defined to include the walls of the blanket which surround the breeder, together with any structural members located within the breeder. The walls must be designed to withstand forces from the helium purge gas pressure, and must also react some or all of the loads on the breeder due to gravity and seismic forces. In general, the walls should provide a large part of the structural rigidity of the first-wall/blanket assembly, to result in the most efficient overall structural system. For some blanket concepts, support members within the breeder zone may be necessary to provide breeder support and to transmit magnetic forces acting on the first wall and multiplier to the main blanket sector structure at the rear of the blanket.

The selected structural concept must satisfy a number of important design requirements. All walls and internal structure must be actively cooled to remove neutronic heat plus heat absorbed from the high-temperature (up to 850°C) breeder regions. The stainless steel structure should be kept at a nominal temperature of $\sim$ 350°C or less, to retain good structural properties and to minimize thermal strain problems. The total volume of structure

should be minimized to maximize tritium breeding. The structural concept should be easily fabricated and assembled as a part of the total first wall and blanket assembly. In particular, the structure design must be integrated with the coolant system mechanical design, and should not constrain the selection of breeder fabrication option.

The evaluation of structural design options concentrated on those most suitable for the selected reference design blanket, which uses U-bend tubes and a neutron multiplier in front of the solid breeder. These options were not analyzed quantitatively but instead were examined qualitatively to determine their ability to satisfy design requirements and to be efficiently integrated into the overall first-wall/blanket design. Some of the specific design options are discussed below.

Internal Frames -- The use of structural frames within the breeder zone is a logical method of transmitting the magnetic forces acting on the multiplier and first wall to the main sector support structure at the rear of the blanket. The forces cause a direct uniform tensile load in the frames. This load can be reacted by using the internal frames as beams to transmit the loads to the sector side walls. A more structurally efficient method would be to tie the internal frames to similar frames within the reflector (or reflector/manifold) zone which would connect the front and back structural walls of that zone. By this means the structure for all zones of the blanket assembly, from the first wall through the reflector, would be tied together structurally to react magnetic, gravity, and seismic loads.

The strongest and most efficient breeder zone internal structure would utilize two sets of frames with their planes perpendicular to each other and to the first wall. However, the second set of frames would be perpendicular to the axes of the straight portions of the U-bend coolant tubes. This would require each frame to be segmented depthwise, with segments and individual tube banks installed sequentially into the breeder zone. Cooling of the individual segments presents a further complication. On the other hand, frames with planes parallel to the coolant tubes can be installed as a single unit and are relatively simple to cool since the frames' cooling channel (or tube) ends can be located near the frame ends, in line with the coolant manifolds at the rear of the blanket. Panel-type structures with integral coolant channels similar to the first wall provide attractive internal frames.

Side and End Walls -- Two basic approaches to the design of the side and end walls were examined. On the first approach, the walls are designed as stiffened flat structural panels each with a separate cooling circuit. The panels are connected to the internal frames and welded to the panel ends to form part of the helium purge gas pressure boundary.

In the second approach, the first wall and second wall (behind the multiplier) coolant panel cross sections are continued without modification down the sides of the blanket to the back of the breeder zone. The panels are welded together along the blanket side to form a structural unit, which in turn, is joined to blanket module end wall panels to form part of the helium pressure boundary. This approach has the advantage of being self-cooling and of minimizing the manifolding problems. The first wall/second wall structural unit also provides adequate support for reacting the loads produced by the helium static pressure.

10.2.5 Reflector

The reflector region is located immediately behind the breeder zone from which it is separated by a stainless steel panel. The reflector serves to reflect low-energy neutrons back into the breeder which results in a slight gain in tritium breeding ratio. As discussed in Sec. 10.2.6, the reflector and manifold zone can be integrated in some design concepts, which results in a less complex design that occupies less volume than two separate zones. The two materials given most attention in the study were graphite and a water/steel combination. These were the most attractive from the standpoints of material compatibility, fabricability, costs, and design integration.

Graphite -- This material offers a number of advantages as a reflector. It is highly stable, low in cost, and requires relatively small thicknesses ($\sim$ 15 cm) for adequate performance. It can be machined or molded into desired configurations and can be bonded to itself. The metal structure surrounding the graphite must be cooled to maintain acceptable structural temperatures ($\lesssim 400°C$). It may also be necessary to cool the interior of the graphite to keep maximum temperatures at acceptable levels (below $\sim 900°C$).

Water/Steel -- For a given thickness, the combination of water and steel is essentially the neutronic equivalent of graphite as a reflector. This is true for most water-to-steel equivalent thickness ratios resulting from practical designs. A reflector could be designed which consists of a steel panel with internal chambers filled with water. The steel would be cooled by the water, but the water itself would have to be circulated continuously through a heat exchanger outside the reactor to remove the heat generated neutronically. The water coolant in the manifold tubes (and headers if present) at the rear of the blanket could also serve as part of the reflector. Bringing the header/manifold system into the reflector zone and removing graphite from that part of the region, is an attractive option from the standpoint of overall blanket design simplicity, and is discussed further in Sec. 10.2.6.

10.2.6 Manifold

In the manifold region, the breeder coolant tubes are connected to the large manifolds which channel the inlet and outlet coolant flow to the blankets. The mechanical design of this zone was governed by a number of important guidelines and goals:

1. maximizing reliability (avoidance of reactor shutdowns caused by coolant system leaks);
2. providing for removal and replacement of a failed blanket module;
3. fabricability; and
4. integration into the reflector zone.

The most complicating factor in achieving a good design is the large number of breeder coolant tubes; a total of $\sim$ 60,000 in the blanket which will require a minimum of $\sim$ 120,000 pressure welds. A second factor was the use of dual coolant circuits. The two circuits are completely isolated from each other. The first wall and second wall, and alternate banks of coolant tubes, are connected to alternate cooling circuits. In the event of a loss of coolant (or flow) from either cooling circuit, cooling provided by the other circuit would be adequate to prevent blanket damage for proposed plasma shutdown scenarios. For reference shutdown conditions, the breeder, multiplier, and structure temperatures will not exceed levels beyond which the

blanket assembly cannot be safely and reliably operated. Examples of damaging conditions would be thermal sintering of the breeder, and embrittlement or loss of cold-worked structural properties of the stainless steel.

The concept given most attention used relatively large-diameter manifold tubes for inlet and outlet flow, located within or behind the reflector zone. The coolant tube ends were connected either directly to the manifolds or to headers which were in turn connected to the manifolds. An alternate concept features coolant flow through large channels of rectangular cross section which span the rear face of the blanket, so that the structure and coolant together serve as both reflector and manifold. These concepts are illustrated in Fig. 10-13.

Tubular Manifolds -- In this option the breeder coolant tubes are welded directly to stubs which extend from the two inlet and two outlet manifold tubes. The manifold tubes extend poloidally along the full length of each module; one inlet/outlet set is used for each of the two coolant circuits. Flexibility in the manifold lines is provided by bellows welded into the manifold at or near the welded joints which connect the manifolds at the intersections of adjacent modules.

The coolant tubes are rerouted near their ends as needed inside the breeder zone to permit the alternate "odd and even" banks of tubes to be conveniently welded to the manifold stubs. Welding would be accomplished by a pre-programmed computer-driven weld head which performs an electron beam weld at the joint. A hand-operated version of such a weld head is in use today. For the diameters of the reference design coolant tubes, required clearances are only 2.5 cm between adjacent tubes and 2.0 cm along the tube to either side of the joint. These clearances are provided without difficulty in this option, assuming that the inside manifold, outside manifold, and sector support frames are sequentially welded into or mechanically attached to the blanket assembly.

The concept using manifolds without headers results in relatively simple operations for blanket module removal and replacement. The only blanket coolant connections which must be cut and rewelded during this fully remote operation are the eight connections of the coolant manifolds at the module ends (one joint at each end of each of four manifold tubes). Modules can be

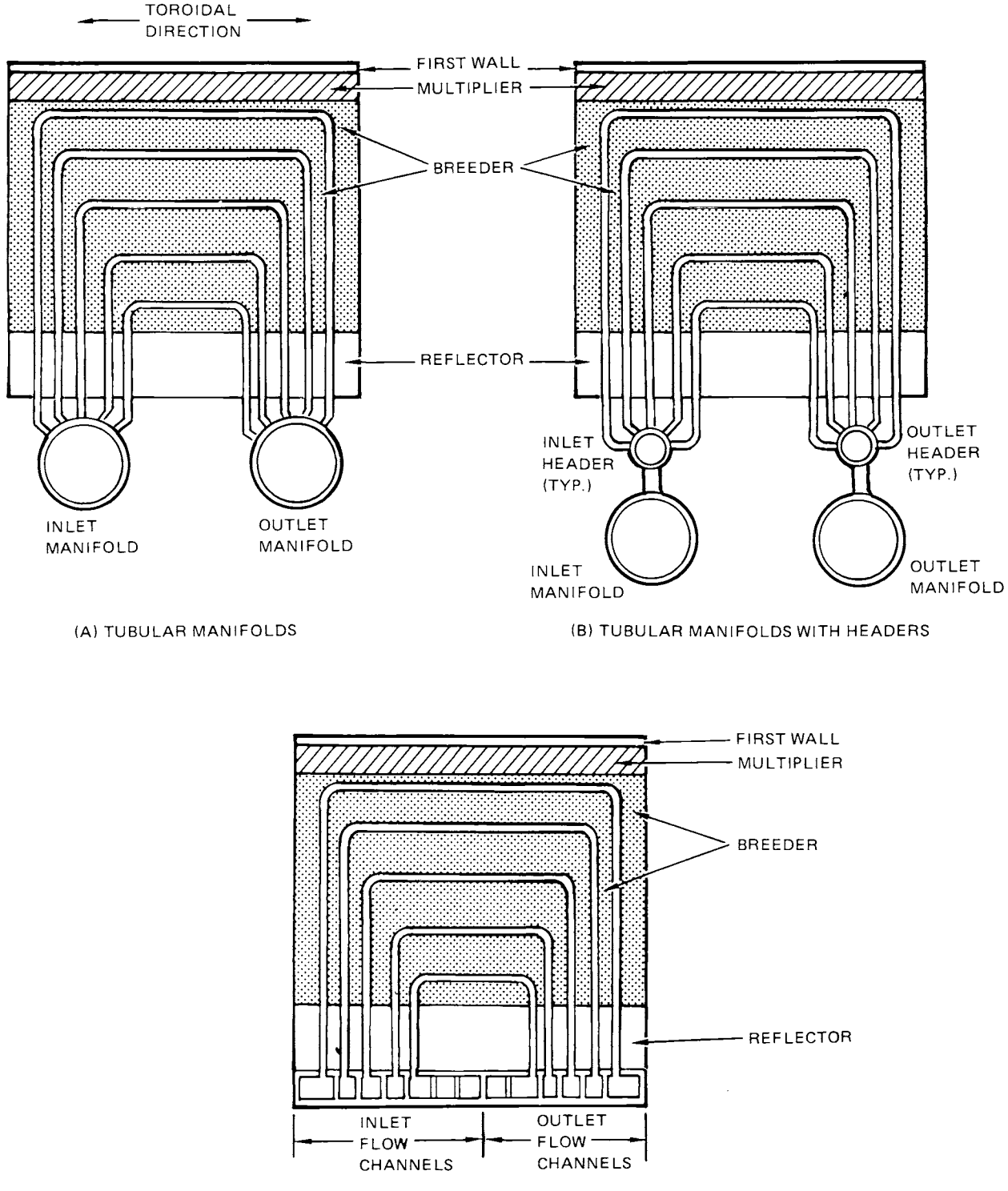

Figure 10-13. Breeder coolant tube options.

physically removed from the blanket sector either to the outside of the sector by cutting or unbolting the sector support frames at the module ends, or to the inside without disturbing the frame by sequentially removing adjacent modules having a "keystone" geometry. Removal without cutting the manifolds is not considered viable for this option because of the very large number of coolant tube connections which would have to be cut and rewelded. One potential disadvantage of the concept is the accumulation of thermal strain along the length of the manifolds in a given module which could arise if one circuit becomes considerably colder than the other during cool down of the blanket following a reactor shutdown.

Tubular Manifolds with Headers -- For this option, the breeder coolant tubes are welded to stubs extending from headers. The headers are in turn connected to the manifolds, and are physically located between the coolant tube ends and the manifolds. The header diameters are significantly less than those of the manifolds and their length is set by the length of the module subassemblies ($\sim$ 60 cm). Thus, for a blanket module of average length, this option would add 12 to 16 headers (three or four for each of two inlet and two outlet manifolds) to the system previously described.

The addition of headers offers several possible advantages. First, the concern over possible thermal strain problems between coolant tubes and manifolds is reduced, since only a fraction of the total number of coolant tubes in the module are connected to any one header. The connections between headers and manifolds also offers an added degree of structural flexibility to the system. Second, it permits the option of fabricating header/tube bank subassemblies and assembling them as a unit into the module. Third, it permits modules to be removed and replaced without cutting and rewelding manifolds. Only the connection pipes between individual headers and manifolds are cut and rewelded (a minimum straight pipe length of 6 cm is required). However, to be replaced the modules must be removed in "keystone" fashion to the inside of the sector, unless the sector frames are moved considerably further to the rear of the blanket to permit sideways removal. This option has the disadvantage of requiring additional volume for the coolant system, which is taken either from the breeder or from the reactor vacuum plenum behind the manifold zone.

Rectangular Channel Manifolds -- This option represents a complete integration of the reflector and manifold zones. The manifold coolant flow is contained in contiguous channels of rectangular cross section which span the width of the blanket module. The channels are formed by connecting the flat plate at the rear of the breeder zone to a similar plate at the rear of the manifold zone by ribs which partition the zone into a number of separate channels. The combination of water and steel also serve as an effective reflector (see Sec. 10.4).

The concept offers significant advantages in simplification of the blanket mechanical design. It eliminates one material, graphite, and the cooling requirements associated with the use of graphite as a reflector. The concept provides an inherently strong "backbone" for individual modules, and when integrated with the sector support frames results in a strong blanket sector structure with minimum deflections from mechanical loads. Because of the relatively small total depth required to adequately serve the functions of both reflector and manifold (10 cm or less), more volume can be provided for the vacuum plenum between the blanket and shield, and/or the reactor size can be slightly reduced to achieve a capital cost saving.

Improved reliability can be achieved by incorporating dual welds around each of the breeder coolant tube joints. This condition can be achieved by making the wall separating the breeder from the manifold out of two separate plates, which are welded together to form a single structural panel. A continuous electron beam weld is made between the plates around each of the tube ends which penetrate the panel, thus forming a small-diameter pressure-tight chamber of near-zero thickness between panels around each tube. The tube ends are welded around their circumference individually to the top and bottom plates of the panel. As a result, in order for coolant in the manifold to contact the breeder through the tube end weld region, both welds at one specific tube end must develop a through-crack. If only the manifold-side tube-to-plate weld leaks, coolant enters the small chamber but is prevented from entering the breeder zone by the reflector-side tube-to-plate weld. If only the reflector-side weld cracks, low-pressure helium enters the small chamber but is retained by the manifold-side weld. Only if both welds develop a through-crack at a given tube end, can the coolant enter the breeder.

This concept was briefly analyzed to demonstrate its basic structural feasibility on a module level but was not analyzed or designed in depth. A number of areas require further development and analysis before the concept can be considered for the reference design blanket:

1. stress concentration regions at rib/wall intersections;
2. thermal strains between the coolant tubes and channel structural assembly;
3. details of manifold connections between modules; and
4. incorporation of dual coolant channel concepts.

10.3 TRITIUM RECOVERY

Tritium recovery from solid tritium-breeding materials has been identified as a key factor in establishing the viability of the solid-breeder concept and an important consideration in the selection of the primary candidate materials (see Sec. 10.1.1). In-situ tritium recovery from fusion blankets is by far the most desirable if not the only viable method of tritium recovery. Mobile solid blanket concepts have been proposed as a means of tritium recovery, however, the feasibility of this concept is questioned primarily on the basis of breeding capability and design complexity, particularly for the tokamak configuration. The economics of a batch-type tritium recovery scenario is generally regarded as unacceptable for a power reactor system.[1]

The emphasis on tailored microstructure of the solid breeding material selection in Sec. 10.1.1 and the concern of radiation-induced sintering arise primarily from the tritium recovery requirement. Also, the blanket design concepts discussed in Sec. 10.2 are greatly influenced by the constraints imposed by the tritium recovery schemes. Also, tritium recovery was a major factor in the selection of ceramic breeding materials over the intermetallic compounds as the primary candidate for STARFIRE.

In the proposed STARFIRE blanket concept, tritium generated in the solid breeder is removed by a low-pressure helium purge stream that circulates through small channels formed in the ceramic (Fig. 10-2). The breeder material is in the form of a low density monolithic structure with a bimodal pore distribution, i.e., a small grain size and fine porosity within particles

that are fairly coarse with a more coarse porosity between the particles. The bred tritium must undergo five steps in the tritium recovery process:

1. bulk diffusion in the grain,
2. desorption of T_2O at the grain surface,
3. migration through interconnected grain boundary porosity to particle surface,
4. "percolation" through the porosity in the packed bed of particles, and
5. convective mass transfer out of the blanket in the helium processing stream.

In addition to the contributions imposed by these kinetic mechanisms, the tritium inventory in the solid breeder is dependent upon the tritium solubility in the grains at the equilibrium T_2O pressure in the gas phase. The T_2O pressure will vary throughout the blanket from a minimum value in the helium channel to a higher value within the grain boundary porosity at points away from the channel.

In the present analysis, the range of materials and operating parameters that will provide acceptable tritium release rates from candidate breeding materials are evaluated from the existing data base (see Sec. 10.1.1 and Appendix E). Estimates of the steady-state tritium inventory are presented for the reference blanket under the anticipated operating conditions.

10.3.1 Analysis of Tritium Release Mechanism

The data base for evaluating the tritium release mechanisms and the steady-state tritium inventory in the solid breeding blanket concepts is very limited. Tritium recovery experiments on solid breeding materials of interest have not been conducted under conditions anticipated in STARFIRE. Also, the data base for evaluating the individual kinetic processes and the thermodynamic equilibria is not sufficient to accurately determine the release rates and the tritium inventory. Both types of data have been analyzed to obtain a best estimate of the most favorable conditions for tritium release from the candidate breeding materials.

10.3.1.1 Analysis of Tritium Recovery Experiments

The tritium recovery experiments that have been performed are limited to short-term, low-temperature irradiations with post-irradiation tritium recovery. Therefore, tritium concentrations generated in these experiments were low, the neutron fluences were low, and the radiation temperatures were below those of interest. The data from these experiments represent a combination of several of the five steps, primarily the first three and part of the fourth step. In order to better understand the processes involved in tritium recovery, a number of models were developed.

Before discussing the five steps and models in detail, a further set of definitions is useful. There are two ideal limiting cases for determination of the tritium inventory. First, one may assume that the tritium inventory is diffusion controlled (i.e., step 1 predominates). Accordingly, Ficks' Laws are solved assuming steady state, a geometry (e.g., spheres), and boundary conditions (e.g., zero surface concentration). The diffusional model gives a tritium inventory corresponding to the concentration gradients within individual grains. Since this model usually assumes that the tritium concentration at the grain edge is zero, the calculated tritium inventory is obviously lower than the true inventory.

Another approach is to assume chemical equilibrium, with a fixed tritium (or T_2O) pressure in the gas phase in equilibrium with the solid. This method assumes uniform concentrations (activities) of tritium throughout the blanket. Because this model does not account for concentration gradients, tritium inventories are again underestimated. For this analysis, the tritium inventory is assumed to be the sum of a diffusive component and an equilibrium component. The total tritium inventory is then the sum of the diffusive inventory and the solubility inventory. In this context, the analysis of tritium release and the five mechanistic steps are discussed below.

Bulk diffusion is considered to be a significant contributor to the tritium inventory. For spherical particles of radius r, assuming zero surface concentration, the tritium inventory I is given by

$$I = \frac{1}{15} \dot{I} \, r^2/D \qquad (1)$$

where $\dot{I}$ = the tritium generation rate and D = diffusivity. It is very significant that the tritium inventory is a function of the square of the particle size. Clearly, small ($\sim$ 1 μm) grain sizes are required for minimum tritium inventory and the grains must not enlarge significantly during the lifetime of a reactor blanket. While diffusivity values for hydrogen have been measured for many solids, there is a rather large uncertainty for what the correct values for tritium in solid breeders will be. Kinetic experiments of post-irradiation tritium release from several candidate solid breeders have been performed. In these experiments, the kinetics are non-steady state and the diffusivity D is given by:

$$D = 0.16\ r^2/\tau \tag{2}$$

where τ is the mean residence time defined as the time required to extract 87.4% of the tritium.[49]

Because the grains in experiments are often very small ($\sim$ 1 μ), non-spherical, and non-uniform, it is very difficult to determine r and, therefore, D in Eq. (2). However, Eqs. (1) and (2) can be combined yielding:

$$I = 0.5\ \dot{I}\ \tau \tag{3}$$

Since τ is readily measured, one can estimate the diffusive inventory in a blanket, provided the particle microstructure in the blanket corresponds to that in the experiments. The tritium generation rate per GWth assuming a breeding ratio of 1.2 and 20 MeV/fusion is 1.87×10^{-3} g/s. Substitution into Eq. (3) yields

$$I = 3.3 \cdot \tau(h) \tag{4}$$

where I = the diffusive tritium inventory in grams per GWth and $\tau(h)$ = the mean residence time determined in post-irradiation annealing experiments. Accordingly, the data of Wiswall[49] were used to obtain the results in Fig. 10-14.

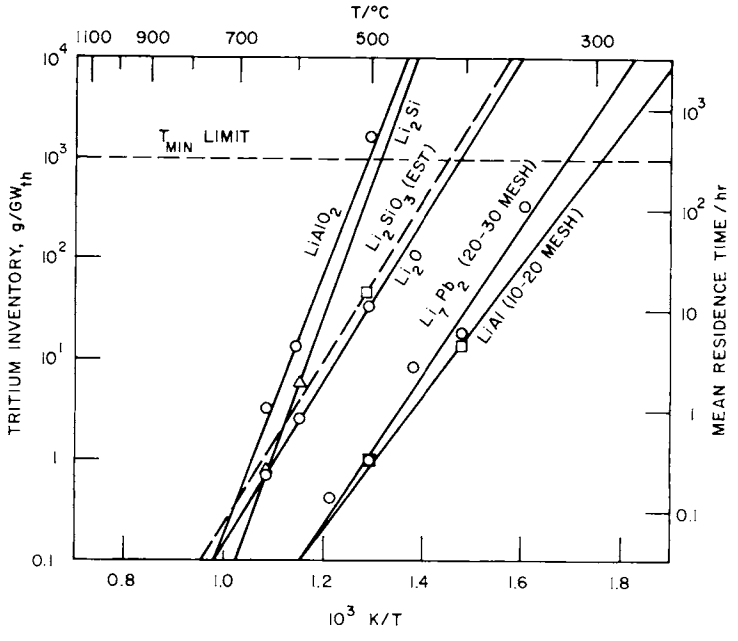

Figure 10-14. Release of tritium from solid breeders.

It can be seen from the results that the estimated inventories are strong functions of temperature. Clearly, the inventories would lower at higher temperatures. However, sintering must not be allowed to occur.

10.3.1.2 Bulk Diffusion Within the Grains

The diffusive inventory can also be calculated directly from hydrogen (tritium) diffusivity. In general, the hydrogen or tritium diffusivities in the candidate breeding materials have not been accurately determined. Since the mechanism of interest here is the diffusion within the grain, single crystal diffusion coefficients should be used. Single crystal diffusivities for some ceramic oxides such as Al_2O_3 and BeO have been measured and are characteristically very low.[14] For example, the reported temperature-dependent single crystal diffusivity of hydrogen in Al_2O_3 is given by

$$D = 3.26 \exp [-57.2/RT] \text{ cm}^2/\text{s} \quad (5)$$

This translates to values of 2.2×10^{-16} cm^2/s at 500°C and 1.7×10^{-17} cm^2/s at 450°C. In terms of temperature, measured diffusivities of hydrogen in BeO do not differ greatly from those in Al_2O_3. Because of the lack of data for the breeding materials of interest, the diffusivity for $LiAlO_2$ is assumed to be similar to that of Al_2O_3. Using Eq. (1) with a grain size of 1 μm and an average tritium generation rate of 6.25×10^{-3} g/s, the calculated diffusive inventories for STARFIRE would be 4.8 or 63 kg if the whole blanket operated at 500 or 450°C, respectively. These values agree quite well with the results shown in Fig. 10-14.

Restructuring, grain growth, or sintering could greatly affect the diffusive inventories since the calculated inventory varies as the square of the grain size. The sintering characteristics of the candidate breeding materials have not been investigated. In general, the thermal sintering characteristics of several stable oxides are similar. Temperatures in excess of 0.8 T_m are required before significant sintering occurs. However, neutron radiation typically enhances the sintering characteristics and lowers the temperatures at which sintering is observed. The effects of radiation are discussed in Sec. 10.3.1.6.

Based on the present model, which combines aspects of diffusion theory with experimental data, the range of operating limitations are defined where bulk diffusion is the rate-limiting step. A minimum temperature is defined as the temperature at which the tritium inventory exceeds 1 kg/GWth (Fig. 10-14). Since, there will be a range of temperatures in the blanket, the inventory distribution must be determined by integrating the tritium generation rate and the temperature distribution throughout the blanket. In the present analysis the meaning of "T_{MIN}" in Fig. 10-14 assumes that no more than 5% of the blanket can be at temperatures below T_{MIN} and none of the blanket can be more than 50° below T_{MIN}. Based upon the above criteria, the minimum temperatures for solid breeders predicted from diffusion controlled processes are given in Table 10-19.

10.3.1.3 Thermodynamic Equilibria

The tritium inventories in the candidate solid tritium-breeding materials that result from the thermodynamic solubility have also been evaluated. The tritium concentrations in the grains are predicted as a function of the

Table 10-19. Temperature Limits for Solid Breeders

Breeder	T_{min} (°C)	T^{*}_{max} (°C)
Li_2O	410	910
$LiAlO_2$	500	850
Li_2SiO_3	420	610
Li_2TiO_3	420	820
Li_2ZrO_3	420	860
Li_2Si	480	350
LiAl	300	310
Li_7Pb_2	320	330
Li_3Bi	320	580

* 0.6 absolute M.P.

tritium or T_2O partial pressures in the gas phase. Since no data have been published on the solubility of tritium in the candidate breeding materials, a thermochemical model was used to estimate the solubilities in the oxides. The assumptions used in the model include: (1) JANAF thermochemical data[50] for hydrogen were used, (2) isotope effects were not considered, (3) tritium was assumed to be in the form of LiOT in solid solution in the breeder, and (4) activity coefficients of all species were assumed to be unity. Assumptions 3 and 4 combined may be considered as Raoult's Law. For a specific example, consider Li_2O:

$$2\ LIOT(c) \rightleftarrows Li_2O(c) + T_2O(g) \qquad (6)$$

$$k_p = \frac{a(Li_2O) \cdot a(T_2O)}{a^2(LiOT)} \approx \frac{p(T_2O)}{X^2} \rightarrow p(T_2O) \approx k_p \cdot X^2$$

where X is the mole fraction of LiOT in Li_2O. For ternary oxides, the relevant equilibrium reaction is expressed as:

$$2\ LiOT + MO_x \rightleftarrows Li_2MO_{x+1} + T_2O \qquad (7)$$

and $$p(T_2O) = X_M \cdot X^2 \cdot K_p$$

In the above expressions, $p(T_2O)$ is the partial pressure of T_2O, X is the mole fraction of LiOT, and X_M is the mole fraction of the binary metal oxide (e.g., Al_2O_3). For the systems of interest, the activities of LiOT and MO_x have not been experimentally determined. The activity of LiOT is probably within a factor of ten of the mole fraction if LiOT is in solution. However, there is a greater uncertainty for the activity of the lithium depleted species, e.g., Al_2O_3, for two reasons:

1. The lithium depleted species may not be a simple metal oxide (Al_2O_3) but most probably is another ternary compound such as $LiAl_5O_8$. Since $LiAl_5O_8$ forms, it is more stable than Al_2O_3, and therefore free energy changes and K_p values for reactions such as (7) may be overestimated.

2. The composition of the breeding material continuously changes during operation of the blanket because the lithium is being burned up. Since tritium is being removed from the blanket, the mole fraction of LiOT will reach a constant value. However, the concentration of the other specie, e.g., Al_2O_3, will continuously increase at a rate of about 1% per year.

Although there is considerable uncertainty in the value of X_M and because it changes with time, a conservative value of $X_M = 0.5\ X$ is assumed for the preliminary scoping studies. Using the above expressions, equilibrium tritium concentrations in solid ceramic breeders for a T_2O partial pressure of 1.3 Pa (10^{-2} torr) were calculated (Fig. 10-15). It is evident that tritium dissolution in Li_2O appears to be unacceptably high for the temperatures of interest. All of the ternary oxides appear to have significantly lower tritium "solubilities" and, with the possible exception of Li_2ZrO_3, have levels of $\sim$ 10 wppm or less. Experimental data are needed to verify the predictions of the model.

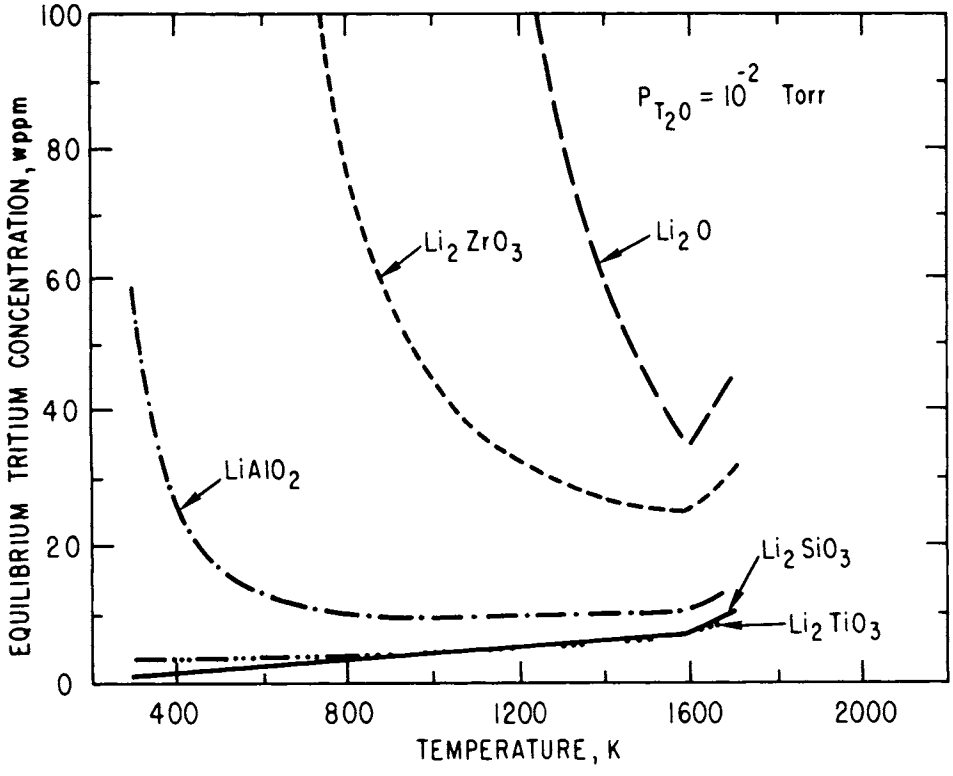

Figure 10-15. Calculated equilibrium tritium concentration in candidate solid breeding materials at P_{T_2O} = 1.3 Pa.

10.3.1.4 Percolation Through Interconnected Porosity

Tritium in the gas phase as T_2O must pass through pores between particles in order to get to the purge channels (Step 4). In order to evaluate this process, the POROUS code was used.[51] This code was originally developed to model gas release in oxide fission fuels. The POROUS code has been modified by Jankus and Rest to model the T_2O transport in the two-phase (T_2O + He) gas mixture. Details of the model are included in Appendix E. The model basically uses Darcy's equations and calculates temperature and pressure profiles of the gas phase species. The four variables in the model and the initial parameters used are defined in Table 10-20. Using the indicated variables, the T_2O pressure and temperature gradients for a blanket region near the first wall are shown in Fig. 10-16. It can be seen that the T_2O pressure rises from 0.1 Pa in the purge stream to over 100 Pa in regions far removed from the purge stream. In addition, the effects of variations in the

Table 10-20. Variables in Percolation Model

Variables (Values Used)

K ≡ Effective diffusion coefficient for T_2O in He, through pores (10^{-3}).

κ ≡ Blanket permeability (10^{-13} cm^2).

ϵ ≡ Blanket porosity (0.09).

S ≡ T_2O generation rate (4×10^{-10} g T_2O/cm^3 s).

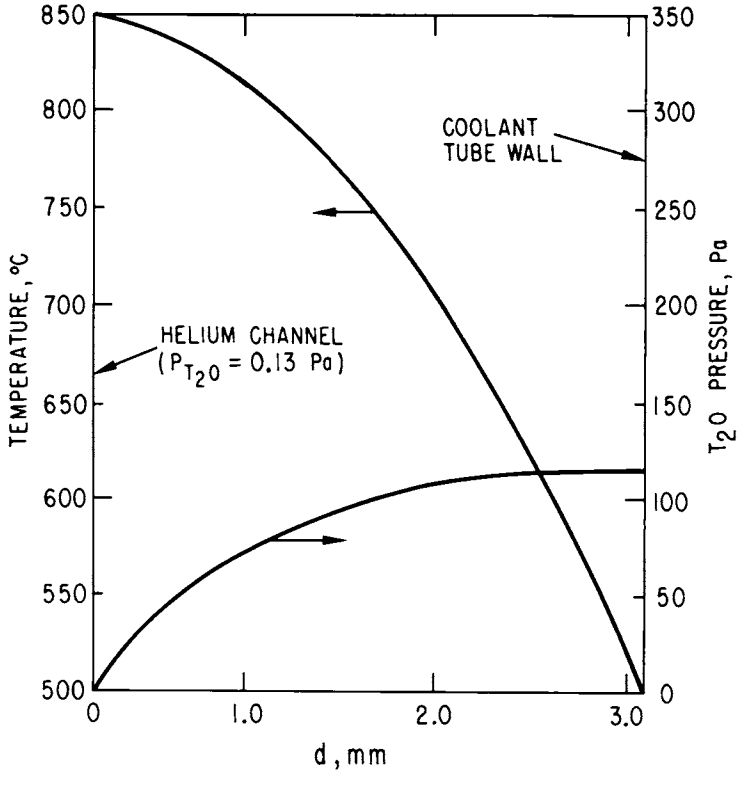

Figure 10-16. Calculated temperature and T_2O pressure profile in solid breeder blanket.

input parameters are shown in Table 10-21. The T_2O pressure buildup is a strong function of blanket porosity ε and the diffusion coefficient K, but only a weak function of the blanket permeability κ. Also, the T_2O pressure buildup is linearly dependent upon the tritium generation rate. The blanket porosity is a function of the theoretical density of the solid breeder and the reference value (ε = 0.09) in the present calculation seems to be a reasonable value for the current STARFIRE design. The value of K is a strong function of tortuosity and pore shape. More detailed analyses are required to more precisely define K. The tritium generation rate is not uniform in the blanket. Thus, the tritium (T_2O) pressure will be considerably higher in regions of the blanket near the first wall, where most of the tritium is being bred. The result of this effect is that the effective T_2O pressure near the first wall will be higher than indicated in Fig. 10-16.

The percolation results presented include only the effects that result from migration in the larger pore structure associated with the $\sim$ 1 mm particles. The T_2O migration in the fine pore structure within the particles, i.e., the interconnected grain boundary porosity, has not been analyzed in detail and the impact on tritium inventory is not included here.

Table 10-21. Parametric Results from the Percolation Model

K	κ/cm^2	ε	P_{MAX} (torr)
10^{-3}	10^{-13}	0.09	0.61
10^{-1}	10^{-13}	0.09	0.0061
10^{-5}	10^{-13}	0.09	59.0
10^{-3}	10^{-15}	0.09	0.67
10^{-3}	10^{-13}	0.009	5.9

10.3.1.5 Convective Mass Transport in the Processing Fluid

In the proposed blanket concept the tritium is transported out of the blanket through small channels formed in the solid breeder material. The processing fluid is a low-pressure ($\sim$ 0.05 MPa) helium stream. In the present analysis, convective mass transfer refers to the total volumetric flow rate required in the purge stream in order to remove the tritium (T_2O). The tritium generation rate is 6.7×10^{-3} g/s assuming a breeding ratio of 1.08, which corresponds to a volumetric T_2O generation rate of 9.3 Pa-m^3/s (70 torr-ℓ/s). As has been discussed by D. K. Sze,[52] if the T_2O pressure in the purge stream is 0.13 Pa (10^{-3} torr), then the required volumetric flow rate of the purge gas in STARFIRE is $\sim$ 10 m^3/s. Since lower T_2O pressures will require even higher volumetric flow rates of purge gas, it can be seen that the minimum tolerable pressure of T_2O in the purge stream is $\sim$ 0.1 Pa. A higher T_2O pressure in the purge gas translates to a higher tritium solubility, and hence a higher tritium inventory, in the solid breeder.

10.3.1.6 Radiation Effects on Tritium Recovery

Irradiation-induced microstructural changes in the solid breeding materials may substantially alter their tritium release characteristics. Radiation effects that have been considered in the present analysis include:

- tritium trapping within the grain
- restructuring and grain growth
- sintering that leads to pore closure

As discussed in Sec. 10.1.1.3, tritium trapping at radiation-induced defects such as cavities may be substantial. Evidence for trapping of hydrogen isotopes in various materials is obtained from ion-bombardment studies. As an example, saturation concentrations of deuterium in several potential first-wall materials after high energy ion-bombardment varied from 0.16 to 0.57 atom fraction.[53] Although the saturation concentrations observed in these types of experiments are typically less at elevated temperatures, concentrations as high as a few percent may be retained. A more conservative estimate of 1 at % tritium in the breeder would correspond to a tritium inventory of a few hundred kilograms in a typical blanket. An increase in the minimum blanket temperatures indicated in Table 10-19 may be required to overcome the trapping.

Wiswall, et al.[49] and Tanifuji, et al.[54] observed significant effects of fluence on the release characteristics of tritium from $LiAlO_2$ and Li_2O. An analysis of Wiswall's data by Smith, et al.,[10] indicated that radiation may increase the diffusive inventory by as much as a factor of ten.

Radiation can enhance restructuring, grain growth and sintering, which could also greatly affect the tritium inventory. Since the calculated diffusive tritium inventory varies as the square of the grain size, significant grain growth would lead to higher tritium inventories. However, grain growth is expected to occur predominantly in the highest temperature regions where the diffusive inventories should be lowest.

Radiation-induced sintering could lead to pore closure which would severely impact the gas-phase tritium transport, i.e., grain boundary migration or percolation. The effects of radiation on the sintering characteristics of the candidate breeding materials have not been investigated; however, the thermal sintering characteristics of stable oxides are generally similar. Although temperatures in excess of 0.8 T_m are required before significant thermal sintering occurs, neutron radiation typically enhances the sintering characteristics and lowers the temperatures at which sintering is observed. For the case of the solid breeding materials, the major radiation damage effect is caused by the high-energy (MeV) tritium and helium recoils from the n-Li reaction. Since the ranges for these particles are much greater than the proposed 1 μm grain size, a substantial impact of radiation on the sintering characteristics is expected. Data from fission reactor oxide fuels, which undergo similar fission product damage, are used to estimate the effects on the ceramic tritium-breeding materials. The impact of temperature on the restructuring of oxide fuels are indicated in Fig. 10-17. The solid line represents initial temperatures (as a fraction of the absolute melting point), as a function of radial distance. After restructuring occurs, a central void if formed and the temperature profile changes (the dashed line). Restructuring during irradiation conditions occurs at regions where the temperature is equal to or greater than $\sim$ 0.6 times the absolute melting point. Therefore, it is anticipated that restructuring of solid fusion breeders may be expected to occur at temperatures equal to or greater than $\sim$ 0.6 of the absolute melting point. Thus, the maximum operating temperatures established for the candidate solid breeding materials are given in Table 10-19.

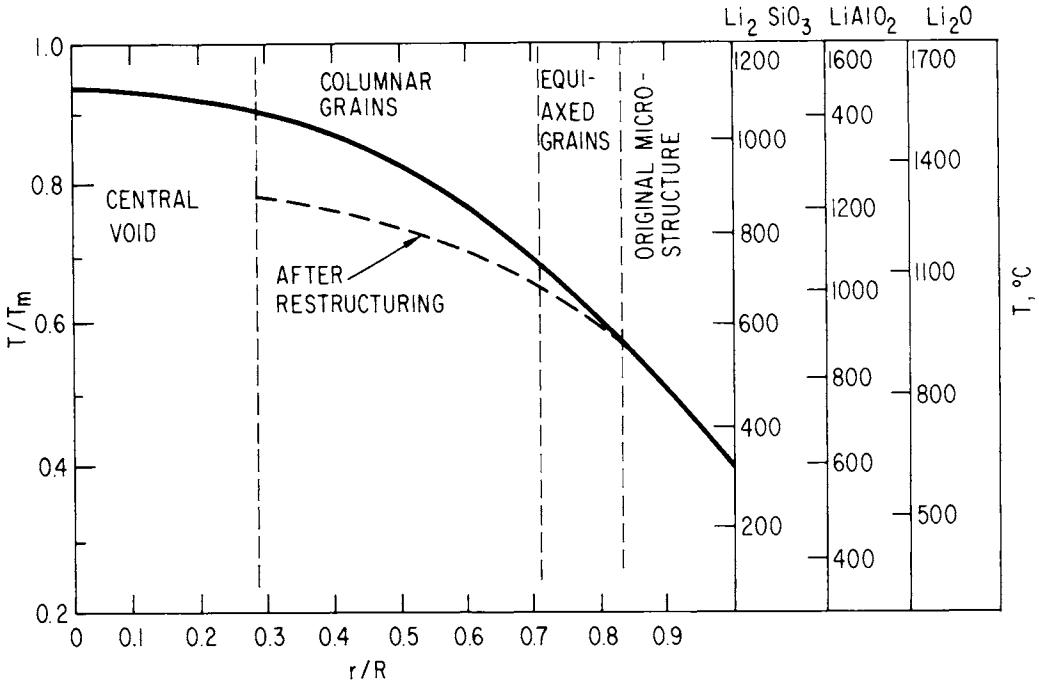

Figure 10-17. Radiation sintering temperatures for candidate solid breeding materials.

10.3.2 Tritium Inventory in the Reference Blanket

Major factors in the selection of $LiAlO_2$ as the reference breeding material for STARFIRE and in the specification of the operating temperature constraints relate to tritium recovery considerations. An important objective of the STARFIRE study was to minimize tritium inventories in the blanket. The results presented here indicate that the ternary oxides offer the most potential of the candidate breeding materials for maintaining low tritium inventories. Based on the models developed in the present study, the steady-state tritium inventory in the reference blanket design with the $LiAlO_2$ breeding material has been estimated for the proposed operating parameters. Results are summarized in Table 10-22 for the five kinetic processes considered, the contribution of thermodynamic equilibria, and the impact of radiation effects.

Table 10-22. Summary of Tritium Recovery Analysis for α-$LiAlO_2$

Assumed Mechanisms	Predicted Effects
KINETIC PROCESSES	
1. Bulk diffusion in grain	Diffusive tritium inventory $\sim$ 0.14 kg for grain size < 1 μm and radiation effects not considered.
2. Desorption from grain	Not studied. Effects believed to be small.
3. Grain boundary migration	Not studied. Could be important.
4. Percolation through packed or sintered bed	Preliminary analyses indicate factor of 10^2 to 10^3 increase in $P(T_2O)$ in bulk of blanket compared to $P(T_2O)$ in processing stream.
5. Convective mass transport	Requires $P(T_2O) \geq 10^{-1}$ Pa in processing stream.
THERMODYNAMICS	
1. Al_2O_3 in ideal solution in $LiAlO_2$	Solubility inventory $\sim$ 8 kg after one year of operation
2. Al_2O_3 forms separate phase	Solubility inventory $\sim$ 0.6 kg
RADIATION EFFECTS	
1. Tritium trapping saturates at 1 at % in $LiAlO_2$	Diffusive inventory $\sim$ 300 kg
2. Tritium trapping increases diffusive inventory by a factor of 10	Diffusive inventory $\sim$ 1.4 kg
3. Sintering and pore closure increases $P(T_2O)$ by two orders of magnitude (both percolation and grain boundary migration)	Solubility inventory would increase by an order of magnitude to $\sim$ 6-80 kg
4. Grain growth	Not expected to be a major problem during normal operation. Thermal excursion could be important.

10.3.2.1 Diffusive Inventory in Reference Design

Estimates of the diffusive inventory in the reference blanket design are based on the analyses just presented and on the thermal-hydraulic analyses presented in Sec. 10.5. The blanket was divided into 100 regions according to the temperature distribution and the inventory in each region was calculated for the average temperature. The total blanket inventory was then obtained by summing the inventory in each region. The detailed calculations are presented in Appendix E. For several different cases the calculations indicate that about 90% of the tritium inventory is located in the coldest 10% of the blanket, i.e., those regions below 550°C. Based on unirradiated tritium diffusion data and the low-fluence, low-temperature irradiations, the predicted diffusive inventory for STARFIRE is calculated to be 140 g.

The impact of radiation on the diffusive inventory is more difficult to assess. Two effects could significantly increase the predicted inventory. Since the calculated diffusive inventory varies as the square of the grain size, any recrystallization or grain growth produced by the radiation could obviously increase the inventory substantially. An effective grain size increase of a factor of two would increase the diffusive inventory by a factor of four. This effect is not expected to be a major problem since the grain growth will occur predominantly in the higher temperature regions where the diffusive inventory is lowest.

The second effect of radiation on the diffusive inventory results from tritium trapping at radiation induced defects such as cavities. As discussed in Secs. 10.1.1.3 and 10.3.1.6, tritium trapping may be significant. Results from energetic ion bombardment studies are considered to be the most relevant data available for assessing this effect. Saturation tritium concentrations of several atom percent may be retained in the solid. Estimates of 1 at % in the STARFIRE breeding material would correspond to a tritium inventory of nearly 300 kg. The factor of ten increase in tritium retention suggested by the analysis[10] of Wiswall's data would increase the diffusive inventory in the STARFIRE blanket to 1.4 kg. As summarized in Table 10-22, a low estimate for the diffusive tritium inventory of a highly irradiated blanket is $\sim$ 1.4 kg and an upper limit is of the order of 300 kg.

10.3.2.2 Solubility Inventory in Reference Design

Estimates of the "solubility" contribution to the tritium inventory in the STARFIRE reference design are also subject to a relatively high degree of uncertainty. The two important effects identified in the present study relate to the (1) T_2O pressure gradient established by the kinetics of the tritium (T_2O) migration through the porosity in the packed or sintered breeding material, and (2) the thermodynamic solubility of tritium in the breeding materials at the appropriate T_2O pressures in the gas phase.

Although more extensive data and analyses are required, the results presented in earlier sections indicate that a reasonable value for the average T_2O pressure in the blanket is $\sim$ 130 Pa (1 torr). For the reference STARFIRE blanket, the solubility inventory for tritium in $LiAlO_2$ in equilibrium with 130 Pa T_2O can be calculated from thermodynamic data for the following reaction:

$$2\ LiOT(c) + Al_2O_3(c) \rightleftarrows 2\ LiAlO_2(c) + T_2O(g) \tag{8}$$

and

$$k_p = \frac{a(LiAlO_2)^2 \cdot a(T_2O)}{a(LiOT)^2 \cdot a(Al_2O_3)} \approx \frac{p(T_2O)}{X^2_{LiOT}\, X_{Al_2O_3}} \tag{9}$$

At 1000 K, $k_p = 3.2 \times 10^6$ atm for the above reaction. If one assumes that the activity coefficient for Al_2O_3 is unity, i.e., ideal solution, an estimate of the tritium inventory early in the blanket life can be calculated. After one year of operation the lithium burnup is on the average about 1%, which corresponds to $X_{Al_2O_3} = 0.005$. Rearranging Eq. (9) and solving for X_{LiOT}:

$$X^2 = \frac{p(T_2O)}{k_p \cdot X_{Al_2O_3}} = \frac{1.3 \times 10^{-3}\ \text{atm}}{(3.2 \times 10^6\ \text{atm})(5 \times 10^{-3})} \tag{10}$$

$$X = 2.85 \times 10^{-4} = 13.0\ \text{wppm tritium in } LiAlO_2$$

Since the blanket breeder inventory is 6.26×10^5 kg of $LiAlO_2$, the calculated tritium solubility inventory is 8.1 kg. The above treatment assumed that the lithium-depleted species was Al_2O_3. In fact, the correct species

is $LiAl_5O_8$. Since $LiAl_5O_8$ forms, it is favored thermodynamically over Al_2O_3, and therefore, the above treatment is likely to underestimate the tritium solubility. However, in the above thermochemical analysis one might assume that Al_2O_3 (or $LiAl_5O_8$) is immiscible in $LiAlO_2$, and hence, form a second phase. Indeed the phase diagram would indicate this behavior if the lithium burnup is significant. In this case the activity of Al_2O_3 (or $LiAl_5O_8$) in Eq. (9) would be unity. The calculated solubility is then 0.92 wppm tritium, which corresponds to an inventory in STARFIRE of 0.57 kg.

Sintering or restructuring of the breeding material could lead to pore closure and increase the average T_2O pressure by orders of magnitude. A two order of magnitude increase in T_2O pressure (0.013 MPa) would raise the calculated inventory to 81 and 5.7 kg for the two thermodynamic models discussed above. Although the thermochemical model requires experimental verification and the calculated solubilities are subject to a rather large degree of uncertainty, the results of the present analyses provide a basis for assessing the potential for tritium recovery from solid breeding materials and for selection of the most viable candidate breeding materials.

10.3.2.3 Summary of Tritium Inventory in Reference Blanket Design

Because of the limited data base there is a relatively high degree of uncertainty in the predicted tritium inventory in the STARFIRE blanket. Estimates of the tritium inventory for two cases are summarized in Table 10-23. The first estimate is based on analyses in which radiation effects are not considered. Also, idealized materials behavior and an optimized microstructure are assumed. The total tritium inventory of $\sim$ 10 kg is believed to be accurate within a factor of ten and the analysis is considered useful for comparing different breeding materials. Although the value of 10 kg is significant, it is generally considered acceptable for a viable blanket design. It is important to note that two of the kinetic processes, viz., desorption and grain boundary migration, have not been included. The desorption step is not expected to produce a major effect; however, the grain boundary migration step could be important.

Table 10-23. Estimated Tritium Inventories in STARFIRE Blanket With and Without Potential Effects of Radiation Included

	With No Adverse Radiation Effects	Predicted Radiation Effects Included
Diffusive Inventory	0.08 - 0.14 kg	1.4 - 300 kg
Solubility Inventory	0.6 - 8.1 kg	6.0 - 80 kg
TOTAL INVENTORY[a]	0.7 - 8.2 kg	7.4 - 380 kg

[a]A total inventory of 10 kg was assumed for the reference design.

The estimated tritium inventory in the blanket is also listed in Table 10-23 for the case where selected effects of radiation are included. There is a higher degree of uncertainty in this estimate because of the lack of data. Radiation-induced trapping of tritium within the grains might increase the diffusive inventory to $\sim$ 300 kg. Also, pore closure could increase the solubility inventory by an order of magnitude (to $\sim$ 80 kg) compared to the unirradiated case. As indicated in the unirradiated case, the desorption step and grain boundary migration step are not included. The grain boundary migration step is of particular concern because of the necessity for maintaining the fine grain size and open porosity. This type of structure is probably more sensitive to radiation effects than a more coarse structure. Grain growth is not expected to be a major factor unless excessive overheating occurs during an off-normal thermal excursion.

For the purposes of the reference design the total blanket tritium inventory was assumed to be 10 kg. This would require that neither significant radiation-induced tritium trapping nor pore closure occur in the breeding material. The estimates presented in this chapter based on the irradiation effects indicate a major concern about tritium release characteristics. An important contribution of the present study is the identification of specific mechanisms or processes that must be investigated before the viability of solid breeder blanket concepts can be more accurately assessed.

10.4 NEUTRONIC ANALYSIS

The three primary functions of a fusion reactor blanket are to convert the fusion energy to sensible heat and to provide for removal of this heat, to breed tritium and to provide for tritium recovery, and to serve as part of the neutron shield for the magnets. As such, the neutronics considerations impact the materials selection and mechanical design aspects of the blanket. The blanket neutronic analyses performed in support of the STARFIRE study are summarized in this section. Important neutronic goals for the blanket are defined and general design concepts considered are presented. The relative neutronic performance characteristics of candidate neutron multiplier materials and tritium breeding materials are analyzed. An assessment of the benefits of neutron multipliers on blanket performance is presented. The relative performance of H_2O versus D_2O cooled blankets are analyzed. The impact of breeding material and neutron multiplier distribution on the breeding characteristics is assessed and the benefits of candidate reflector materials are presented. Finally, the neutronic performance of the reference blanket design based on one- and three-dimensional neutronics models is analyzed.

10.4.1 Neutronic Goals for STARFIRE Blanket Design

The tritium breeding capability of the blanket must be adequate to supply the tritium fuel requirement during the whole plant lifetime as well as generate enough surplus of tritium to start another plant within a reasonable period of time. A tritium doubling time of about seven years is considered adequate for fusion power generation based on the historical growth of the power industry. Based on analyses presented previously,[1] the doubling time for STARFIRE as a function of tritium breeding ratio is given in Fig. 10-18 for a tritium burnup rate of 0.53 kg/day and a tritium inventory of 10 kg. For these conditions, a tritium breeding ratio of 1.02 will produce a doubling time of seven years. A tritium breeding ratio greater than 1.06 will result in doubling time of less than 2.3 years, which is probably excessive. There-

fore, a net tritium breeding ratio of 1.02 to 1.06 is adequate to produce a reasonable doubling time (7 to 2.3 years) for fusion power industry. It should be noted from Fig. 10-18 that lowering the tritium inventory in the STARFIRE plant reduces the doubling time. In the case of 5 kg tritium inventory, the seven years doubling time requires 1.01 net tritium breeding ratio. A larger tritium inventory will require a larger breeding ratio to maintain the same doubling time.

Another blanket design goal is to maximize the blanket energy deposition per fusion neutron within the imposed constraints on the blanket thickness. In addition, it is desirable from the thermal hydraulic and mechanical design point of view to minimize the energy deposition gradient as much as possible.

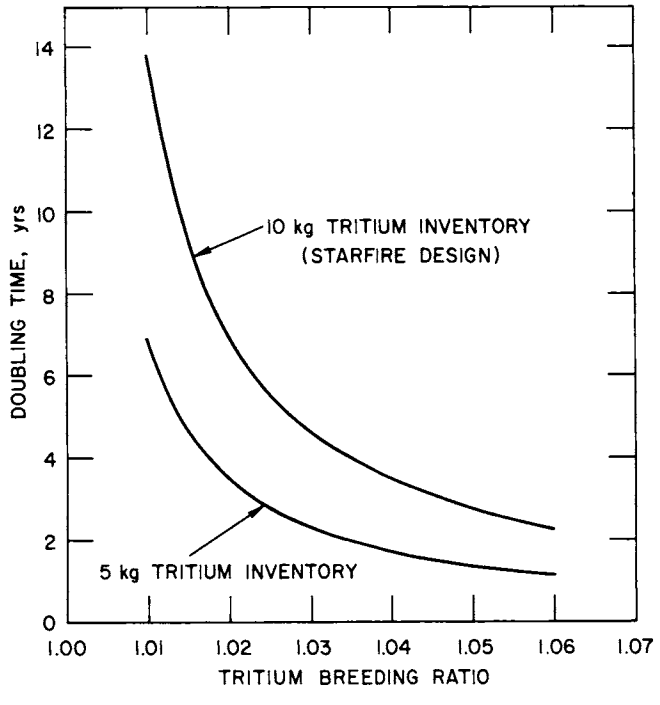

Figure 10-18. Doubling time as a function of tritium breeding ratio for STARFIRE design.

As will be demonstrated later, the energy deposition profile has an exponential shape which is dependent on the material and the geometric configuration used for the different blanket regions. A more uniform energy deposition profile will also reduce the blanket tritium inventory by keeping the breeder temperature profile close to the average design temperature of the breeder.

The energy leakage through the blanket region should be minimized since the heat deposited in the shield region is not usable for generating power. The energy leakage through the blanket should be limited to about one percent of the total energy deposited in the blanket. In general, energy leakage due to streaming through the limiter slot, the rf systems, and other voids will contribute about half of the total energy leakage. This balance in the energy leakage represents an optimum situation for the blanket and shield design.

10.4.2 Blanket Geometry Options

The solid breeder blanket concept with continuous tritium recovery by means of a helium purge stream has been utilized for the STARFIRE design. Unfortunately, the existence of the other elements with the lithium isotopes in the solid breeder material and the high percentage of the structural material result in a tritium breeding ratio of less than one. Consequently, the fusion neutron interactions with these elements reduce the tritium generation from the ^{7}Li isotope. Furthermore, the parasitic neutron interactions with these elements result in less capture in the ^{6}Li isotope for tritium generation. The remedy to this problem is to include a neutron multiplier to produce more neutrons through (n,2n) and (n,3n) interactions.

There are some exceptional solid breeder materials with high lithium content which can produce a tritium breeding ratio greater than one without a neutron multiplier. These solid breeders are Li_2O and LiH. Problems associated with the use of these materials, e.g., large tritium inventory for Li_2O, low melting point for LiH and other safety problems, are discussed in Sec. 10.1 and 10.3.

The neutron multiplier can be incorporated with the solid breeder in three different blanket options. In the first option, the neutron multiplier is placed in a separate zone in front of the breeding zone. In the second option, the first zone consists of both neutron multiplier and breeder followed by a zone consisting only of the breeder. The third option consists of a finer

heterogeneous system of breeder and neutron multiplier. In the first option where the fusion neutrons must pass through the neutron multiplier before reaching the solid breeder, the resulting neutron flux entering the solid breeder is much softer than the first wall neutron flux. However, the neutron flux into the tritium breeding zone is increased. The softer spectrum, which results from the interactions with the neutron multiplier, reduces the probability of neutron interactions with ^{7}Li to produce tritium from the $^{7}Li(n,n\alpha)T$ reaction. The result is to depend on ^{6}Li to produce most of the tritium from the $^{6}Li(n,\alpha)T$ interaction.

The separate zone option has more flexibility to adjust the average operating temperature for each zone independently. The operating temperature of the solid breeder can be adjusted to match the temperature range suggested for the optimum operating conditions as defined by the tritium extraction process. The main drawback in this option is that all the neutrons have to pass through the neutron multiplier and the second wall before reaching the solid breeder zone. This transport process reduces the number of neutrons available for interaction with the solid breeder due to the parasitic neutron interactions in the second wall and the neutron multiplier zone.

In the second option the first zone consists of the solid breeder and the neutron multiplier occupying the same zone in heterogeneous arrangement followed by another zone of the solid breeder. The resulting tritium breeding ratio and the energy deposition per fusion neutron are higher than the corresponding values from the separate zone blanket option. The primary reason for the improved performance is that the neutrons travel less distance to reach the solid breeder, and hence, the parasitic absorption is reduced. However, the design of this option is more difficult, and since it requires more structural material, it is less desirable from the radwaste point of view.

The third option is also intended to further improve the nuclear performance of the blanket and simplify the mechanical design. It consists of two blanket zones similar to the second concept except that the first zone is a homogeneous medium. This homogeneous medium may contain two compounds mixed together (for example, $BeO + LiAlO_2$) or one compound which has lithium and neutron multiplier atoms (for example, Li_2ZrO_3). As anticipated, the nuclear performance can be improved for a particular materials system and

the mechanical design is relatively simple. However, this concept is limited to only a few neutron multiplier and breeding material combinations because of compatibility considerations.

10.4.3 Neutronic Analysis of the Neutron Multipliers

The nuclear data for nonfissionable material were examined to identify elements with (n,2n) or (n,3n) cross sections in the energy range of 0 to 14.1 MeV. Table 10-24 gives a list of the potential candidates along with some relevant parameters for each candidate. The (n,2n) cross section is relatively high and it is of the order of 1 to 2.6 barn for the high-Z materials at 14 MeV neutron energy. For lighter materials, the (n,2n) cross sections are typically lower except for Be and to a lesser extent in D. The (n,2n) cross sections for the low-Z materials remain relatively high down to lower threshold energies compared to the high-Z materials. The other important neutronic considerations are the absorption cross sections, e.g., $\sigma(n,\gamma) + \sigma(n,p) + \sigma(n,\alpha)$, and the inelastic cross sections. These cross sections should be small to qualify the material as a good neutron multiplier from the neutronic point of view. Analysis of the elements with significant (n,2n) and (n,3n) cross sections indicates that Pb, Bi, Be and Zr have the highest potential for neutron multiplication among the candidates listed. Beryllium has been used as a neutron multiplier for several reactor studies,[2,56] and lead has also been suggested[57-59] because it has low absorption cross sections.

In order to compare the performance of the different neutron multipliers, a one-dimensional neutronic analysis was performed to determine the tritium breeding capability, the heat deposition per fusion neutron, and the radioactive isotopes with long half-lives generated from the multiplier materials. The analyses were carried out for two different blanket concepts. In both sets of calculations $LiAlO_2$ solid breeder with 90% ^6Li enrichment, PCA steel structural material and H_2O coolant are used with different neutron multipliers. The separate zone blanket option described in the previous section is employed for these analyses. The differences between the two concepts are related to the neutron multiplier zone design. In the first concept the neutron multiplier is internally cooled by water tubes embedded inside the neutron multiplier material (internally cooled neutron multiplier) while the second concept uses the first wall and second wall water coolant to remove the heat

Table 10-24. Properties of Candidate Neutron Multiplier Materials

Material	Be	BeO	Pb	PbO	Bi	Zr	Zr_5Pb_3	PbBi
Density, g/cm^3	1.85	2.96	11.34	9.53	9.8	7.6	8.93	10.46
Atoms or molecules/ cm^3, x 10^{-24}	0.1236	0.07127	0.03348	0.02571	0.02824	0.04291	0.004680	0.03047
$\sigma(n,2n)$ at 14 MeV, barns	0.5	0.5	2.2	2.2	2.2	0.6	9.2	2.2
$\Sigma(n,2n)$ at 14 MeV, cm cm^{-1}	0.0618	0.0256	0.0737	0.0565	0.0621	0.0257	0.0431	0.0670
Threshold energy for (n,2n) cross section, MeV	1.868	1.868	6.765	6.765	7.442	7.274	6.765	6.765
$\sigma(n,\gamma)$ at 0.0253 eV, barns	0.0095	0.0095	0.17	0.17	0.034	0.18	1.41	0.094
$\Sigma(n,\gamma)$ at 0.0253 eV, cm^{-1}	0.001174	0.0006711	0.005692	0.004369	0.0009602	0.006599	0.002905	0.3534
Radioactivity								
Isotopes	^{10}Be	^{10}Be	^{205}Pb	^{205}Pb	^{210}Po	^{93}Zr	^{93}Zr, ^{205}Pb	^{205}Pb, ^{210}Po
Decay types	B^-	B^-	Ec	Ec	α,γ	B^-	B^-,Ec	Ec, α,γ
Half lives	1.6×10^6 y	1.6×10^6 y	3.0×10^7 y	3.0×10^7 y	138.4 d	1.5×10^6 y	1.5×10^6 y 3×10^7 y	3×10^7 y 138.1 d
Melting point, °C	1278	2520	327.5	888	271.3	1852	1400	125
Thermal conductivity[a] at 25°C, W/m-°K	201	216[b]	35.3	2.8	7.92[c]	22.7	----	2.3[d]

[a] At 25°C

[b] Pure beryllium oxide, hot pressed

[c] Polycrystalline

[d] At 200°C

from the neutron multiplier material (externally cooled neutron multiplier). The zone volumetric compositions for the two blanket concepts are given in Table 10-25. The atomic densities for the different materials used in the neutronic analyses are listed in Table 10-26.

The tritium breeding ratio and the energy deposition per fusion neutron for the internally-cooled multiplier concept are plotted in Figs. 10-19 and 10-20, respectively, as a function of the neutron multiplier thickness. Vanadium, niobium, molybdenum and tungsten neutron multipliers were excluded because of insufficient tritium breeding capability. The beryllium and lead neutron multipliers exhibit the highest tritium breeding ratios for this blanket concept. Lead neutron multiplier exhibits a high tritium breeding ratio in this blanket concept because of its large (n,2n) cross section at the 14 MeV neutron energy and because of its very low capture cross section. The beryllium neutron multiplier produces more neutrons per fusion neutron compared to the other neutron multipliers; however, the maximum breeding ratio

Table 10-25. Blanket Parameters for Internally-Cooled and Externally-Cooled Neutron Multiplier Concepts

Zone Description	Zone Thickness cm	Zone Composition, Vol. %	
		Externally-Cooled	Internally-Cooled
First Wall	1	50% PCA 50% H_2O	50% PCA 50% H_2O
Neutron Multiplier	Variable	100% neutron multiplier	85% neutron multiplier 10% PCA 5% H_2O
Second Wall[a]	1	25% PCA 25% H_2O	No second wall
Tritium Breeder	50	80% $LiAlO_2$[b] 10% PCA 5% H_2O 5% He purge	80% $LiAlO_2$ breeder[b] 10% PCA 5% H_2O 5% He purge
Reflector	15	50% carbon 25% PCA 25% H_2O	50% carbon 25% PCA 25% H_2O

[a] second wall is 50% by volume void

[b] 90% ^6Li.

Table 10-26. Densities of Candidate Neutron Multiplier Materials

Material	Density gm/cm^3	Atom/cm^3 x 10^{24}	
Li_2O*	2.023	O	0.04078
		Li	0.08156
Li_7Pb_2	4.59	Pb	0.01194
		Li	0.04180
$LiAlO_2$	3.40	O	0.06211
		Al	0.03106
		Li	0.03106
Li_2SiO_3	2.52	O	0.05061
		Si	0.01687
		Li	0.03374
Be	1.85	Be	0.1236
BeO	2.96	Be	0.07127
		O	0.07127
Zr	6.5	Zr	0.04291
Pb	11.34	Pb	0.03348
PbO	9.53	Pb	0.02571
		O	0.02571
Zr_5Pb_3	8.93	Zr	0.02340
		Pb	0.01400
H_2O	1.0	H	0.0670
		O	0.0335
D_2O	1.1	D	0.0664
		O	0.0332
Ferritic Steel	7.7	C	0.0003089
		V	0.0001365
		Cr	0.008027
		Fe	0.07404
		Nb	0.00004991
		Mo	0.0004834
		W	0.0001261

* A density factor of 0.6 is used with Li_2O in all the neutronic analysis.

Table 10-26. (Continued)

Material	Density gm/cm^3	Atom/cm^3 x 10^{24}	
PCA Steel	7.81	Fe	0.05486
		Cr	0.01266
		Ni	0.01282
		Mo	0.0009793
		Mn	0.001710
		Ti	0.0002942
		Si	0.0008384
		C	0.0001961
		N	0.00003358
C	1.6	C	0.08023

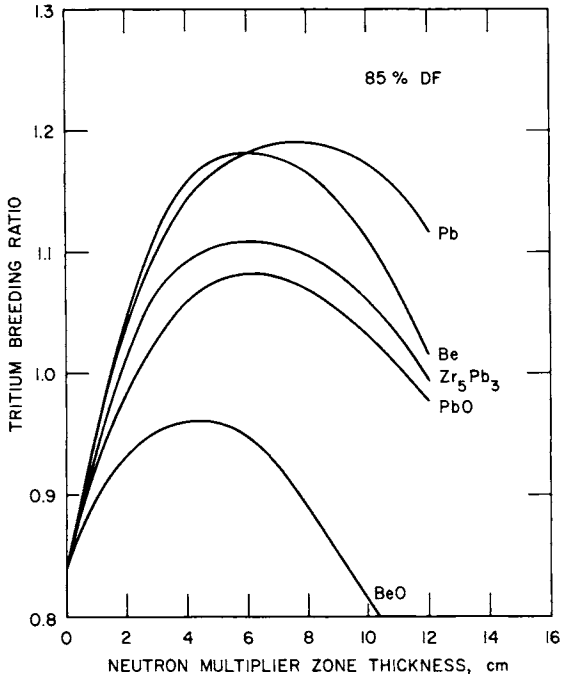

Figure 10-19. Tritium breeding ratio from the separate zone blanket option with different neutron multipliers (internally cooled) with $LiAlO_2$ (90% ^6Li) breeder, H_2O coolant and PCA structure.

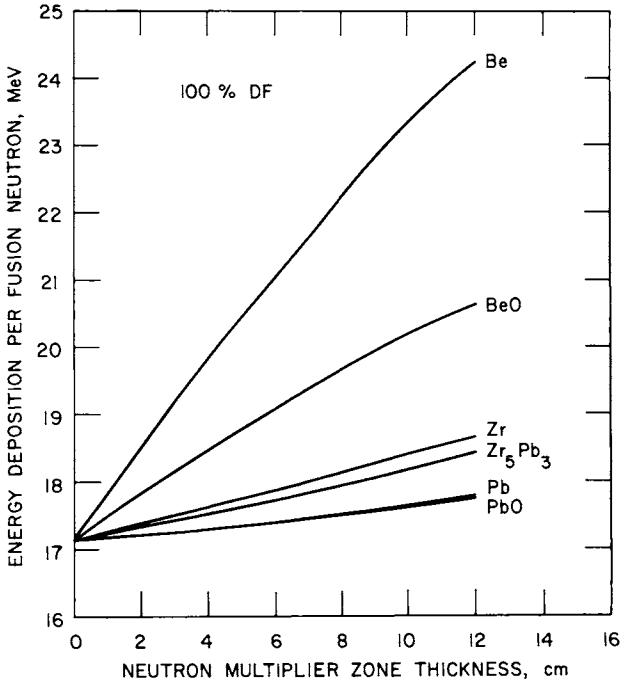

Figure 10-20. Nuclear energy deposition per fusion neutron for the different neutron multipliers (internally cooled) for $LiAlO_2$ (90% ^6Li) breeder, H_2O coolant, and PCA structure.

is about the same as for lead (see Table 10-27). This is due primarily to the softer spectrum from beryllium and the high slowing down power of the H_2O coolant which results in more parasitic neutron interactions in the structural material per fusion neutron as shown in Table 10-27. The unique feature of the beryllium multiplier is the high energy deposition per fusion neutron that is desirable from the economic point of view. The Zr_5Pb_3 and PbO neutron multipliers show a maximum tritium breeding ratio of 1.11 and 1.08, respectively, which is probably insufficient for a practical system. The tritium breeding capability from this blanket concept can be improved by using heavy water (D_2O), which has a lower slowing down power instead of ordinary water (H_2O).

The second concept, in which the neutron multiplier material is cooled externally from both sides (first wall and second wall), provides for a simpler blanket mechanical design and improves the blanket nuclear performance. The tritium breeding ratios and the energy deposition per fusion neutron are plotted in Figs. 10-21 and 10-22, respectively, as a function of the neutron multiplier zone thickness. The beryllium neutron multiplier shows the highest tritium breeding ratio in this blanket concept because the neutron slowing

Table 10-27. Blanket Neutronic Parameters at the Maximum Tritium Breeding Ratio (TBR) from the Separate Zone Blanket Option with Different Neutron Multipliers (internally cooled) for $LiAlO_2$ (90% ^6Li) Breeder/H_2O Coolant/PCA Steel Structure

Neutron Multiplier Material	Pb	Be	Zr_5Pb_3	PbO	BeO
Tritium Breeding Ratio	1.19	1.18	1.11	1.08	0.96
Multiplier Zone Thickness (cm)	7.5	6	6	6	4
Energy per Fusion Neutron (MeV)	17.8	21.1	17.8	17.5	18.3
(n,2n) Reactions from the Neutron Multiplier per Fusion Neutron	0.42	0.61	0.31	0.28	0.24
(n,γ) Reaction from the PCA Structure per Fusion Neutron	0.22	0.34	0.14	0.16	0.13

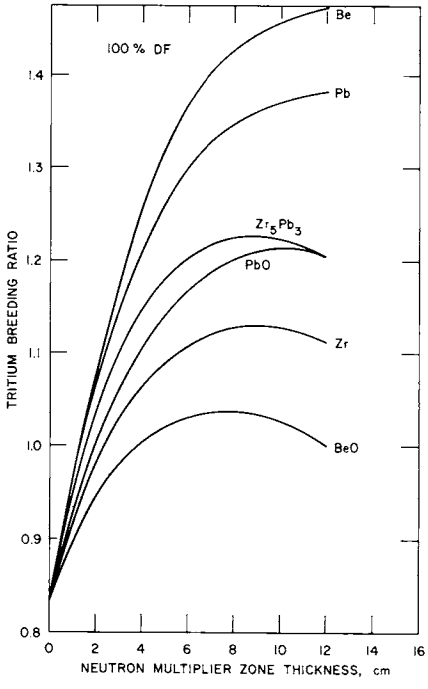

Figure 10-21. Tritium breeding ratio from the separate zone blanket option with different neutron multipliers (externally cooled) with $LiAlO_2$ (90% ^6Li) breeder, H_2O coolant, and PCA structure.

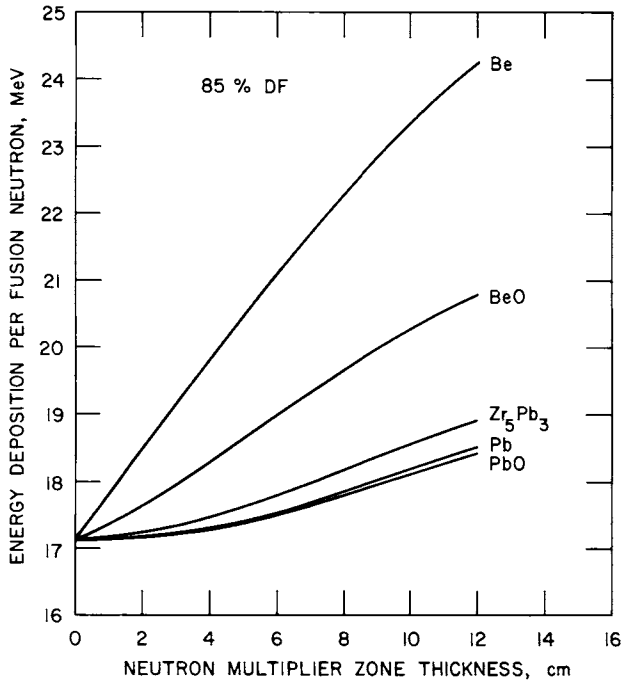

Figure 10-22. Nuclear energy deposition per fusion neutron for the different neutron multipliers (externally cooled) with $LiAlO_2$ (90% ^6Li) breeder, H_2O coolant and PCA structure.

down by the water coolant and the parasitic reactions in the structural material in the neutron multiplier zone are eliminated. Table 10-28 shows the (n,2n) reactions from the neutron multiplier and the (n,γ) reactions from the PCA structure per fusion neutron at a breeding ratio of 1.2 or the maximum tritium breeding ratio attainable if less than 1.2.

It is clear from Tables 10-27 and 10-28 that the performance of the beryllium neutron multiplier is improved in the second blanket concept. The lead neutron multiplier also shows an improvement, and the Zr_5Pb_3 and PbO neutron multipliers provide a breeding ratio greater than 1.2 in the second concept. Since Pb, Bi and PbBi neutron multipliers are quite similar from the neutronic point of view, the neutronic calculations are carried out for lead only.

From the previous results, it appears that Be, Pb, PbBi, Bi, Zr_5Pb_3 and PbO are the potential candidates as neutron multipliers from the neutronic point of view. The choice among these multipliers depends on the physical properties, design criteria and other considerations discussed in Sec. 10.1.

Table 10-28. Blanket Neutronic Parameters at 1.2 or the Maximum Tritium Breeding Ratio from the Separate Zone Blanket Option with Different Neutron Multipliers (externally cooled) for $LiAlO_2$ (90% ^6Li) Breeder/H_2O Coolant/PCA Steel Structure

Neutron Multiplier Material	Be	Pb	Zr_5Pb_3	Zr	PbO	BeO
Tritium Breeding Ratio	1.2	1.2	1.2	1.13	1.2	1.04
Multiplier Zone Thickness (cm)	3.3	3.8	5.9	9	8	8
Energy per Fusion Neutron (MeV)	19.4	17.2	17.7	18.3	17.5	19.7
(n,2n) Reactions from the Neutron Multiplier per Fusion Neutron	0.46	0.43	0.34	0.30	0.40	0.47
(n,γ) Reaction from the PCA Structure per Fusion Neutron	0.14	0.11	0.10	0.11	0.14	0.29

The radioactive isotopes with long half-lives from the different neutron multipliers are given in Table 10-24. A more extensive analysis for the radioactivity in terms of Ci/W from the Be and Zr_5Pb_3 neutron multipliers are given in Chap. 12.

10.4.4 Neutronic Analysis of the Tritium Breeding Materials

The neutronic analyses were carried out for four lithium compounds, $LiAlO_2$, Li_2SiO_3, Li_2O and Li_7Pb_2, representing the potential candidates from the ceramic and intermetallic compounds. The $LiAlO_2$ and Li_2SiO_3 breeder have similar neutronic performance, both need a neutron multiplier to achieve a tritium breeding ratio greater than one. Li_7Pb_2 represents the homogeneous blanket option where the tritium breeding element (Li) exists as a compound with the neutron multiplier element (Pb). Li_2O is one of the few solid breeders that has the potential for tritium breeding without a neutron multiplier.

The separate zone blanket option described in Sec. 10.4.2 with a Zr_5Pb_3 neutron multiplier material, PCA steel structure and H_2O coolant is used for the neutronic analysis of $LiAlO_2$ tritium breeding material. The neutron multiplier material is cooled from the first and second wall to improve the neutronic performance and simplify the mechanical design as discussed in Sec. 10.4.3. In this analysis, the impact of ^6Li enrichment and the neutron multiplier zone thickness on the blanket performance are examined. In addition, the tritium breeding zone thickness and ^6Li burnup are considered in the analysis. The blanket parameters are the same as given in Table 10-25, except a 7-cm thick neutron multiplier and a 50-cm thick reflector (90% C, 5% PCA, and 5% H_2O) are used. The breeding zone thickness and the ^6Li enrichment are variable in this analysis.

The tritium breeding ratio contours as a function of the ^6Li enrichment and the neutron multiplier zone thicknesses are given in Fig. 10-23. The results shown in Fig. 10-23 indicate that a specific tritium breeding ratio can be achieved with different combination of ^6Li enrichment and neutron

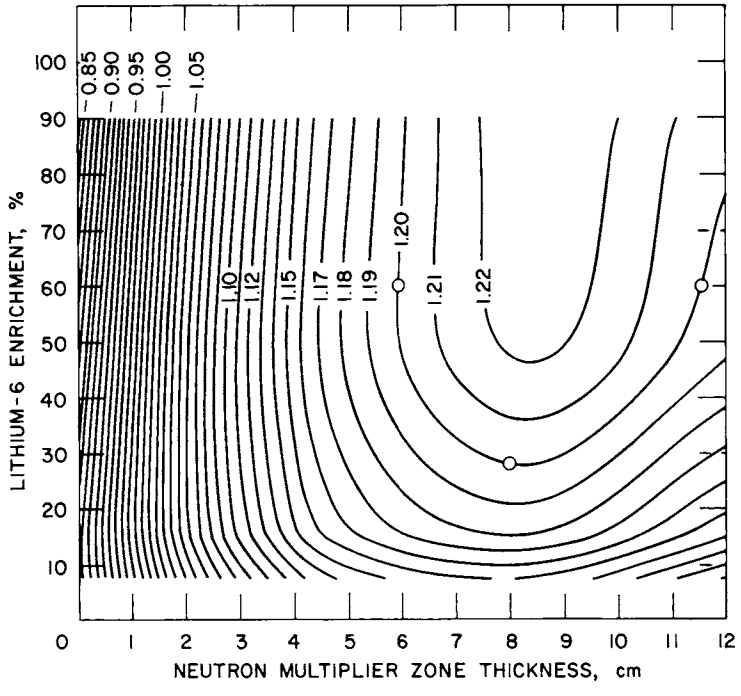

Figure 10-23. Tritium breeding ratio contours from the separate zone blanket option with $LiAlO_2$ breeder, Zr_5Pb_3 neutron multiplier, H_2O coolant, and PCA structure.

multiplier zone thickness. In the range of interest for the STARFIRE design, a tritium breeding ratio of 1.2 is achievable with at least three different cases. The first case with a minimum ^6Li enrichment of 28% requires an 8-cm neutron multiplier zone thickness. The second case with a minimum neutron multiplier zone thickness needs at least a 50% ^6Li enrichment. The third case, which is characterized by a thicker neutron multiplier and a higher ^6Li enrichment, utilizes a 12-cm neutron multiplier zone thickness and a 75% ^6Li enrichment. The differences in the maximum heating rate for these blankets are within 5% as shown in Fig. 10-24. The maximum lithium burnup contours after six years of operation (16.2 MW•yr/m^2) as a function of the ^6Li enrichment and the neutron multiplier zone thicknesses are given in Fig. 10-25.

The maximum lithium burnup increases with both the neutron multiplier zone thickness and the ^6Li enrichment because of an increase in the ^6Li reaction rate. The difference in the maximum burnup between the blanket with minimum ^6Li enrichment and the corresponding one with minimum neutron multiplier zone thickness for a tritium breeding ratio of 1.2 is less than 1%

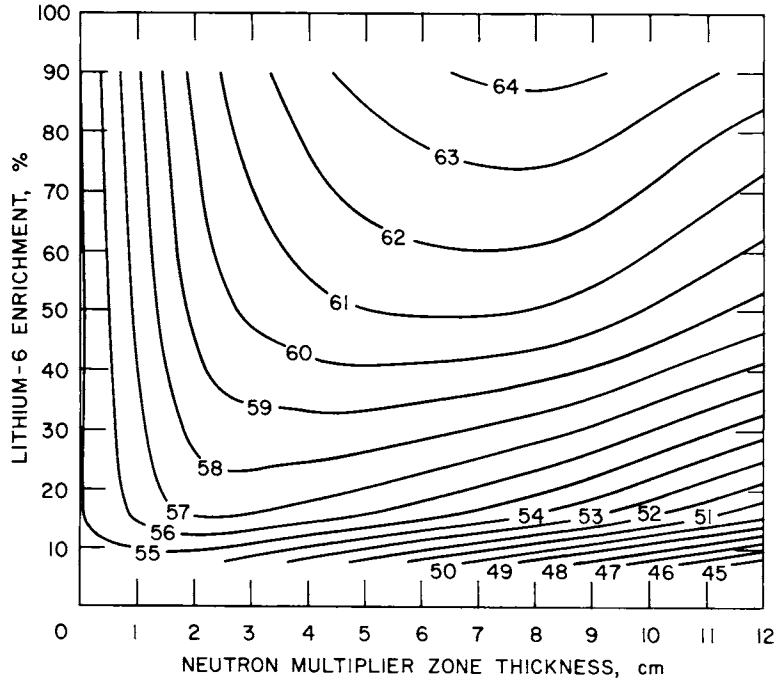

Figure 10-24. Maximum heating rate (W/cm^3) contours in the breeder material from the separate zone blanket option with $LiAlO_2$ breeder, Zr_5Pb_3 neutron multiplier, H_2O coolant and PCA structure.

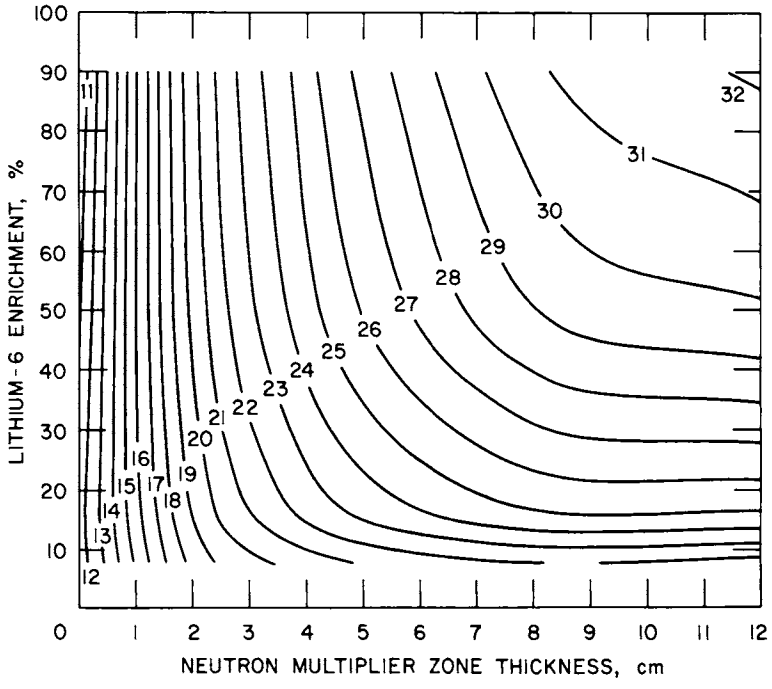

FIgure 10-25. Maximum lithium burnup (%) contours after six years of operation (16.2 MW•yr/m^2) for the separate zone blanket option with $LiAlO_2$ breeder, Zr_5Pb_3 neutron multiplier, H_2O coolant, and PCA structure.

after six years of operation. However, the blanket with a minimum neutron multiplier zone thickness had the lowest maximum temperature in the neutron multiplier zone which is an important design issue in the blanket design as shown in Sec. 10.5. The blanket with the thick neutron multiplier zone and a high ^6Li enrichment has the lowest energy leakage, while the blanket with minimum ^6Li enrichment has an economic advantage derived from the saving in the ^6Li enrichment cost. In the STARFIRE design, the blanket with minimum neutron multiplier zone thickness is employed because it minimizes the beryllium resource requirement and satisfies the maximum temperature criterion for Zr_5Pb_3 with the external multiplier coolant concept.

In order to define the tritium breeding zone thickness, the tritium breeding ratio as a function of the tritium breeding zone thickness was calculated for a blanket design with a 7-cm Zr_5Pb_3 neutron multiplier zone thickness, $LiAlO_2$ (60% ^6Li) tritium breeding material, H_2O coolant and PCA steel structure. The results are summarized in Fig. 10-26. The reflector zone (90% C, 5% PCA, and 5% H_2O) in these calculations is 50 cm thick to assure maximum reflection. The increase in the tritium breeding zone thickness from

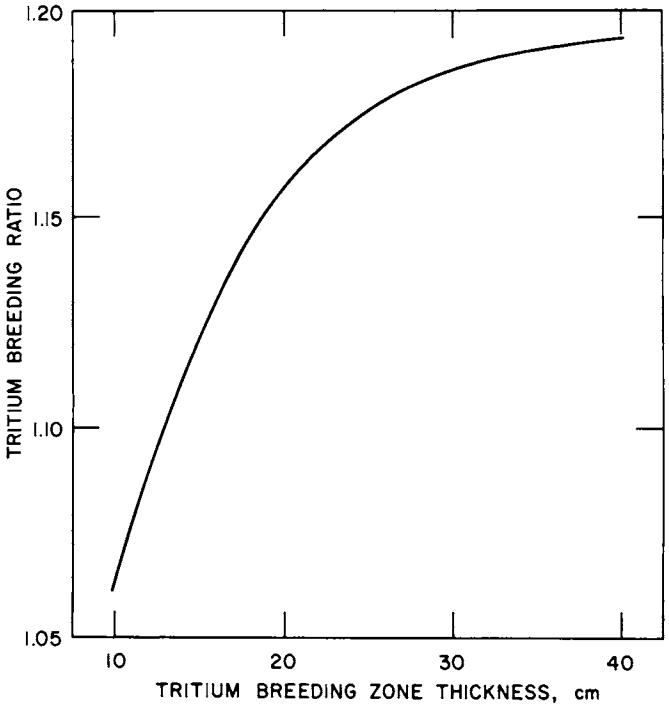

Figure 10-26. Breeding zone thickness from the separate zone blanket option with Zr_5Pb_3 neutron multiplier/$LiAlO_2$ (60%) breeder, H_2O coolant and PCA structure.

30 to 40 cm results in an increase of only 0.6% in the tritium breeding ratio. Therefore, little benefit is gained with a tritium breeding zone greater than 30 cm.

The Li_2SiO_3 breeding material will generate about 0.4% more tritium and deposit 1% less energy per fusion neutron compared to the $LiAlO_2$. However, the main difference between the $LiAlO_2$ and Li_2SiO_3 compounds relates to the radioactivity. Li_2SiO_3 compound does not generate long term radioactive isotopes while $LiAlO_2$ produces ^{26}Al isotope with a half life of 7.3×10^5 yr.

The Li_2O breeding material is a unique candidate because of its potential to breed enough tritium without a neutron multiplier material. Elimination of the neutron multiplier results in much simpler blanket design.

Helium coolant potentially matches the high temperature capability of Li_2O and eliminates the reaction problems associated with water coolant in the tritium breeding zone. Helium coolant occupies large volume fraction of the tritium breeding zone and requires a large amount of structural material which impacts the blanket nuclear performance and increases the blanket thickness. In order to analyze this blanket configuration,

the tritium breeding ratio per 14 MeV fusion neutron as a function of the helium coolant and ferritic steel volume fraction are given in Fig. 10-27. The blanket parameters used in the calculation are listed in Table 10-29. A design similar to STARFIRE would be expected to use 30 to 40% He and 14 to 16% ferritic steel which would result in ∿ 1.2 tritium breeding ratios and ∿ 17.7 MeV energy deposition per fusion neutron.

The use of D_2O coolant with Li_2O tritium breeding material results in a significant improvement in the blanket nuclear performance. Table 10-30 gives the blanket parameters for different tritium breeding zone compositions with Li_2O (natural Li) tritium breeding material and D_2O coolant, while Table 10-31 gives the calculated tritium breeding ratio and the energy deposited per fusion neutron. The D_2O cooled blanket (blanket No. 3 in Table 10-31) gives tritium breeding ratio of ∿ 1.32 with a 60-cm tritium breeding zone thickness compared to 1.2 with 100 cm for the corresponding blanket with a helium coolant. A breeding ratio of 1.2 requires only a 33-cm thick blanket with D_2O coolant compared to 100 cm for the He coolant case. The energy deposited per fusion neutron is ∿ 17.7 MeV for both coolants.

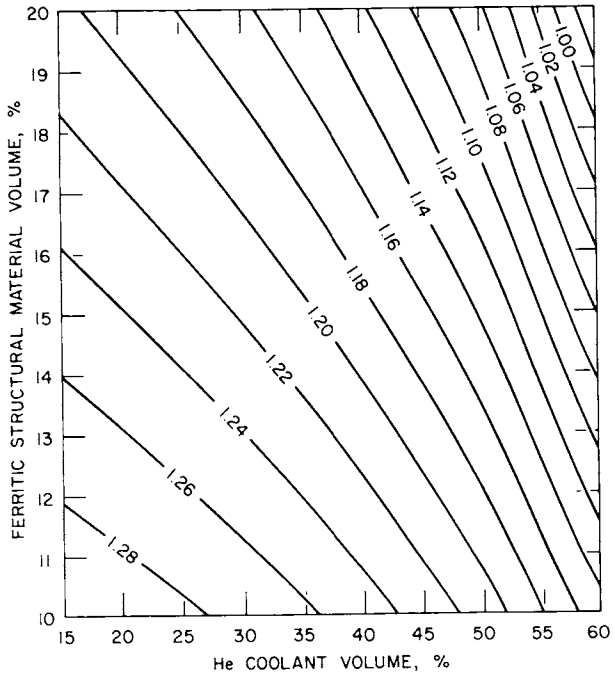

Figure 10-27. Tritium breeding ratio contours for Li_2O breeder, He coolant, ferritic steel structure and with D_2O first wall coolant.

Table 10-29. Blanket Parameters for Different Tritium Breeding Zone Compositions with Li_2O (natural Li) Tritium Breeding Material, Helium Coolant, Ferritic Steel Structure and D_2O Coolant for the First Wall

Zone Description	Zone Thickness cm	Zone Composition Percentage by Volume
First Wall	1	50% ferritic steel structure 50% D_2O coolant
Tritium Breeding Zone	100	(100-X-Y)% Li_2O tritium breeding material X% ferritic steel structure Y% He coolant
Reflector	30	85% carbon reflector material 5% ferritic steel structure 10% He coolant

Table 10-30. Blanket Parameters for Different Tritium Breeding Zone Compositions with Li_2O (natural Li) Tritium Breeding Material, D_2O Coolant and Ferritic Steel Structure

Zone Description	Zone Thickness cm	Zone Composition Percentage by Volume
First Wall	1	50% ferritic steel structure 50% D_2O coolant
Tritium Breeding Zone	60	(100-X-Y)% Li_2O tritium breeding material X% ferritic steel structure Y% D_2O coolant
Reflector	30	90% carbon reflector 5% ferritic steel structure 5% D_2O coolant

Table 10-31. Tritium Breeding Ratio and Nuclear Energy Deposition per Fusion Neutron for Different Tritium Breeding Zone Composition with Li_2O (natural Li) Tritium Breeding Material, D_2O Coolant and Ferritic Steel Structure

Blanket Number	1	2	3	4
Li_2O Tritium Breeding Material, Volume %	90	85	85	80
Ferritic Steel Structure, Volume %	5	5	10	10
D_2O Coolant, Volume %	5	10	5	10
Energy Deposition per Fusion Neutron (MeV)	17.73	17.74	17.74	17.79
$^6Li(n,T)\alpha$ Reaction per Fusion Neutron	0.9395	0.9465	0.9398	0.9463
$^7Li(n,n'T)\alpha$ Reaction per Fusion Neutron	0.4128	0.3941	0.3752	0.3568
Tritium Breeding Ratio (60 cm)	1.3523	1.3406	1.3150	1.3031
Tritium Breeding Zone Thickness for 1.2 Tritium Breeding Ratio (cm)	30	32	33	33

The lithium lead (Li_7Pb_2) provides a high tritium breeding ratio because of the neutron multiplication from lead. The presence of lithium and lead atoms in a homogeneous compound represents a favorable situation for utilizing the secondary neutrons as discussed in Sec. 10.4.2. This situation results in a small blanket thickness to get the required tritium breeding and the nuclear energy. Table 10-32 lists the blanket parameters used for Li_7Pb_2 neutronic analysis. The water-cooled volume fraction is 20% to keep the maximum temperature in the tritium breeding material below the melting point. An increase in ^6Li enrichment for this blanket results in lower values for the tritium breeding ratio and the nuclear heat deposition as shown in Table 10-33. This blanket requires a 24-cm tritium breeding zone thickness and a 5-cm reflector zone thickness to achieve a tritium breeding ratio of 1.2. This small blanket thickness provides an economic advantage.

Table 10-32. Blanket Parameters for Li_7Pb_2 Tritium Breeding Material with H_2O Coolant and Ferritic Steel Structure

Zone Description	Zone Thickness cm	Zone Composition Percentage by Volume
First Wall	1	50% ferritic steel structure 50% H_2O coolant
Tritium Breeding Zone	30	70% Li_7Pb_2 tritium breeding material 10% ferritic steel structure 20% H_2O coolant
Reflector	5	95% H_2O reflector 5% ferritic steel structure

Table 10-33. Tritium Breeding Ratio and Energy Deposition per Fusion Neutron as a Function of the Lithium-6 Enrichment for Li_7Pb_2 Tritium Breeding Material with H_2O Coolant and Ferritic Steel Structure

Lithium-6 Enrichment (%)	Tritium Breeding Ratio	Energy Deposition per Fusion Neutron (MeV)
7.5 (natural)	1.344	18.14
15	1.327	17.92
30	1.304	17.77
45	1.280	17.71
90	1.205	17.64

10.4.5 Neutronic Analysis of Neutron Multiplier versus Non-Neutron Multiplier Blanket

The use of the neutron multiplier material is essential for most of the solid breeders to achieve the required tritium breeding ratio. Also, the use of neutron multiplier material results in a higher energy deposition per fusion neutron and lower neutron energy leakage to the shield. These improvements are obvious from the neutronic analysis of the different neutron multipliers and tritium breeding materials given in the previous sections. However, the use of the neutron multiplier increases the materials compatibility problems in the blanket. There are few solid breeders that can satisfy the tritium breeding requirements without a neutron multiplier. The benefits of using a neutron multiplier with these solid breeders are examined. A Li_2O (natural Li) solid breeder blanket is analyzed for three different blanket configurations. The first blanket is designed without a neutron multiplier, the other two blankets employ a neutron multiplier. Pb and Be are the neutron multipliers used in this analysis. The total blanket thickness is kept constant for the three blanket configurations shown in Table 10-34. The reference breeding zone thickness is defined for a tritium breeding ratio of $\sim$ 1.2 without a neutron multiplier.

The Li_2O blanket without a neutron multiplier achieves a breeding ratio of 1.2 and deposits 17.6 MeV per fusion neutron as shown in Table 10-35. The blankets with neutron multipliers use less Li_2O and generate more tritium per fusion neutron. Both Be and Pb increase the tritium production by $\sim$ 15% relative to the blanket without neutron multiplier. This increase in the tritium breeding ratio is beneficial in two different ways. First, the blanket tritium inventory is reduced because the tritium generation per unit blanket volume is higher since less volume is used compared to the blanket without a neutron multiplier. Second, the reactor cost is decreased with a smaller blanket thickness. In addition, the Be multiplier increases the energy deposition per fusion neutron by $\sim$ 29% which translates to an increase in the reactor power and decreases the cost of electricity. Also, the neutron multiplier decreases the neutron energy leakage per fusion neutron, which is

Table 10-34. Blanket Parameters for Li_2O (natural Li) With and Without Neutron Multiplier Material, Helium Coolant, Ferritic Steel Structure and D_2O Coolant for the First Wall

Zone Description	Zone Thickness cm	Zone Composition Percentage by Volume
A. Blanket Without Neutron Multiplier		
First Wall	1	50% ferritic steel structure 50% D_2O coolant
Tritium Breeding Zone	50	60% Li_2O tritium breeding material 10% ferritic steel structure 30% He coolant and purge stream
Reflector	30	85% carbon reflector material 5% ferritic steel structure 10% He coolant
B. Blankets with Neutron Multiplier		
First Wall	1	50% ferritic steel structure 50% D_2O coolant
Neutron Multiplier	10	85% neutron multiplier material 10% ferritic steel structure 5% D_2O coolant
Tritium Breeding Zone	40	60% Li_2O tritium breeding material 10% ferritic steel structure 30% He coolant and purge stream
Reflector	30	85% carbon reflector material 5% ferritic steel structure 10% He coolant

Table 10-35. Blanket Neutronic Parameters from Three Li_2O (natural Li) Blanket with He Coolant, Ferritic Steel Structure and D_2O Coolant for the First Wall; the First Without a Neutron Multiplier Material, the Second with Be Neutron Multiplier Material, the Third with Pb Neutron Multiplier.

Blanket Parameter	Blanket Parameters		
Multiplier Material	--	Be	Pb
Neutron Multiplier Zone Thickness (cm)	--	10	10
Tritium Breeding Zone Thickness (cm)	50	40	40
Li_2O Material Thickness (cm)	24	19.2	19.2
Neutron Multiplier Material Thickness (cm)	--	8.5	8.5
Total Blanket Thickness (cm)	81	81	81
Tritium Breeding Ratio	1.206	1.386	1.372
Energy Deposition per Fusion Neutron (MeV)	17.6	22.63	17.6
Neutron Energy Leakage per Fusion Neutron (MeV)	0.038	0.026	0.023
Gamma Energy Leakage per Fusion Neutron (MeV)	0.073	0.093	0.064
Total Energy Leakage per Fusion Neutron (MeV)	0.111	0.119	0.087

desirable from the shielding and radioactivity point of view. However, the use of neutron multipliers increases ^6Li consumption per fusion neutron. The increase in ^6Li burnup is about 38% for a tritium breeding ratio of 1.2 compared to the case without a neutron multiplier.

10.4.6 Neutronic Analysis of D_2O versus H_2O Cooled Blanket

The water coolant is the choice for the STARFIRE design as discussed in Sec. 10.1.2. In order to compare the blanket performance with both H_2O and D_2O, a neutronic analysis for both coolants is given in this section for two different blanket concepts. The first blanket concept employs the lead

neutron multiplier in the separate zone blanket option with Li_2SiO_3 (90% ^6Li) tritium breeding material. The second blanket concept utilizes the Li_2O tritium breeding material without a neutron multiplier.

The blanket parameters for the first concept are given in Table 10-36. The resulting tritium breeding ratio from this blanket as a function of the neutron multiplier zone thickness is given in Fig. 10-28 for both coolants. The D_2O cooled blanket gives a maximum tritium breeding ratio of 1.43 compared to 1.23 from the H_2O cooled blanket for neutron multiplier zone thicknesses of 13 and 7.5 cm for D_2O and H_2O, respectively. This difference in the tritium breeding capability is caused primarily by the difference in the slowing down power of D_2O and H_2O. Figure 10-29 shows that the neutron multiplication from Pb(n,2n) reactions for both coolants are the same whereas the neutron capture in the ferritic steel structural material is much higher in the H_2O blanket compared to the D_2O blanket. The H_2O coolant moderates the secondary

Table 10-36. Blanket Parameters for Separate Zone Blanket Option with D_2O or H_2O Coolant, Pb Neutron Multiplier Material, Li_2SiO_3 (90% ^6Li) Tritium Breeding Material and Ferritic Steel Structure

Zone Description	Zone Thickness cm	Zone Composition Percentage by Volume
First Wall	1	50% ferritic steel structure 50% water coolant
Neutron Multiplier	Variable	85% Pb neutron multiplier material 10% ferritic steel structure 5% water coolant
Tritium Breeder	50	80% Li_2SiO_3 tritium breeding material 10% ferritic steel structure 5% water coolant 5% He purge stream
Reflector	20	90% carbon reflector 5% ferritic steel structure 5% water coolant

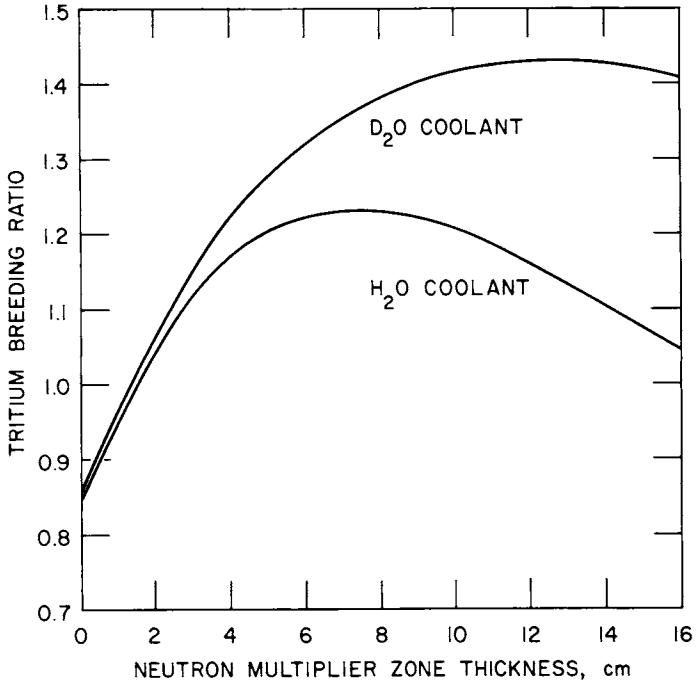

Figure 10-28. Tritium breeding ratio from separate zone blanket option with D_2O and H_2O coolant, Pb neutron multiplier, Li_2SiO_3 (90% ^6Li) breeder and ferritic steel structure.

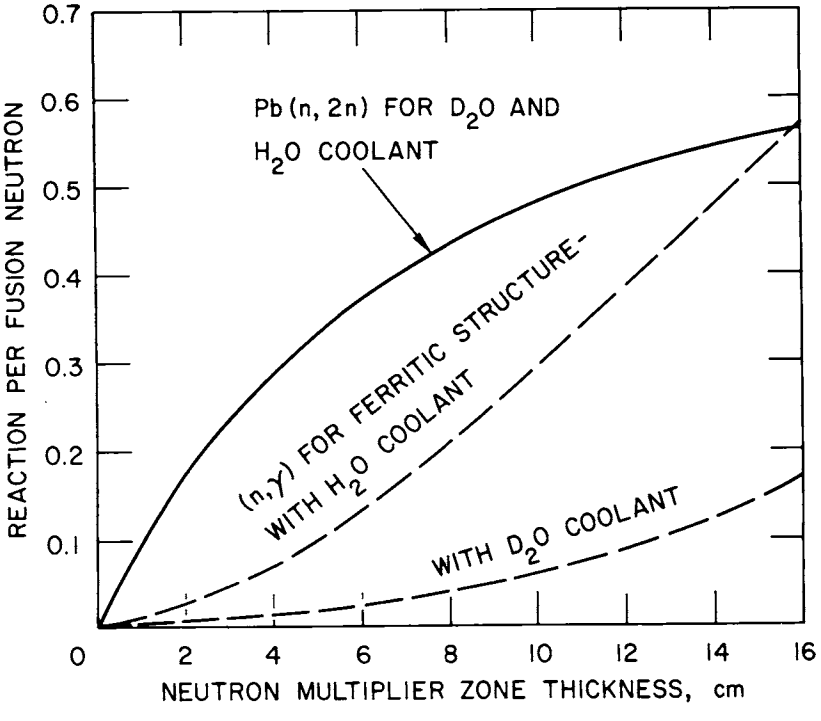

Figure 10-29. Pb(n,2n) neutron interaction and (n,γ) capture in the ferritic structure for D_2O and H_2O cooled blanket with Li_2SiO_3 (90% ^6Li) breeder.

neutrons in the multiplier zone enough to significantly increase the probability for the neutron capture in the ferritic steel structure. More than 95% of the total neutron capture occurs in the first wall and the neutron multiplier structural material. The D_2O coolant does not moderate the neutrons as effectively so that more secondary neutrons proceed into the tritium breeding zone. This also explains the increase in the tritium breeding capability for the blanket with externally cooled neutron multipliers as discussed in Sec. 10.4.3.

The energy per fusion neutron for both coolants is given in Fig. 10-30 as a function of the neutron multiplier zone thickness. The H_2O cooled blanket deposits more energy per fusion neutron. This is due to the increase in the neutron capture in the ferritic structure where the Q value for $Fe(n,\gamma)$ is 7.8 MeV compared to 4.79 MeV for $^6Li(n,\alpha)T$ interaction.

The strong slowing down power of H_2O increases the maximum burnup in the blanket compared to D_2O cooled blankets. Figure 10-31 gives the maximum burnup for both coolants as a function of the neutron multiplier zone

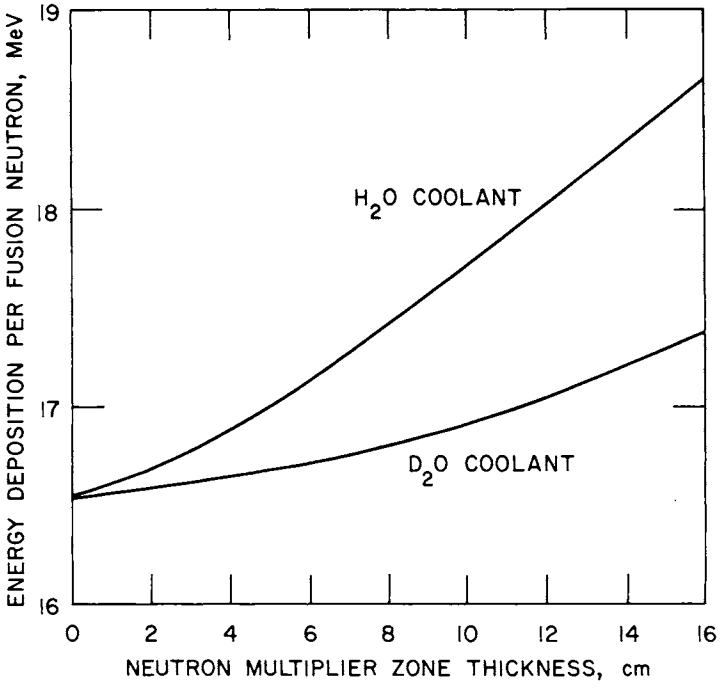

Figure 10-30. Nuclear energy deposition per fusion neutron from separate zone blanket option with D_2O and H_2O coolant, Pb neutron multiplier, Li_2SiO_3 (90% ^6Li) breeder and ferritic steel structure.

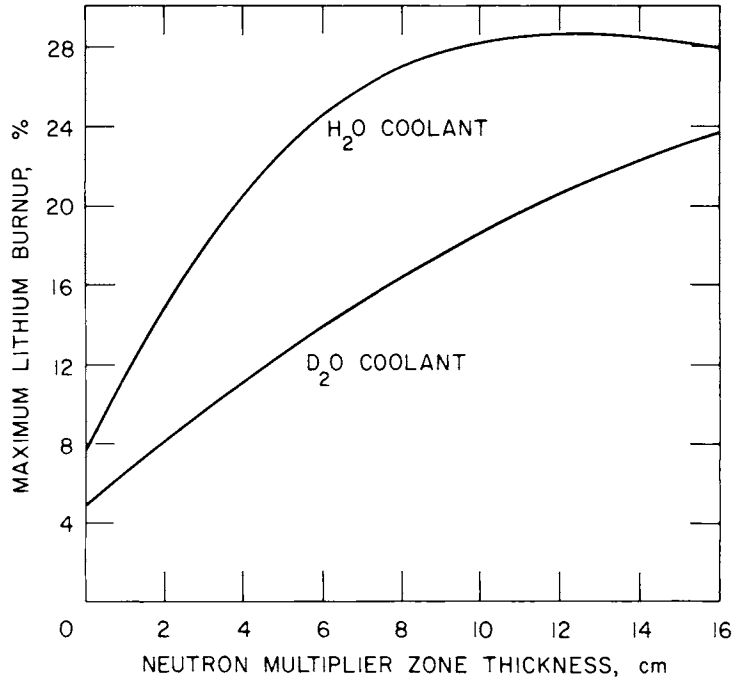

Figure 10-31. Maximum lithium burnup at 16.2 MW•yr/m^2 as a function of the neutron multiplier zone thickness for separate zone blanket option with D_2O and H_2O coolant, Pb neutron multiplier, Li_2SiO_3 (90% ^6Li) breeder and ferritic steel structure.

thickness while Fig. 10-32 gives the same information as a function of the tritium breeding ratio. For a tritium breeding ratio of 1.2, the maximum burnup for H_2O cooled blankets is $\sim$ 22% at 16.2 MW•yr/m^2 exposure (STARFIRE neutron wall loading integrated over the blanket life) compared to $\sim$ 10% for D_2O. This higher maximum burnup will also cause a greater change in the blanket temperature distribution at end of life.

The blanket parameters for the second concept are listed in Table 10-31 for the D_2O coolant. The tritium production, the heat deposition and the neutron leakage are given in Table 10-37 for both coolants. The energy deposition per fusion neutron is almost the same for both coolants. The D_2O cooled blanket gives 1 to 2% more tritium production compared to the H_2O cooled blanket. This increase in the tritium production results from the neutron multiplication from the D(n,2n)P interactions. However, the H_2O cooled blanket has less neutron parasitic interactions due to the excellent H_2O slowing down power that increases the neutron reaction probability with

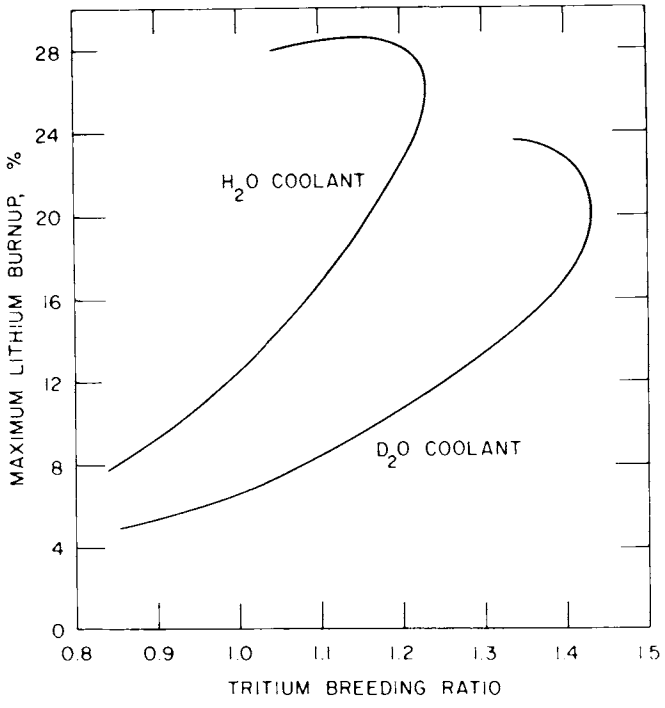

Figure 10-32. Maximum lithium burnup at 16.2 MW·yr/m^2 integrated neutron wall load as a function of the tritium breeding ratio for the separate zone blanket option D_2O and H_2O coolants, Pb neutron multiplier, Li_2SiO_3 (90% ^6Li) breeder and ferritic steel structure; different values for the multiplier zone thickness can yield the same breeding ratio but result in different Li burnup values.

^6Li. Since the $^6Li(n,\sigma)\alpha$ cross section is very large in the low neutron energy range in comparison with the cross sections of the other blanket materials, the slowing down of the neutrons is helping the tritium production for the blanket without a neutron multiplier. For the same reason the neutron leakage from the H_2O cooled blanket is smaller compared to the leakage from the D_2O cooled blanket.

10.4.7 Neutronic Analysis of the Separate Zone versus the Heterogeneous Blanket Option

The separate zone blanket option is selected as the reference blanket option for the STARFIRE design. In this section, a comparison between the separate zone and the heterogeneous blanket option is discussed from the neutronic and material requirements point of view. The neutron multiplier, the tritium breeder, the structural material and the coolant are the same

Table 10-37. Tritium Production, Nuclear Energy Deposition, Neutron Leakage per Fusion Neutron for Different Coolant and Tritium Breeding Zone Composition with Li_2O (natural Li) Tritium Breeding Material and Ferritic Steel Structure

Blanket Number	A	A'	B	B'	C	C'	D	D'
Li_2O Tritium Breeding Material, Volume %	90	90	85	85	85	85	80	80
Ferritic Steel Structure Volume %	5	5	5	5	10	10	10	10
Water Coolant, Volume %	5	5	10	10	5	5	10	10
Type of Water	H_2O	D_2O	H_2O	D_2O	H_2O	D_2O	H_2O	D_2O
Energy Deposition per Fusion Neutron (MeV)	17.75	17.73	17.77	17.74	17.76	17.74	17.77	17.79
$^6Li(n,t)\alpha$ Reaction per Fusion Neutron	0.9276	0.9395	0.9311	0.9465	0.9302	0.9398	0.9355	0.9463
$^7Li(n,n't)\alpha$ Reaction per Fusion Neutron	0.4083	0.4128	0.3875	0.3941	0.3712	0.3752	0.3511	0.3568
Tritium Breeding Ratio	1.3359	1.3523	1.3186	1.3406	1.3014	1.3150	1.2866	1.3031
Neutron Leakage per Fusion Neutron	0.0010	0.0023	0.0008	0.0024	0.0009	0.0021	0.0007	0.0018

for both concepts analyzed. The relevant parameters are listed in Table 10-38. The performance characteristics for both blanket options are compared in Table 10-39. The results indicate about the same tritium breeding ratio, energy deposition per fusion and energy leakage for both cases. However, the material requirements are different. The heterogeneous option requires less tritium breeding material with a high ^6Li enrichment, (90% ^6Li enrichment). Whereas the lithium resources required for the heterogeneous blanket option is half that for the separate zones blanket option, the neutron multiplier material requirements are much greater for the separate zone concept

Table 10-38. Blanket Parameters for Separate Zone and Heterogeneous Blanket Option with Zr_5Pb_3 Neutron Multiplier, $LiAlO_2$ Breeding Material, H_2O Coolant, and PCA Steel Structure

Zone Description	Zone Thickness cm	Zone Composition Percentage by Volume
A. Separate Zone Blanket Option		
First Wall	1	50% PCA steel structure 50% H_2O coolant
Neutron Multiplier	7	100% Zr_5Pb_3 neutron multiplier material
Second Wall	1	25% PCA steel structure 25% H_2O coolant
Tritium Breeding	30	80% $LiAlO_2$ tritium breeding material 10% PCA steel structure 5% H_2O coolant 5% He purge stream
Reflector	15	50% carbon reflector material 25% PCA steel structure 25% H_2O coolant
B. Heterogenous Blanket Option		
First wall	1	50% PCA steel structure 50% H_2O coolant
Tritium Breeding and Neutron Multiplier Material	23	65.2% Zr_5Pb_3 neutron multiplier material 17.4% $LiAlO_2$ tritium breeding material 8.7% PCA steel structure 4.35% H_2O coolant 4.35% He purge stream
Tritium Breeding and Moderator Material	20.5	60.98% C moderator material 19.50% $LiAlO_2$ tritium breeding material 9.76% PCA steel structure 4.88% H_2O coolant 4.88% He purge stream
Reflector	15	50% carbon reflector 25% PCA steel structure 25% H_2O coolant

Table 10-39. Blanket Neutronic Parameters for the Separate Zone Option Versus the Heterogeneous Blanket Option Where Both are Using Zr_5Pb_3 Neutron Multiplier Material, $LiAlO_2$ Tritium Breeding Material, PCA Steel Structure and H_2O Coolant

Blanket Option	Separate Zones	Heterogeneous
Lithium-6 Enrichment (%)	60	90
Neutron Multiplier Material Thickness (cm)	7	12
Tritium Breeding Material Thickness (cm)	24	8
Tritium Breeding Ratio	1.198	1.213
Nuclear Energy Deposition per Fusion Neutron (MeV)	17.88	17.66
Total Energy Leakage per Fusion Neutron (MeV)	0.062	0.088
Neutron Leakage per Fusion Neutron	0.017	0.014
Neutron Energy Leakage per Fusion Neutron	0.033	0.037
Maximum Heating Rate in the Multiplier Material for 3.6 Neutron Wall Loading (w/cm^3)	37.8	29.6

The maximum neutron heating in the neutron multiplier is about 28% higher in the separate zones blanket option. Since there is less tritium breeding material used in the heterogeneous blanket option, the blanket tritium inventory in the heterogeneous blanket option should be less. The average lithium burnup is 3.6% for the separate zones blanket option compared to 10.8% for the heterogeneous option. Although the heterogeneous blanket option has some advantages compared to the separate zone option, the heterogeneous blanket option is more difficult to design from the mechanical and thermal hydraulic point of view.

10.4.8 Blanket Neutron Performance for Different Reflector Materials

In order to analyze the impact of different reflector materials on the blanket performance, a neutronic analysis was performed for the STARFIRE blanket concept with three different reflector materials. Carbon, water (H_2O) and PCA steel are the candidates as reflector materials considered. The blanket parameters for this analysis are listed in Table 10-40. Carbon and water provide the desirable advantage of being low radioactive materials. However, the use of a thick water region is difficult because it requires a heavy container to sustain the high water pressure. The temperature considerations

Table 10-40. Blanket Parameters for Different Reflector Materials with Zr_5Pb_3 Neutron Multiplier Material, $LiAlO_2$ (60% ^6Li) Tritium Breeding Material, PCA Steel Structure and H_2O Coolant

Zone Description	Zone Thickness cm	Zone Composition Percentage by Volume
First Wall	1	50% PCA steel structure 50% H_2O coolant
Neutron Multiplier	7	100% Zr_5Pb_3 neutron multiplier material
Second Wall	1	50% PCA steel structure 25% H_2O coolant
Tritium Breeder	30	80% $LiAlO_2$ tritium breeding material 10% PCA steel structure 5% H_2O coolant 5% He purge stream
Reflector	30	90% reflector material 5% PCA steel structure 5% H_2O coolant

dictate the water pressure to be ∿ 15 MPa. Although the use of steel is simple, it increases the radioactive waste.

The results from the neutronic calculations for the blanket with different reflectors are given in Table 10-41. The tritium breeding zone thickness for these calculations is 30 cm which corresponds to a tritium breeding ratio of 99.3% of the saturation value for the $LiAlO_2$ tritium breeding material. The results indicate that the tritium breeding ratio is about the same for the water and carbon reflectors, and about 1% less for the PCA steel reflector. However, the PCA steel deposits a slightly higher (∿ 0.5%) energy per fusion neutron compared to the other two reflectors. These differences are related to the ratio of the capture to the scattering cross section of the reflector materials. When this ratio is large, more energy is generated and less tritium is produced. The steel reflector also gives the lowest neutron energy leakage per fusion neutron, which is desirable from the shielding point of view. The smaller leakage reduces the power and the radioactivity produced in the shield zone.

10.4.9 Neutronic Analysis of the STARFIRE Reference Design

The selection of the reference STARFIRE blanket design is based on the neutronic analyses presented in the previous sections. A more detailed analysis

Table 10-41. Blanket Neutronic Performance From the Use of Different Reflector Materials with Zr_5Pb_3 Neutron Multiplier Material, $LiAlO_2$ (60% ^6Li) Tritium Breeding Material, PCA Steel Structure and H_2O Coolant

Reflector Material	H_2O	PCA steel	Carbon
Tritium Breeding Ratio	1.181	1.171	1.184
Nuclear Energy Deposition per Fusion Neutron (MeV)	18.02	18.08	18.00
Neutron Energy Leakage per Fusion Neutron (MeV)	0.0059	0.0015	0.0097
Gamma Energy Leakage per Fusion Neutron (MeV)	0.0277	0.0016	0.0209
Total Energy Leakage per Fusion Neutron (MeV)	0.0336	0.0031	0.0306

of the reference design is presented below. A one-dimensional model is used to define the dimensions of the different regions. A three-dimensional neutronics model was developed and used to provide a more accurate evaluation of the nuclear performance of the reference design.

10.4.9.1 One-Dimensional Analysis

The STARFIRE blanket reference design has evolved from the numerous parametric and trade-off studies. The separate zone blanket concept with two neutron multiplier options, viz., Be and Zr_5Pb_3, is selected for the STARFIRE reference design. In this section the thickness of each zone for the reference design is defined.

In order to determine the tritium breeding zone thickness, blankets with a variable tritium breeding zone thickness and a 50-cm carbon reflector are analyzed. The blanket parameters are given in Table 10-42. The resulting tritium breeding ratio and the nuclear energy deposition per fusion neutron are given in Fig. 10-33. The tritium breeding ratio reaches saturation at $\sim$ 40-cm tritium breeding zone thickness with more than 99% of the saturation value achieved at a 30-cm thickness. On the other hand, the nuclear energy deposition per fusion neutron decreases with the increase in the tritium breeding zone thickness because of the difference in the Q value of lithium and iron reactions. Therefore, a 30-cm tritium breeding zone thickness is selected for the STARFIRE reference design.

The ^6Li enrichment is based on the neutronic analysis presented in Sec. 10.4.4. A 60% ^6Li enrichment is used with the Zr_5Pb_3 neutron multiplier whereas natural lithium is used with the Be neutron multiplier.

The analysis for the 30-cm graphite reflector is given in Sec. 10.4.8. The use of the neutron multiplier and water coolant, which produces a soft neutron spectrum at the back of the tritium breeding zone, reduces the importance of the reflector. Therefore, a 15-cm reflector is proposed. The change from a 30 to a 15-cm reflector zone thickness results in only a 0.3% reduction in the tritium breeding ratio and a 0.5% reduction in the nuclear energy deposition per fusion neutron. The fact that the inlet and outlet coolant headers serve as a reflector material increases the effect of the reflector in the STARFIRE design.

Table 10-42. Blanket Parameters for Analysis of Breeding Zone Thickness

Zone Description	Zone Thickness cm	Zone Composition, Percentage by Volume
First Wall	1	50% PCA steel structure 50% H_2O coolant
Neutron Multiplier	7	100% Zr_5Pb_3 neutron multiplier material
Second Wall	1	50% PCA steel structure 25% H_2O coolant
Tritium Breeder	Variable	80% $LiAlO_2$ tritium breeding material 10% PCA steel structure 5% H_2O coolant 5% He purge stream
Reflector	50	90% carbon reflector 5% PCA steel structure 5% H_2O coolant

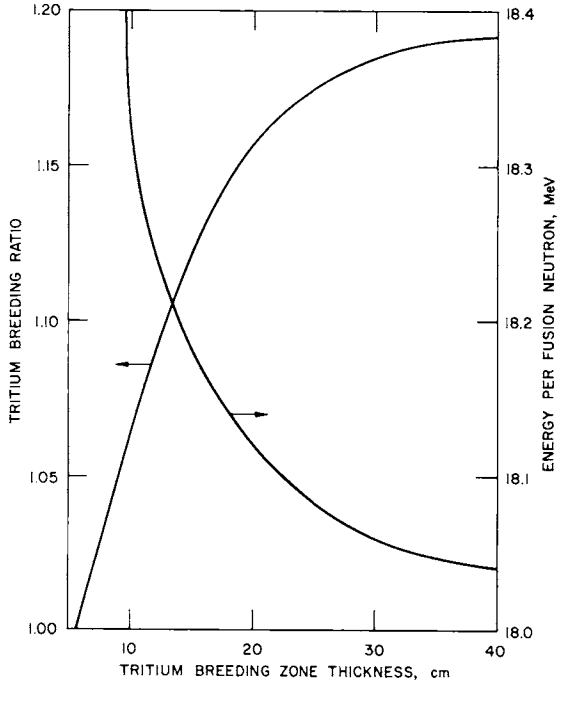

Figure 10-33. Tritium breeding ratio and energy deposition per fusion neutron as a function of the breeding zone thickness with Zr_5Pb_3 neutron multiplier, $LiAlO_2$ (60% ^6Li), PCA structure and H_2O coolant.

The thermal-hydraulic and the stress analyses for the reference design indicate a need for less steel in the second wall and less water in the first and second walls than was used in the neutronic analysis. The implementation of these changes in the first and the second wall thicknesses results in less multiplier zone thickness for the same neutronic performance. Decreasing the neutron multiplier zone thickness is desirable because the maximum temperature of the multiplier is reduced for the same neutron wall loading.

The STARFIRE blanket reference parameters are given in Table 10-43. The same blanket parameters are used for Be neutron multiplier except a natural lithium and a 0.7 density factor for the multiplier zone are imposed on the parameters in Table 10-43. The density factor for the Be neutron multiplier will accommodate any swelling. The tritium breeding material also has a 0.6 density factor to enhance the tritium release characteristics. Therefore, the 30-cm breeding zone thickness of 100% dense $LiAlO_2$ will correspond to a 46-cm breeding zone thickness with 60% dense $LiAlO_2$.

The neutronic performance parameters for the reference design with both the Be and Zr_5Pb_3 multipliers are listed in Table 10-44. Both designs achieve a tritium breeding ratio of $\sim$ 1.2 but the Be design deposits more energy per fusion neutron due to the difference in the Q value of (n,2n) reaction cross sections for both neutron multipliers. However, the energy leakage, the neutron leakage and the maximum lithium burnup are lower with the Zr_5Pb_3 multiplier, which is desirable from the shielding point of view. Figures 10-34 through 10-40 give the nuclear energy deposition rate in each material and zone of the reference blanket design for both neutron multiplier options.

The change in the blanket neutronic performance during the blanket life has also been analyzed to assure satisfactory performance. The neutronic performance of the STARFIRE reference design with the Zr_5Pb_3 neutron multiplier is almost constant during the blanket life of six years or $\sim$ 16.2 $MW \cdot yr/m^2$ integrated neutron wall loading. The tritium breeding ratio drops by 0.7% at the end of life, while the nuclear energy deposition increases by 0.35% because of more neutron capture in the steel.

The blanket neutronic performance with the Be neutron multiplier is more sensitive to the burnup of ^6Li during the blanket life. The burnup analysis

Table 10-43. Blanket Parameters for STARFIRE Reference Design

Zone Description	Zone Thickness cm	Zone Composition, Percentage by Volume
First Wall	1	50% PCA steel structure 27% H_2O coolant
Neutron Multiplier	5	100% Zr_5Pb_3 or 70% Be
Second Wall	1	35% PCA steel structure 17% H_2O coolant
Tritium Breeder	30	80% $LiAlO_2$ tritium breeding material[a] 10% PCA steel structure 5% H_2O coolant 5% He purge stream
Reflector	15	90% carbon reflector 5% PCA steel structure 5% H_2O coolant

[a] Natural Li for Be neutron multiplier or enriched 60% ^6Li for the Zr_5Pb_3 neutron multiplier.

for Be blanket was performed in 3 MW·yr/m^2 steps for a blanket design slightly different from the reference design. The blanket parameters used in this burnup analysis included a higher H_2O fraction (50%) in the first wall, a thicker neutron multiplier zone (5 cm of 100% Be), and a thicker second wall (50% steel, 25% H_2O). The tritium breeding ratio and the nuclear energy deposition per fusion neutron are given in Fig. 10-41. The tritium breeding ratio shows a significant drop at the end of life (16.2 MW·yr/m^2 integrated neutron wall loading). However, for the STARFIRE reactor at any point in time, the average integral neutron wall loading will not exceed 8.1 MW·yr/m^2. This is a result of the maintenance scenario which changes one sixth of the blanket (four blanket segments) every year. This limits the change in the tritium breeding ratio from 1.214 to 1.186 for the reactor. For individual segments, the tritium production will drop by 12% at the end of life and

Table 10-44. Blanket Neutronic Parameters for STARFIRE Reference Design Based on 1-D Model

Neutron Multiplier Material	Zr_5Pb_3	Be
Neutron Multiplier Material Thickness (cm)	5	3.5
^6Li Enrichment (%)	60	Natural
$^6Li(n,\alpha)T$ Reaction per Fusion Neutron	1.186	1.142
$^7Li(n,n\alpha)T$ Reaction per Fusion Neutron	0.020	0.075
Tritium Breeding Ratio	1.206	1.217
Energy per Fusion Neutron (MeV)	17.44	19.87
Neutron Energy Leakage per Fusion Neutron (MeV)	0.041	0.057
Gamma Energy Leakage per Fusion Neutron (MeV)	0.036	0.085
Total Energy Leakage per Fusion Neutron (MeV)	0.077	0.142
Neutron Leakage per Fusion Neutron	0.019	0.038
Maximum Li Burnup at 16.2 MW•yr/m^2 (%)	16.9[a]	21.8[a]
Average Li Burnup at 16.2 MW•yr/m^2 (%)	3.61	3.64

[a] Averaged over the first cm of the breeder zone.

the corresponding increase in the maximum nuclear heating is about 40%. The nuclear energy deposition per fusion neutron increases by 5% at the average neutron wall loading of 8.1 MW•yr/m^2. These changes should be somewhat less for the reference blanket parameters.

10.4.9.2 Three-Dimensional Analysis

The three-dimensional neutronic analysis was performed for the reference design to more accurately determine the nuclear energy deposition in each

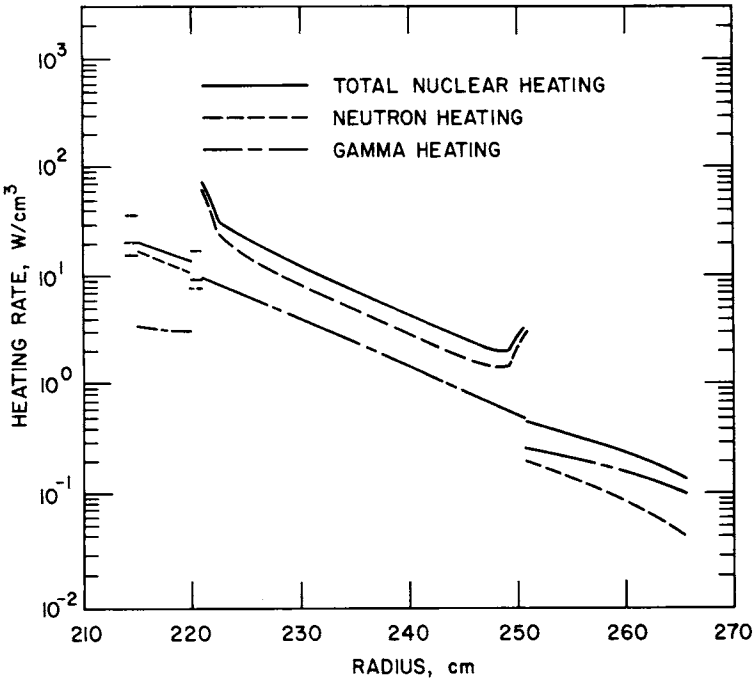

Figure 10-34. STARFIRE nuclear heating rates for Zr_5Pb_3 neutron multiplier option.

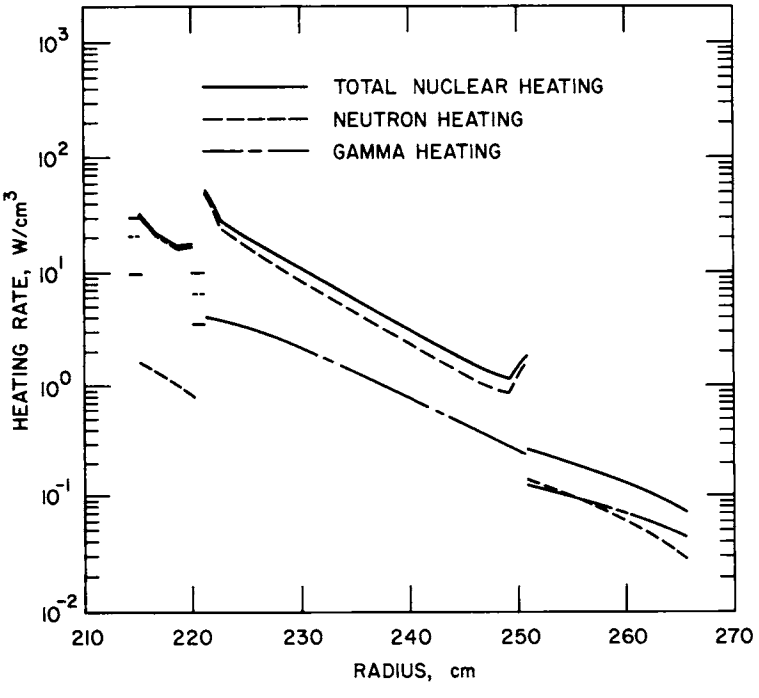

Figure 10-35. STARFIRE nuclear heating rates for Be neutron multiplier option.

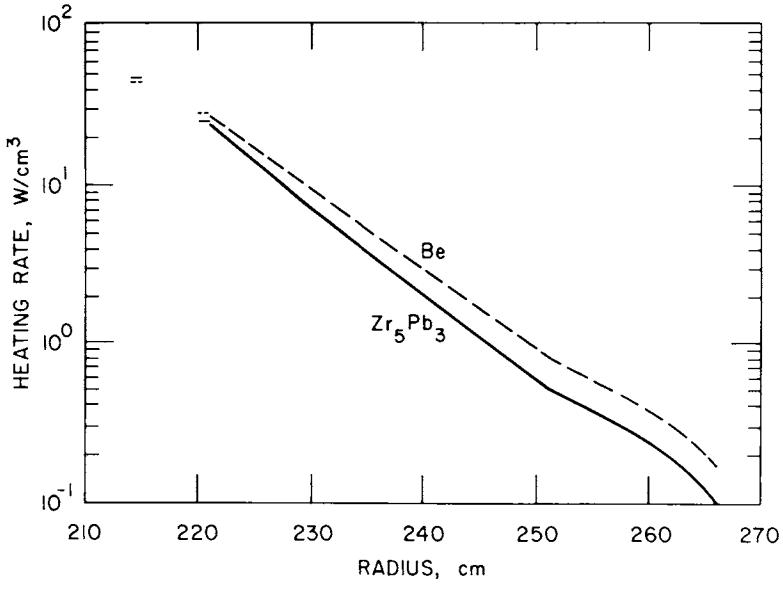

Figure 10-36. Nuclear heating rates in the H_2O water coolant.

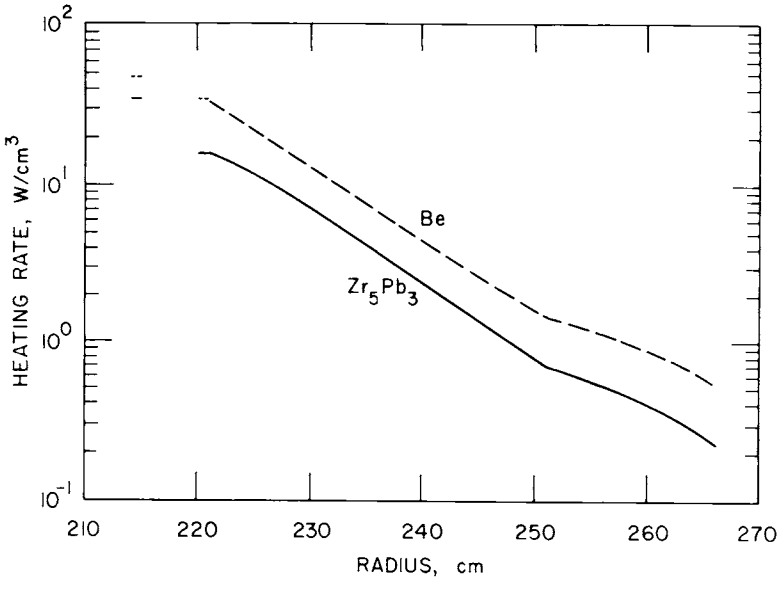

Figure 10-37. Nuclear heating rates in the PCA steel structure material.

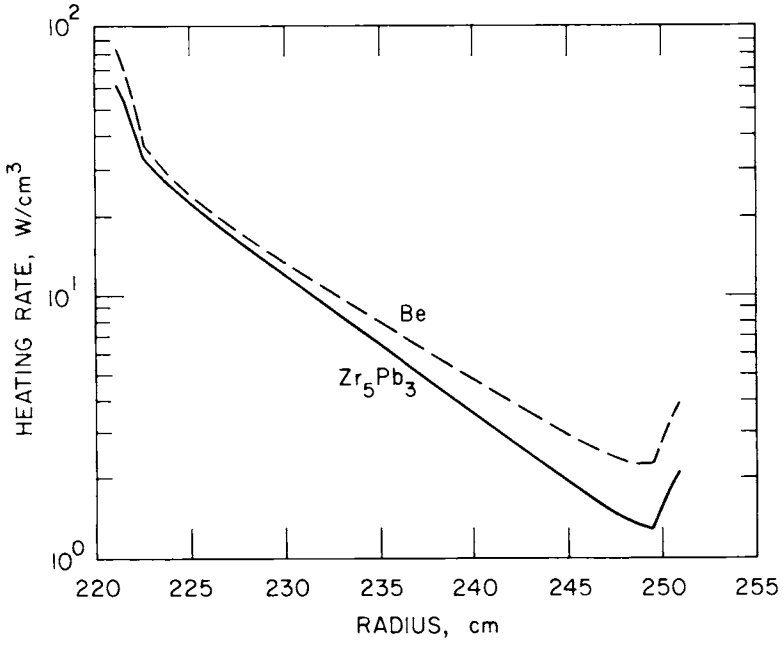

Figure 10-38. Nuclear heating rates in the $LiAlO_2$ tritium breeding material.

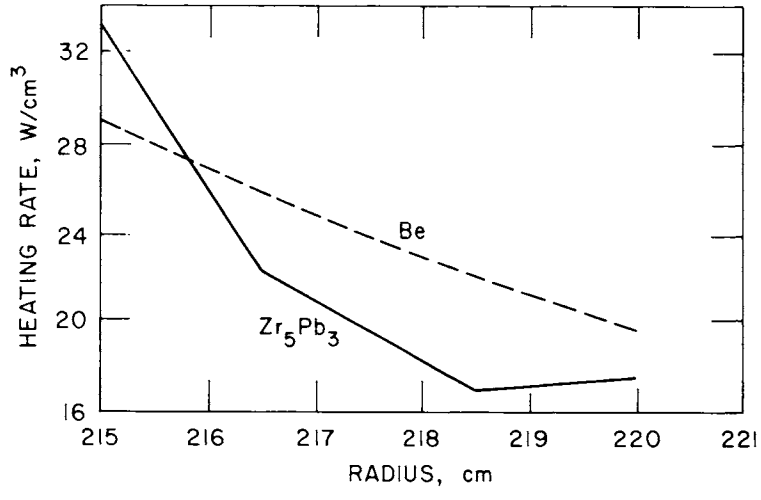

Figure 10-39. Nuclear heating rates in the Zr_5Pb_3 neutron multiplier material.

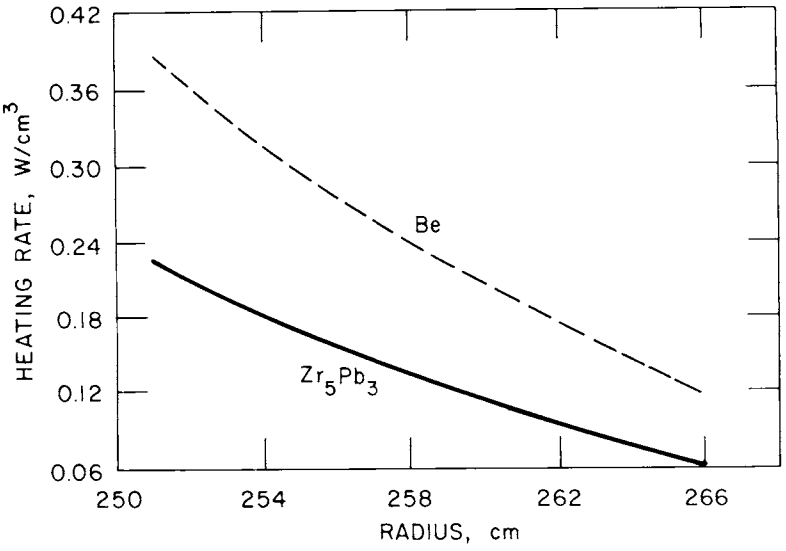

Figure 10-40. Nuclear heating rates in the C reflector material.

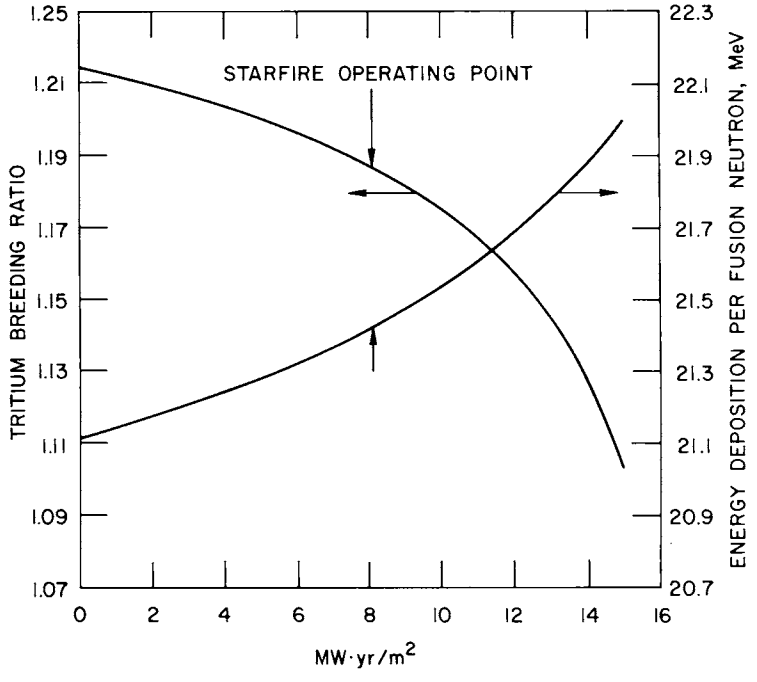

Figure 10-41. Tritium breeding ratio and energy per fusion neutron versus blanket exposure for Be neutron multiplier, $LiAlO_2$ (Li) breeder C reflector, H_2O coolant and PCA structure.

blanket component, the net tritium breeding ratio, and the poloidal heat load on the first wall from the nuclear heating and the radiation from the plasma. The Monte Carlo MORSE-CG code[60] was used for these calculations. A 67 multigroup cross section set (46 neutron and 21 gamma) collapsed from the CTR library[61] with the P_3 approximation used for the calculations. The MACKLIB-IV[62] was employed to calculate the nuclear response functions.

The neutron source distribution for the calculations was determined from the fusion power density as a function of (r,z) as shown in Fig. 10-42. It should be noted that the source is shifted 79 cm from the geometrical center of the reactor chamber towards the outer blanket. The geometry model used in the calculation is shown in Fig. 10-43. The geometry of the blanket, the actual dimension of the individual zones, the limiter system, the rf system, and the geometry change in the poloidal direction are explicitly represented in the model. The inner blanket has a thickness of 28 cm (including 0.6 density factor for the tritium breeding material) with no reflector. The

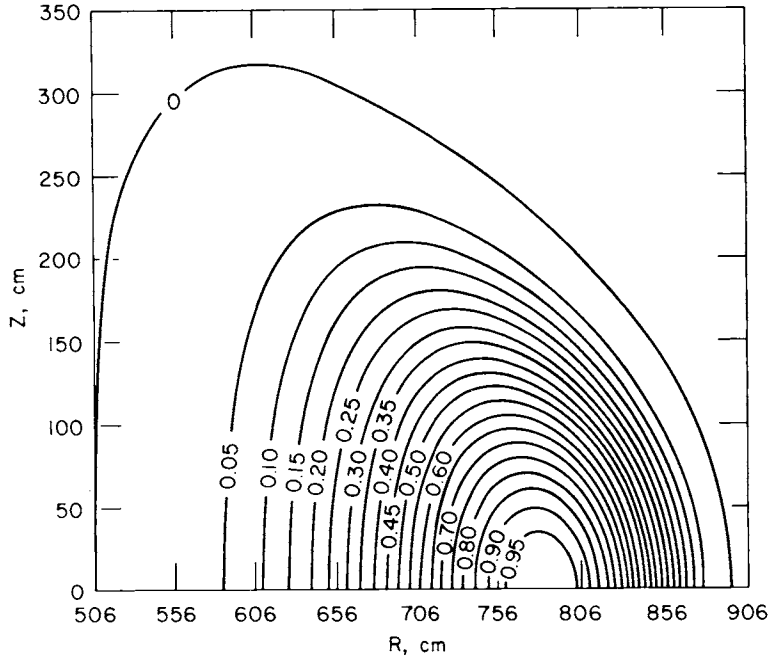

Figure 10-42. Neutron source distribution used in 3-D analysis.

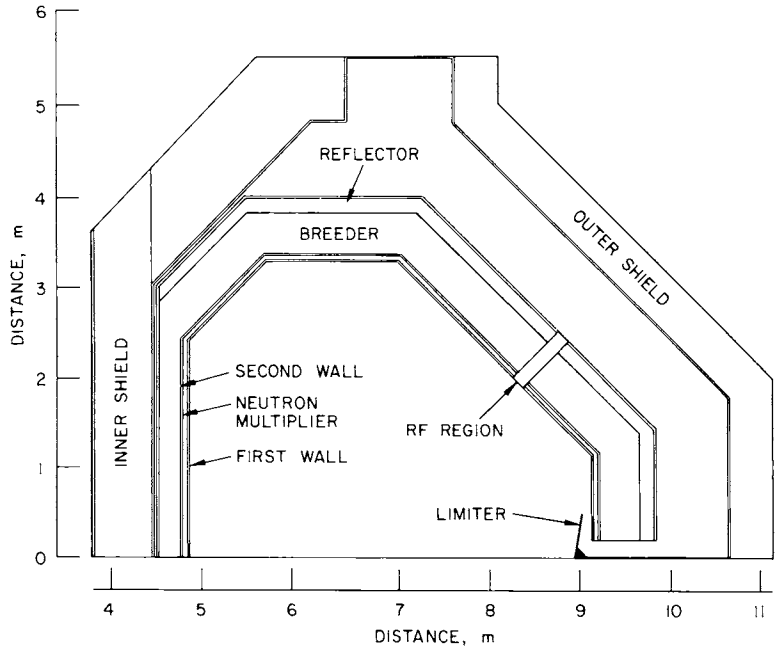

Figure 10-43. Geometry model for 3-D neutronic analysis.

blanket and shield are included in the geometrical model. The Zr_5Pb_3 neutron multiplier option is employed for the three dimensional analysis. The Ta-5W was used in the limiter but it is only one of four candidate materials (see Chap. 8).

Table 10-45 and 10-46 give the nuclear energy deposition and the power generated in the different reactor components. The fractional standard deviation in the calculation is less than 5% for any component. The nuclear heating in the inner shield is $\sim$ 35% of the total energy deposited in the shield regions. As indicated in Table 10-47, the net tritium breeding ratio is 1.044 with a standard deviation of 0.29% for the reference design with Zr_5Pb_3 neutron multiplier option. The corresponding value from the one dimensional model is 1.206 without the limiter and the rf system, with an inner blanket thickness of 46 cm. The doubling time corresponding to a 1.044 net tritium breeding ratio is 1.5 and 3.1 years for a tritium inventory of 5 and 10 kg, respectively. It should be noted that the percentage of H_2O coolant and the PCA structure are assumed to be uniformly distributed throughout the entire breeding zone in these calculations. Since the final thermal-hydraulic analysis calls for less H_2O coolant and PCA structure in the tritium breeding zone, the net tritium breeding ratio should be slightly greater than 1.044.

Table 10-45. Nuclear Energy Deposition in Each Zone From the Three-Dimensional Analysis for the Reference Design with Zr_5Pb_3 Neutron Multiplier

Blanket Component	Energy per Fusion Neutron (MeV)	Fractional Standard Deviation
First Wall	1.1913	0.0071
Neutron Multiplier	3.2897	0.0086
Second Wall	0.4072	0.0093
Tritium Breeding Zone	11.0070	0.0061
Reflector	0.1622	0.0431
Blanket Jacket	0.0771	0.0337
Limiter System	0.8231	0.0402
RF System	0.1480	0.0455
Inner Shield	0.1181	0.0613
Outer Shield	0.2166	0.0573
Total	17.2923	

Table 10-46. Nuclear Power Deposition in Each Zone of STARFIRE Reference Design with Zr_5Pb_3 Neutron Multiplier

Component	MW
First Wall	235.70
Neutron Multiplier	650.87
Second Wall	80.56
Tritium Breeding Zone	2177.73
Reflector	32.09
Blanket Jacket	15.25
Limiter System (Ta-5W)	162.85
rf System	29.28
Inner Shield	23.08
Outer Shield	42.85

Table 10-47. The Net Tritium Breeding Ratio From the Three-Dimensional Analysis for the Reference Design

Reaction Type	Reaction per Fusion Neutron	Fractional Standard Deviation
$^{6}Li(n,\alpha)T$	1.0216	0.0030
$^{7}Li(n,n'\alpha)T$	0.0226	0.0148
Tritium Breeding Ratio	1.0441	0.0029

Although the net tritium breeding ratio satisfies the STARFIRE design requirements, an increase in the tritium production capability is desirable to accommodate any uncertainties in the nuclear data or the calculations. An increase of $\sim$ 5% ($\sim$ 1.1 TBR) in the net tritium breeding ratio can be achieved by increasing the Zr_5Pb_3 neutron multiplier zone thickness from 5 to 7.5 cm or employing the vanadium limiter option. However, it should be noted that the STARFIRE tritium is produced primarily from ^{6}Li for which the uncertainty in the nuclear data is very small compared to ^{7}Li isotope. For the reference design with the Be neutron multiplier, an increase in the multiplier zone thickness gives a larger increase in the tritium production than for the Zr_5Pb_3 neutron multiplier option. Also, the use of heavy water instead of the light water will increase the tritium production. Therefore, an increase in the tritium breeding ratio is possible if it is called for.

The heat load on the first wall consists of two components, viz., surface and volumetric heat load. The first wall surface heating is a result of the radiation from the plasma. The radiation power is the sum of three components, bremsstrahlung, line and recombination radiation power resulting partially from the presence of iodine injected into the plasma. The latter contributions are given by:

$$P_{LR} = N_1 N_I S(T_1) \qquad (11)$$

where P_{LR} is the radiated power in w/m^3 due to line and recombination radiation from iodine, N_1 is the plasma electron density, N_I is the iodine density and T_1 is the electron temperature. The function $S(T_1)$ is taken from the results of Chap. 6 where the zenon data are used since iodine is not listed. The reference density and temperature profiles for the STARFIRE design, as discussed in Sec. 6.7, are used in the above equation. These are given as:

$$
\begin{aligned}
T_1(\hat{\psi}) &= 22.5\ \hat{\psi}^{0.3} \quad \text{keV} \\
N_1(\hat{\psi}) &= 2.5 \times 10^{20}\ \hat{\psi}^{1.1} \quad m^{-3} \\
N_I(\hat{\psi}) &= 1.2 \times 10^{17}\ \hat{\psi}^{1.1} \quad m^{-3}
\end{aligned}
\tag{12}
$$

where $\hat{\psi}$ is the normalized flux function defined as

$$
\hat{\psi} = \frac{\psi_L - \psi}{\psi_L - \psi_m} \tag{13}
$$

where ψ_L and ψ_m are the values of ψ at the limiter and magnetic axis, respectively. The flux function ψ is shown, as a function of (r,z) in Fig. 6-5. By using this flux function, together with the reference profiles and the bremsstrahlung radiation power from Chap. 6, the radiation source is defined for the Monte Carlo calculation. Figure 10-44 shows the surface heat load as a function of the poloidal angle (θ). The average surface heat load is 90.45 w/cm^2, with a maximum and minimum of 117.57 and 62.70 w/cm^2, respectively.

The volumetric heat load caused by the fusion neutrons is shown in Fig. 10-45 as a function of the poloidal angle where the fractional standard deviation is $\sim$ 10% for this calculation. The Monte Carlo point detector estimators were used where the detectors are located at the center of the first wall. Notice that the surface and volumetric heat loads on the first wall are affected by: (1) the spatial distribution of the source strength within the plasma, (2) the MHD shift of the magnetic axis outward from the geometrical axis, (3) the toroidal geometry, and (4) the shape of the first wall in the poloidal cross-section. A more uniform heat load would result if the contour of the first-wall

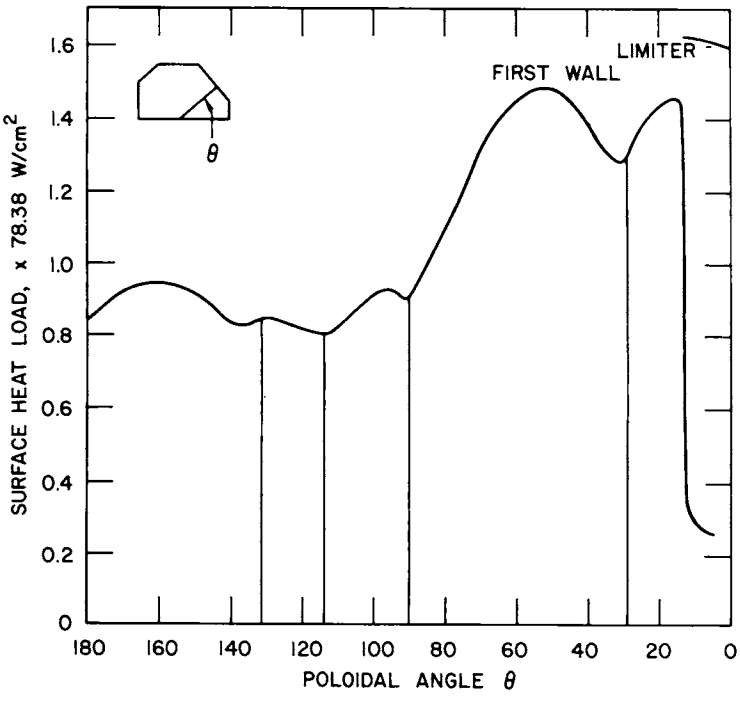

Figure 10-44. Surface heat load on the first wall as a function of the poloidal angle θ.

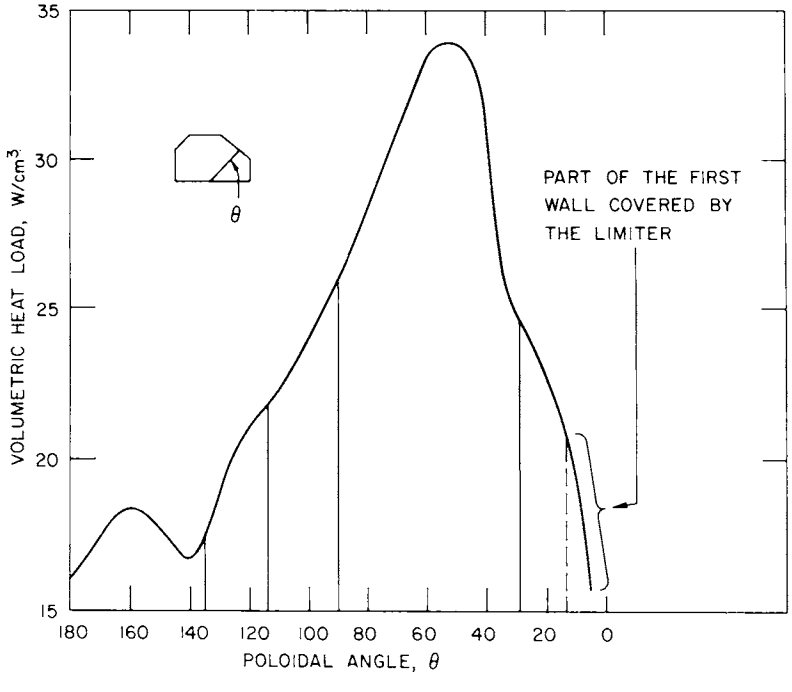

Figure 10-45. First wall nuclear heating as a function of the poloidal angle θ.

more closely approached that of the plasma. A smoother variation in the heat load can be produced by making the first wall closer to circular or D-shaped.

10.5 THERMAL-HYDRAULIC ANALYSES

Both steady-state and transient thermal analyses of the first wall, multiplier, and the breeding blanket were carried out to evaluate the various design concepts for STARFIRE. In carrying out thermal-hydraulic calculations, it appeared prudent to separate the multiplier region, which is sandwiched between the first wall and the second wall coolant panels, from the breeding blanket except for a 1-cm thick breeding region which is cooled by the second wall. Figures 10-1 and 10-2 show the conceptual design of a blanket module consisting of the first wall, multiplier region, second wall and the breeding blanket. Since the energy deposited in the reflector/shield regions is small compared with the above mentioned regions of the blanket modules, no thermal hydraulic calculations were carried out for the reflector and the shield regions.

Thermal-hydraulic calculations were made for both normal operation, as well as for operation under off-design conditions. As STARFIRE operates in continuous mode, as opposed to pulsed mode, normal design/analysis involves evaluation of operating characteristics such as temperature distribution, pressure drop, coolant velocity, pumping-power losses, coolant-tube size selection, coolant- tube layout and evaluation of various material fractions in the breeding region. Only a limited number of off-design scenarios were considered to analyze the behavior of various regions of the first-wall/blanket modules. These include: (1) loss of coolant from both the first and the second wall coolant panels; (2) loss of coolant from the first wall coolant panels only; and (3) plasma disruptions. Since the off-design conditions are transient in nature, the analytical studies are divided into two groups; steady state operation, and transient operation.

10.5.1 Steady-State Operation

Schematic presentation of a typical blanket segment is made in Figs. 10-1 and 10-2. The actual dimensions of blanket modules depend on their location in the torus. The neutron multiplier is sandwiched between two coolant panels - the first wall and the second wall. For the sake of simplicity, the first wall/blanket module is divided into two regions. The segment of the breeder region (about 1 cm thick) that is cooled by the second wall was included in the first wall/multiplier thermal-hydraulic modeling. The

balance of the blanket is analyzed separately. The analytical results are summarized below.

10.5.1.1 Thermal-Hydraulic Analysis of the Blanket

A series of parametric studies of several blanket design concepts was carried out for STARFIRE. Both water and pressurized helium under the current LWR and HTGR design practices, respectively, are used as the heat transport fluid. The analytical results under steady-state operating conditions show that either water or pressurized helium can be used satisfactorily as the heat transport medium. The choice of the coolant will depend primarily on the compatibility of materials with the coolant and method of extraction of tritium from the breeding blanket. The ratio of pumping power to thermal power (RPT) using 1-cm diameter tubes for water is low (RPT $\sim$ 0.3%) compared with that of helium (RPT = 2.5%). However, the pumping power losses for helium can be reduced by a factor of more than 2.5 by raising the helium operating pressure from 5.17 MPa (750 psia) to 8.62 MPa (1250 psia). The actual losses for the overall power conversion system are expected to be higher than these values since the present study is limited to thermal hydraulics of the blanket modules only.

Description of Blanket and Operating Conditions -- A schematic of a typical blanket segment is shown in Fig. 10-1. Figure 10-46 shows a cross section of modular blanket segment. For the thermal-hydraulic calculations, the modular blankets were assumed to be 2.3-m long x 0.6-m wide x 0.46-m thick with separately cooled first-wall panels. The pressurized coolant is carried through stainless steel tubes embedded in a packed bed of granular breeding material. A set of parametric studies was carried out for water and helium as the coolants flowing in tubes varying in size from 0.635 cm (1/4 in.) to 2.54 cm (1 in.). For each coolant tube size, the diameter of the surrounding blanket region was calculated based on (1) coolant inlet and outlet temperature; (2) nuclear heat generation rate; (3) the maximum operating temperature for the breeder; (4) thermal contact resistance between the breeding material and the coolant tube; (5) thermophysical properties of the coolant and the breeder; and (6) heat transfer characteristics of the coolant. For water, the inlet and the outlet temperatures were assumed to be 453°K and 593°K, respectively. For helium, three cases were analyzed by assuming the temperature rise across

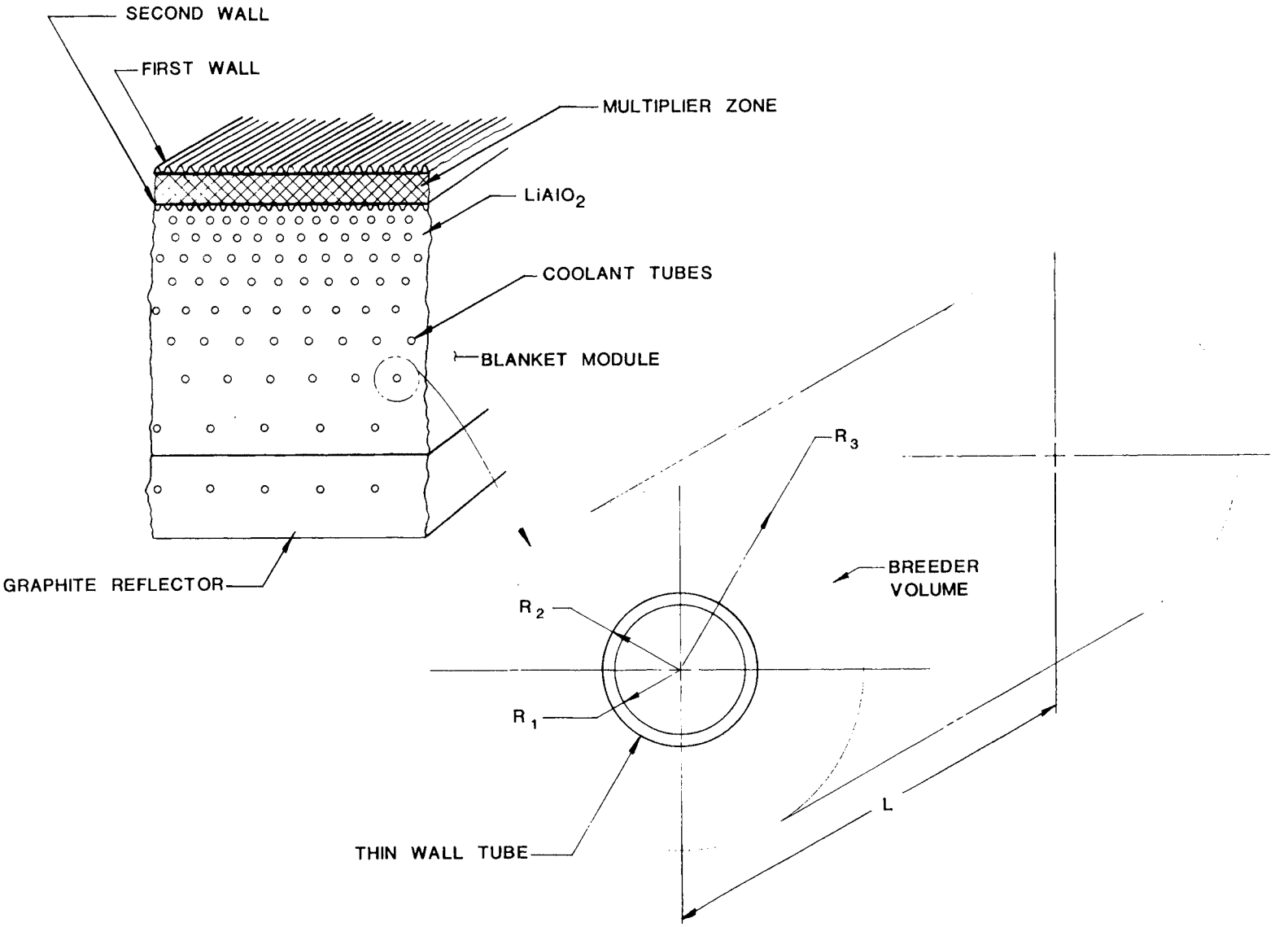

Figure 10-46. First wall/blanket - geometric model of breeder region.

the blanket to be 200°K, 225°K, and 250°K with the coolant entering the blanket at 498°K for each case. Separate helium purge flow channels were assumed to be located uniformly in the space surrounding circular blanket regions (see Fig. 10-2) to provide the necessary capacity for tritium extraction.

Development of Computer Model -- Figure 10-46 shows a typical coolant tube with R_1 and R_2 as the inner and the outer radius, respectively. Each coolant tube is surrounded by a breeder region of radius R_3. The outer radius of the breeding region (R_3) represents an essentially isothermal boundary, except for small breeding regions between a group of coolant tubes where the helium purge flow channels are located (see Fig. 10-2) to extract the tritium from the breeding blanket. The coolant flowing through each coolant channel removes the nuclear heat generated in (1) the coolant; (2) the cladding; and (3) the breeder. The temperature gradient between the coolant stream and the isothermal boundary in the blanket is governed by (1) the heat generated in the various materials; (2) thermal conductivity of cladding and the breeder; (3) interfacial contact resistance between the breeding blanket and the coolant channel outer wall; and (4) the heat transfer characteristics of the coolant.

The differential equation governing the steady-state temperature distribution in a heat-generating cylinder may be represented by

$$\frac{d^2T}{dr^2} + \frac{1}{r}\frac{dT}{dr} + \frac{q'''}{k} = 0 , \qquad (14)$$

where

T = temperature at radial distance r

k = thermal conductivity

q''' = volumetric heat generation rate.

The following boundary conditions were assumed to solve Eq. (14)

$$\frac{dt}{dr} = 0 \quad \text{at} \quad r = R_3 , \qquad (15)$$

$$-k\frac{dT}{dr} = h_f\left(T_{wi} - T_f\right) \quad \text{at} \quad r = R_1 , \tag{16}$$

$$= h_g\left(\Delta T_g\right) \quad \text{at} \quad r = R_2 , \tag{17}$$

where

h_f = coolant heat transfer coefficient

h_g = gap conductance

T_{wi} = coolant channel inner wall temperature

T_{w0} = coolant channel outer wall temperature

T_f = coolant temperature

ΔT_g = temperature drop across the gap.

The maximum breeder temperature (at $r = R_3$), T_{max}, may be expressed as

$$T_{max} = T_{ex} + \frac{q_b''' R_3^2}{4 k_b}\left\{\left(\frac{R_2}{R_3}\right)^2 - 2 \ln\frac{R_2}{R_3} - 1\right\}$$

$$+ \frac{q_b''' R_3^2}{2}\left\{1 - \left(\frac{R_2}{R_3}\right)^2\right\}\left\{\frac{1}{k_s}\ln\frac{R_2}{R_1} + \frac{1}{R_1 h_f}\right\}$$

$$+ \frac{q_b'''}{2 R_2 h_g}\left\{R_3^2 - R_2^2\right\} , \tag{18}$$

where

q_b''' = nuclear heat generation rate in the breeder

k_s = thermal conductivity of clad

T_{ex} = coolant exit temperature

The total heat removed by the coolant, Q_t, may be calculated by

$$Q_t = \pi L\left\{R_1^2 q_c''' + \left(R_2^2 - R_1^2\right)q_s''' + \left(R_3^2 - R_2^2\right)q_b'''\right\} , \tag{19}$$

where

L = coolant channel length

q_c''', q_s''' = nuclear heat generation rate in the coolant and the structure respectively.

From the total heat rate (Q_t) the coolant flow rate ($\dot{w}$) and the coolant velocity (V) may be calculated by

$$\dot{w} = Q_t / \left\{C_p\left(T_{ex} - T_{in}\right)\right\} , \tag{20}$$

$$V = \dot{w}/(A\rho) , \tag{21}$$

where

C_p = coolant heat capacity

T_{in} = coolant inlet temperature

A = cross-sectional area of coolant channels

ρ = average coolant density.

The pumping power and the thermal power may be calculated as follows:

$$\text{Pumping power, PP} = (\dot{w}/\rho)\Delta P \tag{22}$$

$$\text{Thermal Power, TP} = \dot{w}C_p\Delta T_f . \tag{23}$$

The ratio of pumping power to thermal power from Eqs. (22) and (23) is given by

$$RPT = \Delta P / \left(\rho C_p \Delta T\right) , \tag{24}$$

where

ΔP = pressure drop across coolant channel + pressure losses at inlet and outlet headers plus pressure losses at bends, valves, fittings, etc.

ΔT_f = coolant temperature rise = $T_{ex} - T_{in}$.

The volume fraction of the (1) coolant, f_c; (2) structure, f_s (neglecting container structure walls, inlet and outlet coolant channel sections embedded in the blanket); and (3) breeder, f_b, may be represented by

$$f_c = R_1^2/R_3^2 \tag{25}$$

$$f_s = (R_2^2 - R_1^2)/R_3^2 \tag{26}$$

$$f_b = (R_3^2 - R_2^2)/R_3^2 \ . \tag{27}$$

The thermal stress, σ_t, across the coolant tube wall is calculated by

$$\sigma_t = \frac{\alpha E}{2(1 - \nu)} \left(\Delta T_s + \Delta T_v\right) , \tag{28}$$

where

α = coefficient of thermal expansion

E = modulus of elasticity

ν = Poisson's ratio

ΔT_s and ΔT_v = temperature drop across the channel wall due to surface heat flux and volumetric heat generation, respectively.

An examination of the above set of equations shows that some of these equations are interrelated. Hence, an iteration scheme appears to be the simplest method of solution. A computer program was developed to carry out a series of parametric studies by varying the (1) coolant channel diameter; (2) coolant inlet and outlet temperatures; (3) interfacial contact resistance; and (4) coolant pressure (for helium only). Since the nuclear heat generation rate in the blanket decreases exponentially as the blanket regions are removed further and further from the first wall, a series of calculations was carried out by varying the nuclear heat generation from 1% to 100% of the heating rate (100% of the heating rate was assumed to occur at the beginning of the breeder region) in order to select coolant tube size, spacing between the coolant tubes, and spacing between rows of coolant tubes. Table 10-48 summarizes a typical set of calculations for the outer blanket with water as the coolant. The calculations for the inner blanket are summarized in Table 10-49. The tables list (1) the coolant tube diameter (DC); (2) the

Table 10-48. Summary of Analytical Results for Coolant Water (Outer Blanket, $\Delta T = 40°C$, P = 15.5 MPa)

SUMMARY OF CALCULATIONS AT PWF= 1.00D 00 HG= 0.16D 04 QN= 3.12D 01 PIN= 2.20D 03 DTC= 4.00D 01 XL= 2.30D 00 ITR= 6

DC CM	DBR CM	TWI DG.C	TWO DG.C	VEL M/S	DELP PSI	VFC %	VFB %	RPT %	THS PSI
6.350D-01	2.425D 00	3.261D 02	3.661D 02	6.736D 00	3.496D 01	6.462D 00	8.668D 01	1.674D-01	6.157D 03
8.000D-01	2.620D 00	3.263D 02	3.663D 02	4.746D 00	1.460D 01	6.738D 00	8.394D 01	6.990D-02	5.700D 03
1.000D 00	2.835D 00	3.272D 02	3.672D 02	3.539D 00	6.866D 00	6.999D 00	8.056D 01	3.287D-02	5.255D 03
1.200D 00	3.065D 00	3.290D 02	3.690D 02	2.831D 00	3.843D 00	7.052D 00	7.762D 01	1.840D-02	5.019D 03
1.400D 00	3.280D 00	3.308D 02	3.708D 02	2.348D 00	2.370D 00	7.087D 00	7.469D 01	1.135D-02	4.802D 03
1.600D 00	3.495D 00	3.327D 02	3.727D 02	2.015D 00	1.591D 00	7.061D 00	7.198D 01	7.617D-03	4.642D 03
1.800D 00	3.710D 00	3.346D 02	3.746D 02	1.756D 00	1.117D 00	6.993D 00	6.947D 01	5.348D-03	4.522D 03
2.000D 00	3.910D 00	3.364D 02	3.764D 02	1.575D 00	8.387D-01	6.950D 00	6.689D 01	4.015D-03	4.380D 03
2.200D 00	4.125D 00	3.385D 02	3.785D 02	1.434D 00	6.542D-01	6.832D 00	6.472D 01	3.132D-03	4.311D 03
2.540D 00	4.465D 00	3.414D 02	3.814D 02	1.238D 00	4.466D-01	6.684D 00	6.095D 01	2.138D-03	4.148D 03

Table 10-49. Summary of Analytical Results for Coolant Water (Inner Blanket, $\Delta T = 40°C$, P = 15.5 MPa)

SUMMARY OF CALCULATIONS AT PWF= 1.00D 00 HG= 0.16D 04 QN= 3.12D 01 PIN= 2.20D 03 DTC= 4.00D 01 XL= 6.00D 00 ITR= 3

DC CM	DBR CM	TWI DG.C	TWO DG.C	VEL M/S	DELP PSI	VFC %	VFB %	RPT %	THS PSI
6.350D-01	2.425D 00	3.191D 02	3.591D 02	1.781D 01	3.151D 02	6.462D 00	8.668D 01	1.509D 00	6.157D 03
8.000D-01	2.620D 00	3.179D 02	3.579D 02	1.254D 01	1.305D 02	6.738D 00	8.394D 01	6.249D-01	5.700D 03
1.000D 00	2.850D 00	3.174D 02	3.574D 02	9.343D 00	6.074D 01	6.925D 00	8.076D 01	2.908D-01	5.324D 03
1.200D 00	3.080D 00	3.175D 02	3.575D 02	7.470D 00	3.367D 01	6.984D 00	7.784D 01	1.612D-01	5.082D 03
1.400D 00	3.295D 00	3.177D 02	3.577D 02	6.192D 00	2.058D 01	7.023D 00	7.492D 01	9.854D-02	4.861D 03
1.600D 00	3.510D 00	3.181D 02	3.581D 02	5.310D 00	1.370D 01	7.001D 00	7.222D 01	6.560D-02	4.698D 03
1.800D 00	3.725D 00	3.187D 02	3.587D 02	4.670D 00	9.720D 00	6.937D 00	6.971D 01	4.653D-02	4.575D 03
2.000D 00	3.940D 00	3.194D 02	3.594D 02	4.186D 00	7.239D 00	6.844D 00	6.739D 01	3.466D-02	4.481D 03
2.200D 00	4.155D 00	3.202D 02	3.602D 02	3.809D 00	5.604D 00	6.734D 00	6.523D 01	2.683D-02	4.408D 03
2.540D 00	4.510D 00	3.214D 02	3.614D 02	3.312D 00	3.841D 00	6.551D 00	6.173D 01	1.839D-02	4.286D 03

diameter of the surrounding breeder region (DBR); (3) the coolant tube inner wall temperature (TWI); (4) the coolant tube outer wall temperature (TWO); (5) the coolant velocity (V); (6) the pressure drop across the coolant channel (DELP); (7) the volume fraction of structure (VFC); (8) the volume fraction of breeder (VFB); (9) the ratio of pumping power to thermal power (RPT); and (10) the thermal stress across the coolant channel wall (THS). Tables 10-50 through 10-55 list similar sets of data for helium coolant at pressures of 5.17 and 8.62 MPa (750 and 1250 psia) and two different coolant temperature rises (250 and 200°C), respectively.

Temperature Distribution in the Breeding Region - The tritium partial pressure (as T_2O) and hence the tritium retention in the breeder depends on the temperature distribution in the breeding region. To facilitate calculation of tritium inventory due to solubility of tritium in the $LiAlO_2$ breeder (as LiOT), the breeder region surrounding each coolant tube was divided into 100 equi-volume regions (10 in the axial direction and 10 in the radial direction). The temperature distribution in the blanket region may be expressed by

$$T_i = T_{max} - \frac{q_b''' R_3^2}{4 k_b} \left\{ \left(\frac{R_i}{R_3} \right)^2 - 2 \ln \left(\frac{r_i}{R_3} \right) - 1 \right\} , \qquad (29)$$

where

T_i = breeder temperature at radial distance r_i.

For the lithium aluminate solid breeding blanket, the maximum breeder temperature (T_{max}) was assumed to be 850°C for all calculations.

The results presented in the foregoing sections are based on a typical outer blanket segment 2.3 m long x 0.46 m thick. The largest inner blanket segments are 6 m long x 0.28 m thick. From a thermal hydraulics point of view, the major calculational difference between the inner blanket and the outer blanket segments would be the pressure drop across the coolant channels, and hence the ratio of pumping power to thermal power. Table 10-49 lists the analytical results for the blanket regions near the first wall (at 100% of rated power).

Table 10-50. Summary of Analytical Results for Coolant Helium (ΔT = 250°C, P = 5.17 MPa)

SUMMARY OF CALCULATIONS AT PWF= 1.00D 00 HG= 0.16D 04 QN= 3.12D 01 PIN= 7.50D 02 DTC= 2.50D 02 XL= 2.30D 00 ITR= 34

DC CM	DBR CM	THI DG.C	THO DG.C	VEL M/S	DELP PSI	VFC %	VFB %	RPT %	THS PSI
6.350D-01	2.140D 00	2.864D 02	5.364D 02	1.558D 02	1.064D 02	8.298D 00	8.290D 01	1.517D 01	4.586D 03
8.000D-01	2.320D 00	2.918D 02	5.418D 02	1.039D 02	4.149D 01	8.593D 00	7.952D 01	5.654D 00	4.234D 03
1.000D 00	2.520D 00	2.984D 02	5.484D 02	7.553D 01	1.873D 01	8.858D 00	7.540D 01	2.512D 00	3.886D 03
1.200D 00	2.720D 00	3.050D 02	5.550D 02	5.957D 01	1.018D 01	8.955D 00	7.158D 01	1.359D 00	3.645D 03
1.400D 00	2.920D 00	3.114D 02	5.614D 02	4.942D 01	6.257D 00	8.943D 00	6.807D 01	8.325D-01	3.468D 03
1.600D 00	3.120D 00	3.176D 02	5.676D 02	4.246D 01	4.188D 00	8.860D 00	6.484D 01	5.564D-01	3.333D 03
1.800D 00	3.320D 00	3.236D 02	5.736D 02	3.742D 01	2.986D 00	8.732D 00	6.187D 01	3.964D-01	3.226D 03
2.000D 00	3.520D 00	3.292D 02	5.792D 02	3.361D 01	2.235D 00	8.575D 00	5.914D 01	2.966D-01	3.139D 03
2.200D 00	3.720D 00	3.347D 02	5.847D 02	3.064D 01	1.738D 00	8.401D 00	5.662D 01	2.306D-01	3.067D 03
2.540D 00	4.045D 00	3.425D 02	5.925D 02	2.662D 01	1.191D 00	8.144D 00	5.243D 01	1.579D-01	2.928D 03

Table 10-51. Summary of Analytical Results for Coolant Helium (ΔT = 250°C, P = 6.89 MPa)

SUMMARY OF CALCULATIONS AT PWF= 1.00D 00 HG= 0.16D 04 QN= 3.12D 01 PIN= 1.00D 03 DTC= 2.50D 02 XL= 2.30D 00 ITR= 34

DC CM	DBR CM	THI DG.C	THO DG.C	VEL M/S	DELP PSI	VFC %	VFB %	RPT %	THS PSI
6.350D-01	2.140D 00	2.864D 02	5.364D 02	1.128D 02	7.699D 01	8.298D 00	8.290D 01	7.957D 00	4.586D 03
8.000D-01	2.320D 00	2.918D 02	5.418D 02	7.691D 01	3.072D 01	8.593D 00	7.952D 01	3.100D 00	4.234D 03
1.000D 00	2.520D 00	2.984D 02	5.484D 02	5.632D 01	1.396D 01	8.853D 00	7.540D 01	1.397D 00	3.886D 03
1.200D 00	2.720D 00	3.050D 02	5.550D 02	4.454D 01	7.615D 00	8.955D 00	7.158D 01	7.596D-01	3.645D 03
1.400D 00	2.920D 00	3.114D 02	5.614D 02	3.700D 01	4.684D 00	8.943D 00	6.807D 01	4.665D-01	3.468D 03
1.600D 00	3.120D 00	3.176D 02	5.676D 02	3.181D 01	3.137D 00	8.860D 00	6.484D 01	3.122D-01	3.333D 03
1.800D 00	3.320D 00	3.236D 02	5.736D 02	2.804D 01	2.238D 00	8.732D 00	6.187D 01	2.226D-01	3.226D 03
2.000D 00	3.520D 00	3.292D 02	5.792D 02	2.519D 01	1.675D 00	8.575D 00	5.914D 01	1.666D-01	3.139D 03
2.200D 00	3.720D 00	3.347D 02	5.847D 02	2.297D 01	1.303D 00	8.401D 00	5.662D 01	1.296D-01	3.067D 03
2.540D 00	4.045D 00	3.425D 02	5.925D 02	1.996D 01	8.930D-01	8.144D 00	5.243D 01	8.878D-02	2.928D 03

Table 10-52. Summary of Analytical Results for Coolant Helium (ΔT = 250°C, P = 8.62 MPa)

SUMMARY OF CALCULATIONS AT PWF= 1.00D 00 HG= 0.16D 04 QN= 3.12D 01 PIN= 1.25D 03 DTC= 2.50D 02 XL= 2.30D 00 ITR= 34

DC CM	DBR CM	TWI DG.C	TWO DG.C	VEL M/S	DELP PSI	VFC %	VFB %	RPT %	THS PSI
6.350D-01	2.140D 00	2.864D 02	5.364D 02	8.886D 01	6.066D 01	8.298D 00	8.290D 01	4.943D 00	4.586D 03
8.000D-01	2.320D 00	2.918D 02	5.418D 02	6.117D 01	2.443D 01	8.593D 00	7.952D 01	1.962D 00	4.234D 03
1.000D 00	2.520D 00	2.984D 02	5.484D 02	4.494D 01	1.114D 01	8.858D 00	7.540D 01	8.898D-01	3.886D 03
1.200D 00	2.720D 00	3.050D 02	5.550D 02	3.558D 01	6.083D 00	8.955D 00	7.158D 01	4.848D-01	3.645D 03
1.400D 00	2.920D 00	3.114D 02	5.614D 02	2.957D 01	3.744D 00	8.943D 00	6.807D 01	2.981D-01	3.468D 03
1.600D 00	3.120D 00	3.176D 02	5.676D 02	2.543D 01	2.508D 00	8.860D 00	6.484D 01	1.996D-01	3.333D 03
1.800D 00	3.320D 00	3.236D 02	5.736D 02	2.242D 01	1.789D 00	8.732D 00	6.187D 01	1.423D-01	3.226D 03
2.000D 00	3.520D 00	3.292D 02	5.792D 02	2.014D 01	1.340D 00	8.575D 00	5.914D 01	1.066D-01	3.139D 03
2.200D 00	3.720D 00	3.347D 02	5.847D 02	1.837D 01	1.042D 00	8.401D 00	5.662D 01	8.289D-02	3.067D 03
2.540D 00	4.045D 00	3.425D 02	5.925D 02	1.596D 01	7.143D-01	8.144D 00	5.243D 01	5.680D-02	2.928D 03

Table 10-53. Summary of Analytical Results for Coolant Helium (ΔT = 200°C, P = 5.17 MPa)

SUMMARY OF CALCULATIONS AT PWF= 1.00D 00 HG= 0.16D 04 QN= 3.12D 01 PIN= 7.50D 02 DTC= 2.00D 02 XL= 2.30D 00 ITR= 25

DC CM	DBR CM	TWI DG.C	TWO DG.C	VEL M/S	DELP PSI	VFC %	VFB %	RPT %	THS PSI
6.350D-01	2.230D 00	2.838D 02	4.838D 02	2.182D 02	1.918D 02	7.641D 00	8.425D 01	3.495D 01	5.061D 03
8.000D-01	2.410D 00	2.879D 02	4.879D 02	1.390D 02	7.149D 01	7.963D 00	8.102D 01	1.193D 01	4.655D 03
1.000D 00	2.625D 00	2.937D 02	4.937D 02	1.007D 02	3.243D 01	8.163D 00	7.732D 01	5.269D 00	4.325D 03
1.200D 00	2.840D 00	2.996D 02	4.996D 02	7.965D 01	1.784D 01	8.214D 00	7.393D 01	2.869D 00	4.104D 03
1.400D 00	3.040D 00	3.050D 02	5.050D 02	6.560D 01	1.085D 01	8.251D 00	7.054D 01	1.737D 00	3.896D 03
1.600D 00	3.240D 00	3.104D 02	5.104D 02	5.604D 01	7.202D 00	8.216D 00	6.740D 01	1.150D 00	3.736D 03
1.800D 00	3.440D 00	3.155D 02	5.155D 02	4.914D 01	5.100D 00	8.134D 00	6.449D 01	8.135D-01	3.609D 03
2.000D 00	3.640D 00	3.204D 02	5.204D 02	4.395D 01	3.794D 00	8.019D 00	6.179D 01	6.047D-01	3.507D 03
2.200D 00	3.840D 00	3.252D 02	5.252D 02	3.992D 01	2.935D 00	7.884D 00	5.929D 01	4.675D-01	3.422D 03
2.540D 00	4.180D 00	3.329D 02	5.329D 02	3.482D 01	2.031D 00	7.626D 00	5.545D 01	3.234D-01	3.307D 03

Table 10-54. Summary of Analytical Results for Coolant Helium (ΔT = 200°C, P = 6.89 MPa)

SUMMARY OF CALCULATIONS AT PHF= 1.00D 00 HG= 0.16D 04 QN= 3.12D 01 PIN= 1.00D 03 DTC= 2.00D 02 XL= 2.30D 00 ITR= 25

DC CM	DBR CM	THI DG.C	THO DG.C	VEL M/S	DELP PSI	VFC %	VFB %	RPT %	THS PSI
6.350D-01	2.230D 00	2.838D 02	4.838D 02	1.526D 02	1.341D 02	7.641D 00	8.425D 01	1.714D 01	5.061D 03
8.000D-01	2.410D 00	2.879D 02	4.879D 02	1.019D 02	5.240D 01	7.963D 00	8.102D 01	6.416D 00	4.655D 03
1.000D 00	2.625D 00	2.937D 02	4.937D 02	7.476D 01	2.408D 01	8.163D 00	7.732D 01	2.906D 00	4.325D 03
1.200D 00	2.840D 00	2.996D 02	4.996D 02	5.941D 01	1.330D 01	8.214D 00	7.393D 01	1.597D 00	4.104D 03
1.400D 00	3.040D 00	3.050D 02	5.050D 02	4.904D 01	8.110D 00	8.251D 00	7.054D 01	9.709D-01	3.896D 03
1.600D 00	3.240D 00	3.104D 02	5.104D 02	4.194D 01	5.390D 00	8.216D 00	6.740D 01	6.444D-01	3.736D 03
1.800D 00	3.440D 00	3.155D 02	5.155D 02	3.680D 01	3.819D 00	8.134D 00	6.449D 01	4.562D-01	3.609D 03
2.000D 00	3.640D 00	3.204D 02	5.204D 02	3.292D 01	2.842D 00	8.019D 00	6.179D 01	3.394D-01	3.507D 03
2.200D 00	3.840D 00	3.252D 02	5.252D 02	2.991D 01	2.199D 00	7.884D 00	5.929D 01	2.625D-01	3.422D 03
2.540D 00	4.180D 00	3.329D 02	5.329D 02	2.610D 01	1.523D 00	7.626D 00	5.545D 01	1.817D-01	3.307D 03

Table 10-55. Summary of Analytical Results for Coolant Helium (ΔT = 200°C, P = 8.62 MPa)

SUMMARY OF CALCULATIONS AT PHF= 1.00D 00 HG= 0.16D 04 QN= 3.12D 01 PIN= 1.25D 03 DTC= 2.00D 02 XL= 2.30D 00 ITR= 25

DC CM	DBR CM	THI DG.C	THO DG.C	VEL M/S	DELP PSI	VFC %	VFB %	RPT %	THS PSI
6.350D-01	2.230D 00	2.838D 02	4.838D 02	1.187D 02	1.044D 02	7.641D 00	8.425D 01	1.039D 01	5.061D 03
8.000D-01	2.410D 00	2.879D 02	4.879D 02	8.068D 01	4.150D 01	7.963D 00	8.102D 01	4.025D 00	4.655D 03
1.000D 00	2.625D 00	2.937D 02	4.937D 02	5.953D 01	1.918D 01	8.163D 00	7.732D 01	1.843D 00	4.325D 03
1.200D 00	2.840D 00	2.996D 02	4.996D 02	4.741D 01	1.062D 01	8.214D 00	7.393D 01	1.017D 00	4.104D 03
1.400D 00	3.040D 00	3.050D 02	5.050D 02	3.918D 01	6.478D 00	8.251D 00	7.054D 01	6.195D-01	3.896D 03
1.600D 00	3.240D 00	3.104D 02	5.104D 02	3.352D 01	4.307D 00	8.216D 00	6.740D 01	4.116D-01	3.736D 03
1.800D 00	3.440D 00	3.155D 02	5.155D 02	2.942D 01	3.053D 00	8.134D 00	6.449D 01	2.916D-01	3.609D 03
2.000D 00	3.640D 00	3.204D 02	5.204D 02	2.633D 01	2.273D 00	8.019D 00	6.179D 01	2.170D-01	3.507D 03
2.200D 00	3.840D 00	3.252D 02	5.252D 02	2.392D 01	1.759D 00	7.884D 00	5.929D 01	1.679D-01	3.422D 03
2.540D 00	4.180D 00	3.329D 02	5.329D 02	2.087D 01	1.218D 00	7.626D 00	5.545D 01	1.162D-01	3.307D 03

The analytical results for water are shown graphically in Figs. 10-47 through 10-49. Figure 10-47 shows the breeder region diameter as a function of coolant channel diameter for a selected set of power fractions. Figure 10-48 summarizes the pressure drop as a function of coolant channel diameter. The coolant velocity as a function of coolant channel diameter is summarized in Fig. 10-49. The corresponding analytical results for helium at 5.17 MPa (750 psia) are shown in Figs. 10-50 through 10-52.

Coolant Tube Layout -- From an examination of some of the analytical data presented above, one can see that tube layout may be carried out by using different tube sizes and a combination of single pass and multipass (serpentine tubes) flow arrangement. Multipass arrangement with different size tubes will lead to fewer welds and less pressure loss across flow passages. However, from the standpoint of manufacturing cost and quality control, it would be desirable to fabricate all blanket segments utilizing a single tube size. From the total number of coolant tubes (136/m) required for each

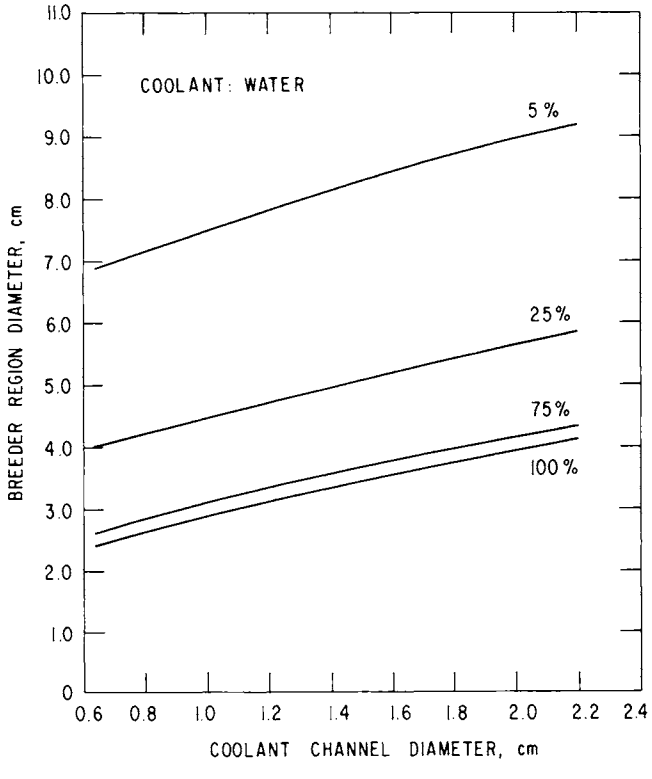

Figure 10-47. Summary of analytical results for water (breeder region diameter vs coolant channel diameter).

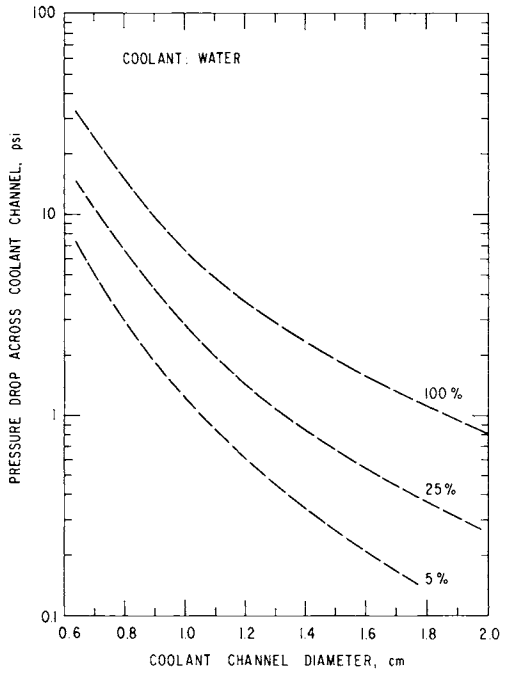

Figure 10-48. Summary of analytical results for water (pressure drop vs coolant tube diameter).

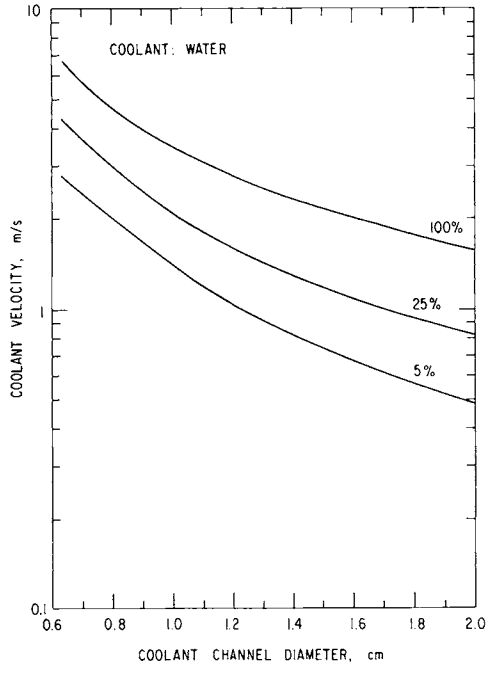

Figure 10-49. Summary of analytical results for water (velocity vs coolant channel diameter).

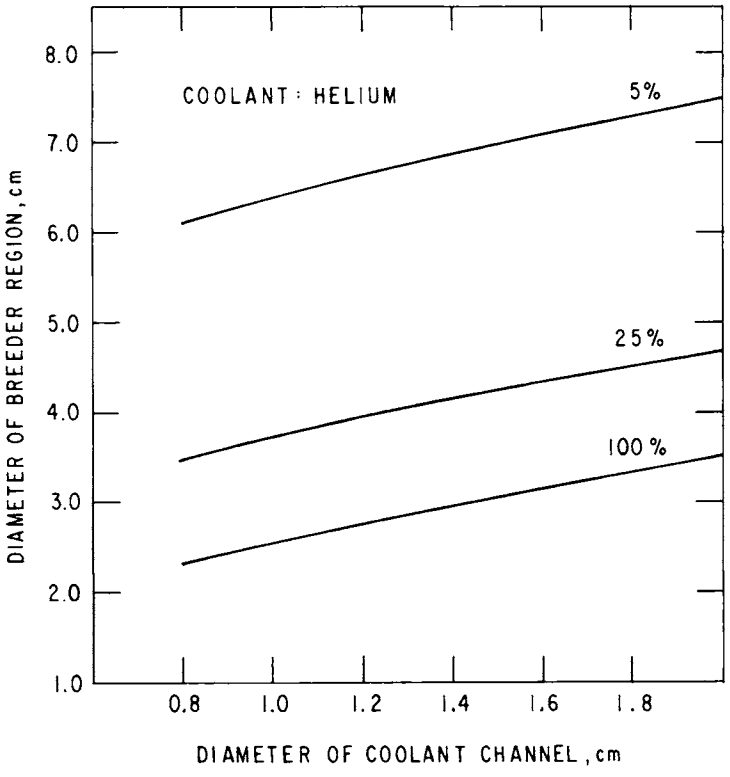

Figure 10-50. Summary of analytical results for helium (breeder region diameter vs coolant channel diameter).

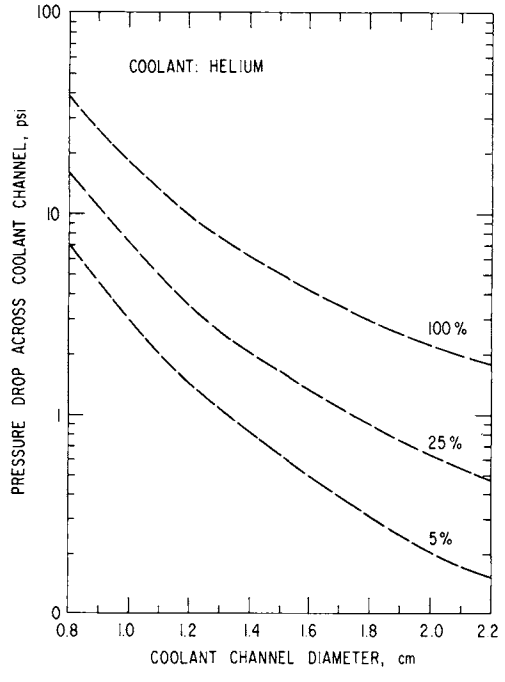

Figure 10-51. Summary of analytical results for helium (pressure drop vs coolant channel diameter).

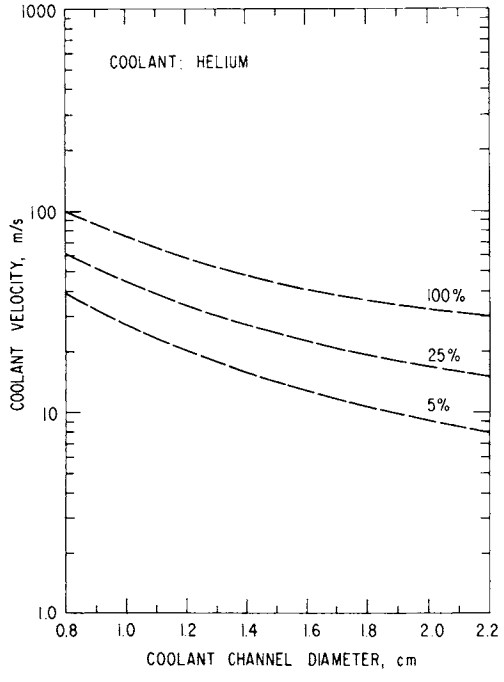

Figure 10-52. Summary of analytical results for helium (velocity vs coolant channel diameter.

segment, the coolant velocity, the pumping power losses, 1-cm diameter tubes appear to be satisfactory for blanket assembly. Table 10-56 summarizes the coolant tube layout for a typical outer blanket segment, consisting of eight rows of tubes. A similar tube layout for an inner blanket module shows six rows of tubes.

Discussion of Results -- Some of the important design goals of the STARFIRE blanket are to achieve (1) low coolant pumping power losses; (2) low structural material temperatures; (3) low coolant and structural material volume fractions; and (4) low coolant velocities. An examination of the results presented in the previous sections shows that the current blanket design meets these goals. The results show that some variations in the operating conditions assumed in the current study may be made to widen the design flexibility. The power loss for water is very small (less than 0.1%), and it is not considered to be a design problem. For helium as the coolant, the pumping power loss at 5.17 MPa (750 psia) is $\sim$ 2.5%. By raising the operating pressure from 5.17 MPa (750 psia) to 8.62 MPa (1250 psia), the pumping power losses for helium can be reduced to about 1%. It should be noted that these pumping power

Table 10-56. Coolant Tube Layout in Outer Blanket Using 1-cm Diameter Tubes

Row No.	Tube Spacing (cm)	Spacing Between (cm)	Pressure Drop (psia)	Coolant Velocity (m/s)
1	3.2	3.4	5.7	3.2
2	3.8	3.9	3.8	2.6
3	4.2	4.4	3.2	2.3
4	4.6	4.9	2.5	2.1
5	5.4	5.8	1.8	1.9
6	6.2	7.0	1.6	1.6
7	7.6	8.7	1.3	1.4
8	9.8	6.9[a]	1.0	1.2

NOTE: The breeder region cooled by the second wall is ∿1 cm. Hence, the eight rows of tubes cool the remaining 45 cm of the blanket.

[a]Spacing for the last row has been adjusted to account for the 46-cm thick blanket.

loss values are for the blanket module only; the total power loss for the overall power conversion system is expected to be higher.

The maximum structural material temperature for the water-cooled blanket is less than 400°C. However, for the helium-cooled blanket modules, the maximum wall temperature approaches 550°C for 1-cm diameter coolant tubes. As the heat loads on the coolant tubes are relatively small, the thermal stresses across the coolant tube wall are negligible. Also, the gap conductance variations between 0.455 W/cm^2-K and 0.91 W/cm^2-K (800 to 1600 Btu/hr-ft^2-°R) at these relatively low flux levels do not significantly affect the structural material temperatures. The coolant velocities (3.5 m/s for water and 76 m/s for helium, respectively) are well within the current design practices.

The water pressure drop across the inner blanket modules (using 1-cm diameter tubes) is 61 psia, which is almost nine times larger than that for the outer blanket modules (see Table 10-56). However, the ratio of pumping power to thermal power is only 0.3%. In order to reduce the large pressure drop, one might consider the use of larger diameter coolant tubes (e.g., 1.4 cm) for the first three rows of tubes. Both the high pumping power losses as well as the excessively high coolant velocities will preclude helium as the coolant for the inner blanket modules.

By reducing the temperature rise for the helium coolant from 250°C to 200°C, the coolant tube wall temperature can be lowered to less than 500°C. However, the pumping power loss for the above case increases from 2.5% to 5.3%, and coolant velocity increases from 76 m/s to 101 m/s (see Table 10-53).

The tritium inventory calculations based on a set of temperature distribution in the blanket (using lithium aluminate as the breeding material) show that the diffusive inventory of tritium is of the order of 1.4 kg. The diffusive inventory is very sensitive to even small temperature variations in the blanket. Hence, the tritium inventory can be reduced even further by tailoring the temperature distribution through proper adjustment of gap conductance, especially at the coolant inlet regions of the blanket segments.

From the results of the parametric studies, it may be concluded that either water or helium can be used satisfactorily as the heat transport fluid. The choice of the coolant will depend, to a large extent, on the method of extraction of tritium and compatibility of materials with the coolant in the high energy neutron environment.

10.5.2 First Wall/Multiplier Regions

One of the conceptual designs of the breeding blanket and multiplier has been to consider separate multiplier and breeding regions with independent cooling capabilities. Of the large number of multiplier and solid breeder combinations, and multiplier thicknesses varying from 35 mm to 80 mm, only the results of beryllium and Zr_5Pb_3 eutectic in combination with $LiAlO_2$ solid breeder are presented here. The thickness of both Be and Zr_5Pb_3 multiplier was assumed to be 50 mm. The 50-mm thick Be multiplier with 70% theoretical density corresponds to a 35-mm thick Be multiplier with 100% density.

Figure 10-53 shows a cross-section of the multiplier in the form of a slab sandwiched between the coolant panels representing the first and the second walls. Also, a section of the blanket that is cooled by the coolant flowing through the coolant channels of the second wall is included in the analysis. Two separate coolant loops, one for the first wall and the other for the second wall, were considered in the analysis to broaden the design flexibility and to enhance the margin of safety in case flow blockage occurs in one of the channels. Only pressurized water, entering at 280°C with a 40°C temperature rise, was considered as the coolant. For the 50-mm multiplier design, no internal coolant was found to be necessary.

For thermal-hydraulic modeling, the complex cross-section of the coolant channels in coolant panels was simplified by representing channels as rectangular flow paths as shown in Fig. 10-54. Steady state calculations were carried out for each design by a three-dimensional conduction code using a 240-node geometric model. The analysis considers surface heat flux on the beryllium coating facing the plasma, internal heat generation in all materials including

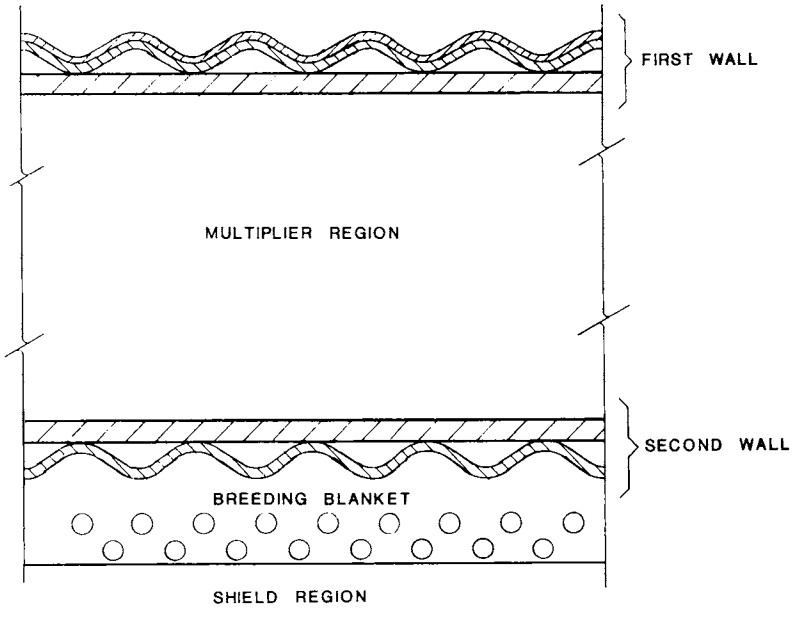

Figure 10-53. First wall/multiplier/blanket schematic.

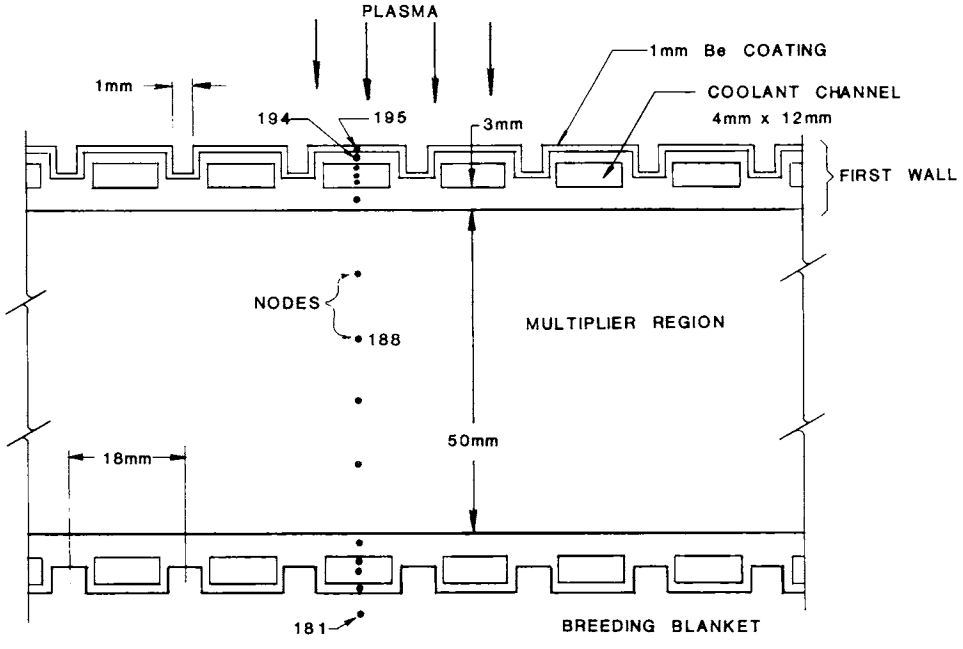

Figure 10-54. First wall/multiplier/blanket - geometric model.

the coolant, and interfacial contact resistance between the multiplier and the first and second wall coolant panels. To facilitate discussion of the results, a selected set of nodes at the coolant exit section are shown in Fig. 10-54.

The steady-state temperature distribution for the combined first-wall/multiplier/breeder regions for the 50-mm Be multiplier are plotted in Fig. 10-55 (note: y-direction represents distance starting from the breeder region towards the first wall). The maximum node temperatures in the breeder, multiplier, structure and Be coating are found to be 805, 493, 403, and 425°C, respectively. As the maximum temperature of the Be multiplier is less than 500°C, no internal coolant channels for the multiplier are needed. The temperatures are well within the design limits.

For the 50-mm thick Zr_5Pb_3 multiplier, the steady-state temperature distribution is shown in Fig. 10-56 . The maximum node temperatures for the breeder, multiplier, structure and beryllium coating are found to be 803, 818, 406 and 427°C, respectively. An examination of the maximum temperature values shows that these temperatures are within the design limits. Also, no internal

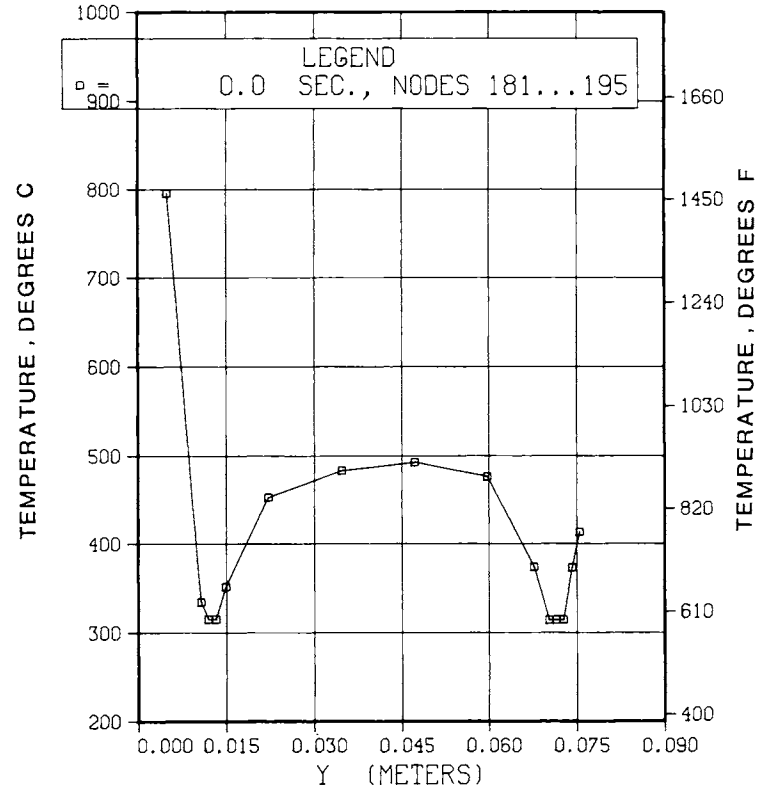

Figure 10-55. Steady state temperature distribution for FW/Be multiplier/blanket.

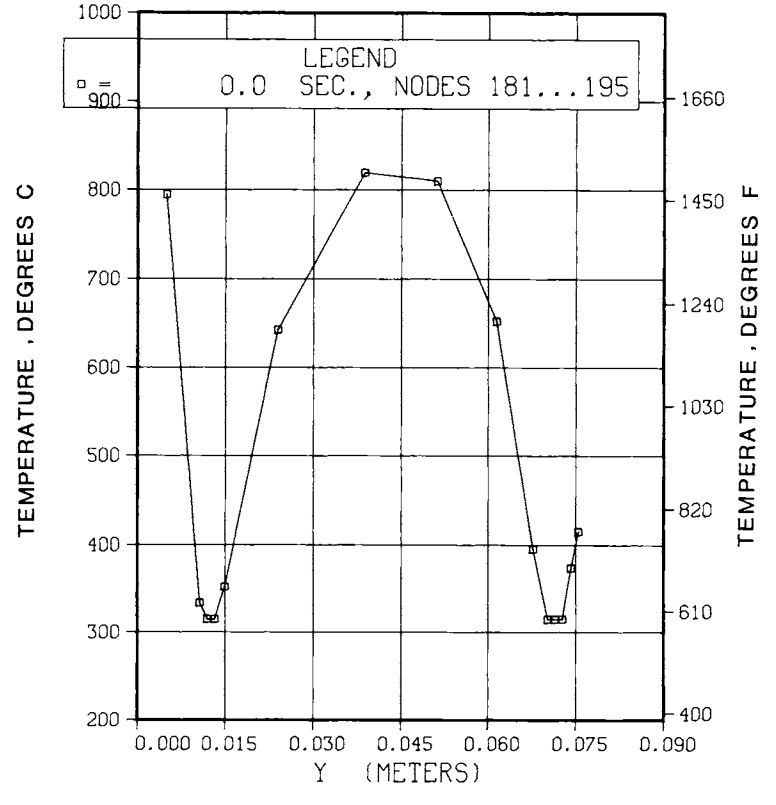

Figure 10-56. Steady state temperature distribution for FW/Zr_5Pb_3 multiplier/blanket.

coolant channels for the multiplier region are needed since the multiplier temperature is less than 820°C, which is significantly below the melting point ($\sim$ 1400°C) of Zr_5Pb_3.

10.5.3 Transient Analysis

In studying the transient operating characteristics of the first-wall/multiplier/blanket combinations, the normal transients that occur during the reactor startup and shutdown were not analyzed. The transients that arise due to flow blockage and plasma disruptions are included in this analysis. The results are summarized below.

10.5.3.1 Flow Blockage

Two separate scenarios for flow blockage were analyzed. The first case considers that both the first wall and the second wall coolant flow channels are blocked. The second case considers flow blockage for the first wall only. In each case, the coolant flow is assumed to decay linearly from its full value to zero in 2 s. It takes 2 s for the instrumentation and control system to detect flow blockage before initiating plasma shutdown. Two plasma shutdown scenarios were envisioned: (1) the first case considers plasma energy to decay linearly to zero in 3 s; and (2) the second case considers plasma shutdown to occur over a duration of 10 s. Following plasma shutdown, only the decay heat in the various materials (except the coolant) remains as a heat source. Because of the limited capability of the computer program used in these analyses, no coolant boiling or coolant expulsion is included in the computer model. Schematic representation of the coolant flow, plasma energy and decay heat for the above flow blockage and plasma shutdown scenarios is included in Fig. 10-57.

Flow Blockage: Both First Wall and Second Wall Channels -- The time temperature history of a selected set of nodes (Nodes 181, 188, 194, and 195, see Fig. 10-54) is shown in Fig. 10-58 and 10-59 for the case consisting of the 50-mm thick beryllium multiplier and 50-mm thick Zr_5Pb_3 multiplier, respectively. Both the breeder and the multiplier temperatures decrease immediately following plasma shutdown. The temperature of the structural material and Be coating increase sharply immediately following flow disruption. Major redistribution of temperature occurs after about 200 s. There

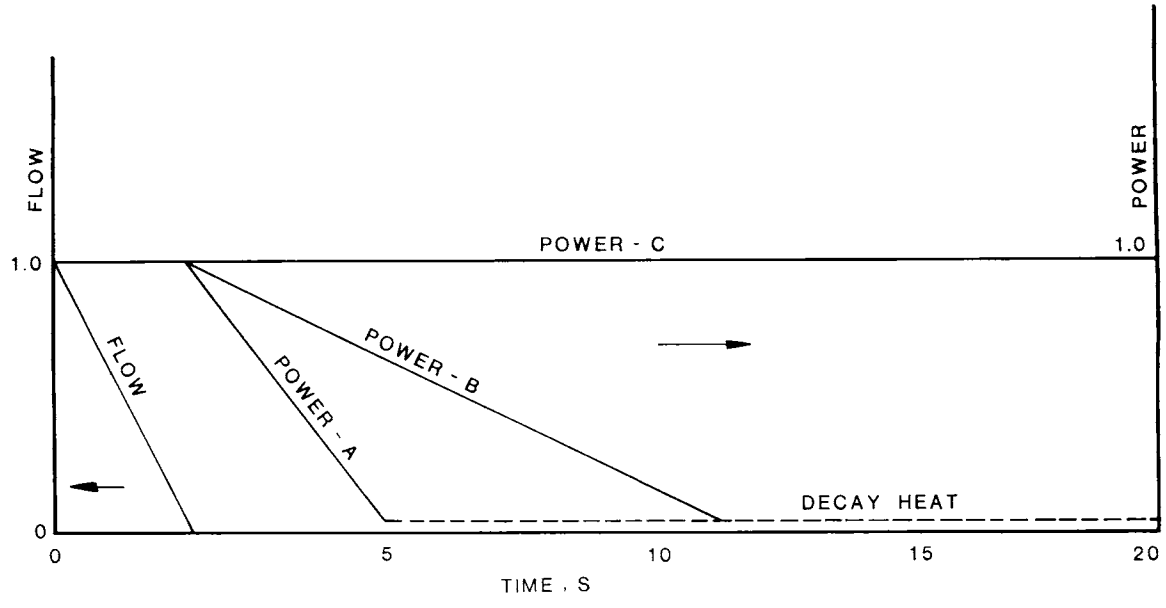

Figure 10-57. Schematic representation of coolant flow, plasma energy and decay heat during plasma shutdown.

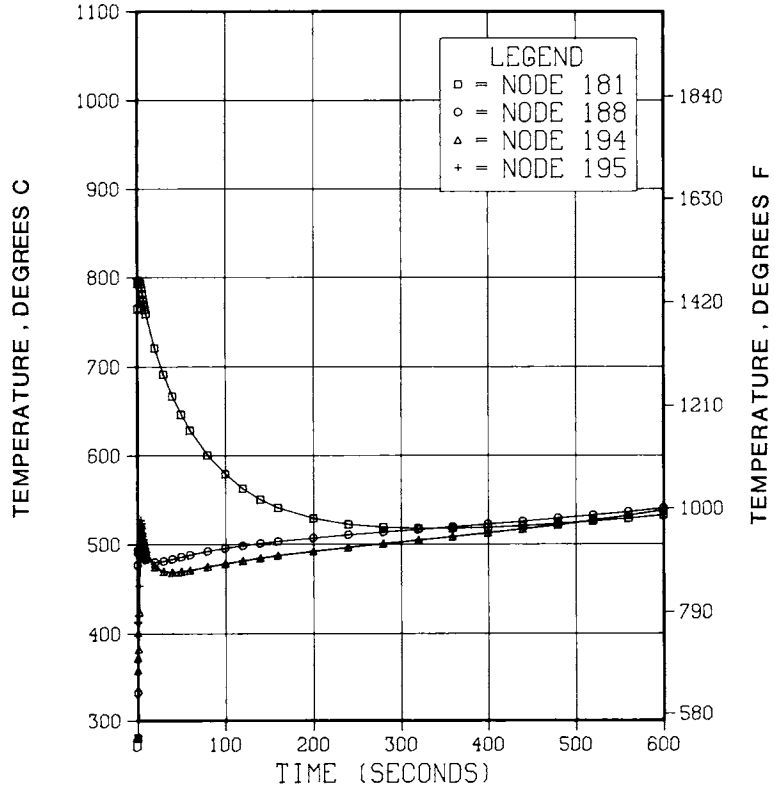

Figure 10-58. Transient temperature response - FW/Be multiplier/blanket (flow blockage of first wall and second wall).

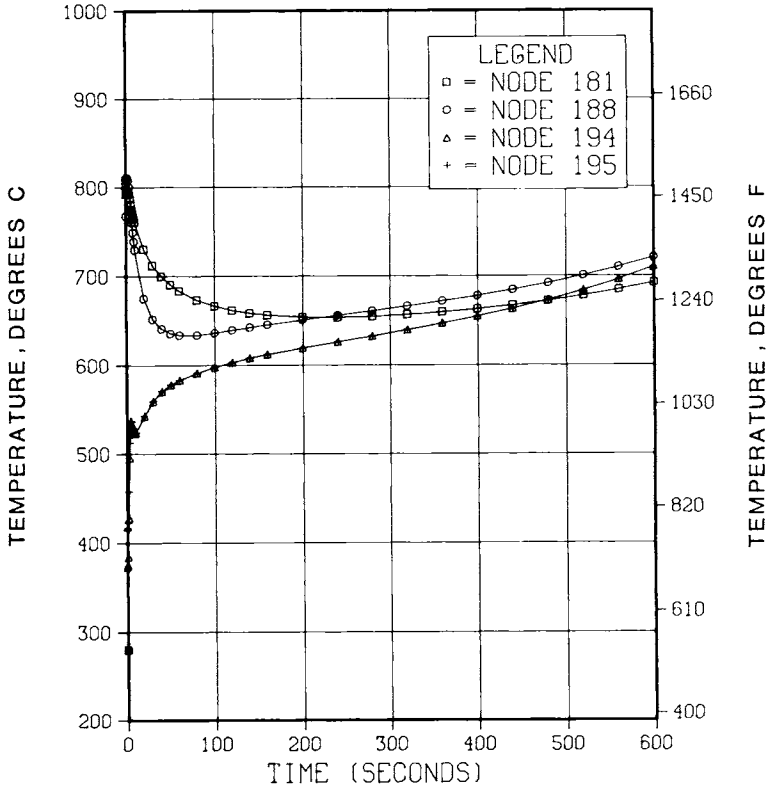

Figure 10-59. Transient temperature response of FW/Zr_5Pb_3 multiplier/blanket (flow blockage of first wall and second wall).

is gradual increase in temperature for all nodes due to decay heat. The temperatures approach 550°C after 600 s of shutdown for the beryllium multiplier. For the case of Zr_5Pb_3 multiplier, the node temperatures approach 700°C after 600 s of flow disruption (see Fig. 10-59).

Flow Blockage: Only First Wall Coolant Blocked -- The analytical procedure for this case is similar to the previous case except that the coolant in the second wall is assumed to flow at its full value during and after the plasma shutdown. As expected, the temperature of the Be coating and the structure increase for a short period ($\sim$ 5 s), and then decrease (see Fig. 10-60, and 10-61). However, both the breeder and the multiplier temperatures commence decreasing immediately following plasma shutdown. All temperatures continue to decrease since the cooling capability of the second wall coolant is more than the decay heat rate (see Fig. 10-60 and 10-61). A temperature rise of the order of 100°C for a brief period of time (less than 50 s) for the structural material and the beryllium coating is not considered to be detrimental for continued safe operation of the first wall.

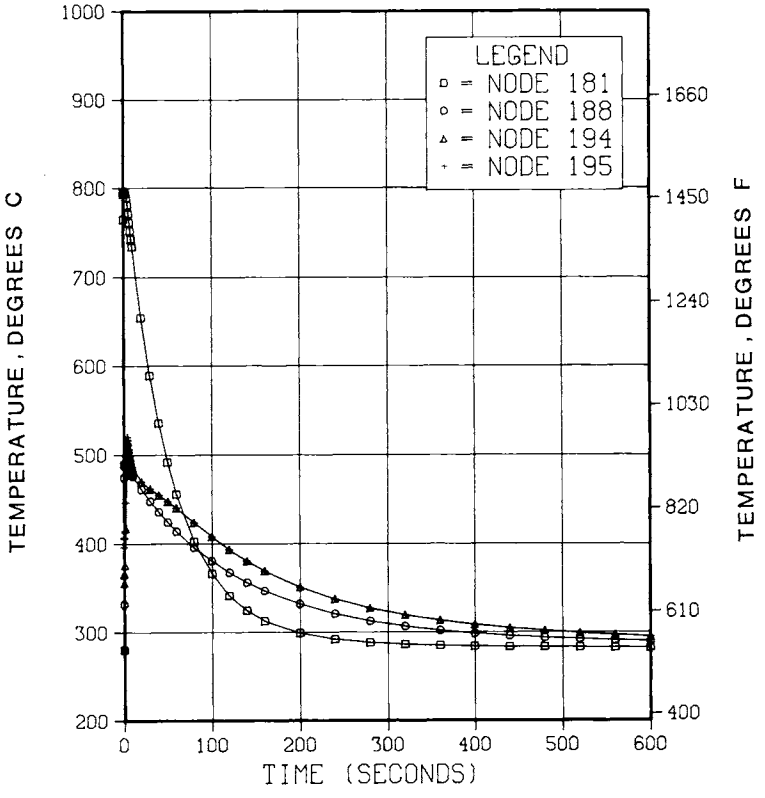

Figure 10-60. Transient temperature response - FW/Be multiplier/blanket (first wall coolant flow blockage).

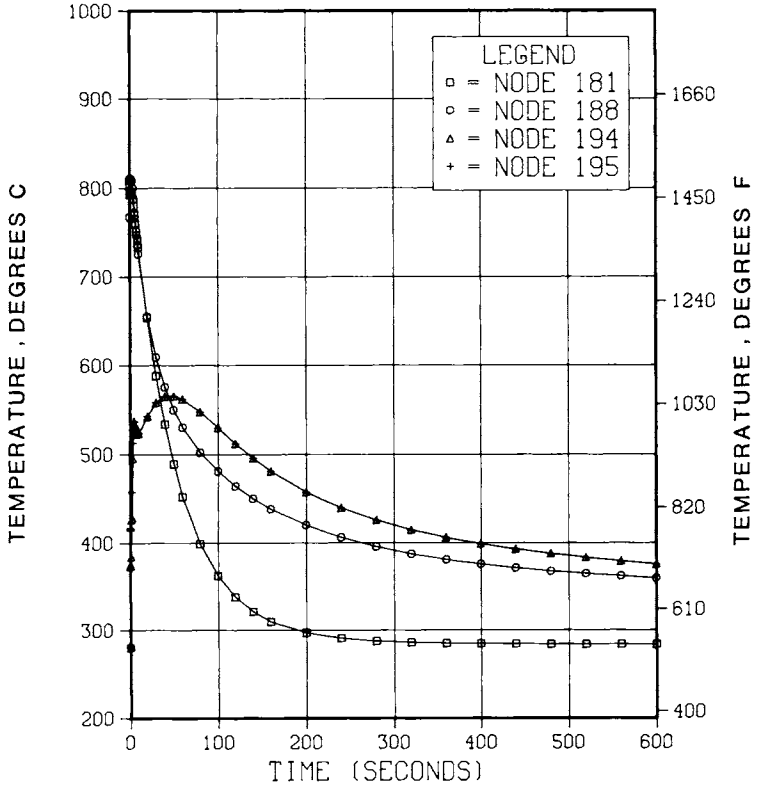

Figure 10-61. Transient temperature response - FW/Zr_5Pb_3 multiplier/blanket (flow blockage of first wall).

The results of the second plasma shutdown scenario (i.e., 10 s plasma shutdown) are similar to the results presented above, except that the transient temperatures of the structural material and the beryllium coating are about 50°C higher than in the previous case.

10.5.3.2 Plasma Disruptions

One of the most severe operating conditions to which the first wall may be subjected is during unstable operation leading to plasma energy dump over a limited surface of the first wall. The severity of this malfunction will depend on the total energy deposited and on the fraction of the wall area over which the plasma energy is dumped. For this study, two plasma disruption scenarios were analyzed, viz., 25 and 100 ms disruptions. The 100 ms disruption is selected as the reference case. In the absence of actual experimental data, the energy dissipation rates are assumed to decrease linearly from maximum to zero during the specified disruption time. The total plasma energy of STARFIRE amounting to 920 MJ is assumed to be deposited uniformly over 30% of the total surface area (the total surface area $\sim$ 800 m^2).

A schematic of the STARFIRE first wall is shown in Fig. 10-62. For the extremely short periods like the plasma disruption times, the first wall surface in contact with the multiplier region may be assumed to be thermally insulated. For thermal hydraulic modeling, the 1-mm Be coating on the first wall surface was divided into five 0.2-mm regions, and the 1.5-mm coolant panel wall was divided into three 0.5-mm thick regions. The transient temperature distribution was calculated by means of a three-dimensional conduction code based on a 225-node geometric model. The nodal representation at the coolant exit section of the first wall is given in Fig. 10-63.

The response of the wall temperature (Be coating and structural material) to plasma disruption are shown in Figs. 10-64 through 10-67. Figure 10-64 shows the time/temperature history for the 100 ms shutdown case over a period of 4 s. The maximum temperatures of the coating and the structural material are found to be respectively 1020 and 790°C. Figure 10-64 shows that both the coating and the structure temperatures approach the coolant temperature 5 s after plasma

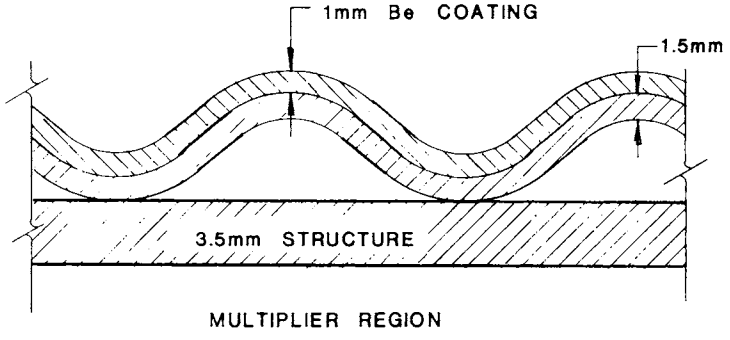

Figure 10-62. Coolant panel schematic.

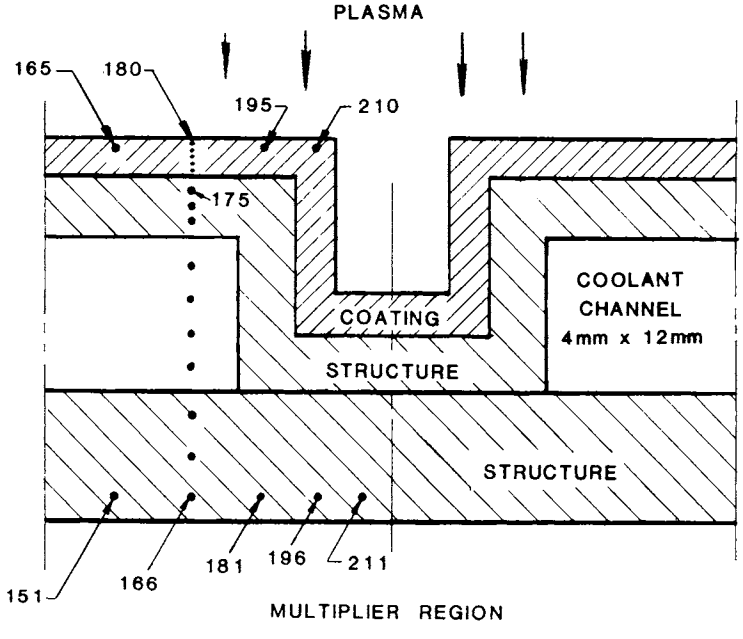

Figure 10-63. Coolant panel geometric model with node representation.

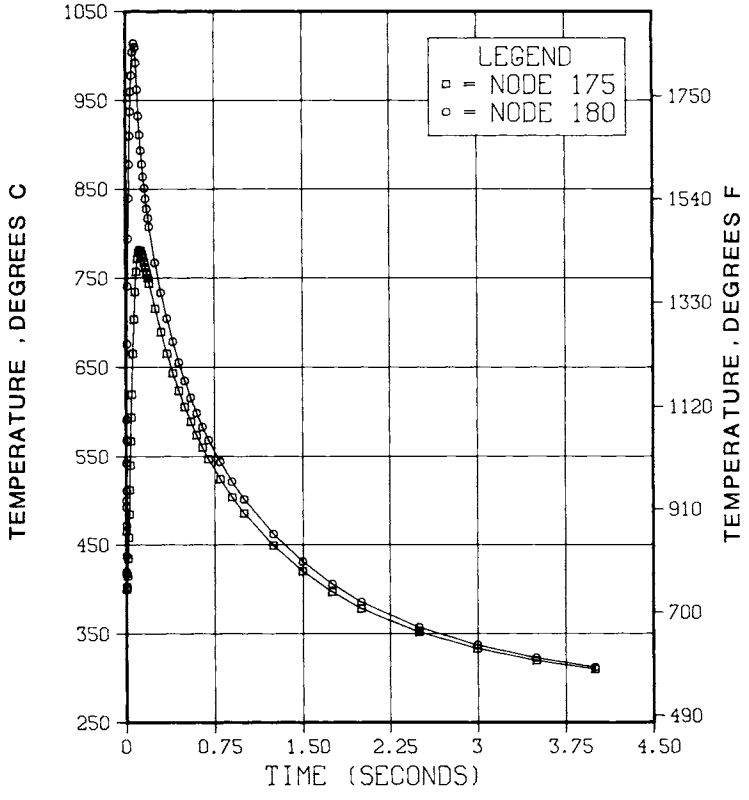

Figure 10-64. Transient temperature response of first wall for 100 ms plasma disruption (0-4 s).

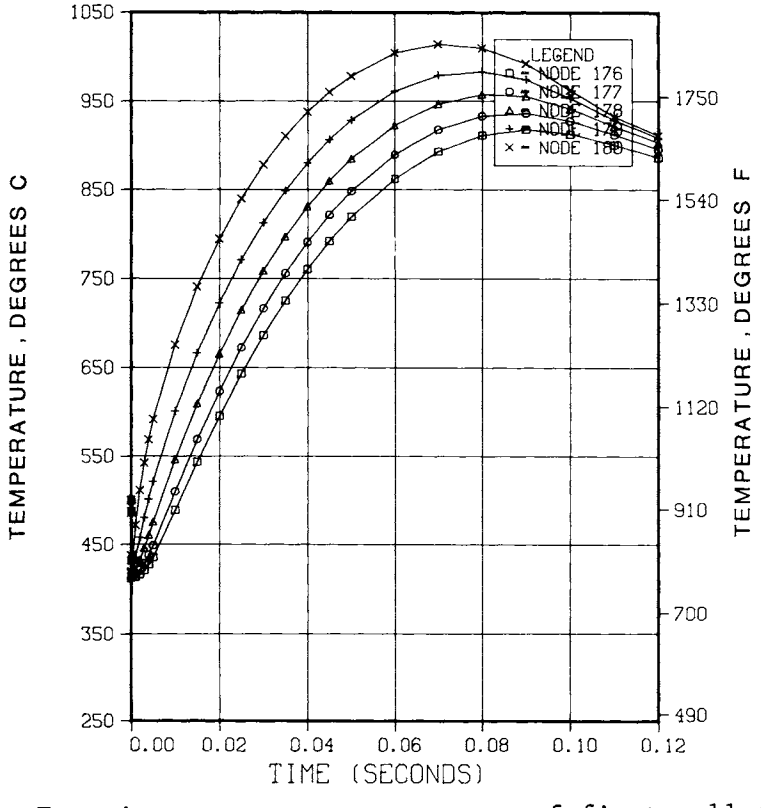

Figure 10-65. Transient temperature response of first wall for 100 ms plasma disruption (0-0.12 s).

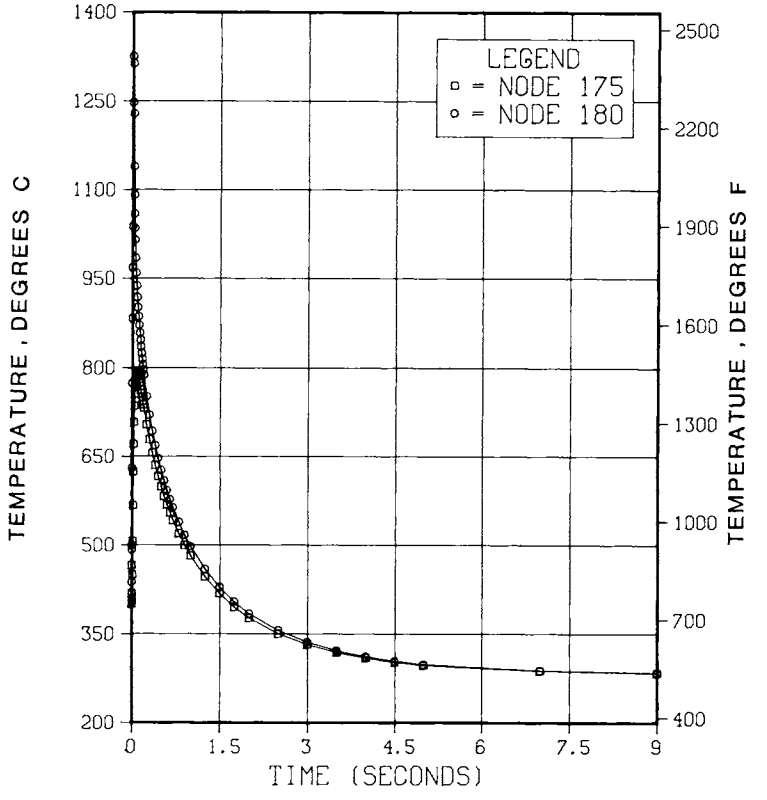

Figure 10-66. Transient temperature response of first wall for 25 ms plasma disruption (0-9 s).

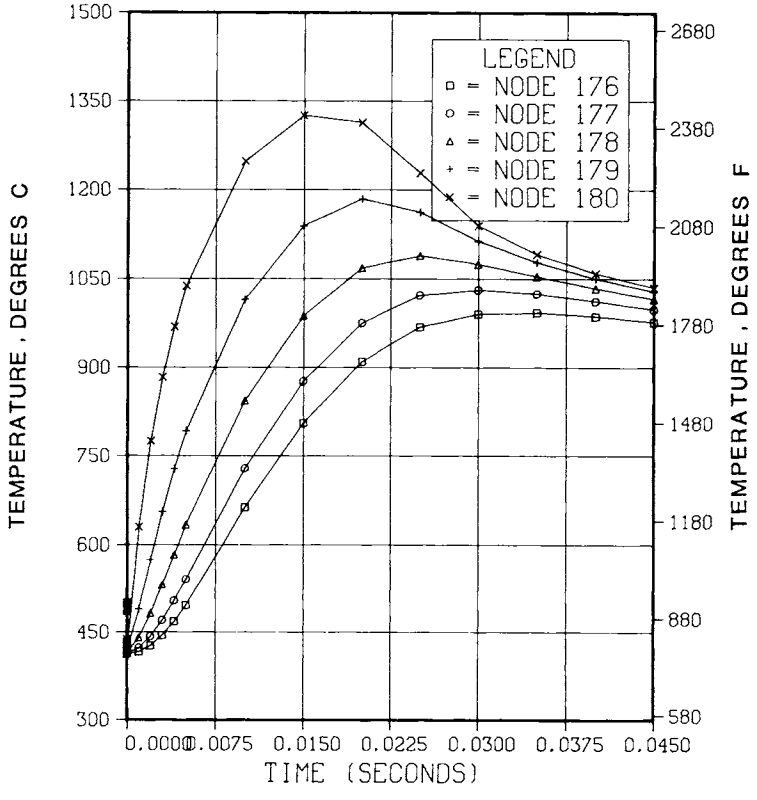

Figure 10-67. Transient temperature response of first wall for 25 ms plasma disruption (0-0.045 s).

disruption. The temperature distribution in the five layers of the Be coating are shown in Fig. 10-65. Temperature differences greater than 200°C in the 1-mm thick Be coating occur during the initial phases of plasma disruption.

Transient temperature distributions for 25 ms plasma disruption are shown in Figs. 10-66 and 10-67. The calculated maximum temperatures of the coating and the structural material are found to be 1325°C and 795°C, respectively. The heat of fusion has not been included in this calculation. The temperature of the coating in the five layers are shown in Fig. 10-67. As in the previous case, these temperatures approach the coolant temperatures in about five seconds. An examination of the peak coating temperature shows that the outermost layer temperature exceeds the melting point of beryllium ($\sim$ 1285°C). Hence, melting of a thin surface layer is likely to occur. Also, since the vapor pressure of beryllium becomes significant at these temperatures (see Sec. 10.1), some vaporization or ablation of the beryllium surface is predicted. Figures 10-65 and 10-67 show that the peak temperatures occur before the plasma energy is completely dissipated. This is due to the fact that the rate of energy deposition or the wall surface decreases linearly with time and becomes very small near the end of the disruption.

In the computer code used for the above analyses, neither meling nor ablation of the beryllium coating was considered. However, these results were used to evaluate the thickness of the melt layer and the extent of evaporation of beryllium during a disruption. The following analysis is based on the more severe disruption, i.e., the 25 ms case. It can be seen from Fig. 10-67 that the outer layer should begin to melt at about 8 ms after the plasma dump. Also, since the coating is surrounded by high vacuum environment, some evaporation of beryllium from its surface will occur as the vapor pressure of beryllium approaches 10 Pa (10^{-4} atm). An attempt was made to estimate the thickness of the melt layer and evaporation of beryllium per plasma disruption.

Melt Layer -- The analytical results allow one to estimate the temperature gradient at the various layers of the coating during plasma disruption. Using these temperature gradients and the thermal conductivity of beryllium, the amount of energy conducted into the coating was estimated between the above

periods θ = 8 ms and θ = 25 ms. The amount of plasma energy during the above time period is known from the nature of plasma decay (i.e., linear decay in 25 ms). The difference between these two quantities of energy must go to melt the coating. The results are summarized below:

Total Plasma Energy	920 MJ
Plasma Energy After 8 ms	417 MJ
Energy Conducted Away	387 MJ
$\therefore$ Energy that goes to melting	30 MJ
The thickness of the melt layer (based on 240 m^2 surface area)	62 μm

Vaporization From Coating Surface -- The evaporation of a substance in high vacuum environment may be calculated from the kinetic theory. At equilibrium, the rate of evaporation of beryllium is equal to the rate of condensation of beryllium. At very low pressures (less than 100 Pa), it may be assumed that the rate of evaporation is independent of the pressure of vapor around it. The rate of evaporation may be expressed by

$$\mu = P\sqrt{\frac{m}{2\pi kT}} \tag{29}$$

where

μ = rate of evaporation (mass per unit area per unit time)

P = vapor pressure

m = molecular weight

k = Boltzmann constant

T = absolute temperature.

The total quantity vaporized may be estimated based on the surface temperature over an interval of time, θ = 0, θ = θ, and the total surface area

$$W = \mu A\theta = A\sqrt{\frac{m}{2\pi k}} \sum \frac{P_i \Delta\theta_i}{\sqrt{T_i}} \tag{30}$$

The temperature T_i at various times θ_i was assumed to be the coating temperature at 0.1 mm below the coating surface as given by the uppermost curve in Fig. 10-67 . The vapor pressure P_i at the corresponding temperature T_i was estimated by interpolation from the following data:

Temperature (K)	Vapor Pressure (Pa)
1125	1×10^{-4}
1265	1×10^{-2}
1465	1×10^{-0}
1610	1×10^{-1}

The total amount of beryllium vaporized between $\theta = 0$ and $\theta = 120$ ms was estimated from Eq. (30), and it was found to be 7.1 g. It may be noted that the bulk of evaporization occurs over a very short period of time ($\theta = 10$ ms to $\theta = 30$ ms).

The above analytical procedure appears to be a reasonable approach both in estimating the thickness of the melt layer as well as the amount of beryllium vaporized during a single plasma disruption. It is expected that a more sophisticated method will be used in the future analyses. These analytical results indicate that for the 25 ms disruption neither melting of a thin layer ($\sim$ 60 μm) over a very short period of time, nor evaporization of only 7 g ($<$ 0.02 μm) of beryllium seems to pose a serious problem as far as choosing 1 mm beryllium coating as a protective layer on the first wall. For the reference case of the 100 ms disruption, no melting occurs and the total evaporation is estimated to be less than 10 mg.

10.6 STRESS ANALYSIS AND LIFETIME MODELS

Preliminary stress and lifetime analyses have been performed to guide the design of the reference first wall and blanket. The stress analyses have focused upon dead weight loads, pressure and thermal stress, and magnetic

loadings resulting from plasma disruptions. The lifetime analyses of the first wall are performed for the primary candidate materials under the reference operating parameters.

10.6.1 Stress Analysis of First-Wall Components

A very conservative stress analysis has been performed for the critical components of the reference first wall and blanket design. The results indicate a considerable degree of reserve capacity for both normal operating conditions and plasma disruptions. This shows that the design is feasible but by no means is the analysis appropriate for a final stress report. A comprehensive stress analysis requires a two-dimensional capability and for critical points even a three-dimensional approach together with a unified constitutive equation that incorporates strain and irradiation hardening, creep, plasticity and thermal effects. Then realistic scenarios can be followed in detail to provide a comprehensive history of these components.

The first wall and the wall that separates the multiplier and breeder zones each consist of a corrugated panel with a coolant under high pressure. The general configuration of each wall is shown in Fig. 10-68, and specific, the corrugation shape is assumed to be described by the function

$$y = \frac{a}{2}\left(1 - \cos\frac{\pi x}{b}\right) \quad 0 \le x \le b \tag{31}$$

for a typical half-channel. Nominal dimensions and thicknesses are taken to be

$$a = 4 \text{ mm},\ b = 9 \text{ mm},\ t_1 = 1.5 \text{ mm},\ t_2 = 3.5 \text{ mm} \tag{32}$$

The region external to each blanket module is considered to be a vacuum whereas the breeder region is maintained at close to atmospheric pressure. Consequently, the primary loading function is a uniform pressure

$$W_1 = 14.7 \text{ psi} \tag{33}$$

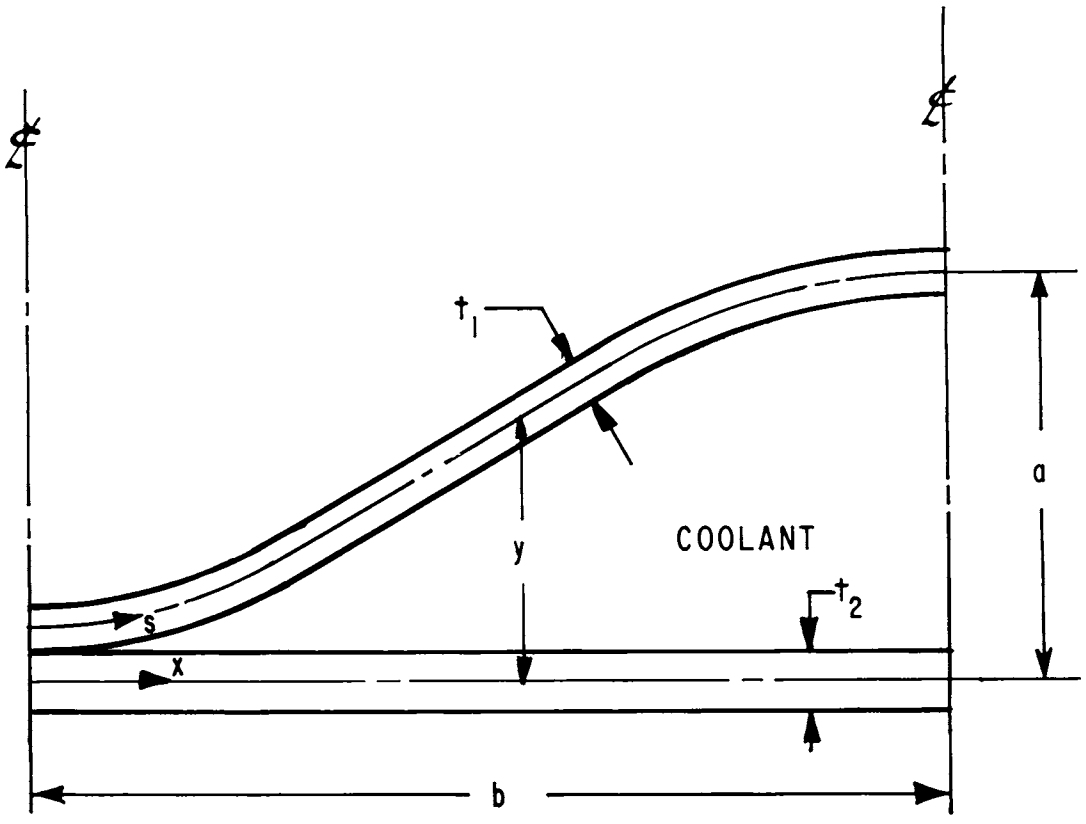

Figure 10-68. Sketch of first-wall structural configuration.

which must be supported by the first wall and module support system. In addition, the dead weight of the multiplier and, perhaps, part of the breeder zone must be taken into account. This load varies with position, with the worst case situation occurring for a module located at the top of the torus. The loading function is taken to be the weight of the multiplier, W_2, which is expressed as mass per unit area. For a multiplier 5 cm thick and a density of approximately 10 gm/cm^3, the resulting nominal loading function is

$$W_2 = 50 \text{ gm/cm}^2 = 4.9 \text{ kPa} \tag{34}$$

If the portion of the breeding material that must be supported by the first wall is assumed to be equivalent to

$$W_3 = 4.1 \text{ kPa} \tag{35}$$

then a reasonable design load is

$$W = W_1 + W_2 + W_3 = 110 \text{ kPa} \tag{36}$$

In addition to dead weight, these components are subjected to thermal stresses. Since the outer panel is subjected to a surface heat flux, and possibly the largest thermal gradient of any segment of the first wall and blanket, a finite element analysis was performed. The heat flux is $q = 0.9 \text{ MW/m}^2$, and on the internal surface the coolant pressure

$$P_c = 15.1 \text{ MPa} \tag{37}$$

acts with an internal wall temperature of $T_i = 340°C$ which is considered constant for the purpose of the stress evaluation.

Since the stresses due to the above loads are steady state, the peak effective stress should be maintained well below the yield stress to preclude plastic deformation or even rupture under a highly irradiated state.

During a plasma disruption, an inward directed pressure is also created. The peak value of this force ranges from 26.6 psi for zero disruption time down to 17 psi for a disruption time of 100 ms. These forces may occur intermittently and occur over a short period of time so that a maximum effective stress close to the ultimate stress is considered acceptable.

10.6.1.1 Dead Weight Analysis

Bending Stiffness of a Corrugated Panel -- Consider a typical panel segment shown in Fig. 10-69. To conduct a stress analysis, the second area moment I is required and ultimately, the second area moment per unit length which is defined to be

$$\hat{I} = I/b \tag{38}$$

For the half-panel shown in Fig. 10-68, the total cross-sectional area is

$$A = t_1 s_1 + t_2 b \tag{39}$$

where

$$ds = \sqrt{dx^2 + dy^2} \quad s_1 = \int_o^{s_1} ds \ . \tag{40}$$

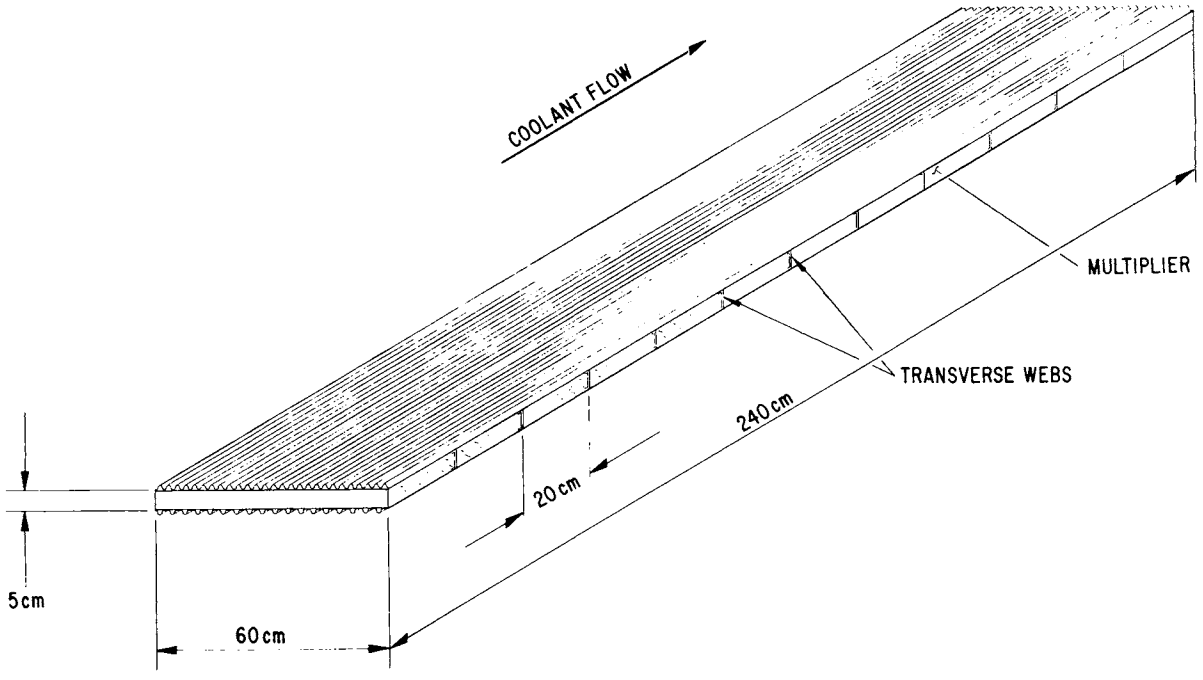

Figure 10-69. First-wall configuration of a typical blanket module.

With the use of Eq. (38)

$$dy = \frac{a\pi}{2b} \sin \frac{\pi x}{b} \, dx \tag{41}$$

and the first two terms of a Taylor's series expansion of Eq. (10) yields

$$ds \simeq \left[1 + \frac{1}{2} \left(\frac{a}{2} \frac{\pi}{b}\right)^2 \sin^2 \frac{\pi x}{b}\right] dx \tag{42}$$

and consequently

$$s_1 = b \left[1 + \frac{1}{4} \left(\frac{a}{2} \frac{\pi}{b}\right)^2\right] = 10.1 \text{ mm} \tag{43}$$

The area of material from Eq. (39) is

$$A = 46.7 \text{ mm}^2 \tag{44}$$

Similarly, the centroid of the cross-section is computed to be

$$\bar{y} = t_1 \int_o^{s_1} y ds/A = 0.65 \text{ mm} \tag{45}$$

which is required in the expression for the second area moment

$$I = \int_o^{s_1} (y-\bar{y})^2 \, t_1 ds + \bar{y}^2 t_2 b \tag{46}$$

$$= 69.6 \text{ mm}^4$$

The second area moment per unit length becomes

$$\hat{I} = 7.8 \text{ mm}^3 \tag{47}$$

For a beam analysis, the bending stiffness EI is required whereas for a plate model, the bending stiffness is $\hat{EI}/(1-\nu^2)$ for Young's modulus, $\bar{E}$, and Poisson's ratio, ν. For the purpose of this analysis, the effect of Poisson's ratio will be ignored.

Rib Stiffeners -- By spot welding at discrete points between each coolant channel, it is possible to consider adding rib stiffeners to the back plate of the cooling panel. These ribs would run transversely to the direction of the coolant flow and spaced a distance d from each other.

Suppose each rib is b_1 mm by h_1 mm and that d is chosen so that the bending stiffness for the composite structure is identical for the two principal directions. Consider a typical segment of width d that contains one rib and ignore any contribution from the corrugation wall of thickness t_1. Then the total area is

$$A = (3.5 \, d + b_1 h_1) \text{ mm}^2 \tag{48}$$

with the centroid given by

$$\bar{y} = \frac{b_1 h_1 \, (1.75 + h_1 \beta)}{A} \text{ mm} \tag{49}$$

Then the second area moment is

$$I = [3.5(d) \, \bar{y}^2 + \frac{1}{12} b_1 h_1^3 + b_1 h_1 \, (1.75 + \frac{h_1}{2} - \bar{y})^2] \text{ mm}^4 \tag{50}$$

which we assign the value of 69.6 mm^4 by appropriate choices of b_1, h_1 and d. For example, with $b_1 = 4$ mm and $h_1 = 10$ mm, it can be shown that d is approximately 270 mm.

Unsupported Length -- Consider a strip of the coolant panel in the direction of the coolant flow as a beam of unit width. Then, the maximum bending stress, σ, is related to the moment, M, by the relation

$$\sigma = \frac{Mc}{\hat{I}} \tag{51}$$

where c is the distance from the centroid to the outer point of the channel. Suppose σ = 300 MPa is the nominal allowable stress. Then with c = 4 mm, the maximum moment allowed for a beam of unit width is

$$M = 585 \text{ N} \tag{52}$$

A similar computation in the orthogonal direction yields a much smaller moment because c = 10 mm.

For a uniform pressure W, the maximum bending moment for a beam of length L and unit width is

$$M = kWL^2 \tag{53}$$

where k = 1/8 for simple supports and k = 1/12 for fixed supports. Similarly for a square plate with side of length L, the maximum moment is also given by Eq. (53) where k = 0.048 for simply-supported boundaries and k = 0.051 for fixed supports. If the plate dimensions are changed to a rectangular plan, then in the limit as the aspect ratio approaches infinity, k approaches the values given for the beam.

Because of symmetry, the assumption of fixed boundaries is most appropriate for beam strips. With k = 1/8 and the use of Eqs. (36) and (53) for the maximum load and moment carrying capacity, respectively, Eq. (53) yields the following value for the maximum unsupported length of a first wall segment

$$L = 0.21 \text{ m} \tag{54}$$

This distance is less than the spacing d, of 0.27 m for transverse ribs required for equal bending rigidity in two directions. The implication is that the use of ribs is not sufficient and instead a component such as webs connecting the two cooling panels is required.

Web Supports -- Assume the maximum module size facing the plasma is 60 cm x 240 cm. As shown in Fig. 10- , the cooling channels are considered to run in the longitudinal direction with the proposed webs (60 cm long) placed transversely with a spacing of 20 cm. These webs, which are attached to the module support system, provide the support required by the cooling panels and serve primarily as a shear support member of a composite structure. For this configuration, the maximum shear stress is very close to the average shear stress,[1] i.e., the maximum shear stress is

$$\tau_{max} \simeq V/A \tag{55}$$

where V is the total shear and A is the cross-sectional area. Since the maximum that can be supported by a material is approximately one-half the tensile stress, and since points in the web also sustain normal bending stresses, a reasonable nominal value for τ_{max} is 100 MPa. The maximum shear occurs at the center (with the assumption of simple end supports for the webs) and is given by

$$V = W \frac{d_w L_w}{2} \tag{56}$$

for web spacing, d_w, and web length, L_w. For W = 110 kPa, d_w = 20 cm, and L_w = 60 cm, the result is

$$V = 6.6 \times 10^3 \text{ N} \tag{57}$$

The web is considered to be h_w = 5 cm high. The width t_w is chosen to satisfy Eq. (55), i.e.,

$$t_w = \frac{V}{\tau_{max} h_w} = 1.3 \text{ mm} \tag{58}$$

This represents the minimum thickness required for the web. For fabrication purposes, a larger value may be desirable, but then problems with heating or neutron multiplication may be a factor. However, even for a 2 mm thick web, the amount of structural material in the multiplier region is only 1%.

Since the web is so thin in a structural sense, there would normally be a possibility of shear buckling. However, if the multiplier can sustain any compressive stress at all, buckling will not be a problem.

10.6.1.2 Pressure and Thermal Stresses in Corrugated Panel

The corrugated panel is subjected to both a high internal pressure and a surface heat flux from the plasma. Because the shape of the panel is not a simple geometrical figure for which closed form solutions are available, a finite element approach was used. Since the panel is a thin-walled member, and the assumption of plane strain is appropriate, the latest version of STRAW[64] is appropriate. This program has a recently-added finite-element heat transfer subroutine which provides the capability of simultaneously determining temperatures and stresses for steady-state or transient problems.

Material properties for highly-irradiated 20% cold-worked 316 stainless steel were used in the analysis. Young's modulus, yield stress and ultimate stress as functions of temperature are given in Appendix E. Since the response is strictly elastic, the slope of the stress-strain curve beyond the yield stress was not required.

An internal pressure of 15.2 MPa (2200 psi) and an inner wall temperature of 340°C were specified. The heat flux was 0.9 MW/m^2.

Figures 10-70 and 10-71 are sketches of the structure and 48-element model. At each element node, nine stations through the thickness were used to obtain an accurate characterization of the transverse distribution of the field variables. Since each station point represented a corner of a thermal finite element, 384 (8 x 48) elements were used for the heat transfer part of the code.

Based on symmetry, cross-sections A-A and B-B were not allowed to rotate. To eliminate rigid-body translations, section A-A was also fixed in space, while section B-B was free to translate in the y-direction but not in the x-direction. This latter condition together with the assumption of plane strain (x-y plane) are actually over restrictive since there will be some expansion in both the y- and z-directions of the base plate. However, since these assumptions provide artificial constraints, the results will be conservative insofar as stresses are concerned.

Since the heat flux is normal to the surface at the cross-sections A-A and B-B, and these sections are constrained, it is not surprising that the critical

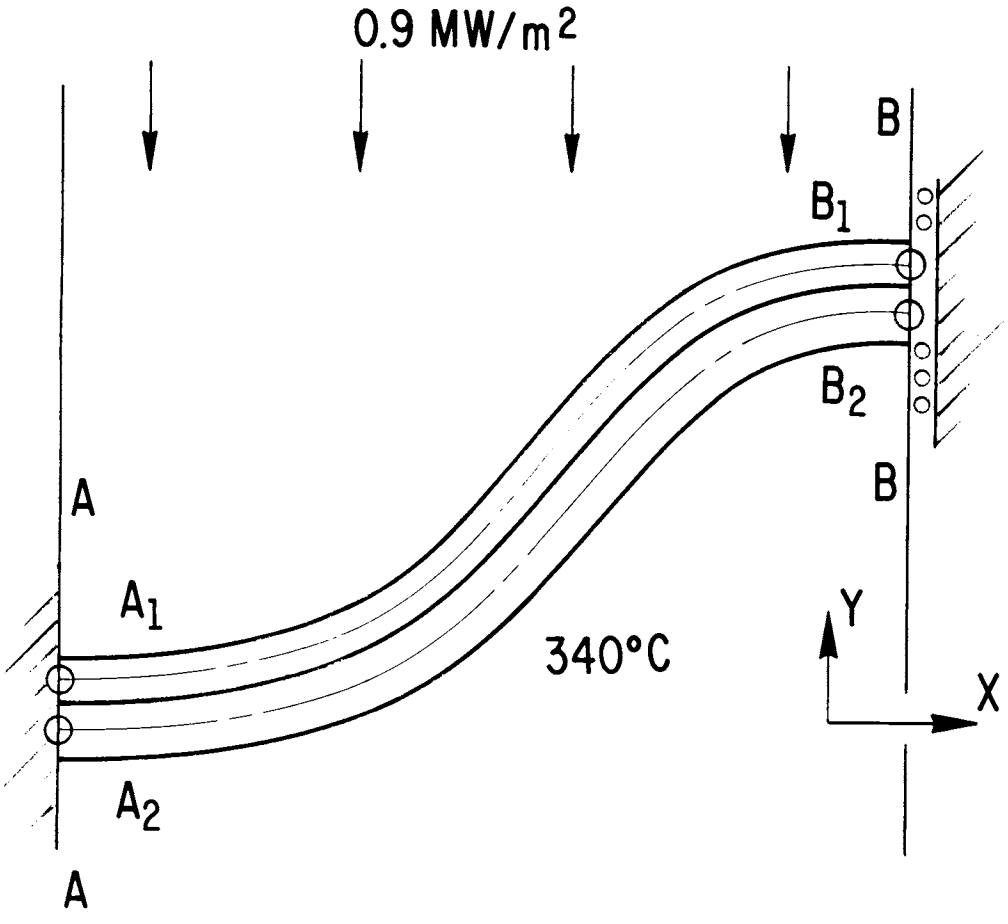

Figure 10-70. Panel configuration and finite element model.

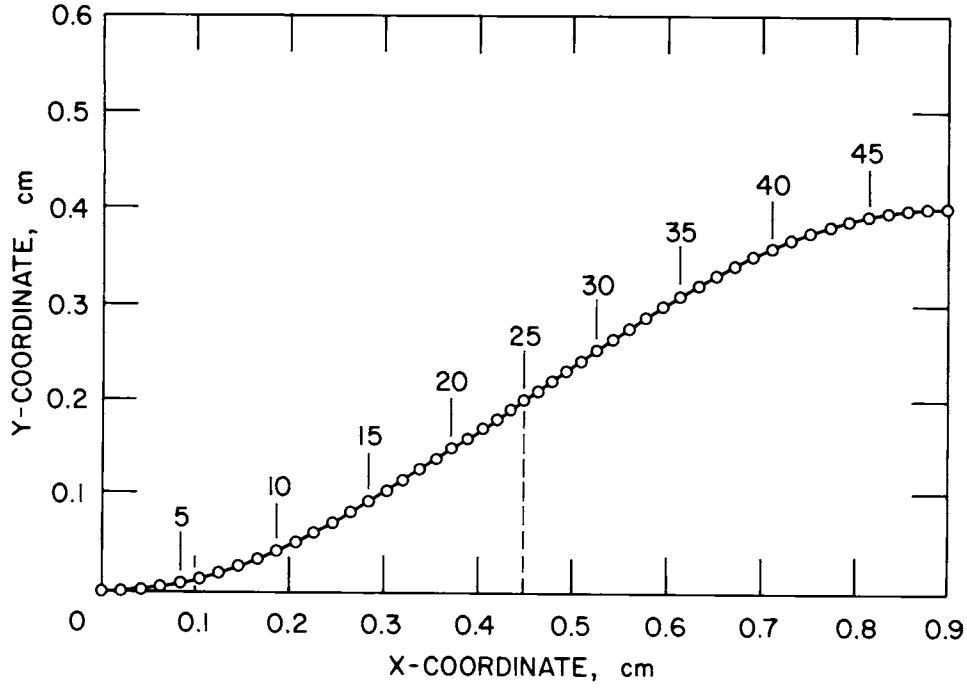

Figure 10-71. Node numbers for finite-element model.

points are located at the corresponding inner and outer surfaces. The temperature, one component of mechanical strain, the two non-zero components of stress, the effective stress and the yield stress for these four points are given in Table 10-57. The displacement field as expressed by the undeformed and deformed configurations is given in Fig. 10-72, while the circumferential component of the stress along the outer and inner surfaces are shown in Fig. 10-73.

The result of this analysis indicates that the maximum effective stress is 73% of the yield stress which indicates that this component will perform satisfactorily under normal operating conditions.

Table 10-57. Key Results of Finite Element Analysis

Point	T, °C	e_{xx}, %,	σ_{xx}, MPa	σ_{zz}, MPa	$\bar{\sigma}$, MPa	σ_y, MPa
A_1	407	0.33	532	- 55	562	771
A_2	340	-0.24	-456	134	536	840
B_1	407	0.01	- 47	-226	207	771
B_2	340	0.12	233	69	207	840

10.6.1.3 Stresses Due to Plasma Disruption

If there is a plasma disruption, an additional equivalent peak pressure of 117 to 183 kPa may be imposed on the first wall. This pressure is of extremely short duration so the loading is more of an impulsive nature. However, if it can be shown that this pressure, treated in a static sense, can be sustained, then the actual dynamic load will not cause any problem. With the maximum dynamic load factor of 2, this implies the possibility of an additional pressure of 366 kPa.

This pressure actually acts like a body force on the multiplier zone. Thus, the primary concern is whether or not the composite structure of the two cooling panels and the multiplier can transmit the loading to the transverse webs. Under normal operating conditions, it was assumed that the cooling

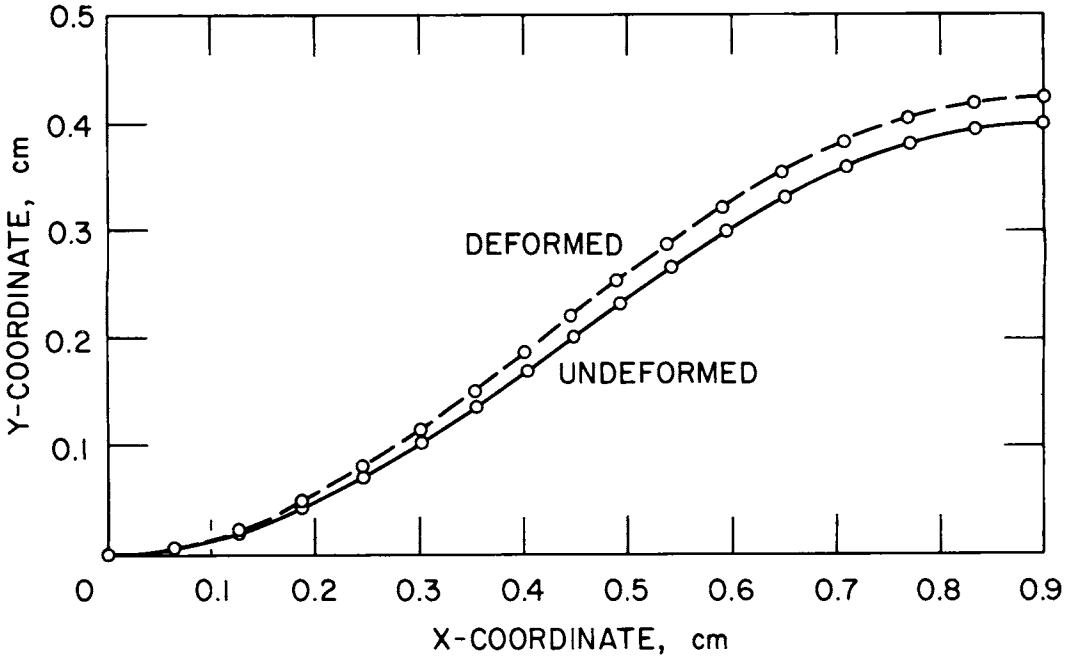

Figure 10-72. Deformation of first wall panel during normal operation.

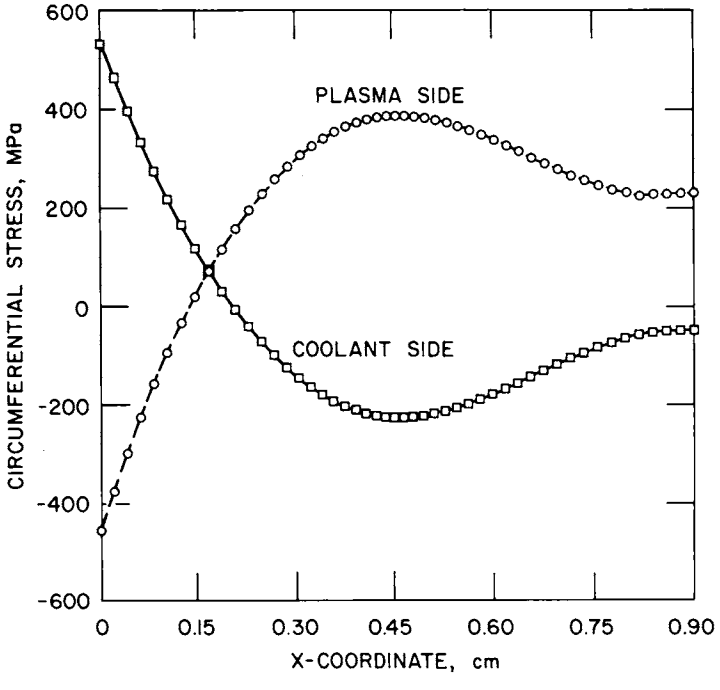

Figure 10-73. Tangential stress components.

panels sustained the entire load because of the possibility of cracking of multiplier material. However, under dynamic conditions, it is reasonable to assume that the multiplier can at least support compressive stresses and the necessary shear. Then the composite section behaves similarly to reinforced concrete with a large moment capacity. Since the specific properties of the multiplier are unknown, an elastic analysis is not possible. However, if the multiplier material can sustain 100 MPa compressive stress then a simple limit analysis can be performed.

The tensile action of the cross-section is completely sustained by the 3.5 mm backing plate of the corrugated panel (see Fig. 10-74). If this plate sustains a large enough strain, then the nominal stress of 300 MPa will be reached. The compressive action occurs over a portion of the multiplier large enough to balance the tensile stress. For 100 MPa uniform maximum stress, this implies a compressive region 10.5 mm thick next to the second wall. The reason for not taking into account the compressive carrying capability of the channel is that the channel may buckle. However, if the buckling is elastic, the channel would snap back to its original configuration when the load is released.

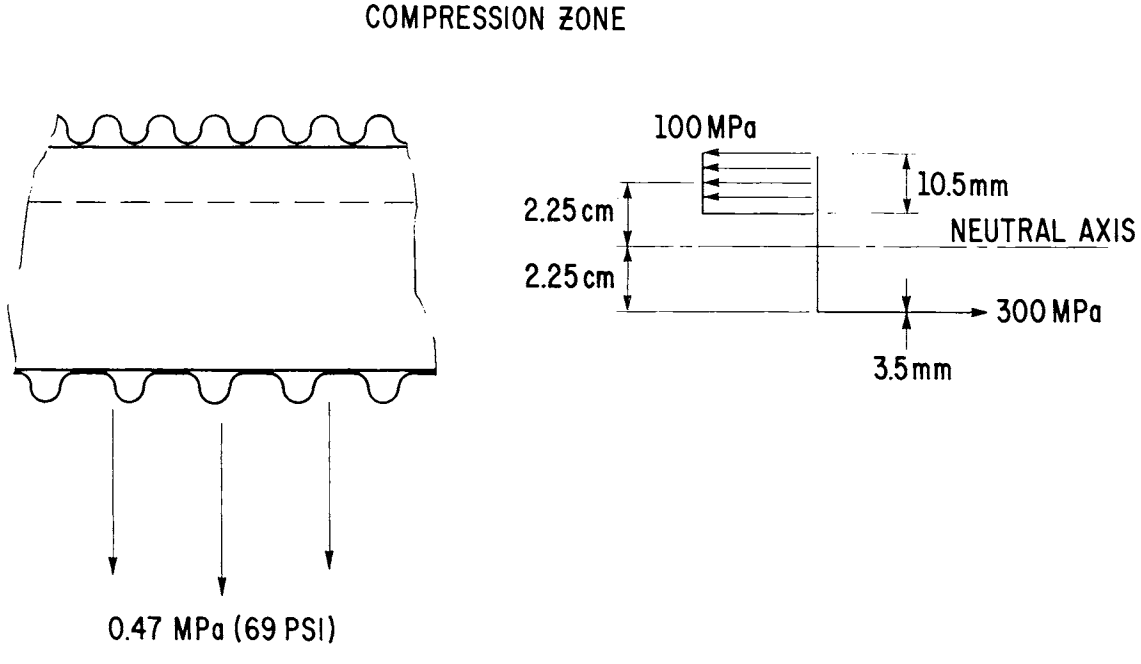

Figure 10-74. Composite action of corrugated panel and multiplier material.

For this stress distribution, the corresponding moment capacity is

$$M_o = (300 \text{ MPa})\ (3.5 \text{ mm})\ (2.25 \text{ cm}) + (100 \text{ MPa})\ (10.5 \text{ mm})\ (2.25 \text{ cm})$$
$$= 4.73 \times 10^4 \text{ Pa/unit width} \quad (59)$$

The total applied moment for a fixed-end beam of unit width is

$$M = \frac{1}{12} WL^2$$
$$= 1.58 \times 10^3 \text{ Pa/unit width} \quad (60)$$

for W = 475 kPa and L = 20 cm. Thus there is no doubt that this load can be sustained although there is a slight possibility of permanent deformation.

For a load of 475 kPa, the transverse web would be subjected to a shear force 4.3 (69/16) times larger than that given in Eq. (57). For a web width of 2 mm, the corresponding shear stress is 285 MPa which is below one-half the ultimate stress for a material such as tungsten or niobium.

10.6.1.4 Support Structure for First Wall Configuration

For the reference design of the multiplier zone, it was shown that a composite plate consisting of two coolant panels and transverse ribs would be a feasible structure from the point of view of allowable stresses. The use of the same composite plate construction in the breeding zone, as shown in Fig. 10-75, is suggested for the following reasons:

1. Standardized manufacturing techniques could be used to construct the plates,

2. Fluid flow for the panels in the breeding zone is in the same direction as the flow in the multiplier zone so that common headers on two sides of a first wall segment can be utilized,

3. The structural material of the internal support members represent a very small percentage of the material in the first wall,

4. The internal support members meet the multiplier and back walls at right angles, if desired,

5. The use of a basic structural element such as a composite plate is easily adapted to first wall segments of various sizes and configurations, and

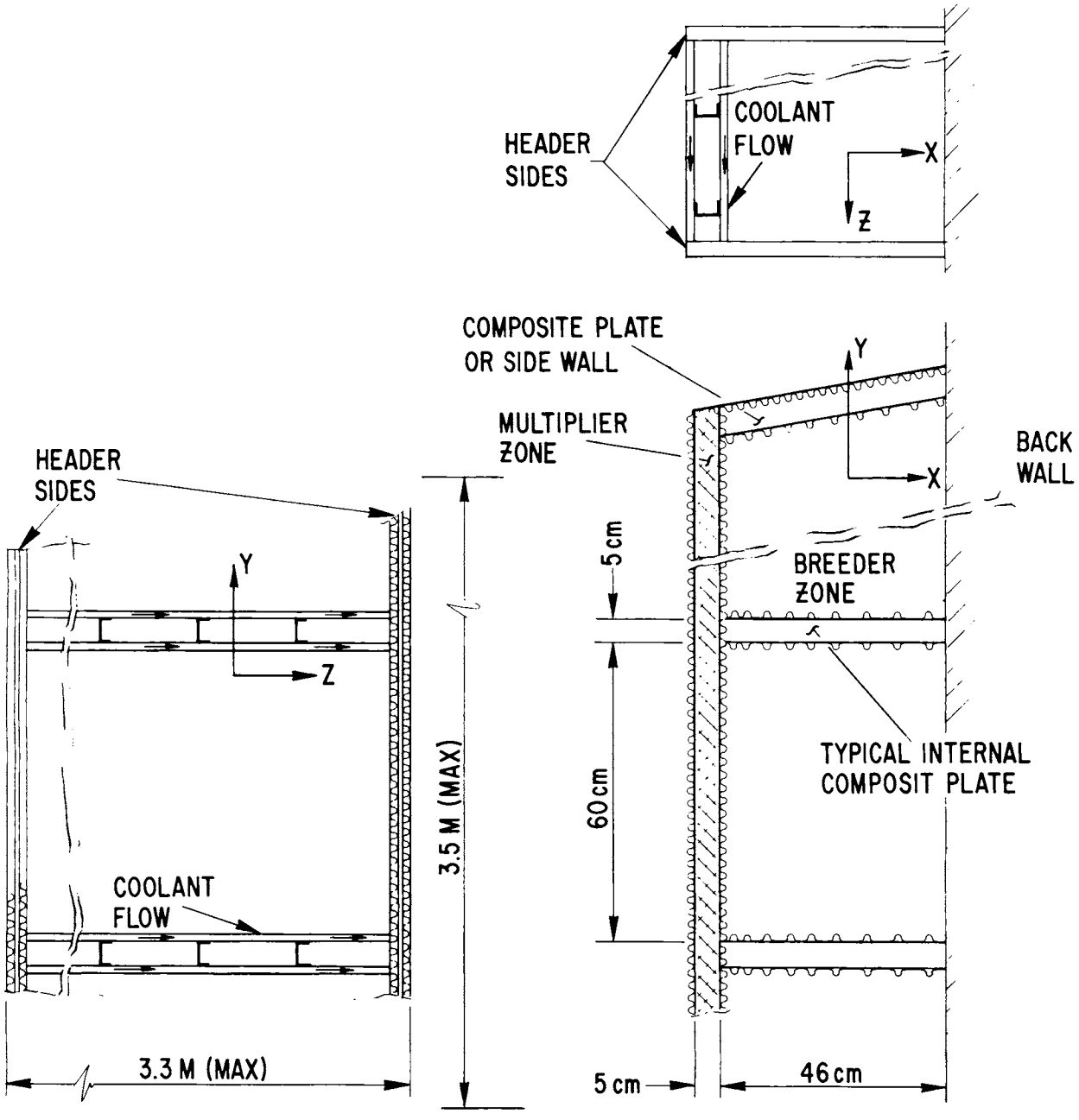

Figure 10-75. Diagram of blanket structure for stress analysis.

6. Breeding material as well as cooling pipes can be placed within the composite plate structure.

Description -- In the figuration shown in Fig. 10-75, each plate segment could be up to 3.3 m long in the direction of fluid flow and 46 cm wide based on the thickness of the breeding zone. This latter dimension is also the length of the transverse webs.

From the previous analysis for the multiplier zone, the transverse webs must be supported every 60 cm or less. This implies that the internal composite plates must be no more than 60 cm apart. It is assumed that the back wall is rigid and that the composite plate can be firmly attached to it. The attachment along the other edge at the multiplier zone will be a difficult construction problem but it is assumed that at least a simple-support type connection can be made (no moment transfer capability). The two plates that form two walls of a module will be subjected to forces similar to that for the multiplier zone so that the previous analysis will be directly applicable. It is assumed that the two walls containing the headers can also support these loads.

Analysis -- Suppose the module is oriented so that gravity acts in the negative x-direction in Fig. 10-75. This is the situation considered for the multiplier zone and discussed previously. For an orientation with gravity acting in the z-direction, it is assumed that the header walls can withstand whatever forces are transmitted. However, if the breeder and multiplier materials can withstand any shear stress, whatsoever, a significant portion of the load will be transferred to the composite plates which form a very stiff structure for forces in the z-direction.

To demonstrate the feasibility of the structure, the very conservative assumption is made that a 20 cm segment (distance between webs) or an internal composite plate can be treated as a cantilevered beam supported by the back wall. The critical loading situation is the case of gravity acting in the negative y-direction. The forces acting on the beam will be a point load, P, due to the multiplier and a uniformly distributed load, W, based on the weight of the breeding material. This loading situation is sketched in Fig. 10-76.

The contributing width for the loading functions is 20 cm and the corresponding depth is 65 cm. The width of the multiplier material is 5 cm

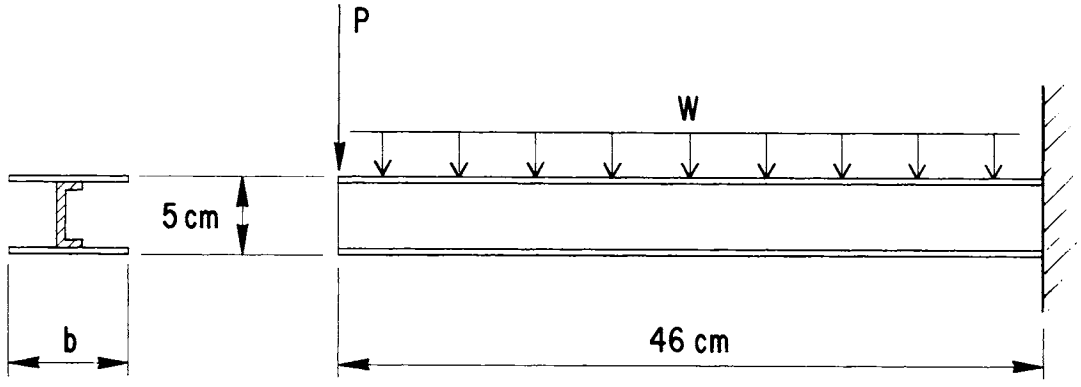

Figure 10-76. Beam model for internal plate structure.

so for mass densities of 10 gm/cm^3 and 2.5 gm/cm^3 for multiplier and breeder material, respectively, it follows that

$$P = (10 \text{ gm/cm}^3)\ (65 \text{ cm})\ (20 \text{ cm})\ (5 \text{ cm}) = 65 \text{ kg} = 640 \text{ N} \quad (61)$$

$$W = (2.5 \text{ gm/cm}^3)\ (65 \text{ cm})\ (20 \text{ cm}) = 3.25 \text{ kg/cm} = 32 \text{ N/cm} \quad (62)$$

The maximum shear occurs at the fixed end and is given by

$$V = P + W(46 \text{ cm}) = 2.1 \times 10^3 \text{ N} \quad (63)$$

which is less than the shear given in Eq. (57) for which the web is designed.

The maximum applied moment also occurs at the fixed end. It is

$$M = P(46 \text{ cm}) + W/2\ (46 \text{ cm})^2 = 63 \times 10^3 \text{ N cm} \quad (64)$$

Suppose that the allowable bending stress in the cooling panel base is σ_a = 300 MPa. Suppose further that a segment of the flange, b = 2 cm wide,

is effective in resisting moment. Then for a flange thickness of t = 0.35 cm and a beam height of h = 5 cm, the allowable moment is

$$M_a = 2(\sigma_a tb)\ h/2 = (300 \times 10^6\ N/m^2)(0.0035\ m)(0.02\ m)(5\ cm)$$
$$= 105 \times 10^3\ n\ cm \qquad (65)$$

which is greater than the maximum applied moment.

For other orientations of a first wall segment (or alternate directions for gravity), the transverse loads will be less while direct tensile stresses will increase. However, the net effect will be a reduction in the maximum stress in an internal plate structure. A similar argument holds for a plate structure that also serves as an end wall with the exception that internal pressure will also be a factor. However, compensation for this load can be made by reducing the spacing to the nearest internal plate structure.

With the conservative assumptions that have been made and with the considerable margin of reserve capacity for nominal loading conditions, it appears that the first wall segment will be able to easily withstand off-normal additional forces. This situation is primarily due to the efficient load carrying capacity of composite plates. For the first wall, the primary difficulty would appear to be that of construction. Also, a detailed analysis to ensure safety under accident conditions is necessary, but because the structure is fairly complex, the use of specialized computer codes will be required to perform this function.

10.6.2 Lifetime and Stress Analysis

The assessment of the first wall and blanket structural materials includes an evaluation of the reactor lifetime. For STARFIRE, the structural material lifetime goal is $\sim$ 20 MW-y/m^2 which corresponds to a lifetime of 6 years. This section will consider the lifetimes of the potential structural materials. The analysis will compare the advanced austenitic alloy, PCA, and a ferritic stainless steel, HT-9, for a specific design and for the expected operating conditions. Before the detailed lifetime analysis is presented, however, several important factors will be considered.

10.6.2.1 General Considerations

The lifetime estimates are expected to depend on such factors as the materials properties, the component design, the reactor power history, and the life-limiting criteria. There are a multitude of materials properties that can potentially influence the lifetime, as shown in Table 10-58. To date, no model has been comprehensive enough to include all of the properties and variables shown in the table. Most models have considered the thermophysical and mechanical properties and have ignored corrosion, transmutation, and sputtering effects, since these properties are considered to have a secondary importance. In addition, most models do not include all relevant variables and interactions between properties. In general, however, the various properties do not act independently of one another, and therefore, it is not strictly correct to consider any property separately. For example, the temperature and stress gradients in a component will result in a swelling gradient. A significant amount of swelling can reduce the thermal conductivity, which will alter the temperature gradient, which will in turn alter the swelling gradient. Such scenarios can be constructed for combinations of other properties.

The reason for not including all properties and variables is that in many cases the relevant data do not exist. Large extrapolations of existing data or the use of properties data from a related material may be required to make a lifetime estimate. In some cases, where no data exist, a property must be modeled theoretically or a best estimate of the property values must be made. Of particular importance is the lack of data on the effect of 14 MeV neutrons on the various properties. At present, radiation effects data are drawn primarily from fission reactor experiments and ion implantation experiments, and thus the influence of the fusion reactor spectrum can only be estimated. Most of the existing data have been obtained using fission reactor materials such as Types 316 and 304 stainless steel and advanced cladding materials such as HT-9. The amount of radiation data for other fusion candidate materials are sparse. The lack of a comprehensive materials data base imposes a significant uncertainty into the lifetime estimates.

The component design will influence the temperature and stress distributions in the material and thus will influence the component lifetime. The implications of this statement are first that the materials lifetime can potentially be enhanced by judicious design and second that the optimum design for one

Table 10-58. Properties Influencing Materials Lifetimes

Property	Important Variables	Influence on Lifetime
Thermal Conductivity	Temperature	Temperature distribution
Thermal Expansion	Temperature	Stress distribution
Specific Heat	Temperature	Rate of temperature and stress change
Young's Modulus	Temperature	Stress distribution
Yield Strength	Temperature, fluence, strain rate	Initial design stress analysis and ability to withstand off normal events
Ultimate Tensile Strength	Temperature, fluence, strain rate	
Uniform Elongation	Temperature, fluence, strain rate	
Total Elongation	Temperature, fluence, strain rate	
Swelling	Temperature, fluence, neutron spectrum	Dimensional changes and stress changes during operation
Creep	Temperature, fluence, stress	
Fatigue	Temperature, fluence, stress, burn cycle frequency, strain range	Crack propagation and failure
Crack Growth	Temperature, fluence, stress intensity burn cycle frequency	
Corrosion	Temperature, fluence, chemistry, environment	Flow blockage, wall thinning Crack propagation and failure
Stress Corrosion Cracking	Temperature, fluence, chemistry, stress, stress intensity, microstructure	
Transmutations	Neutron spectrum, neutron fluence	Potential influence on other properties
Sputtering	Temperature, particle species, particle energy	Wall thinning and defect initiation

material may represent a poor design for another material. The lifetime analysis should therefore consider a particular design, and the estimated lifetime is expected to be valid only for that design. A comprehensive analysis should examine the parameter and property variations in three dimensions, which is beyond the present scope of this investigation. The interactions of the reactor components can also effect the lifetime. For example, the creep and swelling experienced by one component may result in an unintended interaction with a second component which could influence its operating lifetime.

The reactor power history should also be integrated into the lifetime analysis. Obvious factors that are included in the power history are the total neutron fluence, the neutron and surface heat fluxes, and the reactor mode of operation, i.e., cyclic or continuous. STARFIRE will operate in the continuous mode, and as will be shown, this offers a considerable advantage to the structural materials. Less obvious factors that can influence lifetimes are the length and frequency of maintanence operations, off-normal temperature and stress excursions, and the procedures used for ramping the reactor up to or down from full power. Not only is it important to know what reactor events can influence lifetimes, but it is also important to know when these events occur in the reactor history. For example, a temperature or stress transient that occurs early in the reactor history is likely to have less effect on the materials than the same transient that occurs late in the reactor history. Highly irradiated structural materials have lower ductility and are less able to accommodate large amounts of strain before failure.

The lifetime criteria are the limits imposed on the materials properties beyond which a component is considered to fail. The criteria can be divided into two classes: 1) catastrophic failure criteria and 2) dimensional failure criteria. While it is obvious when a component has failed catastrophically by cracking or fracture, it is less obvious when a component has failed due to dimensional changes. In most cases, the allowable dimensional change is determined by how much change can be accommodated before the reactor operation is effected or before it becomes difficult or impossible to replace that component. The allowable dimensional change is therefore likely to be related to the design and function of the various components. One component may be able to tolerate only a 1% dimensional change whereas another component may be able to tolerate a 10% change.

When the factors discussed above are introduced into the analysis, the lifetime estimates contain a rather high degree of uncertainty. The primary purpose of the present materials lifetime study is to determine if the desired lifetime goals are realistic and to determine what parameters and properties are most important in the analysis. The secondary purpose of the study is to determine what future work, both analytical and experimental is necessary to more accurately evaluate the useful lifetime of fusion reactor components.

10.6.2.2 Stress Analysis

Present reactors are designed to insure that designated stress limits are not exceeded. For this purpose, stress design codes have been developed to serve as guidelines in the stress analysis. Fusion reactors will ultimately be designed using such a stress code, and several fusion reactor analysis have used ASME pressure vessel code case 1592 to make their stress and lifetime estimates.[1,65,66] This section will address the questions of stress analysis and the use of pre-existing stress codes in performing the lifetime analysis.

The ASME Code Case 1592 for Class 1 Components in Elevated Temperature Service provides design criteria for components in service at temperatures where creep and other time dependent effects may be significant.[67] The code case is intended to cover a wide variety of design configurations and service conditions, and the design criteria are therefore usually quite conservative. Since different types of stress have different degrees of significance, the code assigns a different allowable stress for each stress classification. The allowable stresses are given in terms of the stress intensity, S_{mt}, which is calculated from the tensile and creep properties of the structural materials. The criteria for calculating S_{mt} are given in Table 10-59.[1] At lower temperatures the value for S_{mt} is a fraction of either the tensile yield or ultimate stress, and at high temperatures S_{mt} is the stress necessary to produce a given amount of creep during the expected component lifetime.

The classes of stresses that are considered by the design codes are the primary stresses, secondary stresses, and peak stresses.[68] A primary stress is a stress developed by the imposed loading which is necessary to satisfy the laws of equilibrium between external and internal forces and moments. The

Table 10-59. Structural Design Criteria

Time-dependent Allowable Stress: S_m (other than bolting)	Lowest value of	1/3 S_u at room temperature 1/3 S_u at temperature 2/3 S_y at room temperature 0.9 S_y at temperature
Time-dependent Allowable Stress: S_t	Lowest value of	2/3 of minimum stress to cause creep rupture in time t 80% of minimum stress to cause tertiary in time t Minimum stress to produce 1% strain in time t
General Primary-membrane Allowable Stress: S_{mt}	Lesser of S_m and S_t at temperature and time.	

S_y = Material Yield Strength

S_u = Material Ultimate Strength

basic characteristic of a primary stress is that it is not self-limiting. If a primary stress exceeds the yield strength of the material, the prevention of failure depends entirely on the strain hardening properties of the material. The primary stresses considered are the primary membrane stress, P_m, local primary membrane stress P_ℓ, and the primary bending stress, P_b. A secondary stress is a stress developed by the self-constraint of the structure. It must satisy an imposed strain pattern rather than being in equilibrium with an external load. The basic characteristic of a secondary stress is that it is self limiting. A peak stress is the highest stress in the region under consideration. The basic characteristic of a peak stress is that it causes no significant distortion and is objectionable mostly as a possible fatigue source. Fatigue analysis is included in the design code and consists of the calculation of the induced strain per cycle, the number of cycles expected for the component

during its lifetime, and then a comparison of those values with fatigue curves given in the code. Safety factors of two in stress or twenty in cycles to failure are built into the code design curves.

The maximum allowable stress intensities for the various categories of stress are given in Table 10-60.[68] The primary membrane stress is limited to a value of S_{mt}, whereas the sum of the primary and secondary stresses at low temperatures, including thermal stresses is limited to a value of 3 S_m. The value of 3 S_m has been suggested assuming that the structure will shakedown to elastic-strain shortly after startup operation of the component. When peak stresses are included, the allowable stress is 2 S_a, where S_a is the allowable stress amplitude calculated from the design fatigue curves. It should be noted that neither corrosion nor radiation effects have been specifically considered in establishing these stress limits. In most cases, the safety margins built into the design codes will allow for changes due to corrosion or radiation damage, but in some cases the allowable stress limits could be non-conservative. The design codes also do not consider crack growth, using fracture mechanics, from a pre-existing defect or crack. For some designs, crack growth is expected to limit the lifetime of a reactor component.

One effect of radiation that has been included in the design codes is the irradiation induced changes in the materials' fracture toughness.[68,70] Several alloys, including HT-9, are known to exhibit a ductile-brittle transition temperature (DBTT) below which the material acts in a brittle fashion and which has been shown to be increased by irradiation.[71] The brittle behavior of these materials can be described by the change in the tensile, the impact, or the crack growth properties, and the design codes provide guidelines for these three properties. In all cases, the allowable limits are related to the nil ductility temperature (NDT) which is defined as the temperature at which the fracture stress for specimens with small flaws is equal to the yield stress for specimens with no flaws. When the tensile properties are used for the prevention of brittle fracture the guidelines are:[68]

1. For $T \leq NDT$, the maximum allowable stress is 41 MPa (6 ksi).
2. For $T > NDT + 17°C$ (30°F), the maximum allowable stress is 1/2 the yield strength.
3. For $T > NDT + 33°C$ (60°F), the maximum allowable stress is the yield strength

Table 10-60. Stress Categories and Maximum Allowable Stress Intensities Current Design Codes

Category	Included in category	Maximum allowable stress intensity
S_1	P_m	S_{mt}
S_2	$P_m+P_b+Q_m(s)$*	$(3/2)S_m$ K_tS_t
S_3	$P_m+P_b+Q_m(s)+Q_m(t)+Q_b(s)+Q_b(t)$	$3S_m$
S_4	$P_m+P_b+Q_m(s)+Q_m(t)Q_b(s)+Q_b(t)+F_t+F_c$	$S_r=2S_a$

*$P_\ell=P_m+Q_m(s)$ = Primary local membrane stress

P_m = primary mean stress.

P_b = primary bending stress.

$Q_m(s)$ = secondary mean stress due to sustained loads.

$Q_m(t)$ = secondary mean stress due to temperature.

$Q_b(s)$ = secondary bending stress due to sustained loads.

$Q_b(t)$ = secondary bending stress due to equivalent linear temperature distribution.

F_t = peak stress due to temperature -- free thermal stress.

F_c = peak stress due to highly localized stress concentration, or highly localized hot spots.

S_a = allowable stress amplitude for any given number of cycles, N

S_r = $2S_a$ = stress range

$$K_t = 1 + K_s\left(1 - \frac{(P_m + Q_m(s))}{S_t}\right)$$

(K_s = 0.25 for shell-type structures)

4. For T > NDT + 67°C (120°F), the maximum allowable stress is the ultimate stress.

The impact properties of materials are usually determined using the Charpy V-notch impact test that measures the energy required for rapid fracture of standardized specimens. The design code for pressure vessels specifies that at T = NDT + 33°C (60°F), the impact energy should be at least 67.8 J (50 ft-lbs) and that the lowest service temperature should be ≥ NDT + 56°C (100°F).[69] If crack growth is to be used as a design guideline, the ASME Pressure Vessel Code prescribes procedures to be used for evaluating the stress intensity of an assumed defect.[7] The calculated stress intensity must be less than the stress intensity at the temperature of operation that is given in a design curve that incorporates the data of several pressure vessel steels. At the NDT the calculated stress intensity must be < 44 MPa-$m^{1/2}$ to prevent brittle failure. The assumed effect of radiation for all types of analysis is to increase the NDT while leaving the shapes of the design data curves uneffected. Thus as the NDT increases, the maximum allowable stress, impact energy, or stress intensity at a given temperature will decrease.

A design code for fusion reactors is likely to contain several changes from the present design codes because of the additional influence of radiation on several properties. Long term dimensional changes are considered in Code Case 1592 to occur via thermal creep. However, dimensional changes in STARFIRE will occur primarily via swelling or radiation creep, and significant changes are expected to occur at temperatures and stresses far below those where such changes would occur by thermal creep. Restriction of the stresses to values that produce a strain allowed by the design codes would result in an unrealistly low allowable primary stress. Radiation damage will also result in significant changes in the yield and ultimate strengths of the materials. Therefore, the values of S_m, which are calculated from tensile strength values will vary with time. Fatigue of structural materials will be influenced by radiation. In the high cycle range where the strain is elastic, radiation may increase the number of cycles to failure, while in the low cycle range where the strain is both elasic and plastic, radiation may reduce the number of cycles to failure.[72] In the absence of a design stress code for fusion reactors, present codes such as ASME code case 1592 provide useful guidelines for component design. It should be recognized, however, that in some cases use of

the present design codes may result in overly conservative designs while in other cases their use could result in non-conservative designs. The addition of radiation effects as an integral past of the stress analysis will be essential for the realistic appraisal of fusion reactor structural components.

10.6.2.3 Comparison of PCA and HT-9

After a thorough review of the different structural materials, the PCA and HT-9 alloys were selected as being the most viable alloys for the STARFIRE first wall/blanket system. A detailed analysis of PCA and HT-9 has been performed to determine if it is feasible for these materials to achieve the lifetime goal of 20 MW yr/m^2 for the operating conditions of STARFIRE.

The properties used in the analysis of the two alloys are the thermophysical, radiation creep, radiation swelling, and crack growth properties, all of which are described in detail in Appendix E. Fatigue and crack growth due to a cyclic stress were not included since STARFIRE operates in a continuous mode. Of the various materials properties, only the thermophysical properties are well known. Several assumptions had to be made concerning the other properties in order to perform the analysis. First, since PCA is similar to Type 316 stainless steel, the unirradiated properties of PCA have been assumed to be those of 20% cold worked type 316 stainless steel. Second, both the thermophysical and crack growth properties have been assumed to be uneffected by irradiation. Because of the lack of crack growth data for HT-9, its crack growth properties are assumed to be the same as PCA. Third, the radiation creep and swelling rates are assumed to be essentially the same as those observed in fission reactors for an equivalent DPA rate. The radiation swelling has been modified slightly to account for the increased helium generation rate in STARFIRE. The radiation swelling has been assumed to be independent of the stress state in the material. Although there is some evidence that stress can influence the swelling, there is not enough evidence for proper analytical treatment.

The design used to make the comparison is a tubular first wall that receives a heat flux from one side. The first wall receives the highest neutron and surface heat flux and is therefore the component which is most likely to fail prior to the desired lifetime. The design, shown in Fig. 10-77, is

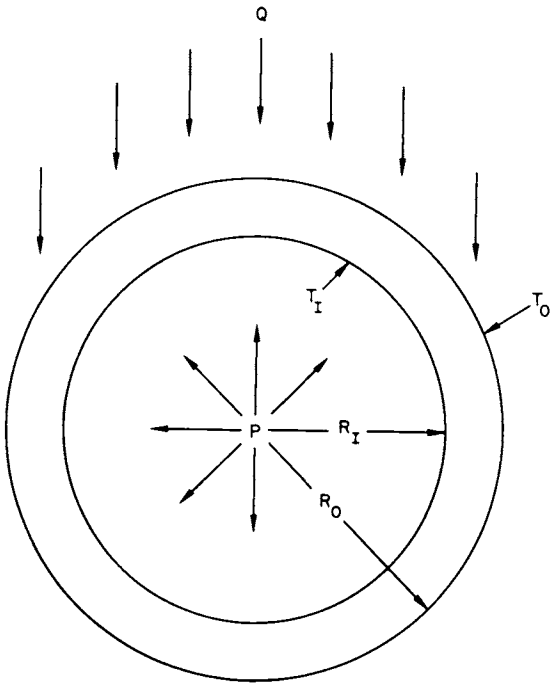

Figure 10-77. First wall model.

a tube of radius R_o and wall thickness $R_o - R_I$ that is placed in a uniform neutron flux ϕ, and receives a heat flux, Q, from one side. The water coolant inside the tube operates at a pressure P. This design was selected because the tubular geometry represents a potentially viable design which can be treated without excessive mathematical complexity. Although this design is not the specific one selected for the STARFIRE first wall, it is similar enough to provide a meaningful evaluation of the two materials. The operational parameters used for the calculations are shown in Table 10-61. The surface heat flux, Q, is assumed to decrease from a peak of 0.85 MW/m^2 at the top surface of the tube facing the plasma to zero at the sides of the tube 90° from the top surface. The neutron fluence is assumed to be uniform through the tube and the water temperature of 320°C is the maximum expected in STARFIRE.

Table 10-61. Design and Operating Parameters for Lifetime Analysis

Tube diameter (cm)	1.0
Wall thickness (mm)	1.5
Coolant pressure (psig)	2000
Coolant temperature (°C)	320
Neutron Wall Load (MW/m^2)	3.5
Surface Heat Flux (MW/m^2)	0.85
dpa rate	11.3[1] (PCA)
($dpa/MW\text{-}yr/m^2$)	11.1[1] (HT-9)
Helium generation rate	147[1] (PCA)
($appm/MW\text{-}yr/m^2$)	110[1] (HT-9)
Initial crack length	100
(μm)	

The initial flaw size is 100 μm, which is assumed to be the minumum flaw size detectable by non-destructive testing.

The life limiting criteria for the analysis are based upon the best estimates of the allowable limits for swelling, creep, and crack growth. The crack length limit is the crack length at which the net section stress equals the ultimate strength of the material. At this point, it is assumed that the tube will fail instantaneously by stress rupture. The allowable limit for creep is based upon the in-reactor creep ductility of Type 316 stainless steel. Recent tests indicate that Type 316 stainless steel should be able to accommodate ∿ 2% plastic strain prior to failing in a neutron field.[73] This value is considerably larger than the creep ductility measured following irradiation. The maximum dimensional change allowed is 4% (creep + swelling), and the maximum level of swelling allowed is 6%. These values are somewhat arbitrary, and probably will vary with the design of each individual component.

The program developed for the analysis calculates tne temperature, stress, and strain distribution in two dimensions. The tube is broken down into 40 segments, each composed of 10 elements, and each element is considered to be at a uniform temperature and stress. Each segment contains a flaw at the tube inner and outer surface whose growth is followed in the program. The inputs required for the program are the tube dimensions, the coolant temperature and

pressure, the neutron wall load, the surface heat flux, and the initial flaw size. The program begins by calculating the temperature, stress and strain distribution in the tube for the input conditions using the assumed thermophysical properties of PCA and HT-9. The initial temperature and stress values are then used to calculate the dimensional and crack growth changes that occur in a small time increment Δt. The dimensional changes are due to radiation swelling and creep. The changes in the dimensions are next used to determine the changes in the stress distribution in the tube. Any changes in crack length are assumed to have no effect on the stress distribution. The process of calculating the dimensional and crack length changes is then repeated with the new stress distribution for the same time increment. The only restriction in this model is that the time increment, Δt, must be chosen such that the changes in crack length dimensions, and stresses are small compared with the original values. In this way the long-term effects of reactor operation can be determined.

The calculated temperature and initial stress distributions in PCA and HT-9 are shown in Fig. 10-78. As expected, PCA exhibits a larger temperature and stress gradient in the tube, because of its lower thermal conductivity and higher thermal expansion. The initial stresses are primarily compressive on the side of the tube facing the plasma and are in tension on the other side of the tube. In both cases, the stresses due to the coolant pressure and thermal gradients are below the design limits of ASME Code Case 1592. The effect of radiation creep is to reduce the stress gradients with time. Figure 10-79 compares the stress distributions of PCA and HT-9 after 1000 h and 3000 h of operation. After 3000 h, the thermal stress gradient has almost been eliminated, leaving only the primary stress due to the coolant pressure. However, a stress gradient, opposite in sign to the initial stress gradient, will be imposed on the tube whenever the temperature gradient is removed. As will be shown, this new stress gradient has important implications if the reactor operation is cyclic.

In order to determine the long term effects of swelling, creep, and crack growth, the calculations were carried out to 50,000 h (5.7 yr) of continuous operation. Crack growth under these conditions was insignificant. The total

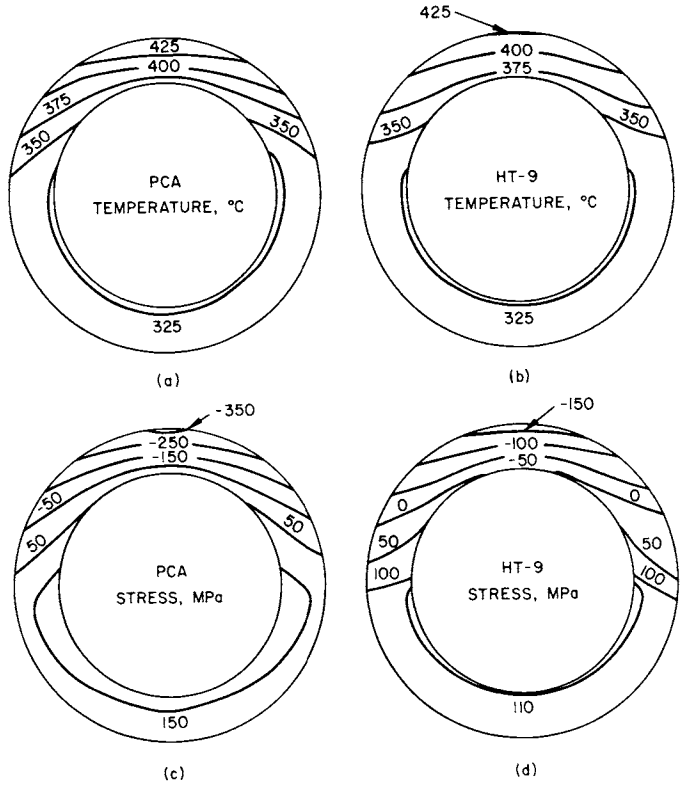

Figure 10-78. (a) temperature distribution - PCA, (b) temperature distribution - HT-9, (c) initial stress distribution - PCA, (d) initial stress distribution - HT-9.

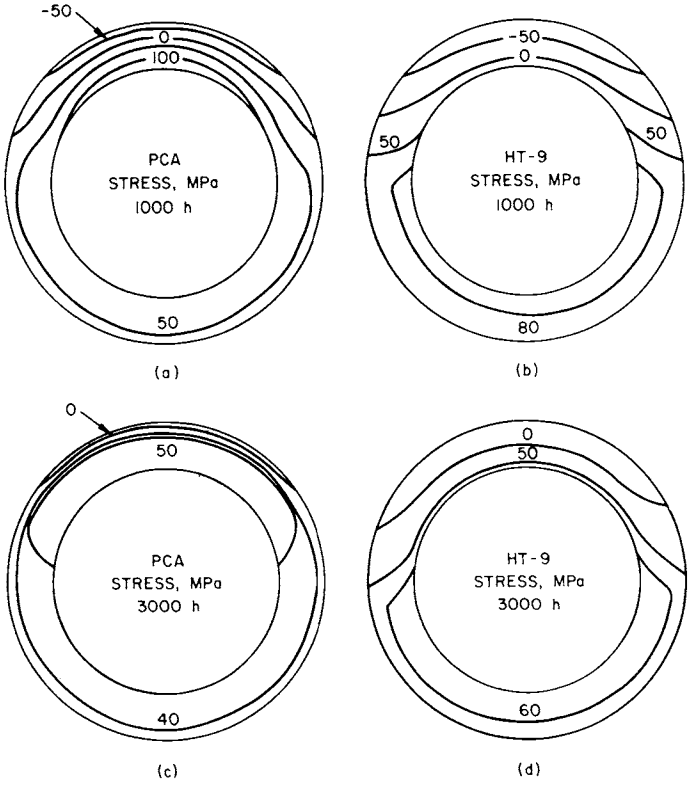

Figure 10-79. Stress distribution in (a) PCA @ 1000 h, (b) HT-9 @ 1000 h, (c) PCA @ 3000 h, (d) HT-9 @ 3000 h.

swelling and creep in PCA and HT-9 in the tube section receiving the highest surface heat flux is shown in Fig. 10-80. For both materials, the total swelling and plastic strain are less than 2%. The swelling of PCA is marginally higher than HT-9, while the radiation creep rate is significantly higher in PCA. At long times, when swelling becomes significant, the temperature gradient in the tube will result in a swelling gradient. A small stress gradient will be established, as shown in Fig. 10-81, that offsets the swelling gradient so that the total change in strain is uniform throughout the tube. The magnitude of the stress gradient will depend on the relative swelling and creep rates of the materials as well as their variation with temperature and stress. The results of these calculations indicate that for continuous operations, both PCA and HT-9 are likely to meet the lifetime goal of 20 MW-yr/m^2.

The importance of a continuous mode of operation on the materials selection can be illustrated by examining the crack growth that would occur during cyclic operation. PCA and HT-9 are again compared for the same conditions shown in Table 10-61. In addition, the effect of a cyclic burn mode as well as the effect of reactor down time for maintenance have been included in the program. It has been assumed that the plasma burn time is 10 minutes, that the plasma is off for 1 minute between burn cycles, and that it requires $\sim$ 0.4 minutes for the temperature gradient to be completely removed when the plasma is turned off. Reactor maintenance is assumed to take 30 days per year. Figure 10-82 shows the growth of cracks from the OD surface of the section of the tube receiving the highest heat flux. Crack growth in PCA is rapid and leads to failure in $\sim$ 7000 h, whereas little crack growth is indicated in HT-9. The rapid crack growth in PCA is due to the larger thermal stresses imposed on the tube. As shown earlier, the large compressive stresses in this section of tubing relax in $\sim$ 3000 h. When the temperature gradient is removed, large tensile stresses are introduced in the tube, increasing the stress intensity at the crack tip. The implication of this result is that the selection of an austenitic stainless steel such as PCA would not be likely for STARFIRE if it operated in a cyclic mode. The introduction of a significant residual tensile stress at low temperatures also presents a problem to the use of HT-9. The DBTT of HT-9 has been shown to be increased considerably above room temperature by neutron irradiation, and the allowable stresses and

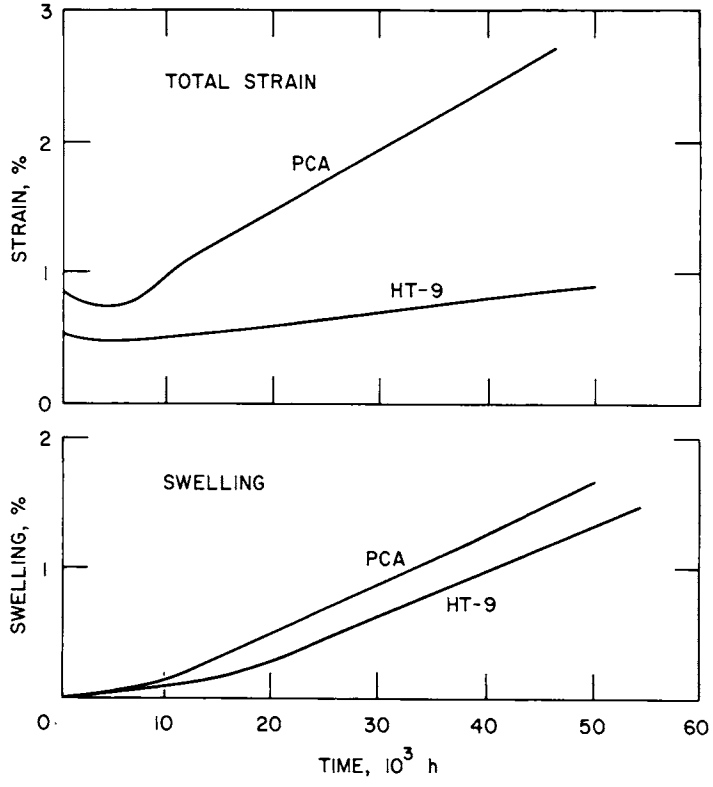

Figure 10-80. Swelling and creep in PCA and HT-9 for section of tube receiving the highest heat flux.

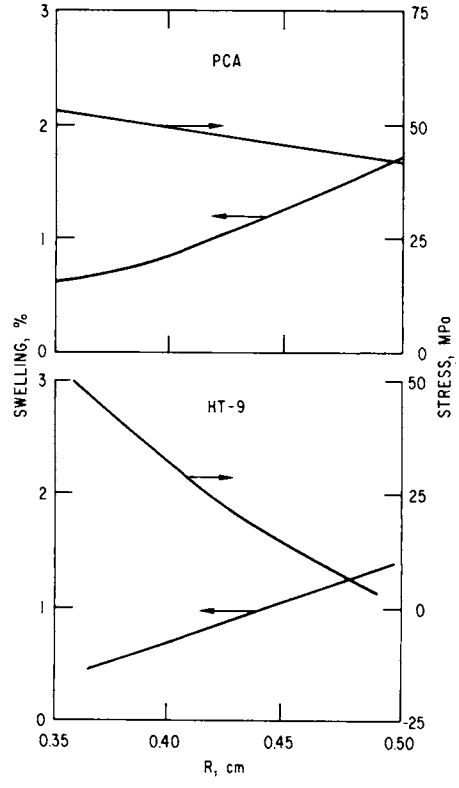

Figure 10-81. Swelling a stress gradient at end of life for tube section receiving highest heat flux, (a) PCA, (b) HT-9.

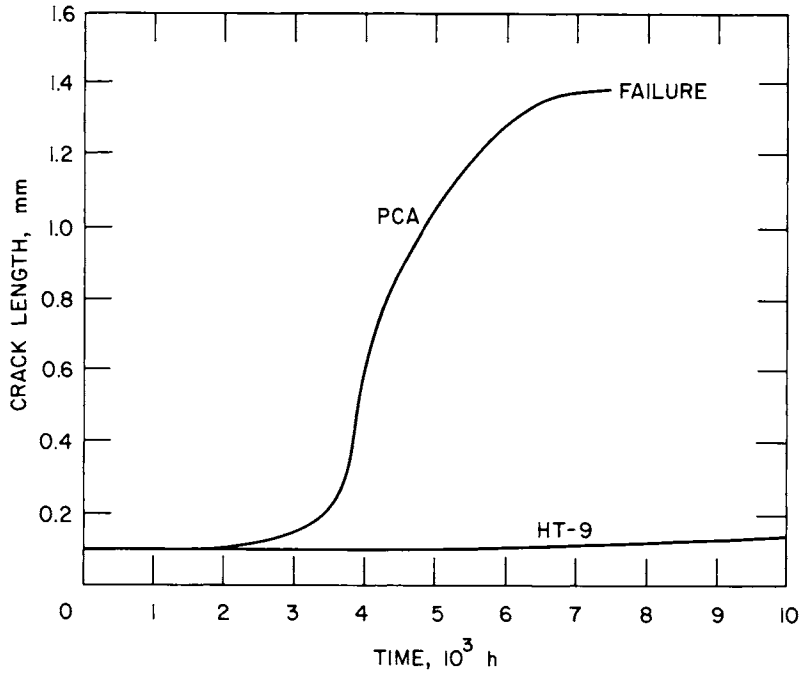

Figure 10-82. Crack growth in PCA and HT-9 for a 10 minute burn time, one minute off time and 30 days/yr maintenance.

and stress intensities would therefore be restricted during maintenance operations. It may be possible to work with these restrictions, but a more detailed analysis is required to determine the feasibility of using HT-9 at low temperatures.

10.6.2.4 Off-Normal Events

Off normal events will result in increased stresses and/or temperatures over those experienced by the materials during normal operation, and can seriously impact on the materials' lifetimes. The consequences of off normal events depends on both the magnitude of the stress or temperature and the duration of the event. The results of the event may include annealing of the microstructure, additional plastic strain, fracture or melting of a component. The melting of a component will depend upon the relative rates of energy input and output and the thermophysical properties of the material. Predicting under what conditions a component will melt can be done using standard thermal-hydraulic calculational techniques. The ability of a material to accommodate

additional plastic strain is dependent upon the effect of radiation on the mechanical properties prior to the off-normal event. Since neutron radiation generally decreases the uniform ductility of metals, the ability of a component to absorb plastic strain is expected to decrease during the lifetime of a component.

The microstructure of the structural materials influence both the mechanical properties and the resistance to radiation damage. The thermomechanical treatment given to PCA (and HT-9) provides a microstructure which optimizes the various properties. During operation, the neutron radiation will alter the microstructure by producing dislocations, voids, helium bubbles, and possibly additional precipitates. If, during an off normal event, the temperature is increased significantly, the microstructure will begin to change due to thermal annealing. The property changes produced by annealing could be either desirable or undesirable. If only the dislocation structure is altered, the material could regain some of its pre-irradiation ductility. However, if helium bubbles migrate to gain boundaries, the material may become more severely embrittled. Also, the initial microstructure is tailored to reduce the total void swelling of the material. Should the microstructure be substantially altered, the rate of swelling during subsequent operation could be greatly increased. Thus, a substantial change in the microstructure during an off-normal event may necessitate immediate replacement of a component even though it has not been otherwise damaged.

A rough estimate of the allowable times at various temperatures can be made from available thermomechanical data. The radiation resistance of PCA has been traced to the presence of a fine distribution of Ti-rich metal carbide precipatates that exist within the grains and at the grain boundaries.[74] The standard procedure for producing the precipatates is to homogenize the alloy at temperatures > 1150°C for $\sim$ 24 h, cool, and then cold work the material 10-25%. The fine precipatates are formed by next heat treating the alloy at $\sim$ 800°C for several hours. The presence of a high dislocation density is crucial to produce the proper precipatate distribution, since the precipatates nucleate on the dislocations. The normal procedure for producing an annealed structure in austenitic stainless steel is to heat the alloy for 1 h at 1050°C. These heat treatments give an indication of the relative stability of the microstructure and therefore a rough approximation of the allowable temperatures

of the material during an off normal event. An event which greatly reduced the dislocation density or swept the helium bubbles to the grain boundaries would result in a material with greatly reduced strength and would prevent the reformation of the Ti-rich carbide structure. Therefore, an off-normal event that resulted in structural temperatures of $\gtrsim$ 1050°C for $\gtrsim$ 30 minutes would probably necessitate replacement. Some coarsening of the microstructure will probably occur if the temperature is allowed to increase to $\sim$ 900°C for any extended period of time. The relative damage produced by such a temperature excursion cannot be determined at this time because of insufficient data.

The thermal mechanical treatment used for HT-9 is different from the one used for PCA since HT-9 is a ferritic material. Normal heat treatment for HT-9 is first an anneal at 1050°C for 30 minutes to completely austenitize and homogenize the material, followed by cooling to produce a martensitic structure.[65] The martensitic structure is then temperated at $\sim$ 780°C for $\sim$ 1 h to achieve the optimum toughness and creep properties. The temperature above which the material begins to transform from a ferritic to an austenitic structure is $\sim$ 820°C.[12] These temperatures and times can again be related to off normal events. First, it is undesirable for a significant fraction of the material to be transformed into austenitic during a temperature transient, since this would result in a complete microstructural change and would lead to the formation of a hard and brittle martensitic structure when the material is cooled. Second, the helium bubbles and voids are likely to be swept to the grain boundaries which would further weaken the structure. This means that an off normal event which produced structural temperatures $\sim$ 850°C for an extended period ($\sim$ 1 h) would significantly alter the microstructure.

A transient is also likely to result in additional stresses in the structure. Since the mechanical strengths of both HT-9 and PCA are markedly decreased at temperatures 600°C, their load carrying capacity will be reduced during a transient. In addition, the ductility of the structural materials will be greatly reduced at temperatures 600°C due to the embrittlement caused by irradiation generated helium. Therefore, the maximum permissible temperatures during a transient could be considerably below those required for

the microstructural changes described above. When stresses are present, the maximum allowable temperatures without component damage are estimated to be 600-700°C, with the exact temperature depending upon the magnitude of the stresses and the duration of the transient.

10.2.6.5 Summary

1. The assessment of the structural materials lifetime depends upon the materials properties, the component design, the reactor power history, and the life limiting criteria. Because of the interrelated nature of these factors, a lifetime estimate can only be considered valid for a particular reactor and component design. The uncertainties introduced into the analysis because of either a lack of pertinent data or the limited scope of the analysis mean that there will be a significant uncertainty in the predicted lifetime.

2. Although present stress design codes provide useful guidelines, the stress analysis of the reactor components will ultimately require a design code specifically intended for materials exposed to radiation. The strict use of present codes could possibly lead to either an overly conservative design, or non-conservative design depending on the effects of radiation on the relevant properties.

3. Both HT-9 and PCA appears to be capable of achieving the lifetime goal of 20 MW/yr/m^2 for the STARFIRE operating conditions. However, use of HT-9 would be difficult at low temperatures since the DBTT is increased above room temperature by radiation. PCA would probably not be used if the reactor operated in a cyclic mode because of the large thermal stresses in the material.

4. The changes in microstructure produced by high temperatures and stresses during an off normal event could necessitate replacement of effected components. For both PCA and HT-9, the combination of stresses and temperatures would likely result in serious damage, if the materials temperature reached 600 to 700°C.

10.7 ELECTROMAGNETIC EFFECTS ON THE FIRST WALL AND BLANKET

10.7.1 Introduction

Because of the close magnetic coupling of the first wall with the plasma and magnet systems, the first wall can participate in four important electromagnetic effects: (1) reducing vertical plasma motion and stabilizing low mode number kink modes, (2) delaying the penetration of ohmic heating (OH) flux and of field changes from the copper correction field (CF) coils into the plasma, (3) protecting against the consequences of a plasma disruption, and (4) experiencing eddy current forces on the blanket modules due to startup, plasma disruption, toroidal field (TF) coil discharge, and unscheduled equilibrium field (EF) coil discharge. The first three of these are described briefly here, and the fourth is somewhat more detailed.

10.7.1.1 Plasma Perturbations

The STARFIRE blanket consists of 24 sectors arranged toroidally. Each sector consists of eight modules arranged poloidally. Induced currents within each module are carried primarily in the multiplier region, which is on the plasma side of the blanket. Modules are connected poloidally and toroidally by jumpers to their neighbors to provide a continuous current path.

Plasma analysis shows that low mode number kinks can be stabilized when the ratio of the blanket minor radius to the plasma minor radius is less than about 1.1. The elongated STARFIRE equilibrium is unstable due to a negative index of curvature of the vertical field, and the uncorrected growth time for this instability is of order 10 μs. Conducting segments of a close-fitting blanket slow this time to the blanket L/R time of 300 ms, which is long enough to permit plasma positional control through external negative feedback with only moderate power requirements. For more detail see Sec. 6.2.

10.7.1.2 Field Penetration

In general, the same L/R time which limits the outward penetration of flux changes from plasma movement, and thus slows down that movement, also limits the inward penetration of field from the CF coils designed to provide long-term correction of that motion. However, calculations show that if the vertical plasma motion is detected by sensors within the blanket, and if the

CF coils can respond quickly enough, then the position correction can begin not with the L/R time characterizing changes in the total current flowing in the blanket but with the much shorter time constant characterizing the distribution of the current through the blanket thickness. Flux change from the OH coils continues for 14 seconds, delay by the first wall is negligible.

10.7.1.3 Plasma Disruption Protection

In the event of a plasma disruption, the collapsing plasma current will be transferred to the first wall. The consequences will be mitigated through the relatively long first wall L/R time.

10.7.1.4 Eddy Current Forces

Eddy current forces due to TF coil discharge and to plasma disruption are described below. Forces due to charging the TF coils or EF coils or to a normal or abnormal EF coil discharge are much smaller than those described for the TF coil discharge and plasma disruption.

10.7.2 Electromagnetic Characterization of the First Wall

10.7.2.1 L/R Time of Toroidal Currents Associated with Plasma Disruption

The current is assumed confined to the multiplier region, either a 3.5 cm thick layer of Be or a 7 cm thick layer of Zr_5Pb_3. The inductance is found from the expression for a hollow torus

$$L = \mu_o R \, [\ell n(8R/a) - 2] = 9.0 \ \mu H \qquad (66)$$

using R = 7 m and a = 2.72 m, which gives an equivalent area. The resistance for an unbroken first wall is given by

$$R = 2\pi R \, \rho/p\delta \qquad (67)$$

where ρ is the resistivity of the multiplier material, δ its thickness and p = 18.6 m is the perimeter of the cross section. For Be, ρ/δ = 12.57 $\mu\Omega$; for ZrPb, ρ/δ = 15.77 $\mu\Omega$. In what follows we use the Be value, which yields

$$R = 29.7 \ \mu\Omega \ .$$

Consequently, the L/R time is τ = 303 ms. Finite resistance of the jumpers will lower that value. Earlier calculations including the resistance of the stainless steel blanket members to the jumper in the back yielded τ = 40 ms. In the following τ = 40 ms and τ = 300 ms will both be considered.

10.7.2.2 L/R Time of Poloidal Currents Associated with TF Coil Discharge

Again the current, in this case poloidal, is assumed confined to the multiplier region. The inductance is found by considering the currents and flux which would follow an instantaneous TF coil discharge. The toroidal field B_{TF} is 5.8 T at the major radius of 7 m, and thus can be written as a function of radius r:

$$B_{TF} = 5.8 \text{ T} \times 7 \text{ m}/r = 40.6/r \tag{68}$$

The flux ϕ is the integral of B_{TF} over a cross section bounded by the first wall

$$\phi = \int B_{TF}\, dA = 137.59 \text{ Wb}$$

10.7.3 Currents

The total plasma current is taken to be I_p = 10 MA. Calculations from plasma flux plots show that if the entire plasma current were instantaneously transferred to the first wall, the current per unit length around the perimeter would vary between 0.50 MA/m and 0.63 MA/m. This deviation from a uniform distribution should not be significant.

For the L/R time τ and an exponential plasma discharge with time constant τ_o, the first wall current is given by

$$I = \frac{I_p}{(1-\tau_o/\tau)} \left[e^{-t/\tau} - e^{-t/\tau_o}\right] \tag{69}$$

The maximum current occurs at time

$$t_{max} = \frac{-\tau_o \, \ell n(\tau_o/\tau)}{(1-\tau_o/\tau)} \tag{70}$$

and is given by

$$I_{max} = \frac{I_p}{(1-\tau_o/\tau)} \left[\left(\frac{\tau_o}{\tau}\right)^{(\tau_o/\tau)(1-\tau_o/\tau)^{-1}} - \left(\frac{\tau_o}{\tau}\right)^{(1-\tau_o/\tau)^{-1}}\right] \tag{71}$$

Values of I_{max} and t_{max} are given in Table 10-62 for various values of τ_o for τ = 40 ms and 300 ms.

Table 10-62. Peak First Wall Current for Different Plasma Discharge Times

τ (ms)	τ_o (ms)	t_{max} (ms)	I_{max} (MA)
40	0	0	10
	10	18.5	6.30
	20	27.7	5.00
	50	44.6	3.28
	100	61.1	2.17
300	0	0	10
	100	165	5.77
	200	243	4.44
	400	345	3.16

10.7.4 Forces

As the current is strictly toroidal, it does not interact with the toroidal field. It interacts with the field from the plasma current and its own field to give a magnetic pressure

$$F/A = IB\Delta\ell/p\Delta\ell = IB/p \tag{72}$$

where p is the perimeter. All the current interacts with the plasma field but only half with the self field, since the self field varies from zero to its peak value across the current thickness.

$$F/A = (B_p + \frac{1}{2} B_s)\ I/p \tag{73}$$

Now
$$B_p = B_o \exp(-t/\tau_o) \tag{74}$$

but B_s is proportional to the current, given by Eq. (69).

$$B_s = B_o\ (1 - \tau_o/\tau)^{-1}\ [\exp(-t/\tau) - \exp(-t/\tau_o)]. \tag{75}$$

The field at the first wall due to the full plasma, B_o is nearly equal to 1.0 T, and is related to the variables in Eq. (72) by

$$B_o = \mu_o I_p/p \tag{76}$$

Hence:

$$F/A = \frac{B_o^2}{2 \mu_o (1 - \tau_o/\tau)^2} [e^{-t/\tau} - (1 - 2 \tau_o/\tau) e^{-2t/\tau_o}$$

$$- 2 \tau_o/\tau e^{-t (1/\tau + 1/\tau_o)}], \tag{77}$$

and

$$B_o^2/2 \mu_o = 398{,}000 \text{ N/m}^2 = 57.7 \text{ psi.}$$

Because Eq. (77) is more complex than Eq. (69), there are no simple relations such as Eq. (70) and (71) to give t_{max} and F/A_{max}. Instead they must be found by trial and error from Eq. (77). The maxima for τ = 40 ms and τ = 300 ms are shown in Table 10-63 for various values of τ_o.

Table 10-63. Maximum Magnetic Pressure on First Wall and Different L/R times τ and Plasma Discharge Times τ_o

τ (ms)	τ_o (ms)	t_{max} (ms)	F/A_{max} (N/m^2)	F/A_{max} (psi)
40	0	0	398,000	57.7
	1	2	369,000	53.4
	10	10	280,000	40.6
	20	16	235,000	34.1
	50	28	171,000	24.8
	100	41	124,000	18.0
300	0	0	398,000	57.7
	100	95	262,000	38.0
	200	145	216,000	31.3
	400	220	166,000	24.1

10.8 SAFETY

One of the primary objectives of the STARFIRE study is the development of a reactor design that has an inherently high degree of safety for the public and for operating personnel. The two principal concerns in achieving this objective were the prevention of tritium release to the environment, and the minimization of both the amount of activated material from the reactor and its level of activation.

The preceding sections of this chapter have discussed various safety considerations of the first-wall/blanket system, primarily from the standpoints of materials compatibility, tritium release from the breeder, and thermal-hydraulic and stress aspects of off-nominal or accident situations. Radioactivity and waste considerations are discussed in Chap. 12.

This section discusses the results of a failure modes and effects analysis (FMEA) performed for the first wall, blanket, and limiter of the STARFIRE design. The analyses are condensed in Tables 10-64 through 10-66. The corrective actions listed are typical rather than comprehensive.

In general, there are three separate failure modes in the first wall which would be cause for concern. These are not necessarily safety-related, but rather are important to reliable operation of the device. The three failure modes are:

- o leak or rupture of one of the coolant channels;
- o leak at the coolant channel/header connection;
- o leak at the module edge.

The first two failure modes lead to water in either the plasma cavity or the breeder region respectively. In the first case the plasma would probably self-extinguish. However, if a leak were detected in the breeder region as in the second mode, it is presumed that an intentional plasma shutdown would be used in order to prevent a plasma disruption. The disruption would result from water vapor blowing out of the module wall through a safety valve and entering the plasma cavity. If this disruption did not occur quickly, a hot spot would form on the first wall. This would also lead to a rapid plasma shutdown, due to ablation of the beryllium coating from the first wall at the

Table 10-64. Failure Mode Analysis for the First Wall

COMPONENT LOCATION	FAILURE MODE	CAUSE(S)	SYMPTOMS AND LOCAL EFFECTS	METHODS OF DETECTION	CORRECTIVE ACTION
1. COOLANT CHANNELS	LEAKAGE OR RUPTURE	a) LOSS OF MATERIALS INTEGRITY b) FAULTY WELD	H_2O LEAKAGE INTO PLASMA CAVITY	PLASMA OR VACUUM MONITOR	a) PLASMA SELF-EXTINGUISHES b) ISOLATE VACUUM PUMPS c) ISOLATE FAILED BLANKET SECTOR d) SHUT REACTOR DOWN e) REPLACE FAILED BLANKET SECTOR
2. COOLANT CHANNEL/ HEADER CONNECTION	LEAKAGE	FAULTY WELD	H_2O LEAKAGE INTO BREEDER REGION	MONITOR ON He PURGE STREAM - PRESSURE - RESIDUAL GAS ANALYZER (RGA)	a) RAPID PLASMA SHUTDOWN b) ISOLATE FAILED BLANKET SECTOR c) SHUT REACTOR DOWN d) REPLACED FAILED SECTOR BLANKET SECTOR
3. MODULE EDGE	LEAKAGE	FAULTY SEAM WELD	He LEAKAGE INTO VACUUM PLENUM	VACUUM MONITOR	a) CONTINUE TO OPERATE UNTIL PLASMA SELF-EXTINGUISHES b) SHUT REACTOR DOWN c) IDENTIFY FAILED BLANKET SECTOR d) REPLACE FAILED BLANKET SECTOR

Table 10-65. Failure Mode Analysis for the Blanket

COMPONENT LOCATION	FAILURE MODE	CAUSE(S)	SYMPTOMS AND LOCAL EFFECTS	METHODS OF DETECTION	CORRECTIVE ACTION
1. COOLANT CHANNELS	LEAKAGE OR RUPTURE	a) LOSS OF MATERIALS INTEGRITY	H_2O LEAKAGE INTO MULTIPLIER OR BREEDER REGION	MONITOR ON He PURGE STREAM - PRESSURE - RESIDUAL GAS ANALYZER (RGA)	a) RAPID PLASMA SHUTDOWN b) ISOLATE FAILED BLANKET SECTOR c) SHUT REACTOR DOWN d) REPLACED FAILED SECTOR
2. COOLANT TUBE/ MANIFOLD, OR MANIFOLD/INLET (OR OUTLET) PIPE CONNECTION	LEAKAGE OR BREAK	a) FAULTY WELD	H_2O LEAKAGE INTO VENTED REFLECTOR/ MANIFOLD REGION	MONITOR ON HEADER/ MANIFOLD - PRESSURE - RGA	a) CONTINUE TO OPERATE UNTIL LEAKAGE RATE BECOMES UNACCEPTABLE b) SHUT DOWN REACTOR c) REPLACE FAILED BLANKET SECTOR
3. He PURGE LINES	LEAKAGE	a) FAULTY WELD	He LEAKAGE INTO VACUUM PLENUM	VACUUM MONITOR	a) CONTINUE TO OPERATE UNTIL PLASMA SELF-EXTINGUISHES b) SHUT REACTOR DOWN c) IDENTIFY FAILED BLANKET SECTOR d) REPLACE FAILED BLANKET SECTOR

Table 10-66. Failure Mode Analysis for the Limiter

COMPONENT LOCATION	FAILURE MODE	CAUSE(S)	SYMPTOMS AND LOCAL EFFECTS	METHODS OF DETECTION	CORRECTIVE ACTION
1. COOLANT CHANNELS	LEAKAGE OR RUPTURE	a) LOSS OF MATERIALS INTEGRITY b) FAULTY WELD	H_2O LEAKAGE INTO PLASMA CAVITY	PLASMA OR VACUUM MONITOR	a) PLASMA SELF-EXTINGUISHES b) ISOLATE VACUUM PUMPS c) ISOLATE FAILED LIMITER SECTOR d) SHUT REACTOR DOWN e) REPLACE ASSOCIATED BLANKET SECTOR
2. COOLANT CHANNEL/ HEADER CONNECTION	LEAKAGE	FAULTY WELD	H_2O LEAKAGE INTO VACUUM PLENUM	VACUUM MONITOR	a) RAPID PLASMA SHUTDOWN (BALANCE SAME AS ABOVE)

hot spot, which would cause the plasma to cool and quench ($\sim$ 0.5 s) from excess impurity ions and electrons. This inherent mechanism should preclude the possibility of the first wall melting due to loss of coolant.

The third failure mode is more subtle and arises due to the fact that the first wall also serves in part as the container for the solid breeder. Helium at approximately 1/2 atm pressure is used as purge gas for tritium removal; thus a faulty seam weld along the module edge would allow helium to leak into the vacuum region. Depending upon the size and location of the helium leak, the reactor may be able to operate for some length of time before the helium level gets too high in the plasma region and the plasma could no longer burn.

Three failure modes have been identified for the blanket. They are as follows:

- o leak or rupture of the coolant tubes in the breeder region internal to the blanket;

- o leak or break at the coolant tube/manifold welds, or the manifold/ inlet or outlet pipe connections;
- o leak of one of the helium purge lines.

The first of these failure modes -- the leakage of water, which would flash to steam and then be superheated -- is a critical area of concern. Safety relief valves on each blanket module, and on the bulk shield which also serves as the vacuum boundary, are essential to be able to accommodate overpressurization resulting from a major coolant leak into the blanket. It is of vital importance to have the capability to quickly detect such a failure and to then isolate that coolant loop before the initial failure leads to failure or flow blockage of adjacent layers of tubes which are on the other cooling loop, or before it leads to overpressurization of the module.

The second-mentioned failure mode -- that is, a leak of coolant at a piping interface weld -- is less critical than the first. All such welds have intentionally been designed to be isolated from the breeder region. Thus a coolant leak at the welds would lead to water leakage into the manifold region which is vented to a vacuum pumping system external to the reactor.

A leak in the helium purge lines would result in a situation similar to that mentioned for the failure of a first wall seam weld, which is not critical.

The following two failure modes which would lead to a loss of coolant have been identified for the limiter:

- o leak or rupture of one of the coolant channels;
- o leak at the coolant channel/header connection.

These failure modes would have the same effect as the first mode for the first wall. However, the pressure of the limiter cooling water is only 4.2 MPa (600 psi) compared to 15.2 MPa for the primary coolant.

10.9 REFERENCE FIRST-WALL/BLANKET DESIGN

A commercial tokamak reactor first-wall/blanket system must perform two primary functions: (1) the breeding of tritium to be used as fuel in the reactor, and (2) conversion of the kinetic energy of fusion neutrons into useful thermal energy. In addition to ensuring the achievement of these requisites, design and materials choices for the STARFIRE reference first-wall/blanket design were made to obtain the overall design which best satisfied system design requirements and project design guidelines of economic and environmental attractiveness, safety to the public and operators, and design credibility. Details of the selected reference design are illustrated in Fig. 10-83. Table 10-67 summarizes the selected materials and mechanical design features of the reference design.

Table 10-67. STARFIRE First-Wall/Blanket Reference Design Description

Selected Materials

- Tritium breeder	$LiAlO_2$ (solid)
- Neutron multiplier	Zr_5Pb_3 (solid) or Be (solid)
- Coolant	Pressurized H_2O (15.2 MPa)
- Tritium processing fluid	Low-velocity helium (0.05 MPa)
- Reflector	Graphite
- Structure	
- High fluence regions	PCA
- Low fluence regions	Low-Mo stainless steel

Selected Design Options

- First wall	Be-coated corrugated panel
- Neutron multiplier	Slab form
- Second wall	Corrugated panel
- Breeder coolant containment	Small-diameter tubes
- Other	
- Two independent primary coolant loops	
- Maintainance by sector removal and replacement	

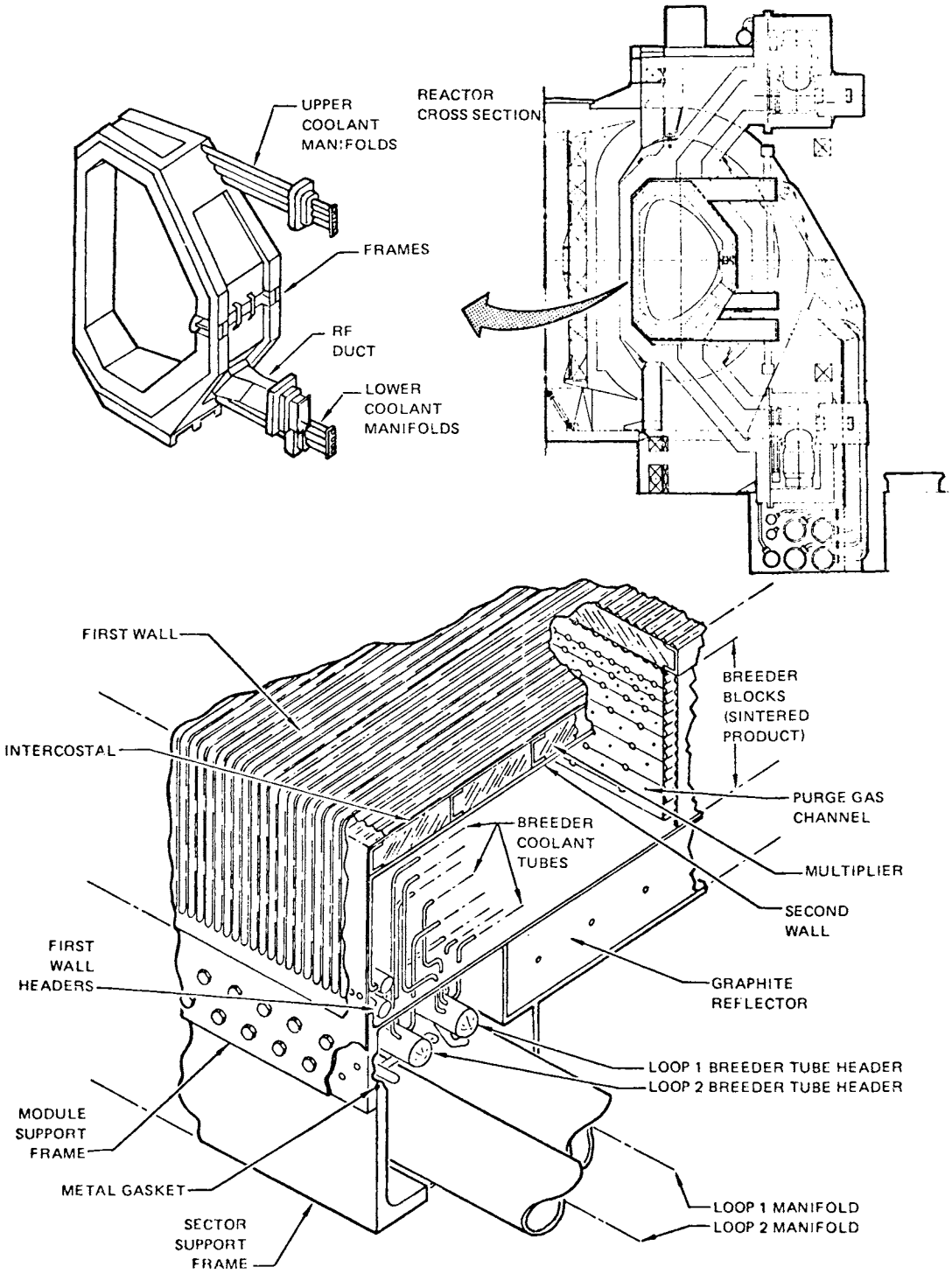

Figure 10-83. STARFIRE first-wall blanket reference design.

The tritium breeding material is solid lithium aluminate, $LiAlO_2$. To obtain adequate tritium breeding, the $LiAlO_2$ is used in conjunction with a neutron multiplier of solid zirconium-lead, Zr_5Pb_3, or solid beryllium. Pressurized H_2O is the coolant for all parts of the first-wall/blanket assembly. The structural material for the high-fluence regions is an advanced austenitic stainless steel (PCA, prime candidate alloy), a titanium-modified Type 316 stainless steel. Solid graphite is used as the reflector.

The first wall which faces the plasma is a water-cooled corrugated panel which removes the surface heat load and cools the front face of the neutron multiplier. The first wall is coated with a 1-mm thick coating of beryllium, to minimize sputtering and erosion and to protect the steel panel; this choice enables a single coating material (Be) to be used for all reactor components that contact the plasma. The back face of the neutron multiplier is cooled by a second corrugated coolant panel. Heat is removed from the breeder by water which passes through tubes surrounded by breeder. Tritium is continuously removed from the breeder by a low-pressure flow of helium purge gas which passes through the sealed breeder zone. The graphite reflector behind the breeder enhances tritium breeding by reflecting low-energy neutrons back into the breeder.

The first-wall/blanket system consists of 24 sectors, each composed of nine separate tritium breeding modules arranged poloidally around the sector. Primary structural support for each sector is provided by large frames at the sector sides; each module is individually connected to the frames. Each module is cooled with two separate but identical coolant circuits. Coolant static pressure is 15.2 MPa, and inlet-to-outlet coolant temperature increase is 40°C. Coolant is directed to and removed from the module in each sector by large tube manifolds which wrap around the outside of the sector.

The following subsections describe the specific materials and elements of mechanical design selected for the first-wall/blanket reference design, and summarizes the rationale for those choices. The rationale for the selected materials is discussed in Sec. 10.9.1. The mechanical design options selected are presented in Sec. 10.9.2 together with the rationale for those choices. The integration of other reactor subsystems into the first-wall/blanket system is presented in Sec. 10.9.3.

10.9.1 Materials Selection

The development of the reference STARFIRE first-wall/blanket design involved numerous tradeoffs in the materials selection process for the breeding material, coolant, structure, low-Z coating, neutron multiplier, and reflector. The important parameters and properties that impact materials selection are presented in the previous sections. The materials selected for the reference STARFIRE blanket design are listed in Table 10-67. Table 10-68 summarizes the key characteristics of the reference materials.

10.9.1.1 Tritium-Breeding Material

The STARFIRE study has focused on the use of solid tritium breeding materials; and hence, liquid lithium, liquid lithium alloys, and molten salts have not been considered. Important criteria considered in the selection of potentially viable solid breeding materials include tritium breeding performance, chemical stability, compatibility, and tritium release characteristics. The α-$LiAlO_2$ is selected on the basis of the best combination of these materials requirements. It is one of the most stable compounds considered and compatibility should not be a major problem. Adequate breeding is attainable with the aid of an effective neutron multiplier. The ceramics are preferred over the intermetallic compounds for the reference solid breeding material because of the larger allowable operating temperature ranges predicted for tritium recovery. On the basis of this criterion, Li_2O and $LiAlO_2$ appear to have an advantage. However, the calculated solubility of tritium in Li_2O at these temperatures and at reasonable T_2O partial pressures in the tritium-processing stream ($> 10^{-1}$ Pa) is much greater than 100 wppm. Since this concentration translates to more than 35 kg of tritium in the blanket, Li_2O is not considered a viable candidate. The primary advantages of α-$LiAlO_2$ compared to γ-$LiAlO_2$ relate to the higher density, which will result in a thinner breeding zone, and the fact that α is the stable phase at temperatures below $\sim$ 900°C. The major disadvantage of Li_2TiO_3 is its poorer breeding performance because of the absorption of titanium. A slight potential advantage of this compound is its lower long-term activation compared to the aluminate. The silicate is similar to the above compounds, but because of its lower melting temperature its chemical stability and compatibility characteristics are not as good.

Table 10-68. Key Features of Selected First-Wall/Blanket Materials

Breeding Material - α-$LiAlO_2$

- Requires effective neutron multiplier for adequate breeding
- Enriched 60% with ^6Li for Zr_5Pb_3 multiplier; natural Li for Be multiplier
- High porosity (40%), fine grain size (< 1 μm) to facilitate tritium recovery
- Highly stable compound; broad operating temperature range
- Good compatibility with coolant, structure, tritium processing fluid
- Predicted tritium release characteristics superior to other candidates
- α-$LiAlO_2$ more dense than γ-$LiAlO_2$, and is stable phase at operating temperatures

Coolant - Pressurized H_2O (15.2 MPa)

- High first-wall heat load capability
- Low void fraction compared to helium
- Results in low operating temperature for structure
- Moderate manifold size requirements
- Very low recirculating power

Structure - Advanced Austenitic Stainless Steel (PCA)

- Adequate wall loading limits and lifetime for steady state operation
- Better radiation damage resistance than Type 316 stainless steel
- Acceptable chemical compatibility in reactor environment
- Good fabricability

Low-Z Coating/Cladding - Be

- Compatible with hydrogen environment
- High thermal conductivity
- Low atomic number
- Withstands high plasma disruption loads
- Low activation
- Applicable to all plasma chamber components
- No stoichiometry effects compared to compounds

Neutron Multiplier - Zr_5Pb_3 or Be

Zr_5Pb_3
- Adequate resources
- Low transmutant gas production
- Results in moderate Li burnup profile in breeder

Be
- Highly effective neutron multiplier
- Low activation and afterheat
- Low density (low mass)
- Effective heat sink for thermal transients
- Low operating temperature
- High energy multiplication

Reflector - Graphite

- Low activation

The microstructural characteristics of the ceramic are critical because of their impact on tritium recovery. A small grain size (< 1 μm) is required for avoiding an excessive diffusion-controlled tritium inventory. Interconnected porosity is necessary to facilitate tritium (T_2O) migration to the tritium processing stream. A bimodal pore distribution is proposed to optimize the tritium migration rate. Although effects of radiation on these ceramics have not been well established, critical mechanisms have been identified. Radiation-induced trapping of tritium at defects could greatly increase the predicted tritium inventory. Grain growth or pore closure caused by restructuring and sintering would also be critical.

10.9.1.2 Coolant Selection

Coolant selection for STARFIRE focused primarily on the tradeoffs between pressurized water, both H_2O and D_2O, and helium. Liquid-metal coolants were not considered in the present study and, except for a lower operating pressure, molten salts have little advantage over water. Since this advantage is outweighed by the disadvantages of higher melting temperatures and greater compatibility problems, the salts are not considered prime candidates. Although steam was given some consideration, any advantages over pressurized water or helium are minimal. Major concerns regarding the use of helium relate to difficult neutron shielding problems, large manifold requirements, leakage into plasma chamber, lower tritium breeding because of the large structure requirements and the high temperatures required for the energy conversion system. An acceptable structural material for use with high temperature helium in a radiation environment has not been identified. Also, design constraints associated with the use of helium as a first-wall coolant appear to be prohibitive. Major advantages of the water coolant are its characteristically low operating temperature and its excellent heat transfer characteristics. However, the use of water with the intermetallic compound breeder materials is probably not acceptable because of the high reactivity, and hence, safety concern. Heavy water (D_2O) has several advantages compared to H_2O. Processing of tritium from the water coolant is less difficult for D_2O and deuterium leakage from the first-wall coolant into the plasma chamber is less detrimental than hydrogen. Another important advantage of D_2O relates to the lithium burnup and energy distribution in the solid breeder. However, the cost of D_2O is considered prohibitive.

10.9.1.3 Selection of the Structural Material

Six classes of materials generally considered as candidates for the first-wall/blanket structure are austenitic stainless steels, high-nickel alloys, titanium alloys, vanadium alloys, niobium alloys, and ferritic steels. Although the structural materials limitations were an important consideration in the selection of other blanket materials, the selection of the structural material is strongly impacted by the choice of coolant and breeder material. Nickel alloys are eliminated primarily on the basis of poor radiation damage resistance (embrittlement), no physical property advantage (thermal stress factor), and limited mechanical property advantage at temperatures required for water coolant. Titanium alloys are not considered viable candidates for the first-wall region because of their affinity for hydrogen. Vanadium and niobium alloys were eliminated because of their poor corrosion resistance in water and limited mechanical advantage at low operating temperatures.

The major focus has been on the tradeoffs between austenitic stainless steels and the ferritic steels. Important factors in the selection of the advanced austenitic stainless steel relate to the following design specific considerations.

- Steady state operation reduces the thermal stress advantage of the ferritic steel.
- The lower structure temperatures characteristic of water-cooled systems reduce the radiation damage advantages of ferritic steels.
- Burnup of the solid breeder poses an additional blanket life limitation.

In addition to these design specific considerations, major advantages of the austenitic steel relate to its ease of fabrication and welding. The primary disadvantages of the ferritic steels relate to their magnetic properties, their sensitivity of mechanical properties to composition, their difficult welding, and their potentially high DBTT.

10.9.1.4 Low-Z Coating

The low-Z coating concept for the first-wall is incorporated as part of the plasma impurity control system. The low-Z coating concept provides flexibility in that the structural material can be selected primarily on the basis

of structural requirements and the coating can be selected primarily on the basis of surface-related properties. Favorable properties such as high thermal conductivity, high heat capacity and compatibility with hydrogen were important considerations in the selection of beryllium as the first-wall coating/cladding material. A primary consideration in the selection of the candidate coating/cladding is that it can be used on all components exposed to the plasma. This is important because considerable redistribution of the material throughout the chamber is expected as a result of sputtering and ablation.

10.9.1.5 Neutron Multiplier

An effective neutron multiplier is required to obtain adequate tritium breeding with the $LiAlO_2$. Two candidate materials are proposed. Beryllium provides good neutronics performance and can be easily incorporated into the blanket design since it has low density, high thermal conductivity and high heat capacity. Because of the concern regarding limited resources of beryllium, an alternate neutron multiplier Zr_5Pb_3 is also proposed. This compound retains some of the beneficial neutronic characteristics of lead but remains solid at the operating temperatures.

10.9.1.6 Reflector

Low activation, low cost and inherent safety characteristics were key factors in the selection of graphite over water and stainless steel as the reflector. An austenitic stainless steel with a low molybdenum concentration is proposed for the reflector structure in order to reduce the long-term activation.

10.9.2 Mechanical Design

The selection of the design elements for incorporation into the reference first-wall/blanket design were most strongly influenced by (1) the primary reactor design guidelines of environmental and economic attractiveness, inherent safety, and credibility of engineering solutions to design problems, and (2) the material choices for tritium breeder, neutron multiplier, and coolant. The materials and design choices were strongly interrelated, and each was

therefore considered in terms of the impact on other areas, rather than as a choice to be made separately.

Table 10-69 summarizes the key features of the first-wall/blanket mechanical design for each of the basic zones. Figures 10-84 and 10-85 illustrate the details of the mechanical design, while Table 10-70 summarizes the operating and design parameters of the system. The remainder of this section describes the mechanical design options selected for each zone together with the rationale for those choices. Design of the first wall, neutron multiplier, breeding and reflector/manifold zones is discussed in Sec. 10.9.2.1 through 10.9.2.4, respectively, while the tritium-breeding inner blanket module is described in Sec. 10.9.2.5.

10.9.2.1 First Wall Zone

The first wall is constructed of actively cooled panels which are attached to the blanket module. The panels are made of PCA stainless steel. Each panel consists of a front (plasma-side) sheet with embossed channel shapes, roughly semi-elliptical in cross section, which is attached to a flat back sheet by a continuous resistance seam weld between the parallel channels which extend across the width of the module and down both sides to the reflector zone. The panels terminate in headers which are joined to the manifolds through connecting pipes.

The 1.5 mm thickness of the embossed plasma-side sheet was selected to keep maximum structural temperature well below 500°C, the level at which the radiation damage resistance and structural properties of the 20% cold worked (CW) stainless steel begin to drop significantly. The maximum steady-state structural temperature of 423°C is reached at the outside of the embossed sheet at the center of the weld land between adjacent flow channels. The 3.5 mm flat sheet thickness was selected to keep total first wall steel thickness to no more than 0.5 cm, to minimize the detrimental effect of neutron absorption on tritium breeding. Flow velocity in the channels approximately 6 m/s.

The basic first wall panels are 60 cm long poloidally. The inlet and outlet ends of these panels terminate in headers located at the sector sides in the reflector zone. The second wall panels, located behind the multiplier, have similar configurations to permit the walls to be joined along the sector

Table 10-69. Key Features of Selected First-Wall/Blanket Mechanical Design Options

First-Wall - Be-Coated Panel

- Minimum water coolant volume compared to tubes
- Thin wall minimizes thermal strain gradients
- Minimal pressure boundary welds
- Separates structural and surface-related requirements
- All plasma chamber components coated with same material
- High surface heat load capability
- Low structural temperature
- Coating vaporization during thermal excursion will quench plasma

Neutron Multiplier Zone - Slab Behind First Wall

- Simple fabrication
- Serves as electrically conductive first wall
- Coolant panels provide barriers to plasma and breeding regions

Breeder Zone - Sintered Ceramic with Coolant in Tubes

- All tube welds located outside of breeder zone in low-fluence region
- High-pressure coolant contained in small-diameter tube
- Tube spacing graded to conform to energy deposition profile
- Low density ceramic to facilitate tritium recovery
- Low-pressure (0.05 MPa), low velocity helium for tritium processing

Reflector/Manifold Zone - Tubular Manifolds and Headers

- Most coolant system welds located within vented secondary containment to accommodate minor leakages while reactor continues to operate
- Graphite, steel, and water all serve as neutron reflectors

Dual Independent Primary Coolant Loops

- Dual loops throughout each module and sector
- Adequate afterheat removal capability even if only one loop is operable

Electrical Conductor Between Sectors - Bimetallic Spring

- Contact near first wall minimizes magnetic induced loads from plasma disruption

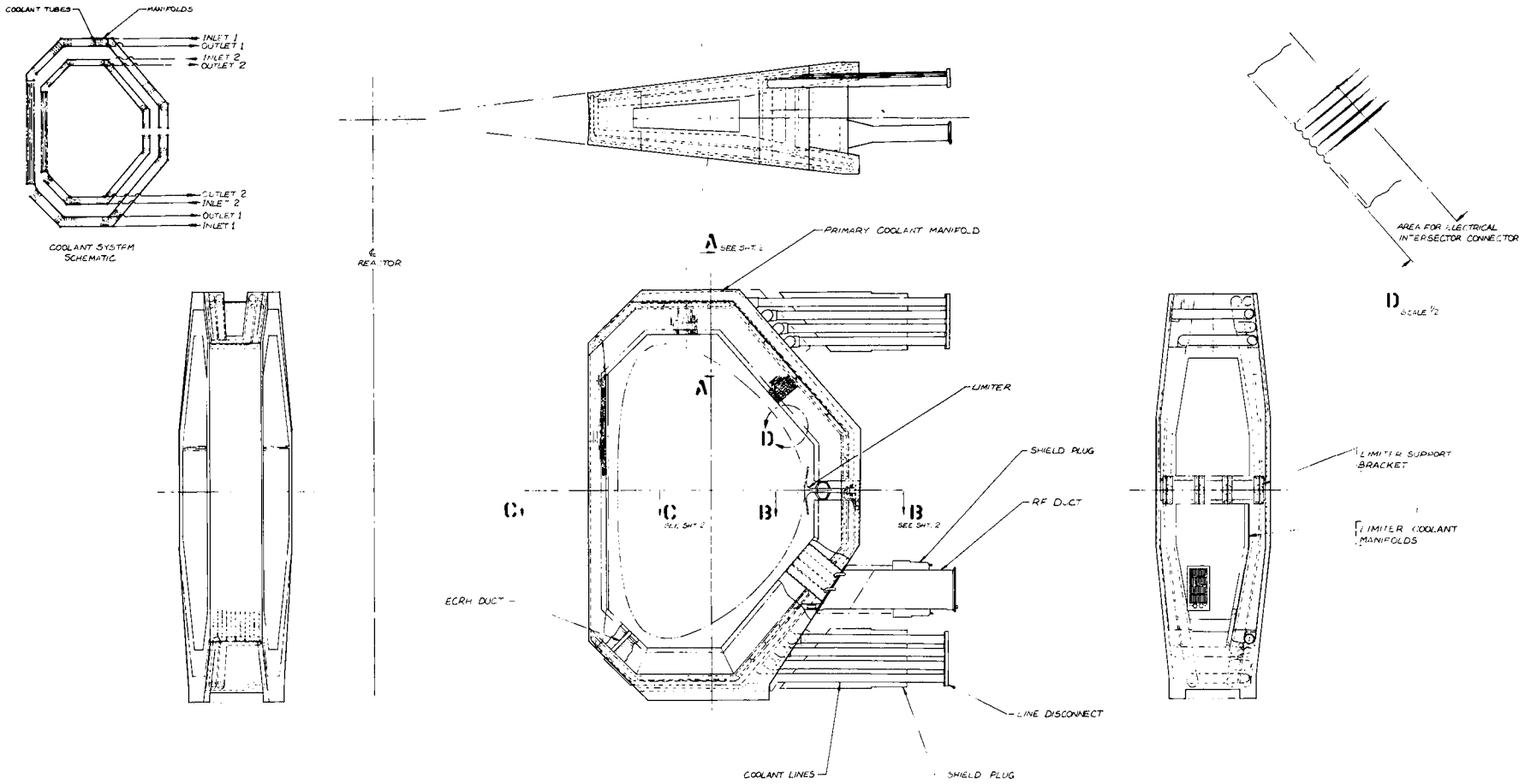

Figure 10-84. Layout of reference design first-wall/blanket.

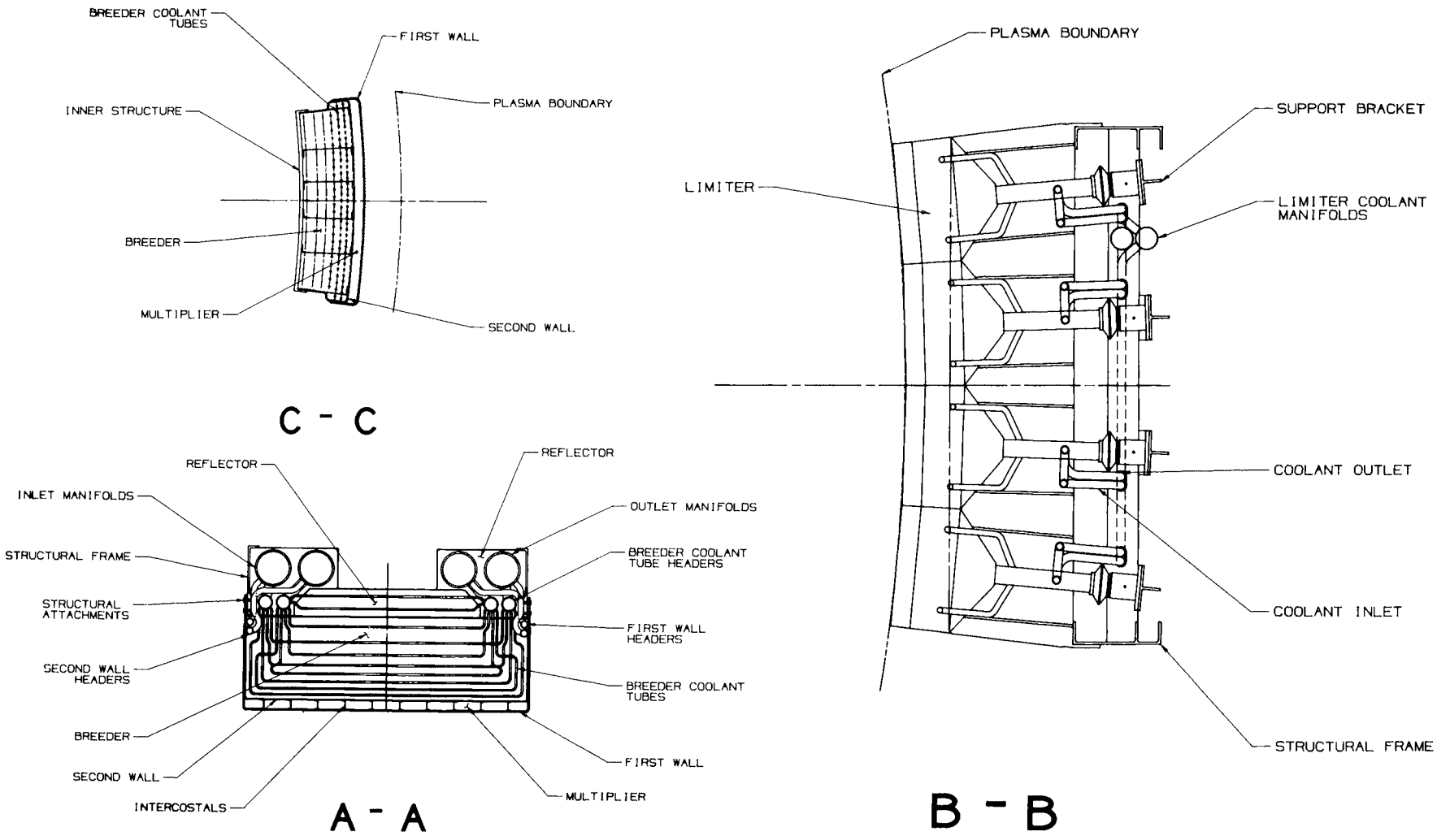

Figure 10-85. Reference design first-wall/blanket - cross sections through sector.

Table 10-70. Design and Operating Parameters of STARFIRE First-Wall/Blanket Reference Design

General Design	
Number of sectors	24 (12 large, 12 small)
Toroidal angle of large sectors	16.2°
Toroidal angle of small sectors	13.8°
Number of modules per sector	9
Mass of blanket sector, tonnes	65 (large) 60 (small)
Coolant mass flow rate per sector, kg/s	8982 (large) 7652 (small)
Fractional composition (% of total volume)	
Structure	2.8
Breeding Material	45.6
Neutron Multiplier	9.5
Coolant	2.7
Void/other	39.4
Total breeding volume, m^3	341.3
Number of independent coolant loops	2
First Wall	
Total area[a], m^2	780
Depth of zone, cm	1.0
Type of design	Internally cooled panel fabricated from two thin sheets, with coolant channels die stamped in plasma-facing sheet
Coating/cladding (facing plasma)	
Material	Be
Thickness, mm	1.0
First Wall area covered, %	100
Structural material	PCA st stl
Weld type	Resistance
Plasma-side sheet	
Thickness, mm	1.5
Channel configuration	Semicircular
Channel size, mm	2.0 (radius)
Channel flow area, cm^2	0.48
Second sheet thickness, mm	4.0
Maximum structural temperature, °C	
During operation	450
During complete LOCA[b]	710 (Zr_5Pb_3); 590 (Be)
Coolant	H_2O
Flowrate (total), kg/s	5811
Flow velocity, m/s	6.1
Pressure, inlet/outlet, MPa	15.2/15.0
Temperature, inlet/outlet, °C	280/320
Neutron Multiplier	
Type	Solid
Depth of zone, cm	5.0
Material	Zr_5Pb_3 (or) Be
Theoretical density, g/cm^3	8.9 1.8
Effective density, %	100 70
Maximum temperature[b], °C	
During operation	818 493
Complete LOCA[b]	270 587
Total mass, kg	356,000 51,800
Type of support	First-wall/second-wall acting as combined beam through intercostals
Second Wall	
Location	Behind neutron multiplier
Depth of zone, cm	1.0
Total area[a], m^2	780
Type of design	Same as first wall except flat sheet contacts back face of neutron multiplier

Table 10-70. (Cont'd)

Structural material	PCA st stl
Breeder-side sheet	
Thickness, mm	1.5
Channel configuration	Semicircular
Channel size, mm	1.25 (radius)
Channel flow area, cm^2	0.48
Multiplier-side sheet thickness, mm	2.5
Coolant	H_2O
Flowrate (total), kg/s	2019
Flow velocity, m/s	6.1
Pressure, inlet/outlet, MPa	15.2/15.0
Temperature, inlet/outlet, °C	280/320

Breeder

Type	Solid
Depth of zone, cm	46.0
Material	α-$LiAlO_2$
Theoretical density, g/cm^3	3.4
Effective density, %	60
^6Li enrichment, %	60 (Zr_5Pb_3); 0 (Be)
Operating temperatures, minimum/maximum, °C	500/850
Maximum temperature[b] during complete LOCA, °C	670 (Zr_5Pb_3); 590 (Be)
Coolant	H_2O
Flowrate (total), kg/s	8668
Flow velocity (maximum), m/s	3.2
Pressure, inlet/outlet, MPa	15.2/15.0
Temperature, inlet/outlet, °C	280/320
Coolant tubes	
Material	PCA st stl
Configuration	U-bend
Number of tubes per meter of module length	136 (poloidally)
Inside diameter, cm	1.0
Wall thickness, cm	0.125
Maximum temperature, °C	< 400
Tritium purge	
Material	He gas
Flow channel diameter in breeder, mm	2
Volumetric flowrate, m^3/s	10
Tritium removed, kg/s	10^{-5}
Pressure, MPa	.05

Reflector/Manifold Zone

Center reflector region	
Depth of zone, cm	15
Material	Graphite
Coolant	H_2O
Coolant manifold region (at sides of sector)	
Depth of zone, cm	30 (avg)
Coolant header inside diameter, cm	7 (avg)
Coolant manifolds	
Number per sector	8 (2 inlet, 2 outlet for each of 2 loops)
Number per module	4 (inlet, 1 outlet for each of 2 loops)
Flow velocity maximum limit, m/s	6 (turbulent flow) 20 (smooth flow)
Coolant header and manifold material	Modified austenitic st stl (low Mo content)

[a] Exclusive of openings, e.g., rf ducts, ECRH ducts.
[b] Temperatures at 600 seconds following complete LOCA for both coolant loops.

sides to form a structural unit and a part of the breeder zone helium purge gas pressure boundary.

The embossed panel concept was selected for the first wall primarily to take advantage of its ability to resist radiation damage. The PCA stainless steel in the panels is much more damage resistant in the 20% CW condition than in the annealed condition. The resistance welded seams which join the two sheets forming the panel are judged to have damage resistance only slightly less than that of the surrounding CW material because the microstructure of the welds are only slightly changed. In addition, the embossed panel configuration minimizes the equivalent volume of water coolant located in front of the multiplier, which enhances tritium breeding; this is especially important for the zirconium-lead multiplier option. Headers are used to terminate the panel coolant channels instead of an embossed manifold because their use results in a simpler design. In addition, locating the headers to the rear of the blanket provides a uniform surface contour along the sector side close to the first wall surface where electrical jumpers between sectors are installed (Sec. 10.9.3).

10.9.2.2 Neutron Multiplier Zone

A neutron multiplier must be added to the blanket in order to achieve adequate tritium breeding with the lithium aluminate breeder. The preferred location for the multiplier is between the first wall and breeder; this location results in the highest tritium breeding ratio and is the least complex from the standpoint of mechanical design. Neutronic heating is removed from the multiplier by the first wall and by a similar cooling panel on the back face of the multiplier.

The reference first-wall/blanket design uses solid beryllium (Be) or zirconium-lead (Zr_5Pb_3) as the multiplier. Parameters for both multipliers are shown in Table 10-70. Beryllium is judged to be technically the better choice. Its internal temperatures are much lower than for Zr_5Pb_3 during operation due to its greater thermal conductivity, and it generates much less afterheat following reactor shutdown. The thickness was set at 5 cm for both multipliers to maintain geometric consistency for the blanket design. The multiplier is fabricated from powder into compressed blocks, the width of which matches the spacing between adjacent parallel intercostals which tie

together the first and second walls in this zone. For beryllium, density of the blocks is only 70% of theoretical density. The resulting spaces between adjacent particles are considered adequate to acommodate helium generated within the beryllium by transmutation during reactor operation. The helium is gradually released from the multiplier blocks and is then removed from the vacuum plenum by the pumps. If future tests show that too much helium is generated to be acceptably vented to the vacuum chamber, the design details of the multiplier zone can be reconfigured to seal it from the vacuum chamber and permit the zone to be vented to pumps located outside the reactor.

The coolant panel between the multiplier and breeder is referred to as the second wall. Its construction is very similar to that of the first wall. The panel provides part of the cooling for both the multiplier and the first centimeter of breeder, which contacts the embossed back surface of the second wall. Channel flow area is less than for the first wall because heat removal requirements are lower (i.e., no surface heat load). Rationale for selection of the embossed panel concept is the same as for the first wall. In addition, the choice permits the first wall and second wall to be more simply combined along the module sides to form a structural unit which forms a part of the helium purge gas pressure boundary around the breeder zone.

10.9.2.3 Breeder Zone

Lithium aluminate, α-$LiAlO_2$, was selected as the solid breeder primarily because it results in an acceptably low steady-state tritium inventory in the blanket, and because it has an acceptably wide range between its minimum and maximum operating temperatures. The compound provides an adequate tritium breeding ratio when used in conjunction with either of the two multipliers, and has acceptable chemical compatibility with water if contact should occur due to a coolant system leak.

The breeder is contained within the helium purge gas pressure boundary, formed by: the first wall/second wall unit on the module sides; module end walls; the second wall; and the back plate between the breeder and reflector zones. The breeder is fabricated as sintered product in the form of blocks which are contoured to fit around the coolant tubes. The 2-mm diameter holes in the blocks for helium purge gas flow are formed during block fabrication,

or subsequently drilled. Breeder volumetric density is 60% of theoretical density, a level which permits adequate migration of tritium between breeder particles to the helium purge stream. The sintered product form of breeder was chosen because it was considered to provide the most uniform breeder density.

The coolant tubes in the breeder zone are arrayed vertically in eight banks as shown in Fig. 10-86. Each tube makes a single pass through the breeder. There are an average of 136 tubes per meter poloidally for each module (except for the inner blanket; see Sec. 10.9.2.5). Each coolant tube is made from seamless PCA tubing in the CW condition, with a 1-cm inside diameter and a 1.25-cm outside diameter. Spacing of the tubes depthwise through the breeder and laterally in each bank is designed to produce a maximum breeder temperature of 850°C, at points approximately equidistant from surrounding coolant tubes. Minimum breeder temperature at the outside surface of the coolant tubes is 500°C. Heat transfer between the tube and breeder surfaces is enhanced by the presence of the low-pressure (0.05 MPa; 8 psig) helium purge gas within the breeder cavity. This breeder temperature range produces an acceptably low steady-state inventory of $\sim$ 10 kg of tritium in the solid breeder during reactor operation. The temperature of the coolant in each tube is raised from 280°C to 320°C over the tube length by using the proper combination of flow rate and flow velocity produced by orificing at the entrance of each tube.

The U-bend tube concept was selected over the straight tube concept because it permits a greater volume of breeder to be used within the module envelope, and because of concerns regarding possible problems with thermal strains in straight coolant tubes which are alleviated in the U-bend tubes by increased flexibility from the two 90° bends.

10.9.2.4 Manifold/Reflector Zone

Evaluation of the various mechanical design and material options for the reflector and manifold zones led to the conclusion that some degree of integration of the two zones would reduce both the complexity and the total volume required for the first-wall/blanket assembly. This was accomplished by bringing the manifold system into the reflector zone to locally replace

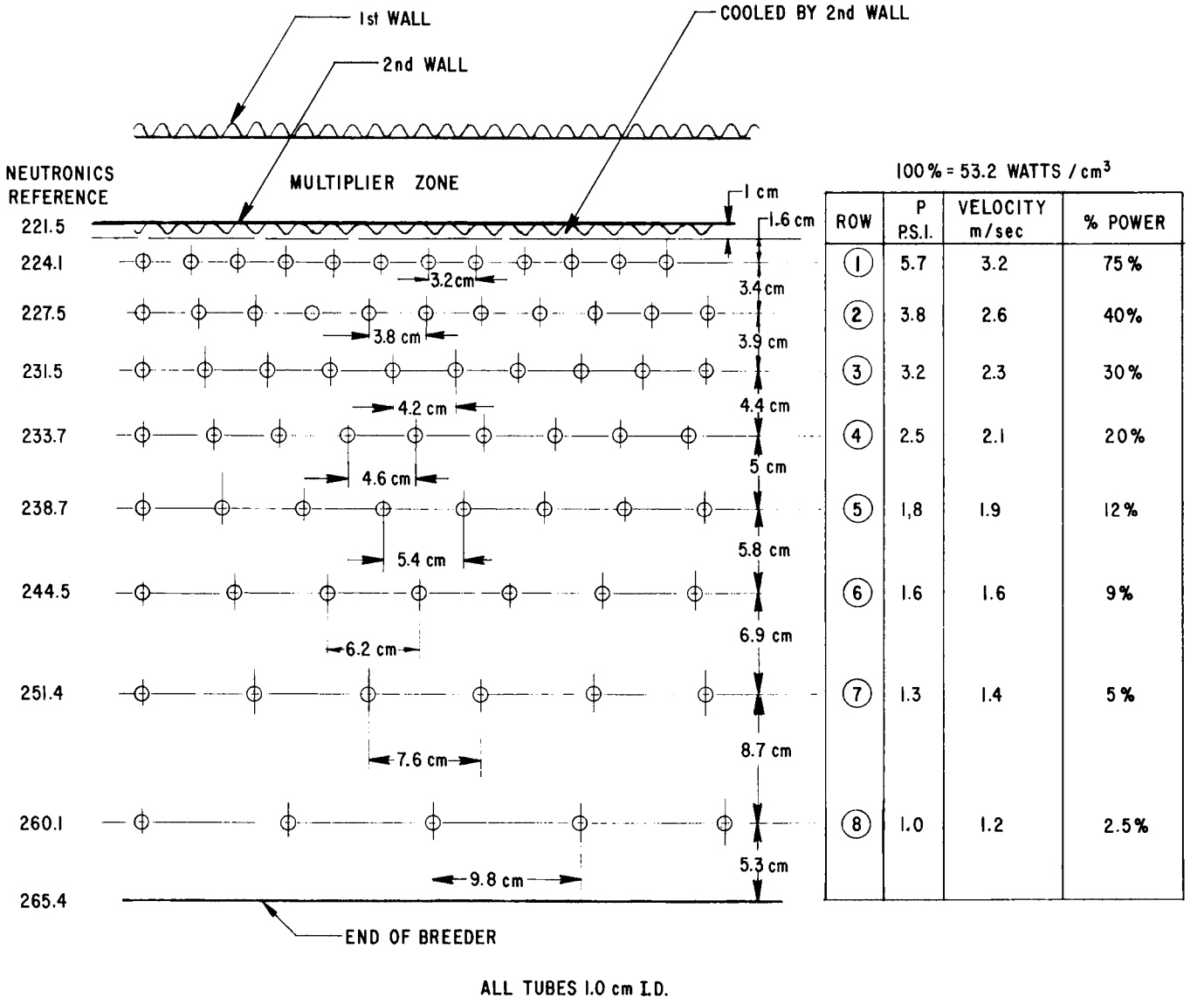

ROW	P P.S.I.	VELOCITY m/sec	% POWER
1	5.7	3.2	75%
2	3.8	2.6	40%
3	3.2	2.3	30%
4	2.5	2.1	20%
5	1,8	1.9	12%
6	1.6	1.6	9%
7	1.3	1.4	5%
8	1.0	1.2	2.5%

Figure 10-86. Breeder coolant tube spacing and parameters

graphite, the basic reflector material. The reflector/manifold zone is thus defined to be all the parts of the blanket assembly which are located to the rear of the breeder zone.

Major design features of the zones are: the manifold and header system which connects to the breeder coolant tubes; a pressure-tight cavity surrounding the manifold/header region; a solid graphite reflector region in the central portion of the module; and a removal and replacement method which does not require cutting or unsplicing of either the sector support frames or the large manifold tubes.

The large manifold tubes begin at the mechanical disconnects which are located outside the shield door and anti-torque panel (see Figs. 10-84 and 10-85), and extend inward toward the reactor centerline to the sector itself. They enter on two different horizontal levels, one approximately level with the uppermost module and the other level with the lowest module. This option was selected over a single level entry at the reactor midplane, to avoid locating large-diameter tees and elbows in the region of the limiter/ vacuum duct which could block particle flow. Four manifold tubes are located at each level, one inlet and one outlet for each of the two coolant circuits. As they join the sector, the inlet tubes each branch into two tubes (to feed the outer and inner regions of the blanket sector) either immediately upon joining the sector or after being directed across the sector to the other side. Flow velocities in the manifold tubes are 20 m/s until the flow is near the sector. The flow then passes through a short transition zone with a 4:1 length-to-radius taper to reduce coolant velocity to 6 m/s for the remainder of the manifold system, to avoid turbulence and flow instability problems in regions of branching flow and rapid changes in flow area. (The previous flow sequence is reversed for outlet tubes.) All manifold tube connections are welded. There are no mechanical (i.e., non-welded) connections for any vent, vacuum, gas or fluid lines within the vacuum boundary of the reactor.

The manifold tubes leading to the mechanical disconnects from both the large (16.2°) and small (13.8°) blanket sectors are located so that blanket removal and replacement operations are simplified. The tube centerlines are perpendicular to the plane of the shield door and anti-torque panel so that those two components can be removed by maintenance devices in a straight line

motion directly away from the reactor centerline. (Vertical and angular movement of the anti-torque panel to clear the EF coils is done after the panel has been pulled clear of the tubes). The vacuum boundary in the tube region is accomplished by elastomeric O-rings, which seal the gap between the outside of the shield door and a seal plate attached to a "pass-through" which surrounds and seals groups of manifold tubes and other lines which penetrate through the door and panel. Force on the seal plate to compress the O-rings -- two at each plate -- is provided through a set of double-motion latches, all of which operate as a unit around the seal plate with a single actuating motion for latching or unlatching. (These latches were developed by McDonnell Douglas for the Gemini space capsule hatch, and a similar design is currently in use on the Space Shuttle Orbiter.)

At the blanket modules the manifolds are each connected to smaller-diameter headers, each approximately 25 cm in length. The ends of the breeder coolant tubes are connected to stubs protruding from the headers. The manifolds and headers are structurally supported from the thick structural panel separating the breeder and reflector/manifold zones. Access is provided for welding of the connections by allowing 4 cm of straight length at the coolant tube/header stub joint, and 6 cm at the header/manifold connection.

The manifolds and headers are enclosed in a pressure-tight cavity, formed by the (1) breeder zone back plate, (2) central reflector zone sidewall, (3) walls extending to the rear from the sides of the back plate, and (4) a closure plate across the back of the zone extending from the partial frames to the central reflector zone walls. All the cavities for each module in a sector are joined together in series by connecting tubes. The cavity in the modules nearest the manifold inlet and outlet are connected to a venting pipe which extends through the shield door to the mechanical disconnects. A vacuum system outside the reactor is connected to this pipe, to pull from the cavities any accumulation of water vapor which would result from leaking of coolant through any of the welds contained in the cavities. Although the mean time between "failure" (leaks) for the coolant system may be relatively high because of the many coolant pressure boundary welds, the use of vented cavities will minimize the impact of the great majority of the potential leaks since the leaked coolant will be vented away and will not enter the

breeder or the vacuum chamber. Therefore, such leaks are not expected to result in reactor shutdown between annual maintenance periods.

The partial frames at the sides of the back plate are designed to be bolted to the L-shaped permanent sector support frames. This permits removal of the module -- from the first wall through the headers -- by unbolting the module along the frames and cutting all header/manifold welds. Access to those welds for cutting and rewelding is gained by cutting out the closure plates. To permit module removal, the walls which seal around the manifold tubes at the poloidal ends of the zones are also cut, then rewelded once the replacement module has been installed.

10.9.2.5 Inner Blanket Module

The importance to reactor capital costs of minimizing tokamak power reactor inner shield and blanket thicknesses has been well demonstrated in previous studies. Accordingly, for the STARFIRE inner blanket it was considered necessary to modify the basic module design to minimize its thickness (depth), while still permitting removal of an adequate amount of thermal power in order to not reduce reactor efficiency. In addition, it was found necessary to breed tritium in the inner blanket to maintain an adequate net breeding ratio for the reactor. Thus, all the major zones and components of the basic module were retained for the inner blanket with the exception of the graphite reflector and the manifold/header system.

The direction of coolant flow in the first wall, second wall and breeder coolant tubes is vertical in the inner blanket rather than horizontal (toroidal) as in outer blanket modules. This permits manifolds and headers to be elimiated except at either end of the inner blanket, where more space is available. As illustrated schematically in Figs. 10-84 and 10-85, two of the four manifold tubes (one inlet, one outlet for each of two coolant circuits) which wrap around the top and bottom of the blanket sector, terminate in headers which feed the first wall, second wall, and odd and even breeder coolant tube banks in the same pattern as established for the other modules. This arrangement retains the dual circuit feature and minimizes the number of headers required for inner blanket coolant.

The thermal-hydraulic parameters calculated for the basic blanket module are slightly changed for the inner blanket to account for the longer flow paths. The manifold dimensions also change slightly to account for the slight nonsymmetry of manifold coolant flow rates which results from the header arrangement selected for the inner blanket. (If each manifold tube at the sector top and bottom terminated in a header for the inner blanket, the manifold flows would be exactly symmetrical for like manifolds both above and below the midplane.)

The blanket sector support frames are continuous from the rear of the outer blanket modules into the sides of the inner blanket modules, so that no additional inner blanket depth is needed to accommodate the frames. The helium purge gas flow is directed vertically through the breeder in the inner blanket, with inlet and outlet headers located in the same region as the coolant headers.

10.9.3 Integration of Other Subsystems

Limiter/Vaccuum -- Four limiter segments are located in each blanket sector, in an opening between outer blanket modules centered on the reactor midplane. This duct is 40 cm wide and extends across the width of each sector. The sector support frames are continuous across the opening, as are the helium purge inlet and outlet lines and the manifold/reflector zone vent lines.

The distance that the limiter penetrates into the plasma scrape-off zone can be adjusted without the blanket being removed from the reactor (see Chap. 8). This is accomplished by varying the pressure of the water coolant supplied to the piston near the rear of the limiter assembly. Limiter position with respect to the blanket is sensed through a set of hydraulic taps along the axis; monitoring of the taps permits coolant pressure to be adjusted to achieve the desired position. The remainder of the limiter is cooled using a separate 4.2 MPa (600 psi) water coolant circuit which is connected in series to each of two adjacent limiter segments in the four-segment set.

The limiter assembly is supported by pads attached to the two module walls which form the vacuum duct, and by brackets suspended from the rear of the same two modules. The limiter coolant circuits and the hydraulic pressure tap leads are routed through the shield door and anti-torque panel as part of a bundle which includes blanket coolant lines. Increased neutron streaming through the duct is accommodated by local modification of the shield or shield door composition in line with the duct.

Plasma Heating (rf) Duct -- The rectangular cross section rf duct assembly enters the second module of the small blanket sector horizontally just below the midplane, and protrudes through the module to the plane of the first wall. The module design is modified locally, with the thermal-hydraulic parameters of the first wall, second wall and breeder coolant tubes being changed in accordance with the reduced module widths. The self-cooled rf duct is supported from the sides of these shortened modules.

ECRH Duct -- This small tubular duct enters the small blanket sector along the bottom of the rf duct, and splits off to continue around the bottom of the sector to the module below the inner blanket. The ECRH duct then protrudes radially through the module to the first wall plane. The module is modified locally to support the duct, but alteration of the basic blanket design parameters is not required. The duct is self-cooling by means of coolant circulating inside the duct's hollow walls.

Tritium Purge -- One inlet line and one outlet line are used for the helium purge gas from the individual blanket sectors. Each line enters the blanket sector with the lower coolant line bundle, and splits through a wye connection to the four outer and five inner modules. The lines pass through the vented manifold/reflector region of each module in turn, along the inside of the frames. The helium is introduced to the breeding zone of each module through a series of connection tubes, spaced $\sim$ 25 cm apart, which extend from the inlet or outlet line through the vented region into the narrow gaps between the ends of the blocks of solid breeder and the lands between embossed channels on the inside of the module side wall, formed by the extensions of the second wall. The helium passes from the inlet plenum to the outlet plenum at the other side of the module through the 2-mm diameter purge gas holes formed in the solid breeder blocks.

Instrumentation -- Definition of the requirements for first-wall/blanket instrumentation has been addressed conceptually. The objective of this system is to be able to detect, on at least the sector level, any off-normal conditions in the first-wall/blanket which either require or cause an immediate reactor shutdown, or which are changing at a rate which could eventually require shutdown. An example of the latter condition would be detection of coolant, in vapor form, accumulating inside the vented manifold/reflector zone as the result of a leaking header/coolant tube weld within the zone.

In the event of a coolant system leak, one of the most important requirements is to be able to detect which of the two separate cooling circuits is involved. This is necessary because, for all but the smallest leaks, it is desirable to minimize the amount of water coolant leaked either into the failed blanket module or into the vacuum chamber. If flow to the leaking circuit can be shut off and the pressure reduced to near-ambient, the amount of cleanup effort and the chances for further damage (e.g., coolant leaking into the hot breeder of the failed module and expanding rapidly as steam inside the module) are minimized. Removal of blanket neutronic afterheat, in the time period between plasma quenching and blanket sector removal, can be easily accomplished for the failed sector by running coolant at a relatively low flowrate and pressure through all the modules of the sector using only the coolant circuit which is not leaking.

To distinguish which of the two circuits is leaking, it is possible conceptually to introduce low-activity, short-lived radioisotopes into the coolant. Sampling from various regions of the vacuum region and blanket can then determine which of the two isotypes is present in a leak situation, and thus indicate which circuit must be shut down when this becomes necessary. Detection of a leak situation and circuit identification will require sampling of:

- o helium purge gas;
- o gas and vapor pumped from sealed zone around manifolds and breeders;
- o gas and vapor pumped from reactor vacuum chamber into main vacuum pumps.

The isotope detection concept was not examined in depth to determine its feasibility. Potential problems include: (a) selection of isotopes meeting the requirements for short half-life and low activity; (b) masking of those isotopes by others produced in the reactor and/or coolant by fusion neutrons; (c) swamping of the detection system by small leaks from both circuits, prior to the occurrence of a larger leak in only one of the circuits. This area is considered to require further research and development effort.

The type of instrumentation required for the first-wall/blanket modules and sectors is identified in Table 10-71. Instrumentation for purposes other than detection of blanket off-nominal conditions (e.g., plasma control) is addressed in other report chapters as appropriate.

Table 10-71. Instrumentation Requirements for First-Wall/Blanket

- Measurements required for each FW/B module:
  - Coolant outlet temperature (in manifold)
- Measurements required for each FW/B sector:
  - Coolant inlet and outlet temperature } in
  - Coolant inlet and outlet pressure } manifolds
  - Helium purge gas outlet temperature, % H_2O, isotope type, and concentration
  - Manifold/header zone: gas/vapor % H_2O, isotope type, and concentration

Electrical Intersector Jumpers -- Plasma control in tokamak power reactors is accomplished in part by making the first wall the electrical equivalent of a continuous conducting shell both toroidally and poloidally. For the sector approach used in the STARFIRE first-wall/blanket design, poloidal electrical continuity between adjacent modules is achieved through the continuous sector support frames to which the individual module support frames are attached in metal-to-metal contact. Designing for toroidal continuity, however, is more difficult because the connection between sectors cannot be permanent, to permit the sectors to be readily removed and replaced during maintenance operations.

For toroidal continuity, the connectors should be located along the facing module sides of adjacent sectors. It is strongly preferred that the electrical intersector connector (EIC) be located at as close to the first wall plane as possible, to minimize the L/R time for the first wall (which minimizes magnetic pressure acting inward on the first-wall/blanket toward the plasma during a disruption) and to minimize torque forces acting on the blanket during a disruption (which are proportional to the distance between the first wall and the EIC). Locating the EIC close to the first wall causes three significant design problems, however. First, the EIC must engage and disengage remotely and/or automatically, since a position near the first wall is virtually inaccessible with all blanket sectors installed. Second, the problems of radiation damage to the materials are greatly increased since the EIC is very close to the plasma. Third, the dimensions of the EIC in the toroidal direction must be kept very small so that significant volume is not taken away from the blanket module itself, which would impact tritium breeding and recoverable thermal power.

Four different concepts for the EIC were examined; these are illustrated in Fig. 10-87. The Bourdon tube and expanding tube concepts each require internal pressurization and depressurization to engage and disengage, which further complicates the blanket mechanical design. In addition, the two concepts each involve initial large-scale plastic deformation of the thin-walled metal tubes, which is considered difficult to achieve reliably on a cyclic basis over the life of the blanket without leaking. The bellows concept utilizes the blanket water coolant pressure to expand elastically to contact the adjacent sector; it retracts upon depressurization of the coolant circuit. The concept takes a minimum of space between sectors, but replaces a small fraction of the neutron multiplier volume with water coolant, which detracts from the tritium breeding ratio. On balance, the bimetallic spring concept was judged the best overall. The device is actuated by its internal temperature increase as a result of blanket pre-heating before plasma ignition, and thus requires no pressure source for actuation, which precludes leakage problems.

The EIC at a first-wall location is recognized as a sub-system requiring further research and development. Among the specific questions which should be addressed are these:

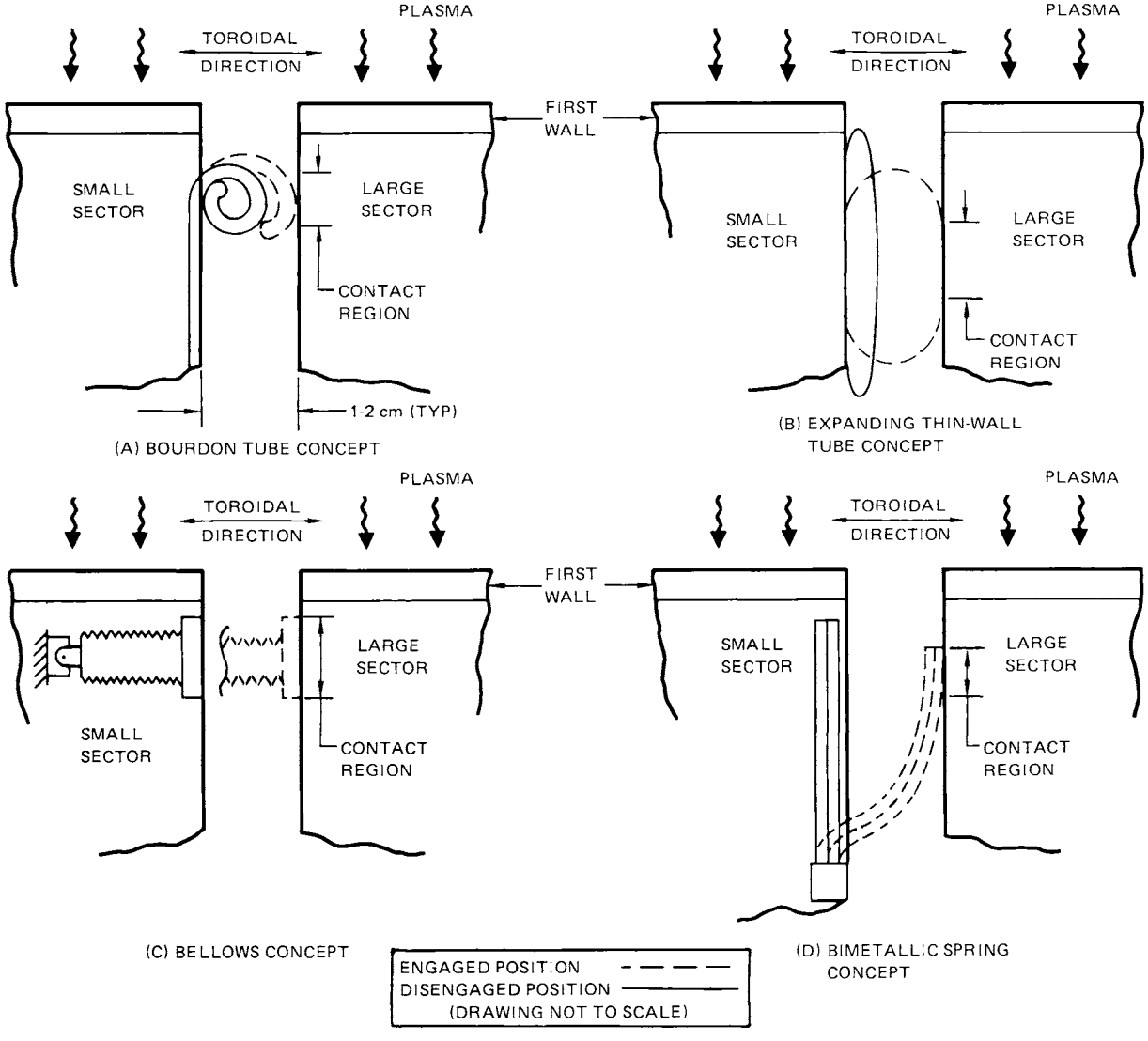

Figure 10-87. Design concepts for electrical intersector connectors.

- o Prevention of vacuum welding or resistance welding of mating EIC contact surfaces from adjacent sectors. (Approximately 2 MA current must be conducted between sectors during a plasma disruption.)
- o Development of two materials for bimetallic spring which (1) are resistant to radiation damage over the blanket design life, and (2) have sufficiently differing thermal expansion coefficients to work acceptably as a spring using the STARFIRE ambient to pre-ignition temperature change.

References

1. D. L. Smith, et al., "Fusion Reactor Blanket/Shield Design Study," joint Argonne National Laboratory/McDonnell Douglas Astronautics Company Report, ANL/FPP-79-1 (July, 1979).

2. B. Badger, et al., "UWMAK-II, A Conceptual Tokamak Power Reactor Design," University of Wisconsin, UWFDM-112 (1975).

3. M. A. Abdou, L. J. Wittenberg and C. W. Maynard, "A Fusion Design Study of Nonmobile Blankets with Low Lithium and Tritium Inventories," Nuclear Technology 26 (1976).

4. D. W. Kearney, et al., "Conceptual Design Study of a Noncircular Tokamak Demonstration Fusion Power Reactor," General Atomic Company, GA-A13992 (November, 1976).

5. R. L. Hagenson, et al., "The Reversed-Field Pinch Reactor (RFPR) Concept," Los Alamos Scientific Laboratory, LA-7973-MS (1979).

6. J. R. Powell, et al., "Preliminary Reference Design of a Fusion Reactor Blanket Exhibiting Very Low Residual Radioactivity," Brookhaven National Laboratory, BNL-19565 (1974).

7. T. Kurasawa, et al., J. Nuclear Materials 80, 48 (1980).

8. D. L. Smith (private communication).

9. A. B. Johnson, et al., "Tritium Production from Ceramic Targets," Battelle Northwest Laboratory, BNWL-2097 (1976).

10. D. L. Smith, R. G. Clemmer and J. W. Davis, Proc. 8th Symposium on Engineering Problems of Fusion Research, San Francisco, p. 433 (1979).

11. R. M. Arons (private communication).

12. R. N. Singh and J. T. Dusek, Proc. 1980 International Symposium on Grain Boundary Phenomena in Electronic Ceramics, Chicago (1980) - In Press.

13. R. M. Arons and J. T. Dusek, Argonne National Laboratory (1980) - Unpublished research.

14. T. S. Elleman, et al., Proc. Third Topical Meeting on the Technology of Controlled Nuclear Fusion, Santa Fe, NM, Vol. 2, p. 763 (1978).

15. W. Bauer, et al., Proc. Second Conference on Surface Effects in Controlled Fusion Devices, San Francisco (1976); also J. Nuclear Materials 63 (1976).

16. G. M. McCracken, et al., Proc. Third International Conference on Plasma Surface Interactions in Controlled Fusion Devices, Abingdon-Oxfordshire, UK (1978); also J. Nuclear Materials 76 & 77 (1978).

17. B. L. Doyle, et al., "Saturation and Isotopic Replacement of Deuterium in Low-Z Materials" - To be published.

18. C. C. Baker, et al., "STARFIRE - A Commercial Tokamak Reactor: Interim Report," Argonne National Laboratory, ANL/FPP/TM-125 (1979).

19. J. S. Karbowski, et al., "Tokamak Blanket Design Study," Oak Ridge National Laboratory, ORNL/TM-6847 (1979); also ORNL/TM-7049 (1980).

20. E. H. VanDeventer, et al., "A Review of Fusion-Related Experimentation on Blanket/Tritium Processing and Hydrogen-Isotope Migration at ANL," Proc. Symposium on Tritium Technology in Fission, Fusion and Isotopic Applications, Dayton, Ohio, CONF-800427, p. 144 (April 29-May 1, 1980).

21. J. W. Davis and D. L. Smith, J. Nuclear Materials 85 & 86, p. 71 (1979).

22. R. E. Nygren, J. Nuclear Materials 85 & 86, p. 861 (1979).

23. F. W. Wiffen, Proc. International Symposium on Effects of Radiation on Structural Materials, Richland, WA, ASTM (July, 1978).

24. A. L. Ward, J. M. Steicher and P. L. Knecht, Irradiation Effects on the Microstructure and Properties of Metals, American Society for Testing and Materials, ASTM STP 611, p. 156 (1976).

25. J. Rawls, Presented Workshop on Ferritic Steels for Fusion Reactor Applications, U.S. Department of Energy, Washington, DC (July 30-31, 1979).

26. "Design Data," Vol. 1, Nuclear Systems Materials Handbook, Hanford Engineering Development Laboratory, TID-26666 (1977).

27. S. F. Pugh and C. A. Little, Editors, Proc. International Conference on Ferritic Steels for Fast Reactors and Steam Generators, British Nuclear Energy Society, London (1978).

28. C. A. Little, J. Nuclear Materials 87, p. 211 (1979).

29. "Alloy Development for Irradiation Performance Quarterly Progress Report for Period Ending June 30, 1979," U.S. Department of Energy (1979).

30. J. A. Spitznagel, et al., J. Nuclear Materials 85 & 86, p. 629 (1979).

31. M. M. Paxton, B. A. Chin, C. R. Gilbert and R. C. Nygren, J. Nuclear Materials 80, p. 144 (1979).

32. E. E. Bloom, J. Nuclear Materials 85 & 86, p. 795 (1979).

33. R. M. Lyon, Editor, Liquid Metals Handbook, Department of the Navy and Atomic Energy Commission, U.S. Government Printing Office, Washington, DC (1954).

34. W. E. Berry, Corrosion in Nuclear Applications, John Wiley and Sons, Inc., New York (1971).

35. Beryllium Sheet and Plate, Kawechi-Berylco Industries, Inc., Bulletin 3027-PD7.

36. I. H. Gelles, V. D. Barth, "Beryllium, Review of Metals," BMI (1973).

37. D. Webster, D. D. Crooks, Met. Trans. 6A, p. 2049 (1975).

38. E. Chandler, H. M. Lindsay, H. Li, D. Pugh and J. S. White, J. Mater. Sci. 8, p. 1788 (1973).

39. C. R. Tipton, Editor, Reactor Handbook, Vol. 1 - Materials, Interscience Publishers, Inc., New York (1960).

40. J. E. Kontorovich, "Surface Hardening of Steel with Beryllium and Boron," Metallovedence i Termicheskaya Obrabotka Metallov, No. 8, 16 (1969).

41. The Metallurgy of Beryllium, Chapman and Hall, Ltd., London (1963).

42. W. R. Griffitts, "Beryllium," United States Mineral Resources, Geological Survey Professional Paper 820, D. D. Brobst, W. P. Pratt, Editors, U.S. Government Printing Office, Washington, DC (1973).

43. "Beryllium," Mineral Commodity Profile, U.S. Bureau of Mines (August, 1979).

44. M. Hansen, Constitution of Binary Alloys, Second Edition, McGraw Hill Book Co., New York (1958).

45. F. A. Shunk, Constitution of Binary Alloys, Second Supplement, McGraw Hill Book Co., New York (1969).

46. J. H. Westbrook, Editor, Intermetallic Compounds, John Wiley and Sons, Inc., New York (1967).

47. K. Farrell, D. N. Brask, "Radiation Damage in a High Strength Ordered Alloy," Metals and Ceramics Division Materials Science Program Annual Progress Report for Period Ending June 30, 1979, Oak Ridge National Laboratory, ORNL-5589, p. 161 (1979).

48. W. M. Stacey, Jr., et al., "Tokamak Experimental Power Reactor Conceptual Design," Argonne National Laboratory, ANL/CTR-76-3 (1976).

49. R. Wiswall and E. Wirsing, "The Removal of Tritium from Fusion Reactor Blankets," Brookhaven National Laboratory, BNL-50748 (1977).

50. JANEF Thermochemical Tables, Dow Chemical Company, Midland, MI (1978).

51. J. R. Hoffman, Nuclear Science and Engineering 68, p. 73 (1978).

52. D. Okula and D. K. Sze, "Tritium Recovery from Solid Breeders: Implications of the Existing Data," University of Wisconsin, UWFDM-351 (1980).

53. B. L. Doyle, et al., "Saturation and Isotopic Replacement of Deuterium in Low-Z Materials," Sandia National Laboratories - To be published.

54. T. Tanifuji, et al., "Tritium Release from Neutron Irradiated Li_2O," Japan Atomic Energy Research Institute, JAERI-Memo-8829 (1980).

55. W. F. Vogelsang, "Breeding Ratio, Inventory and Doubling Time in a D-T Fusion Reactor," Nuclear Technology 15, p. 470 (1972).

56. J. R. Powell, et al., Proc. of the First Topical Meeting on the Technology of Controlled Nuclear Fusion, Vol. I, p. 533 (1976).

57. O. W. Lazareth and J. R. Powell, "Alternatives to Beryllium for Neutron Multiplication for Solid CTR Blankets," Transactions of the American Nuclear Society 22, p. 65 (1975).

58. W. G. Davey, et al., "Use of Tantalum and Liquid Lead in a Fusion Reactor Blanket," Argonne National Laboratory, AP/CTR/TM-21 (1976).

59. Y. Gohar, "An Assessment of Neutron Multipliers for DT Solid Breeder Fusion Reactors," Transactions of the American Nuclear Society 34, p. 52 (1980).

60. M. B. Emmett, "The MORSE Monte Carlo Radiation Transport Code System," Oak Ridge National Laboratory, ORNL-4972 (1975).

61. R. W. Roussin, et al., "The CTR Processed Multigroup Cross Section Library for Neutronics Studies," Oak Ridge National Laboratory, ORNL/RSIC-37.

62. Y. Gohar and M. A. Abdou, "MACKLIB-IV, A Library of Nuclear Response Functions Generated with MACK-IV Computer Program from ENDF/B-IV," Argonne National Laboratory, ANL/FPP/TM-106 (1978).

63. S. P. Timoshenko and G. H. MacCullough, Elements of Strength of Materials, D. Van Nostrand Company, Inc. (1956).

64. D. F. Schoeberle, J. N. Kennedy and T. Belytschko, "Implicit Temporal Integration for Long-Duration Accident in a Structural Response Code - STRAW," Argonne National Laboratory, ANL-8136 (October, 1974).

65. J. M. Rawls, et al., "Assessment of Martensitic Steels as Structural Materials in Magnetic Fusion Devices," General Atomic Company, GA-A15749 (1980).

66. C. K. Youngdahl and D. L. Smith, "Stress and Lifetime of First Wall Structural Materials," J. Nuclear Materials 85 & 86, p. 153 (1979).

67. ASME Boiler and Pressure Vessel Code, 1977 Code Cases - Nuclear Components, 1977 Edition, Case N-47 (1592-10) (1977).

68. D. Gurgren, Design Methods for Power Plant Structures, C. P. Press, Jamaica, New York (1975).

69. ASME Boiler and Pressure Vessel Code, Section III-Rules for Construction of Power Plant Components, Division 1-Subsection NB-Class 1 Components (1977).

70. ASME Boiler and Pressure Vessel Code, Section III-Rules for Construction of Nuclear Power Plant Components, Division 1-Appendix G (1977).

71. Workshop on Ferritic Steels for Fusion Reactors Applications, Eighth ADIP Task Group Meeting, Washington, DC (July 30-31, 1979).

72. D. J. Michel and G. E. Korth, "Effects of Irradiation on Fatigue and Crack Propagation in Austenitic Stainless Steels," Radiation Effects in Breeder Reactor Structural Materials International Conference, Scottsdale, Arizona, p. 117 (June 19-23, 1977).

73. E. E. Bloom and W. G. Wolfer, "In-Reactor Deformation and Fracture of Austenitic Stainless Steel," Effects of Radiation on Structural Materials, ASTM STP 683, p. 656 (1979).

74. P. J. Maziasz and T. K. Roche, "Fabrication of Homogeneous Path A Prime Candidate Alloy," Alloy Development for Irradiation Performance Quarterly Report #8, U.S. Department of Energy, DOE/ET-0058/7, p. 83 (1979).

75. Metals Handbook, 8th Edition, Vol. 8, American Society for Metals, Metals Park, Ohio (1973).

TABLE OF CONTENTS

LIST OF FIGURES

LIST OF FIGURES (Contd.)

LIST OF TABLES

11.1 INTRODUCTION

The functions of the shielding system are: (1) to protect reactor components from radiation damage and nuclear heating, as well as reduce induced activation that may result in maintainability and disposal problems; and (2) to protect workers as well as the general public from radiation exposure at all times during operation, shutdown, scheduled maintenance, and off-normal incidents. The shield system in STARFIRE consists of the blanket, primary bulk shield, penetration shield, component shield, and biological shield.

The interrelations among the shield and reactor components in a fusion reactor are strong and complex. The shield design in STARFIRE has evolved from a comprehensive approach that involved the following: (1) recognition of the importance of the shield system and its impact on reactor component reliability, simplicity, maintainability, and economics; (2) full account of the shielding considerations in the selection process of key reactor subsystems from the early stages of the reactor design; clear examples of this are the choices of the limiter instead of divertor for plasma impurity control and exhaust and the selection of lower-hybrid rf system for plasma auxiliary heating in preference to neutral beams; and (3) comprehensive trade-off analyses for determining the material composition and dimensions of the shield components.

Another unique feature of the STARFIRE design is that the shield system also serves as the vacuum boundary. Compared to the more conventional design concepts in which the boundary is located near the plasma region, the present shield design concept has several important advantages. They are: (1) direct accessibility to the vacuum boundary seals; (2) location of the seals in a low-neutron fluence region; and (3) incorporation of the vacuum pumping system without the inherent design complexities of providing a torus evacuation duct behind the limiter. A detailed study on the shield mechanical design is presented in Sec. 11.4.

This chapter presents the tradeoffs as well as the analysis of the reference design for the bulk shield in Sec. 11.2 and for the penetration shields in Sec. 11.3. Important aspects of radioactivity are discussed in this chapter but only to the extent of their impact on the shield design. Detailed radioactivity calculations are presented in Chap. 12.

11.2 BULK SHIELD

The primary bulk shield circumscribes the blanket and consists of two parts: (1) the inboard shield; and the (2) the outboard shield. The distinction between the inboard and outboard shields is necessary as the design objectives and constraints are quite different in the two regions.

11.2.1 Inboard Shield Design

The main function of the inboard shield is to protect the components of the superconducting toroidal field (TF) coils. The magnet protection requirements[1] are: (1) reduction of the nuclear heating in the magnets to the levels allowed by both the total power required to run the refrigerators and the maximum heating rates imposed by practical limits for coil design; and (2) reduction of the nuclear radiation to the levels allowed by tolerable radiation damage to the components of the superconducting magnets; these components are: (a) the superconductor, (b) the normal conductor (stabilizer), (c) electrical and thermal insulators, and (d) structure.

The most critical design constraint on the inboard shield is the large sensitivity[1] of the reactor performance and economics to the radial thickness Δ_{BS}^{i}, from the first wall to the location of the maximum magnetic field. For a reactor such as STARFIRE with a given size and maximum toroidal-field, an increase of 10 mm in Δ_{BS}^{i} results in a reduction in the fusion power by $\sim$1%. This large sensitivity mandates that the selection of Δ_{BS}^{i} and shielding materials must evolve from a careful optimization of the overall reactor system. This optimization was carried out for STARFIRE using a global parametric systems code as discussed in Chap. 5.

An important factor that makes the above optimization possible is the fact that there is a tradeoff between the radiation level at the magnets (and hence the magnitude of Δ_{BS}^{i}) and the cost of the magnets. The degradation in the critical current density of the superconductor and the increase in the resistivity of the stabilizer can be accommodated by increasing the amounts of superconductor and stabilizer, respectively. Furthermore, magnet annealing recovers most of the damage in the superconductor and stabilizer, with the degree of recovery dependent on the annealing temperature. However, one problem that tends not to be amenable to tradeoffs is the tolerable radiation level in the TF coil insulators. Substantial radiation damage to insulators cannot be

accommodated by a simple increase in the amount of insulator. Furthermore, the problem is compounded by the fact that radiation damage to organic insulators is irreversible. Therefore, the TF coil insulators must be designed to last the lifetime of the plant. It has been shown[2] that if the insulators can withstand a dose of $>10^8$ Gy, then the limiting design constraint on the radiation level at the magnet is generally determined by the increase in the resistivity of the stabilizer, provided that the TF coils are annealed once every ten years or more often. Radiation damage to the insulators is more limiting on the inner shield design if the maximum tolerable dose is $<10^8$ Gy. Fortunately, it was shown recently that Kapton insulators can withstand a radiation dose of up to $\sim 10^8$ Gy at cryogenic temperatures. These experiments are not definitive because the experiments used mostly gamma-ray irradiation while most of the dose in the organic insulators in the TF coils comes from direct neutron interaction. It is assumed here that for the time frame of STARFIRE, organic insulators that can sustain a dose not much less than 10^8 Gy will be available. The subject of radiation effects in the components of superconducting magnets has been covered in several publications that are referenced in a recent review article by Brown.[3]

In the reference design, the value of Δ_{BS}^{i} is 1.2 m. This includes space for 9-cm vacuum gaps between the blanket and shield, shield and TF coils, and thermal insulation inside the TF vacuum tank; 3-cm vacuum tank (Fe14Mn2Ni2Cr); and 7-cm helium vessel (stainless steel). The inner blanket is 37 cm thick (with an average density factor of 0.7) and must breed tritium as the tritium breeding margin with solid breeders is small. Thus the space available for the inboard shield is 64 cm. The optimized composition of the inner shield is shown in Table 11-1. The shield consists primarily of alternating layers of tungsten and boron carbide "mixtures". These mixtures are defined in Table 11-2 and include 10% water and 10% Fe-1422 which consists of iron, 14 wt-% manganese, 2 wt-% nickel, and 2 wt-% chromium. The use of expensive materials such as tungsten and boron carbide is justified because the volume of the inboard shield (being on the inner side of the torus) is relatively small and the additional expense is compensated for by the reduction in reactor size resulting from a smaller Δ_{BS}^{i} when tungsten and boron carbide are used. However, two cautionary remarks are in order. First, price of tungsten tends to fluctuate and projecting future trends in its cost is difficult. Second, there are uncertainties in the nuclear data for tungsten that will have to be resolved by integral

Table 11-1. Toroidal Field Magnet, Inboard Shield, and Inner Blanket Neutronic Parameters for STARFIRE Reference Design

Radius (cm)		Thickness	
From	To	(cm)	Mixture or Element per Zone
236	243	7	Type 304 stainless steel
243	313	70	Low-field portion NbTi mixture[a]
313	366	53	High-field portion Nb_3Sn mixture[a]
366	373	7	Type 304 stainless steel
373	378	5	Thermal insulator
378	381	3	Fe-1422
381	383	2	Vacuum
383	385	2	Fe-1422
385	392.5	7.5	Boron carbide mixture[a]
392.5	400	7.5	Tungsten mixture[a]
400	407.5	7.5	Boron carbide mixture[a]
407.5	415	7.5	Tungsten mixture[a]
415	422.5	7.5	Tungsten mixture[a]
422.5	430	7.5	Boron carbide mixture[a]
430	437.5	7.5	Tungsten mixture[a]
437.5	445	7.5	Tungsten mixture[a]
445	447	2	Fe-1422
447	449	2	Vacuum
449	451	2	PCA steel
451	479	28	Tritium breeding
479	480	1	Second wall
480	485	5	Neutron multiplier
485	486	1	First wall

[a]See Table 11-2.

Table 11-2. Material Composition by Volume for Each Mixture Used in STARFIRE Inboard Reference Design

Mixture	Composition by Volume Percent	Density Factor
Tungsten	80% tungsten	0.95
	10% Fe-1422	1.0
	10% H_2O	1.0
Boron carbide	80% B_4C	0.95
	10% Fe-1422	1.0
	10% H_2O	1.0
NbTi mixture	2% superconductor NbTi	1.0
	32% copper	1.0
	38% Type 304 stainless steel structure	1.0
	24% helium	1.0
	4% insulator	1.0
Nb_3Sn mixture	4% superconductor Nb_3Sn	1.0
	35% copper	1.0
	30% Type 304 stainless steel structure	1.0
	27% helium	1.0
	6% insulator	1.0

experiments. Therefore, the use of tungsten in the inboard shield will have to be reassessed in the future.

Table 11-3 shows the maximum nuclear heating in the TF coils. The maximum heating in the conductor is $\sim 2 \times 10^{-5}$ MW/m^3 which is several orders of magnitude lower than the heat removal capacity in the system dictated by possible Joule losses in off-normal conditions. Table 11-4 shows the maximum absorbed dose to various insulators after 40 yr of operation at an average plant availability factor of 0.75. The maximum dose in the thermal insulator (immediately inside the helium tank) is 2.4×10^7 Gy. A dielectric break is used in the shield as described later in Sec. 11.4. The maximum dose in this dielectric break is 7.4×10^7 Gy and occurs at 50 mm from the back of the shield. Table 11-5 shows the radiation damage-related parameters for the copper stabilizer. The maximum radiation-induced resistivity is 2.2×10^{-10} Ω-m after 40 yr of operation. This result is based on magnet annealing every 10 yr with 83% recovery. Figure 11-1 shows the variation of the induced resistivity with depth in the TF coils.

Table 11-3. Maximum Nuclear Heating Rates in the Inboard Section of the Toroidal Field Coils (MW/m^3)

Component	Neutron	Gamma	Total
Vacuum tank	6.50×10^{-6}	4.11×10^{-5}	4.76×10^{-5}
Helium tank	4.20×10^{-6}	2.76×10^{-5}	3.18×10^{-5}
Superconductor	2.20×10^{-6}	1.32×10^{-5}	1.54×10^{-5}

Table 11-4. Maximum Insulator Dose After 40 yr of Operation at 0.75 Availability Factor (Gy)

Component	Neutron	Gamma	Total
Dielectric break (in the shield, 5 cm from the back)	6.24×10^{7}	1.17×10^{7}	7.41×10^{7}
Thermal insulator	2.10×10^{7}	0.29×10^{7}	2.39×10^{7}
Electrical insulator	1.06×10^{7}	0.16×10^{7}	1.22×10^{7}

Table 11-5. Maximum Irradiation Damage in the Copper Stabilizer

Maximum fast neutron fluence (E > 0.1 MeV) after 40-yr operation	1.87×10^{21} n/m^2
Maximum radiation-induced resistivity after 10-yr operation	1.44×10^{-10} Ω-m
Maximum atomic displacement rate after 10-yr operation	1.34×10^{-4} dpa

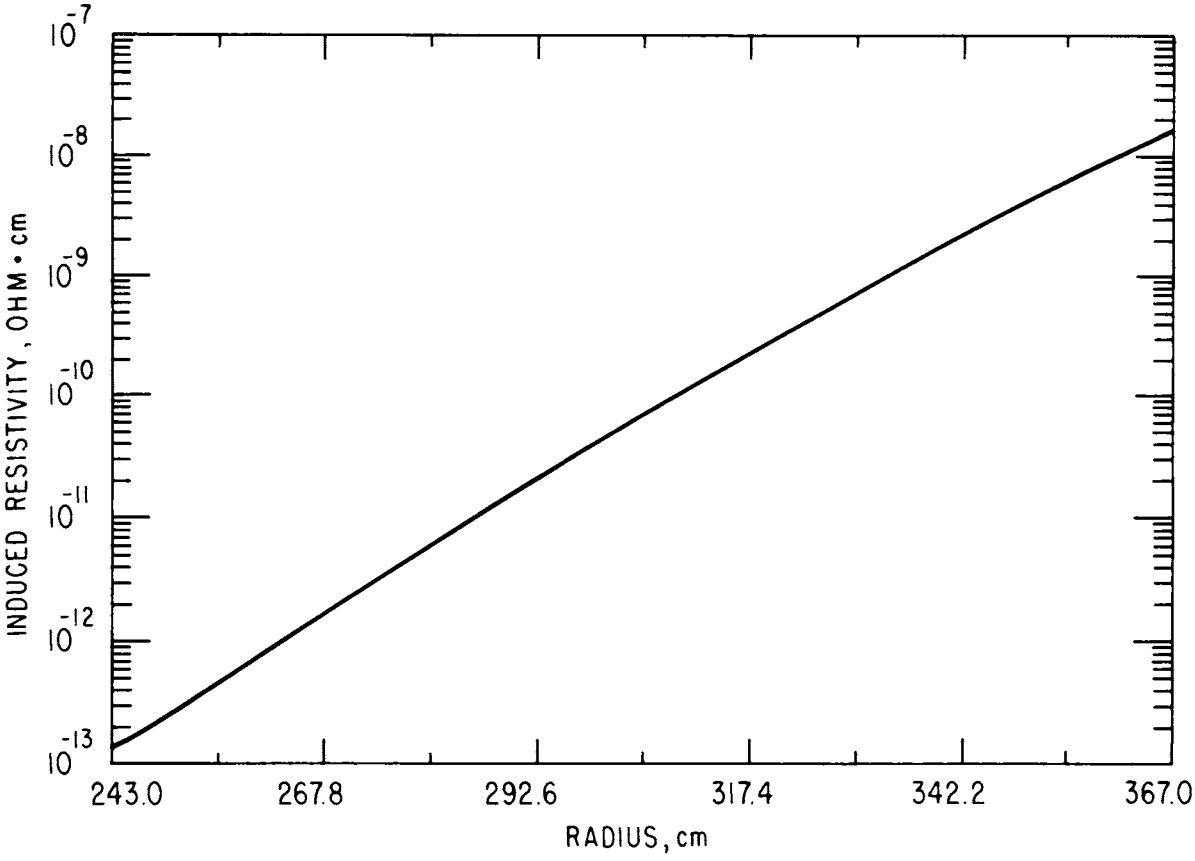

Figure 11-1. Copper-induced resistivity after 10-yr operation.

The reference inboard shield composition was derived as a result of a series of calculations aimed at optimizing the performance and minimizing the cost. Figure 11-2 shows the maximum dose in the thermal insulator after 40-yr operation as a function of the tungsten concentration. A homogeneous mixture of tungsten, water, and boron carbide is used in the 64-cm inboard shield. The volume percentages of tungsten and water are varied as shown in the figure with the balance being B_4C. The results show that increasing the tungsten content from 30 to 50% reduces the dose to the insulators by more than a factor of 2. This beneficial effect is accompanied by an increase in the cost of the shield. At a given tungsten percentage, reducing the water (H_2O) content from 40 to 20% with a corresponding increase in B_4C reduces the dose by $\sim$30%. Figure 11-3 is similar to Fig. 11-2 except that the sensitivity of the induced resistivity of the copper to the tungsten content is shown. The trends are similar in the two figures. Based on these results, the percentage composition was selected, as shown earlier in Table 11-1, to be 50% W, 30% B_4C, 10% H_2O, and 10% Fe-1422. The water serves as a coolant and Fe-1422 is used as a structural and cladding material. In addition to engineering considerations, there are generally some

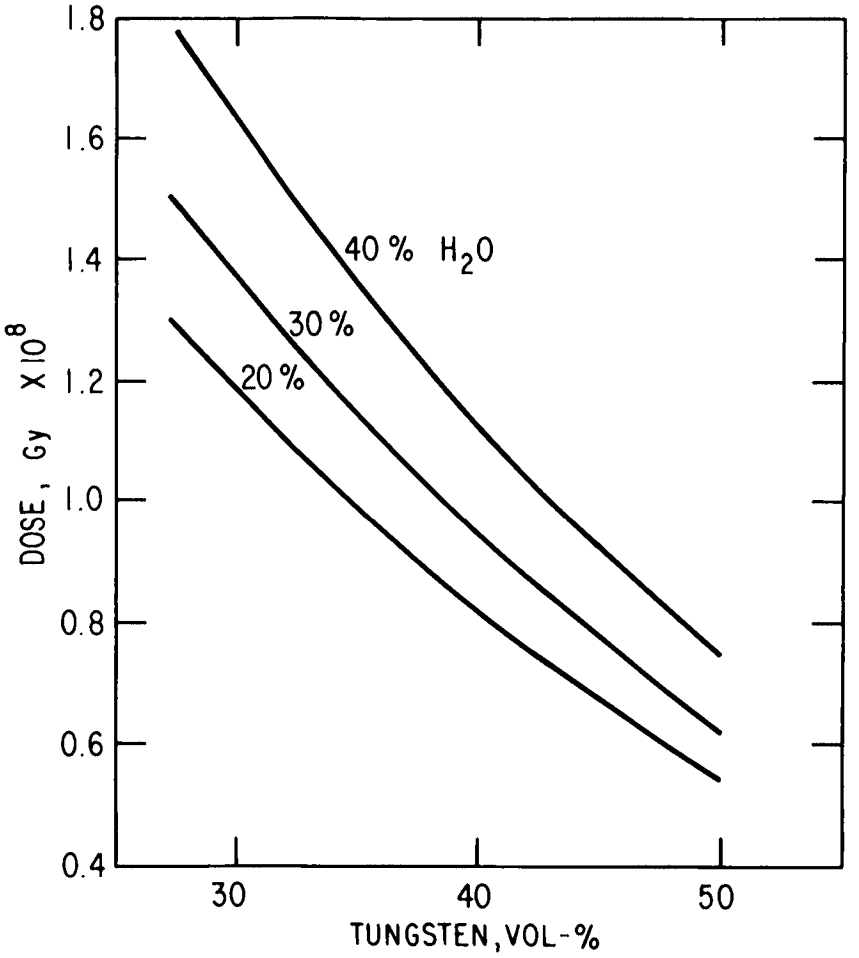

Figure 11-2. Thermal insulator dose after 40 yr of operation as a function of the tungsten concentration in the inboard shield for different water concentrations.

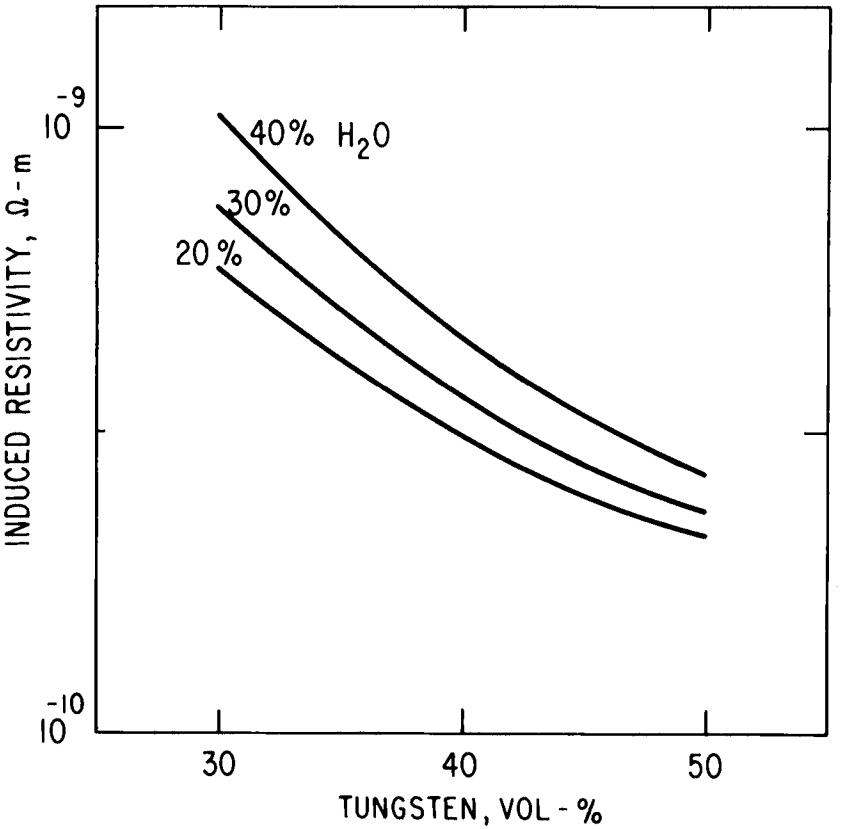

Figure 11-3. Copper-induced resistivity after 10 yr of operation as a function of the tungsten concentration in the inboard shield for different water concentrations.

benefits from heterogeneous arrangements. Table 11-6 shows the effect of several possible heterogeneous arrangements of tungsten and boron carbide on the dose to the dielectric seal and the radiation-induced resistivity in copper, which led to the final arrangement given in Table 11-1.

Table 11-6. Effect of the Material Arrangement on the Dose to the Dielectric Seal (in the Shield) at 40 yr of Operation and on the Maximum Reduced Resistivity in the Copper Stabilizer

	Shield Arrangement								Dose Gy $\times 10^{-8}$	ρ Ω-m $\times 10^{10}$
Magnet	W	W	W	W	W	B_4C	B_4C	B_4C	1.915	3.31
Magnet	W	W	W	B_4C	W	B_4C	W	B_4C	1.826	3.33
Magnet	W	W	B_4C	W	W	B_4C	W	B_4C	1.546	2.95
Magnet	B_4C	B_4C	B_4C	W	W	W	W	W	1.123	1.92
Magnet	B_4C	W	B_4C	W	B_4C	W	W	W	0.926	1.91
Magnet	B_4C	W	B_4C	W	W	B_4C	W	W	0.925	1.85
Magnet	W	B_4C	B_4C	W	W	B_4C	W	W	1.297	2.64

11.2.2 Outboard Bulk Shield Design

One of the functions of the outboard shield is similar to that of the inboard shield; namely, radiation protection of TF coils. The space at the top, bottom, and outer side of the reactor is not as restrictive as that on the inside. However, because of its geometrical location and relatively large volume, the outboard shield must satisfy an additional number of design requirements. Since the volume of materials in the outboard shield is rather large ($\sim$1300 m^3), shielding materials with low long-lived radioactivity should be selected to minimize the need for long-term radwaste storage and to permit recycling. Another important design goal for the STARFIRE shield is that the biological dose rate outside the shield should be about 1 mrem/h at 24 h after shutdown in order to facilitate access into the reactor building for maintenance. Furthermore, the outboard shield should provide neutron attenuation sufficient to prevent significant production of long-lived isotopes in the large volumes of materials in the TF and external EF coils and other reactor components out-

side the shield. Another important requirement is that the reactor building concrete wall should not be significantly activated nor should it require forced cooling because of nuclear heat deposition. All of these design requirements on the outboard bulk shield should, of course, be simultaneously applied to the penetration shield as discussed in the next section.

Multi-dimensional calculations were carried out for STARFIRE. The results of the two- and three-dimensional calculations are presented in the next section which focuses on penetrations and regions in their vicinity. The analysis described in the rest of this section is based on a one-dimensional model described in Table 11-7. The calculations were carried out with ANISN[4] using the S_8P_3 approximations. The associated data libraries, transport cross-section library (46 neutron and 21 gamma groups) and reaction response cross-section library, are taken from the VITAMIN-C[5] and MACKLIB-IV[6] libraries, both of which are processed from ENDF-B/IV.[7] For radioactivity analyses, the generalized activation code, RACC[8] is used along with the associated cross-section/decay data libraries of RACCXLIB and RACCDLIB.[9]

Prior to the final design selection, an extensive analysis on the shield optimization was carried out, focusing on four candidate shielding structural materials of Ti6Al4V, Al-2024, Type 304 stainless steel (304 SS), and Fe14Mn2Ni2Cr (Fe-1422).[10] The material compositions of these candidate alloys are given in Table 11-8. The Fe-1422 alloy composition has much more manganese and much less nickel and chrome than other typical austenitic steels. This alloy seems very attractive as a shield material because in addition to having as good radiation attenuation characteristics as the more conventional iron-base alloys, such as Types 316 and 304 stainless steels, it offers two important advantages. First it tends to produce less long-term activation due primarily to the reduced nickel content. In addition, since isotope ^{56}Mn which is one of the major short-lived radioactive products associated with manganese activation, has a decay life of only $\sim$2.6 h,[11] the reactor room activation shortly after shutdown exhibits a rapid decay which is attractive should maintenance personnel access be necessary. The second important advantage of using Fe-1422 in the shield is the significant reduction in the use of chromium. For example, the use of Fe-1422 in the shield reduces the chromium requirements by approximately 2000 metric tons compared to the case where Fe-1422 is replaced by Type 304 stainless steel. This is important to future commercialization since chromium resources in the United States are limited.

Table 11-7. The Dimensions and Material Composition of the STARFIRE Outboard Blanket/Shield Design Used in the One-Dimensional Analysis

	Component	Outer Radius (m)	Thickness (m)	Composition
1.	Plasma	2.53	2.53	Vacuum
2.	Scrape-off	2.73	0.20	Vacuum
3.	First wall	2.74[a]	0.01	50% PCA + 27% H_2O
4.	Multiplier	2.79	0.05	100% Zr_5Pb_3
5.	Second wall	2.80	0.01	35% PCA + 17% H_2O
6.	Blanket	3.26	0.46	6.55% PCA + 3.26% H_2O + 52.16% $LiAlO_2$[b] + 3.26% He
7.	Reflector	3.41	0.15	5% PCA + 5% H_2O + 90% C
8.	Blanket jacket	3.43	0.02	100% PCA
9.	Coolant header	3.63	0.20	2.5% PCA + 18% H_2O
10.	Plenum	4.13	0.50	Vacuum
11.	Shield jacket	4.15	0.02	100% Fe-1422[c]
12.	HFS shield	4.65	0.50	5% Ti6Al4V + 65% TiH_2 + 15% B_4C + 15% H_2O
13.	MFS shield	5.05	0.40	70% Fe-1422 + 15% B_4C + 15% H_2O
14.	LFS shield	5.33	0.28	100% Fe-1422 (anti-torque panel)
15.	CO_2	5.83	0.50	CO_2
16.	Magnet dewar	5.86	0.03	100% Fe-1422
17.	Gap	5.91	0.05	Vacuum
18.	Helium vessel	5.98	0.07	100% 304 SS
19.	Magnet 1	6.51	0.53	4% Nb_3Sn + 35% Cu + 30% 304 SS + 4% insulator + 27% He
20.	Magnet 2	6.86	0.35	2% NbTi + 32% Cu + 38% 304 SS + 4% insulator + 24% He

(a) Based on the first-wall area of 755.8 m^2 and the major radius of 7 m.

(b) 60% ^6Li enrichment.

(c) Fe14Mn2Ni2Cr.

Table 11-8. Structural Material Composition

Element	PCA Stainless Steel		Type 304 Stainless Steel		Fe14Mn2Ni2Cr		Ti6Al4V	
	wt-%	atom/b-cm	wt-%	atom/b-cm	wt-%	atom/b-cm	wt-%	atom/b-cm
B	0.005	2.188(-5)						
C	0.05	1.971(-4)	0.046	1.813(-4)	0.58	2.309(-3)	0.01	2.267(-5)
N	0.01	3.380(-5)	0.038	1.284(-4)	0.019	6.487(-5)	0.008	1.555(-5)
O							0.065	1.106(-4)
Al	0.03	5.264(-5)					6.0	6.056(-3)
Si	0.5	8.427(-4)	0.47	7.921(-4)	0.23	3.916(-4)	0.01	9.695(-6)
P	0.01	1.528(-5)	0.026	3.974(-5)	0.015	2.316(-5)		
S	0.005	7.382(-6)	0.012	1.772(-5)	0.002	2.983(-6)		
Ti	0.30	2.965(-4)	0.03	2.965(-5)			89.84	5.108(-2)
V	0.10	9.292(-5)					4.0	2.138(-3)
Cr	14.0	1.274(-2)	17.7	1.611(-2)	2.01	1.848(-3)	0.01	5.236(-6)
Mn	2.0	1.723(-3)	1.17	1.008(-3)	14.0	1.219(-2)	0.0025	1.239(-6)
Fe	64.88	5.499(-2)	70.578	5.982(-2)	81.20	6.953(-2)	0.02	9.752(-6)
Co	0.03	2.410(-5)	0.10	8.032(-5)				
Ni	16.0	1.290(-2)	9.3	7.499(-3)	1.94	1.580(-3)	0.005	2.319(-6)
Cu	0.02	1.490(-5)	0.20	1.490(-4)			0.01	4.286(-6)
As	0.02	1.264(-5)						
Nb	0.03	1.529(-5)						
Mo	2.0	9.868(-4)	0.33	1.628(-4)			0.005	1.419(-6)
Sn							0.01	2.294(-6)
Ta	0.01	5.453(-10)						
Density (g/cc)	7.86		7.86		7.94		4.52	

Table 11-8. Structural Material Composition (Contd.)

Element	Type 316 Stainless Steel		Type CE Ferritic Stainless Steel		V15Cr5Ti		Ti4Al2.5V8Sn0.5Si (Ti-4381)	
	wt-%	atom/b-cm	wt-%	atom/b-cm	wt-%	atom/b-cm	wt-%	atom/b-cm
C	0.058	2.286(-4)	0.080	3.089(-4)	0.02	6.118(-5)	0.01	2.267(-5)
N	0.007	2.366(-5)			0.05	1.311(-4)	0.008	1.555(-5)
O					0.05	1.148(-4)	0.065	1.106(-4)
Al					0.004	5.447(-6)	4.0	4.038(-3)
Si	0.460	7.752(-4)			0.03	3.924(-5)	0.5	4.848(-4)
P	0.026	3.974(-5)			0.01	1.186(-5)		
S	0.011	1.624(-5)						
Ti	0.040	3.953(-5)			5.00	2.835(-3)	84.9	4.825(-2)
V			0.150	1.365(-4)	79.794	5.754(-2)	2.5	1.336(-3)
Cr	16.70	1.520(-2)	9.000	8.025(-3)	15.00	1.060(-2)	0.01	5.236(-6)
Mn	1.430	1.232(-3)					0.0025	1.239(-6)
Fe	64.44	5.462(-2)	89.17	7.405(-2)	0.01	6.578(-6)	0.02	9.752(-6)
Co	0.030	2.410(-5)						
Ni	13.90	1.121(-2)			0.001	6.258(-7)	0.005	2.319(-6)
Cu	0.060	4.470(-5)					0.01	4.286(-6)
Ga					0.01	5.270(-6)		
Nb			0.100	4.992(-5)	0.0025	4.996(-7)		
Mo	2.840	1.401(-3)	1.000	4.834(-4)	0.008	3.164(-6)	0.005	1.419(-6)
Sn							8.0	1.835(-3)
Ta					0.003	1.149(-6)		
W			0.500	1.261(-4)	0.0075	1.523(-7)		
Density (g/cc)	7.86		7.70		6.10		4.52	

Figure 11-4 compares the three candidates for the heavy material (which also serve as structural materials) of Fe-1422, Ti6Al4V, and Al-2024 in terms of the radiation attenuation characteristics. Shown for comparison is a dose response of an epoxy-base superconductor insulation material provisionally placed in the outboard shield. The excellent shielding properties of Fe-1422 are clear. It is found that, for a dose limit of 10^6 Gy/MW-yr/m^2, for instance, the reduction in the required shield thickness of Fe-1422 is ∿0.2 m (∿200 m^2 in volume) compared to Ti6Al4V and ∿0.4 m relative to Al-2024.

Figure 11-5 shows the radioactivity concentrations in the first 0.1-m thick outboard shield for the three compositions as a function of time after shutdown following a reactor operation of an integral wall load of 18 MW-yr/m^2. Also shown in the figure is a specific radioactivity level of 10^{-7} MCi/m^3 below which materials are normally classified as low-level waste (LLW) that generally requires no special shield regarding the material handling. Due to the large amount of ^{55}Fe (decay half-life of 2.7 yr, EC decay with no gamma-ray) isotope production, the Fe-1422 shield exhibits a much higher radioactivity level up to 50 yr after shutdown than the Ti6Al4V and Al-2024 shields. The slow decrease in the Fe-1422 shield activation beyond that time period reflects the contribution from ^{63}Ni (100 yr, β^- decay/γ) isotope induced by the ^{62}Ni(n,γ) and ^{64}Ni(n,2n) reactions.

The Al-2024 shield activation shows a rapid decrease as the primary short-lived isotopes ^{24}Na (15 h, β^-/γ), ^{27}Mg (9.5 m, β^-/γ), and ^{28}Al (2.2 m, β^-/γ) decay. The major contribution up to ∿30 yr after shutdown comes from ^{54}Mn (312 d, EC/γ) and ^{55}Fe. Beyond 30 yr the most dominant isotope is ^{63}Ni which is produced in this case, mainly by the ^{63}Cu(n,p) reaction. It is of interest to see that the aluminum alloy exhibits a higher activation level than Fe-1422 after 50 yr because of the larger ^{63}Ni production rate caused by the less effective neutron flux attenuation. The steep decrease in the Ti6Al4V shield activation up to 10 yr after shutdown is very substantial and due primarily to the fast decay of ^{24}Na, ^{45}Ca (165 d, β^-/γ), ^{46}Sc (84 d, β^-/γ), and ^{48}Sc (44 hr, β^-/γ). At times longer than 10 yr, the radioactivity in this shield is determined solely by the impurity activation products such as ^{63}Ni, ^{93m}Nb (13.6 yr, IT/γ), ^{93}Mo (3500 yr, EC/no γ), and ^{14}C (5700 yr, β^-/no γ).

With regard to the potential material recycling within one human generation, e.g., within 30 yr after component replacement or reactor decommissioning, Ti6Al4V seems to be the only candidate among those investigated that can be used

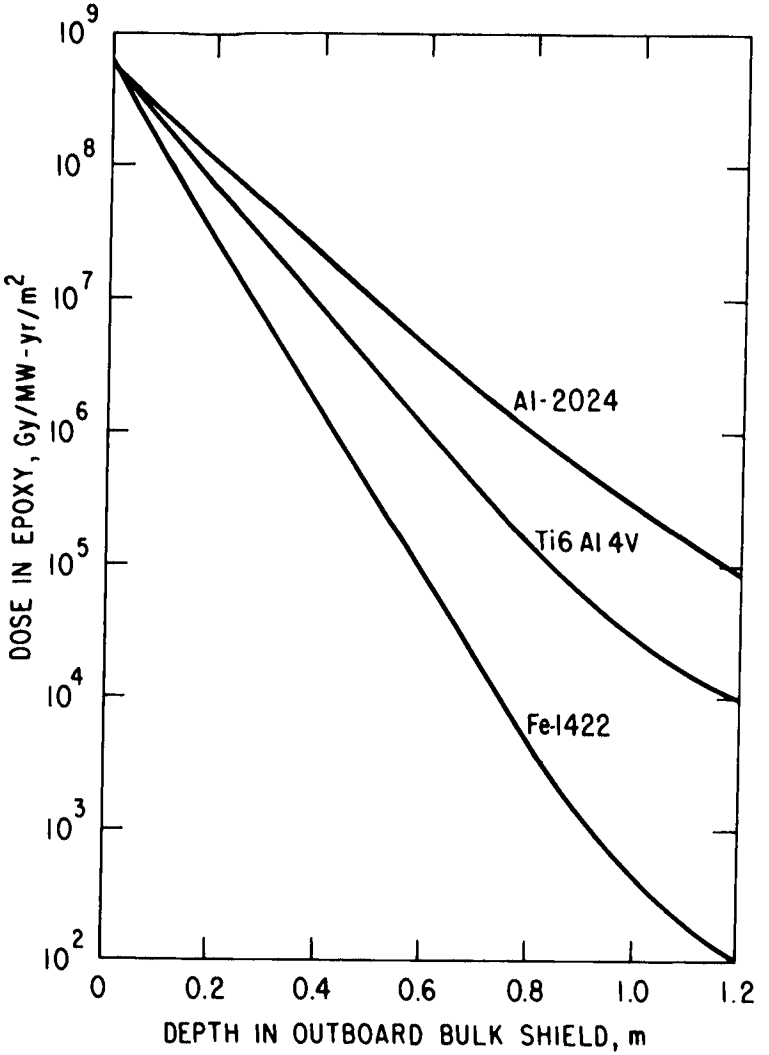

Figure 11-4. A comparison of candidate shield materials on epoxy dose response.

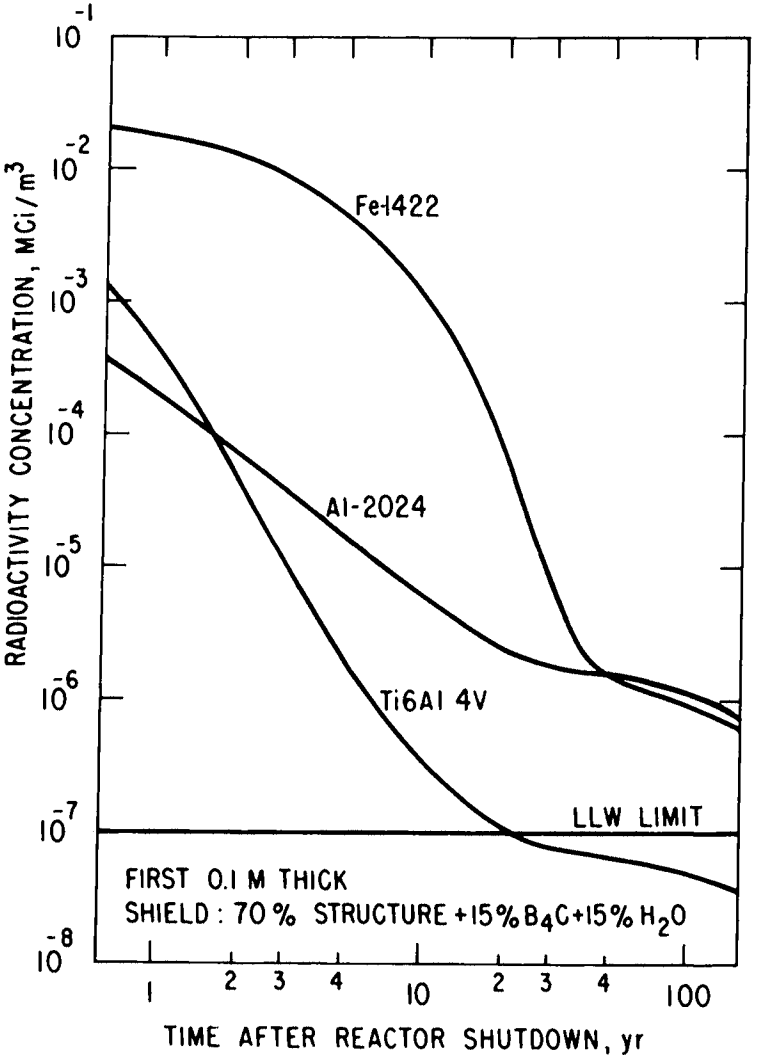

Figure 11-5. A comparison of candidate shield materials on induced radioactivity.

in the high flux shield zone. The results of Figs. 11-4 and 11-5 suggest that the outboard bulk shield be divided into subregions using different shield structural materials by zone, in order to maximize the use of Fe-1422 without inducing any serious high-level activation. Figure 11-6 examines the spatial dependence of the specific radioactivity associated with the Fe-1422 shield. Clearly, in order for the Fe-1422 shield to be recyclable within 30 yr, it must be located at least 0.5 m behind the shield's inner surface. A more detailed activation analysis relevant to the Fe-1422 shield is presented in Chap. 12.

The outboard bulk shield thickness used in the analysis is 1.2 m (including a 0.02-m shield jacket (vacuum boundary) at the front surface) and is divided into three major shield zones of high flux shield (HFS, 0.5 m), medium flux shield (MFS, 0.4 m) and low-flux shield (LFS, 0.28 m). The material compositions are as follows:

HFS: 5% Ti6Al4V + 65% TiH_2 + 15% B_4C + 15% H_2O

MFS: 70% Fe-1422 + 15% B_4C + 15% H_2O

LFS: 100% Fe-1422

It should be noted that the STARFIRE outboard bulk shield is designed to be 1.1 m based on the results presented in this section, reducing the LFS shield zone to 0.18 m.

The use of a large amount of Fe-1422 in the MFS and LFS stems from the following: (1) no significant induction of high-level, long-term activation in these relatively low-flux, soft neutron spectrum regions; (2) excellent radiation attenuation properties; (3) accommodation of the anti-torque support panels which are made of Fe-1422 and serve also as the LFS shield; and (4) material matching to the superconducting magnet dewars and steel liner on the inner surface of the reactor building. Material matching is an important design consideration during the reactor room activation analysis, in particular, when calculating the biological dose after reactor shutdown. Under certain conditions reactor components outside the shield can become a major source for the decay gamma emission inside the reactor building. For example, it is well known, for a given thickness shield that a thin lead layer added at the end of the bulk shield is very useful for drastically reducing post-shutdown decay-gamma rays emerging from the shield. However, under the circumstances where many of the components external to the bulk shield are composed of stainless steel-type

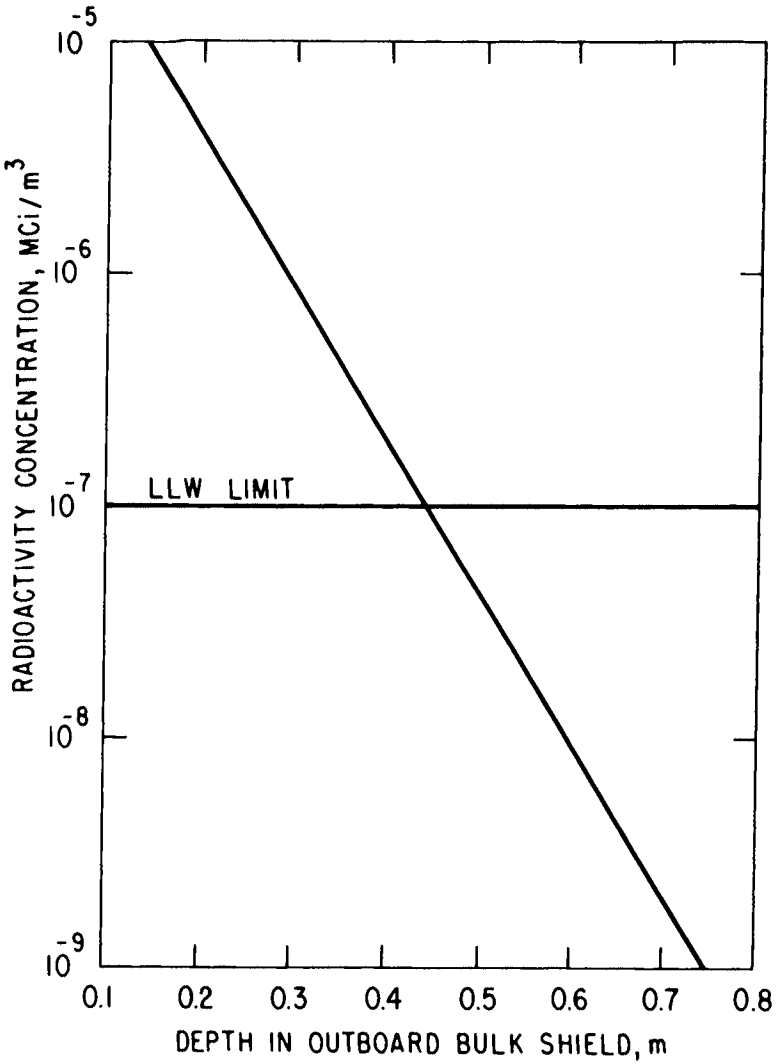

Figure 11-6. Radioactivity concentration at 30 yr after reactor shutdown in a Fe14Mn2Ni2Cr base shield.

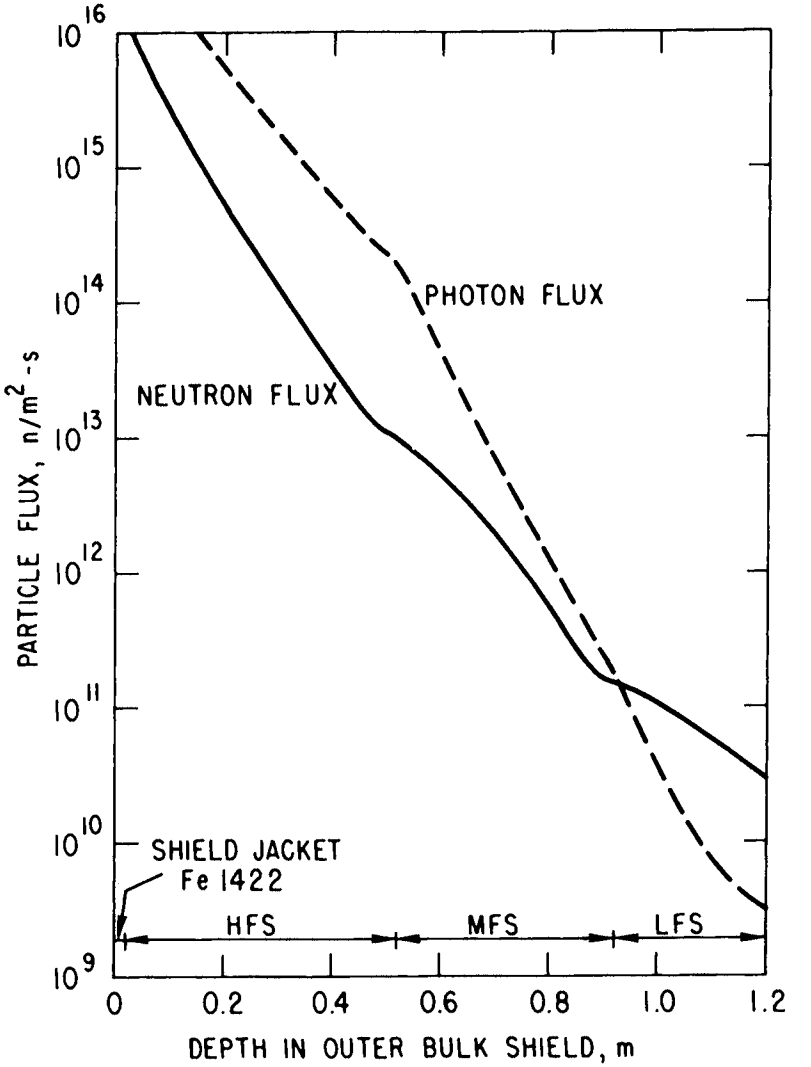

Figure 11-7. Neutron and photon fluxes in outer bulk shield.

materials, the post-shutdown dose level inside the reactor building will be governed largely by decay gamma sources at those stainless steel components. This observation is particularly important when one takes into account the fact that lead is a less effective shielding material in terms of neutron absorption, permitting more neutron leakage and, hence, a rather high-level activation from components external to it.

Figure 11-7 describes the radiation attenuation characteristics for the outboard shield, showing a six-fold neutron flux attenuation and a seven-fold gamma flux attenuation over a 1.2-m thick shield. Figures 11-8 and 11-9 show the neutron and gamma-ray spectra at the midpoint of each shield zone. As shown in Figure 11-8 the relatively slow decrease of the total neutron flux in the LFS zone is associated with the large thermal and epi-thermal flux components, obviously caused by the lack of efficient low-energy neutron absorbers such as B_4C in this zone. However, it should be pointed out that one of the concerns regarding the dose level shortly after shutdown is associated with decay gamma rays of a series of radioactive cobalt isotopes, in particular, of ^{58}Co (71 d, $EC/\beta^+/\gamma$). Most of these cobalt isotopes are induced in nickel elements by the fast neutrons with energies above $\sim$5 MeV (most dominantly above $\sim$10 MeV). Therefore, it is essential to use a large amount of spectrum shifters such as Fe-1422 as in the present design. Thermal neutrons generated in the anti-torque panels LFS zone (Fe-1422) can be absorbed by a thin boron plaster attached to the outer surface of the panels.

As shown in Sec. 11-4, six shield sections contain poloidal dielectric vacuum seal joints in order to minimize the induced toroidal current flow. The dielectric break joints which are made of polymide (kapton) must be designed to last for the entire plant lifetime. The outboard bulk shield also needs to protect elastomer (polyethylene propylene) seals for the shield door sealing. Each shield door is planned to be removed to allow blanket sector replacement at least once every six years for scheduled/unscheduled maintenance. The property deterioration of these seal materials due to radiation damage is of concern. Under the conditions of a neutron wall load of 3.6 MW/m^2, the plant lifetime of 40 yr with 75% plant availability and a blanket replacement interval of 6 yr, the anticipated absorbed nuclear doses in the kapton and elastomer seals are as follows:

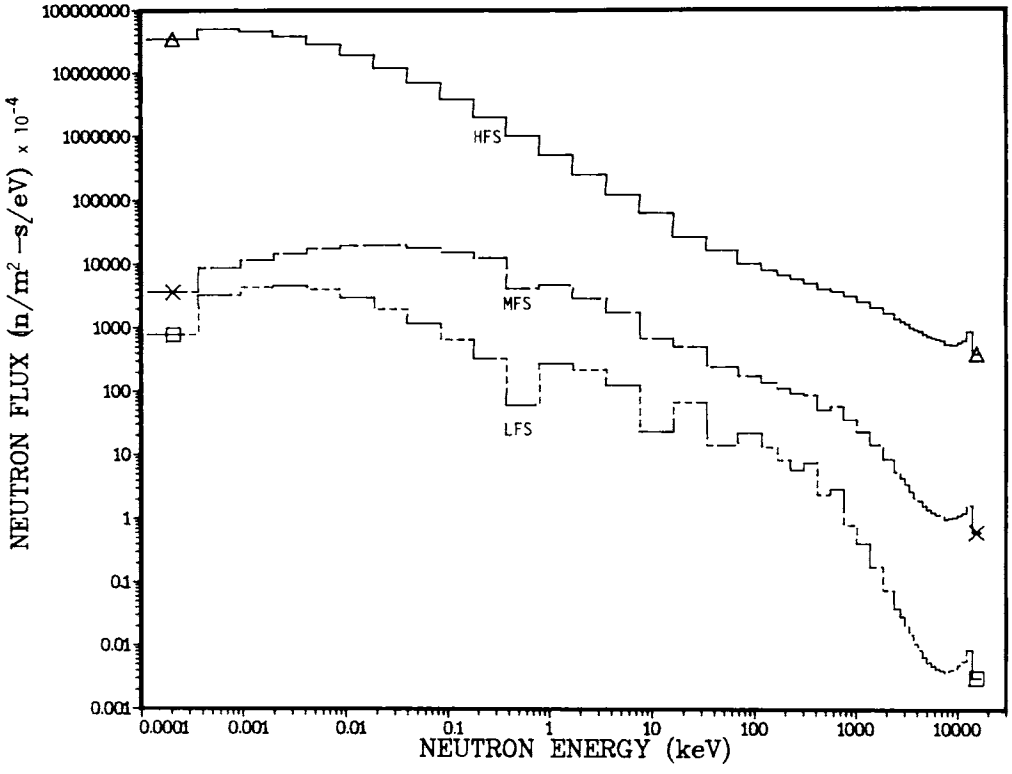

Figure 11-8. Neutron spectra in the outboard bulk shield.

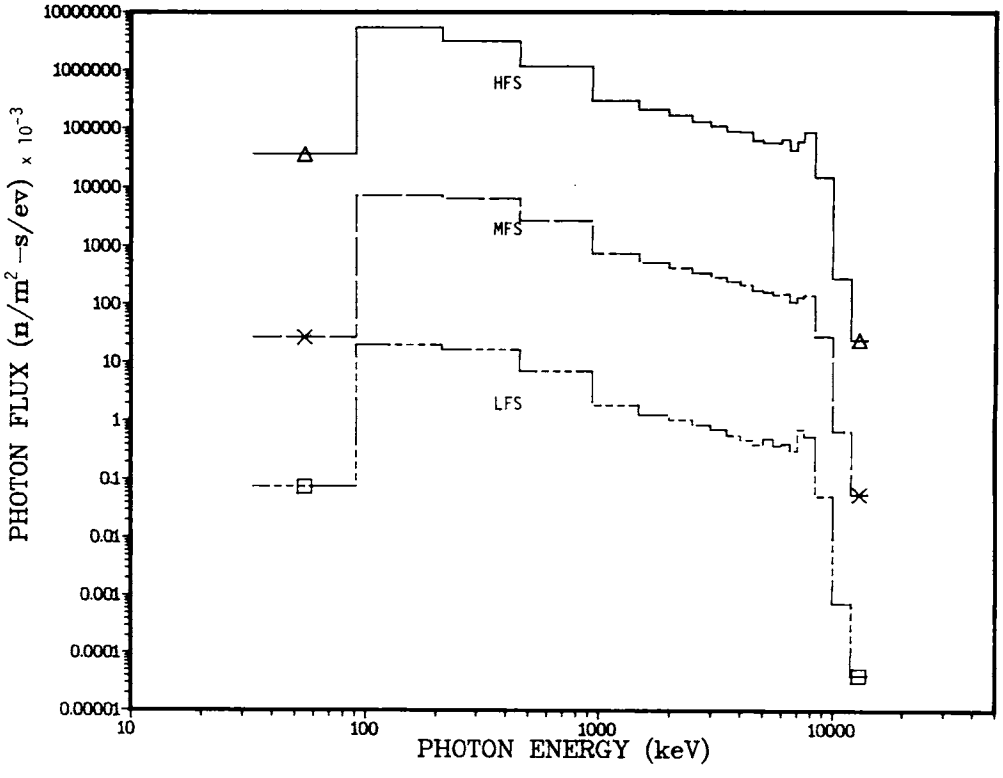

Figure 11-9. Photon spectra in the outboard bulk shield.

	Location from inner surface of the outboard shield	Dose
Kapton	0.60 m	$\sim 5 \times 10^7$ Gy
Elastomer	0.75 m	$\sim 7 \times 10^5$ Gy

Kapton and elastomer are expected to function properly without any serious property degradation up to doses of 10^8 Gy[2] and 10^6 Gy,[12] respectively. The dose rates shown above indicate that both seal materials can be well accommodated within the outboard bulk shield region, giving a degree of design flexibility in the selection of actual locations.

Table 11-9 summarizes the maximum radiation response rates in the outer part of the TF magnets. Since the outboard shield is designed for much more effective attenuation than the inboard shield, the radiation effects in the outer parts of the TF coils are much smaller than those in the inner parts. The relatively thick outboard shield required to permit personnel access into the reactor building shortly after shutdown is, in general, thicker than required for the magnet protection. In particular, when the superconducting magnets are constructed with iron-nickel-chromium-base structural materials which tend to induce significant short-lived radioactive isotopes, the biological shielding requirements become even more restrictive.

Figure 11-10 shows the spatial and time dependence of contact biological dose of the outboard bulk shield system. During reactor operation, the biological dose inside the reactor building is $\sim$100 rem/hr which rules out any possibility of reactor accessibility. More than 90% of the total dose is attributable to neutrons. At reactor shutdown, the reactor room dose decreases to $\sim$100 mrem/h which is still too high to allow personnel access without protection, compared to the current NRC guideline[14] of 2.5 mrem/h for the occupational exposure limit (based on 40 h/wk - 50 wk/yr work in a restricted area). The dose rate at this moment is dominated by the ^{56}Mn (2.6 h, β^-/γ) decay that emits the three major gamma rays of 0.85 MeV (intensity: 98.9%), 1.8 MeV (intensity relative to 0.85 MeV: 27.5%) and 2.1 MeV (relative intensity: 14.5%).[11] The second important gamma source (contributing to the total by $\sim$4%) is ^{54}Mn (312 d, EC/γ) emitting the 0.83-MeV (intensity: 100%) gamma ray. Due to the short half-life of ^{56}Mn and also to the relatively soft gamma spectrum, the reactor room dose decreases very rapidly following shutdown, resulting in $\sim$0.4 mrem/h at 24 h after shutdown. Again, the most dominant isotope in this time

Table 11-9. Maximum Radiation Response Rates[a] in Outer TF Magnets

1.	Neutron fluence, m^{-2}	1.2×10^{19}
2.	Photon fluence, m^{-2}	1.6×10^{18}
3.	Critical current density decrease in Nb_3Sn[b]	negligible
4.	Resistivity increase in copper stabilizer,[c] Ω-m	3.8×10^{-13}
5.	Atomic displacement in copper stabilizer, dpa	2.2×10^{-7}
6.	Dose in insulator, Gy	
	Neutron	5.3×10^{3}
	Photon	1.1×10^{3}
	Total	6.5×10^{3}
7.	Atomic displacement in Type 304 SS structure, dpa	1.4×10^{-7}
8.	Nuclear heating, MW/m^3	
	Stabilizer	1.4×10^{-8}
	Superconductor	1.0×10^{-8}
	Structure	1.1×10^{-8}
	Insulator	9.6×10^{-9}
9.	Average heating in magnets, MW/m^3	9.1×10^{-9}
10.	Total nuclear heating in outer magnets, MW	1.2×10^{-6}

(a) Based on:

Neutron wall load, MW/m^2:	3.6
Integral wall load, $MW\text{-}yr/m^2$:	108
Plant lifetime, yr:	40
Plant availability:	0.75

(b) Based on Ref. 13.

(c) Based on $\rho_r = 3 \times 10^{-9}\ [1 - \exp(-563\ \text{dpa})] \cdot \Omega\text{-m}$ (Ref. 1).

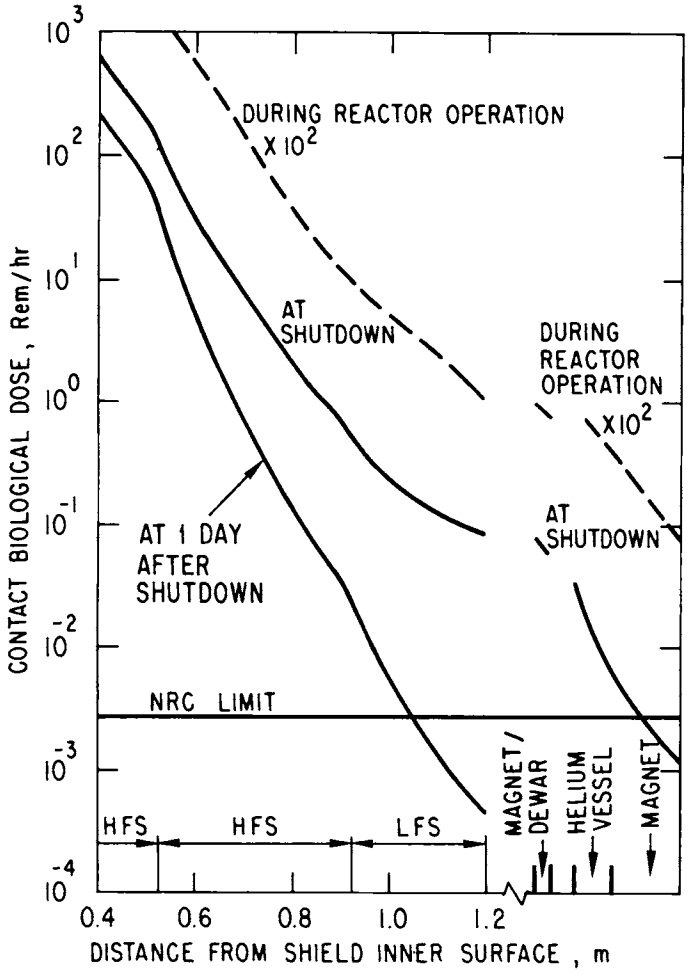

Figure 11-10. Contact biological dose rate for the STARFIRE design.

period is ^{54}Mn. Radioisotope ^{58}Co mentioned earlier contributes to the total dose by less than 5% in the present case by virtue of the substantial spectrum shifting and the lower nickel content in the Fe-1422 shield. Although the STARFIRE plans call for fully remote maintenance, the dose rate of 0.4 mrem/h shows that personnel access into the reactor building with all shielding in place is permissible within one day after shutdown. This provides a degree of confience in improving the plant availability factor, if desired, by allowing some maintenance tasks to be carried out in contact or semi-remote mode. Notice that when the shield thickness is reduced to 1.1 m, the dose rate at 24 h after shutdown is ∿1.5 mrem/h, which is still an acceptably low dose rate. Based on these results, the bulk shield thickness in the final reference design has been reduced to 1.1 m. Repeating the calculations for the 1.1-m case was judged not to be cost-effective since very little would be learned. Therefore,

all the calculations based on the 1.2-m case are retained in this chapter. An estimate of the impact on the design will be noted where it is significant.

A comparison of Fe-1422 and Type 304 stainless steel as the primary shield structural material in the MFS and LFS regions is of interest. Table 11-10 compares the two materials in terms of dose level inside the reactor building and radiation attenuation efficiency. One can notice that the Fe-1422 system offers a nuclear performance which is almost the same as or even better than the Type 304 stainless steel system. The only exception in which the Type 304 stainless steel is favored is the contact biological dose at reactor shutdown. This large difference reflects the effect of the substantial ^{56}Mn decay gamma emission in the Fe-1422 shield as already mentioned earlier. Both systems can meet the post-shutdown dose criterion of 1 mrem/h within one day. With regard to the long-term activation, the Fe-1422 system shows a lower radioactivity, in particular, at times greater than 50 yr after shutdown due to the low nickel content as well as the low molybdenum and niobium impurity levels in Fe-1422.

Table 11-10. A Comparison of Type 304 Stainless Steel and Fe14Mn2Ni2Cr (Fe-1422) Shield Structural Materials on Radiation Shielding and Biological Dose in Reactor Building[a]

	Type 304 Stainless Steel	Fe-1422
	Nuclear Dose (Gy/MW-yr/m^2)	
A. Maximum dose in epoxy-base insulator in TF magnets	81	60
	Biological Dose (mrem/h)	
B. During reactor operation	1.38×10^5	1.04×10^5
C. At shutdown	22.8	84.1
D. At 1 day after shutdown	0.63	0.46

[a]Neutron wall load: 3.6 MW/m^2.

Integral neutron wall load before shutdown: 18 MW-yr/m^2.

Shield composition (total shield thickness: 1.2 m):

HFS: 5% Ti6Al4V + 65% TiH_2 + 15% B_4C + 15% H_2O

MFS: 70% structure + 15% B_4C + 15% H_2O

LFS: 100% structure

Another key material selection for the reference outboard shield design is related to TiH_2 in the HFS region. The material selection for this zone is crucial from the standpoint of minimizing the high-level activation not only in this shield itself but also in the components external to it. A comprehensive scoping study prior to the final material selection resulted in defining the following two HFS material compositions:

(1) 5% Ti6Al4V + 65% TiH_2 + 15% B_4C + 15% H_2O; and

(2) 5% Ti6Al4V + 65% Pb + 15% B_4C + 15% H_2O,

in which Ti6Al4V is used as the primary low-activation structural material as discussed previously, along with the boron carbide neutron absorber and the water coolant. Both TiH_2 and Pb appear attractive in their HFS application because (1) they do not seem to pose a serious long-term activation problem; (2) the prices are relatively low;[15] and (3) their inelastic energy moderation powers are fairly large at neutron energies of interest. For example, at neutron energies of 14 MeV, 10 MeV, and 5 MeV, the respective TiH_2 inelastic cross sections are 0.03 cm^{-1}, 0.06 cm^{-1}, and 0.07 cm^{-1}, while the corresponding lead cross sections are 0.01 cm^{-1}, 0.02 cm^{-1}, and 0.08 cm^{-1}. Table 11-11 compares the two systems with respect to the doses inside the reactor building at shutdown and one day after shutdown. It is seen that the TiH_2 system yields dose rates which are a factor of three to four less than the lead system does. This difference in the dose rate may be translated to a difference in the shield requirement of $\sim$0.1 m for a given dose criterion at one day after shutdown.

Figure 11-11 shows the variation of the maximum biological dose outside the reactor during normal operation as a function of the building wall thickness. The building is assumed to be constructed with ordinary concrete[16] with 5 vol-% iron reinforcement. The calculation is based on a neutron wall load of 3.6 MW/m^2 and the outboard bulk shield thickness of 1.2 m. The building wall thickness is selected to be 1.5 m to satisfy both the radiation protection and structural requirements. As seen from Fig. 11-11, the dose rate at the outer building wall is 0.065 mrem/h for a bulk shield thickness of 1.2 m. When this thickness is reduced to 1.1 m the dose rate increases to $\sim$0.3 mrem/h. This dose permits a person to work immediately outside the building for 40 h/wk on a regular basis. However, personnel on the power plant site occupy buildings whose walls provide additional radiation protection. Furthermore, these buildings are located away from the reactor building. Detailed calculations

Table 11-11. A Comparison of Lead and TiH_2 in the High Flux Shield Zone (HFS) on Biological Dose

	Dose (mrem/hr)[a]	
	Lead	TiH_2
(1) At shutdown:		
• At the end of shield (the anti-torque panel)	307.2	84.1
• At the magnet dewar surface	276.3	76.0
(2) At 1 day after shutdown:		
• At the end of shield (the anti-torque panel)	1.39	0.46
• At the magnet dewar surface	1.10	0.36

[a]Neutron wall load: 3.6 MW/m^2.

Integral neutron wall load before shutdown: 18 $MW-yr/m^2$.

Shield composition (total shield thickness, 1.2 m):

1: 5% Ti6Al4V + 65% (Pb/TiH_2) + 15% B_4C + 15% H_2O

2: 75% Fe-1422 + 15% B_4C + 15% H_2O

3: 100% Fe-1422.

of the dose to every person on the site is beyond the scope of this work. However, it is reasonable to assume that the average dose rate for a person on the plate site is at least a factor of 10 lower than the maximum dose at the reactor building. Therefore, this average dose rate should be <0.03 mrem/h. This is a very low dose rate that translates into radiation exposure of 60 mrem/yr for a person working 40 h/wk. Therefore, a maintenance person working regularly on the site has most of his dose committment reserved for working in the higher radiation fields; e.g. inside the reactor building. Such a low dose rate also guarantees that the dose to the general public outside the site boundary is much less than the 500 mrem/yr suggested by the National Regulatory Commission.

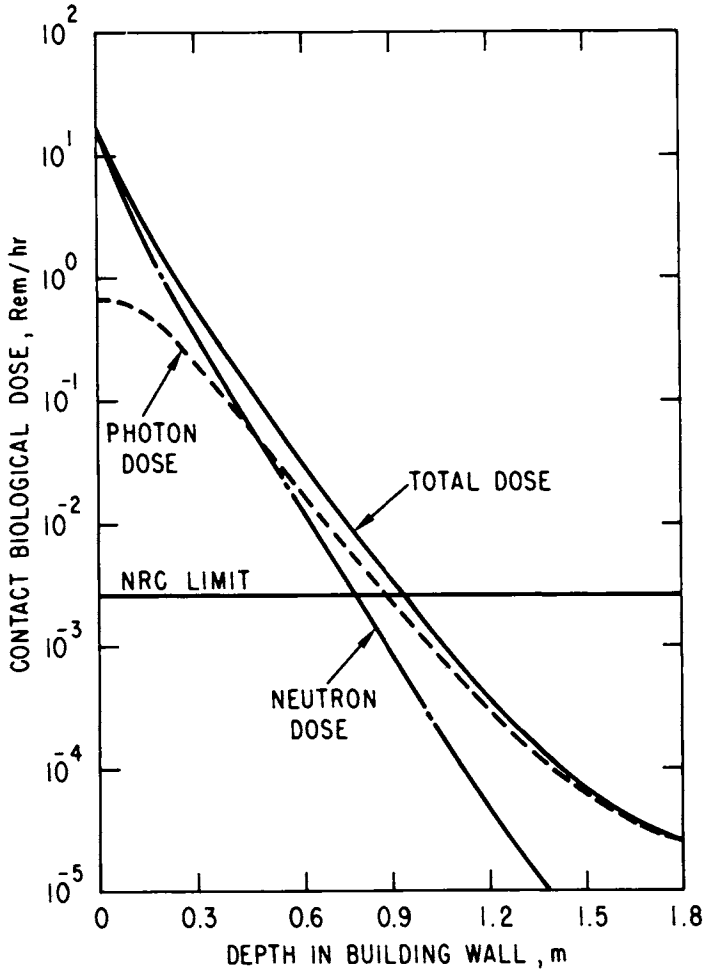

Figure 11-11. Biological dose versus reactor building wall thickness for the STARFIRE design.

11.3 PENETRATION SHIELD

One of the important shield considerations is radiation streaming through void regions that penetrate the blanket and bulk shield regions. In general, the direct radiation flow as seen in neutral beam ports, vacuum pumping ducts, divertors, etc., in tokamak reactor designs is one of the primary sources of design complexity and shielding difficulties. In the STARFIRE design, a serious effort has been devoted to minimizing possible design difficulties associated with these penetrations since the early phases of the conceptual design. A key feature of the STARFIRE vacuum pumping system is the elimination of any direct radiation streaming path from the plasma to the vacuum pumps. The STARFIRE design also features the selection of a lower hybrid rf system in preference to a neutral beam heating system and a limiter impurity control concept rather than divertors. These design features have brought about overall shield design simplicity as well as shielding efficiency.

In this section, three penetration subsystems are analyzed. They are: (1) pumping ports in the bulk shield for torus evacuation; (2) the limiter slot opening leading to the vacuum plenum for plasma impurity control; and (3) rf waveguides for the plasma current drive and plasma heating. The particle transport analyses have been carried out using a Monte Carlo code, MORSE-CG[17] with 20,000 neutron histories and a two-dimensional discrete ordinate code DOT-III[18] with the S_8P_3 approximation.

11.3.1 Vacuum Pumping Ducts

Figure 11-12 shows the computational model of the vacuum duct system used in the Monte Carlo analysis. The vacuum duct is modeled as a combination of three 1-m diameter cylindrical ducts connected in series. As shown in Fig. 11-12, duct 1 penetrates through the bulk shield, starting from the plenum region, and duct 2 is slanted by 40 deg relative to the vertical reactor centerline. Duct 3, whose axis is parallel to the reactor midplane, simulates the vacuum pump housing. The lower two ducts are completely surrounded by a 0.3-m thick (5% Ti6Al4V + 65% TiH_2 + 15% B_4C + 15% H_2O) inner shield and a 0.5-m thick (70% Fe-1422 + 15% B_4C + 15% H_2O) outer shield. Note that these shields compositions are the same as those used in the HFS and MFS regions of the outboard bulk shield design. Also note that these shield thicknesses are provisionally used for the analysis. The final selection of the reference shield thickness will be made based on this analysis as shown below. The vacuum pump chamger is surrounded by a 0.5-m thick shield whose composition is 70% Fe-1422 + 15% B_4C + 15% H_2O.

Nuclear heating due to radiation streaming into the cryopumps is of concern. From Fig. 11-13, it is found that the nuclear heating rates in copper and stainless steel cryopanels are approximately the same and the lowest heat load takes place in an aluminum system which has been selected as the reference material. None of the three candidate materials poses any difficult heat removal problems. The anticipated maximum nuclear heating in the cryopumps of the reference design is presented in Table 11-12.

The penetration shield thickness around the vacuum ducts was determined as a result of detailed analysis. From the numerical analysis standpoint, the vacuum system shielding is of the most adversity in improving the accuracy of the statistical solution by the Monte Carlo technique. This is the result of

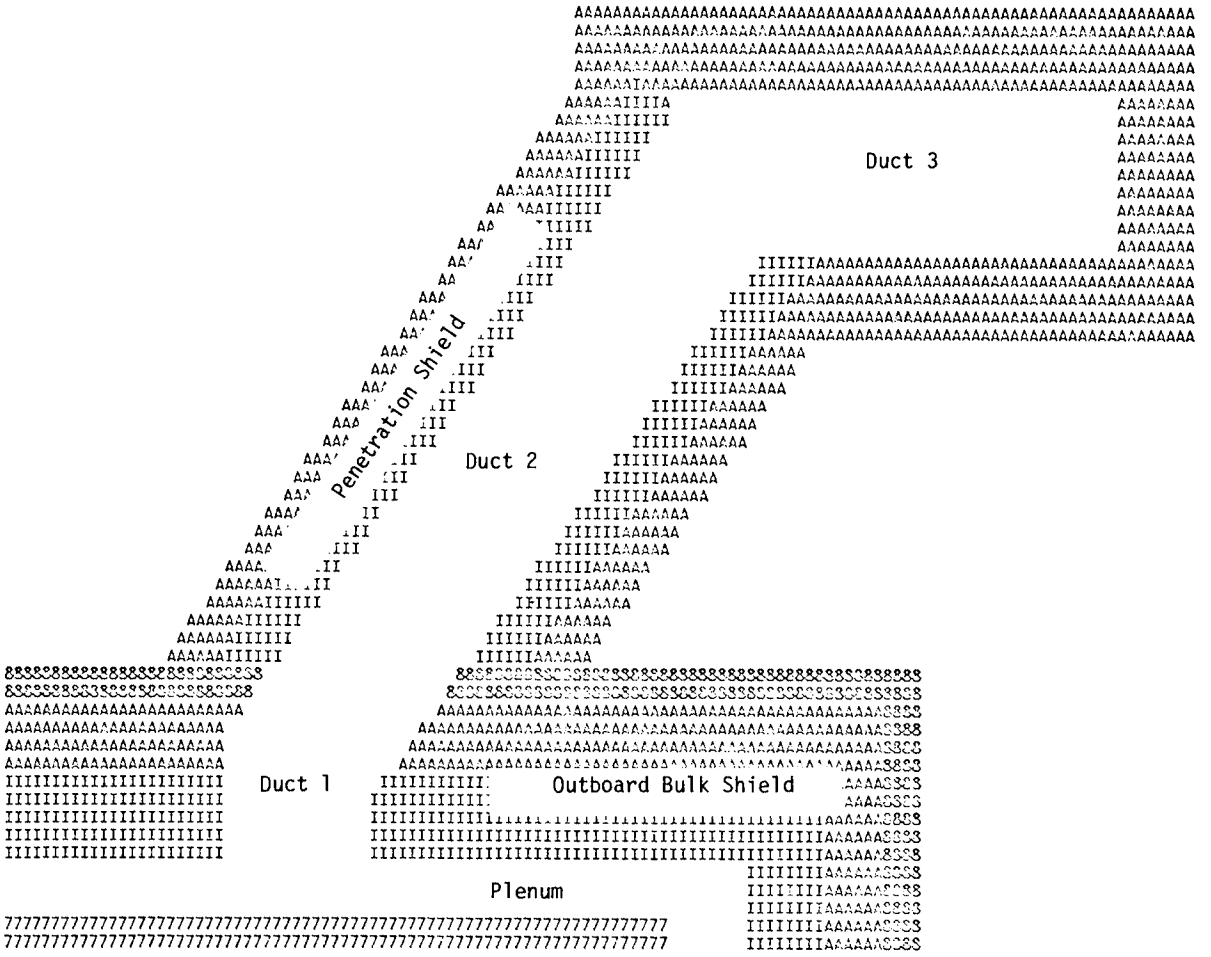

Figure 11-12. The vacuum pumping system model used in the analysis.

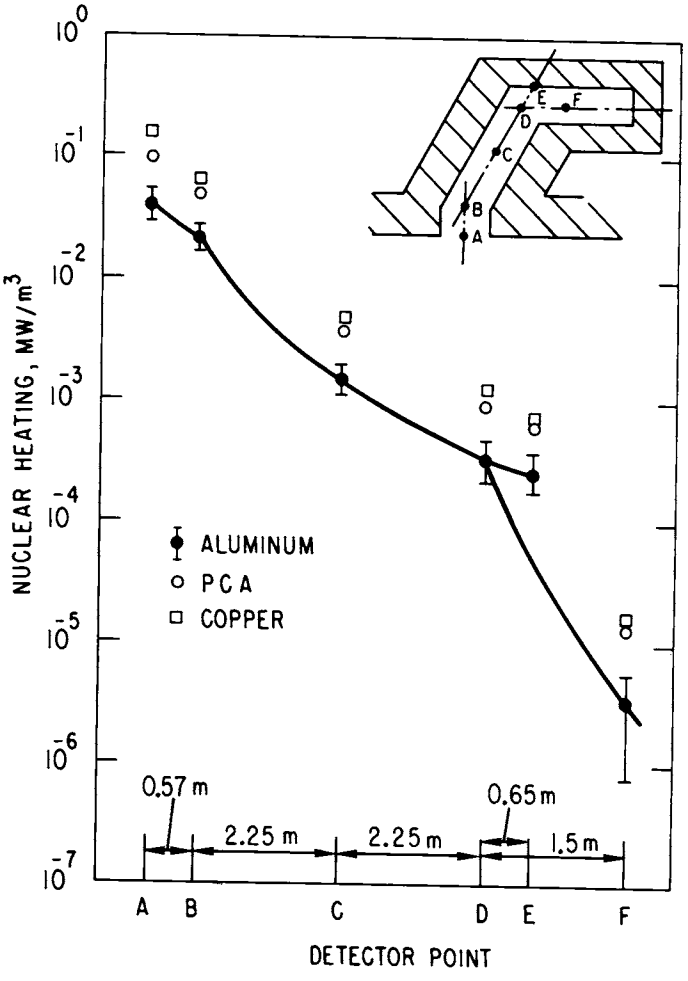

Figure 11-13. Nuclear heating response in vacuum pumping ports.

Table 11-12. The Maximum Nuclear Heating in the Aluminum Cryopanels

	Heating[a] (kW/m^3)
Neutron heating	0.11 (±48%)[b]
Gamma heating	0.15 (±43%)
Total heating	0.26 (±32%)

[a] Based on neutron wall load: 3.6 MW/m^2.

[b] Statistical deviation as estimated by MORSE-CG with neutron histories of 20,000.

a design effort that has been made to reduce radiation streaming into the vacuum pumps. There is no direct path for neutrons from the plasma to the pumps and a number of bends are incorporated into the vacuum ducts. The design criteria for the determination of the penetration shield thickness are: (1) the biological dose rate at any location outside the shield must be about 1 mrem/h within one day after shutdown; and (2) the shield must provide adequate protection of the superconducting magnets around the ducts. Figure 11-14 illustrates the variation of the total neutron flux inside the ducts. The flux attenuation in the second duct is quite small and the 4.5-m long duct offers only about two orders of magnitude reduction in the total flux. This result is quite consistent with the analysis by a discrete ordinate method of Ref. 19.

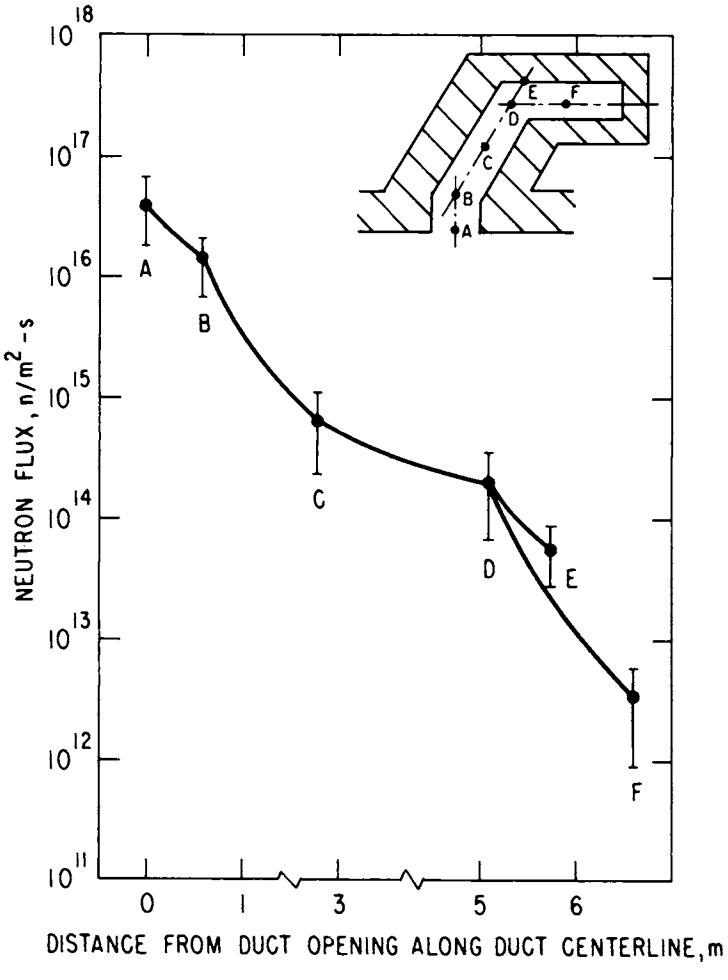

Figure 11-14. Variation of neutron flux in vacuum pumping ports.

Figure 11-15 examines the neutron spectrum change inside the vacuum duct. Plotted in the figure are the spectra at duct points B and D defined in Fig. 11-14. It is found that the majority of neutrons inside the ducts move in the forward direction, substantially lowering neutron population below ∿100 keV by the interactions with the wall materials. As a result, the most significant neutron radiation enhanced by the presence of the ducts is caused by the high energy flux which has survived the neutron capture by the wall materials. In fact, the difference of about two orders of magnitude in the total neutron flux between points B and D is mostly attributable to the spectrum gap below ∿100 keV although the flux at point D for the energy range of 5 to 50 keV appears unduly low because of the large standard deviation. It should be noted that due to the geometrical configuration of the vacuum duct, neutrons entering into the duct are most likely to undergo their first collisions at the upper portion of the duct rather than at the lower portion. In adddition, the first collisions of the fast neutrons will take place in a somewhat deep duct shield region because of the relatively long mean-free path (m.f.p.; typically on the order of a few centimeters for >10 MeV energies). Each collision results in a larger probability of the neutron absorption in the vicinity of the collision site because the absorption cross section is increased as neutron energies are lowered.

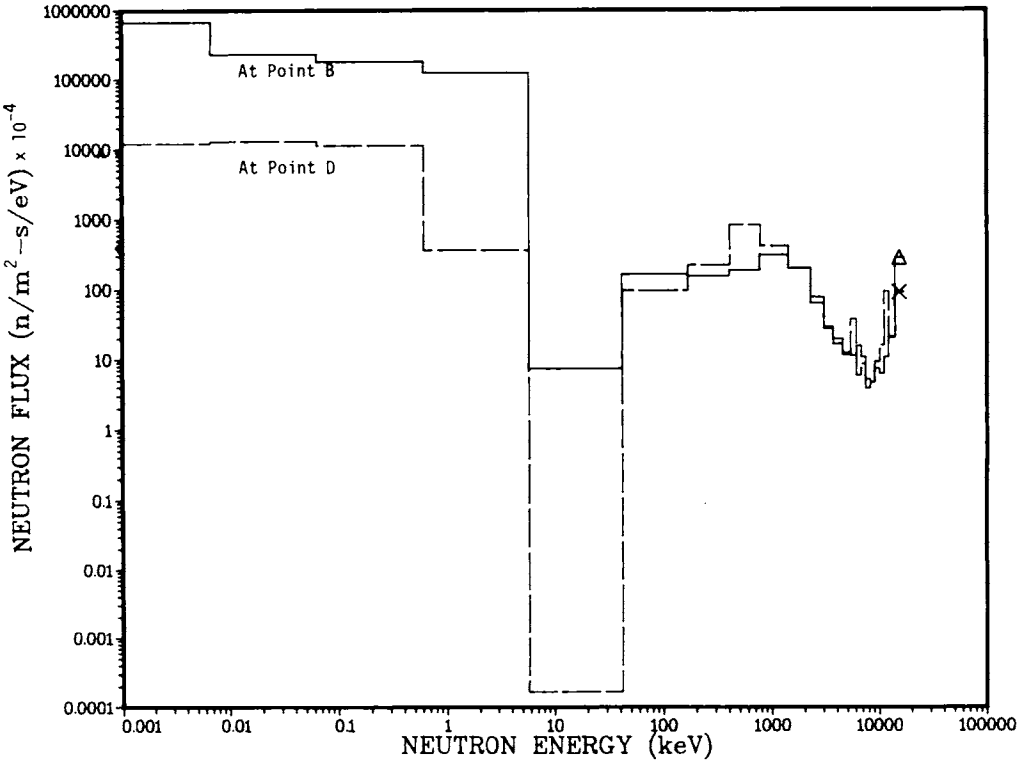

Figure 11-15. Neutron spectrum in vacuum pumping ports.

Therefore, a large fraction of the neutrons entering the duct opening proceed in the forward direction without much background reflection.

Based on this observation, the most important radiation protection from the shielding standpoint is the upper portion of the pumping port system. Figure 11-16 shows the flux variation at three key shield cross sections at lines A, B, and C. Line A runs vertically through the shield from the duct opening center. The shield thickness cut through by line A is ∿1.25 m. Line B starts from the joint center of the second and third ducts, passing vertically through 0.5-m of shielding. Line C originates at the midpoint of the two duct joint centers, and passes horizontally through ∿1.05 m of shield. It is found that the flux attenuation in the penetration shield is large compared to the flux attenuation inside the ducts. In particular, the absorption of low-energy neutron flux is very steep because of the substantially short mfp. For example, the total reaction mfp's in the (70% Fe-1422 + 15% B_4C + 15% H_2O) shield composition are ∿5 mm and ∿1 mm at a few keV and thermal energies, respectively, compared to the source neutron mfp of ∿50 mm, leaving only the high energy neutrons that penetrated the shield. It is important to note that the path lengths of ∿1.25 m, ∿0.5 m, and ∿0.6 m along lines A, B, and C, respectively yield the same level of neutron fluxes outside the shield (within the statistical uncertainties) as does the bulk shield at the reactor midplane.

The absorbed nuclear dose in an epoxy-base insulator of the TF magnets due to the radiation field of point 4 along line C is estimated to be $\sim 3 \times 10^{-6}$ Gy/s for a neutron wall load of 3.6 MW/m^2, resulting in $\sim 10^4$ Gy over the 40-yr plant operation with an availability factor of 75%. Although this dose level is about a factor of two higher than the total dose shown in Table 11-9 (which is based on the system without penetrations), one can conclude that the TF magnets are not likely to be influenced to any appreciable degree by the local radiation enhancement due to the shielded vacuum ducts.

Figure 11-17 describes contact biological doses as a function of depth in the penetration shield around the vacuum ducts. Note that the depth is measured in this case along a line vertical to the duct centerline. Again it is observed that the decay gamma sources are predominantly generated in the upper portion of the duct shield rather than in the lower portion. Based on the results of Fig. 11-17, along with the degree of radiation enhancement to the TF

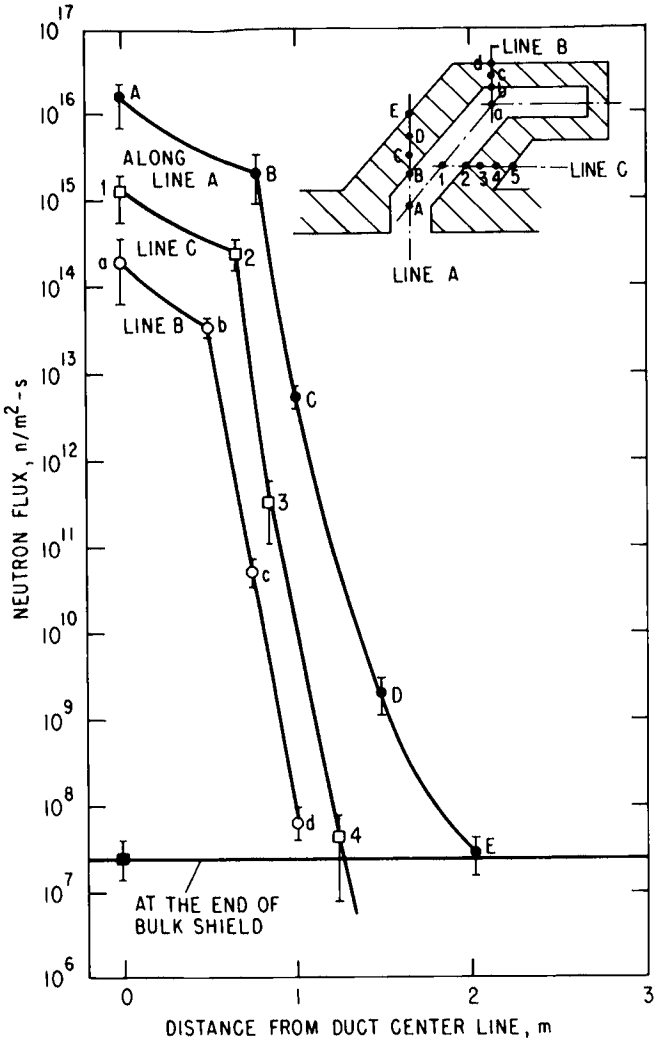

Figure 11-16. Variation of neutron flux in the vacuum pumping duct shield.

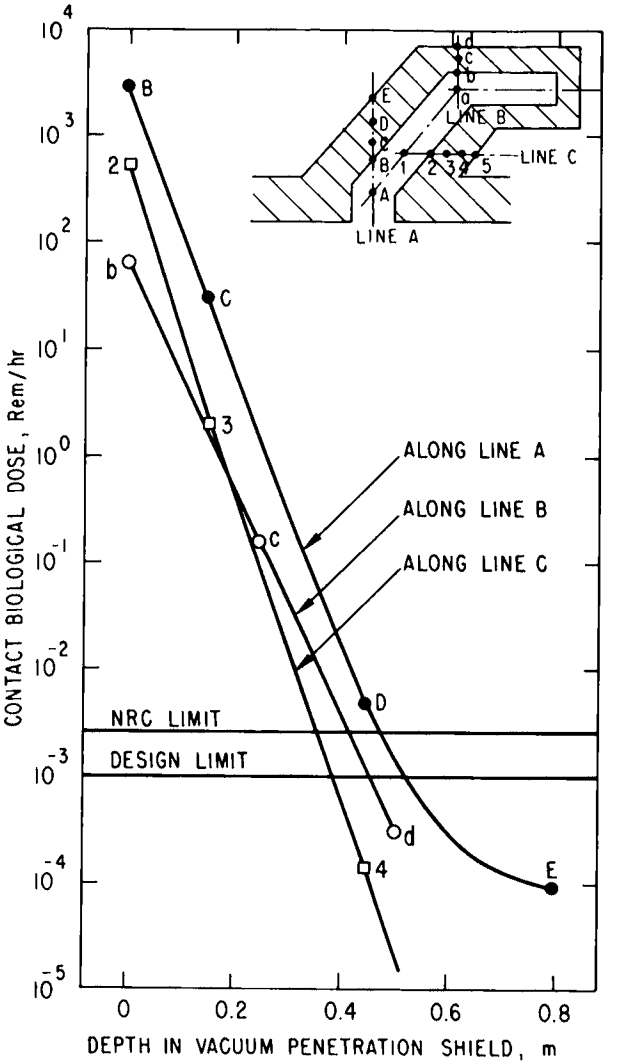

Figure 11-17. Variation of biological dose at 1 day after reactor shutdown for vacuum duct shield.

magnets assessed earlier, the reference shields for the vacuum pumping system are defined as follows:

(1) Shield jacket all around the duct wall: 0.02-m thick shield 1.

(2) Shield for the pump chamber (pod): 0.5-m thick shield 2.

(3) Shield around the vacuum ports:

(a) Upper shield: 0.3-m thick shield 2 followed by 0.28 m thick shield 3

(b) Lower shield: 0.3-m thick shield 2 followed by 0.18-m thick shield 3,

where shield 1 is 100% Fe-1422; shield 2 is 5% Ti6Al4V + 65% TiH_2 + 15% B_4C + 15% H_2O; and shield 3 is 70% Fe-1422 + 15% B_4C + 15% H_2O.

11.3.2 Limiter Slot Opening

A vertical view of the limiter system as modeled in the numerical analysis is shown in Fig. 11-18. The material compositions of three regions, LIMA, LIMB, and LIMC used in the calculations are as follows:

LIMA: 62% structure + 38% H_2O

LIMB: 84% structure + 16% H_2O

LIMC: 10% structure + 15% H_2O + 75% void.

Both the panel region LIMA that is 17-mm thick and 1-m high, and the root section LIMB that is 0.248 m long and 0.08 m high form a toridal belt. The coolant inlet/outlet manifolds in the reference design are arranged discretely in the toroidal direction but this region (LIMC) is approximated in the neutronics calculations here by a homogenous material mixture. The analysis was carried out using the two-dimensional discrete-ordinate transport (S_n) code, DOT-III,[18] with the S_8-P_3 approximation in R-Z cylindrical geometry. The use of the two-dimensional S_N code is based on the observations that (1) the limiter system configuration can be well represented by a two-dimensional model because of the uniformity of the system geometry in the toroidal direction; and (2) a more detailed (deterministic) solution than what the Monte Carlo technique could provide is required for the nuclear response calculations in the limiter

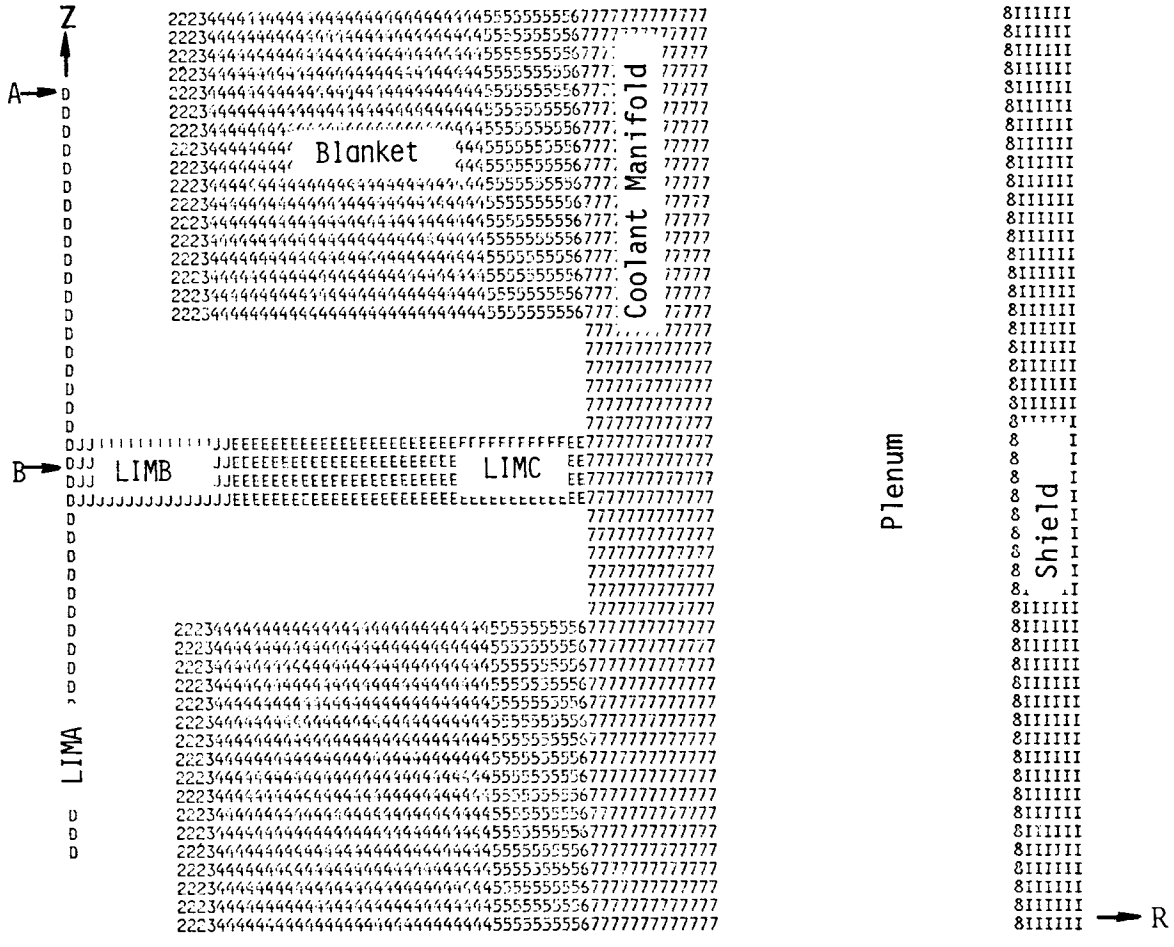

Figure 11-18. The limiter system model used in the analysis.

system. The objective of the analysis in this section is to identify the effect of the limiter slot opening upon the radiation enhancement in the outboard bulk shield region. In particular, the potential increase in nuclear heating in the shield is of concern. As discussed in Sec. 8.4, several candidate materials such as Ta-5W, V-20Ti, and niobium alloys have been considered for the limiter structure. The analysis described here was performed for two of the candidate structural materials: Ta-5W and V-20Ti.

Figure 11-19 shows the total neutron flux variation along the limiter slot opening at the reactor midplane. Also shown in the figure for comparison is the total neutron flux at 1 m from the midplane (i.e., the flux in the bulk blanket/shield region). It is seen that the neutron flux at the midplane drops only by a factor of five between the panel surface (point B in Fig. 11-18) and

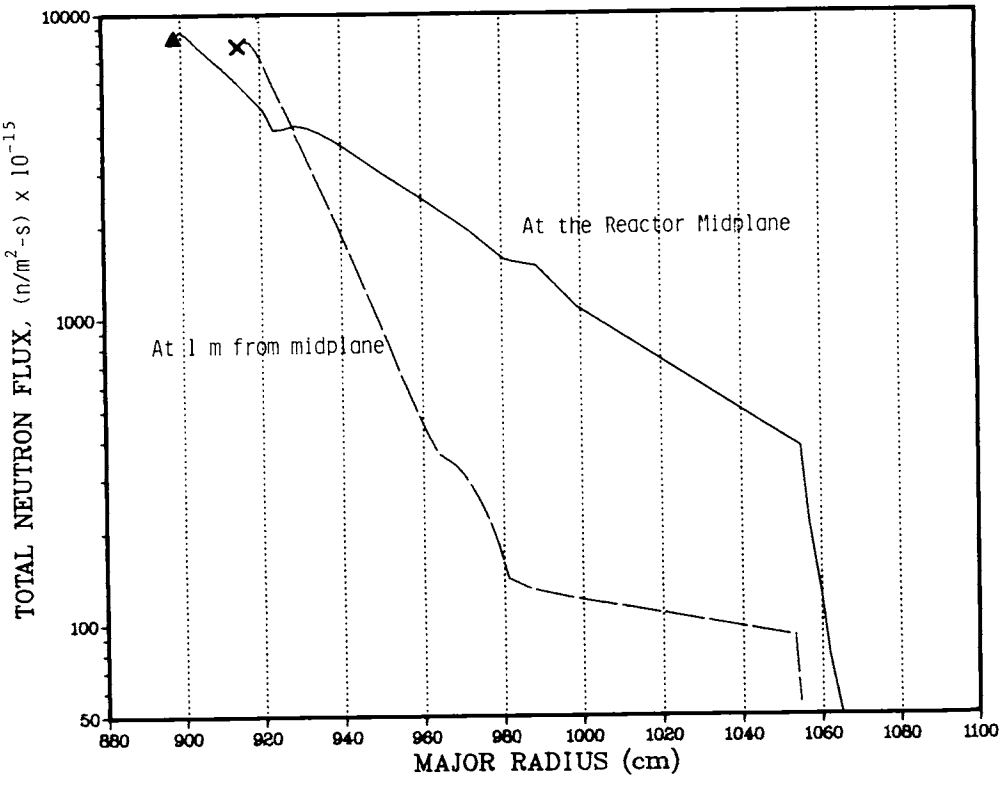

Figure 11-19. Effect of the limiter slot opening on the neutron flux.

the plenum opening area, yielding a total neutron flux at the outboard shield surface that is about an order of magnitude higher than that for the case of complete absence of the opening. This is primarily because of a large component of fast neutrons that directly, or in a few collisions, stream out from the plasma region. The difference in the neutron spectrum between the two systems (with and without limiter) is shown in Fig. 11-20. The spectrum for the case without limiter has been obtained from a one-dimensional ANISN[4] calculation. The spectrum shown in Fig. 11-20 is calculated at the shield jacket (Fe-1422) of the outboard shield. It is found that the fraction of neutrons with energies >10 MeV, for instance, is ∿30% of the total for the limiter system, compared to only ∿5% of the total in the absence of the limiter. There is a lesser difference between the two systems for neutrons with energies <1 keV.

Table 11-13 illustrates the impact of the limiter system upon the nuclear heating in the outboard shield. The maximum heating rate at the shield jacket is enhanced by a factor of ∿10, almost proportionally to the flux increase at

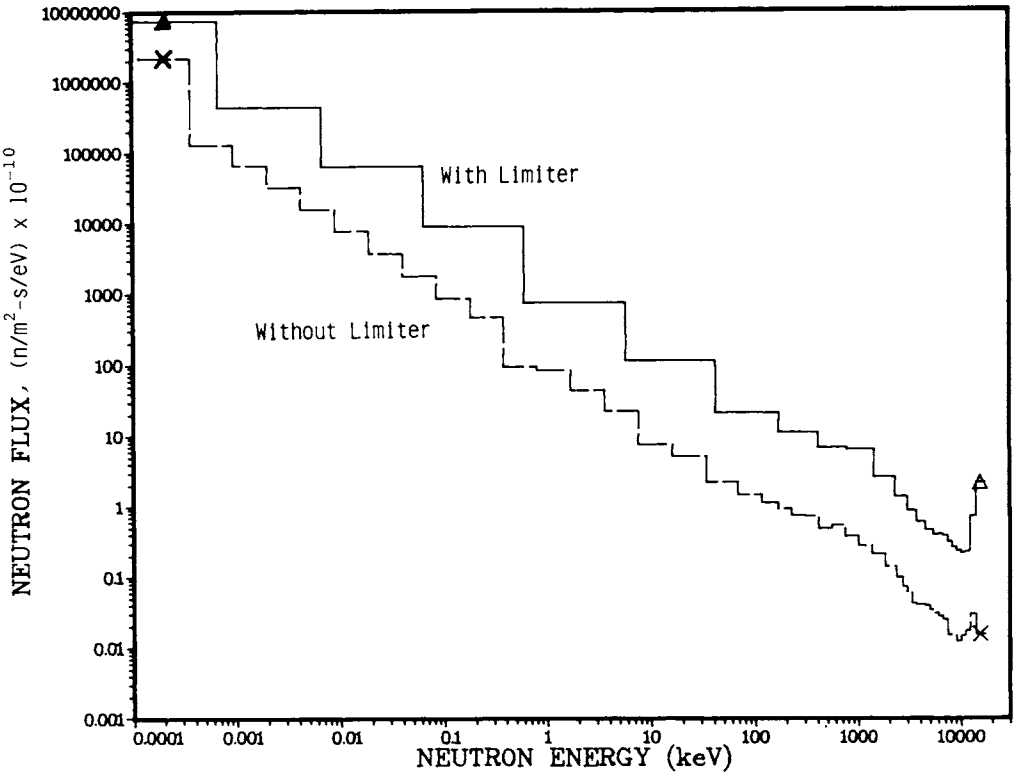

Figure 11-20. Impact of the limiter slot opening on the neutron spectrum.

that point. It appears that the trend toward a higher nuclear heating rate localized near the reactor midplane persistently prevails into the deep shield region although the absolute magnitude of heating rates rapidly decreases. It should be pointed out that the heating rate in this range does not significantly constrain the shield design because the magnitude of the heating rate remains modest. According to the results of Table 11-13, the overall increase of the volumetric nuclear heat generation in the outboard bulk shield region resulting from the presence of the limiter slot opening, is only about 15 MW for both cases of the Ta-5W and V-20Ti limiter designs.

11.3.3 RF Waveguides

The STARFIRE design employs an rf-wave launching method for the plasma heating as well as for the plasma current drive. This dual-function rf system has apparent advantages over the neutral beam injection design. From a radiation shielding standpoint, the rf system is very attractive in that bends can be tolerated in the rf ducts and also that the waveguide structural materials

Table 11-13. The Effect of the Limiter Slot Opening on Nuclear Heating[a] in the Outboard Bulk Shield

	Without Limiter	With Limiter	
		Ta-5W	V-20Ti
1. Nuclear heating at shield jacket[b] (MW/m^3)			
a. at reactor midplane	0.27	2.31	2.64
b. at 1 m from midplane	——	0.70	0.76
2. Nuclear heating at 0.3 m from HFS shield[c] surface (MW/m^3)			
a. at reactor midplane	0.0032	0.052	0.060
b. at 1 m from midplane	——	0.0094	0.010
3. Total heat deposition in outboard shield jacket[b] (MW)	5.4	9.5	10.2
4. Total heat deposition[c] in outboard HFS shield (MW)	10.3	24.9	27.2

[a]Neutron wall load: 3.6 MW/m^2.

[b]100% Fe-1422.

[c]5% Ti6Al4V + 65% TiH_2 + 15% B_4C + 15% H_2O.

(PCA stainless steel in the reference design) along with the water coolant flowing through the structure prevent, to a substantial degree, the direct radiation flow from coming out through the waveguides.

As shown in Chap. 7, the rectangular opening of the rf ducts is 0.77 m × 0.68 m at the first wall, tapering to ∿0.33 m × 0.82 m at an average distance of ∿0.66 m from the wall. After a bend of ∿38 deg toward the reactor midplane, the ducts are extended into the reactor room, protruding through the outboard bulk shield. The neutronics model used for the nuclear analysis by the Monte Carlo method is shown in Fig. 11-21, and consists of a combination of three straight rectangular-shaped ducts, RFA, RFB, and RFC. The cross-sectional dimensions and material compositions of these ducts are as follows:

RFA: 0.77 m × 0.68 m: (22% PCA + 8% H_2O + 70% void);

RFB: 0.77 m × 0.68 m: (58% PCA + 8% H_2O + 34% void); and

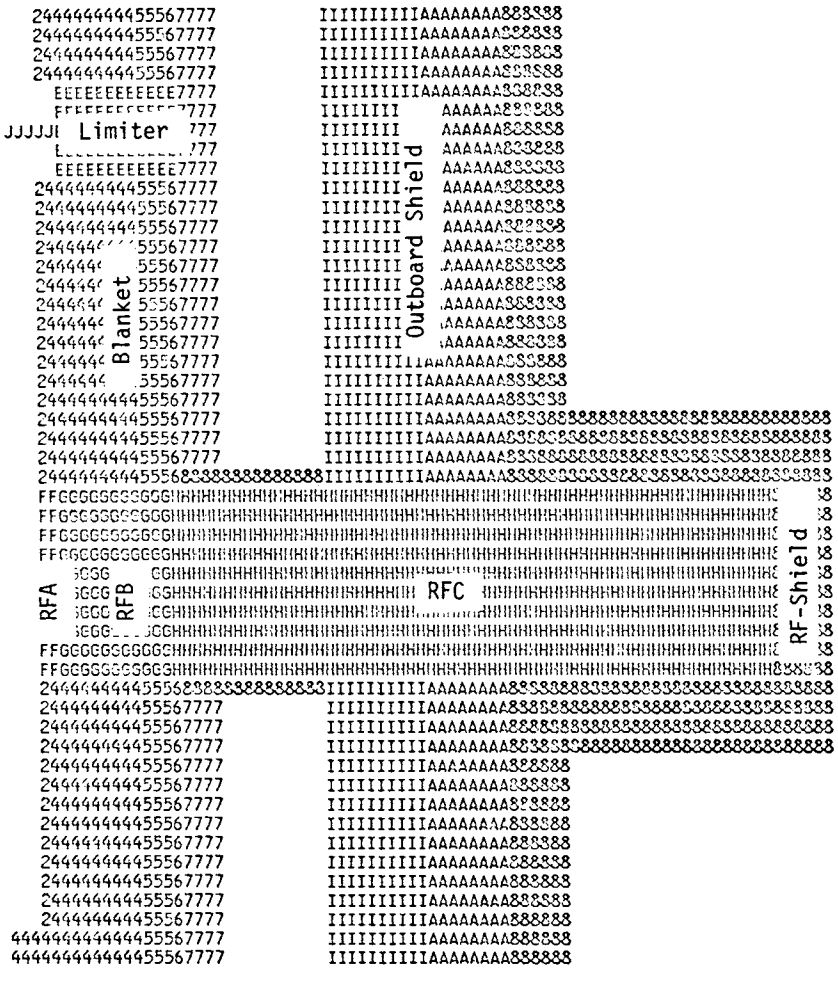

Figure 11-21. The rf system model used in the analysis.

RFC: 0.82 m × 0.33 m: (15% PCA + 11% H_2O + 74% void).

The duct lengths are 0.1 m, 0.56 m, and 2.93 m for RFA, RFB, and RFC, respectively. In order to minimize radiation streaming into the plenum region the duct portion inside the plenum is completely surrounded by a 0.1-m thick Fe-1422 shield. In the initial calculations, the duct portion in the reactor room was fully shielded by 0.3 m of the same material, aiming primarily at reducing the impact of the rf penetration on the potential increase in the post-shutdown biological dose inside the reactor building. As discussed later, the final reference design incorporates only 0.15 m of Fe-1422 shield instead of 0.3 m.

The nuclear analysis in this section is oriented toward identifying (1) the nuclear heat load to the system so as to design an appropriate heat removal system; (2) the degree of radiation-induced property degradation of dielectric

break windows (BeO or Al_2O_3) located ∿12 m from the reactor centerline; and (3) the extent to which the nuclear radiation inside the reactor building is enhanced, and the resultant increase in the dose one day after shutdown. Figure 11-22 describes the total neutron flux attenuation throughout the rf waveguides. Also shown in the figure for purposes of comparison is the neutron flux based on a one-dimensional analysis for the case without any system penetrations, i.e. without the rf ducts or the limiter slot opening. It is importtant to observe that the neutron flux in the waveguides is lower than that for the case without penetrations. There seem to be several reasons leading to this situation. First, the RFB region possesses a higher material density factor and also higher neutron reaction cross sections than the adjacent blanket region. For example, the effective material density in the outboard breeding blanket is only ∿62% due to the breeder porosity required for the tritium extraction, compared to a 66% material density factor in RFB in which 58% of the volume is occupied by a very effective neutron attenuator, PCA stainless steel.

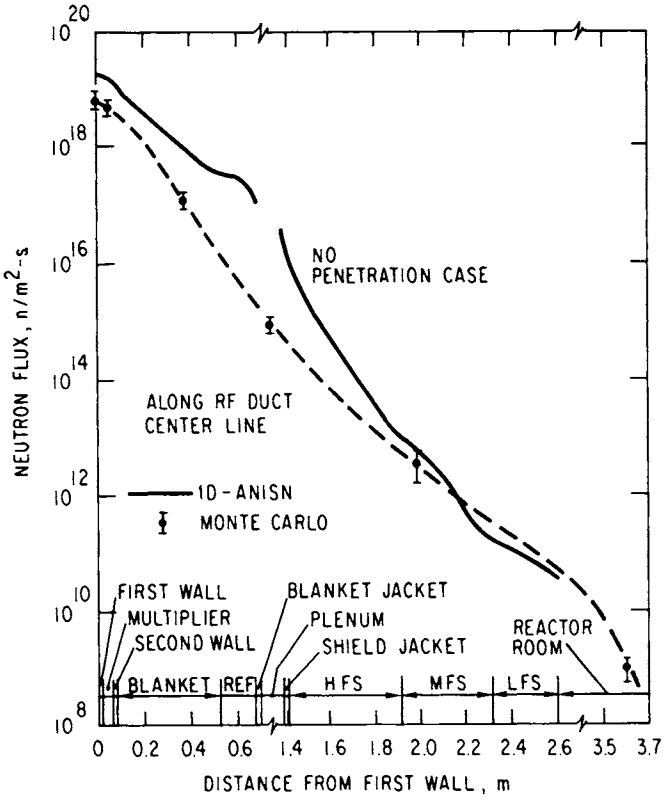

Figure 11-22. Neutron flux variation with distance from first wall along rf duct centerline.

In fact, the mfp's in RFB are ∿75 mm, ∿61 mm, and ∿1 mm at three representative energies of 14 MeV, 10 MeV, and thermal energy, respectively, while the correspondong mpf's in the blanket composition are ∿82 mm, ∿86 mm, and 1 mm. Secondly, the reflector region behind the blanket and also the subsequent vacuum plenum region assist the trend toward the slower neutron attenuation for the case without penetrations. This already reveals that the impact of the rf-waveguide penetration upon the radiation enhancement in the plenum region is insignificant. On the other hand, with regard to the neutron fluxes in the outboard shield region, the difference tends to be smeared out with depth in the shield, reflecting the fact that the outboard bulk shielding material is much more efficient in attenuating the neutron flux than the RFC material composition. Near the first dielectric window location, the total neutron flux is expected to be on the order of 10^7 m^{-2}-s^{-1} or less, resulting in a total fluence of only $\sim 2 \times 10^{14}$ m^{-2} per year, at most, for a plant availability factor of 75%. Under such a low neutron field, neither the ceramic window material of Al_2O_3 nor beryllium oxide will pose radiation-induced swelling problems, but will properly function without any appreciable material deterioration even over the entire plant lifetime of 40 yr. This observation is based on the experimental results obtained by Clinard, et al.[20] and Reed, et al.[21] Based on the observation that beryllium oxide has better thermal conductance properties than Al_2O_3, the reference rf duct design employs beryllium oxide as the dielectric window material.

Tables 11-14 and 11-15 summarize the nuclear heat load to the rf system. The total heat deposition is estimated to be ∿26 MW, almost three-quarters being contributed by the gamma interactions with the PCA grill structure. The maximum nuclear heating rates of ∿20 MW/m^3 in the grill structure and ∿26 MW/m^3 in the water coolant, both of which occur in the RFB region, are within the mechanical and thermal hydraulic design capability. The rf grill structure system is designed to be cooled by 40°C feedwater and the anticipated maximum temperature in the structure is ∿310°C.

As already shown, the neutron flux in the Fe-1422 shield around the projected portion of the rf ducts is quite low and is not likely to influence the overall outboard bulk shield design in terms of biological dose shortly after shutdown. In order to more precisely define the shield thickness around the rf waveguides which protrude through the bulk shield into the reactor room the

Table 11-14. Nuclear Heat Deposition in the rf System

	Nuclear Heating (MW)	
	per Duct	System Total
Section RFA		
Total	0.66	7.86 (±35%)
Neutron	0.25	3.00 (±13%)
Gamma	0.41	4.86 (±55%)
Section RFB		
Total	1.52	18.16 (±26%)
Neutron	0.36	4.26 (±18%)
Gamma	1.16	13.9 (±30%)
Section RFC		
Total	4.08×10^{-4}	4.90×10^{-3} (±18%)
Neutron	1.98×10^{-4}	2.38×10^{-3} (±57%)
Gamma	2.10×10^{-4}	2.52×10^{-3} (±64%)
System Total		
Total	2.18	26.02
Neutron	0.61	7.26
Gamma	1.57	18.76

MORSE Monte Csrlo run with 20,000 neutron histories.
Neutron wall load: 3.6 MW/m^2.

Table 11-15. Nuclear Heating Rate in the rf System

	Heating Rate (MW/m^3)		
	Point A	Point B	Point C
PCA structure			
Total	15.6 (±16%)	20.4 (±32%)	0.45 (±32%)
Neutron	10.7 (±5%)	12.4 (±41%)	0.25 (±34%)
Gamma	4.94 (±51%)	8.05 (±52%)	0.20 (±50%)
H_2O coolant			
Total	25.9 (±13%)	26.2 (±35%)	0.60 (±27%)
Neutron	25.3 (±13%)	25.2 (±36%)	0.57 (±27%)
Gamma	0.63 (±53%)	1.04 (±54%)	0.03 (±52%)

MORSE Monte Carlo run with 20,000 neutron histories.
Neutron wall load: 3.6 MW/m^2.

dose variation at the end of the bulk shield (i.e., at the entrance point into the reactor room) was examined as a function of the penetration shield thickness. At 24 h after reactor shutdown, the dose rates are ∿24 mrem/h, ∿3 mrem/h, ∿0.2 mrem/h, and 1.3×10^{-2} mrem/h at shield depths of 0, 0.1 m, 0.2 m, and 0.3 m, respectively.

Based on this investigation, the final shield thickness for the rf ducts external to the bulk shield is no more than 0.15 m. The corresponding maximum biological doses are estimated to be 2.5 mrem/h and 0.7 mrem/h at reactor shutdown, respectively.

11.4 SHIELD MECHANICAL DESIGN

The shield design has been developed as an integral part of the STARFIRE reactor. The primary function of the shields is radiation protection. Design goals are to minimize activation products and to reduce the radiation levels such that personnel access to the shield exterior is possible within 24 h after shutdown. The shield design also provides the vacuum boundary for the plasma. This vacuum boundary location has several important advantages: (1) to permit direct access to the vacuum boundary seals; (2) to locate the seals in a low neutron fluence region; and (3) to permit incorporation of the vacuum pumping system for the toroidal limiter impurity control system, without the inherent complications of providing a toroidal duct behind the limiter.

A key feature of the shield design is the offset between the limiter slot and the vacuum ducts to eliminate any direct neutron streaming paths from the plasma to the vacuum pumps. This significantly reduces the neutron heating of the cryosorption surfaces as shown in Sec. 11.3.1. Choice of the major subsystems, such as rf heating over neutral beams, and the impurity control limiter over bundle or poloidal divertors has also contributed to overall shield simplicity.

The shield consists of 24 sectors, 12 small sectors (included angle $\sim$12.5 deg), and 12 large sectors (included angle $\sim$17.5 deg) as shown in Fig. 11-23. The 12 small sectors are located symmetrically inside the TF coils and are supported by the room temperature (RT) case. Six of these sectors incorporate poloidal dielectric vacuum seal joints to minimize the induced current flow, which enhances plasma control and permits ohmic heating. Two concentric joints are used at each location for redundancy.

The dielectric break is designed to last for the plant design life. The dielectric joint is installed in the small sector at the factory and then shipped to the reactor site as a unit. This permits use of more sophisticated fabrication processes if required. The reference dielectric seal design utilizes a polymide gasket that is bonded to the adjacent halves of the small sector. The structural load path is provided through a polymide-insulated bolt joint. This technique has been utilized on a smaller scale in vacuum systems in the past.[22] Because the seal is located at the exterior of the shield, the total neutron dose is only 9.25×10^7 Gy at the inner leg of the TF coil over the 40-yr design life at a 75% availability. Recent experimental results[2]

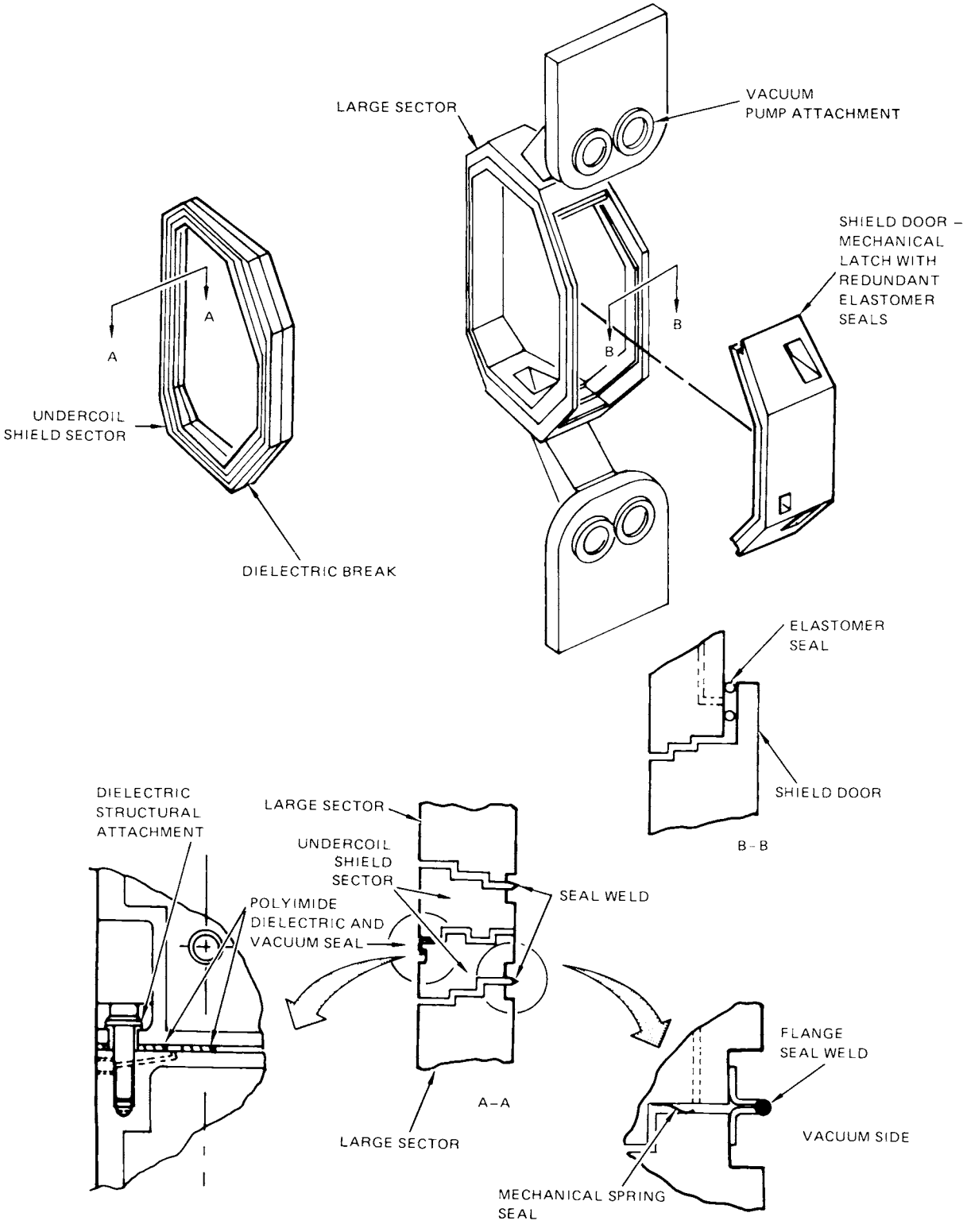

Figure 11-23. Configuration of the STARFIRE shield.

show that (kapton) can sustain 10^8 Gy without serious degradation.

The larger sector fits between the TF coils, but is supported by its room temperature case. This sector is comprised of the basic shield sector, upper and lower vacuum ducts, and an access door. The vacuum ducts are welded to the sector, with all alignments, machining, and testing achieved at the off-site construction location. The door provides for blanket removal, and is checked for fit and function before delivery to the construction site. Without the access door the large sector can be handled by the 600-metric ton overhead crane.

Component weights are as follows:

Large sector (without door and vacuum ducts):	179 tonnes
Shield door:	156 tonnes
Vacuum ducts (each):	116 tonnes
Vacuum pump pod:	160 tonnes
Small sector:	226 tonnes
Total reactor shielding weight:	13,365 tonnes

Because the shield is operated at low temperature ($\sim$50°C) its thermal expansion can be accommodated by the small stepped gap between shield sectors ($\sim$3 mm). Structural attachments to the room temperature TF coil vacuum tanks fix the shield position and react the magnetically induced overturning moments from the blanket and shield. The inner surface of the shield provides a direct support point for the top and bottom of the blanket sectors and constrains any radial and tangential loads.

The shield sectors are designed as life-of-plant components and therefore are not replaced on a regular basis. This permits the flange seal (view AA of Fig. 11-23) between adjacent large and small shield sectors to be welded in place. The inner surface of the shield incorporates inserts that permit installation of a track for a remote seal cutter and welder. These types of devices are currently being planned for TFTR and have been proposed for other conceptual designs.[23,24] Several cutting and welding operations can be accommodated before the weld flange must be replaced. A concentric mechanical seal is provided behind the welded seal to enable detection of leaks through the welded seal by injection of tracer gas.

The basic shield composition is given in Tables 11-1 and 11-7 for the inboard and outboard shields, respectively. The inboard and outboard shield regions are designated in Fig. 11-24. The inboard shield composition changes from tungsten to steel in the areas away from the reactor midplane to minimize shield costs. This change is possible in the neutron fluence with distance from the reactor midplane. Rationale for selection of these materials is given in the previous sections. The vacuum boundary of the inner and outer shield is made of steel (NON-MAG 30).[10]

The mechanical design and construction technique for the shield are shown in Figs. 11-23 and 11-24. A layered series of tubes and shielding material is planned for each of the eight submodules which comprise a toroidal sector. Submodules A through H of Fig. 11-24 have common manifolds at each end to distribute coolant to the layered tubes, which are welded to tube sheets at each manifold. A C-shaped box is first fabricated to form the sides of the shield sector and the wall nearest the blanket. The sides of the box are 40-mm plates to permit machining of the outer surfaces after assembly. Tube sheets are added to each end at the appropriate angle and bulkheads are provided at $\sim$0.7-m spacing between the tube sheets to provide structural support to the module walls. The tubes in the layer against the wall nearest the blanket are welded in first and then sequential layers of shielding material and tubes are built up in the box. An outer sheet is finally added to make structural submodules. The interior of each submodule is vented to the reactor building to prevent pressure buildup if warranted by the vacuum boundary reliability. This vent could be connected to a vacuum pumping system so that cracks through the structural wall would not permit an in-leakage to the plasma. After all submodules are complete they are welded together to form a poloidal sector. The side walls are then faced off by machining to provide proper sector width control and to assure fit.

The vacuum ducts, pump pod, and valve stem covers are constructed of the materials listed in Fig. 11-25. Because of the complex shpae a water tank design approach is used whereby the cladded shielding materials are set into a water bath.

The vacuum ducts are welded to the shield sector to complete the vacuum boundary. Cooling for the 90-MW nuclear heating is provided by 1300 kg/s flow of water coolant at 43°C which enters the lower vacuum duct shields and flows

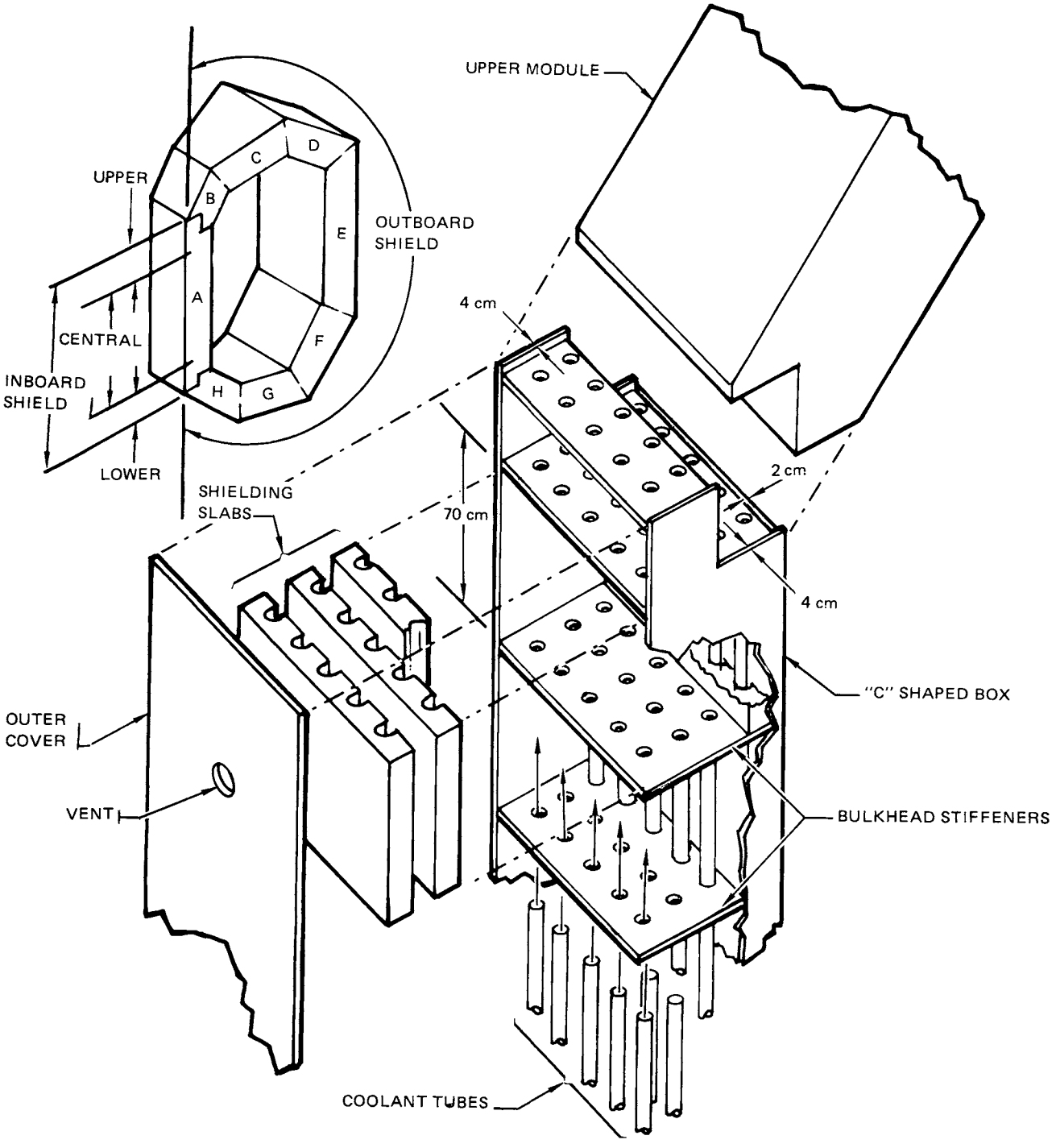

Figure 11-24. Shield — module construction approach.

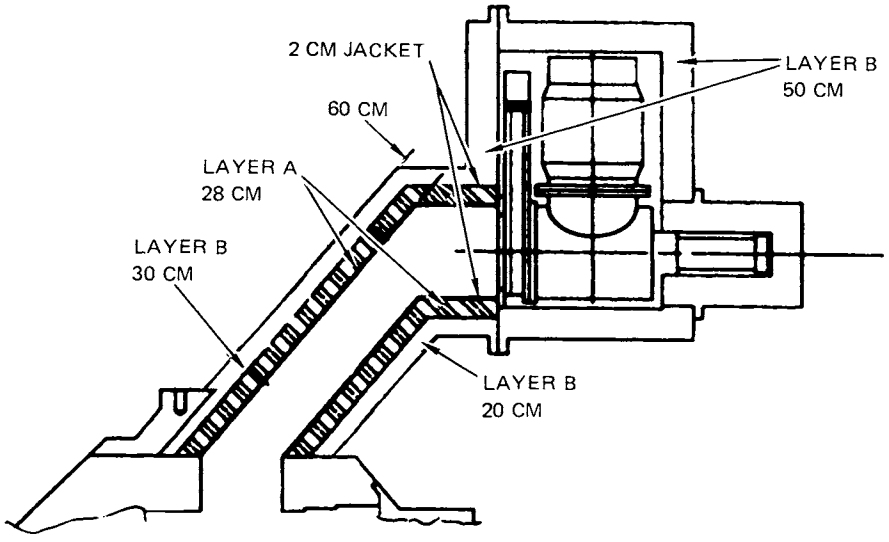

LAYER	THICKNESS
JACKET	
NONMAGNE 30 STEEL	2 CM
LAYER A	30 CM
5% Ti 6AL 4V	
65% Ti H2	
15% B4C	
15% WATER	
LAYER B	18 TO 48 CM
70% NONMAGNE 30 STEEL	PER FIGURE
15% B4C	
15% WATER	

13–3991

Figure 11-25. Vacuum duct composition

upward through the shield sectors where it is piped into a manifold area between submodules. The coolant then flows through the shield sectors and exits from the upper vacuum pump duct at 60°C. The large sectors require a flow rate of 60 kg/s each, and the small sectors require 45 kg/s each. Flow velocity through the shield volume is ∿1 m/s. Inlet pipe diameters are 0.16 m and 0.14 m for the large and small sectors, respectively. The maximum structural temperature of 300°C occurs at the shield midplane directly outboard of the limiter slot. This temperature is based on a 1-m/s flow and a 50% decrease in nuclear heating (relative to the first wall) through the limiter slot. Shield door cooling is provided through an inlet and outlet line routed with the rf duct bundle.

The shield access door is removed to permit blanket sector replacement. Each door is removed one time every six years for scheduled maintenance and approximately one other time every six years for unscheduled blanket replacement (see Chap. 19). Elastomer seals have been chosen over welded seals to provide

the seal replacement and permit use of a simple, reliable latching technique. Metal seals were not chosen because of the large sealing forces required and the lower probability of sealing. The seals are located at the outer shield surface where the radiation dose is 10^6 Gy over six years at a neutron wall load of 3.6 MW/m^2 and 75% availability. Current experience with elastomer seals[12] has shown these fluences are tolerable without loss of sealing capability; however, some hardening is expected. Each time the door is removed the seals will be replaced. The seal material chosen is ethylene propylene diene. It has been evaluated neutronically to determine compound formation (see Sec. 11.2) and judged to be acceptable for the 10^6 Gy dose. Approximately 100 lb/in. of sealing surface is required to effect the seal. This is provided by the atmospheric pressure pushing on the outer door surface. Mechanical latches are provided in the door to minimize the complexity of door removal by remote maintenance. The latches are driven by a standardized drive (Sec. 19.3.2) that is used in other reactor components.

The blanket cooling lines and rf duct protrude through the shield door. This eliminates the need for leak-tight disconnects in the high-pressure coolant lines. A sealed shield plug is provided around each group of coolant lines (see Sec. 19.3.2) to provide the vacuum barrier. This concept is shown in Fig. 11-26. A remotely operated latch is provided on the coolant line plug and a bellows with sealing surface is provided on the shield door The bellows permit deflections without overloading the seal surface. The seal plate is retained by stops to prevent overtravel.

A possible accident condition was identified in which a leak of the 2200-psi blanket coolant into the vacuum cavity could possibly pressurize the vacuum cavity to 300 to 500 psi. To avoid the consequences of this overpressure, a shield vent plug is incorporated into the shield door. The vent plug is shown in Fig. 11-27. The plug fits loosely into a tapered hole, a seal weld between the outer surface and the shield door completes the vacuum boundary. Under normal conditions the atmospheric pressure holds the plug in place and does not load the thin seal. In an overpressure condition, however, the plug is pushed outward and ruptures the seal. The taper provides clearance for venting and a mechanical stop prevents the plug from becoming a projectile. The plug design will operate when the overpressure reaches $\sim$10 psi.

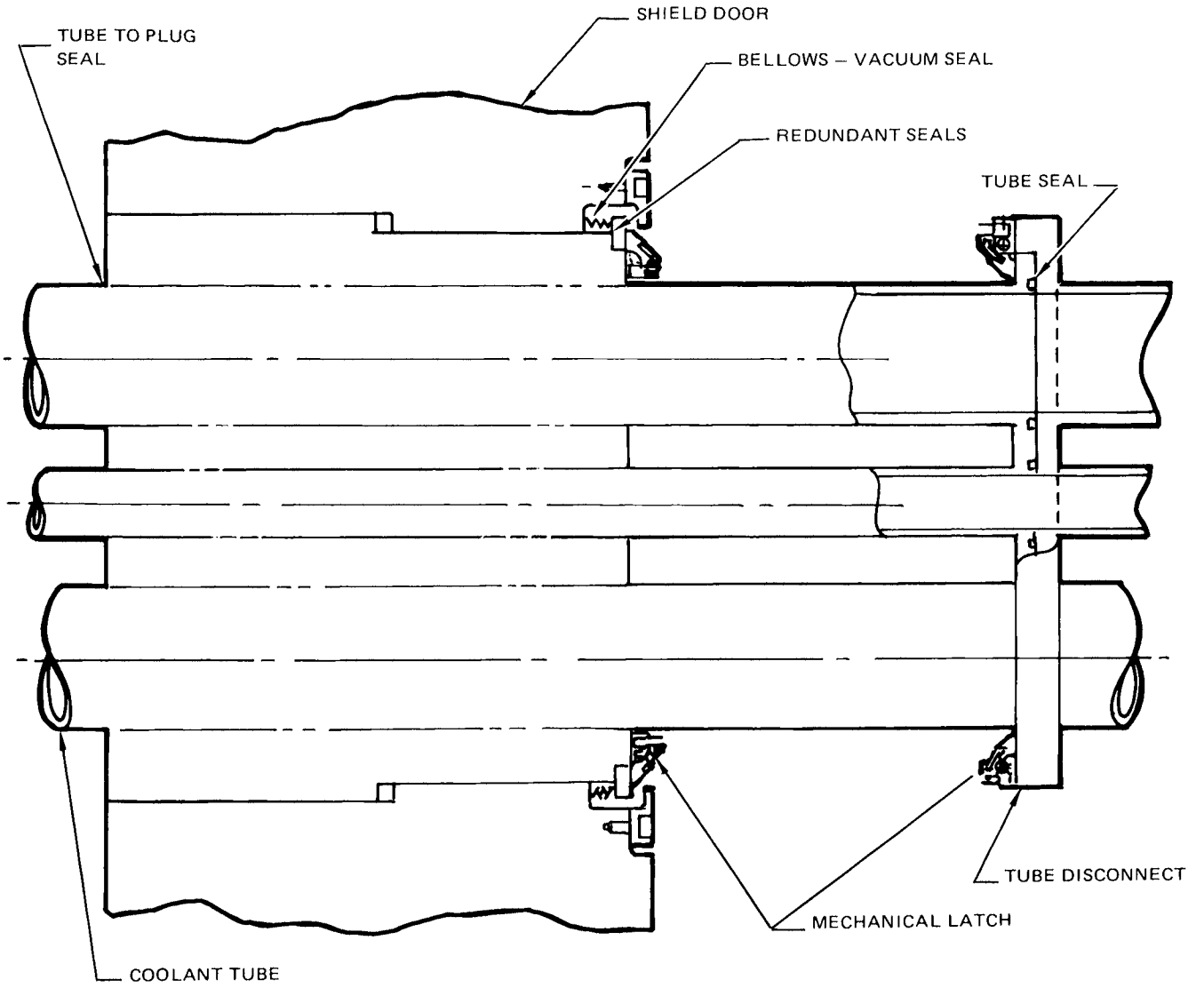

Figure 11-26. Shield door to coolant tube sealing.

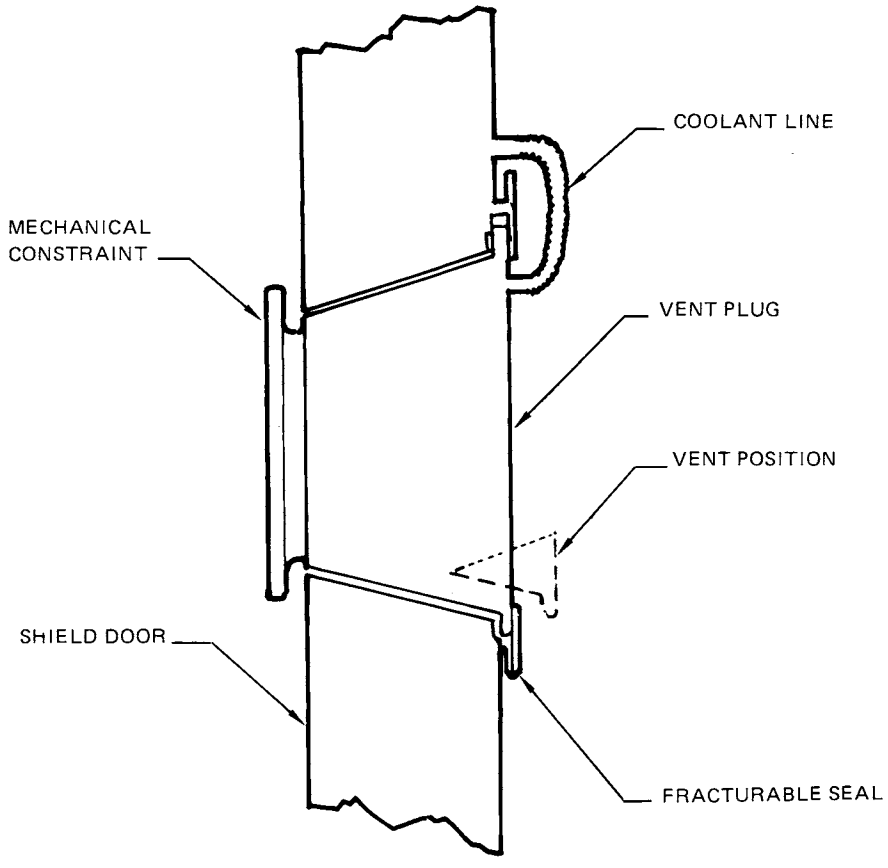

Figure 11-27. Shield door relief valve.

References

1. M. A. Abdou, J. Nucl. Mater. 72, 147 (1978).

2. R. R. Coltman, et al., "Effect of Radiation at 5°K on Organic Insulators for Superconducting Magnets," Proc. 8th Symp. on Engineering Problems of Fusion Research, Vol. III (1979), p. 1694.

3. B. S. Brown, "A Review of Radiation Effects in Superconducting Fusion Magnet Materials," J. Nucl. Mater. (to be published).

4. "ANISN-ORNL: Multigroup One-Dimensional Discrete Ordinates Transport Code with Anisotropic Scattering," Oak Ridge National Laboratory, RSIC/CCC-254 (1973).

5. R. W. Roussin, et al., "VITAMIN-C: The CTR Processed Multigroup Cross Section Library for Neutronics Studies," ORNL/RSIC-37 (ENDF-296), Oak Ridge National Laboratory (1980).

6. Y. Gohar and M. A. Abdou, "MACKLIB-IV: A Library of Nuclear Response Functions Generated with the MACK-IV Computer Program from ENDF/B-IV," Argonne National Laboratory, ANL/FPP/TM-106 (1978).

7. D. Garken (Compiler), "ENDF/B Summary Documentation," Brookhaven Tational Laboratory, BNL-17541 (1975).

8. J. Jung, "Theory and Use of the Radioactivity Code RACC," Argonne National Laboratory, ANL/FPP/TM-122 (1979).

9. J. Jung, "Multigroup Neutron Activation Cross Section Library RACCXLIB and Decay Chain Data Library RACCDLIB for the Radioactivity Calculation Code RACC," Argonne National Laboratory, ANL/FPP Report (to be published).

10. Kobe Steel's Non-magnetic Steel Plate Nonmagne 30, No. A-78B20 (Kobe Steel, Ltd., Kakogawa Work, 1979).

11. C. M. Lederer and V. S. Shirley, eds., Table of Isotopes, 7th ed. (John Wiley and Sons, Inc., New York, 1978).

12. Seal Compound Manual, Catalog C5702 (Park Seal Co., 1968).

13. D. M. Parkin and A. R. Sweeder, "Neutron Irradiation of Nb_3Sn and NbTi Multifilamentary Composites," IEEE Transactions on Magnets, Vol. MAG-11, No. 2, 166 (1975).

14. U. S. National Regulartory Commission, "Standards for Protection Against Radiation," USNRC Rules and Regulations, Title 10, Chap. I, Part 20 (1975).

15. J. W. Davis, McDonnell Douglas Astronautics Company-St. Louis, Personal Communication (1980).

16. A. E. Profio, Radiation Shielding and Dosimetry, A. Wiley, Interscience Publication (John Wiley & Sons, New York, 1979), pp. 414-418.

17. M. B. Emmett, "The MORSE Monte Carlo Radiation Transport Code System," Oak Ridge National Laboratory, ORNL-4872 (1975).

18. W. A. Rhoades and F. R. Mynatt, "The DOT-III, Two-Dimensional Discrete Ordinates Transport Code," Oak Ridge National Laboratory, ORNL/TM-1880 (1973).

19. J. Jung and M. A. Abdou, "Radiation Shielding of Major Penetrations in Tokamak Reactors," Nucl. Technol. 41, 71 (1978).

20. F. W. Clinard, Jr., et al., "Neutron Irradiation Damage in Al_2O_3 and Y_2O_3," in Proc. of Intern. Conf. on Radiation Effects and Tritium Technology for Fusion Reactors, Vol. II (1976), p. II-498.

21. B. W. Reed, et al., "Preliminary Report on the Development of RF Auxiliary Heating Systems for TEPR-1," Princeton Plasma Physics Laboratory, PPPL-1410 (1977).

22. J. C. Jones, "Novel Electrical INSULATOR FOR AN Ultrahigh Vacuum Line," Rev. Sci. Instrum. 46, 4 (1975).

23. "Tokamak Fusion Test Reactor, Final Design Report," Princeton Plasma Physics Laboratory, PPPL-1475 (1978), p. 5-2.

24. A. M. Frank, "Remotely Operable Vacuum Seals," Proc. 7th Symp. on Engineering Problems of Fusion Research, 77CH1267-4NPS (IEEE, 1977).

Distribution for ANL/FPP-80-1

Internal:

M. Abdou	D. Ehst	R. Kustom	D. L. Smith
R. Arons	K. Evans	V. Maroni	R. Smith
C. Baker	P. Finn	R. Martin	H. Stevens
E. Beckjord	R. Fuja	R. Mattas	L. Turner
C. Boley	Y. Gohar	B. Misra	S-T. Wang
J. Brooks	V. Jankus	J. Norem	FP Program (81)
R. Clemmer	J. Jung	J. Rest	ANL Contract File
C. Dennis	M. Kaminsky	J. Roberts	ANL Libraries (2)
J. de Paz	S. H. Kim	H. Schreyer	TIS Files (6)

External:

DOE-TIC, for distribution per UC-20 (117)
Manager, Chicago Operations and Regional Office, DOE
Chief, Office of Patent Counsel, DOE-CORO
President, Argonne Universities Association
Applied Physics Division Review Committee:
- P. W. Dickson, Jr., Clinch River Breeder Reactor Project, Oak Ridge
- R. A. Greenkorn, Purdue U.
- R. L. Hellens, Combustion Engineering, Inc.
- K. D. Lathrop, Los Alamos Scientific Laboratory
- W. B. Loewenstein, Electric Power Research Inst.
- R. Sher, Stanford U.
- D. B. Wehmeyer, Detroit Edison Co.

Accelerator Research Facilities Review Committee:
- H. A. Neal, Indiana U.
- S. D. Putnam, Physics International Co.
- P. H. Rose, Nova Associates, Inc., Beverly, Mass.
- E. M. Rowe, U. Wisconsin, Stoughton
- L. C. Teng, Fermi National Accelerator Lab.

Chemical Engineering Division Review Committee:
- C. B. Alcock, U. Toronto
- R. C. Axtmann, Princeton U.
- P. W. Gilles, U. Kansas

Materials Science Division Review Committee:
- E. A. Aitken, General Electric Co., Sunnyvale
- G. S. Ansell, Rensselaer Polytechnic Inst.
- A. Arrott, Simon Fraser U.
- R. W. Balluffi, Massachusetts Inst. Technology
- S. L. Cooper, U. Wisconsin
- C. Laird, U. Pennsylvania
- M. E. Shank, Pratt & Whitney, East Hartford
- C. T. Tomizuka, U. Arizona
- A. R. C. Westwood, Martin Marietta Labs.

Physics Division Review Committee:
- E. G. Adelberger, U. Washington
- B. Bederson, New York U.
- H. G. Blosser, Michigan State U.
- J. A. Davies, Chalk River Nuclear Labs.
- W. Haeberli, U. Wisconsin
- J. W. Negele, Massachusetts Inst. Technology
- R. O. Simmons, U. Illinois, Urbana

Battelle - Pacific Northwest Laboratory
D. Dingee
Bechtel National, Inc., San Francisco
R. Aronstein
Bell Telephone Laboratories, Inc., Holmdel, New Jersey
S. J. Buchsbaum
Bettis Atomic Power Laboratory, West Mifflin, Pennsylvania
S. D. Harkness
Brookhaven National Laboratory
J. Powell
Burns & Roe, Inc., Oradell, New Jersey
S. Baron
Columbia University
R. A. Gross
Combustion Engineering, Windsor, Connecticut
J. Dietrich
Cornell University
C. Y. Li
Department of Energy
J. Baublitz
D. S. Beard
R. Blanken
J. F. Clarke
M. Cohen
E. Dalder
N. Anne Davies
J. Decker
W. Dove
R. Dowling
W. Ellis
C. Finfgeld
G. Haas
C. Head
R. Impara
M. Murphy
G. Nardella
R. Ng
D. Nelson
E. Oktay
T. Reuther
M. Roberts
S. Staten
P. Stone
K. Zwilsky
EG&G Idaho, Inc., Idaho Falls
J. Crocker
Energy Resource Group, Inc., Arlington, Virginia
R. Bussard
Electric Power Research Institute, Palo Alto
N. Amherd
D. J. Paul
R. Scott
Exxon Nuclear Company, Inc., Bellevue, Washington
H. K. Forsen
D. G. McAlees

Fusion Power Associates, Gaithersburg, Maryland
S. Dean
General Atomic Company
S. Burnett
J. Gilleland
D. Graumann (10)
T. Ohkawa
J. Purcell
P. Sager
General Dynamics, San Diego
R. A. Johnson
General Electric Company, Schenectady
D. J. Anthony
Georgia Institute of Technology, Atlanta
W. Stacey, Jr.
Grumman Aerospace Corporation, Bethpage, New York
R. Botwin
I. G. Hedrick
Hanford Engineering Development Laboratory, Richland
J. Holmes
L. Muhlestein
Iowa State University
A. Husseiny
Lawrence Berkeley Laboratory
R. V. Pyle
Lawrence Livermore Laboratory
G. Carlson
T. K. Fowler
J. D. Lee
R. W. Moir
R. Post
C. E. Taylor
K. I. Thomassen
R. Werner
Los Alamos Scientific Laboratory
J. L. Anderson
H. Cullingsford
H. Dreicer
R. A. Krakowski
J. Rogers
Mathematical Sciences North West, Inc., Bellevue, Washington
P. Rose
H. Willenberg
Maxwell Laboratories, San Diego
A. Kolb
McDonnell Douglas Astronautics Company, St. Louis
D. DeFreece (15)
Massachusetts Institute of Technology
D. Cohn
R. Davidson
M. Kazimi
M. Lidsky
D. Bruce Montgomery
R. Parker
S. Piet
D. J. Rose

Mound Laboratory, Miamisburg, Ohio
W. R. Wilkes
Naval Research Laboratory, Washington, D.C.
A. Robson
Northeast Utility Service Co., Hartford, Connecticut
S. Hale Lull
Nuclear Services Corporation, Campbell, California
S. Naymark
Oak Ridge National Laboratory
L. A. Berry
J. D. Callen
J. Cannon
P. N. Haubenreich
T. Jernigan
R. Langley
M. S. Lubell
O. B. Morgan
M. Rosenthal
J. L. Scott
T. Shannon
D. Steiner
N. A. Uckan
W. Wiffen
Princeton Plasma Physics Laboratory
J. Cecchi
S. Cohen
H. Furth
M. Gottlieb
H. Howe, Jr.
R. G. Mills
P. J. Reardon
P. H. Rutherford
Public Service Electric and Gas Co., Newark, New Jersey
B. Jensen
Purdue University
P. S. Lykoudis
F. J. Loeffler
Science Applications, Inc., McLean, Virginia
S. Locke Bogart
Science Applications, Inc., La Jolla
A. Trivelpiece
Sandia Laboratories, Albuquerque
M. Davis
D. Mattox
The Ralph M. Parsons Company, Pasadena, California
K. Barry (6)
TRW, Redondo Beach, California
K. Moses
J. S. Foster, Jr.
United Technologies Research Center, East Hartford, Connecticut
A. F. Haught
T. Latham
University of California, Los Angeles
F. F. Chen
R. Conn

University of Illinois
J. Gilligan
G. Miley
M. Ragheb
University of Michigan
T. Kammash
University of Missouri - Rolla
A. Bolon
University of Rochester
M. J. Lubin
University of Texas at Austin
K. Gentle
M. Rosenbluth
H. Woodson
University of Washington, Seattle
F. Ribe
G. L. Woodruff
University of Wisconsin
S. Abdel-Khalik
R. Boom
B. Bruggink
J. Feinstein
G. Kulcinski
C. Maynard
R. Rose
K. Symon
D. K. Sze
Westinghouse Electric Corporation, Pittsburgh
C. Flanagan
D. Klein
Z. Shapiro
Bibliotheque, Seine, FRANCE
Bibliothek, Garching, WEST GERMANY
C.E.A. Fusion, Cedex, FRANCE
G. Casini, C.E.A. Ispra(VA), ITALY
C.-H. Chen, Chinese Academy of Sciences, Peking, CHINA
R. Hancox, Culham Laboratory, ENGLAND
Dr. Ing. Albert Knobloch, Max-Planck Institute for Plasmaphysik, WEST GERMANY
Librarian, Culham Laboratory, ENGLAND
Library, Center de Recherches en Physique des Plasma, Lausanne, SWITZERLAND
Library, FOM-Institute voor Plasma-Fysika, THE NETHERLANDS
Thermonuclear Library, Japan Atomic Energy Research Institute, JAPAN
Library Laboratorio Gas Ionizati, Frascatti, ITALY
C.-S. Li, Chinese Academy of Sciences, Peking, CHINA
K. H. Schmitter, Max-Planck Institute fur Plasmaphysik, WEST GERMANY

☆ U.S. GOVERNMENT PRINTING OFFICE: 1981 750-659